제 1 장

2014-15년 한-뉴질랜드-미국 국제공동 연구 (로스해 탐사)

유규철, 이재일, 이민경, 문홍수, 이인애, 윤호일

한국해양과학기술원 부설 극지연구소

요약: 극지연구소 빙붕 K-Polar 사업의 일환으로 2014-15년 한국 쇄빙연구선 아라온호에 한국 연구원 8명, 뉴질랜드 연구원 (퇴적학, 규조 분석 분야) 4명, 미국 연구원 2명 (산호 연구, 퇴적물 연대측정 분야) 이 승선하여 남극 로스해 대륙붕 및 남극해 지역 국제공동 연구를 수행하였다. Sub-bottom Profiler (SBP)와 Multibeam 장비를 통한 지구물리 탐사를 통해 해저 지형 및 퇴적물 분포를 파악하였고, 중력 코어러, 박스 코어러, 롱코어러를 사용하여 총 37 지점에서 총 44점, 총길이 약 161 m의 해양 퇴적물 주상 시료를 획득하였다. 이번 탐사에서는 아라온에 장착된 중력 타입의 jumbo long corer로 극지 현장에서 최초로 길이 15m에 달하는 퇴적물 주상 시료시료를 획득하였다. 또한 2기의 sediment trap을 계류하여 연간 퇴적 및 해양 특성을 조사하였다.

1. 2015년 아라온호 기반 탐사 일정 및 참여 연구원 (그림 1, 2 참조)

2015년 아라온 2항차 탐사 (ANA05B)는 서남극 빙붕변화 관측시스템 구축 및 제4기 해빙사 복원기술 개발 (연구책임자: 윤호일), 서남극 열개구조 진화 연구 (연구책임자: 홍종국), 양극해 환경변화 이해 및 활용연구 (연구책임자: 강성호), 양극해 미래자원 탐사 및 활용기술 개발 (연구책임자: 임정한) 의 4개 과제의 합동 탐사였다. 본 과제는 주로 로스해와 로스해 주변 남극해에서 퇴적물 분포 조사, 퇴적물 코어 채취, 드렛지를 이용한 산호 채취, 그리고 sediment trap의 계류와 회수 작업을 하였다. 본 보고서에는 본 과제의 일환으로 수행된 작업과 그 작업의 수행을 위해 참여한 연구원만을 기술하였다.

극지연구소 고기후팀 참여연구원 : 유규철, 이재일, 이민경, 문홍수, 이태관, 이인애
한국 참여연구원: 정재우 (연세대학교), 이현희 (고려대학교)
뉴질랜드 참여연구원: Gavin Dunbar, Olya Albot (이상 Victoria University of Wellington), Christina Riesselman, Rebecca Parker (이상 University of Otago)
미국 측 참여연구원: Cristina Subt (University of South Florida), Amy Wagner (California State University, Sacramento)

1) 2014년 12월 27일-29일: 연구물품 선적
2) 12월 29일: 뉴질랜드 크라이스트처치 리틀턴 항에서 아라온호 승선
3) 12월 30일: 리틀턴 항 출발
4) 2015년 1월 5일: 남위 60도 통과, SBP survey 시작
5) 1월 12일: Sediment Trap 계류 및 회수
6) 1월 13일: Hell's gate에서 박스코어 3점 및 중력코어 2점 획득, Sediment Trap 계류
7) 1월 14일: 테라노바 만에서 박스코어 1점 획득, 장보고 기지 하역 및 승·하선
8) 1월 15일: 박스코어 1점 획득
9) 1월 16일: 중력코어 2점 획득
10) 1월 19일-20일: Cape Hallet 앞바다에서 long corer 조립 및 설치
11) 1월 21일: Iselin Bank에서 박스코어 1점 및 중력코어 3점 획득
12) 1월 22일: Iselin Bank 서편 Central Basin에서 롱코어 1점 획득 (극지역에서 롱코어러로 최초 시료 획득 : 길이 11.9 m)
13) 1월 24일: Iselin Bank에서 Adare trough로 가는 도중 롱코어 1점 획득
14) 1월 25일: 북서쪽으로 이동중 롱코어 1점 획득.
15) 1월 26-27일: Adare Basin에서 중력코어 1점, 산호 채취를 위한 드렛지 작업 3회
16) 1월 28일: 중력코어 3점 획득
17) 1월 29일: Robertson Bay에서 중력코어 1점 획득
18) 1월 30일: 산호 채취를 위한 드렛지 작업 1회, Moubray Bay에서 중력코어 1점 및 롱코어 1점 획득
19) 2월 1일: Coulman Island 앞에서 중력코어 2점 획득
20) 2월 2일: Coulman Island 북동쪽에서 중력코어 1점 획득
21) 2월 3일: 중력코어 3점 획득

22) 2월 4일: Ross Island 북동쪽에서 중력코어 2점 획득
23) 2월 5일: McMurdo Sound 서쪽에서 중력코어 1점 획득, 이후 피항하며 SBP와 멀티빔 조사
24) 2월 8일: Granite Harbor 바깥에서 중력코어 2점 획득, Mawson Glacier 부근에서 중력코어 2점 획득
25) 2월 9일: Granite Harbor 바깥에서 중력코어 2점 획득, Beaufort Island 서쪽에서 중력코어 2점 획득
26) 2월 10일: Mawson Glacier 북동쪽에서 중력코어 2점 획득
27) 2월 11일: 장보고 기지에서 하계연구인력 승선
28) 2월 12일: r 해체
29) 2월 22일: 남위 60도 통과
30) 2월 25일: 리틀턴항 도착
31) 2월 26-27일: 하선 및 하역 작업, 해양장비 점검
32) 2월 28일-3월 1일: 뉴질랜드 크라이스트처치 출발, 오클랜드 경유 인천공항 도착 (항공박)

2. 탐사 내용 및 결과

2015년 아라온호 기반 국제 공동 승선 연구는 극지연구소 빙붕 K-Polar 사업과 미국, 뉴질랜드의 공동 연구의 일환으로 극지연구소 직원 6명을 비롯한 한국인 연구자 6명, 뉴질랜드 연구자 4명, 미국 연구자 2명이 승선하여 수행되었다 (그림 2). 이 탐사를 통해 그동안 획득되지 않았던 서부 로스해의 멀티빔 자료를 상당부분 확보할 수 있었다. 또 해양 코어 퇴적물 44점 (BC16, GC16-A, GC16-B, BC18, BC19, BC25, GC26, GC27, BC40, GC40, BC41, GC41, GC42, LC42, GC44, GC46, LC47, LC48, GC49, GC53, GC54, GC55, GC57, GC62, LC62, GC64, GC65, GC67, GC68, GC69, GC70, GC71, GC72, GC76, GC77, GC78, GC79, GC80, GC81, GC82, GC83, GC84A, GC84B)을 채취하였으며, Adare Basin 근처에서 드렛지를 총 4회 시도하여 다량의 산호 시료를 채취하였다 (그림 3). 이 연구항해 동안 아라온에 장착된 롱코어러를 사용하여 극지역에서 퇴적물을 획득하는 것이 처음 시도되었고 (그림 4), 총 4점, 45.5 m 길이의 코어 퇴적물을 얻었다. 이 중 가장 긴 것은 14.9 m로 장기간의 고해양 기록을 얻을 수 있을 것으로 기대되었다. 획득된 코어 퇴적물들의 위치 정보와 획득된 길이는 표 1과 그림 1 참조. 이 획득된 코어들에 대해 선상에서 독일 알프레드 베게너 연구소로부터 임대한 Multi Sensor Core Loger

(MSCL)를 사용하여 대자율과 밀도 등 퇴적물 코어의 물리적 특성을 분석하였다 (그림 5). 이후 획득된 퇴적물 코어 시료는 이후 2015년 6월과 8월, 극지연구소에서 두 차례에 걸쳐 sampling party를 열어 분배하였고 미국 연구자 1명, 뉴질랜드 연구자 7명이 참여하여 코어의 관찰과 기재, 시료 분배를 하였다 (그림 6).

Korea-New Zealand-USA International Collaboration (2014-15 Ross Sea expedition, ANA05B)

Kyu-Cheul Yoo, Jae Il Lee, Min Kyung Lee, Heung Soo Moon, Inae Lee, Ho Il Yoon

Korea Polar Research Institute

Abstract: As a part of KOPRI K-Polar project (Monitoring of abrupt environmental change in the ice shelf system and reconstruction of Quaternary deglaciation history in West Antarctica), Korean IBRV Araon-based expedition were conducted during the last 2014 and early 2015. In addition to eight Korean researchers including two students, four New Zealand and two reseachers from USA participated in this cruise in order to collaborate on Ross Sea paleoceanographic research work. In this cruise, geophysical survey using Sub-bottom profiler and Multibeam was conducted to figure out sediment distribution and identify sediment body for deciding where to get cores. Fourty-four sediment cores which is totally containing box cores, gravity cores, and long cores were retrieved, and total length of these cores are nearly up to 161 m. At this time, core sediments were firstly obtained by KOPRI jumbo long corer system in the Polar region. For obtained cores, physical properties such as magnetic susceptibility and gamma density were measured by Multi Sensor Core Loger loaned from Alfred Wegener Institute. Afterward sediment cores were opened, observed, described, and distributed after going through two sampling parties which were held in KOPRI on Jun and August in 2015. One USA researcher and seven researchers from New Zealand participated in this parties.

코어명	시간 (UTC)	위도 (S)	경도	수심 (m)	코어길이 (cm)
RS15-BC16	2015-01-12-17:21	75°39.5707'	165°28.9829'E	848	-
RS15-GC16-A	2015-01-12-17:21	75°39.5707'	165°28.9829'E	848	391
RS15-GC16-B	2015-01-12-17:21	75°39.5700'	165°29.4282'E	850	556
RS15-BC18	2015-01-13-06:39	74°54.8303'	164°31.1914'E	543	-
RS15-BC19	2015-01-13-09:00	75°00.0995'	163°43.4996'E	669	-
RS15-BC25	2015-01-15-06:02	75°49.2232'	165°41.1321'E	499	-
RS15-GC26	2015-01-15-11:00	76°09.8815'	164°57.9113'E	885	263
RS15-GC27	2015-01-15-13:07	76°09.9596'	164°46.8547'E	762	41
RS15-BC40	2015-01-20-11:26	71°36.9904'	178°17.4532'W	1083	-
RS15-GC40	2015-01-20-14:01	71°37.0044'	178°17.4630'W	1083	257
RS15-BC41	2015-01-20-20:50	71°21.9945'	179°01.3429'W	1527	-
RS15-GC41	2015-01-20-22:46	71°23.0785'	178°59.2588'W	1557	540
RS15-GC42	2015-01-21-06:28	71°50.9515'	178°29.8079'E	2073	584
RS15-LC42	2015-01-21-12:05	71°49.3969'	178°34.7602'E	2084	1186
RS15-GC44	2015-01-22-21:49	70°49.9511'	174°43.9427'E	2392	596
RS15-GC46	2015-01-23-18:30	70°36.1129'	172°53.5816'E	2434	666
RS15-LC47	2015-01-24-03:26	70°50.7003'	175°04.1603'E	2417	1387
RS15-LC48	2015-01-25-09:03	68°53.9289'	171°09.8914'E	3167	1491
RS15-GC49	2015-01-25-22:18	69°49.3251'	170°20.2177'E	2442	155
RS15-D52	2015-01-25-18:30	71°48.8572'	171°54.1975'E	525	-
RS15-GC53	2015-01-27-13:02	70°11.2542'	168°02.3390'E	1852	27
RS15-GC54	2015-01-27-20:47	70°10.2535'	170°32.4538'E	2442	544
RS15-GC55	2015-01-28-03:10	70°38.3402'	171°19.1041'E	2346	207
RS15-GC57	2015-01-28-23:15	71°32.2677'	170°03.5376'E	344	576
RS15-GC62	2015-01-30-02:25	72°04.5406'	170°27.4138'E	592	272
RS15-LC62	2015-01-30-04:32	72°04.5415'	170°27.3604'E	575	489
RS15-GC64	2015-01-31-19:17	73°19.5112'	169°15.0580'E	1012	240
RS15-GC65	2015-01-31-22:03	73°14.4859'	169°28.3989'E	644	177
RS15-GC67	2015-02-01-15:24	73°05.1869'	170°52.7400'E	567	104
RS15-GC68	2015-02-02-23:49	75°58.1447'	164°59.5363'E	880	204
RS15-GC69	2015-02-03-02:10	76°00.8773'	164°59.4956'E	855	249
RS15-GC70	2015-02-03-03:59	75°57.5844'	164°54.7049'E	877	221
RS15-GC71	2015-02-03-20:49	77°05.1755'	168°26.2231'E	944	450
RS15-GC72	2015-02-04-03:40	77°14.7225'	167°33.7824'E	944	363
RS15-GC76	2015-02-07-13:11	76°54.9315'	163°21.7774'E	808	317
RS15-GC77	2015-02-07-16:52	76°49.2974'	163°42.7306'E	754	263
RS15-GC78	2015-02-08-00:28	76°15.3160'	163°28.5318'E	821	393
RS15-GC79	2015-02-08-08:47	76°00.3801'	163°27.3877'E	799	430
RS15-GC80	2015-02-08-19:30	76°48.2001'	163°55.6482'E	721	444
RS15-GC81	2015-02-08-21:21	76°49.2834'	163°55.6150'E	711	361
RS15-GC82	2015-02-09-02:27	76°56.6123'	166°17.1496'E	860	582
RS15-GC83	2015-02-09-04:47	76°57.7681'	166°22.9994'E	888	395
RS15-GC84A	2015-02-09-18:51	76°00.4115'	163°27.4285'E	816	385
RS15-GC84B	2015-02-09-20:32	76°00.3845'	163°27.4077'E	816	375
					총 161.81 m

표 1. 2014-15년 아라온 2항차 승선 연구 (ANA05B)를 통해 얻어진 코어 퇴적물 (정점은 그림 2 참조)

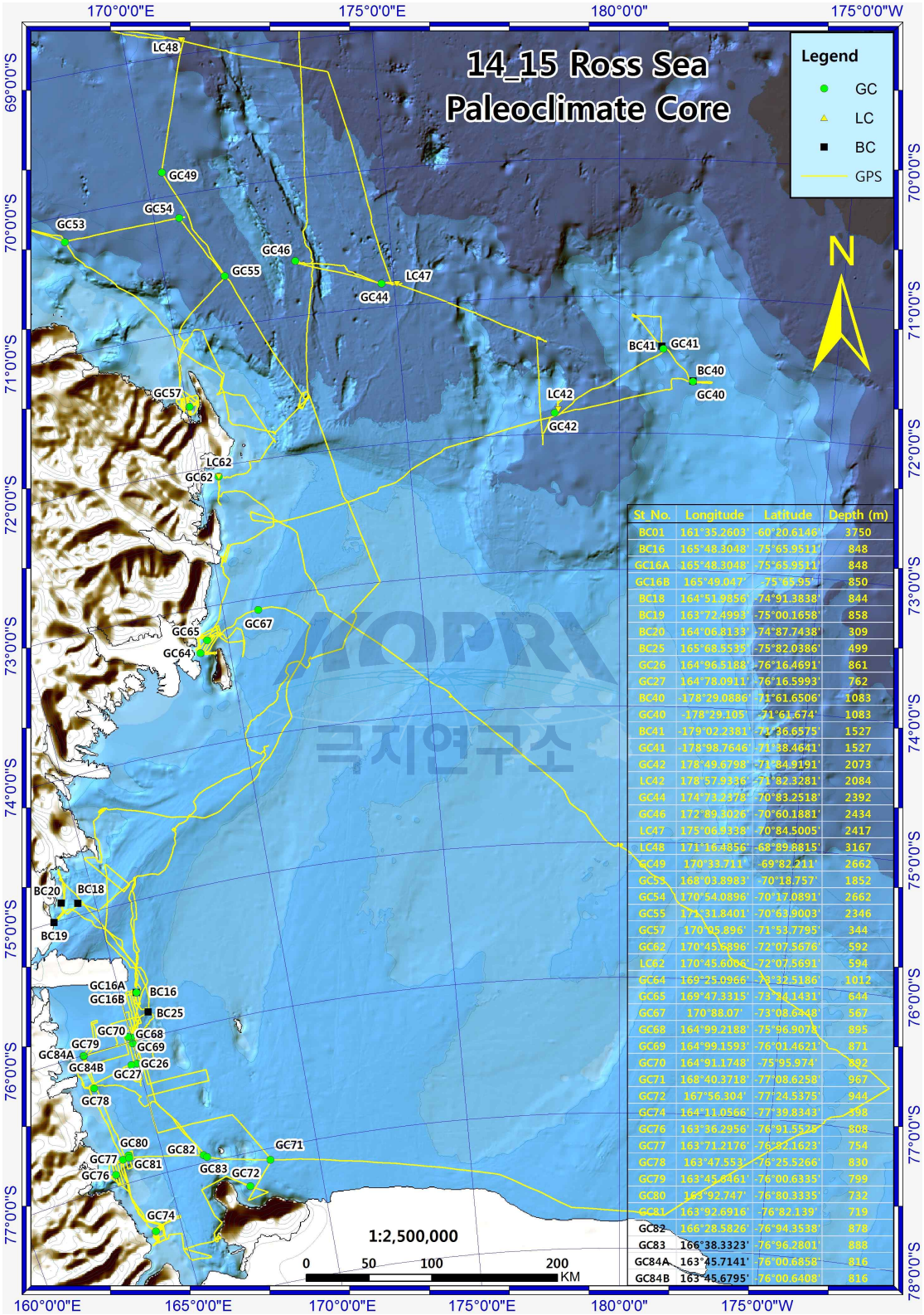

St_No.	Longitude	Latitude	Depth (m)
BC01	161°35.2603'	-60°20.6146'	3750
BC16	165°48.3048'	-75°65.9511'	848
GC16A	165°48.3048'	-75°65.9511'	848
GC16B	165°49.047'	-75°65.95'	850
BC18	164°51.9856'	-74°91.3838'	844
BC19	163°72.4993'	-75°00.1658'	858
BC20	164°06.8133'	-74°87.7438'	309
BC25	165°68.5535'	-75°82.0386'	499
GC26	164°96.5188'	-76°16.4691'	861
GC27	164°78.0911'	-76°16.5993'	762
BC40	-178°29.0886'	-71°61.6506'	1083
GC40	-178°29.105'	-71°61.674'	1083
BC41	-179°02.2381'	-71°36.6575'	1527
GC41	-178°98.7646'	-71°38.4641'	1527
GC42	178°49.6798'	-71°84.9191'	2073
LC42	178°57.9336'	-71°82.3281'	2084
GC44	174°73.2378'	-70°83.2518'	2392
GC46	172°89.3026'	-70°60.1881'	2434
LC47	175°06.9338'	-70°84.5005'	2417
LC48	171°16.4856'	-68°89.8815'	3167
GC49	170°33.711'	-69°82.211'	2662
GC53	168°03.8983'	-70°18.757'	1852
GC54	170°54.0896'	-70°17.0891'	2662
GC55	171°31.8401'	-70°63.9003'	2346
GC57	170°05.896'	-71°53.7795'	344
GC62	170°45.6896'	-72°07.5676'	592
LC62	170°45.6066'	-72°07.5691'	594
GC64	169°25.0966'	-73°32.5186'	1012
GC65	169°47.3315'	-73°34.1431'	644
GC67	170°88.07'	-73°08.6448'	567
GC68	164°99.2188'	-75°96.9078'	895
GC69	164°99.1593'	-76°01.4621'	871
GC70	164°91.1748'	-75°95.974'	892
GC71	168°40.3718'	-77°08.6258'	967
GC72	167°56.304'	-77°24.5375'	944
GC74	164°11.0566'	-77°39.8343'	898
GC76	163°36.2956'	-76°91.5528'	808
GC77	163°71.2176'	-76°82.1623'	754
GC78	163°47.553'	-76°25.5266'	830
GC79	163°45.6461'	-76°00.6335'	799
GC80	163°92.747'	-76°80.3335'	732
GC81	163°92.6916'	-76°82.139'	719
GC82	166°28.5826'	-76°94.3538'	878
GC83	166°38.3323'	-76°96.2801'	888
GC84A	163°45.7141'	-76°00.6858'	816
GC84B	163°45.6795'	-76°00.6408'	816

그림 1. 2014-15 아라온 2항차 (ANA05B)의 이동경로 및 코어획득 위치.

그림 2. 2014-15 아라온 2항차 (ANA05B)에 참여했던 연구원들.

그림 3. Adare Basin 주변에서 드렛지로 채취한 산호 시료.

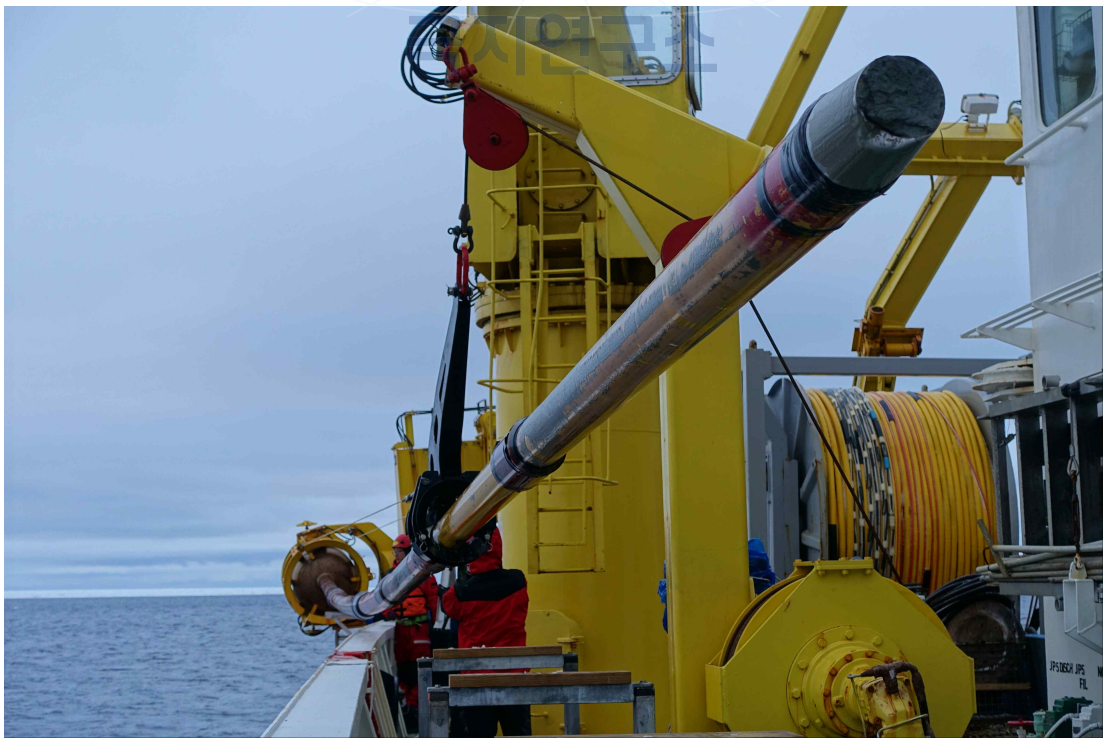

그림 4. 최초로 극지역에서 롱코어러를 이용해 얻어진 RS15-LC42 퇴적물 코어

(길이 11.86 m) 의 채취 장면.

그림 5. 아라온 dry lab에 설치한 MSCL로 퇴적물의 물리적 특성을 분석하는 장면.

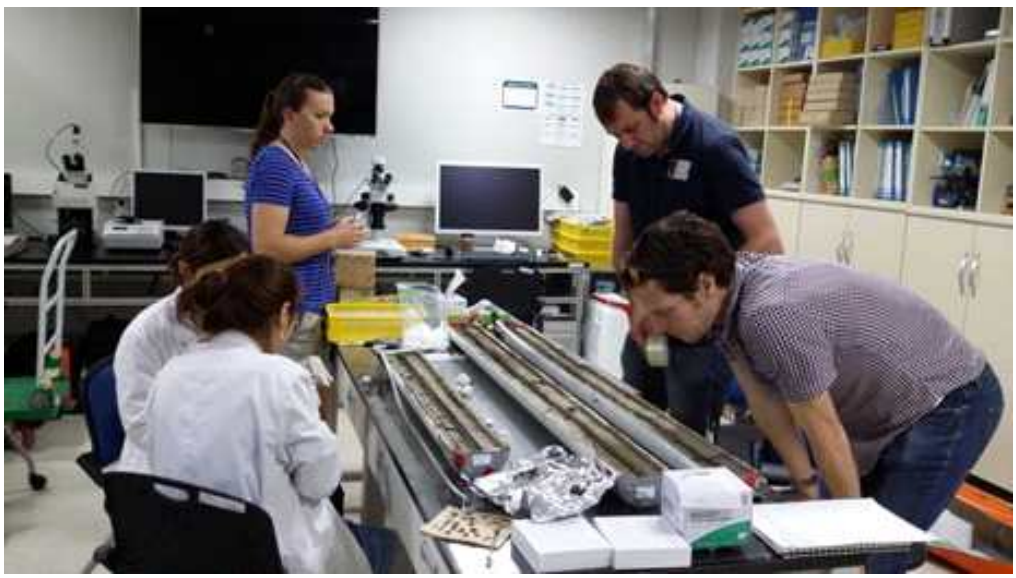

그림 6. 2015년 6월 극지연구소에서 열린 sampling party 중.

제 2 장

2015/16년 남극 로스해 탐사

김기태, 김성한, 문홍수, 황청연, 노연호, 이인애, 윤호일

한국해양과학기술원 부설 극지연구소

요약: 2015년 11월 말부터 12월 말까지 극지연구소 주도로 아라온호 기반 로스해 서안쪽 탐사가 2015년 초에 이어 이루어졌다. 극지연구소 8명의 연구원이 탐사에 참여하였다. 이번 탐사에서 이전에 설치한 퇴적물 트랩2기 중 한기를 회수 및 재설치에 성공하였다. 로스해 서쪽과 빙붕의 과거 환경 변화를 추적하기 위해 로스해 서안 및 로스빙붕 앞에서 박스/중력/롱코어 코어링이 이루어 졌다. 그 중 로스해 바깥 심해에서 획득된 RS15-LC108은 아라온호에 의해서 획득된 롱코어 퇴적물 중 가장 길이가 긴 17.5 m의 퇴적물 시료로 피스톤 타입을 이용하여 획득되었다. 해양생물 연구를 위해 로스해 서안과 로스빙붕 앞에서 CTD 측정이 이루어졌다. 이들 중 일부 CTD 정점에서는 해수 샘플 및 표층퇴적물이 해양 미생물 군집 분석을 위해서 획득되었다.

1. 2015/2016년 아라온호 기반 탐사 일정

조사기간: 2015년 11월 15일부터 12월 31일까지
참여연구원: 표 1 참조
전체적인 조사지역(그림 1-코어링 정점, 그림 2-퇴적물 트랩 정점, 그림 3-CTD 정점 참조)

- 로스해 서부 연안 (장보고 기지 인근)
- 로스빙붕 앞 연안
- 로스해 바깥쪽 심해

1) 11월 22일: 호바트 출발
2) 12월 4일-8일: 장보고 기지 앞 정박 및 하역 작업
3) 12월 8일: 아라온 ice margin으로 이동 및 롱코어 장착 작업 후 CTD 및 multi

beam 작업

4) 12월 9일: BC100 정점에서 CTD 작업, SBP 및 롱코어/박스 코어링(RS15-BC100 및 RS15-LC100)

5) 12월 12일: RS15-BC101 정점에 도착하여 SBP, 박스/중력 코어링(RS15-BC101 및 RS15-GC101). 박스 코어는 퇴적물 회수 실패. RS15-GC102 정점에 도착하여 SBP, 박스/중력 코어링(RS15-BC102 및 RS15-GC102).

6) 12월 13일: CTD 1 정점 도착 및 CTD, SBP, 박스 코어링(10 cm 정도의 퇴적층만 나와 표층시료만 획득)

7) 12월 14일: CTD 3 정점 도착 및 CTD, SBP, 박스 코어링(RS15-BC103). X1 정점에서 세디먼트 트랩 회수

8) 12월 15일: SBP, 박스 코어링 (RS15-BC104)

9) 12월 16일: 장보고 기지 앞 SBP, 박스 코어링(RS15-BC105), 조립한 퇴적물과 함께 bioclasts가 함께 나타나 dredging 시도(망이 엉켜어 해저 바닥 시료 획득 실패). RS15-BC105도 퇴적물은 거의 회수 되지 않음. RS15-BC106에서 박스 코어링을 시도하였으나 거의 회수가 안됨. X1 정점 트랩 재설치

10) 12월 17일: 로스해 대륙붕 지역의 연구항해 종료 및 호바트로 출발

11) 12월 19일: 선스타호 어선 구조 작업 후 RS15-GC107 정점 이동 및 SBP

12) 12월 21일: RS15-GC107 정점 도착 및 박스/중력 코어링 (RS15-BC107 및 RS15-GC107) 후 RS15-LC108 지점으로 이동 및 SBP.

13) 12월 22일: RS15-LC108 정점 도착 및 롱코어 24 m 배럴로 준비 및 롱코어 코어링 (RS15-LC108) 후 롱코어 해체를 위해 해빙이 존재하는 남쪽으로 다시 이동 및 해체 후 크라이스트처치를 향해 출발

14) 12월 28일: 크라이스트처치 도착 및 하선, 해양장비 점검

2. 탐사 내용

가. 코어 퇴적물 획득 및 퇴적물 트랩 회수 및 재설치

남극 로스해 서안과 로스빙붕 앞 연안에서 천해탄성파/다중측심 탐사를 통해, 적합한 퇴적지를 찾아 코어 퇴적물을 획득하였다(그림 1; 코어 정점 참조, 그림 4-6; 각 코어러 타입에 따른 코어 획득 형태 참조). 피스톤 타입 롱코어 퇴적물은 RS15-LC100과 - LC108이며, 중력 코어 퇴적물은 RS15-GC101, -GC102, -GC107

이며, 박스 코어 퇴적물은 RS15-BC100, -BC102, -BC103, -BC104, -BC107이다. 사용된 지구물리 장비는 Multibeam과 SBP이다. 이를 통해 파악된 퇴적층의 두께에 따라 해양퇴적물 획득에 적합하게 중력코어 및 롱코어, 코어 배럴의 길이 등을 달리하였다(표 2). 또한 해양 미생물 군집 분석을 위한 정점의 경우에는 박스 코어링만을 실시하여, 표층해양퇴적물을 획득하였다. 획득된 해양퇴적물은 선상에서 1.5 m 길이로 절단한 후, 캡으로 밀봉 후 냉장실에 보관하였다.

남극 로스해 서안 장보고 기지 앞 해역 트랩 정점 X1(그림 2)에서 예전에 설치되었던 퇴적물 트랩을 회수 및 재설치 하였다(그림 7-8 참조). 회수된 트랩 bottle에 담겨 있는 시료는 따로 냉장 보관하였다.

나. 해양 미생물 연구

남극 로스해 서안과 로스빙붕 앞 연안에서 해양 미생물 연구를 위한 해수 시료 및 해양 퇴적물 시료를 확보하였다(그림 1, 3). 해수 시료 및 해양퇴적물 시료(박스코어)의 수심 및 위경도 정보는 표 2와 표 3에 제시하였다. 채집도구는 Uncontaminated seawater underway sampler, Niskin bottles, 멸균된 주사기 corer, 스패튤라, 각종 여과지 (3.0 μm, 0.8 μm, 0.2 μm 공치수), 포르말린, 피펫 등이다. 박테리아와 바이러스 개체수 측정을 위한 시료의 경우, 현장 해수 시료에 0.2 μm 공치수로 여과한 포르말린을 첨가(최종 농도 2%)한 후 -80°C에 냉동 저장하였다. 해양 퇴적물 시료는 멸균된 주사기 corer 및 스패튤라로 샘플링하여 멸균된 tube에 넣은 후 -80°C에 냉동 저장하였다.

다. 해양 물리 조사

남극 로스해 서안과 로스빙붕 앞 연안에서 해양물리환경을 조사하기 위해 23개의 정점에서 CTD 측정이 이루어졌다(표 3, 그림 3 참조). 조사 항목은 CTD를 이용한 수온, 염분, 전도도, fluorescence 값 등이다. 일부 정점에서는 Niskin bottles을 이용하여 해수 시료를 획득 하였으며, 분석 용도에 맞게 전처리 된 후 동결보관하였다.

3. 향후 연구를 위한 제언

현장 탐사에서 일부 코어링 정점에서 dredging을 두 번 시도하였으나

dredging 망이 엉켜어 올라와 해저 바닥층 샘플을 획득 할 수 없었다. 따라서 추후에도 이러한 상황이 발생하지 않도록 dredging 도구들에 대한 관리가 필요하다고 사료된다.

또한 현장 탐사 중 윈치에 텐션과 관련된 문제가 발생하여 다른 윈치로 대체하여 사용하였으나 이 윈치 역시도 문제가 발생하여 결국 윈치 텐션과 관련된 문제를 해결 하는데 시간이 소요되어, 표층이 잘 보존된 적은 양의 해양퇴적물을 획득하는 박스 코어링에 큰 차질이 있었으며, 일부 정점에서는 박스 코어링을 실시할 수 없는 문제가 발생하였다. 추후 코어링 작업에서 필수적인 윈치와 같은 부분은 출항 전에 항상 점검 및 관리가 필요하다고 사료된다.

2015/2016 Antarctic Cruise: Ross Sea

Kitae Kim, Sunghan Kim, Heungsoo Moon, Chung Yeon Hwang, Younho Noh, Inae Lee, Ho Il Yoon.

Abstract: KOPRI icebreaker Araon based expedition was conducted in the western and southern (proximal to Ross Ice Shelf) Ross Sea from the late November to the late December in 2015. Eight researchers from KOPRI participated in this expedition. During this expedition, one of two sediment traps, previously deployed off the Jangbogo Station, was retrieved and redeployed at the same station. To reconstruct ice shelf advance/retreat history in the past, box/gravity/long-piston corings were carried out in the western coastal and in the Ross Ice Shelf proximal area of the Ross Sea. During this expedition, the longest sediment core (RS15-LC108; 17.5 m), among those obtained by Araon's piston type-long corer in the Polar regions, was retrieved from the deep sea area off the Ross Sea. CTD measurements were also conducted in the western coastal and in the Ross Ice Shelf proximal area of the Ross Sea. Some of sea water samples and core sediments were used for marine microbial analysis.

표 1. 국내 참여 연구원 및 활동 내용

성명	분야	소속	활동 내용
김기태	해양 광화학	극지고환경연구부	현장조사책임 및 시료채집
김성한	지질해양학	극지고환경연구부	퇴적물 시료 채취
문흥수	고해양	극지고환경연구부	코어링 기술
노연호	고해양	극지고환경연구부	코어링 기술
이태관	고해양	극지고환경연구부	코어링 기술
이승준	고해양	극지고환경연구부	코어링 기술
황청연	해양미생물학	극지생명과학연구부	퇴적물 및 해수 시료 채집
이인애	해양미생물학	극지생명과학연구부	퇴적물 및 해수 시료 채집

표 2. Location, water depth and core length of core sediments.

	코어명	위치	정점	수심(m)	길이 (m)
1	RS15-LC100	로스해 서쪽 (장보고 기지 쪽)	75°12.2510S', 164°16.5327'E	1081	9.3
2	RS15-BC100	로스해 서쪽 (장보고 기지 쪽)	75°12.2510S', 164°16.5327'E	1081	0.42
3	RS15-GC101	로스빙붕 앞	77°45.5808S', 178°26.3111'W	690	6.9
4	RS15-GC102	로스빙붕 앞	77°42.277S', 178°54.8966'E	706	3.5
5	RS15-BC102	로스빙붕 앞	77°42.277S', 178°54.8966'E	706	0.6 x 2
6	RS15-BC103	로스해 서쪽 (장보고 기지 쪽)	75°39.5963S', 165°32.0295'E		0.35
7	RS15-BC104	로스해 서쪽 (장보고 기지 쪽)	74°501132S', 166°16.0111'E		0.34
8	RS15-GC107	로스해 바깥 심해	68°04.0741S', 178°37.9066'W	3050	8.4
9	RS15-BC107	로스해 바깥 심해	68°04.0741S', 178°37.9066'W	3050	0.5, 0.46
10	RS15-LC108	로스해 바깥 심해	67°29.6139S', 178°45.1185'W	3690	17.5

표 3. CTD Location and detailed information.

Stn	Date (UTC)	Latitude	Longitude	수심 (m)
1	Dec-8-2015 10:50	74° 45.913'S	164° 8.797'E	168
2	Dec-8-2015 15:00	74° 51.915'S	164° 21.213'E	449
3	Dec-8-2015 15:00	74° 58.197'S	163° 56.980'E	390
4	Dec-8-2015 23:10	75° 12.281'S	164° 16.584'E	1239
5	Dec-9-2015 18:00	75° 21.052'S	164° 43.265'E	680
6	Dec-11-2015 9:30	77° 41.597'S	178° 20.620'E	745
7	Dec-11-2015 15:40	77° 45.172'S	178° 26.222'W	685
8	Dec-12-2015 1:55	77° 42.273'S	178° 54.893'E	720
9	Dec-13-2015 5:15	75° 53.651'S	163° 7.582'E	759
10	Dec-13-2015 9:50	75° 43.474'S	164° 22.451'E	600
11	Dec-13-2015 13:10	75° 39.602'S	165° 32.026'E	850
12	Dec-13-2015 16:05	75° 30.598'S	165° 35.455'E	814
13	Dec-13-2015 18:15	75° 22.148'S	165° 3.229'E	660
14	Dec-14-2015 1:00	75° 4.483'S	165° 15.777'E	1143
15	Dec-14-2015 3:30	74° 47.938'S	165° 8.006'E	718
16	Dec-14-2015 10:10	74° 50.128'S	166° 15.867'E	1081
17	Dec-14-2015 14:05	75° 7.984'S	166° 44.279'E	650
18	Dec-14-2015 22:15	75° 18.313'S	163° 56.426'E	1245
19	Dec-15-2015 5:40	74° 55.374'S	165° 10.893'E	856
20	Dec-15-2015 12:25	74° 58.238'S	163° 56.958'E	385
21	Dec-15-2015 15:00	74° 51.992'S	164° 59.865'E	709
22	Dec-15-2015 16:40	74° 53.568'S	165° 5.314'E	846

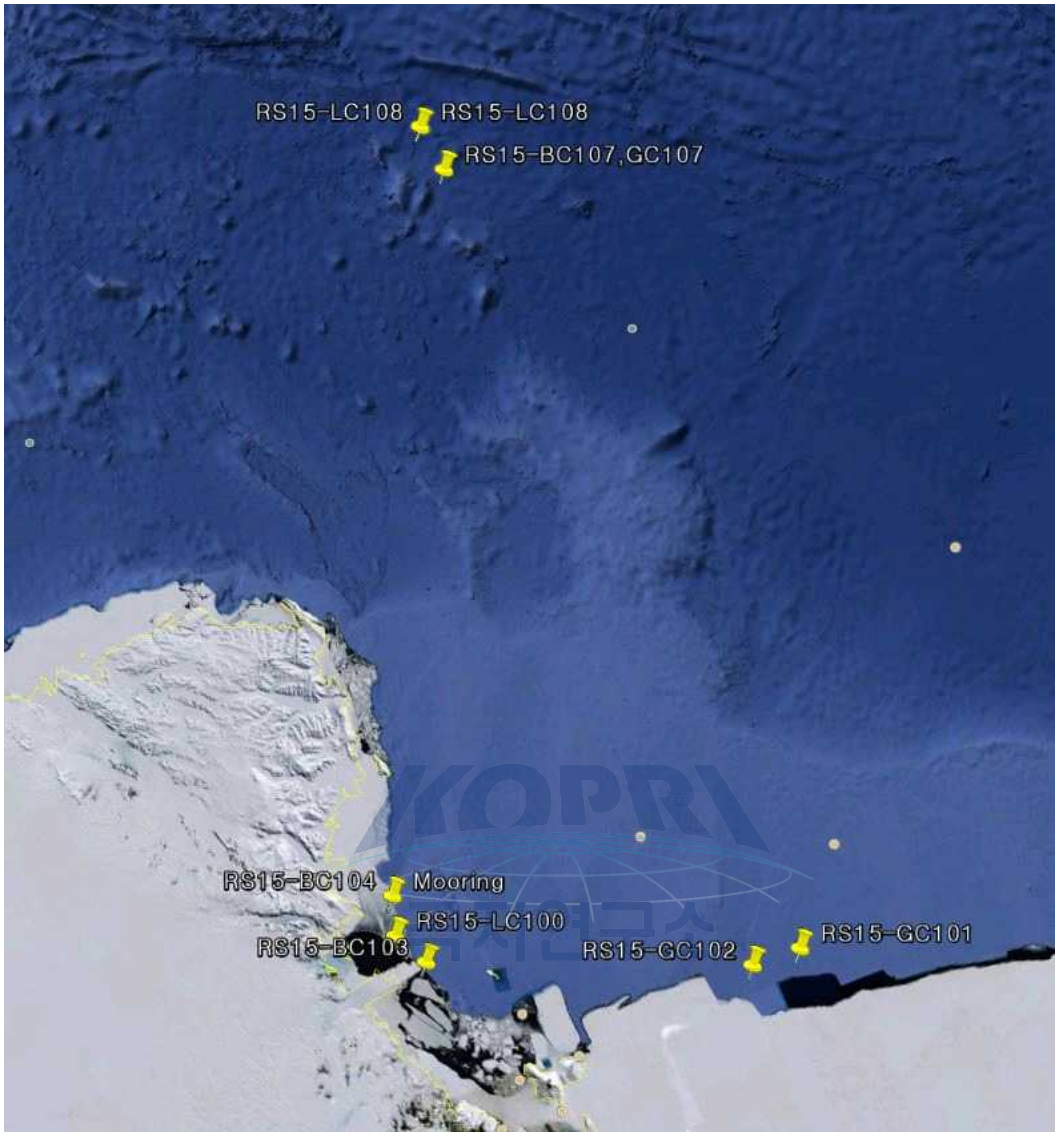

그림 1. Study area and sampling locations for 2015/2016 Antarctic Cruise by IBRV Araon.

그림 2. Location of M-2 sediment trap station (74°33.13′S, 166°15.89′E) in the Ross Sea near Jang Bogo Station

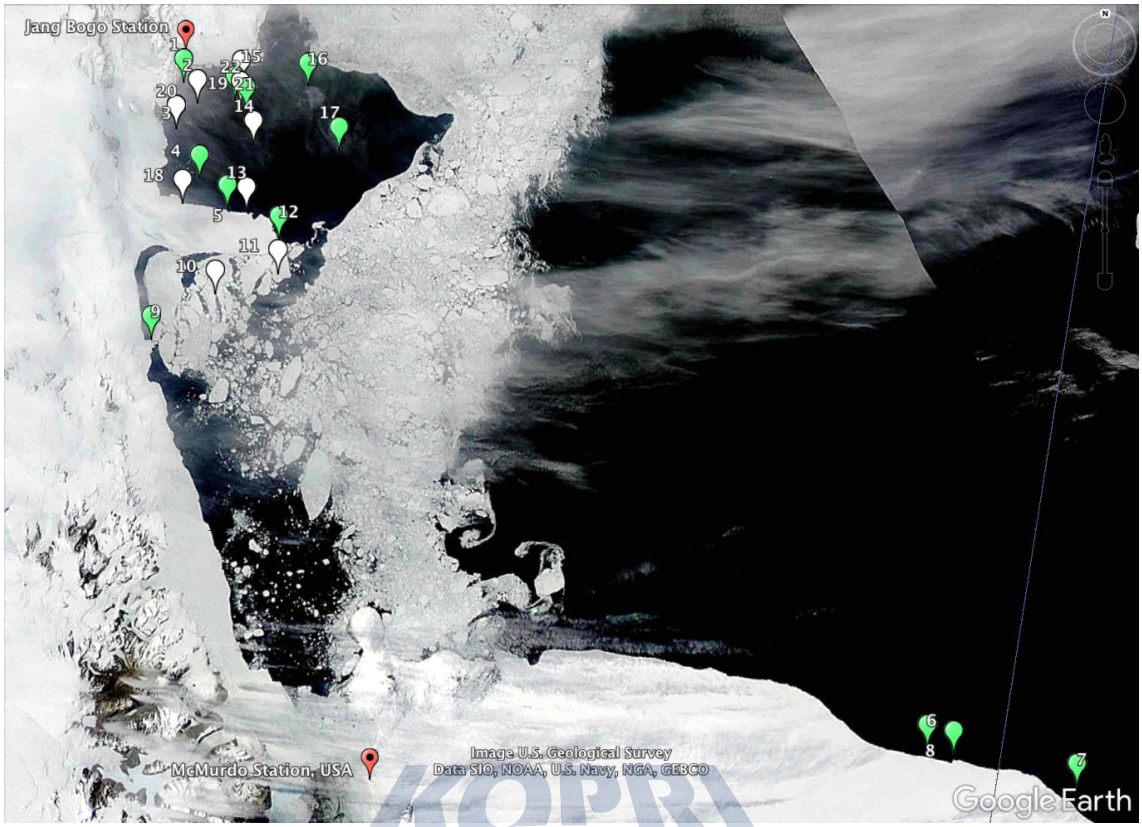

그림 3. Study area and CTD sampling locations for 2015/2016 Antarctic Cruise by IBRV Araon.

그림 4. Retrieving box corer.

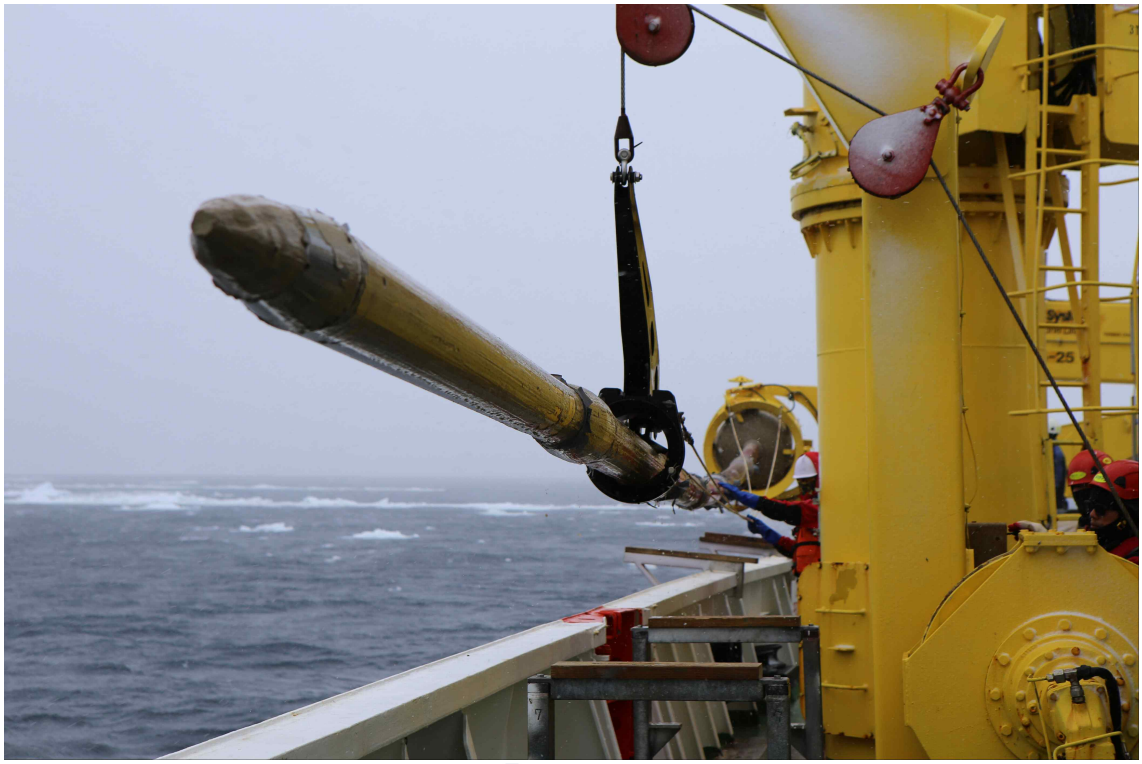

그림 5. Retrieving jumbo piston long corer.

그림 6. Retrieving gravity corer.

그림 7. Image of retrieving sediment trap sampler at X1 station.

그림 8. Image of the retrieved sediment trap.

제 3 장

아미고스 시스템을 이용한 빙붕 장기 모니터링

이춘기

한국해양과학기술원 부설 극지연구소

요약: 빙붕의 이동을 관측하기 위한 고정밀 GPS관측, 기상요소 관측, 빙붕 가장자리의 Calving을 관측할 수 있는 영상 촬영을 동시에 수행할 수 있는 AMIGOS 시스템을 드라이갈스키 빙설, 난센 빙붕, 캠벨 빙붕에 설치하고 연중 연속으로 혹은 이에 준하는 수준의 모니터링을 수행하여, 이를 통해 빙붕의 이동 속도 및 속도변화, 빙붕의 두께변화, 빙붕 변화의 기상요소와의 관계, Calving 특성 등을 파악하려 하였다. 2012년 하계탐사기간중 드라이갈스키 빙설 의 끝단과 중간에 KA1과 KA2, 2기의 AMIGOS시스템을 설치하여 4년간 운용하였다. 이후 2014/2015 하계 기간 중에 난센 빙붕에는 KA4를, 캠벨 빙붕에는 KA5를설치하였으며, 2015/2016 하계 기간에 난센 빙붕에 추가로 KA6를 설치하였다. 드라이갈스키에 설치한 아미고스시스템의 4년간에 걸친 운용을 통해 약 90%이상의 자료회수율을 달성하였으며, 획득된 자료로부터 빙붕의 이동속도를 결정하고 미세한 속도변화를 분석하였다. 드라이갈스키 빙붕 끝단에 설치된 KA1측점에서 GPS 자료로부터 산출된 빙붕의 이동속도는 708m/yr이며 약 25km 상류에 위치한 KA2측점에서 이동속도는 702m/yr로 이 구간에서는 변형에 의한 빙설의 두께 감소는 거의 없는 것으로 보인다. AMIGOS 시스템의 카메라를 통해 관측된 적설량, 빙붕 속도 관측을 통한 변형률 산출, 이전 연구에 따른 Firn 압밀 작용 제거 등을 통해 GPS 고도 변화로부터 빙붕 하부의 용융량을 산출하였다. KA1과 KA2 측점은 매우 큰 하부용융률을 가지는데 그 이유는 빙설의 가장자리에 가깝기 때문인 것으로 보이며, 이는 테라노바만의 폴리냐에 기인하는 것으로 추정된다. 난센빙붕 KA4 측점의 경우 2014년 12월부터 2015년 4월까지의 데이터가 회수되었고, 강한 바람에 의한 피해로 인해 2015년 4월에서 2016년 1월까지의 자료가 손실되었다. 이후 데이터는 2016년/2017년 하계기간 중에 현장에서 회수될 예정이다. 4개월간의 GPS 자료에 의하면 KA4 측점에서의 평균 이동 속도는 약 211m/yr이며, 매우 일정한 속도로 이동하고 있다고 볼 수 있다. 난센빙붕의 하부용융률은 1.4m/yr 로 추정되며, 드라이갈스키 빙설의 KA1과 KA2에 비해

바다로부터 멀리 떨어져 있어 다소 낮은 하부 용융률을 보이는 것으로 추정된다. 난센 빙붕의 KA6 측점은 난센 빙붕 중앙부 중 표면 용융수가 다량 흘러가는 지역으로 이곳의 하부용융률과 표면 용융 상태, 용해호의 변화를 모니터링하기 위하여 아미고스를 설치하였으며, 2016년/2017년 하계 탐사 기간에 자료를 회수할 예정이다. 캠벨 빙하의 지반선으로부터 약 4 km 떨어진 지점에 KA5 아미고스를 설치하였고 이후 약 4개월간의 자료를 획득하였으며 이후 자료는 2016년/2017년 하계 탐사 기간 중에 획득되어질 예정이다.

1. 서론

빙붕의 변화는 빙하의 변동과 해류 및 수온 변화와 밀접한 상관관계를 가지고 있다. 원격탐사나 간헐적인 현장 탐사로는 빙붕의 시간에 따른 변화 양상을 정확히 파악하기에는 한계가 있어 원격으로 유지가능한 지속적인 모니터링이 필요하다. 빙붕의 이동을 규명하기 위한 고정밀 GPS 관측, 기상 요소 관측, 빙붕 가장자리의 Calving을 관측할 수 있는 영상 촬영을 동시에 수행할 수 있는 AMIGOS 시스템을 드라이갈스키 빙붕에 설치하고 연중 연속으로 혹은 이에 준하는 수준의 모니터링을 수년에 걸쳐 장기간 수행하였다. 이를 통해 빙붕의 이동 속도 및 속도변화, 빙붕의 두께변화, 빙붕 변화의 기상요소와의 관계, Calving 특성 등을 파악하고자 하였다.

2. 아미고스 시스템

아미고스(AMIGOS) 시스템(그림 1)은 Automated Meteorology-Ice/Indigenous species-Geophysics Observation System의 약자로서 종합적인 빙하 모니터링 시스템이다. 정밀 측위 GPS, 기상 관측 장치, 웹 카메라 등으로 빙하의 거동을 관측하며, 인공위성 통신을 통하여 자료를 전송하거나 시스템을 컨트롤할 수 있다. 정밀 측위 GPS는 Topcon의 GRS-1 수신기와 안테나로 구성되어 있으며, 수 cm 이하의 정확도로 위치정보를 제공한다. 기상 관측은 주로 Vaisala WXT520 기상 센서로 관측이 이루어지는데 온도, 습도, 풍향, 풍속을 관측하며, 추가적으로 장착된 조도 센서를 이용하여 태양복사와 반사도를 측정한다. Sony SNC-RZ30N/2 웹 카메라를 이용하여 주변 환경 및 장비의 상태를 준 실시간으로 모니터링할 수 있다. 관측된 자료는 이리듐 위성통신 모뎀을 통하여 실시간으로 전송된다. 하지만, 실제 운영시에는 이리듐 송신 요금 및 전력 상황을 고려하여 실시간 전송은 제한하기도 한다.

2.1. 아미고스 시스템의 설치 현황

테라노바 만 주변에 총 5개의 아미고스를 설치하였으며 (그림 2), 현재 드라이갈스키 빙설에 2기(2012~), 난센 빙붕에 2기(2014~), 캠벨 빙하에 1기(2014~)를 운영중이다. 아미고스 운영 현황은 표 1과 같다.

2.2. 드라이갈스키 빙설 모니터링

드라이갈스키 빙설(Drygalski Ice Tongue)은 남극 빅토리아 랜드(Victoria Land) 데이비드 빙하(David Glacier)의 하류에 형성된 남극에서 가장 긴 빙설 중 하나이다. 관측이 시작된 이래로 두 번째 최대 길이인 약 104km(바다쪽으로 돌출된 부분의 길이)에 이르렀던 2005년경, 로스 빙붕(Ross Ice Shelf)으로부터 떨어져나온 B15A와 C16 빙산(iceberg)이 연속적으로 충돌하여 빙설의 끝부분이 C25 빙산으로 분리되어 나갔다(MacAyeal et al., 2008). 드라이갈스키 빙설의 붕괴가 항상 큰 빙산의 충돌에 의해서만 발생하는 것은 아니다. 드라이갈스키 빙설이 약 110km로 가장 길었던 1957년에 약 40km의 전단부가 분리되었는데, 이 시기는 로스 빙붕에서의 빙산 생성과 일치하지 않는다(Jacobs et al., 1986). Frezzotti and Mabin (1994)는 1957년 6월경 발생한 로스해에서의 강한 폭풍에 의해 빙설 전단부의 붕괴가 발생하였다고 제안하였다. 인공위성 영상의 분석에 따르면 현재 드라이갈스키 빙설은 약 700m/yr의 속도로 약 95km의 길이로 성장하고 있으며 붕괴현상이 발생하지 않는다면 약 2030년 경 최대 길이로 성장할 것으로 예상된다. 드라이갈스키 빙설의 성장은 로스해 서부의 해류 변화나 테라노바만(Terra Nova Bay)의 폴리냐 형성에 중요한 영향을 미치고 있어, 드라이갈스키 빙설의 장기적인 모니터링은 향후 로스해의 변화를 예측하는데 중요한 의미를 가진다. 이 연구에서는 드라이갈스키 빙설의 빠른 이동 속도와 방향을 정밀하게 모니터링하여 드라이갈스키 빙설의 거동특성을 파악하고자 드라이갈스키 빙설의 끝단과 중간에 KA1과 KA2를 각각 설치 운영하였다. 자료는 2012년 초부터 2016년초까지 4년간 획득되었다 (그림 3).

2.2.1. 드라이갈스키 빙설지역의 기상

1시간 간격으로 측정된 KA1과 KA2의 기상 자료 (그림 4, 5) 를 바탕으로 4m 높이에서 드라이갈스키 지역의 평균 기온은 -16℃이며, -40℃ ~ 5℃의 분포를 보인다. 기온이 0℃이상으로 상승하는 기간은 연간 평균 약 60-85시간 정도이다.

2012년-2015년 중 2013/2014 하계기간이 가장 따뜻했던 여름인 것으로 관측되었으며, 이 기간에 영상의 기온을 보이는 시간은 약 160시간(약 7일)에 달한다. 반면 -30℃ 이하의 기온을 보이는 시간은 연간 평균 36일 정도이며, 2015년에는 55일로 관측기간 중 가장 추웠던 해로 기록되었다. 습도는 KA1에서 평균 73%이며, 육지에 조금 더 가까운 KA2에서는 71%로 약간 낮다. 기압은 약 984 hPa로 두 측점에서 거의 비슷하다. 카타바틱풍(catabatic wind)에 의해 풍향은 서풍이 단연 우세하며 남서풍도 가끔 불어온다. 평균 풍속은 5.7m/s이며, 최대 풍속은 KA1에서 20m/s, KA2에서 24m/s로 육지에 가까운 KA2에서 바람이 더 강하다. 가장 따뜻했던 2013/2014 하계기간에는 북서풍이 다른 해에 비해 다소 증가한 것으로 보아 북서쪽에서 보다 따뜻한 공기가 유입된 것으로 보인다.

2.2.2. 드라이갈스키 빙설의 이동 특성

아미고스에 탑재된 이중 주파수 GPS를 이용하여 드라이갈스키 빙설의 움직임을 정밀하게 추적하였다. GPS 관측은 6시간 간격으로 20분씩 측정되었으며 GPS 자료 처리는 캐나다 NRC (Natural Resources Canada)의 온라인 PPP (Precise Point Positioning) 프로세싱 서비스를 이용하였다. GPS 위치 정보의 정확도를 확인하기 위하여 장보고기지 인근 암반에 설치된 같은 종류의 GPS 장비로부터 획득된 위치를 분석하였다. 20분간 측정된 GPS 자료의 PPP 처리 정확도에 비해 지각의 움직임은 매우 작아서 암반위 GPS 자료의 표준편차는 처리된 GPS 위치 정보의 오차를 지시한다. 암반위 GPS의 수평방향 표준편차는 3.3-4.5 cm이며, 수직방향 표준편차는 6.1 cm이다.

GPS 자료로부터 산출된 KA1과 KA2에서의 평균 이동 속도는 각각 708 m/yr, 702 m/yr이다 (그림 6). 두 측점에서 속도 차이가 1%이내이므로 이 구간에서는 변형에 의한 빙설의 두께 감소는 거의 없는 것으로 보인다. 하루에 이동하는 최대 속도는 약 1.9 m 이므로 GPS 관측 오차에 의한 일간 속도의 오차는 약 2.6% 이상이다. 수평방향 GPS 관측 오차를 4 cm라 할 때, 20일간의 평균 속도 추정치의 오차는 약 0.7 m/yr이다. 즉, 20일 평균 속도 추정치는 약 0.1%의 오차를 가진다. KA1에서 구한 20일 평균 속도 추정치는 690-740 m/yr의 범위 내에 분포하며 표준편차는 약 8.6 m/yr이다. 특히, 2013/2014년 하계기간에 약 40 m/yr 가량 속도가 갑자기 증가하는 현상이 발생하였다. 이 속도 증가 현상의 원인은 두 가지의 가능성이 있다. 첫째, 2013/2014년 하계 기간 동안 영상의 기온을 나타낸 시간은 160 시간으로, 관측 기간의 여름 중 가장 많다. 이로 인해 표면 용융이 많이 발생한 것으로 보이며, 드라이갈스키 빙설과 육지의 경계부에 융해 연못(melt pond)가 생긴 것이

확인되기도 한다. 표면에서 용융된 물이 빙설과 육지의 경계부로 스며들어 마찰력을 감소시켜 이동 속도가 빨라졌을 가능성이 있다. 둘째, 기상 자료에 의하면 2013/2014년 하계 기간 중 북서풍이 평년에 비하여 증가한 것으로 보인다. 북서풍은 빙설에 남쪽방향의 힘을 가하게 되어 남쪽 방향으로의 속도가 증가했을 가능성도 있다. 보다 명확한 원인은 보다 장기간의 모니터링 자료를 이용한 기상 요소(온도 및 풍향/풍속 등)와 속도 변화 사이의 상관 계수 산출을 통해 규명할 수 있을 것으로 생각된다.

속도변화에 따른 거동 양상을 보다 자세히 살펴보기 위하여 각 지점에서의 평균속도에 따른 이동거리를 제거한 잔여 변위량을 살펴보았다 (그림 7). polar stereographic coordinate system에서 빙붕의 진행 방향에 가까운 X 방향의 성분에 비해 빙설의 진행 방향에 수직에 가까운 Y 방향의 성분에서 보다 큰 잔여 변위량이 확인된다. 즉, 빙설의 진행 방향보다는 빙설에 수직한 방향으로의 속도가 더 크게 변화하고 있다. 잔여 변위량을 공간적으로 표현하면 그림 8과 같다. 드라이갈스키 빙설은 매우 빠른 속도로 동쪽을 향해 이동하고 있지만 속도의 변화는 주로 진행방향에 수직하게 거동한다. 이런 현상은 길게 뻗은 빙설의 형태와 바다로 돌출된 부분에서는 수직방향으로의 움직임을 제한하는 장애물이 적기 때문이다. 수직방향으로 작용하는 힘으로는 해류, 바람, 난센 빙붕과의 접촉, 빙산의 충돌 등이다.

드라이갈스키 빙설에 존재하는 다른 GPS 자료들, InSAR (Interferometric SAR) 속도 자료, Landsat을 이용한 과거 빙설의 이동속도 등을 이용하여 빙설의 이동 속도 변화를 보다 자세히 살펴보았다. 그림 9와 같이 서로 다른 시기에 관측된 InSAR 속도를 비교하였을 때 바다로 돌출된 빙설 지역에서 빙설의 수직 방향 속도가 다소 큰 차이를 보이는 것이 확인된다. 또한 GPS들의 속도 변위를 살펴보면 빙설의 끝으로 갈수록 속도 변위가 증가하고 있으며, 해양으로 돌출된 부분은 하나의 회전축을 중심으로 회전하는 형태의 변위를 보이고 있다. 그 회전축은 빙설이 해양 쪽으로 완전히 돌출되어 육지와의 접촉이 없어지는 지점에 위치한다. 과거의 빙설 속도 변위의 시계열을 살펴보기 위하여 Landsat 인공위성 영상을 이용한 상호 상관을 통한 속도 추출 기법을 적용하여 2000년 이후의 속도 변화를 재현하였다. 속도 변화가 가장 컸을때는 2006년 경이며, 이 시기는 로스 빙붕에서 발생하여 이동해온 B-15A와 C-16 빙산이 드라이갈스키 빙설과 충돌하였던 시기 직후 이다. 빙산들이 충돌하여 빙설의 전단부가 떨어져 나간이후 빙설은 남쪽방향으로의 속도가 약 100 m/yr 증가하였다. 즉, 빙설의 calving 현상이 빙설의 이동 방향에 큰 영향을 주고 있음을 알 수 있다. 남쪽 방향으로 속도가 증가한 것은 빙설의 끝에 작용하던 해류에 의한 전단 응력이 빙설 끝의 붕괴로 인해 약화되었기 때문으로 추정

된다.

2.2.3. 드라이갈스키 빙설의 하부 용융

KA1과 KA2에 설치된 GPS 자료는 수평적인 이동 뿐만 아니라 수직적인 변화도 존재하고 있음을 보여준다. 두 측점 모두 지속적으로 GPS 고도가 낮아지는 현상이 관측된다. 즉, 물에 떠있는 빙붕의 정수 평형을 고려하면 지속적으로 빙붕의 두께가 얇아지고 있음을 의미한다. 빙붕의 두께 변화에 영향을 미치는 요인으로는 적설량(snow accumulation), 하부용융(basal melt), 속도차에 의한 변형률(strain rate), 눈층의 고밀도화(Firn densification) 등이며, 다음 식과 같이 표현할 수 있다.

$$\frac{dH}{dt} = \frac{dA}{dt} - \frac{dB}{dt} - H\epsilon - \frac{df}{dt}$$

여기서, H는 빙붕 두께, A는 적설량, B는 하부용융, ϵ은 변형률, f는 눈층(firn)의 두께를 의미한다. GPS 관측자료는 표면의 고도변화이므로 다음과 같은 정수 평형에 따른 표면고도와 빙붕 두께의 관계를 이용하여 표면 고도변화에 관한 식으로 변형이 가능하다.

$$H = \frac{\rho_w}{\rho_w - \rho_i} h_s - f_c$$

여기서, h_s는 빙붕 표면고도, ρ_w는 해수의 밀도, ρ_i는 얼음의 밀도, f_c는 firn 보정값이다. 이 식을 앞의 식에 대입하면 다음과 같다.

$$\frac{\rho_w}{\rho_w - \rho_i}\frac{dh_s}{dt} = \frac{dA}{dt} - \frac{dB}{dt} - H\epsilon - \frac{df}{dt}$$

장기간 설치된 GPS에 의해 관측되는 고도변화는 빙붕의 표면의 고도변화가 아니라 GPS가 설치된 초기 표면(h_{gps})의 고도 변화이므로 $h_s = h_{gps} + A$를 적용하고 적설량의 하중에 의한 효과를 제거한 GPS 고도를 $h\,(= h_{gps} - \frac{\rho_w}{\rho_w - \rho_i} A)$라고 하면 위 식은 다음과 같이 정리된다.

$$\frac{\rho_w}{\rho_w - \rho_i}\frac{dh}{dt} = -\frac{dB}{dt} - H\epsilon - \frac{df}{dt}$$

그림 10은 KA1과 KA2에서 관측된 GPS 고도 변화와 적설량을 나타낸다. 적설이 발생한 후 눈의 하중에 의해 고도가 낮아지는 것이 관측되며 이 효과를 제거하면 보다 선형적인 변화에 가까워진다. 선형회귀 분석을 이용하여 하중효과가 제거된 고도변화를 산출하였다. KA1에서는 -0.56 m/yr, KA2에서는 -0.42 m/yr의 고도 변화율(dh/dt)이 산출되었으며, 이에 상응하는 두께 변화는 각각 -5.2 m/yr,

-3.9 m/yr이다.

KA1과 KA2간의 속도차이는 약 6 m/yr이며 KA1과 KA2사이의 거리는 약 25km이므로 변형률은 2.4×10^{-4} a^{-1} 이며 빙붕 두께를 약 250 m라고 하면 변형률에 의한 두께변화는 약 6 cm/yr로서 무시할 정도로 작다. KA1과 KA2 지역에서의 눈층 두께 변화에 의한 고도 변화는 약 -0.12 m/r이며 눈층 두께의 변화로 인한 빙설의 두께 변화는 약 1.1 m/yr이다. 결과적으로 위 식에 의해 하부 용융률(basal melt rate)은 각각 4.1 m/yr, 2.8 m/yr 이다. 질량 보존 방법(mass conservation method)을 이용하여 드라이갈스키 빙설의 각 구간별로 구한 하부 용융률(wuite et al., 2009)에 의하면 드라이갈스키 끝단에서는 약 0.7 m/yr의 하부 용융률이 추정되었다. 이 결과와 비교하였을 때 KA1과 KA2 측점은 매우 큰 하부용융률을 가지는데 그 이유는 빙설의 가장자리에 가깝기 때문인 것으로 보인다. Horgan et al. (2011)은 로스 빙붕의 끝단 약 5 km 이내에서는 하부용융률이 급격하게 상승하는 것을 관측하였다. 로스 빙붕과 마찬가지로 드라이갈스키 빙설의 경우도 하부용융률이 빙설의 내부에 비해 가장자리에서 상대적으로 매우 높은 것으로 추정되며 이는 테라노바만의 폴리냐에 기인하는 것으로 추정된다.

2.3. 난센 빙붕 모니터링

난센 빙붕(Nansen Ice Shelf)는 장보고기지 남쪽에 위치한 약 1,800 km2 넓이의 빙붕으로 리브스(Reeves)와 프리슬리(Priestley) 빙하가 배출되어 만들어진 빙붕이다. 건조하고 지속적인 카타바틱풍에 의해 발생하는 풍화와 승화로 인해 난센 빙붕의 중심부는 눈으로 덮혀있지 않고 얼음이 노출되어 있다. 이 곳에서 부는 강한 카타바틱풍은 테라노바만의 폴리냐를 생성시키는 주요 요인이다. 풍화대는 난센 빙붕의 약 40%를 차지하며 풍화율은 약 25 cm/yr로 알려져 있다. 하계기간에는 풍화대에 많은 융해호(melt pond)가 생성되기도 한다.

난센빙붕의 거동과 두께변화를 알아보기 위하여 난센 빙붕의 끝단(KA4)과 중간 지점(KA6)에 아미고스를 설치하여 운영하고 있다. KA4는 2014/2015 하계 기간 중에 설치되었으며, KA6는 2015/2016 하계 기간에 설치되었다 (그림 11).

KA4 측점에서는 강한 바람으로 인한 피해로 인해 2015년 4월에서 2016년 1월까지의 자료가 손실되어, 1년간의 자료가 완전히 회수되지는 않았으나, 영하 38도에서 영상 2도 정도의 기온 분포를 보인다 (그림 12). GPS 자료는 현재까지 2014년 12월부터 2015년 4월까지의 데이터가 회수되었고, 과다한 통신요금으로 인하여 실시간 자료전송은 실시하지 않고 있으며, 2015년 4월 이후 데이터는 2016년/2017년 하계기

간 중에 현장에서 회수될 예정이다.

GPS 자료에 의하면 KA4 측점에서의 평균 이동 속도는 약 211m/yr이며, 약 4개월간 잔여 변위량은 약 10cm이므로 매우 일정한 속도로 이동하고 있다고 볼 수 있다. 수직 성분의 경우 약 19.5cm의 진폭을 가지고 있으며, 평균 조석 진폭은 18.9cm이며 최대 약 50cm 진폭의 조석을 나타내고 있다. 남극 조석 모델인 CATS2008a(www.esr.org)에 의한 모델값으로 조석 성분을 제거하면 약 9.9cm 진폭의 잔차가 남는다. 기압 변화에 따른 해수변 변동 현상을 제거해주는 IBE(Inverse Barometric Effect) 보정을 수행하면 8.6cm 진폭의 잔차가 남게된다.

이 잔차는 조석 모델의 오차나 지역적인 해수면의 변동, 하부용융율의 변동 등 다양한 원인에 기인할 수 있다. 조석 보정과 IBE 보정을 수행한 후의 잔차를 이용하여 산출된 고도 변화율은 -17.5cm/yr이다 (그림 13). KA4가 설치된 지역은 적설이 없고 표면 풍화가 계속되는 지역으로 눈층이 없이 얼음이 노출된 곳이다. KA4 측점에서 관측된 표면 질량 수지(SMB)는 -20.5cm/yr로 이에 의한 표면 고도 변화량은 -2.2cm/yr이다. 변형률에 의한 두께변화는 매우 작을 것으로 추정되므로, 하부용융에 의한 표면 고도 변화량은 -15.3cm/yr이다. 얼음의 밀도를 917kg/m3으로 적용하면 약 1.4m/yr의 하부용융률이 산출된다. 드라이갈스키 빙설의 KA1과 KA2에 비해 바다로부터 멀리 떨어져 있어 다소 낮은 하부 용융률을 보이는 것으로 추정된다.

KA6 측점은 난센 빙붕 중앙부 중 표면 용융수가 다량 흘러가는 지역으로 이곳의 하부용융률과 표면 용융 상태를 모니터링하기 위하여 아미고스를 설치하였다. KA6의 카메라는 인근 표면에 존재하는 용해호(melt pond)의 변화를 살표보기 위하여 설치되었으며 (그림 14), 2016년/2017년 하계 탐사 기간에 자료를 회수할 예정이다.

2.4. 캠벨 빙붕 모니터링

캠벨 빙하는 장보고 기지의 북쪽에 위치한 가장 가까운 빙하로 멜번 화산 옆을 지나 장보고 기지 앞바다로 흘러들어 빙설을 형성하는 작은 빙하이다. 지반선(grounding line) 부근에서 빙설과 빙하 흐름의 상관관계를 모니터링하기 위하여 지반선으로부터 약 4 km 떨어진 지점에 KA5 아미고스를 설치하였다. 현재 설치로부터 약 4개월간의 자료를 획득하였으며 이후 자료는 2016년/2017년 하계 탐사 기간 중에 획득되어질 예정이다. KA5에서의 평균 속도는 188m/yr이며, 잔여 변위량은 ±20cm 정도이다 (그림 15). 일시적으로 잔여 변위량이 증가하는 것이 관찰되는데

이는 일시적인 빙하 이동 속도의 변동이 있음을 의미한다. 즉, 40-50 DOY 부근에서 약 10일에 걸쳐 Y방향의 잔여변위량이 약 20cm정도 증가하는데 이는 약 7m/yr의 속도가 증가하였음을 의미한다. 고도 변화의 경우 80 DOY 이후로 표면 고도의 감소가 관찰되는데 표면고도변화와 앞서 발생한 속도변화 간의 상관관계는 보다 장기간의 자료가 획득된 후에 규명이 가능할 것으로 생각된다.

Ice shelf monitoring using AMIGOS system

Choon-Ki Lee

Korea Polar Research Institute

Abstract: Velocity and thickness variations of the Drygalski Ice Tongue and Nansen Ice Shelf on the west side of the Ross Sea were estimated from four three AMIGOS (Automated Meteorology-Ice/Indigenous species-Geophysics Observation System). The continuous GPS measurements obtained near the front of Drygalski Ice Tongue since early 2012 present the ice velocities of ~708m/yr velocity at KA1 site and ~702m/yr velocity at KA2 site. The ice tongue is stably flowing with residual displacements in the range of ±5m. The elevation of AMIGOS observed by GPS is gradually lowering for four years. By removing the effects of the snow load, firn comfaction, dynamic deformation by strain, we inferred basal melt influence to the elevation of equipment. The basal melt rates beneath the KA1 and KA2 site we obtained are 4.1m/yr and 2.8m/yr respectively. The new estimates of basal melt beneath the Drygalski Ice Tongure is significantly larger than the basal melt under the steady state. The large basal melt rate implies the plausible influence of polynya formed at Terra Nova Bay during austral summer. The ice velocities of Nansen Ice Shelf is very constant (~211m/yr), and the basal melt rate is inferred as 1.4m/yr, which is slightly lower compared to that of Drygalski Ice Tongue.

참고문헌

Jacobs, S. S., MacAyeal, D. R., and Ardai, JR, J. L, 1986,The recent advance of the Ross Ice Shelf, Antarctica, Journal of Glaciology,32, No. 112, 464-474.

MacAyeal, D.R., Okal, E. A., Aster, R. C., and Bassis, J. N., 2008, Seismic and hydroacoustic tremor generated by collding icebergs, J. Geophys. Res, 113, doi:10.1029/2008JF001005.

Frezzotti, M. and Mabin, M. C. G., 1994, 20th century behaviour of Drygalski Ice Tongue, Ross Sea, Antarctica, Annals of Glaciology, 20, 397-400.

Wuite, J., Jezek, K. C., Wu, X., Farness, K., Carnade, R., 2009, The velocity field and flow regime of David Glacier and Drygalski Ice Tongue, Antarctica, Polar Geography, 32, 111-127.

Horgan, H. J., Walker, R. T., Anandakrishnan, S., and Alley, R. B., 2011, Surface elevatino changes at the front of the Ross Ice Shelf: Implications for basal melting, J. Geophys. Res., 116, C02005, doi:10.1029/2010JC006192.

표 1. 아미고스를 이용한 빙붕 모니터링 현황

Site	Location	Latitute	Longitude	Installation	Inst.	Maintenance
KA1	Drygalski	75.4163	165.2527	2011/2012	KAMIGOS version 1	2012.11 Lithium battery 2014.12 Adjustment of weather sensor 2016 - 2017 Repair
KA2	Drygalski	75.3514	164.3447	2011/2012	KAMIGOS version 1	
KA4	Nansen IS	75.0721	163.4274	2014/2015	KAMIGOS version 1	2015.12 Firmware upgrade, Adding 4 gelcell batteries
KA5	Campbell Gl.	74.5405	164.3943	2014/2015	KAMIGOS version 1	2015.12 Firmware upgrade, Adding 4 gelcell batteries
KA6	Nansen IS	74.9511	163.2005	2015/2016	KAMIGOS version 1	


GPS
Iridium Antenna
Camera
Weather Station
Solar Sensor
Solar Panels
Electronics

그림 1. 아미고스 시스템의 구성

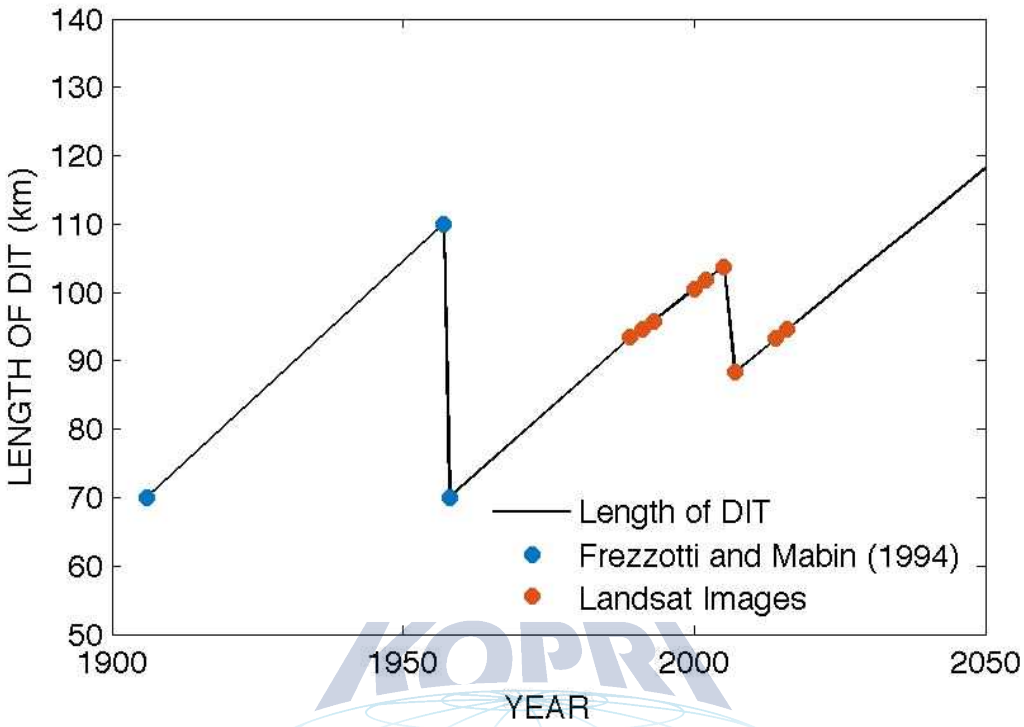

그림 2. 역사 관측 기록과 인공위성 영상을 통해 추정되는 시간에 따른 드라이갈스키 빙설의 길이 변화

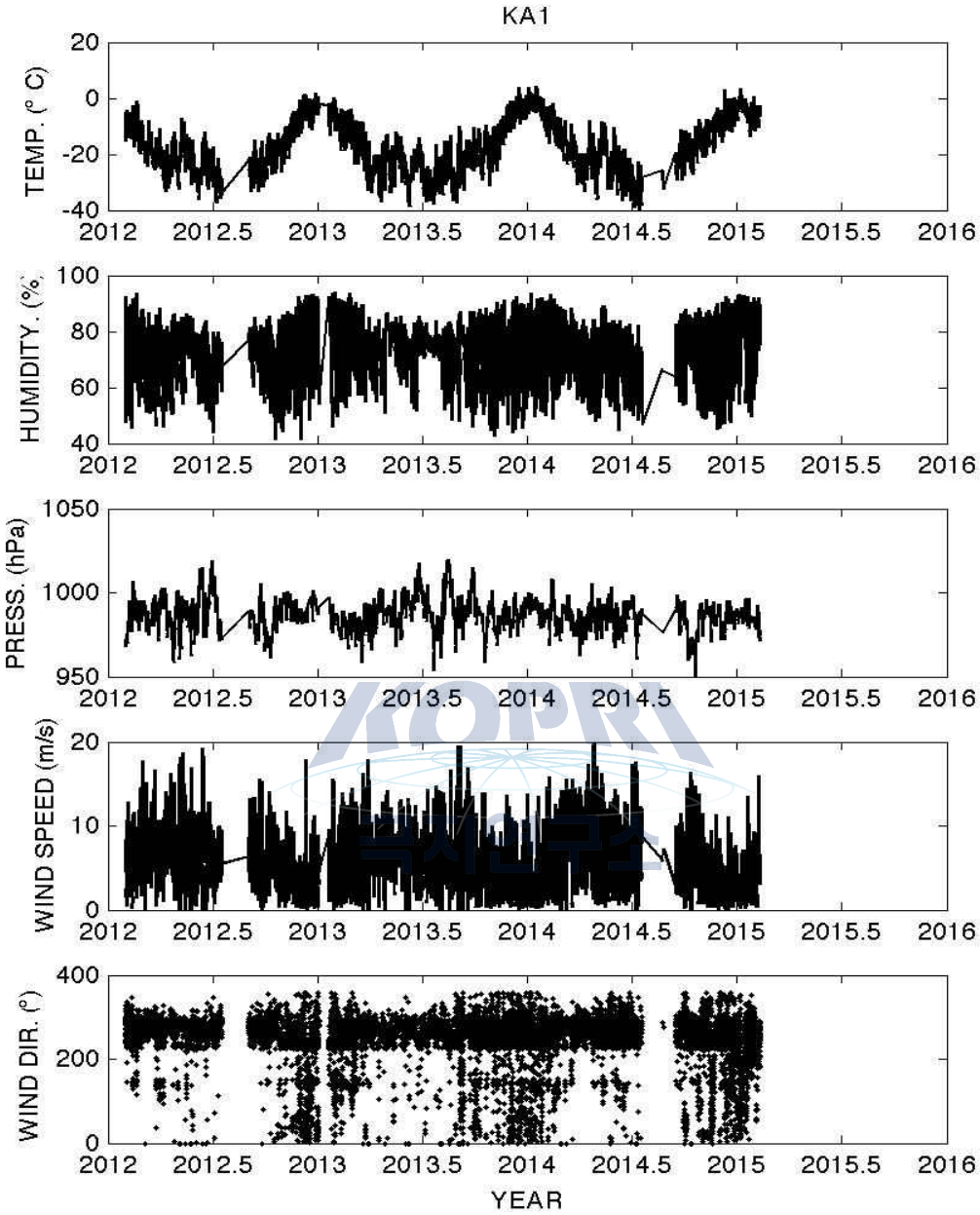
KA1
TEMP. (° C)
HUMIDITY. (%)
PRESS. (hPa)
WIND SPEED (m/s)
WIND DIR. (°)
YEAR
2012
2012.5
2013
2013.5
2014
2014.5
2015
2015.5
2016

그림 3. KA1 기상자료

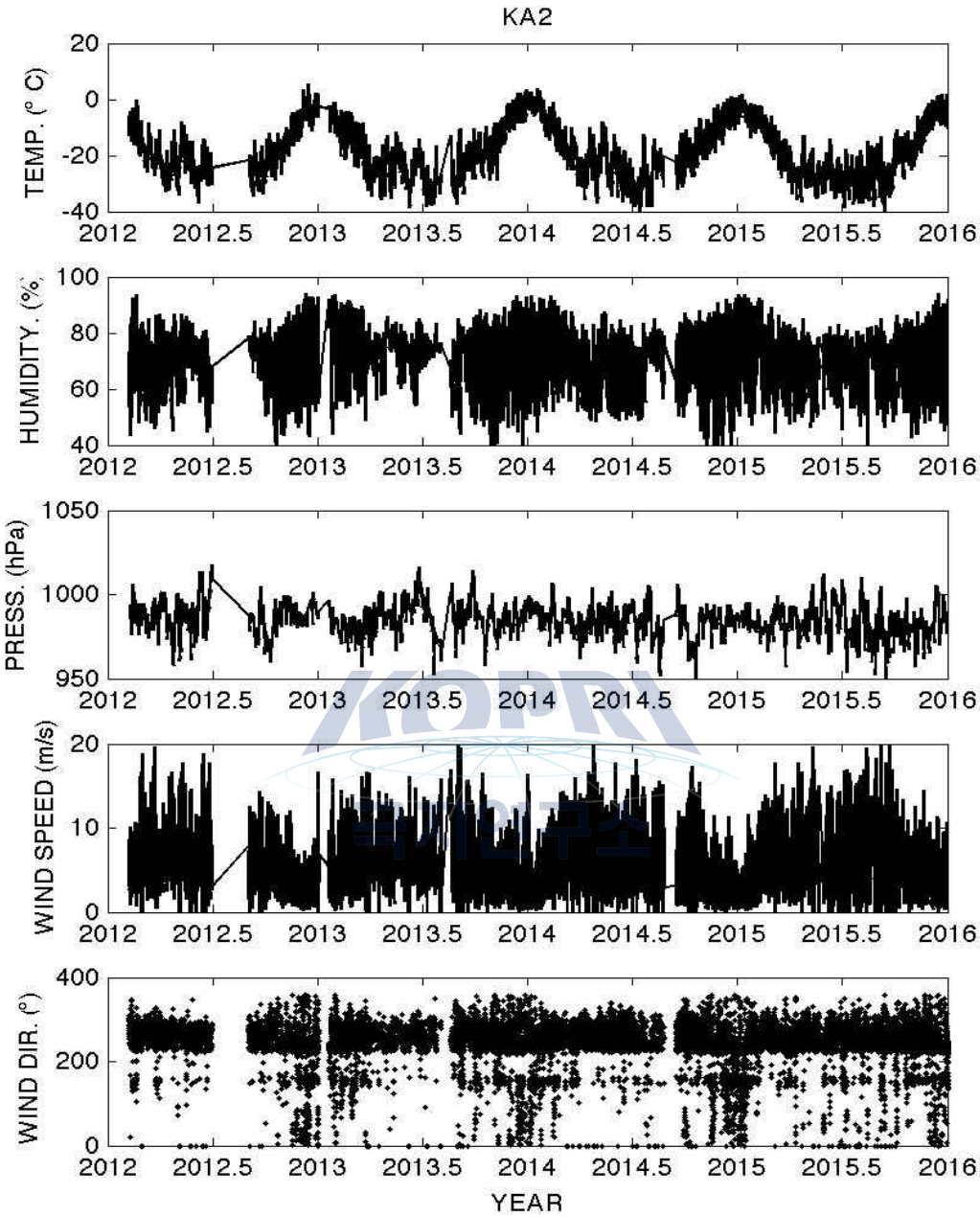

그림 4. KA2의 기상자료

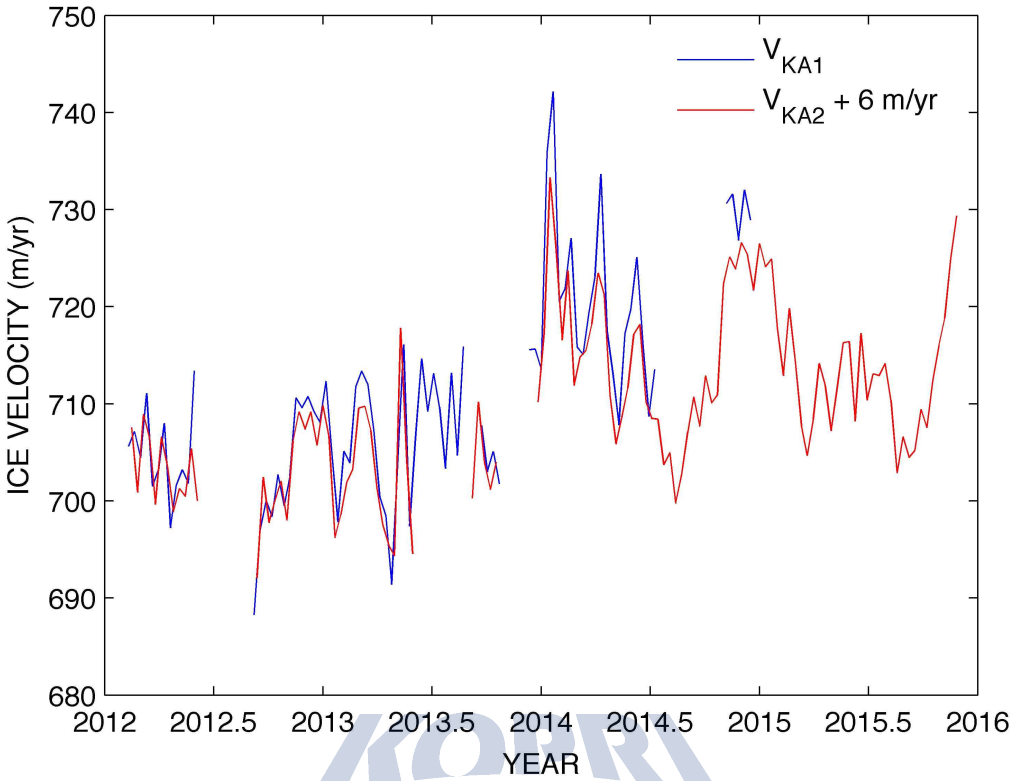

그림 5. 드라이갈스키 빙설의 속도 변화. 비교를 위하여 KA2의 속도에 KA1과 KA2의 평균 속도차인 약 6 m/yr를 더해줌.

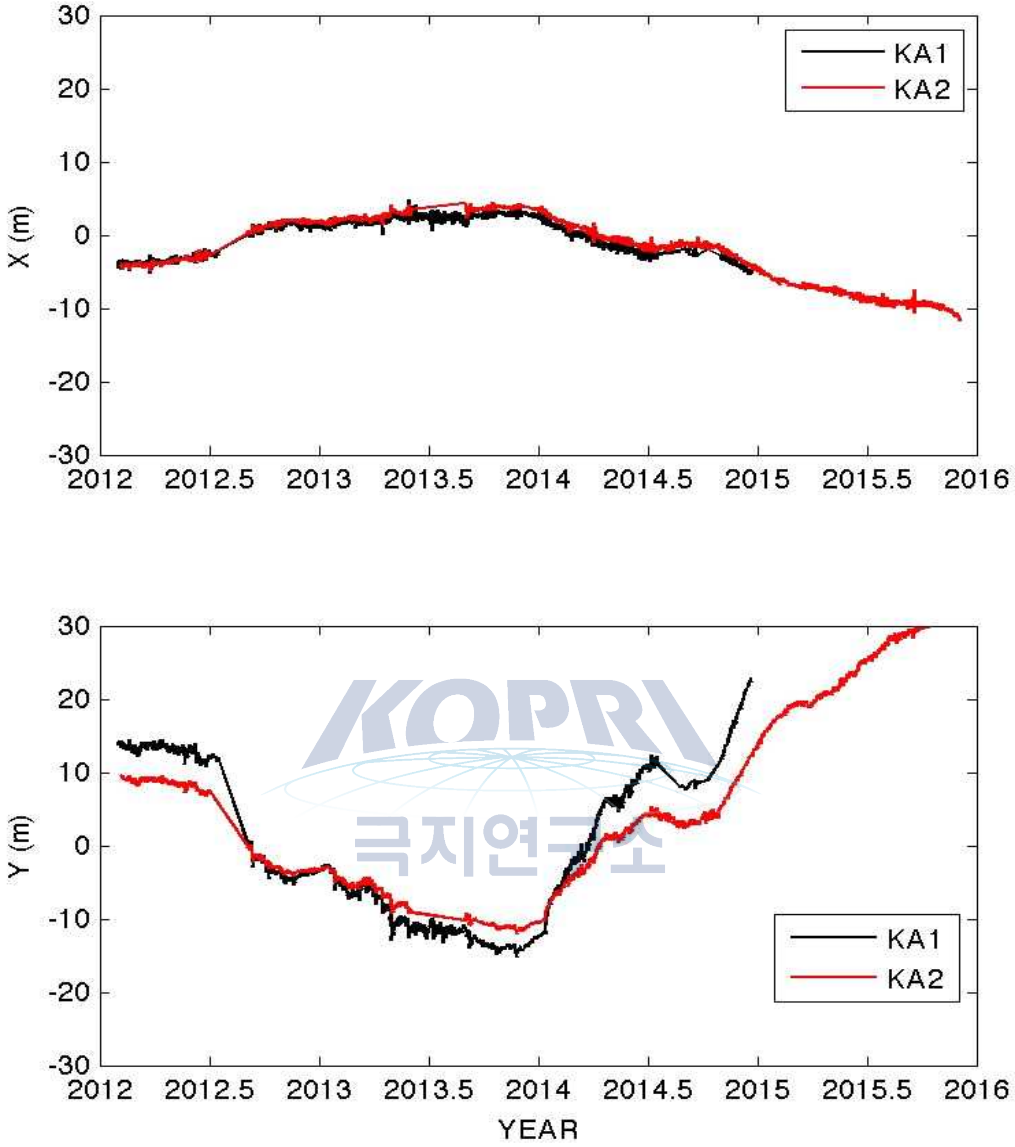

그림 6. 드라이갈스키 빙붕의 평균속도에 의한 이동량을 제거한 잔여 변위량. X와 Y는 polar stereographic coordiante system의 좌표를 의미함.

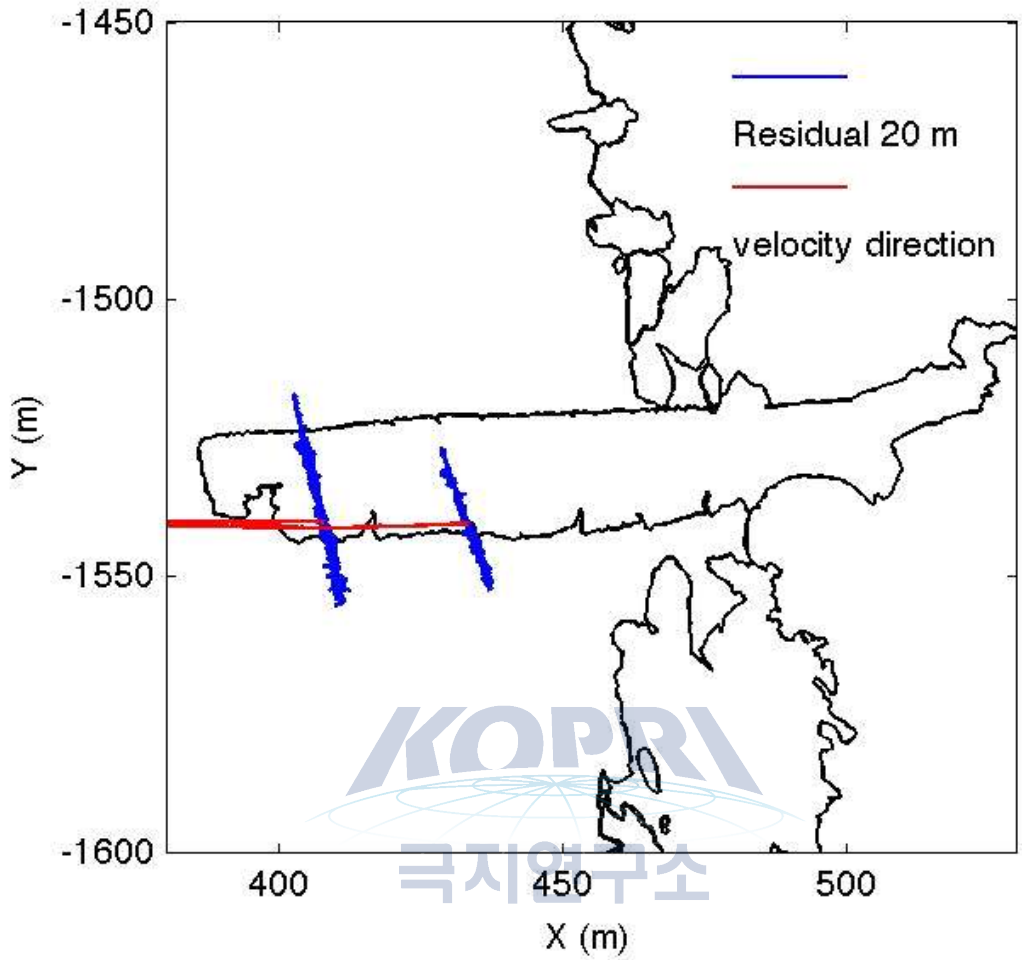

그림 7. 잔여 변위량의 공간적 형태

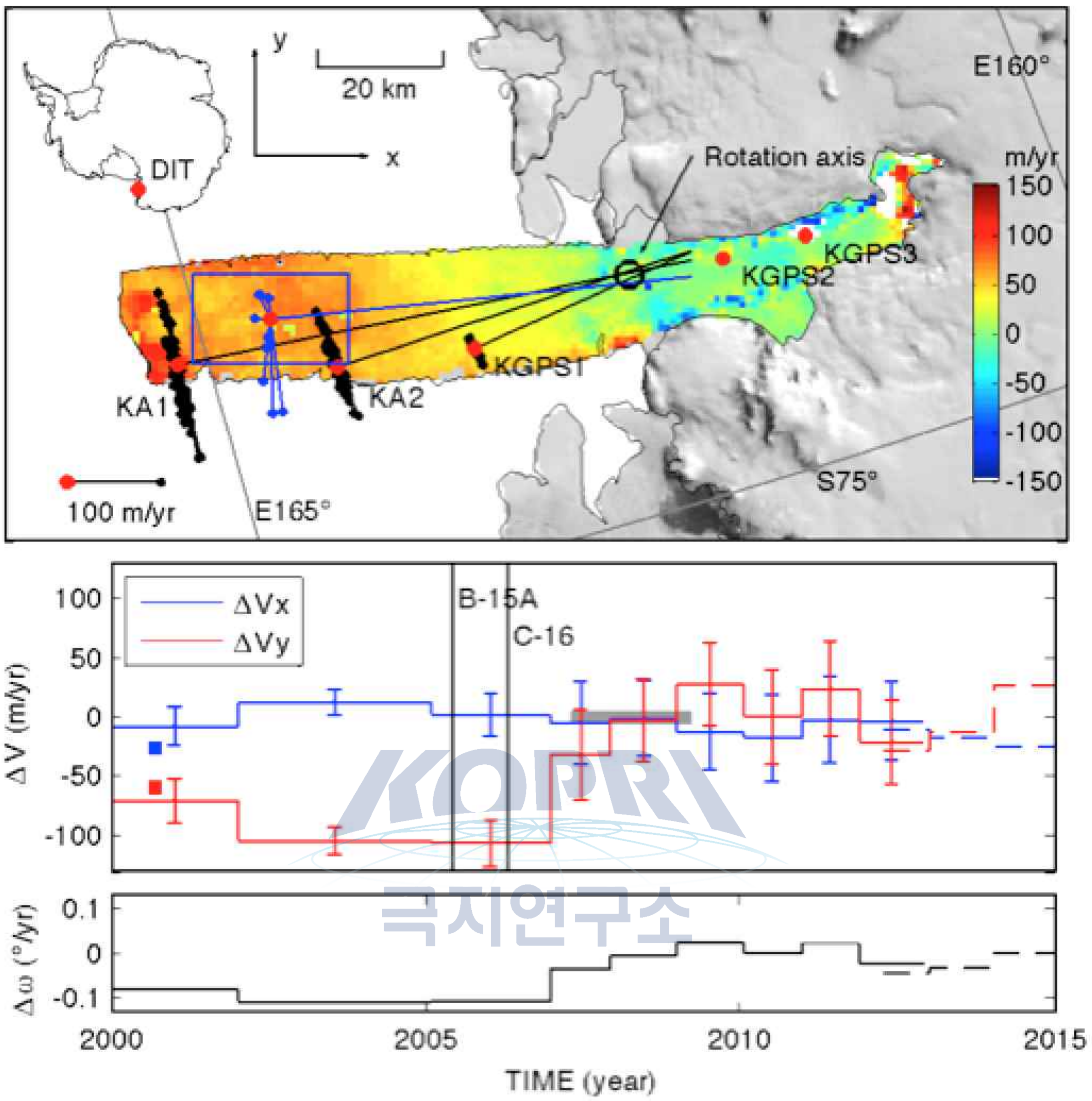

그림 8. (위) 드라이갈스키 빙설의 수평 속도 변화. 빙설에 표시된 색깔은 MEaSUREs와 MAMM InSAR 속도 자료의 y 방향 속도 차이를 표현한다. 흑색점은 GPS 관측자료에서 추출된 20평균 속도의 변화량이며 청색점은 청색 사각형 지역에서 과거 Landsat 위성영상으로부터 계산된 빙설 이동 속도의 변화이다. (중간) Landsat 영상과 KA1 GPS로부터 구한 시간에 따른 속도 변화 양상. 회색 사각형은 MEaSUREs 속도, 사각형은 MAMM 속도를 의미한다. 두 수직선은 B-15A와 C-16 빙산의 충돌 시점을 지시한다. (아래) 흑색점으로 표시된 회전축을 중심으로 한 빙설의 평균 각 속도 변화

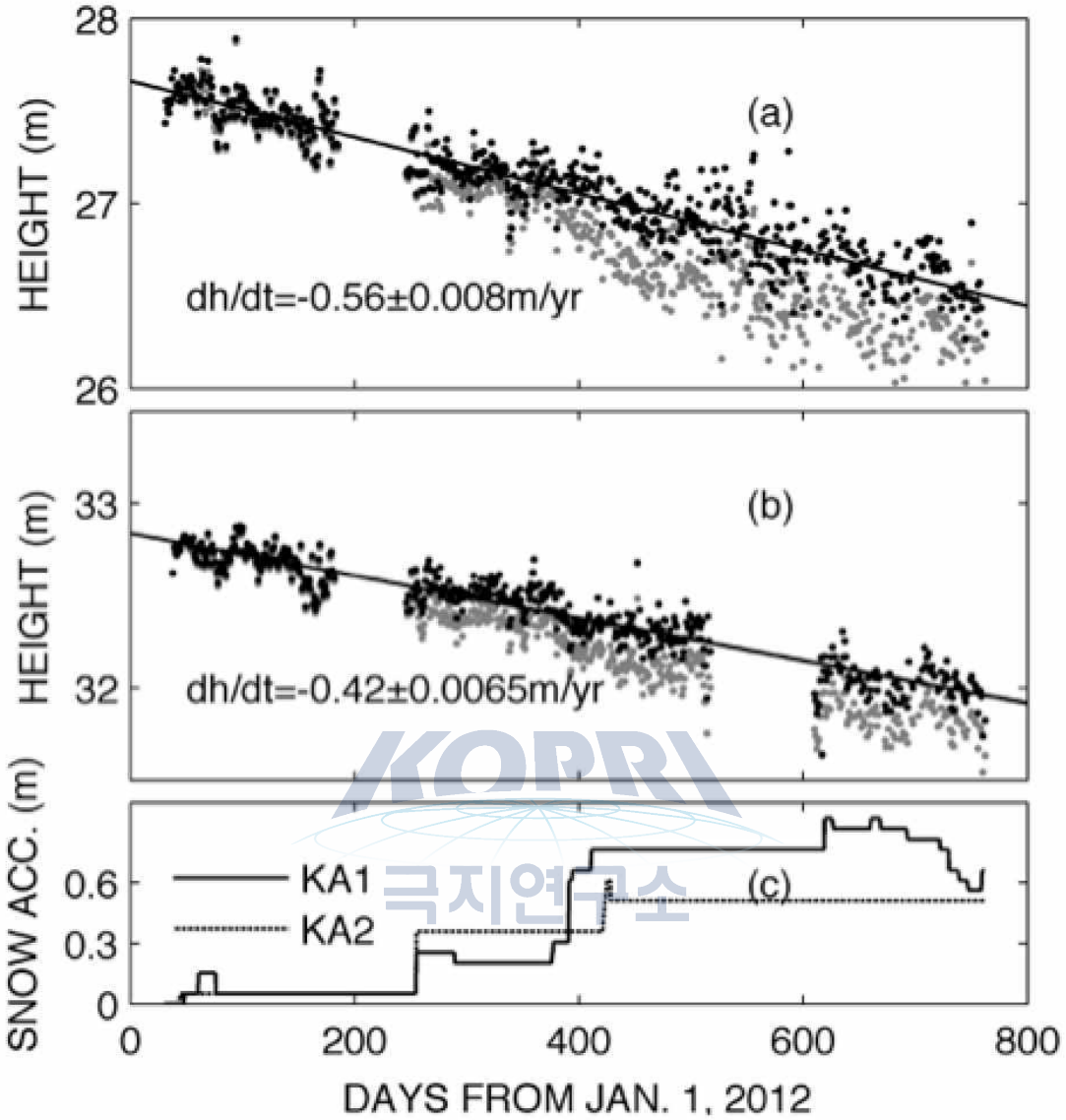

그림 9. KA1과 KA2 측점에서의 표면 고도 변화. 회색점들은 해양조석 및 기압효과를 제거한 GPS 고도를 나타낸다. 적설량은 아미고스 시스템에 장착된 카메라를 통해 관측된 값이다. 흑색점은 적설에 의한 하중 효과를 제거한 표면 고도 변화 양상이다.

그림 10. 난센 빙붕에 설치된 KA6 아미고스, 후방에 관측 대상인 표면 용해호(melt pond)가 보인다.

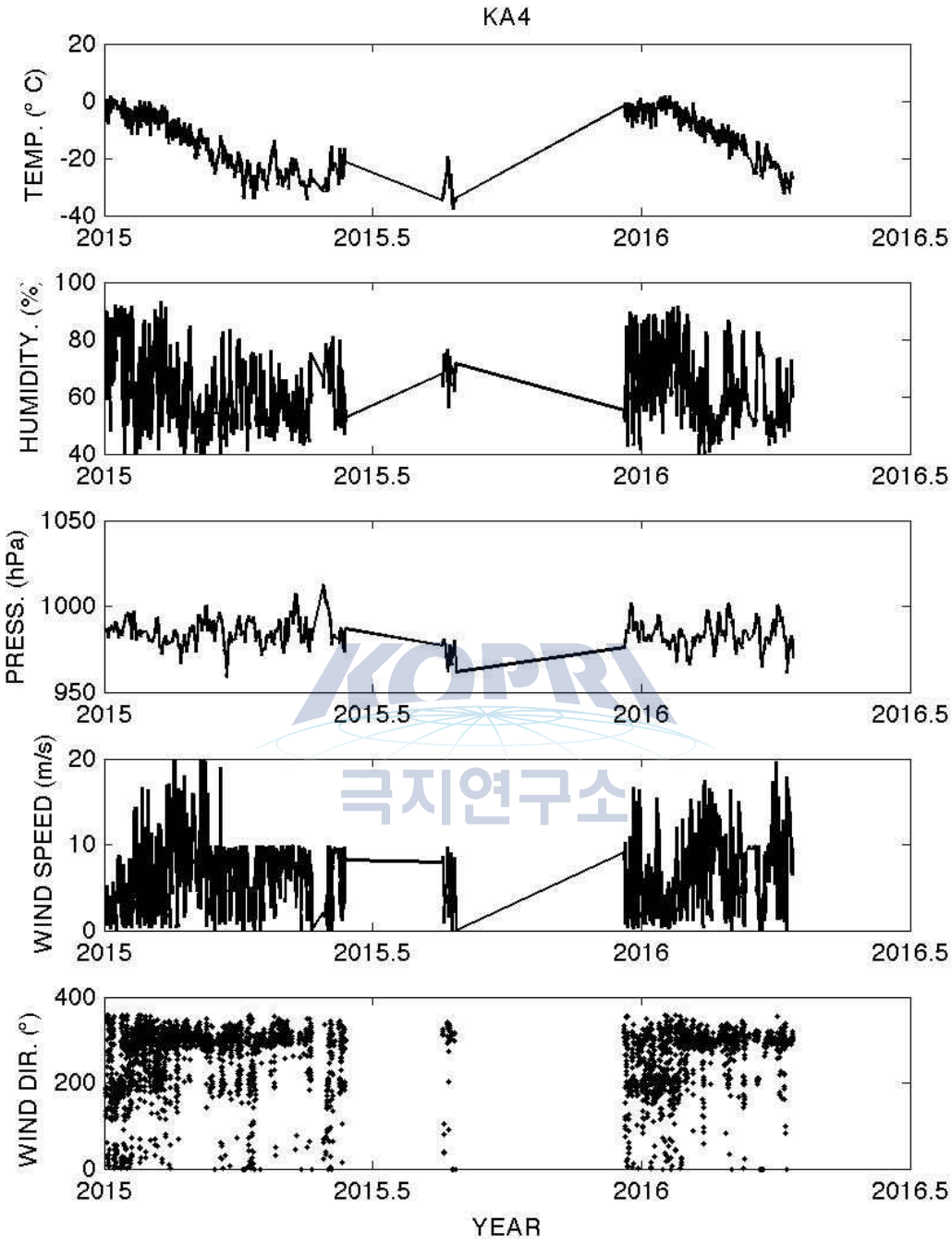

그림 11. 난센빙붕 KA4 측점의 기상자료

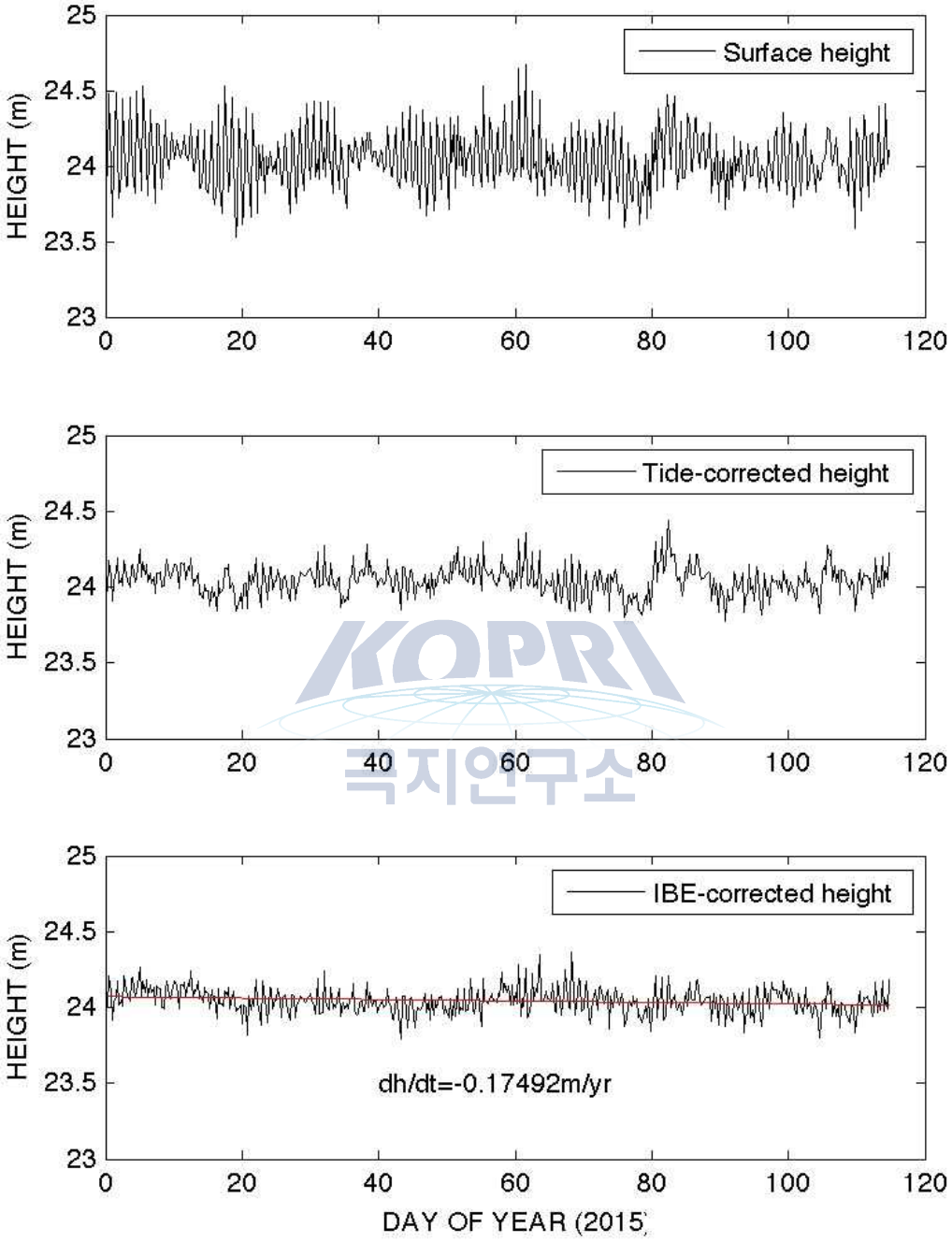

그림 12. KA4에서의 표면 고도 변화 자료. (상) GPS 측정 고도, (중) 조석 보정 후, (하) 기압 보정 후의 표면 고도 변화

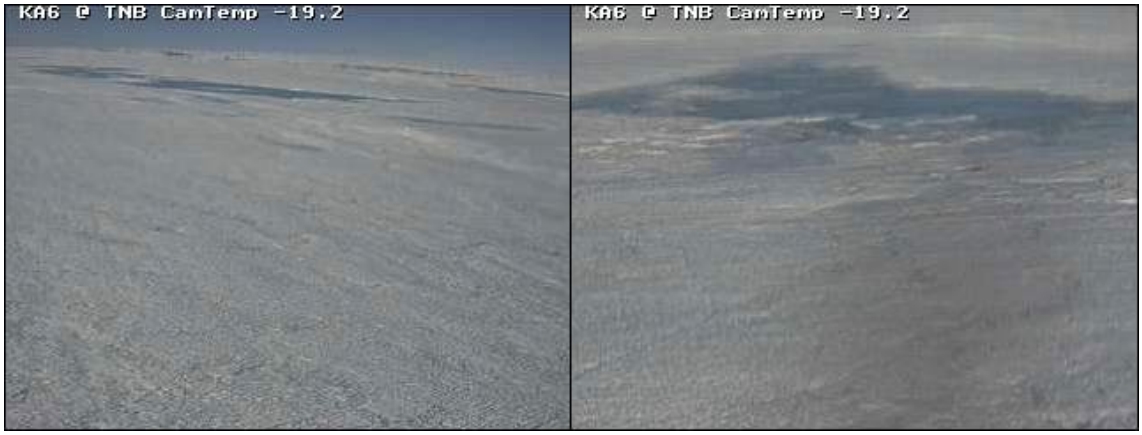

그림 13. KA6에서 관측하는 카메라 영상. 표면 용융에 의해 생기는 표면 융해호를 지속적으로 촬영함.

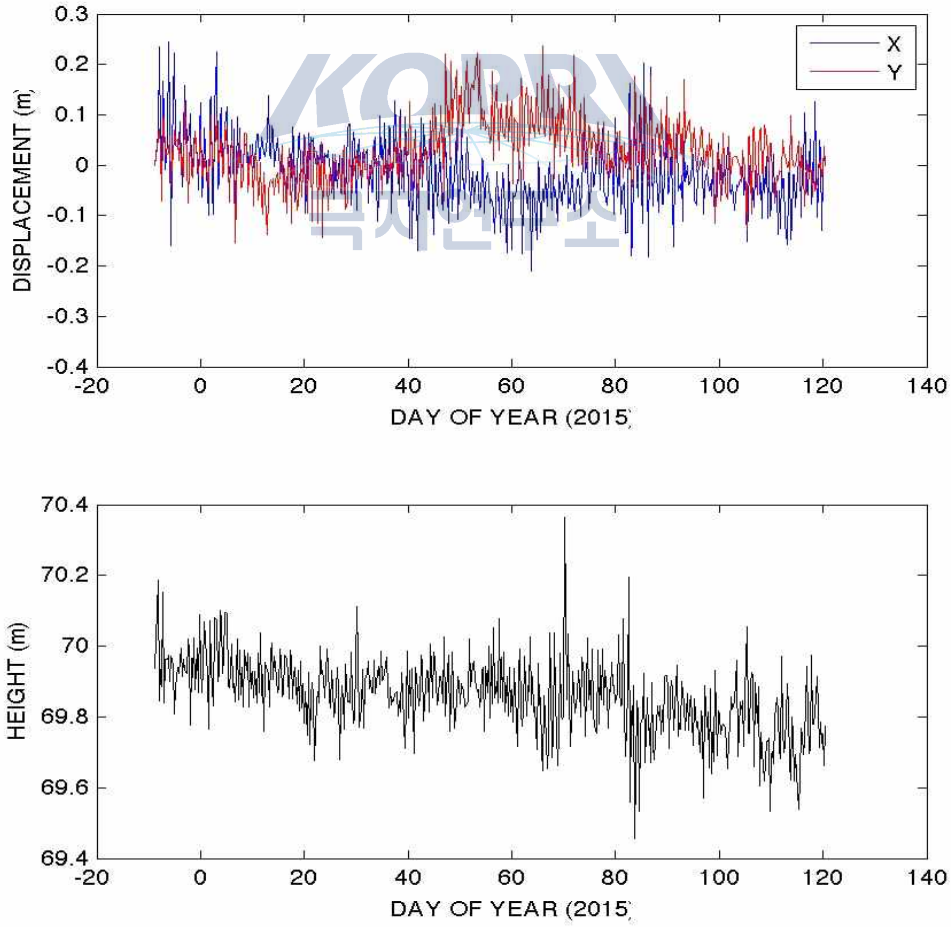

그림 14. (상) 수평 방향의 잔여 변위량, (하) 수직 방향의 표면 고도 변화

제 4 장

남서부 로스해 대륙붕의 아라온 ANA05B 멀티빔 해저 지형 자료 해석[1)]

이재일, 윤호일, 유규철

한국해양과학기술원 부설 극지연구소

요약: 마지막 최대 빙하기 이후 남극 로스해 빙붕 기저부는 대략 남북 방향으로 후퇴한 것으로 생각되어 왔으며 이 가설은 로스해 남서부의 지질학적 증거들을 토대로 서남극 빙상의 후퇴 과정을 해석할 수 있는 근거가 되었다. 로스만에서 바다에 면해있는 빙상의 후퇴 시기와 그 패턴을 보다 정확하게 한정하는 것은 빙붕의 후퇴 기작과 빙붕의 후퇴에 따라 해수면이 얼마나 상승했는지를 이해하는데 있어 중요한 요소이다. 이 보고서에서는 빙하기가 끝난 시점에 동남극으로부터 로스해 쪽으로 흘러온 두꺼운 빙하들이 로스해 남서부의 빙상을 주로 구성하였음을 나타내는 잘 보존된 빙하에 의해 형성된 지형을 확인할 수 있는 새로운 멀티빔 해저지형 자료를 제시하였다. 이 자료들에 의하면 사우스 빅토리아 랜드의 outlet 빙하 계곡은 남동쪽으로 흘렀고 이 방향은 기존의 지질학적 연구결과보다는 서남극 빙상이 로스해 중부에서 홀로세보다 더 일찍부터 후퇴했다는 모델 연구들에서의 후퇴 방향과 잘 맞는다. 이에 따르면 남극횡단산맥의 사면을 따라 나타난 해안가에서의 빙하 후퇴 기록은 로스해에서의 빙하 후퇴의 마지막 부분만을 기록하고 있을 가능성이 높다. 그러므로, 로스해에서 일어난 대규모의 빙상 후퇴의 메커니즘과 정확한 시기를 밝히기 위해서는 로스해 중앙부에서의 연대자료가 필요하다.

1. 서언

2014년 12월부터 2015년 2월까지 극지연구소에서는 로스해 대륙붕 및 심해

1) 이 연구 결과는 다음의 논문으로 2017년 1월 게재승인 되었음: Lee, J.I., McKay, R.M., Golledge, N.R., Yoon, H.I., Yoo, K.-C., Kim, H.J., Hong, J.K. Widespread persistence of expanded East Antarctic glaciers in the southwest Ross Sea during the last deglaciation. Geology.

지역에서 쇄빙연구선 아라온을 이용하여 빙붕 변화 및 고환경 연구를 위한 탐사를 수행하였다 (탐사 번호 ANA05B). 이 탐사 동안 아라온에 장착되어 있는 EM122 멀티빔 해저 지형 탐사 장비를 이용하여 자세한 해저 지형 정보를 획득할 수 있었다. 획득한 멀티빔 해저지형 자료는 CARIS HIPS&SIPS 소프트웨어를 이용하여 처리 후 15m 그리드로 변환하였다. 획득한 지형 자료 중 특히 로스해 남서부 대륙붕 지역에서 획득한 자료로부터 빙하에 의해 형성된 지형을 확인하고 지난 빙하기 이후의 변화를 파악할 수 있는 중요한 단서를 획득할 수 있었다. 이 장에서는 로스해 남서부의 멀티빔 지형 자료를 중심으로 그 의미에 대해 논의하도록 하겠다. 그림 1은 새로 획득한 로스해 남서부 지역에서 새로 획득한 아라온의 멀티빔 해저지형 자료의 위치를 보여주고 있다.

약 2만년 전의 마지막 최대 빙하기 동안 로스해 대륙붕에는 현재보다 더욱 확장된 남극 빙상이 대륙붕의 거의 끝까지 발달하고 있었다 (Anderson et al., 2014). 이 빙상은 동남극 빙상과 서남극 빙상이 로스해 대륙붕에서 합쳐진 형태로 되어 있었다. 로스해 남서부 지역인 사우스 빅토리아 랜드 지역은 미국과 뉴질랜드의 기지가 있는 로스 섬에 가깝기 때문에 비교적 많은 연구가 이루어졌다. 이 지역의 빙하 후퇴 양상이 로스해 다른 지역, 특히 로스해 중심부의 빙하 후퇴와 어떻게 관련이 있는가에 대해서는 논란의 여지가 있다. 이는 맥머도 사운드 주변 지역의 빙하 흐름 양상 해석과 연관이 있다. 로스 섬 주변의 빙퇴석 기원지 연구 결과 LGM 시기의 빙상이 로스해 중앙부에서 로스 섬 북쪽을 지나 남서쪽으로 맥머도 사운드 쪽으로 흘렀다는 주장이 있었다 (Denton and Marchant, 2000). 이런 결과를 바탕으로 로스해 남서부의 빙하 후퇴 양상이 로스해 중앙부와 다른 지역의 빙하 후퇴를 그대로 반영할 것이라는 추정이 가능하다. 하지만 최근의 멀티빔 자료와 퇴적물 코어 연구 결과로는 로스해 중앙부가 로스해 남서부보다 먼저 빙하 후퇴가 일어났으며 서부 해안 쪽의 기록은 지역적인 outlet 빙하들의 기록일 것임이 더 가능성 높아 보인다 (Halberstadt et al., 2016; McKay et al., 2016). 이 경우 남서부 로스해에 존재했던 빙상은 남극횡단산맥을 넘어 동쪽으로 흐른 동남극 빙상의 연장으로, 사우스 빅토리아 랜드의 빙하후퇴 연대는 지역적인 outlet 빙하의 후퇴 시기를 나타내며 로스해 중앙부의 것보다는 훨씬 후의 연대를 지시할 것이다. ANA05B 탐사를 통해 로스해 남서부에서 얻은 새로운 멀티빔 지형 자료는 이런 논란을 해결하는 데 꼭 필요한, 과거 빙하 흐름 방향을 알 수 있는 결정적 자료를 포함하고 있다. 이 장에서는 로스해 남서부의 멀티빔 자료를 바탕으로 해저 지형을 해석하고 그 의미를 토의할 것이다.

2. 해저면 빙하 지형 해석

2.1. 초대형 빙하조선 (MSGL; Mega-Scale Glacial Lineations)

초대형 빙하조선은 길이는 수 킬로미터, 높이는 수 미터, 파장은 수십~수백 미터에 달하는 거대한 곡선의 평행한 언덕들로 이루어진다 (Dowdeswell et al., 2008). 이들은 빠르게 움직이는 빙하 아래에서 변형된 빙퇴석의 일부로 해석된다. 빙하조선은 과거 빙하의 흐름 방향을 명확히 지시하는 구조이다. 드라이갈스키 빙설 남쪽에 있는 모슨 빙하 입구의 해저 지형을 보면 (그림 2) 과거 이 지역에는 지형적으로 두드러진 높은 지역을 중심으로 북동쪽과 동쪽의 두 갈래로 갈라져 흘렀던 빙하가 존재했음을 알 수 있다. 모슨 빙하 입구로부터 동쪽으로 흘렀던 빙하조선은 남쪽으로 150km 이상 추적이 가능하며 처음에는 동쪽으로, 나중에는 남동쪽과 남남동쪽으로 휘어지면서 발달하고 있다 (그림 3). 모슨 빙하의 남쪽에 있는 맥케이 빙하 입구의 Granite Harbor 지역에도 MSGL이 잘 발달하고 있다 (그림 4). 이 지역에서는 수심 700미터 깊이에서 MSGL이 발달하고 있으며 과거 빙하의 흔적이 바다 쪽으로 약 50km 까지 추적 가능하다. 선구조 방향은 맥케이 빙하 입구에서는 남서쪽에서 북동쪽 방향인데 조금 더 바다 쪽으로 가면 보다 동쪽으로 치우치게 된다. 모슨 빙하와 맥케이 빙하로부터 시작된 선구조들은 합쳐져서 동쪽으로 흐른 빙하 흐름을 보인다 (그림 5). 보퍼트 섬 남쪽에서도 남동쪽으로 흐르는 선구조가 발견되며 보다 동쪽으로 가면 이들은 북동쪽으로 휘어 흐르는 경향성을 보이게 된다.

2.2. Grounding-Zone Wedges

Grounding-Zone wedge (GZW)는 단면상에서 봤을 때 비대칭적인 웨지 형태로, 경사면 중 급한 쪽이 빙하가 흘러가는 방향에 해당한다. 빙하가 흘러오는 쪽은 경사가 완만하며 MSGL이 흔히 잘 발달한다. 따라서 MSGL 만으로는 양방향 중 어느 쪽인지를 결정할 수 없으나, GZW이 함께 나타나면 빙하의 흐름 방향을 확정할 수 있다. GZW는 빙하 아래쪽에서 변형된 빙퇴석으로 해석되며 GZW의 정점 위치는 빙하가 후퇴하던 중 잠시 멈추었던 시기의 빙하와 지면의 접점 위치를 반영하는 것으로 알려져 있다 (Batchelor and Dowdeswell, 2015). 맥케이 빙하 동쪽으로는 여러 개의 GZW들이 발견되며 이들은 Granite Harbor로 역추적 가능하다 (그림 4). 이 GZW들은 대개 폭은 10km 미만이지만 비대칭적인 형태로부터 이 골짜기로 전진했던 빙하의 최후 형태는 맥케이 빙하가 확장한 형태였을 것임을 짐작할 수 있

다. 모슨 빙하의 남동쪽에서 GZW들은 규모도 더 크고 더 잘 나타난다 (그림 3). GZW의 stoss 면에는 MSGL이 잘 발달하고 있으며 이들은 GZW와 대략 수직인 방향으로 나타난다. 이곳에서 GZW들은 뒤쪽으로 후퇴하는 형태를 잘 보여주고 있다. MSGL과 GZW 자료들을 종합해 보면 이들은 모슨 빙하 방향으로 후퇴하는 빙하의 흐름을 잘 보여주고 있음을 알 수 있다. 지형적으로 낮은 트러프 지역을 따라 빙하 확장기의 마지막 시기에 모슨 빙하로부터 시작된 빙하의 흐름은 적어도 150km 이상 남동쪽으로 전진하였을 것으로 추정된다.

2.3. Transverse Ridges

GZW와 마찬가지로 transverse ridge들도 MSGL과 거의 수직인 방향성을 보인다. 하지만 이들은 높이가 수 미터 이내로 낮고 부피도 GZW보다 훨씬 적다. 이들은 반복적으로 나타나는 특성이 있는데 파장은 대체로 수십~수백미터 정도가 된다. 이들은 흔히 빠른 후퇴 시기 동안의 연간 ice push를 반영하는 것으로 해석되곤 한다 (Shipp et al., 2002; Dowdeswell et al., 2008). 연구지역에는 Southern Drygalski Trough의 깊은 지역에서 이런 ridge들이 나타난다 (그림 6). 하지만 이 지역에는 형태가 명확한 GZW가 없고 빙하의 흐름 방향을 지시할 만한 다른 구조도 나타나지 않아, 이 ridge를 형성한 빙하의 흐름 방향이나 상대적 시기를 결정하기가 어렵다. 하지만 이 구조가 MSGL 위에 나타나는 점으로 보아 빙상이 타 지역에서는 지면과 접촉해 있으면서 Drygalski Trough의 900미터 이상 깊은 지역 위에 떠 있을 때 형성된 것일 가능성이 있다.

2.4. Channels

로스 섬 부근의 맥머도 사운드 지역에서는 해저면에 channel 시스템이 많은 영역을 차지하고 있으며 빙하 흐름을 지시할 만한 직접적인 구조는 나타나지 않는다 (Greenwood et al., 2012). 이번 연구를 통해 뉴하버 지역에서 100미터 깊이에 1km 폭을 지니면서 깊이 파인, 바닥은 평평하고 옆면은 급경사인 U-자 형태의 channel이 확인되었다 (그림 7). 이 channel은 이 지역의 기반암인 비교적 평평한 plateau를 깎으면서 발달하였는데, 이 plateau에는 미약한 선구조, crag and tail 형태, 그리고 보다 얕게 발달한 channel들이 있는데 이런 것들은 빙하 하부에서 침식된 기반암의 특징이라 할 수 있다 (Pekar et al., 2013). 이 channel은 맥머도 사운드의 깊은 쪽으로 가면서 여러 갈래로 갈라지고 있는데, 이 channel들은 온도가 낮고

퇴적물 함량이 높은 물에 의해 turbidity current가 형성되면서 만들어진 것이라고 제안된 바 있다 (Greenwood et al., 2012). 현재 이 channel들에 turbidity current들이 발생하고 있을 수 있지만 이들 channel 입구에 특별한 fan 구조는 보이지 않으므로 이 channel들이 turbidity current에 의해서만 형성되었다고 보기는 어렵다. Plateau 위에 발달한, 후퇴하는 듯한 ridge들은 Ferrar 빙하 후퇴 시의 proglacial 모레인 퇴적물들로 해석되는데 이런 것들을 보면 channel의 성인을 빙하 기저부에서 만들어진 channel로 보는 것이 더 타당해 보인다. 이런 channel들은 서남극의 대륙붕 안쪽에서 비교적 흔하게 관찰되는데 LGM 이전의 빙하들에 의해 만들어져 이후로도 계속 지속되는 구조일 가능성이 있다 (Graham et al., 2009).

맥머도 사운드 북쪽에는 고저차가 작은 channel 시스템이 발달하고 있는데 이들은 동쪽, 보퍼트 섬 남쪽으로 가면 점차 MSGL로 변하게 된다. 이 channel들은 굴곡이 심하고, 아마도 빙하 하부에서 형성되었을 것으로 해석된 바 있다 (Greenwood et al., 2012). 용융수에 의해 형성되는 channel들은 빙하의 흐름을 직접적으로 지시하지는 않지만 평평한 해저면에 흐르는 meltwater channel들은 전반적으로는 빙상의 표면 경사와 빙하 흐름 방향과 비슷하게 발달한다 (Shreve, 1972).

3. 토의 및 결론

마지막 빙하기 동안 로스해 대륙붕에는 대륙붕단 거의 끝까지 빙상이 발달하였을 것으로 알려져 있으므로, 빙하기 이후 해수면 상승에 대한 남극 비상 용융의 기여 부분 중에서도 로스해 지역의 빙하 후퇴는 상당히 큰 역할을 하였을 것이며 아마도 홀로세 이전의 급격한 해수면 상승에도 일부 기여하였을 것으로 추정된다 (Golledge et al., 2014). 남서부 로스해의 육상에서의 연대측정 결과로는 이 지역에서 대부분의 빙하 후퇴는 홀로세 동안 일어났던 것으로 추정된다 (Denton and Marchant, 2000; Hall et al., 2004; Jones et al., 2015). 이 빙하후퇴시기가 로스해 전역에 걸친 연대와 일치하는가 아니면 지역적인 outlet 빙하의 후퇴 시기를 지시하는가를 결정하는 데는 로스 섬 북쪽의 빙하 흐름 방향이 중요하다. 만약 남서부 로스해의 빙하후퇴 기록인 이 지역의 outlet 빙하의 기록이라면, 로스해의 대부분 지역의 후퇴는 퇴적물 코어 기록과 많은 모델들에서 제시된 바와 같이 홀로세보다 더 먼저 일어났을 것이기 때문이다 (Fig. 1B; Golledge et al., 2014; McKay et al., 2016).

아라온 멀티빔 지형 자료들은 로스해 남서부의 GZW들이 TAM 빙하 방향으로 후퇴하였고, 또한 동남극 빙상의 outlet들이 서부 로스해로, 또 남쪽으로 흘러

로스 섬 방향으로 진행했음을 지시한다. 이는 이 지역에서 과거 빙하 하부에서 형성된 지형에 대한 해석과는 상반되는 것으로 과거에는 빙하의 기원을 특정할 수 없었다 (Greenwood et al., 2012). 따라서 육상 자료에 근거한 빙하 복원 자료와 맞추기 위해, outlet 빙하가 처음에는 TAM으로부터 동쪽으로 진전하였다가 나중에 방향을 정반대로 바꾸어서 로스해 중앙부에 있는 빙상으로부터 북서쪽, 즉 TAM 쪽으로 흘렀다고 해석하였다. 현재 해저면에 보존되어 있는 것은 빙하 이동의 마지막 단계의 기록뿐이지만 과거에 로스해 중앙부에서 북서쪽으로 흘렀던 것으로 해석된 MSGL들이 실제로는 모슨 빙하의 확장에 의해 형성된 것들임이 이번 자료로 명백해졌다. 로스 섬 북쪽에서 빙하 흐름 방향이 반대로 변하는 현상은 발견할 수 없었고 이 지역의 빙하 관련 구조들은 비교적 일관된 빙하 흐름 방향을 반영하는 것으로 보인다 (그림 8).

빙상의 이동 방향은 표면 경사에 의해 좌우되므로, 빙하가 지형적으로 높은 지역을 둘러 흐르는 곡선형의 흐름 형태를 나타내는 것은 비교적 빙상의 경사가 낮았고, 대규모의 "overriding"하는 빙상에 떠밀렸다기 보다는 지형의 영향을 많이 받았음을 지시한다. Denton과 Marchant (2000)는 육상의 기원지 연구에 근거하여 로스해 중앙부에 있던 빙상으로부터 온 북쪽 방향의 흐름에 의해 로스 섬 부근에서 빙하 흐름이 휘어진다고 해석하였는데 이번 연구에서는 그런 현상은 발견할 수 없었다. 이 지역에서 빙하 확장기의 마지막 단계에서 현재 로스해 남서부에 있는 빙하들은 남쪽으로 적어도 100km 이상 로스 섬 방향으로 확장하였고 해저면에 닿았던 것으로 볼 때 두께도 700 미터 이상 되었을 것이다. 이들 outlet 빙하 때문에 isostatic loading의 영향을 받아 사우스 빅토리아 랜드 해안을 따라 융기 해변이 발달할 수 있었을 것으로 보이며, unloading 시기는 대체로 약 7천8백년 쯤이 된다 (Conway et al., 1999; Hall et al., 2004). 맥케이 빙하 가장자리에 발달한 누나택으로부터 측정한 우주기원동위원소 자료를 보면 동남극 outlet 빙하들이 약 7천년 전에 급격하게 얇아졌던 것으로 보이는데, 맥케이 빙하에서 이 시기에는 빙하가 후퇴하면서 해안으로부터 약 70km 떨어진 지형적으로 높은 지역에서 깊은 곳으로 급격히 이동함에 따라 해양 빙상의 불안정성이 발생한 것으로 해석되었다 (Jones et al., 2015). 로스 섬 동쪽의 해양 퇴적물 코어에서는 빙하 후퇴 시기를 이보다 1천6백년 쯤 먼저 일어난 것으로 추정하였는데 (McKay et al., 2016), 이 역시 동남극 outlet 빙상들이 남서부 로스해로 진행했던 시기의 현상들이 로스해 중앙부의 빙상 가설과 무관함을 지시한다. 이런 결과들로 볼 때 보다 큰 규모의 빙상 후퇴 역학을 해석하고자 할 때 구체적인 모델링과 해양 퇴적물 코어 연대 결과를 종합적으로 해석해야 함을 알 수 있다.

멀티빔 자료로는 로스해 중앙부로부터 서쪽으로 흘렀다는 빙하의 흐름을 인지할 수가 없었다. 과거 연구는 anorthoclase phonolite (kenyte) 산출지 및 해안 모레인 내 kenyte 분포에 근거한 기원지 연구 결과에 바탕을 두고 있으므로, kenyte 기원지 문제도 재해석될 필요가 있다. 우선은 산출지로서, 이 암상은 에레부스 산 근처에 널리 퍼져있고 (Esser et al., 2004), kenyte 역은 Cape Bird와 (Denton and Marchant, 2000), Black 섬 (Vella, 1969), 로스 섬 남쪽에서 채취한 앤드릴 AND-1B 코어에서도 발견되므로 Cape Barnes만이 공급지라고 보기는 어렵다. 현재는 얼음으로 덮이거나 남부 맥머도 사운드 해저에 kenyte 산출지가 있을 가능성도 있지만, 여러 곳에서 발견되는 역들은 로스 섬 남쪽에서는 TAM쪽으로, 북쪽에서는 맥케이 빙하와 모슨 빙하로부터의 흐름이 동쪽으로 흘렀던 것으로 해석할 수 있다. 뉴하버 인근에는 남서쪽으로 후퇴하는 proglacial moraine들이 있어 북동 방향으로 흘렀던 빙하가 있었음을 지시하고 있어 kenyte 역의 분포와는 맞지 않는 것처럼 보인다. 여기서는 두 단계의 빙하 흐름을 제시한다. 초기인 최대 빙하기 동안에는 kenyte 역을 운반하던 시기로서 빙하 흐름이 로스 섬에서 뉴 하버 방향으로 진행하였고 이 동안 Ferrar 빙하의 영향은 적었을 것으로 보인다. 이후 맥머도 사운드에서 grounded ice가 물러난 후 Ferrar 빙하는 다시 전진하여 위에 말한 모레인의 흔적을 남기게 되었다.

멀티빔 지형 자료로 보면 남서부 로스해 지역에서 빙하 기록은 동남극 outlet 빙하의 후퇴 기록이며, 중앙부 로스해의 후퇴사와는 무관함을 알 수 있다. 아마도 이미 해양 퇴적물 자료 및 여러 모델 자료에서 제시하듯이, 로스해 중앙부는 로스해 서부보다 수천년 앞서 해빙을 겪었을 것이다 (McKay et al., 2016; Halberstadt et al., 2016). 따라서 중앙부 로스해의 해빙사를 보다 자세히 복원하고 로스해 해빙이 LGM 이후 해수면 상승에 기여한 정도를 정확히 파악하기 위해서는 로스해 서부의 자료보다는 로스해 중앙부에서 믿을 수 있는 연대 측정 자료를 획득하는 것이 필수적이다.

Multibeam bathymetry of the southwestern Ross embayment - Araon ANA05B cruise

Jae Il Lee, Ho Il Yoon, Kyu-Cheul Yoo

Korea Polar Research Institute

Abstract: It has been suggested that the grounding line of the Last Glacial Maximum (LGM) ice sheet in the Ross Sea, Antarctica, receded in an approximately north-to-south pattern during the Holocene. An implication of this hypothesis is that geological evidence from the southwestern Ross Sea has been used widely to interpret retreat histories of the West Antarctic Ice Sheet (WAIS) across the wider Ross Sea embayment. Accurately constraining the timing and pattern of marine-based ice sheet retreat in this embayment is critical to understanding the drivers that may have triggered this event, and its contribution to rapid sea-level rise events. Here, we present new multibeam swath bathymetry data that identifies well-preserved glacial features indicating that thick (>700 m) marine-based ice derived from the East Antarctic Ice Sheet coastal outlet glaciers dominated the ice sheet input into the southwestern Ross Sea during the last phases of glaciation. Subglacial geomorphic features indicate that ice derived from present outlet glacier valleys in South Victoria Land flowed southeastward. This is more consistent with flowlines from model-based interpretations of an earlier retreat of the WAIS in the central Ross Sea than with previous land-based geological reconstructions. This implies that coastal records of deglaciation along the Transantarctic Mountains front record only the final phases of glacial retreat in the Ross Sea. Therefore, chronological data from the central embayment are required to accurately constrain the timing of large scale glacial retreat in the Ross Sea and to identify the mechanisms that drove it.

참고문헌

Anderson, J.B., Conway, H., Bart, P.J., Witus, A.E., Greenwood, S.L., McKay, R.M., Hall, B.L., Ackert, R.P., Licht, K., Jakobsson, M., and Stone, J.O., 2014, Ross Sea paleo-ice sheet drainage and deglacial history during and since the LGM: Quaternary Science Reviews, v. 100, p. 31-54, doi:10.1016/j.quascirev.2013.08.020.

Batchelor, C.L., and Dowdeswell, J.A., 2015, Ice-sheet grounding-zone wedges (GZWs) on high-latitude continental margins: Marine Geology, v. 363, p. 65-92, doi: 10.1016/j.margeo.2015.02.001.

Conway, H., Hall, B.L., Denton, G.H., Gades, A.M., and Waddington, E.D., 1999, Past and Future Grounding-Line Retreat of the West Antarctic Ice Sheet: Science, v. 286, p. 280-283, doi:10.1126/science.286.5438.280.

Davey, F., 2004, Ross Sea Bathymetry, version 1.0, Institute of Geological and Nuclear Sciences Geophysical Map 16: Lower Hutt, New Zealand, Institute of Geological and Nuclear Sciences Ltd, scale 1:2,000,000.

Denton, G.H., and Marchant, D.R., 2000, The Geologic Basis for a Reconstruction of a Grounded Ice Sheet in McMurdo Sound, Antarctica, at the Last Glacial Maximum: Geografiska Annaler. Series A. Physical Geography, v. 82, p. 167-211, doi:10.1111/j.0435-3676.2000.00121.x.

Dowdeswell, J.A., Ottesen, D., Evans, J., Cofaigh, C.?., and Anderson, J.B., 2008, Submarine glacial landforms and rates of ice-stream collapse: Geology, v. 36, p. 819-822, doi:10.1130/G24808A.1.

Esser, R.P., Kyle, P.R., and McIntosh, W.C., 2004, 40Ar/39Ar dating of the eruptive history of Mount Erebus, Antarctica: volcano evolution: Bulletin of Volcanology, v. 66, p. 671-686, doi:10.1007/s00445-004-0354-x.

Golledge, N.R., Menviel, L., Carter, L., Fogwill, C.J., England, M.H., Cortese, G., and Levy, R.H., 2014, Antarctic contribution to meltwater pulse 1A from reduced Southern Ocean overturning: Nature Communications, v. 5, doi:10.1038/ncomms6107.

Graham, A.G.C., Larter, R.D., Gohl, K., Hillenbrand, C.-D., Smith, J.A., and Kuhn, G., 2009, Bedform signature of a West Antarctic palaeo-ice stream reveals a multi-temporal record of flow and substrate control: Quaternary

Science Reviews, v. 28, no. 25-26, p. 2774-2793, doi: 10.1016/j.quascirev.2009.07.003.

Greenwood, S.L., Gyllencreutz, R., Jakobsson, M., and Anderson, J.B., 2012, Ice-flow switching and East/West Antarctic Ice Sheet roles in glaciation of the western Ross Sea: Geological Society of America Bulletin, doi:10.1130/B30643.1.

Halberstadt, A.R., Simkins, L.M., Greenwood, S.L., and Anderson, J.B., 2016, Past Ice-Sheet Behaviour: Retreat Scenarios and Changing Controls in the Ross Sea, Antarctica: The Cryosphere Discussions, p. 1-36, doi:10.5194/tc-2016-33.

Hall, B.L., Baroni, C., and Denton, G.H., 2004, Holocene relative sea-level history of the Southern Victoria Land Coast, Antarctica: Global and Planetary Change, v. 42, p. 241-263, doi:10.1016/j.gloplacha.2003.09.004.

Hall, B.L., Denton, G.H., Heath, S.L., Jackson, M.S., and Koffman, T.N.B., 2015, Accumulation and marine forcing of ice dynamics in the western Ross Sea during the last deglaciation: Nature Geoscience, v. 8, p. 625-628, doi:10.1038/ngeo2478.

Jones, R.S., Mackintosh, A.N., Norton, K.P., Golledge, N.R., Fogwill, C.J., Kubik, P.W., Christl, M., and Greenwood, S.L., 2015, Rapid Holocene thinning of an East Antarctic outlet glacier driven by marine ice sheet instability: Nature Communications, v. 6, p. 8910, doi:10.1038/ncomms9910.

McKay, R., Golledge, N.R., Maas, S., Naish, T., Levy, R., Dunbar, G., and Kuhn, G., 2016, Antarctic marine ice-sheet retreat in the Ross Sea during the early Holocene: Geology, v. 44, p. 7-10, doi:10.1130/G37315.1.

Pekar, S.F., Speece, M.A., Wilson, G.S., Sunwall, D.S., and Tinto, K.J., 2013, The Offshore New Harbour Project: deciphering the Middle Miocene through Late Eocene seismic stratigraphy of Offshore New Harbour, western Ross Sea, Antarctica: Geological Society, London, Special Publications, v. 381, no. 1, p. 199-213, doi: 10.1144/SP381.2.

Shipp, S.S., Wellner, J.S., and Anderson, J.B., 2002, Retreat signature of a polar ice stream: sub-glacial geomorphic features and sediments from the Ross Sea, Antarctica: Geological Society of London, Special Publications, v. 203, p. 277-304, doi:10.1144/GSL.SP.2002.203.01.15.

Shreve, R.L., 1972, Movement of Water in Glaciers*: Journal of Glaciology, v. 11, p. 205-214, doi:10.3198/1972JoG11-62-205-214.

Vella, P., 1969, Surficial geological sequence, Black Island and Brown Peninsula, McMurdo Sound, Antarctica: New Zealand Journal of Geology and Geophysics, v. 12, p. 761-770, doi:10.1080/00288306.1969.10431110.

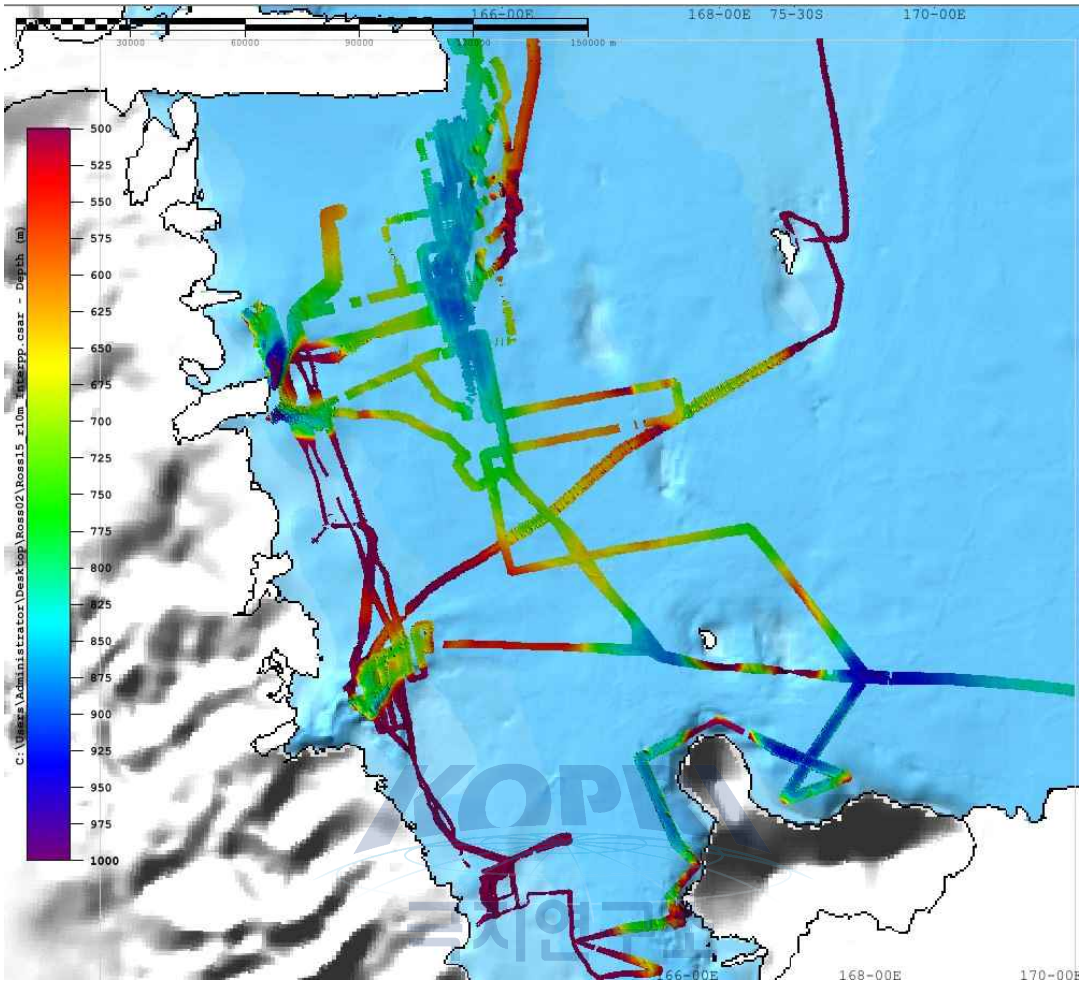

그림 1. 로스해 남서부 대륙붕 지역에서 새로 획득한 아라온의 멀티빔 해저지형 자료의 위치.

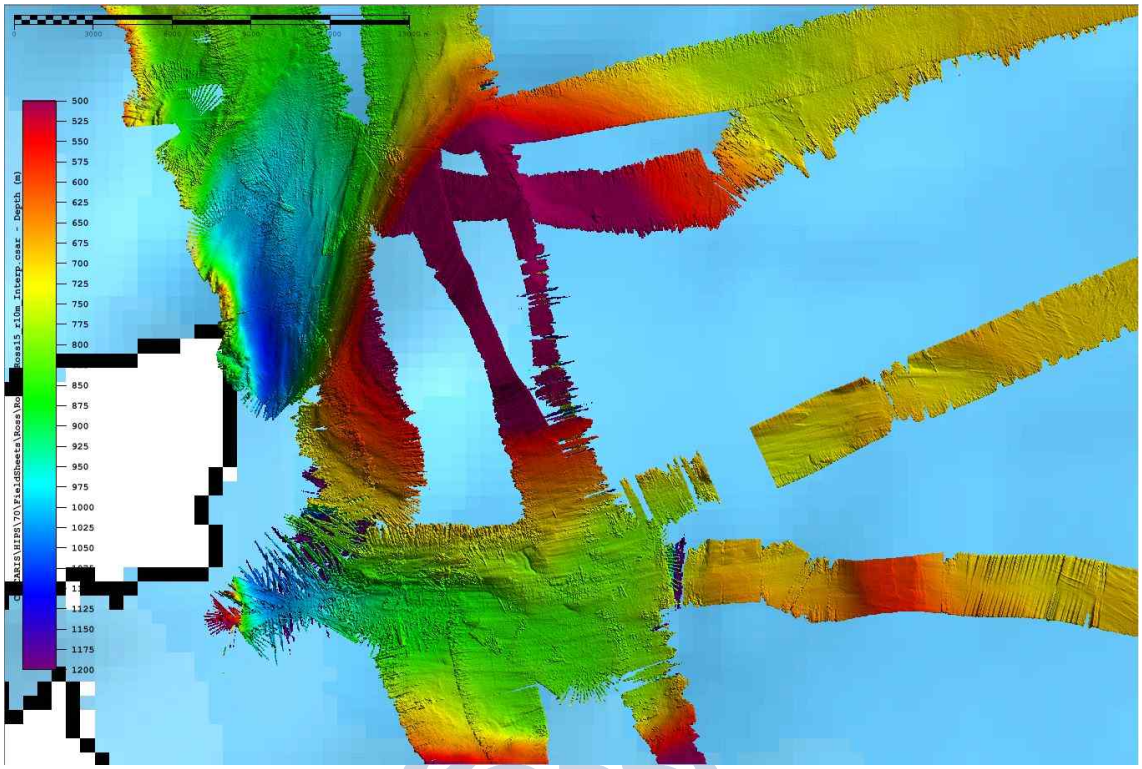

그림 2. 모슨 빙하 입구의 멀티빔 해저지형. 초대형 빙하조선 (MSGL) 방향으로 보면 과거 해저면에 닿았던 빙하는 북동쪽과 동쪽의 두 방향으로 갈라져 흘렀던 것을 알 수 있다.

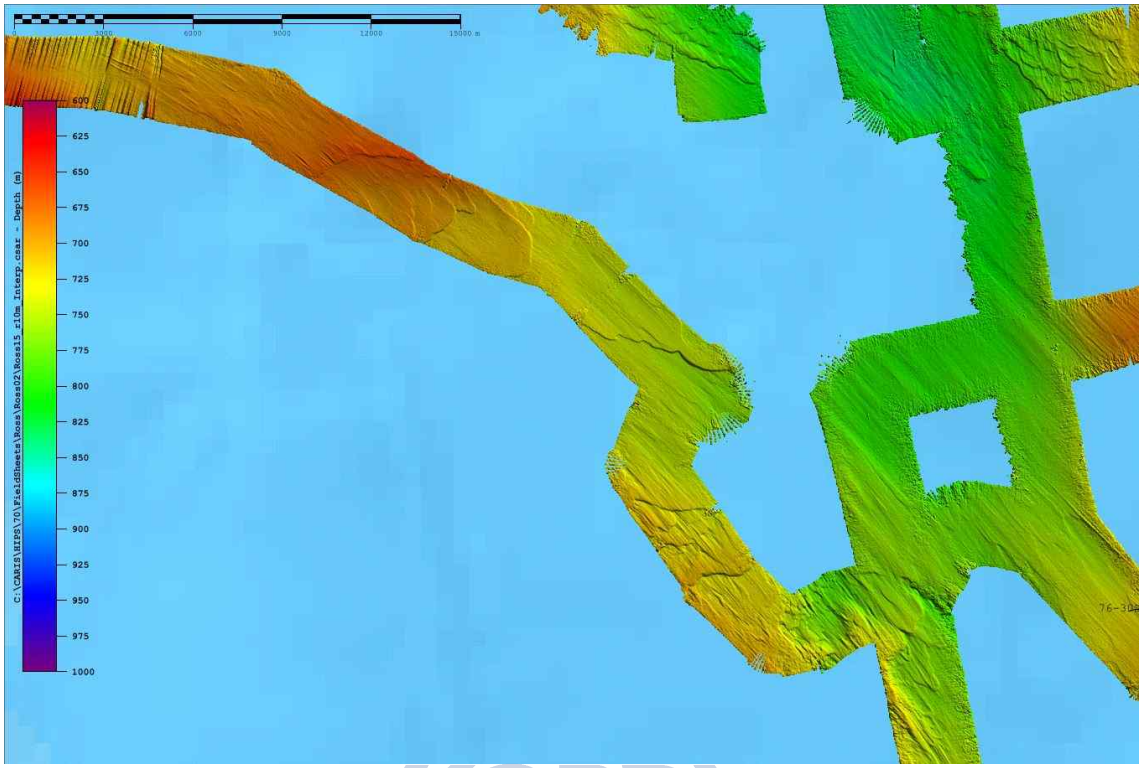

그림 3. 모슨 빙하로부터 남동쪽 방향 해저면의 해저지형. MSGL과 GZW가 잘 발달해 있다. 빙하의 흐름은 북서쪽에서 남동쪽 방향으로 흘렀다.

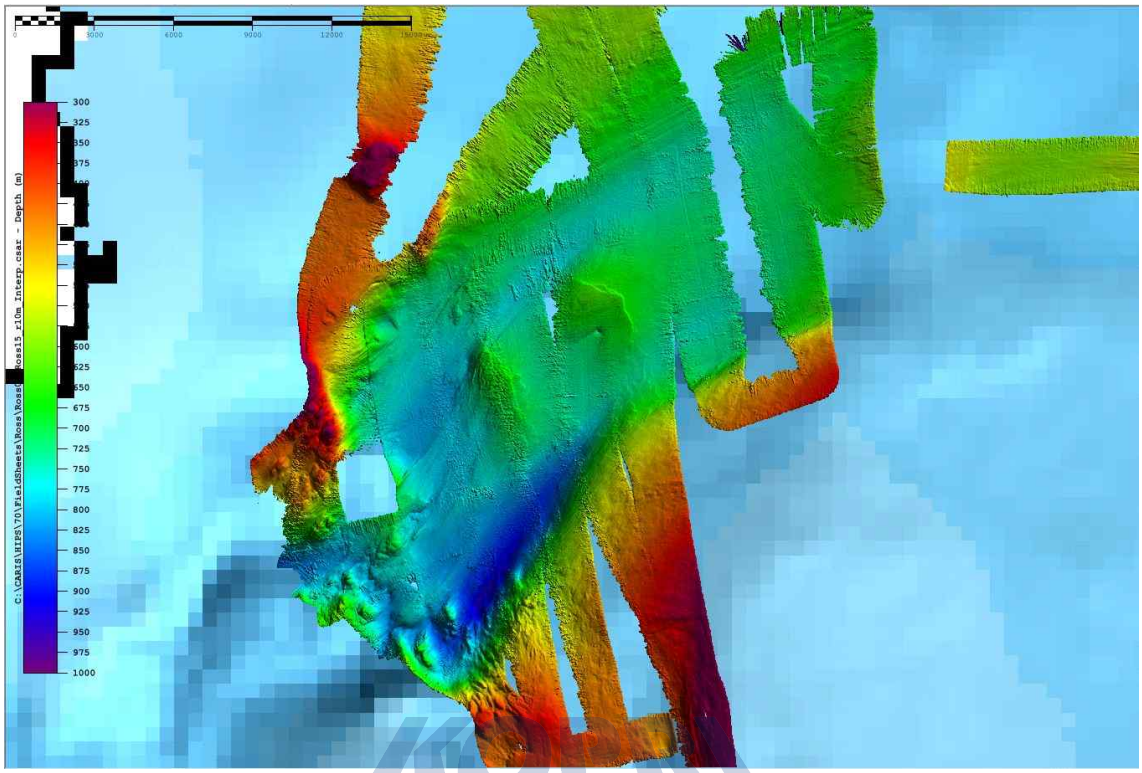

그림 4. Granite Harbor 지역의 멀티빔 해저 지형. MSGL과 Grounding Zone Wedge 구조가 잘 나타난다. 빙하의 흐름은 남서에서 북동쪽 방향이며 좀 더 먼 바다 쪽에서는 동쪽으로 움직였음을 볼 수 있다.

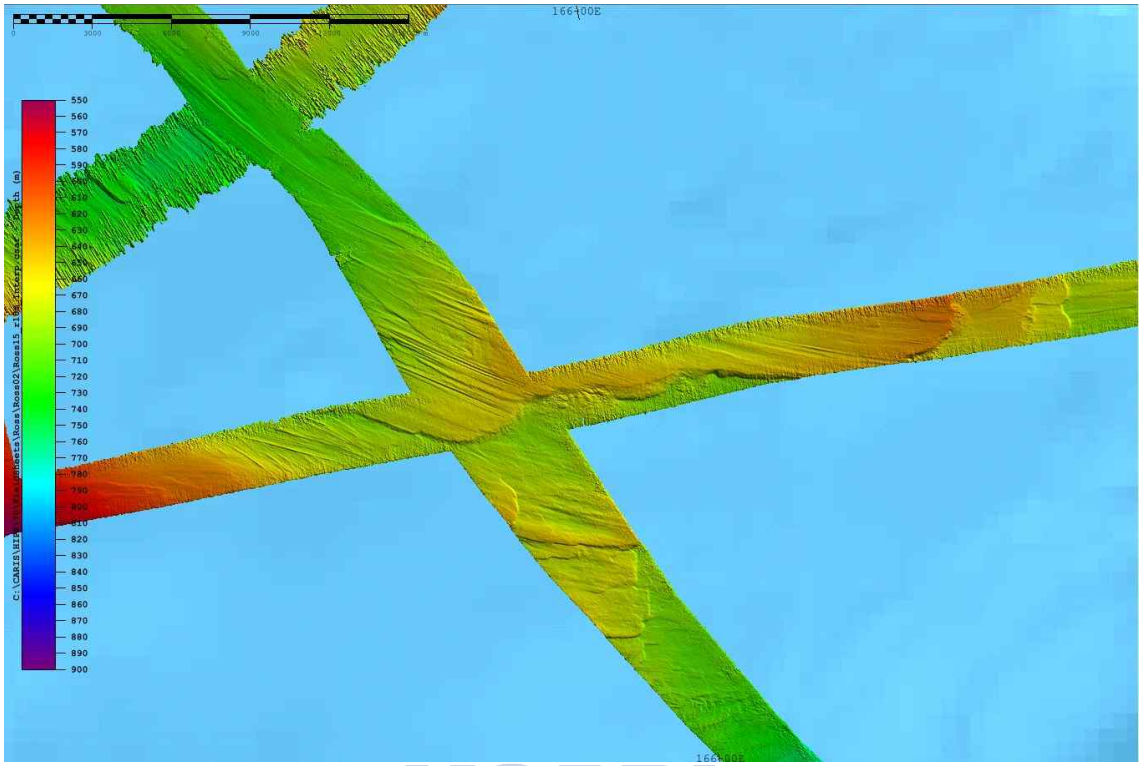

그림 5. 그림 3의 더 남동쪽 지역, 그림 4의 동쪽에서 보이는 해저지형. Grounding zone wedge가 잘 발달하고 있으며, 모슨 빙하로부터 흘러온 남동쪽 방향의 빙하 흐름과 맥케이 빙하로부터 흘러온 동쪽 방향의 빙하 흐름이 합쳐지고 이후로 동쪽으로 빙하가 흘렀음을 알 수 있다.

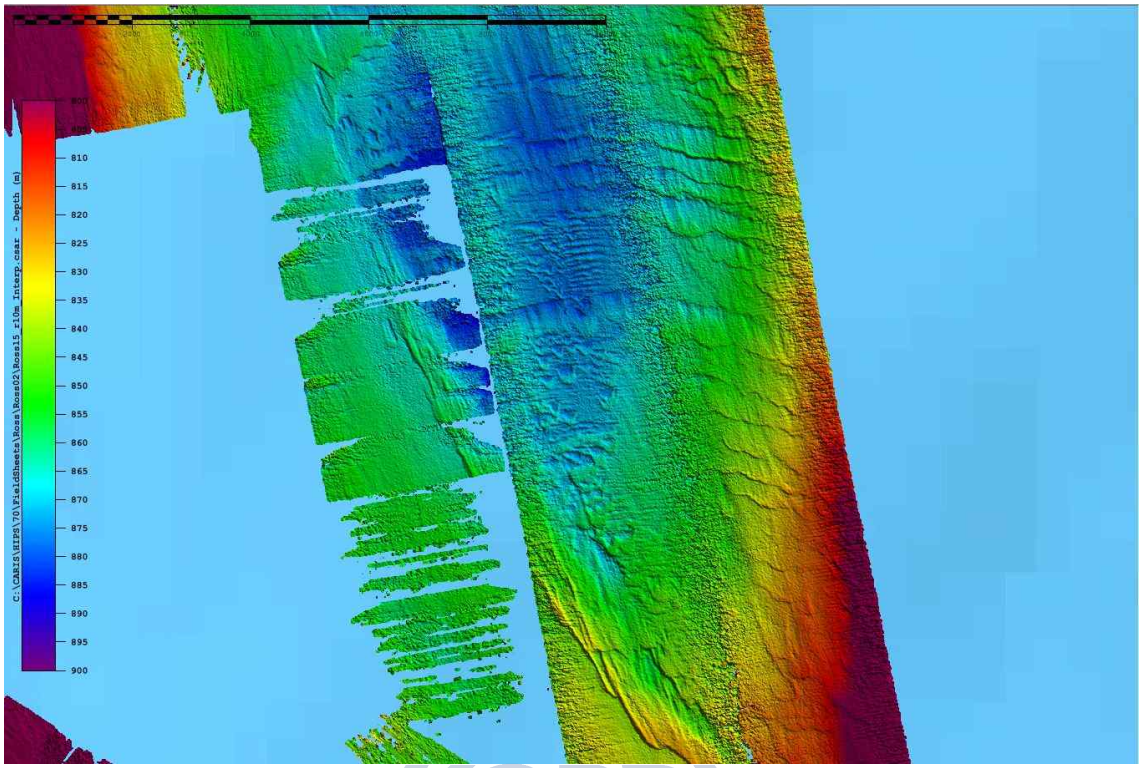

그림 6. Southern Drygalski Trough에 발달하는 transverse ridges.

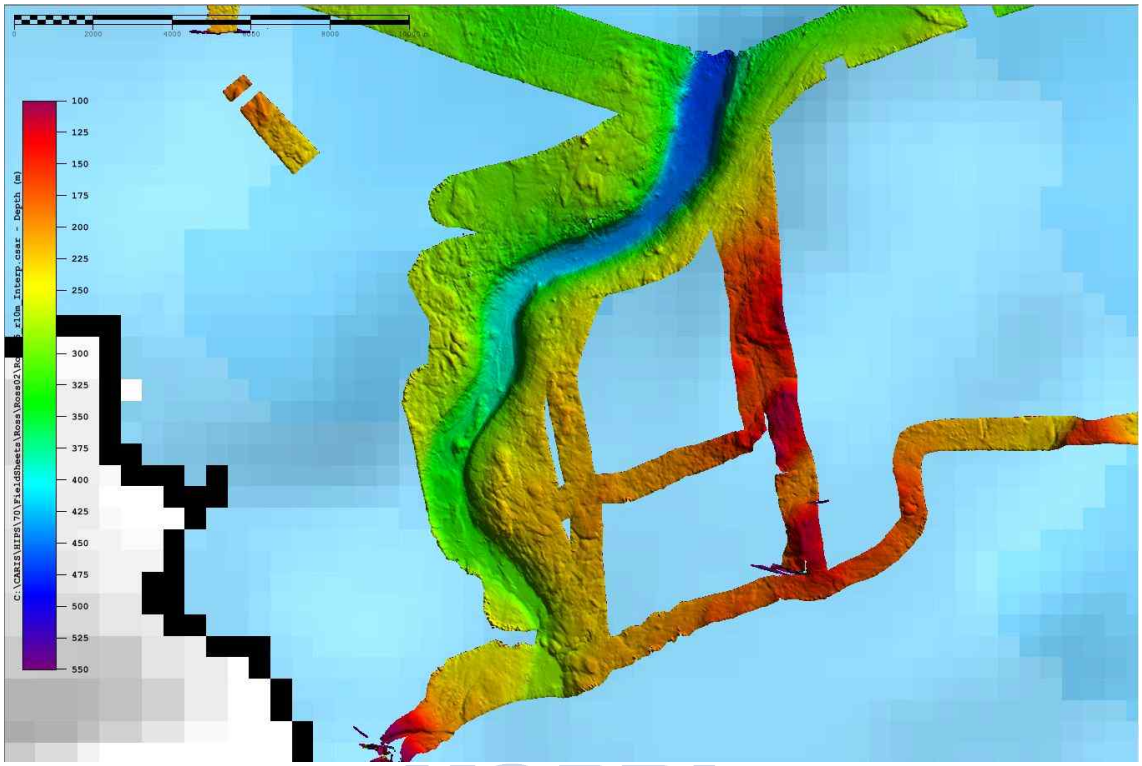

그림 7. New Harbor 근처 해저면에 발달한 U-자 형의 channel.

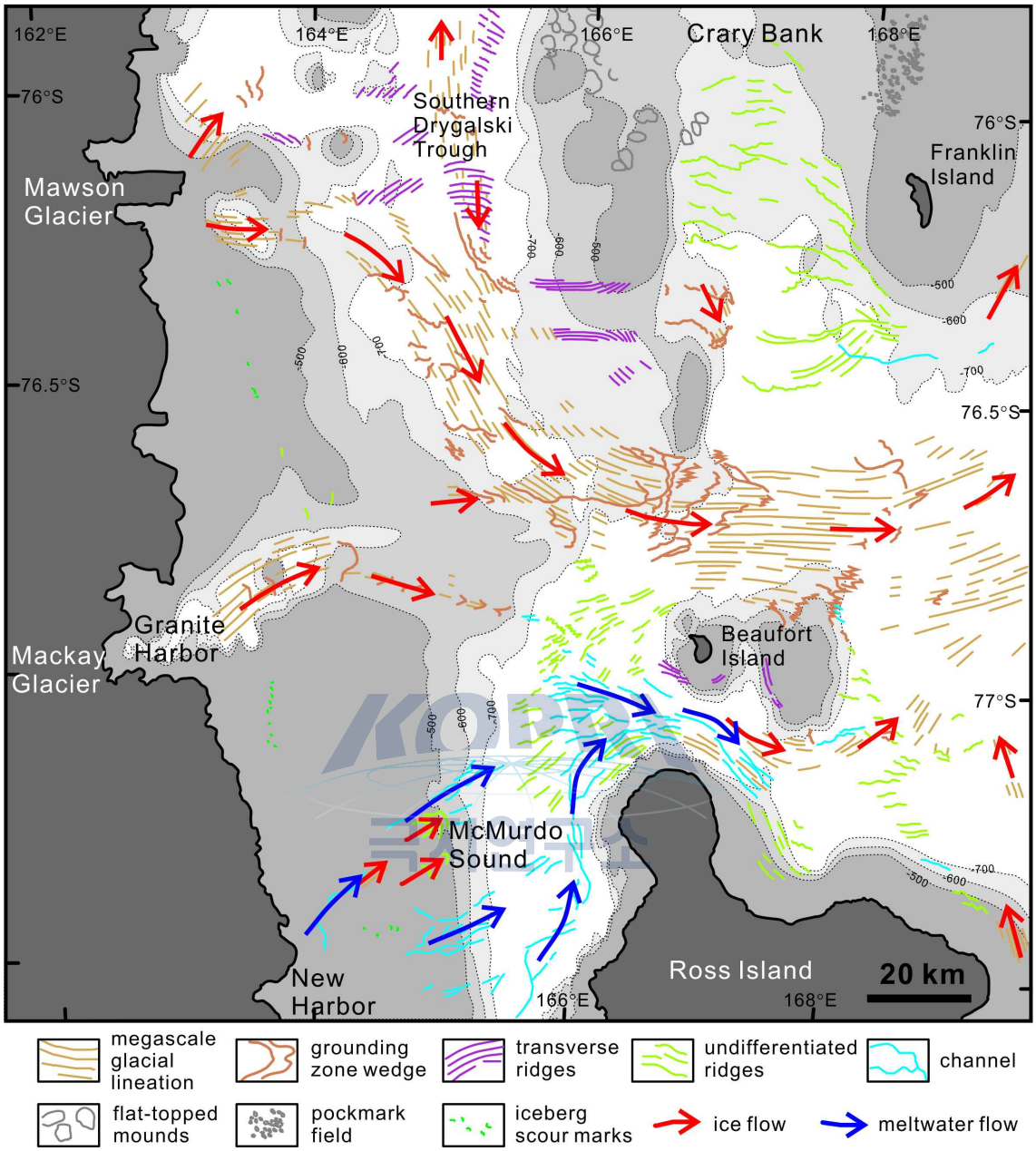

그림 8. 멀티빔 지형자료를 근거로 해석한 마지막 빙하 확장기의 빙하 및 융빙수 흐름 방향 해석.

제 5 장

코어 퇴적물에 나타난 LGM 이후 라슨 C 빙붕의 변화

유규철, 이재일, 김기태, 이민경, 윤호일

한국해양과학기술원 부설 극지연구소

요약: 라슨 C 빙붕에서 획득된 코어 EAP13-GC16B에서 퇴적학적/지화학적/동위원소 분석과 약 10 cm 길이 구간으로 만들어진 슬랩 퇴적물의 이미지 분석을 통해 지난최대빙하기 이후 라슨 C 해역의 빙하 및 빙붕의 변화를 유추하였다. 남극해 빙붕 해역의 지난최대빙하기 이후 기존의 과거 복원들이 매우 제한적이었지만, 라슨 C 코어에 나타난 층리 구조들은 지난최대빙하기 이후 육상빙하의 빙붕 형성과 빙붕단의 변화들을 자세하게 복원할 수 있었다. 라슨 빙붕 북단에 위치한 제임스 로스 섬의 빙하 코어에서 복원된 고해상도 고수온 자료는 이러한 변화들을 유추하는데 큰 도움을 주었다.

1. 서론

라슨 빙붕은 북서 웨델해에 위치하고 있는 길게 연안과 연결된 빙붕이며, 케이프 롱잉(Cape Longing)에서 히어스트 섬(Hearst Island) 남단까지 이어지는 남극반도 동부 연안을 따라 확장되어있다. 이 빙붕은 연안을 따라 특징적인 만들이 차지하고 있는 일련의 빙붕들이며, 구획별로 라슨 A, B, C, D, E, F 그리고 G로 명명되어진다. 현재까지 쇄빙연구선을 통해 이루어진 라슨 빙붕 해양 연구는 라슨 빙붕 C 해역 일부까지 이루어졌고 웨델해에 존재하는 두텁고 많은 얼음들로 인해 나머지 라슨 빙붕 해역들은 탐사된 적이 없다.

실제 라슨 빙붕 해양 연구가 과학계에 관심을 끌게 된 것은 1995년 라슨 빙붕 A의 붕괴가 보고되고(Fox, 2012), 2002년 라슨 빙붕 B가 붕괴되면서 새로운 해양 탐사 영역이 나타난 결과이다. 이러한 붕괴는 현재까지 지속되는 남극반도의 지역적인 온난화로 인한 결과로 사실상 지난 1940년대 이후 매십년 약 0.5℃ 증가한 것으로 알려져 있다(Connor, 2005). 2006년 대기 연구 결과에 따르면(Marshall et

al., 2006), 남극반도 패러데이 기지(Paraday Station)의 대기온도는 1951년부터 2004년까지 2.94℃ 증가하였고, 이는 전지구 관측보다 매우 빠른 경향을 보여준다.

얼음 두께 220 m의 3,250 ㎢의 라슨 B 빙붕이 2002년 붕괴되었고, 현재 완전히 붕괴되었다. 이 빙붕은 지난최대빙하기 이후 전 홀로세에 걸쳐 약 10,000 년간 안정적이었다. 남극해 빙붕 변화는 전지구적인 해수면 변동과 연관되어있어, 인위적인 산업화에 따른 남극해 해빙은 분명 전지구적인 해수면 상승을 유도하지만, 사실 그 수치는 아주 작은 것으로 나타났다. 이러한 지역적인 온난화는 라슨 빙붕들을 위협하지만, 라슨 C 빙붕 또한 라슨 A와 B 빙붕의 붕괴와 유사한 결과를 보여줄 것이라는 예측에도 불구하고 실제 언제 발생할 것인가에 대한 물음에 답을 줄 수 있는 예측은 매우 어려운 문제이다. 라슨 C 빙붕은 규모면으로 남극에서 네번째로 가장 큰 빙붕으로 약 50,000 ㎢의 면적을 차지한다. 최근 2016년 발표된 보고(Adrian et al., 2016)는 500 m 깊이, 91 m 이상 되는 폭, 약 110 ㎞ 길게 이어진 균열이 라슨 C 빙붕에서 존재하고 있으며, 지속적으로 확장되고 있어 향후 이 빙붕의 약 9~12%(6,000 ㎢)가 붕괴될 거라고 예측하고 있다. 만약 전체 라슨 C 빙붕이 붕괴된다면, 지구 해수면이 약 10 cm 정도 상승할 것으로 예측된다.

라슨 C 빙붕 해역은 2005년 독일 탐사선이 들어간 이후 2013년 쇄빙연구선 아라온이 들어가 소중한 탐사 자료를 획득하였다. 특히, 이 해역에서 획득한 해양코어퇴적물은 최초이며, 라슨 C 빙붕의 과거 해빙사를 복원할 수 있는 중요한 시료로 인식된다(그림 1). 이 보고서는 라슨 C 빙붕 퇴적물의 퇴적학적 및 지화학적 분석, 광물분석 및 thin section의 이미지 분석을 통해 지난최대빙하기 이후 라슨 C 빙붕의 변화를 복원하고자 한다.

2. 분석 방법

2.1. 퇴적학적/지화학적 분석 및 광물분석

입도 분석을 위해 코어 절개 면을 따라 4 cm 간격으로 약 5 g의 퇴적물을 채취하였다. 30% H_2O_2와 0.1 N HCl을 이용하여 퇴적물 시료에 포함되어 있는 유기물과 탄산염을 모두 제거한 후, 습식 체질(wet sieving) 방법으로 사질과 니질 퇴적물을 분리하였다. 사질시료는 양이 적어 소형(직경 약 7.6 cm) 체(sieve)를 이용, 5분간 기계적으로 체질한 후 입도별 무게 백분율을 구하였다. 직경 62 μm (4 ϕ) 보다 작은 입자들은 0.1% 확산제(calgon) 용액 내에서 균질분산시킨 후 세립자 분석기(Sedigraph 5000)를 이용하여 분석하였다. 입도 분류는 Folk and Ward (1957) 방

법을 이용하였다(그림 2).

지화학 분석을 위해 약 5 g의 퇴적물 시료를 2 cm 간격으로 채취한 후 60℃에서 24시간 이상 건조시킨 후, 막자사발을 이용하여 균질하게 갈아 분말로 만들었다. 약 10 mg의 분말시료를 취하여 Carlo Erba NA-1500 Elemental Analyzer로 총탄소량(TC, total carbon), 총질소량(TN, total nitrogen), 그리고 총황량(TS, total sulfur) 등을 측정하였다. 약 0.5 g의 분말시료에 10% 염산을 첨가하여 무기탄소(IC, inorganic carbon)를 제거한 후, 약 10 mg의 분말시료를 취하여 총유기탄소량(TOC, total organic carbon)을 측정하였다. 함수량 측정을 위해 코어 절개 면을 따라 약 5 g의 퇴적물 시료를 4 cm 간격으로 주사기로 채취한 후 정확한 무게를 측정하였다. 무게를 측정한 시료는 냉동건조기에서 동결 건조시킨 후 다시 무게를 측정하였다(dry weight)(그림 2).

퇴적물 내에 분포하고 있는 광물 분석을 위해 XRD (bulk,2um)를 이용하여 mineral assemblage가 분석되었으며, XRD를 이용하여 Illite crystallinity가 측정되었다(그림 2).

2.2. 우주선 유발 동위원소 분석

과거 빙붕 활동의 간접적으로 유추하기 위하여 Stone이 1998년에 제시한 Fusion 방법을 선택하여 라슨 C 코어의 전체 해양퇴적물 시료에 대하여 우주선 유발 동위원소 meteoric ^{10}Be이 추출되었고, 한국과학기술연구원(KIST)에 분석을 의뢰하여 우주선 유발 동위원소 meteoric ^{10}Be의 농도가 분석되었다(그림 2).

2.3. 이미지 분석

전체 코어의 고해상도 퇴적상과 층리 구조를 파악하기 위해서 1 cm 폭, 10 cm 길이와 1 cm 두께로 제작된 아크릴 슬랩 내 퇴적물을 레진으로 굳힌 후 0.5 cm 두께의 슬랩의 형태로 제작되었다. 이렇게 만들어진 스랩들이 X-선 촬영으로 이미지가 만들어졌다(그림 3).

2.4. 연대 측정

연대추정을 위해 코어 상부의 일부 구간(0, 6, 10, 14 cm)에서 유공층이 추출되었고, 다른 세 개의 구간(85, 95, 192 cm)에서 퇴적물을 채취하여 총 7개의

AMS ^{14}C 분석이 이루어졌다, 하지만, 퇴적물 시료의 연대 추정값들은 오래된 유기탄소를 포함하고 있어 세 구간은 ramped pyrolysis 분석으로 새로운 연대값들이 제시되었다(표 1).

3. 결과 및 요약

라슨 빙붕 해역에서 얻어진 해양 퇴적물을 통해 복원된 과거 빙붕 변화 연구는 매우 제한적이다. 이 해역들에 대한 쇄빙연구선의 접근이 매우 어려웠기 때문에 해양퇴적물의 시료 자체가 거의 드물다. 기존의 연구 결과들은 라슨 A와 B 빙붕의 붕괴로 인한 기회를 틈타 퇴적물 코어들을 획득하여 얻어진 것들이다. 일반적으로 빙붕 해역은 대륙붕 내에 위치하며 그 대륙붕 내에서 지난최대빙하기 이후 빙하기저부(grounding line)가 후퇴하고 빙붕이 점차 사라지면서 공해상의 여러 기원의 부유물질이 역질 다이아믹톤 위로 해저에 쌓이는 특징적인 퇴적현상을 보여준다(Anderson et al., 1983, 1991; Hambrey et al., 1991). 지난최대빙하기 동안 육상빙하의 기저부가 대부분 대륙붕단까지 전진하면서 이전 간빙기 동안 쌓인 퇴적물들이 대륙붕 내에서 대부분 사라진다. 이 해역에서 일반적인 중력 시추 장비는 빙하운반 역질층을 뚫지 못하기 때문에 사실 중력 시추를 통한 코어 퇴적물은 거의 지난최대빙하기 이후의 역사를 보여준다.

지난최대빙하기 이후 라슨 빙붕 해역의 과거 환경 변화는 라슨 A 빙붕 북동쪽에 위치하는 제임스 로스 섬(James Ross Island)의 빙하 코어로부터 얻어진 고해상도 고수온 복원 자료(그림 4)에서 일부 엿볼 수 있다(Mulvaney et al., 2012). 약 13,000 년 전부터 이 해역에서 홀로세가 시작되었고 약 10,000 년까지 온난기를 거친 후 약 2,500 년 전 부터 신빙하기가 시작된다. 사실 남극해에서 해양퇴적물과 빙하 코어의 과거 기후 복원은 서로 차이가 드러난다. 특히, 해양과 대기 사이에 서로 반응하는 차이로 인해 남극해 대륙붕 내 해양퇴적물과 주변 빙하 코어로부터 복원된 기록들이 시간적으로 상이하게 나타날 수 있다. 또한, 해양퇴적물에서 복원된 연대 추정값들은 빙하 코어에 비해 오류가 많아 상대 비교하기 쉽지 않은 측면도 있다. 현재까지 빙하 코어의 과거 기록 복원들이 해양퇴적물에 비해 상대적으로 적지만, 일부분 과거 기록에 대한 보다 정확한 추정은 빙하 코어에 의존할 수 밖에 없다.

코어 EAP13-GC16B는 약 2 m 길이로 최하부층에 역질 다이아믹톤(diamicton)이 존재한다(그림 5). 역질 다이아믹톤 퇴적상 바로 위에서 측정된 연대값(표 1)은 약 11,577 년 전이다. 코어 위치가 대륙붕단보다 내륙 안쪽에 위치하고

있어 지난최대빙하기가 끝나고 온난기로 접어들면서 중층 해수가 따뜻해지고 대륙붕단의 기저부가 점차 내륙 안쪽으로 후퇴한다. 이에 Mulvaney et al. (2012)의 복원된 홀로세 시작보다 앞서 나타난 코어 퇴적물의 연대 추정값은 빙하기저부의 후퇴에 따른 반응의 결과로 보인다. 특히, 역질 다이아믹톤 위로 약 2 cm 정도 층리가 없다가 상부로 갈수록 희미한 층리에서 점차 뚜렷한 층리를 보이는 것은 지난최대빙하기 이후 홀로세가 시작되면서 빙하기저부가 급격하게 후퇴하다가 빙하기저부의 후퇴 속도가 크게 작아지면서 발생되는 빙하기저부 융빙수의 유출에 따른 층리 형성으로 보인다. 사실 이러한 추정은 빙붕 아래 빙하기저부의 위치와 융빙수 유출량 및 빙붕 두께 모두 빙붕의 안정성과 매우 밀접한 관계를 갖는다. 현재 라슨 C 빙붕의 빙하기저부의 위치는 코어 위치에 그리 멀지 않은 내륙 안쪽에 위치하며, 코어 위치는 라슨 C 빙붕단과 가깝다(그림 1). 지난최대빙하기 이후 코어 위치와 멀지 않은 내륙 안쪽까지 빙하기저부가 급격하게 후퇴하다가 빙하기저부가 더 이상 후퇴하지 않고 들어오는 따뜻한 해수의 영향으로 점차 빙붕 두께가 얇아지면서 층리가 발달되는 것으로 사료된다. 구간 184-148 cm에 나타나는 퇴적상은 점차 하부 퇴적상보다 층리가 뚜렷해지고 층리 두께도 하부 퇴적상보다 두텁게 나타난다. 구간 156-145 cm는 이러한 경향의 최대 정점에 보여주는 퇴적상이다(그림 6, 7, 8과 9). 이는 빙하기저부의 후퇴가 없는 안정된 상태에서 빙붕 안쪽으로 들어오는 따뜻한 해수의 영향으로 점차 빙붕 두께가 얇아지면서 빙하기저부 유출수의 증가로 나타나는 퇴적 현상의 결과로 보인다. 일단 이 시기 동안 우주선기원물질인 10Be 동위원소값의 변동이 없다는 사실은 당시 코어 위치가 계속 빙붕 아래 놓여있었다는 것을 말해준다. 또한, 시간적인 중층 해수의 영향은 일정하기 때문에 탄산염 함량이 지속적으로 증가하고 유기탄소함량은 반대로 감소하는 것은 빙하유출수의 유입량의 증가에 따른 탄산염의 증가와 희석 효과에 따른 유기탄소함량의 감소와 일치하고 있다.

구간 148-80 cm는 두터운 층리구조가 점차 희미해지다가 층리가 없어지는 퇴적상을 보여준다(그림 10, 11, 12, 13, 14, 15와 16). 이 시기는 온난화가 계속 진행되는 것이 아닌 기후적으로 안정기에 접어들거나 최대 온난기를 지나 상대적으로 추워지지만 빙하에 영향을 줄 수 있는 기후인 것으로 생각된다. 당시 라슨 C 빙붕의 빙하기저부가 안정되어있다고 가정하면, 불안정한 층리 구조는 지속적으로 얇아지는 빙붕이 더 이상 지탱되지 못하고 빙붕단(calving line)이 점차 후퇴하면서 빙하기저부 유출에 영향을 준 결과로 보인다. 특히, 이 구간 중에 일부 구간들에서 층리가 보이지 않는 것은 빙붕단이 급격하게 후퇴하거나 일부 붕괴되어 나타나는 결과로 생각된다. 이러한 추정이 가능한 이유는 불안정성이 강하게 나타나는 이 시기

동안에도 10Be 동위원소값들이 낮은 상태로 유지되고 있어 코어 위치가 빙붕 아래 놓여있다는 사실이다(그림 2). 이 구간에서 지속적으로 총무기탄소함량이 낮아지지만 총유기탄소함량은 일정하다는 사실도 불안정성이 강한 이 시기에 빙하기저부 유출량이 줄어들어 희석 효과가 낮아지는 결과로 볼 수 있다. 표 1에서 알 수 있듯이 이 구간 내에 포함된 코어 깊이 95 cm는 약 8,054 년 전이고, 코어 깊이 85 cm는 약 6,021 년 전으로 수온 이상값들(temperature anomaly)이 0℃ 이상을 유지하고 있어서(Mulvaney et al., 2012) 빙붕단의 지속적인 후퇴내지는 일부 빙붕의 붕괴를 예측할 수 있다.

구간 80-36 cm는 얇은 사층리와 층리가 없는 구간이 교호적으로 나타나는 퇴적상을 보여준다(그림 16과 17). Mulvaney et al. (2012)의 연구 결과에서 약 6,000 년부터 약 3,000 년 전까지 수온 이상값들이 약간 증가하는 현상을 보여준다. 이 시기 또한 상부 퇴적상과 마찬가지로 수온 이상값들이 0℃ 이상을 유지하고 있어 빙붕단이 지속적으로 후퇴할 수 있는 충분한 조건이다. 하지만, 상부 퇴적상과 다른 점은 사층리의 존재이다. 10Be 동위원소값들이 점차 증가하고 있어 빙붕단이 코어 위치와 매우 근접하거나 코어 위치 바로 뒤까지 후퇴하였을 가능성을 제시한다. 이 시기 동안 총무기탄소함량이 낮은 값을 유지하고 총유기탄소함량이 증가한다(그림 2). 이는 안정화된 빙하기저부가 약하게 후퇴하고 코어 위치 주변이 공해 상태를 유지하고 있어서 공해의 해양생산력이 코어 주변에 퇴적되기 때문인 것으로 사료된다. 이러한 조건은 라슨 C 빙붕 해역을 비롯해 라슨 A, B 빙붕 내 대륙붕의 일정 부분이 공해 상태였음을 지시한다. 결국 남부 라슨 빙붕의 대륙붕에서 어느 정도 차가운 빙붕수가 형성되어 라슨 C 빙붕 해역부터 A 빙붕 해역을 따라 최북단 남극반도로 올라갈 수 있다. 하지만, 라슨 빙붕 내 대륙붕에 형성된 빙붕수의 방향은 라슨 빙붕 내 빙하기저부의 후퇴 위치에 따라 달라질 수 있고 이 구간에 볼 수 있는 사층리의 방향성은 빙하기저부의 후퇴 위치에 따라 달라지는 결과로 나타날 수 있다. 일부 구간에 나타나는 층리가 없는 구간은 빙붕단의 급격한 후퇴나 붕괴에 따른 결과로 생각된다.

구간 36-0 cm 구간은 희미한 사층리를 보이다가 최상부로 가면서 층리가 사라지는 퇴적상을 보여준다(그림 18, 19와 20). 이 시기 동안 가장 특징적인 변화는 총유기탄소함량이 점차 낮아지고 10Be 동위원소값들이 상당히 높다는 것이다. 또한, 총무기탄소함량이 거의 없다는 사실도 주목할 만하다. 이 구간의 상부 퇴적상에서 빙하기저부와 빙붕단이 다시 후퇴하면서 이 시기에 들어와 코어 위치가 빙하기저부의 영향권에 멀어지고 있음을 보여준다. 또한, 이 당시 빙붕단 위치는 현재와 매우 유사한 장소까지 도달한 것으로 생각된다. 또한, 라슨 C 빙붕 내 대륙붕이 현

재와 유사해 차가운 빙붕수가 상당하게 발달하였을 것으로 생각된다. 사실 공해상에서 높은 생산력이 퇴적물에 반영되어야 함에도 불구하고 차가운 빙붕수는 퇴적되는 유기탄소를 융해시킬 수 있다. 점진적인 총유기탄소함량의 감소는 빙붕단이 코어 위치 안 내륙쪽으로 더 후퇴하면서 차가운 빙붕수의 세력이 확장되어 나타난 결과로 해석된다.

Deglacial history of Larsen C sediment core since the LGM

Kyu-Cheul Yoo, Jae Il Lee, Ki Tae Kim, Min Kyung Lee, Ho Il Yoon

Korea Polar Research Institute

Abstract: We reconstructed deglacial history since the LGM (Last Glacial Maximum) through image analysis of small slab sediments (about 10 cm length, 1 cm wide and 0.5 cm thick) and sedimentological/geochemical/isotopic analyses of core EAP13-GC16B collected from Larsen C embayment. The previous reconstructions of the past glacial history on the eastern AP (Antarctic Peninsula) ice shelf were limited and obscure, but the well-defined sedimentary facies of Larsen C core represents temporal changes of ice shelf from landed glacier including grounding & calving lines. High-resolution paleo-temperatures from ice core of Jame Ross Island (the northern part of Laren ice shelf) were a crucial key to illustrate all traces of them.

참고문헌

Anderson, J.B., Brake, C.F., Domack, E., Myers, N. and Wright, R., 1983, Development of a polar glacial-marine sedimentation model from Antarctic Quaternary deposits and glaciological information. In: Molnia, B.F. (ed.), Glacial Marine Sedimentation. New York, Plenum, 233-264.

Anderson, J.B., Kennedy, D.S., Smith, M.J. and Domack, E.W., 1991, Sedimentary facies associated with Antarcticas floating ice masses. In: Anderson, J.B., Ashley, G.M. (eds.), Glacial Marine Sedimentation: Paleoclimatic Significance, Boulder, Colorado. Geological Society of America. Special Paper, 261, 1-25.

Adrian Luckman, Daniela Jansen, Martin O'Leary, the MIDAS team, 2016. "A growing rift on Larsen C". projectmidas.org.

Connor, Steve, 2005. "Ice shelf collapse was biggest for 10,000 years since Ice Age" The Independent, London (Aug 4).

Fox, Douglas, 2012. "Witness to an Antarctic Meltdown". 307 (1): 54 - 61. doi:10.1038/scientificamerican0712-54.

Folk R.L., Ward W.C., 1957. Brazos River bar: a study in the significance of grain size parameters. *Journal of Sedimentary Petrology* 27:3 - 26.

Hambrey, M.J., Ehrmann, W.U. and Larsen, B., 1991, Cenozoic glacial record of the Prydz Bay continental shelf, East Antarctica. In: Barron, J. and Larsen, B. (eds.), Proceedings of Ocean Drilling Program. Scientific Results, 119, p. 77-131.

Marshall et al., 2006. "The Impact of a Changing Southern Hemisphere Annular Mode on Antarctic Peninsula Summer Temperatures", Journal of Climate, vol. 19, pp. 5388 - 5404.

Mulvaney, R., Abram, N. J., Hindmarsh, R. C. A., Arrow-smith, C., Fleet, L., Triest, J., Sime, L. C., Alemany, O.,and Foord, S., 2012. Recent Antarctic Peninsula warming relative toHolocene climate and ice-shelf history, Nature, 489, 141 - 144,doi:10.1038/nature11391.

Table 1. Ages are reported in blank-corrected ^{14}C years BP and have been calibrated to calendar years BP using Calib 7.1 Marine13 calibration curve with $\Delta R = 831 \pm 50$. Total masses of carbon used for ^{14}C analysis are included for all RP analyses. Isotope dilution Fm values and ^{14}C ages have been corrected for the addition of asurrogate using equations 3 and 4. (Unpublished data from Subt et al.)

Depth (cm)	Type	Mass (μmol of C)	$\delta^{13}C$ (‰)	Fm	± (1σ)	Age (^{14}C yrs BP)	± (1σ)	Calibrated Age (yrs BP)	± (1σ)
85	Isotope Dilution RP1	10.190	-21.95	0.3546	0.0187	8329	424	**6021**	**429**
95	Isotope Dilution RP1	9.790	-24.43	0.2849	0.0118	10087	333	**8054**	**420**
192	Isotope Dilution RP1	11.850	-24.77	0.2017	0.0105	12862	417	**11577**	**479**
0	Foraminiferal Carbonate			0.5661	0.0028	4570	40	**1717**	**90**
6	Foraminiferal Carbonate			0.5261	0.0023	5160	35	**2518**	**84**
10	Foraminiferal Carbonate			0.4447	0.0017	6510	30	**4137**	**79**
14	Foraminiferal Carbonate			0.4419	0.0019	6560	35	**4197**	**83**

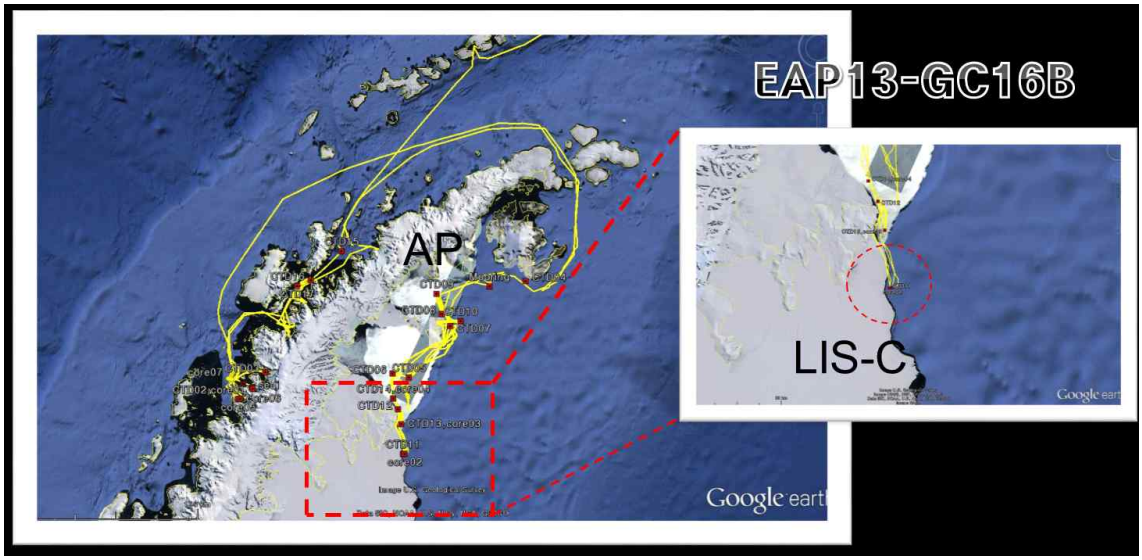

Figure 1 . Study areaand one gravity coring site (red circle). AP = Antarctic Peninsula, LIS-C= Larsen Ice Shelf.

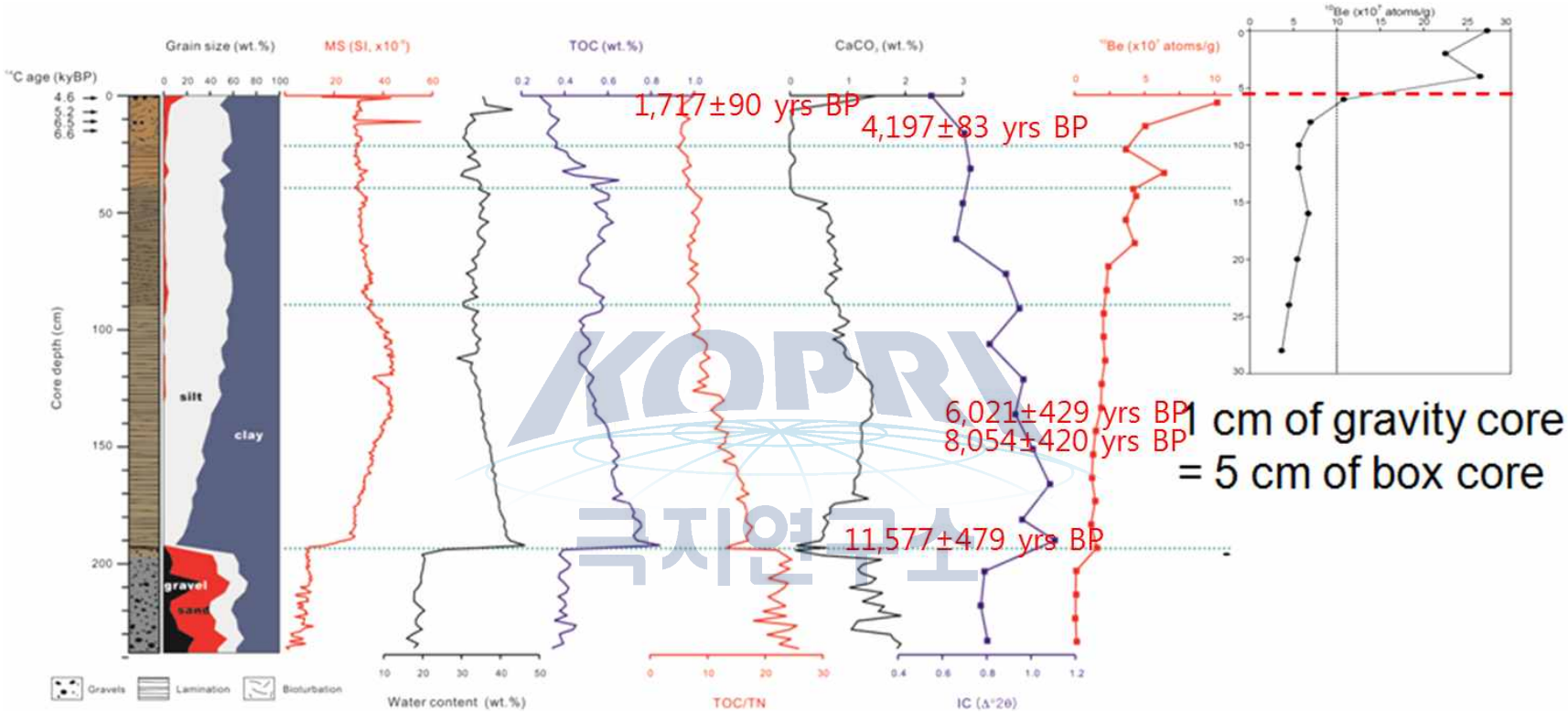

Figure 2. Textural compositions, MS, TOC, $CaCO_3$, TOC/TN, illite crystallity, and 10Be of core EAP13-GC16B.

Figure 3. X-ray images of polished slabs (1×10×0.5 cm) over core EAP13-GC16B.

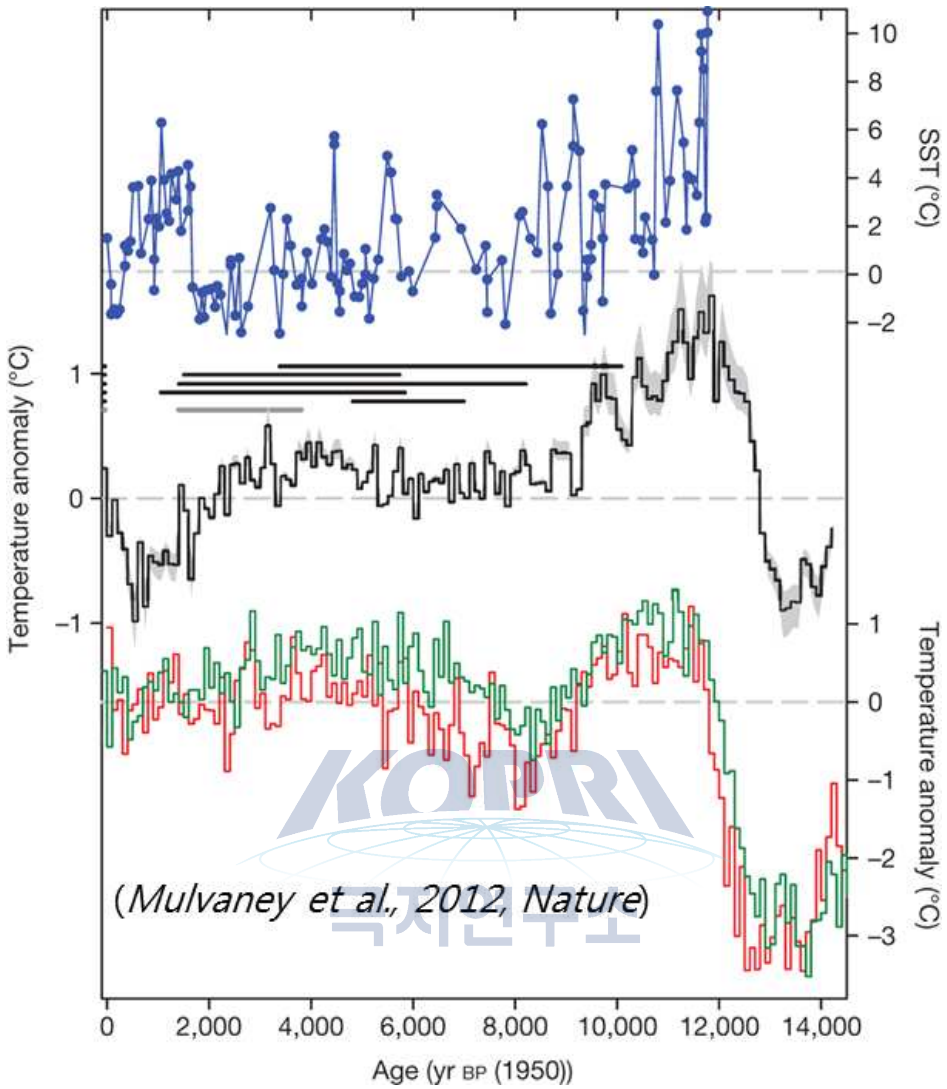

Figure 4. Holocene temperature history of theAntarctic Peninsula. The JRI ice-core temperature reconstruction relative tothe 1961 - 1990 mean (black trace, 100-yr average; the grey bandindicates the standard error of the calibration dependence) is shown alongside a sea surface temperature (SST) reconstructionfrom off the shore of the western Antarctic Peninsula (blue curve), andtemperature reconstructions from the Dome C (red) and Dronning Maud Land(green)30 ice cores from East Antarctica. Horizontal bars show intervals in theHolocene when marine sediment cores indicate that open water was present in thearea of the Prince Gustav (black; top to bottom are north to south core sites;original 14C ages have been calibrated) and Larsen A (grey) ice shelves, whichcollapsed in AD 1995. (Data from Mulvaney et al., 2012)

194-184 cm

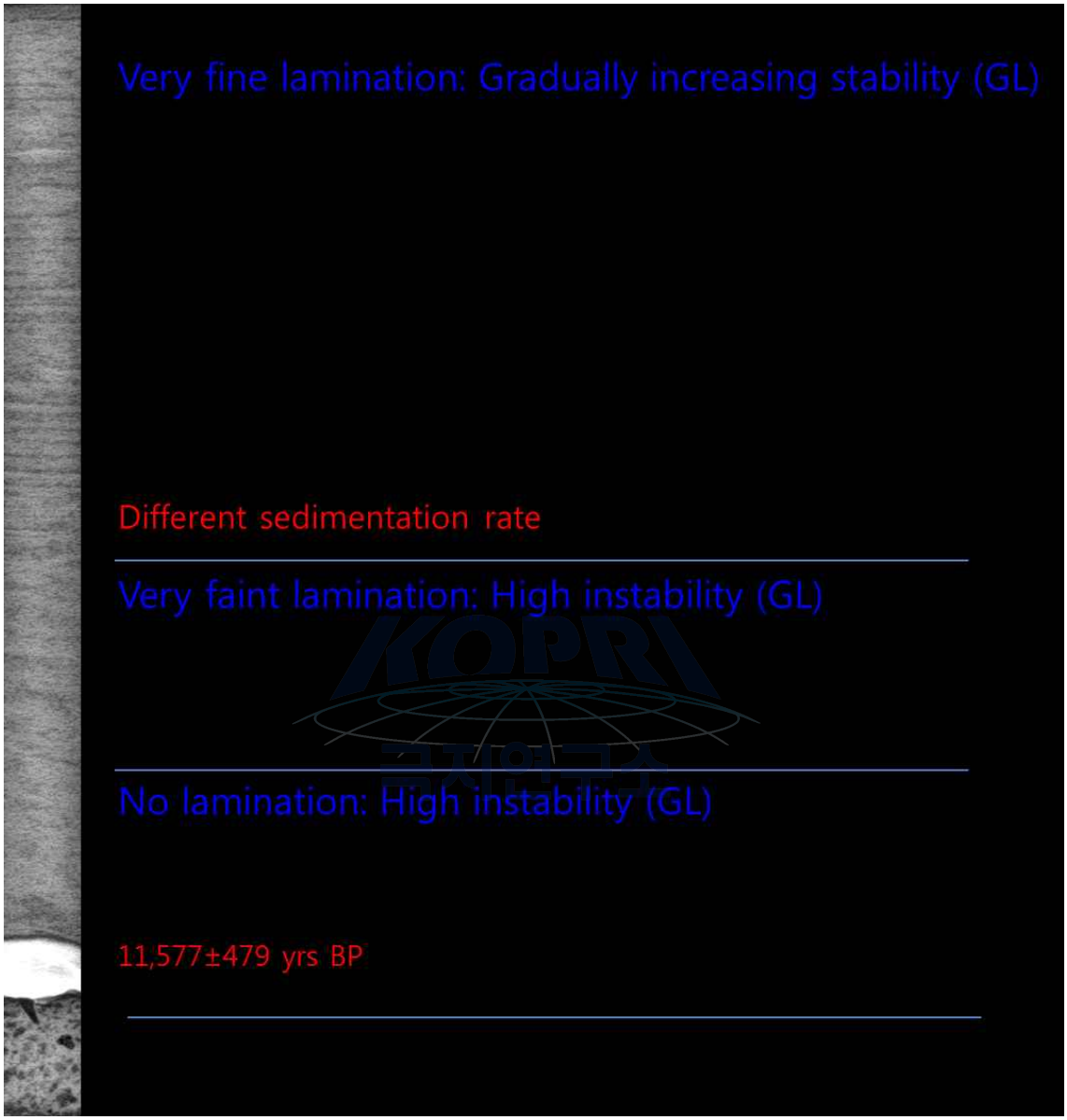

Figure 5. Discription of section 194-184 cm of core EAP13-GC16B.

184-174 cm

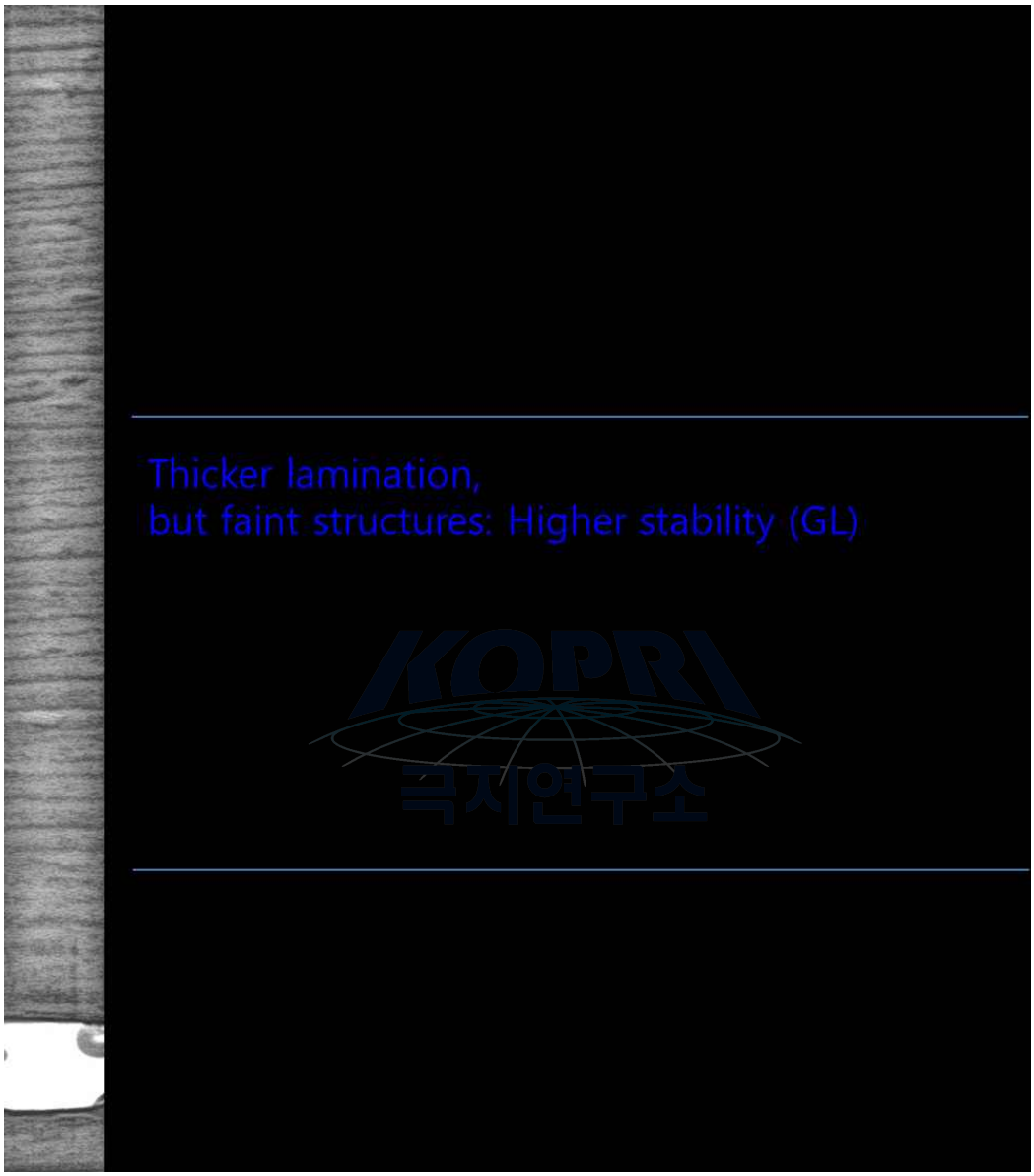

Figure 6. Discription of section 184-174 cm of core EAP13-GC16B.

176-166 cm

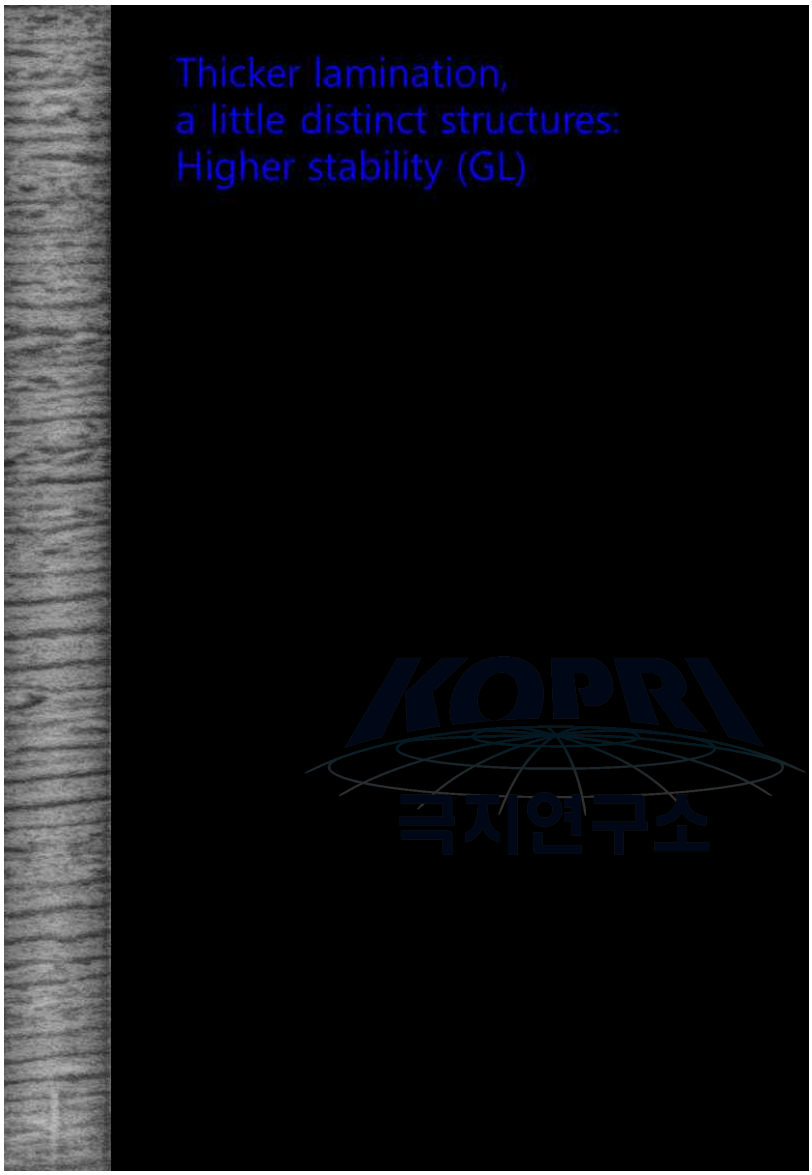

Figure 7. Discription of section 176-166 cm of core EAP13-GC16B.

166-156 cm

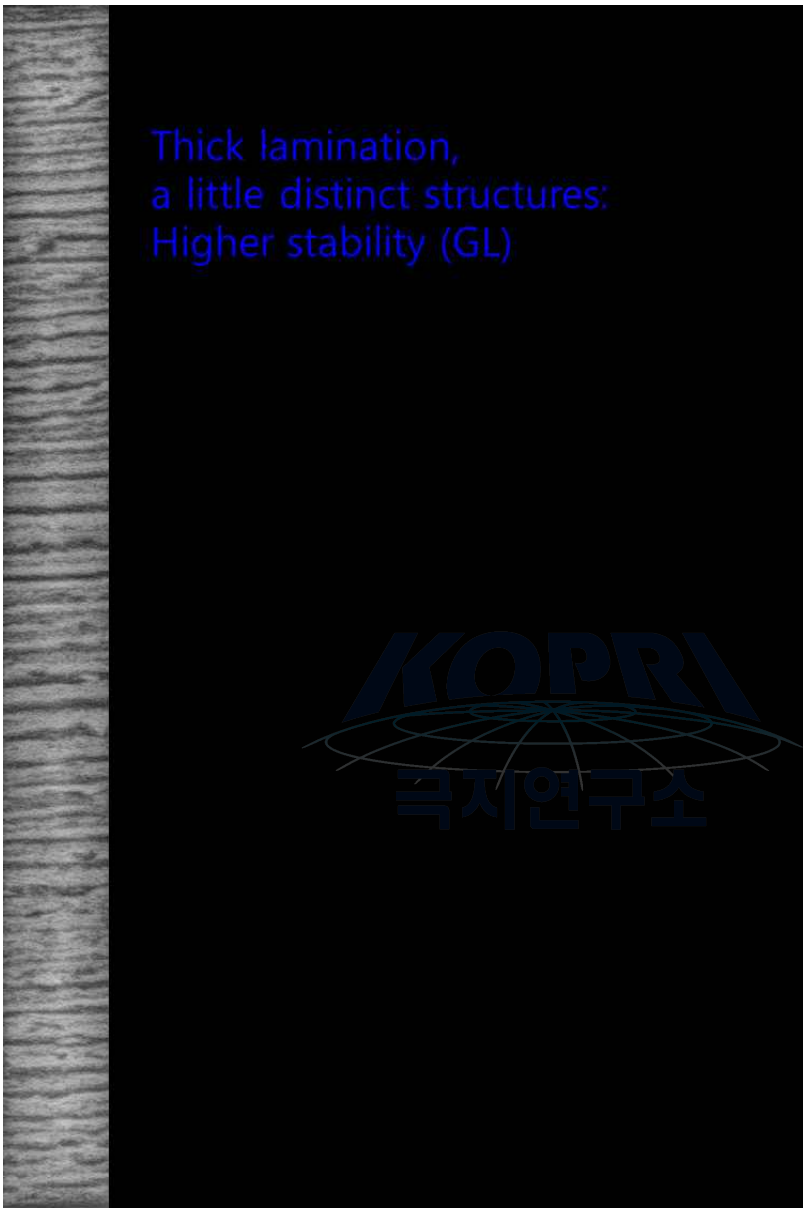

Figure 8. Discription of section 166-156 cm of core EAP13-GC16B.

158-148 cm

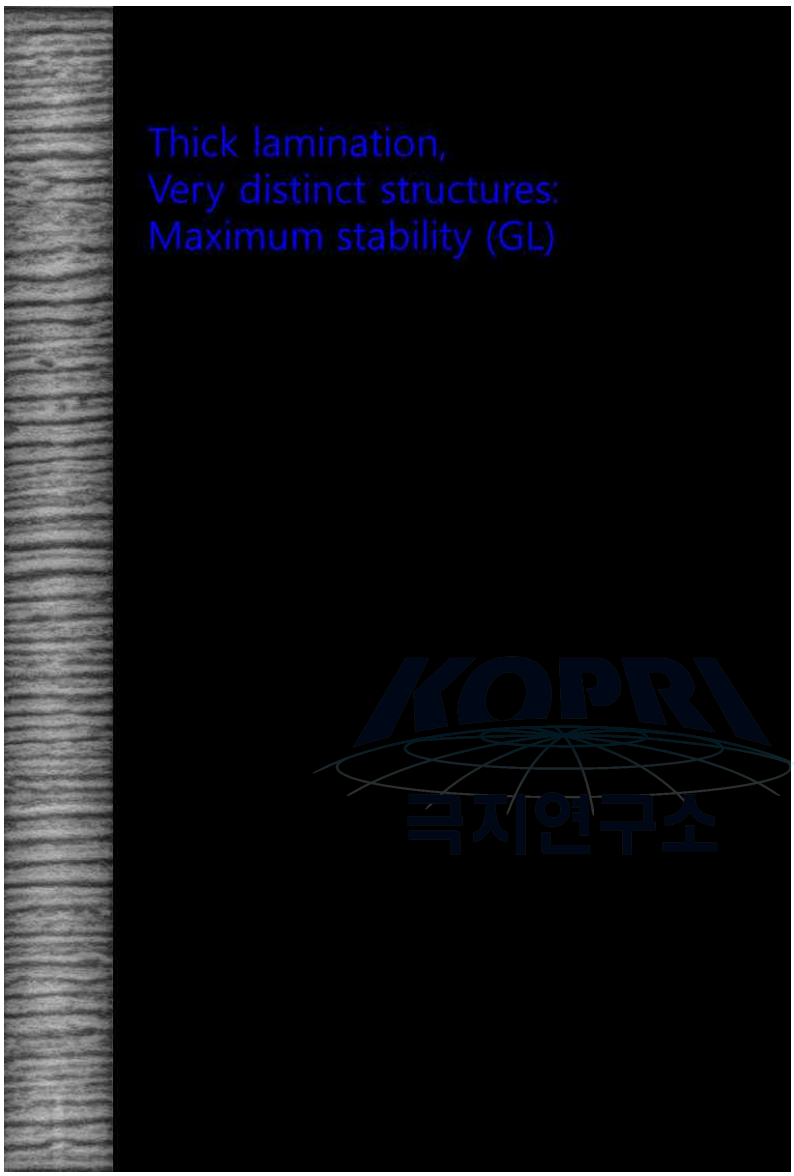

Figure 9. Discription of section 158-148 cm of core EAP13-GC16B.

148-138 cm 140-130.4 cm

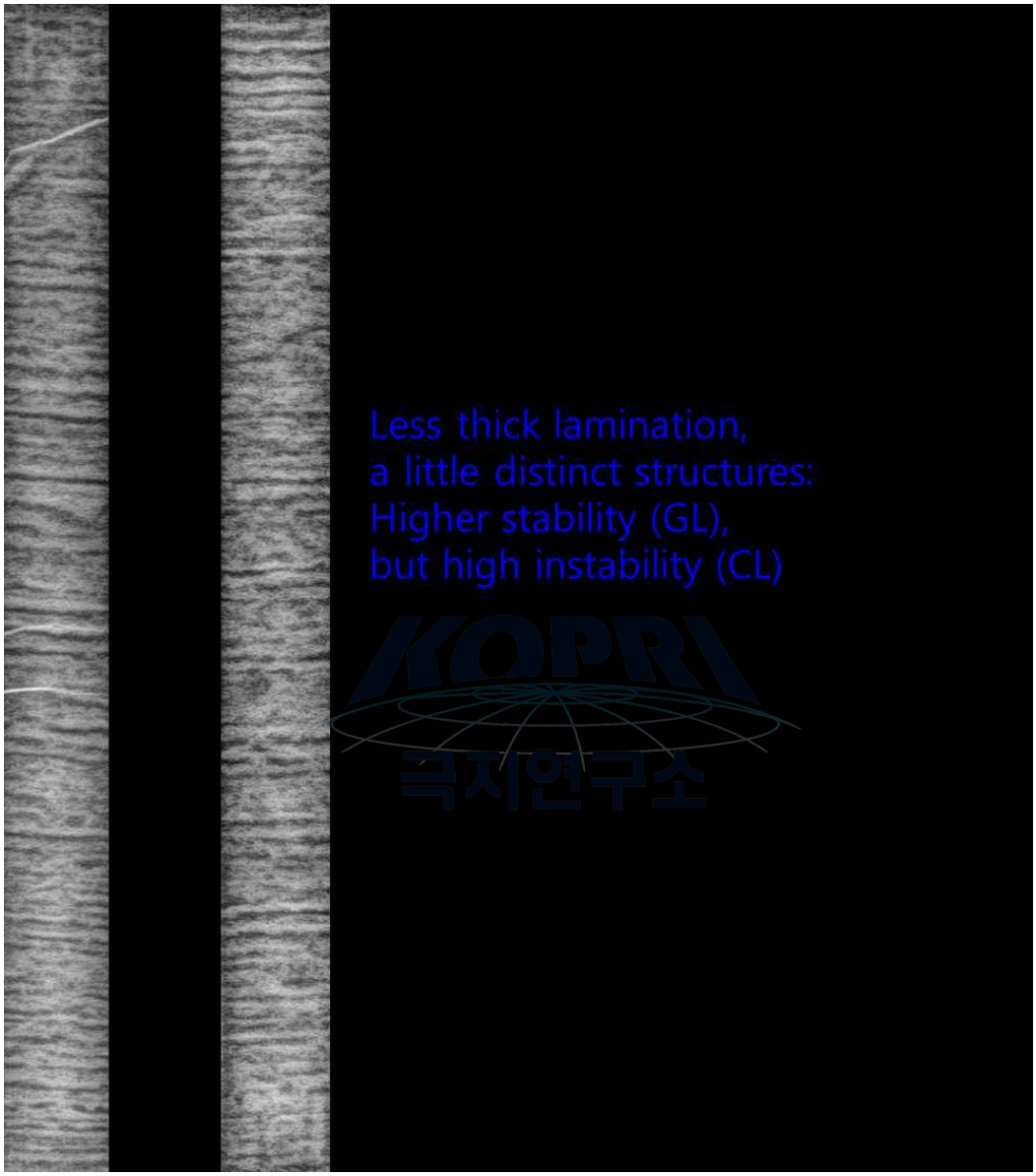

Figure 10. Discription of sections 148-138, 140-130.4 cm of core EAP13-GC16B.

130.4-120.5 cm

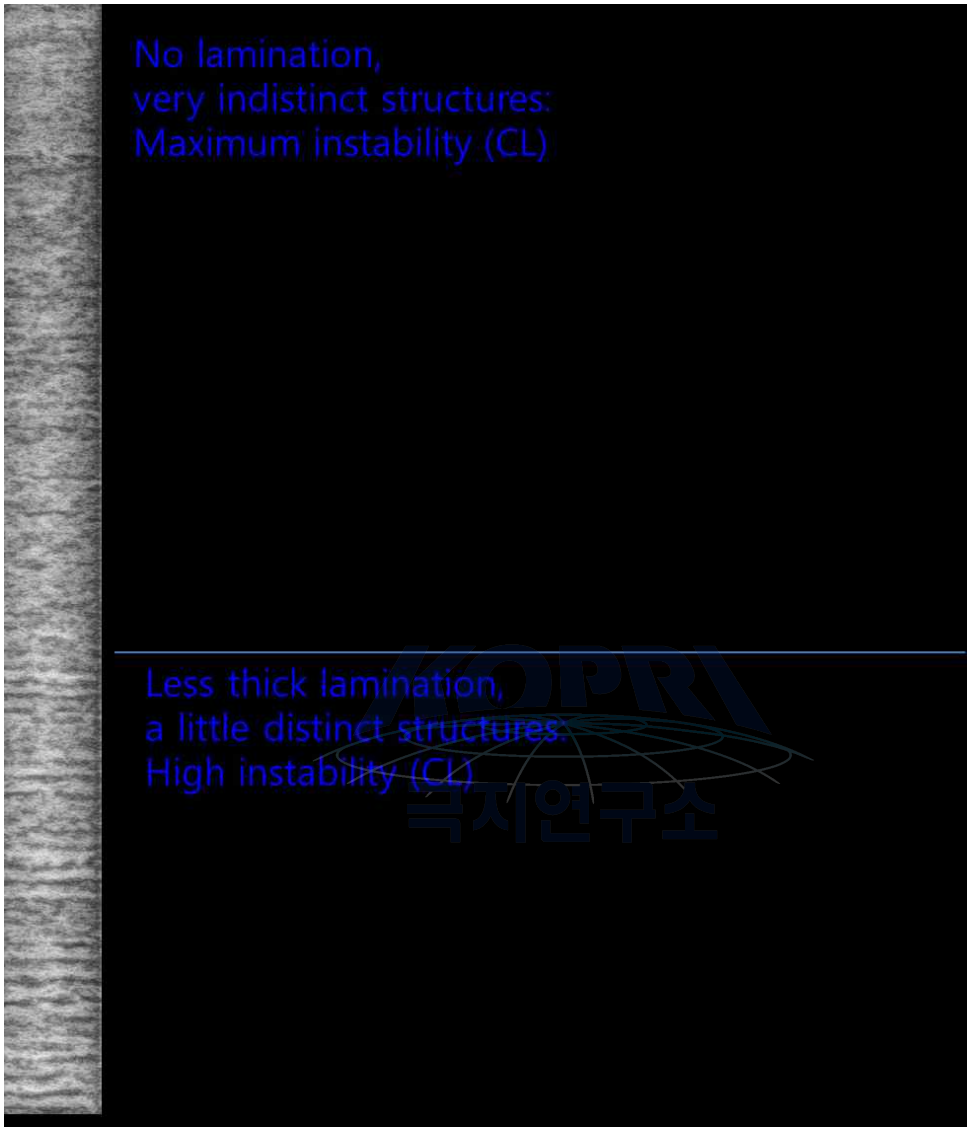

Figure 11. Discription of sections 130.4-120.5 cm of core EAP13-GC16B.

118-108 cm

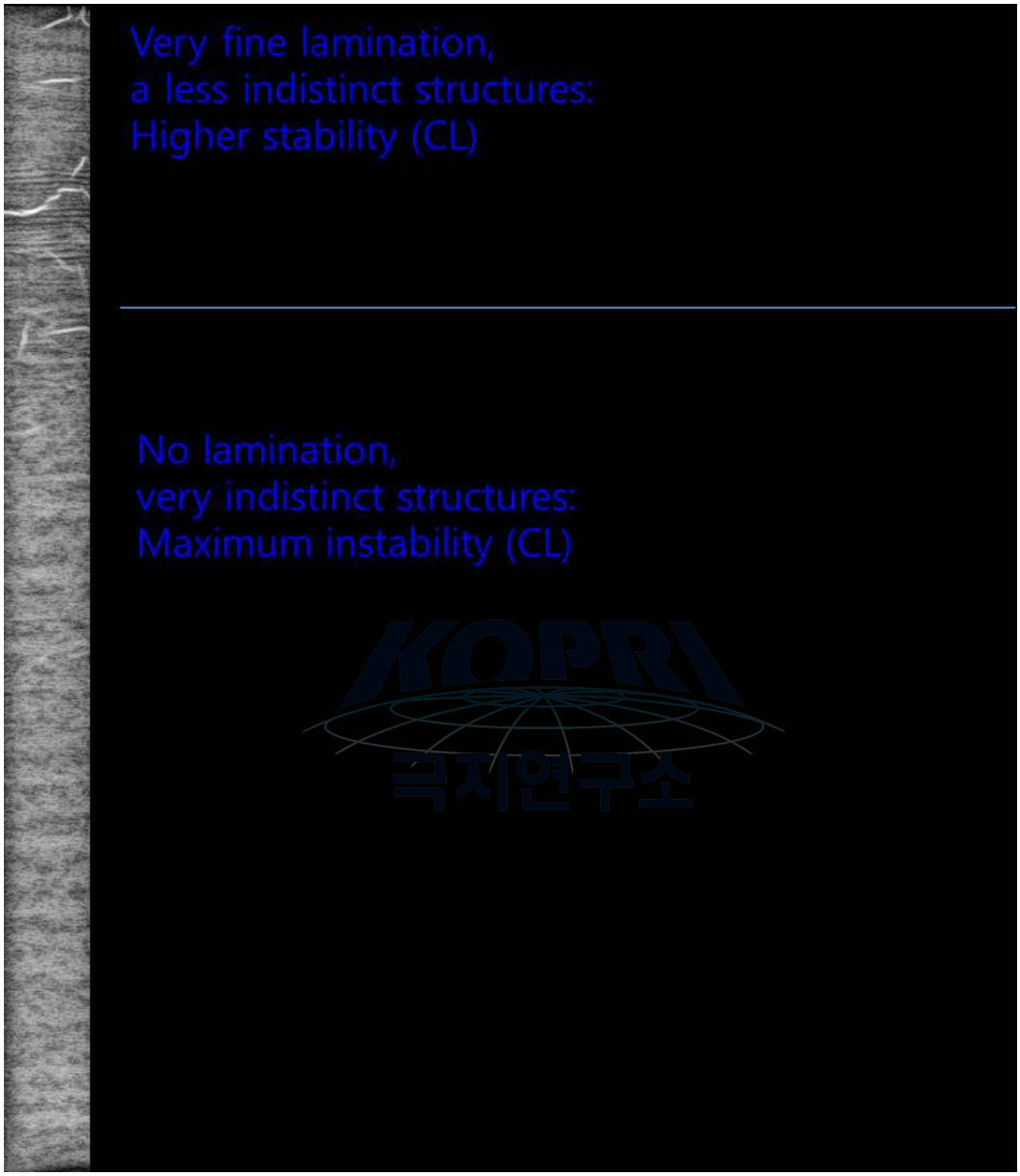

Figure 12. Discription of sections 118-108 cm of core EAP13-GC16B.

110-100 cm

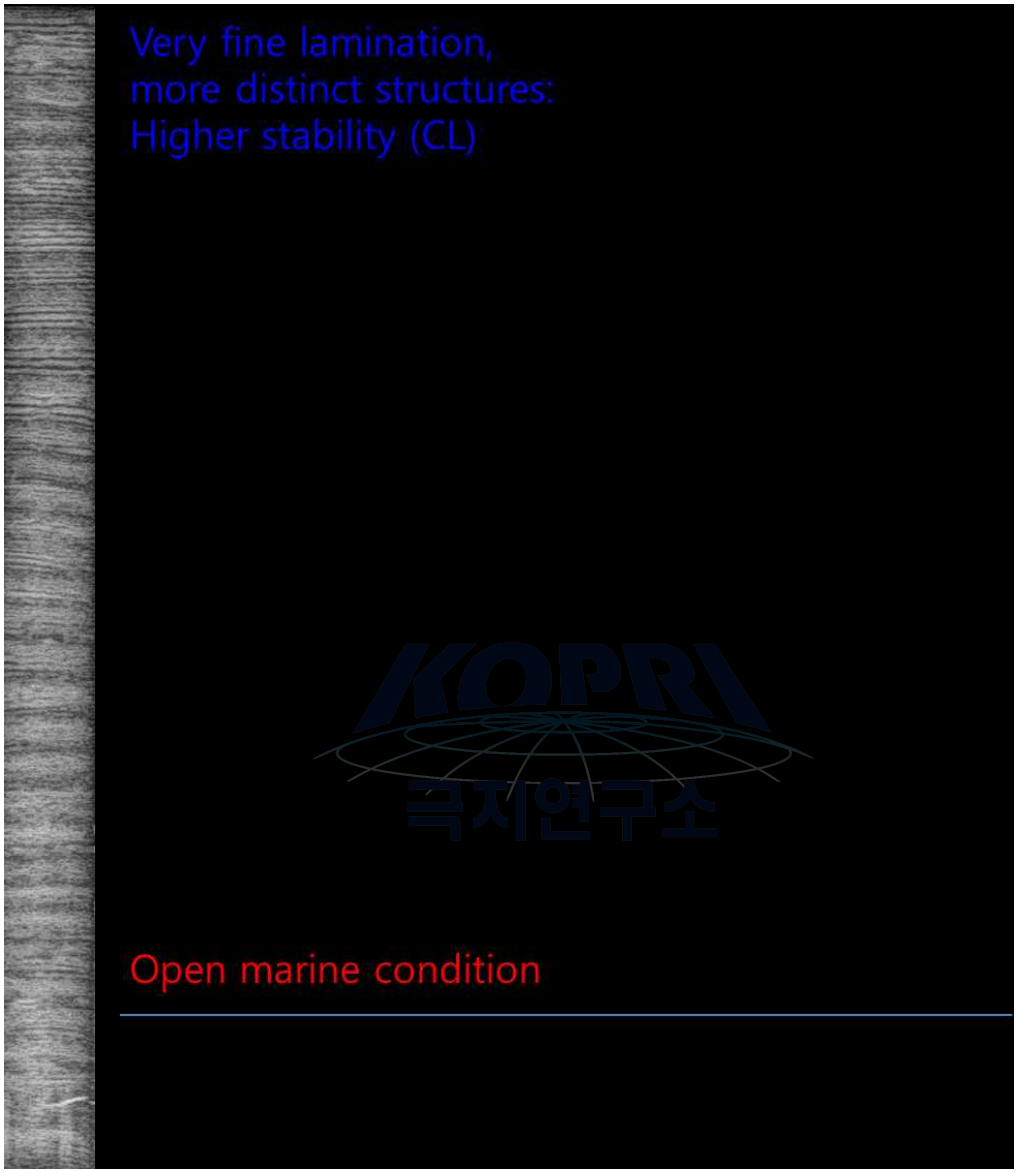

Figure 13. Discription of sections 110-100 cm of core EAP13-GC16B.

100-90 cm

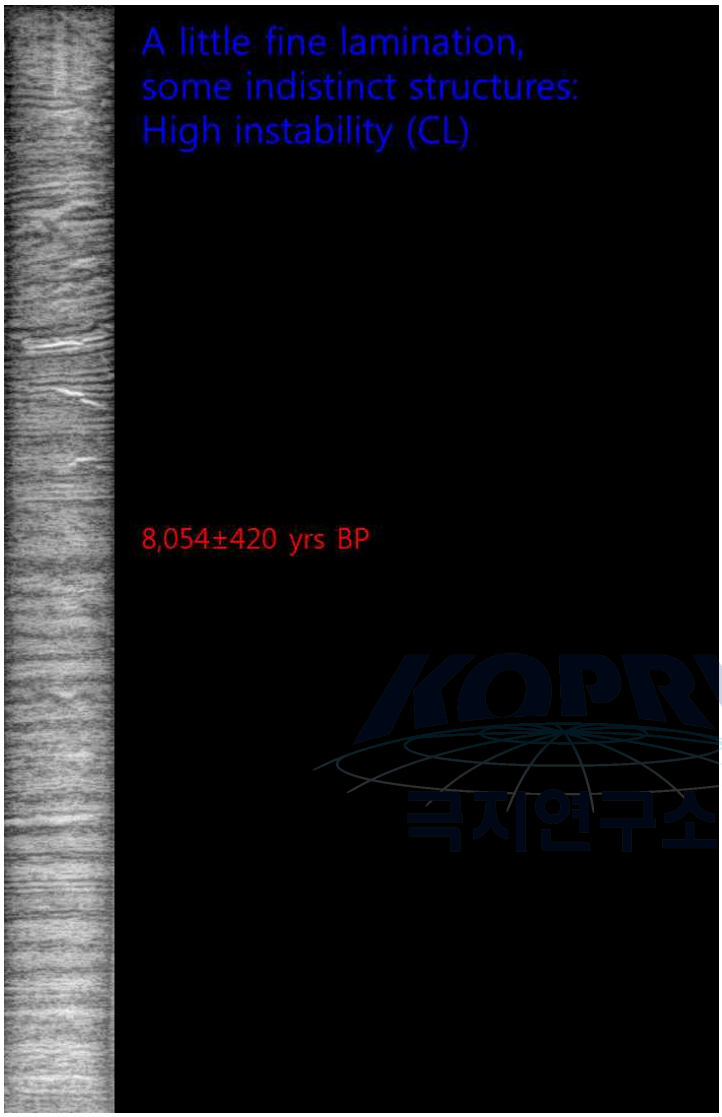

Figure 14. Discription of sections 100-90 cm of core EAP13-GC16B.

91-81.8 cm

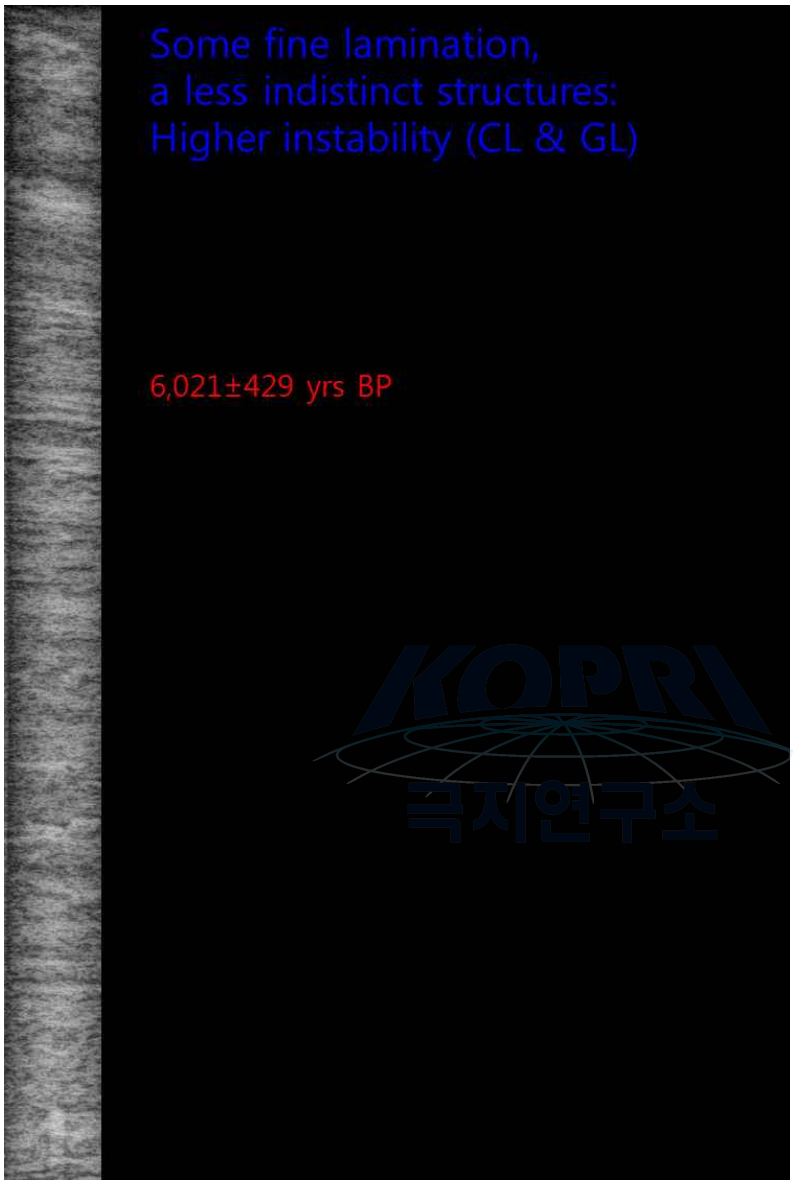

Figure 15. Discription of sections 91-81.8 cm of core EAP13-GC16B.

81.8-71 cm 74-64 cm 64-54 cm

Figure 16. Discription of sections 81.8-71, 74-64, 74-54 cm of core EAP13-GC16B.

56-45 cm 46-36 cm

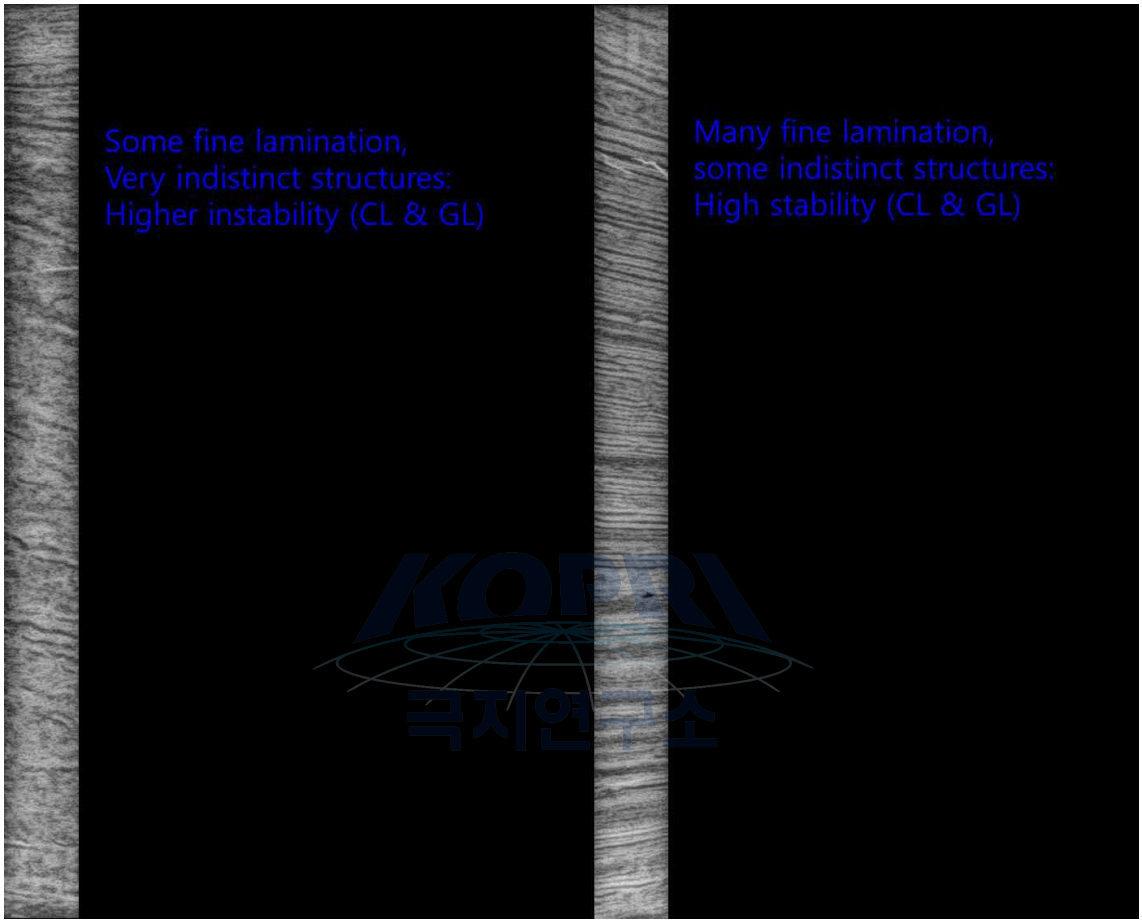

Figure 17. Discription of sections 56-45, 46-36 cm of core EAP13-GC16B.

38-27.9 cm 27.9-18 cm

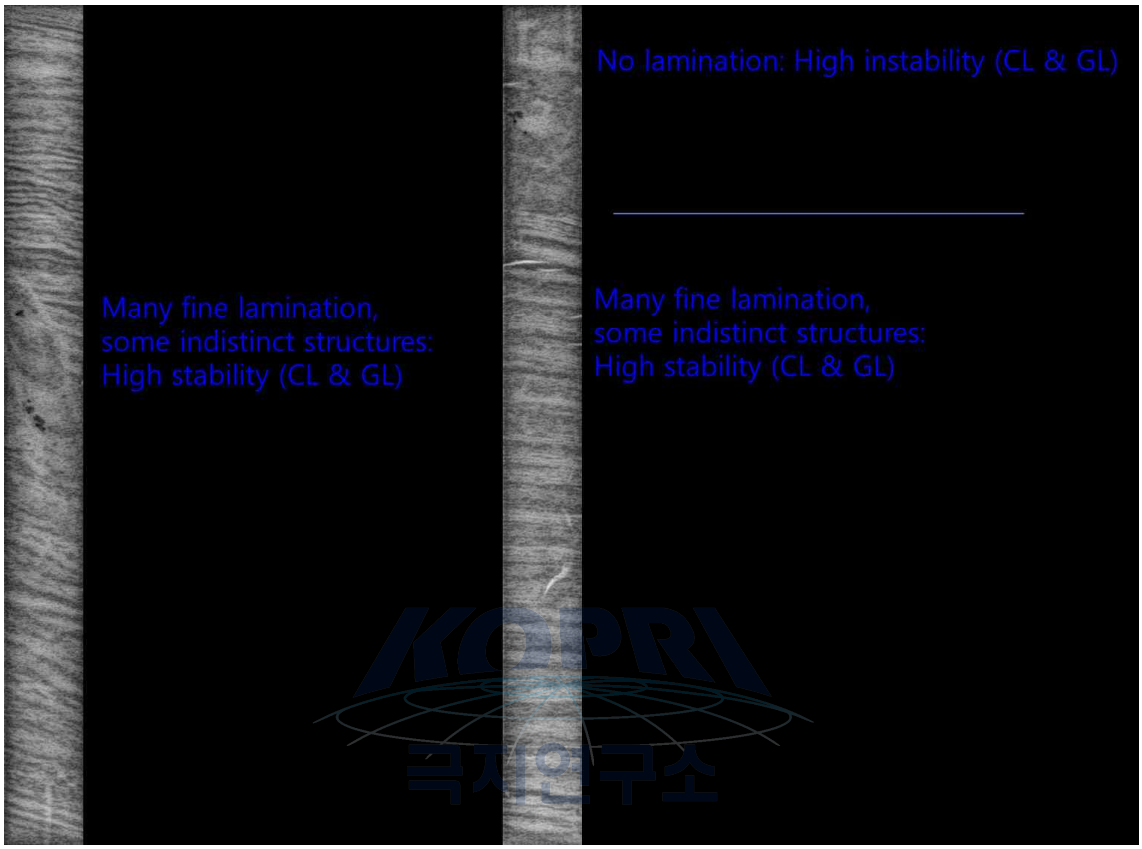

Figure 18. Discription of sections 38-27.9, 27.9-18 cm of core EAP13-GC16B.

20.2-10 cm

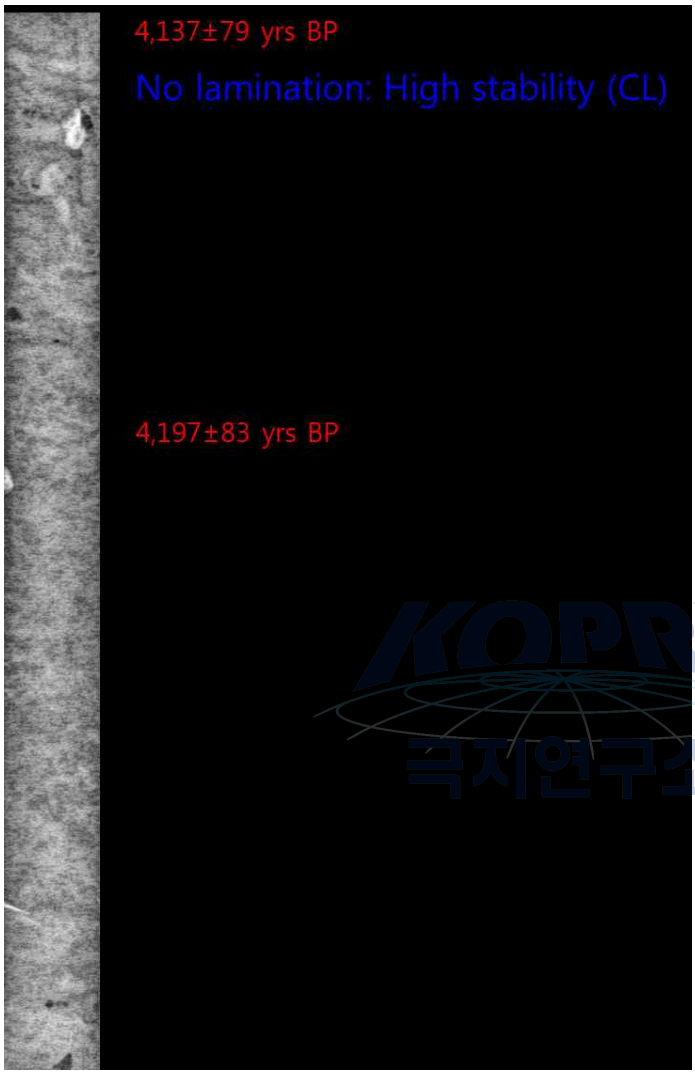

Figure 19. Discription of sections 20.2-10 cm of core EAP13-GC16B.

10-2.3 cm

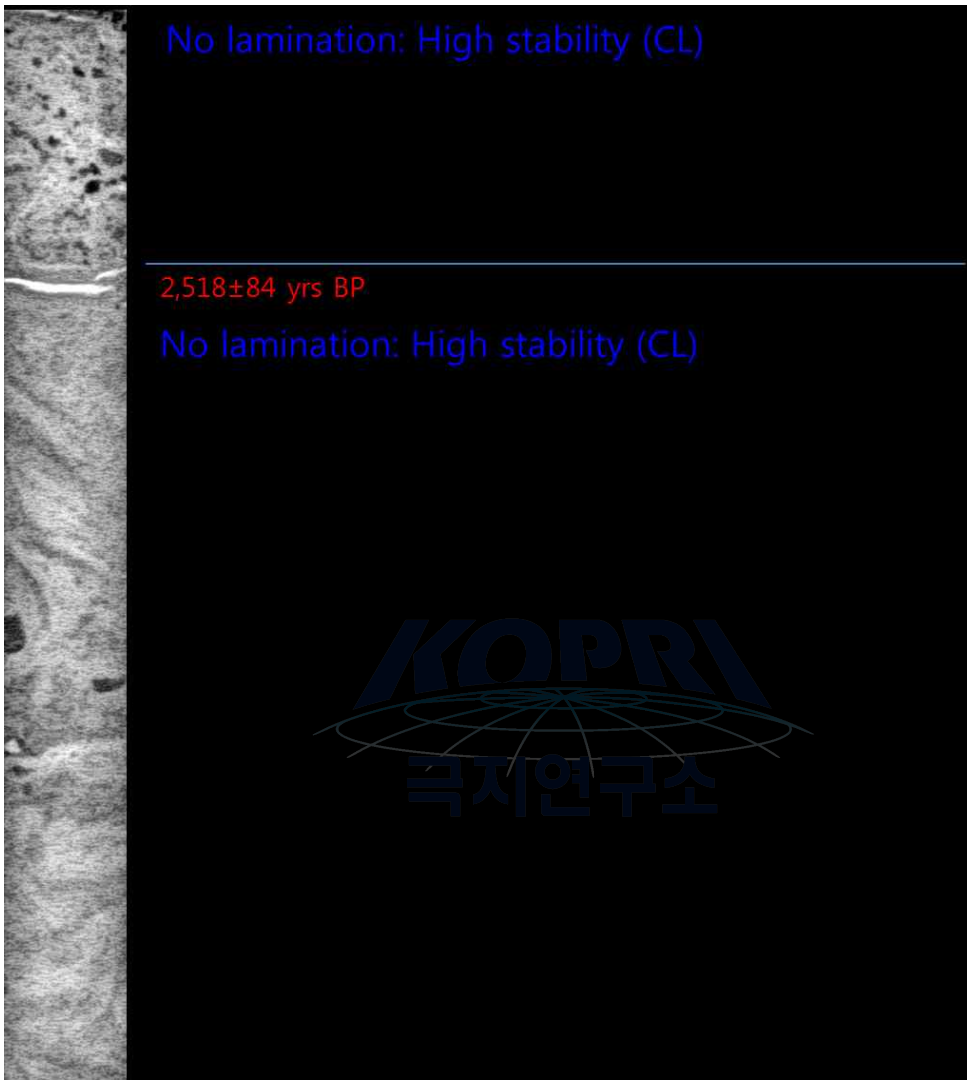

Figure 20. Discription of sections 10-2.3 cm of core EAP13-GC16B.

제 6 장

Hydrography of Marian Cove, King George Island, West Antarctica: implications for ice-proximal sedimentation during summer[2)]

Kyu-Cheul Yoo[1], Min Kyung Lee[1*], Ho Il Yoon[1], Yong Il Lee[2]

[1]Korea Polar Research Institute

[2]Seoul National University

Abstract: During the summer, from 1996 - 2000, vertical profiles of conductivity, temperature and transmissivity were obtained near the tidewater glacier of Marian Cove, King George Island, Antarctic Peninsula. The aims for the study were to determine the short-term variations of water structure due to hydrographic forcings and to understand sedimentation of suspended particulate matter in Antarctic fjord environments. Four distinct water layers were identified in the ice-proximal zone of the cove: i) a surface layer composed of cold and turbid meltwater, ii) a relatively warm Maxwell Bay inflow layer with characteristics of outer fjord water, iii) a turbid/cold mid-depth layer (40 - 70 m) originating from subglacial discharge, and iv) a deep layer comprised of the remnant winter water. The main factor influencing the characteristics of glacial meltwater layers and driving deposition of suspended particles in the cove is tidal forcing coupled with wind stress. The relatively small amount of meltwater discharge in Marian Cove yields low accumulation rates of non-biogenic sedimentary particles in the cove. The response to north-western and western winds, coupled with flood tide, may promote settling and sedimentation of

2) 이 연구 결과는 다음의 논문으로 출판되었음: KYU-CHEUL YOO, MIN KYUNG LEE, HO IL YOON, YONG IL LEE and CHEON YOON KANG. Hydrography of Marian Cove, King George Island, West Antarctica: implications for ice-proximal sedimentation during summer. Antarctic Science 27(2), 185-196 (2015)

suspended particles from turbid layers in the ice-proximal zone of the cove.

1. Introduction

Polar regions in south-east Alaska, Spitsbergen, Greenland and Antarctica have distinct glaciomarine environments in terms of turbid plume sedimentation (Powell 1990, Syvitski et al. 1996). The Antarctic Peninsula has experienced rapid regional warming and, as a result, glaciers from sub-polar to polar fjords have retreated (Cook et al. 2005). This area is characterized by valley and tidewater glaciers, which respond quickly to climatic variations. Very little suspended sediment is produced by meltwater streams from the various sources of the glaciers in most Antarctic fjords (Domack & Williams 1990, Domack et al. 1994, Yoon et al. 1998). Domack et al. (1994) reported the importance of the deposition of non-biogenic particles and transport mechanisms below the surface waters in the ice-proximal zone. The dynamics of ice-proximal plumes are, therefore, key to our understanding of the glaciomarine sedimentation of Antarctic fjords and to building a framework for multidisciplinary research. Sedimentation at the ice-proximal zone is essential not only for understanding modern fjord sedimentation, but also for interpretation of stratigraphic sequences preserved in the rock record (Powell & Molnia 1989). However, our understanding of these plumes remains poor, in part due to the complexity of glacial meltwater discharge and limited accessibility at the glacial terminus.

To understand glaciomarine hydrodynamics and sedimentation in the ice-proximal zone of Antarctic fjords, Marian Cove, King George Island was chosen (Fig. 1). Marian Cove is affected by temperate to sub-polar atmospheric systems, which are very sensitive to climatic variations. Therefore, the cove is a good site for identifying the variation in sedimentation patterns associated with regional climate fluctuations (Khim et al. 2007). Furthermore, research at Marian Cove can provide new information for comparison with other polar fjords (Domack & Williams 1990, Domack et al. 1994). Extensive time series of conductivity/temperature/depth/transmissivity (CTDT) hydrocasts were obtained

in Marian Cove from 1996 - 2000, by the Korea Antarctic Research Program (KARP). In this paper, the characteristics of turbid meltwater plumes from the tidewater glacier are described and discussed. Then, hydrographic variations in glacier-derived plumes and the forcings (tide, wind, glacier status, etc.) controlling their configuration (Cowan 1992, Brandini & Rebello 1994, Klöser et al. 1994) are discussed to explain sedimentation of suspended particulate matter in the cove.

2. Environment

Maxwell Bay, at c. 62°S and c. 58°W, is one of two large fjords on King George Island, which is situated on the northern periphery of West Antarctica (Fig. 1). The main inlets of the bay, which opens towards Bransfield Strait, are Potter Cove, Marian Cove and Collins Harbour. Marian Cove (c. 4.5 km long and c. 1.5 km wide) is bounded by the Weaver Peninsula to the north-west and the Barton Peninsula to the south-east. Much of the bedrock of both peninsulas is covered by glacial till. The geology of the Barton and Weaver peninsulas consists of Palaeocene to Eocene volcaniclastic sediments, tuffs and lavas of andesite and basaltic andesite, that were intruded by Eocene granodiorite (Hur et al. 2001). During summer, some volcanic particles are exposed at the surface of the melted glacier or tephra layers are found at the terminus of the glacier. Landscapes modified by periglaciation are widespread. Marian Cove consists of three basins (outer, central and inner) with a maximum depth of c. 120 m in the ice-proximal zone (Fig. 1). A sub-marine sill (c.70m deep) is located at the mouth of the cove where it enters Maxwell Bay. An additional sill, also c. 70 m deep, separates the middle and inner basins. Ice caps are present on King George Island, and glaciers terminate at vertical or near-vertical calving ice cliffs. The coast is typically gravel beach with steeper slopes in the south than in the north. The tidal regime is of mixed-type and semi-diurnal with a distinct inequality in tidal heights (Yoo et al. 1999). Mean tidal range is 1.5 m with a maximum spring tidal range of 2.8 m. Water exchange between Maxwell Bay and the cove occurs by tidal forcing over the entrance sill and the inner sill (c. 70 m deep) between the central and inner

basins. The cove is ice-free during summer.

Based on meteorological data of King Sejong Station (1988 - 2007) (KOPRI 2009), mean relative humidity is c.90% and annual precipitation is c. 600 mm yr-1. The tidewater glacier entering the cove experienced a retreat rate of c.81m yr-1 between 1994 - 2001 (Park et al. 1998a), compared with c. 12.5 m yr-1 between 1957 - 94, possibly as a consequence of recent rapid warming (Park et al. 1998a). Sea ice in the cove breaks up prior to the beginning of November. During summer, monthly mean air temperature rises > 1.0°C (Fig. 2). Due to relatively high humidity and solar radiation, the snow line rises in elevation through summer. Snow melting and glacier calving at the glacier front begin in early December, introducing large volumes of icebergs and meltwater to the cove (Yoon et al. 1997). Meltwater streams with terrigenous particles persist until late March, when the sea ice begins to form again (Yoo et al. 2002).

3. Methods

The oceanographic data were collected during the summer from 1996 - 2000 to examine the short-term variations of water characteristics due to hydrographic forcings. The vertical profiles of CTDT measurements at the seven stations in Marian Cove are examined in this paper. All measurements were made while the CTDT underwater unit was descending at a rate of 0.3 - 0.5 m s-1. On-board measurements (RV Yuzhmorgeologiya) were conducted along a longitudinal transect (stn 3, 5, 6 and 7).

In particular, continuous time series measurements at an interval of one hour were obtained from stn 5 in the inner basin, where the water depth is c. 110 m. The CTDT castings from stn 1 to stn 4 of the transverse transect were carried out from a rubber boat.

The CTDT profiles were obtained by a SEABIRD model SBE 911 with a SEATECH transmissometer (660 nm wavelength and 25 cm beam pathlength). Data were collected at 24 samples per second. The output data of light transmittance at 660 nm were values of voltage ranging from 0 - 5 V, corresponding to 0 - 100%transmittance. The transmissometer values reflect the suspended sediment load within the water column. All CTDT data were

averaged over 1-m intervals for smoothing the plots of salinity, temperature, depth and transmittance, and are considered to be correct to ± 0.01°C and to ± 0.01 psu.

For the vertical distribution of suspended particulate matter, water samples were collected using a Rosette water sampler containing 12 ea 1 litre Niskin bottles. Three-litre water samples were collected to measure the concentration of suspended particulate matter and to identify its nature. One litre of sampled water was vacuum-filtered through pre-weighed nucleopore filters having a nominal pore size of 0.4 μm. Filters were air dried andre-weighedinthelaboratory.Somefiltered samples were analysed using a scanning electron microscope (SEM). Total suspended sediment concentration was then calculated using the sample volume and sediment weight (Table I). Ten litre water samples were used for grain size analysis (a laser particle size analyser by Malvern) (Table II). Tide data were obtained from a tide gauge installed adjacent to King Sejong Station and meteorological data (air temperature, wind speed, wind direction, etc.) by an automatic observatory at King Sejong Station (Fig. 1). Values on meteorological profiles are presented as daily and/or 10-minute averages.

4. Water structure and glacial meltwater discharge

Longitudinal profiles of CTDT data on 3 January 1996 (Fig. 3) and transverse profiles along the glacier cliff in the ice-proximal zone on 7 February 2000 (Fig. 4) were acquired to illustrate general hydrographic structure in the cove. The approximate ranges for temperature, salinity and transmissivity were -0.7 - 1.5°C, 33.30 - 34.10 and 2.8 - 3.9 V, respectively. Density is controlled mainly by salinity, with temperature only playing a small role (Chang et al. 1990). Near the terminus of the tidewater glacier, four distinct water layers are recognized during summer: i) a surface layer including a turbid and cold meltwater plume, ii) a warm layer having characteristics similar to surface water in Maxwell Bay (Maxwell Bay inflow layer), iii) a turbid and cold mid-depth layer, and iv) a fjord deep water layer comprised of remnant winter water.

The turbid surface layer is stratified within a few metres from the surface (Figs 3 & 4), and is related to local freshwater discharge to the cove. Within the drainage areas, surface heating due to radiation and warm summer temperatures (> 2.0°C) (Fig. 2) causes melting of snow and glaciers, and thus the sediment-laden freshwater input increases significantly. Surface meltwater discharge is concentrated at the head of the cove and its influence decreases towards the mouth (Fig. 3). In the surface layer, the surface plume of supraglacial meltwater discharge exists within 1 m of the surface. Due to vertical mixing by waves and wind, the surface plume does not maintain its integrity from the head to long distances. Thus, the surface plume, as defined by slight horizontal salinity and turbidity gradients, is not considered as a distinct water mass.

Temperature and salinity data measured in Maxwell Bay just off the inlet of Marian Cove (surface water in Maxwell Bay) and at stn 5 in the inner basin of the cove (16 December 2000) are illustrated in Fig. 5. Surface water temperature in the bay is vertically homogeneous in winter, but becomes warm gradually during summer (Yoo et al. 2002). Chang et al. (1990) reported the presence of warm surface water in the upper c. 50 m of the bay: 0.5 – 1.4°C on 27 January 1989, 0.7 – 1.1°C on 4 February 1989, and 0.2 – 0.5°C on 16 January 1990. The high temperatures can be explained by supply of warm surface water in addition to direct solar heating of the surface layer. The sill between the bay and the cove permits free water exchange in the surface layer and the bay strongly affects the temperature distribution within the cove in summer. Because sea ice is formed partly from June to September in the cove, melting of sea ice does not play a significant role in freshening of surface water during summer. Salinity in the cove is consistently lower than that in the bay due to the local freshwater discharge (Yoo et al. 1999, 2000, 2003). On 3 January 1996, mid-depth (52 – 74 m) water with slightly colder temperatures (-0.63 to -0.58°C) and slightly lower transmissivity (3.60 – 3.65 V) than the ambient water (Maxwell Bay inflow layer and deep water) was observed at stn 3 near the glacier front (Fig. 3), which suggests water originating from a subglacial tunnel or grounding line of the glacier. The presence of a turbid/cold mid-depth layer is often reported in the ice-proximal zone of Antarctic fjords (Domack &

Williams 1990, Domack et al. 1994). On 7 February 2000, the turbid/cold feature of the cove was pronounced from 11 - 26 m water depth at stn 1 and stn 2 of the transverse transect (Fig. 4). Dumping of a large amount of sediment at the base of the tide-water glacier can generate down-slope turbidity currents (Domack et al. 1994), but such currents were not observed in the ice-proximal zone of Marian Cove (Yoo et al. 1999, 2000, 2003), suggesting that turbulence is weak near the grounding line of the tidewater glacier. Far-field stations (stn 6 and stn 7) away from the glacier front do not exhibit such a water layer.

The turbid/cold mid-depth layer was clearly visible in profiles from at stations 1 and 2 in front of the north-western glacier of the cove (Fig. 4). The glacier at the calving front is c.50 - 170 m thick and is thicker with increasing water depth (Fig. 6). The starting point of the features in sub-polar fjords is a subglacial meltwater conduit system that is closely associated with the crevasses in summer (Paterson 1981). Supraglacial meltwater can potentially connect to subglacial pathways through crevasses. The presence of the turbid/cold mid-depth layer in the inner cove indicates well developed subglacial networks on the north-western side of the glacier. Figure 6 is a schematic view of the water structures in the cove and subglacial discharges with crevasse conduit systems, consistent with typical Antarctic fjords in terms of water turbidity (Syvitski et al. 1996).

5. Factors influencing water structure and behaviour of meltwater plumes

Tides

A 24-hour time series of CTDT profiles was obtained at stn 5, in the inner basin, at c. 1-hour intervals between 21h00 14 December and 20h00 15 December 1996. A maximum tidal range of c. 220 cm was recorded over c.1.5 semi-diurnal cycles (Fig. 7a).

Closely packed isotherms (< 0.0°C) and low transmissivity (< 2.7 V) were observed in the upper 10 m of the surface water (Fig. 7c & e). During the melt season, a surface layer characterized by low salinities, high turbidity and cold temperatures develops in the cove.

The presence of a sediment plume in the cove indicates freshwater release from the glacier to the cove. From our field observations, a small waterfall near the glacier terminus and small meltwater streams formed by melting of side glaciers or draining of a linked lake were identified. Most of the turbid sediment-laden plumes were restricted largely to the north-western margin of the glacier (Yoon et al. 1998, fig. 8) which is heavily crevassed and terminates on land (Yoon et al. 1998, fig. 2 aerial photograph). The direct thermal melting of ice contributes to the fresh surface plume, but water from this source retains a less turbid character due to a relatively clean glacial face. In Marian Cove, the well-defined turbid fresh surface water is derived from terrestrial and supraglacial meltwater. This turbid water plume was well developed during the first flood tide while it was not clearly observed during the second (Fig. 7e). Considering winds were calm or light during the measurement, plume development is thought to be controlled by air temperature. Air temperature before the measurement maintained at c. 1.0°C and a large supply of increased meltwater could intrude into the cove. From the beginning of the measurement to 09h00 15 December it dropped to 0.0°C. Therefore, due to the colder air temperature, decreased potential of meltwater input into the cove may result in less developed surface water during the second flood tide.

The turbid/cold layer was observed at intermediate depths (c.40 - 70 m), and was characterized by lower temperature (< -0.1°C) and higher turbidity (< 3.1 V) compared to the ambient water (Fig. 7c & e). This observation indicates that the characteristics may have originated from neutrally buoyant water through conduits of the crevasse system. The overarching trend in temperature and transmissivity profiles is the presence of the mid-depth layer during the fl ood tide and disappearance during the ebb tide (Fig. 7c & e). In addition, the presence of this layer was prominent over the first flood tide, while it was less pronounced during the second flood tide. This suggests that the variability of the mid-depth layer may be closely associated with tidal frequencies. The difference between the first and second flood tides may be due to changes in air temperature and the associated extent of supraglacial streams. At higher air temperatures, these streams may supply large volumes of water to crevasse conduits, and thus the mid-depth layer is more prominent during the first flood

tide.

Winds

Yoo et al. (1999) reported that winds played an important role in water exchange of Marian Cove. Their work was based upon 23-hour on-board CTDT profiles obtained at 1-hour intervals at stn 5 on 21 - 22 January 1998 (Fig. 8). The maximum tidal range was c. 90 cm and air temperatures ranged from -0.1 - 3.2°C (Fig. 8a). With the exception of the second flood tide during the measurement period, the feature of closely packed isohalines and low transmissivity was not observed over the measurement when wind was light (< 6.0 m s-1). The most remarkable aspect in the water column is that the Maxwell Bay inflow was not observed for the first 3 hours of the measurement (Fig. 8c). At that time, the Maxwell Bay inflow layer (> 0.8°C) appeared at 15 - 30 m (Fig. 8c). The interaction of tidal effects with the fjord water under calm or light wind is demonstrated in Fig. 7. The variation pattern of Maxwell Bay inflow was nearly consistent with tidally-induced vertical movement of water which extends into the inner cove (Fig. 7c). The disappearance of warm water may be explained by an upwelling event, upward movement of deep water that is colder than the Maxwell Bay inflow.

The upwelling event (shaded in blue in Fig. 8) in the early stage of CTDT measurements (from 15h00 to 18h00 21 January) is probably related to the wind influence prior to the measurements under weak tidal influence (Fig. 8a & b). For 15 hours prior to the measurements (from 00h00 to 15h00 21 January), there was a strong easterly wind with speeds of > 9m s-1. The wind-induced advection can be strong enough to generate upwelling near the head of the cove. There were no icebergs in the inner cove even though ice calving was actively occurring in January, which indicates the movement of icebergs out of the cove by the easterly winds. In an earlier study of Maxwell Bay, Klöser et al. (1994) reported that frequent easterly and katabatic winds at Potter Cove (Fig. 1) could enhance the speed of the outflow and slow down or reverse the inflow, thus the surface water in the ice-proximal zone would be replenished by upwelling water. In addition, Nowosielski (1980) reported that

wind-induced advection caused the generation of outflow and the upwelling along the bottom of the inner bay of Admiralty Bay (Fig. 1).

When wind forcing became weak and the upwelling stopped, the Maxwell Bay inflow appeared in the inner cove (Fig. 8c). After 6 hours, the tide was ebbing and the turbid/cold layer (< 0.7°C, < 4.2 V) was observed at 40 - 55 m (Fig. 8e). This observation may have been controlled by changes in air temperature. Throughout measurement, air temperatures were c. 0.7 - 3.0°C, leading to meltwater production in supraglacial streams and percolation to the glacier bed; thereby facilitating development of the mid-depth layer.

Besides the instability of water column, high turbidity of surface water due to the resuspension of benthic material is accompanied by upwelling. Brandini & Rebello (1994) reported that the surface layer was turbulent and turbid during upwelling periods due to the resuspension of benthic diatoms in the inner inlets (c.10 - 30 m) of Admiralty Bay. In Potter Cove, with shallow depths in the inner basin (< 30 m), resuspension of benthic material was observed (Klöser et al. 1994). In contrast, the resuspension of bottom material in Marian Cove would be insignificant because the depth of the inner basin (c. 120 m) is too deep to cause resuspension of the bottom sediment by upwelling. This interpretation is supported by the low turbidity of the surface water during the upwelling event (Fig. 8e).

Other factors

The Coriolis effect is important only where the fjord width exceeds the Rossby radius of deformation (Gill 1982), which is c.5 - 10 km in typical polar environments. The surface circulation of Maxwell Bay is influenced by a cyclonic gyre associated with the Coriolis effect (Chang et al. 1990). However, Marian Cove is only c. 1.5 km wide, and the Coriolis effect does not seem to be present even at the low speed of outflow from the cove. Nevertheless, the hydrography of the cove appears to be influenced by the surface cyclonic circulation in adjacent Maxwell Bay. The inflowing Maxwell Bay water entrains clastic and suspended particles along the northern shore of the cove and carries them out to Maxwell Bay (Yoo et al. 2000). Indirect evidence for such a current regime is provided by the paths of icebergs calved from Marian Cove glacier;

these flow along the northern shore between head and inlet under calm conditions. This circulation is able to deliver surface water and suspended particles to Maxwell Bay.

The glacier entering Marian Cove is gradually retreating, with active calving in summer. Although most floating icebergs move out of the cove, occasionally abundant icebergs are observed in the cove. Yoo et al. (2000) measured the water column structure and dispersal pattern of suspended particulate matter when the cove contained a large number of floating icebergs. Icebergs were completely stuck in the inner basin of the cove by strong north-western winds (> 7.5 m s-1). The maximum tidal range was c. 140 cm and air temperature ranged from 1.0 - 2.5°C. From the 24-hour CTDT profiles obtained at stn 6 in the central basin (Fig. 1), a cold, clean, fresh surface layer (> 10 m thick) was observed throughout the measurement. This layer may simply be the result of mixing of clean meltwater from icebergs within the inner cove. In the central basin, the turbid/cold structure observed in the ice-proximal zone (stn 5) was not exhibited.

Strong rainfall may be one of the factors affecting short-term meltwater discharge in sub-polar regimes during the summer. Yoo et al. (2003) reported variable meltwater discharges during a rainstorm event. A 12-hour rainstorm resulted in 22.7 mm of rainfall near Marian Cove and supplied freshwater to the glacial drainage basin. Such an event may lead to high-density glacial meltwater discharges into the cove. However, strong rainfalls in summer are infrequent and have a short duration, and thus their records in the cove may not be recognized (i.e. Yoon et al. 1997), although rainstorm-induced event sedimentation is commonly observed at the front of temperate tidewater glaciers (e.g. Cowan et al. 1988).

6. Sedimentation in the cove

Marian Cove is floored with a thin sediment drape (< 6m) on the acoustic basement (Yoon et al. 1997). Park et al.(1998b) reported that the apparent sediment accumulation rate on the floor ranges from 0.15 - 0.43 cm yr-1,much lower than that estimated in many Northern Hemisphere fjord

environments (e.g. Powell & Molnia 1989). Sediment accumulation rate obtained from 210Pb age dating is 0.075 cm yr-1 (Kim 1989) at the central basin of the cove, very similar to the 0.09 cm yr-1 (14C radiocarbon age dating) rate for the upper facies of core sediment obtained from the same basin (Yoon et al. 2004). The core sediment in the upper facies over the cove was composed of basal or supraglacial meltwater-derived sediment (Yoon et al. 1997, 2004). The absence of gravity-flow structures and rhythmic laminations indicates that the sedimentation in the cove was slow, as evidenced by preservation of whole shells (i.e. Yoldia eightsi (Couthouy)) on the floor (Yoon et al. 1997).

Exchange of surface waters between Maxwell Bay and Marian Cove is active, yielding significant lateral transport of suspended particulate matter (SPM) from the cove to the bay (Yoon et al. 1998). The SPM in the fjords and bays of the South Shetland Islands consists of fine silty mud, and SPM in surface waters accounts for > 50 - 90% of the total SPM (Khim et al. 2007). Most SPM in Marian Cove consists of clastic sediments and organic matter from primary production (Yoon et al. 1998, fig. 6). Using data from a sediment trap deployed in the cove, Khim et al. (2007) reported that lithogenic particle fl ux comprises c. 90% of the total flux of terrigenous sediments. The deposition of suspended particles on the sea floor would depend upon their residence time, which is set by fjord circulation patterns within the cove. However, the cove has weak potential for sediment deposition on the bottom due to low SPM concentrations (< 10 mg l-1)(Table I).

From early December to late April, Marian Cove is free from sea ice. At the start of summer, turbidity level rises, which indicates the initiation of sediment flux into the cove. The degree of turbidity decreases with increasing water depth except for the mid-depth layer found only in the inner basin of the cove (Figs 3, 4, 7 & 8). In the surface layer of the cove (Yoon et al. 1998), aggregates of fine-grained lithogenic and organic materials and flocs of biological detritus were observed. In contrast, in the mid-depth layer, only coarse silty materials (mean grain size: c. 51.5 μm) with typical morphoscopic characteristics of glacial-originated sediments, such as conchoidal fractures, step-like features, sharp edges and breakage block, were observed (Fig. 9, Table II). This indicates that the suspended sediments in the mid-depth layer were

transported by horizontal buoyant plume rather than vertically deposited by settling from the supraglacial meltwater plume at the head of the cove. Hydrographically driven fluctuations in the position of the mid-depth layer and associated suspension settling can contribute to the depositional source in the ice-proximal zone.

The contribution of ice-rafted debris (IRD) to ice-proximal sedimentation in Antarctic fjords is known to be much less than that occurring in Alaskan and Greenland fjords (Syvitski et al. 1996). Detachment of the tidewater glacier along a crevasse system of the northern glacier occurs during summer. However, on X-radiographs of core sediment from Marian Cove (Yoon et al. 2004, fig. 5), there is no condensed IRD in the upper facies, but some scattered IRD, indicative of a small influx of IRD. This seems to be due to relatively clean icebergs and/or the short residence time of icebergs in the cove.

In summer, fjord water in Marian Cove is subject to tide and wind forcings, similar to the observations from other fjords in King George Island (Klöser et al. 1994). The wind- and tidally-induced behaviours of surface and mid-depth layers seem to control the depositional processes of SPM in the cove. The easterly wind, coupled with ebb tides, will drive out surface water and accordingly the suspended sediment flux out of the cove would be quite high. In contrast, flood tides coupled with the north-western and western winds allow enhanced sedimentation in the cove by increasing residence time of SPM. The mid-depth layer is no exception to this pattern. The maximum development of the mid-depth layer during flood tides increases the potential for deposition for suspended sediments in the inner basin, while its weak development during ebb tides decreases the potential of sediment deposition. This implies that suspended sediments will be selectively deposited in the ice-proximal zone of the inner basin, leading to the deposition of the laminated sand and mud facies in association with tidal cycles. However, in the upper part of the core sediment from the central basin (Yoon et al. 2004), this facies was not distinct, although some faint laminations associated with seasonal variations of deposition were observed. This observation can be explained by the destabilization of the water column due to strong and frequent wind forcings and/or by the limited influence of mid-depth layer on the deposition of SPM in the ice-proximal zone. Another

explanation for the structureless facies may be the unstable subglacial conditions during summer. Due to the recent warming, the glacial terminus in the cove has retreated rapidly at c.81.2myr-1 from 1994 - 2001 (Park et al. 1998a). Such a rapid retreat rate suggests unstable subglacial conduit networks resulting in low entrainment of glacial meltwater and a weak turbulent jet at the grounding line.

7. Summary

Hydrographic measurements during summer in Marian Cove from 1996 - 2000 reveal the presence of glacial meltwater plumes and their effect on water structures, and provide information on hydrodynamics and depositional processes in the cove. Four distinct layers are recognized in summer: i) a cold and turbid surface layer, i) a warm Maxwell Bay inflow layer with characteristics of surface waters in adjacent Maxwell Bay, iii) a mid-depth turbid/cold layer originated from subglacial meltwater discharge, and iv) a fjord deep layer comprised of remnant winter water. Although Marian Cove is in some ways a typical Antarctic fjord, it has its own unique circulation patterns and morphological features.

Marian Cove is characterized by two turbid sediment-laden meltwater systems. Surface plumes are produced by thermally melting ice due to glacier-water contact melting, waterfalls and meltwater streams. The turbid/cold mid-depth layer close to glacier terminus represents subglacial discharge rising tens of metres to form buoyant plumes. The fluctuations in the position and thickness of the mid-depth layer are best explained by the subglacial meltwater discharge dynamics related to hydrographic conditions (including tide, wind, temperature and rainfall) and tidal flushing of the grounding line from the subglacial conduit system. With no precipitation or icebergs, the time-dependent plumes at the surface and mid-depth in the ice-proximal zone are developed mostly by tides coupled with wind effects. Under weak tidal influence, strong and persistent winds from the eastern direction generated an upwelling event near the cove head, which interrupted the usual development of surface and mid-depth layers within the cove.

The depositional environment of Marian Cove is characterized by

suspension settling of meltwater-derived sediment, and the depositional processes are mainly influenced by the hydrographic and meteorological forcings. Tidal forcing coupled with wind stress played an important role in the ice-proximal distribution and deposition of SPM in the cove.

Wind effects keep sediments of the turbid surface layer in suspension, which facilitates transportation of suspended particles into and out of the cove. However, the north-westerly and westerly winds coupling with flood tides probably caused supraglacial meltwater particles to deposit in the ice-proximal zone. Above all, the turbid/cold mid-depth layer becomes a main contributor to the source of terrigeneous sediments in the inner basin of the cove.

Acknowledgements

We would like to thank the over-wintering party of the King Sejong Station for operation of the rubber boat in Marian Cove during the 1996 - 2000 KARP (Korea Antarctic Research Program) cruise. We are also grateful to the crew of RV Yuzhmorgeologya for all their help during the CTDT on-board measurements. This research was funded by KOPRI Grant PP14010. This manuscript benefited from constructive comments by the Editor Dr Laurence Padman and two anonymous reviewers.

서남극 킹조지 섬 마리안 소만의 수리학적 특성 : 여름동안 얼음 근방에서의 퇴적작용에 대한 연구

유규철[1], 이민경[1*], 윤호일[1], 이용일[2]

[1]한국해양과학기술원 부설 극지연구소
[2]서울대학교

요약: 1996-2000 년의 여름 동안 전도도, 수온, 투과율의 수직 단면도가 남극 반도 킹조지 아일랜드 섬의 마리안 코브 (Marian Cove)의 조수 빙하 근처에서 얻어졌다. 이 연구의 목적은 수로학적 강제력에 의한 수괴의 단기 변동을 파악과 남극 피오르드 환경에서 부유입자물질의 침강을 이해하는 것이다. 4개의 뚜렷한 수괴층이 마리안 코브의 빙하와 가까운 존에서 파악되었다: 1) 차고 탁한 융빙수로 구성된 표층수, 2) 피오르드 바깥쪽 수괴의 특성을 지닌 상대적으로 따뜻한 맥스웰 만 유입층, 3) 탁하고/찬 중층수, 4) 겨울철에 남아 있던 심층수. 빙하의 융빙수 층의 특성에 영향을 미치고 코브 내 부유 입자의 퇴적을 유도하는 주요 요인은 바람의 스트레스와 연관된 조석이다. 마리안 코브 (Marian Cove)에서 비교적 적은 양의 융빙수 배출로 인해 코브에서 비생물 퇴적물 입자의 낮은 축적률이 나타난다. 범람 조류와 결합된 북서풍 및 서풍에 대한 반응은 코브의 빙하 근처 영역의 탁층에서 유입된 부유 입자의 침강과 퇴적을 촉진시킬 수 있다.

참고문헌

Brandini, F.P. & Rebello, J. 1994. Wind field effect on hydrography and chlorophyll dynamics in the coastal pelagial of Admiralty Bay, King George Island, Antarctica. Antarctic Science, 6, 433 - 442.

Chang, K.I., Jun, H.K., Park, G.T. & Eo, Y.S. 1990. Oceanographic conditions of Maxwell Bay, King George Island, Antarctica (austral summer 1989). Korean Journal of Polar Research, 1, 27 - 46.

Cook, A.J., Fox, A.J., Vaughan, D.G. & Ferrigno, J.G. 2005. Retreating glacier fronts on the Antarctic Peninsula over the past half-century. Science, 308, 541 - 544.

Cowan, E.A. 1992. Meltwater and tidal currents: controls on circulation in a small glacial fjord. Estuarine Coastal and Shelf Science, 34, 381 - 392.

Cowan, E.A., Powell, R.D. & Smith, N.D. 1988. Rainstorm-induced event sedimentation at the tidewater front of a temperate glacier. Geology, 16, 409 - 412.

Domack, E.W. & Williams, C.R. 1990. Fine structure and suspended sediment transport in three Antarctic fjords. Antarctic Research Series, 50, 71 - 89.

Domack, E.W., Foss, D.J.P., Syvitski, J.P.M.& Mclennen, C.E. 1994. Transport of suspended particulate matter in an Antarctic fjord. Marine Geology, 121, 161 - 170.

Gill, A.E. 1982. Atmosphere-ocean dynamics, New York, NY: Academic Press, 662 pp.

Hur, S.D., Lee, J.I., Hwang, J. & Choe, M.Y. 2001. K-Ar age and geochemistry of hydrothermal alteration in the Barton Peninsula, King George Island, Antarctica. Ocean Polar Research, 23, 11 - 21. [Korean].

Khim, B.K., Shim, J., Yoon, H.I., Kang, Y.C. & Jang, Y.H. 2007. Lithogenic and biogenic particle deposition in an Antarctic coastal environment (Marian Cove, King George Island): seasonal patterns from a sediment trap study. Estuarine Coastal and Shelf Science, 73, 111 - 122.

Kim, K.H. 1989. Measurement of radioactivity in sediments and estimation of sedimentation rate. KORDI report, BSPG 00081-246-7.

Ansan: Korea Ocean Research and Development Institute, 470 - 485.

Klöser, H., Ferreyra, G., Schloss, I., Mercuri, G., Laturnus, F. & Curtosi, A. 1994. Hydrography of Potter Cove, a small fjord-like inlet on King George Island (South Shetland). Estuarine Coastal and Shelf Science, 38, 523 - 537.

KOPRI. 2009. Annual weather report, King Sejong, Korean Antarctic Station (2007). KOPRI report, BSPE08030. Ansan: Korea Ocean Research and evelopment Institute, 18 - 20.

Nowosielski, L. 1980. Meteorological conditions at Arctowski Station in 1978 (King George Island, South Shetland Islands). Polish Polar Research, 1, 83 - 93.

Park, B.K., Chang, S.K., Yoon, H.I. & Chung, H. 1998a. Recent retreat of ice cliffs, King George Island, South Shetland Islands, Antarctic Peninsula. Annals of Glaciology, 27, 633 - 635

Park, K.H., Han, J.H., Yoon, H.I. & Kim, Y. 1998b. Estimation of sediment accumulation rate and sediment mixing rate using excess lead-210 in the sea around King George Island, West Antarctica. KORDI report, BSPP 98001-04-1149-7. Ansan: Korea Ocean Research and Development Institute, 71 - 89.

Paterson, W.S.B. 1981. The physics of glaciers. New York, NY: Pergamon, 380 pp.

Powell, R.D. 1990. Glacimarine processes at grounding-line fans and their growth to ice-contact deltas. In DOWDESWELL, J.A. & SCOURSE, J.D., eds. Glacimarine environments: processes and sediments. Geological Society London Special Publication, No. 53, 53 - 73.

Powell, R.D. & Molina, B.F. 1989. Glacimarine sedimentary processes, facies and morphology of the south-southeast Alaska shelf and fjords. Marine Geology, 85, 359 - 390.

Syvitski, J.P.M., Andrews, J.T. & Dowdeswell, J.A. 1996. Sediment deposition in an iceberg-dominated glacimarine environment, East Greenland: basin fill implications. Global and Planetary Change, 12, 251 - 270.

Yoo, K.-C., Kang, C.Y., Yoon, H.I., Suk, D.W. & Oh, J.-K. 2002. Seasonal water column properties and dispersal pattern of suspended particulate

matter (SPM) in Marian Cove, King George Island, South Shetland Islands. Journal of Geological Society of Korea, 38, 573 - 593. [Korean].

Yoo, K.-C., Yoon, H.I., Oh, J.-K., Kang, C.Y. & Khim, B.K. 2000. Water column structure and dispersal pattern of suspended particulate matter (SPM) in a floating ice-dominated fjord, Marian Cove, Antarctica during austral summer. The Sea, 5, 295 - 304. [Korean].

Yoo, K.-C., Yoon, H.I., Oh, J.-K., Kim, Y. & Kang, C.Y. 1999. Water column properties and dispersal pattern of suspended particulate matter (SPM) of Marian Cove during austral summer, King George Island, West Antarctica. Journal of the Korean Society of Oceanography, 4, 266 - 274. [Korean].

Yoo, K.-C., Yoon, H.I., Oh, J.-K., Kang, C.Y., Kim, Y. & Bae, S.-H. 2003. Wind- and rain-induced variations of water column structures and dispersal pattern of suspended particulate matter (SPM) in Marian Cove, the South Shetland Islands, West Antarctica during the austral summer 2000. The Sea, 8, 357 - 368. [Korean].

Yoon, H.I., Park, B.K., Domack, E.W. & Kim, Y. 1998. Distribution and dispersal pattern of suspended particulate matter in Maxwell Bay and its tributary, Marian Cove, in the South Shetland Islands, West Antarctica. Marine Geology, 152, 261 - 275.

Yoon, H.I., Han, M.W., Park, B.K., Oh, J.-K. & Chang, S.K. 1997. Glaciomarine sedimentation and paleo-glacial setting of Maxwell Bay and its tributary embayment, Marian Cove, in the South Shetland Islands, West Antarctica. Marine Geology, 140, 265 - 282.

Yoon, H.I., Yoo, K.-C., Park, B.K., Kim, Y., Khim, B.-K. & Kang, C.-Y. 2004. The origin of massive diamicton in Marian and Potter coves, King George Island, West Antarctica. Geosciences Journal, 8, 1 - 10.

Table I. Concentration ($mg\ l^{-1}$) of suspended particles in the ice-proximal zone of Marian Cove.

Depth (m)	1996	1998*	1998	1998	2000*
0	9.5	5.1	5.6	3.0	3.6
7	8.7				
10		4.1	4.7	3.3	
14	8.8				
20	8.9		6	3.1	2.7
28	8.8				
30			4	1.5	
40					1.3
42	8.5				
45		3.2			
50		2.4	13.9	1.9	3.6
55			3		
60	9.4	2.7			2.5
70	8.9				2.6
80		3.1		3.0	3.2
90					2.8
96					3.1
Date	15 Dec	22 Jan	31 Jan	31 Jan	26 Jan
Time	10h00	13h00	09h00	14h00	22h00
Tidal range	210 cm	40 cm	130 cm	180 cm	130 cm
Tidal level	Ebb	Flood	Flood	Ebb	Flood
Tidal height	90 cm	133 cm	203 cm	27 cm	185 cm

*After Yoo *et al.* 1999, 2003.

Table II. Mean grain diameter (μm) of suspended particles with water depth in the ice-proximal zone of Marian Cove measured in 1998.

Depth (m)	Grain size (μm)
0	35.5
7	34.9
40	16.7
42	51.5

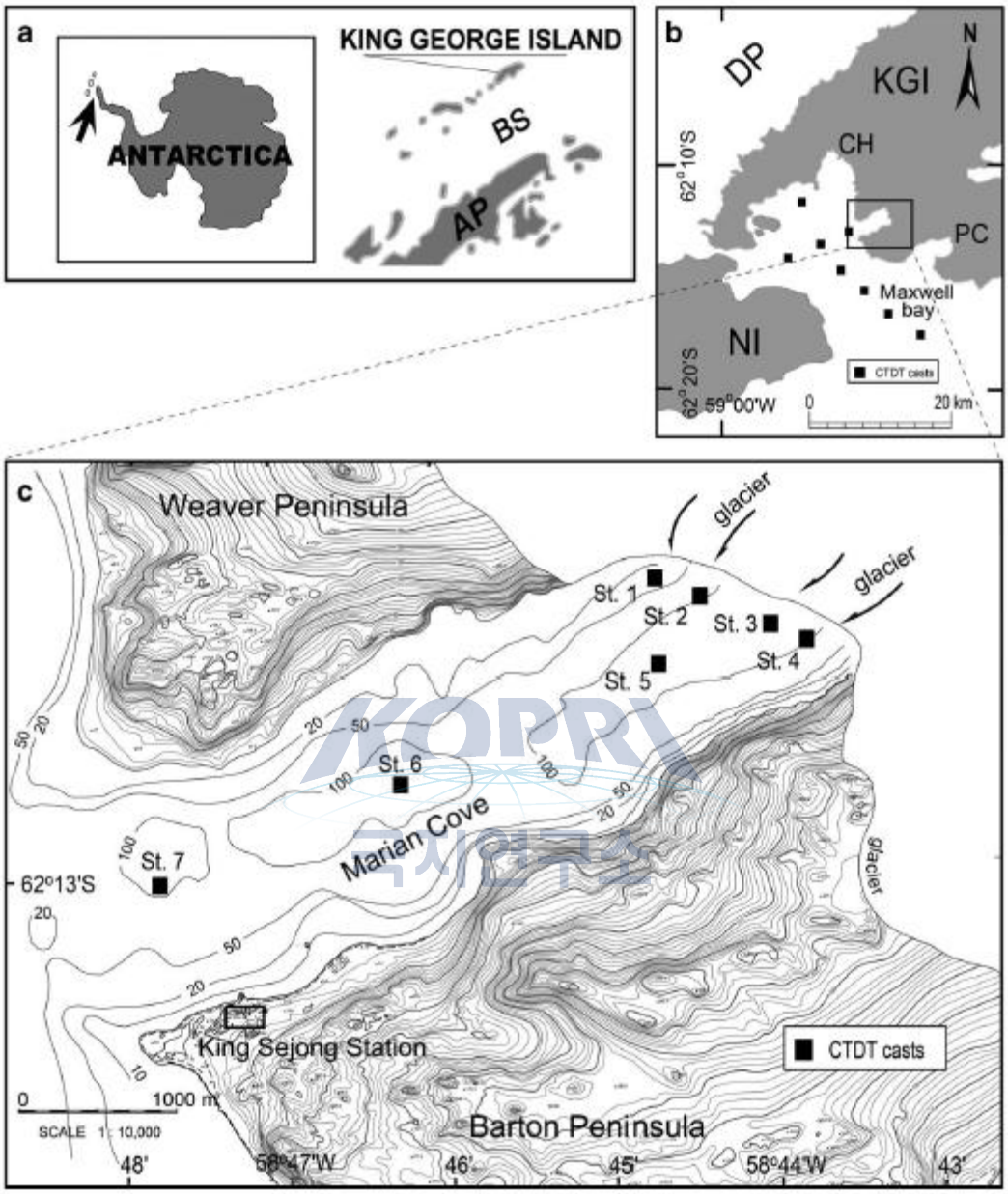

Fig. 1. Location of a. King George Island, b. Maxwell Bay, and c. Marian Cove in the western Antarctic Peninsula. The CTDT measurements in the bay (eight stations) and the cove (stations 1 - 7) are represented by black squares. AP: Antarctic Peninsula, BS: Bransfield Strait, CH: Collins Harbour, DP: Drake Passage,K GI: King George Island, NI: Nelson Island, PC: Potter Cove.

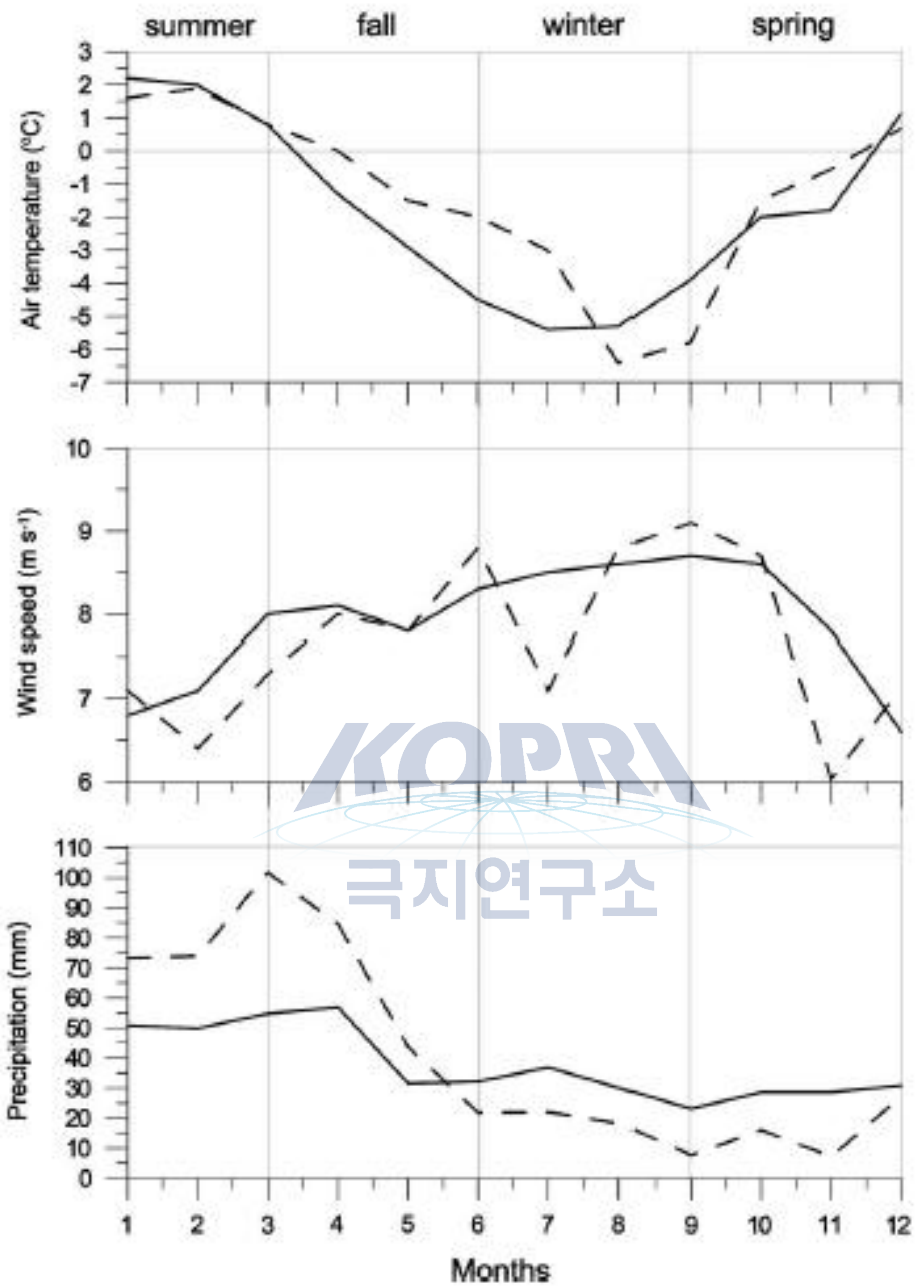

Fig. 2. Typical monthly variation in air temperature (°C), wind speed (m s-1) and precipitation (mm) at King Sejong Station (see Fig. 1 for location). Solid line = mean between 1988 and 2000, and dashed line = mean in 2000.

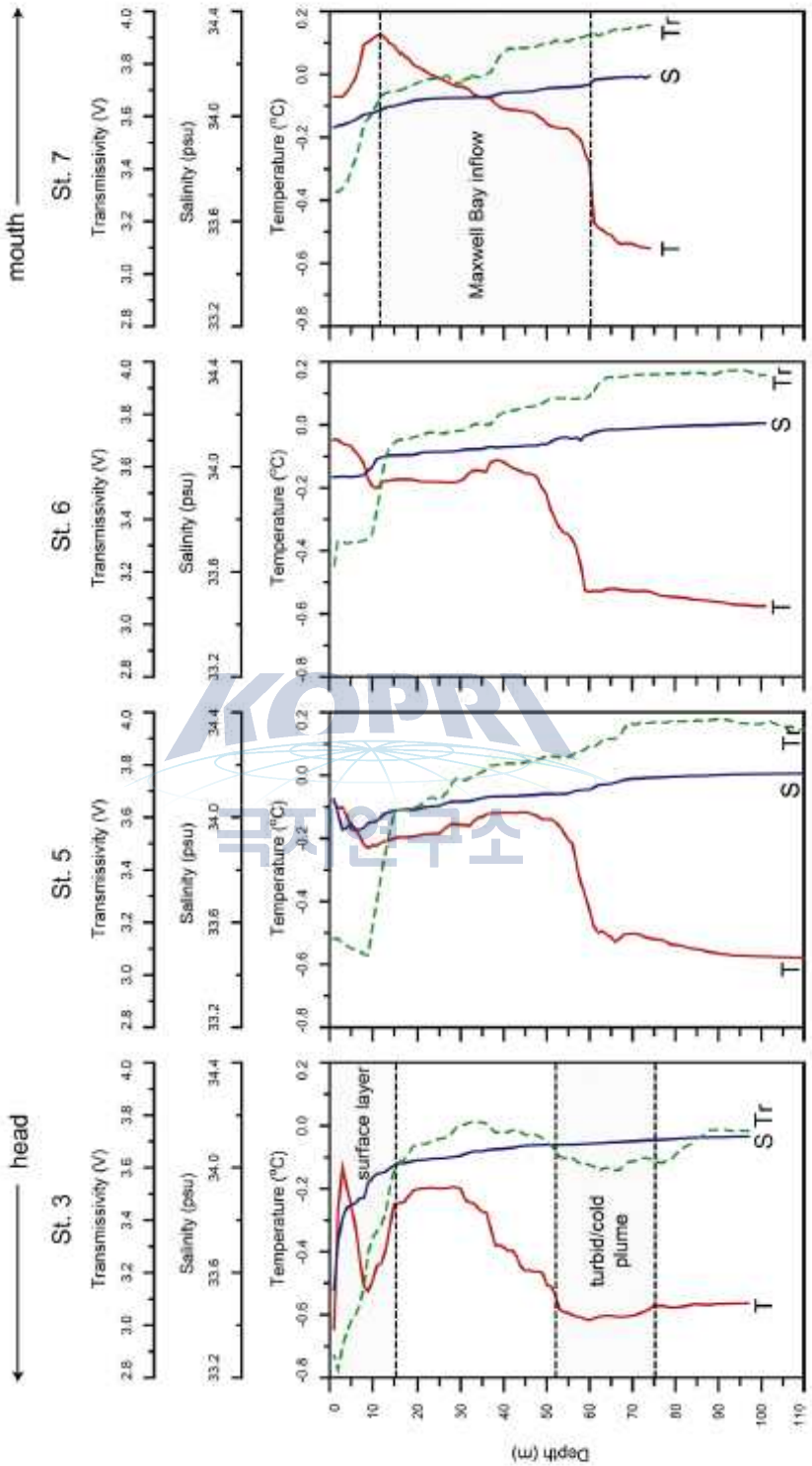

Fig. 3. Vertical profiles of temperature (T), salinity (S) and transmissivity (Tr) along the axis of Marian Cove on 3 January 1996.

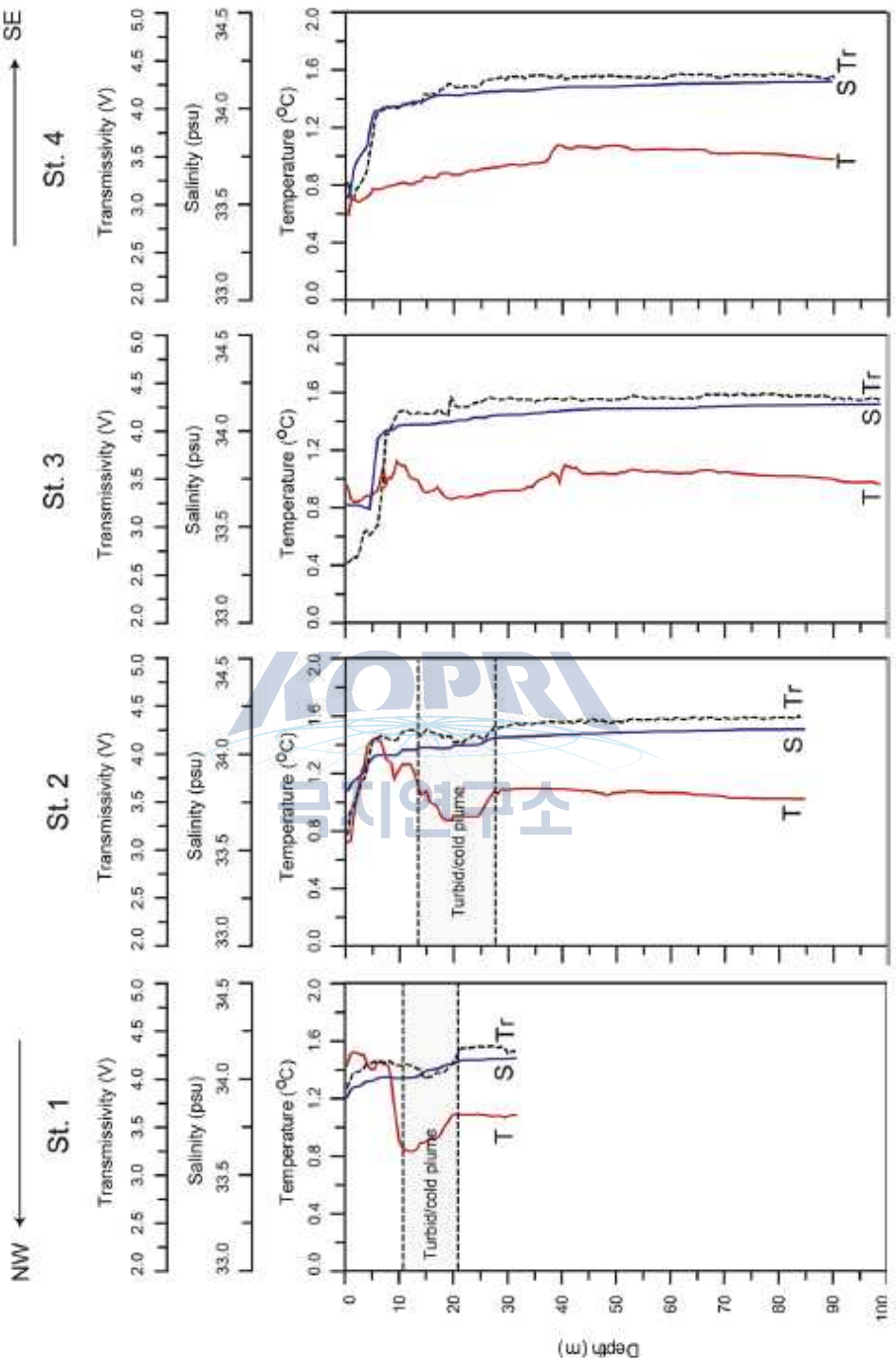

Fig. 4. Vertical profiles of temperature (T), salinity (S) and transmissivity (Tr) along the strike of the ice-proximal zone of Marian Cove measured on 7 February 2000 (modified from Yoo et al. 2002).

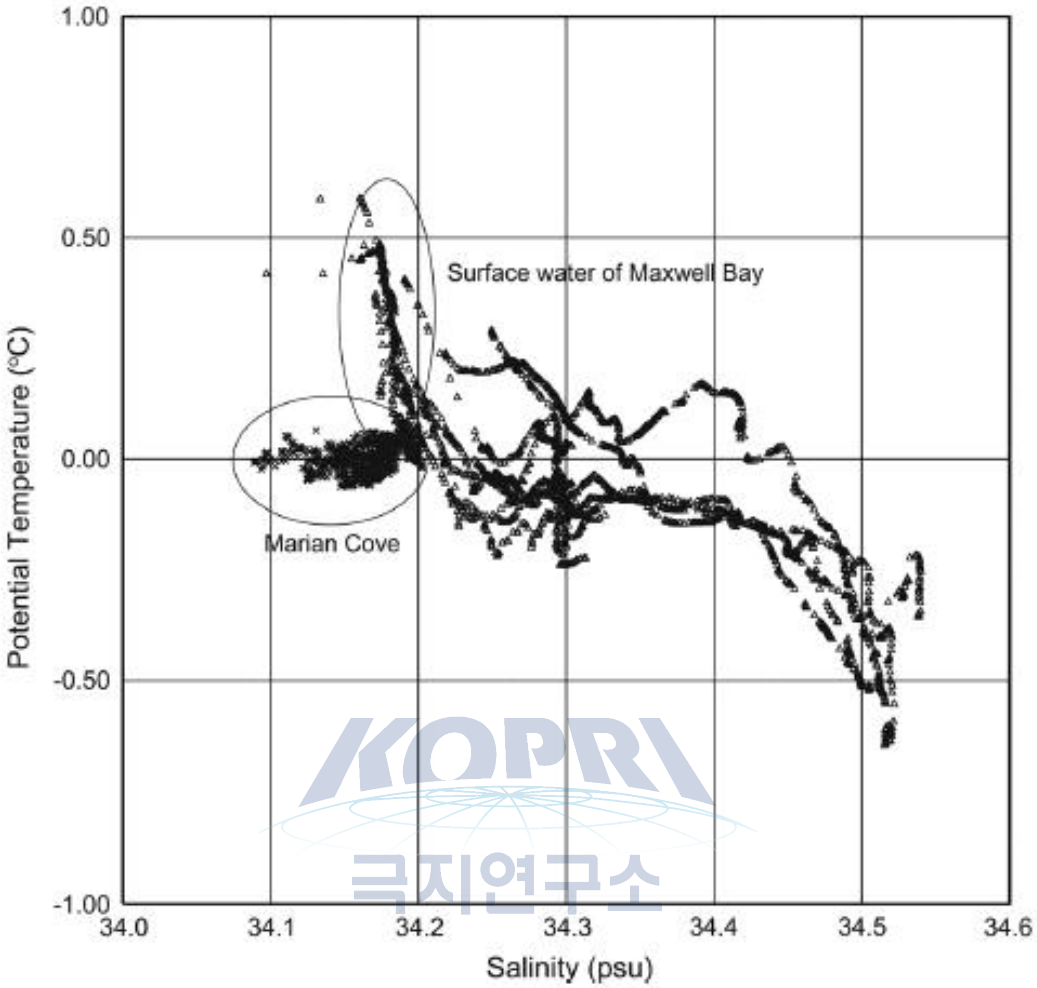

Fig. 5. Temperature-salinity diagram of Marian Cove (near stn 5) and Maxwell Bay (8 stations) (see Fig. 1 for location). The data were obtained on 14 - 16 December 2000.

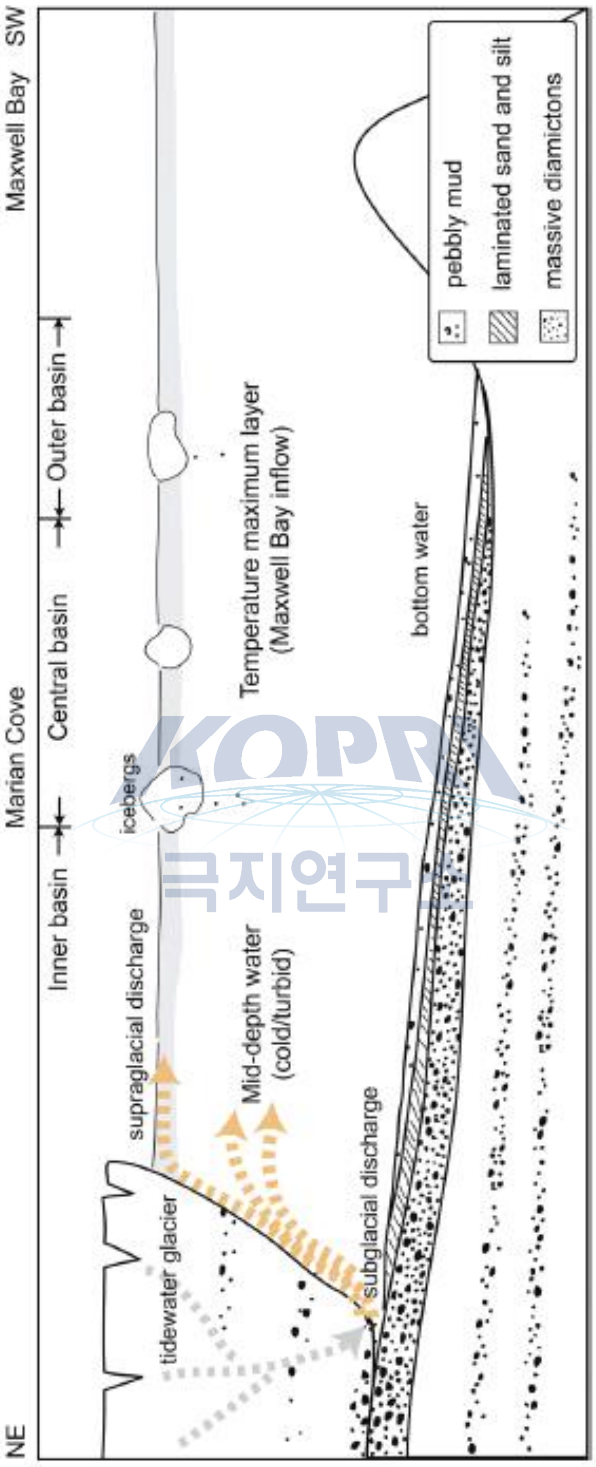

Fig. 6. Schematic diagram of water structures and glacial meltwater discharges (supra- and subglacial discharges) in Marian Cove during summer (modified from Yoon et al. 1997). The sedimentary facies in the cove are also shown.

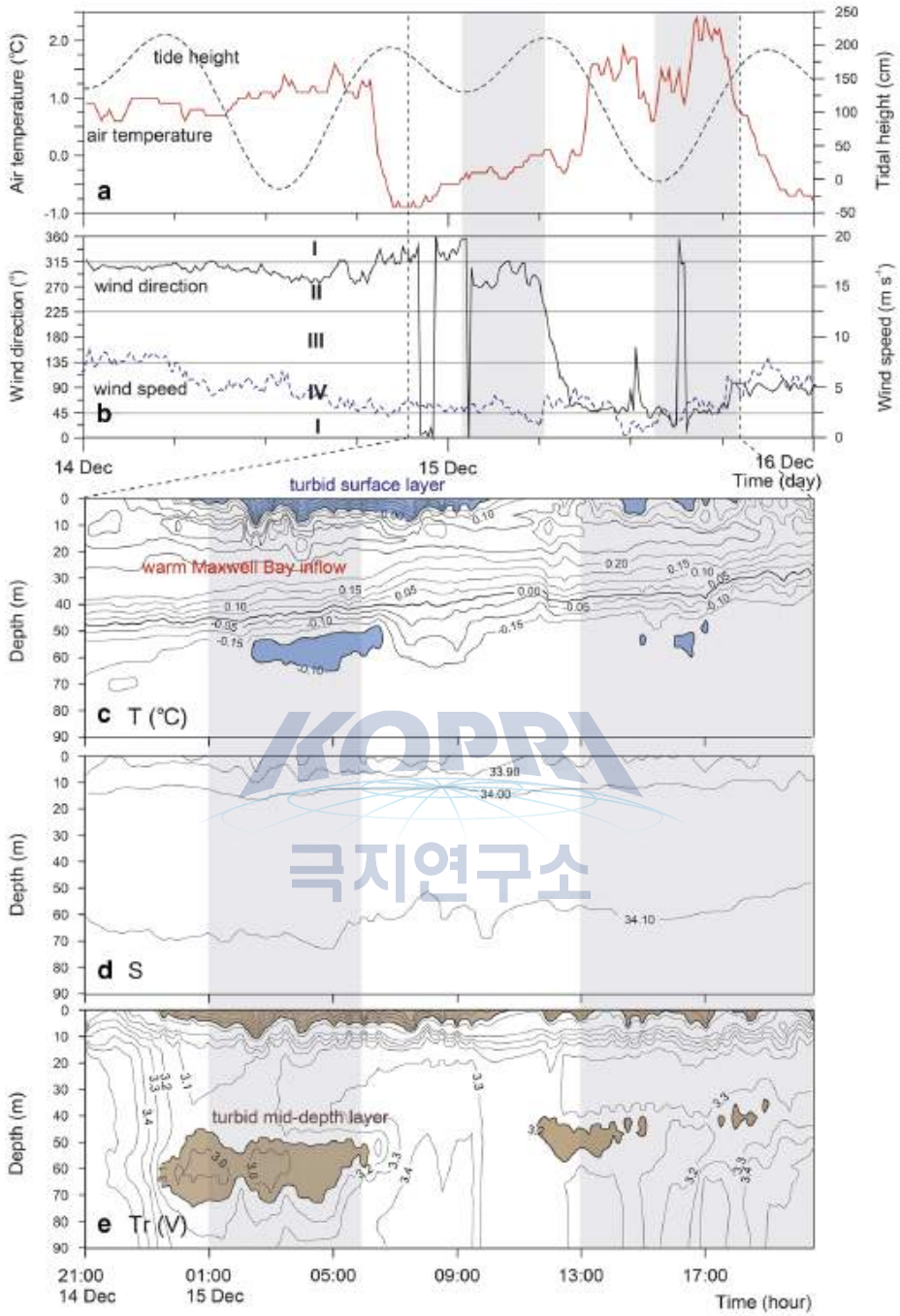

Fig. 7. Vertical and temporal variations of a. air temperature (°C) and tidal height (cm) (dashed line), b. wind direction (°) (I: northern sector, II: western sector, III: southern sector, IV: eastern sector) and wind speed (m s-1) (dashed line), c. temperature (°C), d. salinity, and e. transmissivity (V) of seawater at station 5 during CTDT casting on 14 and 15 December 1996. The two flood periods are shaded in grey. Turbid/cold surface and mid-depth layers are shaded in blue in c. and brown in e., respectively.

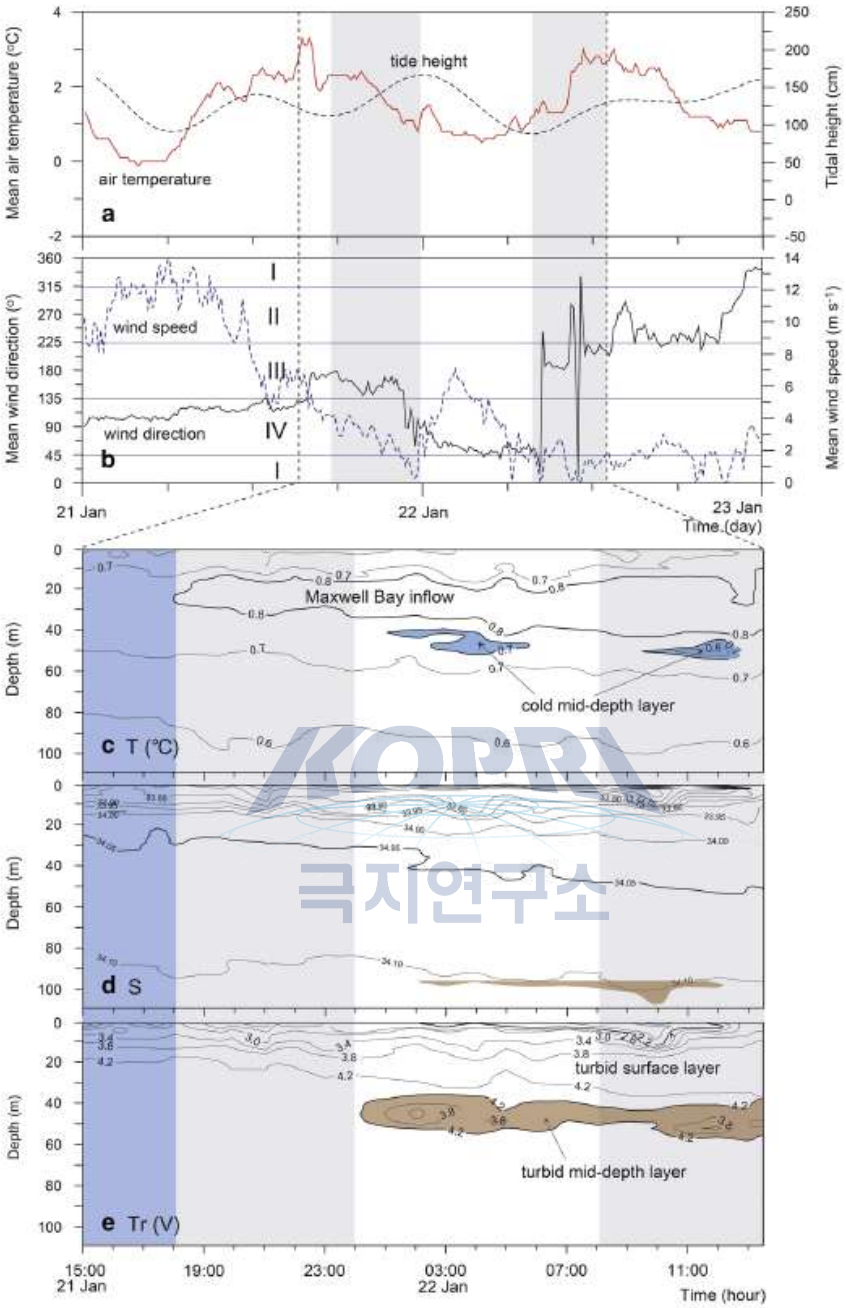

Fig. 8. Vertical and temporal variations of a. air temperature (°C) and tidal height (cm) (dashed line), b. wind direction (°) (I: northern sector, II: western sector, III: southern sector, IV: eastern sector) and wind speed (m s-1) (dashed line), c. temperature (°C), d. salinity, and e. transmissivity (V) of seawater at station 6 on 21 and 22 January 1998 (modified from Yoo et al. 1999). Two flood periods are shaded in grey, turbid/cold surface and mid-depth layers in blue in c. and brown in e., respectively, and upwelling event period in blue in c., and e. (from 15h00 to 18h00 21 January).

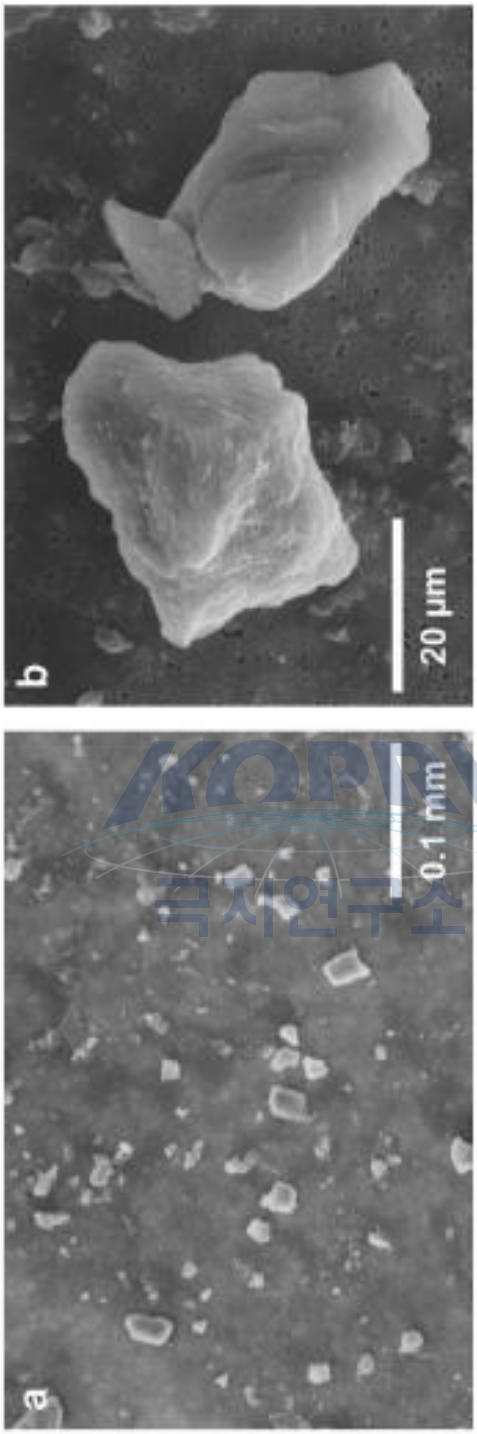

Fig. 9. Scanning electron microscope photomicrographs of suspended particulate matters in the cold/turbid tongue of mid-depth layer (42 m; referred in Table II). a. Filtered particles and b. angular to sub-angular particles with sharp edges, cleavage block and step-like features.

제 7 장

남극반도 북단 남극해의 대자율 조절요인 - 빙산의 분리 대기 순환의 연관

김성한, 유규철, 이재일, 이민경, 김기태, 윤호일, 문흥수

한국해양과학기술원 부설 극지연구소

요약: 스코시아해의 해양퇴적물의 대자율은 빙하 코어에 기록된 칼슘 이온 농도(non-sea salt Ca^{2+} concentration)와 강한 상관관계가 나타났다. 이는 남빙양에서 대기 순환의 역할이 중요하다는 것을 보여준다. 둘의 강한 상관관계를 통해서 남빙양에서 해양퇴적물의 연대 설정의 강력한 툴로서 사용될 수 있다는 것을 의미한다. 그러하 스코시아해의 해양퇴적물의 대자율 변동의 조절요인은 명확하지 않다. 이 연구에서는 남극반도 북쪽의 남빙양에서 해양퇴적물의 입도분석을 통해서 대자율의 변동과 관련된 입도 크기를 확인하고 이 크기의 입자들의 유입 기작을 밝히고자 한다. 스코시아해에서 획득된 코어들의 대자율의 값은 점토질 입자와 평균 입도와 음의 상관관계를 가지는 반면, 사질 입자와는 양의 상관관계를 가지는 것을 통해서, 남극반도 북쪽의 남빙양에서 해양퇴적물의 대자율은 사질 입자의 양에 의해 조절된다는 것을 확인하였다. 게다가, 사질 입자는 빙하쇄설성 퇴적물로서 스코시아해에 유입되는 것으로 생각되며, 사질 입자가 빙하쇄설성 퇴적물의 유입을 대표하는 것으로 생각된다. 그러므로 해양퇴적물의 대자율과 빙하 코어의 더스트 기록의 강한 상관관계는 빙하의 붕괴 활동과 대기 순환 및 남반구 편서풍의 강도가 밀접하게 연관되어 있다는 것을 시사한다.

1. 서론

남빙양은 심층수의 형성 (Orsi et al., 1995) 및 생물펌프 (Takahashi et al., 2002) 등을 통해 전지구적 기후 변화에 있어서 중요한 역할을 담당하고 있다. 그러나 남빙양에서의 고기후/고해양학적 연구들은 유공충의 부재와 오래된 탄소의 유입으로 인해서 연대 설정이 어렵다고 알려져 있다 (Gordon and Harkness, 1992; Nakada et al., 2000; Anderson et al., 2002; Heroy and Anderson, 2005; The

RAISED Consortium et al., 2014). 스코시아해의 해양퇴적물의 대자율은 더스트 유입을 지시하는 빙하코어에 기록된 비해염 칼슘의 농도 변화와 잘 일치한다 (Rothlisberger et al., 2004; Lambert et al., 2011; Weber et al., 2012). 스코시아해 해양퇴적물의 대자율 기록과 빙하코어의 비해염 칼슘의 농도 변화 기록의 시각적인 연결을 통해서 남빙양의 해양퇴적물의 연대를 고해상으로 설정 가능하게 되었다 (Pugh et al., 2009; Allen et al., 2011; Weber et al., 2012; Xiao et al., 2016).

대기 순환이 스코시아해에의 대자율의 변동을 조절하는 중요한 기작으로 제안된바 있다 (Weber et al., 2012). 스코시아해에서 수행된 일부 이전 연구 결과들과 잘 일치한다 (Hofmann, 1999; Pugh et al., 2009). 비록 파타고니아가 주요 더스트 기원지이지만 (Haberzettl et al., 2009), 스코시아해에서 파타고니아에서 멀어지는 거리에 따른 경향성이 나타나지 않았다 (Diekmann et al., 2000; Weber et al., 2012; Xiao et al., 2016) (그림 1). 게다가, 스코시아해의 퇴적물 코어의 칼슘 이온 기록과 빙하코어의 비해염 칼슘 농도 기록과 잘 일치하지만 (Weber et al., 2012) 이것이 육성기원 물질의 유입이 더스트에 의한 것이라는 것을 의미하는 것은 아니다. 게다가 Diekmann et al. (2000)은 지화학적 광물학적 분석을 통해 세립 퇴적물은 더스트 유입에 의해 파타고니아에서 유입되는 것이 아니라, 다양한 기원지에서 해류에 의해 유입된다고 보고하였다. 남오크니고원과 남스코시아해에서 해양퇴적물의 대자율과 사질 입자의 양이 함께 변동한다고 보고된바 있다 (Yoon et al., 2005; Lee et al., 2010). 스코시아해에서 해양퇴적물의 대자율과 빙하 코어의 더스트 기록과의 강한 상관관계에도 불구하고, 대자율이 더스트 유입에 의해 조절된다는 직접적인 증거는 없다.

최근 남극반도 북쪽의 남빙양은 웨델해에서 유입되는 빙산이 지나는 주요 경로이다 (그림 1, Reid and Anderson, 1990; Diekmann and Kuhn, 1999). 빙하기에 해빙 및 빙하가 확장되었기 때문에 (Gersonde et al., 2005; Minzoni et al., 2015), 남스코시아해와 포웰분지에서 빙권의 영향은 지난 빙하기 동안에 강해서 더 많은 빙하쇄설성 퇴적물과 높은 대자율 값을 나타낸다. 서남극 반도에서 높은 대자율 값은 많은 빙하쇄설성 퇴적물의 유입과 함께 나타난다 (예, Brachfeld and Banergee, 2000; Christ et al., 2015; Peck et al., 2015). 그러나, 빙하쇄설성 퇴적물의 유입 변동은 스코시아해에서 대자율의 값과 일치하지 않았기 때문에, 빙하쇄설성 퇴적물의 유입은 대자율의 값을 조절하는 요인에서 제외되었다 (Diekmann et al., 2000; Weber et al., 2012). 그러나, 북대서양에서 빙하쇄설성 퇴적물은 자갈 크기 입자들에만 국한되지 않기 때문에 (Andrews, 2000; Jonkers et al., 2012, 2015), 이전 연구들에서 사용된 적은 수의 큰 크기의 입자들이 빙하쇄설성 퇴적물을 대표하지 못할

수 있다. 예로, 남반구와 북반구 고위도 지역에서 사질 입자가 빙하쇄설성 퇴적물을 지시하는 인자로서 사용된바 있다 (Kanfoush et al., 2000; Sakamoto et al., 2005, 2006; Peck et al., 2007, 2015; Bailey et al., 2013; Teitler et al., 2015). 그러므로 대자율 값의 변동에 대한 빙하쇄설성 퇴적물의 역할에 대해 재평가가 필요하다.

이 연구에서 남극반도 북단의 남빙양의 퇴적물 입도 분석 자료와 대자율 값을 통해, 어떤 입도가 대자율의 변화와 관련이 되며, 이 입자들이 어떻게 들어오는지에 대해서 이해하고자 한다.

2. 재료 및 방법

퇴적물 코어들의 대자율 값 측정은 Bartington MS-2B 대자율 측정기를 사용하여 1 cm 간격으로 측정하였다. 퇴적물에서 생물기원 구성 물질들을 제거한 후, 4 cm 간격으로 입도 분석을 실시하였다. 63 μm 보다 큰 입자들에 대해서는 체를 이용하여 분석하였고, 세립 입자들에 대해서는 세디그라프를 통해서 분석하였다.

3. 결과 및 토의

코어들의 대자율 값은 기존에 스코시아해에서 보고된 값들과 비슷한 변동 양상을 보였다 (그림 2). 코어 MD07-3134는 스코시아해에서 보고된 기존 연구 결과들 중에서 가장 긴 코어이며, 빙하코어의 비해염 칼슘 이온 농도와 강한 상관관계를 보인다 (Weber et al., 2012). 이 연구에서 사용된 퇴적물 코어들의 대자율 값들을 MD07-3134의 대자율과 비교를 하였다 (그림 2). AnalySeries software (Pillard et al., 1996)을 이용하여 시각적 연결을 적용하였다. 이를 통해 계산된 선형 상관계수는 0.75 이상이었다 (표 1). 대자율 값들의 강한 상관관계는 이들 지역에서 대자율 값을 조절하는 요인이 서로 다른 해양학적 특성을 보임에도 같다는 것을 의미한다 (그림 1). 높은 대자율 값을 가지는 구간은 사니질 층이 나타나는 반면 대자율 값이 낮은 구간에서는 니질 층이 나타난다.

3.1. 대자율의 변화와 관련되는 입자 크기

해양퇴적물 코어들의 대자율의 변동 패턴은 사질 입자의 변동과 비슷하며, 평균 입도 및 니질 입자의 변동과는 반대 양상을 나타내었다 (그림 3). 대자율 값과 사질 입자의 양, 평균 입도, 니질 입자의 양과의 강한 상관관계는 통계적으로 확인

되었다 (그림 4). 이러한 결과들은 남극반도 북쪽의 남빙양에서의 해양퇴적물의 대자율의 변동은 니질 입자에 의한 것이 아니라 명확하게 사질 입자에 의해서 조절된다는 것을 보여주며, 이것은 더스트 유입이 대자율 값의 변동에 주요 요인이 아니라는 것을 의미한다. 사질 입자 중에서도 비교적 세립한 사질 입자들이 대부분을 차지하였다.

3.2. 사질 입자의 운송 기작

사질 입자의 운송 기작과 관련하여, 니질 입자는 해양퇴적물의 대자율과 음의 상관관계를 보였기 때문에 (그림 3), 풍성기원은 대자율의 주요 조절 요인에서 제외하였다. 중국 서쪽의 타클리마칸과 구반턴구트 사막에서 바람에 의해 세립한 사질 입자가 잘 운송된다고 보고되었지만, 이렇게 운송되는 입자들은 대부분 75 μm 보다 작다 (Biscaye et al., 1997; Ding et al., 2001; Bory et al., 2003). 그러므로, 남극반도 북쪽의 남빙양에서 남반구의 편서풍에 의해서 운송되는 풍성기원 더스트 입자들도 75 μm 보다 작을 것으로 생각된다. 만약에 사질 입자가 풍성기원이라면, 사질 입자의 분포는 남빙양의 넓은 지역에 분포할 것이다. 따라서, 아문젠 해의 사질 입자와 대자율 값의 불일치는 풍성기원이 대자율을 조절하는 요인이 아니라는 것을 의미한다.

스코시아해에서 선생된 연구 (Diekmann et al., 2000)은 세립한 입자들은 해류에 의해서 운송된다고 보고하였다. Hofmann (1999)는 서로 다른 해류 시스템을 가지는 지역에서 비슷한 대자율 변동 패턴을 나타내는 것을 보고하였고, 다른 해양학적 특성을 보이는 남스코시아해와 포웰분지의 북쪽에서도 비슷한 대자율 변동 패턴을 보였다 (Orsi et al., 1995). 게다가, 이러한 사질 입자가 해류에 의해서 운송되기는 어렵다. 반면, 사질 입자는 남샌드위치섬에서 화산기원에 의해서 운송될 수 있다 (Nielsen et al., 2007). 하지만 화산과 관련된 대자율 값의 피크는 연속적으로 나타나지 않는다 (Xiao et al., 2016). 결0과적으로 간헐적인 화산물질의 유입이 연속적으로 높게 나타나는 대자율의 값을 설명하기는 어렵다.

남빙양에서 저층류에 의해서 형성되는 컨투어라이트 퇴적층이 잘 발견된다 (Diekmann, 2007). 스코시아해는 웨델해심층수와 남극순환류의 영향을 받기 때문에, 저층수에 의한 퇴적물의 운송도 고려되어야 한다. MAldonado et al. (2003)과 Gilbert et al. (1998)은 스코시아해 중앙 지역과 웨델해 북서쪽에 다양한 컨투어라이트가 발달해 있다고 보고하였다. Yoon et al. (2005)도 남 스코시아해에서 저층수의 증거를 보고한바 있다. 컨투어라이트 퇴적층은 깊은 채널의 끝 자리를 따라 약

하게 흐르는 지역에서 나타나기 때문에, 저층수는 연구지역에서 세립한 퇴적물들을 운송하고 퇴적하는 역할을 할 것으로 보인다. 하지만 높은 대자율 값을 가지는 사니질 층이 세립한 입자들의 위노잉에 의해서 초래될 수도 있다. 하지만 높은 대자율 값은 스코시아해에서 지난 빙하기에 나타난다 (Diekmann et al., 2000; Diekmann, 2007; Weber et al., 2012; Xiao et al., 2016). 추운 기후에서 웨델해 서쪽에서는 약한 심층수가 보고되었고, 빙하기 동안 탄산염이 잘 보존되었다. 그러므로 저층해류 순환에 의해서 사질 층이 운송되었다고 보기 힘들다.

오호츠크해에서 해빙이 빙하쇄설성 퇴적물의 주요 운송기작으로서 작용하기 때문에 (Kimura and Wakatsuchi, 1999; Sakamoto et al., 2005, 2006), 해빙의 역할에 대해서도 논의가 필요하다. 그러나 Weber et al. (2012)는 남극에서 해빙은 세립한 퇴적물을 운송하기 힘들다고 보고했기 때문에 사립입자가 해빙에 의해서 운송되기는 더욱 힘들 것으로 보인다. 오늘날 겨울철 해빙은 스코시아해를 부분적으로 덮고 포웰분지는 완전히 덮는다 (그림 1). 그러나 박스 코어에서 얻은 표층퇴적물의 대자율 값은 스코시아해의 표층퇴적물의 대자율 값과 비슷하다. 하지만 빙하기 동안에는 여름철과 겨울철의 해빙의 범위가 더 북쪽까지 전진하기 때문에 (Allen et al., 2011; Ferry et al., 2015), 해빙이 빙산을 운송하는 보조적인 수송역할을 담당했을 수 있다.

빙산의 유입을 지시하는 빙하쇄설성 퇴적물의 기록은 스코시아해의 해양퇴적물의 대자율과 비교된바 있지만 (Diekmann et al., 2000; Kanfoush et al., 2000; Weber et al., 2012, 2014), 빙하쇄설성 퇴적물은 대자율 값과 잘 일치하지 않아서 스코시아해에서 대자율 값은 빙하쇄설성 퇴적물에 의해 조절되는 것이 아니라는 결론으로 이어졌다. 하지만 빙하쇄설성 퇴적물이 조립한 입자들에만 국한되는 것이 아니기 때문에 (Andrews, 2000; Jonkers et al., 2012, 2015), 조립한 입자만을 빙하쇄설성 퇴적물로 간주한 기존의 연구에 대한 고찰이 필요하다. Licht et al. (1999)는 해양퇴적물에서 2 mm 이상의 입자는 코어러의 직경을 고려할 때 대표성이 없다고 주장했고, 이 연구에서도 자갈 사이즈는 사질 입자나 대자율과 어떠한 상관관계도 나타나지 않았다. 대서양 남동쪽 극전선 지역에서 150 μm - 2 mm의 사질 입자를 빙하쇄설성 퇴적물로서 사용하였고, Teitler et al. (2015)에서도 150 μm - 2 mm의 입자를 남빙양에서 빙하쇄설성 퇴적물로서 검정하였다. Hillenbrand et al. (2009)도 빙하쇄설성 퇴적물의 유입은 자갈 및 모래 입자에 의해서 반영된다고 보고하였다. 해양퇴적물의 대자율 값과 사질 입자의 강한 상관관계는 대자율 값의 변화가 빙하쇄설성 퇴적물의 유입과 관련된다는 것을 의미한다. 그리고 남극반도 북쪽 남빙양은 빙산이 지나가는 주요 경로이다 (Tournadre, 2015; Meriro et al.,

2016).

4. 결론

남극반도 북쪽의 남빙양의 해양퇴적물 대자율 값은 사질 입자와 양의 상관관계를 가지지만, 니질 입자와 평균 입도와는 음의 상관관계를 가지는 것으로 나타났다. 이러한 결과들은 연구지역에서 대자율의 값이 세립한 사질 입자의 유입에 의해 조절된다는 것을 의미하고 이러한 입자들은 빙산에 의해서 운송되는 것으로 보인다. 이러한 결론은 남빙양에서 빙하쇄설성 퇴적물의 크기에 대한 재고찰을 요한다. 해양퇴적물의 대자율 값과 빙하 코어의 더스트 기록의 잘 일치하는 것은 빙산의 떨어져 나가는 활동이 대기 순환 및 남반구 편서풍의 강도 사이에 강한 연관성이 있다는 것을 의미한다.

Controls on magnetic susceptibility of the Southern Ocean off the northern Antarctic Peninsula - Coupling of iceberg calving and atmospheric circulation

Sunghan Kim, Kyu-Cheul Yoo, Jae Il Lee, Min Kyung Lee, Kitae Kim, Ho Il Yoon, Heung Soo Moon

Korea Polar Research Institute

Abstract: Magnetic susceptibility (MS) values in Scotia Sea sediments showed strong correlations to ice core non-sea salt Ca^{2+} concentration (dustinput), which emphasizes the role of atmospheric circulation in the Southern Ocean. As a result, the correlation between them was suggested as a powerful tool for age reconstruction of marine sediments in the Southern Ocean. However, controls for MS variation in Scotia Sea sediments were not clear. In this study, we document grain size analysis record of sediment cores from the Southern Ocean off the northern Antarctic Peninsula (the south Scotia Sea and the northern Powell Basin) to reveal which size fraction is responsible for MS variation and discuss the transport mechanism for the size fraction. MS values of all cores have negative correlations to clay fraction and mean grain size (Φ) and have positive correlations to sand fraction (63 μm to 2 mm, especially from 63 μm to 250 μm), which implies that MS variation in the Southern Ocean off the northern Antarctic Peninsula is related to the content of sand fraction, not clay fraction (i.e., dust input). The main transport mechanism for sand fraction is considered as iceberg transport. In addition, the sand fraction seems to be representative of ice-rafted debris (IRD) in the Southern Ocean off the northern Antarctic Peninsula. Thus, the strong correlations between MS values in marine sediments and ice core dust record imply a strong coupling between iceberg calving activity and atmospheric circulation/intensity of the Southern Hemisphere Westerlies in the high latitude in the Southern Hemisphere.

참고문헌

Allen, C.S., Pike, J., Pudsey, C.J., 2011. Last glacial-interglacial sea-ice cover in the SW Atlantic and its potential role in global deglaciation. Quat. Sci. Rev. 30, 2446 - 2458.

Anderson, J.B., Andrew, J.T., 1999. Radiocarbon constraints on icesheet advance and retreat in the Weddell Sea, Antarctica. Geology 27, 179 - 182.

Anderson, J.B., Shipp, S.S., Lowe, A.L., Wellner, J.S., Mosola, A.B., 2002. The Antarctic Ice Sheet during the Last Glacial Maximum and its subsequent retreat history: a review. Quat. Sci. Rev. 21, 49 - 70.

Andrews, J., 2000. Icebergs and iceberg rafted detritus (IRD) in the North Atlantic: Facts and assumptions. Oceangraphy 13(3), 100 - 108.

Bailey, I., Hole, G.M., Foster, G.L., Wilson, P.A., Storey, C.D., Trueman, C.N., Raymo, M.E., 2013. An alternative suggestion for the Pliocene onset of major nothern hemisphere glaciation based on the geochemical provenance of North Atlantic Ocean ice-rafted debris. Quat. Sci. Rev. 75, 181 - 194.

Bennett, L.H., Page, C.H., Swartzendruber, L.J., 1978. "Comments on units in magnetism". J. Res. Natl. Inst. Stan. 83(1), 9 - 12.

Brachfeld, S., Banergee, S.K., 2000. A new high-resolution geomagnetic paleointentisy record for the North American Holocene: a comparison of sedimentary and absolute intensity data. J. Geophys. Res. 105(B1), 821 - 834.

Christ, A.J., Talaia-Murray, M., Elking, N., Domack, E.W., Leventer, A., Lavoie, C., Brachfeld, S., Yoo, K. - C., Gilbert, R., Jeong, S. - M., Petrushak, S., Wellner, J., the LARISSA Group, 2015. Late Holocene glacial advance and ice shelf growth in Barilari Bay, Graham Land, west Antarctic Peninsula. Geol. Soc. Am. Bull. 127(1 - 2), 297 - 315, doi:10.1130/B31035.1.

Diekmann, B., Kuhn, G., 1999. Provenance and dispersal of glacial-marine surface sediments in the Weddell Sea and adjoining areas, Antarctica: ice-rafting versus current transport. Mar. Geol. 158, 209 - 231.

Diekmann, B., 2007. Sedimentary patterns in the late Quaternary Southern Ocean. Deep-Sea Res. II 54, 2350 - 2366.

Diekmann, B., Kuhn, G., Rachold, V., Abelmann, A., Brathauer, U., Fütterer, D.K., Gersonde, R., Grobe, H., 2000. Terrigenous sediment supply in the

Scotia Sea (Southern Ocean): response to Late Quaternary ice dynamics in Patagonia and on the Antarctic Peninsula. Palaeogeogr. Palaeoclimatol. Palaeoecol. 162, 357 - 387.

Ferry, A.J., Crosta, X., Quilty, P.G., Fink, D., Howard, W., Armand, L.K., 2015. First records of winter sea ice concentration in the southwest Pacific sector of the Southern Ocean. Paleoceanography 30, 1525 - 1539, doi:10.1002/2014PA002764.

Fischer, H., Fundel, F., Ruth, U., Twarloh, B., Wegner, A., Udisti, R., Becagli, S., Castellano, E., Morganti, A., Severi, M., Wolff, E., Littot, G., Röthlisberger, R., Mulvaney, R., Hutterli, M.A., Kaufmann, P., Federer, U., Lambert, F., Bigler, M., Hansson, M., Jonsell, U., De Angelis, M., Boutron, C., Siggaard-Andersen, M.-L., Steffensen, J.P., Barbante, C., Gaspari, V., Gabrielli, P., Wagenbach, D., 2007. Reconstruction of millennial changes in dust emission, transport and regional sea ice coverage using the deep EPICA ice cores from the Atlantic and Indian Ocean sector of Antarctica. Earth Planet. Sci. Lett. 260, 340 - 354.

Folk, R.L., Ward, W.C., 1957. Brazos River bar [Texax]; a study in the significance of grain size parameters. J. Sediment. Res. 27(1), 3 - 26.

Gersonde, R., Crosta, X., Abelmann, A., Armand, L., 2005. Sea-surface temperature and sea ice distribution of the Southern Ocean at the EPILOG Last Glacial Maximum - a circum-Antarctic view based on siliceous microfossil records. Quat. Sci. Rev. 24, 869 - 896.

Gilbert, I.M., Pudsey, C.J., Murray, J.W., 1998. A sediment record of cyclic bottom-current variability from the northwest Weddell Sea. Sediment. Geol. 115, 185 - 214.

Gordon, J.E., Harkness, D.D., 1992. Magnitude and geographic variation of the radiocarbon content in Antarctic marine life: Implications for reservoir corrections in radiocarbon dating. Quat. Sci. Rev. 11, 697 - 708.

Haberzettl, T., Anselmetti, F.S., Bowen, S.W., Fey, M., Mayr, C., Zolitschka, B., Ariztegui, D., Mauz, B., Ohlendorf, C., Kastner, S., Lücke, A., Schäbitz, F., Wille, M., 2009. Late Pleistocene dust deposition in the Patagonian steppe - extending and refining the paleoencironmental and tephrochronological record from Laguna Potrok Aike back to 55 ka. Quat. Sci. Rev. 28, 2927 - 2939.

Heroy, D.C., Anderson, J.B., 2005. Ice-sheet extent of the Antarctic Peninsula region during the Last Glacial Maximum (LGM) - Insights from glacial geomorphology. Geol. Soc. Am. Bull. 117, 1497 - 1512.

Hofmann, A., 1999. Kurzfristige Llimaschwankungen im Scotiameer und Ergebnisse zur Kalbungsgeschichte der Antarktis während der letzten 200000 Jahre - Rapid Climate oscillations in the Scotia Sea and results of the calving history of Antarctica during the last 200000 years, Geowissenschaften. Universität Bremen, Bremen, 178 p.

Jonkers, L., Prins, M.A., Moros, M., Weltje, G.J., Troelstra, S.R., Brummer, G. - J.A., 2012. Temporal offsets between surface temperature, ice-rafting and bottom flow speed proxies in the glacial (MIS 3) northern North Atlantic. Quat. Sci. Rev. 48, 43 - 53.

Jonkers, L., Barker, S., Hall, I.R., Prins, M.A., 2015. Correcting for the influence of ice-rafted detritus on grain size-based paleocurrent speed estimates. Paleoceanography 30, 1347 - 1357, doi:10.1002/2015PA002830.

Kanfoush, S.I., Hodell, D.A., Charles, C.D., Guilderson, T.P., Mortyn, P.G., Ninnemann, U. S., 2000. Millennial-scale instability of the Antarctic Ice Sheet during the Last Glaciation. Science 288, 1815 - 1818.

Kimura, N., Wakatsuchi, M., 1999. Processes controlling the advance and retreat of sea-ice in the Sea of Okhotsk. J. Geophy. Res. 104(C5), 11137 - 11150.

Lambert, F., Bigler, M., Steffensen, J.P., Hutterli, M., Fischer, H., 2011. The calcium-dust relationship in high-resolution data from Dome C, Antarctica. Climate of the Past Discussions 7, 1113 - 1137.

Larter, R.D., Anderson, J.B., Graham, A.G.C., Gohl, K., Hillenbrand, C-D., Jakobsson, M., Johnson, J.S., Kuhn, G., Nitsche, F.O., Smith, J.A., Witus, A.E., Bentley, M.J., Dowdeswell, J.A., Ehrmann, W., Klages, J.P., Lindow, J., Cofaigh, C.O., Spiegel, C., 2014. Reconstruction of changes in the Amundsen Sea and Bellingshausen Sea sector of the West Antarctic Ice Sheet since the Last Glacial Maximum. Quat. Sci. Rev. 100, 55 - 86.

Lee, J.E., Bak, Y.S., Yoo, K.C. Lim, H.S., Yoon, H.I., Yoon, S.H. 2010. Climate changes in the South Orkney Plateau during the last 8600 years. The Holocene 20(30), 395 - 404.

Mackiewicz, N.E., Powell, R.D., Carlson, P.R., Molnia, B.F., 1984. Interlaminated

ice-proximal glacimarine sediments in Muir Inlet, Alaska. Mar. Geol. 57, 113 - 147.

Minzoni, R.T., Anderson, J.B., Fermandez, R., Wellner, J.S., 2015. Marine record of Holocene climate, ocean, and cryosphere interactions: Herbert Sound, James Ross Island, Antarctica. Quat. Sci. Rev. 129, 239 - 259.

Molnia, B.F., 1983. Distal glacial marine sedimentation: abundance, composition and distribution of North Atlantic Pleistocene ice rafted sediment, in Glacial marine sedimentation, edited by Molnia, B. F., pp. 593 - 626, Plenum Press, New York.

Nakada, M., Kimura, R., Okuno, J., Moriwaki, K., Miura, H., Maemoku, H., 2000. Late Pleistocene and Holocene melting history of the Antarctic ice sheet derived from sea-level variations. Mar. Geol. 167, 85 - 103.

Nielsen, S.H.H., Hodell, D.A., Kamenov, G., Guilderson, T., Perfit, M.R., 2007. Origin and significance of ice-rafted detritus in the Atlantic sector of the Southern Ocean. Geochem. Geophy. Geosy. 8, 1 - 23.

Orsi, A.H., Whitworth, T., Nowlini Jr., W. D., 1995. On the meridional extent and fronts of the Antarctic circumpolar current. Deep Sea Res. I 42(5), 641 - 673.

Paillard, D., Laeyrie, L., Yiou, P., 1996. Macintosh Program Performs Time-series Analysis, vol. 77. EOS Transactions American Geiophysical Union, Washington D.C., p. 379.

Peck, V.L., Hall, I.R., Zahn, R., Grousset, F., Hemming, S.R., Scourse, J.D., 2007. The relationship of Heinrich events and their European precursors over the past 60 ka BP: multi-proxy ice-rafted debris provenance study in the North East Atlantic. Quat. Sci. Rev. 26, 862 - 875, doi.org/10.1016/j.quascirev.2006.12.002.

Peck, V.L., Allen, C.S., Kender, S., McClymont, E.L., Hodgson, D.A., 2015. Oceanographic variability on the West Antarctic Peninsula during the Holocene and the influence of upper circumpolar deep water. Quat. Sci. Rev. 119, 54 - 65.

Petit, J.R., Mounier, L., Jouzel, J., Korotkevitch, Y., Kotlyakov, V., Lorius, C., 1990. Paleoclimatological implications of the Vostok core dust record. Nature 343, 56 - 58.

Pugh, R.S., MaCave, I.N., Hillenbrand, C.-D., Kuhn, G., 2009. Circum-Antarctic age modeling of Quaternary marine cores under the Antarctic Circumpolar Current: ice-core dust-magnetic correlation. Earth Planet. Sci. Lett. 284, 113-123.

Reid, D.E., Anderson, J.B., 1990. Hazards to Antarctic exploration and production, in *Antarctic as an Exploration Frontier - Hydrocarbon Potential Geology and Hazards*, edited by B. St. John, pp. 31-46. American Association of Petroleum Geologists Studies in Geology 31, Tulsa, Oklahoma.

Röthlisberger, R., Bigler, M., Wolff, E.W., Joos, F., Monnin, E., Hutterli, M.A., 2004. Ice core evidence for the extent of past atmospheric CO_2changeduetoironfertilisation.Geophys.Res.Lett.31,L16207,doi:10.1029/2004GL020338.

Ruddiman, W.F., 1977. Late Quaternary deposition of ice-rafted sand in the subpolar North Atlantic (late 40 to 65 N). Geol. Soc. Amer. Bull. 88, 1813-1827.

Sakamoto, T., Ikehara, M., Aoki, K., Iijima, K., Kimura, N., Nakatsuka, T., Wakatsuchi, M., 2005. Ice-rafted debris (IRD)-based sea-ice expansion events during the past 100 kyrs in the Okhotsk Sea. Deep-Sea Res. II 52, 2275-2301.

Sakamoto, T., Ikehara, M., Uchida, M., Aoki, K., Shibata, Y., Kanamatsu, T., Harada, N., Iijima, K., Katsuki, K., Asahi, H., Takahashi, K., Sakai, H., Kawahata, H., 2006. Millennial-scale variations of sea-ice expansion in the southwestern part of the Okhotsk Sea during the past 120 kyr: Age model and ice-rafted debris in IMAGES Core MD01-2412. Global Planet. Change 53, 58-77.

Sun, J.M., 2002. Source regions and formation of the loess sediemnts on the high mountain regions of northwestern China. Quaternary Research 58, 341-351.

Takahashi, T., Sutherland, S.C., Sweeney, C., Poisson, A., Metzl, N., Tilbrook, B., Bates, N., Wanninkhof, R., Feely, R.A., Sabine, C., Olafsson, J., Nojiri, Y., 2002. Global sea-air CO_2fluxbasedonclimatologicalsurfaceoceanpCO_2,andseasonalbiologicalandtemperatureeffects.Deep-SeaRes.II 49, 1601-1622.

Teitler, L., Florindo, F., Warnke, D.A., Filippelli, G.M., Kupp, G., Taylor, B., 2015. Antarctic Ice Sheet response to a long warm interval across Marine Isotope Stage 31: A cross-latitudinal study of iceberg-rafted debris. Earth Plan. Sci. Lett. 409, 109 - 119.

The RAISED Consortium et al., 2014. A community-based geological reconstruction of Antarctic Ice Sheet deglaciation since the Last Glacial Maximum. Quat. Sci. Rev. 100, 1 - 9.

Weber, M.E., Kuhn, G., Sprenk, D., Rolf, C., Ohlwein, C., Ricken, W., 2012. Dust transport from Patagonia to Antarctica - a new stratigraphic approach from the Scotia Sea and its implications for the last glacial cycle. Quat. Sci. Rev. 36, 177 - 188.

Weber, M.E., Clark, P.U., Kuhn, G., Timmermann, A., Sprenk, D., Gladstone, R., Zhang, X., Lohmann, G., Menviel, L., Chikamoto, M.O., Friedrich, T., Ohlwein, C., 2014. Millennial-scale variability in Antarctic ice-sheet discharge during the last deglaciation. Nature 510, 134 - 138.

Xiao, W., Frederichs, T., Gersonde, R., Kuhn, G., Esper, O., Zhang, X., 2016. Constraining the dating of late Quaternary marine sediment records from the Scotia Sea (Southern Ocean). Quat. Geochronol. 31, 97 - 118, doi.org/10.1016/j.quageo.2015.11.003.

표 1. 인근 코어 MD07-3134와 연구 코어들의 대자율 연결점

GC04-G03 (cm)	GC02-SS02 (cm)	GC03-C2 (cm)	GC03-C4 (cm)	MD07-3134 (cm)
	9	419	460	894
27				1341
110	232	715	745	1527
		806	823	1645
170	258			1688
209				1856
251	296			2040
294	340			2214
383	381			2469
501	467			2667
535				2780

표 2. 그림 1에 나타난 코어들의 정보

Core ID	Latitude	Longitude	Water depth (m)	Source
GC02-SS02	59°29′S	49°36′W	4043	This study
GC03-C2	60°34′S	55°55′W	3750	This study
GC03-C4	60°33′S	55°52′W	3778	This study
GC04-G03	61°19′S	49°48′W	2907	This study
MD07-3133	57°26′S	43°27′W	3101	Weber et al., 2012
MD07-3134	59°25′S	41°28′W	3663	Weber et al., 2012
PS2319-1	59°47′S	42°41′W	4320	Diekmann et al., 2000
PS2515-3	53°33′S	45°19′W	3522	Diekmann et al., 2000
PS67/197-1	55°08′S	44°06′W	3837	Xiao et al., 2016
PS67/219-1	57°57′S	42°28′W	3619	Xiao et al., 2016

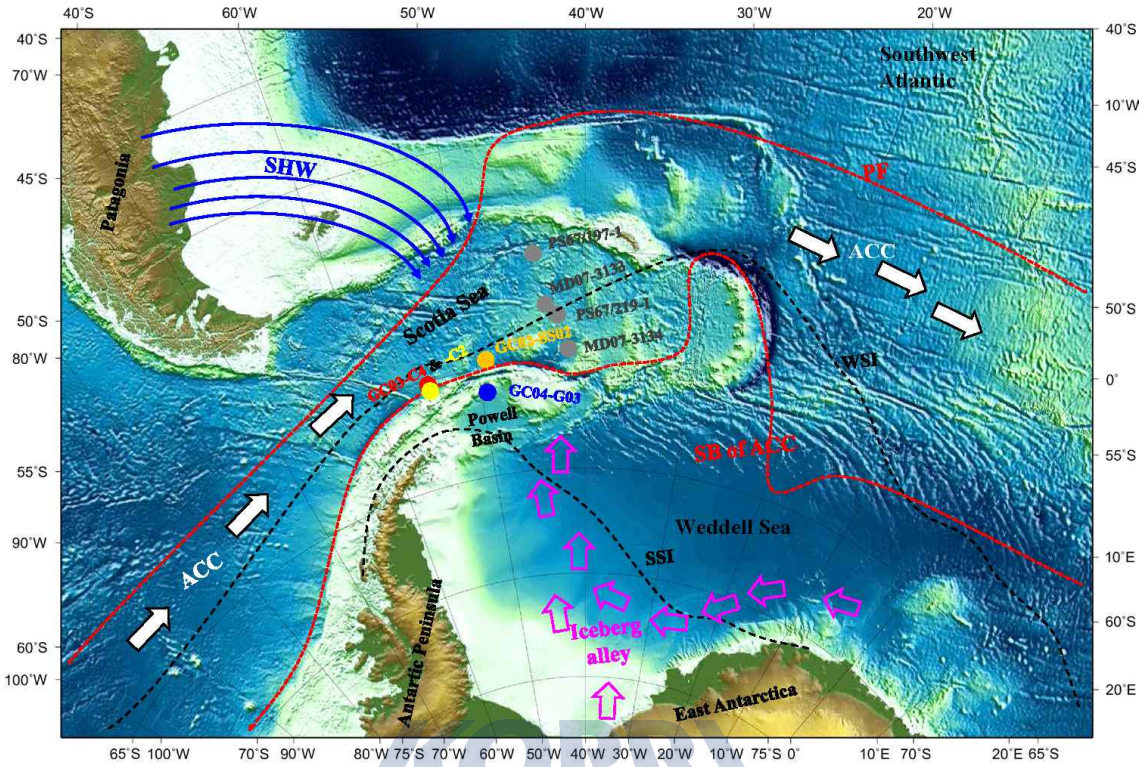

그림 1. 연구지역

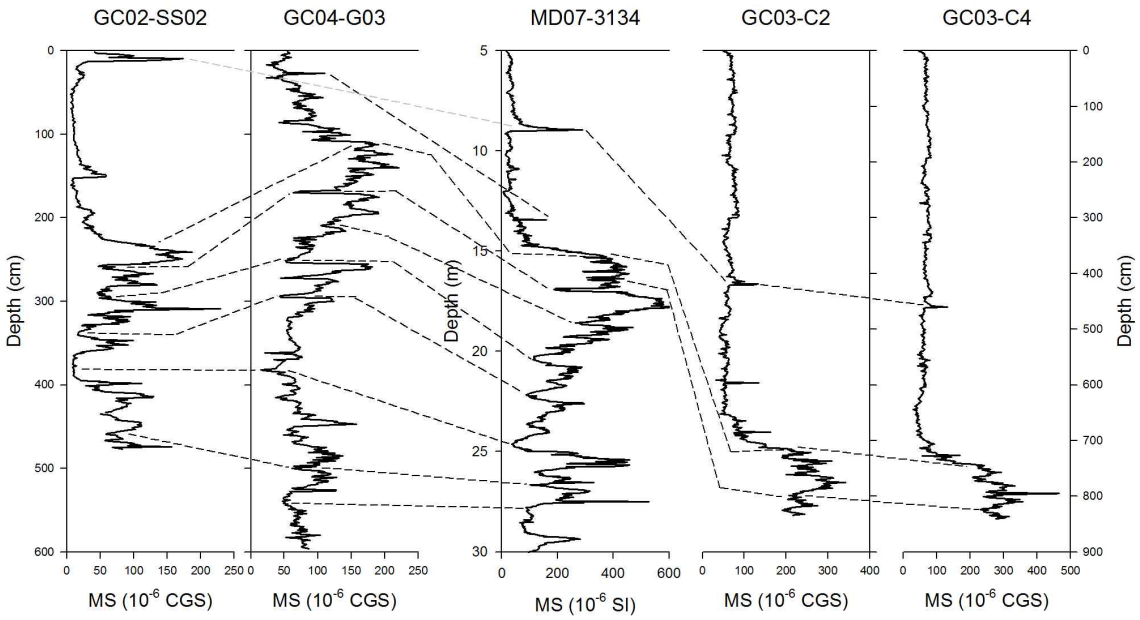

그림 2. 코어 MD07-3134의 대자율 값과 연구 코어들의 대자율 값의 대비

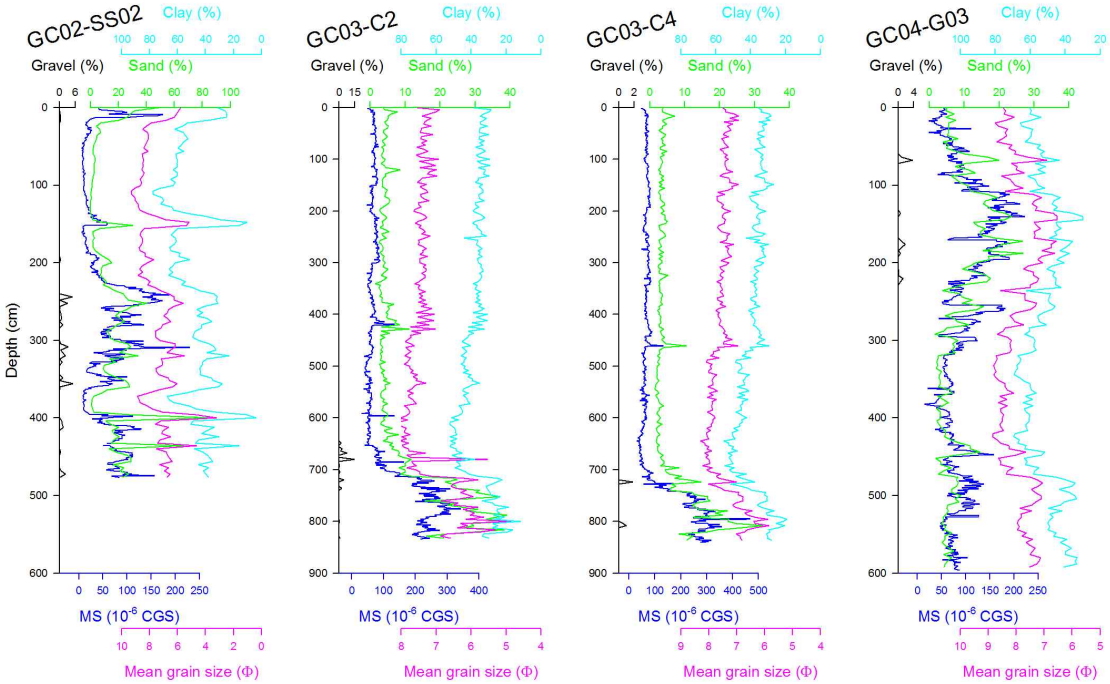

그림 3. 연구 코어들의 대자율 및 입도 변화

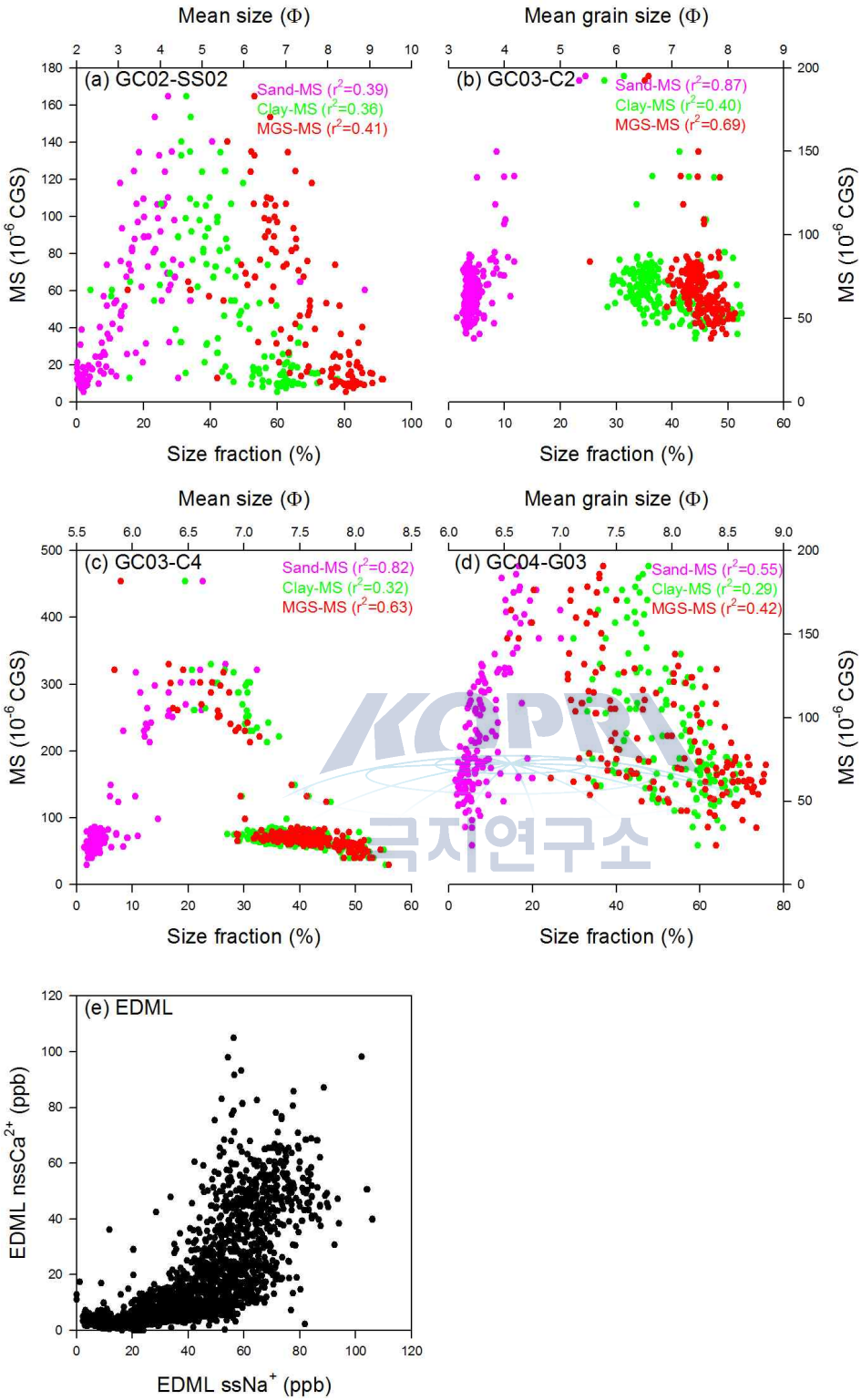

그림 4. 사질 입자-대자율, 니질 입자-대자율, 평균 입도-대자율의 상관관계

제 8 장

Late Holocene glacial advance and ice shelf growth in Barilari Bay, Graham Land, west Antarctic Peninsula[3)]

Kyu-Cheul Yoo, Ho Il Yoon

Korea Polar Research Institute

Abstract: Three marine sediment cores were collected along the length of the fjord axis of Barilari Bay, Graham Land, west Antarctic Peninsula (65°55′S, 64°43′W). Multi-proxy analytical results constrained by high-resolution geochronological methods (^{210}Pb, radiocarbon, ^{137}Cs) in concert with historical observations capture a record of Holocene paleoenvironmental variability. Our results suggest early and middle Holocene (>7022 - 2815 cal. [calibrated] yr B.P.) retreated glacial positions and seasonally open marine conditions with increased primary productivity. Climatic cooling increased sea ice coverage and decreased primary productivity during the Neoglacial (2815 to cal. 730 cal. yr B.P.). This climatic cooling culminated with glacial advance to maximum Holocene positions and expansion of a fjord-wide ice shelf during the Little Ice Age (LIA) (ca. 730 - 82 cal. yr B.P.). Seasonally open marine conditions were achieved and remnant ice shelves decayed within the context of recent rapid regional warming (82 cal. yr B.P. to present). Our findings agree with previously observed late Holocene cooling and glacial advance across the Antarctic Peninsula, suggesting that the LIA was a regionally significant event with few disparities in timing and magnitude. Comparison of the LIA Antarctic Peninsula record to the rest of the Southern Hemisphere demonstrates close synchronicity in the southeast Pacific and southern most Atlantic region but less coherence for the southwest Pacific and Indian Oceans. Comparisons with the Northern Hemisphere demonstrate that

3) 이 연구 결과는 다음의 논문으로 출판되었음: Christ, A. J., Talaia-Murray, M., Elking, N., Domack, E. W., Leventer, A., Lavoie, C., ... & Petrushak, S. (2015). Late Holocene glacial advance and ice shelf growth in Barilari Bay, Graham Land, west Antarctic Peninsula. Geological Society of America Bulletin, 127(1-2), 297-315.

the LIA Antarctic Peninsula record was contemporaneous with pre-LIA cooling and sea ice expansion in the North Atlantic - Arctic, suggesting a global reach for these events.

1. Introduction

The Antarctic Peninsula (AP) is among the fastest-warming regions on the planet, with atmospheric temperatures rising at a rate of +3.4 °C per century, exceeding five times the global rate (Vaughn et al., 2003). Ice shelf retreat and collapse in the AP—notably documented by the breakup of Larsen Inlet in A.D. 1989 (Skvarca et al., 1999) and of the Prince Gustav Channel and northern Larsen A ice shelves in A.D. 1995 (Rott et al., 1998), and the catastrophic and unprecedented collapse of the Larsen B in A.D. 2002 (Scambos et al., 2003; Domack et al., 2005)—have occurred within the period of recent rapid regional warming, suggesting the southward movement of the -5 °C to -9 °C isotherms, the limit of ice shelf viability (Morris and Vaughn, 2003). Recent removal of ice shelves has facilitated and accelerated grounded ice loss (Scambos et al., 2004; Ferrigno et al., 2008; Berthier et al., 2012). Regionally, 87% of 244 observed glacier fronts in the AP have retreated from historical positions since A.D. 1953 (Cook et al., 2005). Ice shelf collapse and associated ice loss in the AP therefore will contribute to future global sea-level rise as regional and global climatic warming continues (Mercer, 1978; Vaughn et al., 2003; Bentley et al., 2009).

The stability and behavior of ice shelves across the AP varied spatially and temporally during the Holocene (Pudsey and Evans, 2001; Brachfeld et al., 2003; Gilbert and Domack, 2003; Bentley et al., 2005; Hodgson et al., 2006), suggesting a set of complex forcing factors that control the regional climate system. The recent warming trend should be placed in the context of the entire Holocene climate history, specifically with respect to records of ice shelf expansion and collapse. Furthermore, late Holocene records must be documented, specifically millennial- to century-scale climate oscillations (such as the Little Ice Age, LIA), to distinguish the climate events and environmental changes that immediately precede the current regional warming trend and further resolve

complexities in the regional and global climate system.

The most recent and severe climate anomaly of the Neoglacial period, the LIA, is classically defined as the period of glacial advance to maximum Holocene positions in the European Alps between A.D. 1550 and 1800 (Lamb, 1985; Grove, 1988, 2004). This "event" was initially constrained by the recognition of frontal moraines that stood down-valley of the glacial margins that existed at the time. The LIA was hence named irrespective of the actual climate forcing responsible for the late Holocene re-advance of the glaciers. Locally, as in the European Alps, colder, wetter conditions could be linked to the LIA "event," and so this characteristic response was assigned climatic significance. Because the LIA was originally an alpine phenomenon, global extrapolation of this event to glaciated terrains resulted in an asynchronous record, because a multitude of factors besides strict regional temperatures changes can induce a glacial response. For instance, in Southern Patagonia, increased intensity of moisture-bearing westerly winds can induce glacial advance for systems facing the west, despite warming regional temperatures that induce recession for glacial systems with non-westerly aspect (Holmlund and Fuenzalida, 1995). Further, western outlet glaciers of the Northern Patagonian Ice Field are more responsive to changes in precipitation than temperature during the Holocene (Bertrand et al., 2012). Given these issues and chronologic inconsistencies, the global recognition of a "LIA event(s)" has become problematic.

The Antarctic Peninsula (AP) represents an important testing ground for ideas related to the LIA. This is because the region today remains heavily glaciated with a general lack of terrestrially exposed relict moraines. The tidewater character of these glaciers also implies an ice margin dynamic typically considered more complex than that of terrestrially terminating glaciers (Mann, 1986). Most importantly, the AP represents a transitional glacial climate system between temperate, ablation-dominated systems (i.e., Patagonia, South Georgia) and polar systems governed by iceberg calving and ice shelf processes. We proceed by first presenting marine evidence for late Holocene glacial advance, followed by retreat (the classic definition of the LIA from Europe), and

then relate these observations to a glacial climate reconstruction that is consistent with facies models for ice shelf and glacio-marine sedimentation. We close by comparing our results to the regional and hemispheric information related to LIA glacial fluctuations, then speculating as to the differences in forcing and timing revealed therein.

2. The LIA in the Antarctic Peninsula

South of the polar front in the AP and surrounding sub-Antarctic islands, the available terrestrial glacial and marine sedimentary records indicate glacial advance and climatic cooling broadly during the LIA. On King George Island in the South Shetland Islands, radiocarbon dates of mosses incorporated into Holocene moraines suggest LIA advance of the Collins Ice Cap after 650 cal. (calibrated) yr B.P. (A.D. 1300) (Hall, 2007). Further southeast at James Ross Island in the northeastern AP, a Holocene climate history extracted from an ice core documents a period of late Holocene cooling that supported regional ice shelf expansion beginning at 2500 yr B.P. with a particularly cold span between 800 and 400 yr B.P., but does not indicate a LIA event correlative with the Northern Hemisphere event (Mulvaney et al., 2012). In the eastern AP, apparent exposure ages of glacial erratics indicate expanded ice cover between 600 and 100 yr B.P., suggesting glacial advance and expansion of the Larsen A and Prince Gustav ice shelves during the late Holocene. Radiocarbon and ^{210}Pb activity series (Gilbert and Domack, 2003) and geomagnetic paleointensity chronologies (Brachfeld et al., 2003) of sediment cores collected in the former Larsen A ice shelf area confirm expansion at a maximum age of 700 yr B.P. and minimum age of 400 yr B.P., followed by modern disintegration in A.D. 1995. On Anvers Island in the northwestern Antarctic Peninsula, terrestrial organic matter exposed by recent glacial retreat indicate that the Marr Ice Piedmont was at or landward of present glacial positions 970 - 700 cal. yr B.P. (A.D. 1050 - 1250) (Hall et al., 2010).

Late Holocene climate records from sediment cores extracted from the west AP indicate a similar Neoglacial cooling trend and suggest the presence of a LIA climate signature between 700 and 150 yr B.P. (A.D. 1300 and 1850)

(Brachfeld et al., 2002; Domack and Ishman, 1993; Domack et al., 1995, 2001; Domack and McClennen, 1996; Leventer et al., 1996, 2002; Shevenell et al., 1996; Harris et al., 1999; Taylor et al., 2001; Warner and Domack, 2002; Milliken et al., 2009; Allen et al., 2010; Hodgson et al., 2013). In Lallemand Fjord, the advance of the Müller Ice Shelf at ca. 400 yr B.P. (ca. A.D. 1600) is recognized as a decline in productivity and an increase in fine-grained siliciclastic sedimentation, but is ultimately inferential with regard to any change in the grounding line position (Domack et al., 1995). While evidence for the LIA climate exists in the west AP, the precise timing of LIA glacial advance and retreat is constrained at only a few sites and is otherwise poorly documented across the region, particularly in glacial marine environments (Bentley et al., 2009).

In this paper we present the first precise chronology of LIA glacial advance and subsequent retreat in Graham Land, west AP. Sediment cores were collected from the entire length of the Barilari Bay during the LARISSA (Larsen Ice Shelf System, Antarctica) cruise in early 2010 aboard the RV/IB Nathaniel B. Palmer (NBP10-01). Prior to NBP10-01, Barilari Bay had not been subjected to extensive scientific study. This fjord closes a geographic data gap along the west AP between the Danco Coast (Domack and Ishman, 1993; Domack and McClennen, 1996; Griffith and Anderson, 1989; Harris et al., 1999) and Palmer Deep (Domack et al., 2001; Leventer et al., 2002; Warner and Domack, 2002; Shevenell and Kennett, 2002; Domack et al., 2005) to the north, and Crystal Sound and Lallemand Fjord to the south (Domack et al., 1995, 2003; Domack and McClennan, 1996; Shevenell et al., 1996; Taylor et al., 2001). Unlike Lallemand Fjord and the Danco Coast, Barilari Bay is not geographically protected from the Bellingshausen Sea, and thus, is more susceptible to oceanic influence. Barilari Bay is also situated at a sub-polar latitude, whereas Lallemand Fjord lies fully south of the Antarctic Circle.

3. Study Area

Barilari Bay (65°55′S, 64°43′W; Fig. 1) was discovered during the first French Antarctic Expedition of 1903–1905 (Charcot, 1905) and re-charted

by the British Graham Land Expedition of 1934–1937 (Rymill, 1938). Historic voyages to Barilari Bay recorded seasonally marine conditions since its discovery. Barilari Bay is a re-entrant in the Graham Land coast with the attribute of a fjord system. It is defined by a northwest-southeast-trending fjord 34 km long and 4.8–11 km wide (Figs. 1 and 2). The fjord can be divided into three sections: the glacier-proximal inner fjord, the middle fjord, and more oceanic outer fjord. The inner fjord of Barilari Bay is characterized by the tidewater fronts of the Bilgeri, Weir, Lawrie, and Birley Glaciers. Swath multibeam bathymetric surveys of the inner fjord revealed a prominent grounding zone 5.2 km, 6.3 km, and 4.8 km seaward of the present positions of the Weir, Lawrie, and Birley Glaciers, respectively. The middle fjord is characterized by over-deepened and flatted basins and reaches a depth of 610 m where a zone of at least 35 m of ponded sediment is observed. The outer fjord consists of isolated over-deepened basins (670 m depth) with up to 25 m of ponded sediment, crudely streamlined bedforms including drumlinized and elongated "channel"-appearance bedforms, and crag-and-tail bedforms.

The Otlet, Birley, Lawrie, Weir, and Bilgeri Glaciers and several unnamed glaciers draining the Bruce Plateau terminate into Barilari Bay. A shift toward a general trend of glacial retreat between 64°S and 66°S in the AP initiated between A.D. 1955 and 1969 (Cook et al., 2005). This 20th-century pattern is expressed in some ice fronts in Barilari Bay by the demise of small, remnant ice shelves since the 1940s and the retreat of the calving fronts of the Birley Glacier and a small unnamed glacier in the inner fjord in the 1960s (Ferrigno et al., 2008). The Bilgeri Glacier, however, experienced a mean ice advance within this time period, although the extent of advance was not delineated by Ferrigno et al. (2008). The other glaciers draining Barilari Bay have maintained ice-front stability since the 1980s (Ferrigno et al., 2008) (Fig. 2). The recent advance and relative stability of ice fronts in this region of the AP versus mean retreat elsewhere suggests accelerated ice discharge from the Bruce Plateau within the past 50 years. Barilari Bay is 12 nautical miles from the ice core recently drilled at Site Beta on the Bruce Plateau by the Byrd Polar Research Center at the Ohio State University (USA) in 2010, providing the most direct comparison between the marine sedimentary and glacial ice records in the

Antarctic.

4. Methods

4.1.. Multi-proxy analyses

4.1.1. Core descriptions

Cores KC-54 and KC-55 were opened, described, and sampled soon after collection during NBP10-01. Core JPC-126 was opened, described, and sampled at the Antarctic Research Facility at Florida State University (USA) in 2010. Sediments were described following the procedures established by Kaharoeddin et al. (1988) with the addition of the use of the term “diamicton” following the discussions after Flint et al. (1960).

4.1.2. Particle size

Grain size was determined using the Malvern Mastersizer/E particle size analyzer and Malvern software suite at Hamilton College (New York, USA). Bulk sediment samples were dispersed in a dispersant solution (sodium hexametaphosphate) and rinsed once. The grain size classification used is: clay (<3.9 μm), fine- and medium-grained silt (3.9 - 31.00 μm), coarse-grained silt (31.00 - 62.5 μm), and sand (>62.50 μm) (Wentworth, 1922). This method of sample preparation and data analysis has been utilized successfully in previous similar studies (e.g., Warner and Domack, 2002).

4.1.3. Lamination and Ice-Rafted Debris Indices

X-rays of each core were used to quantify the number of ice-rafted debris (IRD) grains and laminations present within 5 cm intervals of each core. X-ray images for cores KC-55 and JPC-126 were developed at the Korean Polar Research Institute (KOPRI), Republic of Korea, and for core KC-54 at Hamilton College. The IRD index was determined by counting grains greater

than 2 mm in size, excluding grains present at the base of turbidite sequences and clasts in diamict. Laminations were defined by sequences bounded using the color contrast in X-ray radiographs.

4.1.4. Bulk Organic Geochemistry

Bulk organic geochemistry was evaluated on acid-washed dried sediment using a Delta Plus Ion ratio mass spectrometer with a COSTECH elemental analyzer. Standards and operating procedures are provided online (see http://www.hamilton.edu/EMSI). Values of percent total organic carbon (%TOC) and δ^{13}Corg were determined from a suite of analyses, and results were adjusted using standard processing procedures.

4.1.5. Physical Properties

Magnetic susceptibility (MS) was measured for cores KC-54 and KC-55 aboard the Nathaniel B. Palmer using a Bartington MS2E surface scanning sensor. MS was measured on split cores for JPC-126 using a Bartington MS2C at the Antarctic Marine Geology Research Facility at Florida State University. MS data were measured at an interval of every centimeter. Water content was measured according to the laboratory procedure at Hamilton College.

4.1.6. Diatoms

Diatom analyses were conducted at Colgate University (New York, USA) and at KOPRI where quantitative diatom slides were prepared following the settling technique described by Scherer (1994). Diatoms were counted along transects at 1000× magnification on a Zeiss Primostar microscope. Where possible, a total of 400 valves were counted, but where diatom abundances were extremely low, a total of 10 transects were counted. Diatom abundances are calculated as millions of valves per gram dry sediment (mvpgs). Relative abundances of the dominant genus, Chaetoceros, were calculated based on the total abundance counts described above. However, these data are not calculated

or presented for counts where absolute diatom abundances were so low that counting was stopped after 10 transects well prior to counting 400 valves. In these samples, diatom abundances were simply too low for a statistically accurate presentation of the contribution of any species to the total assemblage.

4.2.. Chronology

4.2.1. Cesium-137 A.D. 1963 "Bomb Spike"

The upper 20 cm of core KC-55 was analyzed to determine the calendar year A.D. 1963 A.D. (47 yr B.P. relative to A.D. 2010) using ^{137}Cs. This method has been previously used in the Antarctic to determine anomalously high ^{137}Cs activity attributed to atmospheric fallout from global nuclear weapons testing (Appleby et al., 1995). Samples were collected at the University of Houston and analyzed at Core Scientific International (Winnipeg, Manitoba, Canada).

4.2.2. Lead-210 Activity Series

The recent chronologies of cores KC-54 and KC-55 were constrained using ^{210}Pb activity series. This method has been used (Gilbert and Domack, 2003) in determining short-term chronologies in marine sediment cores in the Southern Ocean and Antarctic fjords. The sediment-water interface was well preserved in both cores as observed at the time of core splitting, and the water content profiles display a logarithmic decrease down core with a mixed surface layer. Subsamples of sediment were taken at intervals of 1 cm (KC-54) and every other centimeter (KC-55) from the surface to 10 cm (KC-54) and 13 cm (KC-55) depth in anticipation of defining the unsupported 210Pb activity, and at progressively greater intervals to 17 cm (KC-54) and 60 cm (KC-55) depth to determine the supported ^{210}Pb activity. Background levels of supported 210Pb were identified in both cores. By calculating the slope (m) of sample depth versus the natural log of the activity (lnA), one can obtain a linear sedimentation rate (LSR) from LSR = $-\lambda m$, where λ is the ^{210}Pb radioactive decay constant (0.0311 yr^{-1}). Stepped accumulation rates were calculated for

both cores based on ^{210}Pb activity, and then each core was assigned a chronology in terms of years before present relative to A.D. 2010.

4.2.3. Radiocarbon Dating

Calcareous foraminifera and some mollusk fragments were used for ^{14}C-radioisotope dating, and samples were sent to the National Ocean Sciences Accelerator Mass Spectrometry (NOSAMS) facility in Woods Hole, Massachusetts (USA). Foraminifera consisted of mostly mono-specific assemblages of clean Bulimina aculeata that were in abundance in most intervals within the cores. Results are presented in the text as calibrated ages (cal. yr B.P.) and were calibrated using CALIB ^{14}C calibration program (version 6.0; Stuiver and Reimer, 1993) with the MARINE09 curve (Reimer et al., 2009) (http://calib.qub.ac.uk/calib/). The intervals selected for age determination were chosen based on proximity to unit horizons as well as to interpreted specific sedimentologic events.

Radiocarbon dating in the Southern Ocean is notoriously difficult due to the dominance of upwelling of old deep water derived in large part from the Northern Hemisphere at the Antarctic Divergence (Ingólfsson et al., 1998; Hall, 2009). Deep water is depleted in ^{14}C, and modern marine species that use carbonate from this water typically yield radiocarbon “ages” that are older than 1000 yr (Stuiver et al., 1981; Gordon and Harkness, 1992; Berkman and Forman, 1996). This reservoir effect is not uniform, however, across the Antarctic margin, and regional as well as species-specific disparities (vital fractionations) do occur (Domack, 1992; Domack et al., 2005).

The calibration routine for this study utilized a reservoir correction based on a surface age of 1390 yr B.P. on foraminifera taken from the innermost Barilari Bay core KC-54, from 0 to 3 cm (Table 1). This age is somewhat older than that of living foraminifera observed on the eastern side of the Antarctica Peninsula at 880 ± 45 yr (Domack et al., 2005) and 1040 ± 70 for the nearby Gerlache Strait (Domack, 1992). It is likely that bioturbation has resulted in a slightly older age than the published reservoir ages because the living microfauna would be mixed with deeper, dead microfauna. At present there are

no modern ages on living foraminifera within the Graham Land coast region. For these reasons we must assume that the near-surface age of 1390 yr B.P. is a realistic reservoir correction for Barilari Bay. Facies interpretation of each core, the proximity of the surface date, and the fit of the calibration curve to the data points were all considered when choosing the appropriate age model.

5. Results

5.1.. Core KC-54

Core KC-54 was collected from the edge of the relict grounding zone in the inner fjord of Barilari Bay at a depth of 341 m, 6.3 km seaward of the calving front of the Lawrie Glacier (Fig. 2), and is 134 cm in length. KC-54 is the most glacial-proximal core. The core was divided into: unit 1 (0 - 11.5 cm); unit 2, which was subdivided to unit 2a (11.5 - 38 cm) and unit 2b (38 - 49 cm); and unit 3 (49 - 134 cm) (Fig. 3).

Unit 3 (134 - 49 cm) is a medium to dark gray, structureless, poorly sorted, sandy, homogenous diamicton that extends 90 cm upcore from the core bottom. MS values are highly variable compared to values in overlying units. We do not identify the clasts in unit 3 as IRD. %TOC is at the lowest levels in the entire core (~0.035%), and δ^{13}Corg values are at their most negative, varying between -23.4‰ and -24.5‰. Total diatom abundance is two orders of magnitude lower in unit 3 than in the overlying units, with an average value of 0.055 mvpgs and a maximum value of only 0.223 mvpgs. Total diatom abundance was so low that relative contributions of species to the total assemblage could not be counted with confidence.

At 49 cm there is a sharp contact between unit 3 and unit 2b. Unit 2b (49 - 39 cm) is a bluish-gray clayey silt. MS values are lower relative to unit 2a and unit 3. IRD content is sparse within unit 2b. There is a limited but notable increase in %TOC and increase of δ^{13}Corg values relative to unit 3. Total diatom abundance increases and ranges between 0.05 and 4.7 mvpgs, and percent Chaetoceros averages 81%. While these are signs of a limited increase in upper ocean biologic activity, eight laminations and no signs of bioturbation

were observed in this unit, hence only minimal benthic activity is inferred.

Unit 2b grades into unit 2a (39 - 11.5 cm), a dark olive gray, sandy silt containing gravel- to cobble-sized IRD grains. We do not classify unit 2a as a diamict, based on the total fewer number of clasts set in a finer-grained matrix observed in the X-ray image and slightly higher water content relative to unit 3. MS values and IRD are increased in unit 2a relative to unit 2b. IRD content increases upcore from 33 grains at the contact with unit 2b to a maximum of 57 grains between 20 and 25 cm depth, and then decreases to 27 grains at the contact with unit 1. %TOC and diatom abundance are relatively low throughout most of unit 2a. Percent Chaetoceros shows variability between 68.6% and 90%. Grain size fines upward between 14 and 11.5 cm, and %TOC increases from 0.04% to 0.1%. δ^{13}Corg values increase upcore into unit 1, and range from -22.9‰ to -24.2‰. Diatom total abundance also increases, ranging between 0.1 and 0.5 mvpgs, with only one sample having a higher abundance of 2 mvpgs at 26 - 27 cm. Few laminations are observed between 10 and 20 cm depth.

At 11.5 cm there is a sharp contact between unit 2 and unit 1 (11.5 - 0 cm), which consists of water saturated, bioturbated, diatomaceous, light olive gray clayey silt. Between 11.5 and 10 cm there is an interval of gray gravel and cobbles. MS values gradually decrease upcore, corresponding to higher water content, higher diatom abundance, and lower IRD abundance. δ^{13}Corg is more positive relative to unit 2a but decreases from 5 cm to the core top. %TOC increases upcore from ~0.11% at the lower contact at 11.5 cm to ~0.24% near the sediment-water interface. Diatoms are abundant as indicated by the olive color of the sediment, and total diatom abundance increases an order of magnitude upcore, from 2.6 mvpgs at 11.5 cm to a maximum of 23 mvpgs at 3 - 4 cm. No laminations were observed in this unit. The water content in the upper 15 cm of the core exhibits a logarithmically decreasing downcore trend, indicating that the sediment-water interface was preserved.

Two methods were utilized to establish the chronology for core KC-54: ^{210}Pb activity series and radiocarbon dating. The 210Pb activity series generated an activity profile from which ten ages were calculated. The deepest unsupported 210Pb activity at 13 cm had a calculated age of 98 yr B.P. (A.D. 1912) (Table 1 and Fig. 4). The implied sedimentation rate is 1.33 mm/yr and

thus places the bottom of unit 1 (11.5 cm) roughly at A.D. 1925. Three radiocarbon ages were obtained for KC-54: a surface date from foraminifera at 0 - 3 cm, a date from foraminifera in the laminated silt between 38 and 42 cm (unit 2a-2b contact), and a date from reworked mollusk fragments in unit 3 (69 - 75 cm). Results are presented in Table 2 and Figure 3.

5.2.. Core JPC-126

Core JPC-126 is 21.46 m in length and was collected from an isolated basin of ponded sediment ~10 km from the grounding line at a water depth of 642 m (Figs. 2 and 5). The core was divided into three units: unit 1 (0 - 1.9 m), unit 2 (3.07 - 18.75 m), and unit 3 (19.10 - 21.46 m). There are core recovery gaps between each unit attributed to the coring process.

Unit 3 (21.46 - 19.10 m) consists of olive green diatomaceous, mottled, pebbly sandy silt. MS is lower relative to unit 2 above, reflecting higher diatom content. IRD abundance is enhanced within this interval and reaches a maximum count of 41 grains between 20.47 and 20.52 m. Preserved primary productivity is higher within this unit as indicated by the olive green color and the maximum values of %TOC and δ13Corg of 0.398% and -23.5‰, respectively. Total diatom abundance increases from the core bottom to an average of 72.6 mvpgs, with a maximum value of 222.2 mvpgs at 20.11 m. Percent Chaetoceros shows a general decreasing upcore trend.

Following a core recovery gap between 19.10 and 18.85 m, unit 2 (18.75 - 3.07 m) is a gray laminated silt interbedded with sandy turbidite sequences. Turbidite sequences were recognized by (1) sand and silty sand at the base, which fine upward to clayey silt, (2) peaks in MS that correspond to the sand and silty sand horizons, and (3) overlying silt laminae. Within the laminated intervals, grain size consists of primarily fine and medium silt and sand with little coarse silt and little to no clay. IRD is generally near zero throughout unit 2, with a maximum value of only 4 grains. Productivity within this unit is relatively low, as δ^{13}Corg values and %TOC are depleted and reduced relative to the units above and below. Diatom abundance is low relative to unit 3, with an average of 17.7 mvpgs, and increases to as much as 53.4 mvpgs at 12.005 m.

Following a core recovery gap between 3.07 and 1.9 m, unit 1 (1.9 - 0 m) is a pebbly, homogenous sandy silt with streaks of green organic-rich silt. MS within in this interval is generally lower than that of the rest of the core, reflecting high water content. The most notable characteristic of this unit is the absence of turbidite sequences and marked increase in IRD relative to unit 2. δ^{13}Corg values and %TOC values are increased relative to unit 2 below. Total diatom abundance is similar to that of unit 2 below, at an average of 11.4 mvpgs, but increases to as much as 35.5 mvpgs at 40.5 cm.

Four samples were isolated and prepared for radiocarbon dating in core JPC-126: (1) a complete, undisturbed scaphopod at 7.70 m (unit 2), (2) mollusk fragments at 14.13 m (unit 2), (3) fragments from a single scaphopod at 1880 cm (unit 2), and (4) a complete mollusk at 1920 cm (unit 3) (Table 2 and Fig. 5). There is no radiocarbon age from unit 1. As there is not age control for the top of the core and the sedimentology suggests variable sedimentation rates throughout unit 2, a continuous age model was not developed for JPC-126.

5.3. Core KC-55

Core KC-55 was collected from an over-deepened basin in the outer fjord in a water depth of 652 m and is 425 cm in length (Figs. 2 and 6). The logarithmic decrease in water content in the upper 25 cm of the core indicates that the sediment-water interface was well preserved during core extraction. KC-55 can be divided into three units: unit 1 (0 - 20 cm), unit 2 (20 - 82 cm), and unit 3 (82 - 425 cm).

Unit 3 (425 - 82 cm) is a dark olive green, diatomaceous, pebbly, mottled clayey silt, and displays a general upcore trend of increasing MS and IRD content and decreasing preserved primary productivity. Between 425 and 255 cm, MS and IRD content is decreased below their respective average values for the entire core while %TOC, δ^{13}Corg, total diatom abundance, and percent Chaetoceros are higher than average. Enhanced biologic activity is evidenced by the maximum %TOC value of 0.89% at 306 cm, total diatom abundance of 1624 mvpgs at 296 cm, and nine burrows observed between 365 and 395 cm. Enhanced preserved productivity is interrupted within this interval of unit 3 by

a sandy silt turbidite between 330 and 341 cm, which is marked by a layer of very fine-grained sand that fines upward into a greenish gray silt. Between 255 and 135 cm, MS values are fairly stable but increased relative to values below 225 cm. This depth interval has generally higher IRD content; the maximum IRD abundance, 38 grains, is recorded between 195 and 200 cm. δ^{13}Corg, %TOC, total diatom abundance, and percent Chaetoceros values decrease below the core average within this interval. Between 135 and 82 cm, grain size fines upward, MS values increase upcore, and IRD is reduced. %TOC decreases from 0.71% to 0.59%, total diatom abundance decreases significantly from 750 to 290 mvpgs, and percent Chaetoceros decreases. The decline in organic carbon, however, is paralleled by increased δ^{13}Corg values. These upcore trends in productivity and physical properties continue into unit 2 above.

Unit 3 grades into unit 2 (82 - 20 cm), a light olive gray, mottled, diatomaceous clayey fine silt. The increase in fine terrigenous sediment is paralleled by an enhanced MS signal above the core average value. IRD is lower in unit 2 relative to unit 3 and unit 1. %TOC decreases from 0.6% at the contact with unit 3 to the core minimum of 0.28% at 38 cm. δ^{13}Corg values are generally less than the average value for the entire core and range between -23.9‰ and -21.9‰. Total diatom abundance decreases significantly within this interval from 291 mvpgs at 82 cm to as little as 58 mvpgs at 21 cm. Percent Chaetoceros also decreases below average values in this interval. Within unit 2, the decrease in diatoms is coincident with increased clay content. Laminations were not observed in unit 2.

Unit 2 grades into unit 1 (20 - 0 cm), a pebbly, mottled, diatomaceous dark olive grayish clayey silt that coarsens upward to a pebbly, mottled, diatomaceous, olive gray silt. MS decreases upcore due to elevated water content. IRD is slightly increased relative to unit 2. %TOC rebounds within unit 1 from 0.3% to 0.6% but does not exceed the core average value. It should be noted, however, that %TOC in core KC-55 is generally an order of magnitude greater than in the other Barilari Bay cores, reflecting its more open, oceanic setting. δ^{13}Corg demonstrates variability with no discernable trend, varying between -22.9‰ at the lower unit contact, -21.9‰ at 14 cm, and -23.5‰ at the sediment-water interface. Total diatom abundance remains decreased at

values similar to those of unit 2. This reflects a general upcore trend of decreasing total diatom abundance initiated at 140 cm in unit 3. Percent Chaetoceros is variable but is lower than the core average. Laminations were not observed in unit 1.

The chronology of core KC-55 was constrained using the A.D. 1963 cesium "bomb spike" (47 yr B.P. relative to A.D. 2010), ^{210}Pb activity series, and radiocarbon dating. The 1963 Cs bomb spike was determined to be at 15 - 16 cm, with an inferred sedimentation rate of 3.2 - 3.4 mm/yr (Fig. 6). ^{210}Pb activity series profiles allowed calculation of 14 dates, the oldest at 139 yr B.P. (A.D. 1871) at 16 cm, with an overall sedimentation rate of 1.21 mm/yr (Table 1 and Fig. 4). Radiocarbon dating complements the above geochronological methods and provides a continuous time series and polynomial age model. Six intervals were selected for foraminifera collection: (1) 19 - 24 cm (units 1 and 2 contact), (2) 49 - 54 cm (middle of unit 2), (3) 80 - 84 cm (units 2 and 3 contact), (4) 200 - 205 cm (unit 3), (5) 250 - 254 cm (unit 3), and (6) 400 - 405 cm (core bottom). Table 2 shows the complete radiocarbon results for KC-55. The six radiocarbon dates from KC-55 represent a continuous sedimentation record for the late Holocene in Barilari Bay (Fig. 6) spanning the last 3863 cal. yr B.P. Depth is converted to age using a third-order polynomial derived from the combined radiocarbon dates and 210Pb activity series from KC-55. Under this age model, the sedimentation rate decreases downcore from 1.19 mm/yr at the surface to 0.033 mm/yr at the core bottom.

6. Discussion

Seasonally open marine conditions (i.e., seasonally sea ice covered and seasonally open) have been recorded in Barilari Bay since its discovery in the early 20th century (Charcot, 1905; Rymill, 1938), followed by the loss of small remnant ice shelves around the periphery of the fjord since the 1940s, minor glacial retreat since the 1960s, and stable ice front positions at the head of the fjord since the 1980s (Cook et al., 2005; Ferrigno et al., 2008). We propose a sequence of paleoenvironmental variability in Barilari Bay that constrains the glacial and environmental history based on historical observations, the

sedimentary record, and a lithofacies model described below. The Holocene paleoenvironmental history of Barilari Bay is summarized in a space-time diagram (Fig. 7) that displays the shifts in environmental setting across the fjord through time.

6.1. Lithofacies Model

Sediment lithofacies assigned to the cores within Barilari Bay are based upon decades of information obtained from fjords along the AP. What is unique in this particular setting is that the cores were strategically acquired in position to optimize understanding of the subsurface reflectors and integrated within the multi-beam seafloor morphology. We recognize the following lithofacies: (1) compact, structureless diamicton, (2) laminated silt and clay, (3) graded ensembles of interbedded sand and mud, and (4) diatomaceous mud and diatom-bearing mud with variable content of outsized gravel and pebbles. These lithofacies are interpreted respectively as: (1) sub-glacial till, (2) near - grounding line plume and undermelt deposits, (3) turbidite sediment gravity flow deposits, and (4) hemipelagic and ice-rafted deposits. The facies succession as follows from Walther's Law then allows us to infer changes in depositional environment with constraints upon these various sediments imposed by changing ice shelf cover and glacier extent.

6.2.. Early and Middle Holocene—Retreated Glacial Positions and Seasonally Open Marine Conditions

Retreated glacial positions during the early Holocene are evidenced by the presence of a mollusk fragment at 69 - 75 cm depth in core KC-54. The radiocarbon age of this mollusk fragment, 7022 cal. yr B.P. (5072 B.C.), suggests that a younger glacial advance transported and incorporated the mollusk fragments from somewhere further in to the head of the fjord. Similar evidence for retreated glacial positions in the early to middle Holocene is found in shelly tills on Brabant Island (Hansom and Flint, 1989) and organic fragments recently revealed from beneath the ice cap margin on Anvers Island (Hall et al., 2010).

While the chronology of core KC-55 does not constrain the onset of the middle Holocene, the outer fjord record confirms regional observations of enhanced productivity during the middle Holocene (Domack et al., 2001, 2003). Between 3863 and 2815 cal. yr B.P. (1913 - 865 B.C.), higher %TOC and less-negative δ^{13}Corg relative to the entire KC-55 core indicate greater productivity. Within this interval, total diatom abundance is greater and the assemblage consists primarily of Chaetoceros resting spores, considered an indicator of high productivity (Leventer et al., 1996), and thus this interval is interpreted as representing productive seasonally marine conditions. Reduced gravel abundance in unit 3 of KC-55 suggests greater distance from calving ice fronts.

Similar evidence for enhanced productivity during the middle Holocene exists in Neny Fjord, Marguerite Bay (Allen et al., 2010), Lallemand Fjord and Crystal Sound (Domack et al., 1995; Shevenell et al., 1996; Taylor et al., 2001), the Palmer Deep (Brachfeld et al., 2003; Domack et al., 2003), and Maxwell Bay, South Shetland Islands (Milliken et al., 2009). Generally, biological productivity is associated with reduced sea ice coverage and prolonged growing seasons. There is an exception in Maxwell Bay where decreased sea-surface temperature and increased sea ice coverage enhanced productivity (Milliken et al., 2009). Recently, Hodgson et al. (2013) suggested extended middle Holocene regional warming on Horseshoe Island, northern Marguerite Bay, likely related to periods of reduced lacustrine-ice cover that stimulated production.

6.3. Neoglacial－Climatic Cooling

At 2815 cal. yr B.P. (865 B.C.), productivity began to decline as reflected in the %TOC, δ^{13}Corg, and total diatom abundance proxies in core KC-55 under open marine conditions with greater sea ice coverage. IRD increases upcore in unit 3, suggesting increasing glacial proximity as the calving fronts in Barilari Bay advanced, but seasonally open marine conditions were maintained. In the middle fjord, the late portion of the Neoglacial event is captured in unit 3 of core JPC-126 (>~730 cal. yr B.P.; A.D. 1220), which marks open marine and more productive conditions and the absence of active turbidity currents

associated with advanced glacial positions discussed in the “Little Ice Age” section.

The Neoglacial event is observed at a number of sites in the western AP and initiated between 3500 – 2500 years ago (Domack et al., 2003). Allen et al. (2010) presented a sedimentary record of Neny Fjord in Marguerite Bay where the Neoglacial began ca. 2800 cal. yr B.P. (850 B.C.). Taylor et al. (2001) proposed that the Neoglacial initiated at 2880 cal. yr B.P. (930 B.C.) in Lallemand Fjord, but increased sea ice coverage may have begun as early as 4420 cal. yr B.P. (2470 B.C.). Further north at the Palmer Deep, the Neoglacial began at 3360 cal. yr B.P. (1410 B.C.) and is marked by a decline in productivity and sedimentation rates (Leventer et al., 1996; Domack et al., 2001, 2003). In Maxwell Bay, this period is placed between 2600 yr B.P. and the present, although the sedimentological character shows little evidence of this climatic event (Milliken et al., 2009).

While δ^{13}Corg in the outer fjord of Barilari Bay is enriched between ca. 1325 cal. yr B.P. and 626 cal. yr B.P. (A.D. 625 – 1324), we do not observe strong evidence for a Medieval Warm Period (MWP) event. Productivity in the outer fjord remains decreased as indicated by decreasing %TOC, total diatom abundance, and percent Chaetoceros within this same time interval. The MWP is recognized regionally in the western AP by enhanced productivity in more oceanic settings such as the Palmer Deep and Crystal Sound between 1150 – 700 yr B.P. (A.D. 850 – 1300), but is less evident in glacial-proximal environments such as Lallemand Fjord (Domack et al., 2003).

6.4. Little Ice Age (LIA)

6.4.1. Glacial Advance and Ice Shelf Development

All three sediment cores provide evidence for climatic cooling and glacial advance with associated development of an ice shelf during the LIA between ca. 730 and 82 cal. yr B.P. (A.D. 1220 and 1868). In the inner fjord, core KC-54 lies at the edge of the fluted grounding zone wedge and captures the maximum Holocene glacial position (Fig. 8A). Unit 3 of KC-54 documents the inner fjord

in a sub-glacial environment during the last glacial advance in Barilari Bay. The poorly sorted homogenous diamicton with generally lower water content suggests deposition from sub-glacial processes. Very low %TOC and total diatom abundance and highly negative δ^{13}Corg indicate lower primary productivity caused by light limitation and other biologic activity.

Glacial advance in Barilari Bay altered sedimentological processes across the entire fjord. In core JPC-126, the transition to the LIA is recognized at ca. 730 cal. yr B.P. (A.D. 1220) by a shift to gray laminated silt with interbedded sandy turbidite sequences (unit 2) deposited as glaciers advanced to the edge of the grounding line. At these advanced positions, meltwater pulsing along the grounding line ejected sediment plumes into the fjord, depositing laminated silts and clays. Fluctuations of the ice margin at this advanced position caused portions of the edge of the grounding zone wedge to collapse, and turbidity currents carried sediment through channels toward the zone of ponded sediment in the middle fjord. Both of these depositional processes likely increased sedimentation rates within the middle fjord relative to seasonally open marine conditions.

The decay of remnant ice shelves demonstrated in historic records and our sedimentological evidence suggests that a prehistoric ice shelf expanded across Barilari Bay during the LIA. This environment is marked by both low IRD abundance and decreased productivity within this time interval. In the presence of the ice shelf, and thus absence of iceberg calving processes, entrained glacial debris is not rafted from the ice margin and deposited across the fjord. Sub - ice shelf conditions precluded primary productivity as expressed in the decreased %TOC, more-negative δ^{13}Corg values, reduced total diatom abundance, and fewer Chaetoceros within this interval. However, enhanced sedimentation rates under the advanced glacial position may partially mask biogenic sedimentation in this interval and region of the fjord. An open marine influence was maintained near the ice shelf margin as diatoms were likely transported under the ice shelf by wind-driven surface currents.

In the outer fjord of Barilari Bay, the LIA is captured between 626 and 82 cal. yr B.P. (A.D. 1324 - 1868) in unit 2 of core KC-55, which is marked by a fining of grain size and decreased primary productivity. The fining in grain

size and increasing upcore trend in MS reflects increased fine-grained siliciclastic sedimentation, preservation instead of dissolution of fine-grained magnetite in the zone of low %TOC, and reduction in biogenic input from diatoms. The negative shift in δ^{13}Corg, and decrease in %TOC, total diatom abundance, and percent Chaetoceros, are attributed to the expansion of the ice shelf into or near the outer fjord and more pervasive sea ice coverage. This reduction in productivity and fining of particle size is comparable to trends observed in Lallemand Fjord when the Müller Ice Shelf expanded during the LIA 400 yr B.P. (Domack et al., 1995; Shevenell et al., 1996). Given the olive gray color, diatomaceous nature of the sediment, and %TOC values that are an order of magnitude greater than in the middle and inner fjord in this interval, proximity to the ice shelf front and seasonally marine conditions, albeit with greater sea ice coverage, must have been maintained. A bathymetric rise northeast of the mouth of the fjord may have served as a pinning point for the expanded ice shelf. Under this scenario, IRD in unit 2 of KC-55 may have been sourced from the grounding line of the advanced Otlet Glacier, where basal melt-out could have supplied IRD grains.

The precipitation accumulation zone and rate must have increased to allow glacial advance, and the ablation zone and rate must have decreased for the ice shelf to expand. Further south on the AP (75°55′S, 84°15′W), the ice core from Siple Station records relatively warmer conditions and decadal-scale periods of increased snow accumulation rate, possibly due to intensification of the Southern Westerlies between A.D. 1500 and 1900 (Mosley-Thompson et al., 1990). While increased snow accumulation could have caused a positive shift in the mass balance for western AP glaciers, higher temperatures contradict the expansion of an ice shelf in Barilari Bay, as it implies that the -5 to -9 °C isotherm did not migrate north during the LIA. We propose, therefore, a shift in oceanographic conditions that decreased frontal melting and undermelting of glacier fronts, allowing the expansion of the Barilari Bay ice shelf. Reduced upwelling of warm, saline circumpolar deep water (CDW) during the LIA interval may have permitted the formation of the ice shelf in Barilari Bay. The advance of the Müller Ice Shelf at 400 yr B.P. (Domack et al., 1995) further south in Lallemand Fjord suggests a regional climatic shift that encouraged ice

shelf growth during the LIA and has also been attributed to decreased presence of CDW.

6.4.2. Ice Shelf Recession and Glacial Retreat

At the edge of the grounding zone in core KC-54, the sharp contact between diamict (unit 3) and laminated clayey silt (unit 2b) marks initial glacial retreat. The appearance of IRD, fining in grain size, and decrease in MS values relative to unit 3 indicate a transition from sub-glacial deposition to pelagic sedimentation. Laminations suggest deposition related to meltwater pulsing near the grounding zone. The limited increase in %TOC and δ^{13}Corg reflects continued low primary productivity under sub-ice shelf conditions. Reduced biologic activity is also evidenced by the bluish gray color of the unit, low abundance of microfossils, and preservation of laminations that would otherwise be disturbed by bioturbation under more productive conditions. Unit 2b was deposited in proximity to grounded ice, but some distance from the calving front of the ice shelf; thus the transition between units 3 and 2b represents an ice "back-off" event from the edge of the grounding line and occurred sometime prior to 252 ± 137.5 cal. yr B.P. (A.D. 1698). This suggests that the maximum extent of ice advance during the LIA occurred in the first half of the LIA (730 to >252 cal. yr B.P.; A.D. 1220 to >1698) followed by slow, gradual retreat until 82 cal. yr B.P. (A.D. 1868).

The demise of the LIA ice shelf in Barilari Bay may be analogous to recent observations below the ice shelf extending from the Pine Island Glacier in West Antarctica, where an ice "back-off" event was observed at Pine Island Glacier in the late 1970s (Jenkins et al., 2010). Jenkins et al. (2010) suggested that although the ridge feature along the edge of the grounding line initially impeded influx of warm, saline CDW to the base of the glacier, thinning of the ice shelf from above by increased atmospheric temperatures and from below by CDW enlarged the cavity between the edge of the grounding line and glacier base, ultimately increasing and accelerating ice retreat. While the ice shelf in Barilari Bay may have receded in a similar fashion, the timing of the initial ice "back-off" event some time prior to 252 cal. yr B.P. suggests that ice recession

in this study area was much more gradual.

Unit 2a in core KC-54 signifies that the complete transition from sub-ice shelf to open marine conditions in the inner fjord occurred between 252 ± 137.5 cal. yr B.P. (A.D. 1698) and 98 yr B.P. (A.D. 1912). Although the first French Antarctic Expedition recorded seasonally open marine conditions in Barilari Bay between A.D. 1903 and 1905, expedition records are not specific regarding conditions in the inner fjord (Charcot, 1905). The charts produced by the British Graham Land Expedition, however, explicitly record seasonally open marine conditions in Barilari Bay between A.D. 1934 and 1937 (Rymill, 1938). Grain size gradually coarsens upwards, with enhanced IRD deposition indicating increasing input of terrigenous sediment as entrained debris fell out of the receding ice shelf, similar to observations at the former Prince Gustav Channel and Larsen A ice shelves (Gilbert and Domack, 2003). The increased flux of terrigenous sediment into the inner fjord masked the input of biologic components as shown by the decreased %TOC. The maximum number of IRD grains occurring between 20 and 25 cm marks the point in time when the calving front was most proximal to the KC-54 collection site. Above 20 cm, IRD abundance and MS values decrease, followed by significantly increased productivity proxies indicating that the calving front retreated landward toward its present position, affording more open marine conditions at the site.

6.5. Modern Warming

Unit 1 in core KC-54 represents the modern open marine conditions that facilitate primary productivity as indicated by maxima in %TOC and δ^{13}Corg. Benthic activity is indirectly documented by bioturbation. IRD and MS decrease upcore, marking greater distance from the core collection site to, and less terrigenous sediment input from, the glacier fronts. The horizon of cobbles and gravel at 10 cm is interpreted as an ice rafting event where the calving front was landward of the KC-54 collection site. The reduced flux of terrigenous sediment also enhances the biologic signal preserved in unit 1. Figure 8B illustrates Barilari Bay under seasonally open marine conditions.

In the middle fjord, the transition from sub-ice shelf to seasonally open

marine conditions occurs between unit 2 and unit 1 in JPC-126. Due the core recovery gap that exists between 1.87 and 3.07 m, the exact timing of this climatic shift is not constrained in the middle fjord. Unit 1 of core JPC-126, however, indicates an environmental shift toward open marine conditions. The most notable changes are the absence of sandy turbidite sequences and presence of IRD relative to unit 2. As glacial positions retreated, the ice margin no longer stood at the edge of the grounding zone. As a result, meltwater pulsing along the grounding line ceased along with slope instability and associated turbidity currents. Glacial retreat and the gradual demise of the ice shelf also increased calving events and consequently IRD deposition. Interestingly, total diatom abundance and percent Chaetoceros do not rebound in the upper unit; however, the sediment-water interface, and thus possibly the transition to more productive open water conditions, was not well preserved in JPC-126.

In the outer fjord, ice shelf recession and glacial retreat was completed by 82 cal. yr B.P. (A.D. 1868), and the modern seasonally open marine conditions are represented by unit 1 in KC-55. This environmental shift toward seasonally open marine conditions is expressed by a rebound in productivity and coarsening of grain size upcore, with a related reduced MS signal. Total diatom abundance continues to decrease upcore in unit 1 however, despite an increase in %TOC. This suggests that primary productivity increased as a consequence of increased abundance of groups other than diatoms—presumably a soft-bodied algae, perhaps cryptophytes, as have been observed to be associated with increased glacial meltwater and lower sea surface salinities (Moline et al., 2004). The variability in δ^{13}Corg may further reflect oceanographic changes that may have affected the local biological community.

6.6. Comparison with Late Holocene Glacial Records in the Southern Hemisphere

The timing and magnitude of LIA glacial advance in Barilari Bay corresponds to regional enhanced climatic cooling and glacial advance in the AP, but the LIA is asynchronous with glacial records from elsewhere in the Southern Hemisphere. Compiled late Holocene glacial records from middle to high latitudes in the Southern Hemisphere are presented in Figure 9. The

following chronology summary will be discussed in terms of calendar years (B.C./A.D.) where possible, or in terms originally used by the authors where conversion to calendar years was not possible.

South of the polar front and across both the western and eastern AP, the Barilari Bay record confirms a tightly constrained period of glacial advance between A.D. 1200 and 1400. Glacial advance in Barilari Bay is broadly coincident with the advance of the Müller Ice Shelf at ca. A.D. 1600 (Domack et al., 1995), and regional cooling and decreased productivity across the western AP between A.D. 1300 and 1850 (Domack et al., 2003). The terrestrial glacial record on Anvers Island is also in agreement, as the Marr Ice Piedmont advanced sometime after A.D. 1250 (Hall et al., 2010). The Barilari Bay record corresponds to the glacial advance in the eastern AP where both terrestrial (Balco et al., 2013) and glacial marine (Gilbert and Domack, 2003; Brachfeld et al., 2003) evidence indicates late Holocene glacial advance and re-establishment of the Prince Gustav Channel and Larsen A ice shelves between A.D. 1300 and 1600. The Collins Ice Cap on King George Island in the South Shetland Islands advanced at A.D. 1300 (Hall, 2007). Late Holocene glacial advances in the AP and the South Shetland Islands coincide with two periods (A.D. 1275 – 1300 and A.D. 1430 – 1455) of abrupt and intensified cooling and sea ice growth around Iceland and Arctic Canada, attributed to volcanic forcing (Miller et al., 2012), but predate the classically defined period of LIA alpine glacial advance in the European Alps (Lamb, 1985).

North of the polar front on South Georgia, a late Holocene advance occurred at A.D. 900 and predates glacial advance in the AP and South Shetlands (Clapperton et al., 1989; Bentley et al., 2007). This advance was during a period of relatively warmer conditions and reduced ice extent in the western AP (Domack et al. 2003). Glacial advance on South Georgia is attributed to increased precipitation afforded by southern excursion of the Southern Westerlies, warmer temperatures, and reduced sea ice conditions, leading to the anti-phase relationship with AP glacial records (Bentley et al., 2007). Glaciers in the Kerguelen Islands in the southern Indian Ocean were at maximum Holocene positions in the late 19th century (Frenot et al., 1993).

In southern South America, there is general synchronicity with the AP

for glacial advance between A.D. 1200 and 1400, but the records later diverge, as additional pulses of glacial advance are observed during the classically defined LIA period. In Tierra del Fuego, the Ema Glacier advanced in sync with AP glaciers at 695 14C yr B.P. but then readvanced between 379 14C yr B.P. and 60 yr B.P. (Strelin et al., 2008). In the Gran Campo Nevado (Chile), Glaciar Lengua advanced to maximum Holocene positions between A.D. 1280 and 1460, followed by overall retreat and six smaller, punctuated advances between A.D. 1628 and 1941 (Koch and Kilian, 2005). Further north in the Monte Fitz Roy region (Argentina), glaciers reached maximum LIA positions later, in the A.D. late 1500s to early 1600s (Masiokas et al., 2009). In the Southern Patagonian Ice Field and Northern Patagonian Ice Field, LIA glacial advance ages range from A.D. 1220 to 1890, but a majority of Southern Patagonian Ice Field glaciers advanced after A.D. 1600 (Glasser et al., 2004). Most of the outlet glaciers in the Northern Patagonian Ice Field advanced later, between A.D. 1650 and 1766, and retreated from their maximum late Holocene positions between A.D. 1860 and 1870 (Harrison et al., 2007). In the northern sector of the Northern Patagonian Ice Field, the Gualas Glacier advanced to maximum Holocene positions between 2230 B.C. and A.D. 1100, and experienced three smaller advances between A.D. 1790 and 1940 (Bertrand et al., 2012).

In New Zealand, late Holocene glacial advance occurred out of sync with the AP and southern South America and at the end of the classic LIA time period. On the western side of the divide of the Southern Alps, the Strauchon Glacier advanced prior to the AP and southern South America glaciers at 390 B.C., A.D. 310, and A.D. 910 (Winkler, 2009). The Franz Josef Glacier, however, advanced during the classic LIA time frame, with the most extensive advance some time before A.D. 1600 and smaller advances at A.D. 1600 and A.D. 1800 (McKinzey et al., 2004). On the eastern side of the Southern Alps, glaciers advanced to maximum positions in the early and middle Holocene. Late Holocene glacial advance on the eastern side of the Southern Alps occurred slightly later than in the AP and southern South America. The Mount Cook glaciers advanced at A.D. 1440 (Schaefer et al., 2009), and the Cameron Glacier advanced at A.D. 1362 and A.D. 1492, followed by smaller advances after A.D. 1770 (Putnam et al., 2012). On the North Island, Mount Taranaki glaciers retreated after A.D.

1500 (Brook et al., 2011). The asynchronous behavior of New Zealand glaciers during the classic LIA has been attributed to a shift to a negative phase of the Interdecadal Pacific Oscillation (Schaefer et al., 2009) and the southern migration of the Intertropical Convergence Zone (Putnam et al., 2012), both of which bring warmer and drier conditions to New Zealand.

The timing of LIA glacial advances is increasingly younger to the north from the AP toward the Northern Patagonian Ice Field, indicating that the LIA was not a synchronous event across the southeast Pacific sector. This chronological progression may be in response to northward migration of the Southern Westerlies, which control storm tracks, regional precipitation, cloud cover, and temperature patterns that influence local glacial behavior (Holmlund and Fuenzalida, 1995; Bertrand et al., 2012). Alternatively, the overall pattern may reflect the response time of the glacial system under a uniform climatic shift. If climatic episodes appropriate to induce glacier growth take place across the entire region (Patagonia to AP) and are of limited duration, then asynchronous response may simply indicate the lag time for colder and more sluggish systems (i.e., those in the AP). If the forcing factor is of long enough duration, then a delayed response across the region should reflect the varying response times across glacial dynamic boundaries. We suggest that the AP glaciers indeed may be sluggish, as their calving lines are not as easily stabilized by sediment provisioning in deep water, and fast ice to ice shelf transitions may take several decades, under a generally colder climate. Indeed, sediment delivery rates are higher and ice flow dynamics are greater for Patagonian glaciers than their counterparts in the AP (Boldt et al., 2013).

7. Conclusions

Based on our observations and the historical record, we propose this high-resolution chronology of paleoenvironmental history in Barilari Bay (Fig. 7):

1. Early Holocene and middle Holocene (>2815 cal. yr B.P.; >865 B.C.) retreated glacial positions and seasonally open marine conditions with enhanced primary productivity;

2. Neoglacial (2815 to ca. 730 cal. yr B.P.; 865 B.C. to A.D. 1220) seasonally open marine conditions with increased sea ice coverage—we do not observe strong evidence for a MWP event in Barilari Bay;
3. Little Ice Age (ca. 730 – 82 cal. yr B.P.; A.D. 1220 – 1868) glacial advance to maximum Holocene positions and development of a fjord-wide ice shelf—prehistoric glacial retreat and gradual recession of the ice shelf initiated some time prior to 252 cal. yr B.P. (A.D. 1698);
4. Modern seasonally open marine conditions and loss of remnant ice shelves within the context of recent rapid regional warming (82 cal. yr B.P. to present; A.D. 1868 to present).

The late Holocene record from Barilari Bay is the first precisely constrained LIA glacial advance and ice shelf expansion record in Graham Land, western AP, that is concurrent with the classic definition of the LIA in the Northern Hemisphere (Lamb, 1985; Grove, 1988). Prior efforts in the western AP were inferential in terms of the actual advanced position of ice shelves and/or terrestrial termini, but no grounding limits had been defined (Domack et al., 1995, 2003; Shevenell, et al., 1996, Hall, 2007; Hall et al., 2010). The Barilari Bay sedimentary record will be greatly bolstered by results from the Site Beta ice core on the Bruce Plateau collected only 12 nautical miles east of Barilari Bay. This combined data set will provide the most direct correlation of marine sedimentary and cryospheric climatic records in Antarctica to date.

The Barilari Bay record further supports a regional LIA climate signature in the AP but highlights intra-hemispheric and global disparities in the timing and magnitude of the latest Holocene glacial advance. The overall asynchronous late Holocene glacial record across the Southern Hemisphere demonstrates the issues involved in globally extrapolating the original definition of the LIA in the European Alps. In comparing glacial records across the Southern Hemisphere, there is evidence for broad late Holocene advance, but the exact timing varies according to region. The synchronicity of glacial advance in the AP, and to some degree in southern South America, during periods of abrupt and intensified cooling and sea ice growth in Arctic Canada and Iceland (A.D. 1275 – 1300 and A.D. 1430 – 1455) strengthens the case for the onset of

global LIA cooling due to volcanic forcing (Miller et al., 2012), but intra-hemispheric disparities remain. The late Holocene glacial record of southern South America, however, diverges from the AP, as additional advances occurred during the classic LIA period and were progressively younger northwards. This broad asynchronous trend in the southeast Pacific sector may reflect changes in the migration of the Southern Westerlies. Late Holocene glacial behavior in New Zealand is asynchronous with the southeast Pacific, suggesting that the colder, wetter conditions of the classic LIA were not globally distributed to the southwest Pacific. While the timing of late Holocene glacial advance is asynchronous, ongoing rapid retreat over the past 150 years in the Southern Hemisphere, particularly within the AP, reaffirms that anthropogenic climate forcing is manifested globally.

서남극 그레이엄 랜드 배릴러리 만에서 홀로세 후기 동안 빙하의 전진 및 빙붕의 성장

유규철, 윤호일

Korea Polar Research Institute

요약: 서남극 반도 그레이엄 랜드의 Barilari Bay (65°55′S, 64°43′W)의 피오르드 축을 따라 세 개의 해양퇴적물 코어를 획득하였다. 고해상도의 지질연대 측정법 (210Pb, 방사성 탄소, 137Cs)에 의해 연대가 설정된 멀티-프록시 분석 결과는 홀로세의 고환경 변화의 기록을 반영한다. 우리의 결과는 초기와 중기 홀로세 (> 7022-2815 cal. yr B.P.)는 빙하가 후퇴하고 생산력이 증가하는 공해 환경이었다. 신빙하기 (2815 - 730 cal. yr B.P.) 기후 냉각은 해빙 면적을 증가 시켰고 표층 생산성을 감소시켰다. 이 기후 냉각은 소빙하기 (LIA) (약 730-82 cal. yr B.P.) 동안 피오르드 전역에 해당하는 빙붕이 확장하였고, 홀로세 동안 빙하가 가장 전진한 시기이다. 계절적인 공해 환경은 최근 급격한 지역적인 온난화 (82 cal. yr B.P.부터 오늘날까지)로 남아 있던 빙붕이 후퇴하였다. 우리의 연구 결과는 소빙하기가 시기와 규모면에서 지역적으로 중요한 사건이었다는 것을 시사하는 기존의 연구 결과와 잘 일치한다. 남극 반도의 소빙하기 기록과 남반구의 다른 나머지 지역과의 비교는 태평양 남동쪽과 남반구의 대서양 지역과 비슷하지만, 태평양 남서쪽과 인도양은 일관성이 떨어진다. 북반구와의 비교는 남극반도의 소빙하기 기록은 북대서양- 북극의 소빙하기 이전 한랭화와 해빙의 확장시기와 동일 시기임을 의미하며, 이 것은 이 사건이 전지구적인 영향을 끼쳤음을 시사한다.

참고문헌

Allen, C.S., Oakes-Fretwell, L., Anderson, J.B., and Hodg-son, A., 2010, A record of Holocene glacial and oceanographic variability in Neny Fjord, Antarctic Peninsula. The Holocene, v. 20, p. 551 - 564, doi: 10 .1177 /0959683609356581.

Appleby, P.G., Jones, V.J., and Ellis-Evans, J.C., 1995, Radiometric dating of lake sediments from Signy Is-land (maritime Antarctic): Evidence of recent climate change. Journal of Paleolimnology, v. 13, p. 179 - 191, doi: 10 .1007 /BF00678106 .

Balco, G., Schaefer, J.M., and LARISSA Group, 2013, Ex-posure-age record of Holocene ice sheet and ice shelf change in the northeast Antarctic Peninsula. Quater-nary Science Reviews, v. 59, p. 101 - 111, doi: 10 .1016 /j .quascirev .2012 .10 .022.

Bentley, M.J., Hodgson, D.A., Sugden, D.E., Roberts, S.J., Smith, J.A., Leng, M.J., and Bryant, C., 2005, Early Holocene retreat of the George VI Ice Shelf, Antarc-tic Peninsula. Geology, v. 33, p. 173 - 176, doi: 10 .1130 /G21203 .1 .

Bentley, M.J., Evans, D.J.A., Fogwill, C.J., Hansom, J.D., Sugden, D.E., and Kubik, P.W., 2007, Glacial geomor-phology and chronology of deglaciation, South Geor-gia, sub-Antarctic. Quaternary Science Reviews, v. 26, p. 644 - 677, doi: 10 .1016 /j .quascirev .2006 .11 .019.

Bentley, M.J., Hodgson, D.A., Smith, J.A., Ó Cofaigh, C., Domack, E.W., Larter, R.D., Roberts, S.J., Brachfeld, S., Leventer, A., Hjort, C., Hillenbrand, C.D., and Evans, J., 2009, Mechanisms of Holocene palaeo-environmental change in the Antarctic Peninsula region. The Holocene, v. 19, p. 51 - 69, doi: 10 .1177 /0959683608096603.

Berkman, P.A., and Forman, S.L., 1996, Pre-bomb radiocar-bon and the reservoir correction for calcareous marine species in the Southern Ocean. Geophysical Research Letters, v. 23, p. 363 - 366, doi: 10 .1029 /96GL00151.

Berthier, E., Scambos, T.A., and Shuman, C.A., 2012, Mass loss of Larsen B tributary glaciers (Antarctic Penin-sula) unabated since 2002.

Geophysical Research Let-ters, v. 39, L13501, doi: 10 .1029 /2012GL051755.

Bertrand, S., Hughen, K.A., Lamy, F., Stuut, J.B.W., Torrejon , F., and Lange, C.B., 2012, Precipitation as the main driver of Neoglacial f uctuations of Gualas glacier, Northern Patagonian Icef eld. Climate of the Past, v. 8, p. 519 - 534.

Boldt, K.V., Nittrouer, C.A., Hallet, B., Koppes, M.N., For-rest, B.K., Wellner, J.S., and Anderson, J.B., 2013, Modern rates of glacial sediment accumulation along a 15° S-N transect in fjords from Antarctic Peninsula to southern Chile. Journal Geophysical Research, v. 118, p. 2072 - 2088, doi: 10 .1002 /jgrf .20145.

Brachfeld, S.A., Banerjee, S.K., Guyodo, Y., and Acton, G.D., 2002, A 13,200 year history of century to mil-lennial-scale paleoenvironmental change magnetically recorded in the Palmer Deep, western Antarctic Pen-insula. Earth and Planetary Science Letters, v. 194, p. 311 - 326, doi: 10 .1016 /S0012 -821X (01)00567 - 2.

Brachfeld, S., Domack, E., Kissel, C., Laj, C., Leventer, A., Ishman, S., Gilbert, R., Camerlenghi, A., and Eglin-ton, L.B., 2003, Holocene history of the Larsen-A Ice Shelf constrained by geomagnetic paleointen-sity dating. Geology, v. 31, p. 749 - 752, doi: 10 .1130 /G19643 .1.

Brook, M.S., Neall, V.E., Stewart, R.B., Dykes, R.C., and Birks, D.L., 2011, Recognition and paleoclimatic im-plications of late-Holocene glaciation on Mt Taranaki, North Island, New Zealand. The Holocene, v. 21, p. 1151 - 1158, doi: 10 .1177 /0959683611400468.

Charcot, J.B., 1905, The French Antarctic Expedition. The Geographical Journal, v. 26, p. 497 - 516, doi: 10 .2307 /1776355.

Clapperton, C.M., Sugden, D.E., Birnie, J., and Wilson, M.J., 1989, Late-glacial and Holocene glacier f uctuations and environmental change on South Georgia, Southern Ocean. Quaternary Research, v. 31, p. 210 - 228, doi: 10 .1016 /0033 -5894 (89)90006 - 9.

Cook, A.J., Fox, A.J., Vaughan, D.G., and Ferrigno, J.G., 2005, Retreating glacier fronts on the Antarctic Penin-sula over the past half-century. Science, v. 308, p. 541 - 544, doi: 10 .1126 /science .1104235.

Domack, E.W., 1992, Modern carbon-14 ages and reservoir corrections for the Antarctic Peninsula and Gerlache Strait area. Antarctic Journal of the United States, v. 27, p. 63 - 64.

Domack, E.W., and Ishman, S., 1993, Oceanographic and physiographic controls on modern sedimentation within Antarctic fjords. Geological Society of America Bulletin, v. 105, p. 1175 - 1189, doi: 10 .1130 /0016 -7606 (1993)105 <1175: OAPCOM>2 .3 .CO;2.

Domack, E.W., and McClennen, C.E., 1996, Accumulation of glacial marine sediments in fjords of the Antarctic Peninsula and their use as Late Holocene paleoenvi-ronmental indicators, in Ross, R.M., Hofmann, E.E., and Quetin, L.B., eds., Foundations for Ecological Research West of the Antarctic Peninsula. American Geophysical Union Antarctic Research Series 70, p. 135 - 154, doi: 10 .1029 /AR070p0135.

Domack, E.W., Ishman, S.E., Stein, A.B., and Jull, A.J.T., 1995, Late Holocene advance of the Müller Ice Shelf, Antarctic Peninsula: Sedimentological, geochemical and palaeontological evidence. Antarctic Science, v. 7, p. 159 - 170, doi: 10 .1017 /S0954102095000228.

Domack, E.W., Leventer, A., Dunbar, R., Taylor, F., Brach-feld, S., Sjunneskog, C., Cowan, E., Daniels, J.W., Escutia, C., Evans, A., Eyles, N., Guyodo, Y., Ioio, M., Iwai, M., Kyte, F., Lauer, C., Maldonado, A., Morez, T., Osterman, L., Pudsey, C., Schuffert, J., Vigar, K., Wein-heimer, A., Williams, T., Winter, D., and Wolf-Welling, T.C.W., 2001, Chronology of the Palmer Deep site, Ant-arctic Peninsula: A Holocene palaeoenvironmental ref-erence for the circum-Antarctic. The Holocene, v. 11, p. 1 - 9, doi: 10 .1191 /095968301673881493.

Domack, E.W., Leventer, A., Root, S., Ring, J., Williams, E., Carlson, D., Hirshorn, E., Wright, W., Gilbert, R., and Burr, G., 2003, Marine sedimentary record of natural en-vironmental variability and recent warming in the Ant-arctic Peninsula, in Domack, E., Leventer, A., Burnett, A., Bindschadler, R., Convey, P., and Kirby, M., eds., Antarctic Peninsula Climate Variability: Historical and Paleoenvironmental Perspectives. American Geophysi-cal Union Antarctic Research Series 79, p. 205 - 224.

Domack, E.W., Duran, D., Leventer, A., Ishman, S., Doane, S., McCallum, S., Amblas, D., Ring, J., Gilbert, R., and Prentice, M., 2005, Stability of the Larsen B ice shelf on the Antarctic Peninsula during the Holocene epoch. Nature, v. 436, p. 681 - 685, doi: 10 .1038 /nature03908 .

Ferrigno, J.G., Cook, A.J., Mathie, A.M., Williams, R.S., Jr., Swithinbank, C., Foley, K.M., Fox, A.J., Thomson, J.W., and Sievers, J., 2008, Coastal-change and glacio-logical map of the Larsen Ice Shelf area, Antarctica: 1940 - 2005. U.S. Geological Survey Geological Inves-tigations Map I-2600-B, 1 map sheet, 28 p. text.

Flint, R.F., Sanders, J.E., and Rodgers, J., 1960, Diamictite, a substitute term for symmictite. Geological Society of America Bulletin, v. 71, no. 12, p. 1809 - 1810, doi: 10 .1130 /0016 -7606 (1960)71 [1809: DASTFS]2 .0 .CO;2

.Frenot, Y., Gloaguen, J.C., Picot, G., Bougere, J., and Benja-min, D., 1993, Azorella selago Hook. used to estimate glacier f uctuations and climatic history in the Ker-guelen Islands over the last two centuries. Oecologia, v. 95, p. 140 - 144.

Gilbert, R., and Domack, E.W., 2003, Sedimentary record of disintegrating ice shelves in a warming climate, Ant-arctic Peninsula: Geochemistry Geophysics Geosys-tems, v. 4, no. 4, p. 1 - 12, doi: 10 .1029 /2002GC000441.

Glasser, N.F., Harrison, S., Winchester, V., and Aniya, M., 2004, Late Pleistocene and Holocene palaeoclimate and glacier fluctuations in Patagonia. Global and Planetary Change, v. 43, p. 79 - 101, doi: 10 .1016 /j .gloplacha .2004 .03 .002.

Gordon, J.E., and Harkness, D.D., 1992, Magnitude and geo-graphic variation of the radiocarbon content in Antarc-tic marine life: Implications for reservoir corrections in radiocarbon dating. Quaternary Science Reviews, v. 11, p. 697 - 708, doi: 10 .1016 /0277 -3791 (92)90078 - M .

Griffth, T.W., and Anderson, J.B., 1989, Climatic control of sedimentation in bays and fjords of the northern Ant-arctic Peninsula. Marine Geology, v.

85, p. 181 – 204, doi: 10 .1016 /0025 -3227 (89)90153 - 9 .

Grove, J.M., 1988, The Little Ice Age. London and New York, Methuen, 520 p.

Grove, J.M., 2004, Little Ice Ages: Ancient and Modern. London and New York, Routledge, 718 p.

Hall, B.L., 2007, Late-Holocene advance of the Collins Ice Cap, King George Island, South Shetland Islands. The Holocene, v. 17, p. 1253 – 1258, doi: 10 .1177 /0959683607085132.

Hall, B.L., 2009, Holocene glacial history of Antarctica and the sub-Antarctic islands. Quaternary Science Reviews, v. 28, p. 2213 – 2230, doi: 10 .1016 /j .quascirev .2009 .06 .011.

Hall, B.L., Koffman, T., and Denton, G.H., 2010, Reduced ice extent on the western Antarctic Peninsula at 700 – 970 cal. yr B.P. Geology, v. 38, p. 635 – 638, doi: 10 .1130 /G30932 .1.

Hansom, J.D., and Flint, C.P., 1989, Holocene ice f uc-tuations on Brabant Island, Antarctic Peninsula. Antarctic Science, v. 1, p. 165 – 166, doi: 10 .1017 /S0954102089000246 .

Harris, P.T., Domack, E., Manley, P.L., Gilbert, R., and Leventer, A., 1999, Andvord drift: A new type of inner shelf, glacial marine deposystem from the Antarctic Peninsula. Geology, v. 27, p. 683 – 686, doi: 10 .1130 /0091 -7613 (1999)027 <0683: ADANTO>2 .3 .CO;2.

Harrison, S., Winchester, V., and Glasser, N.F., 2007, The timing and nature of recession of outlet glaciers of Hielo Patagonico Norte, Chile, from their Neogla-cial IV (Little Ice Age) maximum positions. Global and Planetary Change, v. 59, p. 67 – 78, doi: 10 .1016 /j .gloplacha .2006 .11 .020.

Hodgson, D.A., Bentley, M.J., Roberts, S.J., Smith, J.A., Sugden, D.E., and Domack, E.W., 2006, Examining Holocene stability of Antarctic Peninsula ice shelves. Eos (Transactions, American Geophysical Union), v. 87, p. 305 – 308, doi: 10 .1029 /2006EO310001.

Hodgson, D.A., Roberts, S.J., Smith, J.A., Verleyen, E., Sterken, M., Labarque, M., Sabbe, K., Vyverman, W., Allen, C.S., Leng, M.J., and Bryant, C., 2013, Late Quaternary environmental changes in Marguerite Bay, Antarctic Peninsula, inferred from lake sediments and raised beaches.

Quaternary Science Reviews, v. 68, p. 216 - 236, doi: 10 .1016 /j .quascirev .2013 .02 .002.

Holmlund, P., and Fuenzalida, H., 1995, Anomalous glacier response to 20th century climate changes in Darwin Cordillera, southern Chile. Journal of Glaciology, v. 41, p. 465 - 473.

Ingólfsson, Ó., Hjort, C., Berkman, P.A., Björck, S.E.C., Goodwin, I.D., Hall, B., Hirakawa, K., Melles, M., Möller, P., and Prentice, M.L., 1998, Antarctic glacial history since the Last Glacial Maximum: An over-view of the record on land. Antarctic Science, v. 61, p. 326 - 344.

Jenkins, A., Dutrieux, P., Jacobs, S.S., McPhail, S.D., Per-rett, J.R., Webb, A.T., and White, D., 2010, Observa-tions beneath Pine Island Glacier in West Antarctica and implications for its retreat. Nature Geoscience, v. 3, p. 468 - 472, doi: 10 .1038 /ngeo890.

Kaharoeddin, F.A., Russell, M.D., Weiterman, S.D., Cooper, C.R., Lang, T.H., Clark, D.R., Covington, J.M., Firth, J.V., Applegate, J.L., Knuttel, S., and Breza, J.R., 1988, The United States Antarctic Research Program in the western Ross Sea, 1979 - 1980: The sediment descrip-tions. Sedimentology Research Laboratory Contribu-tion No. 53, Department of Geology, Florida State University, Tallahassee, 230 p.

Koch, J., and Kilian, R., 2005, 'Little Ice Age' glacier fluctuations, Gran Campo Nevado, southernmost Chile. The Holocene, v. 15, p. 20 - 28, doi: 10 .1191 /0959683605hl780rp.

Lamb, H.H., 1985, Climatic History and the Future. Prince-ton, New Jersey, Princeton University Press, 835 p.

Leventer, A., Domack, E.W., Ishman, S.E., Brachfeld, S., McClennen, C.E., and Manley, P., 1996, Productiv-ity cycles of 200 - 300 years in the Antarctic Peninsula region: Understanding linkages among the sun, atmo-sphere, oceans, sea ice, and biota. Geological Society of America Bulletin, v. 108, p. 1626 - 1644, doi: 10 .1130 /0016 -7606 (1996)108 <1626: PCOYIT>2.3 .CO;2.

Leventer, A., Domack, E., Barkoukis, A., McAndrews, B., and Murray, J., 2002, Laminations from the Palmer Deep: A diatom-based interpretation.

Paleoceanogra-phy, v. 17, no. 3, p. PAL 3-1 - PAL 3-15.

Mann, D.H., 1986, Reliability of a fjord glacier's f uctua-tions for paleoclimatic reconstructions. Quaternary Research, v. 25, p. 10 - 24, doi: 10 .1016 /0033 -5894 (86)90040 - 2.

Masiokas, M.H., Luckman, B.H., Villalba, R., Delgado, S., Skvarca, P., and Ripalta, A., 2009, Little Ice Age fluctuations of small glaciers in the Monte Fitz Roy and Lago del Desierto areas, south Patagonian Andes, Argentina. Palaeogeography, Palaeoclimatology, Palaeoecology, v. 281, p. 351 - 362, doi: 10 .1016 /j .palaeo .2007 .10 .031.

McKinzey, K.M., Lawson, W., Kelly, D., and Hubbard, A., 2004, A revised Little Ice Age chronology of the Franz Josef Glacier, Westland, New Zealand. Journal of the Royal Society of New Zealand, v. 34, p. 381 - 394, doi: 10 .1080 /03014223 .2004 .9517774.

Mercer, J.H., 1978, West Antarctic ice sheet and CO2 greenhouse effect: A threat of disaster. Nature, v. 271, p. 321 - 325, doi: 10 .1038 /271321a0.

Miller, G.H., Geirsdottir, A., Zhong, Y.F., Larsen, D.J., Otto-Bliesner, B.L., Holland, M.M., Bailey, D.A., Ref-snider, K.A., Lehman, S.J., Southon, J.R., Anderson, C., Bjornsson, H., and Thordarson, T., 2012, Abrupt onset of the Little Ice Age triggered by vol canism and sustained by sea-ice/ ocean feedbacks: Geo-physical Research Letters, v. 39, L02708, doi: 10 .1029 /2011GL050168.

Milliken, K.T., Anderson, J.B., Wellner, J.S., Bohaty, S.M., and Manley, P.L., 2009, High-resolution Holocene climate record from Maxwell Bay, South Shetland Islands, Antarctica. Geological Society of America Bulletin, v. 121, p. 1711 - 1725, doi: 10 .1130 /B26478 .1.

Moline, M., Claustre, H., Frazer, T.K., Schof eld, O., and Vernet, M., 2004, Alteration of the food web along the Antarctic Peninsula in response to a regional warming trend. Global Change Biology, v. 10, p. 1973 - 1980, doi: 10 .1111 /j .1365 -2486 .2004 .00825 .x.

Morris, E.M., and Vaughn, D.G., 2003, Spatial and tem-poral variation of surface temperature on the Antarctic Peninsula and the limit of viability of ice shelves, in Domack, E., Leventer, A., Burnett, A., Bindschadler,

R., Convey, P., and Kirby, M., eds., Antarctic Peninsula Climate Variability: Historical and Paleoenvironmental Perspectives. American Geophysical Union Antarctic Research Series 79, p. 61 - 68.

Mosley-Thompson, E., Thompson, L.G., Grootes, P.M., and Gundestrup, N., 1990, Little Ice Age (Neoglacial) paleo environmental conditions at Siple Station, Ant-arctica. Annals of Glaciology, v. 14, p. 199 - 204.

Mulvaney, R., Abram, N.J., Hindmarsh, R.C.A., Arrow-smith, C., Fleet, L., Triest, J., Sime, L.C., Alemany, O., and Foord, S., 2012, Recent Antarctic Peninsula warming relative to Holocene climate and ice-shelf history. Nature, v. 489, p. 141 - 144, doi: 10 .1038 /nature11391.

Pudsey, C.J., and Evans, J., 2001, First survey of Antarctic sub-ice shelf sediments reveals mid-Holocene ice shelf retreat. Geology, v. 29, p. 787 - 790, doi: 10 .1130 /0091 -7613 (2001)029 <0787: FSOASI>2 .0 .CO;2.

Putnam, A.E., Schaefer, J.M., Denton, G.H., Barrell, D.J.A., Finkel, R.C., Andersen, B.G., Schwartz, R., Chinn, T.J.H., and Doughty, A.M., 2012, Regional climate control of glaciers in New Zealand and Europe during the pre-industrial Holocene. Nature Geoscience, v. 5, p. 627 - 630, doi: 10 .1038 /ngeo1548 .

Reimer, P.J., Baillie, M.G.L., Bard, E., Bayliss, A., Beck, J.W., Blackwell, P.G., Ramsey, C.B., Buck, C.E., Burr, G.S., Edwards, R.L., Friedrich, M., Groo-tes, P.M., Guilderson, T.P., Hajdas, I., Heaton, T.J., Hogg, A.G., Hughen, K.A., Kaiser, K.F., Kromer, B., McCormac , F.G., Manning, S.W., Reimer, R.W., Rich-ards, D.A., Southon, J.R., Talamo, S., Turney, C.S.M., van der Plicht, J., and Weyhenmeyer, C.E., 2009, INTCAL09 and MARINE09 radiocarbon age calibra-tion curves, 0 - 50,000 years cal BP. Radiocarbon, v. 51, p. 1111 - 1150.

Rott, H., Rack, W., Nagler, T., and Skvarca, P., 1998, Climati cally induced retreat and collapse of northern Larsen Ice Shelf, Antarctic Peninsula. Annals of Glaci-ology, v. 27, p. 86 - 92.

Rymill, J.R., 1938, British Graham Land Expedition, 1934 - 37. The Geographical Journal, v. 91, p. 297 - 312, doi: 10 .2307 /1788186.

Scambos, T.A., Hulbe, C.L., and Fahnestock, M., 2003, Climate-induced ice shelf disintegration in the Antarc-tic Peninsula, in Domack, E.W., Leventer, A., Burnett, A., Bindschadler, R., Convey, P., and Kirby, M., eds., Antarctic Peninsula Climate Variability: Historical and Paleoenvironmental Perspectives. American Geophysi-cal Union Antarctic Research Series 79, p. 79 - 92.

Scambos, T.A., Bohlander, J.A., Shuman, C.A., and Skvarca, P., 2004, Glacier acceleration and thinning after ice shelf collapse in the Larsen B embayment, Antarctica. Geophysical Research Letters, v. 31, L18402, doi: 10 .1029 /2004GL020670 .

Schaefer, J.M., Denton, G.H., Kaplan, M., Putnam, A., Finkel , R.C., Barrell, D.J.A., Andersen, B.G., Schwartz, R., Mackintosh, A., Chinn, T., and Schlüchter, C., 2009, High-frequency Holocene glacier f uctuations in New Zealand differ from the northern signature. Sci-ence, v. 324,. 622 - 625, doi: 10 .1126 /science .1169312.

Scherer, R.P., 1994, A new method for the determination of absolute abundance of diatoms and other silt-sized sedi mentary particles. Journal of Paleolimnology, v. 12, p. 171 - 179, doi: 10 .1007 /BF00678093.

Shevenell, A.E., and Kennett, J.P., 2002, Antarctic Holocene climate change: A benthic foraminiferal stable isotope record from Palmer Deep. Paleocenaography, v. 17, no. 2, p. PAL 9-1 - PAL 9-10.

Shevenell, A.E., Domack, E.W., and Kernan, G.M., 1996, Record of Holocene palaeoclimate change along the Antarctic Peninsula: Evidence from glacial marine sediments, Lallemand Fjord: Papers and Proceedings of the Royal Society of Tasmania, v. 130, p. 55 - 64.

Skvarca, P., Rack, W., Rott, H., and Ibarzábal y Donángelo, T., 1999, Climatic trend and the retreat and disintegra-tion of ice shelves on the Antarctic Peninsula: An over-view. Polar Research, v. 18, p. 151 - 157, doi: 10 .1111 /j .1751 -8369 .1999 .tb00287 .x.

Strelin, J., Casassa, G., Rosqvist, G., and Holmund, P., 2008, Holocene glaciations in the Ema Glacier Valley, Monte Sarmiento Massif, Tierra del Fuego. Palaeogeography, Palaeoclimatology, Palaeoecology, v. 260, p. 299 - 314, doi: 10 .1016 /j .palaeo .2007 .12 .002 .

Stuiver, M., and Reimer, P.J., 1993, Extended ^{14}C database and revised CALIB radiocarbon calibration program. Radiocarbon, v. 35, p. 215 - 230.

Stuiver, M., Denton, G.H., Hughes, T.J., and Fastook, J.L., 1981, History of the marine ice sheet in West Antarc-tica during the last glaciation: A working hypothesis, in Denton, G.H., and Hughes, T.J., eds., The Last Great Ice Sheets: New York, John Wiley and Sons, p. 319 - 436.

Taylor, F., Whitehead, J., and Domack, E., 2001, Holocene paleoclimate change in the Antarctic Peninsula: Evi-dence from the diatom, sedimentary and geochemical record: Marine Micropaleontology, v. 41, p. 25 - 43.

Vaughan, D.G., Marshall, G.J., Connolley, W.M., Parkinson, C., Mulvaney, R., Hodgson, D.A., King, J.C., Pudsey, C.J., and Turner, J., 2003, Recent rapid regional climate warming on the Antarctic Peninsula. Climatic Change, v. 60, p. 243 - 274.

Warner, N. R., and Domack, E. W., 2002, Millennial- to decadal-scale paleoenvironmental change during the Holocene in the Palmer Deep, Antarctica, as recorded by particle size analysis. Paleoceanography, v. 17, no. 3, p. PAL 5-1 - PAL 5-10.

Wentworth, C.K., 1922, A scale of grade and class terms for clastic sediments. The Journal of Geology, v. 30, p. 377 - 392, doi: 10 .1086 /622910.

Winkler, S., 2009, First attempt to combine terrestrial cosmo-genic nuclide (10Be) and Schmidt hammer relative-age dating: Strauchon Glacier, Southern Alps, New Zea-land. Central European Journal of Geosciences, v. 1, p. 274 - 290.

TABLE 1. RADIOCARBON CHRONOLOGY

Lab ID	Core number	Depth interval (cm)	Sample material	^{14}C age (yr B.P.)	Age error (yr B.P.)	δ^{13}C	Δ^{14}C	Calibrated age* (cal. yr BP)	Calibrated error*† (cal. yr B.P.)	
									Positive deviation	Negative deviation
OS-86511	KC-54	0–3	Foraminifera	1390	40	−0.80	−165.17	0	0	0
OS-86534	KC-54	38–42	Foraminifera	1600	25	−0.04	−186.73	252	138	137
OS-86510	KC-54	69–75	Shell fragments	7500	45	−0.44	−609.83	7022	146	167
OS-92296	JPC-126	769.5	Complete, undisturbed scaphopod	1770	30	0.76	−202.39	418	78	113
OS-92299	JPC-126	1413	Mollusk fragment	2010	25	−0.13	−226.51	596	69	78
OS-92300	JPC-126	1680	Scaphopod fragments	2180	35	0.80	−242.02	736	131	88
OS-87515	JPC-126	1920	Complete mollusk	2170	25	0.14	−242.78	728	139	90
OS-92187	KC-55	19–24	Foraminifera	1450	45	−0.38	−171.52	82	32	82
OS-92260	KC-55	49–54	Foraminifera	1820	50	−0.35	−209.64	462	42	37
OS-92177	KC-55	80–84	Foraminifera	2050	50	−0.11	−230.93	626	43	60
OS-102267	KC-55	200–205	Foraminifera	3450	45	−0.22	−353.71	2110	64	84
OS-92276	KC-55	250–254	Foraminifera	4030	60	−0.29	−399.09	2815	52	75
OS-92190	KC-55	400–405	Foraminifera	4880	55	−0.20	−459.49	3863	93	73

*Calibrated with Marine09 dataset (Reimer et al., 2009); 1390 yr reservoir age (Ballari Bay, KC-54), Delta R = 990 ± 40.
†One-sigma error.
Note: All sediment cores were collected on cruise NBP 10-01.

TABLE 2. LEAD-210 ACTIVITY SERIES CHRONOLOGY

Core number	Sample depth interval (cm)	^{210}Pb activity (Bq/g)	Assigned date (A.D.)	Accumulation rate (mm/yr)
KC-54	0–1	0.326	2010	N/A
KC-54	1–2	0.333	2005	1.83
KC-54	2–3	0.272	1998	1.54
KC-54	3–4	0.197	1992	1.46
KC-54	4–5	0.193	1985	1.54
KC-54	5–6	0.142	1977	1.21
KC-54	6–7	–	1972*	2.26*
KC-54	7–8	0.099	1969	3.23
KC-54	8–9	0.089	1960	1.06
KC-54	9–10	0.077	1952	1.38
KC-54	10–12	–	1945*	1.38*
KC-54	12–13	0.060	1925	0.49
KC-54	13–16	–	1912*	0.81*
KC-54	16–17	0.018	Supported level	†
KC-55	0–1	0.579	2010	N/A
KC-55	1–2	0.492	2006	2.53
KC-55	2–3	–	2002*	2.55*
KC-55	3–4	0.481	1998	2.18
KC-55	4–5	0.396	1991	1.52
KC-55	5–6	–	1986*	1.91*
KC-55	6–7	0.274	1981	2.00
KC-55	7–8	–	1976*	2.20*
KC-55	8–9	0.185	1970	1.49
KC-55	9–10	–	1961*	1.12*
KC-55	10–12	0.161	1949	0.83
KC-55	12–14	0.101	1929	0.51
KC-55	14–16	–	1913*	0.62*
KC-55	16–18	0.043	1871	0.23
KC-55	18–20	–	–	–
KC-55	20–22	0.037	Supported level	†
KC-55	22–24	–	–	–
KC-55	24–25	0.038	Supported level	†
KC-55	25–32	–	–	–
KC-55	32–33	0.026	Supported level	†
KC-55	33–40	–	–	–
KC-55	40–41	0.038	Supported level	†
KC-55	41–50	–	–	–
KC-55	50–51	0.034	Supported level	†
KC-55	51–60	–	–	–
KC-55	60–61	0.036	Supported level	†

Note: Bg/g—Becquerels per gram of sediment. "–" means no sample was analyzed for this depth. N/A—upper-most sample depth; accumulation rate could not be calculated.

*Interpolated value.

†As this sample was at supported level activity, no accumulation rate could be calculated.

Note: All sediment cores were collected on cruise NBP 10-01.

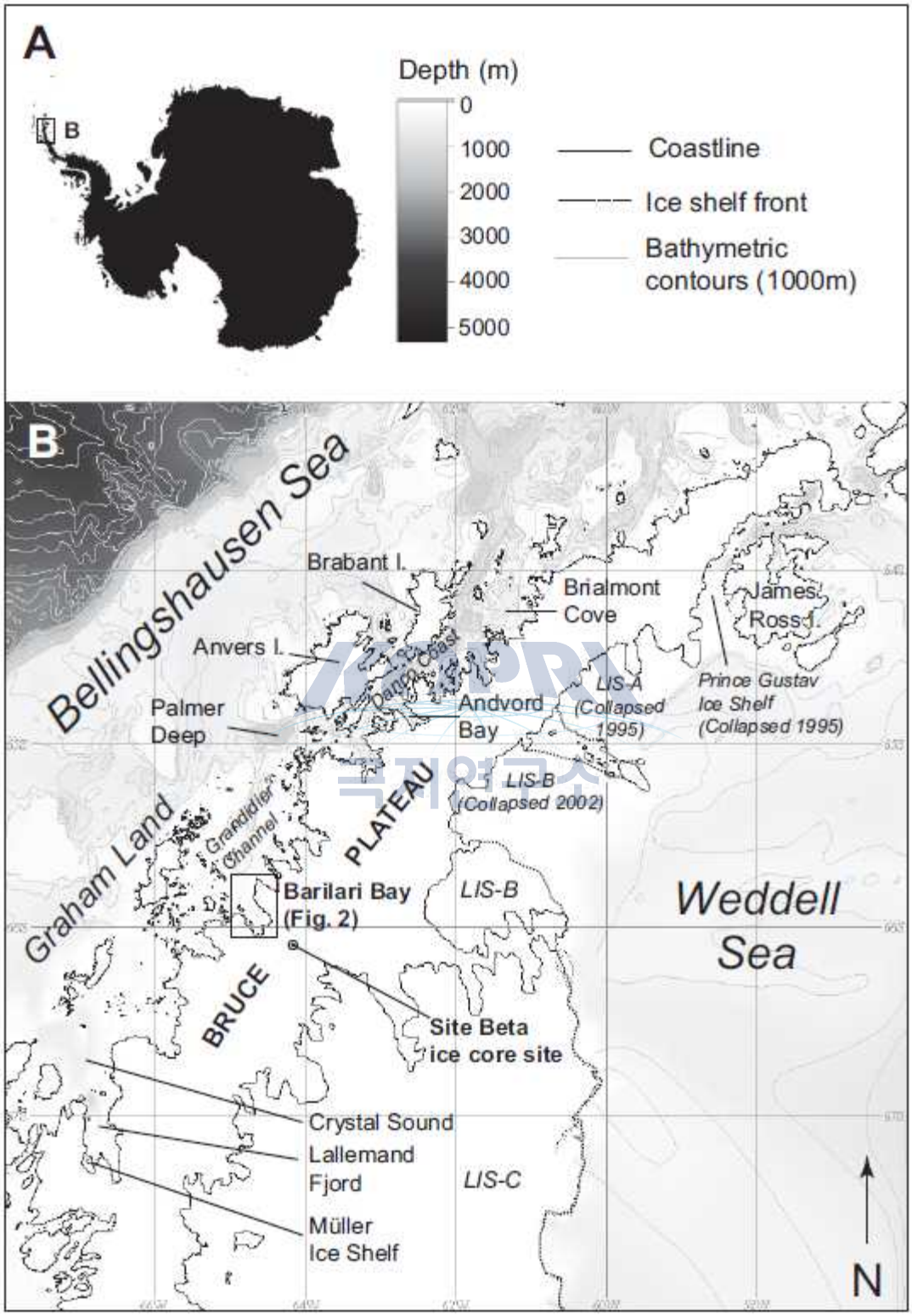

Figure 1. (A) Location of the northern Antarctic Peninsula in Antarctica. (B) North Antarctic Peninsula. Locations with late Holocene records are marked, as well as the location of the Site Beta ice core on the Bruce Plateau.

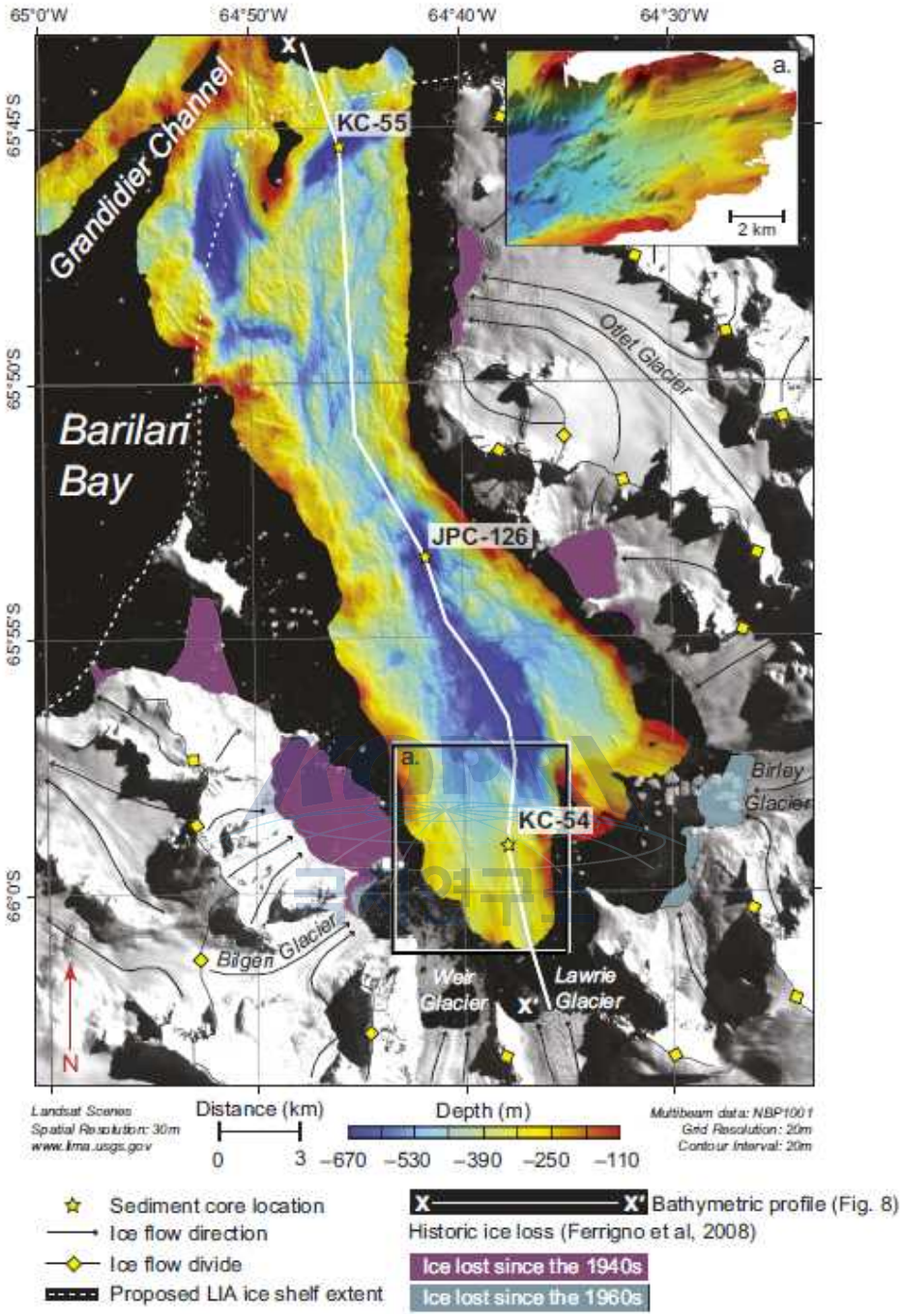

Figure 2. Surface satellite imagery and multibeam swath bathymetry of Barilari Bay. Sediment core locations are marked. Present glacial fl ow lines and fl ow divides are indicated. Bathymetric profi le line used in Figure 8 is drawn for reference. Historic ice loss is delineated from Ferrigno et al. (2008). Proposed Little Ice Age ice shelf extends to the outer fjord. Inset (a): Oblique view of grounding line and grounding zone wedge in inner Barilari Bay (4× vertical exaggeration).

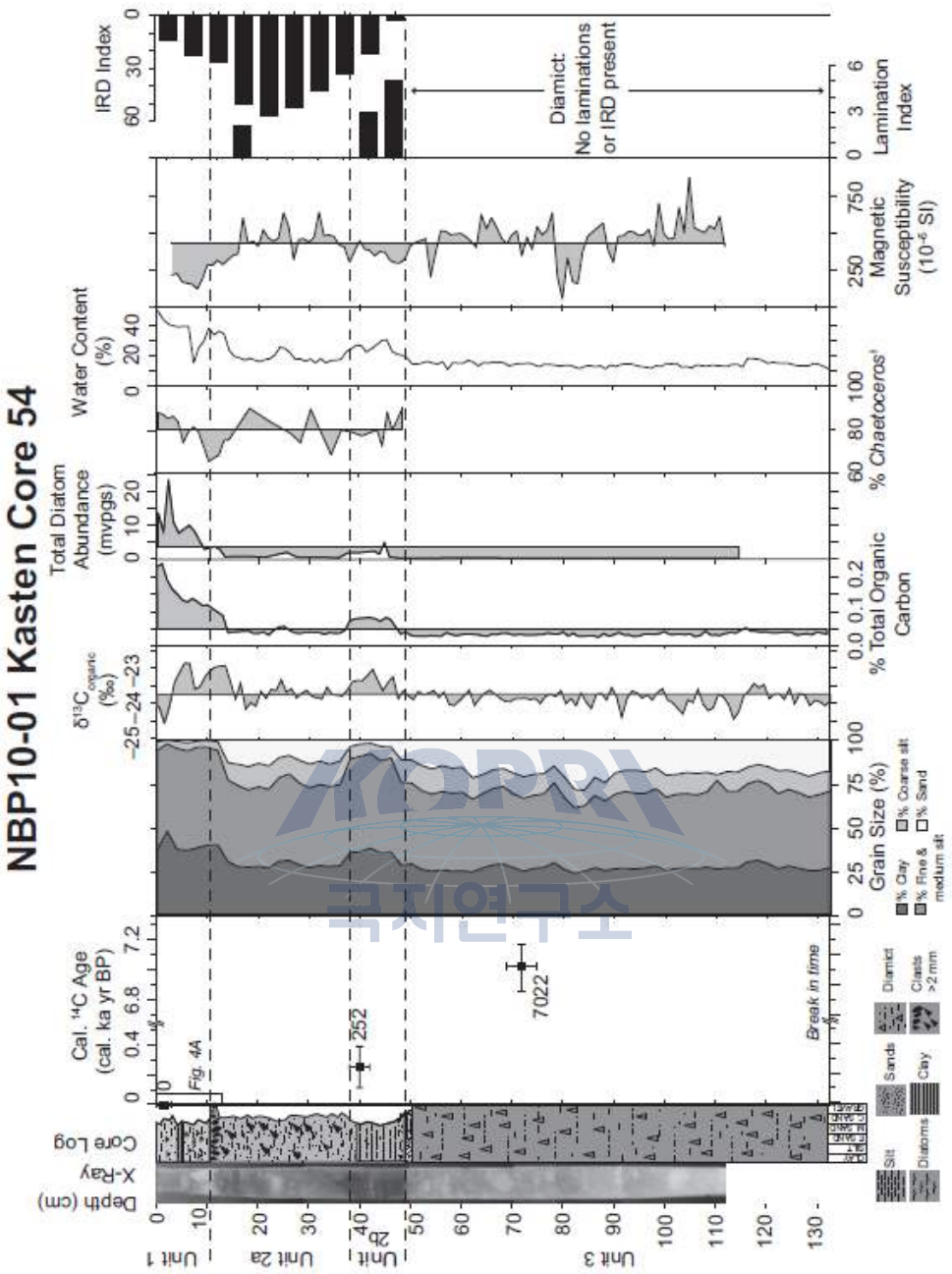

Figure 3. Multi-proxy results and chronology for Kasten Core 54 (KC-54). Multi-proxy results are shaded with respect to the average value for each individual proxy. Note the change in scale for radiocarbon chronology. Interval used in Figure 4 for the short-term chronology assigned by 210Pb activity series is noted. ǂDue to extremely low total diatom abundances in unit 3, diatom assemblages were not determined (see "Diatoms" section for details). cal.—calibrated; mvpgs—millions of valves per gram dry sediment; IRD—ice-rafted debris.

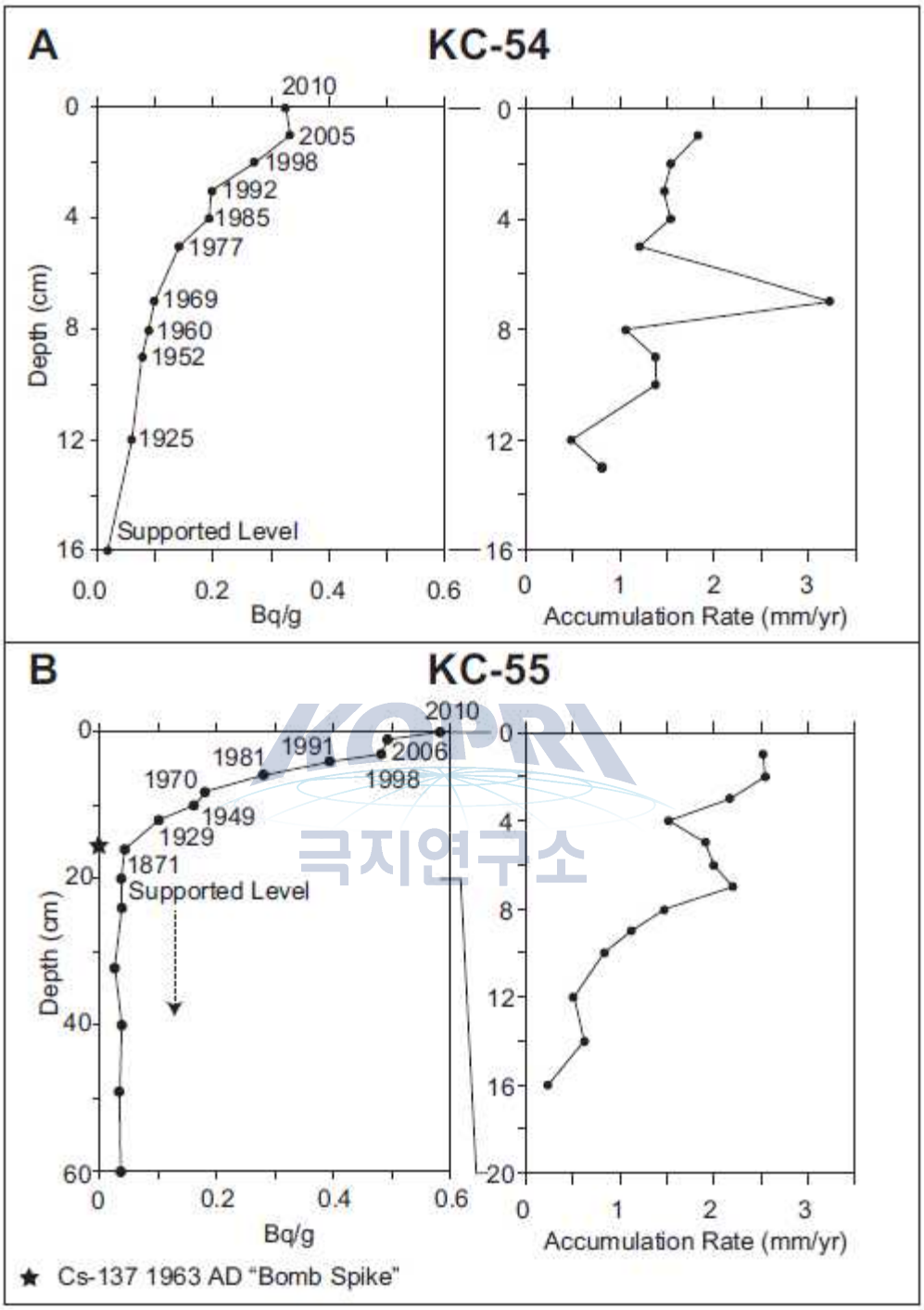

Figure 4. Calculated dates (in A.D.) and sediment accumulation rates from ^{210}Pb activity for cores KC-54 (A) and KC-55 (B). Bq/g is Becquerels per gram of sediment and quantifi es the radioactivity of 210Pb in sediment. The 137Cs A.D. 1963 "bomb spike" is shown for KC-55.

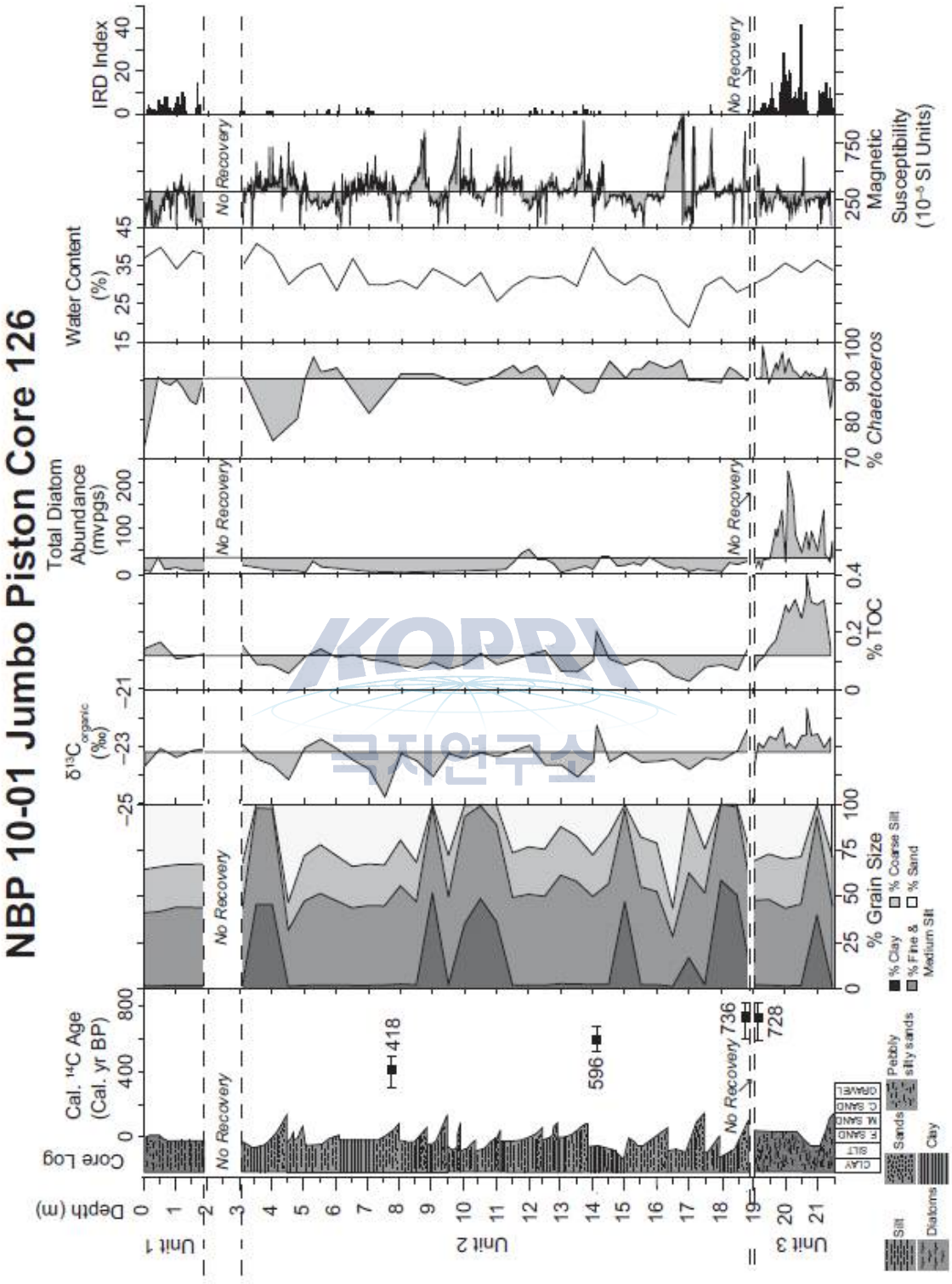

Figure 5. Multi-proxy results and chronology for Jumbo Piston Core 126 (JPC-126). Multi-proxy results are shaded with respect to the average value for each individual proxy. cal.－calibrated; TOC－total organic carbon; mvpgs－millions of valves per gram dry sediment; IRD－ice-rafted debris.

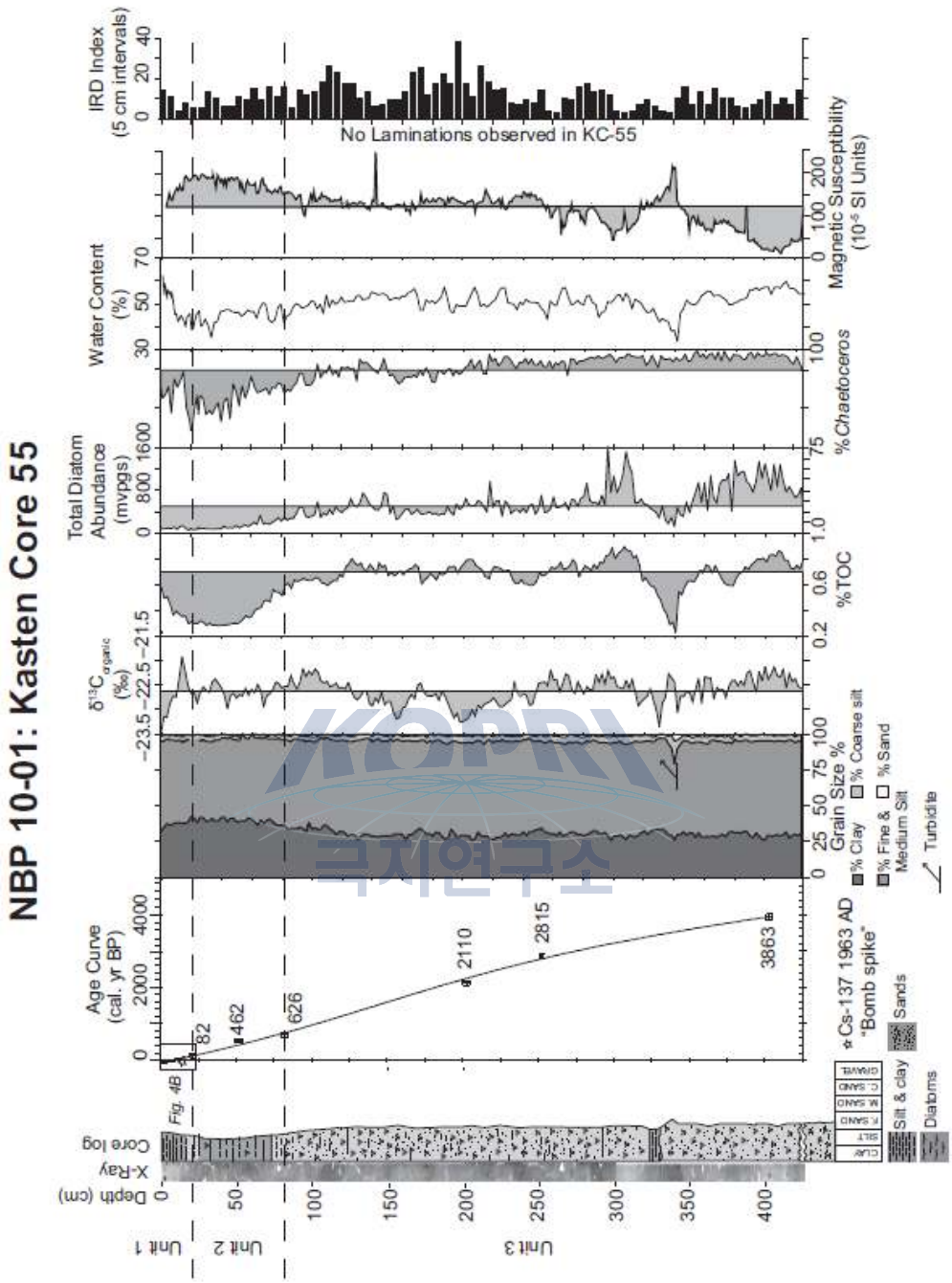

Figure 6. Multi-proxy results and chronology for Kasten Core 55 (KC-55). Multi-proxy results are shaded with respect to the average value for each individual proxy. Interval used in Figure 4 for the short-term chronology assigned by 210Pb activity series is noted. The age model is defi ned by the equation y = -5E-5x3 + 0.0241x2 + 8.4025x (R^2 = 0.99859) where x is depth (cm) and y is age (cal. yr B.P.). cal.—calibrated; TOC—total organic carbon; mvpgs—millions of valves per gram dry sediment; IRD—ice-rafted debris.

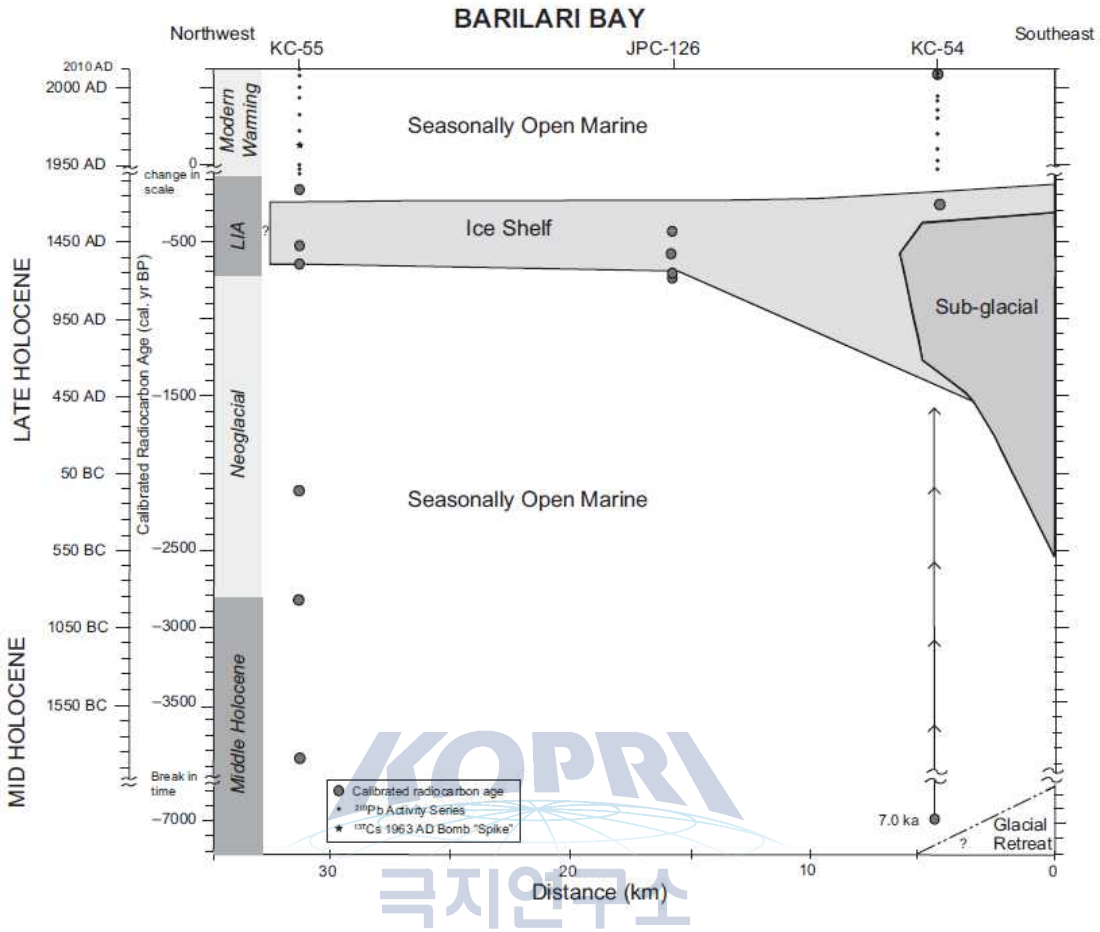

Figure 7. Space-time diagram of late Holocene paleoenvironments and climatic history in Barilari Bay. Location of sediment cores is indicated, along with chronological data for each: calibrated radiocarbon ages (black circles with gray fi ll), ^{210}Pb activity series (small black dots), and ^{137}Cs A.D. 1963 bomb spike (small black star). Note change of time scale on right at A.D. 1950 and 4000 yr B.P. LIA—Little Ice Age.

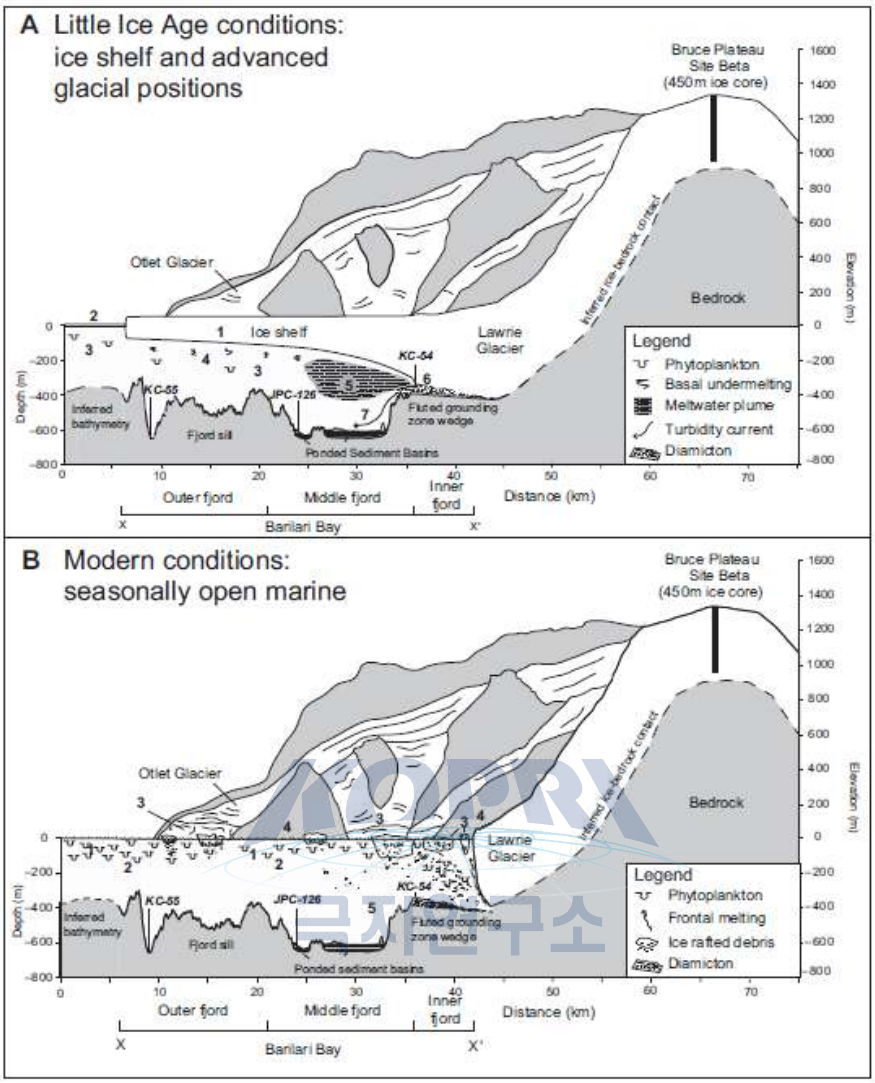

Figure 8. Schematic diagram of Barilari Bay. The bathymetric profile traced along the fjord axis in A and B can be found in Figure 2. Cross-section view is looking to the northeast. Numbers refer to environmental and sedimentological processes active during this each climate event. (A) Little Ice Age conditions: 1－fjord-wide ice shelf; 2－increased sea ice coverage and fast ice; 3－decreased primary productivity; 4－reduced basal melting of the ice shelf; 5－ejection of meltwater plumes of fi ne-grained siliciclastic sediment; 6－glacial advance to maximum Holocene positions over a fluted grounding zone wedge; 7－turbidity currents emanating from the grounding line. (B) Modern seasonally marine conditions in Barilari Bay: 1－seasonally open marine conditions; 2－increased primary productivity; 3－increased iceberg calving and ice-rafted debris deposition; 4－retreated glacial positions with frontal melting at the calving

fronts; 5－absence of turbidity currents and meltwater plumes.

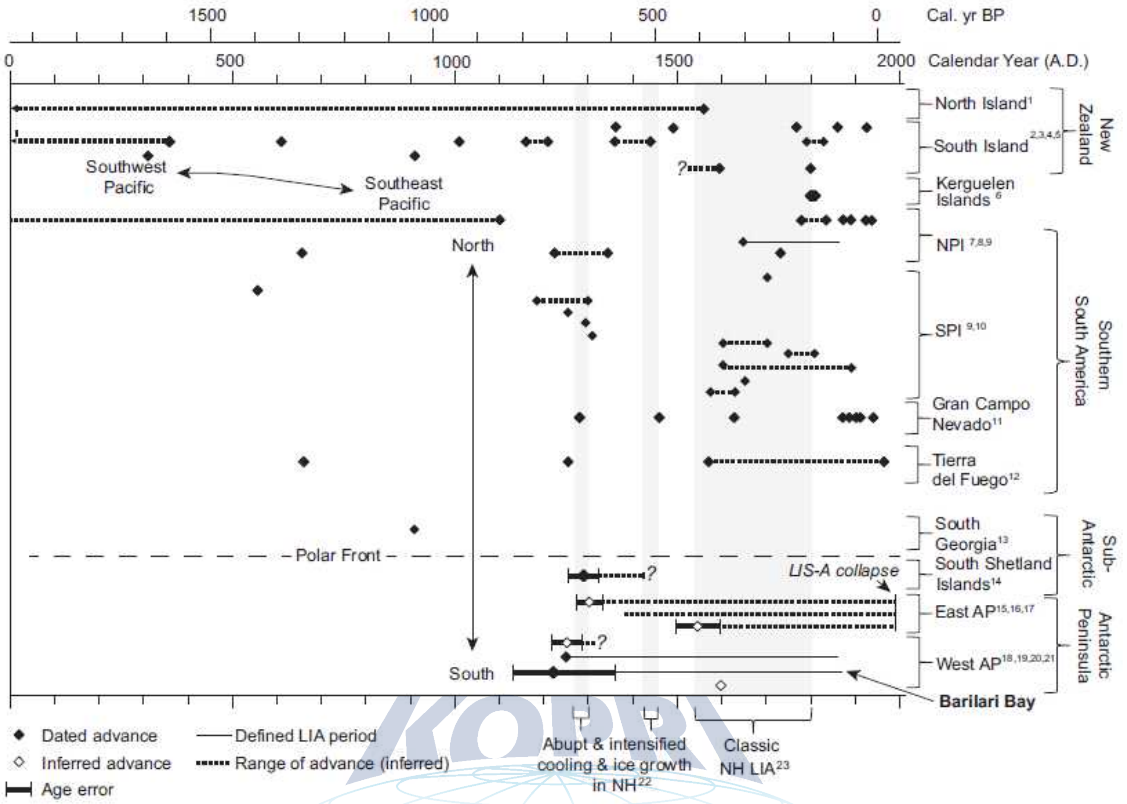

Figure 9. Late Holocene glacial advance and defi ned Little Ice Age (LIA) glacial intervals in the Southern Hemisphere. Cal.－calibrated; NPI－Northern Patagonian Ice Field; SPI－Southern Patagonian Ice Field; AP－Antarctic Peninsula; NH－Northern Hemisphere; LIS-A－ Larsen Ice Shelf A. Black diamonds indicate dated glacial deposits. Hollow black diamonds indicate inferred ages of glacial advance. Black diamonds with dotted lines between them bracket possible advance age ranges. Solid black line indicates defi ned LIA glacial period. Age error bars are included for AP records where appropriate. Periods of abrupt (A.D. 1275 - 1300) and intensifi ed (A.D. 1430 - 1455) cooling and ice growth in Iceland and Arctic Canada attributed to volcanic forcing (Miller et al., 2012) are shaded in gray, as is the classic Northern Hemisphere LIA (A.D. 1550 - 1800). Superscripts refer to the following references: [1]Brook et al., 2004; [2]Putnam et al., 2012; [3]Schaefer et al., 2009; [4]Winkler, 2009; [5]McKinzey et al. 2004; [6]Frenot et al., 1993; [7]Bertrand et al., 2012; [8]Harrison et al., 2007; [9]Glasser et al., 2004; [10]Masiokas et al., 2009; [11]Koch and Kilian, 2005; [12]Strelin et al., 2008; [13]Bentley et al., 2007; [14]Hall, 2007; [15]Gilbert and Domack, 2003; [16]Balco et al., 2013; [17]Brachfeld et al., 2003; [18]Hall et al., 2010; [19]Domack et al., 2003; [20]This study (Barilari Bay); [21]Domack et al., 1995; [22]Miller et al., 2012; [23]Lamb, 1985.

제 9 장

Configuration of the Northern Antarctic Peninsula Ice Sheet at LGM based on a new synthesis of seabed imagery[4)]

Kyu-Cheul Yoo, Ho Il Yoon

Korea Polar Research Institute

Abstract: We present a new seafloor map for the northern Antarctic Peninsula (AP), including swath multibeam data sets from five national programs. Our map allows for the examination and interpretation of Last Glacial Maximum (LGM) paleo-ice-flow paths developed on the seafloor from the preservation of mega-scale glacial lineations, drumlin-ized features, and selective linear erosion. We combine this with terrestrial observations of flow direction to place con-straints on ice divides and ice domes on the AP continental shelf during the LGM time interval. The results show a flow bifurcation as ice exits the Larsen B embayment. Flow em-anating off the Seal Nunataks (including Robertson Island) is directed toward the southeast, then eastward as the flow transits toward the Robertson Trough. A second, stronger "streaming flow" is directed toward the southeast, then south-ward as ice overflowed the tip of the Jason Peninsula to reach the southern perimeter of the embayment. Our reconstruction also refines the extent of at least five other distinct paleo-ice-stream systems that, in turn, serve to delineate seven broad regions where contemporaneous ice domes must have been centered on the continental shelf at LGM. Our reconstruction is more detailed than other recent compilations because we followed specific ice-flow indicators and have kept tributary flow paths parallel.

4) 이 연구 결과는 다음의 논문으로 출판되었음: C. Lavoie, E. W. Domack, E. C. Pettit, T. A. Scambos, R. D. Larter, H.-W. Schenke, K. C. Yoo, J. Gutt, J. Wellner, M. Canals, J. B. Anderson, and D. Amblas., 2015. Configuration of the Northern Antarctic Peninsula Ice Sheet at LGM based on a new synthesis of seabed imagery. The Cryosphere, 9, 613-629.

1. Introduction

The reconstruction of paleo-ice sheets/stream-flow directions depends first upon an accurate assessment of ice domes, ice divides, and outlet flow paths (Andrews, 1982). Studies of the configuration of the Antarctic Peninsula Ice Sheet (APIS) during the Last Glacial Maximum (LGM; time interval ~ 23 - 19 kyr BP) suggest that the grounded ice reached the continental-shelf break (e.g., Larter and Barker, 1989; Banfield and Anderson, 1995; Larter and Vanneste, 1995; Wellner et al., 2001; Canals et al., 2002; Evans et al., 2005; Heroy and Anderson, 2005; Amblas et al., 2006; Wellner et al., 2006; Simms et al., 2011). The seafloor of the Antarctic Peninsula (AP) continental shelf is characterized by over-deepened troughs and basins where mega-scale glacial lineations (MSGLs) (Clark, 1993; Clark et al., 2003) and large-scale flow line bedforms such as glacial flutes, mega-flutes, grooves, drumlins, and crag-and-tails provide geomorphic evidence for former regional corridors of fast-flowing ice and drainage directions of the APIS on the continental shelf. Also of importance is their synchroneity as the ice flows change during the ice sheet evolution from ice sheet to ice stream to ice shelf (Gilbert et al., 2003; Dowdeswell et al., 2008). Our capability to image specific flow directions and styles on the Antarctic continental shelf is critical to any glacial reconstruction because they help us to understand the present and future ice sheet's behavior. Recently, Livingstone et al. (2012) published an inventory of evidence for paleo-ice streams on the continental shelf of Antarctica at LGM. Their reviews are in agreement with previous studies and highlight that the western (Pacific) AP continental shelf is characterized by preferred regional ice-flow pathways on the middle shelf through cross-shelf troughs connected to major flow paths on the outer shelf (e.g., Evans et al., 2004; Heroy and Anderson, 2005). On the other side, the eastern (Weddell Sea) AP continental shelf is less well defined but characterized by multiple deep tributaries on the inner shelf that converge in shallow troughs on the mid- to outer shelf (e.g., Evans et al., 2005). Nevertheless, our knowledge on the APIS configuration at the LGM time interval, such as paleo-flow paths in the Larsen B embayment, is limited and particularly relevant to the ice sheet reconstruction, where the broad continental

shelf served as a platform for extension of the glacial systems that spilled off the Detroit and Bruce Plateau ice caps. In fact, the AP is believed to have experienced the largest percentage change in areal extent of glacial cover of any sector of the Antarctic margin through the last glacial cy-cle (i.e., MIS stages 2 to 1). For instance, our reconstruction shows that the current APIS covers ~ 23 % of the total area of grounded ice coverage at LGM. The APIS system in par-ticular is a significant bellwether system in the evolution of the Antarctic Ice Sheet because it is

1 the one system today that is most closely tied to surface-driven ablation and accumulation change (Rebesco et al., 2014) rather than driven mainly by oceanographic change such as in the West Antarctic Ice Sheet, hav-ing equilibrium lines above sea level (a.s.l.) as a conse-quence of significantly warm summer temperatures;
2. exposed to a contrasting oceanographic regime of cold and warm water on the eastern and western sides, re-spectively; and
3. the most northern of the ice sheet systems and is ex-posed to southward excursions in westerly winds and the Antarctic Circumpolar Current.

In this paper, we examine and interpret the paleo-ice-flow di-rections of the APIS based on a new synthesis of single and swath bathymetry data and provide a comprehensive assess-ment of the flow paths, ice divides, and ice domes pertaining to the glacial history of the northern APIS at the LGM time interval. These ice divides can either be ice ridges or local ice domes with their own accumulation centers, which are ice divides with a local topographic high in the ice surface and flow emanating in all directions (although not necessar-ily equally). The shape of an ice dome may range from cir-cular to elongated; elongated ridge-like ice domes are com-mon amongst the present-day ice streams of West Antarc-tica. The spatial coverage of the bathymetric data is exten-sive (Fig. 1) and for this and the above reasons we focus on regional systems by dividing it into seven sectors. These in-clude the (1) Larsen B embayment, (2) Larsen A and James Ross Island, (3) Joinville Archipelago Platform, (4) Brans-field Strait, (5) Gerlache - Croker - Boyd straits, (6) Palmer Deep and Hugo Island Trough, and (7) Biscoe Trough. First, we highlight the

geomorphic features that define the specific flow paths at LGM and glacial tributaries across the inner to outer shelf. We combine this with terrestrial observations of flow direction to place constraints on ice divides and ice domes that controlled the APIS flow drainage and subsequent retreat history. Finally, we discuss the characteristics of the reconstructed northern APIS and its regional significance for ice sheet modeling.

2. Methods

2.1. Data sets

Extensive multibeam swath bathymetry data have been ac-quired from several regions including those recently uncovered by the collapse of the Larsen Ice Shelf system. Ice-flow directions within the Larsen B embayment are indicated by a series of interconnected (1) multibeam surveys begin-ning with a USAP program in 2000 and followed by the British Antarctic Survey (2002), additional USAP surveys (2001 and 2006), Alfred Wegener Institute, Helmholtz Centre for Polar and Marine Research surveys (2007 and 2011), Korea Polar Research Institute survey (KOPRI, 2013) under the LARISSA project, and (2) single-beam sonar data from USAP in 2005. Detailed observations of the seafl oor morphology in the Larsen A embayment, the area surrounding James Ross Island and offshore from Joinville Archipelago were collected by the USAP program between 2000 and 2002, 2005 and 2007, and in 2010 and 2012, including work by the British Antarctic Survey (2002) and United Kingdom Hydrographic Office (2006 – 2008). The Bransfield Strait has been covered by the Spanish Antarctic program between 1991 and 1997, USAP program (1995 – 1997, 1999 – 2002, and 2005 – 2011), and United Kingdom Hydrographic Office (2006 – 2008, 2010 and 2012). The multibeam swath bathymetry data from the Gerlache – Croker – Boyd Strait, Palmer Deep and Hugo Island Trough, and Biscoe Trough are from the USAP program (1995 – 1997, 1999 – 2002, and 2005 – 2012), the Spanish Antarctic program in 1996 – 1997 and 2001 – 2002, and KOPRI (2013). The data set was gridded at a cell size of 30 m × 30 m and analyzed with illu-mination at variable azimuths. The high-resolution seabed images were

gridded at a cell size of 25 m × 25 m. Addi-tional single-beam sonar data from NOAA National Geo-physical Data Center Marine Trackline Geophysical database (http://ngdc.noaa.gov/mgg/geodas/trackline.html) were used to support the delineation of the continental-shelf ice domes.

2.2. Bedform mapping

We assume that our 詮굇w line reconstructions over sedimen-tary deposits are contemporaneous to the LGM time interval and that observed seafl oor lineations over resistant substrate were carved last by the APIS at LGM, although formation of the latter may derive from time-integrated glacial processes (e.g., Nývlt et al., 2011). While it is possible that some por-tion of the preserved flow line features we examine are repre-sentative of the "death mask" state of the APIS (i.e., Wellner et al., 2006) rather than the mature LGM stage of the system, we suggest that this in general is not the case. We base this hypothesis upon specific observations and assumptions that include

1. only slight modification of flow trajectory as preserved along recessional grounding zones (i.e., Evans et al., 2005, Fig. 7), and such flow relationships are easily re-solved;
2. a general shelf slope gradient that does not, except very locally, provide signi ficant reversal in relief to have in-fluenced evolving flow paths as ice would have thinned (drawn-down) and receded toward the coast;
3. clear association of converging flow paths from areas that would have provided divergent flow during stages of retreat (i.e., as from shelf ice domes).

From the observed seafloor lineations, we establish a cen-tral flow line at the root of each tributary glacier adjacent to areas of reasonable coverage in the multibeam data. We pre-served these central flow lines by forcing tributary contribu-tions to remain parallel and consistent with observed seafloor lineations. In this way converging flow can be evaluated more easily than by using "idealized" single-line flow arrows (as has been done on previous reconstructions). The number of lines in a given flow path is defined by the

number of tribu-taries and is only a visual approximation of the ice discharge for that flow path. In some cases, ice flow across the seafloor diverged around obstacles but remained parallel within the larger confining troughs or fjords. Small-scale basal-flow di-vergence patterns such as these were not preserved in our reconstruction.

The orientation of the bedrock striations at Cape Framnes and Foyn Point (Larsen B embayment; Fig. 2) were measured with a Brunton Compass, corrected for regional declination, and compared to visual data of large-scale bedrock fluting from overflights during 2010 (USAP-ship-based helicopters during LARISSA NBP10-01 cruise).

2.3. Ice volume estimation and assumptions

We utilize two different algorithms to estimate volumes of the ice sheet, depending upon the type of system, streaming flow, or ice domes. The average depths along the flow paths are estimated from our swath bathymetry map and the Inter-national Bathymetric Chart of the Southern Ocean (IBCSO) map gridded at 500 m (Arndt et al., 2013). For the mini-mum volumes, we assume that the ice streams were lightly grounded until the shelf break or to the end of the defined flow path (except for Larsen B/Jason Trough), where the ice thickness must be about 10 % more than the average depth to prevent flotation (allowing the deepest areas to be sub-glacial lakes rather than full of ice). We assume a minimal surface slope (0.001) similar to the lowest sloping modern ice streams. For the maximum volumes, we assume that the ice was grounded to the continental-shelf break (except for Larsen B/Jason Trough). We assume the surface slope of the ice was steeper (0.005) but not too steep to exceed the nearby ice divide elevations. The real slope will depend on the geol-ogy. A softer more malleable bed would favor a lower profile ice stream, while a stiffer bed would lead to a slightly steeper profile. For the ice domes in this reconstruction, we use a ra-dially symmetric Bodvarsson - Vialov model as presented in Bueler et al. (2005). This model assumes the shallow-ice ap-proximation (no sliding bed) and Glen-type ice flow with a softness that depends on the average temperature. The model can directly predict the

thickness as a function of distance from the dome center (r = 0) as

$$H(r) = \left(2^{(n-1)}\frac{\dot{b}}{\Gamma}\right)^{1/(2n+2)} (L^{1+1/n} - r^{1-1/n})^{n/(2n+2)}, \quad (1)$$

$$\Gamma = \frac{2A(\rho g)^n}{n+2}, \quad (2)$$

where H is the ice thickness, $\dot{b}$ is the accumulation rate, L is the lateral extent of the ice dome, assuming it is circular, and n = 3 for typical Glen-type ice flow. Γ is a parameter that depends on the ice softness, A, which is temperature dependent, the density (ρ) of ice, and gravity (g). The specific values of A used are for warm ice 6.8e−15 s−1 kPa−3 and cold ice 4.9e−16 s−1 kPa−3 (Cuffey and Paterson, 2010). Because we lack specific data for LGM accumulation rate and ice temperature, we use our best guesses to bound the ice thicknesses and volumes as follows. We assume that the same strongly orographic precipitation occurred during LGM interval as to-day and the ice temperature was around 0 ○C (mostly temper-ate) for the western AP domes and averaging −20 ○C for the domes located on the eastern side. For the modern AP, the western side has higher average temperatures than the eastern side, suggesting that, in the past, the ice domes on the western side were warmer on average than the eastern side. We based the minimum and maximum dome volumes on a low-end and high-end approximation of the accumulation rates, respectively. In these accumulation rate assumptions, we took into account that some domes are more exposed to the prevailing storm direction and some will be in the lee, result-ing in higher or lower accumulation rates. Also, we take the geologically defined aerial dome extent and assume a dome base of circular area that has the same area as the geologically defined dome. The approximation of a circular dome with the same average radius as

the estimated bathymetric features will introduce additional source of uncertainty into the volume estimates. This circular dome assumption may overestimate volume if the real feature is a oval ridge shape, but it may underestimate the volume if the dome is bounded by thick ice streams. Without more constraints, we feel the uncertainties due to the circular dome assumption are small compared to the uncertainties due to the accumulation rate and temperature assumptions.

3. Results

3.1. Larsen B embayment

The major collapse of the Larsen B Ice Shelf in 2002 (Scam-bos et al., 2003), unprecedented in the Holocene history of this glacial system (Domack et al., 2005; Curry and Pud-sey, 2007), has provided a unique opportunity for seafl oor mapping. This work reveals a far more detailed flow pattern in Larsen B embayment than that inferred by general orientation of bathymetric troughs derived from sparse swath or single-line bathymetric data. Such earlier approaches sug-gested that all Larsen B ice flowed out toward the Robertson Trough (e.g., Evans et al., 2005; Davies et al., 2012; Living-stone et al., 2012). By using a more detailed analysis of flow indicators avail-able from the swath data, we now recognize two distinct flow trajectories that split the Larsen B embayment into two outlets (Fig. 2). The first relates to the attenuated drumlin-ized bedforms and highly attenuated MSGLs observed in the northern perimeter of the Larsen B embayment. The ice flow emanating off the Seal Nunataks and Robertson Island di-rected flow toward the southeast and then eastward as the flow transits toward the Robertson Trough, a feature that con-nects Larsen A and B (Evans et al., 2005). This flow pattern extends across relatively shallow depths of less than 500 m and was probably fed by small tributary confluence.

In contrast, the southern perimeter is marked by stronger “streaming fl ow” indicators fed by large tributaries draining the APIS, including the Crane Glacier and most likely the Evans, Green, and Hektoria glaciers. The well-defi

ned drum-linized bedforms with crescentic scour and MSGLs indicate that ice fl ow was funneled into the Cold Seep Basin (Fig. 3a) and moved toward the southeast from the interior. From the southern edge of Scar Inlet (Larsen B Ice Shelf), the swath bathymetric map shows evidence of a northeastward flow (Fig. 3b) that shifted in a downstream direction toward the southeast, thus convergent with the flow streaming from the Cold Seep Basin corridor. The Scar Inlet ice stream system was fed by the tributaries of the Starbuck, Flask, and Leppard glaciers. Our flow line bedform compilation suggests that the southeastward flow in the southern part of the Larsen B em-bayment changed to a southward direction with ice overflow-ing the tip of the Jason Peninsula, offshore the northern re-gion of the Larsen C Ice Shelf (Figs. 2 and 3c), to reach the Jason Trough. This southward flow orientation is supported by east-southeast bedrock striations and flute orientations at Cape Framnes, Jason Peninsula (Fig. 4), that are in similar orientation to the flow indicators found directly offshore.

Finally, the southernmost swath bathymetry data at the edge of the northern Larsen C Ice Shelf indicate a southeast-ward ice-flow orientation on a seafloor deeper than 400 m. Recent seismic reflection soundings close to the northern ice shelf front and inward show a uniform water cavity thickness beneath the ice shelf of around 220 to 240 m (Brisbourne et al., 2014).

3.2. Larsen A and James Ross Island

Our mapped flow pattern of the Larsen A and James Ross Island sector differs only in fine detail to those of earlier re-constructions (e.g., Evans et al., 2005; Johnson et al., 2011; Davies et al., 2012). The data show the establishment of two major outlets: the Robertson Trough system and the Erebus - Terror system (Fig. 5). The Robertson Trough system col-lected flow out of the Larsen A, southern Prince Gustav Channel, and portions of Admiralty Sound. The ice flowed from the Larsen A, derived mainly from the Detroit Plateau (AP), toward the south and then east. It then coalesced with the southern Prince Gustav Channel flow across the shelf to-ward the southeast and finally directly east (Pudsey et al., 2001; Gilbert et al., 2003; Evans et al., 2005). On the outer shelf the ice flow coalesced with the northern perimeter of the Larsen B fl

ow to form a major ice-flow trend in the Robert-son Trough.

The Erebus - Terror system captured flow out of the northern Prince Gustav Channel, Antarctic Sound, and Admiralty Sound. The northern Prince Gustav Channel shows evidence of a main eastern flow direction fed by tributaries from ice caps on Trinity Peninsula and James Ross Island before coa-lescing with the Antarctic Sound and Admiralty Sound flows into the Erebus and Terror Gulf to reach the shelf break. Flow within the Prince Gustav Channel was separated from the south Larsen A system by an ice divide that extended from the Detroit Plateau across to James Ross Island (Camerlenghi et al., 2001). Recent observations and cosmogenic isotope exposure age dating on erratic boulders on James Ross Is-land by Glasser et al. (2014) suggest that the ice divide that crossed the central Prince Gustav Channel may only have been developed during the post-LGM recession.

3.3. Joinville Archipelago platform

The platform surrounding the northernmost extension of the AP terrain (D'Urville, Joinville, and Dundee Islands) has very limited multibeam coverage. Only two distinctive troughs have been imaged and flow lines are conjectural and defined (as in earlier approaches) by recognition of bathy-metric troughs. Portions of the flow out of the Larsen Chan-nel, between D'Urville Island and Joinville Island, and out of Active Sound between Joinville Island and Dundee Is-land ran in a southwestern direction, coalescing with the Antarctic Sound fl ow to the Erebus - Terror system. The other portion shows evidence of east and southeast flows. South of Joinville Island, the multibeam data imaged drumlin-like features indicating that ice was grounded on the Joinville Plateau, suggesting that the APIS extended across the shelf (Smith and Anderson, 2011; their Fig. 6).

3.4. Bransfield Strait

The continental shelves off the Trinity Peninsula (e.g., Lawver et al., 1996; Canals et al., 2002) and the South Shet-land Islands (Simms et al., 2011)

reveal paths of paleo-ice streams that drained into the Bransfield Strait. This narrow and deep (greater than 1000 m) strait was formed by rifting, actively spreading for the past 4 million years in response to subduction in the South Shetland Trench (Barker, 1982). Based on seafloor evidence, the grounded ice fl ow along the Bransfield Basin's perimeter transitioned to an ice shelf in deeper water (floating glacier ice that was not in contact with the seafloor). This system must have been confined to the Bransfield Basin between tributary flow out of the Orleans Strait, off the Trinity Peninsula, and the South Shetland Is-lands (Figs. 5 and 6). As indicated by the curvature of bed-forms on the surface of the grounding zone fans (i.e., mouths of both Maxwell and Admiralty bays) and major troughs (i.e., Lafond, Laclavere, and Mott Snowfield Troughs) that extend into Bransfield Strait, flow of the ice shelf was conjectured to involve a northeastern direction more or less parallel to the trend of the basin (Canals et al., 2002; Willmott et al., 2003). Outlets in the eastern portions of the basin are even less well defined but must have involved partitioned grounded fl ow out across the northern end of the South Shetland Platform (just northeast of King George Island), out beyond Elephant Is-land, and into the Powell Basin (Fig. 6). According to the swath bathymetry data, it is likely that there was a small ice dome over Elephant Island providing a plug to the northeast-flowing Bransfield Ice Shelf system.

3.5. Gerlache - Croker - Boyd straits

In the Gerlache - Croker - Boyd straits, the streaming ice flow is confined in a spectacular bundle structure 100 km long and flowing to the north-northwest (Canals et al., 2000). Almost the entire ice drainage out of the Gerlache Strait was fun-neled through the Croker Passage, which included glaciers draining the eastern side of Anvers and Brabant islands and the western flank of the Bruce Plateau (Domack et al., 2004; Evans et al., 2004). These tributary systems converged at various depths (submarine hanging valleys) where fjord val-leys joined the Gerlache Strait and the Croker Passage. This, along with the large number of tributaries, requires consider-able constriction of parallel arrangement of flow lines within the Croker Passage and

Boyd Strait outlet path (Fig. 5). Near, near the shelf break the grounding line system shows a spread of flow trajectories out toward the shelf break (Canals et al., 2003; their Fig. 2b).

3.6. Palmer Deep and Hugo Island Trough

The outflow from the Palmer Deep and Hugo Island Trough is one of the three major tributary systems that terminate as an outlet system along the western AP continental-shelf edge (Fig. 5). This flow system was delineated first by Pudsey et al. (1994), then by Vanneste and Larter (1995), and later out-lined in detail by Domack et al. (2006). The systems include tributary glaciers from the Graham Land Coast between 65 and 66° S and ice which flowed out of Dallmann Bay around the northeast corner of Anvers Island (Fig. 5). Along the Gra-ham Land Coast the ice flow emanating from the fjords di-rected flow to the northeast, coalescing with the Palmer Deep ice flow in Hugo Island Trough, and crossed the mid-shelf in a northern direction to the outer shelf (Domack et al., 2006). On the outer shelf the ice flow coalesced with the Dallmann Bay flow that runs out around the north end of Anvers and Brabant islands.

3.7. Biscoe Trough

The cross-shelf Biscoe Trough system consists of three flow branches with overly deepened troughs up to 800 m depth, a topographic ridge of 300 m high crosses the main branch of the Biscoe Trough system in a southwest and northeast di-rection, and a smoother surface toward the shelf edge at 400 - 500 m depth (Canals et al., 2003; Amblas et al., 2006). The flow line bedforms show a general converging westward flow directions toward the shelf edge. The Biscoe Trough system also shows a spread of flow trajectories out toward the shelf break. This system was fed by ice flow primarily off Renaud Island archipelago but notably also contains indications of ice flow off mid- to outer shelf banks, with a distinct flow di-vide between the Biscoe Trough and Palmer Deep and Hugo Island Trough systems, and south along the trend defined by

Hugo Island.

4. Interpretation and discussion

Based on the above observations we recognized six major outlets for paleo-ice-stream drainage off the APIS during the LGM and refined the locations of their ice divides (Fig. 5). In addition, the patterns revealed by our fl ow direction re-construction indicate the locations and areal dimensions of at least seven major ice domes centered on the middle to outer AP continental shelf. Below we focus on a comprehensive interpretation of the new seabed morphology and discuss the regional implications regarding flow paths, ice divides, and ice domes.

4.1. Flow bifurcation in Larsen B embayment

Our observations of streamed bedforms in the Larsen B em-bayment indicate that the modern glaciers (i.e., Crane, Lep-pard, and Flask Glaciers) were not tributaries of the Robert-son mid-outer shelf paleo-ice stream as previously inter-preted by Evans et al. (2005) and highlighted in previous re-views (e.g., Davies et al., 2012; Livingstone et al., 2012).

Keeping in mind that there are no surface expressions of seismic stratigraphic boundaries on the shelf interpreted as a LGM ice stream bifurcation (Smith and Anderson, 2009), we provide two possible explanations to explain the flow di-vergence we observe in the Larsen B embayment. The first explanation is based on the hypothesis of a non-uniform geo-logical framework. The diverging flow could be explained by the southeastward extension of the Seal Nunatak and Robertson Island post-Miocene volcanic sequence, in contact with Mesozoic rocks in the Larsen embayment. We infer from some seismic data (M. Rebesco, personal communication, 2014) the presence of Mesozoic mudrocks similar to the Nor-denskö ld Formation (Jurassic black shale; Reinardy et al., 2011) and Cretaceous sedimentary sequences of Robertson Island within the Larsen B embayment. These are known to have influenced bed deformation within tills derived from them (Reinardy et al., 2011). One hypothesis, therefore,

would suggest that the divergence of flow was related to faster flow and was funneled out of the inner Larsen B em-bayment by a bed that was more easily deformed (mud base) than the higher friction of the sandy volcaniclastic palagonite units that comprise the Seal Nunatak massif. Detailed petro-graphic analysis of the respective tills could test this hypothesis.

We also consider the pre-determined topography and glacial dynamics that could have split the flow direction on the mid-shelf. The existence of a slightly elevated seabed over the middle shelf could have acted as a prow between the Robertson Trough and Jason Trough, thus causing di-verging flow. This hypothesis cannot be fully tested at this time because heavy ice cover in this particular region makes navigation and acquisition of key swath bathymetry very dif-ficult. However, some bathymetric data and seismic profiles from shipboard surveys south of Jason Peninsula do exist (Sloan et al., 1995) and these show evidence of shallow shelf banks at less than 300 m water depth. Such topographic highs could have divided the glacial flow (Fig. 5). The examination of a time series of MODerate-resolution Imaging Spectro-radiometer (MODIS) images from the northeastern AP also shows unequivocal evidence of several previously unknown reef and shoal areas based on their influence on sea ice drift and grounding of small icebergs (Table 1, Fig. 7, Supplement S1, and video S2; see also http://nsidc.org/data/iceshelves_images/index_modis.html). Luckman et al. (2010) demon-strated the reliability of using satellite remote-sensing tools to identify western Weddell Sea grounded tabular icebergs and to estimate their draft, which they interpreted as max-imum water depth. In the 12-year series of images, shoal areas appear as frequent stranding areas of small icebergs, particularly during heavy winter sea ice periods. Larger ice-bergs (having 200 - 350 m keels) show drift paths strongly controlled by the shoals. Stranding of icebergs (especially for the informally named Bawden, Robertson, and Jason shoal or reef areas; see Table 1) indicates the shallowest areas of the region. These high areas could have served as centers of glacial nucleation similar to the model proposed for shallows across the Bellingshausen Sea continental shelf (Domack et al., 2006).

The two mechanisms described above could have inter-acted to cause the divergence of the flow observed from the Larsen B embayment; a process

combination of a de-formation of weak bed material and a bifurcation of the ice around a topographic high. Divergence of flow lines has been observed at the margin of the Greenland Ice Sheet and Antarctica. A modern example that shows fast-flowing ice bifurcation can be observed on the flow velocity field map of the northeast Greenland Ice Stream, where the southern flow feeds Storstrømmrn and flows into the northern out-let glaciers of Zachariæ Isstrøm and Nioghalvfjerdsfjorden (Joughin et al., 2001, 2010). Modern analogs such as Siple Dome show diverging flow of marine-based ice streams (bed 600 to 700 m b.s.l. - below sea level) around a topographic high only 300 to 400 m b.s.l. (Fretwell et al., 2013). In the Siple Coast region, only a 200 to 300 m topographic differ-ence is sufficient to create diverging flow separated by ice domes. In addition to these real-world examples, modeling has shown that either a relative topographic high or a relative increase in the basal drag can lead to divergence of ice flow and formation of an elongated ice dome between them. A number of researchers have modeled the surface expression of variability in bed topography or bed properties; a compre-hensive analysis is provided by Gudmundsson (2003).

4.2. Evidence of ice divides

We define an ice divide as a boundary separating divergent ice-flow directions, i.e., the line that separates neighboring drainage systems, analogous to a water divide. The separa-tion of the west and east AP along the Bruce Plateau and De-troit Plateau on the Trinity Peninsula and the Graham Land Coast formed the primary ice divide for the AP during LGM. Our results, based on details of the ice-flow directions and modern subaerial and submarine topography, suggest that secondary ice divides split off from the primary ice divide creating several large draining basins (Fig. 5). On the eastern side of the peninsula, we define four major ice divides:

1. from the AP across the Seal Nunatak and Robertson Is-land to divide the ice flow between the northeast Larsen B embayment and the western area of Larsen A;
2. from the Bruce Plateau (AP) to Cape Longing to di-vide flows between

Larsen A and southern Prince Gustav Channel;

3. from the Detroit Plateau (AP) southeast across the Prince Gustav Channel and up across the center of James Ross Island (Camerlenghi et al., 2001), before continuing across Admiralty Sound and Seymour Island to split the ice flow between the southern and northern Prince Gustav Channel, dividing the ice flow on James Ross Island and Admiralty Sound; and
4. from the Trinity Peninsula to the Joinville Island Group and along the axis of D'Urville Island, across the Larsen Channel, Joinville Island, and Dundee Island according to the seabed morphology in the Antarctic Sound.

On the western AP, the boundary of major ice divides runs

1. along the South Shetland archipelago;
2. from the AP across the Orleans Strait, Trinity Island, and along a series of shelf banks at the western end of the Bransfield Strait that divide the ice flow between the Bransfield Strait and Gerlache - Boyd Strait;
3. from the Bruce Plateau (AP) across Gerlache Strait, Wiencke Island, the southern edge of Anvers Island, Schollaert Channel, and up along the crest of Brabant Island to explain the constriction of flow lines in the Gerlache Strait; and
4. along Anvers Island and Renaud Island to explain the Palmer Deep and Hugo Island Trough ice-flow system and its separation from the Biscoe Trough.

Ice divides typically evolve into elongated ice domes with topographic highs that influence the spatial pattern of accu-mulation rate and the ice-flow directions. These divides are not stationary and can evolve under variations in climate or boundary conditions (e.g., Nereson et al., 1998; Marshall and Cuffey, 2000). Indeed, an entire ice dome can change shape as climate conditions change on a timescale of a few hun-dred to thousand years, depending on the accumulation rate and size of the divide (Nereson et al., 1998; Marshall and Cuffey, 2000).

4.3. Inferred ice domes on the continental shelf

The existence of two separate shelf ice domes at LGM, one covering the northern AP and the other upon the South Shet-land Islands, was suggested by early work that recognized centers of ice accumulation over the highest existing bedrock topography (Banfield and Anderson, 1995; Bentley and An-derson, 1998). Our LGM ice-flow reconstruction of at least six distinct systems across the northern AP continental shelf and evidence of ice divides serves to delineate at least seven broad regions where additional ice domes may have been centered out on the continental shelf. The presence of the domes is required to constrain lateral spreading of each of the paleo-ice-stream outlets and also to explain the observa-tion of radial flow that, in part, converges with flow within several of the paleo ice stream trajectories. We define each of these features here by assigning names associated with the nearest prominent headland for each ice dome; head-lands likely provided some axial orientation to the ice dome. These include Hugo Dome, Marr Dome, Brabant Dome, Liv-ingston Dome, Snow Hill Dome, Robertson Dome, and Hek-toria Dome (Fig. 5).

The exact dimensions and character of each of these domes is difficult to define because these areas of the con-tinental shelf are generally devoid of multibeam coverage. Furthermore, extensive iceberg scouring across these banks has largely obscured original glacial flow indicators, which might have provided some sense of paleo-ice-flow direction. Nevertheless, some small troughs and lineated features do exist for at least three of the inferred domes. For the Marr, Brabant, and Livingston domes some radial flow indicators can be seen in small troughs that drain the mid-point divides in about the middle of the continental shelf (Fig. 5). Further-more, the Hugo Dome can be seen to have directed flow into the Biscoe Trough from a position considerably far out on the continental shelf. Hence, this evidence does indicate that the mid-shelf hosted ice domes as centers of ice accumula-tion which contributed ice drainage contemporaneous with the large paleo ice streams (Fig. 5). In this hypothesis, the continental-shelf ice domes do not necessarily require exces-sive elevation, only sufficient height to have grounded the system and allowed each dome to constrain the surrounding paleo-ice streams. Our hypothesis for these ice domes

is not without precedent; some work on the East Antarctic margin has postulated a similar situation, where major divides were diverted and constrained by large ice domes that rested upon shelf banks (Eittreim et al., 1995). Also, an independent ice dome centered over the west of the Alexander Island, west-ern AP, persisted through the LGM and deglaciation (Gra-ham and Smith, 2012). Furthermore, there are existing mod-ern ice domes that separate fast-flowing, marine-based ice in West Antarctica, including Siple Dome (with surface eleva-tion of 600 m a.s.l. and an ice thickness of 1000 m; Gades et al., 2000; Conway et al., 2002).

The seaward extent of each of the shelf ice domes would seem to correspond to the outer continental shelf, as outlet systems are uniformly constrained out to the grounding line position (the outer shelf) in each of the systems we examined. The exception to this is the broad apron of the grounding line associated with the Gerlache - Croker - Boyd Strait and Biscoe ice streams. In those cases diverging flow is clearly imaged out across the continental-shelf break, indicating spreading flow toward the grounding line. Indeed, the extensive relief of Smith Island (maximum elevation of 2100 m a.s.l.) would likely have blocked any ice flow associated with the Bra-bant Dome from reaching the outermost shelf (Fig. 5). This spreading flow is similar to that observed for unrestricted paleo-ice-stream fans such as in the Kveithola Trough off Svalbard (Rebesco et al., 2011).

While the areal dimensions of the ice domes are fairly cer-tain, their thickness is less well defined. We can assume that these features were thick enough to have served as effec-tive lateral constraints to ice stream outlets and to have al-lowed the dome to have been grounded across a bathymetry of approximately 350 m on average. The thickness of an ice dome in steady state depends on the regional accumulation rate average, the temperature of the ice, and the aerial extent of the dome outlined in Sect. 2.3 (Bueler et al., 2005). Fig-ure 8 shows the results of our model with red ellipses defin-ing the range of possible ice thickness values for each dome. We assume that the western-side domes (Marr, Livingston, Brabant, and Hugo) have an average ice temperature of 0 ∘C (Fig. 8a), while the eastern-side domes have an average ice temperature of −20 ∘C (Fig. 8b). The colder ice is stiffer, which can result

in thicker domes when all other parame-ters are the same. The minor axis of the red ellipses shows a possible range of error in the ice radius associated with the irregular aerial extent of the real ice dome.

For accumulation rates, we base our assumptions on the modern AP, which has a strong orographic precipitation gra-dient that ranges from 4 m yr−1 on the western side to less than 0.1 m yr−1 on the eastern side. High accumulation sites will result in thicker ice domes if all other parameters are equal. In the LGM case, the distribution of domes will create multiple precipitation highs and lows as each dome creates its own pattern of orographic precipitation (Roe and Lindzen, 2001). Therefore, we predict the highest accumulation rates for Brabant, Livingston, and Hugo Domes. Marr Dome will likely be shielded somewhat from the highest accumulation. On the eastern side, Hektoria and Snow Hill Domes are likely to have slightly higher accumulation than Robertson Dome, as they may receive some precipitation from the Weddell Sea. We have selected a broad range of accumulation rates be-cause we have only general atmospheric patterns from which to draw our assumptions. Despite this large range of input values, we can bracket the ice thicknesses for each dome as presented in Fig. 8 and estimate volumes as shown in Table 2.

4.4. Regional implications

We have presented a compilation of paleo-ice-flow indicators for the northern AP and used the resulting map to infer ice-flow patterns, ice divides, and ice domes. This allows an inte-grated view over the full extent of the APIS at the LGM. This mapping effort suggests that the seabed topography and the complex geology influenced the ice-flow route and regime at the LGM. The bifurcation of the flow lines in the Larsen B embayment affected the character of the basal ice erosion mechanisms. In general, diverging ice flow is associated with an area of decelerating flow (e.g., Stokes and Clark, 2003). Moreover, the increased flux of ice and debris flowing around a topographic high could provide a powerful feedback where an ice stream could deepen existing depressions (Knight et al., 1994). However, the flow convergences (strongest near the mid-shelf in the northern AP) led to an increase in flow speed at the mid- and

upper end of the ice streams, promoting high basal shear stress and significant basal sediment trans-port (e.g., Boulton, 1990).

It should also be kept in mind that the ice stream catch-ments include deep basins (i.e., Palmer Deep) that serve as deposystems for thick interglacial mud and ooze deposits. For instance, typical thicknesses for Holocene mud within the Palmer Deep are about 100 m, while across the broader shelf the interglacial muds are no more than 6 - 8 m thick. This mud could serve as basal lubrication as ice systems advance out across the shelf and eventually ground within the deep inner shelf, thus enhancing streaming flow within the trough trajectory via bed deformation. Once ice streaming was initi-ated in areas where interglacial sediments provided lubrica-tion, the interglacial sediment would be completely removed by ice; streaming would continue, having been established through regional flow patterns, by eroding the underlying bedrock for more lubricating material and thus enhancing the focus of the trough through multiple cycles.

The presence of multiple APIS ice domes centered on the mid-shelf implies that ice thickness was not uniform on the northern AP continental shelf during the maximum extension of the APIS at LGM. These domes may have harbored sig-nificant ice volume above buoyancy, even under minimal sce-narios of ice thickness due to their large areal extent. Com-paring the estimated total area of the ice domes with the one estimated for the flow paths (Tables 2 and 3) shows that the ice domes were at least as important, if not more so, as the paleo-ice streams, in terms of areal coverage. The minimum estimate for total ice volume of the domes and the paleo-ice streams are similar. However, because the convergent flow paths have significantly deeper beds (as they flow in troughs) the ice streams contain 43 % more maximum ice than the domes.
The presence of multiple ice domes on the shelf would have influenced the ice sheet dynamics (e.g., basal melting and sliding parameters) and the sediment transport to be-yond the margin of the ice. The ice velocity would have been slower near the ice divides with lower sediment trans-port rates than at the peripheral regions where the domes fed out into fast-flowing ice streams with high sediment transport rates. Because of feedbacks between ice dome formation and the orographic precipitation, all of these domes may not have reached their

largest extent at the same time; the growth of one dome may “starve” another of its accumulation (e.g., Roe and Lindzen, 2001).

Finally, the delineation of ice domes and faster-flowing outlets is important because it would help to gauge the rel-ative contribution of each system to post-glacial eustatic rise in sea level or, conversely, how each system might have re-sponded to a eustatic or ocean-climate event. For instance, recent models for glacial recession within the Palmer Deep and along the East Antarctic margin suggest a calving bay re-entrant model, wherein ice streams retreat preferentially landward thus creating a linear “fjord-like” bay surrounded by slower-flowing ice of the domes (Domack et al., 2006; Leventer et al., 2006). This model and others (i.e., Kilfeather et al., 2011) deserve consideration in that our reconstruc-tion clearly outlines differences in the boundary conditions of fl ow, thickness, bed character, accumulation, and ice sourc-ing for the domes and converging flow systems. Thus the two systems would logically be expected to respond differently to any forcing factors involved in deglaciation.

The identification of ice domes, ice divides, and diverg-ing/converging fl ows help us to understand ice-sheet evolu-tion and processes. While considerable effort has been put forward recently toward understanding the character and tim-ing of the retreat of the APIS, more work needs to focus on the reconstruction and detailed vitality of the APIS during the last glacial cycle. The features we recognize have im-portant implications for this effort and the future siting of ice cores and marine drilling sites. Finally, they provide im-portant constraints for glaciohydrology, past and future ice-sheet modeling used, for instance, to look at sediment fluxes (Golledge et al., 2013) or provide more realistic predictions, ice-sheet modeling in response to changing environments, and sea level modeling. The existing challenge includes ar-ranging models of ice-flow and geological data so that they resemble each other, especially when geological features are small compared to the grid scale of ice-flow paths. While the evidence for the ice domes out on the shelf is largely circum-stantial, there likely exists today remnants of these features as is the case for the ice cap on Hugo Island, which stands as a prominent feature in the middle of the AP continental shelf.

5. Conclusions

Our results provide considerable improvement in the assess-ment of ice flow and thereby the dynamics that may have governed the expansion, stabilization, and eventual demise of the ice mass which comprised the APIS. We now not only recognize six spatially defined paleo-ice streams but we can also infer with some confidence the source areas and number of tributaries which fed them. In addition, our study high-lights the need to understand the extent and behavior of seven large shelf ice domes that best explain the confi guration of the ice-flow directions and serve as lateral constraints to the paleo-ice-stream flow. These ice domes had slower-flowing ice and were likely frozen to their beds, exhibiting some-what different behavior from the paleo-ice streams which were fed almost exclusively from convergence of tributary glaciers draining the elevated spine of the AP and surround-ing islands. Also, while the timing of paleo-ice-stream re-cession is known in a general way from recent syntheses (Ó Cofaigh et al., 2014), the detailed rates and step backs are far from resolved. Our reconstruction allows focus on the vary-ing character of each ice stream and how this might have influenced differential response to the forcing factors (i.e., eustasy, atmospheric and ocean temperature) and accumula-tion rates which may have induced instability in the region (Livingstone et al., 2012).

Future research including strategic multibeam coverage, marine sediment cores, and modeling considering the glacio-isostatic rebound are needed to confi rm the existence of the ice domes, define their characteristics, and constrain the tim-ing of their ice retreat. When combined with high-resolution dating efforts, our flow reconstruction will help elucidate the retreat history of the ice sheet and, therefore, those forces that acted to destabilize the system and initiate the most re-cent deglaciation of the APIS.

해저면 이미지의 새로운 합성에 따른 마지막 빙하기의 남극 반도 북부 빙상의 상대적 배치

유규철, 윤호일

한국해양과학기술원 부설 극지연구소

요약: 5개의 국가 프로그램에서 얻은 멀티빔 자료를 이용하여 남극반도 북쪽의 해저면 지형도를 새로이 제시하였다. 이 지형도는 해저면 위에 발달된 빙하의 흔적들을 통해 마지막 최대 빙하기의 과거 얼음의 흐름 방향을 파악하고 해석할 수 있게 한다. 우리는 이러한 것과 육상에서의 방하 흐름 방향과 조합하여 마지막 최대 빙하기 동안 남극반도 대륙붕의 아이스돔을 구분하였다. 결과는 Larsen B 만에서 빙하가 빠져나가는 흐름 모양을 보였다. 강한 유출 흐름이 남동쪽을 향하고 그리고 얼음이 Jason 반도의 끝단에서 만의 남쪽 둘레에 이르기 까지 흘렀다. 우리의 복원은 7개의 넓은 지역에 얼음을 유입하는 적어도 5개의 다른 뚜렷한 과거 빙하 흐름 시스템이 있었다는 것을 확인하였다. 우리의 복원은 다른 연구 보다 더욱더 자세한데, 그것은 우리가 특정 얼음의 유출 흔적들을 따라서 분석하였기 때문이다.

참고문헌

Amblas, D., Urgeles, R., Canals, M., Calafat, A. M., Robesco, M.,Camerlenghi, A., Estrada, F., De Batist, M., and Hughes-Clarke, J. E.: Relationship between continental rise development and palaeo-ice sheet dynamics, Northern Antarctic Peninsula Pacific margin, Quaternary Sci. Rev., 25, 933 - 944, 2006.

Andrews, J. T.: On the reconstruction of pleistocene ice sheets: a review, Quaternary Sci. Rev., 1, 1 - 30, 1982.

Arndt, J. E., Schenke, H. W., Jakobsson, M., Nitsche, F. O., Buys, G., Goleby, B., Rebesco, M., Bohoyo, F., Hong, J., Black, J., Greku, R., Udintsev, G., Barrios, F., Reynoso-Peralta, W., Taisei, M., and Wigley, R.: The International Bathymetric Chart of the Southern Ocean (IBCSO) Version 1.0 - a new bathymetric com-pilation covering circum-Antarctic waters, Geophys. Res. Lett., 40, 3111 - 3117, 2013.

Banfield, L. A. and Anderson, J. B.: Seismic facies investgation of the late Quaternary glacial history of Bransfield Basin, Antarc-tica, in: Geology and Seismic Stratigraphy of the Antarctic Mar-gin, edited by: Cooper, A. K., Barker, P. F., and Brancolini, G., Antarct. Res. Ser. 68, American Geophysical Union, Washing-ton, D.C., 123 - 140, 1995.

Barker, P. F.: The Cenozoic subduction history of the Pacific margin of the Antarctic Peninsula: ridge crest-trench interactions, J.Geol. Soc., 139, 787 - 801, 1982.

Bentley, M. J. and Anderson, J. B.: Glacial and marine geological evidence for the ice sheet configuration in the Weddell Sea-Antarctic Peninsula region during the Last Glacial Maximum, Antarct. Sci., 10, 309 - 325, 1998.

Boulton, G. S.: Sedimentary and sea level changes during glacial cycles and their control on glacimarine facies architecture, in: Glacimarine Environments: Processes and Sediments, edited by: Dowdeswell, J. A. and Scourse, J. D., Geological Society Special Publication 53, The Geological Society, London, 15 - 52, 1990.

Brisbourne, A. M., Smith, A. M., King, E. C., Nicholls, K. W., Holland, P. R.,

and Makinson, K.: Seabed topography beneath Larsen C Ice Shelf from seismic soundings, The Cryosphere, 8, 1 - 13, doi:10.5194/tc-8-1-2014, 2014.

Bueler, E., Lingle, C. S., Kallen-Brown, J. A., Covey, D., and Bow-man, L. N.: Exact solutions and verification of numerical models for isothermal ice sheets, J. Glaciol., 51, 291 - 306, 2005. Camerlenghi, A., Domack, E. W., Rebesco, M., Gilbert, R., Ish-man, S., Leventer, A., Brachfeld, S., and Drake, A.: Glacial mor-phology and post-glacial contourites in northern Prince Gustav Channel (NW Weddell Sea, Antarctica), Mar. Geophys. Res., 22, 417 - 443, 2001.

Canals, M., Urgeles, R., and Calafat, A. M.: Deep seafloor evidence of past ice streams off the Antarctic Peninsula, Geology, 28, 31 - 34, 2000.

Canals, M., Casamor, J. L., Urgeles, R., Calafat, A. M., Domack, E. W., Baraza, J., Farran, M., and De Batist, M.: Seafloor evidence of a subglacial sedimentary system off the northern Antarctic Peninsula, Geology, 30, 603 - 606, 2002.

Canals, M., Calafat, A. M., Camerlenghi, A., De Batist, M., Urgeles, R., Farran, M., Geletti, R., Versteeg,W., Amblas, D., Rebesco, M., Casamor, J. L., Sànchez, A., Willmott, V., Lastras, G., and Imbo, Y.: Uncovering the footprint of former ice streams off Antarctica, EOS, 84, 97 - 108, 2003.

Clark, C. D.: Mega-sclae glacial lineations and cross-cutting ice-flow landforms, Earth Surf. Proc. Land., 18, 1 - 29, 1993.

Clark, C. D., Tulaczyk, S., Stokes, C. R., and Canals, M.: A groove-ploughing theory for the production of mega-scale glacial lineations, and implications for ice-stream mechanics, J. Glaciol., 49, 240 - 256, 2003.

Conway, H., Catania, G., Raymond, C. F., and Gades, A. M.: Switch of flow direction in an Antarctic ice stream, Nature, 419, 465 - 467, 2002.

Cuffey, K. M. and Paterson, W. S. B. (Eds.): The Physics of Glaciers, Elsevier Inc., Oxford, UK, 2010.

Curry, P. and Pudsey, C. J.: New Quaternary sedimentary records from near the Larcen C and former Larsen B ice shelves; evidence for Holocene stability, Antarct. Sci., 19, 355 - 364, 2007. Davies, B. J., Hambrey, M. J., Smellie, J. L., Carrivick, J. L., and Glasser, N. F.: Antarctic Peninsula

Ice Sheet evolution during the Cenozoic Era, Quaternary Sci. Rev., 31, 30 - 66, 2012.

Domack, E. W., Canals, M., Camerlenghi, A., Gilbert, R., Amblas, D., Wilmott, V., Calafat, A. M., Urgeles, R., DeBatist, M., Casamor, J. L., and Rebesco, M.: Complete swath map coverage of the Gerlache Boyd Strait paleo ice stream: an example of col-laborative seafloor mapping in the Antarctic Peninsula, XXVIII SCAR Open Science Conference, Bremen, Germany, 26 - 28 July 2004, Abstract S11/P08, 2004.

Domack, E., Duran, D., Leventer, A., Ishman, S., Doane, S., Mc-Callum, S., Amblas, D., Ring, J., Gilbert, R., and Prentice, M.: Stability of the Larsen B ice shelf on the Antarctic Peninsula dur-ing the Holocene epoch, Nature, 436, 681 - 685, 2005.

Domack, E., Amblas, D., Gilbert, R., Brachfeld, S., Camerlenghi, A., Robesco, M., Canals, M., and Urgeles, R.: Subglacial mor-phology and glacial evolution of the Palmer deep outlet system, Antarctic Peninsula, Geomorphology, 75, 125 - 142, 2006.

Dowdeswell, J. A., Ottesen, D., Evans, J., Ó Cofaigh, C., and Anderson, J. B.: Submarine glacial landforms and rates of ice-stream collapse, Geology, 26, 819 - 822, 2008.

Eittreim, S. L., Cooper, A. K., and Wannesson, J.: Seismic stratigraphic evidence of ice-sheet advances on the Wilkes Land mar-gin of Antarctica, Sediment. Geol., 96, 131 - 156, 1995.

Evans, J., Dowdeswell, J. A., and Ó Cofaigh, C.: Late Quaternary submarine bedforms and ice-sheet flow in Gerlache Strait and on the adjacent continental shelf, Antarctic Peninsula, J. Quaternary Sci., 19, 397 - 407, 2004.

Evans, J., Pudsey, C. J., Ó Cofaigh, C., Morris, P., and Domack, E. W.: Late Quaternary glacial history, flow dynamics and sed-imentation along the eastern margin of the Antarctic Peninsula Ice Sheet, Quaternary Sci. Rev., 24, 741 - 774, 2005.

Fretwell, P., Pritchard, H. D., Vaughan, D. G., Bamber, J. L., Bar-rand, N. E., Bell, R., Bianchi, C., Bingham, R. G., Blankenship, D. D., Casassa, G., Catania, G., Callens, D., Conway, H., Cook, A. J., Corr, H. F. J.,

Damaske, D., Damm, V., Ferraccioli, F., Fors-berg, R., Fujita, S., Gim, Y., Gogineni, P., Griggs, J. A., Hind-marsh, R. C. A., Holmlund, P., Holt, J. W., Jacobel, R. W., Jenk-ins, A., Jokat, W., Jordan, T., King, E. C., Kohler, J., Krabill, W., Riger-Kusk, M., Langley, K. A., Leitchenkov, G., Leuschen, C., Luyendyk, B. P., Matsuoka, K., Mouginot, J., Nitsche, F. O., Nogi, Y., Nost, O. A., Popov, S. V., Rignot, E., Rippin, D. M., Rivera, A., Roberts, J., Ross, N., Siegert, M. J., Smith, A. M., Steinhage, D., Studinger, M., Sun, B., Tinto, B. K., Welch, B. C., Wilson, D., Young, D. A., Xiangbin, C., and Zirizzotti, A.: Bedmap2: improved ice bed, surface and thickness datasets for Antarctica, The Cryosphere, 7, 375 – 393, doi:10.5194/tc-7-375-2013, 2013.

Gades, A., Raymond, C. F., Conway, H., and Jacobel, R.: Bed prop-erties of Siple Dome and adjacent ice streams, West Antarctica, inferred from radio-echo sounding measurements, J. Glaciol., 46, 88 – 94, 2000.

Gilbert, R., Domack, E. W., and Camerlenghi, A.: Deglacial history of the Greenpeace Trough: ice Sheet to Ice Shelf transition in the Northwestern Weddell Sea, Antarct. Res. Ser., 79, 195 – 204, 2003.

Glasser, N. F., Davies, B. J., Carrivick, J. L., Rodés, A., Hambrey, M. J., Smellie, J. L., and Domack, E.: Ice-stream initiation, du-ration and thinning on James Rosse Island, northern Antarctic Peninsula, Quaternary Sci. Rev., 86, 78 – 88, 2014.

Golledge, N. R., Levy, R. H., McKay, R. M., Fogwill, C. J., White, D. A., Graham, A. G. C., Smith, J. A., Hillenbrand, C.-D., Licht, K. J., Denton, G. H., Ackert Jr., R. P., Maas, S. M., and Hall, B. L.: Glaciology and geological signature of the Last Glacial Maximum Antarctic ice sheet, Quaternary Sci. Rev., 78, 225-247, 2013.

Graham, A. G. C. and Smith, J. A.: Palaeoglaciology of the Alexan-der Island ice cap, western Antarctic Peninsula, reconstructed from marine geophysical and core data, Quaternary Sci. Rev., 35, 63 – 81, 2012.

Gudmundsson, G. H.: Transmission of basal variability to a glacier surface, J. Geophys. Res.-Solid Earth, 108, ETG 9-1 – 19, 2003.

Heroy, D. C. and Anderson, J. B.: Ice-sheet extent of the Antarctic Peninsula region during the Last Glacial Maximum (LGM) – in-sights from

glacial geomorphology, Geol. Soc. Am. Bull., 117, 1497 - 1512, 2005.

Johnson, J. S., Bentley, M. J., Roberts, S. J., Binnie, S. A., and Freeman, S. P. H. T.: Holocene deglacial history of the north-east Antarctic Peninsula - a review and new chronological con-straints, Quaternary Sci. Rev., 30, 3791 - 3802, 2011.

Joughin, I., Fahnestock, M., MacAyeal, D. R., Bamber, J. L., and Gogineni, P.: Observation and analysis of ice flow in the largest Greenland ice stream, J. Geophys. Res., 106, 34021 - 34034, 2001.

Joughin, I., Smith, B. E., Howat, I. M., Scambos, T., and Moon, T.: Greenland flow variability from ice-sheet-wide velocity mapping, J. Glaciol., 56, 415 - 430, 2010.

Kilfeather, A. A., ÓCofaigh, C., Lloyd, J. M., Dowdswell, J. A., Xu, S., and Moreton, S. G.: Ice-stream retreat and ice-shelf history in Marguerite Trough, Antarctic Peninsula: Sedimentological and foraminiferal signatures, Geol. Soc. Am. Bull., 123, 997 - 1015, 2011.

Knight, P. G., Sugden, D. E., and Minty, C. D.: Ice flow around large obstacles as indicated by basal ice exposed at the margin of the Greenland ice sheet, J. Glaciol., 40, 359 - 367, 1994.

Larter, R. D. and Barker, P. F.: Seismic stratigraphy of the Antarctic Peninsula Pacific margin: a record of Pliocene - Pleistocene ice volume and paleoclimate, Geology, 17, 731 - 734, 1989.

Larter, R. D. and Vanneste, L. E.: Relict subglacial deltas on the Antarctic Peninsula outer shelf, Geology, 23, 33 - 36, 1995. Lawver, L. A., Sloan, B. J., Barker, D. H. N., Ghidella, M. E., von Herzen, R. P., Keller, R. A., Klinkhammer, G. P., and Chin, C. S.: Distributed, active extension in Bransfield Basin, Antarctic Peninsula: evidence from multibeam bathymetry, GSA Today, 6, 1 - 6, 1996.

Leventer, A., Domack, E., Dunbar, R., Pike, J., Stickley, C., Mad-dison, E., Brach field, S., Manely, P., and McClennan, C.: Marine sediment record from East Antarctica margin reveals dynamics of ice-sheet recession, GSA Today, 16, 4 - 10, 2006.

Livingstone, S. J., Ó Cofaigh, C., Stokes, C. R., Hillenbrand, C. D.,Vieli, A., and Jamieson, S. S. R.: Antarctic palaeo-ice streams, Earth-Sci. Rev., 111,

90 – 128, 2012.

Luckman, A., Padman, L., and Jansen, D.: Persistent iceberg groundings in the western Weddell Sea, Antarctica, Remote Sens. Environ., 114, 385 – 391, 2010.

Marshall, S. J. and Cuffey, K. M.: Peregrinations of the Greenland Ice Sheet divide in the last glacial cycle: implications for central Greenland ice cores, Earth Planet. Sc. Lett., 179, 73 – 93, 2000. Nereson, N. A., Hindmarsh, R. C. A., and Raymond, C. F.: Sensi-tivity of the divide position at Siple Dome, West Antarctica, to boundary forcing, Ann. Glaciol., 27, 207 – 214, 1998.

Nývlt, D., Košler, J., Mlˇcoch, B., Mixa, P., Lisá, L., Bubík, M., and Hendriks, B. W. H.: The Mendel Formation: Evidence for Late Miocene climatic cyclicity at the northern tip of the Antarctic Peninsula, Palaeogeogr. Palaeoclimatol. Palaeoecol., 299, 363 – 384, 2011.

Ó Cofaigh, C., Davies, B. J., Livingstone, S. J., Smith, J. A., John-son, J. S., Hocking, E. P., Hodgson, D. A., Anderson, J. B., Bent-ley, M. J., Canals, M., Domack, E., Dowdeswell, J. A., Evans, J., Glasser, N. F., Hillenbrand, C. D., Larter, R. D., Roberts, S. J., and Simms, A. R.: Reconstruction of ice-sheet changes in the Antarctic Peninsula since the Last Glacial Maximum, Quaternary Sci. Rev., 100, 87 – 110, 2014.

Pudsey, C. J., Barker, P. F., and Larter, R. D.: Ice Sheet retreat from the Antarctic Peninsula shelf, Cont. Shelf. Res., 14, 1647 – 1675, 1994.

Pudsey, C. J., Evans, J., Domack, E. W., Morris, P., and Del Valle, R. A.: Bathymetry and acoustic facies beneath the former Larsen-A and Prince Gustav ice shelves, north-west Weddell Sea, Antarct. Sci., 13, 312 – 322, 2001.

Rebesco, M., Liu, Y., Camerlenghi, A., Winsborrow, M., Laberg, J. S., Caburlotto, A., Diviacco, P., Accettella, D., Sauli, C., Wardell, N., and Tomini, I.: Deglaciation of the western margin of the Bar-ents Sea Ice Sheet – a swath bathymetric and sub-bottom seis-mic study from the Kveithola Trough, Mar. Geol., 279, 141 – 147, 2011.

Rebesco, M., Domack, E., Zgur, F., Lavoie, C., Leventer, A., Brach-feld, S., Willmott, V., Halverson, G., Truffer, M., Scambos, T., Smith, J., and

Pettit, E.: Boundary condition of grounding lines prior to collapse, Larsen-B Ice Shelf, Antarctica, Nature, 345, 1354 - 1358, 2014.

Reinardy, B. T. J., Larter, L. D., Hillenbrand, C. D., Murray, T.,Hiemstra, J. F., and Booth, A. D.: Streaming flow of an Antarctic Peninsula palaeo-ice stream, both by basal sliding and deforma-tion of substrate, J. Glaciol., 57, 596 - 608, 2011.

Roe, G. H. and Lindzen, R. S.: The mutual interaction between continental-scale ice sheets and atmospheric stationary waves, J. Climate, 14, 1450 - 1465, 2001.

Scambos, T. A., Hulbe, C. L., and Fahnestock, M.: Climate-induced ice shelf disintegration in the Antarctic Peninsula, in: Antarctic Peninsula Climate Variability, edited by: Domack, E. W., Leven-ter, A., Burnett, A., Bindschadler, R., Convey, P., and Kirby, M., Antarct. Res. Ser. 79, American Geophysical Union, Washing-ton, D.C., 79 - 92, 2003.

Simms, A. R., Milliken, K. T., Anderson, J. B., and Wellner, J. S.: The marine record of deglaciation of the South Shetland Is-lands, Antarctica since the Last Glacial Maximum, Quaternary Sci. Rev., 30, 1583 - 1601, 2011.

Sloan, B. J., Lawver, L. A., and Anderson, J. B.: Seismic stratigra-phy of the Larsen Basin Eastern Antarctic Peninsula, in: Geol-ogy and Seismic Stratigraphy of the Antarctic Margin, edited by: Cooper, A. K., Barker, P. F., and Brancolini, G., Antarctic Res. Ser. 68, American Geophysical Union, Washington, D.C., 59 - 74, 1995.

Smith, R. T. and Anderson, J. B.: Ice-sheet evolution in James Ross Basin,Weddell Sea margin of the Antarctic Peninsula: the seis-mic stratigraphic record, Geol. Soc. Am. Bull., 122, 830 - 842, 2009.

Smith, T. and Anderson, J. B.: Seismic stratigraphy of the Joinville Platform: implications for regional climate evolution, in: Tec-tonic, Climatic and Cryospheric Evolution of the Antarctic Peninsula, edited by: Anderson, J. B. and Wellner, J. S., Ameri-can Geophysical Union Special Publication 063, American Geo-physical Union, Washington, D.C., 51 - 62, 2011.

Stokes, C. R. and Clark, C. D.: The Dubawnt Lake palaeo-ice stream: evidence for dynamic ice sheet behaviour on the Cana-dian Shield and insights

regarding the controls on ice-stream lo-cation and vigour, Boreas, 32, 264 - 279, 2003.

Vanneste, L. E. and Larter, R. D.: Deep-tow boomer survey on the Antarctic Peninsula Pacific Margin: an investigation of the morphology and acoustic characteristics of Late Quaternary sed-imentary deposits on the outer continental shelf and upper slope, in: Geology and Seismic Stratigraphy of the Antarctic Margin, Part 1, edited by: Cooper, A. K., Barker, P. F., and Brancolini, G., American Ggophysical Union, Washington, D.C., 97 - 121, 1995.

Wellner, J. S., Lowe, A. L., Shipp, S. S., and Anderson, J. B.: Dis-tribution of glacial geomorphic features on the Antarctic conti-nental shelf and correlation with substrate: implications for ice behavior, J. Glaciol., 47, 397 - 411, 2001.

Wellner, J. S., Heroy, D. C., and Anderson, J. B.: The death mask of the antarctic ice sheet: comparison of glacial geomorphic fea-tures across the continental shelf, Geomorphology, 75, 157 - 171, 2006.

Willmott, V., Canals, M., and Casamor, J. L.: Retreat history of the Gerlache - Boyd ice stream, Northern Antarctic Peninsula: an ultra-high resolution acoustic study of the deglacial and post-glacial sediment drape, in: Antarctic Peninsula Climate Variabil-ity, edited by: Domack, E. W., Leventer, A., Burnett, A., Bind-schadler, R., Peter, C., and Kirby, M., Antarct. Res. Ser., 79, 183 - 194, 2003.

Table 1. Reef and shoal areas in the northwestern Weddell Sea*.

Latitude	Longitude	Notes
65.237° S 65.183° S	59.251° W to 58.213° W	"Robertson reef": 49 km long, bearing numerous 005° high points, shallow depth (est. ~ 100 m depth)
66.912° S 66.813° S	60.133° W to 59.468° W	"Bawden reef": extending 34 km from southern end of ice rise, arcuate, bearing numerous 020° high points, shallow depth (est. ~ 100 m depth)
66.174° S 66.177° S 66.025° S	58.968° W W 58.721° W E 58.806° W N	"Jason shoals": 12 × 18 km region, 3–4 high points, shallow depth at west end (est. 100–150 m depth)
65.784° S	58.237° W	"Hektoria 1 shoal", single point (est. > 150 m depth)
65.849° S	57.276° W	"Hektoria 2 shoal", single point (est. > 150 m depth)
65.692° S	56.956° W	"Hektoria 3 shoal", single point (est. > 150 m depth)
66.292° S	56.975° W	"Hektoria 4 shoal", single point (est. > 150 m depth)

* Based on sea ice and small iceberg strand sites and winter sea ice fracture loci seen in MODIS image data archived at http://nsidc.org/data/iceshelves_images/index_modis.html.

Table 2. Continental-shelf domes estimated area and minimum and maximum estimated ice volumes using the simple Bodvarsson–Vialov model (Bueler et al., 2005).

Continental ice dome	Area (km^2)	Ice volume (km^3)	
		Minimum	Maximum
Hugo Dome	13 675	10 000	11 200
Marr Dome	4950	2500	3300
Brabant Dome	12 850	8200	10 200
Livingston Dome	8075	5000	5500
Snow Hill Dome	14 835	10 800	14 000
Robertson Dome	7560	5000	6200
Hektoria Dome	12 920	9300	12 000
Total	74 865	50 800	62 400

Table 3. Flow path systems estimated area (continental shelf) and minimum and maximum estimated ice volumes.

Flow path system	Area (km^2)	Approximate length (km)	Ice volume (km^2)	
			Minimum	Maximum
Biscoe Trough	4625	125	2842	4254
Palmer Deep and Hugo Island Trough	15 000	230	9570	17 255
Barbant	850	60	564	719
Gerlache–Croker–Boyd straits	10 675	300	9234	16 402
South Bransfield Strait streams	5600	110	4211	5834
Erebus–Terror	7125	190	3905	6935
Robertson Trough	18 300	330	13 066	26 149
Larsen B embayment	10 700	217	6736	11 937
Total	72 875	1562	50 128	89 485

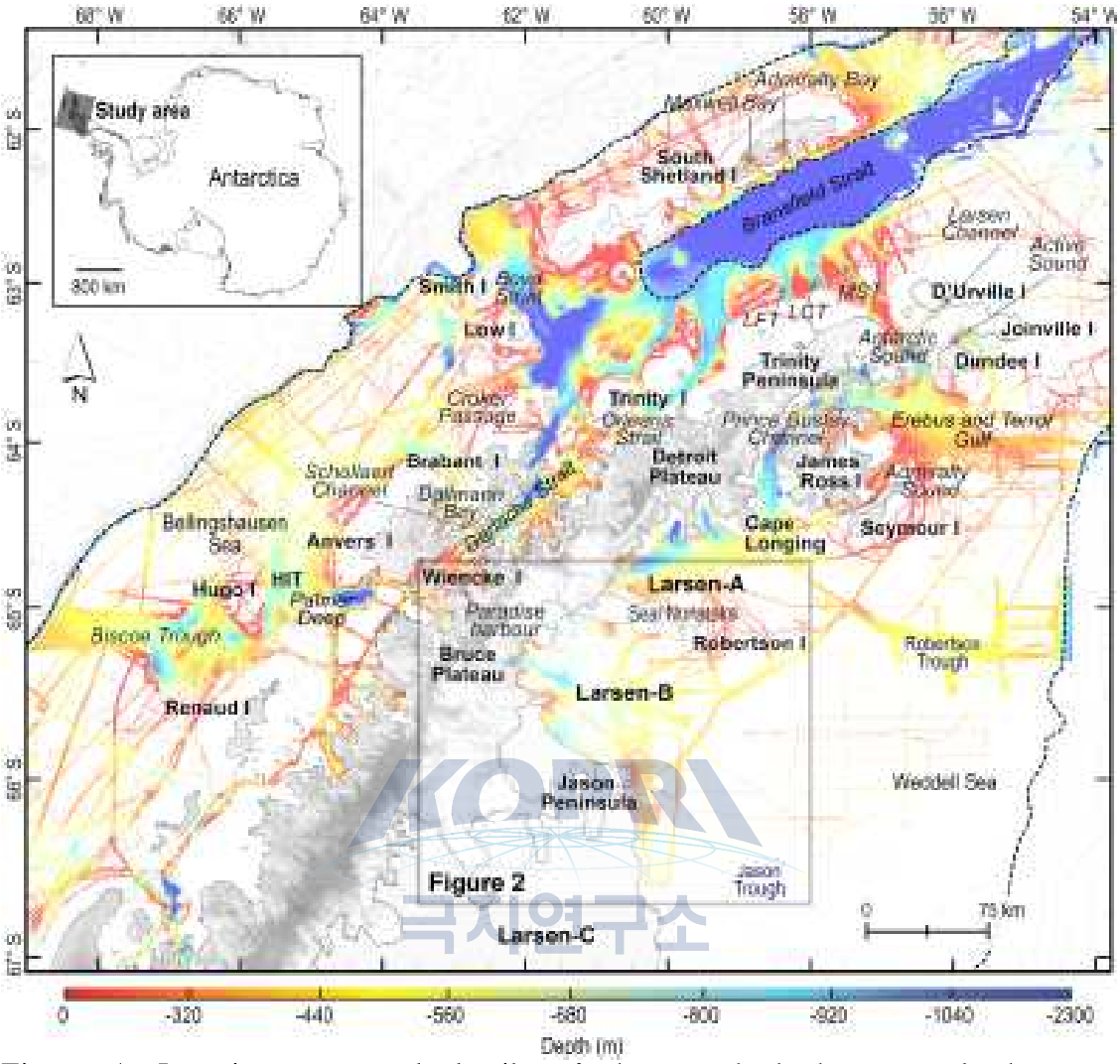

Figure 1. Location map and details of the swath bathymetry database, as compiled up to 2013, around the northern Antarctic Peninsula (AP). Offshore topography is gridded at 30 m. The shelf break is shown as a black dashed line. The gray box indicates the regions detailed in Fig. 2. The background image on land is from RAMP AMM-1 SAR Image 125 m Mosaic of Antarctica; the coastline is from the British Antarctic Survey (BAS; http://www.add.scar.org/); the bathymetry contour interval of 250 m is from IBCSO (Arndt et al., 2013). The inset shows the location of the northern AP in Antarctica. Abbreviations: HIT - Hugo Island Trough, LFT - Lafond Trough, LCT - Laclavere Trough, MST - Mott Snowfield Trough.

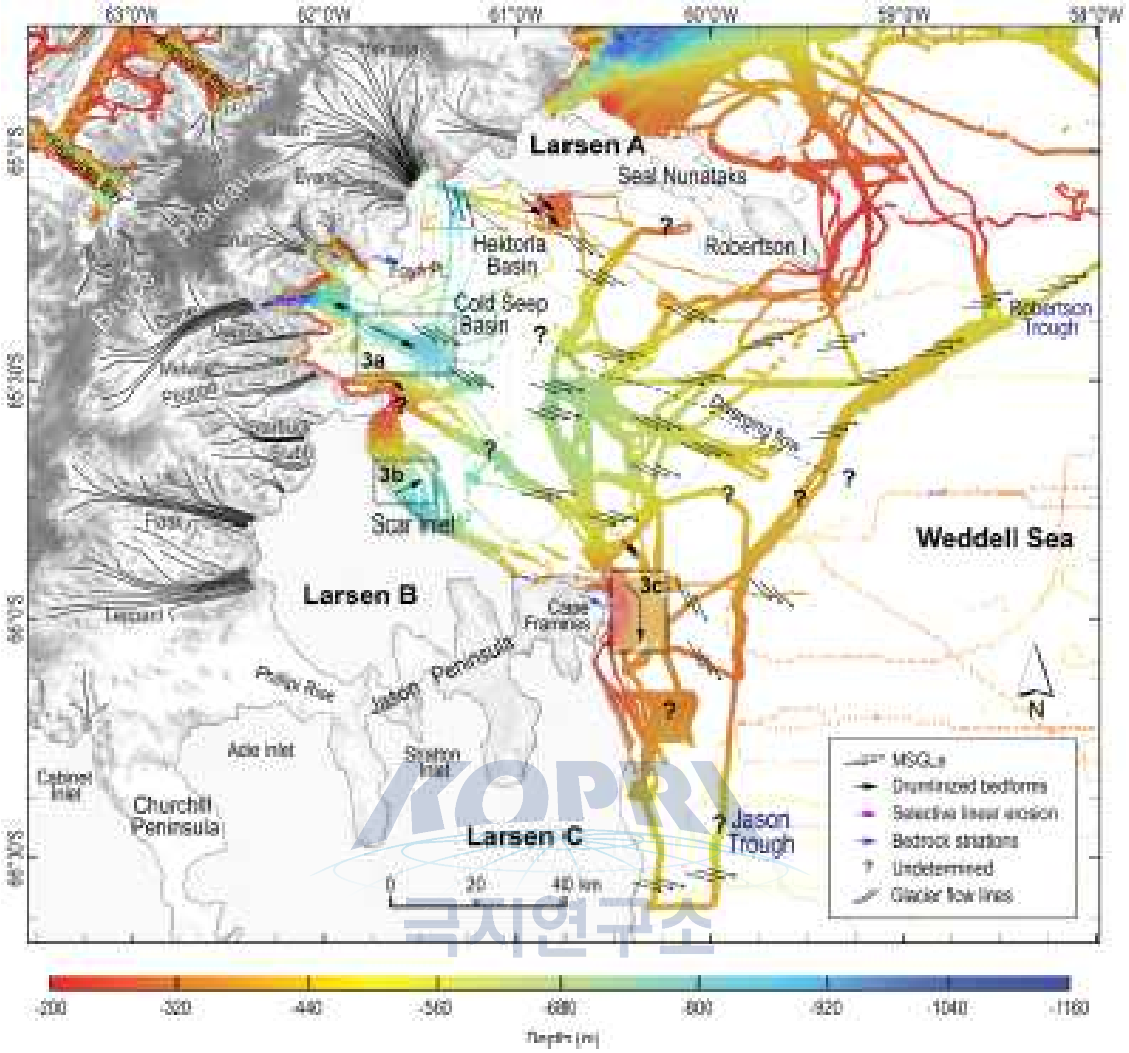

Figure 2. Details of seabed morphology in Larsen B embayment associated with paleo-flow-line trajectories based on examination of swath bathymetry imagery of the seafloor. Distinct flow trajectories split the Larsen B embayment into two outlets by ice-flow bifurcation. The bathymetry contour interval of 250 m is from IBCSO (Arndt et al., 2013). The gray boxes show the regions detailed in Fig. 3. For location see Fig. 1.

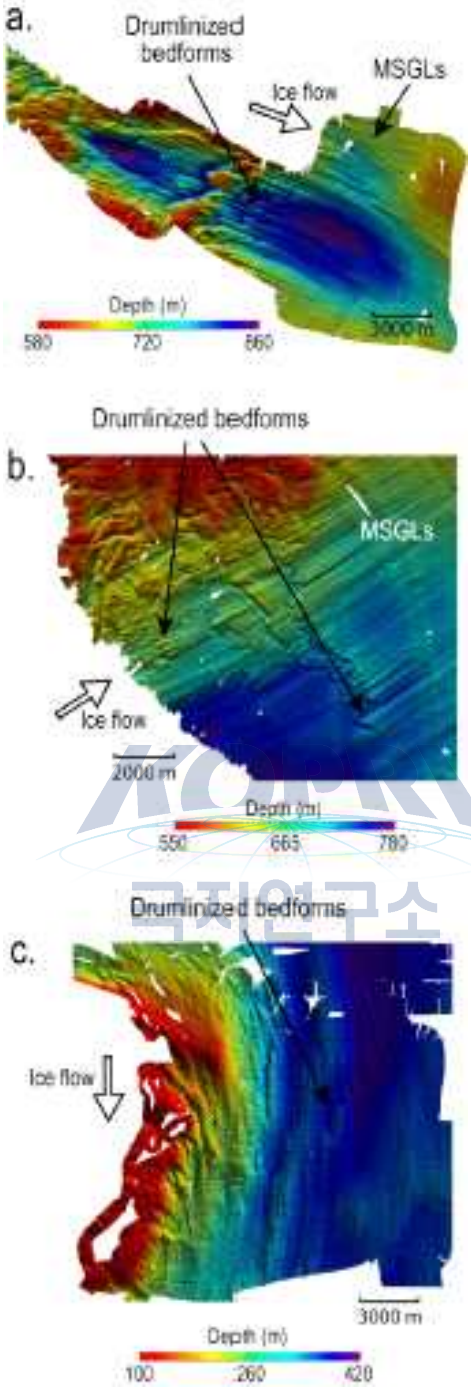

Figure 3. Close-up on the seabed morphology and swath bathymetry perspective views. The location of (a) - (c) is presented in Fig. 2. Offshore topography is gridded at 25 m and shown with a vertical exaggeration of X3. (a) Bathymetry image shows the Cold Seep Basin region with drumlinized bedforms and mega-scale glacial lineations (MSGLs) associated with a paleo-ice-flow direc-tion, (b) Scar Inlet, and (c) Cape Framnes, south of the Jason Penin-sula. The paleo-ice-flow direction is indicated by the white arrows.

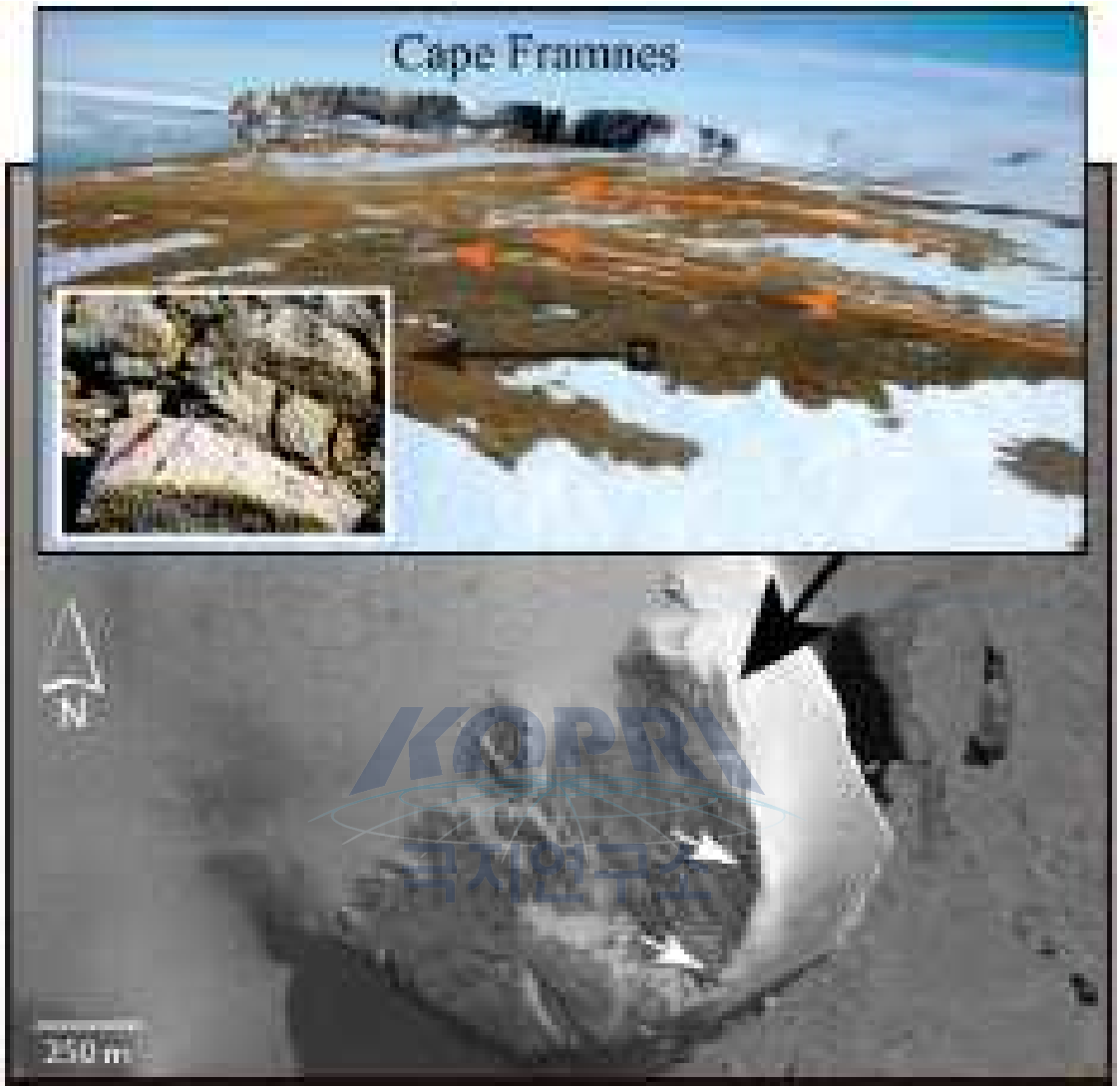

Figure 4. Photograph from Cape Framnes showing bedrock stria-tions and flute orientations ESE in agreement with the southward flow orientation observed on the seafloor (this study). The location of the photograph and its aspect are indicated by the black arrow on the Landsat Scenes LIMA. The insets show an isolated bedrock rib, its location on the landscape, and the flow direction of striations and bedrock flutes (orange and white arrows) in each case (figure mod-ified from a map compiled by Spences Niebuhr, Polar Geospatial Center).

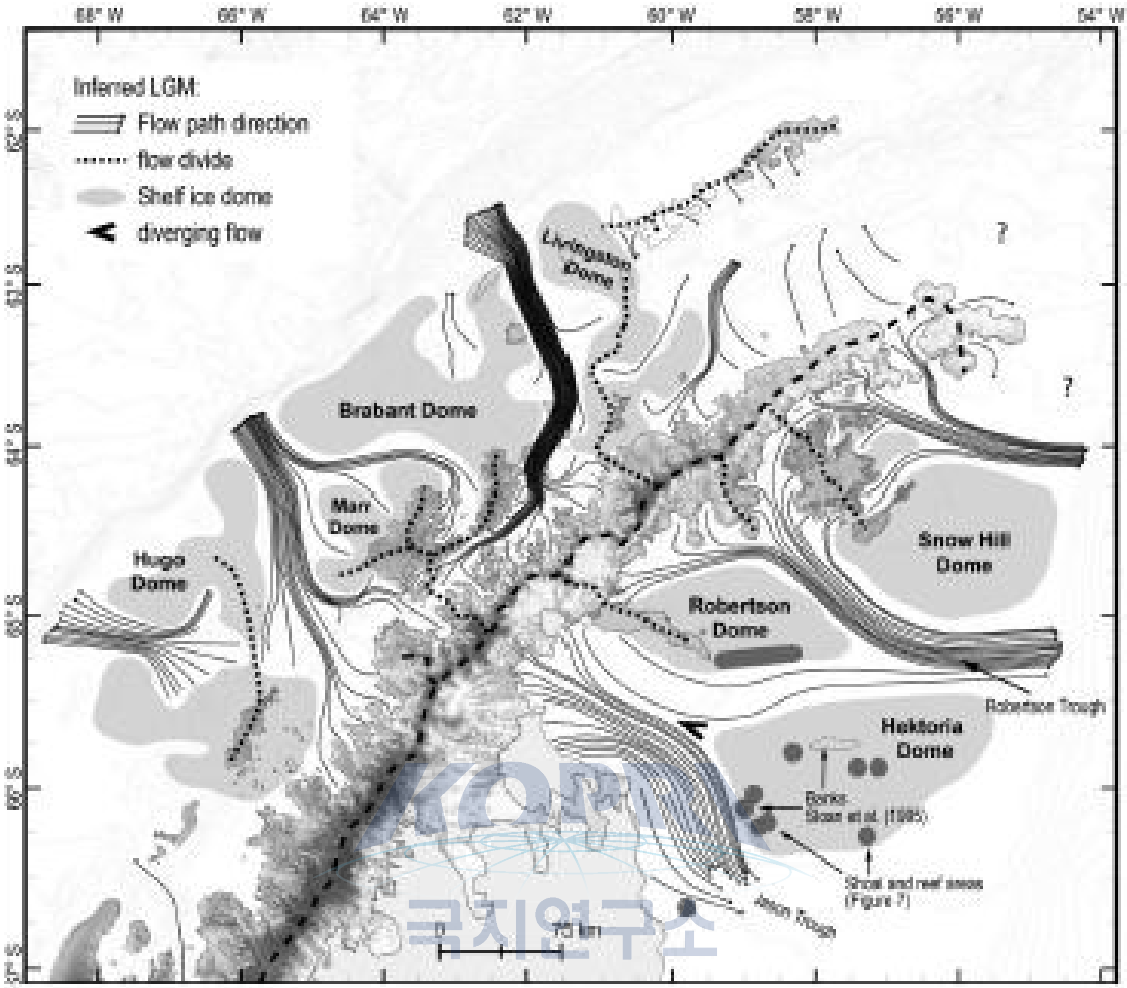

Figure 5. Inferred paleo-ice-flow directions and continental-shelf ice domes around the northern AP continental shelf at LGM showing ice divides (black short-dashed lines), shelf ice domes (gray areas), and the bifurcating flow in the Larsen B embayment. The modern divide along the AP (black dash line) is probably not at the same location of the LGM divide, but it is close. Also identi fied are the topographic banks by Sloan et al. (1995) and the shoal and reef areas of Fig. 7. The bathymetry contour interval of 250 m is from IBCSO (Arndt et al.,2013).

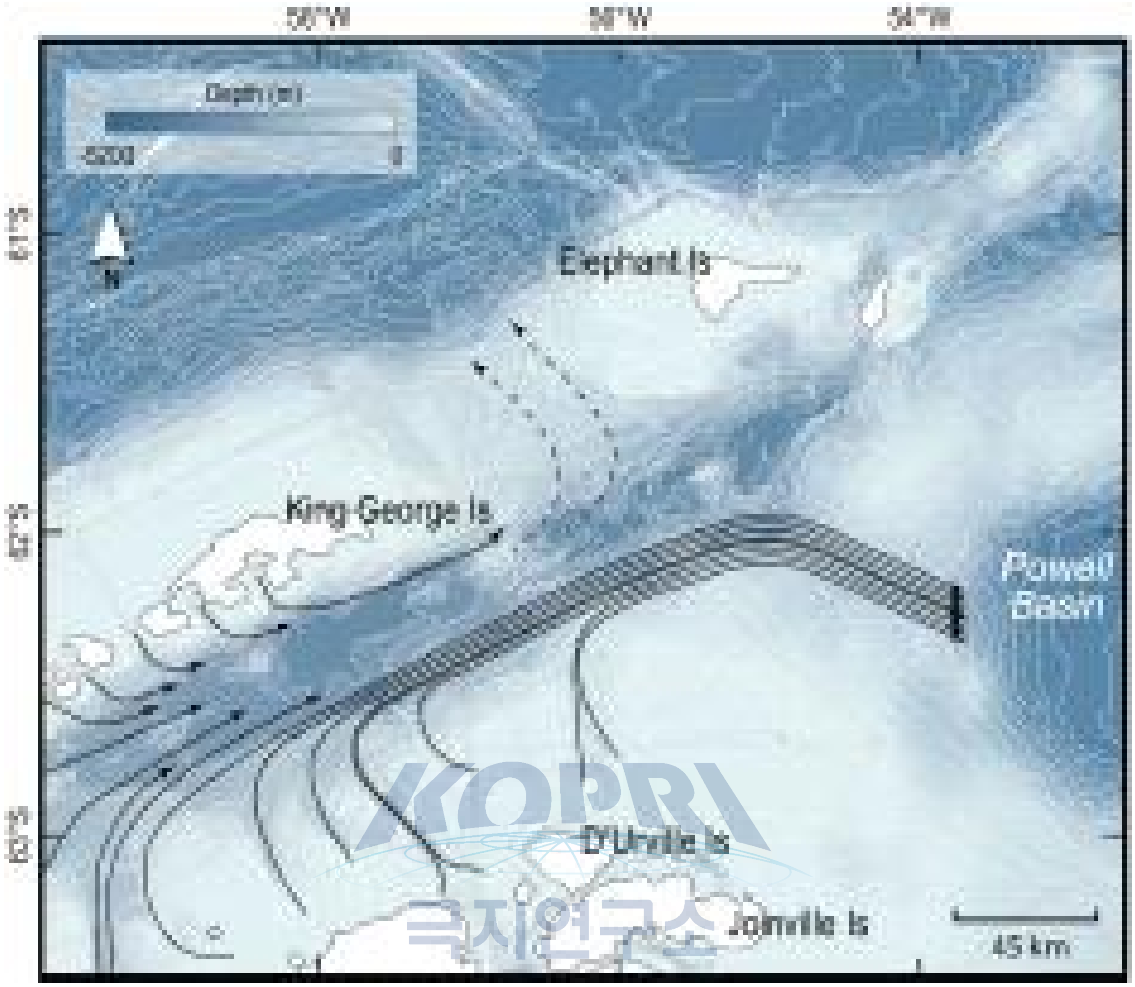

Figure 6. Seabed morphology in Bransfield Strait showing the in-ferred paleo-fl ow-line trajectories based on the multibeam imagery (black arrows) and assumptions (black dashed arrows). Background image is from BedMap2 (Fretwell et al., 2013); the island coast-line is from the British Antarctic Survey (BAS; http://www.add. scar.org/); the bathymetry contour interval of 250 m is from IBCSO (Arndt et al., 2013).

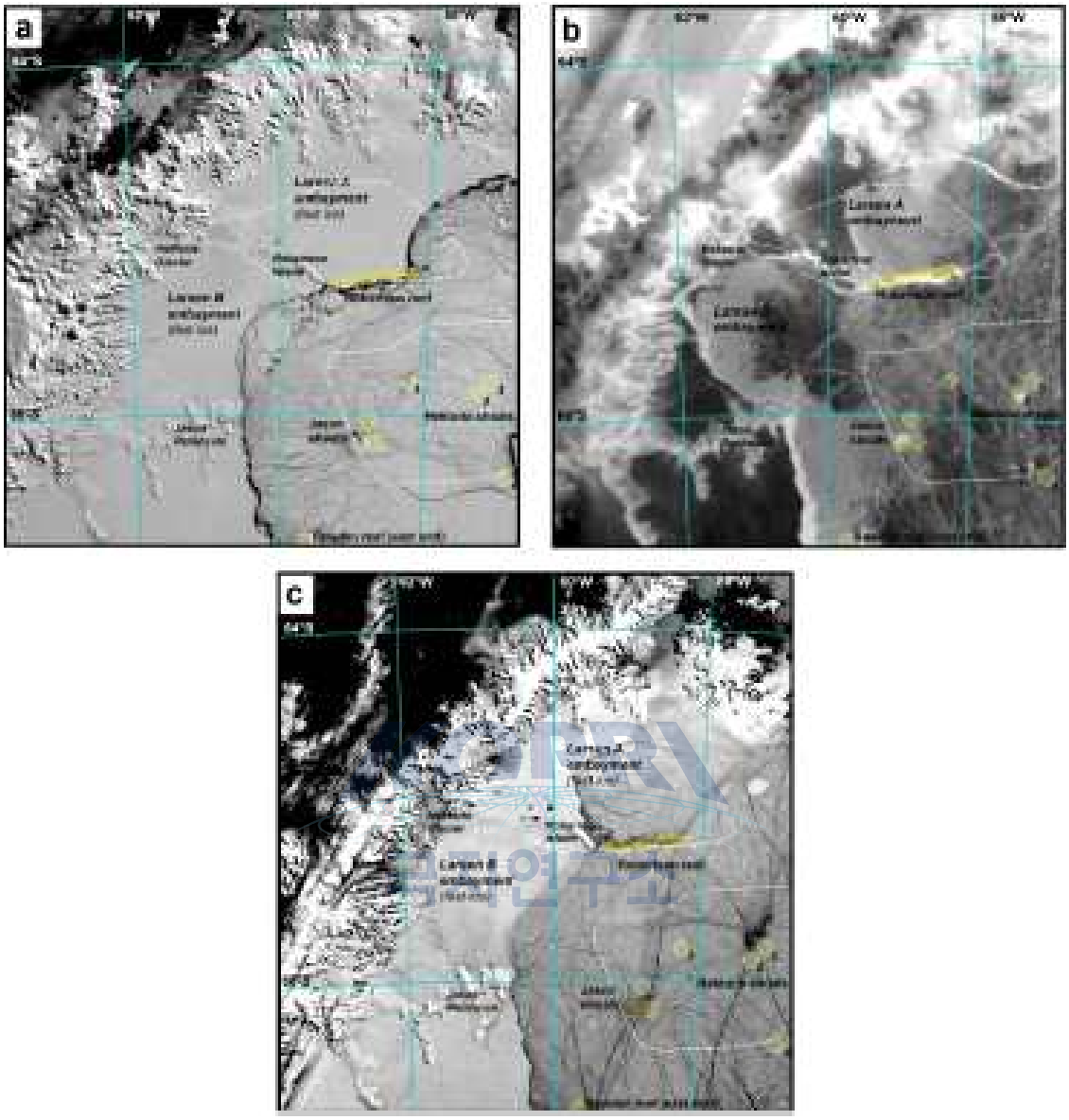

Figure 7. MODerate-resolution Imaging Spectroradiometer (MODIS, 36-band spectrometer) images showing unequivocal evidence of sev-eral shoal and reef areas (yellow circle) in the northwestern Weddell Sea, based on sea ice drift and grounding of small icebergs (see also Table 1). The shelf ice domes Hektoria and Robertson are showed in dashed white lines. (a) 5 October 2007, band number (BN) 02 (band-width 841 - 876 nm, spatial resolution of 250 m); (b) 20 August 2010, BN 32 (bandwidth 11770 - 12270 nm, spatial resolution of 1000 m); and (c) 26 January 2013, BN 02 (bandwidth 841 - 876 nm, spatial resolution of 250 m).

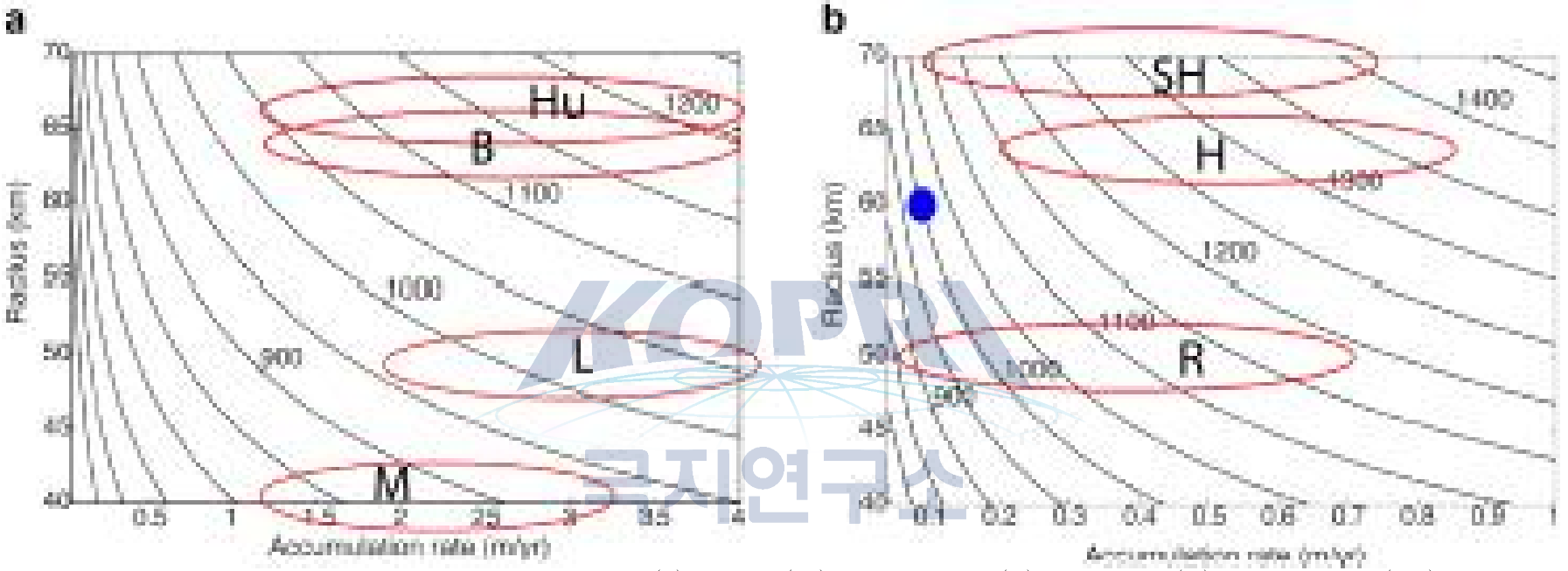

Figure 8. Range of ice thickness expected from (a) Marr (M), Livingston (L), Brabant (B), and Hugo (Hu) west AP continental-shelf domes with ice temperature averaging 0 ○C and (b) Robertson (R), Hektoria (H), and Snow Hill (SH) east AP continental-shelf domes with ice averaging −20 ○C using the Bodvarsson - Vialov model (Bueler et al., 2005). The blue dot is the modern analog, 1000 m thick Siple Dome in West Antarctica that fits well the model. See Fig. 5 for the location of the domes.

제 10 장

Late quaternary climate changes around the elephant islands, Antarctic Peninsula[5)]

Young Suk Bak[1*], Kyu-Cheul Yoo[2], Ho Il Yoon[2]

[1]Chonbuk Naiotnal University
[2]Korea Polar Research Institute

Abstract: Sixty-seven species of diatoms of 28 genera were identified in Core GC03-C2 acquired from the north slope of Elephant Island, Antarctic Peninsula. The number of diatom valves per gram of dry sediment ranged from 0.2~17.3×107g−1, and these were dominated by Fragilariopsis kerguelensis (65.8%). Diatom assemblage analysis reconstructed the Quaternary paleoclimatic change the Elephant Islands. Four diatom assemblage zones were identified according to the frequency of critical taxa as follows: zone I, from 830 to 710 cm (Antarctic Cold Reversal); zone II, from 700 to 550 cm (Deglaciation zone); zone III, from 540 to 260 cm (warm period; Holocene); and zone IV, from 250 to 0 cm (cool period; Holocene). The high abundance of reworked species includes Actinocyclus ingens, Denticulopsis hustedtii, D. praedimorpha, and D. dimorpha appeared in Zone I by turbidity currents and ice rafting in the area during the glaciations-deglaciation event.

5) 이 연구 결과는 다음의 논문으로 출판되었음: Bak, Y. S., Yoo, K. C., & Yoon, H. I. (2014). Late quaternary climate changes around the elephant islands, Antarctic Peninsula. Geosciences Journal, 18(4), 495-501.

1. Introduction

Diatom assemblage analysis provides one of the best sources of paleoenvironmental information and is widely used to determine biological productivity or sea ice during the late Quaternary in the high-latitude regions (Medlin and Priddle, 1990; Stoermer and Smol, 1999; Armand et al., 2005; Crostaet al., 2005; Gersonde et al., 2005; Stickley et al., 2005). Further, diatoms serve as one of the most sensitive proxies for oceanographic reconstructions of the Southern Ocean where theyare extremely abundant and diverse, with many species restricted to particular environments. Their opaline silica skeletons, which are particularly well preserved in Antarctic sediments, provide apaleoenvironmental record. Diatom distribution is controlled by environmental conditions, including water temperature, salinity, and stability as well as light, nutrient availability, and sea-ice cover (Defelice and Wise, 1981; Dunbar et al., 1985; Leventer and Dunbar, 1996; Zielinski and Gersonde, 1997; Cunningham and Leventer, 1998). There are some areas for glacial-interglacial research in Antarctica (Hall, 2009; Allenet al., 2011). Recently, there have been a few studies about the climate change using diatom during the late Quaternary around the Elephant Islands (Bak et al., 2010, 2011). The objective of this paper is provide a new analysis of down-core change of diatom assemblages in core GC03-C2 from the northern region of Elephant Island, which was studied to reveal climate change during the Late Quaternary.

2. Oceanographic setting

Elephant Island is located northeast of the South Shetland Islands, and is adjacent to the Bransfield Strait and the Drake Passage. Elephant Island is situated close to the Shackleton Fracture Zone and the South Scotia Ridge, which are active transform plate boundaries (Klepeis and Lawver, 1996; Kimet al., 1997). Elephant Island is 90% ice-covered and was uplifted by approximately 100 m since 6.4 Ma (Rebesco et al., 1997; Trouw et al., 2000). Elephant Island is surrounded by complex ocean currents that traverse the Bellingshausen Sea, Bransfield Strait, Drake Passage, and the Weddell Sea. On the shelves of

Elephant Island, the waters, which are referred to as Antarctic Peninsula shelf waters (Deacon and Foster, 1977; Patterson and Sievers, 1980; Amos, 2001; Prid-dle et al., 1994; Hofmann et al., 1996; Zhou et al., 2010), are strongly influenced by intrusions of the Antarctic Circumpolar Current (ACC), local runoff, and cooling. The northward and southward excursions of the ACC in the southern Drake Passage have been characterized (Orsi et al., 1993, 1995; Hofmann et al., 1996; Amos, 2001; Schodlok et al., 2002; Zhou et al., 2010).

The waters associated with the ACC are as follows: the warm Antarctic Surface Water (ASW), the cold Winter Water (WW) below the ASW, and the warm Circumpolar Deep Water (CDW) (Nowlin and Klinck, 1986; Orsi et al., 1995; Hoffmann et al., 1996; Schodlok et al., 2002; Sprintall, 2003). The temperature (<0.1°C) and low salinity (<34.6 ‰) of the ASW extend to a depth of approximately 200 m (Carmack and Foster, 1975). The current of Wedell Sea Water are flowing in the Elephant Island region (Gordon and Nowlin, 1978;Whitworth et al., 1994), input from upstream regions along the western Antarctic Peninsula (Stein, 1986, 1988, 1989; Niiler et al., 1991; Capella et al., 1992; Garcia et al., 1994; Hofmann et al., 1996). The CDW of the Bransfield Strait is the coldest, originating from the Weddell Sea and exerting a local cooling influence (Zhou et al., 2010). Further, depths greater than 800 m are referred to as the high-density Weddell Sea Deep Water (- 0.7 °C < T < 0 °C) and the Weddell Sea Bottom Water (<0.7°C) (Orsi et al., 1993; Matano et al., 2002).

3. Materials and methods

The gravity core GC03-C2 (830cm long; 61°07.3′S,61°01.2′W) was obtained at a depth of approximately 3200 mnorth of Elephant Island (Fig. 1).

Eighty-three samples were collected from the core at 10 cm intervals for diatom analysis (Fig. 1). The dry samples were placed in the beaker with 25 ml of 30% hydrogen peroxide (H_2O_2). 10% Hydrochloric acid (HCl) was then added to remove organic carbonate for another 24 h. They were then centrifuged three times at 1,700 rpm for 15 second; samples were washed with distilled water to remove chemical residue and salt crystals between centrifuging. Washed samples

were prepared for quantitative diatom abundance analysis using conventional microscope slides according to the random settling method of Scherer (1994). All diatoms were countedin a minimum of 200 specimens, excluding resting spores of Chaetoceros spp. Diatoms were identified using a Nikon E400 microscope at magnifications of ×400 and ×1000. The number of microfossils per gram was calculated as follows: Abundance = ((A×B)/(C×D))/E (A = number of specimens counted; B = area of the settling chamber; C = number of fields of view; D = area of field of view; E = mass of sample). The age of the sediment, was determined by AMS (accelerator mass spectrometry) ^{14}C dates. Five radiocarbon accelerator ages were obtained from the core.

4. Results and discussion

Sixty-seven diatom species belonging to 28 genera were recognized, and the most abundant species was Fragilariopsis kerguelensis (65.8%) (Fig. 2). Also present were Thalassiosira antarctica, Actinocyclus cuvatulus, Rhizosolenia styliformis, Eucampia antarctica var. recta, and E.var. antarctica. Samples of bulk sediment were radiocarbon-dated using accelerator mass spectrometry and ages were corrected using a local reservoir age of 1160 years (Bjorck et al., 1991) (Table 1). In marine sediments, MS is in turn a function of terrigenous source composition and dilution by biogenic material. While the low magnetic susceptibility values may be ascribed to biogenic dilution of magnetic minerals, the high values are likely to reflect variations in mineralogy and grain size (Yoonet al., 2009).

4.1. Diatom Assemblages

Four assemblage zones are established from the entire core according to the abundance of diatom valves, the vertical distributions of major species and magnetic susceptibility (Fig. 2).

4.1.1. Diatom assemblage zone I: (830 - 710 cm)

The number of diatom valves per gram of dry sediment was very low, ranging from 0.2 to 1.5×107g−1. The high abundance of Actinocyclus curvatulus indicates neritic environment (Romero et al., 2002). Eucampia antarctica is reportedto two varieties as E. antarctica var. antarctica and Eucampia antarctica var. recta (Fryxell and Prasad, 1990; Fryxell, 1991). The high abundance of the polar form of Eucampia antarctica (Eucampia antarctica var. recta) in assemblage zone I is consistent with the low abundance of the subpolar form of E. antarctica (E. antarctica var. antarctica) (Fig. 2). Thalassiosira antarctica is widespread in Antarctic water sand is generally associated with the relatively open-water primary production of marginal ice-edge environments (Leventer and Dunbar, 1987, 1988, 1996; Fryxell and Kendrick, 1988; Leventer, 1992; Leventer et al., 1993; Taylor et al., 1997; Zielinski and Gersonde, 1997). The GC03-C2 is located at a transitional zone between winter sea-ice zone and summer sea-ice zone. The vegetative valves of T. antarctica were not detected in diatom assemblage zone I, but Eucampia antarctica var. recta is abundant. Moreover, the lowest primary productivity and relatively high magnetic susceptibility values (132~342) are associated with glacial environment (Vanderaveroet et al., 1999). It was because the grain-size is better sorted than glacial ones during interglacial stages, and is silt-dominated. Contradistinctively, the glacial sediments are richer clay or sand size particles, poorly-sorted (Vanderaveroet et al., 1999). At the upper part of 780 cm horizon, MS value indicates a relatively high than the lower part. Conversely, there is a rapid decrease in F. kerguensis (open water species) in the upper part of 780 cm horizon. This change in the diatom assemblage zone I indicates cooling condition, and correlates with the Antarctic Cold Reversal (ACR) following the end of AIM1 (Antarctic Isotopic Maximum) (Stenni et al., 2010). Also, this is consistent with the results of radiocarbon dating (700 cm: ca. 14,340 yr).

4.1.2. Diatom assemblage zone II: (710 - 550 cm)

The range of diatom valves per gram of dry sediment was 0.3 - 11.1×$10^{7}g^{-1}$, and is higher than that of assemblage zone I. The abundance of A. curvatulus gradually decreased, although that of E. antarctica var. recta increased from lower to upper levels. The relative abundances of open-water

species such as F. kerguelensis and R. styliformis increased in assemblage zone II. F. kerguelensis is a valuable paleoindicator used to identify open marine environments. Today, it predominates between 52 - 63°S (Burckle et al., 1987) where summer surface water temperatures exceed 0°C (Krebs et al., 1987). The abundance of F. kerguelensis is inversely correlated with sea-ice distribution (Burckle and Cirilli, 1987), and this species is present in the ACC and PF (Bathmann et al., 1997; Zielinski and Gersonde, 1997; Crosta et al., 2004). Rhizosolenia styliformis is most abundant in open-water environments where the sea ice does not freeze or forms for short durations during winter (Crosta et al., 2005). The magnetic susceptibility values drastically decreased while the number of open-water species increased. This zone corresponds to the deglaciation period of gradual warming beyond the end of the Antarctic cold Reversal.

4.1.3. Diatom assemblage zone III: (550 - 260 cm)

The number of diatom valves per gram of dry sediment ranged between 2 and $17.3\times10^{7}g^{-1}$ and was the highest of all zones. However, the abundances of A. curvatulus and E.antarctica var. recta were markedly reduced. The subpolar form of E. antarctica increased in the upper part of assemblage zone III compared with zone II, and the abundance of open-water species such as F. kerguelensis and T. antarctica increased. As mentioned before, Fragilariopsis kerguelensis is dominant between 52−63°S (Burckle et al., 1987), and a paleoindicator suggests open marine deposition. Therefore, this assemblage corresponds to the warm period of the mid-Holocene climatic optimum (Table 1) with low magnetic susceptibility values and high diatom valve abundance (Fig. 2), and is accompanied by a marked increase in the abundance of T. antarctica.

4.1.4. Diatom assemblage zone IV: (260 - 0 cm)

The number of diatom valves per gram of dry sediment ranged between 2.5 and $14.4\times10^{7}g^{-1}$, representing a decrease compared with that of assemblage zone III and sea-ice species (E. antarctica var. recta and F. curta) shows a marked increase in abundance; however, T. antarctica was not detected. F. curta is highly abundance near the sea ice edge (Kangand Fryxell, 1992, 1993; Leventer and Dunbar, 1996). Therefore, this assemblage may have been present

during a period of climatic cooling (Table 1) compared to the period of assemblage zone III. Reworked diatom species such as A. ingens, Denticulopsis hustedtii, D. dimorpha, and D. praedimorpha were present in high abundance in assemblages I to II. These species correspond to Miocene - Pleistocene periods (Table 2), but increased from the last glacial to deglaciation periods (Fig.3). Pudsey (2000) suggests a supply of old sediment by turbidity currents and ice rafting in the area during the glaciation-deglaciation event. The results of the study areas (GC03-C2) are not unlike the results from the surrounding sediment core GC03-C1, showing the palaeoclimatic change from the LGM (Last Glacial Maximum) to Neoglacial (Bak et al., 2010,2011). There is no deposit of the LGM in the GC03-C2 core wherein, deglaciation appears from the lowest horizon, no evidence of neoglacial cooling event. However, diatom assemblages from GC03-C2 core show the cooling event (Antarctic Cold Reversal) in the periods of deglaciation.

The paleoclimatic changes between late glacial-deglacial periods can be reconstructed from the GC03-C2 core date. The magnetic susceptibility and the diatom faunal reveals that a marked cooling event in the area during the ACR. While following the deglaciation, F. keruelensis and valve abundanceare characterized by consistently high values. The mid-Holoceneclimatic optimum, represented by the core interval between550 and 260 cm, is expressed by a decrease in the E. antarctica var. recta. After a warming, the diatom data showing anincrease of E. antarctica var. recta and F. curta suggest acolder interval between 260 and 0 cm.

5. Conclusion

We identified four distinct diatom assemblage zones in the GC03-C2 core sediment taken from the north slope of Elephant Island, Antarctic Peninsula based on the vertical distribution of diatom species and magnetic susceptibility values. These zones are defined as follows: zone I (830 - 710cm, Antarctic Cold Reversal period); zone II (710 - 550 cm, Deglaciation period); zone III (550 - 260 cm, Holocene);and zone IV (260 - 0 cm, Holocene).

The Antarctic Cold Reversal period is characterized by the increase of

sea-ice species in association with the lowest primary productivity and high magnetic susceptibility values. The Deglaciation period is characterized by a high abundance of open-water species. The Holocene of Zone III corresponds to the warm period characterized by a marked increase in the abundance of T. antarctica. The Holocene of Zone IV is characterized by a marked increase in sea-ice species (E.antarctica var. recta and F. curta) during the cooling events.

남극 반도 엘리펀트 섬의 홀로세 후기 기후변화

박영숙[1*], 유규철[2], 윤호일[2]

[1]전북대학교
[2]한국해양과학기술원 부설 극지연구소

요약: 남극 반도의 엘리펀트 섬 (Elephant Island) 북쪽 사면에서 획득한 GC03-C2에서 28속 67 종의 규조가 확인되었다. 단위 g 당 규조 수의 수는 0.2 ~ 17.3 × 107/g이었고, Fragilariopsis kerguelensis (65.8 %)가 우점하였다. 규조 종조성 분석을 통해 엘리펀트 섬의 제 4기 고기후 변화를 복원하였다. 주요 종의 산출에 따라 4 개의 규조 종조성 존(존 1: 830-710 cm-남극냉각역전기, 존 2: 700-550 cm-해빙기, 존 3: 540-260 cm-홀로세 온난기, 존 4: 250-0 cm-홀로세 한랭기)으로 나누었다. 존 1에 나타나는 Actinocyclus ingens, Denticulopsis hustedtii, D. praedimorpha와 같은 재동된 종은 빙기/해빙기 사건 동안 터비다이트 해류와 빙하에 의해서 운송되었다.

참고문헌

Allen, C.S., Pike, J., and Pudsey, C.J., 2011, Last glacial-interglacial sea-ice cover in the SW Atlantic and its potential role in global deglaciation. Quaternary Science Reviews, 30, 2446 - 2458.

Amos, A.F., 2001, A decade of oceanographic variability in summertime near Elephant Island, Antarctica. Journal of Geophysical Research, 106, 22401 - 22423.

Armand, L., Crosta, X., Romero, O., and Pichon, J.J., 2005, The biogeography of major diatom taxa in Southern Ocean sediments. 1. Sea ice related species. Paleogeography Paleoclimatology Paleoecology, 223, 93 - 126.

Bak, Y.S., Lee, J.D., Yoon, H.I., Yoo, K.C., and Lee, S.J., 2010, Holocene paleoclimate change in the area around Elephant Island, Antarctica: evidence from the diatom record. Journal of the Geological Society of Korea, 46, 111 - 117. (In Korean with English abstract)

Bak, Y.S., Yoo, K.C., Lee, J.D., Yoon, H.I., Lee, J.I., Kim, H.J., and Lee, S.J., 2011, Deglacial environments in the northeastern of South Shetland Islands, Antarctica: evidence from the high resolution diatom record. Journal of the Geological Society of Korea, 47, 363 - 369. (In Korean with English abstract)

Baldauf, J.G. and Barron, J.A., 1991, Diatom biostratigraphy: Kerguelen Plateau and Prydz Bay regions of the Southern Ocean. In: Barron, J., Larsen, B. et al. (eds.), Proceedings of the Ocean Drilling Program Scientific Results, 119, Ocean Drilling Program, College Station, TX, 547 - 598.

Bathmann, U.V., Scharek, R., Klaas, C., Dubischar, C.D., and Smetacek, V., 1997, Spring development of phytoplankton biomass and composition in major water masses of the Atlantic sector of the Southern Ocean. Original Research Article Deep Sea Research Part II: Topical Studies in Oceanography, 44, 51 - 67.

Bjorck, S., Hjort, C., Ingolfsson, O., and Skog, G., 1991, Radiocarbon dates from the Antarctic peninsula region — problems and potential. In: Lowe, J.J. (ed.), Radiocarbon Dating: Recent Applications and Future Potential. Quaternary Research Association, Cambridge, Quaternary

Proceedings 1, p. 55 - 65.

Burckle, L.H. and Cirilli, J., 1987, Origin of diatom ooze belt in the Southern Ocean; implications for late Quaternary paleoceanography. Micropaleontology, 33, 82 - 86.

Burckle, L.H., Jacobs, S.S., and McLaughlin, R., 1987, Late spring diatom distribution between New Zealand and the Ross Sea: correlation with hydrography and bottom sediments. Micropaleontology, 33, 74 - 81.

Capella, J.E., Ross, R.M., Quetin, L.B., and Hofmann, E.E., 1992, A note of the thermal structure of the upper ocean in the Bransfield Strait-South Shetland Islands region. Deep-Sea Research, 39, 1221 - 1229.

Carmack, E.C. and Foster, T.D., 1975, On the flow of water out of the Weddell Sea. Deep-Sea Research I, 22, 711 - 724.

Ciesielski, P.F., 1983, The Neogene and Quaternary diatom biostratigraphy of subantarctic sediments, Deep Sea Drilling Project Leg 71. In: Ludwig, W.J. and Krasheninnikov, V.A. (eds.), Initial Reports of the Deep Sea Drilling Project. 71, p. 635 - 666. Washington: U.S. Government Printing Office.

Crosta, X., Sturm, A., Armand, L., and Pichon, J.J., 2004, Late quaternary sea ice history in the Indian sector of the Southern Ocean as recorded by diatom assemblages. Marine Micropaleontology, 50, 209 - 223.

Crosta, X., Romero, A., Armand, L., and Pichon, J.J., 2005, The biogeography of major diatom taxa in Southern Ocean sediments. 2. Open Ocean related species. Paleogeography Paleoclimatology Paleoecology, 223, 66 - 92.

Cunningham, W.L. and Leventer, A., 1998, Diatom assemblages in surface sediments of the Ross Sea; Relationship to present oceanographic conditions. Antarctic Science, 10, 134 - 146.

Deacon, G.E.R. and Foster, T.D., 1977, The boundary region between the Weddell Sea and Drake Passage currents. Deep-Sea Research 24, 505 - 510.

Defelice, D.R. and Wise, S.W., 1981, Surface lithofacies, biofacies and diatom diversity patterns as models for delineation of climatic change in the south east Atlantic Ocean. Marine micropaleontology, 6, 29 - 70.

Dunbar, R.B., Anderson, J.B., Domack, E.W., and Jacobs, S.S., 1985, Oceanographic influences on sedimentation along the Antarctic continental shelf. Antarctic Research Series, 43, 291 - 312.

Fryxell, G.A., 1991, Comparison of winter and summer growth stages of the diatom Eucampia antarctica from the Kerguelen Convergence Zone. In: Barron, J.A. and Larsen, B. (eds.), Proceedings of the Ocean Drilling Program, Scientific Results 119. College Station, TX (Ocean Drilling Program), 675 - 685.

Fryxell, G.A. and Kendrick, G.A., 1988, Austral spring microalgae across the Weddell Sea ice edge; spatial relationships found along a northward transect during AMERIEZ 83. Deep-Sea Research Part A 8212. Oceanographic Research Papers, 35, 1 - 20.

Fryxell, G.A. and Prasad, A.K.S.K., 1990, Eucampia antarctica var. recta (Mangin) stat. nov. (Biddulphiaceae, Bacillariophyceae): life stages at the Weddell Sea ice edge. Phycologia 29, 27 - 38.

Garcia, M.A., Lopez, O., Sospedra, J., Espino, M., Garcia, V., Morrison, G., Rojas, P., Figa, J., Puigdefabregas, J., and Arcilla, A.S., 1994, Mesoscale variability in the Bransfield Strait region (Antarctica) during austral summer. Annales Geophysicase, 12, 856 - 867.

Gersonde, R. and Burckle, L.H., 1990, Neogene diatom biostratigraphy of ODP Leg 113, Weddell Sea (Antarctic Ocean). In: Barker, P.F., Kennett, J.P. et al. (eds.), Proceedings of the Ocean Drilling Program, Scientific Results, College Station, TX (Ocean Drilling Program), 113, 761 - 790.

Gersonde, R. Crosta, X. Abelmann, A., and Armand, L., 2005, Sea surface temperature and sea ice distribution at the EPILOG last glacial maximum – a circum-Antarctic view based on siliceous microfossil records. Quaternary Science Reviews, 24, 869 - 896.

Gordon, A.L., and Nowlin, Jr. W.D., 1978, The basin waters of the Bransfield Strait. Journal of Physical Oceanography, 8, 258 - 264.

Hall, B.L., 2009, Holocene glacial history of Antarctica and the sub-Antarctic islands. Quaternary Science Review, 28, 2213 - 2230.

Hofmann, E.E., Klinck, J.M., Lascara, C.M., and Smith, D.A., 1996, Water mass

distribution and circulation west of the Antarctic Peninsula and including Bransfield Strait. In: Ross, R., Hofmann, E., and Quetin, L. (eds.), Antarctic Research Series, 70, American Geophysical Union, Washington, D.C, p. 61 - 80.

Kang, S.H. and Fryxell, G.A., 1992, Fragilariopsis cylindrus (Grunow) Krieger: the most abundant diatom in water column assemblages of Antarctic marginal ice edge zones. Polar Biology, 12, 609 - 627.

Kang, S.H. and Fryxell, G.A., 1993, Phytoplankton in the Weddell Sea, Antarctica — composition, abundance and distribution in watercolumn assemblages of the marginal ice-edge zone during austral autumn. Marine Biology, 116, 335 - 348.

Kellogg, D.E. and Kellogg, T.B., 1986, Diatom biostratigraphy of sediment cores from beneath the Ross Ice Shelf. Micropaleontology, 32, 74 - 94.

Kim, Y., Jin, Y.K., and Nam, S.H., 1997, Crustal structure of the Shackleton Fracture Zone in the southern Drake Passage, Antarctica. In: Ricci, C.A. (ed.), The Antarctic Region: Geological Evolution and Processes. Tipologia Senense, Siena, Italy, 661 - 667.

Klepeis, K.A. and Lawver, L.A., 1996, Tectonics of the Antarctic- Scotia plate boundary near Elephant and Clarence Islands, West Antarctica. Journal of Geophysical Research 101,B9, 20211 - 20231.

Krebs, C.J., Gilbert, B.S., Boutin, S., and Boonstra, R., 1987, Estimation of snowshoe hare population density from turd transects. Canadian Journal of Zoology, 65, 565 - 567.

Leventer, A., 1992, Modern distribution of diatoms in sediments from the George V Coast, Antarctica. Marine Micropaleontology, 19, 315 - 332.

Leventer, A. and Dunbar, R., 1987, Diatom flux in Mcmurdo Sound, Antarctica. Marine Micropaleontology, 12, 49 - 64.

Leventer, A. and Dunbar, R.B., 1988, Recent diatom record of McMurdo Sound, Antarctica: implications for history of sea ice extent. Paleoceanography, 3, 259 - 274.

Leventer, A. and Dunbar, R., 1996, Factors influencing the distribution of diatoms and other algae in the Ross Sea. Journal of Geophysical Research, 101, 18,489 - 18,500.

Leventer, A., Dunbar, R., and DeMaster, D.J., 1993, Diatom evidence for Late Holocene climatic events in Granite Harbor, Antarctica. Paleoceanography, 8930, 373 - 386.

Matano, R.P., Gordon, A.L., Muench, R.D., and Palma, E.D., 2002, A numerical study of the circulation in the northwestern Weddell Sea. Deep-Sea Research II, 49, 4827 - 4841.

Medlin, L. and Priddle, J., 1990, Polar Marine Diatoms. British Antarctic Survey, Cambridge, 214 p

Niiler, P.P., Amos, A., and Hu, J.-H., 1991, Water masses and 200 m relative geostrophic circulation in the western Bransfield Strait region. Deep-Sea Research, 38, 943 - 960.

Nowlin, W.D. and Klinck, J.M., 1986, The physics of the Antarctic Circumpolar Current. Reviews of Geophysics, 24, 469 - 491.

Orsi, A.H., Nowlin Jr., W.D., and Whitworth III, T., 1993, On the circulation and stratification of the Weddell Gyre. Deep-Sea Research I, 40, 169 - 203.

Orsi, A.H., Whitworth III, T., and Nowlin Jr., W.D., 1995, On the meridional extent and fronts of the Antarctic Circumpolar Current. Deep Sea Research, 42, 641 - 673.

Patterson, S.L. and Sievers, H.A., 1980, The Weddell-Scotia Confluence. Journal of Physical Oceanography 10, 1584 - 1610.

Priddle, J., Brandini, F., Lipski, M., and Thorley, M.R., 1994, Pattern and variability of phytoplankton biomass in the Antarctic Peninsula region: an assessment of the BIOMASS druises. In: El-Sayed, S.Z. (ed.), Southern Ocean Ecology: The BIOMASS Perspective. Cambridge University Press, Cambridge, p. 49 - 61.

Pudsey, C.J., 2000, Sedimentation on the continental rise west of the Antarctic Peninsula over the last three glacial cycles. Marine Geology, 167, 313 - 338.

Rebesco, M., Larter, R.D., Barker, P.F., Camerlenghi, A., and Vanneste, L.E., 1997, The history of sedimentation on the continental rise west of the Antarctic Peninsula. In: Barker, P. F. and Cooper, A.K. (eds.), Geology and Seismic Stratigraphy of the Antarctic Margin II. AGU Antarctic Research Series, 29 - 50.

Romero, O., Boeckel, B., Donner, B., Lavik, G., Fischer, G., and Wefer, G., 2002, Seasonal productivity dynamics in the pelagic central Benguela System inferred from the flux of carbonate and silicate organisms. Journal of Marine Systems, 37, 259 - 278.

Scherer, R.P., 1994, A new method for determination of absolute abundance of diatoms and other siltsized sedimentary particles. Journal of Paleolimnology, 12, 171 - 179.

Schodlok, M.P., Hellmer, H.H., and Beckmann, A., 2002, On the transport, variability and origin of dense water masses crossing the South Scotia Ridge. Deep Sea Research II, 49, 4807 - 4825.

Sprintall, J., 2003, Seasonal to interannual upper-ocean variability in the Drake Passage. Journal of Marine Research 61, 27 - 57.

Stein, M., 1986, Variability of water masses and currents off the Antarctic Penninsula during SIBEX. Arch Fischerewiss, 37, 25 - 50.

Stein, M., 1988, Variation of geostrophic circulation off the Antarctic Peninsula and in the south west Scotia Sea, 1975 - 1985. In: Sahrhage, D. (ed.), Antarctic Ocean and Resources Variability. Springer-Verlag, Berlin, p. 81 - 91.

Stenni, B., Buiron, D., Frezzotti, M., Albani, S., Barbante, C., Bard, E., Barnola, J.M., Baroni, M., Baumgartner, M., Bonazza, M., Capron, E., Castellano, E., Chappellaz, J., Delmonte, B., Falourd, S., Genoni, L., Iacumin, P., Jouzel, J., Kipfstuhl, S., Landais, A., Lemieux-Dudon, B., Maggi, V., Masson-Delmotte, V., Mazzola, C., Minster, B., Montagnat, M., Mulvaney, R., Narcisi, B., Oerter, H., Parrenin, F., Petit, J.R., Ritz, C., Scarchilli, C., Schilt, A., Schüpbach, S., Schwander, J., Selmo, E., Severi, M., Stocker, T.F., and Udisti, R., 2010, Expression of the bipolar see-saw in Antarctic climate records during the last deglaciation. Nature geosciences, 4, 46 - 49.

Stickley, C.E., Pike, J., Leventer, A. Dunbar, R., Domack, E.W., Brachfeld, S. Manley, P., and McClennen, C., 2005, Deglacial ocean and climate seasonality in laminated diatom sediments, Mac.Robertson Shelf, Antarctica. Palaeogeography Palaeoclima tology Palaeoecology, 227, 290 - 310.

Stoermer, E.F. and Smol, J.P., 1999, The Diatoms: Applications for the Environmental and Earth Sciences. Cambridge University Press, Cambridge, 469 p.

Taylor, F., McMinn, A., and Franklin, D., 1997, Distribution of diatoms in surface sediments of Prydz Bay, Antarctica. Marine Micropaleontology, 32, 209 - 230.

Trouw, R.A.J., Passchier, C.W., Valeriano, C.M., Simoes, L.S., Paciullo, F.V.P., and Ribeiro, A., 2000, Deformational evolution of a Cretaceous subduction complex: Elephant Island, South Shetland Islands, Antarctica. Tectonophysics, 319, 93 - 110.

Vanderaveroet, P., Averbuch, O., Deconinck, J.-F., and Chamley, H., 1999, A record of glacialrinterglacial alternations in Pleistocene sediments off New Jersey expressed by clay mineral, grain-size and magnetic susceptibility data. Marine Geology, 159, 79 - 92.

Whitworth III, T., Nowlin Jr, W.D., Orsi, A.H., Locarnini, R.A., and Smith, S.G., 1994, Weddell Sea Shelf Water in the Bransfield Strait and Weddell-Scotia Confluence. Deep-Sea Research I, 41, 629 - 641.

Yoon, H.I., Yoo, K.-C., Bak, Y.-S., Lee, Y.I., and Lee, J.I., 2009, Corebased reconstruction of paleoenvironmental conditions in the southern Drake Passage (West Antarctica) over the last 150 ka. Geo-Marine Letters, 29, 309 - 320

Zielinski, U. and Gersonde, R., 1997, Diatom distribution in Southern Ocean surface sediments (Atlantic sector): implications for paleoenvironmental reconstructions. Palaeogeography Palaeoclimatology Palaeoecology, 129, 213 - 250.

Zhou, M., Zhu, Y., Dorland, R.D., and Measures, C.I., 2010, Dynamics of the current system in the southern Drake Passage. Deep-Sea Research I, 57, 1039 - 1048.

Table 1. Radiocarbon ages of the GC03-C2 core sediment

Depth (cm)	Lab code	^{14}C age[uc] (yr BP)	^{14}C age[c] (yr BP)	Materials
0	NZA21512	3573 ± 70	2413	Bulk sediment
70	NZA21513	6195 ± 85	5035	Bulk sediment
200	NZA21514	7227 ± 50	6067	Bulk sediment
320	NZA21515	9394 ± 40	8234	Bulk sediment
500	NZA21516	12296 ± 50	11136	Bulk sediment

[uc]uncorrected for reservoir effect; [c]corrected for reservoir effect.

Table 2. Age of selected diatom species from GC 03-C2

Datum	species	Age (Ma)	Reference
LO	*Actinocyclus ingens*	0.62	Kellogg & Kellogg, 1986
LO	*Denticulopsis hustedtii*	4.5	Ciesieiski, 1983
LCO	*D.dimorpha*	10.1	Baldauf & Barron, 1991
LO	*D. praedimorpha*	10.5	Ciesieiski, 1983
FO	*D.dimorpha*	11.9 (12.2)	Baldauf & Barron, 1991
FO	*D. praedimorpha*	12.6	Gersonde & Burckle, 1990
FO	*D. hustedtii*	14.2	Gersonde & Burckle, 1990

FO: first occurrence, LO: last occurrence, LCO: last common occurrence.

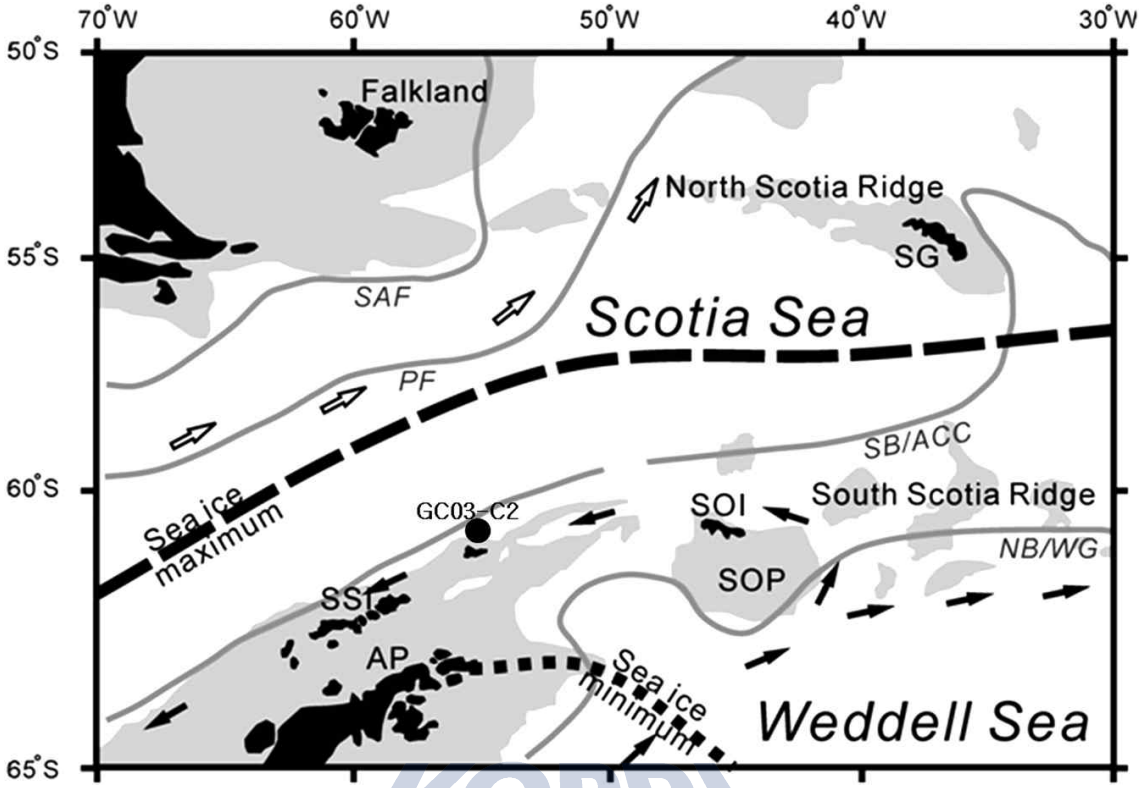

Figure 1. Location of the GC03-C2 core. Gray lines indicate fronts and boundaries of the ocean current systems: SAF, Sub-Antarctic Front; PF, Polar Front; SB/ACC, southern boundary of the ACC; NB/WG, northern boundary of the Weddell Gyre (Orsi et al., 1993, 1995; Whitworth et al., 1994).

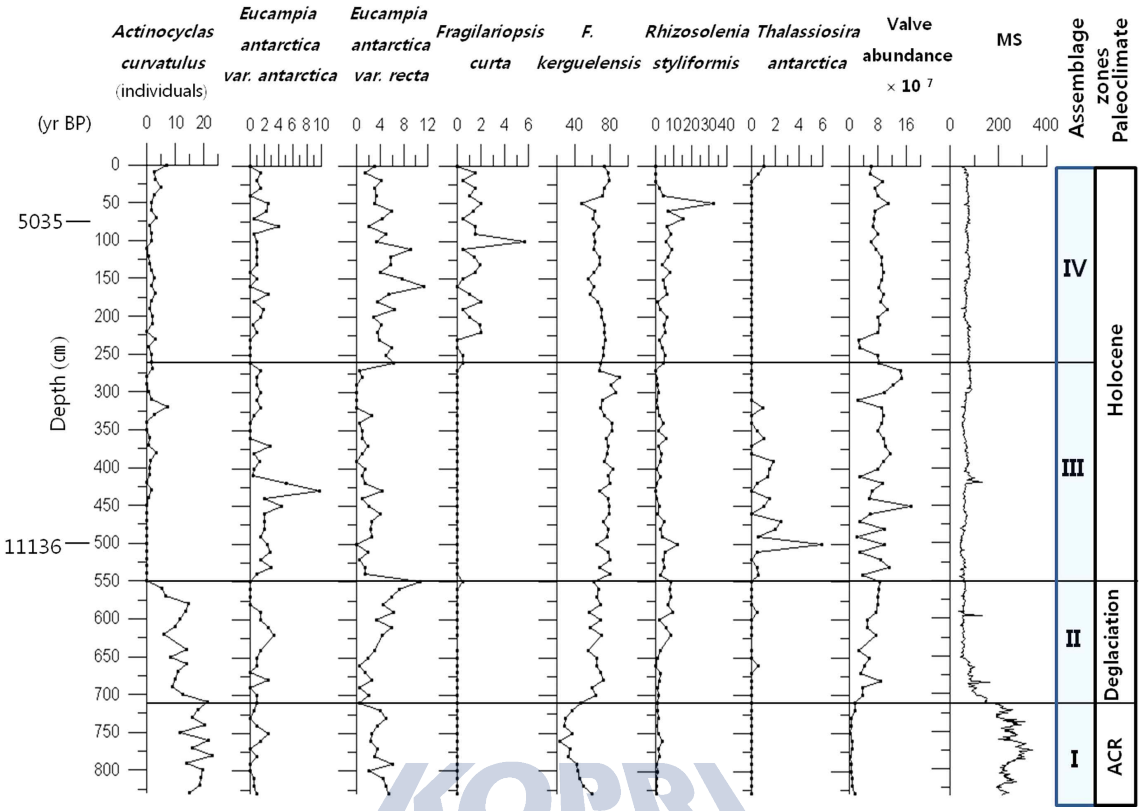

Figure 2. Assemblage zones and vertical distribution of selected indicators from GC03-C2. ACR; Antarctic Cold Reversal (Stenni et al., 2010).

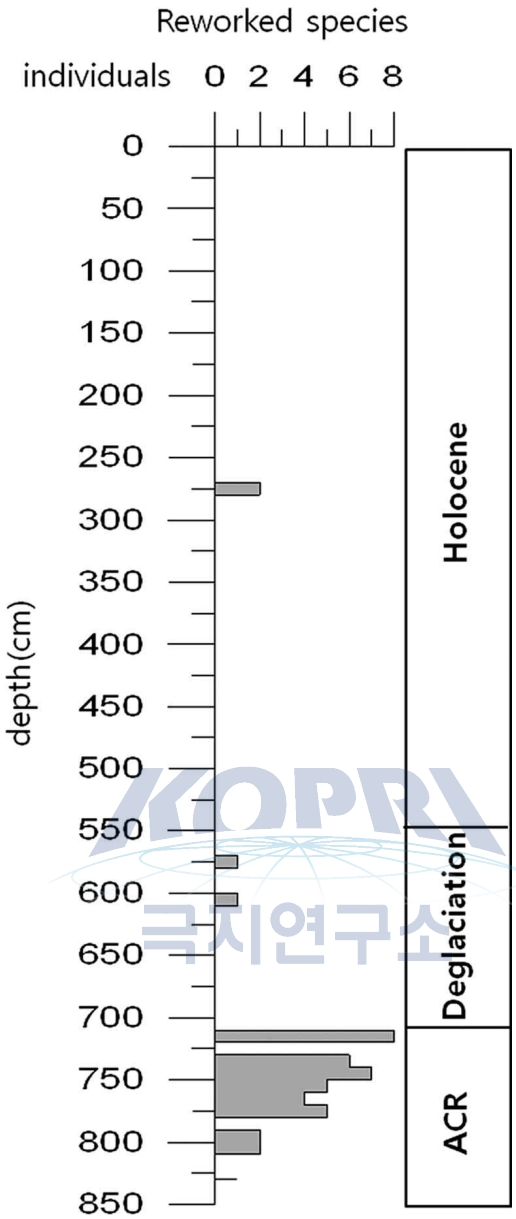

Figure 3. Summary of reworked diatoms present in core GC03-C2.

제 11 장

Geochemical characteristics of meltwater and pondwater on Barton and Weaver Peninsulas of King George Island, West Antarctica[6)]

Jin-Yong Lee[1], Ho Il Yoon[2]

[1]Kangwon National University
[2]Korea Polar Research Institute

Abstract: In Antarctica, the geochemical properties of meltwater and pondwater are very sensitive to global warming. Therefore, understanding the geochemical properties of the meltwater and pondwater is crucial to evaluating global climate change. This study was performed to examine the chemical and isotopic compositions of the meltwater and pondwater at the Barton and Weaver Peninsulas of King George Island, Antarctica, to understand their spatial variation and to evaluate factors controlling the surface water chemistry. The meltwater, pondwater and seawater were sampled at 50 sites of the Barton and Weaver Peninsulas during the period from 23 December 2010 to 5 January 2011. The chemical compositions of the meltwater and pondwater were mainly influenced by sea salt. Additionally, the influence of water-rock interaction was observed in some meltwater and pondwater. The LREE/HREE ratios of some of the pondwater in the Barton Peninsula showed a decreasing trend by influence of water-rock interaction. The influences of sea salt and water-rock interaction were more dominant at the Barton Peninsula than the Weaver Peninsula. The $\delta^{18}O$ and δD of the meltwater and pondwater showed a wide range. Little evaporation losses were observed at the Barton Peninsula but evaporation losses did not occurred at the Weaver Peninsula.

6) 이 연구 결과는 다음의 논문으로 출판되었음: Lim, H. S., Park, Y., Lee, J. Y., & Yoon, H. I. (2014). Geochemical characteristics of meltwater and pondwater on Barton and Weaver Peninsulas of King George Island, West Antarctica. Geochemical Journal, 48(4), 409-422.

1. Introduction

The Antarctic environment is highly sensitive to global warming because of the extreme cold (Knap et al.,1996). Most climate change models predicted that the climate of Antarctica will become warmer and wetter (IPCC, 2001; SCAR, 2009). Recently, ice-free regions in summer have been rapidly expanding in Antarctica due to global warming (Vaughan et al., 2001). Additionally, the collapse of ice shelves and retreat of glacier have occasionally been observed (Vaughan and Doake, 1996; Parket al., 1998). Thus, the monitoring of these environmental changes is important because it is one of the methods used to evaluate global climate change. For this reason, research on monitoring environmental changes has been actively conducted in Antarctica (Knap et al., 1996; King and Turner, 1997; Quayle et al., 2002; Kejna et al., 2013).

The meltwater (MW) and pondwater (PW) in Antarctica are mainly distributed in periglacial environments, where environmental changes due to global warming can be relatively easily observed compared with in other environments. It has been found that the chemical compositions of MW and PW are mainly controlled by precipitation, sea salt and weathering and are not significantly influenced by anthropogenic factors (Brown, 2002; Borghini and Bargagli, 2004; Hodson et al., 2010; Stumpfet al., 2012). However, the contamination due to heavy metals and organic matters has been reported in some regions, mainly around scientific stations after International Geophysical Year (1957~1958) (Santos et al., 2005; Caiet al., 2012).

The influence of sea salt on MW and PW is significant in the coastal regions of Antarctica because of strong winds (Wagenbach et al., 1998; Kerminen et al., 2000). The concentrations of Na^+, Cl^- and SO_4^{2-} in MW and PW in the coastal regions were found to be higher than those in inland (Kerminen et al., 2000; Aristarain and Delmas,2002). Additionally, the Cl^-/Na^+ ratios of snow, streams (MW) and lakes (PW) at the inland stations were found to be lower than those in coastal regions (Wagenbach et al., 1998; Kerminen et al., 2000). Therefore, the concentrations of Na^+, Cl^- and SO_4^{2-} and Cl^-/Na^+ ratios are used in many areas including Antarctica to evaluate influence of sea salt.

The chemical weathering in Antarctica has been actively discussed to this day. It is generally known that little chemical weathering has occurred in Antarctica (Lee et al., 2004; Santos et al., 2007). Chemical weathering was mainly observed in periglacial environments (Levyet al., 2011). The ionic concentrations, including dissolved silica, gradually increase along flow path of stream water. Therefore, these trends have been used with evidenceof chemical weathering (Stumpf et al., 2012). In addition, the dissolution of carbonate minerals and the oxidation of sulfide minerals were observed near hydrothermally altered regions of West Antarctica (Jeong, 2003). Nevertheless, the sources of dissolved components in MW and PW are unclear because the fractionation of components in minerals or whole rocks, such as Ca^{2+}, Mg^{2+}, Na^{+} and rare earth elements (REE), are induced during water-rock interaction (Webster et al., 1994; Ji et al., 2004).

This study was performed at the Barton and Weaver Peninsulas of King George Island (KGI), West Antarctica. The response to environmental change around KGI has been rapid because the island is located in the marginal area of West Antarctica and the access to KGI is easier than other regions. Therefore, numerous studies in various fields such as environmental change, the petrogenesis of volcanic rocks, soil formation, sedimentation in coastal environments, the isotopic compositions of seawater and dry deposition have been conducted (Khim et al., 1997; Park et al., 1998; Lee et al., 2004; Yeo et al., 2004; Santos et al., 2007; Leal et al., 2008). However, there has been little work on the geochemical properties of MW and PW at the Barton and Weaver Peninsulas. The chemical and isotopic compositions of MW and PW can demonstrate hydrogeological processes such as water-rock interaction, dilution and evaporation. Therefore, this study was executed to examine the chemical and isotopic compositions of MW and PW, to understand their spatial variations and to evaluate factors control-ling the water chemistry. The results of this study may further understanding of the hydrogeological processes in the Antarctic environment, and the results can be used as basic data to assess environmental changes in Antarctica.

2. Study Area

2.1. Natural environments

KGI is located in the South Shetland Islands, West Antarctica (Fig. 1). Its surface area is approximately 1,310 km^2. The fjord morphology of areas such as the Admiralty and Maxwell bays and the Marian Cove has been developed by glaciers (Chang et al., 2003; Santos et al., 2007). The approximately 92% of KGI is covered with glaciers, which have a maximum thickness of 395 m (Lealet al., 2008). However, retreat of glacier rapidly occurs because of climate change (Park et al., 1998). The mean annual temperature shows the increasing trend of 0.02°C/year during the past several decades, (Kejna et al., 2013). This trend was significantly observed in winter, 0.04°C/year compared with summer (Ferron et al., 2004). The annual precipitation is approximately 500 mm, and slightly decreased by 48.7 mm in 1996 compared with the average of the annual precipitation occurred during the period from 1978 to 1989 (Kejna and Láska, 1999). Then, the snow cover depth ranges 2~73 cm (Kejna and Láska, 1999), and snow mainly melts in summer (November to March) (Wen et al., 1998). The Barton and Weaver Peninsulas are located in the southwestern areas of KGI. The southwestern coastal areas of the Barton and Weaver Peninsulas in summer season from December to February are ice-free. MW and PW are densely distributed in coastal areas compared with those in inland areas (Fig. 1). At the Barton Peninsula, it is known that the active layer depth was approximately 1 m and that permafrost is present below the active layer (Jeong and Yoon, 2001; Lee et al., 2004). According to climatic data collected at the King Sejong Station in the Barton Peninsula from 1988 to 1996, the Barton Peninsula is warm, wet and windy, with an average annual temperature, relative humidity, precipitation and wind velocity of -1.8°C, 89%, 438 mm and 7.9 m/s, respectively, with winds predominantly from the NW and SW (Lee et al., 1997).

2.2. General geology

The Barton and Weaver Peninsulas consist mainly of lavas, pyroclastics and

Paleocene to Eocene hypabyssal and plutonic rocks. The lowermost Sejong Formation is distributed along the southern and southwestern coastal area of the Barton Peninsula and is widespread in the central part of the Weaver Peninsula. The Sejong Formation consists of mostly volcaniclastic sediments. Additionally, plant fossils have been observed in the fine-grained sand-stone of the Sejong Formation (Yeo et al., 2004). Most volcanic rocks over the Sejong Formation are widely distributed in the Barton Peninsula. Ancient volcanic centers remain with nunataks (Barton, 1965). The volcanic rocks consist of several units ranging from basalt to andesite. Lapilli tuffs are inserted in the volcanic rocks (Yeo et al.,2004). Granodiorite is exposed in the southwestern region of Noel Hill. Hydrothermal alteration is observed at the boundary between the volcanic rock and the granodiorite in the central part of the Barton Peninsula(Lee et al., 2004; Hwang et al., 2011). The altered volcanic rocks contain various secondary minerals, such as hornblende, actinolite, epidote, chlorite, calcite, hematite, ilmenite and pyrite. The pyrite of these minerals has also been observed in fresh volcanic rocks (Hwang et al., 2011). Additionally, various metamorphic minerals, such as quartz, pyrite, illite and kaolinite, have been observed in hydrothermally altered rocks (Jeong, 2003). Pyrite is especially abundant, and most are highly altered (Jeong, 2003).

3. Method

MW, PW and seawater were sampled from 23 December 2010 to 5 January 2011 at the Barton (38 ea) and Weaver (12 ea) Peninsulas. The collected samples were filtered with a 0.45 μm micropore membrane filter, and part of each filtered sample was acidified with HNO_3 (to approximately pH = 2). All samples were refrigerated for later analysis. The water temperature, pH and electric conductivity (EC) of the samples were measured on site. The dissolved carbon species were calculated from the alkalinity, which was measured according to the Gran method (Wetzel and Likens, 1991), which assumes that dissolved carbon species mainly contribute to the alkalinity. Major cations (Ca^{2+}, Mg^{2+}, Na^{+} and K^{+}) and anions (Cl^{-}, NO_3^{-} and SO_4^{2-}) were analyzed using ICP-AES and IC, respectively, at the Sangji University. Rare earth elements

(REEs) were analyzed at the Seoul Center of the Korea Basic Science Institute (KBSI). The data quality was evaluated using charge balance. In this study, data showing a charge balance below 30% were used. Oxygen and hydrogen isotopic compositions of samples were analyzed using IRMS at the Ochang Center of KBSI. The analyzed data were reported by δ notation relative to the Vienna Standard Mean Ocean Water (VSMOW). The analytical reproducibility of the $\delta^{18}O$ and δD was ±0.1 and ±1‰, respectively.

4. Results and Discussion

4.1.. Chemical properties

Table 1 shows the water temperature, pH and EC of MW and PW at the Barton and Weaver Peninsulas. The ambient air temperature was well reflected by the water temperature of the MW and PW. The water temperature of the PW was typically higher than that of the MW. At the Barton Peninsula, the pH and EC of the MW ranged 4.38~8.80 and 32.6~390 μS/cm, respectively, and those of the PW ranged 5.00~7.47 and 33.2~27,900 μS/cm, respectively. The variation of the pH and EC in the MW were significantly distinguished from those of the PW. However, the EC of the PW had a range of 33.2~432 μS/cm in most samples (except MW-4 and MW-23), which is slightly high compared with the MW. The EC was especially high at MW-4 (8,730 μS/cm) and MW-23 (27,900μS/cm). At the Weaver Peninsula, the pH and EC of the MW showed ranges of 5.11~5.78 and 42.1~98.4 μS/cm, respectively, and those of the PW had ranges of 4.98~5.79 and 69.1~196 μS/cm, respectively. In total, the variation ranges of the pH and EC at the Weaver Peninsula were narrow compared with those of the Barton Peninsula. The pH of the MW was not distinguished from that of the PW. The EC of the MW was relatively low compared with that of the PW.

The chemical compositions of the MW and PW at the Barton and Weaver Peninsulas are also summarized in Table 1. The values of the standard deviation for each ion showed very wide ranges of 0~1,057. These results are attributed to the vertical and spatial inhomogeneity of snow and glaciers

(Maupetit and Delmas, 1992; Fortner et al., 2009). The concentrations of most ions of the PW at the Barton Peninsula were higher than those at the MW, as was especially clear in the Mg^{2+}, Na^{+}, K^{+} and Cl^{-}. The average concentrations of Mg^{2+}, Na^{+}, K^{+} and Cl^{-} in the PW were higher by approximately 77, 62, 25 and 30 times, respectively, compared with those in the MW. These ions may mainly come from sea salt. The concentrations of Mg^{2+}, Na^{+}, Cl^{-} and SO_4^{2-} in the snow sampled at coastal regions of Antarctica were higher than those inland (Aristarain and Delmas, 2002). Additionally, the average concentrations of Ca^{2+}, SO_4^{2-}, HCO_3^{-} and H_4SiO_4 in the PW were higher by approximately 3.4, 9.8, 1.4 and 1.5 times, respectively, than those in the MW. These ions are associated with water-rock interaction between carbonate, sulfide and silicate minerals and surface water (Caulkett and Ellis-Evans, 1997; Borghini and Bargagli, 2004; Grasby et al., 2010; Stumpf et al., 2012). Therefore, the influence of sea salt and chemical weathering may be more dominant in the PW than in the MW.

At the Weaver Peninsula, the chemical compositions of the MW and PW did not show difference as large as at the Barton Peninsula. While the average concentrations of Mg^{2+}, Na^{+} and Cl^{-} in the PW increased by approximately 3.4, 2.1 and 1.5 times, respectively, compared with those in the MW, those of Ca2+, $SO4_2^{-}$ and HCO_3^{-} in the MW increased by approximately 1.1, 1.3 and 1.2 times, respectively, compared with those of the PW. In addition, the average concentration of H_4SiO_4 of the PW was 0.57, but that of the MW did not detected. These results indicate that the influences of sea salt and chemical weathering at the Weaver Peninsula were small compared with those at the Barton Peninsula because of the high altitude and steep slope at the Weaver Peninsula.

The chemical compositions of all samples were plotted on a piper diagram (Fig. 2). The MW was not distinguished from the PW at the Barton and Weaver Peninsulas, respectively. However, the contributions of SO_4^{2-} of the MW and PW at the Barton Peninsula were higher than those at the Weaver Peninsula. These results may be attributed to the influence of alteration of sulfide minerals at the geothermal alterations area of the Barton Peninsula. Most samples were plotted on the area of the Ca - Cl type. MW-4 and MW-23 showing high EC levels wereplotted near the seawater. The typical fresh water

generally shows Na - HCO_3 or Ca - HCO_3 types in the volcanic rock area. However, fresh water affected by sea salt or seawater in a coastal region can be changed to Ca - Cl or Na - Cl types (El Yaouti et al., 2009). Therefore, these results indicate that the MW and PW may be influenced by sea salt.

4.2.. Rare earth element chemistry

Table 2 shows the concentrations of REEs in the MW and PW at the Barton and Weaver Peninsulas. The standard deviation for concentrations of REEs has wide range from 0.001 to 2.001, which is attributed to vertical and spatial inhomogeneity of REEs of snow and glacier (Boryet al., 2010). At the Barton Peninsula, the average concentrations of REEs of the PW were higher than those of the MW. Ce and Nd were dominant in the MW and PW. Ho, Tm and Lu were not detected in the MW. At the Weaver Peninsula, contrary to the Barton Peninsula, the average concentrations of REEs of the MW at the Weaver Peninsula were higher than those of the PW. Additionally, Eu, Tb Ho, Er, Tm, Yb and Lu of the MW and PW were not detected. These results indicate that the contributions of the factors controlling the REE levels such as aerosol are different, and the influence of aerosol was predominant in samples at the PW of the Barton Peninsula among the sampling sites. It is known that snow, glacier and surface water at KGI were affected by aerosol from marine spray, particles by weathering and anthropogenic materials occurred around scientific stations (Santos et al., 2005; Leal et al., 2008), and aerosol such as mineral particles can be one of REEs sources in the coastal areas (Bory et al., 2010). To clearly understand the reasons for these results, additional research on the source identification of the REEs is necessary.

The Ce, Nd, La and Pr of the total REEs of the MW and PW at the Barton Peninsula were 93.7 and 84.5%, respectively, and those of the total REEs of the MW and PW at the Weaver Peninsula were 95.7 and 95.8%, respectively. These results are due to the absence or very low concentrations of heavy REEs (Gd, Tb, Dy, Ho, Er, Tm, Yb and Lu), in addition to Gd and Dy, at the Weaver Peninsula (Table 2).

4.3. Oxygen and hydrogen isotopic composition

Figure 3 shows that the $\delta^{18}O$ and δD of the MW and PW of the Barton and Weaver Peninsulas did not exhibit mixing trend with seawater. This result indicates that all MW and PW were not directly influenced by seawater. At the Barton Peninsula, the $\delta^{18}O$ and δD of the MW had ranges of −14.8~−9.0 and −111~−70‰, respectively, and those of the PW had ranges of −13.2~−8.8 and −101~−66‰, respectively. The $\delta^{18}O$ and δD of the MW and PW showed a wide variation range. These results are due to vertical and spatial inhomogeneity of snow and glaciers (Simões et al., 2004; Wang et al., 2010). The $\delta^{18}O$ andδD of the PW were slightly enriched compared with those of the MW. Additionally, the regression lines for the MW and PW were $\delta D = 7.23\delta^{18}O - 4.26$ ($n = 23$, $r^2 = 0.99$) and $\delta D = 7.76\delta^{18}O + 0.72$ ($n = 13$, $r^2 = 0.99$), respectively. The slopes of the regression lines were somewhat different compared with the slopes of the global meteoric water line (GMWL; $\delta D = 8\delta^{18}O + 10$) (Craig, 1961) and the local meteoric water line of precipitation at Frei Station of KGI ($\delta D = 7.1\delta^{18}O - 2.2$) (Simões et al., 2004).

At the Weaver Peninsula, the $\delta^{18}O$ and δD of the MW had ranges of −12.5~−10.2 and −96~−78‰, respectively, and those of the PW had ranges of −14.3~−10.2 and −112~−79‰, respectively. The $\delta^{18}O$ and δD were slightly depleted and showed narrow variation ranges compared with those of the Barton Peninsula. In addition, the regression lines for the MW and PW were $\delta D = 8.18\ \delta^{18}O + 5.34$ ($n = 5$, $r^2 = 0.99$) and $\delta D = 8.02\delta^{18}O + 3.28$ ($n = 6$, $r^2 = 0.99$), respectively. The slopes of the regression lineswere similar to those of GMWL, but showed large values compared with those at the Barton Peninsula. These results suggest that the MW and PW at the Barton Peninsula may undergo little evaporation losses because the MW and PW at the Barton Peninsula were plotted near the GMWL. However, the MW and PW at the Weaver Peninsula did not undergo the evaporation losses.

4.4. Influence of sea salt

The MW and PW of the coastal regions of Antarctica can be generally influenced by sea salt transported by strong winds (Hall and Wolff, 1998). To assess the influence of sea salt on the MW and PW, MW-43 and MW-44 were considered with the end-member of MW uncontaminated by sea salt. The sampling sites of these end-members are located inland of the Barton Peninsula, and they showed very low EC levels (33 and 37 μS/cm, respectively).

Figure 4 shows the relationship between the ECs and major ions. In Fig. 4, the dotted lines represent hypothetical mixing lines for each ion. Most major ions, except HCO_3^- of MW-4 and MW-23 with high EC levels (8,730 and 27,900 μS/cm, respectively), showed a thorough mixing trend between the freshwater and seawater. The influence of seawater was significantly observed at the MW-4 and MW-23. The Mg^{2+}, Cl^- and SO_4^{2-} of many of the samples were plotted around hypothetical lines of the mixing trend. These trends were more dominant at theBarton Peninsula than those at the Weaver Peninsula. Cl^- and SO_4^{2-} were mainly supplied from sea salt in the coastal areas (Kerminen et al., 2000; Aristarain and Delmas, 2002). However, Ca^{2+}, some of Mg^{2+}, Na^+ and HCO_3^- did not show significant mixing trends. These results indicate that sea salt is not main factor supplying Ca^{2+}, some Mg^{2+}, Na^+ and HCO_3^-. It is known that Ca^{2+}, Mg^{2+} and HCO_3^- are associated with the dissolution of carbonate minerals. The water-rock interaction will be explained in next section.

Generally, the ionic ratios of major ions have been used to identify sources because the ratios are conservative parameters (Hall and Wolff, 1998; Borghini and Bargagli, 2004). Figure 5 shows the ionic ratios of the MW and PW at the Barton and Weaver Peninsulas. The Ca^{2+}/Cl^- (1.203), SO_4^{2-}/Cl^- (0.868) and HCO_3^-/Cl^- ratios (0.798) of the end-member were higher than the Ca^{2+}/Cl^- (0.015), SO_4^{2-}/Cl^- (0.128) and HCO_3^-/Cl^- ratios (0.004) of the seawater. The Na^+/Cl^- (0.275) and Mg^{2+}/Cl^- ratios (0.012) of the end-member were lower than the Na^+/Cl^- (0.431) and Mg^{2+}/Cl^- ratios (0.042) of the seawater. If sea salt and glaciers were the main factors controlling the chemistry of the MW and PW, all samples should be distributed between the end-member of the freshwater and the seawater. Most samples from the Weaver Peninsula were distributed in the mixing area between two end-members, but some samples from the Barton Peninsula were distributed

outside of mixing areas. These trends are distinctly shown in the SO_4^{2-}/Cl^- ratios of the samples from the Barton Peninsula. These results indicate that the chemistry of the MW and PW at the Weaver Peninsula is greatly influenced by sea salt. However, the chemistry of the MW and PW at the Barton Peninsula is mainly controlled by sea salt and is only slightly influenced by other factors, which may be the water-rock interaction and dry depositions. An additional study on sources of dissolved components in the MW and PW will be necessary to clearly understand them.

According to previous works (e.g., Borghini and Bargagli, 2004), Na^+/Cl^- ratios show a positive relation with distance from the coast line because sea salt is mainly transported by wind. However, these trends were not obviously observed in this study because the study area is small, and most sampling sites are influenced by wind. Therefore, the influence of sea salt on the MW and PW may be controlled more by the exposure time to air than by wind in the study area.

4.5. Evaluation of the water-rock interaction

According to the previous works, there has been little chemical weathering in the Barton Peninsula (Lee et al., 2004), and the clay minerals in the soil were mainly formed by the glacial erosion of rocks (Jeong et al., 2004). However, chemical weathering evidence such as carbonate mineral dissolution and the alteration of plagioclase, in thin sections (Jeong, 2003). Therefore, this study evaluated of the water-rock interaction using the chemical compositions of the rock, soil and surface water (MW and PW). Figure 6 shows the chemical compositions of the basaltic andesite (data from Yeo et al., 2004) and the soils on the basaltic andesite (data from Lee et al., 2004) at the Barton Peninsula. The average concentrations of Ca, Mg, Na and K were 4.21, 2.88, 2.72 and 1.24%, respectively, in the soils and 8.19, 4.05, 3.28 and 0.76%, respectively, in the rocks. The concentrations of the Ca, Mg and Na of the soils were lower than those of the rocks. This result may be associated with carbonate mineral dissolution and alteration of silicate minerals (Tranter et al., 2002; Wadham et al., 2007). However, the K concentrations ofthe soils were higher than those of

the rocks, which maybe attributable to the accumulation of K^+ from sea salt. Additionally, Jeong (2003) did not observe the alterationof K-feldspar in the bedrocks of the Barton Peninsula. Additionally, H_4SiO_4 concentrations were very low (0.37~9.07 mg/L), which indicates that the alteration of silicate minerals did not occur actively. Therefore, the influence of the water-rock interaction on the MW and PW was evaluated using the Mg/Ca and Mg/Na of the MW, PW, seawater, soils and rocks. In Fig. 7, the Mg/Ca and Mg/Na of end-member of the MW were relatively low compared with those of the seawater, soils and rocks. Additionally, the Mg/Na of seawater was relatively low compared with that of the soils and rocks because Na^+ is more abundant in the seawater than in the soils and rocks. Therefore, if the influence of sea salt increases gradually, the Mg/Ca of the MW and PW will show a gradually increasing trend. In addition, if the influence of the water-rock interaction increases gradually, the Mg/Na and Mg/Ca of the MW and PW will have a gradually increasing trend together. Figure 7 shows that the MW and PW chemistry was controlled by sea salt and the water-rock interaction. The water-rock interaction dominantly occurred in the PW of the Barton Peninsula.

In Fig. 8, the heavy REEs (HREEs) and light REEs (LREEs) represent La and Nd and Gd and Yb, respectively. The LREE/HREE ratios of the seawater rangedfrom 16.1 to 24.0 and those of the soils and rocks ranged from 3.07 to 7.40. Most samples are plotted near the seawater or above (Fig. 8). Additionally, REE mobility is mostly influenced by weathering condition and stability of mineral bearing REE (Aubert et al., 2001). Therefore, REEs of the MW and PW may be mainly supplied from sea salt rather than water-rock interaction. However, the LREE/HREE ratios of some of the samples from the Barton Peninsula were lower than those of the seawater, perhaps due to the influence of the water-rock interaction. These ratios were especially low in MW-24 (5.43) and MW-48 (11.1).

5. Conclusions

In this study, the geochemical properties of the MW and PW at the Barton and Weaver Peninsulas were demonstrated, and the water-rock interaction was evaluated using Mg/Ca, Mg/Na and REEs. The MW and PW at the Barton and Weaver Peninsulas showed the Ca - Cl type by the influence of sea salt. The influence of sea salt was more obvious in the PW than in the MW and at the Barton Peninsula compared with the Weaver Peninsula. However, some of the Ca^{2+}, Mg^{2+}, Na^{+}, SO_4^{2-}, HCO_3^{-} and REEs may be released by the water-rock interaction. According to previous works, the water-rock interaction does not occur significantly at KGI, and the soils were mainly formed by glacial erosion. Additionally, there has been little research on the water-rock interaction in the MW and PW at the Barton and Weaver Peninsulas. However, some of the Ca^{2+}, Mg^{2+} and Na^{+} in the MW and PW are controlled by sea salt and the water-rock interaction, including carbonate mineral dissolution and the alteration of sulfate minerals. Additionally, REEs of some PW (MW-24 and MW-48) at the Barton Peninsula were influenced by the water-rock interaction. The water-rock interaction was more distinctly observed at the Barton Peninsula than the Weaver Peninsula. However, the water-rock interaction was not the main factor controlling the surface water chemistry at the Barton and Weaver Peninsulas. The $\delta^{18}O$ and δD of the MW and PW showed a wide range because of the inhomogeneity of the glacier and snow. The MW and PW of the Barton Peninsula underwent evaporation losses but those of the Weaver Peninsula did not undergo.

서남극 킹조지 섬 바톤 반도와 위버 반도의 융빙수와 연못물의 지화학적 특성

이진용[1], 윤호일[2]

[1]강원대학교, [2]한국해양과학기술원 부설 극지연구소

요약: 남극에서 융빙수와 연못물의 지화학적 특성은 지구 온난화에 매우 민감하다. 그러므로 융빙수와 연못물의 지화학적 특성을 이해하는 것은 전지구적 기후 변화를 평가하는 데 중요하다. 이 연구는 표층수의 화학을 조절하는 요인을 찾고 공간적인 변동을 이해하기 위해 남극 킹 조지 섬의 바턴 반도와 위버 반도의 융빙수와 연못물의 화학적 및 동위원소 조성을 조사를 수행하였다. 2010년 12 월 23 일부터 2011년 1 월 5 일까지 바턴 반도와 위버 반도에서 50 개 지점에서 융빙수, 연못물 및 해수를 획득했다. 게다가, 물-암석 상호 작용의 영향은 일부 융빙수 및 연못물에서 관찰되었다. 바턴 반도의 일부 연못물의 LREE/HREE 비는 물-암석 상호 작용의 영향으로 감소하는 경향을 보였다. 해염과 물-암석 상호 작용의 영향은 바턴 반도에서 위버 반도보다 더 지배적이었다. 융빙수와 연못물의 δ18O와 δD는 넓은 값의 범위를 보였다. 바턴 반도에서는 약간의 증발 손실이 관찰되었지만, 위버 반도에서는 증발 손실이 발생하지 않았다.

참고문헌

Aristarain, A. J. and Delmas, R. J. (2002) Snow chemistry measurements on James Ross Island (Antarctic Peninsula) showing sea-salt aerosol modification. Atmos. Environ. 36, 765 - 772.

Aubert, D., Stille, P. and Probst, A. (2001) REE fraction during granite weathering and removal by waters and suspended load: Sr and Nd isotope evidence. Geochim. Cosmochim. Acta 65, 387 - 406.

Barton, C. M. (1965) The geology of the South Shetland Is-lands: III. The stratigraphy of King George Island. British Antarctic Survey Scientific Report 44, 33 pp.

Borghini, F. and Bargagli, R. (2004) Change of major ion concentrations in melting snow and terrestrial waters from northern Victoria Land, Antarctica. Antarctic Sci. 16, 107 - 115.

Bory, A., Wolff, E., Mulvaney, R., Jagoutz, E., Wegner, A., Ruth, R. and Eldefield, H. (2010) Multiple sources supply eolian mineral dust to the Atlantic sector of coastal Antarctica: Evidence from recent snow layers at the top of Berkner Island ice sheet. Earth Planet. Sci. Lett. 291, 138 - 148.

Brown, G. H. (2002) Glacier meltwater hydrochemistry. Appl. Geochem. 17, 855 - 883.

Cai, M., Yang, H., Xie, Z., Zhao, Z., Wang, F., Lu, Z., Sturm, R. and Ebinghaus, R. (2012) Per- and polyfluoroalkyl substances in snow, lake, surface runoff water and coastal seawater in Fildes Peninsula, King George Island, Antarctica. J. Hazard. Mater. 209 - 210, 335 - 342.

Caulkett, A. P. and Ellis-Evans, J. C. (1997) Chemistry of streams of Signy Island, maritime Antarctic: sources of major ions. Antarctic Sci. 9, 3 - 11.

Chang, S. K., Lee, J. I., Choe, M. Y. and Hur, S. D. (2003) Geology around the King Sejong Station, King George Island off the Antarctic Peninsula. J. Geol. Soc. Korea 39,271 - 286 (in Korean with English abstract).

Craig, H. (1961) Isotopic variations in meteoric waters. Science 133, 1702 - 1703.

El Yaouti, F., El Mandour, A., Khattach, D., Benavente, J. and Kaufmann, O.

(2009) Salinization processes in the unconfined aquifer of Bou-Areg (NE Morocco): A geostatistical, geochemical and tomographic study. Appl. Geochem. 24, 16 - 31.

Ferron, F. A., Simões, J. C., Aquino, F. E. and Setzer, A. W.(2004) Air temperature time series for King George Island, Antarctica. Pesqisa Antártica Brasileira 4, 155 - 169.

Fortner, S. K., Lyons, W. B., Fountain, A. G., Welch, K. A. and Kehrwald, N. M. (2009) Trace element and major ion concentrations and dynamics in glacier snow and melt: Eliot Glacier, Oregon Cascades. Hydrol. Processes 23, 2987 - 2996.

Grasby, S. E., Osborn, J., Chen, Z. and Wozniak, P. R. J. (2010) Influence of till provenance on regional groundwater geochemisty. Chem. Geol. 273, 225 - 237.

Hall, J. S. and Wolff, E. W. (1998) Causes of seasonal and daily variations in aerosol sea-salt concentrations at a coastal Antarctic station. Atmos. Environ. 32, 3669 - 3677.

Hodson, A., Heaton, T., Langford, H. and Newsham, K. (2010) Chemical weathering and solute exprt by meltwater in a maritime Antarctic glacier basin. Biogeochemistry 98, 9 - 27.

Hwang, J., Xiangshen, Z., Ripley, E. M., Lee, J. I. and Shin, D.(2011) Isotope geochemistry of volcanic rocks from the Barton Peninsula, King George Island, Antarctica. J. Earth Sci. 22, 40 - 51.

IPCC (2001) Climate Change 2001: Impacts, Adaptation, and Vulnerability. Cambridge Univ. Press, 1031 pp.

Jeong, G. Y. (2003) Chemical weathering of glacial debris of the Barton Peninsula of King George Island, South Shetland Island, Antarctica: Microtextural evidences. J. Mineral. Soc. Korea 16, 181 - 189 (in Korean with English abstract).

Jeong, G. Y. and Yoon, H. I. (2001) The origin of clay minerals in soils of King George Island, South Shetland Island, West Antarctica, and its implications for the clay mineral com-positions of marine sediment. J. Sedimentary Res. 71, 833 - 842.

Jeong, G. Y., Yoon, H. I. and Lee, S. Y. (2004) Chemistry and microstructures

of clay particles in smectite-rich shelf sediment, South Shetland Islands, Antarctica. Mar. Geol. 209,19 - 30.

Ji, H., Wang, S., Quyang, Z., Zhang, S., Sun, C., Liu, X. and Zhou, D. (2004) Geochemistry of red residua underlying dolomites in karst terrains of Yunnan - Guizhou Plateau II.The mobility of rare earth elements during weathering. Chem. Geol. 203, 29 - 50.

Kejna, M. and Láska, K. (1999) Weather conditions at Arctowski Station, King George Island, South Shetland Islands, Antarctica in 1996. Pol. Polar Res. 20, 203 - 220.

Kejna, M., Ara´zny, A. and Sobota, I. (2013) Climate change on King George Island in the years 1948 - 2011. Pol. Polar Res.34, 213 - 235.

Kermimen, V. M., Teinila, K. and Hillamo, R. (2000) Chemistry of sea-salt particles in the summer Antarctic atmosphere. Atmos. Environ. 34, 2817 - 2825.

Khim, B. K., Park, B, K. and Yoon, H. I. (1997) Oxygen isotopic compositions of seawater in the Maxwell Bay of King George Island, West Antarctica. Geosci. J. 1, 115 - 121.

King, J. C. and Turner, J. (1997) Antarctic Meteorology and Climatology. Cambridge Univ. Press, 409 pp.

Knap, W. H., Oerlemans, J. and Grdée, M. (1996) Climate sensitivity of the ice cap of King George Island, South Shetland Islands, Antarctica. Ann. Glaciol. 23, 154 - 159.

Leal, M. A., Joppert, M., Licínio, M. V., Evangelista, H., Maldonado, J., Dalia, K. C., Lima, C., Barros Leite, C. V.,Correa, S. M., Geiza Medeiros and Dias da Cunha, K. (2008) Atmospheric impacts due to anthropogenic activities in remote area: The cast study of Admiralty Bay/King George Island/Antarctic Peninsula. Water Air Soil Pollut. 188, 67 - 80.

Lee, B. Y., Won, Y. and Oh, S. N. (1997) Meteorological characteristics at King Sejong Station, Antarctica (1988 - 1996). Report BSPE 97604-00-1020-7, Korea Ocean Research and Development Institute, 517 - 599.

Lee, Y. I., Lim, H. S. and Yoon, H. I. (2004) Geochemistry of soils of King George Island, South Shetland Island, West Antarctica: Implication

for pedogenesis in cold polar regions. Geochim. Cosmochim. Acta 68, 4319 - 4333.

Levy, J. S., Fountain, A. G., Gooseff, M. N., Welch, K. A. and Lyons, W. B. (2011) Water tracks and permafrost in Taylor Valley, Antarctica: extensive and shallow groundwater connectivity in a cold desert ecosystem. Geol. Soc. Am. Bull.123, 2295 - 2311.

Maupetit, F. and Delmas, R. J. (1992) Chemical composition of falling snow at Dumont D'urville, Antarctica. J. Atmos. Chem. 14, 31 - 42.

Park, B. K., Chang, S. K., Yoon, H. I. and Chung, H. (1998) Recent retreat of ice cliff, King George Island. South Shet-land Islands, Antarctic Peninsula. Ann. Glaciol. 27, 633 - 635.

Quayle, W., Peck, L. S., Peat, H., Ellis-Evans, J. C. and Harrigan, P. R. (2002) Extreme responses to climate changein Antarctic lakes. Science 295, 645.

Santos, I. R., Silva-Filho, E. V., Schaefer, C. E. G. R., Albuquerque-Filho, M. R. and Campos, L. S. (2005) Heavy metal contamination in coastal sediments and soils near the Brazilian Antarctic Station, King George Island. Mar. Pollut. Bull. 50, 185 - 194.

Santos, I. R., Fávaro, D. I. T., Schaefer, C. E. G. R. and Silva-Filho, E. V. (2007) Sediment geochemistry in coastal maritime Antarctica (Admiralty Bay, King George Island): Evidence from rare earths and other elements. Mar. Chem. 107,464 - 474.

SCAR (2009) Antarctic Climate Change and the Environment. Victoire Press, Cambridge.

Simões, J. C., Ferron, F. A., Bernardo, R. T., Aristarain, A. J., Stiévenard, M., Pourchet, M. and Delmas, R. J. (2004) Ice core study from the King George Island, South Shetland, Antarctica. Pesqisa Antártica Brasileira 4, 9 - 23.

Stumpf, A. R., Elwood Madden, M. E., Soreghan, G. S., Hall, B. L., Keiser, L. J. and Marra, K. R. (2012) Glacier meltwater stream chemistry in Wright and Taylor Valleys, Antarctica: Significant roles of drift, dust and biological processes in chemical weathering in a polar climate. Chem. Geol.322 - 323, 79 - 90.

Tranter, M., Huybrechts, P., Munhoven, G., Sharp, M. J., Brown,G. H., Jones, I. W., Hodson, A. J., Hodgkins, R. and Wadham, J. L. (2002) Direct effect of ice sheets on terrestrial bicarbonate, sulfate and base cation flux during the last glacial cycle: minimal impact of atmospheric CO2 concentrations. Chem. Geol. 190, 33 - 44.

Vaughan, D. G. and Doake, C. S. M. (1996) Recent atmospheric warming and retreat of ice shelves on the Antarctic Peninsula. Nature 418, 291 - 292.

Vaughan, D. G., Marshall, G. J., Connolley, W. M., King, J. C. and Mulvaney, R. (2001) Climate change: Devil in the de-tail. Science 293, 1777 - 1779.

Wadham, J. L., Cooper, R. J., Tranter, M. and Bottrell, S. (2007) Evidence for widespread anoxia in the proglacial zone ofan Arctic glacier. Chem. Geol. 243, 1 - 15.

Wagenbach, D., Ducroz, F., Mulvaney, R., Keck, L., Minikin, A., Legrand, M., Hall, J. S. and Wolff, E. W. (1998) Sea-salt aerosol in coastal Antarctic regions. J. Geophys. Res.103, 10961 - 10974.

Wang, Y., Hou, S., Masson-Delmotte, V. and Jouzel, J. (2010) A generalized additive model for the spatial distribution of stable isotopic composition in Antarctic surface snow. Chem. Geol. 271, 133 - 141.

Webster, J. G., Brown, K. L. and Vincent, W. F., (1994) Geochemical processes affecting meltwater chemistry and the formation of saline ponds in the Victoria Valley and Bull Pass region, Antarctica. Hydrobiologia 281, 171 - 186.

Wen, J., Kang, J., Han, J., Xie, Z., Liu, L. and Wang, D. (1998) Glaciological studies on King George Island ice cap, South Shetland Islands, Antarctica. Ann. Glaciol. 42, 45 - 58.

Wetzel, R. G. and Likens, G. E. (1991) Limnological Analysis. 2nd ed., Springer-Verlag, 391 pp.

Yeo, J. P., Lee, J. I., Hur, S. D. and Choi, B. G. (2004) Geochemistry of volcanic rocks in Barton and Weaver Peninsulas, King George Island, Antarctica: Implications for arc maturity and correlation with fossilized volcanic centers. Geosci. J. 8, 11 - 25.

Table 1. Chemical compositions of meltwater and pondwater in the Barton and Weaver Peninsulas of King George Island, Antarctica

Type		pH	T	EC	Ca^{2+}	Mg^{2+}	Na^{+}	K^{+}	H_4SiO_4	Cl^{-}	NO_3^{-}	SO_4^{2-}	HCO_3^{-}
Barton Peninsula													
Meltwater (n = 23)	Minimum	4.83	0.2	32.6	2.95	0.03	0.81	0.11	0.53	0.49	3.55	2.38	0.61
	Maximum	8.80	8.3	390	9.52	1.38	9.71	0.91	9.07	30.2	3.55	43.8	9.15
	Mean	6.36	2.3	129	5.67	0.39	3.59	0.50	2.08	13.4	3.55	11.5	3.89
	Standard deviation	0.97	1.7	87.0	1.56	0.34	2.13	0.33	0.74	7.00	0	10.4	2.19
Pondwater (n = 14)	Minimum	5.00	0.2	33.2	3.65	0.14	1.31	0.11	0.45	3.21	—	2.03	0.61
	Maximum	7.47	9.2	27,900	99.5	226	2,210	58.3	8.24	3,901	—	816	22.6
	Mean	6.00	3.8	2,738	19.3	30.4	222	12.2	3.22	405	—	113	5.30
	Standard deviation	0.66	2.6	7,320	27.9	68.3	598	21.2	0.72	1,057	—	223	5.51
Seawater (n = 1)		8.12	2.5	42,200	212	642	6,743	179	1.92	13,672	0.61	1,935	54.8
Weaver Peninsula													
Meltwater (n = 5)	Minimum	5.11	2.0	42.1	4.52	0.08	0.45	—	—	6.42	1.10	3.14	7.32
	Maximum	5.78	3.8	98.4	5.53	0.09	3.33	—	—	12.8	1.10	5.70	11.0
	Mean	5.43	2.6	69.2	5.04	0.08	1.50	—	—	8.56	1.10	4.50	8.91
	Standard deviation	0.23	0.7	19.6	0.32	0.01	1.02	—	—	2.38	0	1.01	1.20
Pondwater (n = 6)	Minimum	4.98	1.2	69.1	2.65	0.08	1.89	0.32	0.37	1.80	—	2.29	5.49
	Maximum	5.79	8.3	196	6.69	0.71	5.85	0.35	0.75	24.9	—	4.04	9.15
	Mean	5.35	4.1	122	4.79	0.28	3.14	0.33	0.57	13.1	—	3.36	7.32
	Standard deviation	0.29	2.4	51.4	1.18	0.22	1.44	0.02	0.06	8.02	—	0.67	1.22
Seawater (n = 1)		5.70	3.4	43,800	281	712	6,997	226	2.37	18,950	—	2,164	67.1

Unit of water temperature and EC is °C and μS/cm, respectively.
Unit of concentrations of the major ions are mg/L.

Table 2. Concentrations of REEs in the meltwater and pondwater in the Barton and Weaver Peninsulas of the King George Island, Antarctica

Type		La	Ce	Pr	Nd	Sm	Eu	Gd	Tb	Dy	Ho	Er	Tm	Yb	Lu
Barton Peninsula															
Meltwater (n = 23)	Minimum	0.378	0.986	0.047	0.567	0.034	0.002	0.021	0.003	0.001	—	0.002	—	0.009	—
	Maximum	1.169	2.587	0.275	1.557	0.200	0.041	0.182	0.003	0.088	—	0.043	—	0.028	—
	Mean	0.730	1.765	0.141	1.040	0.096	0.014	0.078	0.003	0.024	—	0.016	—	0.017	—
	Standard deviation	0.192	0.400	0.055	0.252	0.040	0.016	0.037	—	0.021	—	0.015	—	0.007	—
Pondwater (n = 14)	Minimum	0.476	1.228	0.068	0.739	0.045	0.007	0.042	0.033	0.003	0.032	0.006	0.012	0.002	0.006
	Maximum	3.698	9.264	1.210	6.815	1.329	0.313	1.515	0.132	0.894	0.128	0.413	0.012	0.276	0.006
	Mean	1.084	2.750	0.270	1.754	0.240	0.077	0.242	0.082	0.155	0.080	0.113	0.012	0.076	0.006
	Standard deviation	0.803	2.001	0.285	1.528	0.329	0.109	0.385	0.049	0.258	0.048	0.145	—	0.100	—
Seawater (n = 1)		0.593	1.828	0.134	0.946	0.097	—	0.096	—	0.011	—	0.008	—	—	—
Weaver Peninsula															
Meltwater (n = 5)	Minimum	0.607	1.509	0.101	0.872	0.066	—	0.050	—	0.003	—	—	—	—	—
	Maximum	0.793	1.883	0.146	1.065	0.098	—	0.089	—	0.006	—	—	—	—	—
	Mean	0.695	1.699	0.123	0.965	0.083	—	0.068	—	0.005	—	—	—	—	—
	Standard deviation	0.068	0.150	0.018	0.077	0.012	—	0.015	—	0.001	—	—	—	—	—
Pondwater (n = 6)	Minimum	0.541	1.354	0.090	0.777	0.055	—	0.046	—	0.003	—	—	—	—	—
	Maximum	0.763	1.828	0.132	1.085	0.119	—	0.076	—	0.010	—	—	—	—	—
	Mean	0.650	1.597	0.114	0.921	0.080	—	0.057	—	0.005	—	—	—	—	—
	Standard deviation	0.072	0.161	0.017	0.102	0.020	—	0.013	—	0.003	—	—	—	—	—
Seawater (n = 1)		0.714	1.828	0.136	1.031	0.097	—	0.073	—	0.011	—	—	—	—	—

Unit of concentrations of REEs is μg/L.

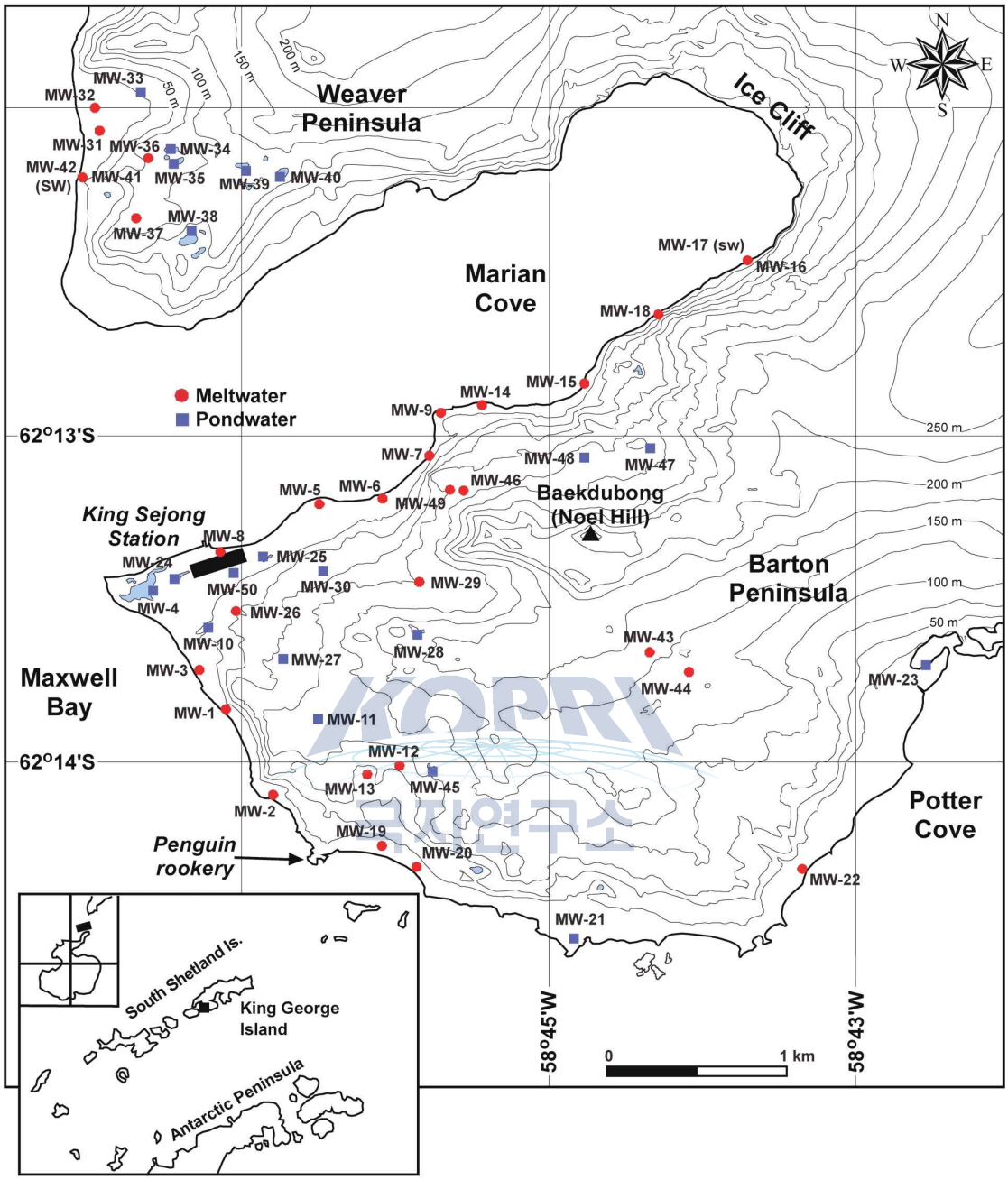

Figure 1. Location of the Barton and Weaver Peninsulas of the King George Island, Antarctica and sampling sites of the meltwater and pondwater.

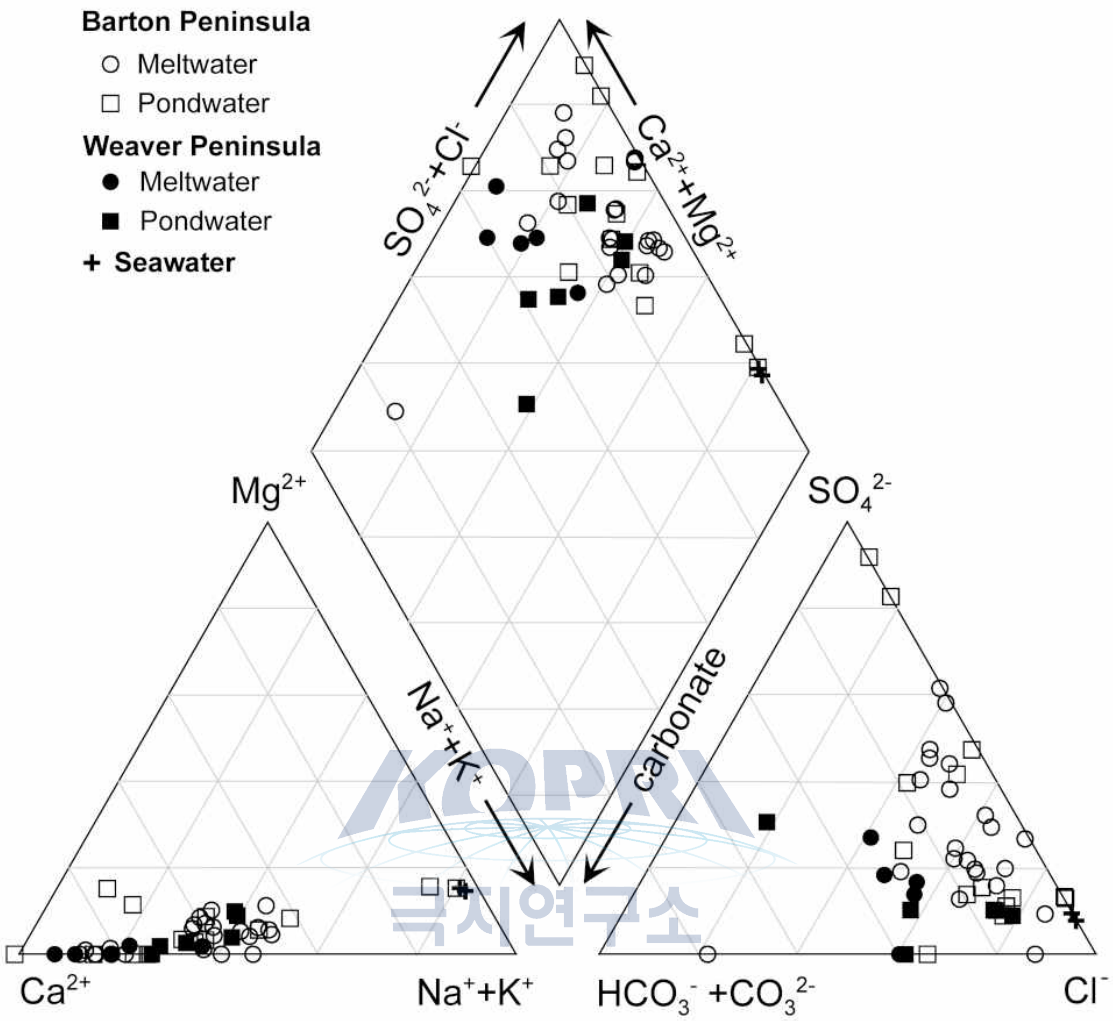

Figure 2. Chemical compositions of the meltwater and pondwater in the Barton and Weaver Peninsulas.

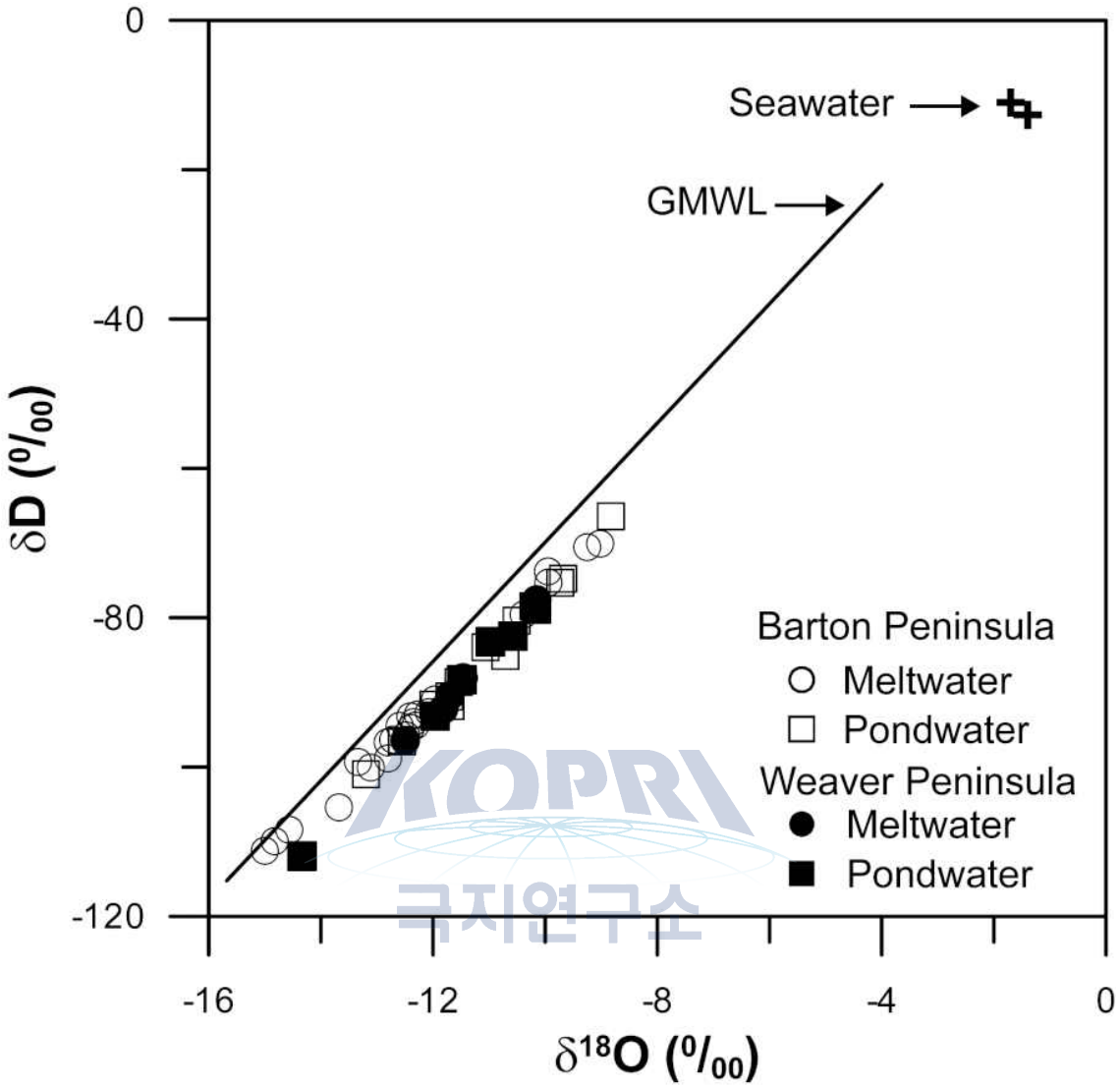

Figure 3. Oxygen and hydrogen isotopic compositions of the meltwater and pondwater in the Barton and Weaver Peninsulas. GMWL (the solid line) represents global meteoric water line after Craig (1961).

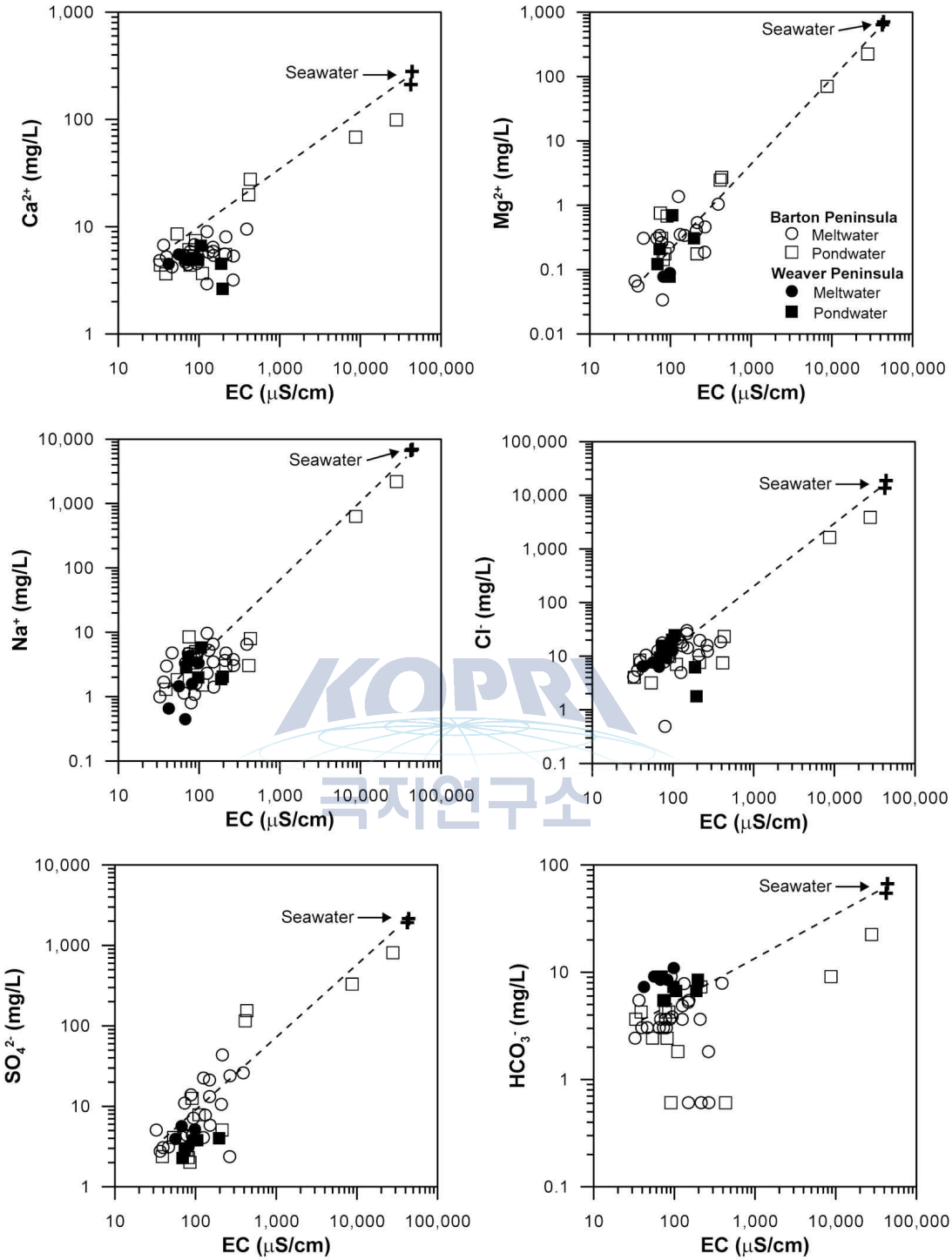

Figure 4. Relations between the major ions and EC of the meltwater and pondwater in the Barton and Weaver Peninsulas. The dotted lines represent hypothetical lines of mixing reactions between end-member of meltwater and seawater. The end-member of meltwater is MW-43 and MW-44 in inland of the Barton Peninsula.

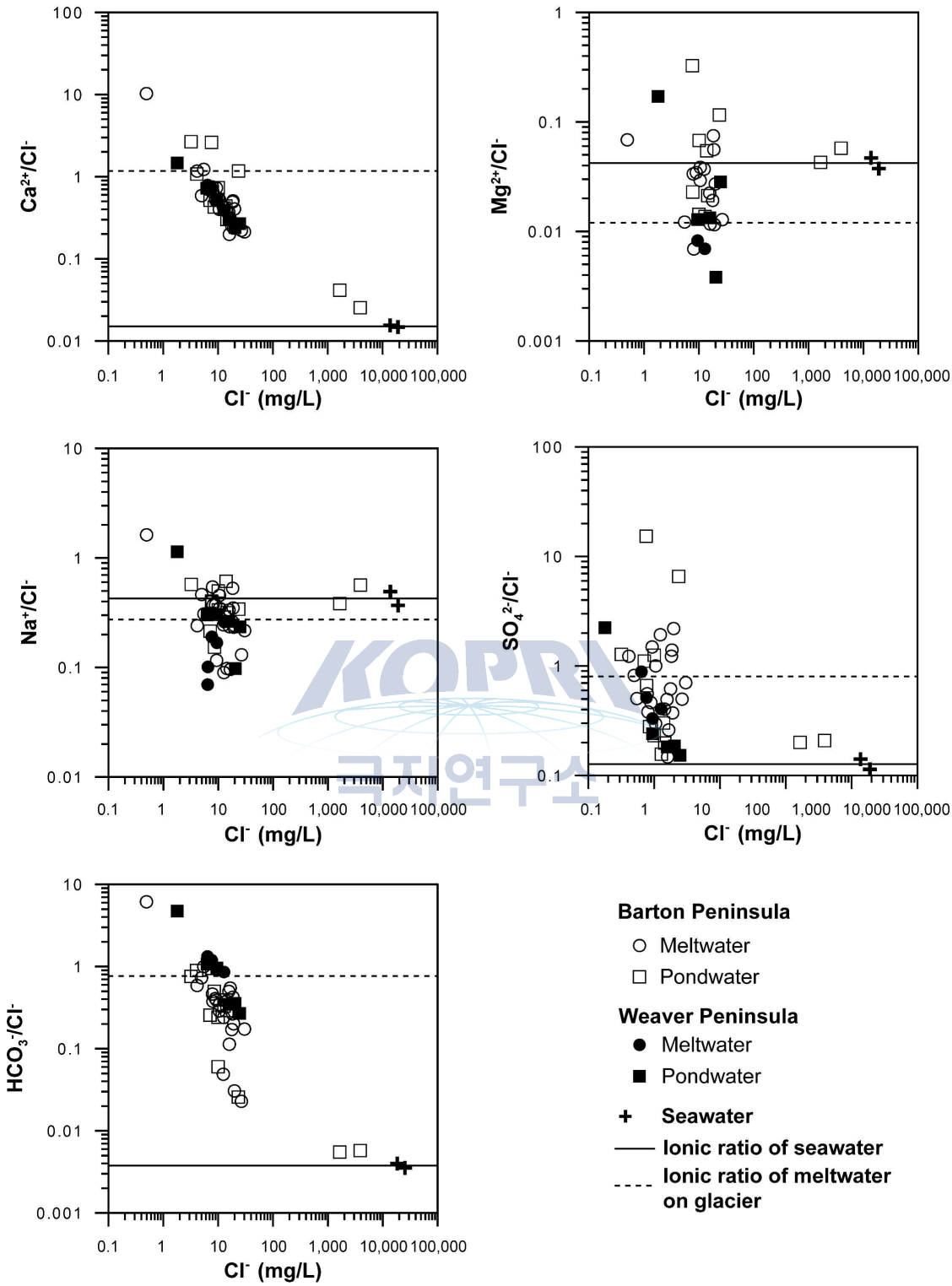

Figure 5. Ionic ratios of the major ions for Cl^- of the meltwater and pondwater in the Barton and Weaver Peninsulas. The end-members calculating the ionic ratios of the meltwater are same in Fig. 3.

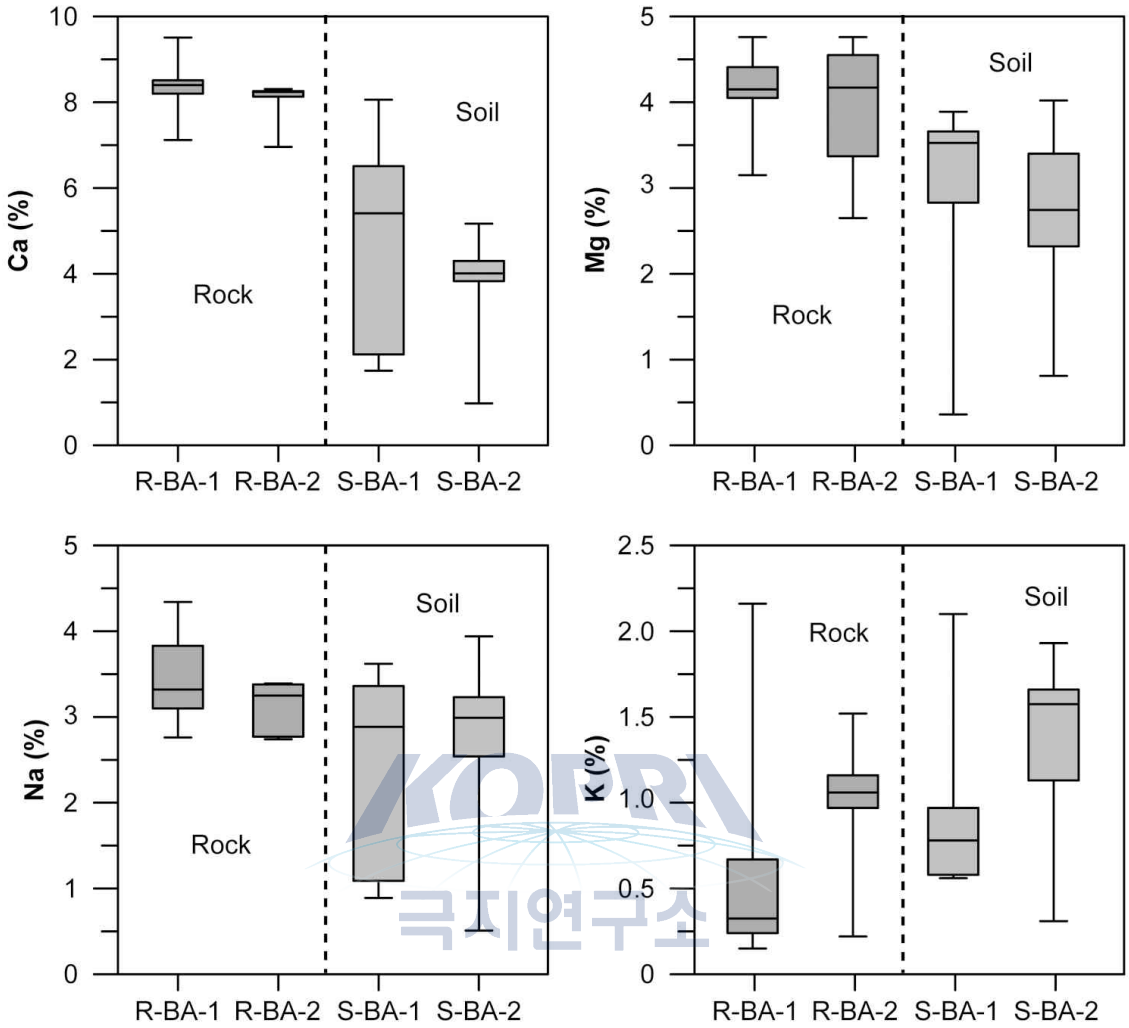

Figure 6. Comparison of chemical compositions of rocks with those of soils in the Barton Peninsula. The chemical compositions of rocks and soils are collected from Yeo et al. (2004) and Lee et al. (2004), respectively.

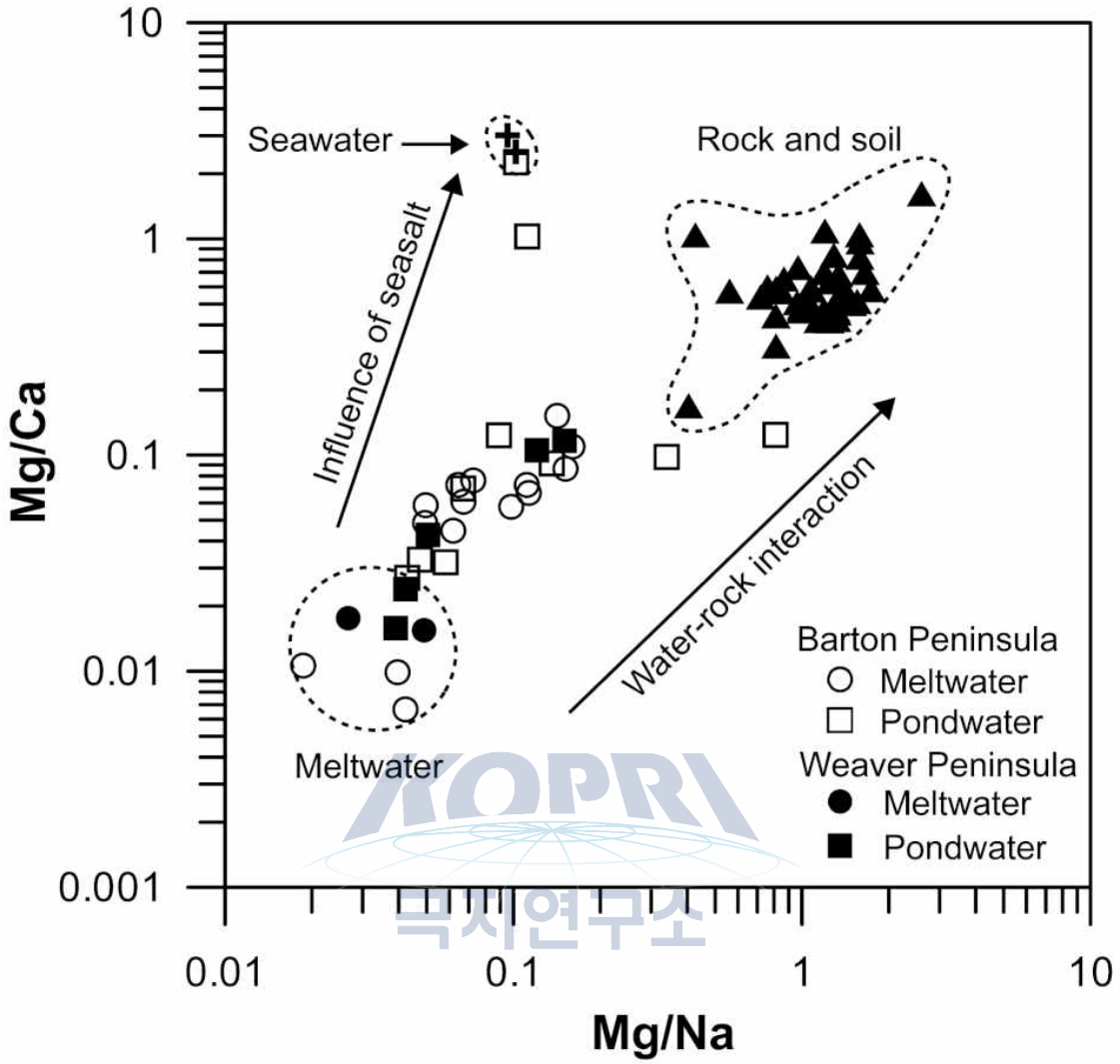

Figure 7. Mg/Na vs. Mg/Ca for the meltwater, pondwater, rocks and soils in the Barton and Weaver Peninsulas. The end-members calculating Mg/Na and Mg/Ca of the meltwater are same in Fig. 3. The chemical compositions of rocks and soils are from Yeo et al. (2004) and Lee et al. (2004), respectively.

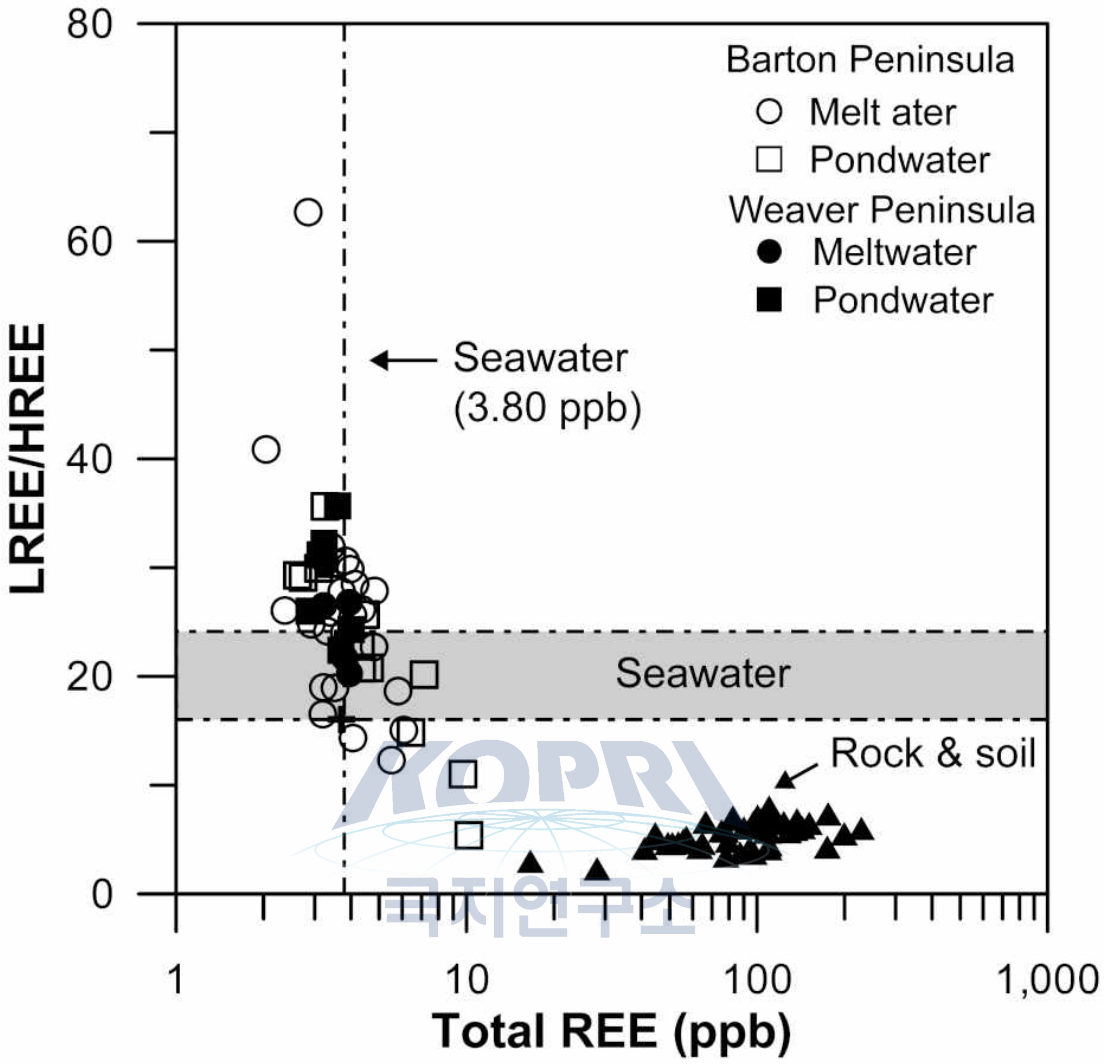

Figure 8. Evaluation of the water-rock interaction using REEs of the meltwater, pondwater, rocks and soils in the Barton and Weaver Peninsula. The chemical compositions of rocks and soils are from Yeo et al. (2004) and Lee et al. (2004), respectively.

제 12 장

Enhanced Removal of Hexavalent Chromium in the Presence of H_2O_2 in Frozen Aqueous Solutions[7)]

Kitae Kim[1], Wonyong Choi[2], Ho-Il Yoon[1*]

[1]Korea Polar Research Institute

[2]Pohang Univerisity of Science and Technology

Abstract: The reductive transformation of Cr(VI) to Cr(III) by H_2O_2 in ice was compared with that in water. The reduction of Cr(VI) was significant at -20 °C (ice), whereas the reduction efficiency was very low at 25 °C (water). This enhanced reduction of Cr(VI) in ice was observed over a wide range of H_2O_2 concentration (20-1000 μM), pH (3-11), and freezing temperature (-10 to -30 °C). The observed molar ratio of consumed [H_2O_2] to reduced [Cr(VI)] in ice was in close agreement with the theoretical (stoichiometric) molar ratio (1.5) for H_2O_2-mediated Cr(VI) reduction through proton-coupled electron transfer (PCET). The synergistic increase in Cr(VI) reduction in water by increasing the H_2O_2 and proton concentrations confirms that the freeze concentration of both H_2O_2 and protons in the liquid brine is primarily responsible for the enhanced Cr(VI) reduction in ice. In comparison, the one-electron reduction of Cr(VI) to Cr(V) and subsequent re-oxidation of Cr(V) to Cr(VI) is the major reaction mechanism in aqueous solution. The reduction efficiency of Cr(VI) by H_2O_2 in the frozen aqueous electroplating wastewater was similar to that in the frozen aqueous deionized water, which verifies the enhanced reduction of Cr(VI) by freezing in real Cr(VI)-contaminated aquatic systems.

7) 이 연구는 극지연구소(PP15010), Basic Science Research Program, Space Core Technology Development Program(미래창조과학부) 공동 지원으로 수행되었으며 그 결과는 다음의 논문으로 출판되었음. Kitae Kim, Jaesung Kim, Alok D. Bokare, Wonyong Choi, Ho-Il Yoon, Jungwon Kim "Enhanced removal of hexavalent chromium in the presence of H2O2 in frozen aqueous solutions" Environ. Sci. Technol. 2015, 49, 10937-10944

1. Introduction

Chemical reactions at temperatures above the freezing point (i.e., in aqueous solution) may be different from those at temperatures between the freezing and eutectic points (i.e., in the mixture of ice crystals and liquid brine).(Bartels-Rausch et al, 2014, Park et al, 2010, Boxe et al, 2009, Boxe et al, 2008) Reaction rates in ice crystals are usually lower than those in aqueous solution because of the lower temperature in ice crystals. However, some chemical reactions can be accelerated and enhanced by freezing. The oxidation of nitrite to nitrate in water was markedly accelerated by freezing.(Takenaka et al, 1992, Takenaka et al, 1996, Takenaka et al, 2007) In addition, the dissolution of metal oxides, such as iron oxide and manganese oxide, by organic compounds in frozen aqueous solution was accelerated.(Kim et al, 2012, Jeong et al, 2012) Recently, it was also reported that the reduction of chromate by organic compounds under acidic conditions is enhanced by freezing.(Kim et al, 2011, Dong et al, 2014) These enhanced chemical reactions are mainly ascribed to the freeze concentration phenomenon, which refers to the increased concentrations of both solutes (e.g., nitrite, metal oxide particles, and organic compounds) and protons in the liquid brine by exclusion from ice crystals during the freezing process.(Bartels-Rausch et al, 2014, Takenaka et al, 1992, Takenaka et al, 1996, Takenaka et al, 2007, Betterton et al, 2001, Heger et al, 2005) Chemical reactions below the eutectic temperature are generally stopped because the liquid brine is completely solidified. The photochemical degradation mechanism and products of organic compounds in ice can be different from those in water because the coupling/dimerization reactions are enhanced in ice.(Klán et al, 2002, Klán, P. et al, 2003, Klánová, J. et al, 2003, Bláha, L. et al, 2004) The different chemical kinetics and mechanisms between ice and water required various laboratory and field studies of chemical reactions in ice to explain the cycling and fate of contaminants in the cryosphere (e.g., permafrost, polar regions, high latitudes, and midlatitudes during the winter season) and the upper troposphere.(Bartels-Rausch et al, 2014, Grannas et al, 2013, McNeill et al, 2012) Various industries, such as metallurgy, wood preservation, leather tanning, metal electroplating, and pigment manufacturing, use chemical reagents containing high

concentrations of chromium,(Barnhart et al, 1997) which results in a large amount of wastewater containing chromium that needs to be treated. In addition, chromium pollution can naturally occur from weathering and dissolution of chromium-bearing minerals and volcanic eruptions.(Vaiopoulou et al, 2012) Chromium is commonly found as trivalent chromium (Cr(III)) and hexavalent chromium (Cr(VI)) in water, and its toxicity, water solubility, and environmental fate are greatly dependent on the oxidation state.(Costa et al ,2003) Between these two chromium species, Cr(III) and Cr(VI), Cr(VI) is more toxic, water soluble, and difficult to remove using physical treatment processes (e.g., adsorption, ion exchange, and precipitation) than Cr(III).(Barrera-Díaz et al, 2012) In this regard, the pre-reduction of Cr(VI) to Cr(III) is considered a desirable process in chromium removal.

Hydrogen peroxide (H_2O_2) is ubiquitous in aquatic environments. H_2O_2 can be produced through the photochemical reactions of natural organic matter with dioxygen and by biological processes mediated by algae.(Clark et al , 2008, Mö ller et al , 2009) In addition, it is well known that H_2O_2 is present in snow/ice and plays important roles in oxidation reactions in the polar regions as an oxidant and a precursor of hydroxyl radicals (• OH).(Neftel et al, 1984. Kamiyama et al, 1996) The interest in redox reactions between H_2O_2 (or • OH) and pollutants in snow/ice has increased because the concentration of H_2O_2 in snow/ice has increased by 50% over the past 200 years.(Sigg et al, 1991) In water treatment processes, H_2O_2 has been widely used as an oxidant for the degradation of aquatic pollutants.(Chang et al, 2001) In addition, H_2O_2 can be used as a reducing agent for easily oxidizable metals, such as Fe(III) and Cr(VI), and kinetic and mechanistic investigations of metal reduction by H_2O_2 in water have been extensively performed.(Griend et al, 2002, Pettine et al, 2002, Perez-Benito et al, 1997, Liu et al, 2011, Walling et al, 1973) However, the reduction of Cr(VI) by H_2O_2 in ice has not been studied despite the high probability of the coexistence of H_2O_2 and Cr(VI). The concentrations of chromium and hydrogen peroxide in the cryosphere vary from a few to 470 ppt and 600 ppb, respectively, depending on region, season, and depth from the surface.(De Velde et al, 1999, Gabrielli et al, 2005, Sigg et al, 1988, Chu et al, 2005) The reaction between Cr(VI) (discharged from natural and anthropogenic

sources) and H_2O_2 (in-situ naturally generated) in frozen aqueous environment might be different from that in aqueous environment, which results in the different fate of Cr(VI) depending on region, altitude, and weather.

In this work, we investigated the reduction of Cr(VI) by H_2O_2 as a reductant in ice and compared it with the corresponding reaction in water. The reduction of Cr(VI) by H_2O_2 in water was limited, whereas it was significant in ice. The reduction process in ice and water was compared as a function of various experimental parameters, such as H_2O_2 concentration, pH, and freezing temperature. Furthermore, the reaction mechanism between H_2O_2 and Cr(VI) in ice was discussed and compared with that in water. The reduction efficiency of Cr(VI) by H_2O_2, which is the ratio of (initial [Cr(VI)] - final [Cr(VI)])/(initial [Cr(VI)]), in the frozen aqueous electroplating wastewater containing various metals was similar to that in the frozen aqueous deionized water, which verifies the enhanced reduction of Cr(VI) by freezing in real Cr(VI)-contaminated aquatic systems.

2. Experimental

2.1. Chemicals and Reagents.

The chemicals and reagents used in this work include the following: sodium dichromate dihydrate ($Na_2Cr_2O_7$ $2H_2O$, Cr(VI), Aldrich), hydrogen peroxide (H_2O_2, Samchun chemicals), acetone (CH_3COCH_3, Junsei), sulfuric acid (H_2SO_4, Aldrich), 1,5-diphenylcarbazide ($C_6H_5NHNHCONHNHC_6H_5$, DPC, Aldrich), benzoic acid (C_6H_5COOH, BA, Aldrich), 4-hydroxybenzoic acid ($HOC_6H_4CO_2H$, 4-HBA, Aldrich), N,N-diethyl-1,4-phenylenediamine ($(C_2H_5)_2NC_6H_4NH_2$, DPD, Aldrich), peroxidase from horseradish (type VI-A, POD, Aldrich). All chemicals were of analytical grade. The deionized water was ultrapure (18 MΩ cm) and prepared using a Barnstead purification system. The electroplating wastewater was obtained from a local electroplating plant in Korea.

2.2. Experimental Procedure

An aqueous solution containing the desired concentrations of Cr(VI) and H2O2 (usually 20 μM and 100 μM, respectively), which was adjusted to the desired pH value using a $HClO_4$ or NaOH solution, was put in a conical centrifuge tube (15 mL). For the reaction in ice, the conical centrifuge tube was placed in a stainless steel tube rack in a cryogenic ethanol circulator cooled to the desired temperature (usually -20 ℃) for freezing. The point when the aqueous samples were added to the cryogenic ethanol circulator was defined as time zero (t = 0) in the measurements of reaction kinetics. To melt the frozen aqueous samples within 10 min, the conical centrifuge tubes were placed in a beaker containing lukewarm water (35 ℃). The Cr(VI) reduction experiments in aqueous solution were performed at 25 ℃ using the same experimental system. Multiple (two or more) experiments were performed for a given condition to confirm data reproducibility. Error bars represent one standard deviation from the mean value.

2.3. Analysis

The concentrations of Cr(VI) and H_2O_2 were measured spectrophotometrically using the DPC39 and DPD40 methods, respectively. For the DPC method, 100 μL of the DPC reagent (containing 25 mL of acetone, 250 μL of H_2SO_4, and 0.05 g of DPC) was added to a vial containing a diluted sample (2.5 mL of deionized water and 0.5 mL of the sample solution). The vial was mixed vigorously and kept in the dark before the analysis. After 30 min, the absorbance measurements at 540 nm (ε = 6850 M^{-1} cm^{-1})(Eaton et al, 1995) were performed using a UV-visible spectrophotometer (Biochrom Libra S22). For the DPD method, 0.05 mL of the DPD reagent (containing 0.1 g of DPD and 10 mL of H_2SO_4 (0.1 M)), 0.05 mL of POD solution (containing 0.01 g of POD and 10 mL of deionized water), and 0.4 mL of phosphate buffer (0.5 M, pH = 6.0) were added to a diluted sample (2.0 mL of deionized water and 1.0 mL of the sample solution). The solution was mixed vigorously, and its absorbance was measured at 551 nm (ε = 21000 M^{-1} cm^{-1})(Bader et al, 1988) after 1 min.

The production of hydroxyl radicals ($\bullet$OH) was indirectly monitored by

measuring the concentration of 4-hydroxybenzoic acid (4-HBA), which was generated from the reaction between benzoic acid (BA) and •OH.(Liu et al, 2013, Joo et al, 2005) The concentration of 4-HBA was quantified by comparing the chromatography peak area of the samples with that of the authentic standard at the same retention time using high-performance liquid chromatography (HPLC, Agilent 1100) equipped with a UV-visible detector and a ZORBAX 300SB C-18 column (4.6 mm × 150 mm). The mobile phase was a binary mixture of a 0.1% phosphoric acid solution and acetonitrile (8:2 by volume) at a flow rate of 1.0 mL/min, and the detection wavelength was 254 nm.

The chemical composition of the electroplating wastewater was analyzed using inductively coupled plasma-optical emission spectroscopy (ICP-OES, Thermo iCAP 6300 Duo), which was operated under the conditions of RF power 1150 W, pump rate 50 rpm, auxiliary gas flow 0.5 L/min, and nebulizer gas flow 0.7 L/min.

3. Results and Discussion

Cr(VI) Reduction by H_2O_2 in Water and Ice. Because the eutectic temperature of H_2O_2 solution is below than -50 °C,(Foley et al, 1951) the reaction system in this study was not completely solidified. Therefore, the term "ice" in this study refers to the mixture of ice crystals and liquid brine, without indicating a fully frozen state. The reduction of Cr(VI) to Cr(III) by H_2O_2 in ice (more precisely, in the liquid brine) was compared to that in water (Figure 1a). Under the conditions of [H_2O_2] = 100 μM, [Cr(VI)] = 20 μM, and pH = 3.0, the reduction of Cr(VI) by H_2O_2 was stopped in 2.5 and 15 min in water and ice, respectively. The degree of Cr(VI) reduction after 5 min was markedly different between ice and water. The overall reduction of Cr(VI) by H_2O_2 was very small (less than 3 μM) in water, but 100% reduction was achieved in ice. We compared the reduction of Cr(VI) by H_2O_2 in water under both vigorous stirring and non-stirring conditions. However, the results were almost the same in both cases. This result indicates that the limited reduction of Cr(VI) in water cannot

be attributed to diffusion limitation. Although the reduction of Cr(VI) in ice continuously proceeded even in the absence of H2O2 through a proton-mediated reduction process (i.e., $4HCr^{VI}O_4^- + 16H^+ \rightarrow 4Cr^{3+} + 3O_2 + 10H_2O$; $E^0 = 0.15$ V_{NHE}),11 its effect was minor in H_2O_2-mediated Cr(VI) reduction (20 μM of Cr(VI) reduction in the presence of H_2O_2 within 15 min vs. 1 μM of Cr(VI) reduction in the absence of H_2O_2 for 30 min). In accordance with the higher Cr(VI) reduction in ice, the decrease in the H_2O_2 concentration in ice was higher than that in water (Figure 1b), which indicates that the reaction between H_2O_2 and Cr(VI) is more favored in ice than water. The concentration of H_2O_2 did not decrease in the absence of Cr(VI) in both water and ice.

Cr(VI) can be reduced to Cr(III) by H2O2 through proton-coupled electron transfer (PCET, reaction 3), which is obtained from the half-reduction reactions of Cr(VI) (reaction 1) and dioxygen (reaction 2).(David et al, 1996) According to reaction 3, the reduction of Cr(VI) by H_2O_2 should be favored at high concentrations of H_2O_2 and protons.

$$HCr^{VI}O_4^- + 7H^+ + 3e^- \rightarrow Cr^{3+} + 4H_2O; \quad E_1^0 = 1.35\ V_{NHE} \tag{1}$$
$$E_1 = E_1^0 - 0.14pH - 0.02\log([Cr^{3+}]/[HCr^{VI}O_4^-])$$

$$O^2 + 2H^+ + 2e^- \rightarrow H_2O_2; \quad E_2^0 = 0.70\ V_{NHE} \tag{2}$$
$$E_2 = E_2^0 - 0.06pH - 0.03\log([H_2O_2]/[O_2])$$

$$2HCr^{VI}O_4^- + 3H_2O_2 + 8H^+ \rightarrow 2Cr^{3+} + 3O_2 + 8H_2O;$$
$$E_3^0 = E_1^0 - E_2^0 = 0.65\ V_{NHE} \tag{3}$$
$$E_3 = E_1 - E_2$$
$$= 0.65 - 0.08pH + 0.02\log([HCr^{VI}O_4^-]/[Cr^{3+}]) + 0.03\log([H_2O_2]/[O_2])$$

The solutes and protons are excluded from the ice crystals into the liquid brine during freezing.(Bartels-Rausch et al, 2014, Takenaka et al, 1992, Takenaka et al, 1996, Takenaka et al, 2007, Betterton et al, 2001, Heger et al, 2005) As a result, the concentrations of the solutes and protons in the liquid brine increase by freezing. This freeze concentration phenomenon (i.e., the increased concentrations of H_2O_2 and protons in the liquid brine by freezing) can enhance

the reduction of Cr(VI) to Cr(III) by providing better conditions for PCET reaction (reaction 3).

In ice, the concentration of H_2O_2 rapidly decreased in the initial period but did not decrease further after 15 min (Figure 1b). This behavior is consistent with the complete removal of Cr(VI) (behaving as an electron acceptor) within 15 min (Figure 1a). Thus, 35 μM of H_2O_2 (added [H_2O_2] - residual [H_2O_2]) reduced 20 μM of Cr(VI) in ice neglecting reduced [Cr(VI)] in the absence of H_2O_2, which amounts to a molar ratio value of H_2O_2 to Cr(VI) (consumed [H_2O_2]/reduced [Cr(VI)]) equal to 1.75. This value is close to the theoretical (stoichiometric) molar ratio of 1.5 according to reaction 3. Therefore, reaction 3 accounts for the major consumption of H_2O_2 and all other side reactions are very minor in ice. In contrast, the reduction of Cr(VI) in aqueous solution was stopped after 2.5 min, although high concentrations of both Cr(VI) and H_2O_2 still remained in aqueous solution (Figure 1a and b). In addition, the concentration of H_2O_2 continuously decreased without the reduction of Cr(VI) (Figure 1a and b). These results imply the existence of other pathways for the reaction between H_2O_2 and Cr(VI) in water.

The reaction mechanism between Cr(VI) and H_2O_2 is critically dependent on the solution pH. Under acidic conditions, the complete reduction of Cr(VI) to Cr(III) by H_2O_2 is favored through PCET reaction (reaction 3).(Pettine et al, 2002) On the other hand, under neutral and basic conditions, the tetraperoxochromate(V) anion ($[Cr^{V}(O_2)_4]^{3-}$) is preferentially formed by the simultaneous single-electron transfer from H_2O_2 to Cr(VI) and sequential substitution of oxo ligands by peroxo groups (reaction 4).(Griend et al, 2002) However, $[Cr^{V}(O_2)_4]^{3-}$ is easily decomposed into $[Cr^{VI}(O_2)_3(O)]^{2-}$ with the generation of "OH (reaction 5),(Peters et al, 1975,Kawanishi et al, 1986) which creates a null cycle combining with reaction 4 (Cr(VI) → Cr(V) → Cr(VI)).

$$2[Cr^{VI}O_4]^{2-} + (7 + 2n)H_2O_2 + 2OH^- \rightarrow 2[CrV(O_2)_4]^{3-} + (8 + 2n)H_2O + nO_2 \quad (4)$$

$$[CrV(O_2)_4]^{3-} + H^+ \rightarrow [Cr^{VI}(O_2)_3(O)]^{2-} + OH \quad (5)$$

In addition, the intermediate Cr(V) species generated from reaction 4 can react with residual H_2O_2 to regenerate Cr(VI) with producing • OH (reaction

6),(Perez-Benito et al, 1997,Bagchi et al, 2002) and •OH generated from reactions 5 and 6 can re-oxidize Cr(V) back to Cr(VI) (reaction 7).

$$Cr(V) + H_2O_2 \rightarrow Cr(VI) + {}^{\bullet}OH + OH^- \quad (6)$$

$$Cr(V) + {}^{\bullet}OH \rightarrow Cr(VI) + OH^- \quad (7)$$

These coupled redox reactions (reaction 4 + reaction 5, 6, or 7) consume H_2O_2 without the reduction of Cr(VI) to Cr(III). Because the concentration of the protons in water at pH = 3.0 should not be sufficient to drive reaction 3, the reduction of Cr(VI) to Cr(III) was very small. Alternatively, Cr(V) should be primarily formed by the single-electron transfer from H_2O_2 to Cr(VI) (reaction 4) and then re-oxidized back to Cr(VI) (reactions 5-7). These null reactions that occur in water limit the reduction of Cr(VI) to Cr(III) with continuously consuming H_2O_2.

To provide convincing evidence of different reaction mechanisms between Cr(VI) and H_2O_2 in water and ice (i.e., reactions 4-7 in water vs. reaction 3 in ice), the production of •OH was monitored by measuring the production of 4-hydroxybenzoic acid (4-HBA) that was generated from the reaction between •OH and benzoic acid (BA) (Figure 2). If the reaction between Cr(VI) and H_2O_2 is initiated through the single-electron transfer (reaction 4), •OH should be generated through the decomposition of Cr(V) (reaction 5) or the reaction between Cr(V) and H_2O_2 (reaction 6). In contrast, ″OH is not produced in the course of Cr(VI) reduction by H_2O_2 through PCET reaction (reaction 3).

As shown in Figure 2, the production of 4-HBA, which is directly proportional to the production of ″OH, gradually increased in the aqueous Cr(VI)/H_2O_2 system. This result indicates that the single-electron transfer from H_2O_2 to Cr(VI) (i.e., the formation of Cr(V), reaction 4) and subsequent re-oxidation of Cr(V) to Cr(VI) (reactions 5-7) is favored in water. However, the formation of 4-HBA was negligible in the frozen aqueous Cr(VI)/H_2O_2 system. Therefore, the formation of Cr(V) by single-electron transfer from H_2O_2 to Cr(VI) (reaction 4) can be ruled out in ice, with the PCET reaction (reaction 3) proposed as the major reaction pathway between H_2O_2 and Cr(VI).

Cr(VI) Reduction by H_2O_2 in Various Conditions. The effect of the H_2O_2 concentration on Cr(VI) reduction was investigated in both water and ice (Figure 3a). The reduction of Cr(VI) increased with increasing H_2O_2 concentration in water. However, approximately 40% of Cr(VI) (8 μM) still remained even at $[H_2O_2]$ = 1 mM, which should be attributed to the fact that the complete reduction through PCET reaction (reaction 3) is less favorable than the coupled redox reactions (reaction 4 + reaction 5, 6, or 7) in water. In contrast, the reduction of Cr(VI) (20 μM) was completed at $[H_2O_2] \geq 50$ μM in ice. At $[H_2O_2]$ = 20 μM and [Cr(VI)] = 20 μM, 14 μM of Cr(VI) was reduced and 20 μM of H_2O_2 was completely consumed after 2 h. Because 2 μM of Cr(VI) was reduced for 2 h in the absence of H_2O_2 (Figure 1a), the observed molar ratio of H_2O_2 to Cr(VI) (consumed $[H_2O_2]$/(reduced [Cr(VI)] - 2 μM)) was 1.67, which was similar to the theoretical (stoichiometric) value of 1.5 (reaction 3). This result also corroborates the proposed PCET reaction between H_2O_2 and Cr(VI) in ice.

The effect of the pH on Cr(VI) reduction by H_2O_2 was also investigated (Figure 3b). The reduction of Cr(VI) gradually decreased from pH 3 to pH 11 in both ice and water. This behavior is expected because the reduction of Cr(VI) to Cr(III) through PCET reaction is favored under acidic conditions. However, it should be noted that approximately 45% of Cr(VI) (9 μM) was reduced in the presence of 100 μM of H_2O_2 at neutral pH in ice, whereas the reduction in water was very small under the same conditions. This result implies that the enhanced reduction of Cr(VI) by H_2O_2 in ice is not particularly restricted to acidic conditions only. A significant portion of Cr(VI) in natural waters (e.g., river water, lake water, and groundwater), where the pH is generally neutral, can be reduced to Cr(III) in the presence of H_2O_2 by freezing. The reduction of Cr(VI) in ice at neutral pH was negligible in the absence of H_2O_2, which implies that the reduction of Cr(VI) is initiated only by H_2O_2 at neutral pH in contrast to acidic pH.

It has been estimated that the concentration of protons in the liquid brine increases by 2-3 orders of magnitude compared to that in aqueous solution.(Heger et al, 2006, Robinson et al, 2006) If so, the pH in water can be changed from 7.0 up to 4.0 by freezing. However, the reduction of Cr(VI) at pH

= 7.0 in ice was more significant than that at pH = 4.0 in water, which indicates that the pH decrease by freezing is not the only reason for the enhanced Cr(VI) reduction in ice. In addition to protons, H_2O_2 can be concentrated in the liquid brine during freezing. This behavior should result in a synergistic enhancement of the Cr(VI) reduction through PCET reaction, because reaction 3 is also favored at high concentrations of H_2O_2. The alkaline aqueous solution may become more basic by freezing due to the accumulation of OH^- in the liquid brine, which constitutes an unfavorable condition for PCET reaction (reaction 3). Therefore, the observed positive effect of freezing on Cr(VI) reduction at basic conditions should be ascribed to only the increased concentration of H_2O_2 in the liquid brine.

Figure 3c shows the temperature-dependent kinetic profiles of Cr(VI) reduction at the same [H_2O_2]. The apparent Cr(VI) reduction rate, which is the ratio of (initial [Cr(VI)] - final [Cr(VI)])/(reaction stop time), in the ice samples increased with decreasing freezing temperature (0.52 μM/min at -10 °C, 0.93 μM/min at -20 °C, and 1.21 μM/min at -30 °C). The freezing temperature should have an effect on the volume of the liquid brine by affecting the freezing speed. The size of the ice crystals should be larger at higher freezing speed (i.e., at lower freezing temperature). Therefore, the volume of the liquid brine, which is inversely proportional to the size of the ice crystals, should be smaller at lower freezing temperatures. The smaller volume of the liquid brine (i.e., more highly concentrated H_2O_2 and protons) at lower freezing temperature increases the apparent reduction rate of Cr(VI).

The Cr(VI) reduction efficiency, which is the ratio of (initial [Cr(VI)] - final [Cr(VI)])/(initial [Cr(VI)]), seems to be independent of the freezing temperature because all experiments were performed above the eutectic temperature (i.e., the reduction of Cr(VI) was not stopped by complete solidification). However, more Cr(VI) was reduced at higher freezing temperatures (16.5 μM at -10 °C, 14.5 μM at -20 °C, and 12.5 μM at -30 °C). This result is consistent with the previous report that the freeze concentration phenomenon is more significant at higher freezing temperatures.(Kim et al, 2011) Highly concentrated dioxygen may completely inhibit the reduction of Cr(VI) to Cr(III) through PCET reaction (reaction 3) with Cr(III) generated from Cr(VI) reduction by reducing the driving

force (i.e., E_3 value). The concentration of dioxygen should be higher at lower freezing temperatures because dioxygen can also be more confined in the smaller liquid brine.6, 7 This can help explain why the efficiency of Cr(VI) reduction by H_2O_2decreased with decreasing freezing temperature. In order to confirm the dioxygen concentration-dependent Cr(VI) reduction efficiency in ice, the Cr(VI) reduction efficiency at -20 °C of the sample purged with Ar or O_2 prior to freezing was measured and compared with that of the sample under air-equilibrium conditions (Figure 3d). The reduction efficiency of Cr(VI) increased by Ar purge (i.e., in relatively O_2-poor condition), but decreased after O_2 purge (i.e., in relatively O_2-rich condition). This result supports that the faster increase of dioxygen concentration at lower freezing temperature stops the Cr(VI) reduction process earlier and then subsequently decreases the reduction efficiency of Cr(VI).

Verification of Freeze Concentration Phenomenon. The enhanced reduction of Cr(VI) in ice should be due to the freeze concentration of H_2O_2 and protons in the liquid brine. To verify the freeze concentration phenomenon as the reason for the enhanced Cr(VI) reduction in ice, we investigated the reduction of Cr(VI) in water at high H_2O_2 (1 mM) and/or proton concentrations (pH = 2.0) and compared their results to those of the reference experiment ([H_2O_2] = 100 μM and pH = 3.0) (Figure 4). The reduction of Cr(VI) by H_2O_2 was enhanced when the concentration of either H_2O_2 or protons increased by 10 times. In addition, the reduction of Cr(VI) in water was more significant and comparable to that in ice when both the concentration of H_2O_2 and protons increased by 10 times. Therefore, the enhanced reduction of Cr(VI) in ice should be attributed to the freeze concentration of both protons and H_2O_2 (not protons or H_2O_2 alone) in the liquid brine.

H_2O_2-Mediated Reduction of Cr(VI) in Electroplating Wastewater in Water and Ice. To verify the enhanced H_2O_2-mediated Cr(VI) reduction by freezing in real Cr(VI)-contaminated aquatic systems, the reduction of Cr(VI) in the diluted electroplating wastewater was investigated in both water and ice (Figure 5). The electroplating wastewater was obtained from a local electroplating plant in

Korea and its chemical composition is listed in Table 1. The concentration of Cr(VI) in the electroplating wastewater was ~ 0.6 M and the pH was ~ 0.4. The raw electroplating wastewater was diluted ~ 30,000 times with deionized water. After the addition of H2O2 (100 mM, 100 μL) to the diluted electroplating wastewater ([Cr(VI)] ≈ 20 μM, 99.9 mL), the pH of the diluted electroplating wastewater containing H_2O_2 ([Cr(VI)] = 20 μM, [H_2O_2] = 100 μM, and pH = 5.1) was adjusted to the desired pH (i.e., pH = 3.0, 4.0, or 5.0) with a $HClO_4$ solution. The reduction of Cr(VI) in the electroplating wastewater by H_2O_2 was also markedly enhanced by freezing at all pH ranges tested (pH 3-5). In addition, the reduction efficiency of Cr(VI) in the electroplating wastewater was similar to that in the deionized water despite the presence of other metals, which implies that H_2O_2 can selectively reduce Cr(VI) among the various metals.

4. Conclusion

Both Cr(VI) and H_2O_2 are ubiquitous in atmospheric water, natural waters, and soil,(Cooper et al, 1988, Saputro et al, 2014) and chemical reactions in ice can occur in various geographical regions, such as permafrost, polar regions, high latitudes, and midlatitudes during the winter season, and the upper troposphere. Therefore, the reaction in ice between Cr(VI) and H_2O_2 can significantly influence the concentrations of both Cr(VI) and H_2O_2 in the global environment. In particular, the pH of atmospheric water, such as rain and clouds, is in the range of (Takenaka et al, 1996, Park et al, 2010, Boxe et al, 2009, Boxe et al, 2008, Takenaka et al, 1992,Herrmann et al, 2013) which is a good condition for the proposed ice/Cr(VI)/H_2O_2 process. Therefore, the freezing of atmospheric water containing both Cr(VI) and H_2O_2 in the cryosphere and the upper troposphere can significantly reduce its toxicity and potential risk through the reduction of Cr(VI) to Cr(III).

Cr(VI) is one of the most notorious pollutants generated from various industries due to its high production volume and toxicity, and the pH of Cr(VI)-contaminated wastewaters is very low.(Chen et al, 2007) In addition, the pH of acid mine drainage (AMD), which contains high concentrations of chromium (up to 15 mM), is usually lower than 5.0.(Sheoran et al, 2006,

Regenspurg et al, 2005) The results of this study imply that a respectable amount of Cr(VI) in Cr(VI)-contaminated wastewater and AMD can be removed by reacting with naturally generated H_2O_2 in cold environments.

We investigated the reduction of Cr(VI) by H_2O_2 in frozen aqueous solutions compared with the corresponding reaction in aqueous solutions. In water, the reaction between Cr(VI) and H_2O_2 is very slow and the intermediate Cr(V) species, which is generated from the one-electron reduction of Cr(VI) by H_2O_2, is immediately re-oxidized back to Cr(VI). Therefore, the reduction of Cr(VI) to Cr(III) by H_2O_2 was limited in water. In contrast, the reduction of Cr(VI) by H_2O_2 proceeded rapidly at pH = 3.0 in ice until either Cr(VI) or H_2O_2 was completely consumed. The reaction between Cr(VI) and H_2O_2 in ice was primarily initiated by a proton-coupled electron transfer (PCET) mechanism and the observed H_2O_2 to Cr(VI) molar ratio value ~ 1.5 satisfied the theoretical (stoichiometric) requirements. The enhanced reduction of Cr(VI) in ice should be attributed to the freeze concentration of both H_2O_2 and protons in the liquid brine, which provide a better reaction medium for the reduction of Cr(VI) to Cr(III) through PCET reaction. The observed synergistic effect of higher H_2O_2 concentration and lower pH on Cr(VI) reduction in water corroborates the freeze concentration phenomenon as the reason for the enhanced Cr(VI) reduction in ice. The reduction efficiency of Cr(VI) by H_2O_2 in ice varied depending on the H_2O_2 concentration, pH, and freezing temperature. However, the reduction of Cr(VI) in ice was more significant than that in water under all experimental conditions. This study provides useful information for understanding the fate and cycling of Cr(VI) in the cryosphere and the upper troposphere. However, the exact concentrations of H_2O_2 and proton in the liquid brine are unknown at this stage. Based on precise modeling and/or in-situ measurement of H_2O_2 and proton concentrations in the liquid brine during freezing, more detailed quantitative investigations of the Cr(VI) reduction kinetics in ice need to be performed.

얼음 내에서 향상된 과산화수소에 의한 6가 크롬의 제거 반응

김기태[1], 최원용[2], 윤호일[1]

[)]한국해양과학원부설 극지연구소
[2]POSTECH 환경공학부

요약: 과산화수소에 의한 독성 6가 크롬의 제거반응을 액상과 얼음상에서 비교 실험하였다. 액상(영상 25도)에서 매우 느리게 진행되던 6가크롬의 환원반응이 얼음(영하 20도)상에서 매우 빠르게 진행되는 것을 확인하였다. 얼음 상에서 향상된 6가 크롬의 환원반응은 다양한 과산화수소의 농도범위(20~1000 uM) 및 온도 범위(영하 10도 ~ 영하 30도)에서 일어났다. 측정된 과산화수소 소모량과 6가크롬의 제거량의 몰 비(molar ratio)는 이론적 몰 비인 1.5와 유사하게 나왔으며 이는 수소와 전자의 동시 전달에 의한 반응결과로 예상된다. 또한, 얼음상에서 빨라진 6가 크롬의 제거 반응은 얼음 내 준액체층에서 동결농축효과에 의한 과산화수소와 수소이온의 농도(pH 강하)때문인 것으로 생각되어진다. 액상과 얼음상에서 상이한 6가 크롬의 환원 반응 메카니즘을 본문에 제시하였다. 국내 폐수공정에서 배출된 6가 크롬 오염폐수를 대상으로 동일한 실험ㅇ르 수행한 결과 실험실 결과와 유사하게 나왔으며 이는 동결에 의한 6가크롬의 제거기작을 실제 폐수공정에 적용할 수 있음을 시사한다.

참고문헌

Bartels-Rausch, T.; Jacobi, H.-W.; Kahan, T. F.; Thomas, J. L.; Thomson, E. S.; Abbatt, J. P. D.; Ammann, M.; Blackford, J. R.; Bluhm, H.; Boxe, C.; Domine, F.; Frey, M. M.; Gladich, I.; Guzm?n, M. I.; Heger, D.; Huthwelker, T.; Kl?n, P.; Kuhs, W. F.; Kuo, M. H.; Maus, S.; Moussa, S. G.; McNeill, V. F.; Newberg, J. T.; Pettersson, J. B. C.; Roeselov?, M.; Sodeau, J. R. A review of air-ice chemical and physical interactions (AICI): liquids, quasi-liquids, and solids in snow. Atmos. Chem. Phys. 2014, 14, 1587-1633.

Bader, H.; Sturzenegger, V.; Hoign?, J. Photometric method for the determination of low concentrations of hydrogen peroxide by the peroxidase catalyzed oxidation of N,N-diethyl-p-phenylenediamine (DPD). Water Res. 1988, 22, 1109-1115.

Bagchi, D.; Stohs, S. J.; Downs, B. W.; Bagchi, M.; Preuss, H. G. Cytotoxicity and oxidative mechanisms of different forms of chromium. Toxicology 2002, 180, 5-22.

Barnhart, J. Occurrences, uses, and properties of chromium. Regul. Toxicol. Pharmacol. 1997, 26, S3-S7.

Barrera-Díaz, C. E.; Lugo-Lugo, V.; Bilyeu, B. A review of chemical, electrochemical and biological methods for aqueous Cr(VI) reduction. J. Hazard. Mater. 2012, 223-224, 1-12.

Betterton, E. A.; Anderson, D. J. Autoxidation of N(III), S(IV), and other species in frozen solution-a possible pathway for enhanced chemical transformation in freezing systems. J. Atmos. Chem. 2001, 40, 171-189.

Bláha, L.; Klánová, J.; Klán, P.; Janošek, J.; Škarek, M.; Růžička, R. Toxicity increases in ice containing monochlorophenols upon photolysis: environmental consequences. Environ. Sci. Technol. 2004, 38, 2873-2878.

Boxe, C. S.; Saiz-Lopez, A. Influence of thin liquid films on polar ice chemistry: implications for Earth and planetary science. Polar Sci. 2009, 3, 73-81.

Boxe, C. S.; Saiz-Lopez, A. Multiphase modeling of nitrate photochemistry in the

quasi-liquid layer (QLL): implications for NOx release from the Arctic and coastal Antarctic snowpack. Atmos. Chem. Phys. 2008, 8, 4855-4864.

Chang, K. L. B.; Tai, M.-C.; Cheng, F.-H. Kinetics and products of the degradation of chitosan by hydrogen peroxide. J. Agric. Food Chem. 2001, 49, 4845−4851.

Chen, S.-S.; Cheng, C.-Y.; Li, C.-W.; Chai, P.-H.; Chang, Y.-M. Reduction of chromate from electroplating wastewater from pH 1 to 2 using fluidized zero valent iron process. J. Hazard. Mater. 2007, 142, 362−367.

Chu, L.; Anastasio, C. Formation of hydroxyl radical from the photolysis of frozen hydrogen peroxide. J. Phys. Chem. A 2005, 109, 6264−6271.

Clark, C. D.; De Bruyn, W. J.; Jakubowski, S. D.; Grant, S. B. Hydrogen peroxide production in marine bathing waters: implications for fecal indicator bacteria mortality. Mar. Pollut. Bull. 2008, 56, 397−401.

Cooper, W. J.; Zika, R. G.; Petasne, R. G.; Plane, J. M. C. Photochemical formation of hydrogen peroxide in natural waters exposed to sunlight. Environ. Sci. Technol. 1988, 22, 1156−1160.

Costa, M. Potential hazards of hexavalent chromate in our drinking water. Toxicol. Appl. Pharmacol. 2003, 188, 1−5.

CRC Handbook of Chemistry and Physics, 77th ed.; David, R. L., Ed.; CRC Press: New York, 1996; pp 10−189.

De Velde, K. V.; Ferrari, C.; Barbante, C.; Moret, I.; Bellomi, T.;Hong, S.; Boutron, C. A 200 year record of atmospheric cobalt, chromium, molybdenum, and antimony in high altitude alpine firn and ice. Environ. Sci. Technol. 1999, 33, 3495−3501.

Dong, X.; Ma, L. Q.; Gress, J.; Harris, W.; Li, Y. Enhanced .Cr(VI) reduction and As(III) oxidation in ice phase: important role of dissolved organic matter from biochar. J. Hazard. Mater. 2014, 267, 62−70.

Foley, W. T.; Giguère, P. A. Hydrogen peroxide and its analogues: II. phase equilibrium in the system hydrogen peroxidewater. Can. J. Chem. 1951, 29, 123−131.

Gabrielli, P.; Barbante, C.; Boutron, C.; Cozzi, G.; Gaspari, V.; Planchon, F.;

Ferrari, C.; Turetta, C.; Hong, S.; Cescon, P. Variations in atmospheric trace elements in Dome C (East Antarctica) ice over the last two climatic cycles. Atmos. Environ. 2005, 39, 6420−6429.

Grannas, A. M.; Bogdal, C.; Hageman, K. J.; Halsall, C.; Harner, T.; Hung, H.; Kallenborn, R.; Klán, P.; Klánová, J.; Macdonald, R. W.; Meyer, T.; Wania, F. The role of the global cryosphere in the fate of organic contaminants. Atmos. Chem. Phys. 2013, 13, 3271−3305.

Griend, D. A. V.; Golden, J. S.; Arrington, C. A., Jr. Kinetics and mechanism of chromate reduction with hydrogen peroxide in base. Inorg. Chem. 2002, 41, 7042−7048.

Heger, D.; Jirkovský, J.; Klán, P. Aggregation of methylene blue in frozen aqueous solutions studied by absorption spectroscopy. J. Phys. Chem. A 2005, 109, 6702−6709.

Heger, D.; Klánová, J.; Klán, P. Enhanced protonation of cresol red in acidic aqueous solutions caused by freezing. J. Phys. Chem. B 2006, 110, 1277−1287.

Herrmann, H. Kinetics of aqueous phase reactions relevant for atmospheric chemistry. Chem. Rev. 2003, 103, 4691−4716.

Jeong, D.; Kim, K.; Choi, W. Accelerated dissolution of iron oxides in ice. Atmos. Chem. Phys. 2012, 12, 11125−11133.

Joo, S. H.; Feitz, A. J.; Sedlak, D. L.; Waite, T. D. Quantification of the oxidizing capacity of nanoparticulate zero-valent iron. Environ. Sci. Technol. 2005, 39, 1263−1268.

Kamiyama, K.; Motoyama, H.; Fujii, Y.; Watanabe, O. Distribution of hydrogen peroxide in surface snow over antarctic ice sheet. Atmos. Environ. 1996, 30, 967−972.

Kawanishi, S.; Inoue, S.; Sano, S. Mechanism of DNA cleavage induced by sodium chromate(VI) in the presence of hydrogen peroxide. J. Biol. Chem. 1986, 261, 5952−5958.

Kim, K.; Choi, W. Enhanced redox conversion of chromate and arsenite in ice. Environ. Sci. Technol. 2011, 45, 2202−2208.

Kim, K.; Yoon, H.-I.; Choi, W. Enhanced dissolution of manganese oxide in ice compared to aqueous phase under illuminated and dark conditions.

Environ. Sci. Technol. 2012, 46, 13160−13166.

Klán, P.; Klánová, J.; Holoubek, I.; Čupr, P. Photochemical activity of organic compounds in ice induced by sunlight irradiation: the Svalbard project. Geophys. Res. Lett. 2003, 30, 1313.

Klán, P.; Holoubek, I. Ice (photo)chemistry. ice as a medium for long-term (photo)chemical transformations-environmental implications. Chemosphere 2002, 46, 1201−1210.

Klánová, J.; Klán, P.; Nosek, J.; Holoubek, I. Environmental ice photochemistry: monochlorophenols. Environ. Sci. Technol. 2003, 37, 1568−1574.

Liu, J.; Wu, J.-Y.; Kang, C.-L.; Peng, F.; Liu, H.-F.; Yang, T.; Shi, L.; Wang, H.-L. Photo-fenton effect of 4-chlorophenol in ice. J. Hazard. Mater. 2013, 261, 500−511.

Liu, L.; Yuan, Y.; Li, F.-b.; Feng, C.-h. In-situ Cr(VI) reduction with electrogenerated hydrogen peroxide driven by iron-reducing bacteria. Bioresour. Technol. 2011, 102, 2468−2473.

McNeill, V. F.; Grannas, A. M.; Abbatt, J. P. D.; Ammann, M.; Ariya, P.; Bartels-Rausch, T.; Domine, F.; Donaldson, D. J.; Guzman, M. I.; Heger, D.; Kahan, T. F.; Klán, P.; Masclin, S.; Toubin, C.; Voisin, D. Organics in environmental ices: sources, chemistry, and impacts. Atmos. Chem. Phys. 2012, 12, 9653−9678.

Möller, D. Atmospheric hydrogen peroxide: evidence for aqueous-phase formation from a historic perspective and a one-year measurement campaign. Atmos. Environ. 2009, 43, 5923−5936.

Neftel, A.; Jacob, P.; Klockow, D. Measurements of hydrogen peroxide in polar ice samples. Nature 1984, 311, 43−45.

Park, S.-C.; Moon, E.-S.; Kang, H. Some fundamental properties and reactions of ice surfaces at low temperatures. Phys. Chem. Chem. Phys. 2010, 12, 12000−12011.

Pettine, M.; Campanella, L.; Millero, F. J. Reduction of hexavalent chromium by H2O2 in acidic solutions. Environ. Sci. Technol. 2002, 36, 901−907.

Perez-Benito, J. F.; Arias, C. A kinetic study of the chromium(VI)-hydrogen peroxide reaction. role of the diperoxochromate(VI) intermediates. J. Phys. Chem. A 1997, 101, 4726−4733.

Peters, J. W.; Bekowies, P. J.; Winer, A. M.; Pitts, J. N., Jr. An investigation of potassium perchromate as a source of singlet oxygen. J. Am. Chem. Soc. 1975, 97, 3299−3306.

Regenspurg, S.; Peiffer, S. Arsenate and chromate incorporation in schwertmannite. Appl. Geochem. 2005, 20, 1226−1239.

Robinson, C.; Boxe, C. S.; Guzmán, M. I.; Colussi, A. J.;Hoffmann, M. R. Acidity of frozen electrolyte solutions. J. Phys. Chem.B 2006, 110, 7613−7616.

Saputro, S.; Yoshimura, K.; Matsuoka, S.; Takehara, K.; Narsito; Aizawa, J.; Tennichi, Y. Speciation of dissolved chromium and the mechanisms controlling its concentration in natural water. Chem. Geol. 2014, 364, 33−41.

Sheoran, A. S.; Sheoran, V. Heavy metal removal mechanism of acid mine drainage in wetlands: a critical review. Miner. Eng. 2006, 19, 105−116.

Sigg, A.; Neftel, A. Evidence for a 50% increase in H2O2 over the past 200 years from a Greenland ice core. Nature 1991, 351, 557−559.

Sigg, A.; Neftel, A. Seasonal variations in hydrogen peroxide in polar ice cores. Ann. Glaciol. 1988, 10, 157−162.

Standard Methods for the Examination of Water and Wastewater, 19th ed.; Eaton, A. D.; Clesceri, L. S.; Greenberg, A. E., Ed.; APAH: Washington, DC, 1995.

Takenaka, N.; Ueda, A.; Maeda, Y. Acceleration of the rate of nitrite oxidation by freezing in aqueous solution. Nature 1992, 358, 736−738.

Takenaka, N.; Ueda, A.; Daimon, T.; Bandow, H.; Dohmaru, T.; Maeda, Y. Acceleration mechanism of chemical reaction by freezing: the reaction of nitrous acid with dissolved oxygen. J. Phys. Chem. 1996, 100, 13874−13884.

Takenaka, N.; Bandow, H. Chemical kinetics of reactions in the unfrozen solution of ice. J. Phys. Chem. A 2007, 111, 8780−8786.

Vaiopoulou, E.; Gikas, P. Effects of chromium on activated sludge and on the performance of wastewater treatment plants: a review. Water Res. 2012, 46, 549−570.

Walling, C.; Goosen, A. Mechanism of the ferric ion catalyzed decomposition of hydrogen peroxide. effect of organic substrates. J. Am. Chem. Soc.

1973, 95, 2987−2991.Abbatt, J. P. D.; Thomas, J. L.; Abrahamsson, K.; Boxe, C.; Granfors, A.; Jones, A. E.; King, M. D.; Saiz-Lopez, A.; Shepson, P. B.; Sodeau, J.; Toohey, D. W.; Toubin, C.; von Glasow, R.; Wren, S. N.; Yang, X. Halogen activation via interactions with environmental ice and snow in the polar lower troposphere and other regions. Atmos. Chem. Phys. 2012, 12 (14), 6237−6271.

element[a]	Al	As	B	Ca	Cr	Cs	Cu	Fe	Mg	Mo	Na	Pb	Tl
concentration (ppm)[a]	56	100	62	306	39524	9104	281	1348	69	50	125	75	37

a concentrations of other elements (Ag, Ba, Be, Cd, Co, Mn, Ni, Sb, Se, Si, Ti, V, and Zn) were negligible.

Table 1. Chemical composition of the electroplating wastewater.

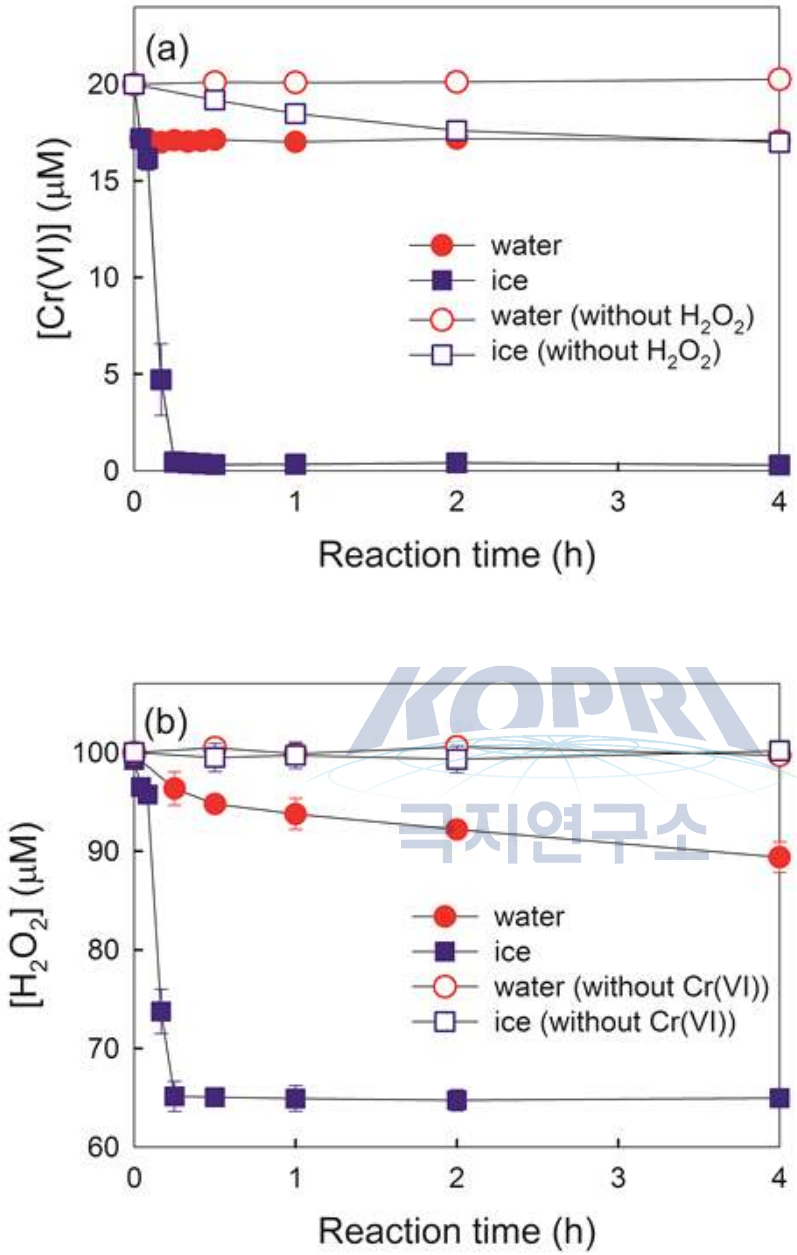

Figure 1. Time profiles of (a) Cr(VI) and (b) H_2O_2 concentrations in water and ice. Experimental conditions were as follows: $[Cr(VI)]_i$ = 20 μM, $[H_2O_2]_i$ = 100 μM, pHi = 3.0, and reaction temperatures = water at 25 °C and ice at -20 °C.

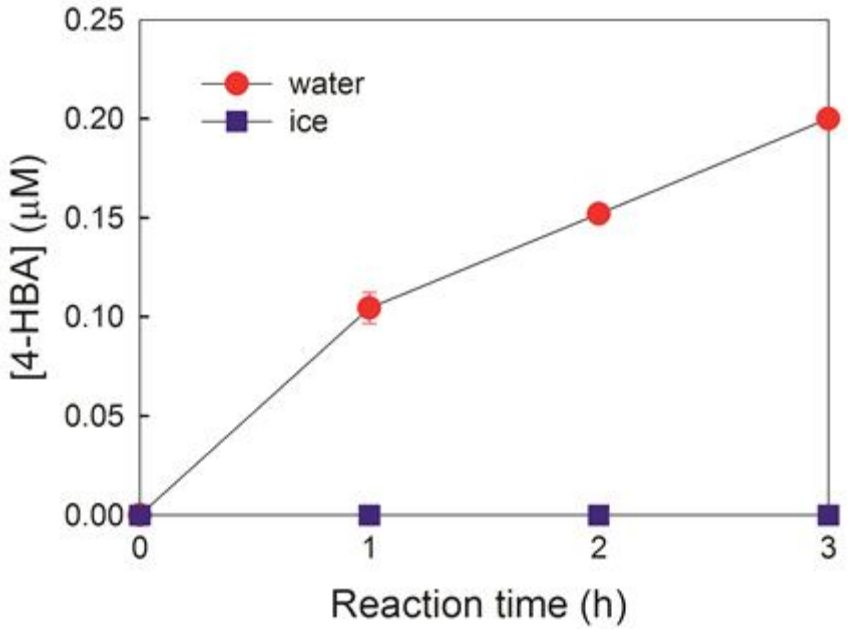

Figure 2. Time profiles of ˙OH production in water and ice. Experimental conditions were as follows: $[Cr(VI)]_i$ = 20 μM, $[H2O2]_i$ = 100 μM, $[BA]_i$ = 1 mM, pHi = 3.0, and reaction temperatures = water at 25 °C and ice at −20 °C.

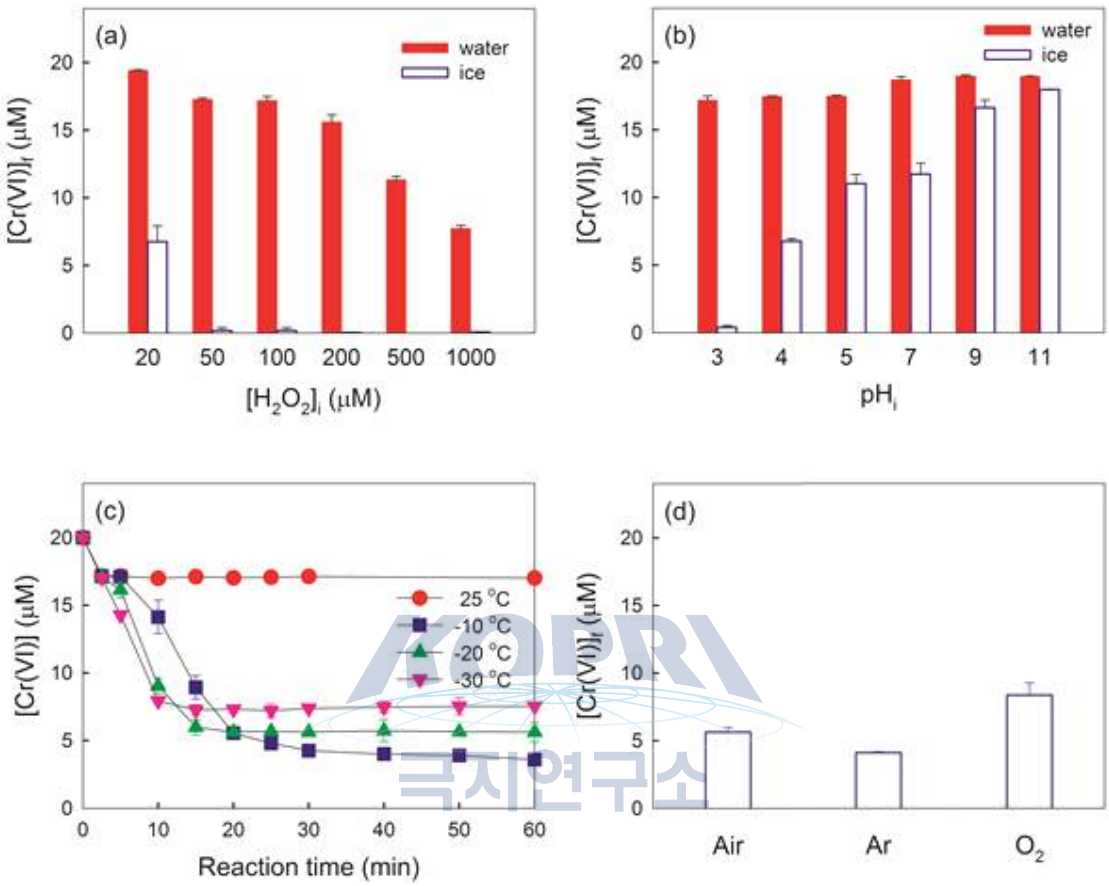

Figure 3. Effect of (a) H_2O_2 concentration, (b) pH, (c) temperature, and (d) dioxygen concentration on Cr(VI) reduction in water and ice. Experimental conditions were as follows: $[Cr(VI)]_i$ = 20 μM, $[H_2O_2]_i$ = 100 μM (for b, c, and d), pH_i = 3.0 (for a), pH_i = 4.0 (for c and d), reaction temperatures = water at 25 °C and ice at −20 °C (for a, b, and d), and reaction time = 2 h (for a, b, and d). A conical centrifuge tube containing Cr(VI) and H_2O_2 was sealed with a rubber septum. Then, Ar or O_2 (99.999%) was purged for 30 min prior to freezing (for d).

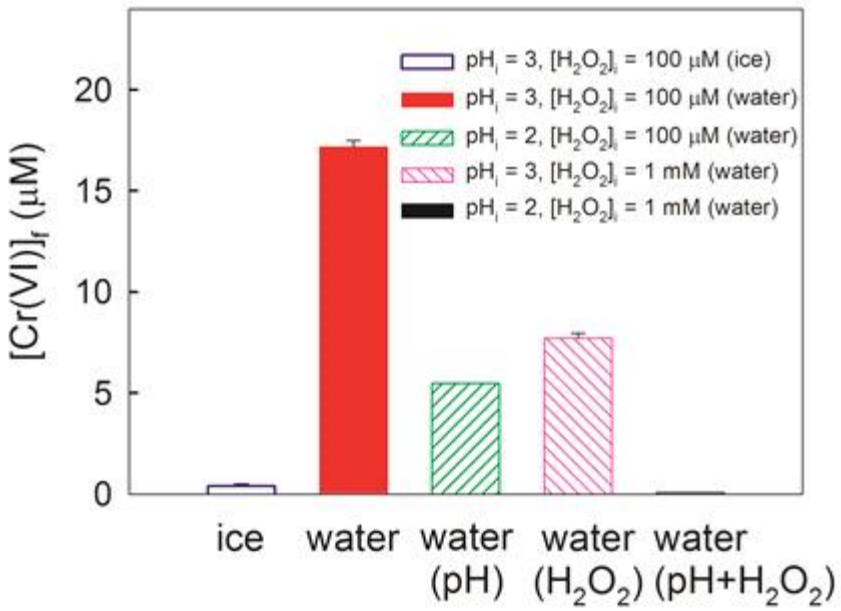

Figure 4. Effect of H_2O_2 concentration and pH on Cr(VI) reduction in water and ice. Experimental conditions were as follows: $[Cr(VI)]_i$ = 20 μM, reaction temperatures = water at 25 ℃ and ice at -20 ℃, and reaction time = 2 h.

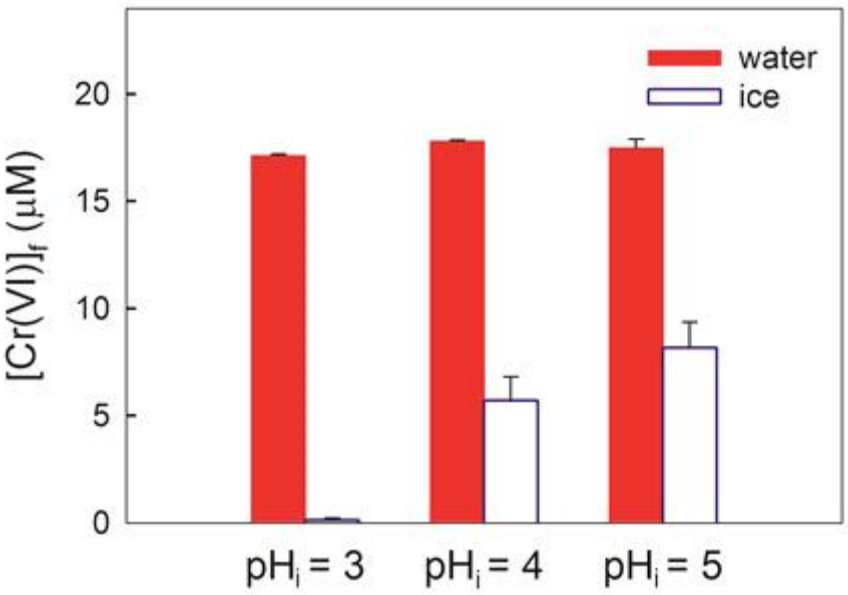

Figure 5. Reduction of Cr(VI) in the electroplating wastewater by H2O2 at various pH in water and ice. The electroplating wastewater was diluted to the desired concentration, H_2O_2 was added, and then the pH was adjusted with a $HClO_4$ solution. Experimental conditions were as follows: $[Cr(VI)]_i$ = 20 μM, $[H2O2]_i$ = 100 μM, reaction temperatures = water at 25 °C and ice at −20 °C, and reaction time = 2 h.

제 13 장

Freezing-Enhanced Dissolution of Iron Oxides: Effects of Inorganic Acid Anions[8)]

Kitae Kim[1], Dae Wi Min[2], and Wonyong Choi[2]

[1]Korea Polar Research Institute
[2]Pohang University of Science and Technology

Abstract: Dissolution of iron from mineral dust particles greatly depends upon the type and amount of copresent inorganic anions. In this study, we investigated the roles of sulfate, chloride, nitrate, and perchlorate on the dissolution of maghemite and lepidocrocite in ice under both dark and UV irradiation and compared the results with those of their aqueous counterparts. After 96 h of reaction, the total dissolved iron in ice (pH 3 before freezing) was higher than that in the aqueous phase (pH 3) by 6−28 times and 10−20 times under dark and UV irradiation, respectively. Sulfuric acid was the most efficient in producing labile iron under dark condition, whereas hydrochloric acid induced the most dissolution of the total and ferrous iron in the presence of light. This ice-induced dissolution result was also confirmed with Arizona Test Dust (AZTD). In the freeze− thaw cycling test, the iron oxide samples containing chloride, nitrate, or perchlorate showed a similar extent of total dissolved iron after each cycling while the sulfate-containing sample rapidly lost its dissolution activity with repeating the cycle. This unique phenomenon observed in ice might be related to the freeze concentration of protons, iron oxides, and inorganic anions in the liquid-like ice grain boundary region. These results suggest that the ice-enhanced dissolution of iron oxides can be a potential source of

8) 이 연구 결과는 다음의 논문으로 출판되었음: Daun Jeong, Kitae Kim, Dae Wi Min, and Wonyong Choi 2015. Freezing-Enhanced Dissolution of Iron Oxides: Effects of Inorganic Acid Anions. Environ. Sci. Technol. 015, 49, 12816−12822

bioavailable iron, and the acid anions critically influence this process.

1. Introduction

Iron is an essential but limiting nutrient to marine organisms in about 30% of the open ocean (HNLC; high nutrient low chlorophyll).1−3 Among 16 Tg of iron deposited to the open ocean each year, only a small portion of it (i.e., around 0.02 to 1 nM) is in a form bioavailable to marine organisms.4 This lack of bioavailable iron is mainly caused by the low solubility of ferric ion, which is the most stable form at pH 8, and also by removal through adsorption on sinking particles.5,6 The major source of iron in the open ocean is the atmospheric deposition of mineral dust aerosols, which accounts for 95% of the atmospheric iron budget.4,7 Aeolian dust aerosols undergo various chemical and physical weathering processes that enhance their solubility and thus provide bioavailable iron upon deposition to the open ocean. Extensive laboratory, field, and model studies have been carried out to investigate the factors controlling iron dissolution processes and these include the effect of light, pH, organic and inorganic ligands, and the characteristics (e.g., source, size, struc-ture, etc.) of iron-containing dust.7−10

Reactions in the ice matrix can undergo different pathways compared to the aqueous counterparts. Although an apparent frozen material seems completely solid, it may contain some amount of liquid when frozen above its “eutectic point”.11,12 This liquid content exists between solid ice crystals and is often referred to as “liquid-like boundary” or “ice grain boundary”.

In this ice boundary region, solutes, protons, and dissolved gases can be extremely concentrated (i.e., freeze concentration effect), which provides a unique reaction environment that is very dif-ferent from the normal aqueous media.13−15 For example, nitrite oxidation has been reported to be accelerated by 105 times upon freezing.13 It is interesting to note that even the exothermic hy-dration of 2-oxopropanoic acid to 2,2-dihydroxypropanoic pro-ceeded down to 250 K in ice.16 Our recent studies found that the dissolution of iron oxide particles can be greatly enhanced upon freezing both in the dark and under

photoirradiation because of thefreezeconcentration effect of protons, iron oxides, and organic ligands in the grain boundaries.17,18 A similar ice-enhanced dis-solution was also observed for manganese oxide.19 The extent of iron (or manganese) release depended on the presence of light, pH, freezing temperature, surface area of iron oxides, and the type of organic ligands present.

Iron-containing atmospheric dust particles are one of the most efficient ice nuclei in forming cirrus clouds.20−22 The presence of atmospheric dust facilitates the ice formation (i.e., heterogeneous freezing) at relatively low humidity and high temperature compared to a condition in which ice can form in the absence of any nuclei (i.e., homogeneous freezing).23,24 Recent studies also indicate that ice residues frequently contain organic/inorganic compounds from anthropogenic or natural sources.25 In the aqueous phase, these compounds can influence the dissolution of iron by forming mono- or multidentate complexes between the ligands and the iron oxide surface.6,8,26 Therefore, iron oxides trapped in atmo-spheric ice might undergo unique chemical and physical reactions in the presence of these ligands.

In this study, we investigated the roles of inorganic acid anions on the dissolution of iron oxides in ice under both dark and UV irradiation. Atmospheric dust particles can often be coated with high concentrations of sulfate, chloride, and nitrate in the acidic deliquescence layer on the surface.27,28 Moreover, many studies have reported the coexistence of these inorganic anions and dust particles in atmospheric ice residuals.21,22 To better understand the roles of inorganic acid anions in producing bioavailable iron in ice, we conducted dissolution experiments with maghemite and lepidocrocite in both aqueous and ice phases in the presence of sulfate, chloride, nitrate, and perchlorate.

2. Materials and methods

Materials. Maghemite (Aldrich, BET surface area 36 m2/g), lepidocrocite (LANXESS Corp, 75 m2/g), and Arizona fine test dust (Power Technology Inc., ISO 12103-1 A2 test dust) were used as received for iron oxide dissolution experiments. Arizona test dust (AZTD) is typically composed of 2−5wt%ofFe2O3 and hasbeenusedasareferencematerial for mineral dust. Detailed

information on AZTD can be found at www.powdertechnologyinc. com. Inorganic acids such as sulfuric acid, hydrochloric acid, nitric acid, and perchloric acid were all purchased from Aldrich and were diluted with ultrapure (18 MΩ cm) deionized water as desired.

Experimental Procedures. A total of 50 mL of 0.2 g/L iron oxide suspension was prepared in ultrapure (18 MΩcm) deionized water and sonicated for 3 min for better dispersion. After sonication, pH of the iron oxide suspensions was adjusted with H2SO4,HCl, HNO,or HClO. The initial pH condition was mainly adjusted to 3 in order to mimic a low pH atmospheric aerosol environment. Five mL of this suspension was placed in a quartz tube, sealed with septa, and put in a merry-go-round photolysis reactor in the ethanol bath set at −5 °C. The temperature of the ethanol bath was then gradually lowered to−20 °C(witharate of0.5°Cmin−1) to prevent the breakage of the tubes. A 100-W mercury lamp (Ace Glass Inc.) surrounded by a pyrex jacket (transmitting λ > 300 nm) was immersed in an ethanol (transparent to the irradiation of λ >300 nm)bath for uniform irradiation. The UV light intensity incident on the immersed quartz tube reactor was estimated to be 3.0 × 10−4 Einstein min−1 L−1 (λ > 300 nm) by ferrioxalate actinometry.17 For dissolution experiments under dark condition, 5 mL of the iron oxide suspension was placed in a conical tube (15 mL) and put in an ethanol bath cooled at −20 °C or kept at ambient tem-perature (20−25 °C) for aqueous samples. After each reaction time (i.e., 24, 48, 72, 96 h), sample tubes were thawed in warm water (40 °C) for further analysis. The thawing process was completed within 10 min and the thawed samples were filtered with a 0.45-μm filter to remove particles prior to the analysis of dissolved iron. The reprecipitation of dissolved iron was negligible withinthistime ofthesampletreatments. Inthecaseoffreeze− thaw cycling experiments, the experimental procedure was the same but the temperature of the ethanol bath was adjusted repeatedly between 25 °Cand −20 °Cevery 12hfor4 days.After each cycle, the sample tubes were withdrawn and analyzed.

Analysis. The dissolved iron was determined colorimetri-cally after filtering the suspension samples through a 0.45-μm filter. For ferrous (Fe2+) analysis, 2 mL of 1,10-phenanthroline and 1.5 mL of ammonium acetate buffer were added to a 5-mL conical tube containing 1.5 mL of the sample. The same samples were

also analyzed for the total dissolved iron (Fetot = Fe2+ +Fe3+) by adding 100 μL of hydroxylamine hydrochloride for ferric reduction to ferrous. After an hour, absorbance of the samples was measure with a UV/visible spectrophotometer (Libra S22, Biochrom) at 510 nm. ζ-Potential and hydrodynamic diameter of the iron oxide samples were measured using an electrophoretic light-scattering spectrophotometer (ELS 8000, Otsuka). The extent of aggregation of iron oxides was analyzed with TEM. The TEM samples were prepared using a freeze-drying method to minimize a possible effect of drying process on the aggregation state of the iron oxide particles. One drop of iron oxide suspension containing the acid anions (i.e., Cl− or SO42−) was applied to a TEM sample grid, frozen at −80 °C, and then dried in a freeze drier for 12 h prior to TEM analysis.

3. Results and discussion

Anion Effects on Iron Oxide Dissolution in Ice under Dark Condition. Figure 1 compares the production of total dissolved iron from the dissolution of maghemite (a) and lepidocrocite (b) in the presence of various acid anions both in the ice and aqueous phases. The dissolved iron concentra-tion was markedly enhanced in the ice phase for all types of acids used, while a negligible concentration of dissolved iron was observed in the aqueous phase. In the absence of light (Figure 1), most of the dissolved iron was in the ferric form, which indicates a nonreductive dissolution.18 The iron dissolving efficiency of the inorganic anions was in the order of sulfate > chloride > nitrate ≈ perchlorate. After 96 h of reaction of maghemite in ice, the samples with sulfate and chloride yielded the highest concen-trations (45(±13) μMand31(±8) μM, respectively) of total dissolved iron, while nitrate and perchlorate produced much lesser amounts (8.4(±1) μMand13μM, respectively). In the aqueous phase, approximately 1 μM of labile iron was released with all types of inorganic anions. This ice-induced iron dis-solution was also observed for lepidocrocite (Figure 1b) and AZTD (Figure 2). The extent of iron dissolution in ice was dependent upon the initial acid anion concentration in the sample. With increasing the concentration of sulfate and chloride (i.e., up to 10 mM), the

dissolved iron increased (Supporting Information (SI) Figure S1). Another factor that might influence the dissolution rate is the surface area of iron oxide samples. Although a higher dissolution rate is expected with a higher surface area, lepidocrocite (of which BET surface area is twice as large as that of maghemite) exhibited a lower dissolution rate than maghemite (compare Figure 1avs 1b). This implies that other factors such as the crystallinity and inorganic acid anion are more critical in determining the dissolution rate.

The accelerated dissolution of iron oxides in ice under dark condition can be related to the "freeze concentration effect" of iron oxides, protons, and inorganic anions in the liquid-like ice grain boundary region. Studies showed that dissolved ions are distributed unequally between the ice and aqueous phases when freezing. This inequality develops an electric potential (so-called "freezing potential"), which induces OH− or H3O+ to be preferentially accumulated in the ice grain boundary region resulting in a pH change.29 For example, NaCl induces the accumulation of OH− ions (pH increase) in the liquid-like boundary region through the preferential incorporation of Cl− ions in the ice matrix (i.e., negative potential in the ice side and positive potential in the liquid side) while Na2SO4 may have the opposite effect (inducing pH decrease).30,31 However, in our study, the presence of iron oxides makes the chemistry more complex since the iron oxides, which contain amphoteric surface hydroxyl groups, can buffer the change of pH to some extent. It seems that the freezing-induced accumulation of protons32,33 and anions can enhance the interfacial iron dissolution processes (eqs 1 and 2) in the ice grain boundary region. The increased proton mobility in frozen media could be an important factor in the dissolution process. Proton mobility in a frozen media has been reported to be comparable to or even greater than that in the liquid counterpart.34 As expected, the initial pH had significant influence on enhancing the total dissolved iron in ice, and the iron dissolution was higher at lower pH (SI Figure S2), which should be ascribed to the proton-assisted dissolution (eq 1).

$$\equiv Fe^{III} - OH + H^+ \rightarrow Fe^{3+}_{(aq)} + H_2O \quad (1)$$

$$\equiv Fe^{III} - OH + L^- + H^+ \rightarrow \equiv Fe^{III}L + H_2O \rightarrow [Fe^{III}L]_{(aq)} + H_2O \quad (2)$$

Because the pH of all other dissolution experiments was con-trolled at pH 3 in this study (Figure 1), theobserveddifference in the iron dissolution rate with diff erent acid anions should be ascribed mainly to the effect of the anions, ligand-promoted dis-solution (eq 2). The presence of anion ligands may modify the dissolution process of iron oxides depending on their strength and mode of adsorption on the solid oxide surfaces.

The nonreductive ligand-promoted dissolution of iron oxides is initiated by the adsorption of inorganic ligand on the iron oxide surface. This weakens the Fe−O bonds and the ferric complex is detached from the iron oxide surface to be dissolved into the bulk solution (eq 2). Many studies have reported metal oxide dissolution promoted by sulfate and chloride. In particular, sulfate can strongly adsorb on oxide surfaces by displacing the surface hydroxyl groups and forming monodentate or bidentate complexes6,35,36 with surface iron.37 Being a divalent ion, sulfate tends to show stronger affinity on iron oxide surfaces and also promote more proton adsorption compared to monovalent anions.37,38 Therefore, sulfate can extract labile iron from iron oxides more efficiently compared to monovalent ions.32,38 The ice-enhanced release of labile iron in the presence of sulfate was also confirmed with AZTD, which is a reference material for mineral dust (Figure 2). Different types of monovalent ions also show disparate affinities on iron oxide surfaces. Among the monovalent ions, studies showed that chloride accelerates the dissolution of iron by forming strong complexation with ferric species and by directly coordinating to the solid oxide surface. In contrast, perchlorate and nitrate adsorb on the surface by forming weak outer-sphere complexes and are therefore considered inert electrolytes compared to sulfate and chloride.6,26,37,38 In the ice grain boundary regions, sulfate, chloride, and protons can be con-centrated, leading to both

ligand- and proton-assisted dissolution of iron. Moreover, the enhanced protonation of the iron oxide surface in the grain boundary increases the positive surface charge density, which further facilitates the electrostatic attraction of negatively charged chloride and sulfate anions.6,26

Anion Effects on Iron Oxide Dissolution in Ice under UV Light. Iron oxide dissolution experiments were also per-formed in the presence of light to investigate the solar irradi-ation effect, and the results are shown in Figure 3. In the ice phase, the production of both total dissolved iron and ferrous ion was markedly enhanced in the presence of light compared to the dark dissolution, which implies that a photoreductive dis-solution mechanism is operating in this case.17 This trend was also confirmed with thedissolutionfrom AZTD in thepresenceof sulfate (Figure 2). It should be noted that, under irradiation, the order of iron dissolution efficiency of the inorganic acid anions decreases in the order of chloride > sulfate > perchlorate > nitrate, which is different from that in the dark condition.

The photoreductive dissolution of iron oxide in ice can be largely explained by two mechanisms: the photoexcitation of surface iron complexes (e.g., ligand-to-metal charge transfer39−41) and the bandgap excitation of semiconducting iron oxides.17 As for the first case, the surface complexation of ligands promotes the photodissolution of iron.39−41 In the absence of ligands, sur-face coordinated water or hydroxyl groups donate an electron to surface ferric ion producing surface-bound ferrous species,42 which should be subsequently detached from the surface. The concen-tration of inorganic anions such as sulfate and chloride in the ice grain boundary region should promote their surface complexation, which subsequently accelerates the iron dissolution. On the other hand, the semiconductor model is based on the bandgap excita-tion of iron oxide with generating electron−hole pairs in the oxide lattice. The photogenerated conduction band (CB) electrons reduce the surface ferric ions (eq 3), while the holes can be scavenged by electron donors present in the surface region.

$$\equiv Fe^{III} - OH + e_{cb}^{-} \rightarrow \equiv Fe^{II} - OH \rightarrow Fe^{2+}_{(aq)} \qquad (3)$$

Among inorganic acid anions, chloride may react with the photogenerated valence band (VB) holes (Cl− +hvb+ → Cl□: E0(Cl□/Cl−) = 2.2 VNHE) to enhance the overall photoreductive dissolution of iron oxide, which may explain why the photo-dissolution of maghemite was the most efficient in the presence of chloride (see Figure 3). The VB edge potential of maghemite is positive enough to oxidize chloride ion to chlorine radical (Evb(maghemite) = 2.6 VNHE).43 This explanation is supported by the data shown in Table 1. Although the photoproduction of total dissolved iron in ice was highest with chloride, the produc-tion of Fe(III) was highest with sulfate (as in the dark dis-solution in Figure 1). Note that the photogeneration of Fe(II) is outstanding with chloride compared with other anions, which supports the role of chloride as a hole scavenger. The highest efficiency of maghemite/chloride system for the photodis-solution can be explained by the semiconductor mechanism where chlorides serve as a hole scavenger. Although this semi-conductor mechanism has been suggested as not effective because of the fast charge recombination in iron oxide,44,45 the ice system where the hole scavengers (e.g., chloride) can be highly concentrated in the ice grain boundary may be different from the aqueous system. Moreover, the iron oxide particles are excluded from the ice crystals and extensively aggregated in the grain boundary region.17 This agglomeration of semiconductor nanoparticles (iron oxide) may facilitate the charge-pair sepa-ration by electron hopping through the particle grain bound-aries when they are trapped in the frozen phase.17,46

An alternative explanation for the higher photogeneration of Fe(II) in the presence of chloride is the photoactivity of Fe(III)−Cl complex that leads to the generation of ferrous ions. Once ferric ions ([FeIII(H2O)5(OH)]2+ or simply FeOH2+)are dissolved through eqs 1 and 2, they can be complexed with chloride ions (eq 4). These Fe(III)−Cl complexes ([FeIII(H2O)5Cl]2+ or simply FeCl2+) are photoactive at UV and visible regions to reduce ferric to ferrous ion.7,47 At the low pH condition, the dominant species in the presence of chloride are FeCl2+ and FeCl2+ with FeOH2+ being present only in very low level. FeCl2+ can be pho-toreduced under solar irradiation (eq 5), which is twice as active as the photoreduction of FeOH2+ (eq 6). Such complex formation of FeCl2+ should

be more favored in the ice grain boundary region (where ferric ions and chlorides are concentrated) with facilitating the photogeneration of Fe2+ ions. Both the iron complex model and the semiconductor excitation model can explain the higher photoproduction of Fe(II) in the presence of chloride.

$$[Fe^{III}(H_2O)_5(OH)]^{2+} + Cl^- + H^+ \rightarrow [Fe^{III}(H_2O)_5Cl]^{2+} + H_2O \quad (K = 5.34\ M^{-1}) \tag{4}$$

$$[Fe^{III}(H_2O)_5Cl]^{2+} + H_2O + h\nu \rightarrow [Fe^{II}(H_2O)_6]^{2+} + {}^{\bullet}Cl \quad (\Phi_{347nm} = 0.5) \tag{5}$$

$$[Fe^{III}(H_2O)_5(OH)]^{2+} + H_2O + h\nu \rightarrow [Fe^{II}(H_2O)_6]^{2+} + {}^{\bullet}OH \quad (\Phi_{347nm} = 0.21) \tag{6}$$

On the other hand, in the presence of nitrate that is a very weak complexing ligand, the reductive process can be suppressed by a strong oxidant (i.e., □OH) produced by the photolysis of nitrate.50,49 Similarly, Fe(III)−sulfate complexes may also have photochemical properties suppressing the reduction of ferric to ferrous ions.7 The adsorption of sulfate on iron oxide surfaces replaces OH groups,37 whichareknowntoreduceferricions.42 Accordingly, sulfate that showed the highest iron dissolution in the dark also produced the highest amount of Fe(III) under the photoirradiation but the lowest amount of Fe(II) (see Table 1). This indicates that the Fe(III)−sulfate complexes retard the photo-reduction of ferric species as was also observed in case of the photodissolution of α -FeOOH.7

Simulated Freeze−Thaw Cycling Process. Iron oxide particles may undergo a series of freeze−thaw cycles in the natural environment. To simulate the freezing-induced weath-ering process, the iron oxide suspensions were frozen and then thawed for repeated cycles and were analyzed for total dissolved iron after each process (Figure 4). After the first 12 h of reaction in ice, a significant amount of dissolved iron was observed for all types of acid anions, as expected. For the next 12 h, the samples were maintained in an aqueous phase by raising the temperature from −20 to 25 °C. After 12 h in a

thawed state, approximately half of total dissolved iron was reduced from its initial value for all types of anion samples. This should be ascribed to the precip-itation of ferric ions which have a low solubility at pH 3.51 During the four successive freeze−thaw cycles, the iron dissolution and precipitation showed a reversible behavior (i.e., dissolution upon freezing and reprecipitation after thawing) in the presence of chloride, nitrate, or perchlorate. It seems that the number of the freeze−thaw cycles has an insignificant influence on the steady-state level of dissolved iron with these acid anions. However, the sulfate system showed a markedly different behavior. In the presence of sulfate, the behavior of iron dissolution and pre-cipitation was irreversible and the freezing-induced dissolution of iron was significantly reduced after the first freeze−thaw cycle and gradually decreased with repeating the cycle. As a result, the iron dissolution with sulfate was the lowest after the fourth cycle among the compared samples while the presence of sulfate induced the highest level of dissolved iron after the first cycle.

This unique iron dissolution profile obtained in the presence of sulfate might be ascribed to the difference in the extent of aggregation of maghemite particles. Table 2 shows the ξ-potential and the dynamic light scattering (DLS) measurements of maghemite at the initial stage and after 6 h reaction in ice and aqueous phase, respectively. In the presence of sulfate, the initial ξ-potential of maghemite was the lowest (14 mV) among 4 types of inorganic acid anions and the hydrodynamic diameter was the largest both before and after the reaction in the aqueous and ice phase. In particular, the size of sulfate-containing iron oxide agglomerates after reaction in ice was about 5 times larger than those of chloride-, nitrate-, or perchlorate-containing iron oxide sample. This extensive aggregation of iron oxide particles caused by sulfate was also confirmed by TEM images (see Figure 5).

On the other hand, the iron oxide samples containing other acid anions showed much less change in the hydrodynamic size and the agglomeration after the freeze−thaw cycle. Being a divalent anion, sulfate has a high affinity for positively charged iron oxide surface and subsequently reduces the positive surface charge more efficiently than other monovalent anion.37,38 This is refl ected in the lowest zeta-potential of maghemite in the presence of sulfate (see

Table 2). In addition, the freeze concentration of divalent sulfate ions within the ice grain boundary region highly enhances the ionic strength, which induces the aggregation of iron oxide particles more efficiently than monovalent ions. As a result, the electrostatic repulsion force between iron oxide particles is weakest in the presence of sulfate and therefore the largest agglomerates are formed.35,37 The iron oxide particles are forced to be aggre-gated in the confined space of ice grain boundaries but might be deaggregated after thawing. However, the presence of sulfate seems to stabilize the state of agglomeration as shown in Figure 5b. The large aggregates reduce the number of active surface sites eventually diminishing the dissolution rate.52,53

Environmental Implications. The present study demon-strates that the presence and kind of inorganic acid anions can critically influence the freezing-induced dissolution of bioavail-able iron from mineral particles both in the dark and under photoirradiation. The ice-enhanced dissolution of iron oxides in the dark condition was most efficient in the presence of sulfate, whereas the dissolution under the photoirradiation was the highest in the presence of chloride. During the freeze−thaw cycle, the presence of sulfate facilitated the aggregation of iron oxide particles with gradually reducing the iron dissolution e fficiency. Iron-containing dust particles in the atmosphere can be transported long-range and undergo multiple freeze−thaw cycles.14,54 In the presence of acid anions, the pH of iron-containing aerosols may decrease to pH 1−2.54 Thus, acidic aerosols containing inorganic anions have been suggested as a source of bioavailable iron.7,8 This study showed that the extent of iron dissolution is markedly enhanced in the ice phase in the presence of sulfate or chloride. Therefore, any changes in the anthropogenic and natural emissions of sulfur- and chlorine-containing compounds, which are the precursors of inorganic anions in the atmosphere, might be related with modifying the freezing-induced dissolution of iron-containing atmospheric aerosols. The freezing-induced dissolution of iron oxides is suggested as an important source of bioavailable iron that will eventually influence the ocean carbon cycle upon deposition to the open ocean.1,4 Further laboratory studies and field obser-vations should be carried out to investigate and assess the effects of various inorganic and organic ligands on the freezing-induced dissolution of iron

oxides in cold environments such as the upper atmosphere and polar regions.

얼음 반응에 의해 촉진되는 철 산화물의 용해에 무기산 음이온이 미치는 효과

김기태[1], 민대위[2], 최원용[2]

[1]한국해양과학기술원 부설 극지연구소
[2]포항공과대학교

요약: 광물먼지입자에서 철의 용해는 공존하는 무기 음이온들의 형태와 양에 크게 좌우된다. 이 연구에서 우리는 환산염, 염화물, 질산염, 과염소산의 마그네마이트와 레피도크로사이트의 얼음에서 어둡고 UV 광조건에서의 역할을 조사하였고, 수층에서의 반응 결과와 비교하였다. 반응 96 시간 이후, 총 용존 철은 얼음(pH 3-얼리기 전)에서 물에서 보다 6-28배 높았고, 어둡고 UV 광조건 보다 10-20배 높았다. 황산이 암조건에서 철을 생산하는데 가장 효율적이었으나, 염산은 빛 조건에서 2가 철과 총철의 가장큰 용해를 이끌었다. 이렇게 얼음에 의한 용해 결과는 아리조나 테스트 먼지를 통해 확인되었다. 결빙-용융 순환 테스트에서 염화물, 질산염, 과염소산을 가지는 철산화물은 비슷한 총용존철의 용도를 보였으나, 황산염을 넣은 시료에서는 용해도가 크게 감소하였다. 이러한 얼음에서 관측된 유일한 현상은 아마도 얼음의 준액체층에 있는 양성자, 철산화물, 무기 음이온의 농도와 관련되는 것으로 보인다. 이러한 결과들은 엄음에 의해 강화된 철 산화물의 용해는 생물이 이용가능한 철의 소스가 될 수 있고, 산성 음이온들이 이 과정에 큰 영향을 줄 수 있다는 것을 의미한다.

참고문헌

(1) Martin, J. H.; Gordon, R. M.; Fitzwater, S. E. Iron in Antarctic waters. Nature 1990, 345, 156−158.

(2) Boyd, P. W.; Jickells, T.; Law, C. S.; Blain, S.; Boyle, E. A.; Buesseler, K. O.; Coale, K. H.; Cullen, J. J.; De Baar, H. J. W.; Follows, M.; Harvey, M.; Lancelot, C.; Levasseur, M.; Owens, N. P. J.; Pollard, R.; Rivkin, R. B.; Sarmiento, J.; Schoemann, V.; Smetacek, V.; Takeda, S.; Tsuda, A.; Turner, S.; Watson, A. J. Mesoscale iron enrichment experiments 1993−2005: Synthesis and future directions. Science 2007, 315, 612−617.

(3) Shi, Z.; Krom, M. D.; Jickells, T. D.; Bonneville, S.; Carslaw, K. S.; Mihalopoulos, N.; Baker, A. R.; Benning, L. G. Impacts on iron solubility in the mineral dust by processes in the source region and the atmosphere: A review. Aeolian Research 2012, 5,21−42.

(4) Turner, D. R.; Hunter, K. A. The Biogeochemistry of Iron in Seawater; John Wiley & Sons: Chichester, UK, 2001; Vol. 7, p 396.

(5) Johnson, K. S.; Gordon, R. M.; Coale, K. H. What controls dissolved iron concentrations in the world ocean? Mar. Chem. 1997, 57, 137−161.

(6) Cornell, R. M.; Schwertmann, U. The Iron Oxides: Structure, Properties, Reactions, Occurrence and Uses; Wiley-VCH: New York,

(7) Rubasinghege, G.; Lentz, R. W.; Scherer, M. M.; Grassian, V. H. Simulated atmospheric processing of iron oxyhydroxide minerals at low pH: Roles of particle size and acid anion in iron dissolution. Proc. Natl. Acad. Sci. U. S. A. 2010, 107, 6628−6633.

(8) Chen, H.; Grassian, V. H. Iron dissolution of dust source materials during simulated acidic processing: The effect of sulfuric, acetic, and oxalic acids. Environ. Sci. Technol. 2013, 47, 10312−10321.

(9) Cwiertny, D. M.; Young, M. A.; Grassian, V. H. Chemistry and photochemistry of mineral dust aerosol. Annu. Rev. Phys. Chem. 2008, 59,27−51.

(10) Shi, Z.; Bonneville, S.; Krom, M. D.; Carslaw, K. S.; Jickells, T. D.; Baker, A. R.; Benning, L. G. Iron dissolution kinetics of mineral dust at

low pH during simulated atmospheric processing. Atmos. Chem. Phys. 2011, 11, 995−1007.

(11) Pincock, R. E.; Kiovsky, T. E. Kinetics of reactions in frozen solutions. J. Chem. Educ. 1966, 43, 358−360.

(12) Takenaka, N.; Bandow, H. Chemical kinetics of reactions in the unfrozen solution of ice. J. Phys. Chem. A 2007, 111, 8780−8786.

(13) Takenaka, N.; Ueda, A.; Maeda, Y. Acceleration of the rate of nitrite oxidation by freezing in aqueous solution. Nature 1992, 358, 736−738.

(14) Grannas, A. M.; Jones, A. E.; Dibb, J.; Ammann, M.; Anastasio, C.; Beine, H. J.; Bergin, M.; Bottenheim, J.; Boxe, C. S.; Carver, G.; Chen, G.; Crawford, J. H.; Dominé, F.; Frey, M. M.; Guzmán, M. I.; Heard, D. E.; Helmig, D.; Hoffmann, M. R.; Honrath, R. E.; Huey, L. G.; Hutterli, M.; Jacobi, H. W.; Klán, P.; Lefer, B.; McConnell, J.; Plane, J.; Sander, R.; Savarino, J.; Shepson, P. B.; Simpson, W. R.; Sodeau, J. R.; Von Glasow, R.; Weller, R.; Wolff, E. W.; Zhu, T. An overview of snow photochemistry: Evidence, mechanisms and impacts. Atmos. Chem. Phys. 2007, 7, 4329−4373.

(15) Kim, K.; Choi, W. Enhanced Redox Conversion of Chromate and Arsenite in Ice. Environ. Sci. Technol. 2011, 45, 2202−2208.

(16) Guzman, M. I.; Hildebrandt, L.; Colussi, A. J.; Hoffmann, M. R. Cooperative hydration of pyruvic acid in ice. J. Am. Chem. Soc. 2006, 128, 10621−10624.

(17) Kim, K.; Choi, W.; Hoffmann, M. R.; Yoon, H. I.; Park, B. K. Photoreductive Dissolution of Iron Oxides Trapped in Ice and Its Environmental Implications. Environ. Sci. Technol. 2010, 44, 4142−

(18) Jeong, D.; Kim, K.; Choi, W. Accelerated dissolution of iron oxides in ice. Atmos. Chem. Phys. 2012, 12, 11125−11133.

(19) Kim, K.; Yoon, H. I.; Choi, W. Enhanced Dissolution of Manganese Oxide in Ice Compared to Aqueous Phase under Illuminated and Dark Conditions. Environ. Sci. Technol. 2012, 46, 13160−13166.

(20) Cziczo, D. J.; Froyd, K. D. Sampling the composition of cirrus ice residuals. Atmos. Res. 2014, 142,15−31.

(21) Cziczo, D. J.; Froyd, K. D.; Hoose, C.; Jensen, E. J.; Diao, M. H.; Zondlo, M. A.; Smith, J. B.; Twohy, C. H.; Murphy, D. M. Clarifying the Dominant Sources and Mechanisms of Cirrus Cloud Formation. Science 2013, 340, 1320−1324.

(22) DeMott, P. J.; Cziczo, D. J.; Prenni, A. J.; Murphy, D. M.; Kreidenweis, S. M.; Thomson, D. S.; Borys, R.; Rogers, D. C. Measurements of the concentration and composition of nuclei for cirrus formation. Proc. Natl. Acad. Sci. U. S. A. 2003, 100, 14655−

(23) Archuleta, C. M.; DeMott, P. J.; Kreidenweis, S. M. Ice nucleation by surrogates for atmospheric mineral dust and mineral dust/sulfate particles at cirrus temperatures. Atmos. Chem. Phys. 2005, 5, 2617−2634.

(24) DeMott, P. J.; Rogers, D. C.; Kreidenweis, S. M. The susceptibility of ice formation in upper tropospheric clouds to insoluble aerosol components. J. Geophys. Res. 1997, 102, 19575−

(25) Kamphus, M.; Ettner-Mahl, M.; Klimach, T.; Drewnick, F.; Keller, L.; Cziczo, D. J.; Mertes, S.; Borrmann, S.; Curtius, J. Chemical composition of ambient aerosol, ice residues and cloud droplet residues in mixed-phase clouds: single particle analysis during the Cloud and Aerosol Characterization Experiment (CLACE 6). Atmos. Chem. Phys. 2010, 10, 8077−8095.

(26) Cornell, R. M.; Posner, A. M.; Quirk, J. P. Kinetics and mechanisms of the acid dissolution of goethite (α-FeOOH). J. Inorg. Nucl. Chem. 1976, 38, 563−567.

(27) Sullivan, R. C.; Guazzotti, S. A.; Sodeman, D. A.; Tang, Y.; Carmichael, G. R.; Prather, K. A. Mineral dust is a sink for chlorine in the marine boundary layer. Atmos. Environ. 2007, 41, 7166−7179.

(28) Sullivan, R. C.; Guazzotti, S. A.; Sodeman, D. A.; Prather, K. A. Direct observations of the atmospheric processing of Asian mineral dust. Atmos. Chem. Phys. 2007, 7, 1213??236.

(29) Workman, E. J.; Reynolds, S. E. Electrical Phenomena Occurring during the Freezing of Dilute Aqueous Solutions and Their Possible Relationship to Thunderstorm Electricity. Phys. Rev. 1950, 78, 254−

259.

(30) Cobb, A. W.; Gross, G. W. Interfacial Electrical Effects Observed during Freezing of Dilute Electrolytes in Water. J. Electrochem. Soc. 1969, 116, 796−804.

(31) Robinson, C.; Boxe, C. S.; Guzman, M. I.; Colussi, A. J.; Hoffmann, M. R. Acidity of frozen electrolyte solutions. J. Phys. Chem. B 2006, 110, 7613−7616.

(32) Teir, S.; Revitzer, H.; Eloneva, S.; Fogelholm, C. J.; Zevenhoven, R. Dissolution of natural serpentinite in mineral and organic acids. Int. J. Miner. Process. 2007, 83,36−46.

(33) Hamer, M.; Graham, R. C.; Amrhein, C.; Bozhilov, K. N. Dissolution of ripidolite (Mg, Fe-chlorite) in organic and inorganic acid solutions. Soil Sci. Soc. Am. J. 2003, 67, 654−661.

(34) Takenaka, N.; Ueda, A.; Daimon, T.; Bandow, H.; Dohmaru, T.; Maeda, Y. Acceleration mechanism of chemical reaction by freezing: The reaction of nitrous acid with dissolved oxygen. J. Phys. Chem. 1996, 100, 13874−13884.

(35) Rao, S. M.; Sridharan, A. Mechanism of sulfate adsorption by kaolinite. Clays Clay Miner. 1984, 32, 414−418.

(36) Zhu, M. Q.; Northrup, P.; Shi, C. Y.; Billinge, S. J. L.; Sparks, D. L.; Waychunas, G. A. Structure of Sulfate Adsorption Complexes on Ferrihydrite. Environ. Sci. Technol. Lett. 2014, 1,97−101.

(37) Harrison, J. B.; Berkheiser, V. E. Anion interactions with freshly prepared hydrous iron oxides. Clays Clay Miner. 1982, 30,97−102.

(38) Rietra, R. P. J. J.; Hiemstra, T.; van Riemsdijk, W. H. Electrolyte anion affinity and its effect on oxyanion adsorption on goethite. J. Colloid Interface Sci. 2000, 229, 199−206.

(39) Waite, T. D.; Morel, F. M. M. Photoreductive Dissolution of Colloidal Iron Oxides in Natural Waters. Environ. Sci. Technol. 1984, 18, 860−868.

(40) Voelker, B. M.; Morel, F. M. M.; Sulzberger, B. Iron redox cycling in surface waters: Effects of humic substances and light. Environ. Sci. Technol. 1997, 31, 1004−1011.

(41) Borer, P.; Sulzberger, B.; Hug, S. J.; Kraemer, S. M.; Kretzschmar, R.

Photoreductive Dissolution of Iron(III) (Hydr)oxides in the Absence and Presence of Organic ligands: Experimental Studies and Kinetic Modeling. Environ. Sci. Technol. 2009, 43, 1864−1870.

(42) Miller, W. L.; King, D. W.; Lin, J.; Kester, D. R. Photochemical redox cycling of iron in coastal seawater. Mar. Chem. 1995, 50,63??7.

(43) Beydoun, D.; Amal, R.; Low, G.; Mcevoy, S. Occurrence and prevention of photodissolution at the phase junction of magnetite and titanium dioxide. J. Mol. Catal. A: Chem. 2002, 180, 193−200.

(44) Leland,J.K.; Bard,A.J. Photochemistry of colloidal semiconducting iron oxide polymorphs. J. Phys. Chem. 1987, 91, 5076−5083.

(45) Cherepy, N. J.; Liston, D. B.; Lovejoy, J. A.; Deng, H.; Zhang, J. Z. Ultrafast studies of photoexcited electron dynamics in ɣ- and ɑ -Fe2O3 semiconductor nanoparticles. J. Phys. Chem. B 1998, 102, 770−

(46) Lakshminarasimhan, N.; Kim, W.; Choi, W. Effect of the agglomerated state on the photocatalytic hydrogen production with in situ agglomeration of colloidal TiO2 nanoparticles. J. Phys. Chem. C 2008, 112, 20451−20457.

(47) Lim, M.; Chiang, K.; Amal, R. Photochemical synthesis of chlorine gas from iron(III) and chloride solution. J. Photochem. Photobiol., A 2006, 183, 126−132.

(48) Nadtochenko, V. A.; Kiwi, J. Photolysis of FeOH2+ and FeCl2+ in aqueous solution. Photodissociation kinetics and quantum yields. Inorg. Chem. 1998, 37, 5233−5238.

(49) De Laat, J.; Truong Le, G.; Legube, B. A. comparative study of the effects of chloride, sulfate and nitrate ions on the rates of decomposition of H2O2 and organic compounds by Fe(II)/H2O2 and Fe(III)/H2O2. Chemosphere 2004, 55, 715−723.

(50) Hsu, C. L.; Wang, S. L.; Tzou, Y. M. Photocatalytic reduction of Cr(VI) in the presence of NO3− and Cl− electrolytes as influenced by Fe(III). Environ. Sci. Technol. 2007, 41, 7907−7914.

(51) Free, M. L. Hydrometallurgy: Fundamentals and Applications; John Wiley & Sons: Hoboken, NJ, 2013.

(52) Cwiertny, D. M.; Handler, R. M.; Schaefer, M. V.; Grassian, V. H.; Scherer, M. M. Interpreting nanoscale size-effects in aggregated Fe-oxide suspensions: reaction of Fe(II) with goethite. Geochim. Cosmochim. Acta 2008, 72, 1365－1380.

(53) Rubasinghege, G.; Kyei, P. K.; Scherer, M. M.; Grassian, V. H. Proton-promoted dissolution of alpha-FeOOH nanorods and micro-rods: Size dependence, anion effects (carbonate and phosphate), aggregation and surface adsorption. J. Colloid Interface Sci. 2012, 385, 15－23.

(54) Rubasinghege, G.; Elzey, S.; Baltrusaitis, J.; Jayaweera, P. M.; Grassian, V. H. Reactions on Atmospheric Dust Particles: Surface Photochemistry and Size-Dependent Nanoscale Redox Chemistry. J. Phys. Chem. Lett. 2010, 1, 1729－1737.

Table 1. Photo-Dissolution of Iron (Fe(II) + Fe(III)) from Maghemite in Ice in the Presence of Various Inorganic Anions[a]

anion type	dissolved iron (μM)		
	Fe(II)	Fe(III)	total Fe
SO_4^{2-}	9.8 ± 0.7 (11%)[b]	80.0 ± 0.4	89.8 ± 1.1
Cl^-	70.0 ± 3.0 (54%)	60.2 ± 0.6	130.1 ± 3.6
NO_3^-	14.2 ± 1.7 (30%)	33.2 ± 0.8	47.4 ± 0.9
ClO_4^-	27.8 ± 3.3 (35%)	51.0 ± 5.7	78.9 ± 2.4

[a]Experimental conditions: [γ-Fe_2O_3] = 0.2 g/L, pH 3, reaction time 96 h under UV irradiation at −20 °C. [b]Percentage of Fe(II) in the total dissolved iron.

Table 2. Properties of Maghemite before and after Reaction in Water and Ice[a]

anion type	ζ-potential (mV)	hydrodynamic diameter (nm)		
	initial	initial	aq[b]	ice[b]
SO_4^{2-}	14 ± 0	1303 ± 137	1934 ± 10	3127 ± 28
Cl^-	44 ± 1	512 ± 18	672 ± 30	696 ± 42
NO_3^-	43 ± 2	451 ± 29	497 ± 61	624 ± 0
ClO_4^-	52 ± 4	503 ± 112	420 ± 26	574 ± 47

[a]Experimental conditions: [γ-Fe_2O_3] = 0.2 g/L, pH 3, reaction time 6 h under dark condition at 25 °C and −20 °C. [b]Hydrodynamic diameter measured after 6 h of reaction.

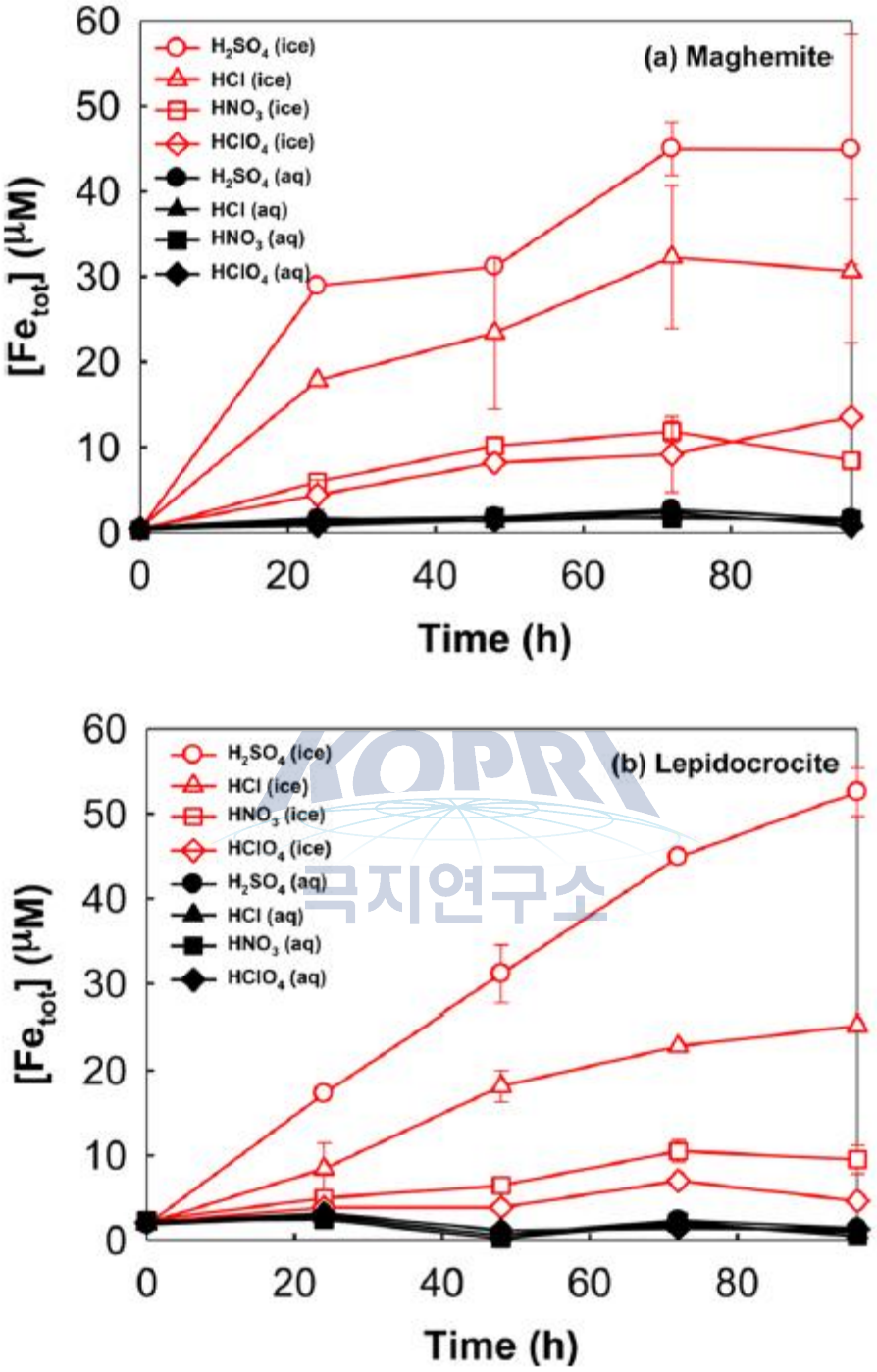

Figure 1. Production of total dissolved iron from (a) maghemite (ɣ-Fe2O3)and (b)lepidocrocite (ɣ-FeOOH) under dark condition in the presence of various inorganic anions after reaction in water (25 °C) and ice (−20 °C) . Experimental conditions: pHi =3(±0.05),[iron oxide] = 0.2 g/L.

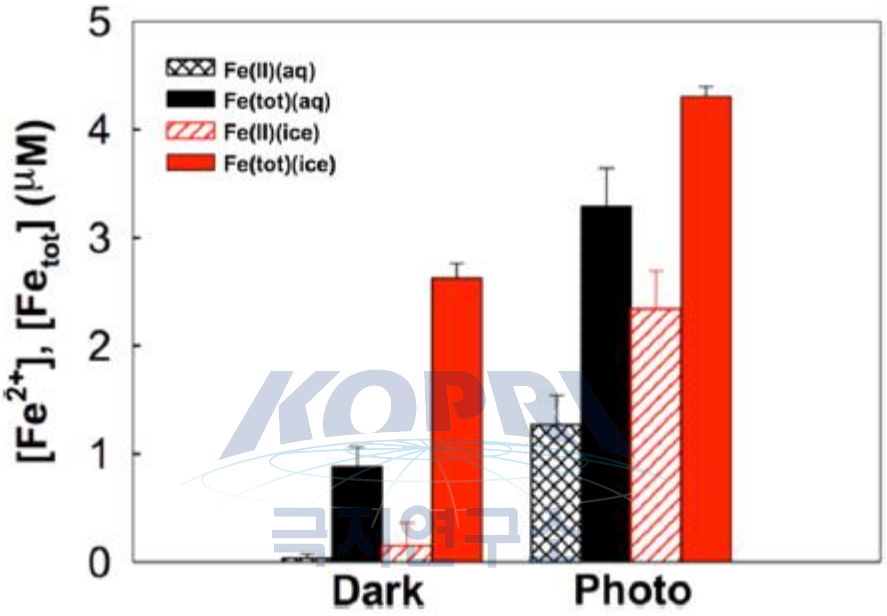

Figure 2. Comparison of total dissolved iron and ferrous ion from AZTD (Arizona test dust) between water (25 °C) and ice (−20 °C) under dark and UV irradiation. Experimental conditions: pHi =3± 0.05 (adjusted with H2SO4), [AZTD] = 2 g/L, reaction time 48 h.

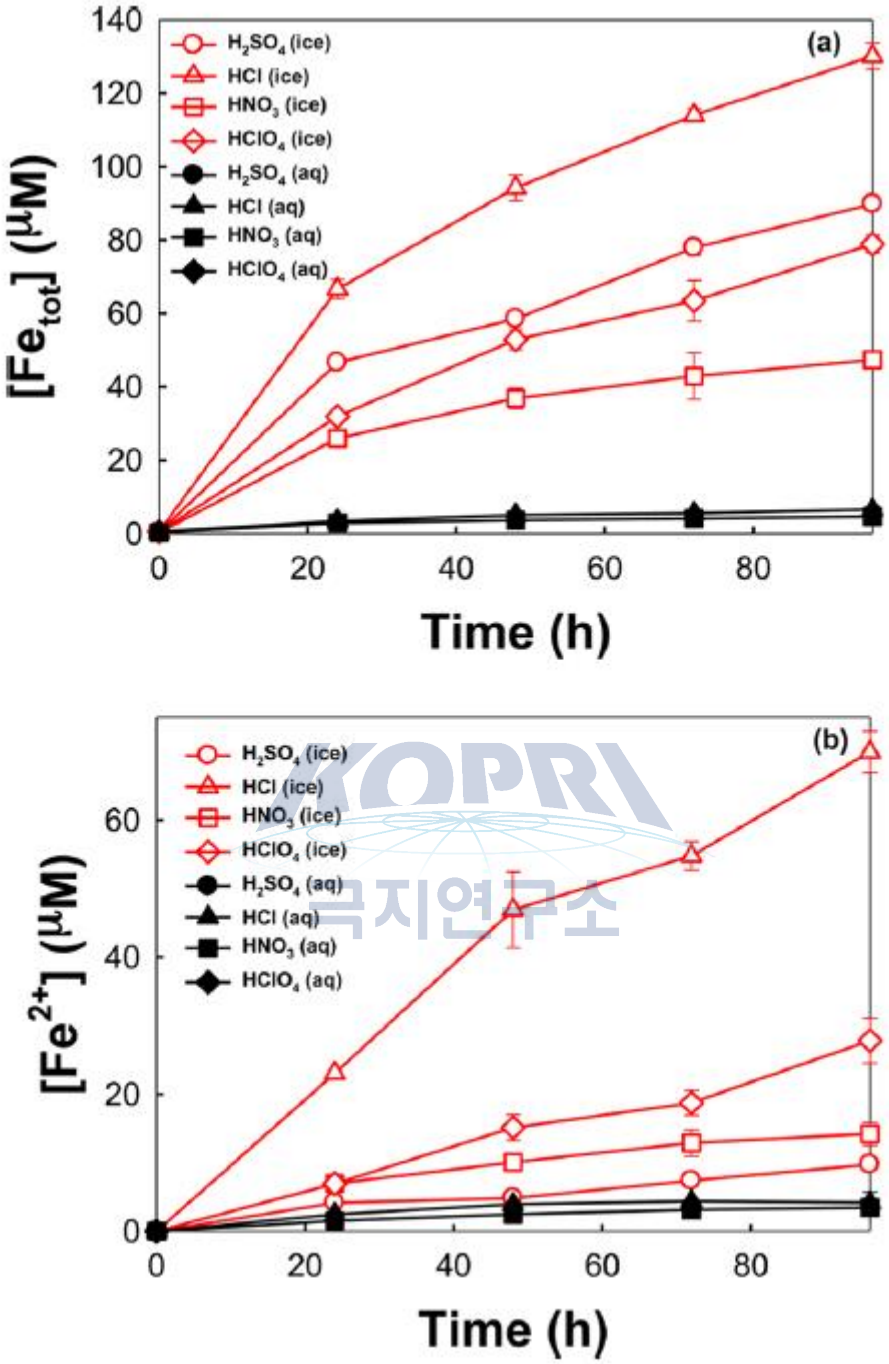

Figure 3. Photoirradiation-induced production of (a) total dissolved iron and (b) ferrous (Fe(II)) ion from maghemite under UV irradia-tion in the presence of various inorganic anions after reaction in water (25 °C) and ice (−20 °C). Experimental conditions: pHi =3(±0.05),[γ-Fe2O3] = 0.2 g/L.

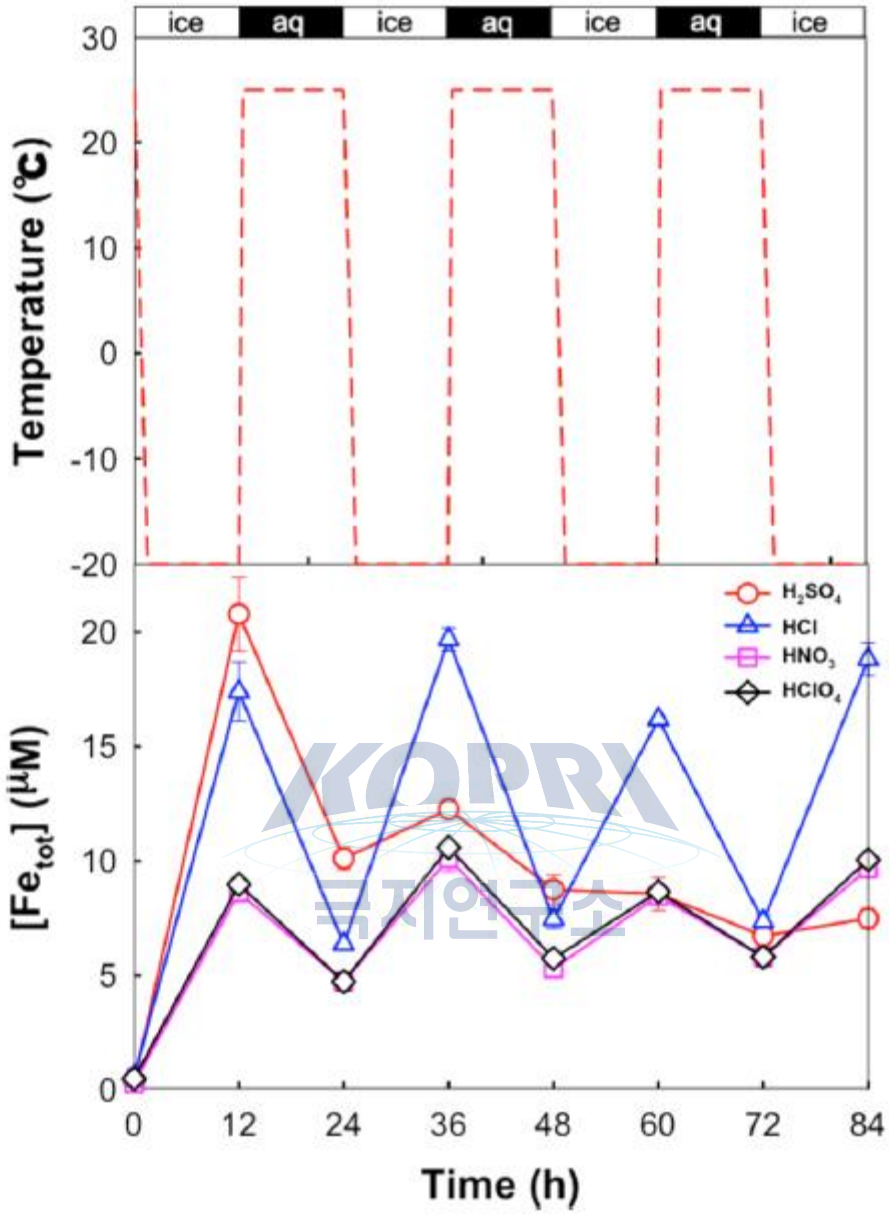

Figure 4. (a) Temperature variation profile and (b) the accompanying production of total dissolved iron from maghemite (ɣ-Fe2O3)duringthe freeze−thaw cycling experiment under the dark condition. Aqueous phase maintained at 25 °C and ice phase at −20 °C. Experimental conditions: pHi =3 ± 0.05, [ɣ-Fe2O3] = 0.2 g/L.

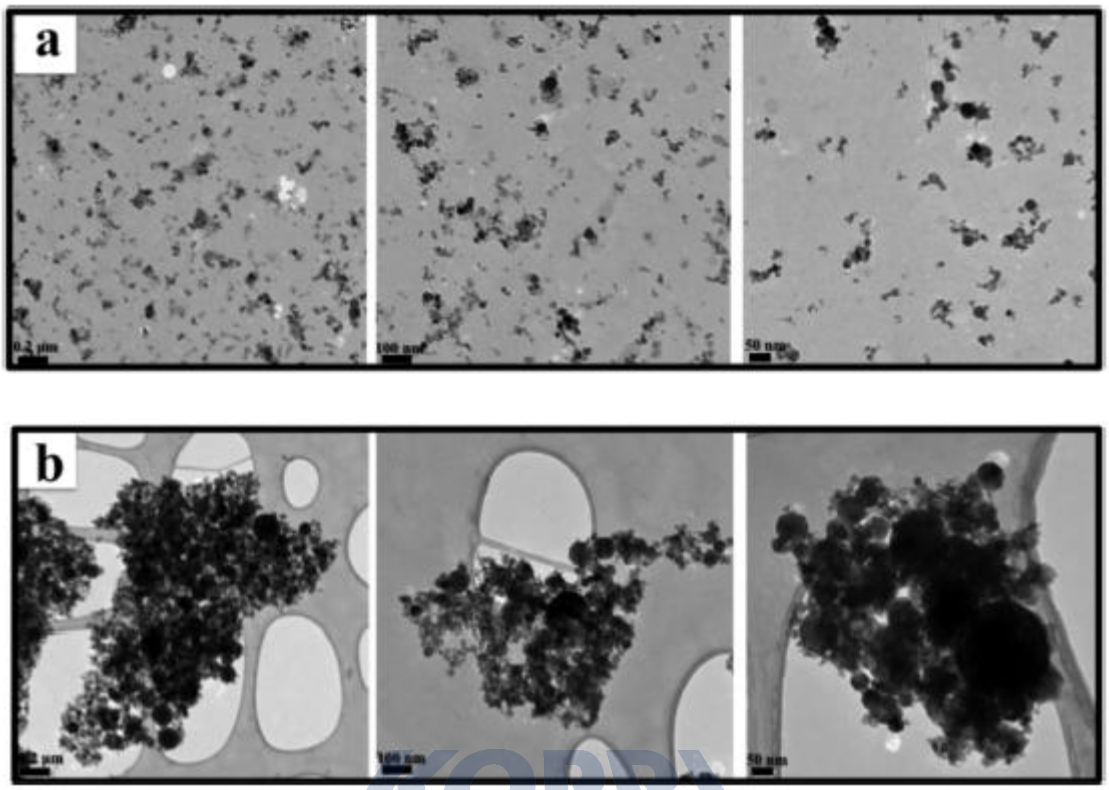

Figure 5. TEM images of maghemite particles in the presence of (a) chloride and (b) sulfate after 6 h reaction in the ice phase (−20 °C) under dark condition. Experimental conditions: pHi =3± 0.05,[γ-Fe2O3]=0.2 g/L.

제 14 장

남극 엽층리 퇴적물로부터 규조 종을 이용한 고기후 변화 연구[9)]

박영숙[1*], 윤호일[2], 유규철[2]

[1]전북대학교 자연과학대학 지구환경과학과
[2]한국해양연구원 부설 극지연구소 극지기후연구센터

요약: 남극 브랜스필드 해협의 동부분지로부터 획득한 GC08-EB01 코어퇴적물의 고해상 엽층리로부터 규조를 이용하 여 고기후변화를 연구하였다. 규조 정량 분석의 결과 규조 개체수 농도는 0.4-4.2×108 g 로 매우 풍부하게 산출되었으며, 엽층리는 생물기원의 규조가 풍부한 층과 육성기원 퇴적물이 풍부한 층으로 구분된다. 규조 엽층리는 Corethron crilophilum, Eucampia antarctica, Fragilariopsis curta, F. kerguelensis, Odontella weissflogii, Proboscia inermis, R. styliformis, Thalassiosira antarctica와 Chaetoceros resting spores 등의 번성이 특징적이며, 육원성 엽층리에서는 규조군집이 혼합되어 나타나는 것이 특징이다. 홀로세 후기 동안 Fragilariopsis curta+F. cylindrus)/Thalassiosira antarctica의 산출 수직 분포비가 급격히 증가하는 구간은 해빙의 확장을 지시하며, 연구 코어 GC08-EB01 코어퇴적물이 퇴적되는 동안 적어도 5번의 한랭기가 있었음을 알려준다.

9) 이 연구 결과는 다음의 논문으로 출판되었음: 박영숙1,*·윤호일2·유규철2·이영엽1, 2015. 남극 엽층리 퇴적물로부터 규조 종을 이용한 고기후 변화. J. Korean Earth Sci. Soc., v. 36, no. 2, p. 190.

1. 서론

엽층리성 해양 퇴적물은 표층수로부터 계속적으로유입된 고해상 기록을 가지고 있다(Grimm et al., 1997; Kemp et al., 1998). 엽층리성(laminated sediments) 해양 퇴적물의 보존은 연안의 용승류 아래나 분지의가장자리에서 산소가 적고 생물교란을 받지 않는환경에서 잘 형성되는 것으로 알려져 있으나 지난 수십년간 동태평양 적도부근과 북대서양의 심해에서도 엽층리성 규조 연니가 발견되었다. 심해에서 엽층리의 보존은 저층수의 혐기성 때문이 아니라 오히려단단한 규조의 활발한 대량 유입 때문으로 생각된다(Brodie and Kemp, 1994; Bodén and Backman, 1996; Bull et al., 2000; Kemp et al., 1995; King et al., 1995). 남극 반도의 해양 생태계는 연안, 대륙붕대와 계절적인 해빙대로 특징지워지는데 여름철 최소해빙대와 겨울철 최대 해빙대의 사이인 경계지역(marginal ice zone)에서는 빙하가 녹는 동안과 여름철에 1차 생산자인 식물성플랑크톤의 대증식이 일어난다. 또한, 여름동안의 일차 생산력은 빈영양 상태에서부터 높은 클로로필 농도를 가진 용승류에 이르기까지 다양한 해수 환경의 영향을 받는다(Holm-Hansen and Mitchell, 1991; Basterretxea and Artistegui, 1999; Figueiras et al., 1999).

규조는 남대양에서 1차 생산자의 약 75%를 차지하고 규소와 탄소의 지구적 순환에 매우 중요한 역할을 하고 있으며(Treguer et al., 1995), 일차 생산력에서의 변화는 주로 해빙의 변화와 표층수의 안정성및 성층화에 의해 일어난다. 브랜스필드 해협(Bransfield Strait)은 기후와 해양의 변화에 매우 민감하며, 지난수천년 동안 이 지역에서의 일차생산력은 일반적으로감소하는 경향을 보였다(Bárcena et al., 1998). 또한,브랜스필드 해협에서 규조 생산량의 변화는 약 250년 주기를 가진 대자율, 유기탄소등의 변화와 일치한다(Leventer et al., 1996; Bárcena et al., 1998). 남극브랜스필드 해협의 엽층리성 해양 퇴적물로부터 규조를 연구하는 것은 과거의 기후 변화 동안 기후와 해양의 변화 양상에 대한 정보를 상세히 얻는데 매우중요한 자료가 된다. 본 연구는 브랜스필드 해협 동부분지에서 채취한 중력코어퇴적물(GC08-EB01)에서 규조가 풍부한 생물기원과 육원성 퇴적물 기원의엽층리로부터 규조를 관찰하여 규조 군집의 변화를알아보고, 기후변화와 규조종의 변화를 대비하여 보고자 한다.

2. 연구 지역 및 방법

2.1. 연구지역

브랜스필드 해협은 남북으로 남극반도와 남쉐틀랜드 군도사이에 위치하는 반폐쇄성 분지(semi-enclosed basin)이다. 브랜스필드 분지는 세 개의 소분지로 나눠진다. 연구 지역은 동부 소분지로서 남동쪽으로 연장되어 있으며, 중앙 소분지보다 좁고, 약 2,500 m깊이에 달한다(Bárcena et al., 2002). 브랜스필드 해협에서 표층수 순환은 벨링스하우젠해(Bellingshausen Sea)와 웨델해(Weddell Sea)로부터 유입되며, 벨링스하우젠 해수는 비교적 따뜻하고 저염인 반면에 웨델해수는 차갑고 고염의 특성을 가진다 (García et al., 2002). 브랜스필드 해협에서 계절적인 해빙(sea-ice)의분포는 매우 복잡한 양상을 가지며, 겨울철 해빙의최대 크기가 남극반도의 57oS의 범위까지 확장되나여름철에는 완전히 해빙의 영향을 벗어난다. 해빙의영향을 벗어난 공해 (open-water)환경의 시기동안 규질의 유기물들이 대량 유입되는 반면에, 해빙으로 덮여 있는 동안에는 유입되는 규질 유기물의 양이 매우 적다 (Abelmann and Gersonde, 1991).

2.2. 연구 방법

연구에 사용한 코어퇴적물 GC08-EB01은 62o02.0′S, 56o13.0′W의 위치에서 채취하였으며(Fig. 1), 총 길이796 cm의 엽층리상 퇴적물에서 밝은 색의 규조연니층과 어두운 색의 퇴적물로부터 총 97개의 시료를획득하였다. 규조 분석을 위해 각 시료당 2g을 취하여 박영숙 외(2007)의 시료처리과정을 토대로 실험하였다. 또한, 규조의 정량분석을 위한 슬라이드 준비를 위해서 Scherer (1994)의 연구 방법을 사용하였고, 계산식 Abundance=((A×B)/(C×D))/E (A=number of specimens counted; B=area of settling chamber; C=number of field of view in microscope; D=area of field of view; E=mass of sample)에 의해 절대개체수 농도를 계산하였다.

Chaetoceros resting spores의 경우, 다량 산출되는 층준이 많아서 각 view field 에서 전체 개체수를 산정하였고 각 시료의 개체 수에는 포함시키지 않았으나, 특정 층준에서 폭발적으로 산출되는 규조종의 경우에는 전체 산출 개체수에 포함시켰다.

연구 코어퇴적물의 퇴적시기를 알아보기 위하여 한국해양연구원 극지기후연구센터에서 측정한 탄소동위원소 절대연령은 다음과 같다(Table 1).

3. 결과

3.1. 규조 군집

브랜스필드 해협 동부 소분지에서 채취한 GC08-EB01 코어퇴적물의 전체 층준에서 규조화석이 매우풍부하게 산출되었으며 총 23속 59종의 규조 화석이감정되었다. 특히, 생물기원의 엽층리에서 특정 종의출현이 폭발적으로 증가하는 경향을 보였고, 육원성엽층리에서는 폭발적인 증가 보다는 여러 종들이 고루 산출되었다. 규조 개체수 농도의 범위는 0.4-4.2×108 g 으로 매우 풍부하게 산출되었다. 규조 화석 군집 조성을 살펴보면 Fragilariopsis curta가 전체 산출의 16.1%, F. kerguelensis 10.6%, Proboscia inermis 12.3%, Rhzosolenia styliformis 9.6%와 Thalassiosira antarctica 12.9%가 우세하게 산출되었으며 전체의61.5%를 차지한다.

3.2. 규조 번성종

연구 코어퇴적물 GC08-EB01로부터 산출된 종들 중 Corethron crilophilum, Eucampia antarctica, Fragilariopsis curta, F. kerguelensis, Odontella weissflogii, Proboscia inermis, Rhizosolenia styliformis, Thalassiosira antarctica와 Chaetoceros resting spores는 특정한 층준에서 폭발적으로 개체수가 증가하는경향을 보인다(Fig. 2).

Corethron crilophilum은 웨델해의 늦겨울에 해빙의 가장자리 부근에 나타나는 식물성 플랑크톤 군집의 중요한 구성원으로서(Marra and Boardman, 1984), 336 cm 층준에서 다량 산출된다.

Eucampia antarctica var. recta는 해빙과 관계가있는 종(Fryxell and Prasad, 1990; Fryxell, 1991)으로 모든 층준에서 꾸준히 산출되며 167 cm 층준에서 산출량은 증가한다. 공해환경을 지시하는 E. antarctica var. antarctica는 하부 층준인 686-790 cm 구간에서매우 풍부하다.

Fragilariopsis curta는 해빙의 하부에서 나타나는주요 해빙 종으로서(Hendey, 1981), 전체적으로 풍부하게 산출되는 경향을 보이며, 545, 758 cm 층준에서가장 풍부하게 산출된다.

F. kerguelensis는 브랜스필드 분지 서쪽에 분포하는 남극 순환수(Antarctic circumpolar current)나 벨링스하우젠해로부터 따뜻한 해류의 유입을 지시하며(Zielinski and Gersonde, 1997), 전체적으로 고루 산출되나 특히 520, 567,

608, 686 cm 층준에서 풍부하게 산출된다.

*Odontella weissflogii*는 전형적인 여름철 남극종(Pike et al., 2008)으로서 4, 24, 61, 180, 232, 255, 502, 666 cm 층준에서 상대적으로 풍부하게 산출된다.

*Proboscia inermis*와 *Rhizosolenia styliformis*는 해빙환경과는 연관이 없이 공해 환경에서 풍부한 종들이다(Zielinski and Gersond, 1997). 이들의 산출은 435 cm 이하의 층준에서는 상대적으로 산출이 적고P. inermis는 167, 435 cm 층준에서, R. styliformis는79, 89, 287 cm에서 다량 산출된다.

*Thalassiosira antarctica*는 여름과 가을철에 대번성하는 종으로 알려져 있다. 남극반도 주변에서 초여름식물성 플랑크톤의 주 구성원이며(Sommer, 1991), 성층화되지 않거나 약하게 형성된 남극 표층수에서대번성을 일으키는 주 구성원이다(Cremer et al., 2003). 연구지역에서는 T. antarctica cold type과 T. antarctica warm type (Buffen et al., 2007)이 전 층준에 걸쳐 꾸준히 산출되며, 특히 T. antarctica warm type이 273 cm 층준에서 급증한다.

*Chaetoceros resting spores*의 산출빈도는 융빙수의 유입에 의해 이루어진 안정되고 성층화된 해수에 서 풍부하며, 해빙단(sea-ice edge) 부근에서 염분이나 질소의 부족으로 인하여 휴면포자를 형성하게 된다(Leventer, 1991, 1992; Crosta et al., 1997). 연구코어 퇴적물에서의 휴면포자의 산출은 하부에서 상부층준까지 꾸준하며, 특히 폭발적으로 급증하는 구간은 147, 545, 579 cm 층준이다.

3.3. 고환경 해석

GC08-EB01 코어퇴적물에서 폭발적인 번성을 나타낸 종들의 계절적인 특징을 살펴 보면 Chaetoceros resting spores와 Corethron criophilum은 특별히 초봄에 대번성을 일으키며(Stickley et al., 2005), 공해에서는 늦봄과 여름에 해저로 유입되는 규소가 풍부해지기 때문에 성층의 파괴가 일어나서 혼합양상을 보인다. Chaetoceros spp.은 해빙이 녹고 표층수가 성층화 되는 봄 동안에 우세하게 나타나는 반면 F.curta와 F. cylindrus는 초봄에 해빙이 존재할 때 나타난다(Denis et al., 2006; Maddison et al., 2005, 2006). F.kerguelensis는 해빙이 후퇴하고 표층수가 따뜻한 여름동안에 지속되며, Thalassiosira antarctica는 여름/가을 시기에 풍부하게 산출된다(Crosta et al., 2008).남극반도에서 홀로세 후기에 나타나는 Rhizosolenia spp.가 풍부한 엽층리는 대번성 후에 빠른 침전으로인해 형성된 것이며(Leventer and Dunbar, 1996), 늦은 봄에서 초여름까지 전이기간동안 Rhizosolenia spp.가 풍부하게 산출된다. Rhizosolenia spp.과 Proboscia spp.의 대번성은 여름철 표층수가

강하게 성층화된동안에 수온약층의 아래에서 나타나며 이들의 대량퇴적은 가을철에 수온약층이 약해져서 혼합될 때 일어난다.

연구코어의 686-796 cm 구간에서는 따뜻한 공해환경을 지시하는 Eucampia antarctica var. antarctica가풍부하게 산출되며, 520-686 cm 구간에서는 초봄 해빙을 지시해주는 Fragilariopsis curta와 융빙수의 유입을 지시하는 Chaetoceros resting spores가 상부로갈수록 증가한다. 349-520 cm 구간에서는 가을철에 대량퇴적되는 Proboscia inermis, 232-349 cm 구간에서는 초봄 지시종인 Corethron criophilum, 여름 지시종인 Thalassiosira antarctica (warm type), Odontella weissflogii의 순으로 번성한다. 99-232 cm 구간에서는여름 지시종인 Odontella weissflogii, Proboscia inermis, 초봄 지시종인 Chaetoceros resting spores의순으로 번성한다. 최상부 층준인 4-99 cm 구간에서는최하부에 Rhizosolenia styliformis, Odontella weissflogii순으로 공해종이 번성한다. 이들의 산출양상은 전반적으로 장기간동안의 해빙의 영향이 매우 적은 환경에서 퇴적되었음을 시사하며, 좀 더 세밀하게는 계절적인 해빙의 확장과 축소로 인한 규조 군집의 변화가 잘 나타나 있음을 알 수 있다.

엽층리상 퇴적층은 해빙의 계절적인 후퇴와 순환에의해서 일어나는 생물학적, 퇴적학적과정에 의해서형성된다. 각각의 엽층리는 규조의 생산적 변화를 나타내며 간빙기동안에 형성된다(Domack et al., 2003).엽층리상 퇴적물은 해빙에서의 계절적인 변화를 뚜렷이 반영한다. Fragilariopsis curta+F. cylindrus/Thalassiosira antarctica의 수직분포비는 추운 기후를의미한다. 또한, 공해 환경에서 Fragilariopsis curta가 다량 나타나는 것은 해빙이 빠르게 확장되고 있음을 의미한다(Burckle et al., 1987; Pichon et al., 1992). 연구코어에서 Fragilariopsis curta+F. cylindrus/Thalassiosira antarctica의 수직분포비를 조사한 결과,연구지역은 전반적인 경향이 공해환경이 주를 이루면서 계절적인 해빙의 영향 하에 놓여 있었으나, GC08-EB01 코어퇴적물이 퇴적되는 동안 각 43, 140, 545, 732, 758 cm 층준에서 최소 5번의 한랭기가 있었음을 알 수 있다(Fig. 3).

4. 결 론

GC08-EB01 코어퇴적물로부터 총 23속 59종의 규조 화석이 감정되었으며, 규조 개체수 농도의 범위는 0.4-4.2×108 g 으로 매우 풍부하게 산출되었다. 특히,생물기원의 엽층리에서 특정종의 출현이 폭발적으로증가하는 경향을 보였고, 육원성 엽층리에서는 폭발적인 증가보다는 혼합된 양상을 보였다. 특징종은Corethron

crilophilum, Eucampia antarctica, Fragilariopsis curta, F. kerguelensis, Odontella weissflogii, Proboscia inermis, Rhizosolenia styliformis, Thalassiosira antarctica와 Chaetoceros resting spores이다. 특징 종들의 폭발 적인 대번성은 계절적인 변화에 의한 표층수의 성층화 때문에 특정 규조종이 엽층리를 형성하는 것으로생각된다. GC08-EB01 퇴적물이 퇴적되는 동안, 전체적인 퇴적환경은 공해환경이 주를 이루면서 계절적인해빙의 분포 변화가 있었다. 또한, 기후변화를 지시해주는 Fragilariopsis curta+F. cylindrus/Thalassiosira antarctica의 상대적인 수직분포비에 의하면 퇴적되는동안 적어도 5번 정도의 한랭기가 있었음을 알 수 있다.

Diatom Succession Representing the Paleoclimatic Change from Laminated Sediments around Antarctica

Young-Suk Bak[1*],, Ho Il Yoon[2],, Kyu-Cheul Yoo[2]

[1]Department of Earth and Environmental Sciences
[2]Korea Polar Research Institute

Abstract: This study investigated the paleoclimatic change using diatoms that were extracted from the high-resolution laminated layers of diatom ooze sediment cores GC08-EB01 in the eastern basin of the Bransfield Strait, Antarctica. The range of diatom valves per gram of dry sediment was from 0.4 to 4.2×108 g in quantitative diatom assemblage analysis. Laminations are classified using visually dominant diatom species and terrigenous content. Biogenic diatom ooze laminae characterised by bloom of Corethron crilophilum, Eucampia antarctica, Fragilariopsis curta, F. kerguelensis, Odontella weissflogii, Proboscia inermis, R. styliformis, Thalassiosira antarctica, and Chaetoceros resting spores. Terrigenous laminae characterised by mixed diatom assemblage. The ratio of (Fragilariopsis curta+F. cylindrus)/Thalassiosira antarctica increase in horizons, suggesting increased sea-ice cover in the study area during the late Holocene (cold events). As a result, five cold events are identified on the basis of frequency of the critical taxa throughout the section.

참고문헌

박영숙, 이종덕, 윤혜수, 윤호일, 김향숙, 2001, 서남극 브랜스필드 동부 분지내 코아 퇴적물(A9-EB01)의 방산충. 한국지구과학회지, 22(2), 130-137.

박영숙, 이종덕, 윤호일, 이재일, 2007, 남극 사우스오크니제도 서부 해역의 코어퇴적물에서 산출된 규조 군집. 지질학회지, 43(1), 33-42.

Abelmann, A. and Gersonde, R., 1991, Biosiliceous particle flux in the Southern Ocean. Marine Chemistry, 35, 503-536.

Bárcena, M.Á., Gersonde, R., Ledesma, S., Fabres, J., Calafat, A. M., Canals , M., Sierro, F.J. and Flores, J. A., 1998, Record of Holocene glacial oscillations in

Bransfield Basin as revealed by siliceous microfossil assemblages. Antarctic Science, 10(3), 269-285.

Bárcena, M.Á., Isla, E., Plaza, A., Flores, J.A., Sierro, F.J., Masque, P., Sanchez-Cabeza, J.A. and Palanques, A., 2002, Bioaccumulation record and its relation with paleoclimatic evolution in the weastern Bransfield Strait. Deep-Sea Reserch II, 49(4-5), 935-950.

Basterrexea, G. and Aristegui, J., 1999, Phytoplankton biomass and production during late austral spring (1991) and summer (1993) in the Bransfield Strait. Polar Biology, 21, 11-22.

Berkman, P.A., Andrew, J.T., Bjorck, S., Colhoun, E.A., Emslis, S., Goodwin, I.D., Hall, B.L., hart, C.P., Hirakawa, K., Igarashi, A., Ingolfson, O., Lopez Martinez, J., Lyons, W.B., Mabin, M.C.G., Quilty, P.G., Taviani, M. and Yoshida, Y., 1998, Circum-Antarctic coastal environmental shifts during the Late Quaternary reflected by emerged marine deposits. Antarctic Science 10, 345-362.

Bóden, P. and Backman, .J., 1996. A laminated sediment sequence from northern North Atlantic Ocean and its climatic record. Geology, 24, 507-510.

Brodie, I. and Kemp, A.E.S., 1994. Pelletal structures in Peruvian upwelling sediments. Journal of the Geological Society, 15(1), 141-150.

Buffen, A., Leventer, A., Rubin, A. and Hutchins, T., 2007, Diatom assemblages in surface sediments of the northwestern Weddell Sea, Antarctic Peninsula. Marine Micropaleontology, 62, 7-30.

Bull, D., Kemp, A.E.S., Weedon, G.P., 2000. A 160-k.y.-old record of El Nino-Southern Oscillation in marine production and coastal runoff from Santa Barbara Vasin, California, USA. Geology, 28 (11), 1007-1011.

Burckle, L.H., Jacobs, S.S and McLaughlin, R.B., 1987, Late austral spring diatom distribution between New Zealand and the Ross Ice Shelf, Antarctica: hydrographic and sediment correlations. Micropaleontology, 33, 74-81.

Cremer M, Kupper K, Wagler B, Wizelman L, von Hase J, Weiland Y, Kreja L, Diebold J, Speicher MR, Cremer T., 2003, Inheritance of gene density-related higher order chromatin arrangements in normal and tumor cell nuclei. Journal of Cell Biology, 162, 809-820.

Crosta, X., J.-J. Pichon and M. Labracherie, 1997, Distribution of Chaetoceros resting spores in modern peri-Antarctic sediments. Marine Micropaleontology, 29, 283-299.

Crosta, X., Denis, D. and Ther, O., 2008, Sea ice seasonality during the Holocene, Adélie Land, East Antarctica. 66, 222-232.

Denis, D., Crosta, X., Zaragosi, S., Romero, O., Martin, B. and Mas, V., 2006, Seasonal and subseasonal climate changes recorded in laminated diatom ooze sediments, Adélie Land, East Antarctica. The Holocene, 16(8), 1137-1147.

Domack, E.W., Leventer, A., Root, S., Ring, J., Williams, E., Carlson, D., Hirshorn, E., Wright, W., Gilbert, R. and Burr, G., 2003, Marine sedimentary record of natural environmental variability and recent warming in the Antarctic Peninsula. In: Domack, E., Leventer, A., Burnett, A., Bindschadler, R., Convey, P., Kirby, M. (Eds.), Antarctic Peninsula Climate Variability: Historical and Paleoenvironmental Perspectives. American Geophysical Union, Washington, D.C., 205-224.

Figueiras, F.G, Arbones, B and Estrada, M, 1999, Implications of bio-optical modelling of phytoplankton in Antarctic waters: further evidence of no light limitation in the Bransfield Strait. Limnology and Oceanography, 44, 1599-1608.

Fryxell, G.A., 1991, Comparison of winter and summer growth stages of the diatom Eucampia antarctica from the Kerguelen Convergence Zone. In:

Barron, J.A. and Larsen, B. (eds.), Proceedings of the Ocean Drilling Program, Scientific Results 119. College Station, TX (Ocean Drilling Program), 675-685.

Fryxell, G.A. and Prasad, A.K.S.K., 1990, Eucampia antarctica var. recta (Mangin) stat. nov. (Biddulphiaceae, Bacillariophyceae): life stages at the Weddell Sea ice edge. Phycologia, 29, 27-38.

Garcia, M.A., Castro, C.G., Rios, A.F., Doval, M.D., Roson, G., Gomis, D. and Lopez, O., 2002, Water masses and distribution of physico-chemical properties in the Western Bransfield Strait and Gerlache Strait during Austral summer 1995/96. Deep-Sea Research II, 49, 585-602.

Grimm, K.A., Lange, C.B. and Gill, A.S., 1997, Selfsedimentation of phytoplankton blooms in the geologic record. Sedimentary Geology, 110, 151-161.

Hendey, Q.B. 1981. The geological succession at Langebaanweg, Cape Province, and global events of the late Tertiary. South African Journal of Science 77, 33-38.

Holm-Hansen, O. and Mitchell, B.G., 1991, Spatial and temporal distribution of phytoplankton and primary production in the western Bransfield Strait region. Deep Sea Research, 38, 961-9811.

Kemp, A.E.S., Baldauf, J.G., Pearce, R.B., 1995. Origins and paleoceanographic significance of laminated diatom ooze from the eastern equatorial Pacific Ocean.Proceedings of the Ocean Drilling Program. Scientific Results, 138, 641-645.

Kemp, A.E.S., Pearce, R.B., Pike, J., Marshall, J.E.A., 1998, Microfabric and microcompositional studies of Pliocene and Quaternary sapropels from the Eastern Mediterranean. In:Robertson, A.H.F., Emeis, K.-C., Richter, C., Camerlenghi, A. (Eds.), Proceedings of the Ocean Drilling Program, Scientific Results, 160, 333-348.

King, S.C., Kemp, A.E.S., Murray, J.W., 1995. Benthic foraminifera assemblages in Neogene laminated diatom ooze deposits in the east equatorial Pacific Ocean (Site 844). Proceedings of the Ocean Drilling Program, Scientific Results Leg 138, 665 p. Leventer. A., 1991, Sediment trap diatom assemblages from the northern Antarctica Peninsula region. Deep Sea

Research, 38, 1127-1143.

Leventer, A., 1992, Modern distribution of diatoms in sediments from the George V Coast, Antarctica. marine Micropaleontology, 19, 315-332.

Leventer, A. and Dunbar, R., 1996, Factors influencing the distribution of diatoms and other algae in the Ross Sea. Journal of Geophysical Research. 101, 18489-18500.

Maddison, E.J., Pike, J., Leventer, A. and Domack, E.W., 2005, Deglacial seasonal and sub-seasonal diatom record from Palmer Deep, Antarctica. Journal of Quaternary Science, 20, 435-446.

Maddison, E.J., Pike, J., Leventer, A., Dunbar, R., Brachfeld, S., Domack, E.W. Manley, P. and McClennen, C., 2006,. Post-glacial seasonal diatom record of the Mertz Glacier Polynya, East Antarctica. Marine Micropaleontology, 60, 66-88.

Marra, J. and Boardman, D.C., 1984, Late winter chlorophyll a distributions in the Weddell Sea. Marine Ecoogy Progress Series, 19, 197-205.

Orsi, A.H., Nowlin Jr., W.D. and Whitworth III, T., 1993, On the circulation and stratification of the Weddell Gyre. Deep Sea Research I, 40, 169-203.

Orsi, A.H., Whitworth III, T. and Nowlin Jr., W.D., 1995, On the meridional extent and fronts of the Antarctic Circumpolar Current. Deep Sea Research, 42, 641-673.

Sommer, U., 1991. Comparative nutrient status and competitive interactions of two Antarctic diatoms (Corethron criophilum and Thalassiosira antarctica). Journal of Plankton Research, 13, 61-75.

Pichon, J.J., Labeyrie, L.D., Bareille, G., Labracherie, M., Duprat, J. and Jouzel, J., 1992, Surface water temperature changes in the high latitudes of the southern hemisphere over the last glacial-interglacial cycle. Paleoceanography, 7, 289-318.

Pike, J., Allen, C.S., Leventer, A., Stickley, C.E. and Pudsey, C.J., 2008, Comparison of contemporary and fossil diatom assemblages from the western Antarctic Peninsula shelf. Marine Micropaleontology, 67, 274-287.

Scherer, R.P., 1994. A new method for the determination of absolute abundance of diatoms and other silt-sized sedimentary particles. Journal of

Paleolimnology, 12(2), 171-180

Stickley, C.E., Pike, J., Leventer, A., Dunbar, R., Domack, E.W., Brachfeld, S., Manley, P. and McClennen, C., 2005, Deglacial ocean and climate seasonality in aminated diatom sediments, Mac. Robertson Shelf, Antarctica. Palaeogeography, Palaeoclimatology, Palaeoecology, 227, 290-310.

Treguer, P., Nelson, D.M., van Bennekom, A.J., DeMaster, D.J., Leynaert, A. and Queguiner, B., 1995, The silica balance in the world ocean: a re-estimate. Science, 268, 375-379.

Whitworth III, T., Nowlin Jr, W.D., Orsi, A.H., Locarnini, R.A. and Smith, S.G., 1994, Weddell Sea Shelf Water in the Bransfield Strait and Weddell-Scotia Confluence. Deep-Sea Research I, 41, 629-641.

Zielinski, U. and Gersonde, R., 1997, Diatom distribution in Southern Ocean surface sediments (Atlantic sector): implications for paleoenvironmental reconstructions. Palaeogeography, Palaeoclimatology, Palaeoecology, 129, 213-250.

Table 1. Results of AMS ^{14}C datings of core GC08-EB01

Depth (cm)	Age (^{14}CyrB.P.)		Material	Lab code
	Uncorrected	Corrected[a]		
83	1,790±20	490±20	shell	UGAMS#344
443	3,950±25	650±25	shell	UGAMS#7347

[a]A 1300-yr correction was applied to all ages of core GC08-EB01. This correction is also based upon the fact that the Antarctic marine reservoir effect averages 1,300 yr (Berkman et al., 1998)

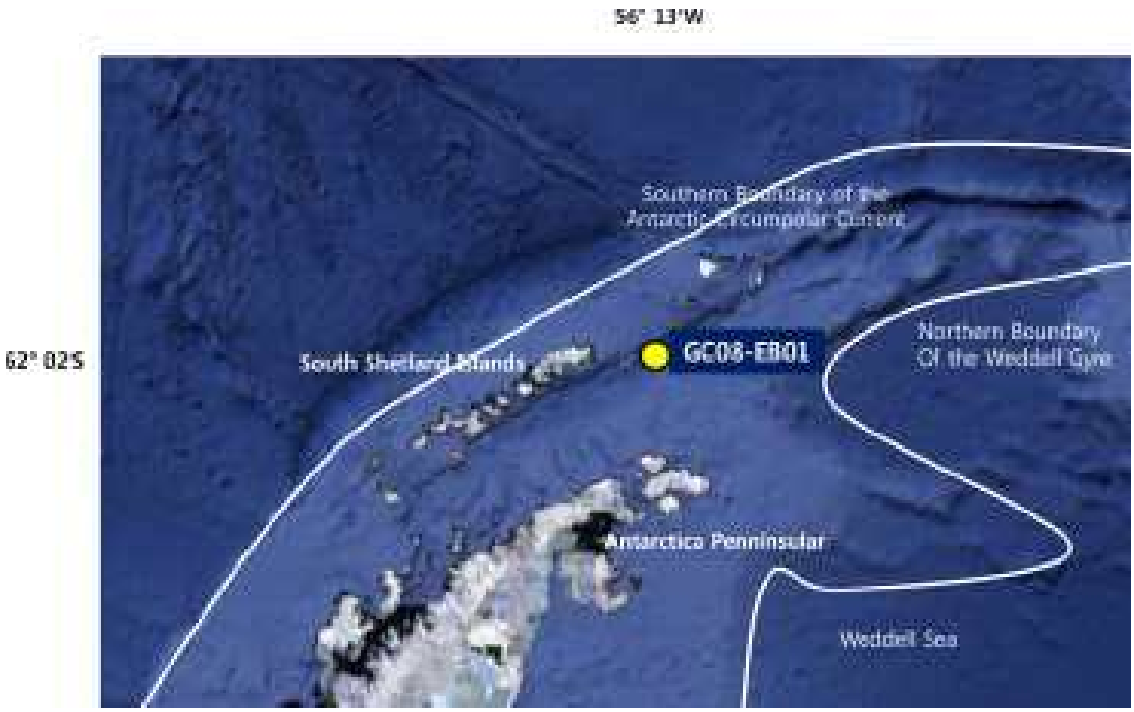

Fig. 1. Locality map of core sediment, GC08-EB01, in Antarctica. White lines shoe fronts and boundaries of the ocean current systems: southern boundary of the Antarctic Circumpolar Current, northern boundary of the Weddell Gyre (Orsi et al., 1993, 1995; Whitworth et al., 1994).

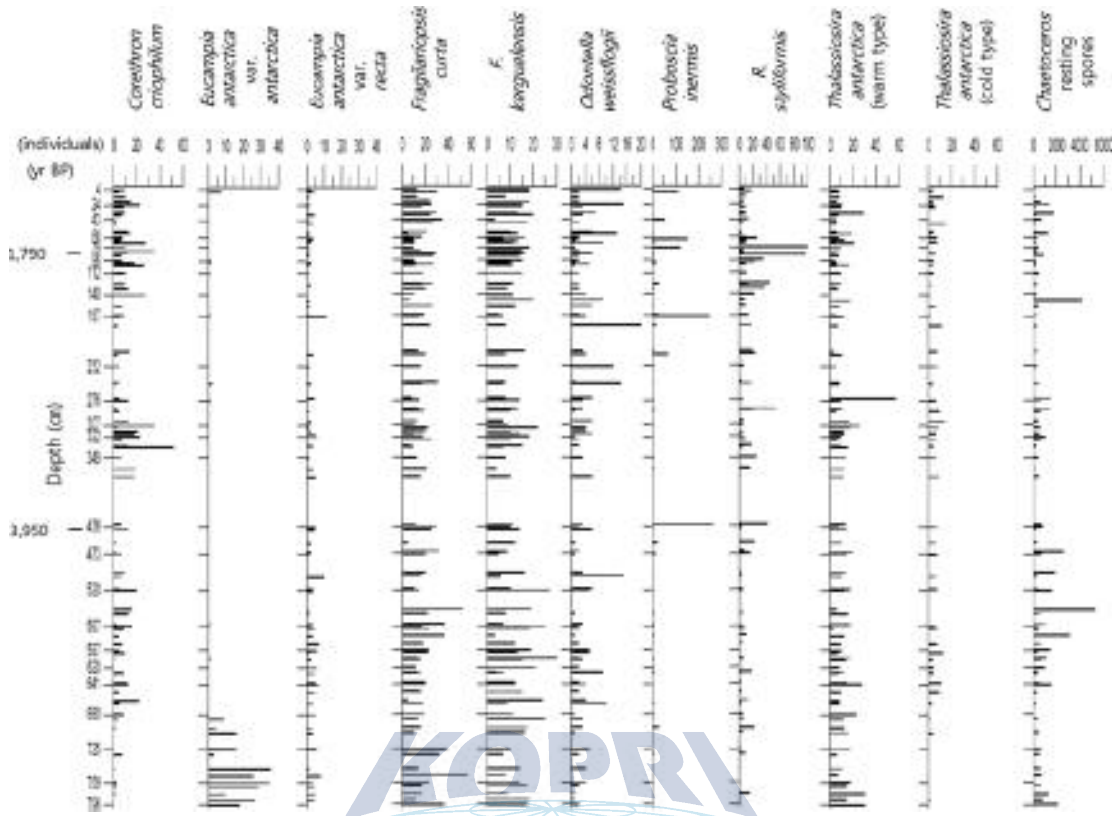

Fig. 2. Down-core variations of relative abundance of the characteristic species (Corethron criophilum, Eucampia antarctica var. antarctica, Eucampia antarctica var. recta, Fragilariopsis curta, F. kerguelensis, Odontella weissflogii, Proboscia inermis, R. styli-formis, Thalassiosira antarctica (warm type), Thalassiosira antarctica (cold type) and Chaetoceros resting spores. ucyr BP. : Uncorrected Age.

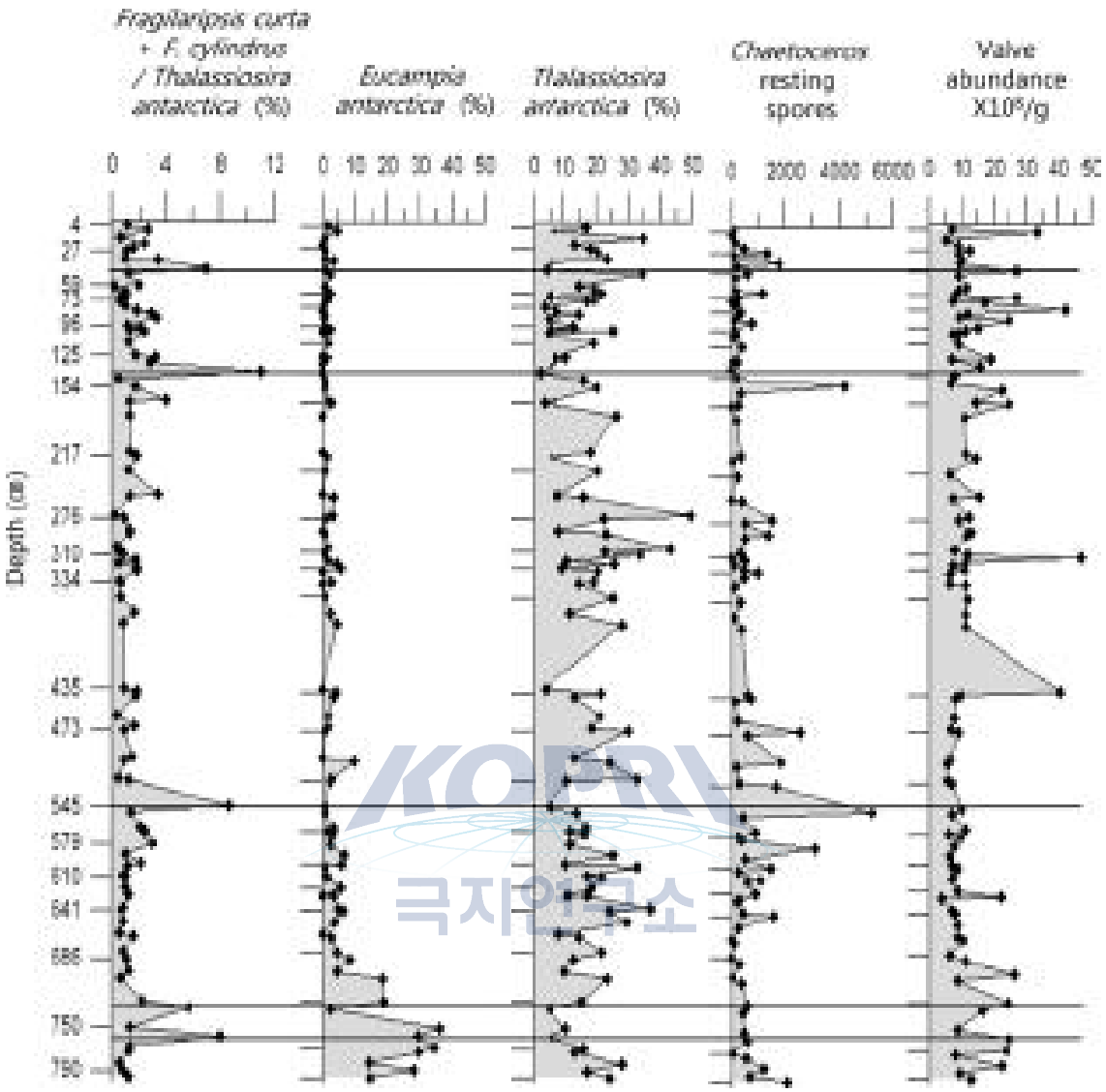

Fig. 3. Ratio of (Fragilariopsis curta+F. cylindrus)/Thalassiosira antarctica and down-core variations relative abundances of Eucampia antarctica (%), Thalassiosira antarctica (%), Chaetoceros resting spores, and number of valves per gram of sediment.

제 15 장

Production of molecular iodine and triiodide in the frozen solution of iodide: implication for polar atmosphere[10)]

Kitae Kim[1], Dae Wi Min[2], Ho-Il Yoon[1] and Wonyong Choi[2*]

[1]Korea Polar Research Institute

[2]Pohang University of Science and Technology

Abstract: The chemistry of reactive halogens in the polar atmosphere plays important roles in ozone and mercury depletion events, oxidizing capacity, and dimethylsulfide oxidation to form cloud condensation nuclei. Among halogen species, the sources and emission mechanisms of inorganic iodine compounds in the polar boundary layer remain unknown. Here, we demonstrate that the production of triiodide (I_3^-) via iodide oxidation, which is negligible in aqueous solution, is significantly accelerated in frozen solution – both in the presence and absence of solar irradiation. Field experiments carried out in the Antarctic region (King George Island, 62°13′S 58°47′W) also showed that the generation of triiodide via solar photooxidation was enhanced when iodide was added to various ice media. The emission of gaseous I_2 from the irradiated frozen solution of iodide to the gas phase was detected by using cavity ring down spectroscopy, which was observed both in the frozen state at 253 K and after thawing the ice at 298 K. The accelerated (photo)oxidation of iodide and the subsequent formation of triiodide and I_2 in ice appear to be related with the freeze concentration of iodide and dissolved O_2 trapped in the ice crystal grain

10) 이 연구는 본 과제와 극지연구소(PP16010, PAP) 지원으로 수행되었으며 그 결과는 다음의 논문으로 출판되었음. Kitae Kim, Akihiro Yabushita, Masanori Okumura, Alfonso Saiz-Lopez, Carlos A. Cuevas, Christopher S. Blaszczak-Boxe, Dae Wi Min, Ho-Il Yoon, Wonyong Choi. "Production of Molecular Iodine and Tri-iodide in the Frozen Solution of Iodide: Implication for Polar Atmosphere" Environ. Sci. Technol. 2016, 50, 1280-1287

boundaries. We propose that an accelerated abiotic transformation of iodide to gaseous I_2 in ice media provides a previously unrecognized formation pathway of active iodine species in the polar atmosphere.

1. Introduction

Reactive halogens play various key roles in the global environment. In particular, the presence of gaseous halogens in the polar and marine boundary layers is of great interest as these highly reactive species can affect the oxidative capacity of Earth's atmosphere.(von Glasow et al, 2008, Pratt, K. A. et al, 2013, Saiz-Lopez et al, 2014, Abbatt et al, 2012, Saiz-Lopez et al, 2012, Saiz-Lopez et al, 2008, Schroeder et al, 1998, Simpson et al, 2015, Simpson et al, 2007) The sources and impacts of iodine in polar atmospheric chemistry are much less understood in comparison with chlorine and bromine. Although active iodine compounds (e.g., IO and I_2) in the polar regions have been observed by ground and satellite based techniques, the sources and mechanisms of this large iodine emission are still being debated.(Abbatt et al, 2012, Saiz-Lopez et al, 2012, Saiz-Lopez et al, 2008, Saiz-Lopez et al, 2010, Frieß et al, 2010) In this aspect, it is of particular interest how the heterogeneous chemistry of iodine can be affected by the presence of frozen media in cold environments such as the polar region. Some chemical and photochemical reactions in frozen solutions are reported to be quite different from their aqueous counterparts and highly accelerated, because solutes are concentrated in liquid-like grain boundary regions (freeze concentration effect) (Betterton et al, 2001, Grannas et al, 2007, Takenaka et al, 1992, Klanova et al, 2003, Cheng et al, 2010, Kim et al, 2010, Kim et al, 2011, Jeong et al, 2012, Kim et al, 2012) and brine channels in sea ice (Mock et al, 2008, Atkinson et al, 2014) as they are segregated from the crystalline ice lattice.

A number of atmospherically relevant oxidation reactions, such as nitrite to nitrate and sulfite/sulfide to sulfate, are known to be promoted when dilute solutions are frozen.(Betterton et al, 2001, O'Driscoll et al, 2008, Takenaka et al, 1996) O'Driscoll et al.(O'Driscoll et al, 2008) reported that the enhanced release of active and ozone-depleting gases such as nitric oxide (NO) and iodine

molecule (I_2) from the solidification of sea-salt aerosol components containing nitrite and iodide ion (NO_2^-/I^-). They observed the production of I_3^- spectrophotometrically in the frozen solution of $NaNO_2$/KI at pH 6. Sullivan and Sodeau(O'Sullivan and Sodeau et al, 2010) investigated the freeze-induced formation of interhalogen species from frozen halide ion solutions which can be a potential mechanism for the release of interhalogens to the atmosphere in polar regions. In this study, they observed the freeze-induced production of dibromoiodide ion, IBr_2^- from mixed solutions containing iodide, bromide and nitrite ions under slightly acidic conditions up to pH 5.1 which is relevant to snow in polar region. They also verified the effects of various experimental conditions such as a ratio of $[Br^-]/[I^-]$, pH, and the presence of oxidants (nitrite and hydrogen peroxide) and dioxygen. Diao and Chu also investigated the heterogeneous reactions of gaseous HONO with HCl, HBr, and HI on ice surface at 191 K in a fast flow-tube reactor.(Diao et al, 2005) The results showed that the reaction probability of HONO on HI-treated ice surface is higher than that on HCl-treated or HBr-treated ice surface. The reaction probability increased with the surface coverage of HI and the product INO rapidly converted to I_2 on the HI-treated ice surface. However, chemical or photochemical conversion kinetics and mechanisms of iodide alone in frozen solution are unknown and needed to be investigated.

In this study, we investigated the oxidation of iodide to form I_3^- and I_2 in frozen solution, which is even more enhanced under simulated solar irradiation. The effects of various experimental parameters on the freezing-enhanced iodide oxidation were systematically investigated to understand this anomalous chemical process. A modeling study was also carried out to reproduce the experimental results. This finding proposes a previously unrecognized source of gaseous I_2 through abiotic process in the polar region.

2. Experimental

2.1. Materials

KI (99.5%, Samchun Chemical) was used as the iodide source. N_2 (BOC

Gases, 99.999% purity) and O_2 (Sinan Gases, Korea, 99.999% purity) gases were used when the effect of the dissolved gas was investigated. Ultrapure deionized water (18 MΩ·cm) prepared by a Barnstead purification system was used in all experiments.

2.2. Laboratory Experiments of Iodide Oxidation in Ice

The initial iodide concentration employed in this work ranged in 1 1000 μM for the oxidation either in the dark or under photoirradiaion. The pH of the solutions was adjusted with HCl or NaOH solution to a desired value prior to freezing. Iodide solution (5 mL) was added to 12×125-mm quartz tubes, sealed with septa, and put into the ethanol bath precooled at -5°C. The temperature of the freezing bath was gradually lowered from -5°C to -20°C within 30 minutes for complete solidification. The whole ice column was irradiated by a lamp (for photooxidation) after the freezing process. Sample tubes (maximum 16 tubes) were located in a merry-go-round photolysis reactor that was rotated at a constant speed (0.8-1.0 rpm) around a 100-W mercury lamp (Ace Glass Inc.) for uniform irradiation. Light was filtered by a pyrex jacket (transmitting > 300 nm; see Figure 1C) surrounding the mercury lamp that was immersed in the ethanol bath. For the photooxidation experiments in oxygen or nitrogen saturated conditions, the sample tubes were purged with O_2 or N_2 gas for 30 minutes prior to freezing and irradiation. The dark oxidation experiments were also carried out in the same way except for the photoirradiation.

All irradiated ice samples were thawed for sampling and the subsequent analysis for I_3^-. Although there is a possibility that the concentration of triiodide in frozen solution might be changed after thawing, we assumed that this effect is negligible in this study. Aqueous photochemical reactions of iodide were also carried out as a control at 25 °C using the same experimental setup. The concentration of photogenerated triiodide (I_3^-) was determined by measuring the absorbance at 352 nm (εm = 26400 $M^{-1}cm^{-1}$)23 using a UV/visible spectrophotometer (Libra S22). The detection limit of this analysis method is about 0.1 M of triiodide. The absorption spectrum of oxygen-saturated solution of iodide was obtained with direct O_2 purging in a 1cm-pathlength quartz cell

sealed with septa.

2.3. Outdoor Experiments

The experiments for iodide photooxidation were also carried out under ambient solar radiation. The outdoor experiments were conducted in the Antarctic region, King George Island (62°13′S 58°47′W, sea level) from December 1st to 17th, 2010. Quartz tubes containing the desired concentration of iodide were frozen in a refrigerator (at -20°C) before exposing to sunlight. The solidified ice samples were placed on the surface of ambient snow horizontally for exposure to incident solar radiation. The irradiated samples remained solid during the entire exposure to sunlight. Control photolyses of aqueous samples containing iodide were carried out simultaneously under the same irradiation conditions. In order to prevent the freezing of the aqueous samples under ambient exposure, the samples were placed on an electrically heated mat on the snow.

The concentrations of photogenerated I_3^- were immediately determined by UV/visible spectrophotometer after solar irradiation in the Korea Polar Research Institute (KOPRI) the King Sejong Station (King George Island). The ambient temperature ranged between -4.5 and 2.3°C (average temperature was -3.5°C during experiments). The integrated solar irradiance as measured at the King Sejong Station in King George Island varied from 0.2 to 8.6 W/m^2 for UV band of $315 < \lambda < 380$ nm, depending on the angular position of the sun and the weather condition with an average intensity of 3.1 W/m^2 during photooxidation experiment (corresponding to about 9.0 Einstein $m^{-2}s^{-1}$ assuming 350 nm photons). The snow samples for iodide spiking experiment were collected 100 m far from The King Sejong Station and about 50 m far from sea ice and sea water. The initial pH of collected snow and glacier ice after melting was 5.30 and 5.45, respectively. The glacier ice samples were obtained from drifting icebergs detached from Marian Cove Glacier and the outer part of glacier was removed in order to eliminate contamination. The collected snow and glacier were thawed at room temperature and resolidified after iodide spiking (adding 1

mM iodide) at -20°C for photolysis under natural solar irradiation

2.4.. Gaseous I_2 Measurement by Cavity Ring-Down Spectroscopy

Gaseous iodine molecule was measured by cavity ring-down spectroscopy (CRDS). The principle of CRDS and pertinent experimental details (Figure S1) are described elsewhere,(Sakamoto et al, 2009) and a brief description is given here. The photooxidation of iodide in frozen solution proceeded in a Pyrex glass cell (41 mm internal diameter and 54 cm length) coupled with two valves on both sides of the cell (total volume = 770±10 mL). The glass cell consists of a double pipe. To minimize possible secondary reactions, the inner side of the cell was washed by deionized water and methanol before each experiment, and dried. Aqueous NaI solutions ([NaI] = 1, 5, 10, 50 and 100 M, volume = 50 mL) were prepared by reagent grade NaI (Sigma-Aldrich, ≥ 99.5%) in 18 MΩ″cm deionized water. Deoxygenated water was also used for control experiments. Dissolved oxygen was removed from deionized water by bubbling nitrogen gas through the water, and the concentration of which was measured with a dissolved oxygen meter. Typical concentrations of dissolved oxygen were 8.2-8.4 mg/L and 0.0-0.2 mg/L, before and after nitrogen gas bubbling, respectively. Solution pH was adjusted to pH 3 by adding HCl. The temperature of the inner side of the cell was regulated by flowing a mixture of ethylene glycol and water through the outer side of a double pipe cell over the range of 253 to 298 K. The sample solution was filled into the cell at 265 K, and the temperature of the inner side of the cell was gradually decreased. It took about 40 minutes for the temperature of the ice sample to reach 253 K. The temperature of the sample ice was monitored by a thermocouple, which was located near the ice surface.

The sample ice (surface area of 145 cm^2) kept at 253 K was illuminated through a Pyrex glass cell by two 20-W fluorescence lamps (TOSHIBA, FL-20S-BLB, 58 cm length, centered at 365 nm) in a closed batch reactor. Each lamp was fixed above the cell. The distance between the center of the lamp and the ice surface was 7.0(±0.2) cm and the incident irradiation power was 8.25(±0.25) mW cm^{-2}, corresponding to about 1.5×1016 photons cm^{-2} s^{-1}. After irradiation for 3 h,

the sample ice was thawed at 298 K. It took about 10 minutes for the temperature of the sample solution to reach 298 K, and then the molten solution was rest for 15 minutes to achieve equilibrium. The CRDS detection region was 18.3(±1) mm above the surface of the sample solution. The I_2 concentration was monitored with a Nd^{3+}:YAG pumped dye laser (Lambda Physik, SCANmate) at 532.8 nm for the $B_3\Pi - X_1\Sigma^+$ band. The CRDS measurements of gaseous I_2 were usually carried out after thawing the ice at 298 K. In a separate control experiment, I_2 was measured both before and after melting the ice to investigate whether gaseous I_2 is emitted over the frozen state at 253 K. The measurement was performed immediately after two valves on both sides of the reactor cell were opened and no apparent sign of I_2 loss was observed during the measurement. The I_2 signal baseline was taken at the same wavelength after refreshing the cell completely by N_2(g) flow. The detection limit of I_2 was estimated to be 1.5 1010 molecules cm^{-3}. All photochemical reactions and measurements were performed at atmospheric pressure. The pressure in the cell was monitored by a pressure gauge.

2.5. Modeling

We use the multiphase model, CON-AIR (Condensed Phase to Air Transfer Model).28,29 The model treats the coupling of ice photochemistry (i.e., in the brine layer (BL)), and atmospheric boundary layer and condensed phase chemistry. The model is comprised of reactions involving O, H, C, N, S, Cl, Br, and I, incorporating heterogeneous uptake, halogen recycling on deliquesced airborne sea-salt aerosols and wet/dry deposition. Full model details with a list of the condensed phase reactions, phase transfer processes, and photochemical reactions used in the model can be found elsewhere.(Saiz-Lopez et al, 2015, Boxe et al, 2008) A list of BL reactions and the Henry´s law constants included in the model is attached in SI (Table S1 and S2). The dependence of the Henry's law constants on the salinity was not considered due to the lack of the experimental data. Halogen species exchange between the BL and gas phase is treated via phase equilibration as well onto the sea-ice surface. The solubility of species is taken into account by including a diurnal variation of the typical

temperature profile during polar springtime (i.e., ~ 260 T/K ~270).(Launiainen et al, 2013) CON-AIR is parameterized with: $[I^-]_0$ = 1.3 × 10-7 M; a BL thickness of 500 μm; volumetric = 1.14 × 10^{-6} (cm^3 (BL)/cm^3 (atmosphere), $[O_2]$(sea ice) = 1 × 10^{-4} M,(Zhou et al, 2014) which is applied to aqueous phase reaction rates; and the first-order transfer rate constant, kt = 1.25 × 10^{-5} s^{-1} (Gong et al, 1997, Michalowski et al, 2000) and the dimensionless Henry's law constant (H′ = HRT, H is a species' Henry's law constant, R is the gas constant, 0.08206 L atm K^{-1} mol^{-1} and T is the temperature (K) are used to quantify the rate of transfer of species from the BL to the atmosphere via k(BL →Atmosphere) = (k_t × [species concentration])/(H′).(Saiz-Lopez et al, 2015 ,Boxe et al, 2008) We have implemented in CON-AIR the experimentally-derived Reaction 1 (vide infra) and the equilibrium between triiodide and I_2. For a detailed description of CON-AIR, please refer to the previous studies.(Saiz-Lopez et al, 2015 ,Boxe et al, 2008) This allows us to study the effect of the proposed mechanism, under a range of aqueous iodide concentrations and pH values, on the release of active iodine to the atmosphere and the resulting contribution to iodine levels in the polar boundary layer.

3. Results and Discussion

Iodide Oxidation to Tri-iodide in Various Conditions. Iodide can be oxidized to triiodide slowly in the presence of O_2 in acidic condition through reaction 1.25,34

$$O_2(aq) + 4H^+ + 6I^- \rightarrow 2H_2O + 2I_3^- \quad (1)$$

The rate constant of reaction 1 was firstly measured in ambient aqueous solution and determined to be 2.16 10^{-2} ($mol^{-2}.L^2.s^{-1}$) (see supporting information (Table S3 and Figure S2) for details). We found that the oxidative formation of triiodide (reaction 1), which occurs extremely slowly in aqueous solution, is significantly accelerated in the frozen solution (both under dark and photoirradiation conditions) (see Figure 1a). The inset (Figure 1a) clearly shows the appearance of the triiodide peak, which has two absorption bands centered at 288 and 352 nm (with molar absorption coefficients of 40,000 and 26,400 $M^{-1}cm^{-1}$, respectively). To confirm the occurrence of reaction 1 even in the

absence of light, the absorbance band (at 352 nm) was monitored as a function of time under dark condition in a highly concentrated iodide solution (1 M): Figure 1b show that the triiodide absorbance gradually increased with time, which indicates that I_3^- is generated in-situ as a result of the reaction between iodide and dissolved O_2. The oxygen purging of the iodide solution further accelerated the production of triiodide (Figure 1b), which confirms the role of O_2 in reaction 1. However, reaction 1 is negligible in aquatic environmental condition where the iodide concentration is much lower. Upon observing the enhancement of iodide oxidation in frozen solution, we systematically studied the iodide activation in ice medium as a new unknown environmental transformation path and investigated the oxidation of iodide to triiodide (I_3^-) in ice and the subsequent emission of gaseous I_2 to the gas phase.

Table 1 summarizes the production of I_3^- in aqueous solution and ice under different experimental conditions (i.e., in the presence and absence of light and O_2, various pH, solar radiation in the polar environment): the formation of I_3^- in ice was significantly accelerated in all tested conditions compared to those in the liquid state. The production of triiodide was observed in ice even in the dark acidic condition whereas that in aqueous solution was negligible below the detection limit. Under solar irradiation ($>$ 300 nm), the rate of triiodide formation was significantly enhanced in ice although iodide ions do not absorb light in this wavelength region (Figure 1c). Although the photogeneration of triiodide (under solar-simulating condition) gradually decreased from pH 3 to pH 6, the enhanced production of triiodide in the ice phase was still observed over a wide range of pH (pH 3-9) (Figure 2). In the absence of light, the generation of triiodide in ice exhibited a similar pH-dependence although the dark production rates were much lower than the photo-production rates. The ice-induced production of I_3^- under dark was about 7 times lower than that under solar irradiation (at pH 3) and became insignificant above pH 6.

The dissolved gas (air, N_2 and O_2) also critically influenced the photooxidation of iodide as shown in Table 1. Since the efficiency of iodine atom formation via photoexcitation of iodide ion is highly enhanced in the presence of a suitable electron acceptor such as dioxygen,(Yeo et al, 2009) the photooxidation of iodide was negligible in both aqueous and frozen solutions in the absence of O_2. The

photogeneration of triiodide in aqueous solution was markedly enhanced in oxygen-saturated conditions in an acidic environment, which confirms the role of dioxygen in the photooxidation of iodide. However, it is noted that there was no significant change of triiodide formation between air-equilibrated and O_2-saturated conditions in the ice phase, which implies that O_2 is saturated in ice grain boundaries even in air-saturated conditions. Previous studies also showed a similar result indicating that the dissolved O_2 can be accumulated in the ice grain boundary upon freezing.(Takenaka et al, 1992, Takenaka et al, 1996)

The photooxidation of iodide was also investigated as a function of initial iodide concentration in ice phase at acidic pH range (Figure 3). The generation of triiodide in ice gradually increased with increasing initial concentration of iodide and was more efficient at lower pH condition in the whole concentration range tested. We also carried out the iodide photooxidation experiments at various temperature (-10, -20, and -30 °C), which are shown in Figure S3. A similar enhancement of iodide oxidation was observed at different freezing temperatures and we did not observe any formation of KI precipitates during the experiments.

Mechanism for Enhanced Oxidation of Iodide in Ice. At lower pH and higher iodide concentrations, the generation of triiodide in ice is higher (Figure 2 and Figure 3). The observed accelerated generation of triiodide in illuminated and dark ice conditions can be ascribed to the freeze concentration effect of iodide and O_2 (in reaction 1) at ice grain/surface boundaries. The local concentration of solutes in the ice grain boundary region can be enhanced by several orders of magnitude from their respective aqueous concentrations.(Heger et al, 2006, Robinson et al, 2006, Heger et al, 2005) Reaction 1 is negligible in diluted aqueous solutions but can be markedly accelerated in high concentrations found in the ice grain boundary region. Furthermore, the elevated local concentrations of substrates in the ice grain boundary region may affect the photochemical kinetics and mechanisms.(Heger et al, 2006, Kahan et al, 2010) Our results show that the photogeneration of triiodide in ice was higher at lower pH (as shown in Fig. 1a and 2a), because reaction 1 is favored under acidic condition.

Although iodide itself does not absorb in the wavelength region of > 300 nm (Figure 1c), it can form a charge transfer (CT) complex with O_2 ($I^- \cdot$

O_2).(Levanon et al, 1969) The absorption spectrum of a concentrated iodide solution is different between the air-saturated and O_2-saturated condition (Figure 1c): a new absorption band at 280 – 330 nm appeared in an O_2-saturated solution (see Figure S4 for detailed spectrum), which agrees with the reported absorption spectrum of the CT complex ($I^- \cdot O2$) in aqueous solution.40 The CT-complexation (enabling the light absorption above 300 nm) should be enhanced in the ice grain boundary region, where both iodide and dioxygen can be concentrated, which subsequently accelerates the photoinduced oxidation of iodide (via reaction 2). In the presence of excess iodide in the grain boundary, I atom recombines with I^- to produce I_2^- at a diffusion-limited rate, which subsequently generates triiodide through disproportionation (reactions 3,4).(Gardner et al, 2009) In the confined environment of ice grain boundary, the bimolecular reactions among various reactive iodine species (I, I_2 , I_3^-) and O_2 might be highly accelerated, which is associated with the marked photoeffect observed in iodide oxidation in ice.

$$I^- + O_2 \rightarrow (I^- \cdot O2) \rightarrow I\cdot + O_2^- \quad (2)$$

$$I\cdot + I^- \rightarrow I_2^- \quad (3)$$

$$I_2^- + I_2^- \rightarrow I_3^- + I^- \quad (4)$$

Verification of Freeze Concentration Effect. To investigate the concentration effect of iodide and protons on the photooxidation kinetics of iodide, we monitored the formation of triiodide in the aqueous phase via elevating the concentration of either iodide or proton (lowering pH) (Figure 4). The generation of triiodide in aqueous solution was markedly enhanced when the iodide concentration is increased by 100-fold (1 mM → 100 mM) or the proton concentration was raised by 100-fold (pH 3 → pH 1). Hence, although the iodide photooxidation in aqueous solution at 1 mM and pH 3 is negligible, its kinetics in ice are significantly enhanced.

Direct Detection of Gaseous I_2 with CRDS. The production of triiodide implies the presence of I_2, that should be in equilibrium with triiodide ($I_2 + I^- \leftrightarrow I_3^-$: K = 700).(Yeo et al, 2009, Rahn et al, 1997) The I_2 molecule generated in ice can be released to the headspace. In laboratory experiments, the release of gaseous I_2 emitted from the irradiated frozen solution was directly detected by cavity

ring-down spectroscopy (CRDS) (Figure 5a). The results show that the concentration of gaseous I_2 linearly increased with increasing iodide concentration (Figure 5b). The photogeneration of I_2 was observed in the irradiated frozen solution containing iodide as low as 1 M (or about 0.1 ppm), which is close to a lower detection limit. The I_2 concentration produced at $[I^-] <$ 1 M could not be quantified. The effects of O^2, photoirradiation, and freezing on the generation of gaseous I_2 are compared in Figure 5c, which reconfirms that the freezing process and the presence of O_2 are critical for the production of I_2. Although the in-situ generated I_2 might react with other halide species such as chloride and bromide, it does not seem to be significant. Note that the photogeneration of I^2 (Figure 5c) was measured in the presence of excess amount of chloride (1 mM HCl, 100 fold higher than the iodide concentration). An additional control test in the presence of 1 mM Br^- (in the condition of Figure 5c) did not reduce the I_2 emission at all.

In a separate set of experiments, the concentration of gaseous I^2 was measured at the frozen state (irradiated for 3 h, $[I^-]_0$ = 10 μM) at 253 K, then clean N_2 gas purged the reactor to clear out I_2. It took about 10 minutes for the irradiated ice to thaw at 298 K under dark condition. After the molten solution was equilibrated for 15 minutes, gaseous I2 was measured again. The emission of gaseous I_2 was observed both before and after thawing the ice, which yielded the concentration of 3.8(±1.6) and 3.9(±1.2) (10^{12} molecules cm^{-3}), respectively. This observation implies that the gaseous I_2 can be emitted directly over the irradiated ice/snow containing iodide even without melting the frozen media, which can also explain IO observation in inner Antarctica where no surface melt occurs.(Atkinson et al, 2012, Schönhardt et al, 2008) Moreover, this also implies that the in-situ generated I_2 can diffuse successfully through the ice grain boundaries to the air above the ice surface.

Incidentally, the I_2 emission flux from the irradiated ice surface is roughly estimated as an example at a specific experimental condition (Figure 5c: pHi = 3, $[I^-]_0$ = 10 μM, air-equilibrated ice at 253 K, assuming that the production rate of I_2 is linear during the 3 h irradiation): the calculated photogeneration flux of I_2 in the CRDS reactor is 2.8 109 molecules cm^{-2} s^{-1}. Although this number should not be taken as an index for a real polar I_2 emission flux (since the

laboratory experimental condition has much higher [I^-] and UV flux and lower pH than those of the natural polar condition), it may provide an upper limit. On the other hand, the flux of I_2 emission via the dark aqueous reaction at 298 K (reaction 1) can be estimated on the basis of the experimentally-determined rate law (see SI, Table S3 and Figure S2) and the assumption that the production rate of I2 is equal to that of I_3^- and all I_2 molecules are fully volatilized to the gas phase. The calculated I_2 flux under the dark aqueous condition in the same CRDS reactor would be 6.3 106 molecules cm^{-2} s^{-1}, which is lower by three orders of magnitude than the above mentioned photogenerated flux of I_2.

Outdoor Experiments. Finally, the photooxidation of iodide (spiked into the molten snow/glacier samples) was investigated in the Antarctic region (King George Island, 62°13′N, 58°47′E) to confirm the laboratory-observed phenomenon under Antarctic solar radiation. The field experiments were carried out using the frozen solutions of iodide (in distilled water) and the refrozen solutions of molten snow/glacier (spiked with iodide), both of which were irradiated under the same Antarctic solar condition (Table 1). The outdoor experiments confirmed the laboratory results. The frozen samples irradiated under the Antarctic sun generated a significant amount of triiodide and I_2 (also confirmed by the appearance of the brownish color), which was more efficient at lower pH and higher iodide concentration.

Multiphase Modeling. We next incorporated the experimentally-derived rate constant of reaction 1 into a multiphase model(Saiz-Lopez et al,2015, Boxe et al, 2008) that considered the iodide oxidation and the reactions among active halogen species within the ice gran boundary and its associated air-condensed phase equilibrium, to calculate the effect of the proposed mechanism upon the gas phase levels of iodine in the polar atmosphere. Competition between chloride, bromide, and iodide is quantitatively expressed in CON-AIR.(Saiz-Lopez et al,2015, Boxe et al, 2008) To show that the model replicates the laboratory experimental data, we conducted a modelling exercise to reproduce the range of I_2 production in the CRDS reactor condition ($[I^-]_0$ = 1 to 10 M), which indeed exhibits a good match (with Figure 5b) as shown in Figure S5.

The model results indicate that the photooxidation of iodide in ice, and the subsequent phase equilibration of I_2, produces the following gas phase IO levels

under typical springtime Antarctic irradiation conditions: 0.25 pptv and 1.5 pptv with $[I^-]_0$ = 10 nM at pH 6 and 3, respectively; 0.5 pptv and 2.5 pptv with $[I^-]_0$ = 130 nM for pH 6 and 3, respectively. These model results were obtained with a modeling framework based on available experimentally- and field-derived data; however, please note that uncertainties still remain when modeling processes at the ice-air interface, for instance, on the concentration effects applied to reaction rates, salinity dependence of Henry's law coefficients and brine layer thickness. This range of IO concentrations are in agreement with satellite observations around King George Island.45 The modelled IO dependence on pH reflects the enhanced production of triiodide at acidic condition, as observed in the laboratory experiments. The pH of the sea-ice/snowpack at Antarctica ranges in 4.5-6.5.(Ali et al, 2010) Our results suggest that higher levels of reactive iodine are expected to be transferred to the gas phase in regions with higher iodide concentrations. However, we should mention that the total I_2 emission from the solar irradiated ice surface in the polar environment is not comparable (in a global scale) to the total iodine emission from seawater, considering that the sea surface area is far larger than the frozen surface on earth.

4. Conclusion

We have shown that the abiotic oxidation mechanism of iodide to triiodide and I_2 in the ice phase, under solar irradiation, leads to the emission of gaseous reactive iodine. The experimental studies were carried out with varying the reaction conditions (e.g., pH, light intensity, iodide concentration, dissolved gas) and the observed phenomenon may have significant environmental implications since iodine compounds can influence the chemistry and radiative balance of the polar atmosphere. The modeling calculation done with employing the environmentally relevant condition confirmed that the proposed iodide oxidation process can be important in the polar environment. Furthermore, the strong enrichment of iodine in Antarctic meteorites and snow, which has recently been measured,(Frieß et al, 2010, Heumann et al, 1987) might be related with the enhanced production of volatile I_2 and IO over the solar irradiated ice. Freezing-induced chemical reactions involving iodine compounds,

which have not been recognized before, may have significant impacts on polar environments. This kind of phenomenon might be extended to other halide species concentrated in brine channels in sea ice and should be further investigated.

극지방 대기 요오드 대량생성 메카니즘 연구

김기태[1], 민대위[2], 윤호일[1], 최원용[2],

[1]한국해양과학원부설 극지연구소
[2]포항공과대학교

요약: 극지방 대기중의 할로겐 물질들은 오존 및 수은농도 감소, 대기산화력, 황화합물의 산화등 큰 영향을 미치고 있다. 다양한 할로겐 물질 중 대기 중 비생물학적 요오드에 대한 연구는 많이 수행되지 않았으며 그 생성원 및 거동등도 아직 명확하지 않다. 본 연구에서는 수중에 존재하는 요오드(I^-, iodide)가 얼음 내에서 일어나는 독특한 화학반응으로 인해 산화되어 I_3^-를 생성하고 이후 대기중으로 I_2 기체를 방출하는 현상에 대해 연구를 수행하였다. 액상에서 거의 진행되지 않던 요오드의 산화반응이 얼음상에서 매우 빠르게 진행되는 것을 실험을 통하여 확인하였다. 남극 세종과학기지에서 현장실험을 수행한 결과 실험실의 결과와 마찬가지로 얼음상에서만 요오드의 광산화 반응이 매우 빠르게 일어남을 재차 확인하였다. 요오드의 산화반응으로 생성된 I_3^-가 실제로 대기중으로 방출되는지 확인하기 위하여 Cavity Ring Down Spectroscopy 를 이용하여 I_2 기체를 검출하였다. 얼음 내에서 향상된 요오드 이온의 활성화 반응은 동결농축효과로 얼음 결정주위 준액체층에서 높아진 요오드 이온과 산소의 농도 때문인 것으로 생각되어진다. 본 연구결과는 기존에 알려지지 않았단 극지방 얼음에 의한 비-생물학적 무기 요오드의 생성 메카니즘을 최초로 밝혔다는데 과학적 의미가 있다.

참고문헌

Ali, K.; Sonbawane, S.; Chate, D. M.; Siingh, D.; Rao, P. S. P; Safai, P. D.; Budhavant, K. B. Chemistry of snow and lake water in Antarctic region. J. Earth Syst. Sci. 2010, 119 (6), 753−762.

Atkinson, H. M.; Huang, R.-J.; Chance, R.; Roscoe, H. K.; Hughes, C.; Davison, B.; Schönhardt, A.; Mahajan, A. S.; Saiz-Lopez, A.; Hoffmann, T.; Liss, P. S. Iodine emissions from the sea ice of the Weddell Sea. Atmos. Chem. Phys. 2012, 12 (22), 11229−11244.

Atkinson, H. M.; Hughes, C.; Shaw, M. J.; Roscoe, H. K.; Carpenter, L. J.; Liss, P. S. Halocarbons associated with Arctic sea ice. Deep Sea Res., Part I 2014, 92, 162−175.

Betterton, E. A.; Anderson, D. J. Autoxidation of N(III), S(IV), and other species in frozen solution − A possible pathway for enhanced chemical transformation in freezing systems. J. Atmos. Chem. 2001, 40 (2), 171−189.

Boxe, C. S.; Saiz-Lopez, A. Multiphase modeling of nitrate photochemistry in the quasi-liquid layer (QLL): implications for NO(x) release from the Arctic and coastal Antarctic snowpack. Atmos. Chem. Phys. 2008, 8 (16), 4855−4864.

Cheng, J.; Soetjipto, C.; Hoffmann, M. R.; Colussi, A. J. Confocal fluorescence microscopy of the morphology and composition of interstitial fluids in freezing electrolyte solutions. J. Phys. Chem. Lett. 2010, 1 (1), 374−378.

Couto, A. B.; De Souza, D. C.; Sartori, E. R.; Jacob, P.; Klockow, D.; Neves, E. A. The catalytic cycle of oxidation of iodide ion in the oxygen/nitrous acid/nitric oxide system and its potential for analytical applications. Anal. Lett. 2006, 39 (15), 2763−2774.

Diao, G.; Chu, L. T. Heterogeneous reactions of HX + HONO and I2 on ice surfaces: Kinetics and linear correlations. J. Phys. Chem. A 2005, 109 (7), 1364−1373.

Frieß, U.; Deutschmann, T.; Gilfedder, B. S.; Weller, R.; Platt, U. Iodine monoxide in the Antarctic snowpack. Atmos. Chem. Phys. 2010, 10

(5), 2439−2456.

Gardner, J. M.; Abrahamsson, M.; Farnum, B. H.; Meyer, G. J. Visible light generation of iodine atoms and I−I Bonds: Sensitized I− oxidation and I3− photodissociation. J. Am. Chem. Soc. 2009, 131 (44), 16206−16214.

Gong, S. L.; Barrie, L. A.; Blanchet, J. P. Modeling sea-salt aerosols in the atmosphere 1. Model development. J. Geophys. Res. 1997, 102 (3), 3805−3818.

Grannas, A. M.; Jones, A. E.; Dibb, J.; Ammann, M.; Anastasio, C.; Beine, H. J.; Bergin, M.; Bottenheim, J.; Boxe, C. S.; Carver, G.; Chen, G.; Crawford, J. H.; Dominé, F.; Frey, M. M.; Guzmań, M. I.; Heard, D. E.; Helmig, D.; Hoffmann, M. R.; Honrath, R. E.; Huey, L. G.; Hutterli, M.; Jacobi, H. W.; Klań, P.; Lefer, B.; McConnell, J.; Plane, J.; Sander, R.; Savarino, J.; Shepson, P. B.; Simpson, W. R.; Sodeau, J. R.; von Glasow, R.; Weller, R.; Wolff, E. W.; Zhu, T. An overview of snow photochemistry: evidence, mechanisms and impacts. Atmos. Chem. Phys. 2007, 7 (16), 4329−4373.

Heger, D.; Jirkovsky, J.; Klan, P. Aggregation of methylene blue in frozen aqueous solutions studied by absorption spectroscopy. J. Phys. Chem. A 2005, 109 (30), 6702−6709.

Heger, D.; Klanova, J.; Klan, P. Enhanced protonation of cresol red in acidic aqueous solutions caused by freezing. J. Phys. Chem. B 2006, 110 (3), 1277−1287.

Heumann, K. G.; Gall, M.; H, W. Geochemical investigations to explain iodine-overabundances in Antarctic meteorites. Geochim. Cosmochim. Acta 1987, 51 (9), 2541−2547.

Jeong, D.; Kim, K.; Choi, W. Accelerated dissolution of iron oxides in ice. Atmos. Chem. Phys. 2012, 12 (22), 11125−11133.

Kahan, T. F.; Donaldson, D. J. Benzene photolysis on ice: implications for the fate of organic contaminants in the winter. Environ. Sci. Technol. 2010, 44 (10), 3819−3824.

Kim, K.; Choi, W. Enhanced redox conversion of chromate and arsenite in ice. Environ. Sci. Technol. 2011, 45 (6), 2202−2208.

Kim, K.; Choi, W.; Hoffmann, M. R.; Yoon, H.-I.; Park, B.-K. Photoreductive dissolution of iron oxides trapped in ice and its environmental implications. Environ. Sci. Technol. 2010, 44 (11), 4142−4148

Kim, K.; Yoon, H.-I.; Choi, W. Enhanced dissolution of manganese oxide in ice compared to aqueous phase under illuminated and dark conditions. Environ. Sci. Technol. 2012, 46 (24), 13160− 13166.

Klanova, J.; Klan, P.; Nosek, J.; Holoubek, I. Environmental ice photochemistry: monochlorophenols. Environ. Sci. Technol. 2003, 37 (8), 1568−1574.

Launiainen, J., Vihma, T. On the surface heat fluxes in the Weddell Sea. In The Polar Oceans and Their Role in Shaping the Global Environment; Johannessen, O. M., Muench, R. D., Overland, J. E.; Geophys. Monogr. Ser., Vol. 85, Eds.; AGU: Washington, D.C., 2013; pp 399−419.

Levanon, H.; Navon, G. The spectrum and stability of oxygen iodide charge-transfer complex. J. Phys. Chem. 1969, 73, 1861−1868.

Michalowski, B. A.; Francisco, J. S.; Li, S.-M.; Barrie, L. A.; Bottenheim, J. W.; Shepson, P. B. A computer model study of multiphase chemistry in the Arctic boundary layer during polar sunrise. J. Geophys. Res. 2000, 105 (D12), 15131−15145.

Mock, T.; Thomas, D. N. Psychrophiles: from Biodiversity to Biotechnology. In Microalgae in Polar Regions: Linking Functional Genomics and Physiology with Environmental Conditions; Margesin, R., Schinner, F., Marx, J. C., Gerday, C., Eds.; Springer: Heidelberg, Germany, 2008; pp 285−308.

O'Driscoll, P.; Minogue, N.; Takenaka, N.; Sodeau, J. Release of nitric oxide and iodine to the atmosphere from the freezing of sea-salt aerosol components. J. Phys. Chem. A 2008, 112 (8), 1677−1682.

O'Sullivan, D.; Sodeau, J. R. Freeze-induced reactions: formation of iodine-bromine interhalogen species from aqueous halide ion solutions. J. Phys. Chem. A 2010, 114 (46), 12208−12215.

Pratt, K. A.; Custard, K. D.; Shepson, P. B.; Douglas, T. A.; Pöhler, D.; General, S.; Zielcke, J.; Simpson, W. R.; Platt, U.; Tanner, D. J.; Gregory Huey, L.; Carlsen, M.; Stirm, B. H. Photochemical production of molecular bromine in Arctic surface snowpacks. Nat.eosci. 2013, 6 (5),

351－356.

Rahn, R. O. Potassium iodide as a chemical actinometer for 254 nm radiation:use of iodate as an electron scavenger. Photochem. Photobiol. 1997, 66 (4), 450－455. .

Robinson, C.; Boxe, C. S.; Guzman, M. I.; Colussi, A. J.; Hoffmann, M. R. Acidity of frozen electrolyte solutions. J. Phys. Chem. B 2006, 110 (15), 7613－7616

Saiz-Lopez, A.; Blaszczak-Boxe, C. S.; Carpenter, L. J. A mechanism for biologically-induced iodine emissions from sea-ice. Atmos. Chem. Phys. 2015, 15 (17), 9731－9746.

Saiz-Lopez, A.; Mahajan, A. S.; Salmon, R. A.; Bauguitte, S. J. -B.; Jones, A. E.; Roscoe, H. K.; Plane, J. M. C. Boundary layer halogens in coastal antarctica. Science 2007, 317 (5836), 348－351.

Saiz-Lopez, A.; Plane, J. M. C.; Baker, A. R.; Carpenter, L. J.; von Glasow, R.; Gómez Martín, J. C.; McFiggans, G.; Saunders, R. W. Atmospheric chemistry of iodine. Chem. Rev. 2012, 112 (3), 1773－ 1804.

Saiz-Lopez, A.; Plane, J. M. C.; Mahajan, A. S.; Anderson, P. S.; Bauguitte, S. J. -B.; Jones, A. E.; Roscoe, H. K.; Salmon, R. A.; Bloss, W. J.; Lee, J. D.; Heard, D. E. On the vertical distribution of boundary layer halogens over coastal Antarctica: implications for O3, HOx, NOx and the Hg lifetime. Atmos. Chem. Phys. 2008, 8 (4), 887－900.

Saiz-Lopez, A.; Saunders, R. W.; Joseph, D. M.; Ashworth, S. H.; Plane, J. M. C. Absolute absorption cross-section and photolysis rate of I2. Atmos. Chem. Phys. 2004, 4 (5), 1443－1450.

Saiz-Lopez, A.; von Glasow, R. Reactive halogen chemistry in the troposphere. Chem. Soc. Rev. 2012, 41 (19), 6448－6472.

Sakamoto, Y.; Yabushita, A.; Kawasaki, M.; Enami, S. Direct emission of I2 molecule and IO radical from the heterogeneous reactions of gaseous ozone with aqueous potassium iodide solution. J. Phys. Chem. A 2009, 113 (27), 7707－7713.

Schönhardt, A.; Begoin, M.; Richter, A.; Wittrock, F.; Kaleschke, L.; Gómez Martín, J. C.; Burrows, J. P. Simultaneous satellite observations of IO and BrO over Antarctica. Atmos. Chem. Phys. 2012, 12 (14), 6565－

6580.

Schönhardt, A.; Richter, A.; Wittrock, F.; Kirk, H.; Oetjen, H.; Roscoe, H. K.; Burrows, J. P. Observations of iodine monoxide columns from satellite. Atmos. Chem. Phys. 2008, 8 (3), 637−653.

Schroeder, W. H.; Anlauf, K. G.; Barrie, L. A.; Lu, J. Y.; Steffen, A.; Schneeberger, D. R.; Berg, T. Arctic springtime depletion of mercury. Nature 1998, 394 (6691), 331−332.

Simpson, W. R.; Brown, S. S.; Saiz-Lopez, A.; Thornton, J. A.; von Glasow, R. Tropospheric Halogen Chemistry: Sources, Cycling, and Impacts. Chem. Rev. 2015, 115 (10), 4035−4062.

Simpson, W. R.; von Glasow, R.; Riedel, K.; Anderson, P.; Ariya, P.; Bottenheim, J.; Burrows, J.; Carpenter, L. J.; Frieß, U.; Goodsite, M. E.; Heard, D.; Hutterli, M.; Jacobi, H.-W.; Kaleschke, L.; Neff, B.; Plane, J.; Platt, U.; Richter, A.; Roscoe, H.; Sander, R.; Shepson, P.; Sodeau, J.; Steffen, A.; Wagner, T.; Wolff, E. Halogens and their role in polar boundary-layer ozone depletion. Atmos. Chem. Phys. 2007, 7 (16), 4375−4418.

Takenaka, N.; Ueda, A.; Daimon, T.; Bandow, H.; Dohmaru, T.; Maeda, Y. Acceleration mechanism of chemical reaction by freezing: the reaction of nitrous acid with dissolved oxygen. J. Phys. Chem. 1996, 100 (32), 13874−13884.

Takenaka, N.; Ueda, A.; Maeda, Y. Acceleration of the rate of nitrite oxidation by freezing in aqueous solution. Nature 1992, 358 (6389), 736−738.

Von Glasow, R. Sun, sea and ozone destruction. Nature 2008, 453 (7199), 1195−1196.

Yeo, J.; Choi, W. Iodide-mediated photooxidation of arsenite under 254 nm irradiation. Environ. Sci. Technol. 2009, 43 (10), 3784− 3788.

Zhou, J.; Delille, B.; Brabant, F.; Tison, J.-L. Insights into oxygen transport and net community production in sea ice from oxygen, nitrogen and argon concentrations. Biogeosciences 2014, 11 (23), 5007−5020.

Table 1. Production of I3- (uM) in aqueous solution and ice

	Dark		Light						Antarctic Solar			
Phase	Aq	Ice	Aq			Ice			Aq (DW)‡	Ice (DW)	Snow	Glacier
Gas†	Air	Air	Air	O_2^*	N_2^*	Air	O_2^*	N_2^*	Air	Air	Air	Air
pH 3	*nd*	6.1±1.3	2.9	11.0±1.7	*nd*	44.3±3.5	47.3±1.2	0.3±0.1	4.0±0.1	29.4±1.5		
pH 4	*nd*	2.5±0.8	0.3±0.1	1.3±0.3	*nd*	15±2.1	19.9±0.2	0.2±0.1	0.8±0.2	13.2±1.2		
pH 5	*nd*	0.7±0.2	0.1	0.1	*nd*	2.9±0.5	2.6±0.3	*nd*	*nd*	1.8±0.1	1.5±0.1	0.4
pH 6	*nd*	0.1	*nd*	*nd*	*nd*	2.3	0.6±0.1	*nd*	*nd*	*nd*		

Experimental conditions : [I-]0 = 1 mM, 6 h irradiation, snow and glacier samples were also spiked with 1 mM iodide.

† kind of dissolved gas prior to freezing. *O2 or N2 was purged for 30 min before freezing and irradiation. ‡ DW: distilled water. nd: not detected

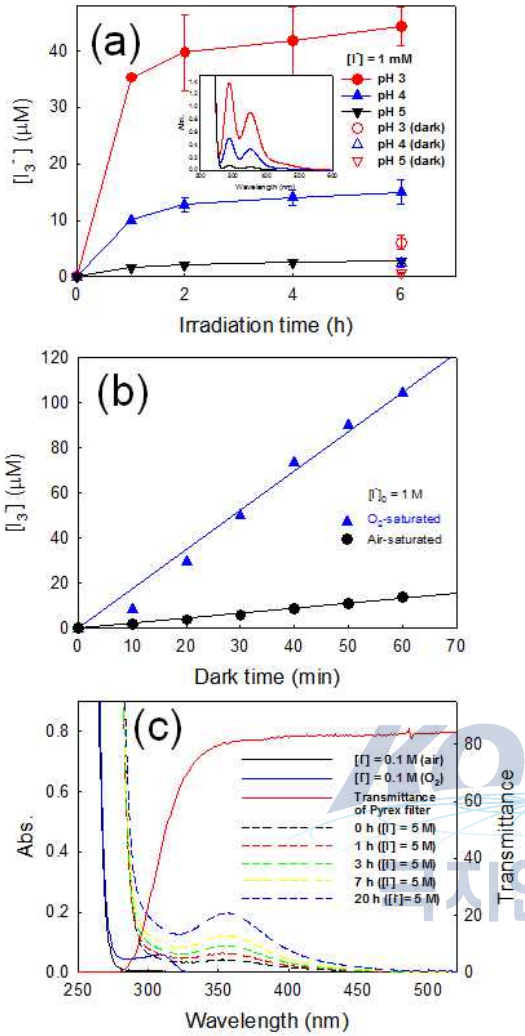

Figure 1. Iodide oxidation to I3- in frozen and aqueous solution. (a) The time profiles of the photogeneration of triiodide in ice phase (-20°C) measured at different pH along with the dark control oxidation of iodide shown. (inset: UV-visible absorption spectra of I3- formed in ice containing [I-]0 = 1 mM, after 2 h irradiation). (b) The time profiles of dark production of triiodide from a concentrated iodide solution that was continuously purged with pure O2 or air flow ([I-]0 = 1 M, pHi =3). (c) UV-visible absorption spectra of iodide solutions. Dashed lines represent the spectral change of an iodide solution ([I-]0 =5 M, pHi =6.5, air-equilibrated, dark condition) with time with the accompanying production of I3-. Note the appearance of (I ″O2) charge transfer (CT) complex band in O2-saturated solution (blue solid line, [I-]0 = 0.1 M). The transmittance of the pyrex filter employed for photoexperiments was also shown (red solid line) for comparison.

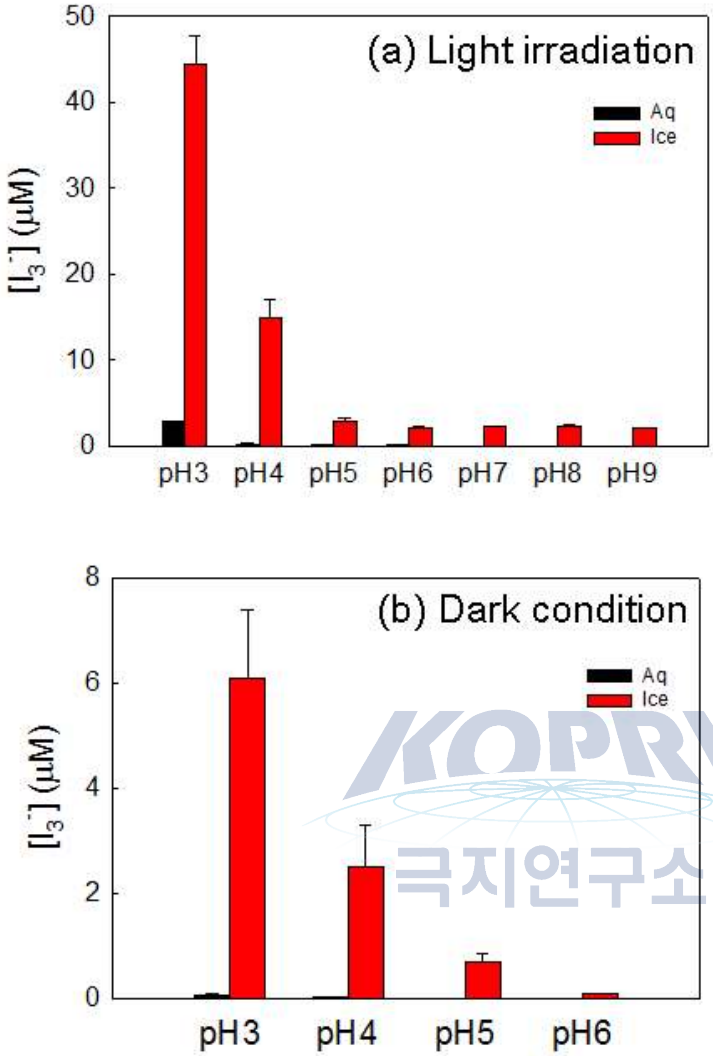

Figure 2. Generation of I3- at various pH range in aqueous solution at 25 °C (black bar) and in ice at -20 °C (red bar). (a) under light irradiation (λ > 300 nm) (b) in the dark. [I-]0 = 1 mM, reaction time 6 h

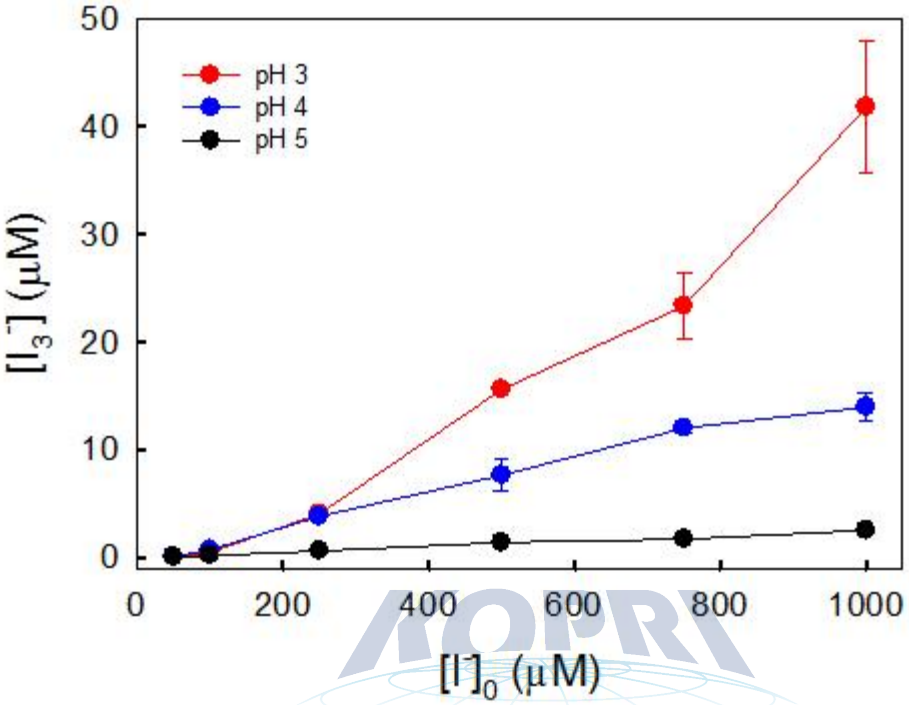

Figure 3. Photo-induced production of I3- from iodide oxidation in ice. The triiodide concentration generated after 6 h solar-simulating irradiation in ice phase (-20°C) was measured as a function of the initial iodide concentration and pH.

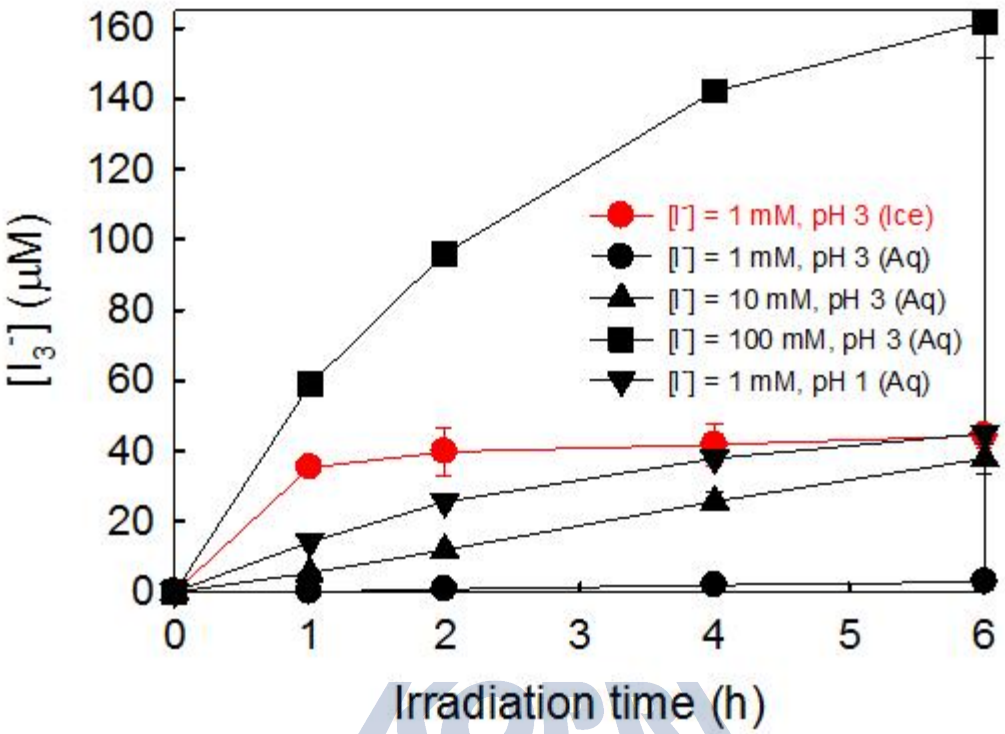

Figure 4. Effects of pH and iodide concentration on the photooxidation of iodide in aqueous solution and ice.

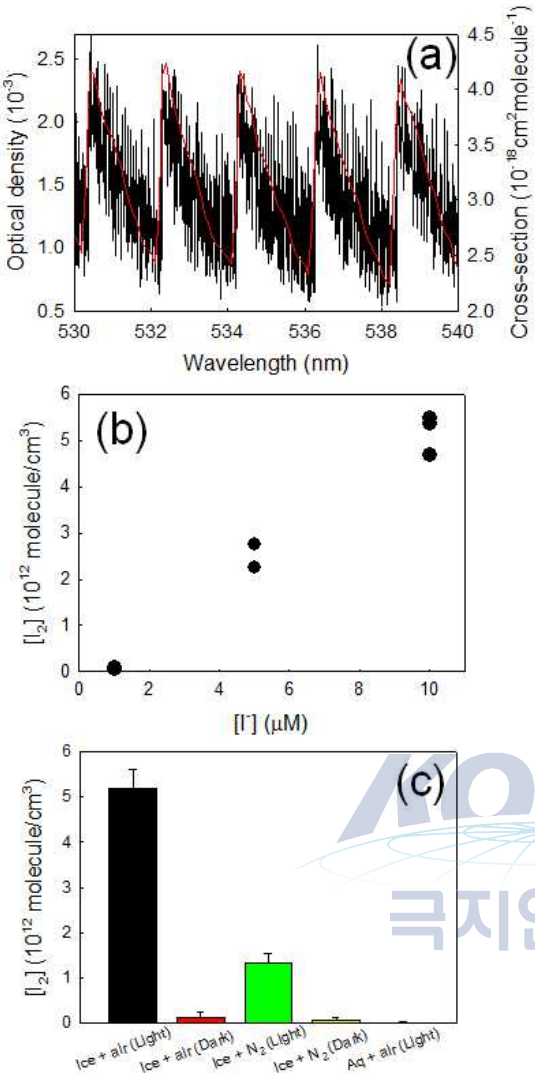

Figure 5. Detection of gaseous I2 by CRDS. (a) CRD spectrum of gaseous I2 formed as a result of iodide photooxidation in frozen NaI solution (10 μM, pHi = 3) for 3 h at 253 K. The spectrum was measured after the frozen solution was thawed (at 298 K). (Red line) I2 absorption cross-section reported in the literature.48 (b) Concentration of gaseous I2 emitted (after thawing) from the frozen iodide solution irradiated for 3 h at 253 K, as a function of the iodide concentration before freezing. The 3σ detection limit of I2 (σ: the standard deviation of the baseline noise) was estimated to be 1.5 1010 molecules cm-3, which corresponded to the case of [I-]0 = 0.8 ?M under the present experimental condition. (c) Comparison of I2(g) concentrations under various experimental conditions (pHi = 3, [I-]0 = 10 μM, ice temperature at 253 K, equilibrium temperature after thawing at 298 K)

제 16 장

Late Neogene sediment properties in the Wilkes Land continental rise (IODP Exp. 318 Hole U1359A), East Antarctica[11)]

Boo-Keun Khim, Buhan Song

Pusan National University

Abstract: On the basis of the variations of sediment properties such as biogenic opal, grain size, natural gamma radiation (NGR), and clay mineralogy, we differentiate two types of late Neogene marine sediments that record paleoclimate changes associated with the growth and retreat of the East Antarctic Ice Sheet (EAIS) and associated changes in sea ice cover. The first type of sediments are massive muds characterized by high biogenic opal (30~55%), low NGR (15~30 counts per second (cps)), large mean grain size (>8.3 μm), and low smectite/(illite + chlorite) [S/(I + C)] ratios (<~0.2). We interpret these sediments as the result from deposition by hemipelagic sedimentation during interglacial conditions. In contrast, the second type of sediments are lam-inated muds characterized by low biogenic opal (5~7%), high NGR (45~67 cps), small mean grain size (<6.3 μm), and high S/(I+ C) ratios (>~0.2). We interpret these sediments as the result from deposition by either turbiditic or contouritic processes during glacial conditions. All these sediment properties indicate that the Wilkes Land continental rise recorded late Neogene paleoclimatic changes in terms of surface water productivity, sediment provenance and transport pathway, and depositional processes that are related to

11) 이 연구 결과는 다음의 논문으로 출판되었음: Boo-Keun Khim, Buhan Song, Hyen Goo Cho, Trevor Williams, and Carlota Escutia. Late Neogene sediment properties in the Wilkes Land continental rise (IODP Exp. 318 Hole U1359A), East Antarctica. Geosciences Journal Vol. 21, No. 1, p. 21-32, February 2017

the growth and retreat of EAIS. In addition, the decreased maxima of biogenic opal content at Hole U1359A highlights the temporal climatic change between the late Pliocene (~2.0 Ma to ~3.7 Ma) and the early Pliocene to late Miocene (~3.7 Ma to ~6.3 Ma), confirming the important role of sea ice to the surface water productivity associated with the global cooling trend in the East Antarctica.

1. INTRODUCTION

Quaternary sediments on the Wilkes Land continental rise consist of an alternation between interglacial massive mud and glacial laminated mud (Hampton et al., 1987; Busetti et al., 2003; Escutia et al., 2003; Carburlotto et al., 2010). The interglacial massive mud is characterized by (1) the lack of laminations and grading and the presence of pervasive bioturbation, suggesting a low-energy environment, (2) good preservation of open-ocean diatom species and high biogenic opal content, indicating an increase of surface water productivity, and (3) the occurrence of sparse fine- to coarse-grained Ice-rafted debris (IRD), representing the continuous sediment input from icebergs. In contrast, the glacial laminated mud is characterized by (1) planar and/or cross laminations, implying an interval of stronger current activity, (2) rare to occasionally-isolated dropstones, suggesting extensive sea ice cover, and (3) absence or rare to poor preservation of sea-ice diatoms and low biogenic opal content, indicating the decrease of surface water productivity. Similar sedimentary features were also reported on the continental rise of the Antarctic Peninsula and the Prydz Bay, showing interglacial bioturbation related to hemipelagic sedimentation and glacial lamination related to either turbiditic or contouritic processes (McGinnis et al., 1997; Pudsey and Camerlenghi, 1998; Pudsey, 2000; O'Cofaigh et al., 2001; Lucchi et al., 2002; Hillenbrand and Ehrmann, 2005).

Biogenic opal productivity in the Antarctic Ocean is mainly controlled by the extent of sea ice coverage and the rate of upwelling of cold nutrient-rich water, which controls the availability of light and micronutrients, respectively (e.g., Ebert et al., 1995; de Baar et al., 2005). In particular, biogenic opal

productivity in seasonally ice-covered areas is related more to sea ice conditions because the annual diatom production occurs during the limited months with open-water conditions (Abelmann and Gersonde, 1991; Wefer and Fischer, 1991). Thus, biogenic opal productivity linked to sea ice distribution in the Antarctic Ocean is mainly coupled to glacial and interglacial climate cycles. For example, Charles et al. (1991) reported that the biogenic opal deposition decreased at the places south of the present Antarctic Polar Front (APF) in the Atlantic sector of the Southern Ocean during glacial intervals because of the increased areal expansion of sea ice distribution. Dezileau et al. (2003) also found the same result of low opal deposition south of the APF in the Indian sector of the Southern Ocean during glacial cycles. In the Wilkes Land continental rise far south of the APF (Fig. 1), late Pleistocene interglacial massive mud (hemipelagic sedimentation) is characterized by relatively high opal content (up to 15%) as it is composed of abundant open-ocean diatoms whereas late Pleistocene glacial laminated mud (turbidites or contourites) is characterized by low opal content represented as mostly fragmented diatoms (Busetti et al., 2003; Escutia et al., 2003).

Clay minerals in Antarctic marine sediments are typically of detrital origin (Chamley, 1989). The clay mineral distribution is mainly controlled by the composition of the source rocks, physical-chemical weathering, transport, and depositional mechanisms, which are ultimately related to climate changes. Thus, clay minerals on the Antarctic continental margins reflect changes in source areas and weathering processes in relation to paleoclimate and glacial history (Ehrmann et al., 1992, 2005; Hillenbrand and Ehrmann, 2001; Junttila et al., 2005; Verma et al., 2014). In the Wilkes Land continental rise, different contents of individual clay minerals in late Pleistocene interglacial massive and glacial laminated mud are controlled by the interplay between different source areas and the main sedimentary processes (Damiani et al., 2006). Junttila et al. (2005) also reported that similar short-term fluctuations in the clay mineral assemblages during the mid-Pliocene can be correlated with the lithological variations influenced by glacial activity at ODP Site 1165 on the Wild Drift (Prydz Bay, East Antarctica).

Integrated Ocean Drilling Program (IODP) Expedition 318 drilled seven

sites on the Wilkes Land continental shelf and rise at water depths between ~400 and 4000 m. The principal drilling objective at this Wilkes Land continental margin is to reveal a long-term history of Antarctic glaciation and its relationships with global paleoclimatic and paleoceanographic changes (Escutia et al., 2011). IODP Expedition 318 drilled Site U1359 (64°54.24′S, 143°57.68′E, 3020.9 m deep; Fig. 1) at the Wilkes Land continental rise (East Antarctica) (Fig. 1). The main drilling objective for Site U1359 was to obtain the late Neogene to Quaternary record in order to provide a long-term and orbital-scale history of climate and paleoceanographic variability concerning on the stability of the EAIS (Escutia et al., 2011). The EAIS appears to have been very dynamic, waxing and waning in response to global climate change. In addition, the EAIS in the Wilkes Subglacial Basin is grounded below sea level and may have been more sensitive to climate changes in the late Neogene (Escutia et al., 2005). However, little is known about the behavior of EAIS from the continental margin sediment properties.

In this study, we documented diverse sediment properties such as biogenic opal, physical property, grain size, and clay minerals at Hole U1359A in order to reveal the climate and ice sheet history with a view to late Miocene glacial activity in the Wilkes Subglacial Basin.

2. MATERIALS AND METHODS

The Wilkes Land continental margin has formed during an extensional tectonic episode in mid-Jurassic/Cretaceous time, resulting from the separation of the Australia from the Antarctic continent (Cande and Mutter, 1982). The acoustic basement across this continental margin is composed of block-faulted continental crust, thinned and intruded transitional crust, and oceanic crust (Eittreim, 1994). An integrated seismic stratigraphic survey reveals that, above the acoustic basement, about 8-km thick sedimentary sequence records the long-term history of glacial advance and retreat across the EAIS margin (Eittreim et al., 1995; Escutia et al., 1997, 2005; De Santis et al., 2003; Donda et al., 2003).

Site U1359 was drilled on the eastern levee of the Jussieau submarine

channel in an upper fan environment of the Wilkes Land continental rise (Expedition 318 Scientists, 2011). The Jussieau submarine channel is one of the intricate networks of slope canyons that develop downslope into channels and coalescing deep-sea fans in the Wilkes Land continental margin (Escutia et al., 2000). Four holes U1359A (193.5 m), U1359B (252.0 m), U1359C (168.7 m) and U1359D (602.2 m) were drilled at this site (Expedition 318 Scientists, 2011). A total of 133 core samples from U1359A-6H-1 (38.85 mbsf) to U1359A-22X-CC (189.96 mbsf) were obtained at Hole U1359A for this study. Based on visual core descriptions and smear slide analyses (Expedition 318 Scientists, 2011), Site U1359 was divided into three (Unit I, Unit II, Unit III) lithostratigraphic units. Hole U1359A preserves Unit I (1H-1 through 6H-4: 0 - 43.54 mbsf: Pleistocene), Subunit IIa (6H-4 through 12H-3: 43.54 - 99.87 mbsf: early to late Pliocene) and Subunit IIb (12H-3 through 22X-CC: 99.87 to 190.26 mbsf: early Pliocene to late Miocene). For more detail information on the sediment lithology, one can refer to Expedition 318 Scientists (2011).

The preliminary shipboard age-depth model of Hole U1359A was the integrated biostratigraphy from microfossils (diatom and radiolarian) and incorporation of magnetostratigraphic age constraints of Hole U1359A (Fig. 2; Expedition 318 Scientists, 2011). The biostratigraphic controls in the lower part of Hole U1359A were further improved significantly by magnetostratigraphy of Holes U1359B and U1359C. Tauxe et al. (2012) determined age constraints of the composite core for the reconstruction of whole magnetostratigraphy. The polarity log constructed from the magnetization/demagnetization behavior was correlated with the geomagnetic polarity timescale of Gradstein et al.(2004). The lowermost sediment of Hole U1359A was estimated to be about 6.3 Ma old (Fig. 2).

The physical properties program including natural gammy radiation (NGR) measurement for Site U1359 were conducted onboard during the expedition with the routine runs on the Whole-Round Multisensor Logger (WRMSL), which was used to correlate the four holes (U1359A-U1359D) and to define a composite stratigraphic record (Expedition 318 Scientists, 2011). We analyzed the biogenic silica content of 133 sediment samples from Hole U1359A using a wet alkaline extraction method (DeMaster, 1981). The analytical

precision as a relative standard deviation (±1σ) is 1%. The biogenic opal content was calculated by multiplying biogenic silica content by 2.4 (Mortlock and Froelich, 1989). A S3500 laser diffraction particle analyzer (Microtrac) was used to measure the grain size on the selected 24 sediment samples. Sediments were treated using 30% hydrogen peroxide to remove the organic matter and then boiled with deionized water. Carbonate was not removed because of insignificantly low content (Expedition 318 Scientists, 2011). Clay mineral particles sized <2 ❍m for the selected 23 sediment samples were analyzed using a SIEMENS/BRUKER D5005 diffractometer by X-ray diffraction on air-dried and ethylene-glycolated oriented mounts prepared by the 'smear-on-glass slide' method (Stokke and Carson, 1973). Identification of clay minerals follows the classification of Brown and Brindley (1980) and Moore and Reynolds (1989). Semi-quantitative estimates of major clay minerals (illite, smectite, kaolinite, and chlorite) were based on the method described by Biscaye (1965). Sediment constituents of some horizons representing high and low biogenic opal contents were examined using scanning electron microscopy (SEM; HITACHI S3500N).

3. RESULTS

The long-term trend of biogenic opal content is discernible at Hole U1359A, showing the upward decrease of high biogenic opal contents (Fig. 3). Variation of biogenic opal content is small in the upper part of Subunit IIa, corresponding to the late Pliocene (~2.0 Ma to ~3.7 Ma), whereas it is large in the lower part of Subunit IIa and entire Subunit IIb, belonging to the early Pliocene to late Miocene (~3.7 Ma to ~6.3 Ma). In particular, the lowermost part of Hole U1359A at about 6.0 Ma is characterized by very high biogenic opal content (more than 50%). The short-term scale fluctuations of biogenic opal contents are distinct throughout the core. The low biogenic opal content is almost constant (5~7%) throughout the core whereas the high biogenic opal contents are in the range from about 30% to 55%. In particular, the high peaks of biogenic opal content are low (about 30%) during the late Pliocene, but they are high (up to 55%) during the early Pliocene to late Miocene.

Frequent fluctuations of NGR are similar to that of the biogenic opal content

(Fig. 3), showing that low NGR values correspond to high biogenic opal content and vice versa. Thus, there is an inverse relationship between these two properties (Fig. 4a). This is because NGR is emitted principally by clay minerals in this setting, and the clay mineral content is controlled to a large degree of dilution by biogenic opal. Based on the onboard description of sediment facies (Expedition 318 Scientists, 2011), high biogenic opal and low NGR interval generally corresponds to the massive muds whereas low biogenic opal and high NGR interval coincide with the laminated muds.

Figure 3 also shows the mean grain sizes of 24 selected whole sediment samples. These mean grain sizes appear to be divided into two groups, i.e., the smaller mean grain size (<6.3 μm) for the low opal content and the larger mean grain size (8.3~16.8 μm) for the high opal content. Such a division was confirmed by a linear relationship between two properties (Fig. 4b). Thus, similarly to biogenic opal content, smaller mean grain size corresponds mostly to the laminated intervals, whereas larger mean grain size relates to the massive interval. Based on the pattern of grain size distribution (Fig. 5), the modes of grain size between these two groups are not much different. It is discernible that the sediments of smaller mean grain size are limited to the fine-grained particle fraction, whereas those of larger mean grain size contain the distinct coarse-grained fraction tail.

Clay mineral compositions in 23 selected sediments of Hole U1359A show that illite (56% to 76%) is dominant, followed by considerable smectite concentrations (4% to 33%) (Fig. 3). Chlorite concentrations are less than 16%, and kaolinite typically occurs in trace amounts (about 7%), with a maximum value of 10%. Smectite content is correlated negatively with illite and chlorite contents, respectively (Figs. 4c and d), showing that downcore distribution of smectite is opposite to that of illite and chlorite. Biogenic opal content seems to exhibit the positive relationship with illite content, despite very low correlation coefficient (Fig. 4e). Similarly, biogenic opal content is negatively correlated with smectite/(illite + chlorite) [S/(I + C)] ratios (Fig. 4f). S/(I + C) ratios are different between the massive mud (<~0.2) and the laminated mud (>~0.2) at Hole U1359A. More high resolution S/(I + C) ratios of Hole U1359B show the almost similar pattern of variation to those of Hole U1359A (Verma et al., 2014).

4. DISCUSSION

4.1. Late Neogene Two Sediment Types in the Wilkes Land Continental Margin

The Wilkes Land continental margin experienced a series of glacial-interglacial changes during the late Cenozoic. Core sediments from the Wilkes Land continental rise consist of different components as a result of the interplay of sedimentary process (e.g., hemipelagite or turbidite), depending on the environmental condition controlled by the sea level fluctuations (Escutia et al., 2002, 2003; Busetti et al., 2003; Donda et al., 2003; Caburlotto et al., 2010). These depositional processes in the Wilkes Land continental margin are similar to those of other Antarctic margins, such as the western Antarctic Peninsula (McGinnis et al., 1997; Pudsey and Camerlenghi, 1998), Prydz Bay (O'Brien et al., 2004), and the Weddell Sea (Michels et al., 2001; O'Cofaigh et al., 2001).

At IODP Site U1361 (64°24.57′S, 143°53.20′E, 3465.5 m deep; Fig. 1) spanning a Pliocene interval between 5.3 and 3.3 Ma, high biogenic opal contents coincide with abundant diatom tests and high Ba/Al ratios, pointing to the increased biological productivity related to less sea ice and warmer sea surface temperatures (Cook et al., 2013). At Hole U1359A, biogenic opal contents reflect the degree of diatom productivity, extent of sea ice distribution, and climatic conditions related to the glacial activity in the Wilkes Land continental margin similar to the other areas of the Antarctic Ocean (Charles et al., 1991; Mortlock et al., 1991; Bareille et al., 1998; Chase et al., 2003; Dezileau et al., 2003; Bradtmiller et al., 2009; Escutia et al., 2009; Sprenk et al., 2013). Figure 3 shows the long-term trend of biogenic opal content at Hole U1359A, highlighting the temporal climatic change between the late Pliocene (~2.0 Ma to ~3.7 Ma) and the early Pliocene to late Miocene (~3.7 Ma to ~6.3 Ma). Low biogenic opal contents indicating low diatom productivity are consistent throughout the whole interval, which we interpret to be due to wide and extensive sea ice distribution, suggesting that the cold glacial climate condition was similar throughout this interval. However, biogenic opal contents are higher during the early Pliocene to late Miocene (~50%) than during the late Pliocene

(~30%) (Fig. 3). We interpreted that this indicates much warmer climatic conditions favorable for enhanced diatom productivity during the latest Miocene to early Pliocene compared to the late Pliocene on the Wilkes Land continental margin. This also supports the early Pliocene warmth at Site U1361 (Cook et al., 2013; Patterson et al., 2014). Similarly, a significant increase in the biogenic opal deposition and sea ice reduction occurred during late Miocene to early Pliocene at the Prydz Bay continental rise and the Antarctic Peninsula margin (Grützner et al., 2005; Escutia et al., 2009). The high biogenic opal content at about 6.0 Ma in the lower part of Hole U1359A seems to correspond to the biogenic bloom since roughly 6.5 Ma (Diekmann et al., 2003). It implies the Southern Ocean wide impact associated with variations in EAIS stability and sea ice coverage during the early Pliocene to late Miocene.

In addition, the variability of biogenic opal content at Hole U1359A (Fig. 3), in particular, the positive correlation between high biogenic opal and massive sediments, and between the low biogenic opal and laminated sediments, also responds to changes in the context of the sea ice distribution. Massive and laminated muds have been also described in Quaternary sediments of the Wilkes Land continental rise and interpreted in terms of the sedimentary deposition, as representing interglacial and glacial conditions, respectively (Escutia et al., 2002, 2003; Busetti et al., 2003; Donda et al., 2003; Caburlotto et al., 2010). Such a contrast of sedimentary structures representing interglacial and glacial conditions was also reported on the Antarctic Peninsula continental rise (McGinnis et al., 1997; Pudsey and Camerlenghi, 1998; Pudsey, 2000; O'Cofaigh et al., 2001; Lucchi et al., 2002; Hillenbrand and Ehrmann, 2005). The biogenic opal content at Hole U1359A reflects the degree of the late Neogene diatom productivity, related to variations of sea ice cover in the Wilkes Land continental margin. Busetti et al. (2003) reported that Quaternary massive sediments in the Wilkes Land continental rise contained well-preserved diatom assemblages deposited in an open marine environment during interglacial times. Thus, we infer that high opal content in the massive sediments at Hole U1359A indicates high productivity during warm climate conditions with an increase of light availability due to the decrease of sea ice cover during the late Neogene.

NGR represents the amount of radiation emitted by radioactive isotope

decay within the sediments, thus, it has been used as a proxy to indicate the amount of fine-grained terrigenous particles enriched in the radioisotope elements (e.g., Blum 1997). The opposite relationship (r2 = 0.57) between biogenic opal content and NGR is fairly good, which implies that these two properties are coupled closely (Fig. 4a). The density of biogenic opal (2.2 g/cm3) is lower than that of terrigenous particles (2.6 - 2.75 g/cm3). Because of such a density contrast, the sediments depleted in biogenic opal show an increase in P-wave velocity (Weber, 1998). Intervals of high biogenic opal content and low NGR at Hole U1359A may be related to the warm period when the distribution of sea ice is relatively low, providing that high diatom production relatively overwhelmed the deposition of fine-grained particle in the Wilkes Land continental rise. In particular, these late Neogene sediments, characterized by high biogenic opal content and low NGR, are generally massive whereas those of low biogenic opal content and high NGR show the lamination structures, confirming the independent depositional processes during the Quaternary climatic stages (Escutia et al., 2002, 2003; Busetti et al., 2003; Donda et al., 2003; Caburlotto et al., 2010).

It is worthwhile to note that a strong positive relationship (r2 = 0.75) between biogenic opal content and mean grain size was observed at some selected sediments of Hole U1359A (Fig. 4b). The laminated sediments are characterized by low biogenic opal content and small mean grain size. In contrast, the massive sediments are characterized by high biogenic opal content and large mean grain size. However, such large mean grain size also could be partly due to a relative increase in IRD during interglacials. These two types of late Neogene sediments are also differentiated by the grain size distribution pattern (Fig. 5); all sediments show the distinct single mode that is not much different between two types of sediments. However, the grain size range of smaller mean grain size is limited to the fine-grained particle fraction, whereas that of larger mean grain size contain the coarse-grained fraction tail including the IRD. SEM observation of these sediment constituents confirms the different pattern of grain size distribution (Fig. 6). Sediments of smaller mean grain size contain mostly very fine-grained clastic particles with less biogenic remains that are very small and fragmented (Fig. 6). The low NGR interval in the massive

muds generally corresponds to high biogenic opal contents mainly contributed to the dilution by the coarse-grained particles of IRDs and additional whole diatoms. Carburlotto et al. (2010) reported that the laminated intervals in the Wilkes Land continental rise are composed of mainly fine-grained particles associated with transport by bottom current. Most of these fragmented diatoms may be reworked Neogene tests (Busetti et al., 2003). On the other hand, sediments of larger mean grain size preserve the original form of diverse diatom species (Fig. 6). Although IRD particles are scattered in the massive layers of the Quaternary sediments in the Wilkes Land continental rise (Escutia et al., 2003; Busetti et al., 2003; Caburlotto et al., 2010), the large size of well-preserved diatom valves accounts for coarse-grained particles in the late Neogene massive sediments that were deposited by hemipelagic sedimentation under the warm climate with limited sea ice cover.

4.2. Clay Mineral Provenance and Depositional Processes in the Wilkes Land Continental Margin

Short-term fluctuations of clay mineral assemblages in the various regions of the Antarctic Ocean have been interpreted in terms of changes of the ice volume related to the glacial retreat and advance patterns (e.g., Antarctic Peninsula by Hillenbrand and Ehrmann (2001), Prydz Bay by Juntila et al. (2005) and Escutia et al. (2009), and Wilkes Land margin by Damiani et al. (2006)). Clay mineral compositions in some selected sediments of Hole U1359A are similar to those of Quaternary sediments on the Wilkes Land continental rise, which was first reported by Busetti et al. (2003). Smectite content is correlated negatively with both illite and chlorite contents (Figs. 4c and d), and consequently, correlation between S/(I + C) ratios and biogenic opal content is also fairly negative (Fig. 4f). It indicates that the clay mineral assemblages in terms of S/(I + C) ratios are also divided into the massive mud and the laminated mud. Thus, the laminated mud seems to have relatively high S/(I +C)ratios (>~0.2), whereas the massive mud appears to show low S/(I + C) ratios (<~0.2).

The sources of clay minerals in the Wilkes Land continental rise have

been elucidated by several studies (Busetti et al., 2003; Juntila et al., 2005; Damiani et al., 2006; Verma et al., 2014). Illites are detrital and typical products of physical weathering and subglacial erosion from continental crystalline rocks (Ehrmann, 1998). Gneisses, granulites, metamorphosed mafic dykes, granites and granitoids, phyllite are widespread outcrop in the hinterland of Mertz and Ninnis glaciers along Geroge V coast (Oliver and Fanning, 2002; Talarico and Kleinschmidt, 2003). Verma et al. (2014) reported that the illite in the Wilkes Land continental rise was derived from biotite-rich rocks because of high enrichment in Fe-Mg cation in its lattice. Chlorite in this margin is also considered as detrital product, and two main sources were suggested (Damiani et al., 2006). One source is the hinterland of Mertz glacier where chlorite can derive from the physical weathering of low grade, chlorite-bearing metamorphic and basic source rocks (Talarico and Kleinschmidt, 2003). Another possible source is Victoria Land green schist and chlorite was transported by the westward flowing Antarctic Bottom Water (Henjes-Kunst and Schussler, 2003). Kaolinite cannot form under polar conditions, because it is mostly generated from intense chemical weathering (e.g., Chamley, 1989.). In the present Antarctic Ocean, kaolinite represents the reworked product of older sediments and paleosoils (Hambrey et al., 1991; Ehrmann et al., 1992). Thus, the source of kaolinite in the Wilkes Land continental rise is considered to be the Paleozoic sedimentary sequences of Beacon Supergroup in the Transantarctic Mountains (Piper and Pe, 1977). Although smectite formation is closely related to the chemical weathering, smectite is considered to be detrital in recent Antarctic marine sediments, derived either from weathering of volcanic rocks (Ehrmann et al., 1992) or from reworking of paleosoils (Claridge, 1965) and tills (Bardin, 1982). Damiani et al. (2006) reported that smectites in the Wilkes Land continental rise are dioctahedral because of enrichment in Al and Fe, which excludes an authigenic origin. These detrital smectites were also confirmed by their chemical compositions (Verma et al., 2014).

Although clay mineral contents complement each other, a clear inverse relationship of smectite with illite and chlorite (Figs. 4c and d) and a fairly negative relationship between S/(I+ C) and biogenic opal contents (Fig. 4f) provide a close linkage between depositional processes and paleoclimate

conditions. The deposition of massive mud at Site U1359A, characterized by low S/(I + C) ratios, is attributed primarily to the hemipelagic sedimentation during the warm climate, whereas the deposition of laminated mud, characterized by high S/(I + C) ratios, results from a complex interplay of gravity flows and bottom currents during the cold climate (Escutia et al., 2002, 2003; Busetti et al., 2003; Donda et al., 2003; Caburlotto et al., 2010). Low S/(I + C) ratios during the warm climate are due to the high amounts of illite and subordinated chlorite derived directly from the hinterland of George V Land transported by ice sheets and/or tongues and additional contribution reworked from the sediment deposits on the continental shelf and slope by downslope gravitational movements.

In contrast, high S/(I + C) ratios during the cold climate could be related to the delivery of smectite by westward bottom contour currents along the Wilkes Land continental rise from basic volcanic rocks of McMurdo group in the Transactartic Mountains and the Ross Sea including the volcanic Balleny Islands (Ehrmann, 1998; Setti et al., 2000; Veevers and Saeed, 2011), rather than from a local source of Ferrar Dolerite sills exposed limitedly in the hinterland of the Ninnis glacier (Roland et al., 2000). Gordon and Tchernia (1972) observed that Antarctic Bottom Water produced in the Ross Sea flows westward along the Wilkes Land continental rise. However, Verma et al. (2014) argued that smectite-rich sediment was transported to the Wilkes Land continental margin by surface or bottom water currents during the times of ice retreat. Thus, smectite provenance should be further disclosed by more investigations in this region.

5. CONCLUSIONS

IODP Expedition 318 drilled Site U1359 at the crest of a levee in an upper fan environment of the Wilkes Land continental rise. Diverse sediment properties using a total of 133 core samples from Hole U1359A (196.4 m long) were analyzed to provide the paleoceanogrpahic evidence on the late Neogene glacial activity in the Wilkes Subglacial Basin. Late Neogene marine sediments at Site U1359A are divided distinctly into two types which are characterized by the paleoclimate changes associated with the growth and retreat of the EAIS.

The first type sediments are characterized by the high biogenic opal, low NGR, the large mean grain size, and low S/(I + C) ratios, whereas the second type sediments are characterized by the low biogenic opal, high NGR, the small mean grain size, and high S/(I + C) ratios. In particular, the first type sediments generally consist of the massive mud and the second type sediments are composed of the laminated mud, which indicate the different depositional processes. Thus, the former sediments were deposited by hemipelagic sedimentation during the interglacial condition whereas the latter sediments were deposited by either turbiditic or contouritic processes during the glacial condition. The long-term trend of biogenic opal content at Hole U1359A highlights the temporal climatic change. The maxima of biogenic opal content at Hole U1359A decreased from the early Pliocene and late Miocene (~3.7 Ma to ~6.3 Ma) to the late Pliocene (~2.0 Ma to ~3.7 Ma). It indicates the surface water productivity changes due to the increased sea ice cover in the Wilkes Land continental margin which is associated with global cooling trend. Thus, the sediment properties at Hole U1359A in the Wilkes Land continental rise implies the Southern Ocean wide impact associated with advance and retreat of the EAIS and sea ice coverage during the late Neogene.

동남극 윌크스 랜드 대륙대 ((IODP Exp. 318 Hole U1359A)) 신제3기 후기 퇴적물의 특성

김부근, 송부한

부산대학교

요약: 생물기원 오팔, 입도, 자연감마선, 점토광물과 같은 퇴적 특성의 변동에 의거해 우리는 동남극 빙상의 성쇠와 해빙의 면적 변동과 관련되는 고기후 변화를 기록하고 있는 신제3기 후기의 퇴적층을 2 개의 타입으로 구분하였다. 첫 번째 타입은 높은 생물기원 오팔(30-55%), 낮은 NGR 값(15-30 cps), 큰 입자크기 (>8.3 μm), 낮은 스멕타이트/(일라이트+클로라이트), S/(I+C), 비(<0.2)를 가지는 균질한 퇴적물이다. 반면 다른 타입은 낮은 생물기원 오팔(5-7%), 높은 NGR 값(45-67 cps), 작은 입자크기 (<6.3 μm), 높은 스멕타이트/(일라이트+클로라이트), S/(I+C), 비(>0.2)를 가지는 엽리층 머드이다. 우리는 이 퇴적물을 빙하기 동안의 터비다이트나 컨투어라이트 프로세스에 의한 퇴적으로 해석하였다. 모든 퇴적 특성들이 윌크스랜드의 대륙대가 신제3기 후기 고기후학적 변화들(동남극 빙상의 성쇠와 관련된 표층생산성, 퇴적물의 기원 및 운송 경로, 퇴적과정)을 기록하고 있다. 게다가 Hole U1359A에서 플라이오세 후기와 마이오세 후기-플라이오세 전기동안의 생물기원 오팔 함량의 최대값 감소는 동남극에서 전지구적인 한랭화와 관련되어 해빙이 표층생산성의 감소에 중요한 요인이라는 것을 보여준다.

참고문헌

Abelmann, A. and Gersonde, R., 1991, Biosiliceous particle flux in the Southern Ocean. Marine Chemistry, 35, 503 - 536.

Bardin, V.I., 1982, Composition of east Antarctic moraines and some problems of Cenozoic history. In: Craddock, C. (ed.), Antarctic Geoscience. University of Wisconsin Press, Madison, p. 1069 - 1076.

Bareille, G., Labracherie, M., Bertrand, P., Labeyrie, L., Lavaux, G., and Dignan, M., 1998, Glacial-interglacial changes in the accumulation rates of major biogenic components in Southern Indian Ocean sediments. Journal of Marine Systems, 17, 527 - 539.

Bindoff, N.L., Rosenberg, M.A., and Warner, M.J., 2000, On the circulation and water masses over the Antarctic continental slope and rise between 80 and 150°E. Deep-Sea Research II, 47, 2299 - 2326

Biscaye, P.E., 1965, Mineralogy and sedimentation of recent deep-sea clay in the Atlantic Ocean and adjacent seas and oceans. Geological Society of America Bulletin, 76, 803 - 832.

Blum, P., 1997, Physical properties handbook: a guide to the shipboard measurement of physical properties of deep-sea cores. ODP Technical Note 26. http://www-odp.tamu.edu/publications/tnotes/tn26/INDEX.HTM

Bradtmiller, L.I., Anderson, R.F., Fleisher, M.Q., and Burckle, L.H., 2009, Comparing glacial and Holocene opal fluxes in the Pacific sector of the Southern Ocean. Paleoceanography, 24, 2214. http://dx.doi.org/10.1029/2008PA001693

Brown, G. and Brindley, G.W., 1980, X-ray diffraction procedures for clay mineral identification. In: Brindley, G.W. and Brown, G. (eds.), Crystal structures of clay minerals and their X-ray identification. Mineralogical Society, London, p. 305 - 359.

Busetti, M., Carbulotto, A., Armand, L., Damiani, D., Giorgetti, R.G., Lucchi, P.G., Quilty, P.G., and Villa, G., 2003, Plio-Quaternary sedimentation on the Wilkes Land continental rise. Preliminary results. Deep-Sea Research II, 50, 1529 - 1562.

Cande, S.C. and Mutter, J.C., 1982, A revised identification of the oldest sea-floor spreading anomalies between Australia and Antarctica. Earth and Planetary Science Letters, 58, 151 - 160.

Carburlotto, A., Lucchi, R.G., De Santis, L., Marcci, P., and Tolotti, R., 2010, Sedimentary processes on the Wilkes Land continental rise reflect changes in glacial dynamics and bottom water flow. International Journal of Earth Sciences, 99, 909 - 926.

Chamley, H., 1989, Clay Sedimentology. Springer, Berlin, 623 p. Charles, C.D., Froelich, P.N., Zibello, M.A., Mortlock, R.A., and Morley, J.J., 1991, Biogenic opal in southern ocean sediments over the last 450,000 years: implications for surface water chemistry and circulation. Paleoceanography, 6, 697 - 728.

Chase, Z., Anderson, R.F., Fleisher, M.Q, and Kubik, P.W., 2003, Accumulation of biogenic and lithogenic material in the Pacific sector of the Southern Ocean during the past 40,000 years. Deep-Sea Research II, 50, 799 - 832.

Claridge, G.G.C., 1965, The clay mineralogy and chemistry of some soils from the Ross dependency, Antarctica. New Zealand Journal of Geology and Geophysics, 3, 186 - 200.

Cook, C.P., van de Flierdt, T., Williams, T., Hemming, S.R., Iwai, M., Kobayashi, M., Jimenez-Espejo, F.J., Escutia, C., Gonzaez, J.J., Khim, B.K., McKay, R.M., Passchier, S., Tauxe, L., Sugisaki, S., Lopez, A., Patterson, A.M.O., Bohaty, S.M., Riesselman, C.R., Sangiorgi, F., Pierce, E.L., Brinkhuis, H., and IODP Expedition 318 Scientists, 2013, Dynamic behaviour of the East Antarctic Ice Sheet during Pliocene warmth. Nature Geoscience, 6, 765 - 769.

Damiani, D., Giorgetti, G., and Turbanti, I.M., 2006, Clay mineral fluctuations and surface textural analysis of quartz grains in Pliocene - Quaternary marine sediments from Wilkes Land continental rise (east-Antarctica): paleoenvironmental significance. Marine Geology, 226, 281 - 295.

de Baar, H.J.W., Boyd, P.W., Coale, K.H., Landry, M.R., Tsuda, A., Assmy, P., Bakker, D.C.E., Bozec, Y., Croot, P.L., Gervais, F., Gorbunov, M.Y., Harrison, P.J., Hiscock, W.T., Lann, P., Lancelot, C., Law, C.S.,

Levasseur, M., Marchetti, A., Millero, F.J., Nishioka, J., Nojiri, Y., Oijen, T.V., Rieesell, U., Rijkenberg, M.J.A., Saito, H., Takeda, S., Timmermans, K.R., Veldhuis, M.J.W., Waite, A.M., and Wong, C.S., 2005, Synthesis of iron fertilization experiments: from the iron age in the age of enlightenment. Journal of Geophysical Research (Ocean) 110, C09S16. http://dx.doi.org/10.1029/2004jc002601

DeMaster, D.J., 1981, The supply and accumulation of silica in the marine environment. Geochimica et Cosmochimica Acta, 45, 1715 - 1732.

De Santis, L., Brancolini, G., and Donda, F., 2003, Seismic-stratigraphic analysis of the Wilkes Land continental margin (East Antarctica). Influence of glacially-driven processes on the Cenozoic deposition. Deep-Sea Research II, 50, 1563 - 1594.

Dezileau, L., Reyss, J.L., and Lemoine, F., 2003, Late Quaternary changes in biogenic opal fluxes in the Southern Indian Ocean. Marine Geology, 202,143 - 158.

Diekmann, B., Falker, M., and Kuhn, G., 2003, Environmental history of the south-eastern South Atlantic since the Middle Miocene: evidence from the sedimentological records of ODP Sites 1088 and 1092. Sedimentology, 50, 511 - 529.

Donda, F., Brancolini, G., De Santis, L., and Trincardi, F., 2003, Seismic facies and sedimentary processes on the continental rise off Wilkes Land (East Antarctica): Evidence of bottom current activity. Deep- Sea Research II, 50, 1509 - 1528.

Ebert, E., Schramm, J., and Curry, J., 1995, Disposition of solar radiation in sea ice and the upper ocean. Journal of Geophysical Research (Ocean), 100, 15965 - 15975.

Ehrmann,W., 1998, Implications of late Eocene to early Eiocene clay mineral assemblages in McMurdo Sound (Ross Sea, Antarctica) on paleoclimate and ice dynamics. Palaeogeography Palaeoclimatology Palaeoecology, 139, 213 - 231.

Ehrmann, W.U., Melles, M., Kuhn, G., and Grobe, H., 1992, Significance of clay mineral assemblages in the Antarctic Ocean. Marine Geology, 107, 249 - 273.

Ehrmann, W., Setti, M., and Marinoni, L., 2005, Clay minerals in Cenozoic sediments off Cape Robert (McMurdo Sound, Antarctica) reveal palaeoclimatic history. Palaeogeography Palaeoclimatology Palaeoecology, 229, 187 - 211.

Eittreim, S.L., 1994, Transition from continental to oceanic crust on the Wilkes - Adelie margin of Antarctica. Journal of Geophysical Research, 99, 24189 - 24205.

Eittreim, S.L., Cooper, A.K., and Wannesson, J., 1995, Seismic stratigraphic evidence of ice-sheet advances on the Wilkes Land margin of Antarctica. Sedimentary Geology, 96, 131 - 156.

Escutia, C., Barcena, M.A., Lucchi, R.G., Ballegeer, A.M., Gonzalez, J.J., and Harwood, D.M., 2009, Circum-Antarctic warming events between 4 and 3.5 Ma recorded in marine sediments from the Prydz Bay (ODP Leg 188) and the Antarctic Peninsual (ODP Leg 178) margins. Global and Planetary Change, 69, 170 - 184.

Escutia, C., Brinkhuis, H., Klaus, A., and the Expedition 318 Scientists, 2011, Proceedings of the IODP, vol. 318. Integrated Ocean Drilling Program Management International, Inc., Tokyo, 59 p. http://dx.doi.org/10.2204/iodp.proc.318.101.2011

Escutia, C., De Santis, L., Donda, F., Dunbar, R.B., Cooper, A.K., Brancolini, G., and Eittereim, S.L., 2005, Cenozoic ice sheet history from East Antarctic Wilkes Land continental margin sediments. Global and Planetary Change, 45, 51 - 81.

Escutia, C., Eittreim, S.L., and Cooper, A.K., 1997, Cenozoic glaciomarine sequences on the Wilkes Land continental rise, Antarctica. Proceedings of the 7th International Symposium of Antarctic Earth Sciences on the Antarctic Region: Geological Evolution and Processes, Sienna, Sept. 10 - 15, p. 791 - 795.

Escutia, C., Eittreim, S.L., Cooper, A.K., and Nelson, C.H., 2000, Morphology and acoustic character of the Antarctic Wilkes Land turbidite systems: ice-sheet sourced vs. river-sourced fans. Journal of Sedimentary Research, 70, 84 - 93.

Escutia, C., Nelson, C.H., Acton, G.D., Cooper, A.K., Eittreim, S.L., Warnke, D.A.,

and Jaramillo, J., 2002, Current controlled deposition on the Wilkes Land continental rise. In: Stow, D.A.V., Pudsey, C.J., Howe, J.A., Faugeres, J.C., and Viana, A.R. (eds.), Deep-Water Contourite Systems: Modern Drifts and Ancient Series, Seismic and Sedimentary Characteristics. Memoirs of Geological Society of London, 22, p. 373 - 384.

Escutia, C., Warnke, D.A., Acton, G.D., Barcena, A., Burckle, L., Canals, M., and Frazee, C.S., 2003, Sediment distribution and sedimentary rocesses across the Antarctic Wilkes Land margin during the Quaternary. Deep-Sea Research II, 50, 1481 - 1508.

Expedition 318 Scientists, 2011, Site U1359. In: Escutia, C., Brinkhuis, H., Klaus, A., and the Expedition 318 Scientists (eds.), Proceedings of the IODP, vol. 318. Integrated Ocean Drilling Program Management International, Inc., Tokyo, 121 p. http://dx.doi.org/ 10.2204/iodp.proc.318.107.2011

Gordon, A.L. and Tchernia, P., 1972, Waters of the continental margin off Adelie coast, Antarctica. In: Hayes, D.E. (ed.), Antarctic Oceanology II: The Australian - New Zealand Sector. Antarctic Research Series, vol. 19, American Geophysical Union, Washington, p. 59 - 69.

Gradstein, F.M., Ogg, J.G., and Smith, A.G., 2004, A Geologic Time Scale 2004. Cambridge University Press, Cambridge, 401 p.

Grutzner, J., Hillenbrand, C.-D., and Rebesco, M., 2005, Terrigenous flux and biogenic silica deposition at the Antarctic continental rise during the late Miocene to early Pliocene: implications for ice sheet stability and sea ice coverage. Global and Planetary Change, 45, 131 - 149.

Hampton, M.A., Kravitz, J.H., and Luepke, G., 1987, Geology of sediment cores from the George V continental margin, Antarctica. In: Eittreim, S.L. and Hampton, M.A. (eds.), The Antarctic Continental Margin: Geology and Geophysics of Offshore Wilkes Land. CPCEMR Earth Science Series, vol. 5A: Circum Pacific Council for Energy and Mineral Resources, p. 75 - 88.

Henjes-Kunst, F. and Schussler, U., 2003, Metasedimentary Units of the Cambro-Ordovician Ross Orogen in Northern Victoria Land and Oates Land: Implications for Their Provenance and Geotectonic Setting from

Geochemical and Nd-Sr Isotope Data. Terra Antarctica, 10, 105 - 128.

Hillenbrand, C.-D. and Ehrmann, W., 2001, Distribution of clay minerals in drift sediments on the continental rise west of the Antarctic Peninsula, ODP Leg 178, Sites 1095 and 1096. In: Barker, P.F., Camerlenghi, A., Acton, G.D., and Ramsay, A.T.S. (eds.), Proceedings of Ocean Drilling Program, Scientific Results, 178, College Station, p. 1 - 29.

Hillenbrand, C.-D. and Ehrmann, W., 2005, Late Neogene to quarter nary environmental changes in the Antarctic Peninsula region: evidence from drift sediments. Global and Planetary Change, 45, 165 - 191.

Juntila, J., Ruikka, M., and Strand, K., 2005, Clay-mineral assemblages in high-resolution Plio-Pleistocene interval at ODP Site 1165, Prydz Bay, Antarctica. Global and Planetary Change, 45, 151 - 163.

Lucchi, R.G., Rebesco, M., Camerlenghi, A., Busetti, M., Tomadin, L., Villa, G., Persico, D., Morigi, C., Bonci, M.C., and Giorgetti, G., 2002, Mid-late Pleistocene glacimarine sedimentary processes of a high latitude, deep-sea sediment drift (Antarctic Peninsula Pacific margin). Marine Geology, 189, 343 - 370.

McGinnis, J.P., Hayes, D.E., and Driscoll, N.W., 1997, Sedimentary processes across the continental rise of the southern Antarctic Peninsula. Marine Geology, 141, 91 - 109.

Michels, K.H., Rogenhagen, J., and Kuhn, G., 2001, Recognition of contour current influence in mixed contourite-turbidite sequences of the western Weddell Sea, Antarctica. Marine Geophysical Research, 22, 465 - 485.

Moore, D.M. and Reynolds, R.C., 1989, X-ray diffraction and the identification and analysis of clay minerals. Oxford University Press, Oxford, 332 p.

Mortlock, R.A. and Froelich, P.N., 1989, A simple method for the rapid determination of biogenic opal in pelagic marine sediments. Deep- Sea Research, 36, 1415 - 1426.

Mortlock, R.A., Charles, C.D., Froelich, P.N., Zibello, M.A., Saltzman, J., Hats, J.D., and Burckle, L.H., 1991, Evidence for lower productivity in the Antarctic Ocean during the last glaciation. Nature, 351, 220 - 223.

O'Brien, P.E., Cooper, A.K., Florindo, F., Handwerger, D.A., Lavelle, M.,

Passchier, J.J., Pospichal, P.G., Quilty, P.G., Richter, C., Theissen, K.M., and Whitehead, J.M., 2004, Prydz channel fan and the history of extreme ice advances in Prydz Bay. In: Cooper, A.K., O'Brien, P.E., and Richter, C. (eds.), Proceedings of Ocean Drilling Program, Scientific Results, 188, College Station, p. 1 - 32.

O'Cofaigh, C., Dowdeswell, J.A., and Pudsey, C.J., 2001, Late Quaternary iceberg rafting along the Antarctic Peninsula continental rise and in the Weddell and Scotia Seas. Quaternary Research, 56, 308 - 321.

Oliver, R.L. and Fanning, C.M., 2002, Proterozoic geology east and southeast of Commonwealth Bay, George V land, Antarctica, and its relationship to that of adjacent Gondwana terranes. In: Gamble, J.A., Skinner, D.N.B., Henry, S., and Lynch, R. (eds.), International Symposium of Antarctic Earth Sciences 1999: Antarctic at the close of a millennium. Royal Society of New Zealand, Wellington, p. 51 - 58.

Patterson, M.O., McKay, R., Naish, T., Escutia, C., Jimenez-Espejo, F.J., Raymo, M.E., Meyers, S.R., Tauxe, L., Brinkhuis, H, and IODP Expdition 318 Scientists, 2014, Orbital forcing of the East Antarctic ice sheet during the Pliocene and Early Pleistocene. Nature Geoscience, 7, 841 - 847.

Piper, D.J.W. and Pe, G.G., 1977, Cenozoic clay mineralogy from D.S.D.P. Holes on the continental margin of the Australia-New Zealand sector of Antarctica. New Zealand Journal of Geology and Geophysics, 20, 905 - 917.

Pudsey, C.J., 2000, Sedimentation on the continental rise west of the Antarctic Peninsula over the last three glacial cycles. Marine Geology, 167, 313-338.

Pudsey, C.J. and Camerlenghi, A., 1998, Glacial-interglacial deposition on a sediment drift on the pacific margin of the Antarctic Peninsula. Antarctic Science, 10, 286 - 308.

Roland, N.W., Henjes-Kunst, F., Kleinschmidt, G., and Talarico, F., 2000, Petrographical, geochemical, and radiometric investigations in Northern Victoria Land, Oates Land and George V Coast: towards a better understanding of plate boundary processes in Antarctica. Terra Antarctica Reports, 5, 57 - 65.

Setti, M., Marinoni, L., Lopez-Galindo, A., and Delgado-Hubertas, A., 2000, Compositional and morphological features of the smectites of the sediments of CRP-2/2A, Victoria Land Basin, Antarctica. Terra Antarctica, 7, 581 - 587.

Sprenk, D., Weber, M.E., Kuhn, G., Rosen, P., Molina-Kescher, M., Liebetrau, V., and Rohling, H.G., 2013, Southern Ocean bioproductivity during the last glacial cycle-new detection method and decadal-scale insight from the Scotia Sea. In: Hambrey, M., Barker, P., Barrett, P., Bowman, V., Davies, B., Smellie, J., and Tranter, M. (eds.), Antarctic Palaeoenvironments and Earth-Surface Processes.

Geological Society of London, Special Publications, vol. 381, p. 245 - 261. http://dx.doi.org.10.1144/SP381.17

Stokke, P.R. and Carson, B., 1973, Variation in clay mineral X-ray diffraction results with the quantity of sample mounted. Journal of Sedimentary Petrology, 43, 957 - 964.

Talarico, F. and Kleinschmidt, G., 2003, Structural and metamorphic evolution of the Mertz Shear Zone (East Antarctic Craton, George V Land): implications for Australia/Antarctica correlations and East Antarctic Craton/Ross Orogen relationships. Terra Antarctica Reports, 10, 229 - 248.

Tauxe, L., Stickley, C., Sugisaki, S., Bijl, P., Bohaty, S., Brinkhuis, H., Escutia, C., Flores, J.A., Iwai, M., Jimenez-Espejo, F., Mckay, R., Passchier, S., Pross, J., Riesselan, C., Rohl, U., Sangiorgi, F., Welsh, K., Klaus, A., Fehr, A., Bendle, J.A.P., Dunbar, R., Gonzalez, J., Hayden, T., Olney, M.P., Pekar, S.F., Shrivastava, P.K., van de Fleridt, T., Williams, T., and Yamane, M., 2012, Chronostratigraphic framework for the IODP expedition 318 cores from the Wilkes Land margin: Constraints for paleoceanographic reconstruction. Paleoceanography, 27, 2214. http://dx.doi.org/10.1029/2012PA002308

Veevers, J.J. and Saeed, A., 2011, Age and composition of Antarctic bedrock reflected by detrital zircons, erratics, and recycled microfossils in the Prydz Bay - Wilkes Land - Ross Sea - Marie Byrd Land sector (70° - 240°E). Gondwana Research, 20, 710 - 738.

Verma, K., Bhattacharya, S., Biswas, P., Shrivastava, P.K., Pandey, M., Pant, N.C., and IODP Expedition 318 Scientific Party, 2014, Clay mineralogy of the ocean sediments from the Wilkes Land margin, east Antarctica: implications on the paleoclimate, provenance and sediment dispersal pattern. International Journal of Earth Sciences, 103, 2315 - 2326.

Weber, M.E., 1998, Estimation of biogenic carbonate and opal by continuous non-destructive measurements in deep-sea sediments: application to the eastern equatorial Pacific. Deep-Sea Research I, 45, 1955 - 1975.

Wefer, G. and Fischer, G., 1991, Annual primary production and export flux in the Southern Ocean from sediment trap data. Marine Chemistry, 35, 597 - 613.

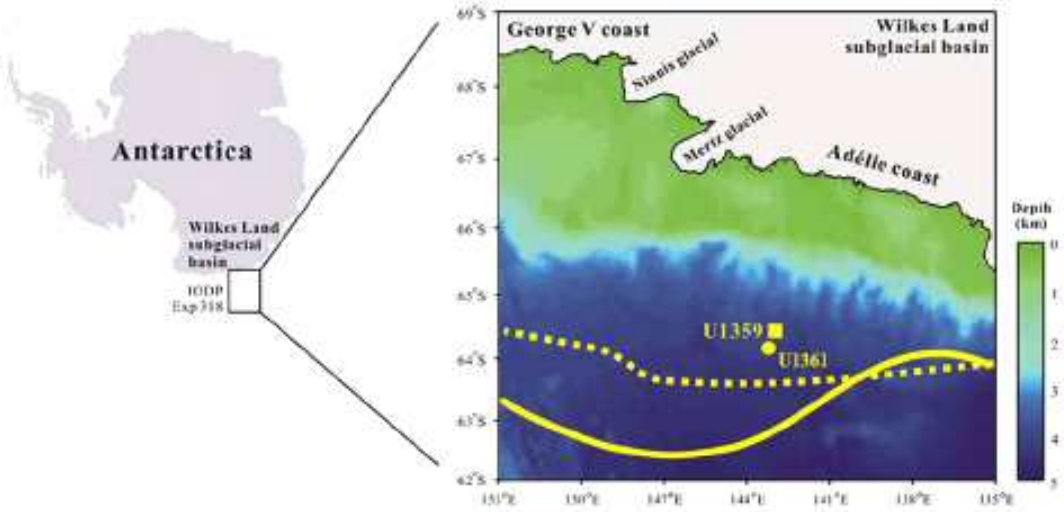

Fig. 1. Map showing the drilling site of Hole U1359A in the Wilkes Land continental rise (East Antarctica). Location of Antarctic Divergence (yellow solid line) and Southern Boundary of the Antarctic Circumpolar Current (yellow dotted line) are adopted from Bindoff et al. (2000).

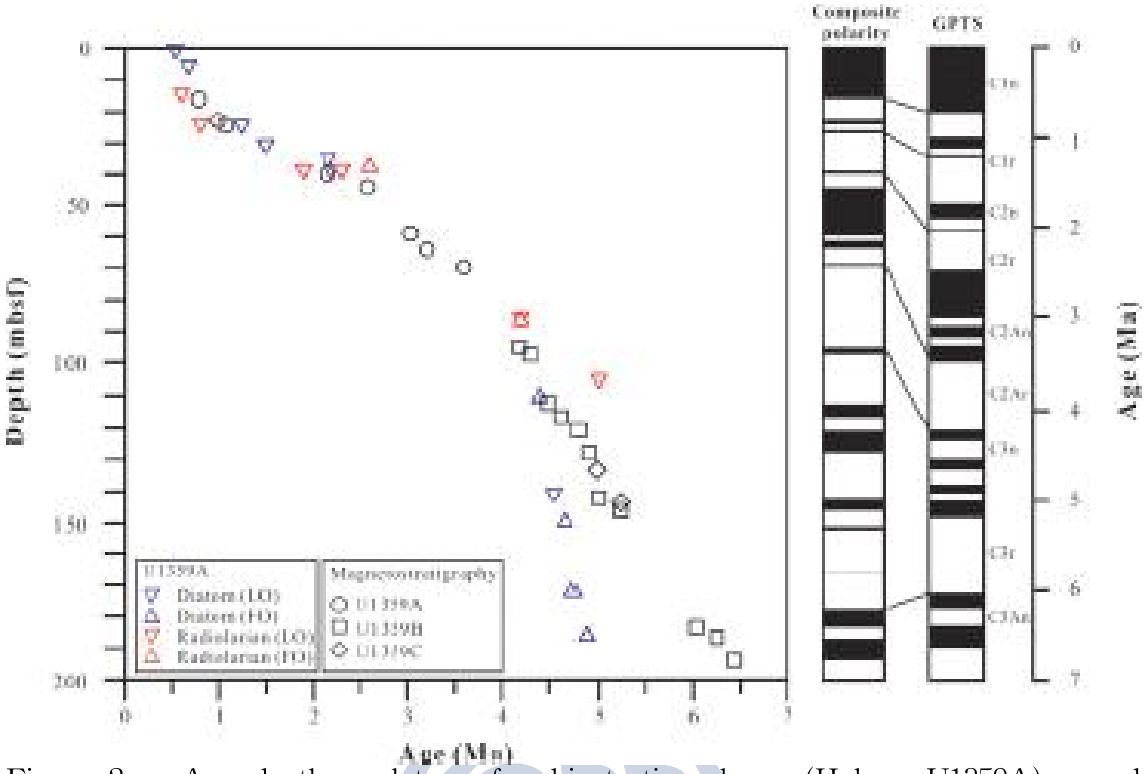

Fig. 2. Age-depth plot of biostratigraphy (Hole U1359A) and magnetostratigraphy (Site U1359) (modified from Tauxe et al., 2012). Composite polarity magnetostratigraphyof Site U1359 was correlated to GPTS for the age determination.

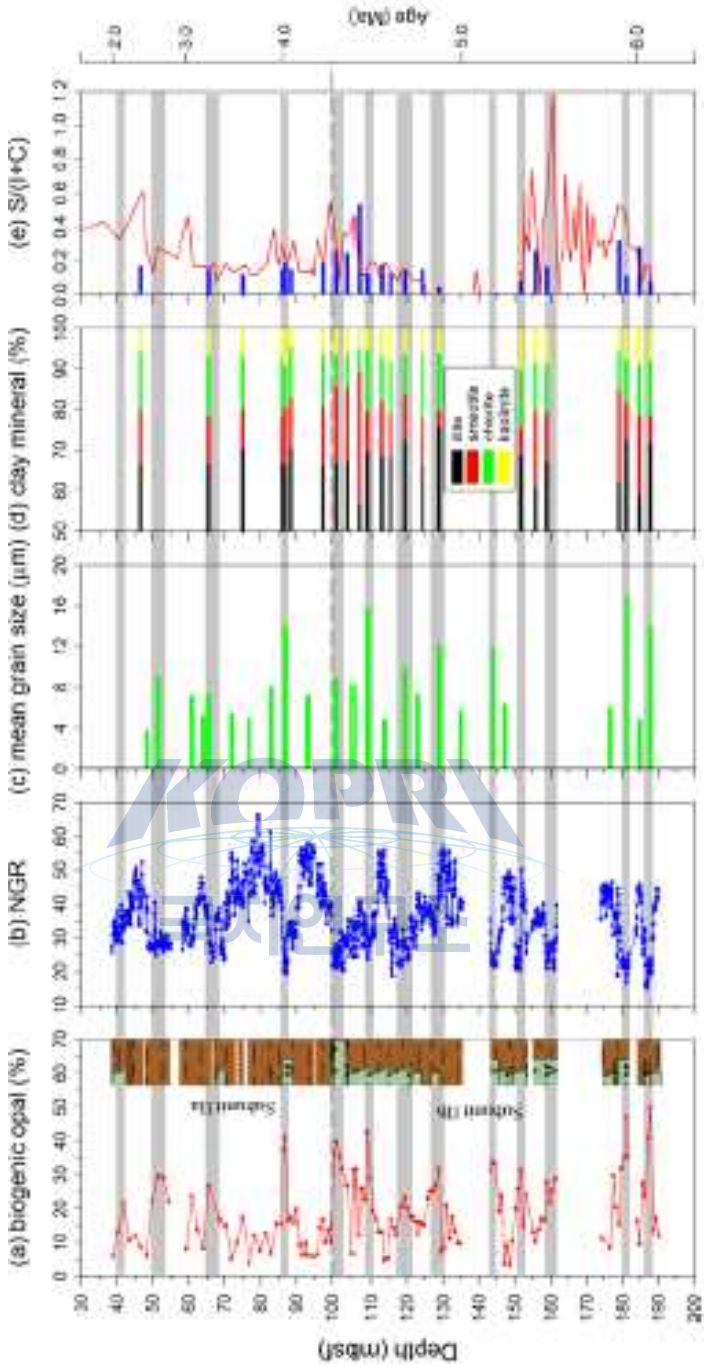

Fig. 3. Downcore profile of (a) biogenic opal content, (b) natural gamma radiation (NGR), (c) mean grain size, (d) clay mineral contents, and (e) smectite/(illite + chlorite) [S/(I + C)] ratios of Hole U1359A (horizontal color bar) and Hole U1359B (red line: Verma et al., 2014). Gray shading represents a series of massive mud layers. Brown and green lithologic symbols represent clayey silty clay layer and diatom ooze layer, respectively (Expedition 318 Scientists, 2011).

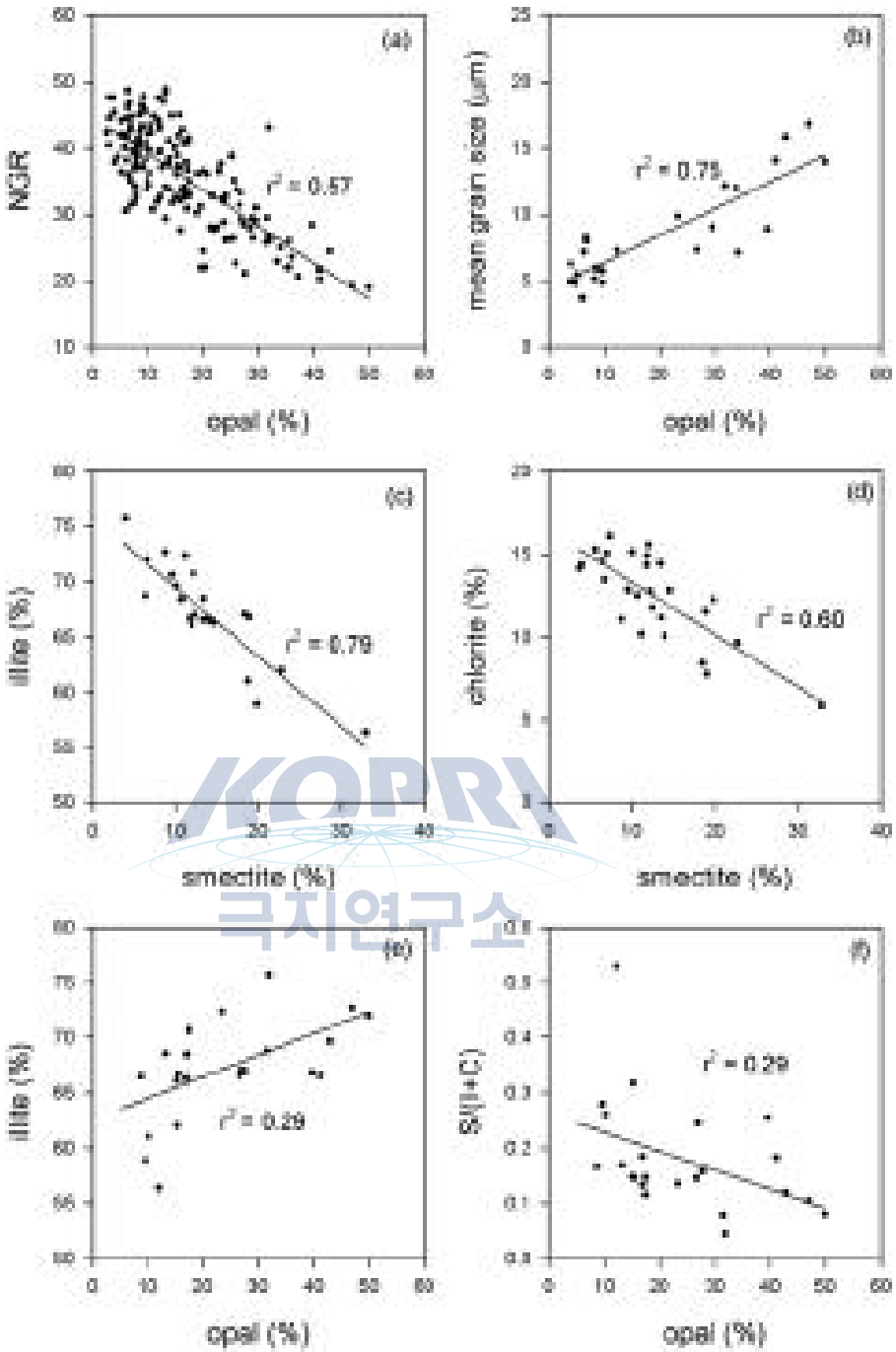

Fig. 4. Correlations between (a) biogenic opal content and NGR, (b) biogenic opal content and mean grain size, (c) smectite and illite con-tents, (d) smectite and chlorite contents, (e) biogenic opal and illite contents, and (f) biogenic opal content and S/(I + C) ratios of Hole U1359A.

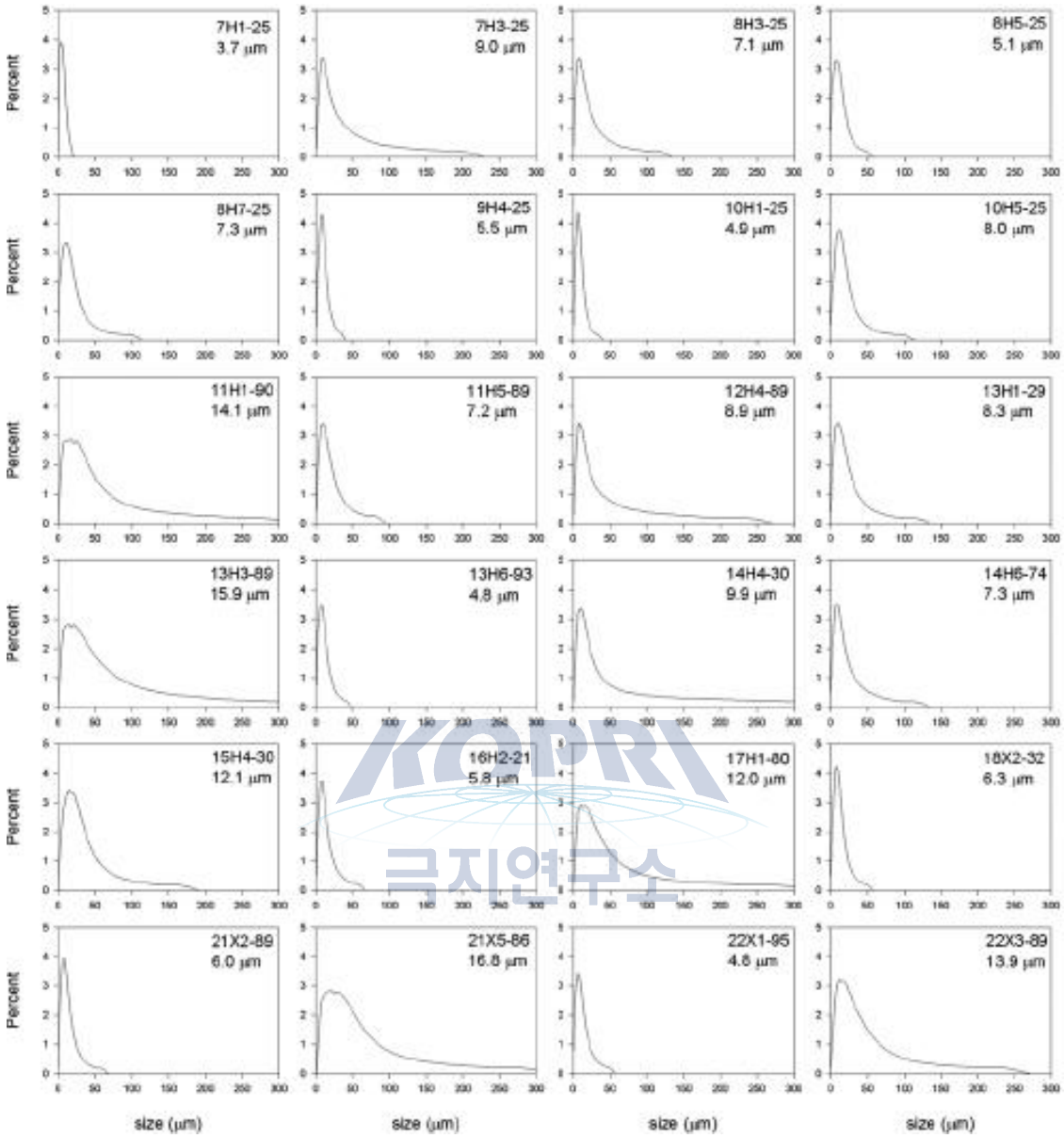

Fig. 5. Grain size distribution patterns of 24 selected sediment samples of Hole U1359A. Each plot shows the sample code and mean grain size.

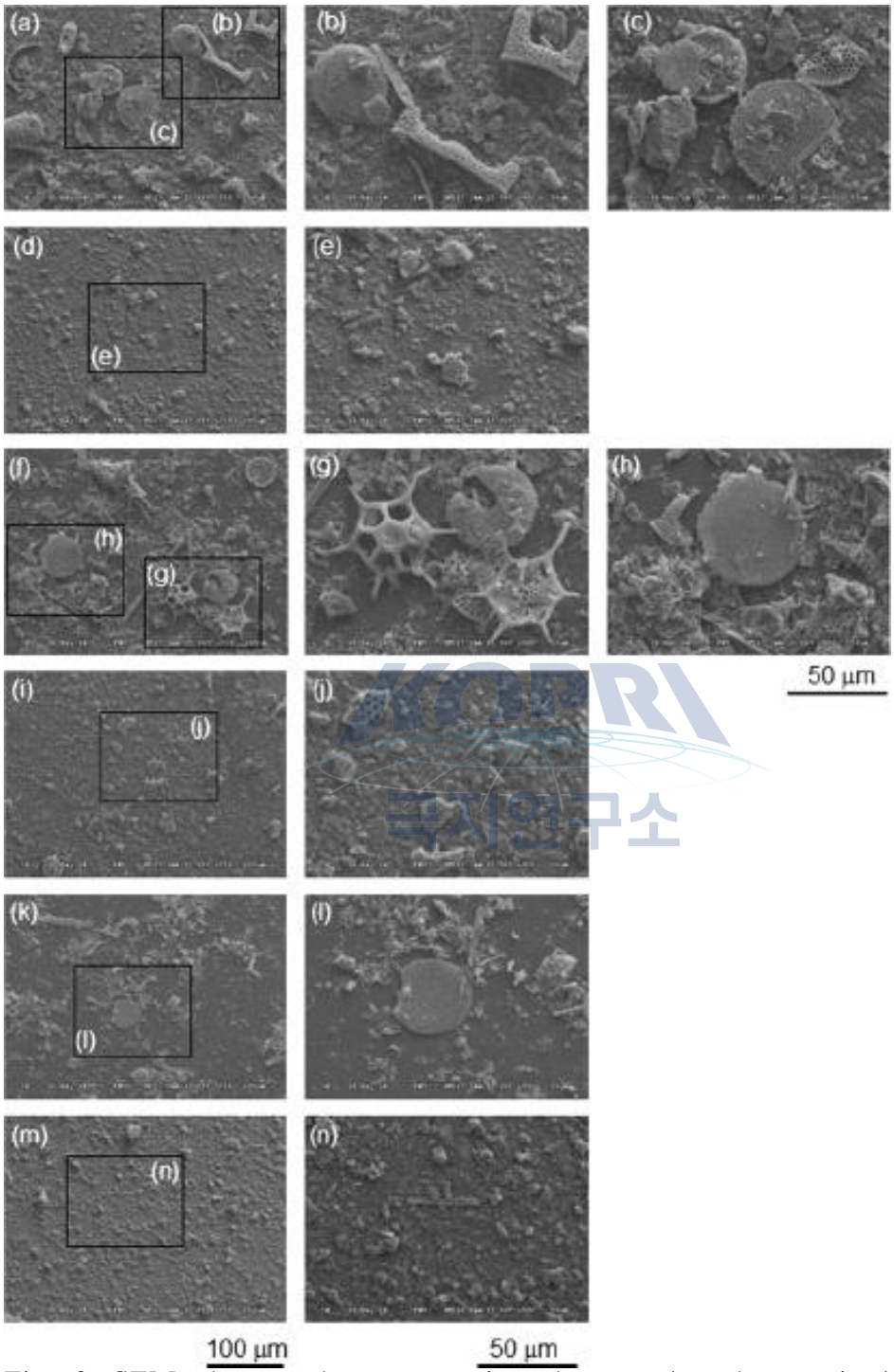

Fig. 6. SEM photographs representing the samples characterized by the large mean grain size (a, d, f) and small mean grain size (i, k, m).(a) 6H3-25 (41.85 mbsf), (d) 7H1-25 (48.35 mbsf), (f) 13H3-89 (108.99 mbsf), (i) 13H6-93 (113.52 mbsf), (k) 21X5-86 (181.06 mbsf), (m) 22X1-95 (184.85 mbsf). Scale bar (a, d, f, I, k. m): 100 um, Scale bar (b, c, e, g, h, j, l, n): 50 um.

제 17 장

웨델해와 로스해 빙붕 주변 해역의 미생물 분포 특성 연구

황청연, 이인애, 윤수정

한국해양과학기술원 부설 극지연구소

요약: 빙붕 주변 해역의 미생물 분포 특성을 이해하기 위해 분자생물학적 기법을 이용한 세균, 고세균 및 바이러스 다양성 연구를 수행하였다. 웨델해와 로스해 빙붕의 코어 퇴적물 시료를 대상으로 미생물(세균, 고세균)의 유전자 마커(16S rRNA gene)에 대한 대용량 염기서열 분석법을 이용하여 깊이에 따른 군집 변화를 조사하였다. 심해 퇴적물에 서식하는 배양 가능한 세균의 특성 연구를 위해 평판 배지 배양법을 이용하여 세균을 분리하였으며, 유전자 마커의 서열 분석을 통해 종 동정을 수행하였다. 웨델해 해수의 RNA 바이러스 군집 특성 연구를 위해 대용량 염기서열 분석법을 이용한 메타게놈분석을 수행하였다. 남극 웨델해(라슨C) 빙붕 해역 퇴적물 코어(약 1.8 m)의 미생물 군집 구조를 분석한 결과, 다양한 분류군에 속하는 5,715개의 미생물 종(OTUs; operation taxonomic units)이 출현하였으며 깊이에 따라 우점군의 분포가 변화하는 특징을 보였다. 특히 50cm와 170cm 부근을 경계로 미생물 군집 구조의 큰 변화를 보였는데, 이는 퇴적 당시의 퇴적물 조성 또는 미생물 조성 차이에 의한 영향으로 여겨진다. 로스해 빙붕에서 획득된 퇴적물 코어에서 퇴적물의 깊이에 따른 우점 박테리아 군집의 변화가 나타났으며, 40 cm 이하의 깊이에서 OP9 박테리아가 50% 정도를 차지하고 있어, 해당 깊이에서의 생지화학적 순환에 중요할 가능성을 보였다. 심해 퇴적물 미생물에서 4종의 신규 미생물을 분리하였으며, 이 중 1종(*Marinobacterium profundum*)에 대한 생리·생화학 특성 및 유전체 특성 분석을 완료하였다. 웨델해 표층수에 포함된 RNA 바이러스 군집에 대한 대용량 염기서열 분석을 통해 다수(120,233개)의 고품질 서열을 확보하였다. 결과적으로 식물 플랑크톤에 특이적인 바이러스 Picornavirus가 우점하고 있는 것으로 나타나, 대번식(bloom) 이후 식물플랑크톤의 사망에 바이러스가 중요한 역할을 담당할 가능성을 시사하였다.

1. 서론

해양 박테리아와 바이러스는 해양 환경에 널리 분포하고 있으며, 생지화학적 순환에 중요한 역할을 한다(Azam 1998, Fuhrman 1999). 해양 박테리아 군집은 주변의 물리·화학적 요인에 의해 영향을 받기 때문에, 미생물의 군집 구조와 환경 요인과의 관련성을 연구하는 것은 기초 생태계를 이해하는데 필수적이다. 또한 대용량 염기서열 분석 기법(예, pyrosequencing 기법; Margulies et al. 2005)의 발전에 힘입어 박테리아 군집과 환경 요인과의 연관성에 대한 연구가 확대되어, 최근에는 해양 퇴적물 코어에서 박테리아의 군집 구조가 생지화학 자료의 분포와 밀접하게 연관되어 있음이 알려지기도 하였다(Jorgensen et al. 2012). 해양 바이러스는 현재까지 DNA 바이러스에 대한 연구가 주로 수행되었으나, 진핵생물과 관련성이 있을 것으로 추정되는 RNA 바이러스의 중요성이 해양 미생물 연구에서 새롭게 대두되고 있다(Steward et al. 2013). 본 과제에서는 남극 빙붕 주변의 해수 및 퇴적물 시료에 대해 분자생물학적 기법을 이용하여 군집 구조 특성을 이해하고자 하였다.

2. 국내외 기술개발 현황

웨델해 라슨C 빙붕에서 퇴적물 박테리아의 다양성에 대한 연구는 국내·외에서 알려진 바가 없다. 남극 반도 서안에서의 RNA 바이러스 군집에 대한 연구는 수행된 바 있으나(Miranda et al. 2016), 남극 반도 동안에 위치한 웨델해 해역의 RNA 바이러스 군집에 대한 연구는 알려진 바가 없다.

3. 연구개발수행 내용 및 결과

3.1. 연구 방법

2013년 아라온 탐사 중 웨델해의 라슨C 빙붕에서 획득한 심해 퇴적물 코어(EAP13-GC16B; 약 1.8 m의 길이) 시료 중 37개 깊이의 퇴적물 시료로부터 DNA를 추출하였고, 군집 분석을 위한 PCR (16S rRNA gene)을 수행한 후, 454 GS-FLX pyrosequencing을 진행하였다(Jorgensen et al. 2012). 2012년 로스해 Drygalski Ice Tongue 부근에서 획득한 퇴적물 코어(DG12-06; 약 4 m의 길이)를 대상으로 19개 깊이에서 DNA를 추출하였고, 대용량 염기서열 분석법을 이용하여 16S rRNA 유전

자 서열을 확보하였다 (그림 1).

배양 가능한 심해 퇴적물 박테리아를 분리하기 위해 평판 배지법(marine agar 또는 메탄올만을 탄소원으로 첨가된 최소영양배지)을 이용하였다(Hwang et al. 2016). 박테리아의 순수 분리는 4회 이상의 콜로니 계대 배양을 실시하여 수행하였으며, 박테리아의 종 동정은 16S rRNA gene에 특이적인 universal primers (Lane 1991)를 이용한 PCR과 sequencing 방법을 이용하였다. 특이적인 미생물의 생리·생화학 특성 연구는 Hwang & Cho (2008)의 방법을 이용하였다.

RNA 바이러스 군집 연구를 위해 2013년 4월 아라온 탐사에서 웨델해 및 남극 반도 서안 표층수를 채수하였고, Miranda et al. (in press)의 방법에 따라 염기서열을 대량 확보하였다.

3.2. 연구 결과

3.2.1. 퇴적물 박테리아 군집 연구

3.2.1.1. 웨델해 라센 C 빙붕 퇴적물

웨델해 라센 C 퇴적물 코어 시료를 대상으로 미생물 마커(16S rRNA 유전자)에 대한 대용량 염기서열 분석 기법(pyrosequencing)을 이용하여 105,298개의 서열을 확보하였다(표 1). 다양한 분류군에 속하는 5,715개의 미생물 종(OTUs; operation taxonomic units)이 파악되었으며, 코어 깊이에 따라 우점군의 분포가 변화하는 특징을 보였다(표 1).

특히 50cm와 170cm 부근을 경계로 미생물 군집 구조의 큰 변화를 보였는데(그림 2), 이는 퇴적 당시의 퇴적물 조성 또는 미생물 조성 차이에 의한 영향으로 여겨진다. 흥미롭게도 철환원 미생물 군집은 IC와 유의한 양의 상관 관계를 보였는데, 이는 라센 C 퇴적물의 생지화학적 순환에서 미생물이 중요한 역할을 담당하고 있음을 시사한다.

3.2.1.2. 로스해 빙붕 퇴적물

로스해의 Drygalski Ice Tongue 부근에서 획득한 퇴적물 코어(DG12-06; 약 4 m의 길이)를 대상으로 16S rRNA 유전자 서열을 확보하였다. 퇴적물의 깊이에 따른 우점 박테리아 군집의 변화가 나타났으며, 특히 40 cm 이하의 깊이에서 OP9 박테리아가 50% 정도를 차지하고 있어(그림 3), 해당 깊이에서의 생지화학적 순환에 중요할 가능성을 보였다.

3.2.1.3. 웨델해와 로스해 퇴적물 코어의 박테리아 군집 비교 연구

웨델해와 로스해 빙붕 퇴적물에서 출현한 박테리아 군집을 비교한 결과, 두 퇴적물에서 공통적으로 Proteobacteria와 Chloroflexi 그룹이 전체 깊이에서 우점하였다(그림 4). 특징적으로 웨델해와 로스해 퇴적물에서는 각각 Planctomycetes 그룹과 OP9 그룹이 우점하는 차이를 보여(그림 4), 해당 그룹의 미생물들이 생지화학적 순환에서 중요할 가능성을 보였다.

3.2.2. 배양 가능한 심해 퇴적물 박테리아 연구

남극 동부분지 퇴적물 코어(GC08-EB01)에서 26개의 균주를 분리하였으며, 16S rRNA 유전자 서열을 분석하여 종 동정을 완료하였다(표 2). 분리된 박테리아는 대부분 *Alphaproteobacteria* (38%), *Bacteroidetes* (27%), *Gammaproteobacteria* (23%) 그룹에 속하였다(표 2). 이 중 3개 균주는 기존에 알려진 종들(*Gilvimarinus polysaccharolyticus*, *Marinobacter antarcticus*, *Lacinutrix copepodicola*)과 비교할 때, 유사도가 97.4-98.1%로 낮았다(표 2). 이들 균주들에 대한 계통분류학적 분석을 수행한 결과, 각 균주들은 새로운 신종일 가능성이 높았다(그림 5).

동해 심해 퇴적물로부터 메탄을 이용 가능성이 있는 박테리아 (*Marinobacterium profundum*)를 분리하여 생리·생화학 특성, 계통분류학, 유전체 특성 분석을 수행하였고(그림 6, 표 3), 이를 통해 신종 미생물임을 밝혔다(Hwang et al. 2016).

3.2.3. RNA 바이러스 군집 연구

웨델해 및 남극 반도 서안 표층수에 포함된 RNA 바이러스 군집에 대한 대용량 염기서열 분석을 통해 120,233개 (251 Mbp)의 고품질 서열을 확보하였다. Picornavirales에 속하는 RNA 바이러스가 13-77% (평균 38%)로 우점하는 것으로 나타났다(그림 7). 특히 식물 플랑크톤에 특이적인 RNA 바이러스의 출현 비율이 높았는데, 이는 남극 식물 플랑크톤의 대번식(bloom) 이후 바이러스가 식물 플랑크톤의 사망에 중요한 역할을 담당할 가능성을 시사한다. 또한 미지의 바이러스가 평균 43%를 차지하고 있다는 본 연구 결과는 남극 해양에서의 바이러스 연구에 대한 필요성을 보여준다.

Research on distributions of microorganisms in the vicinity of ice shelves of Weddell Sea and Ross Sea

Chung Yeon Hwang, Inae Lee, Soo Jung Yoon

Korea Polar Research Institute

Abstract: To understand distributions of microorganisms in the vicinity of ice shelves, diversities of bacteria, archaea and viruses were studied using molecular techniques. Community structures of microorganisms (bacteria and archaea) along a depth of the sediment cores obtained from ice shelves in Weddell Sea and Ross Sea were investigated using pyrosequencing of 16 rRNA genes. To characterize culturable bacteria in deep-sea sediments, bacteria were isolated using culture media plates and identified based on 16S rRNA gene sequences. RNA viral community in surface waters of Weddell Sea was investigated using a metagenomic approach. Community structures of bacteria and archaea in a sediment core (ca. 1.8 m long) from the ice shelf (Larsen C) of Weddell Sea showed a high diversity of 5,715 OTUs (operation taxonomic units), which varied along a depth. Specifically, rapid changes of community structures at 50 and 170 cm might reveal an abrupt change of sediment components or microorganisms compositions during the past sedimentations. In a sediment core from the ice shelf of Ross Sea, predominant taxa varied along a depth with a dominance of OP9 bacteria (50%) at >40 cm depth, indicating that OP9 played an important role in biogeochemical cycles at those depths. Four bacterial strains of candidate new species were isolated from deep-sea sediments. One of them, Marinobacterium profundum, was characterized with a respective of physiological, biochemical and genomic features. RNA viral community structures were investigated with high-quality metagenome sequences of 120,233 by massive nucleotide sequencing. Picornavirus which is related to phytoplankton was dominant, suggesting that viruses might cause lysis of phytoplankton during bloom period in the study area.

참고문헌

Azam, F., 1998, Microbial control of oceanic carbon flux: the plot thickens, Science, 280: 694-696.

Fuhrman, J.A., 1999, Marine viruses and their biogeochemical and ecological effects, Nature, 399: 541-548.

Hwang, C.Y., Yoon, S.J., Lee, I., Baek, K., Lee, Y.M., Yoo, K.C., Yoon, H.I., Lee, H.K., 2016, Marinobacterium profundum sp. nov., a marine bacterium from deep-sea sediment. International Journal of Systematic and Evolutionary Microbiology, 66: 1561-1566.

Hwang C.Y., Cho, B.C., 2008, *Cohaesibacter gelatinilyticus* gen. nov., sp. nov., a marine bacterium that forms a distinct branch in the order *Rhizobiales*, and proposal of *Cohaesibacteraceae* fam. nov. International Journal of Systematic and Evolutionary Microbiology, 58: 267-277.

Jorgensen SL *et al.* (2012) Correlating microbial community profiles with geochemical data in highly stratified sediments from the Arctic Mid-Ocean Ridge. Proceedings of the National Academy of Sciences, 109: E2846-E2855.

Margulies, M., Egholm, M., Altman, W.E., Attiya, S., Bader, J.S., Bemben, L.A., Berka, J. et al., 2005, Genome sequencing in microfabricated high-density picolitre reactors. Nature, 437: 376-380.

Miranda, J.A., Culley, A.I., Schvarcz, C.R., Steward, G.F., RNA viruses as major contributors to Antarctic virioplankton. Environ. Microbiol. (in press)

Steward, G.F, Culley, A.I., Mueller, J.A., Wood-Charlson, E.M., Belcaid, M., Poisson, G. 2013, Are we missing half of the viruses in the ocean? The ISME Journal, 7: 672-679.

da Silva MAC et al. (2013) Phylogenetic identification of marine bacteria isolated from deep-sea sediments of the eastern South Atlantic Ocean. Springerplus 2: 127.

Hardies SC, Hwang YJ, Hwang CY, Jang GI & Cho BC (2013) Morphology, physiological characteristics, and complete sequence of marine bacteriophage RIO-1 Infecting *Pseudoalteromonas marina*. Journal of Virology 87: 9189 - 9198.

Hwang CY, Lee I, Cho Y, Lee YM, Jung YJ, Baek K, Nam SI, Lee HK (2015) *Sediminicola arcticus* sp. nov., a psychrophilic bacterium isolated from deep-sea sediment, and emended description of the genus *Sediminicola*. International Journal of Systematic and Evolutionary Microbiology, 65: 1567 - 1571.

Jorgensen SL *et al.* (2012) Correlating microbial community profiles with geochemical data in highly stratified sediments from the Arctic Mid-Ocean Ridge. Proceedings of the National Academy of Sciences 109: E2846 - E2855.

Kim YG, Choi DH, Hyun S, Cho BC (2007) *Oceanobacillus profundus* sp. nov., isolated from a deep-sea sediment core. International Journal of Systematic and Evolutionary Microbiology, 57: 409 - 413.

Lane DJ (1991) 16S/23S rRNA sequencing. In Nucleic Acid Techniques in Bacterial Systematics, pp. 115-175. Edited by E. Stackebrandt & M. Goodfellow. Chichester: Wiley.

표 1. 웨델해 라센 C의 퇴적물 코어(EAP13-GC16B)에서 확보된 염기 서열 수(reads numbers), 관찰된 OTU (operation taxonomic unit), 종 풍부도(species richness) 결과

Sample ID	Depth (cm)	Reads numbers	Observed OTU* (97%)	Species richness (Chao1)
1	0~1	1556	458	1238
2	2~3	1017	427	1102
3	4~5	1222	359	707
4	6~7	1290	287	459
5	8~9	2072	251	479
6	10~11	3183	294	518
7	12~13	2036	268	489
8	14~15	2538	297	568
9	16~17	2243	305	579
10	18~19	2078	277	539
11	20~21	3161	288	507
12	25~26	3579	221	370
13	30~31	2224	303	606
14	35~36	1888	245	467
15	40~41	3324	231	377
16	45~46	3562	257	562
17	50~51	1802	537	1354
18	55~56	2301	246	547
19	60~61	4008	225	478
20	65~66	7411	229	592
21	70~71	3726	189	382
22	75~76	2777	181	333
23	80~81	2200	297	634
24	85~86	3898	241	532
25	90~91	4553	191	541
26	95~96	3249	235	564
28	105~106	2144	259	665
29	110~111	3907	256	524
30	115~116	4029	239	438
31	120~121	1855	363	751
37	150~151	2615	250	421
38	155~156	1153	405	924
39	160~161	3329	210	388
40	165~166	1428	362	669
41	170~171	4387	200	460
42	175~176	3309	211	560
43	180~181	4244	154	408
	Total	105,298		
	Average	**2,846**	**277**	**587**

표 2. 남극 동부분지 퇴적물 코어(GC08-EB01)에서 분리한 박테리아의 균주 리스트 (볼드체로 표시된 3개 균주들은 계통분류학적 분석 결과, 신종일 가능성이 높은 균주들임).

근연종	유사도 (%)	균주 수	그룹
Salinibacterium amurskyense KMM 3673(T)	99.4-99.5	3	*Actinobacteria*
Sphingorhabdus flavimaris SW-151(T)	99.3-99.7	7	*Alphaproteobacteria*
Thalassospira lohafexi 139Z-12(T)	99.9-100	3	*Alphaproteobacteria*
***Gilvimarinus polysaccharolyticus* YN3(T)**	**97.4**	**1**	***Gammaproteobacteria***
Halomonas titanicae BH1(T)	99.4	2	*Gammaproteobacteria*
***Marinobacter antarcticus* ZS2-30(T)**	**97.4**	**1**	***Gammaproteobacteria***
Marinobacter guineae M3B(T)	99.9-100	2	*Gammaproteobacteria*
Algoriphagus aquimarinus LMG 21971(T)	100	5	*Bacteroidetes*
***Lacinutrix copepodicola* DJ3(T)**	**98.1**	**1**	***Bacteroidetes***
Aequorivita antarctica SW49(T)	99.4	1	*Bacteroidetes*

표 3. 신종 *Marinobacterium profundum* PAMC 27536^{T}과 근연종(*M. rhizophilum*)의 생리·생화학 특성, 유전체 특성의 비교 결과

Characteristic	PAMC 27536^{T}	*M. rhizophilum* KCCM 42386^{T}
Temperature range (°C) for growth (optimum)	4–32 (25–30)	10–34 (25–30)
Salinity range (%, w/v) for growth (optimum)	1–4 (3)	1–6 (3)
pH range for growth (optimum)	6.0–9.0 (7.0–7.5)	6.0–9.0 (7.0)
α-Glucosidase	−	+
Acid production from:		
D-Adonitol, D-arabitol, L-arabitol, cellobiose, D-glucose, inositol, inulin, methyl α-D-glucopyranoisde, trehalose, turanose, xylitol	−	+
Raffinose	+	−
Utilization as sole carbon and energy source:		
N-Acetyl-D-glucosamine	−	+
Melibiose	+	−
DNA G+C content (mol%; HPLC analysis)	56.1 (57.2)*	61†

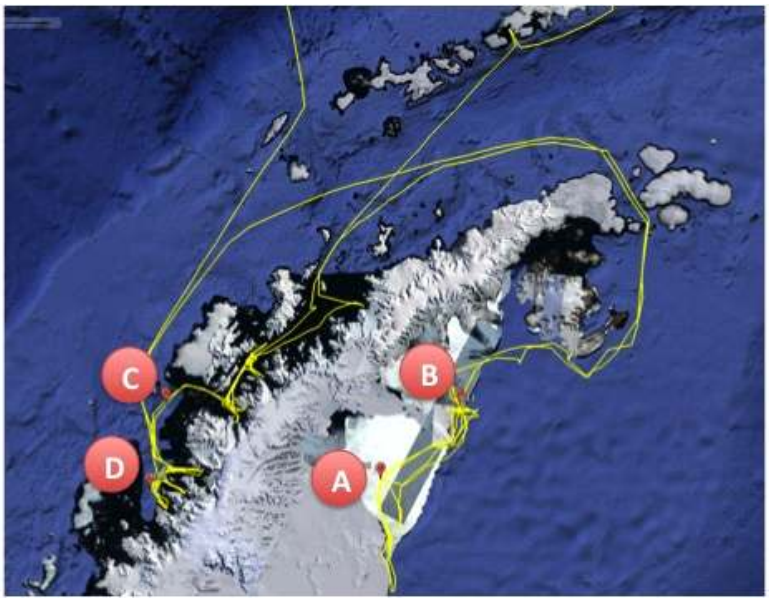

그림 1. 표층 바이러스 군집 연구를 수행하였던 웨델해 및 남극 반도 서안의 정점 지도

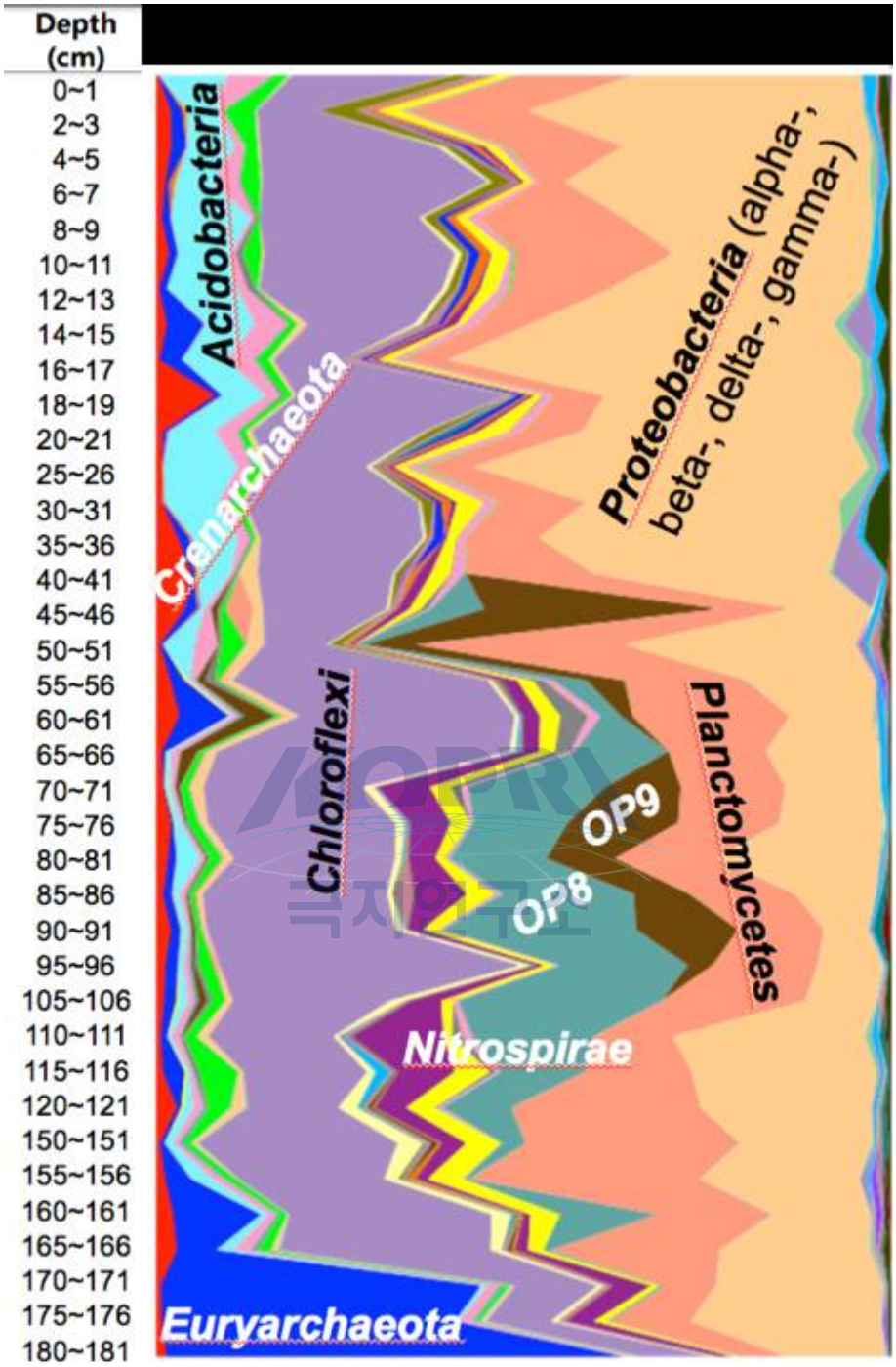

그림 2. 웨델해 라센 C의 퇴적물 코어(EAP13-GC16B)에서 출현한 미생물 그룹의 수직 분포

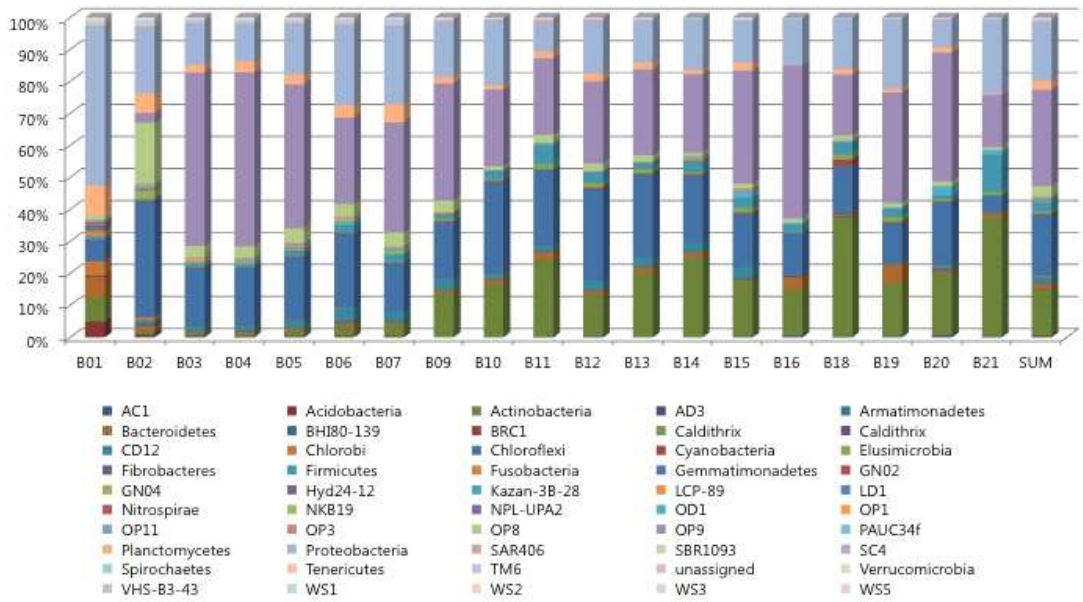

그림 3. 로스해 빙붕 퇴적물 코어(DG12-06)에서 출현한 미생물 그룹의 수직 분포

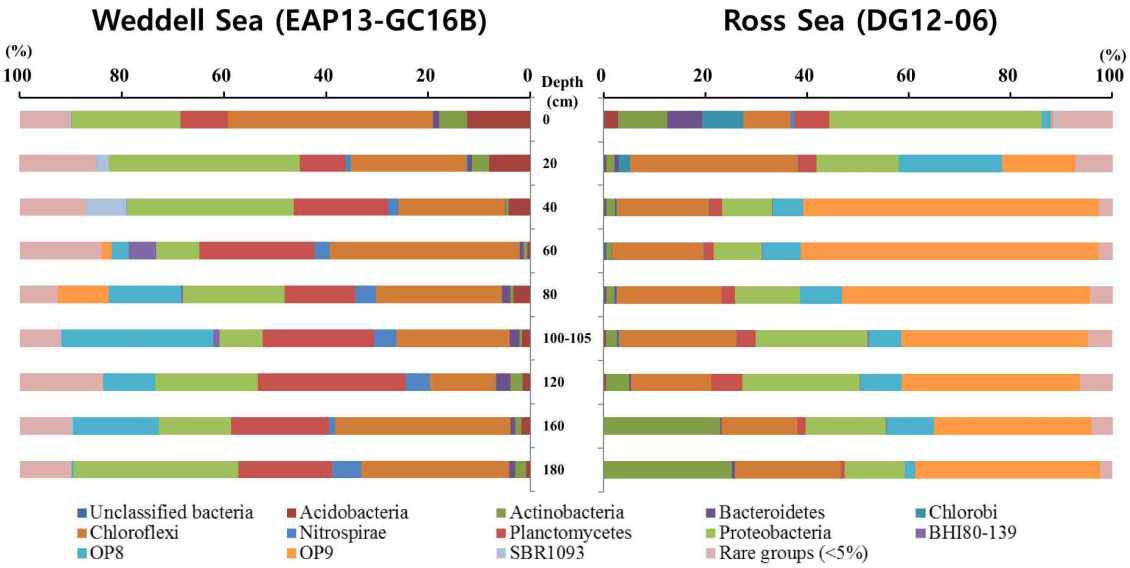

그림 4. 웨델해와 로스해 빙붕 퇴적물에서 출현한 미생물 그룹의 비교

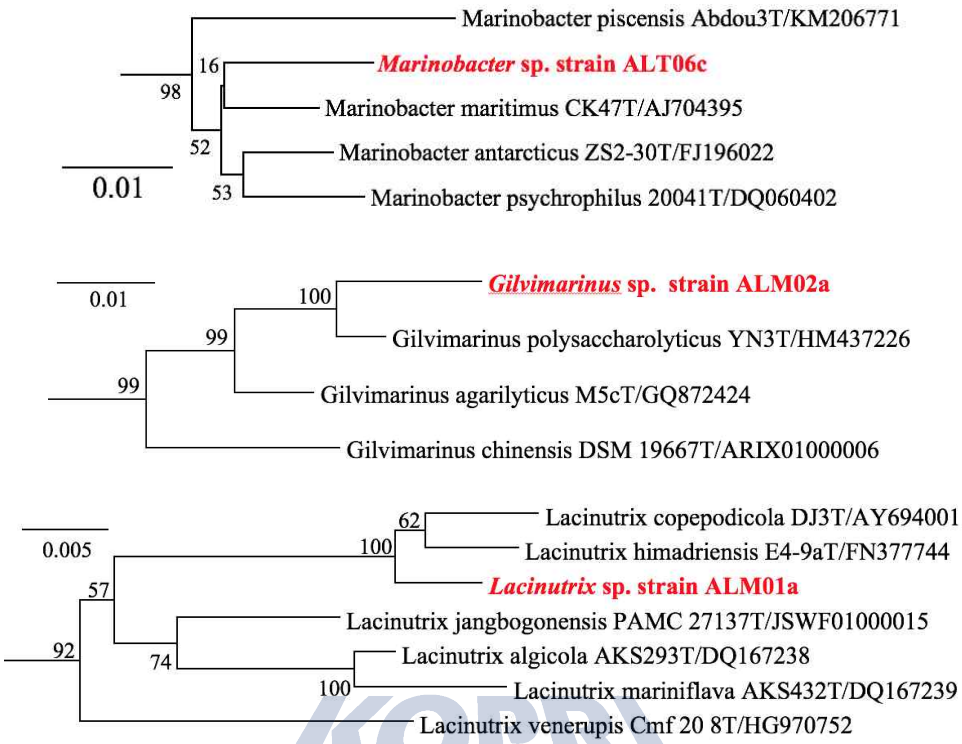

그림 5. 남극 동부분지 퇴적물 코어(GC08-EB01)에서 분리한 신종 후보 균주들의 16S rRNA 유전자에 대한 계통수

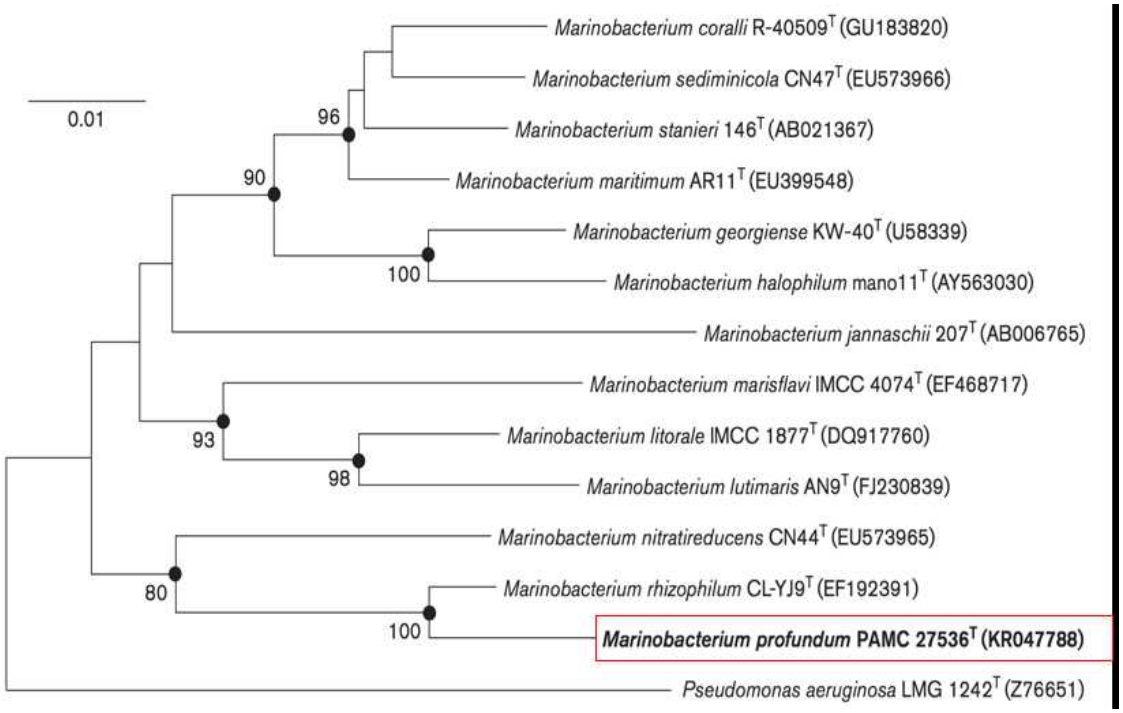

그림 6. 신종 *Marinobacterium profundum* PAMC 27536^{T} 및 관련 종들과의 16S rRNA 유전자 계통수

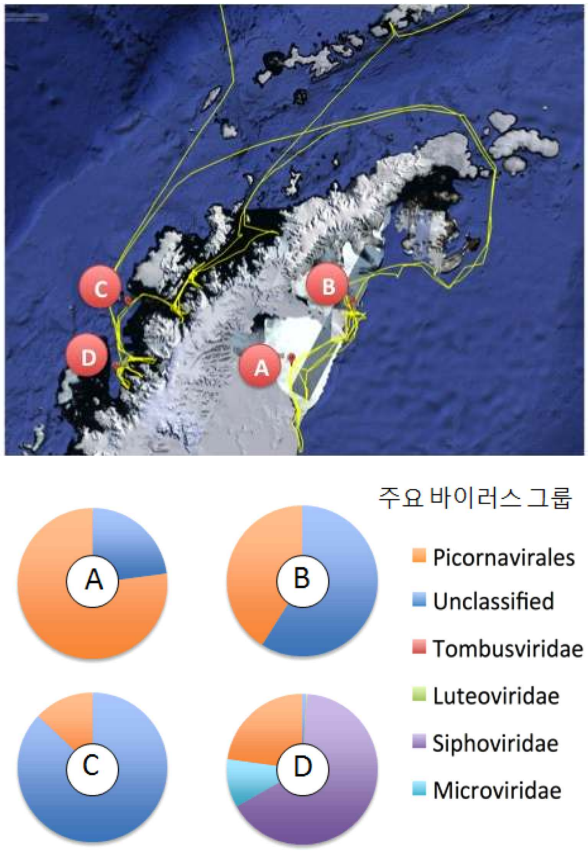

그림 7. 남극 웨델해와 남극 반도 서안의 표층수에 출현한 RNA 바이러스 그룹의 분포

제 18 장

서남극지역에서의 동물플랑크톤 분포 및 먹이습성에 관한 연구

최은정, 김지훈

한국해양과학기술원 부설 극지연구소

요약: 본 연구지역은 빙붕이 빠르게 무너지는 지역으로써 이 연구지역의 해양생태계의 구조적이고 기능적인 변화를 연구함으로써 급변하게 변하는 해양생태계의 반응을 연구하고 미래를 예측할 수 있는 기반을 모색해 보고자 한다. 본 연구의 현장조사는 2013.04.04 ~ 2013.05.14에 걸쳐서 대한민국의 쇄빙연구선인 아라온을 이용하여 해양탐사가 이루어졌다. 상대적으로 높은 수온 및 클로로필 농도와 낮은 염분범위를 보인 서남극반도 부근에서는 주로 식물플랑크톤을 먹이로 하는 종들이 많이 출현한 반면, 낮은 수온 및 클로로필 농도와 높은 염분범위를 보인 동남극반도 주변에서는 주로 다른 동물플랑크톤을 포식하는 종들이 다수 출현하여 뚜렷한 지역차이를 확인할 수 있었다.

1. 서 론

서남극지역의 경우 기후변화에 대한 남극 해양생태계의 반응에 민감한 지역으로써 특히 남극의 빙붕이 붕괴된 연구지역에서의 해양환경자료 및 생물상, 그리고 그들의 섭식관계는 그 해역의 환경을 이해하는데 매우 유용한 자료가 될 것이라 생각되어진다.

안정동위원소는 주로 어떤 원소의 동위원소의 질량의 차이로 인하여 물리화학적인 작은 변화에 의해 일어나는 동위원소 분별(Isotope fractionation)에 의해 자연 물질에서 동위원소의 존재량의 차이가 나타난다. 이러한 동위원소의 분별에 의한 안정 동위원소비를 이용하여 물질의 기원과 생성환경을 해석하는 연구방법으로 지질학, 고고학, 환경화학, 생물학, 해양학, 농학, 지구과학, 식품화학 등의 분야에서 광범위하게 응용 연구되고 있다. 최근에는 질량분석 기기의 눈부신 발달은 동위원소를 이용한 과학 분야의 질과 심도를 급격히 확장시켜왔다. 동위원소 분석방법에

있어서의 감도와 정밀도가 향상됨에 따라서 동위원소 연구의 응용범위는 더욱 넓어져서 물질의 기원 및 생성환경을 연구하는 과학자들에게는 동위원소가 강력하고 효과적인 연구수단으로 자리 잡게 되었으며 최근에는 생물의 먹이망을 통한 물질의 순환과정 평가에 이용되기 시작하였다. 특히 1960년대 후반부터 수소($^{2}H(D)/^{1}H$), 산소($^{18}O/^{16}O$), 탄소($^{13}C/^{12}C$), 질소 ($^{15}N/^{14}N$), 황($^{34}S/^{32}S$) 등의 환경 동위원소가 지구과학에 이용되기 시작하여 최근에 와서는 이의 응용분야도 방대하다. 국제적으로 이와 같은 높은 응용연구에도 불구하고 국내의 안정 동위원소의 분석연구는 이미 1979년부터 시작되었으나 기술습득 및 기본적인 연구를 수행하는 수준에서 진행되고 있다.

먹이망 구조를 연구하는 전통적인 방법은 소비자의 위 내용물을 분석하는 것이었다. 그러나 이러한 방법은 많은 시료들을 분석해야 하고 많은 시간과 노력이 요구될 뿐만 아니라 먹이생물로서의 다양한 생물종을 대상으로 연구를 수행해야 하며, 소화가 진행된 먹이, 먹이생물의 크기가 작은 경우나 형태적인 특징이 잘 나타나지 않는 생물의 경우 동정이 어렵고, 이미 소화되고 난 후의 파편이나 일부만 섭취된 생물들을 대상으로 할 수도 있다는 연구방법상의 단점을 가지고 있다. 또한 소화관 내용물 분석 방법으로 고차소비자로 갈수록 소비자가 이용하는 유기물의 기원을 추적하기는 어렵다. 이와 같은 단점들을 보완하고 소비자가 이용하는 유기물 기원을 추적하기 위해 탄소와 질소 안정동위원소 비값($\delta^{13}C$와 $\delta^{15}N$)을 이용하는 방법이 효과적으로 이용될 수 있다(Fry & Sherr, 1984; Michener & Schell, 1994; DeNiro & Epstein, 1981.) (그림 1).

이 방법은 소비자가 먹이를 섭취하게 되면 대사과정을 거치면서 기원물질이 가지는 원래의 특성은 사라지는 반면 생산자의 탄소와 질소의 안정동위원소 조성이 소비자의 안정동위원소 조성에 반영된다는 특성에 근거하여 그 동물이 실제로 이용하는 먹이의 기여도를 평가할 수 있다. 또한 체성분 중 안정동위원소 조성은 상당기간 동안 그들의 섭식활동을 반영한 결과이기 때문에 이들이 서석하고 있는 먹이환경을 해석할 수도 있다. 또한 안정동위원소 비 값을 분석할 경우 먹이와 소비자(prey-predator) 사이에 각 영양 단계를 따라 탄소는 1‰ 이내, 질소는 3 ~ 4‰ 정도가 높아지는 동위원소 분별효과(fractionation effect)가 나타난다. 따라서 안정동위원소 조성 분석을 통하여 소비자가 이용하는 유기물 기원의 추적이 가능하며 소비자의 영양단계를 연구하는데 있어 유용하게 이용될 수 있다(그림 2).

서남극 빙붕과 주변 빙상, 해양의 입체적 관측 시스템 구축을 통해 최근 급속히 진행되는 서남극 빙붕 붕괴 현상을 사전에 예측할 수 있는 장기 관측 시스템을 구축하고 빙붕 붕괴의 원인을 규명하며, 과거 유사한 환경 복원을 통해 향후 빙

붕 붕괴시 일어날 수 있는 급격한 지구환경 변화의 규모 및 파급효과를 예측하는데 필요한 기초자료를 제공하고자 한다. 본 연구지역은 빙붕이 빠르게 무너지는 지역으로써 이 연구지역의 해양생태계의 구조적이고 기능적인 변화를 연구함으로써 급변하게 변하는 해양생태계의 반응을 연구하고 미래를 예측할 수 있는 기반을 모색해 보고자 한다.

2. 재료 및 실험방법

본 연구의 현장조사는 2013.04.04 ~ 2013.05.14에 걸쳐서 대한민국의 쇄빙연구선인 아라온을 이용하여 해양탐사가 이루어졌다. 해양환경조사 연구정점들 중, 수직해양조사 정점 22개 정점에서 CTD 및 영양염, 입자유기탄소 및 질소, 입자유기물의 거대입자물질 분석을 위한 시료채집 및 전처리를 수행하였고, 남극반도 해양환경에 대한 폭 넓은 이해를 위해, 총 20개의 표층정점에서 수온, 염분 및 클로로필 농도, 색소 분석등의 환경 데이터 조사를 위한 시료 채집 및 전처리를 실시하였다. 또한 남극반도 연안의 동물플랑크톤 군집의 지역적 분포특성을 파악하기 위해 총 15개의 정점에서 수심별 수직채집 (0-100m, 0-300m)을 실시하여 다양한 해양환경조사를 수행함. 정점별 동물플랑크톤의 출현량과 종조성, 공간분포 및 먹이원에 대한 연구를 위해 시료를 종 수준까지 동정 및 분류 후 먹이원 파악을 위한 탄소 및 질소 안정동위원소 비 분석을 수행하였다.

본 연구에서 동위원소 분석을 위한 carrier gas로는 헬륨 (He) 가스를 이용하였고, 원소분석기의 온도를 1030℃로 조절하여 모든 유기물을 완전 연소시킨 후 CO_2와 N_2 가스를 헬륨으로 안정동위원소 질량분석기로 주입하여 각 원소를 측정하고 위의 식에 따라 국제 표준에 맞는 동위원소 비값을 계산하였다. 이를 위해서 내부 표준물질로 동위원소 비 값을 알고 있는 peptone을 이용하였다. 한편, 각각 총 20개의 peptone과 lysine을 이용하여 안정동위원소를 분석한 결과 standard deviation은 탄소에서 ± 0.1‰과 질소에서 ± 0.2‰을 나타내어 매우 높은 정밀도와 재현성을 나타내었다.

3. 결과 및 토의

3.1. 해양환경조사 및 동물플랑크톤 연구

2013년 4월 15일 부터 29일까지 총 15일간 남극 반도 주변의 해양환경 조사를 위한 다양한 실험을 대한민국 쇄빙연구선인 아라온을 이용하여 수행하였다. 연구 정점은 총 59개 정점으로 그 중에서 CTD를 이용한 해양조사 정점이 39개였고 (그림 4), 그 중 23개 정점에서 해수분석을 실시하였다. 이동 중 표층해수를 이용한 환경조사 를 20개 정점에서 수행하였으며, 네트를 이용한 플랑크톤 채집을 15개 정점에서 수행하였다. 주로 남극반도 주변 연안해역을 중심으로 브랜스필드 해협과 드레이크 해협 등의 지역에서 조사를 실시하였다. 남극반도 주변해역의 해수특성을 파악하기 위해 총 39개의 정점에서 CTD를 이용, 주요 수심별 채수 및 환경 데이터 조사를 수행하였다. 모든 정점에서 기본적 물리데이터인 수온과 염분을 수심에 따라 측정하였고, 23개 정점에서 주요 수심별 해수분석을 통한 다양한 환경데이터 도출을 위해 해수를 채집하였다. 또한 미리 선정된 주요 정점에서 해수 시료를 이용해, 현장과 실험실 환경에서 기초생산력을 측정하였다. 영양염 분석 등을 포함한 여러 화학적 분석을 준비 중에 있으며, 이를 위해 아라온에서 미리 모든 정점의 해수를 여과하여 전처리하였다.

남극반도 연안의 동물플랑크톤 군집의 지역적 분포특성을 파악하기 위해 총 15개의 정점에서 수심별 수직채집 (0-100m, 0-300m)을 실시하여 다양한 해양환경 조사를 수행함. 정점별 동물플랑크톤의 출현량과 종조성, 공간분포 및 먹이원에 대한 연구를 위해 시료를 종 수준까지 동정 및 분류 후 먹이원 파악을 위한 탄소 및 질소 안정동위원소비 분석 수행 예정임. 출현한 주요 동물플랑크톤 분류군은 요각류와 패형류, 크릴 그리고 화살벌레로 나타남. 요각류와 패형류가 높은 출현비율을 나타냈고, 살파와 단각류도 일부 정점에서 출현하였다 (그림 5).

주요동물플랑크톤의 탄소 및 질소안정동위원소비 결과를 보면 Oithona는 탄소 및 질소안정동위원소비가 -25.1±0.4‰, 8.0±0.7‰을 나타내어 가장높은 trophic level을 보였고, Sagitta의 경우 -26.5±0.2‰, 4.19±0.3‰을 나타내였다. Clione의 경우 -28.0±0.7‰, 5.0±0.4‰로 가장 낮은 탄소안정동위원소비 값을 보였으며, Calanus의 경우에는 -22.4±0.3‰, 6.8±0.5로 가장 높은 탄소안정동위원소비값을 나타내었다 (그림 6). 동물플랑크톤의 분포를 보면 상대적으로 높은 수온 및 클로로필 농도와 낮은 염분 범위를 보인 서남극반도 부근에서는 주로 식물플랑크톤을 먹이로 하는 종들이 많이 출현한 반면, 낮은 수온 및 클로로필 농도와 높은 염분범위를 보인 동남극반도 주변에서는 주로 다른 동물플랑크톤을 포식하는 종들이 다수 출현하여 뚜렷한 지역차이를 확인할 수 있었다 (그림 7). 향후 이들간의 먹이와 포식관계를 안정동위원소비 결과를 통해 밝혀진다면 남극 해양생태계의 동물플랑크톤의 먹이습성의 차이를 이해하는 자료가 될 것이라 판단된다.

4. 결 론

주요동물플랑크톤의 탄소 및 질소안정동위원소비 결과를 보면 Oithona는 탄소 및 질소안정동위원소비가 -25.1±0.4‰, 8.0±0.7‰을 나타내였고, Sagitta의 경우 -26.5±0.2‰, 4.19±0.3‰을 나타내였다. Salpa의 경우 -28.0±0.7‰, 5.0±0.4‰로 가장 낮은 탄소안정동위원소비 값을 나타내였으며, Calanus의 경우에는 -22.4±0.3‰, 6.8±0.5로 가장 낮은 탄소안정동위원소비값을 나타내었다. 또한, 상대적으로 높은 수온 및 클로로필 농도와 낮은 염분 범위를 보인 서남극반도 부근에서는 주로 식물플랑크톤을 먹이로 하는 종들이 많이 출현한 반면, 낮은 수온 및 클로로필 농도와 높은 염분범위를 보인 동남극반도 주변에서는 주로 다른 동물플랑크톤을 포식하는 종들이 다수 출현하여 뚜렷한 지역차이를 확인할 수 있었다. 향휴 더 넓은 해역과 더 많은 종들에서의 해양환경자료와 동위원소비 바료를 비교하여 먹이습성의 차이가 해역환경의 차이인지 지속적으로 모니터링할 필요가 요구되어 진다.

Research on distributions of zooplankton and the trophic links between primary organic matter sources and dominant zooplankton in West Antarctica

Eun Jung Choy, Ji Hoon Kim

Korea Polar Research Institute

Antarctic oceanographic surveys were carried out from April 2013 to May 2013 using Korean icebreaker Araon. The goal of this expeditions are to understand the marine biological structure and functions to abruptly changing marine ecosystems. To understand the trophic links between primary organic matter sources and dominant zooplankton taxa, we measured the carbon and nitrogen stable isotope ratios. There were a distinct differences of zooplankton dominant species between western Antarctic peninsula and eastern Antarctic peninsula and carbon and nitrogen stable isotope ratios.

참고문헌

DeNiro, N.J., Epstein, S., 1981. Influence of diet on the distribution of nitrogen isotopes in animals. Geochimca et Cosmochimca Acta 45, 341-351.

Fry, B., Sherr, E.B., 1984. $\delta^{13}C$ measurements as indicators of carbon flow in marine and freshwater ecosystems. Contributions in Marine Science 27, 13-47.

Michener RH, Schell DM 1994. Stable isotope ratios as tracers in marine aquatic food webs. In: Lajtha K, Michener RH (eds) Stable isotopes in ecology and environmental science. Blackwell Scientific Publications, Oxford, p 138-157

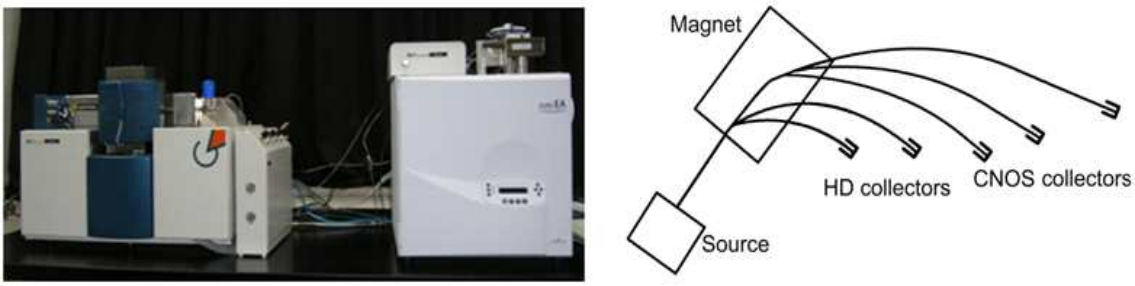

그림 1. 안정동위원소 질량분석기(Isotope Ratio Mass Spectrometry, IRMS)

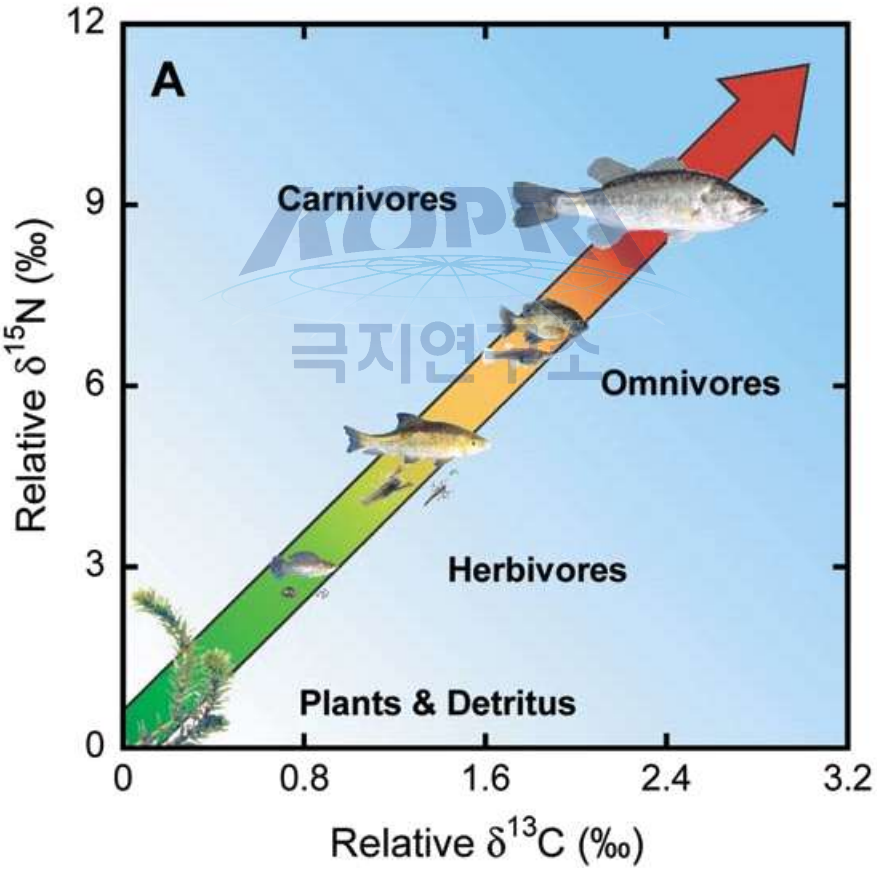

그림 2. 탄소와 질소안정동위원소비의 먹이망에 따른 분별효과

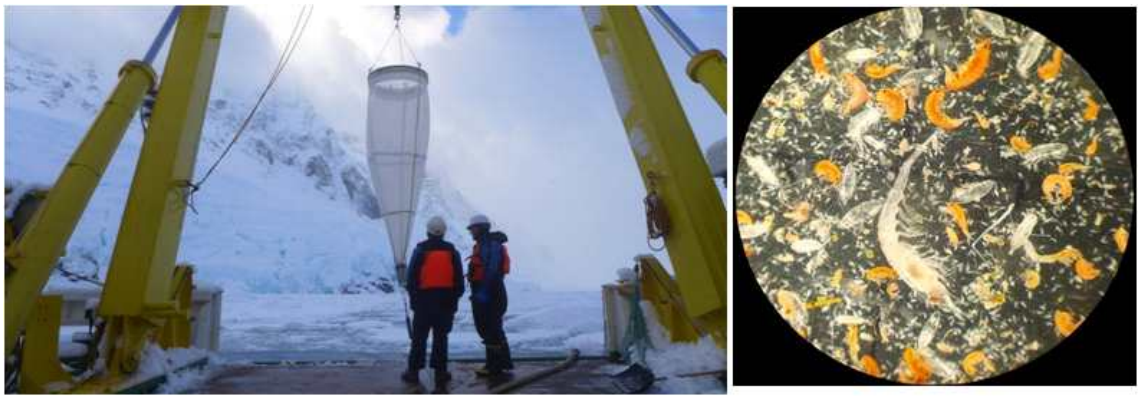

그림 3. 동물플랑크톤 채집광경(좌)과 동물플랑크톤 시료 (우)

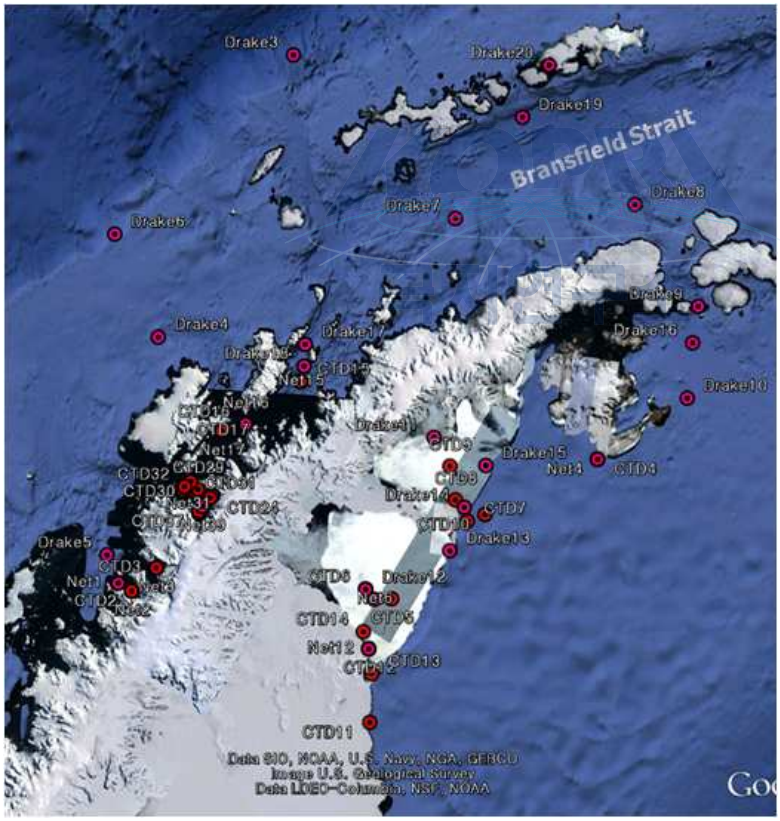

그림 4. 2013년 아라온 크루즈를 통한 남극반도 주변 연안 해양환경 조사 정점

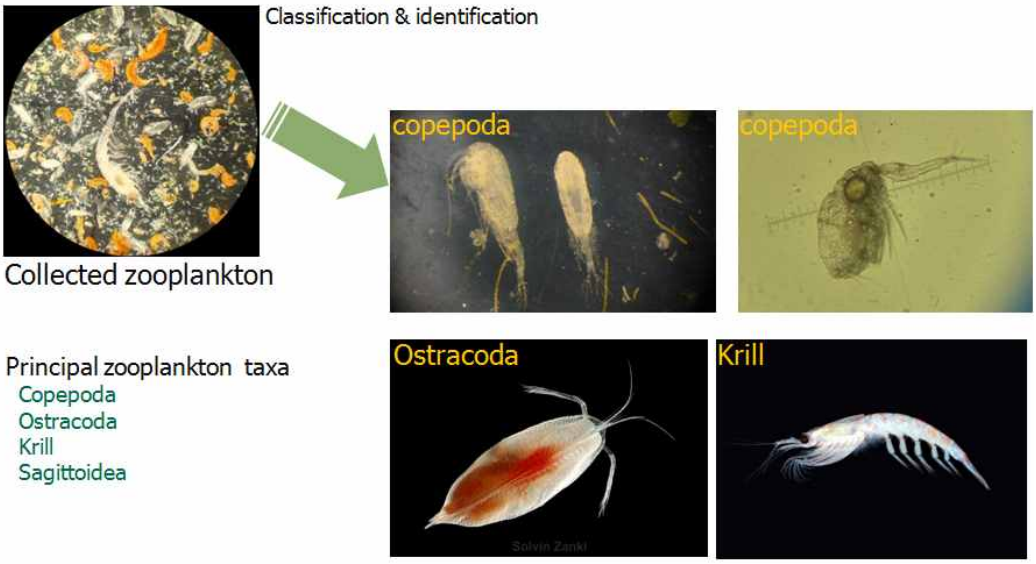

그림 5. 남극반도 주변 연안 해역에서 우점하여 출현하는 동물플랑크톤 그룹

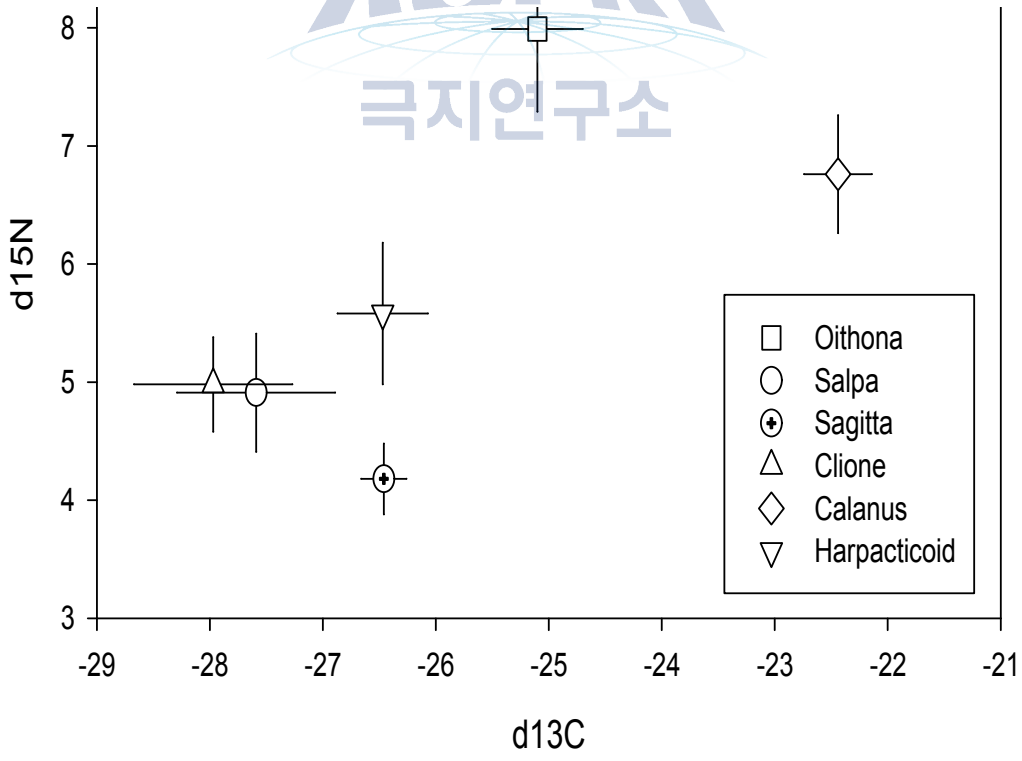

그림 6. 주요동물플랑크톤 분류군의 탄소 및 질소안정동위원소비

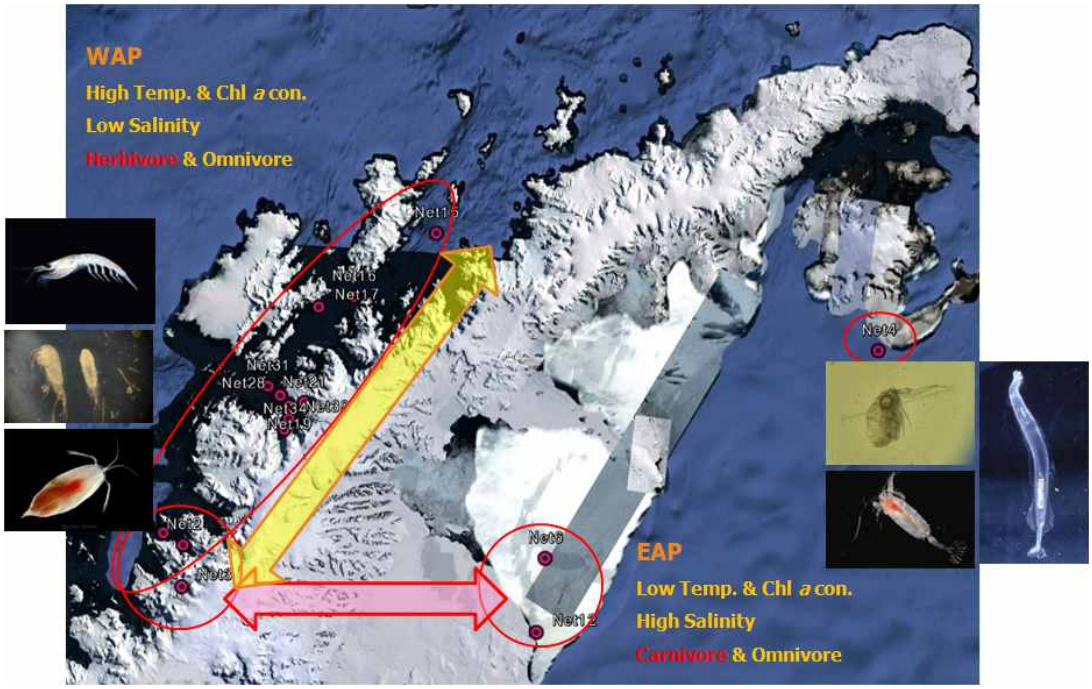

그림 7. 출현하는 동물플랑크톤 우점종의 지역별 차이

제 19 장

Thermal characteristics of soil and water during summer at King Sejong Station, King George Island, Antarctica[12)]

Jin-Yong Lee[1], Ho Il Yoon[2]

[1]Kangwon National University
[2]Korea Polar Research Institute

Abstract: Soil temperatures, water temperatures, and weather parameters were monitored at a variety of locations in the vicinity of King Sejong station, King George Island, Antarctica, during sum-mer 2010 - 2011. Thermal characteristics of soil and water were ana-lysed using time-series analyses, apparent thermal diffusivity (ATD), and active layer thickness. The temperatures of pond water and nearby seawater showed the distinctive diurnal variations and cor-related strongly with solar radiation (r = 0.411 - 0.797). Soil tem-perature (0.1 - 0.3 m depth) also showed diurnal fluctuations that decreased with depth and were directly linked to air temperature (r = 0.513 - 0.783) rather than to solar radiation; correlation decreased with depth and the time lag in the response increased by 2 - 3 hours per 0.1 m of soil depth. Owing to the lack of snow cover, summertime soil temperature was not decoupled from air temperature. Estimated ATD was between 0.022 and 29.209 mm2/sec, showed temporal and spatial variations, and correlated strongly with soil moisture content. The maximum estimated active layer thickness in the study area was a 41 - 70 cm, which is consistent with values reported in the previous work.

12) 이 연구 결과는 다음의 논문으로 출판되었음: Jin-Yong, Lee Hyoun Soo, Lim, Ho Il Yoon. Thermal characteristics of soil and water during summer at King Sejong Station, King George Island, Antarctica. eosciences Journal Vol. 20, No. 4, p. 503 ~516, August 2016

1. Introduction

Temperatures of the ground surface and the soil active layer in the Arctic and Antarctic are highly sensitive to outer atmo-spheric conditions and are good indicators of climate change (Guglielmin, 2004, 2006; Conovitz et al., 2006; Kim et al., 2007; Adlam et al., 2010; Wu et al., 2010). Because the active layer controls heat flux from the atmosphere to the perma-frost (Smith, 1990; Lachenbruch, 1994), understanding the thermal behaviour of the active layer is crucial to predicting the long-term behaviour and stability of permafrost (Guglielmin, 2006; Kowalewski et al., 2006; Iijima et al., 2010). Recent studies have focused on the thermal properties of soil in order to estimate the influence of climate on the seasonal freezing and thawing depths of permafrost (Pavlov, 1994; Osterkamp and Romanovsky, 1996, 1999; Jin et al., 2000; Pringle et al., 2003; Potter, 2004; Osterkamp, 2005; Han et al., 2006; Zhang et al., 2008).

Soil temperature varies according to a somewhat regular pattern that expresses both diurnal and annual cyclicity (Burgess et al., 2000; Hinkel et al., 2001; Ikard et al., 2009), but its most obvious controls are air temperature, incoming solar radiation, and cloud and snow cover (Bockheim and Hall, 2002; Guglielmin, 2004; Kowalewski et al., 2006). In addi-tion, heat transfer is controlled by soil moisture and texture (Hinkel et al., 2001; Pringle et al., 2003). Consequently, the (apparent) thermal diffusivity of a soil changes with time and season and is generally higher in winter than in summer (Han and Jung, 1994; Pringle et al., 2003; Ikard et al., 2009).

In this study, temperatures of soil, meltwater ponds, and seawater were measured hourly during the austral summer of 2010 - 2011 (21 December 2010~9 January 2011) in the vicinity of King Sejong station, King George Island, Antarctica. Time-series analyses, including auto-correlation, cross-cor-relation, and spectral density functions, were conducted for the monitored data to enhance understanding of the thermal behaviour of this region. Thermal diffusivities of soil layers at six locations were estimated using temperature data from 0.1, 0.2, and 0.3 m depths and three different methods, and then were compared by location. The effect of soil moisture on the estimated thermal diffusivities was also evaluated. Using the vertical profiles of soil temperature at the six

locations, the thickness of the active layer at each location was deter-mined and compared with findings by other studies in the Antarctic Peninsula and its offshore islands (e.g., Bockheim and Hall, 2002; Bockheim et al., 2007; Adlam et al., 2010). The results add to the understanding of the thermal characteristics of this coastal region of Antarctica.

2. Methods and materials

2.1. Study Site

The study area is in a coastal area of the Barton Penin-sula, King George Island, west Antarctica (Fig. 1), where a Korean Antarctic Research Station (King Sejong Station) has been operating since 1988. Research facilities at the sta-tion, which covers about 0.4 km2 (Kim et al., 2007) at topographic elevations between 5 and 15 m above sea level, include a weather monitoring system and an aerosol observatory. The weather monitoring system records wind speed, wind direction, air temperature, relative humidity, air pressure, precipitation, and solar radiation every 10 minutes.

The climate of the study area is cold but humid owing to the maritime effect (Lee et al., 2004; Kim et al., 2007; Lim et al., 2014). Climatic data for 1988 to 2006 at the station (Cho et al., 2008) indicate an annual mean air temperature of −1.6 °C, with a summer mean of 1.7 °C and a winter mean of −5.1 °C. The annual mean precipitation for the study year was 484.0 mm, and about 30% of total precipitation was delivered in summer. The annual mean wind speed was 8.0 m/sec, and winds were predominantly from the northwest and southwest (Chung et al., 2004; Kim et al., 2007). Annual mean relative humidity was 88.9%, and humidity expressed very little annual variation. According to Lee et al. (2008), the annual mean air temperature during 1956 to 2006 grad-ually increased at a rate of 0.037 °C per year, and total pre-cipitation also increased over the last 20 years (1988–2007).

2.2. Temperature Monitoring

Temperature was monitored in water and soil. Hourly water temperature monitoring was performed at six locations, including five pond or meltwater areas (OB1 and OB3 – OB6) and one seawater location (OB2; Fig. 1). Automatic sensors (LT or LTC Levelogger, Solinst, Canada) measured temperature, water level, and/or electrical conductivity at depths of 0.5 to 2 m below the pond or seawater surface. The operating tem-perature of these sensors is –20 to 80 °C and the tempera-ture resolution is 0.1 °C.

Soil temperature loggers (iButton, Dallas Semiconductor, USA) were installed at six locations (SJ1 – SJ6) at depths of 0.1, 0.2, and 0.3 m (Fig. 1). These thermochrons perform poorly when soil is water-saturated. Thus, prior to installation, each thermochron was inserted into a 50 mL glass bottle filled with soil from the installation location and then sealed. Delay in the temperature response of the thermochron associated with this extra complexity appears to be minimal (Lee et al., 2013). The sensor range is from –40 to 85 °C, in increments of 0.5 °C. The thermochrons collected temperature data at 1-hour inter-vals. One thermochron went missing during the study and was probably stolen by Antarctic skuas.

In addition to automatic temperature monitoring, manual measurement of soil temperature (mostly surface soil) was conducted at 28 locations in the vicinity of the research sta-tion using a probe (5TE, Decagon Devices, USA) that also measured soil moisture content (volumetric). The temperature range of this probe is –40 to 50 °C at a resolution of ±0.1 °C. At the end of the automatic temperature monitoring (9 Jan-uary 2011), the vertical distributions of soil temperature and moisture (depths = 0.1, 0.2, and 0.3 m) were also investigated at the six locations (SJ1 – SJ6).

Grain size analyses of soils at the six locations (0.1 – 0.3 m depth soil column) were conducted with a laser particle size analyzer (Mastersizer 2000, Malvern Instruments, UK). Table 1 shows results of the grain size analyses. The effective grain size (de) ranged from 0.006 to 0.024 cm, and the uniformity coefficients (Cu) were between 5.99 and 13.53, indicating generally poorly sorting, which is a common characteristic of Antarctic soils (Lee et al., 2004). Soil characteristics in this area are quite variable at a local scale: soils at SJ1 and SJ5 are dominated by very fine material, whereas those at SJ2 and SJ3 are

generally coarser.

2.3. Time-series Analysis

Time-series analysis has been widely used to analyse both continuously and regularly monitored data, and to identify characteristics such as inter-dependency of successive values and repetitive behaviours (Lee et al., 2013). The most com-monly used functions are auto-correlation, cross-correlation, and spectral density. Auto-correlation identifies the degree of self-dependency and any memory effect, whereas cross-correlation shows the relationship between two suites of time-series data (Angelini, 1997; Larocque et al., 1998). Spectral density, a Fourier transformation of the auto-correlation, reveals any periodic variation in time-series data (Lee and Lee, 2000). Time-series analysis using these three functions was applied to hourly data gathered during this study. Prior to the time-series analysis, the data were de-trended using linear regres-sion to highlight more distinct short-term variations and to remove low-frequency noise (Lee et al., 2013). Water-level data were adjusted according to coeval atmospheric pressure measurements.

2.4. Thermal Diffusivity and Active Layer Depth

Thermal diffusivity (♋) is a measure of the ease with which a soil changes temperature (Hinkel et al., 2001; Pringle et al., 2003). This study used three methods of estimating (apparent) thermal diffusivity (ATD) of soil layers using time-series temperature data; only one-dimensional heat conduction was considered (e.g., Hinkel, 1997; Hinkel et al., 2001; Guglielmin, 2004; Han et al., 2006; Ikard et al., 2009). The first method used was the equation for amplitude attenuation with depth (Hinkel et al., 1990; Hinkel, 1997; Guglielmin, 2006; Roberto, 2012),

$$\alpha = \frac{\omega}{2}\left[\frac{z_2 - z_1}{\ln(\Delta T_1/\Delta T_2)}\right]^2, \qquad (1)$$

where ω is the fundamental angular frequency, z1 and z2 are the measured depths, and ΔT1 and ΔT2 are the amplitudes of the soil temperature fluctuations at z1 and z2, respectively (Gug-lielmin, 2004). Amplitude was determined in this study using the maximum and minimum temperatures in one cycle (Koo et al., 2003). The second method uses the equation for time lag with depth,

$$\alpha = \frac{1}{2\omega}\left[\frac{z_2 - z_1}{\delta t}\right]^2, \qquad (2)$$

where Δt is the phase lag observed at depths of z1 and z2 (Guglielmin, 2004). The third method is a logarithmic equation based on the Fourier series solution for heat conduction (Seemann, 1979; Verhoef et al., 1996; Koo et al., 2003),

$$\alpha = \frac{2\omega(z_2 - z_1)^2}{\left[\ln\frac{(T_1 - T_3)^2 + (T_2 - T_4)^2}{(T_1' - T_3')^2 + (T_2' - T_4')^2}\right]^2}, \qquad (3)$$

where Ti and Ti′ are the temperatures measured every π/2ωhours at depths z1 and z2, respectively. The calculated apparent thermal diffusivities using the three methods were then compared.

The active layer depth (thickness), defined as the maxi-mum depth of the 0 °C isotherm, can be determined using a mechanical probe (Gooseff et al., 2007; Ramos et al., 2007; Ikard et al., 2009) or by the 0 °C intercept of the annual max-imum soil temperature profile (Burn, 1998; Gugliemin et al., 2003; Adlam et al., 2010). In this study, the date of the annual thermal maximum was when the soil temperature at the deepest monitored depth (0.3 m) reached its maximum.

3. RESULTS AND DISCUSSION

3.1. Atmospheric Conditions and Water Temperatures

Hourly atmospheric data from 17 December 2010 to 10 Jan-uary 2011 for the weather monitoring system at the research station (Fig. 2) show that hourly precipitation (mostly rainfall) was between 0 and 4.3 mm, with most of the rainfall occurring on 27 and 28 December. Air temperature ranged between -1.32 and 8.69 °C (mean = 1.64 °C) and slowly increased with time, but with some non-periodic fluctuation (not daily). The peak air temperature was recorded at 15:00 on 3 January 2011. Air pressure gradually increased (range = 966 - 1006 mb and mean = 987 mb), with some fluctuations (not daily). Solar radiation ranged from a low of 0.46 W/m2 to a high of 962 W/m2, with a mean of 185.5 W/m2, and showed the most striking daily variation of all of the data types. The most subdued varia-tion in solar radiation was on the days having the most pre-cipitation (27 and 28 December).

Figure 3 shows water levels, electrical conductivities (ECs), and temperatures of seawater and pond water. Seawater levels in Bransfield Strait showed a combination of diurnal and semi-diurnal variations (Vidal et al., 2012); the greatest ampli-tude of the fluctuation was approximately 1.35 m. Water lev-els in ponds varied little but increased distinctly with an effect attributed to the influx of meltwater in summer. The ECs of seawater (OB2) were between 24.01 and 30.06 mS/cm (mean = 28.98 mS/cm), but were relatively stable and did not cor-relate with tidal cycles. The ECs at OB1 (pond water), which was located immediately adjacent to the shore (seawater), were very high (range = 2.15 - 25.79 mS/cm, mean = 10.75 mS/cm), but showed decreasing trends that were also attributable to the influx of fresh meltwater (Lim et al., 2014). Other ponds (OB3, OB4) also exhibited decreasing EC, although the trends were somewhat less clear and the EC values were very low (0.07 - 0.31 mS/cm for OB3 and 0.02 - 0.06 mS/cm for OB4). Water temperatures exhibited daily variations with differ-ent amplitudes (Fig. 3c). Temperature fluctuations of pond waters were generally greater than those of seawater. A very subdued temperature fluctuation on 28 December was prob-ably related to the very weak variations in the solar radiation on that rainy day (Fig. 2b). In general, water temperature increased gradually over the monitoring interval.

3.2. Soil Temperatures

Soil temperatures at 0.1, 0.2, and 0.3 m depths ranged from 0 to 9 °C at SJ1, −0.5 to 4 °C at SJ2, 0 to 13 °C at SJ3, 0.5 to 11 °C at SJ4, −0.5 to 7.5 °C at SJ5, and 0.5 to 5 °C at SJ6 (Fig. 4). Soil temperatures showed distinct daily variations and an overall increase during the study; the magnitude of the vari-ation decreased with depth. A phase shift (time lag) was present with depth due to the time required to transmit heat from the ground's surface (Hinkel, 1997; Pringle et al., 2003; Guglielmin, 2006; Isaksen et al., 2011). Daily fluctuation was absent on 28 December owing to rainy conditions.

Surface temperatures measured on 5 to 7 January 2011 at 28 locations around the research station varied markedly with time (Fig. 5). The highest temperatures, ranging from 4.7 to 9.2 °C, were in the afternoon (14:00 – 17:00), and the lowest temperatures, ranging from 2.4 to 4.6 °C, were recorded in the morning (08:00 – 09:00) and evening (19:00 – 20:00). Mois-ture content did not show any significant daily variation, rang-ing from 0.017 to 0.302 m3/m3 (total mean = 0.102 m3/m3). The highest moisture contents were at locations near the beach (around SJ6).

3.3. Auto-correlations

Figure 6 shows the auto-correlation and spectral density functions of the weather parameters, water levels, electrical conductivities, and water temperatures. The auto-correlation of precipitation decreased most rapidly, with a brief lag time, which is characteristic of the random behaviour of precip-itation (Angelini, 1997; Lee and Lee, 2000). Although both air temperature and solar radiation varied periodically, solar radiation showed a more distinct diurnal periodicity (Fig. 6b). Air pressure varied on a relatively longer time scale, with only a few peaks of spectral density at lower frequencies. Auto-correlation of pond water levels showed longer duration and long lag times (Fig. 6c), which indicates that ponds were not generally affected by short-term phenomena such as tides, precipitation, or air pressure. Instead, pond water lev-els should be most strongly affected by the influx of inland meltwater. Seawater level exhibited distinctive, short-term variations including diurnal and

semidiurnal periodicities (Fig. 6d). Auto-correlations of the ECs showed relatively slowly decreasing trends, indicating longer periodicities, which is supported by spectral density peaks at very low frequen-cies (Fig. 6f). Water temperatures showed the most peculiar periodic (daily) variations (Fig. 6g), as was expected. Seawater temperature (OB2) exhibited a less distinct repetitive behaviour than did pond water, because of a behaviour that may be a function of the very large heat capacity of seawater relative to pond water.

Figure 7 shows auto-correlation and spectral density functions of soil temperatures with different depths at six loca-tions. The auto-correlations showed very similar patterns, but stronger interdependency and a longer memory effect were generally observed with deeper depth. Auto-correlations of SJ1 and SJ5 showed shorter memory effects than those for SJ2 and SJ3. This result may be due to the much higher proportion of fine material at these sites (Table 1), although other factors, including soil moisture and organic matter, can strongly affect the thermal response (Hinkel et al., 2001). Fine-grained material can quickly attenuate thermal stress with a short propagation length (Peters-Lidard et al., 1998; Abu-Hamdeh and Reeder, 2000). All of the spectral density functions of the subsur-face temperatures exhibited distinctive diurnal frequencies, but the peculiar peaks at frequencies below 0.01 indicate the existence of much longer cyclic behaviours, such as biweekly or semi-monthly variations.

3.4. Cross-correlations

Figure 8 shows cross-correlations among solar radiation, air temperature, and water temperature. The solar radiation exhibited a high correlation with air temperature with a very short lag time ($r = 0.474$ with 1 hour delay), which indicates that they are directly linked (Cho et al., 2008). Air temperature also showed strong correlation ($r = 0.424 - 0.622$; mean = 0.495) with seawater and pond water temperatures, with lag times of 12 to 14 hours (mean = 12.8 hours). Solar radiation correlated strongly with water temperature ($r = 0.411 - 0.797$; mean = 0.657) with lag times of 14 to 15 hours (mean = 14.2 hours). Based on the lag times among the three parameters, it is inferred that high incoming

radiation caused high air temperatures and hence high water temperatures in summer (Guglielmin, 2004; Adlam et al., 2010).

Figure 9 presents the cross-correlations among air temperature, solar radiation, and soil temperatures. Air temperature cor-related strongly with soil temperature (0.623 - 0.709 for SJ1, 0.657 - 0.783 for SJ2, 0.513 - 0.633 for SJ3, 0.709 - 0.714 for SJ4, 0.597 - 0.683 for SJ5, and 0.642 - 0.713 for SJ6) with substantial time lags (16 - 23 hours at SJ1, 18 - 23 hours at SJ2, 15 - 20 hours at SJ3, 15 - 19 hours at SJ4, 17 - 22 hours at SJ5, and 18 - 21 hours at SJ6). Correlation generally decreased with depth, and the time lag increased by 2 to 3 hours per 10 cm depth increase. Solar radiation also correlated strongly with soil temperature (0.509 - 0.732 for SJ1, 0.289 - 0.405 for SJ2, 0.436 - 0.659 for SJ3, 0.653 - 0.778 for SJ4, 0.473 - 0.627 for SJ5, and 0.510 - 0.650 for SJ6) although the correlation was weaker than that with air temperature and lag time was greater (18 - 24 hours at SJ1, 19 - 23 hours at SJ2, 17 - 22 hours at SJ3, 17 - 20 hours at SJ4, 18 - 24 hours at SJ5, and 20 - 22 hours at SJ6). Considering the correlations and time lags of air temperature and solar radiation with soil temperature, air temperature had a stronger influence on soil temperature in summer (Zhang et al., 1997; Conovitz et al., 2006; Bockheim et al., 2007; Adlam et al., 2010). Soil temperatures were not decoupled from air temperatures because no snow was present (Guglielmin, 2004; Farbrot et al., 2011).

3.5. Thermal Diffusivity and Active Layer

Figure 10 summarizes ATD, as estimated using the three methods. The ATD values for depths of 0.1 to 0.3 m in the study area ranged from 0.022 to 29.209 mm2/sec (0.125 - 21.221 mm2/sec for SJ1, 0.058 - 29.209 mm2/sec for SJ2, 0.161 - 29.209 mm2/sec for SJ3, 0.262 - 29.209 mm2/sec for SJ4, 0.022 - 21.221 mm2/sec for SJ5, and 0.125 - 5.305 mm2/sec for SJ6), with median values 0.4 - 3.3 mm2/sec (mean = 1.3 mm2/sec) greater than values reported in a previous study performed in the area in winter (0.8 - 1 mm2/sec for 0.4 - 0.6 m depth; June 2003 and August 2004; Han et al., 2006). The ATD values of upper soils in summer in this study are much larger because heat transfer is affected not only by conduction (as in winter) but also by other factors such as percolating

rain water (Hinkel, 1997). Thermal diffusivity correlated strongly with moisture content (r2 = 0.91; Fig. 11).

Estimated ATD values showed very large temporal vari-ations, but they were generally greatest on 28 and 29 Decem-ber, which were the days of the heaviest and most frequent rainfall (Fig. 2). Percolating rainwater enhances soil moisture content, which facilitates thermal transfer downward through soils (Hinkel, 1997; Hinkel et al., 2001; Ikard et al., 2009; Iijima et al., 2010). The ATD estimates varied according to the method used, but no systematic trend was present. Spatial variations and generally increasing trends in ATD values are attributed to increasing moisture content with depth (0.2 - 0.3 m).

Table 2 shows the active layer thickness estimated using the highest temperatures of the deepest soils (0.3 m) in the area. The maximum active layer thickness ranged from 0.41 to 0.70 m (mean = 0.54 m), which is consistent with values from elsewhere in the Antarctic islands (0.4 - 1.5 m) but is larger than those of inland and upland valleys (0.15 - 0.4 m) and plateau fringe areas (Bockheim and Hall, 2002). Prox-imity to a coast is known to be a controlling factor in active layer thickness, and this is probably the best explanation for the relatively large values in the study area. Jeong and Yoon (2001) and Lee et al. (2004) had reported the active layer depth as 1 m, but their estimate was not based on temperature measurement or mechanical probing, and the estimates in this study are considered to be more reliable.

4. Conclusions

Study of thermal characteristics of soil and water in the vicinity of King Sejong station, King George Island, West Antarctica, during summer (December 2010 to January 2011) produced the following conclusions.

1) Air and water temperatures slowly increased during the monitoring time, with different daily variations. Soil tempera-ture showed distinct daily variations with increasing trends, and the magnitude of the variations decreased with depth.

2) Auto-correlation of soil temperatures indicated similar patterns, but stronger interdependency and longer memory effects were generally observed

with deeper depth. All of the spectral density functions of the subsurface temperatures showed distinctive diurnal frequencies.

3) Air temperature correlated strongly with soil temperature; correlation decreased with depth. Solar radiation also correlated with soil temperatures, but with more significant time lags.

4) The ATD values for depths of 0.1 to 0.3 m ranged from 0.022 to 29.209 mm2/sec, and median values were somewhat greater than winter values. Thermal diffusivity correlated very strongly with moisture content. Active layer thickness ranged from 0.41 to 0.70 m, with a mean of 0.54 m; these values are reli-able because they are based on soil temperature measurements.

Future work in this area should include multi-year mon-itoring, measurement of soils to deeper depths (>0.3 m), and inclusion of more locations at different elevations above sea level.

남극 킹조지섬 세종 기지의 여름 동안 토양가 물의 열적 특성

이진용[1], 윤호일[2]

[1]강원대학교, [2]한국해양과학기술원 부설 극지연구소

요약: 토양의 온도, 수온, 기후 변수들이 남극 킹조지섬의 세종기지 인근의 여러지점에서 2010-2011년 동안 모니터링 되었다. 토양과 물의 열적인 특성은 시계열적 분석, ATD, 활성층의 두께를 이용하여 분석하였다. 연못 물의 수온과 가까운 해수온은 뚜렷한 일주기의 변동성을 나타내었고, 태양광과 강하게 연동되어 있었다. 토양의 온도는 태양광 보다 대기온도와 관련되어 있었다. 상관관계는 토양의 깊이가 깊어짐에 따라 감소하였고 2-3시간/0.1m의 갭이 존재하였으나, 일주기 변동성을 보였다. 눈이 덮여 있지 않은 여름철 토양의 온도는 대기 온도와 잘 일치 하였다. 추정된 ATD는 0.022-29.209 mm^2/sec였고, 시공간적인 변동을 보였으며, 토양의 습도와 강한 상관관계를 보였다. 연구지역에서 최대 활성층 두께는 41-70 cm로 이전 연구들에서 보도된 것과 잘 일치 한다.

참고문헌

Abu-Hamdeh, N.H. and Reeder, R.C., 2000, Soil thermal conductivity, effects of density, moisture, salt concentration, and organic matter. Soil Science Society of America Journal, 64, 1285 - 1290.

Adlam, L.S., Balks, M.R., Seybold, C.A., and Campbell, D.I., 2010, Temporal and spatial variation in active layer depth in the McMurdo Sound Region, Antarctica. Antarctic Science, 22, 45 - 52.

Angelini, P., 1997, Correlation and spectral analysis of two hydrogeological systems in Central Italy. Hydrological Sciences Journal, 42, 425 - 439.

Bockheim, J.G., Campbell, I.B., and McLeod, M., 2007, Permafrost distribution and active-layer depths in the McMurdo Dry Valleys, Antarctica. Permafrost and Periglacial Processes, 18, 217 - 227.

Bockheim, J.G. and Hall, K.J., 2002, Permafrost, active-layer dynamics and periglacial environments of continental Antarctica. South African Journal of Science, 98, 82 - 90.

Burgess, M., Smith, S.L., Brown, J., Romanovsky, V., and Hinkel, K., 2000, Global Terrestrial Network for Permafrost (GTN-P): permafrost monitoring contributing to global climate observations. Current Research 2000-E14, Geological Survey of Canada, p. 1-8.

Burn, C.R., 1998, The active layer: two contrasting definitions. Permafrost and Periglacial Processes, 9, 411 - 416.

Cho, H.K., Kim, J., Jung, Y., Lee, Y.G., and Lee, B.Y., 2008, Recent changes in downward longwave radiation at King Sejong Station, Antarctica. Journal of Climate, 21, 5764 - 5776.

Chung, H., Lee, B.Y., Chang, S-K, Kim, J.H., and Kim, Y., 2004, Ice cliff retreat and sea-ice formation observed around King Sejong Station in King George Island, West Antarctica. Ocean Polar Research, 26, 1 - 10.

Conovitz, P.A., MacDonald, L.H., and McKnight, D.M., 2006, Spatial and temporal active layer dynamics along three glacial meltwater streams in the McMurdo Dry Valleys, Antarctica. Arctic, Antarctic and Alpine Research, 38, 42 - 53.

Farbrot, H., Hipp, T.F., Etzelmüller, B., Isaksen, K., Ødegard, R.S., Schuler, T.V.,

and Humlum, O., 2011, Air and ground temperature variations observed along elevation and continentality gradients in southern Norway. Permafrost and Periglacial Processes, 22, 343 - 360.

Gooseff, M.N., Barrett, J.E., Northcott, M.L., Bate, B., Hill, K.R., Zeglin, L.H., Bobb, M., and Takacs-Vesbach, C.D., 2007, Controls on the spatial dimensions of wetted hydrologic margins of two Antarctic lakes. Vadose Zone Journal, 6, 41 - 848.

Guglielmin, M., 2004, Observations on permafrost ground thermal regimes from Antarctica and the Italian Alps, and their relevance to global climate change. Global and Planetary Change, 40, 159 - 167.

Guglielmin, M., 2006, Ground surface temperature (GST), active layer and permafrost monitoring in continental Antarctica. Permafrost and Periglacial Processes, 17, 133 - 143.

Guglielmin, M., Balks, M.R., and Paetzold, R., 2003, Towards and Antarctic active layer and permafrost monitoring network. Proceedings of the 8th International Conference on Permafrost, Zurich, July 21 - 25, p. 337 - 341.

Han, U. and Jung, H.C., 1994, Temperature response in the permafrost at the Sejong Station, Antarctica. Journal of the Korean Earth Science Society, 15, 170 - 176.

Han, U., Lee, C.K., Jeong, S., Lee, B.Y., and Nam, S.H., 2006, The studies on the temperature and thermal properties of the active layer soil at the Sejong Station, Antarctica. Journal of the Geological Society of Korea, 42, 577 - 586.

Hinkel, K.M., 1997, Estimating seasonal values of thermal diffusivity in thawed and frozen soils using temperature time series. Cold Region Science and Technology, 26, 1 - 15.

Hinkel, K.M., Outcalt, S.I., and Nelson, F.E., 1990, Temperature variation and apparent thermal diffusivity in the refreezing active layer, Toolik Lake, Alaska. Permafrost and Periglacial Processes, 1, 265 - 274.

Hinkel, K.M., Paetzold, F., Nelson, F.E., and Bockheim, J.G., 2001, Patterns of soil temperature and moisture in the active layer and upper permafrost at Barrow, Alaska: 1993 - 1999. Global and Planetary

Change, 29, 293 - 309.

Iijima, Y., Fedorov, A.N., Park, H., Suzuki, K., Yabuki, H., Maximov, T.C., and Ohata, T., 2010, Abrupt increases in soil temperatures following increased precipitation in a permafrost region, central Lena River basin, Russia. Permafrost and Periglacial Research, 21, 30 - 41.

Ikard, S.J., Gooseff, M.N., Barrett, J.E., and Takacs-Vesbach, C., 2009, Thermal characterization of active layer across a soil moisture gradient in the McMurdo Dry Valleys, Antarctica. Permafrost and Periglacial Processes, 20, 27 - 39.

Isaksen, K., Ødegård, R.S., Etzelmüller, B., Hilbich, C., Hauck, C., Farbrot, H., Eiken, T., Hygen, H.O., and Hipp, T.F., 2011, Degrading mountain permafrost in Southern Norway: Spatial and temporal variability of mean ground temperatures, 1999 - 2009. Permafrost and Periglacial Processes, 22, 361 - 377.

Jeong, G.Y. and Yoon, H.I., 2001, The origin of clay minerals in soils of King George Island, South Shetlands, West Antarctica, and its implications for the clay-mineral compositions of marine sediments. Journal of Sedimentary Research, 71, 833 - 842.

Jin, H., Li, S., Cheng, G., Shaoling, W., and Li, X., 2000, Permafrost and climatic change in China. Global and Planetary Change, 26, 387 - 404.

Koo, M.H., Kim, Y., Suh, M., and Suh, M.S., 2003, Estimating thermal diffusivity of soils in Korea using temperature time series data. Journal of the Geological Society of Korea, 39, 301 - 317.

Kim, J.H., Ahn, I.Y., Lee, K.S., Chung, H., and Choi, H.G., 2007, Vegetation of Barton Peninsular in the neighbourhood of King Sejong Station (King George Island, maritime Antarctic). Polar Biology, 30, 903 - 916.

Kowalewski, D.E., Marchant, D.R., Levy, J.S., and Head, J.W., 2006, Quantifying low rates of summertime sublimation for buried glacier ice in Beacon Valley, Antarctica. Antarctic Science, 18, 421 - 428.

Lachenbruch, A.H., 1994, Permafrost, the active layer, and changing climate. U.S. Geological Survey Open-File Report, 94-694, Menlo Park, 43 p.

Larocque, M., Mangin, A., Razack, M., and Banton, O., 1998, Contribution of correlation and spectral analyses to the regional study of a karst

aquifer (Charente, France). Journal of Hydrology, 205, 217 - 231.

Lee, J., Jin, Y.K., Hong, J.K., Yoo, H.J., and Shon, H., 2008, Simulation of a tidewater glacier evolution in Marian Cove, King George Island, Antarctica. Geosciences Journal, 12, 33 - 39.

Lee, J.Y. and Lee, K.K., 2000, Use of hydrologic time series data for identification of recharge mechanism in a fractured bedrock aquifer system. Journal of Hydrology, 229, 190 - 201.

Lee, J.Y., Lim, H.S., Yoon, H.I., and Park, Y., 2013, Stream water and groundwater interaction revealed by temperatures analyses in the Haean basin, Korea. Water, 5, 1677 - 1698.

Lee, Y.I., Lim, H.S., and Yoon, H.I., 2004, Geochemistry of soils of King George Island, South Shetland Islands, West Antarctica: Implications for pedogenesis in cold polar regions. Geochimica et Cosmochimica Acta, 68, 4319 - 4333.

Lim, H.S., Park, Y., Lee, J.Y., and Yoon, H.I., 2014, Geochemical characteristics of meltwater and pond water on the Barton and Weaver peninsulas of King George Island, West Antarctica. Geochemical Journal, 48, 409 - 422.

Osterkamp, T.E. and Romanovsky, V.E., 1996, Characteristics of changing permafrost temperatures in the Alaskan Arctic, U.S.A. Arctic and Alpine Research, 28, 167 - 273.

Osterkamp, T.E. and Romanovsky, V.E., 1999, Evidence for warming and thawing of discontinuous permafrost in Alaska. Permafrost and Periglacial Processes, 10, 17 - 37.

Osterkamp, T.E., 2005, The recent warming of permafrost in Alaska. Global and Planetary Change, 49, 187 - 202.

Pavlov, A.V., 1994, Current changes of climate can permafrost in the Arctic and Sub-Arctic of Russia. Permafrost and Periglacial Processes, 5, 101 - 110.

Pereira, E.B., 1990, Radon-222 time series measurements in the Antarctic peninsula (1986 - 1987). Tellus, 42B, 39 - 45.

Peters-Lidard, C.D., Blackburn, E., Liang, X., and Wood, E.F., 1998, The effect of soil conductivity parameterization on surface energy fluxes and

temperatures. Journal of the Atmospheric Sciences, 5, 1209 - 1224.

Potter, C., 2004, Predicting climate change effect on vegetation, soil thermal dynamics, and carbon cycling in ecosystems of interior Alaska. Ecological Modeling, 175, 1 - 24.

Pringle, D.J., Dickinson, W.W., Trodahl, H.J., and Pyne, A.R., 2003, Depth and seasonal variations in the thermal properties of Antarctic Dry Valley permafrost from temperature time series analysis. Journal of Geophysical Research, 108, 2474. DOI: 10.1029/ 2002JB002364

Ramos, M., Vieira, G., Gruber, S., Blanco, J.J., Hauck, C., Hidalgo, M.A., Tomé, D., Neves, M., and Trindade, A., 2007, Permafrost and active layer monitoring in the maritime Antarctic: Preliminary results from CALM sites on Livingston and Deception Islands. USGS OF-2007-1047, Short Research Paper 070, U.S. Geological Survey and the National Academies. DOI: 10.3133/of 2007-1047. srp070

Roberto, F.M.M., Carlos, E.G.R.S., Everton, L.P., Felipe, N.B.S., Elpidio, I.F.F., and James, G.B., 2012, Active layer temperature in two Cryosols from King George Island, Maritime Antarctica. Geomorphology, 155 - 156, 12 - 19.

Seemann, J., 1979, Measuring technology. In: Seeman, J., Chirkov, Y.I., Lomas, J., and Primault, B. (eds.), Agrometeorology. Springer- Verlag, Berlin, p. 40 - 45.

Smith, M.W., 1990, Potential responses of permafrost to climatic change. Journal of Cold Regions Engineering, 41, 29 - 37.

Verhoef, A., van den Hurk, B.J.J.M., Jacobs, A.F.G., and Heusinkveld, B.G., 1996, Thermal soil properties for vineyard (EFEDA-I) and savanna (HAPEX-Sahel) sites. Agricultural and Forest Meteorology, 78, 1 - 18.

Vidal, J., Berrocoso, M., and Fernández-Ros, A., 2012 Study on tides and sea levels at Deception and Livingston islands, Antarctica. Antarctic Science, 24, 193 - 201.

Wu, Q., Zhang, T., and Liu, Y., 2010, Permafrost temperatures and thickness on the Qinghai-Tibet Plateau. Global and Planetary Change, 72, 32 - 38.

Zhang, T., Osterkamp, T.E., and Stamnes, K., 1997, Effects of climate on the active layer and permafrost on the North Slope of Alaska, USA.

Permafrost and Periglacial Processes, 8, 45 - 67.

Zhang, Y., Chen, W., and Riseborough, D.W., 2008, Transient projects of permafrost distribution in Canada during the 21st century under scenarios of climate change. Global and Planetary Change, 60, 443 - 456.

Table 1. Results of grain size analyses for active layer (soil for 0.1–0.3 m depth)

Location	d_{60} (mm)	d_{10} (mm)	Uniformity coefficient (C_u)	Sorting	Effective grain size (d_e, cm)
SJ1	0.84	0.06	13.53	Poor	0.006
SJ2	2.53	0.24	10.45	Poor	0.024
SJ3	1.90	0.14	13.24	Poor	0.014
SJ4	1.19	0.15	7.97	Poor	0.015
SJ5	0.43	0.05	8.29	Poor	0.005
SJ6	0.94	0.16	5.99	Moderate	0.016
Mean	1.31	0.13	9.91	Poor	0.013

Table 2. Active layer thickness calculated using profiles of the maximum soil temperatures. Date of occurrence was selected at the date of the maximum soil temperature at 0.3 m

Location	Date (mm/dd/yy)	$T_{0.1\,m}$ (°C)	$T_{0.2\,m}$ (°C)	$T_{0.3\,m}$ (°C)	Active layer thickness (m)
SJ1	05/01/11	7.0	5.5	4.0	0.56
SJ2	04/01/11	3.5	2.5	1.5	0.45
SJ3	05/01/11	10	8.5	6.5	0.67
SJ4	06/01/11	9.0	7.5	6.0	0.70
SJ5	05/01/11	7.0	4.5	2.5	0.41
SJ6	05/01/11	na	5.0	3.0	0.45
Mean	–	–	–	–	0.54

Note: na is not available.

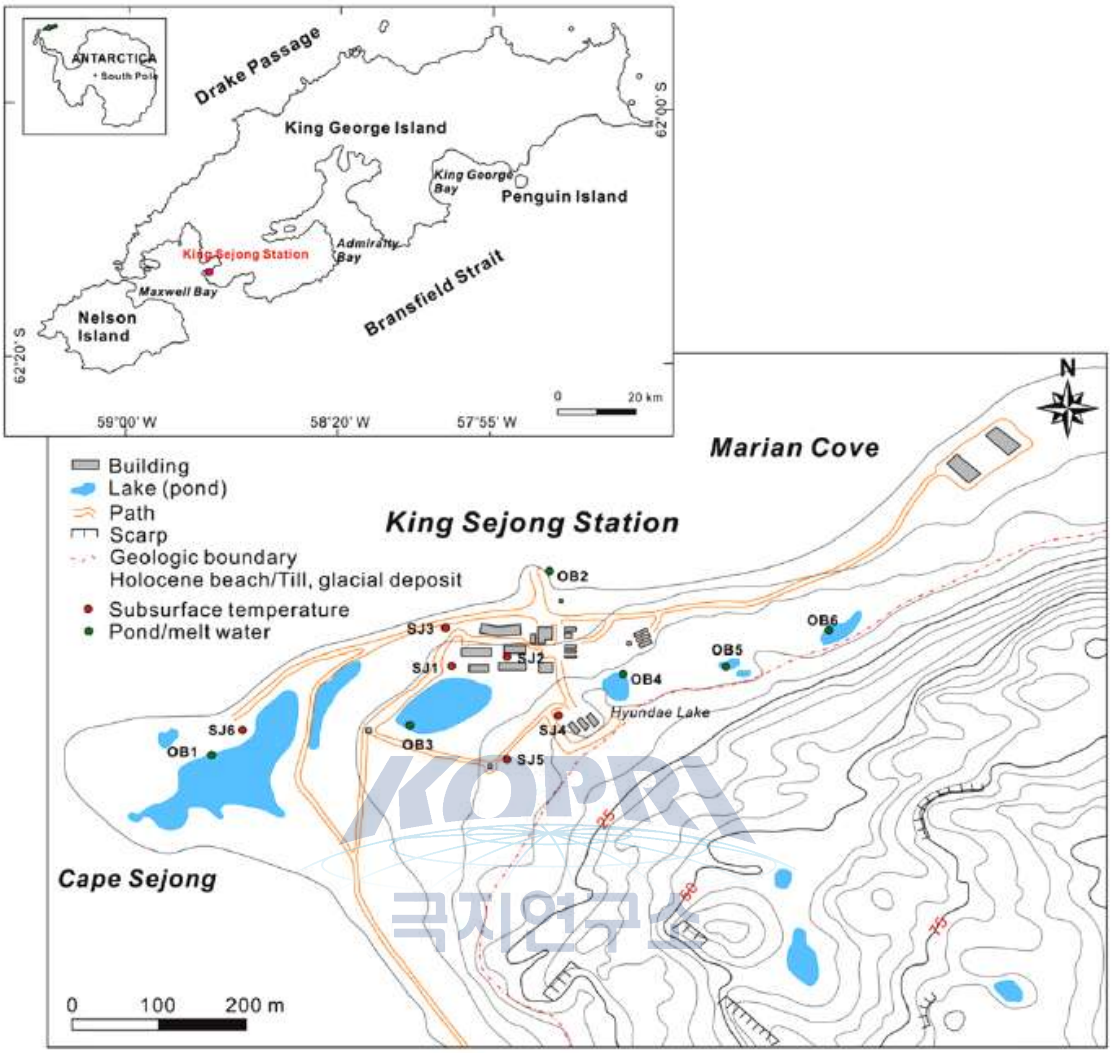

Fig. 1. Location of the study area showing monitoring points for subsurface (SJ1 – SJ6), pond water (OB1, OB3 – OB6), and seawater (OB2) temperatures.

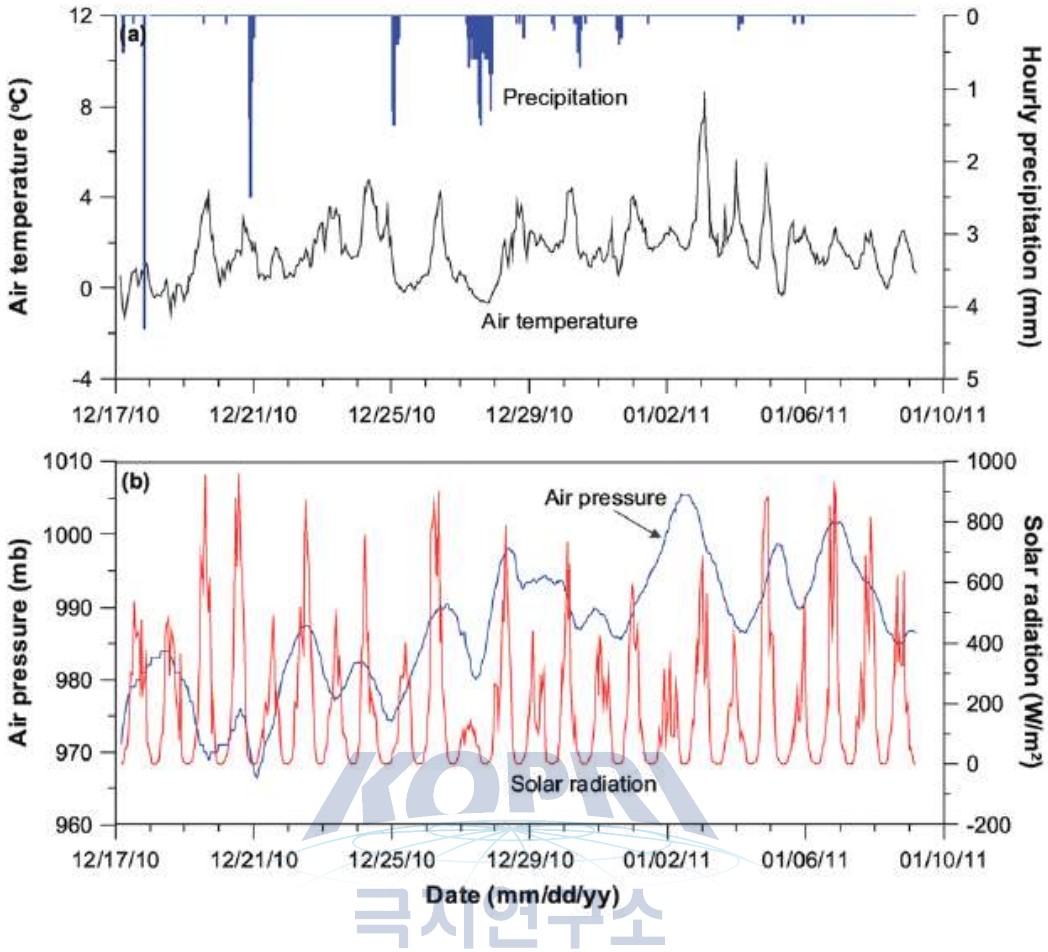

Fig. 2. Atmospheric conditions measured at a weather station at King Sejong Station from 17 December 2010 to 10 January 2011.

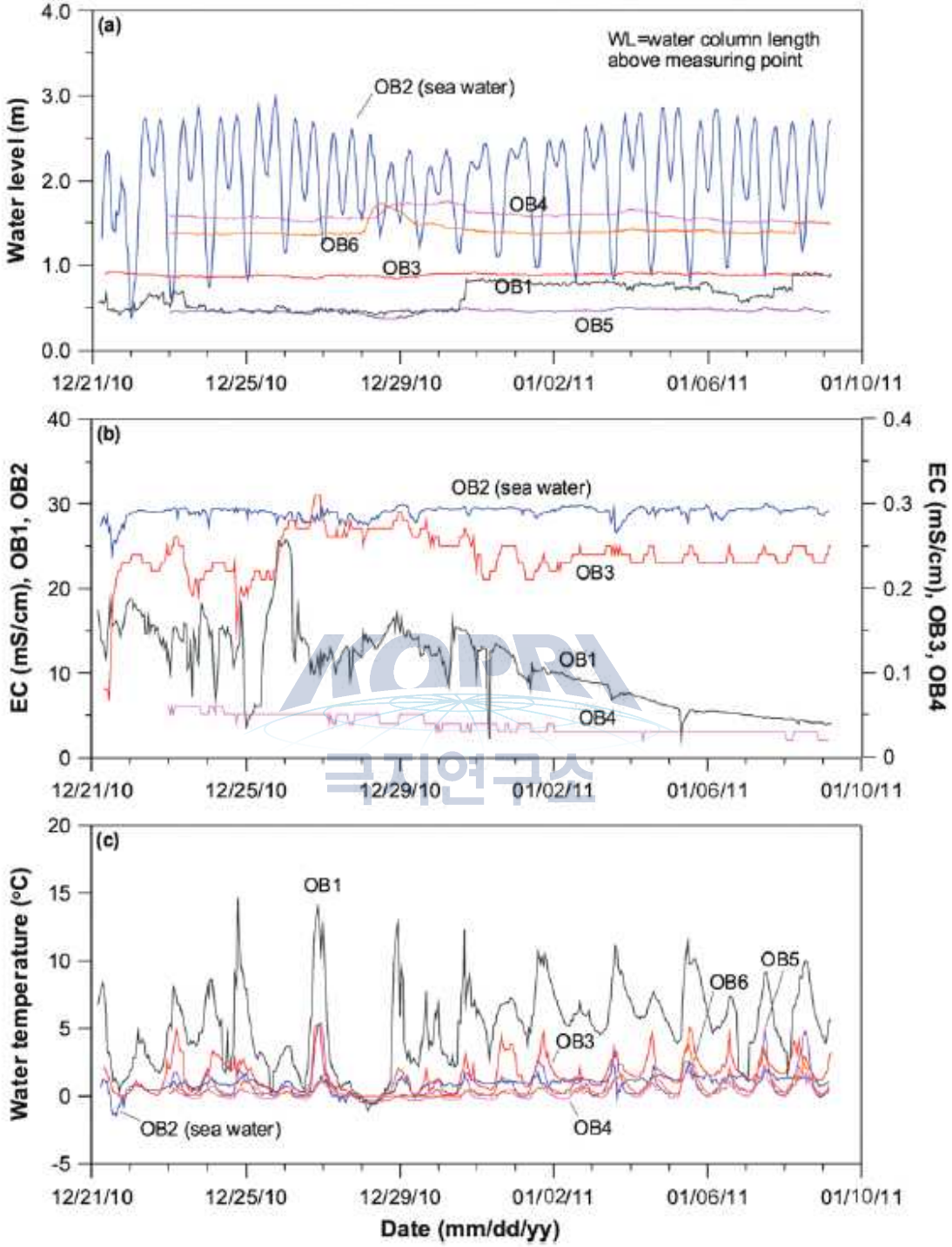

Fig. 3. Variations in (a) water level (water column length above measuring point), (b) electrical conductivity, and (c) water temperature.

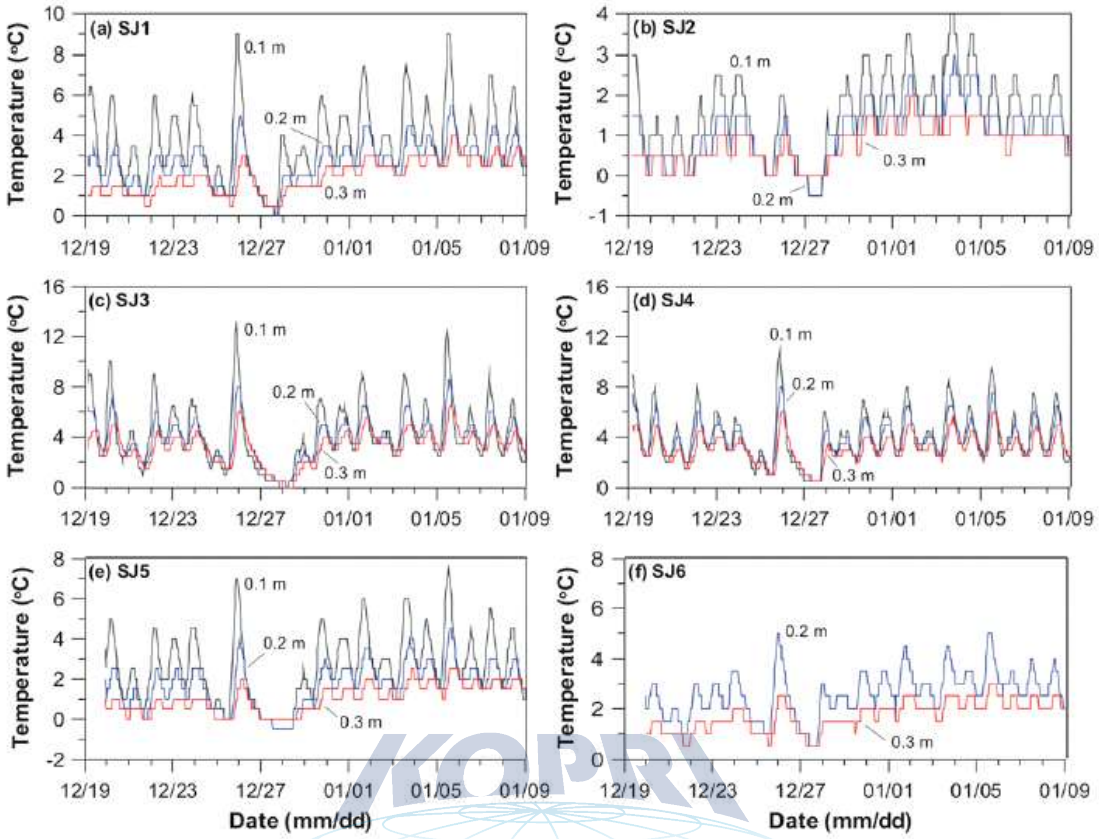

Fig. 4. Subsurface temperature at each monitoring location at depths of 0.1, 0.2, and 0.3 m. Temperature data for 0.1 m depth at SJ6 are not shown because the thermocouple went missing.

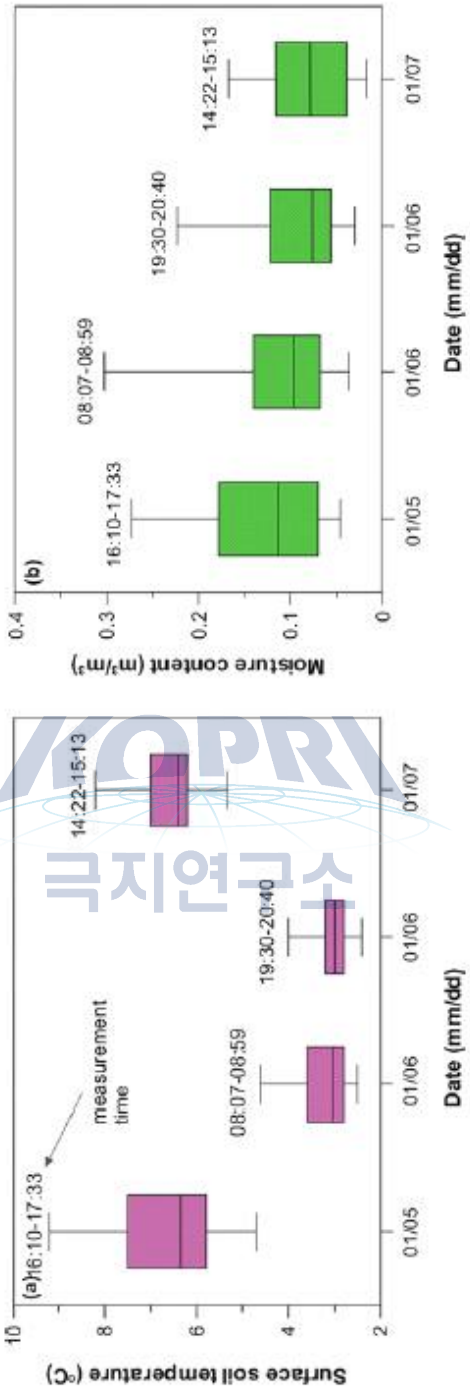

Fig. 5. Temperature and moisture content of surface soil at 28 locations around King Sejong Station.

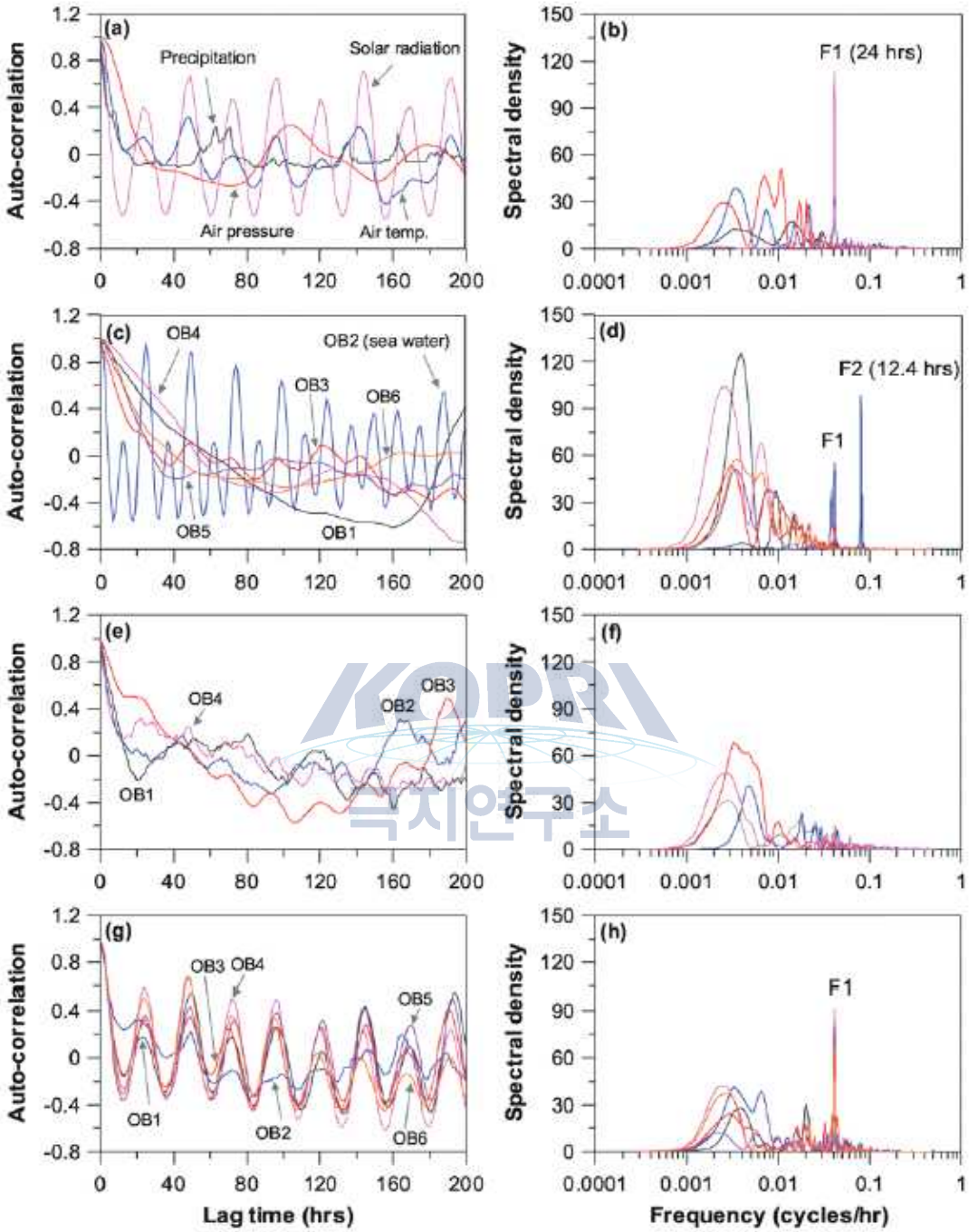

Fig. 6. Autocorrelation and spectral density functions for weather conditions (a and b), water levels (c and d), electrical conductivities (e and f), and water temperatures (g and h). The truncation period for auto-correlation was 200 hours.

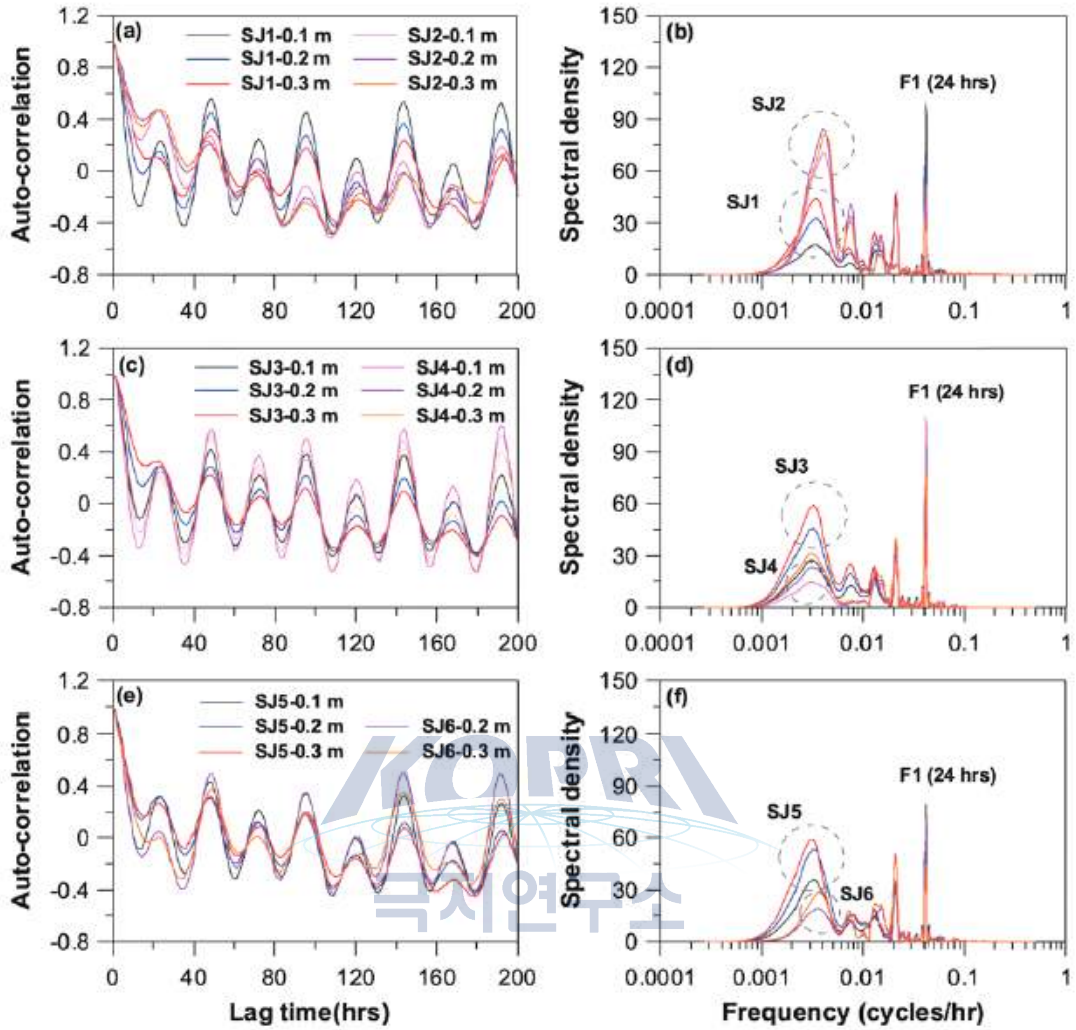

Fig. 7. Autocorrelation and spectral density functions of subsurface temperatures at different depths (0.1 - 0.3 m) at SJ1 and SJ2 (a and b), SJ3 and SJ4 (c and d), and SJ5 and SJ6 (e and f). The truncation period for auto-correlation was 200 hours.

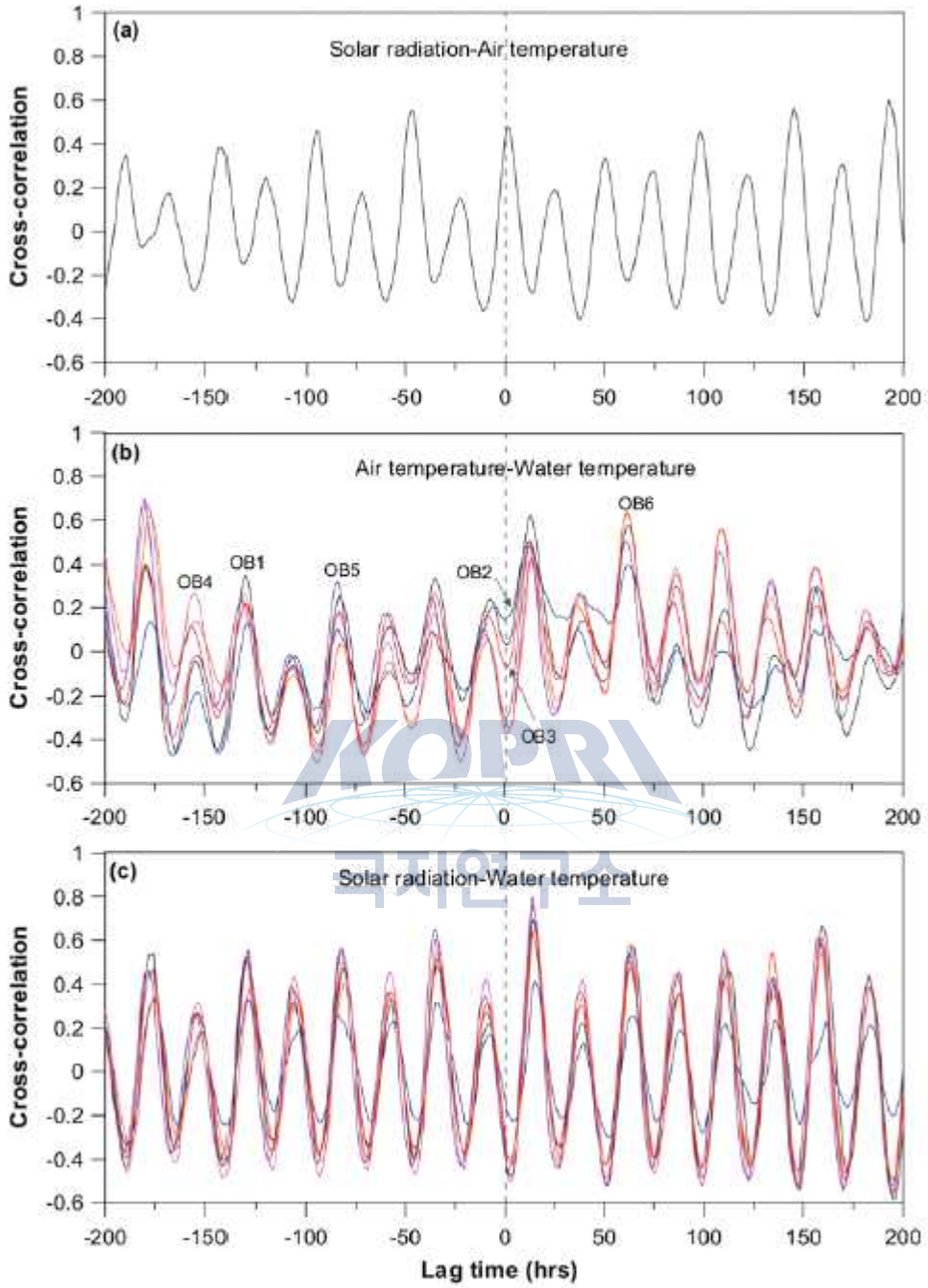

Fig. 8. Cross-correlations between (a) solar radiation and air temperature, (b) air temperature and water temperature, and (c) solar radiation and water tem-perature. The truncation period was 200 hours.

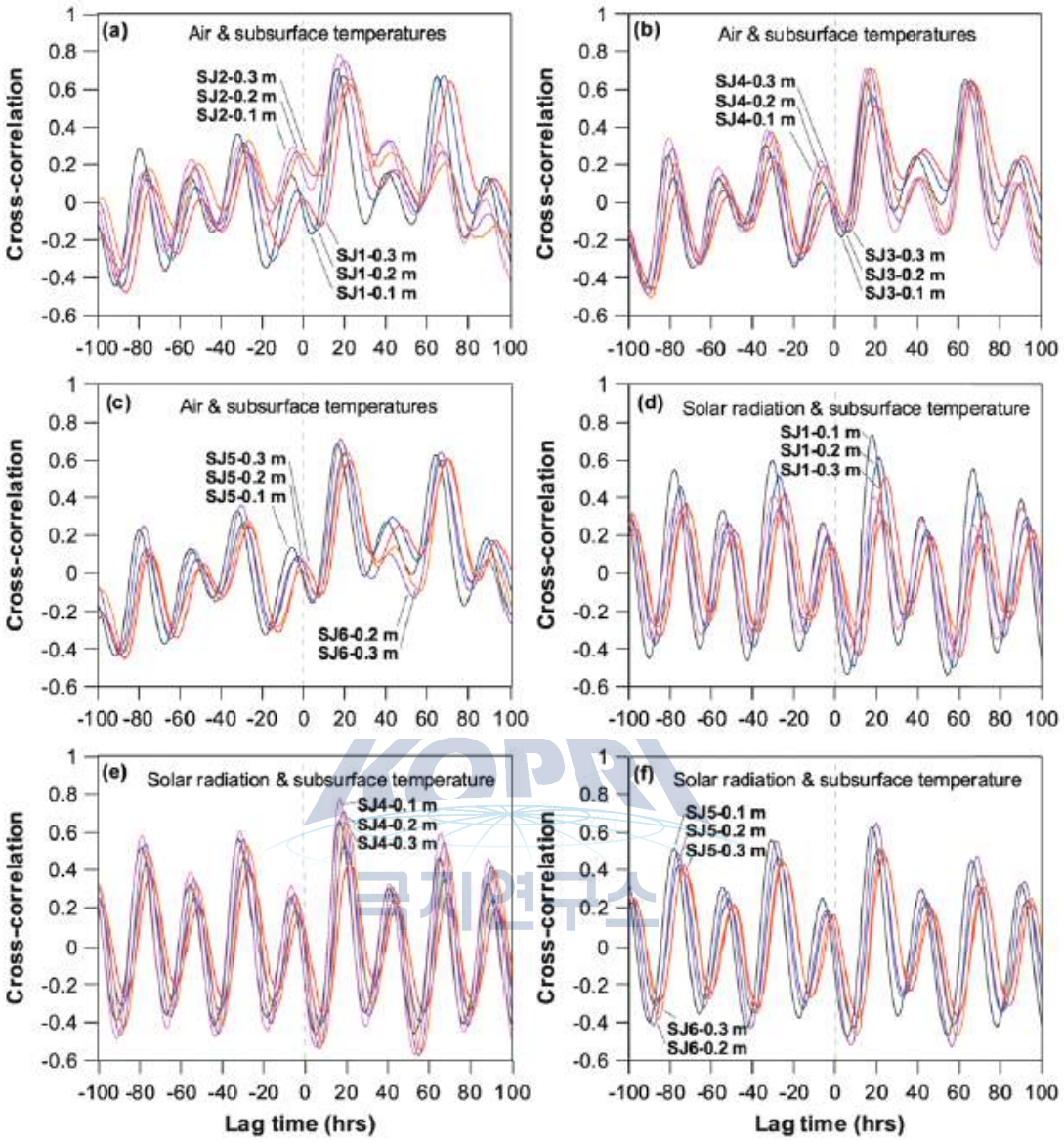

Fig. 9. Cross-correlations between air temperature and subsurface temperature at different depths at SJ1 to SJ6 (a, b, and c) and between solar radiation and subsurface temperatures (d, e, and f). The truncation period was 100 hours.

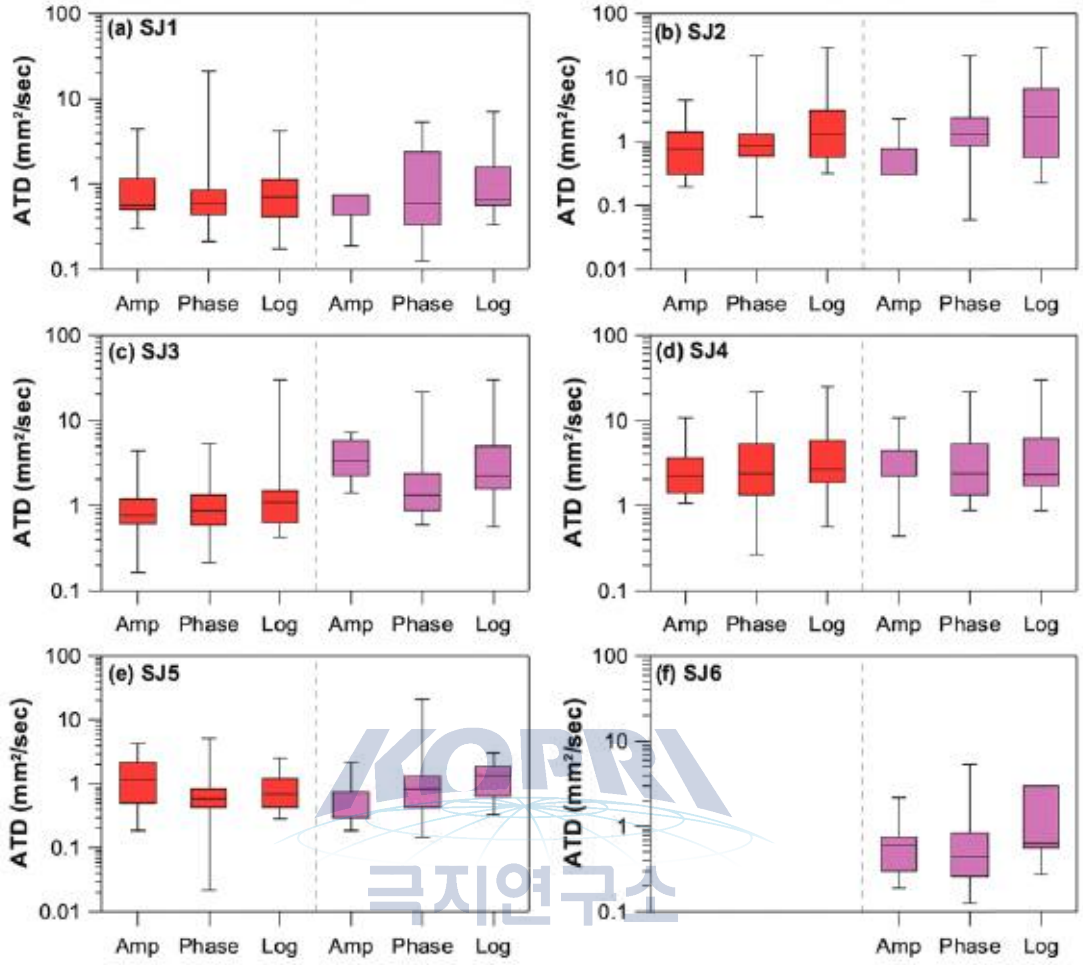

Fig. 10. Estimates (n = 21) of apparent thermal diffusivity for different depth intervals (the first three are for 0.1 - 0.2 m depth and the second three are for 0.2 - 0.3 m depth) using three methods: the amplitude and phase methods (Pringle et al., 2003) and a logarithmic equation (Seeman, 1979; Verhoef et al., 1996).

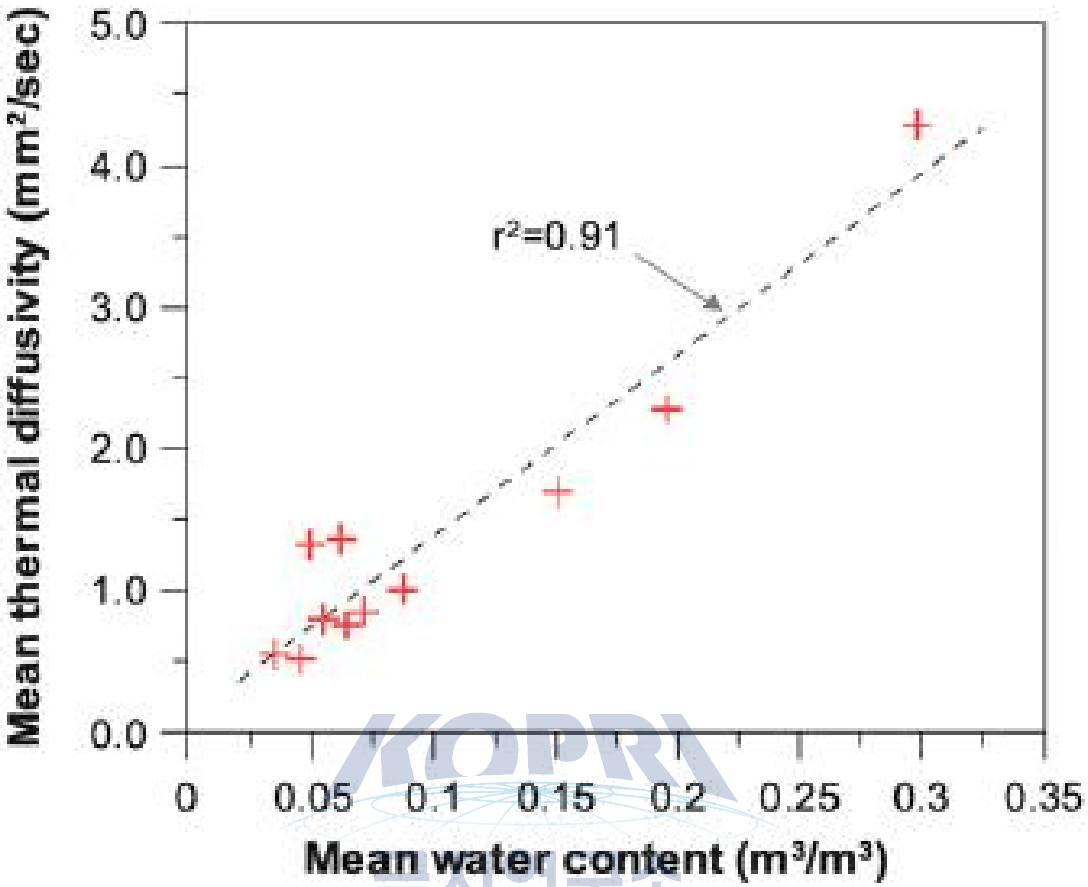

Fig. 11. Relationship between soil moisture content and calculated apparent thermal diffusivity, based on mean moisture content (9 January 2011) for each interval (0.1 - 0.2 and 0.2 - 0.3 m) and mean thermal diffusivity (three methods).

제 20 장

Late Quaternary glaciation in the Nun-Kun massif, northwestern India[13)]

Yeong Bae Seong[1*], Ho Il Yoon[2], Kyu-Cheul Yoo[2]

[1]Korea National University
[2]Korea Polar Research Institute

Abstract: The late Quaternary glacial history of the Nun-Kun massif, located on the boundary between the Greater Himalaya and the Zanskar range in northwestern India, was reconstructed. On the basis of morphostratigraphy and 10Be dating of glacial landforms (moraines and glacial trimlines), five glacial stages were recognized and defined, namely: (i) the Achambur glacial stage dated to Marine Oxygen Isotope Stage 3 to 4 (38.7 – 62.7 ka); (ii) the Tongul glacial stage dated to the early part of the Lateglacial (16.7 – 17.4 ka); (iii) the Amantick glacial stage dated to the later part of the Lateglacial (14.3 ka, 11.7 – 12.4 ka); (iv) the Lomp glacial stage dated to the Little Ice Age; and (v) the Tanak glacial stage, which has the youngest moraines, probably dating to the last few decades or so. Present and former equilibrium-line altitudes (ELAs) were calculated using the standard area accumulation ratio method. The average present-day ELA of ~4790 m above sea level in the Greater Himalaya is lower than those in the Ladakh and Zanskar ranges, namely 5380 and ~5900 m a.s.l., respectively. The ELA in the Zanskar range is higher than in the Ladakh range, possibly due to the higher peaks in the Ladakh range that are able to more effectively capture and store snow and ice. ELA depressions decrease towards the Ladakh range (i.e. inner Plateau). Peat beds interbedded with aeolian deposits that cap the terminal moraine of Tarangoz Glacier suggest

13) 이 연구 결과는 다음의 논문으로 출판되었음: Lee, S. Y., Seong, Y. B., Owen, L. A., Murari, M. K., Lim, H. S., Yoon, H. I., & Yoo, K. C. (2014). Late Quaternary glaciation in the Nun-Kun massif, northwestern India. Boreas, 43(1), 67-89.

millennial-time-scale climate change throughout the Holocene, with soil formation times at c. 1.5, c. 3.4 and c. 5.2 ka, probably coinciding with Holocene abrupt climate change events. Given the style and timing of glaciation in the study area, it is likely that climate in the Nun-Kun region is linked to Northern Hemisphere climate oscillations with teleconnections via the mid-latitude westerlies.

1. Introduction

The Himalayan - Tibetan orogen has the greatest mass of glaciers outside of the polar realms and is considered the third largest component of the Earth's cryosphere (Qiu 2008). An understanding of the nature of climate change and associated glacial and hydrological responses in this region is important for modelling future climate change both regionally and globally. The impressive glacial and associated landforms preserved in the valleys of the orogen allow reconstructions of former glacier advances. In recent years numerous researchers began to develop glacial chronologies throughout the region (Sharma & Owen 1996; Phillips et al. 2000; Richards et al. 2000a, b; Taylor & Mitchell 2000; Sch[a WITH DIAERESIS]fer et al. 2001, 2008; Owen et al. 2002, 2003a, b; Tsukamoto et al. 2002; Yi et al. 2002; Zech et al. 2003, 2009; Barnard et al. 2004a, b, 2006; Meriaux et al. 2004; Chevalier et al. 2005; Abramowski et al. 2006; Seong et al. 2007, 2009; Koppes et al. 2008; Kong et al. 2009; Scherler et al. 2010; Chevalier et al. 2011; Hedrick et al. 2011). These studies show the complexity of the glacial record and the possible complex interactions between the south Asian monsoon and the mid-latitude westerlies in driving glaciation (Overpeck et al. 1996; Owen et al. 1997, 2001, 2008, 2012; Benn & Owen 1998; Finkel et al. 2003; Zech et al. 2005, 2009; Dortch et al. 2010b; Scherler et al. 2010; Hedrick et al. 2011).

We examine the evidence for glaciation around the Nun-Kun massif in the semi-arid Himalayan region of northern India, which is situated at a key location just within the present-day northernmost limit of the south Asian monsoon, to help determine the importance of the south Asian monsoon and mid-latitude westerlies in driving the glaciation. Mayewski et al. (1984), using the chemistry of an ice core from the Sentick Glacier in Ladakh near Nun-Kun,

showed that the south Asian monsoon is the dominant climate system responsible for supplying moisture to the region. However, the age of the ice within the core of Mayewski et al. (1984) was not well constrained, and it is therefore difficult to use the ice-core data directly to reconstruct the temporal variation of glacier oscillations back into the Quaternary and to infer the dominant climatic driving force throughout the past. Röthlisberger & Geyh (1986), however, were able to define the timing of past glacial oscillations for Sentick Glacier in the Nun-Kun area using humic acid and the total organic method for radiocarbon dating, and suggested that glaciations in the Nun-Kun massif are synchronous with those in the European Alps over the late Quaternary, where Northern Hemisphere climate oscillations dominate. This implies that the mid-latitude westerlies are the dominant forcing factor for driving glaciation in this region, as they teleconnect with the Northern Hemisphere climate oscillations. Strengthened glaciation in the Northern Hemisphere pushes the mid-latitude westerlies farther southwards, which provides more precipitation in the mid-latitude area. By further developing the glacial chronology for the Nun-Kun massif, we aim to examine role of the various climate systems is in this region in driving glaciation. We use field-mapping aided by remote sensing and apply ^{10}Be Terrestrial Cosmogenic Nuclides (TCN), Optically Stimulated Luminescence (OSL), and radiocarbon dating to define the ages of glacial and associated landforms. In addition, we calculate and present former equilibrium-line altitudes (ELAs) of a region from the Greater Himalaya to the Ladakh range to help quantify the degree of glaciation and define topographic influences on glacier growth and retreat.

2. Study area

The Nun-Kun massif, comprising the peaks of Nun (7135 m above sea level (a.s.l.)) and Kun (7077 m a.s.l.), is located between the NW-trending Greater Himalaya and the far western ranges of Zanskar in Northern India. Both the Greater Himalaya and the Zanskar range have an average elevation of ~ 6000 m a.s.l. (Fig 1). Our study areas are situated on north-facing slopes of the Nun-Kun massifs in the Suru Valley, which is drained by the Suru River. The

Suru River defines the western and northern boundaries of the Zanskar range and ultimately flows into the Indus River. The valley preserves extensive glacial and fluvial landforms, including U-shaped valleys and moraines, alluvial fans, river terraces and floodplains. There are two vegetation zones recognized with altitude - alpine meadow and alpine tundra. Alpine meadows, which comprise grasses and shrubs, are usually present along the bottom of the valley, whereas alpine tundra - dominated by lichen and moss - exists on the snow-free rock surfaces. Most of the glaciers are fed by snow avalanche from the steep slopes and direct snowfall, with little rock debris on their surfaces. They exist as isolated cirques or separated by steep icefalls as a result of glacial retreat, possibly during historical times.

The Nun-Kun massif receives precipitation from two climate systems: the Indian monsoon during the summer; and mid-latitude westerlies during the winter (Fig. 1). Previous studies have concluded that two-thirds of the annual precipitation in the Zanskar range is presently supplied by the Indian summer monsoon (Murakami 1987; Benn & Owen 1998). Weather data are rarely recorded in remote regions of the Himalaya, and direct weather and climate data have not yet been measured in the Suru Valley. A 30-year record of climate from the Leh station (34.09°N, 77.34°E; 3514 m a.s.l.) shows that annual precipitation is ~115 mm a−1, with 41% of this falling from July to September and 35% falling from December to March. Precipitation in spring and autumn is <10 mm month−1 (Osmaston et al. 1994; Taylor & Mitchell 2000). In contrast, the area to the west of Leh, including Dras and Kargil, receives winter precipitation that is five times greater than that during summer (Walter & Lieth 1960 - 1967). Dras has considerable precipitation in both winter and spring (~90 mm month^{-1}), and two-thirds of this total annual precipitation is in the form of snow (Osmaston et al. 1994). Apart from Srinagar, the three areas near the Nun-Kun massif have substantial winter precipitation, implying that the nature of regional precipitation changes rapidly across the high mountain ranges of the Himalaya and Karakoram (Fig. 2).

Complex mountain topography generates abrupt and systematic changes in climatic conditions and, in particular, in temperature and precipitation, even over very short distances (Becker & Bugmann 1997; Beniston 2006). Therefore,

the measured climate data from the Leh and the other four stations may not be truly representative of the entire western Zanskar and Himalaya ranges.

Precipitation gradient data from the Greater Himalaya to the Ladakh range were obtained from the Satellite Tropical Rainfall Measuring Mission (TRMM), which is hosted by the National Aeronautics and Space Administration (NASA) Giovanni TRMM Online Visualization and Analysis System (TOVAS) (Fig. 2). The Greater Himalaya receives precipitation of ~800 mm a^{-1}, and the Lahul receives 800 - 900 mm a^{-1}. The Suru and Puga valleys in the western Zanskar range have precipitation of 400 - 600 and 600 - 800 mm a^{-1}, respectively. Annual precipitation in the Ladakh range decreases to 200 - 400 mm a^{-1}. To compare precipitation on a seasonal basis, precipitation data in 2011 were divided into four seasons (March - May, June - August, September - November, and December - February; Fig. 3). Precipitation in all four seasons decreases from SW to NE, reflecting the effects of the topographic barrier of the high ranges on precipitation. At latitudes above 34°N in the Himalaya, winter precipitation is greatest, whereas at latitudes below 34°N, summer precipitation is dominant. The influence of the Indian monsoon and mid-latitude westerlies on the glaciation in northern India probably varied considerably throughout the late Quaternary (Benn & Owen 1998: fig. 1).

3. Methods

3.1. Geomorphological mapping

Topographic maps were generated from 3-arcsecond (~90-m surface resolution) Shuttle Radar Topography Mission (SRTM) Digital Elevation Models (DEMs) in ArcGIS 9.3. Glacial and non-glacial landforms in the study area were identified and mapped in the field aided by Google Earth imagery (Google 2009). Some of the names and locations of glaciers and glacial features were obtained from the reconnaissance maps of Workman (1908). Topographic maps were revised through comparison with landforms identified in the field utilizing GPS and photography.

3.2. ^{10}Be TCN surface exposure age dating

The relative stratigraphy of the various moraines was constructed using morphostratigraphic observations prior to sampling. Three glaciers (Tarangoz, Sentick and Rantac) in the Suru Valley were chosen for study, as their similar size, altitude, proximity, and valley aspect mean that they are likely to have responded synchronously to climatic fluctuations.

A sampling strategy for 10Be TCN dating was devised based on the moraine morphostratigraphy we developed. Where lateral moraines with sharp ridges and little evidence of post-depositional modification were chosen for sampling. End and hummocky moraines were not sampled in order to avoid sampling moraines that are unstable for long periods of time, as shown by Zech et al. (2005) and Dortch et al. (2010a, b) in their studies in the Pamir and Alaska, respectively. The relatively flat ridge moraines (ST2 and ST3) were sampled for dating, however, owing to the lack of moraines with sharp ridges in Sentick Glacier valley. The bedrock was mostly quartz-rich, crystalline rock, which is suitable for 10Be dating. However, most boulders on Tarangoz Glacier moraine (TG3) were composed of carbonate rocks and were not suitable for ^{10}Be dating. At least five moraine boulders were sampled from each moraine ridge for 10Be dating, except for the Tarangoz Glacier moraine (TG3), where only two boulders were sampled.

To avoid the depositional effects of snow and loess, boulders with heights of ~1 m or more (except for a few samples) on a convex surface of a sharp ridge were sampled. The sampling locations were recorded using a GPS, along with a field sketch and photograph of the relative topography (Appendix S1 in the Supporting Information). Skyline angles from each sampling site to the horizon were measured at 10° intervals using a hand-held inclinometer and compass to calculate for topographic shielding. Samples were collected on a sufficiently extensive, flat, and horizontal boulder surfaces. The geomorphic characteristics of the boulders including lithology, texture, and the degree of lichen development and weathering features were recorded.

All the physical and chemical procedures for 10Be dating were performed in the Geochronology Laboratories of Korea University (Korea) and the

University of Cincinnati (USA) following conventional methods described by Kohl & Nishiizumi (1992) and briefly summarized as follows. Rock samples were first crushed and sieved. The 250 - 500 μm size fraction was cleaned to remove carbonates, organics and metals by leaching for >12 h in a mixture of HCl and HNO3. To separate quartz, the sample was chemically leached using 1 and 5% HF and HNO_3 for 3 days at 66°C in an ultrasonic bath. The remaining feldspar and heavy minerals were removed using heavy liquid (LST, lithium heteropolytungstate) and magnetic separation. As it is important to eliminate minerals such as feldspar before dissolution of quartz, the purity of quartz was measured using infrared stimulated luminescence with a Riso OSL Reader. Subsequently, 15 - 30 g of pure quartz was dissolved in a high-concentration mixture of HF and HNO_3. Be and Al standard carriers were gravimetrically added to the quartz. After the quartz was completely dissolved, the solution was evaporated to dryness on a hotplate. Fluoride was removed from the samples by fuming three times with a mixture of HNO_3 - $HClO_4$, and then the sample was dissolved in HCl for stepwise Be separation using anion and cation exchange chromatography. The extracted Be fractions were re-precipitated and neutralized by the addition of ammonium hydroxide. $Be(OH)_2$ was then combusted at 750°C in a quartz crucible. ^{10}Be concentrations were measured on a mixture of BeO with Nb powder in steel targets at the PRIME laboratory of Purdue University (USA).

3.3. OSL dating

The aeolian deposit on Tarangoz Glacier moraine (TG1) was sampled for OSL dating (full geomorphic details of the sampling site are given in the glacial landforms and aeolian deposits in the Nun-Kun area section below). Aeolian deposits are most suitable for OSL dating because they are likely to be nearly perfectly bleached by sunlight or daylight during sediment transportation (Olley et al. 1999). The aeolian deposit has a total thickness of 260 cm in the thickest part of this sediment package. Three samples were obtained at 65, 143 and 236 cm below the surface, where each bed was interbedded with a peaty layer. The aeolian deposit is mainly silt and fine sand with massive structure,

and contains no evidence of bioturbation. Samples were collected in light-tight plastic tubes to prevent exposure to light. The centre part of each sample was preprocessed to measure its luminescence. Samples were sieved using 90 and 125 μm sieves, before 10% HCl, 10% H_2O_2 and 40% HF etching. To identify feldspar contamination, infrared stimulation with infrared-light-emitting diodes (870 nm, 150 mW cm^{-2}) was applied to all quartz samples. Luminescence measurements were conducted on quartz from each sample using a Riso Automated TL/OSL reader following the Single Aliquot Regenerative (SAR) method of Murray & Wintle (2000). Blue-light-emitting diodes (470 nm, 50 mW cm^{-2}) filtered using a green long-pass GG-420 filter were used for stimulating the quartz grains. A 52-mm diameter photomultiplier tube (9235B) filtered through a Hoya U-340 filter was used to detect the OSL signal. Aliquots with poor recuperation (10%) were excluded from the age calculations. All sample preparation and OSL dating was undertaken at the University of Cincinnati.

Samples from both ends of the sampling tubes were used for measuring the dose rate at the Korea Basic Science Institute in O-Chang, Korea. The beta attenuation was assumed as 0.93, and the cosmic contribution was presumed as 0.13 (Gy ka^{-1}). The water content is likely to be variable owing to groundwater conditions in the field, which could possibly affect the dose rate. However, given the arid climate and that the sampling location is ~100 m above the present river, we do not consider that the aeolian deposit had any significant variation in water content throughout its history. Dose rates were recalculated taking into account cosmic ray effects.

3.4.. Radiocarbon dating and $\delta^{13}C$ analysis

Dark brown amorphous peaty layers intercalated with aeolian deposits on the Tarangoz moraine (TG1) were sampled for $\delta^{13}C$ analysis as well as for conventional radiocarbon dating (more details of the site are discussed in glacial landforms and aeolian deposits in the Nun-Kun area section below). All three samples (NKTC1 - 3) were processed following standard procedures and methods, and measured at the Accelerator Mass Spectrometry Facility of the

Korea Institute of Geoscience and Mineral Resources, Daejeon, Korea. All the radiocarbon ages presented in our study and previously published ages were calibrated using CalPal (CalPal 2007).

3.5. ELA analysis

Conventionally, the ELA of a glacier is defined as points on a glacier where annual accumulation exactly balances annual ablation (Benn & Evans 2010). This definition was developed for high-latitude glaciers type, but it is unsuitable for glaciers experiencing a distinct dry season, such as glaciers in the Himalaya (Benn et al. 2005). Therefore, for the present study, use of the steady-state ELA is preferred, which is the average altitude at which annual accumulation balances annual ablation (Benn et al. 2005).

Palaeoprecipitation gradients make it possible to understand past atmospheric circulation patterns and track moisture sources (Miller et al. 1975; Benn & Lehmkuhl 2000). Comparison of ELAs among regions provides an important source of palaeoclimatic gradient data in mountain regions and information on the effect of topography on the health of glaciers along a mountain range, individually responding to similar climate forcing. Thus, it is possible to construct more robust climatological and hydrological models for the prediction of future climate change (Benn & Lehmkuhl 2000).

In addition to the numerical dating of moraines, the precise location of moraines is also required to determine the ELA. The location data of well-preserved end and lateral moraines observed in prior studies were rechecked in the field using GPS data and Google Earth imagery map overlain on DEMs (Google 2009). The three-dimensional aspect of Google Earth image maps was particularly useful in delineating the boundary of palaeoglaciers, essentially identifying trimlines. When enough detailed information was obtained on the past glacier positions, the former glacial extent could be reconstructed in detail, taking into account the valley shape.

A number of variables such as snow supply by avalanche and debris cover can affect ELA analysis, although it was not possible to rigorously account for these in this study owing to a lack of glaciological and

meteorological data. The ELA was calculated using the standard Area Accumulation Ratio (AAR) method. This method assumes a fixed accumulation area relative to glacier area under steady-state conditions (Benn et al. 2005). Previous studies have concluded that the present-day average AAR value of Indian glaciers is 0.48, which indicates that these glaciers are under negative mass balance (Ahmad et al. 2004). However, an ELA construction for the Himalaya showed that the AAR value is typically 0.60 - 0.65 (Owen & Benn 2005), and for the Ladakh and Zanskar ranges the ELA reconstructed using the AAR method yields a value of 0.65 (Burbank & Fort 1985). We used a value of 0.65 for the AAR method in our study.

The Toe-to-Headwall Altitude Ratio (THAR) assumes that the ELA is located at a fixed proportion of vertical distance between head and toe altitudes, making it simple to calculate the ELA (Benn & Lehmkuhl 2000). We used a THAR of 0.5, although we note that some debris-covered glaciers in other regions have a THAR of 0.6 - 0.8 (Clark et al. 1994).

4. Glacial landforms and aeolian deposits in the Nun-Kun area

4.1. Moraines

There are three small valley glaciers on the northwestern slope of the Nun-Kun massif: Sentick, Rantac and Tarangoz glaciers. All three glaciers are located at similar elevations, and advanced into the Suru Valley in the past (Fig. 4). The Suru Valley is U-shaped and displays glacial and associated landforms, including moraines and paraglacial fans. Glacial trimlines produced by a main trunk valley glacier that extended down the Suru Valley are eroded into bedrock on the valley walls at ~300 - 400 m above the present-day valley floor. Bedrock on the trimline east of Sentick Glacier was sampled (NK9 - 11 and NKB1) to date the retreat of the main valley glacier. Samples were obtained at an altitude of ~3700 m a.s.l. along the southern side of the Suru Valley. Moraine remnants of this main glacier are absent, most probably due to erosion by paraglacial processes.

A succession of three moraines is present at the northern mouth of

Sentick Glacier. The outermost moraines (ST1) have a pair of distinctive NW-trending ridges. The oldest moraines have well-preserved sharp ridges. Seven samples (NK15 - 21) for ^{10}Be dating were collected from boulders on the northeastern moraine. A rock glacier in the bottom of the valley is located between the ST1 and ST2 moraines. Very poorly sorted cobbles and boulders cover the surface of the rock glacier. Jagged ice under the patchily distributed sediment is 100 m wide and 300 m long. Two lateral moraines are present along the gorge of Sentick Glacier. The older moraine (ST2) is located behind a younger moraine (ST3). The ST2 and ST3 moraines have denuded slopes and blunt moraine ridges on the western side of the gorge. These two moraines are likely to have formed at a similar time, given the close proximity of ST2 and ST3. Metre-sized boulders are present on the ST2 moraine ridge. These boulders have surfaces characterized by abundant lichen and millimetre-sized weathering pits. Four samples (NK5 - 8) were collected from the boulders for ^{10}Be dating. A further four samples (NK1 - 4) were collected from boulders on the most highly elevated site of ST3 (Figs 4, 5).

A pair of lateral moraines (RT1) is located at the contact of Rantac Glacier with the main valley. Several moraine ridges occur as a latero-frontal moraine complex. In particular, one moraine has an arc-shaped ridge, which bifurcates in front of Tongul village. The fronts of the moraines have been severely eroded by the Suru River in the main valley. Slope deposits and/or alluvial fans cover the down-ice slope of the lateral moraines, and rare boulders are present on top of the moraine ridge. Therefore, on the basis of morphostratigraphy, RT1 was assigned to the same group as TG1 and ST1 (Figs 4, 6).

Tarangoz Glacier valley contains the most distinctive moraine groups, and we therefore use the moraine groups in the Tarangoz Valley for correlation with moraines in adjacent glacial valleys. The TG1 and TG2 moraines are present at the confluence of a tributary and the main Suru Valley. A steep north - south-trending ridge bounds the outermost and oldest pair of moraines (TG1). The moraine ridge on the northwestern side is surrounded by three alluvial fans along the mountain ridge. Another moraine ridge extends for ~500 m along the valley and has a steep slope that has been incised into a deep

gorge. Abundant large boulders, with limited evidence of weathering, are present on the surface of the moraine. Seven samples (NK22 - 28) for ^{10}Be dating were collected from boulders on top of a sharp crested moraine ridge. Three samples (NK26 - 28) were collected from low-lying rather denuded moraines. Notably, an aeolian deposit, that is 260 cm thick and is exposed for more than 4 m, overlies till on the outer edge of the eastern part of the TG1 moraine. This deposit is described in the next section.

Two subdued moraines (TG2) are located ~500 m above the TG1 moraines. These moraines have a pair of parallel moraine ridges with heights of ~1 - 2 m. Given the low relief and parallel nature of the moraine ridges, it is likely that the glacier stagnated at this point or that the ridges were associated with now-melted, buried glacial ice that was below the till after the glacier retreated. Numerical dating of these moraines was not undertaken because large boulders suitable for ^{10}Be dating could not be found on the moraine surface. We consider these moraines to be recessional features, based on their morphostratigraphy we correlate them with the ST2 and ST3 moraines.

Two asymmetric moraines (TG3) are present upstream along the Tarangoz Valley, at ~600 m above the TG2 moraine. The moraine to the east has a ~500-m-long sharp ridge that is largely unvegetated, whereas the moraine to the west forms a lower-lying and more subdued ridge. The boulders on the TG3 moraines are of different lithologies from those on other moraines, comprising carbonates, which are not suitable for 10Be dating. However, two granite - gneiss samples (NK29 - 30) were collected from the proximal part of the TG3 moraine.

The TG4 moraine has a sharp unvegetated ridge covered with cobbles and boulders, and is located ~1.5 km downstream from the snout of the contemporary glacier. Given its close proximity to the contemporary glacier and small amount of weathering, this moraine was assigned to the youngest TG moraine (Figs 4, 7).

4.2.. Aeolian and slope deposits in the Tarangoz Valley

An exposure in the TG1 moraine (34.065°N, 75.928°E; 3425 m a.s.l.)

reveals an interesting succession of sediments (Fig. 8). The sediment at the base of the exposure is composed of a massive, matrix-supported diamict of very poorly sorted grey silt and sand, containing boulders. The middle part of the exposure contains stratified sands and gravels deposits. The upper part of the exposure is composed of pale yellow brown massive fine sand and silt beds (referred to as Unit A) interbedded with centimetre- to decimetre-thick dark brown organic-rich beds (which we refer to as Unit B) and slopes parallel to the surface of the lower units. The lower and middle units are interpreted as till and glaciofluvial sediment, respectively. The upper beds are interpreted as being formed by aeolian (Unit A-1 - 3), colluvial and soil processes and are numbered (Unit B-1 - 3) as shown in Fig. 8. The base of Unit A-1 is an aeolian deposit that is 130 cm thick. This unit comprises fine sand and contains two pebbly layers at 50 and 103.5 cm above its base. The granule lamination is the result of a preferred orientation of granules, which are elongate down-slope, and the unit probably formed as a sheet-flow deposit. Samples were collected at 24 cm (NKTO1) and 118 cm (NKTO2) above the base of this unit for OSL dating. In Unit B-1, dark brown peat (15 cm thick) is dominant. One sample (NKTC1) was collected from this unit for radiocarbon dating. The boundary between this and the underlying Unit B-2 is sharp. The left side of this bed is exposed on the surface by erosion. Unit A-2 comprises silt (10 cm thick) and lacks any distinctive soil structure. The boundary of this bed is poorly defined. Unit B-2 is ~10 cm thick and contains dark brown peat and rare plant root material. To avoid contamination by potentially modern biomass, one sample (NKTC2) was collected for radiocarbon dating from an intact part of this unit. Unit A-3 is ~ 18 cm thick and complex in nature, varying between an aeolian deposit and peat. Fine sand is dominant in Unit A-3. Unit B-3 is a mottled dark brown peat that is 8 cm thick, and contains only rare modern plant root material. A sample (NKTC3) for radiocarbon dating was collected from Unit B-3, as it is uncontaminated by modern plant material. The uppermost bed comprises massive fine sand that is 69 cm thick, which we interpret to be an aeolian deposit. Diffuse dark brown laminations occur in the middle of Unit B-3. One sample (NKTO3) was collected for OSL dating from the homogeneous sand of Unit B-3 (Fig. 8).

5. Results

There has been considerable debate regarding how the distribution of TCN ages for boulders on a moraine should be used to date a moraine. A number of studies have asserted that the oldest boulder age is the most appropriate to assign to a moraine (Hallet & Putkonen 1994; Zreda et al. 1994; Putkonen & Swanson 2003; Zech et al. 2009; Applegate et al. 2010; Heyman et al. 2011). While inheritance of TCNs by prior exposure of boulders is rare, other studies have suggested that statistical analysis should be used to assign an age (Finkel et al. 2003; Owen et al. 2005; Schaefer et al. 2009; Dortch et al. 2010b, 2011; Hedrick et al. 2011). In our study, the ages used to date the moraines are the mean and maximum boulder ages, after elimination of any ages that are not within 2σ of the mean, of each set of ages on a moraine.

There has been much controversy about the appropriate scaling models and geomagnetic corrections for ^{10}Be production to calculate ^{10}Be ages (e.g. Pigati & Lifton 2004; Staiger et al. 2007). To facilitate comparison with other studies, we used the time-constant scaling models of Lal (1991) and Stone (2000) in CRONUS 2.2. The age differences resulting from the various scaling systems are shown in detail in Appendix S2.

5.1. Achambur glacial stage

The width of the Suru Valley abruptly increases, reaching its maximum near Achambur village (34.089°N, 75.936°W) in the study area. The U-shaped valley and trimline on the valley bedrock show that the main valley contained an extensive glacier linked to the tributary glaciers, although end or lateral moraines are absent. ^{10}Be dating of bedrock on the right-hand trimline upstream of Sentick Glacier yields ages of between 38.7 and 62.7 ka (n=6; NK9 - 14; Fig. 9).

The apparent ^{10}Be ages conservatively indicate when the glacier retreated from the bedrock, and not when the glacier extended to this point. Therefore, the glacier probably advanced to the area before c. 60 ka, and the glacier wasted down and retreated from the sampling sites between c. 30 and 60

ka. The scattered ages may be a real feature reflecting the gradual downwasting of the glacier with time, or may be associated with site-specific conditions of the bedrock surface. For example, any remaining glacier ice or covering loess/soil on the bedrock would result in an underestimation of age by partially blocking cosmic ray bombardment. Samples were collected from a narrow range, and therefore there is no strong correlation between bedrock ages and sampling locations at this point. Given the distribution of 10Be ages, the trunk valley glaciation probably occurred during Marine Oxygen Isotope Stage (MIS) 4 or MIS 3, although it may have been earlier in MIS 5. Therefore, it is likely that the glacier extent reached a maximum during the early part of the Last Glacial (Tables 1, 2).

5.2. Tongul glacial stage

Three moraines (ST1, TG1 and RT1) were assigned to the Tongul glacial stage and all are latero-frontal moraines located just before the confluence with the main valley. Therefore, the extent of glacier advance was less extensive than the main valley glaciation. Fourteen samples were collected from two moraines (ST1 and TG1) with sharp crest ridges and abundant boulders on their surface.

The ST1 moraine has ^{10}Be ages that range from 8.1 to 16.7 ka (n=7; NK15 - 21), with a mean age of 13.7 ka. This moraine shows a scatter in 10Be ages; however, it has a mean age of 14.5 ka after elimination of outliers (that lie outside 2σ). The mean age of ST1 is not consistent with the chronology of ST2 and ST3. The maximum age of the ST1 moraine is 16.7 ka.

The TG1 moraine has ^{10}Be ages that range from 14.8 to 20.0 ka (n=7; NK22 - 28) with a mean age of 17.4 ka. There is no distinct outlier in this data set. The maximum age of TG1 is 20.0 ka. The distribution of ^{10}Be ages from the TG1 moraine reflects denudation of the moraine. TG1 has a sharp crest ridge that is ~500 m long, from which samples were collected. Three samples (NK23 - 25) were collected from the middle of moraine ridge with <1° in inclination, and three samples (NK26 - 28) were taken from the terminus of the moraine with 1 - 3° inclination. Consequently, the ^{10}Be ages of NK26 - 28 (14.8 -

16.3 ka) probably underestimate the true age of TG1. The remaining sample (NK22; 20.0 ka) was collected at the contact between the moraine ridge and mountain bedrock.

In summary, the average of ^{10}Be ages of the Tongul glacial-stage moraines of two valleys is 16.7 - 17.4 ka. Röthlisberger & Geyh (1986) undertook ^{14}C dating of Rantac Glacier moraine (RT1) and obtained a humic acid age of 19 490±1630 a BP (23 396±2003 cal. a BP) and a total organic age of 15 670±770 a BP (c. 18 830±851 cal. a BP). Given the ^{10}Be age distribution, we consider that the glaciers advanced to the moraines during the early Lateglacial (Tables 1, 2).

5.3. Amantick glacial stage

Three moraines (ST2, ST3 and TG2) are assigned to the Amantick glacial stage. These moraines are unpaired lateral moraines. The TG2 moraine was not sampled, because the moraine ridge is very low and contains few large boulders on its surface. 10Be age data for the Amantick glacial stage moraine appear to be less reliable than for the other moraines, as the range of 10Be ages is large, and some ages are not consistent with field evidence. To interpret the complex range of 10Be ages, other factors such as boulder type, moraine shape, and sampling position should be considered. Unfortunately, such an approach is difficult when only a small number of sample ages are available.

Four samples (ST2; NK5 - 8) have ^{10}Be ages that range from 13.7 to 24.1 ka with a mean age of 17.3 ka. The calculated mean age is 14.3 ka after elimination of outliers, and, similarly, the maximum ^{10}Be age without outliers is 15.9 ka. The 10Be age of NK5 appears to be an outlier. NK6 and NK7 were obtained on lower surfaces than NK5. Boulder NK6 has a low height, which can cause age underestimation. NK7 was collected on a 170-cm-high boulder covered by abundant, large (<15 cm) lichen of pink, white and grey colour. Therefore, NK7 is likely to provide the most representative age. Although it is difficult to assign a robust age to the moraine, we conservatively suggest that, based on the mean age, this glacier advanced at c. 14.3 ka.

^{10}Be ages for ST3 moraine boulders are scattered from 1.5 to 16.3 ka,

with an average age of 10.3 ka. Excluding outliers, the ST3 moraine yields a maximum and a mean age of 12.4 ka and 11.7 ka, respectively. The outlier sample (NK2) was collected from a boulder that appears very fresh and has little lichen or rock varnish. It is likely that NK2 was exhumed by moraine degradation, as indicated by its anomalously young age of 1.5 ka.

Two TG2 moraines with three low ridges belong to the Amantick glacial stage. These moraines have gentle relief, and boulders suitable for ^{10}Be surface exposure dating are rare on this moraine. Therefore, the age of these moraines was not determined. Outer moraines (ST2) of the Amantick glacial-stage moraine in the Sentick glacial valley have an age of 14.3 ka, corresponding to the time when the glacier reached its greatest length. After the glacier retreated from this maximum position, it temporarily halted at a position marked by the inner moraine (ST3) cluster of the Amantick glacial stage. The glaciers then completely retreated after 11.7 - 12.4 ka (Tables 1, 2).

5.4. Lomp glacial stage

TG3 moraines in the Tarangoz Valley belong to the Lomp glacial stage. Two samples (TG3; NK29 - 30) have ages of 0.4 and 0.5 ka. As only two samples were collected from the TG3 moraines, since nearly all the moraine boulders were composed of carbonates, the certainty of the moraines age is low.

Moraines at 3800 - 3900 m a.s.l. in the study by Röthlisberger & Geyh (1986) can be correlated with the TG3 moraine on the basis of altitudes and characteristics of moraines. Röthlisberger & Geyh (1986) provided two different radiocarbon ages on the moraines. One sample (~3800 m) on a downstream moraine had a humic acid age of 2230±95 a BP (2224±105 cal. a BP) and a total organic age of 3280±90 a BP (3526±99 cal. a BP). A second sample collected 100 m upstream from the first sample had a humic acid age of 7405±185 a BP (8214±168 cal. a BP) and a total organic age of 12 750±1190 a BP (15 189±456 cal. a BP). Given that all the radiocarbon ages from the upstream second moraine are older than the first samples located farther down from the glacier snout, old organic materials were likely to be incorporated during glacier advance. Alternatively, although the second moraine is located upstream from

the first one, the two moraines could have formed during independent advances. If the latter event really occurred, it is likely to be synchronous with Amantick glacial-stage moraines. Given that ^{14}C ages from humic acid may include contributions from older organic material, these ages are likely to be maximum ages. Thus, on the basis of the well-bracketed ^{10}Be age and their proximity to the present glacier snout, we tentatively assign the Lomp glacial-stage moraines to the Little Ice Age (Tables 1, 2).

5.5. Tanak glacial stage

The TG4 moraines are located in the uppermost Tarangoz Valley, but these are not dated. Given that TG4 moraines are located between the present snout of the glacier and the Little Ice Age moraine (TG3), these moraines probably formed after retreat from the position of TG3, or as a glacial re-advance associated with climate deterioration in the past few centuries (Table 2).

5.6. Regional comparison of ELAs

The results of previous glacial studies in the Greater Himalaya, Zanskar and Ladakh ranges are summarized by location, chronology and glacial stage in Table 3 for regional comparisons. The present-day ELAs, former ELAs and ELA depressions (ΔELA) calculated using the AAR and THAR methods are compiled in Table 4. The AAR method was used mainly to interpret the extent of glaciation in the three ranges for ease of comparison with prior research. A comparison of glaciation in the Nun-Kun massif and five adjacent regions (Fig. 10; Lahul, Nimaling, Puga Valley, Karzok Valley and Bagzo) yields a picture of glaciation in the Nun-Kun massif and the presence of a precipitation gradient over the region. Precipitation across the Transhimalayan region decreases northwards moving into the continental interior and would be affected by the east - west-trending ranges (Fig. 2). Moraines with location data and clearly identified source areas and boundaries were selected for ELA reconstruction.

In the Lahul region, four glacial stages have been identified: the Chandra

(oldest), Batal, Kulti and Sonapani (youngest) (Owen et al. 1995, 1997, 2001). Most of the moraines are latero-frontal moraines formed by extensive valley glaciers. Therefore, moraines with small areas, including two contemporary glaciers, three moraines from the Kulti glacial stage, and one moraine from the Sonapani glacial stage, were used to reconstruct ELAs. Batal Glacier, whose snout head faces NE, has a present-day ELA at 4737 m a.s.l., and its ΔELA during the Sonapani glacial stage was 70 - 100 m. The present-day ELA for Sissu Nala Glacier, which is on the northwestern side of Batal Glacier, is 4851 m a.s.l. The Kulti glacial stage had a ΔELA of >325 m, perhaps due to the very large former area of this glacier. The Lahul region has the lowest ELAs for present glaciers and palaeoglaciers amongst the studied regions. Similarly, the present distribution of glaciers shows that glacier cover in the Greater Himalaya is greater than in the Zanskar and Ladakh ranges, perhaps because the Greater Himalaya preferentially receive moist winds from the Indian summer monsoon and mid-latitude westerlies. This influence of aspect on the extent of glaciation is also apparent in the fact that Sissu Nala Glacier on a southern slope extends farther than Batal Glacier on a northwestern slope.

The Nun-Kun region lies on the boundary between the Zanskar range and the Greater Himalaya, and has two tributary valley glaciers (Sentick and Tarangoz). Sentick Glacier yields a modern ELA of 5531 m a.s.l., a ΔELA for the Amantick glacial stage (dated at 11.7 - 14.3 ka) of 570 m, and a ΔELA of 620 m for the Tongul glacial stage (dated at c. 17.4 ka), which indicates it was the most extensive tributary valley glacier. In its downstream region, there is rock glacier that might affect estimation of the present-day ELA, for example through debris cover on the glacier. The present-day ELA of Tarangoz Glacier is 5089 m a.s.l., which is ~500 m lower than that of Sentick Glacier, owing to snow supply by avalanche to Tarangoz Glacier. Calculation of palaeo-ELAs for Tarangoz Glacier shows that the ΔELA of the Lomp glacial stage (dated at 0.4 - 0.5 ka) was 204 m, and the ΔELA of the Tongul glacial stage (dated at 16.7 - 17.4 ka) was 340 m. These ΔELA values are approximately half of those for Sentick Glacier.

ELAs of four present-day and eight past glaciers from four regions in the Zanskar range have been calculated. ELAs in the Nimaling region (Damm

2006), located between the Nun-Kun and the Bagzo regions (Owen et al. 2006), have also been calculated, although numerical dating of moraines in this region has not been undertaken. The present-day tributary glaciers number ~5 - 6, and they flowed into the main valley where there is moraine present that represents the Nimaling glacial stage. Present-day ELAs have values of 5796 - 5946 m a.s.l., which are similar to the values of 5640 - 6700 m a.s.l. as determined by Damm (2006) (Table 3).

The Puga and Karzok valleys in the southern Zanskar range are located between the Lahul and Ladakh regions (Hedrick et al. 2011). The present-day ELA value for the Puga Valley is 5968 m a.s.l. Palaeo-ELA reconstructions indicate that the ΔELA of the PM3 glacial stage (0.6 ka) was >154 m, which is similar to the ΔELA of the Lomp glacial stage for Sentick Glacier, and that the ΔELA for PM2 (dated at c. 4.2 ka) was >237 m. Only small (<1 km^2) glaciers are present upstream in the Karzok Valley, which were not considered for calculation of the present ELA. The KM1 glacial stage (dated at 12.5 and 50 ka) can be compared with the Amantick glacial stage in the Nun-Kun area, which indicates that the ELA during KM1 was ~5608 m a.s.l. The ELA was lower at the glacial head by >452 m, which is approximately equivalent to the ΔELA of the Amantick glacial stage. The calculated ELA of the KM3 glacial stage is ~5671 m a.s.l. The ELAs determined for KM1 to KM3 in this study should be regarded as minimum values, given that these are lateral moraines.

ELAs in the Ladakh range were calculated for Bagzo, Phyang and Leh glaciers. Present-day ELA values range between 5295 and 5547 m a.s.l. Numerical ages were not obtained for the Khalling and Kar glacial stages (Table 3). The Barzok glacial stage (dated at 41 - 74 ka) has a ΔELA of 131 - 344 m, indicating a smaller glacier advance in the Ladakh range than in the Zanskar range. Given that the ΔELA of the Tongul glacial stage of the Lateglacial period was ~600 m, the Achambur glacial stage (dated at 32.0 - 60.4 ka) in the Nun-Kun area was likely to have been even more extensive, with ΔELA values >600 m. Therefore, ΔELA variations in the Greater Himalaya range were greater than in the Ladakh range.

5.7. Chronology of aeolian and slope deposits in the Tarangoz Valley

Two different dating methods (^{14}C and OSL dating) were applied to the peat-rich layers and fine sediments of the aeolian and slope deposits. The dating results are plotted in depth - age profiles in Fig. 8B, and details are presented in Tables 5 and 6. The apparent ages systematically increase with depth and show a high degree of correlation (R2=0.987). Aliquots with poor recuperation (>10%) were not used in the age calculations. The ages of NKTO1 and NKTO3 are reliable, as the equivalent dose values are clustered. However, the equivalent dose values of NKTO2 are scattered. This sample might be partially bleached, which in turn OSL measurements on each grain would give a different equivalent dose (Olley et al. 1999). The mean ages are 9.8±1.4, 5.7±2.2 and 1.0±0.2 ka. As described previously, the aeolian deposit on the moraine dips gently to the north. Therefore, the apparent rate (24.5 cm ka^{-1}) of mass accumulation of the aeolian deposit may be only a lower limit, because the surface of the aeolian deposit is likely to have been susceptible to surface erosion.

Radiocarbon dating indicates that the dark brown peats have ages of 1620±40 a BP (1498±56 cal. a BP), 3150±40 a BP (3388±37 cal. a BP) and 4480±40 a BP (5155±99 cal. a BP), which are consistent the results of Röthlisberger & Geyh (1986) with ages of 4680±60 a BP (5583±72 cal. a BP). $\delta^{13}C$ values range from −26.2‰ to −22.7‰, consistent with C3 plant material that typically grows in cold and humid environments. Some studies have suggested that δ13C values of C3 plants growing under humid conditions in Tibet range from 32.6‰ to −23.2‰ (O'Leary 1988; Chengjun et al. 2003).

6. Discussion

6.1. Multiple late Quaternary glacial advances

Five glacial stages were defined in this study using the morphostratigraphy and TCN chronology of the Nun-Kun region. The oldest glacial stage was characterized by the maximum main valley ice extent during MIS 3 and/or 4 and was assigned to the Achambur glacial stage. There is no

evidence to suggest that glaciers ever occupied the main Suru Valley after this glacial stage.

Three pairs of moraines formed during the Tongul glacial stage. These moraines still have sharp ridges, even though they formed at 16.7 – 17.4 ka. Our 10Be ages agree with radiocarbon ages obtained for this moraine by Röthlisberger & Geyh (1986), namely a humic acid age of 19 490±1630 a BP (23 396±2003 cal. a BP) and a total organic age of 15 670±770 a BP (c. 18 830±851 cal. a BP). These moraines appear to have formed during the early Lateglacial, and are approximately synchronous with the Mungo glacial stage in the central Karakoram, where glaciers advanced with major influences from the Northern Hemisphere climate oscillations (Seong et al. 2007).

Moraines produced in the Amantick glacial stage have low continuous ridges. The ^{10}Be ages obtained from the ST2 and ST3 moraines by ^{10}Be dating show that the glaciers formed massive moraines at 14.3 ka, and that these glaciers re-advanced or temporarily stagnated during recession between 11.7 and 12.4 ka. This glacial stage also coincides with tributary valley glacier advances in the central and northern Karakoram (Seong et al. 2007, 2009), areas that have precipitation patterns similar to those in our study area. As such glaciation(s) in the Nun-Kun massif might broadly correlate with glaciation(s) in the central and northern Karakoram, the Pamir and Tien Shan (Owen et al. 2002, 2012; Abramowski et al. 2006; Seong et al. 2007). This may indicate that the Nun-Kun area has been mostly affected by mid-latitude westerlies and that the Greater Himalaya has effectively obstructed northward intrusion of the Indian summer monsoon.

A range of data (e.g. Wang et al. 2005; more references therein) indicates that the coldest period in the late Quaternary was likely the global Last Glacial Maximum (LGM) in MIS 2. However, the maximum extent of ice in our study area was during MIS 3 – 4. This extensive ice advance prior to the LGM is characteristic of many regions in the Himalaya – Tibetan region. Based on changes in ELAs, the extent of glacier advance has decreased with time through to the present-day. The progressive uplift of the Himalaya to the south and/or the Karakoram mountains to the west possibly caused the precipitation decrease that, in turn, has reduced glacial extent with time (Seong et al. 2009; Owen et al.

2012).

Alternatively, longitudinal erosion modelling of glacial valleys has shown that the valley bottom shape can be changed into a concave shape by glacial erosion (Oerlemans 1984; MacGregor et al. 2000). As such, when a glacier re-advances, the absolute distance of the renewed advance might decrease, as a concave valley bottom is longer than a linear valley bottom. Therefore, the glacial snout will retreat even though the total volume of the glacier may remain constant. Changes in longitudinal valley form caused by glacial incision might thus constrain the horizontal extent of advancing glaciers. More research on the feedback between the intensity of glacial erosion and changes in longitudinal valley form in high-mountain areas is required in order for the potential role of multiple glacial incisions on ELA reconstructions to be understood.

6.2. Precipitation gradients inferred from ELA analysis

Present-day ELAs reconstructed for the three high-mountain ranges show that topographic effects influence precipitation gradients. All the regions fall in a narrow latitude belt between 32°N and 35°N, and most of the present-day glaciers are at altitudes >4000 m a.s.l., and hence receive most of their precipitation as snowfall even during the summer months. As such, glaciers in these regions are possibly influenced by changes in precipitation rather than in temperature (Kaser & Osmaston 2001). Therefore, ELA analysis primarily reflects precipitation gradients in these regions, and allows examination of the relationship between glaciation and precipitation through the Greater Himalaya, and the Zanskar and Ladakh ranges.

The present-day ELA of the Lahul region is the lowest amongst the regions considered here, presumably because it is located on the windward side of the Greater Himalaya where there is a large amount of topographically controlled precipitation produced by the Indian summer monsoon and mid-latitude westerlies. Satellite data show that there are extensive present-day glaciers in the Greater Himalaya, particularly on the windward side of the range, although the Lahul region is located at relatively low latitudes.

The Zanskar and Ladakh ranges to the north of the Greater Himalaya are located in the interior of the Tibetan Plateau, where moist winds carried by mid-latitude westerlies and the Indian monsoon are less likely to penetrate. Precipitation tends to decrease towards the interior, as is evident from Figs 2 and 4. It is notable that the present-day ELA of the Ladakh range is on average ~450 m lower than that of the Zanskar range, which is contrary to the general prediction of a northward increase in present-day ELA, if it were modulated primarily by precipitation. The present-day ELA of the Leh region in the Ladakh range is on average 5384 m a.s.l., whereas the present-day ELA of the Zanskar range is on average ~5903 m a.s.l. Burbank & Fort (1985) suggested that bedrock influences ELAs and glaciations in both ranges. However, there is no significant difference in the bedrock of these ranges that could account for the observed ELA trends. The overall ELA trends from past to present mirror those of the distribution pattern of present-day glaciers. Topographic precipitation influenced by the presence of high mountains appears to dominantly control the past and present-day glacier distribution and ELAs. The present-day glaciers are juxtaposed continuously in the Ladakh range owing to this topographical barrier of ~5500 m a.s.l. high mountains being arranged in an east - west direction (Figs 1, 10). However, high mountains (~5500 m a.s.l.) are sporadically distributed in the Zaskar range, which means that they do not represent as an effective topographic barrier to cause and control precipitation. Present-day glaciers are also more sporadic and scattered in distribution on the high peaks of the Zanskar range.

Moreover, all the studied areas in the Zaskar range are on leeside, NW-facing slopes. In the Ladakh range, glaciers in the Nubra Valley on the leeside slope have ELAs that are ~100 m lower than glaciers on the windward aspect (Dortch et al. 2010b). Topographic effects on glacier distribution and variations in ELA identified in our study imply that the aspect of a glacier basin is closely related to the ELAs of both present-day and former glaciers in the Himalaya - Tibetan orogen (Oskin & Burbank 2005).

Our comparisons of ELAs and timings of glacier oscillations require further study, as the timing of glaciation in the Ladakh range dates back to 100 ka whereas for the Lahul range it dates back to 20 ka, meaning that these

comparisons should be made cautiously. However, there is a strong relationship between location and timing of glaciation. The outermost range (Greater Himalaya) has relatively young moraines, such as those produced in the early Holocene, whereas the inner range (Ladakh) has relatively older moraine groups with long intervals of time between their formations. Both moraine age and the time interval between the formation of different moraine groups increase towards the east in the Zanskar range. This indicates that strong moist air systems were likely to have reached the interior regions across the high topography. In the case of the Indian summer monsoon, the strength of summer insolation controls fluctuations of monsoon behaviour. As such, only periods of strong monsoons can penetrate far into the interior of the plateau, whereas a precipitation increase caused by both weak and strong monsoon events can affect the glaciers of the outer ranges of the Himalaya - Tibetan orogen (Owen et al. 2012).

6.3. The relationship between moraine and aeolian-slope deposits

Radiocarbon ages from peat beds within the aeolian and slope deposit on the TG1 moraine show periodic formation at c. 1498±40, 3388±37 and 5155±99 cal. a BP. δ13C values from the dark brown peat vary from −32.6‰ to −23.2‰, implying that the peats were formed under humid conditions influenced by increased precipitation. As mid-latitude westerlies shift to a more southward position when the climate of the Northern Hemisphere becomes colder, this could have supplied more precipitation to the Nun-Kun massif. Consequently, precipitation increased and average temperature dropped during these cold periods. At this time, fine sand and silt produced from the glacier upvalley were preferentially transported to the leeward slopes of moraines downvalley. Vegetation would also grow on aeolian deposits during increased precipitation periods and, simultaneously, the glacier would be more likely to advance upvalley. Typically, the formation of loess during the Quaternary is related to cold - dry climates when glaciers advance, followed by pedogenic modification of the loess during warm - wet climates when glaciers retreat (Catt 1991; Derbyshire et al. 1995; Kemp 2001; Srivastava et al. 2009). The formation of loess

in the southern Himalaya has been interpreted as a response to the oscillating glaciers (Srivastava et al. 2009). The formation of aeolian deposits in the Nun-Kun massif region has a clear inverse relationship with strengthening of westerlies as compared with the southern Himalaya, where glacial advance was forced by cold periods. Peat ages broadly coincide with the glaciation of Muztag Ata in the Pamir (38°44′N, 75°02′E, 3310 m a.s.l.) when the glacier advanced at 1.4±0.1 and 3.3±0.6 ka (Seong et al. 2009). This observation further supports the hypothesis that mid-latitude westerlies affected the glaciation of the Nun-Kun area. However, the formation of aeolian deposits does not correspond with the formation of moraines by glacier advance in the upper Tarangoz Glacier valley. Given the substantial difference (~300 m) in elevation, these areas are likely to have evolved differently, with a minor glacier advance upvalley but vegetation growth downvalley as a response to increased precipitation.

$\delta^{18}O$ measurements of stalagmite calcite from the Dongge cave in China (25°17′N, 108°5′W, 680 m a.s.l.) show that the weak Eastern Asian Summer monsoon (strengthened mid-latitude westerlies) can be correlated with North Atlantic climate. A weak Eastern Asian Summer monsoon coincides with millennial cycles in the northern Atlantic (Denton & Karlén 1973) and peat formation at 1.6 and 5.5 ka in our study area. Therefore, the timing of peat formation coincides with periods of weakened Eastern Asian monsoon or periods of strengthened mid-latitude westerlies (Fig. 11), supporting our view that the glaciation of the Nun-Kun massif was sensitive to changes in precipitation modulated by mid-latitude westerlies and the Indian monsoon, although some lag time might exist in the processes of peat-bed formation in the study area.

7. Conclusions

^{10}Be, ^{14}C and OSL dating methods applied to moraines and peat-bearing aeolian sediments define the timing of five Quaternary glacial stages, namely the Achambur, Tongul, Amantick, Lomp and Tanak glacial stages, and three shorter-term, millennial-scale climate fluctuations during the Holocene in the Nun-Kun massif. The most extensive glacial advance occurred during the Achambur glacial stage, when a trunk valley glacier advanced down the Suru

Valley. Trimlines in bedrock in the main trunk valley indicate that the glacier retreated from an altitude of ~3700 m a.s.l. between c. 38.7 and 62.7 ka. Three moraines formed from 16.7 to 17.4 ka during the Tongul glacial stage, representing a ΔELA for Sentick glacier of 620 m and for Tarangoz glacier of 340 m, when glaciers advanced down the tributary valley to the Suru Valley. Moraines of the Amantick glacial stage date to between 14.3 and 11.7 - 12.4 ka, representing a ΔELA for the ST2, 3 moraine in Sentick glacier of 570 m. These indicate that Sentick glacier advanced down to the confluence in the main Suru Valley at 14.3 ka and temporarily halted its retreat at 11.7 - 12.4 ka. The Lomp glacial stage was a period of glacier advance during the Little Ice Age and produced a pair of latero-frontal moraines located ~1 km away from the present glaciers, and the ΔELA was ~200 m. The moraines closest to the present-day snout of Tarangoz Glacier were not dated, but formed during historical glacial advances (Tanak glacial stage). The timing of glaciation in the Nun-Kun massif is similar to that in the northern and central Karakoram, with both appearing to be strongly influenced by mid-latitude westerlies. The progressively declining extent of glacial advances during the late Quaternary might reflect regional tectonic uplift, causing an increase in the topographic barrier effect, or a response to landform change resulting from repeated glaciations. Changes in ELAs of the three ranges from the Greater Himalaya to the Ladakh Range reflect a topographic barrier effect, which controls the precipitation gradient towards the interior of the Tibetan Plateau. The present-day ELA is lowest in the outer and southernmost Greater Himalaya owing to topographic precipitation from the Indian summer monsoon and mid-latitude westerlies. ELAs become higher towards the interior, although the highest ELAs are defined in the Zanskar range because of the sporadic distribution of high mountains in this range, which allows substantial penetration of moist winds. Owing to this topographic barrier, it is likely that only strong moist winds can penetrate into the deep interior, for example to the Ladakh range, which preserves one of the oldest moraine records (Indus Valley: 130 - 385 ka, Table 3) in Tibet. The ΔELA for the Barzok glacial stage (41 - 74 ka) was 131 - 344 m, indicating less glacial advance. In contrast, glaciers in the outermost part of the ranges responded to weak as well as to strong climate

perturbations; for example, the Kulti glacial stage was at 10.6 - 11.4 ka with a ΔELA of ~325 m. In the Nun-Kun region, a, ΔELA for the Amantick glacial stage (11.7 - 14.3 ka) was 570 m, and a ΔELA for the Tongul glacial stage (17.4 ka) was 620 m. Therefore, ΔELA variations in the Greater Himalaya were greater than in the Ladakh range. Peat-rich beds intercalated with aeolian deposits were cyclically formed at c. 1.5, c. 3.4 and c. 5.2 ka, synchronous with known periods of abrupt climate change during the Holocene. As such, glaciers in the Nun-Kun massif have responded to short-term climate oscillations occurring on millennial time scales, superimposed on longer-term, orbitally driven, Quaternary climate cycles.

제4기 후기 인도 북서부의 Nun-Kun 대산괴의 빙하작용

성영배[1*], 윤호일[2], 유규철[2]

[1]고려대학교

[2]한국해양과학기술원 부설 극지연구소

요약: 인도 북서부의 히말라야 산맥과 잔 스카르 산맥 사이에 위치한 Nun-Kun 대산괴의 제 4 기 후기 빙하기 역사가 복원되었다. 빙하기 지형의 지형평년진과 10Be 연대에 의해 5 단계의 빙하기 단계가 확인되었고 정의되었다: 1) Achambur 빙하 단계 (38.7-62.7 ka), 2) Tongul 빙하 단계 (16.7-17.4 ka), 3) Amantick 빙하 단계 (14.3 ka, 11.7-12.4 ka), 4) Lomp 빙하 단계 (소빙기), Tanak 빙하 단계 (가장 최근 빙퇴석). 현재와 과거의 형형라인고도(ELA)는 표준지역 축적비 방법을 통해 계산되었다. 오늘날의 평균 ELA는 히말라야에서의 해발 4790 m는 Ladakh 5380 m, 잔 스카르 5900 m 보다 낮다. 잔 스카르 산맥에서 ELA는 Ladakh 산맥 보다 높고, 아마도 Ladakh 산맥에서 더 높은 눈과 얼음을 더 효율적으로 저장할 수 있는 봉우리 때문인 것 같다. ELA의 침하는 Ladakh 산맥 쪽으로 감소한다. Tarangoz 빙하의 빙퇴석을 덮는 풍성 퇴적층 사이의 이탄층은 홀로세 동안 천년단위의 기후변화를 시사한다. 1.5, 3.4, 5.2 ka의 토양 형성 시기는 홀로세의 급격한 기후 변화와 연관된다. 연구지역에서의 빙하기의 스타일과 시기를 감안하면, Nun-Kun 지역의 기후가 북반구 기후변화와 관련되어 있다는 것을 의미한다.

참고문헌

Bae, S.H., Yoon, H.I., Park, B.-K., Kim, Y.,, 2003. Late Quaternary stable isotope record and meltwater discharge anomaly events to the south of the Antarctic Polar Front, Drake Passage. Geo-Marine Letters 23, 110 - 116.

Abramowski, U., Bergau, A., Seebach, D., Zech, R., Glaser, B., Sosin, P., Kubik, P. & Zech, W. 2006: Pleistocene glaciations of Central Asia: results from 10Be surface exposure ages of erratic boulders from the Pamir (Tajikistan), and the Alay - Turkestan range (Kyrgyzstan). Quaternary Science Reviews 25, 1080 - 1096.

Ahmad, S., Hasnain, S. I. & Selvan, M. T. 2004: Morpho-metric characteristics of glaciers in the Indian Himalayas. Asian Journal of Water Environment and Pollution 1, 109 - 118.

Applegate, P. J., Urban, N. M., Laabs, B. J. C., Keller, K. & Alley, R. B. 2010: Modeling the statistical distributions of cosmogenic exposure dates from moraines. Geoscientific Model Development 3, 293 - 307.

Barnard, P. L., Owen, L. A. & Finkel, R. C. 2004a: Style and timing of glacial and paraglacial sedimentation in a monsoonal influenced high Himalayan environment, the upper Bhagirathi Valley, Garhwal Himalaya. Sedimentary Geology 165, 199 - 221.

Barnard, P. L., Owen, L. A., Finkel, R. C. & Asahi, K. 2006: Landscape response to deglaciation; in a high relief, monsoon-influenced alpine environment, Langtang Himal, Nepal. Quaternary Science Reviews 25, 2162 - 2176.

Barnard, P. L., Owen, L. A., Sharma, M. C. & Finkel, R. C. 2004b: Late Quaternary landscape evolution of a monsoon-influenced high Himalayan valley, Gori Ganga, Nanda Devi, NE Garhwal. Geomorphology 61, 91 - 110.

Barry, R. G. & Chorley, R. J. 2003: Atmosphere, Weather, and Climate, eighth ed. 279pp.

Becker, A. & Bugmann, H. 1997: Predicting global change impacts on mountain hydrology and ecology: integrated catchment hydrology/altitudinal

gradient studies. Workshop report: documentation resulting from an International Workshop, Kathmandu, Nepal, 30 March 1996. Global Change Report.

Beniston, M. 2006: Mountain weather and climate: a general overview and a focus on climatic change in the Alps. Hydrobiologia 562, 3 – 16.

Benn, D. I. & Evans, D. J. A. 2010: Glaciers and Glaciation. 802 pp. Hodder Education, Oxford.

Benn, D. I. & Lehmkuhl, F. 2000: Mass balance and equilibrium-line altitudes of glaciers in high-mountain environments. Quaternary International 65, 15 – 29.

Benn, D. I. & Owen, L. 1998: The role of the Indian summer monsoon and the mid-latitude westerlies in Himalayan glaciation: review and speculative discussion. Journal of the Geological Society 155, 353 – 363.

Benn, D. I., Owen, L. A., Osmaston, H. A., Seltzer, G. O., Porter, S. C. & Mark, B. 2005: Reconstruction of equilibrium-line altitudes for tropical and sub-tropical glaciers. Quaternary International 138, 8 – 21.

Bookhagen, B., Thiede, R. C. & Strecker, M. R. 2005: Late Quaternary intensified monsoon phases control landscape evolution in the northwest Himalaya. Geology 33, 149 – 152.

Burbank, D. W. & Fort, M. B. 1985: Bedrock control on glacial limits: examples from the Ladakh and Zanskar ranges, north-western Himalaya, India. Journal of Glaciology 31, 143 – 149.

Calpal. Available at: http://www.calpal.de/ (accessed 18.01.2011).

Catt, J. A. 1991: Soils as indicators of Quaternary climatic change in mid-latitude regions. Geoderma 51, 167 – 187.

CrossRef | Web of Science® Times Cited: 24Chengjun, Z., Fahu, C. & Ming, J. 2003: Study on modern plant C-13 in western China and its significance. Chinese Journal of Geochemistry 22, 97 – 106.

Chevalier, M.-L., Hilley, G., Tapponnier, P., Van Der Woerd, J., Liu-Zeng, J., Finkel, R. C., Ryerson, F. J., Li, H. & Liu, X. 2011: Constraints on the late Quaternary glaciations in Tibet from cosmogenic exposure ages of moraine surfaces. Quaternary Science Reviews 30, 528 – 554.

Chevalier, M.-L., Ryerson, F. J., Tapponnier, P., Finkel, R. C., Van Der Woerd, J., Haibing, L. & Qing, L. 2005: Slip-rate measurements on the Karakoram Fault may imply secular variations in fault motion. Science 307, 411 - 414.

Clark, D. H., Clark, M. M. & Gillespie, A. R. 1994: Debris-covered glaciers in the Sierra Nevada, California, and their implications for snowline reconstructions. Quaternary Research 41, 139 - 153.

CRONUS 2008: Cronus-Earth online calculators. Available at: http://hess.ess.washington.edu (accessed 06.01.2011).

Damm, B. 2006: Late Quaternary glacier advances in the upper catchment area of the Indus River (Ladakh and western Tibet). Quaternary International 154, 87 - 99.

Denton, G. H. & Karlén, W. 1973: Holocene climatic variations - their pattern and possible cause. Quaternary Research 3, 155 - 205.

Derbyshire, E., Keen, D. H., Kemp, R. A., Rolph, T., Shaw, J. & Meng, X. 1995: Loess - palaeosol sequences as recorders of palaeoclimatic variations during the last glacial - interglacial cycle: some problems of correlation in north-central China. Quaternary Proceedings 4, 7 - 18.

Dortch, J. M., Owen, L. A. & Caffee, M. W. 2010b: Quaternary glaciation in the Nubra and Shyok valley confluence, northernmost Ladakh, India. Quaternary Research 74, 132 - 144.

Dortch, J. M., Owen, L. A., Caffee, M. W. & Brease, P. 2010a: Late Quaternary glaciation and equilibrium line altitude variations of the McKinley River region, central Alaska Range. Boreas 39, 233 - 246.

Dortch, J. M., Owen, L. A., Schoenbohm, L. M. & Caffee, M. W. 2011: Asymmetrical erosion and morphological development of the central Ladakh Range, northern India. Geomorphology 135, 167 - 180.

Finkel, R. C., Owen, L. A., Barnard, P. L. & Caffee, M. W. 2003: Beryllium-10 dating of Mount Everest moraines indicates a strong monsoon influence and glacial synchroneity throughout the Himalaya. Geology 31, 561 - 564.

Google 2009: Google Earth. Available at: http://www.google.com/intl (accessed 24.03.2011).

Hallet, B. & Putkonen, J. 1994: Surface dating of dynamic landforms: young boulders on aging moraines. Science 265, 937 – 940.

Hedrick, K. A., Seong, Y. B., Owen, L. A., Caffee, M. C. & Dietsch, C. 2011: Towards defining the transition in style and timing of Quaternary glaciation between the monsoon-influenced Greater Himalaya and the semi-arid Transhimalaya of Northern India. Quaternary International 236, 21 – 33.

Heyman, J., Stroeven, A. P., Harbor, J. M. & Caffee, M. W. 2011: Too young or too old: evaluating cosmogenic exposure dating based on an analysis of compiled boulder exposure ages. Earth and Planetary Science Letters 302, 71 – 80.

Kaser, G. & Osmaston, H. 2001: Tropical Glaciers. 161 pp. Cambridge University Press, Cambridge.

Kemp, R. A. 2001: Pedogenic modification of loess: significance for palaeoclimatic reconstructions. Earth-Science Reviews 54, 145 – 156.

Kohl, C. & Nishiizumi, K. 1992: Chemical isolation of quartz for measurement of in-situ-produced cosmogenic nuclides. Geochimica et Cosmochimica Acta 56, 3583 – 3587.

Kong, P., Fink, D., Na, C. & Huang, F. 2009: Late Quaternary glaciation of the Tianshan, Central Asia, using cosmogenic 10Be surface exposure dating. Quaternary Research 72, 229 – 233.

Koppes, M., Gillespie, A. R., Burke, R. M., Thompson, S. C. & Stone, J. 2008: Late Quaternary glaciation in the Kyrgyz Tien Shan. Quaternary Science Reviews 27, 846 – 866.

Lal, D. 1991: Cosmic ray labeling of erosion surfaces- in situ nuclide production rates and erosion models. Earth and Planetary Science Letters 104, 424 – 439.

CrossRef | CAS | Web of Science® Times Cited: 879 | ADSMacGregor, K. R., Anderson, R., Anderson, S. & Waddington, E. 2000: Numerical simulations of glacial-valley longitudinal profile evolution. Geology 28, 1031 – 1034.

Mayewski, P. A., Lyons, W. B., Ahmad, N., Smith, G. & Pourchet, M. 1984: Interpretation of the chemical and physical time-series retrieved from

Sentik Glacier, Ladakh Himalaya, India. Journal of Glaciology 30, 66 - 76.

Meriaux, A.-S., Ryerson, F. J., Tapponnier, P., Van der Woerd, J., Finkel, R. C., Xu, X., Xu, Z. & Caffee, M. W. 2004: Rapid slip along the central Altyn Tagh Fault: morphochronologic evidence from Cherchen He and Sulamu Tagh. Journal of Geophysical Research 109, B06401, doi: 10.1029/2003JB002558.

Miller, G., Bradley, R. & Andrews, J. 1975: The glaciation level and lowest equilibrium line altitude in the high Canadian Arctic: maps and climatic interpretation. Arctic and Alpine Research 2, 155 - 168.

Murakami, T. 1987: Effects of the Tibetan Plateau. In Chang, C. P. & Krishamurti, T. N. (eds): Monsoon Meteorology, 235 - 270. Oxford University Press, Oxford.

Murray, A. S. & Wintle, A. G. 2000: Luminescence dating of quartz using an improved single-aliquot regenerative-dose protocol. Radiation Measurements 32, 57 - 73.

O'Leary, M. H. 1988: Carbon isotopes in photosynthesis. Bioscience 38, 328 - 336.

Oerlemans, J. 1984: Numerical experiments on glacial erosion. Zeitschrift fur Gletscherkunde und Glazialgeologie 20, 107 - 126.

Olley, J., Caitcheon, G. & Roberts, R. 1999: The origin of dose distributions in fluvial sediments, and the prospect of dating single grains from fluvial deposits using optically stimulated luminescence. Radiation Measurements 30, 207 - 217.

Oskin, M. & Burbank, D. W. 2005: Alpine landscape evolution dominated by cirque retreat. Geology 33, 933 - 936.

Osmaston, H., Frazer, J. & Crook, S. 1994: Human adaptation to environment in Zanskar. Buddhist Himalayan Villages in Ladakh, Bristol: Environment, resources, society and religious life in Zangskar, Ladakh. ed. / HA Osmaston ; Crook; H J . University of Bristol, 37 - 110.

Overpeck, J., Anderson, D., Trumbore, S. & Prell, W. 1996: The southwest Indian Monsoon over the last 18 000 years. Climate Dynamics 12, 213 - 225.

Owen, L., Benn, D., Derbyshire, E., Evans, D., Mitchell, W., Thompson, D., Richardson, S., Lloyd, M. & Holden, C. 1995: The geomorphology and landscape evolution of the Lahul Himalaya, Northern India. Zeitschrift für Geomorphologie 39, 145 - 174.

Owen, L. A., Bailey, R. M., Rhodes, E. J. & Coxon, W. A. M. 1997: Style and timing of glaciation in the Lahul Himalaya, northern India: a framework for reconstructing late Quaternary palaeoclimatic change in the western Himalayas. Journal of Quaternary Science 12, 83 - 109.

Owen, L. A. & Benn, D. I. 2005: Equilibrium-line altitudes of the Last Glacial Maximum for the Himalaya and Tibet: an assessment and evaluation of results. Quaternary International 138, 55 - 78.

Owen, L. A., Caffee, M. W., Bovard, K. R., Finkel, R. C. & Sharma, M. C. 2006: Terrestrial cosmogenic nuclide surface exposure dating of the oldest glacial successions in the Himalayan orogen: Ladakh Range, northern India. Geological Society of America Bulletin 118, 383 - 392.

Owen, L. A., Caffee, M. W., Finkel, R. C. & Seong, Y. B. 2008: Quaternary glaciation of the Himalayan-Tibetan orogen. Journal of Quaternary Science 23, 513 - 531.

Owen, L. A., Chen, J., Hedrick, K. A., Caffee, M. W., Robinson, A. C., Schoenbohm, L. M., Yuan, Z., Li, W., Imrecke, D. B. & Liu, J. 2012: Quaternary glaciation of the Tashkurgan Valley, Southeast Pamir. Quaternary Science Reviews 47, 56 - 72.

Owen, L. A., Finkel, R. C., Barnard, P. L., Haizhou, M., Asahi, K., Caffee, M. W. & Derbyshire, E. 2005: Climatic and topographic controls on the style and timing of Late Quaternary glaciation throughout Tibet and the Himalaya defined by 10Be cosmogenic radionuclide surface exposure dating. Quaternary Science Reviews 24, 1391 - 1411.

Owen, L. A., Gualtieri, L., Finkel, R. C., Caffee, M. W., Benn, D. I. & Sharma, M. C. 2001: Cosmogenic radionuclide dating of glacial landforms in the Lahul Himalaya, northern India: defining the timing of Late Quaternary glaciation. Journal of Quaternary Science 16, 555 - 563.

Owen, L. A., Kamp, U., Spencer, J. Q. & Haserodt, K. 2002: Timing and style of Late Quaternary glaciation in the eastern Hindu Kush, Chitral,

northern Pakistan: a review and revision of the glacial chronology based on new optically stimulated luminescence dating. Quaternary International 97/98, 41 – 56.

Owen, L. A., Ma, H., Derbyshire, E., Spencer, J. Q., Barnard, P. L., Zeng, Y. N., Finkel, R. C. & Caffee, M. W. 2003b: The timing and style of Late Quaternary glaciation in the La Ji Mountains, NE Tibet: evidence for restricted glaciation during the latter part of the Last Glacial. Zeitschrift für Geomorphologie 130, 263 – 276.

Owen, L. A., Spencer, J. Q., Ma, H., Barnard, P. L., Derbyshire, E., Finkel, R. C., Caffee, M. W. & Zeng, Y. N. 2003a: Timing of Late Quaternary glaciation along the southwestern slopes of the Qilian Shan, Tibet. Boreas 32, 281 – 291.

Phillips, W. M., Sloan, V. F., Shroder J. F. Jr, Sharma, P., Clarke, M. L. & Rendell, H. M. 2000: Asynchronous glaciation at Nanga Parbat, northwestern Himalaya Mountains, Pakistan. Geology 28, 431 – 434.

Pigati, J. S. & Lifton, N. A. 2004: Geomagnetic effects on time-integrated cosmogenic nuclide production with emphasis on in situ 14C and 10Be. Earth and Planetary Science Letters 226, 193 – 205.

Putkonen, J. & Swanson, T. 2003: Accuracy of cosmogenic ages for moraines. Quaternary Research 59, 255 – 261.

Qiu, J. 2008: China: the third pole. Nature News 454, 393 – 396.

Richards, B. W. M., Benn, D. I., Owen, L. A., Rhodes, E. J. & Spencer, J. Q. 2000a: Timing of Late Quaternary glaciations south of Mount Everest in the Khumbu Himal, Nepal. Geological Society of America Bulletin 112, 1621 – 1632.

Richards, B. W. M., Owen, L. A. & Rhodes, E. J. 2000b: Timing of Late Quaternary glaciations in the Himalayas of northern Pakistan. Journal of Quaternary Science 15, 283 – 297.

Röthlisberger, F. & Geyh, M. 1986: Glacier variations in Himalayas and Karakorum. Journal of Glaciology and Geocryology 4, 237 – 249.

Schaefer, J. M., Denton, G. H., Kaplan, M., Putnam, A., Finkel, R. C., Barrell, D. J. A., Andersen, B. G., Schwartz, R., Mackintosh, A. & Chinn, T. 2009: High-frequency Holocene glacier fluctuations in New Zealand

differ from the northern signature. Science 324, 622 – 625.

Schaefer, J. M., Oberholzer, P., Zhao, Z., Ivy-Ochs, S., Wieler, R., Baur, H., Kubik, P. W. & Schlüchter, C. 2008: Cosmogenic beryllium-10 and neon-21 dating of late Pleistocene glaciations in Nyalam, monsoonal Himalayas. Quaternary Science Reviews 27, 295 – 311.

Schaefer, J. M., Tschudi, S., Zhao, Z., Wu, X., Ivy-Ochs, S., Wieler, R., Baur, H., Kubik, P. W. & Schluchter, C. 2001: The limited influence of glaciations in Tibet on global climate over the past 170000 yr. Earth and Planetary Science Letters 194, 287 – 297.

Scherler, D., Bookhagen, B., Strecker, M. R., von Blanckenburg, F. & Rood, D. 2010: Timing and extent of late Quaternary glaciation in the western Himalaya constrained by 10Be moraine dating in Garhwal, India. Quaternary Science Reviews 29, 815 – 831.

Seong, Y. B., Owen, L. A., Bishop, M. P., Bush, A., Clendon, P., Copland, L., Finkel, R., Kamp, U. & Shroder, J. F. 2007: Quaternary glacial history of the Central Karakoram. Quaternary Science Reviews 26, 3384 – 3405.

Seong, Y. B., Owen, L. A., Yi, C. & Finkel, R. C. 2009: Quaternary glaciation of Muztag Ata and Kongur Shan: evidence for glacier response to rapid climate changes throughout the Late Glacial and Holocene in westernmost Tibet. Geological Society of America Bulletin 121, 348 – 365.

Sharma, M. C. & Owen, L. A. 1996: Quaternary glacial history of NW Garhwal Himalayas. Quaternary Science Reviews 15, 335 – 365.

Srivastava, P., Rajak, M. & Singh, L. 2009: Late Quaternary alluvial fans and paleosols of the Kangra basin, NW Himalaya: tectonic and paleoclimatic implications. Catena 76, 135 – 154.

Staiger, J., Gosse, J., Toracinta, R., Oglesby, B., Fastook, J. & Johnson, J. V. 2007: Atmospheric scaling of cosmogenic nuclide production: climate effect. Journal of Geophysical Research – Solid Earth 112, B02205, doi:10.1029/2005JB003811.

Stone, J. O. 2000: Air pressure and cosmogenic isotope production. Journal of Geophysical Research-Solid Earth 104, B10.

Taylor, P. J. & Mitchell, W. A. 2000: The Quaternary glacial history of the Zanskar Range, north-west Indian Himalaya. Quaternary International 65, 81 - 99.

Tsukamoto, S., Asahi, K., Watanabe, T., Kondo, R. & Rink, W. J. 2002: Timing of past glaciation in Kanchenjunga Himal, Nepal by optically stimulated luminescence dating of tills. Quaternary International 97/98, 57 - 68.

Walter, H. & Lieth, H. 1960 - 1967: Klimadiagramm-weltatlas. G. Fischer Verlag, Jena.

Wang, Y., Cheng, H., Edwards, R. L., He, Y., Kong, X., An, Z., Wu, J., Kelly, M. J., Dykoski, C. A. & Li, X. 2005: The Holocene Asian monsoon: links to solar changes and North Atlantic climate. Science 308, 854 - 857.

Workman, W. H. 1908: An exploration of the Nun Kun mountain group and its glaciers. The Geographical Journal 31, 12 - 39.

Yi, C., Li, X. & Qu, J. 2002: Quaternary glaciation of Puruogangri: the largest modern ice field in Tibet. Quaternary International 97/98, 111 - 123.

Zech, R., Glaser, B., Sosin, P., Kubik, P. W. & Zech, W. 2005: Evidence for long-lasting landform surface instability on hummocky moraines in the Pamir Mountains (Tajikistan) from 10Be surface exposure dating. Earth and Planetary Science Letters 237, 453 - 461.

Zech, R., Zech, M., Kubik, P. W., Kharki, K. & Zech, W. 2009: Deglaciation and landscape history around Annapurna, Nepal, based on 10Be surface exposure dating. Quaternary Science Reviews 28, 1106 - 1118.

Zech, W., Glaser, B., Abramowski, U., Dittman, C. & Kubik, P. W. 2003: Reconstruction of the Late Quaternary Glaciation of the Macha Khola valley (Gorkha Himal, Nepal) using relative and absolute (14C, 10Be, dendrochronology) dating techniques. Quaternary Science Reviews 22, 2253 - 2265.

Zreda, M. G., Phillips, F. M. & Elmore, D. 1994: Cosmogenic 36Cl accumulation in unstable landforms 2. Simulations and measurements on eroding moraines. Water Resources Research 30, 3127 - 3136.

Table 1. ^{10}Be ages and details of sample locations and dated material.

Sample name	Moraine group	Latitude	Longitude	Altitude	Boulder size	Thickness	Shielding	Quartz mass	Be carrier[2]	^{10}Be/^{9}Be ratio	^{10}Be atoms[3] (per g of quartz)	Age[4]
		(°N)	(°E)	(m a.s.l.)	h/w/w[1] (cm)	(cm)	correction	(g)	(g)	ratio ± error	atoms ± error	(ka)
NK1	ST-3	34.0466	75.9473	3506	140/210/170	3.5	0.971	23.0521	0.3525	$60.8\pm2\times10^{-14}$	$66.362\pm1.4080\times10^{4}$	16.3 ± 1.5
NK2	ST-3	34.0466	75.9473	3506	130/155/210	4.5	0.950	18.5199	0.3520	$54.0\pm4\times10^{-15}$	$58.088\pm2.2750\times10^{3}$	1.5 ± 0.1
NK3	ST-3	34.0466	75.9473	3506	130/155/210	3.0	0.971	17.5704	0.3510	$32.5\pm1\times10^{-14}$	$45.522\pm1.4019\times10^{4}$	11.1 ± 1.0
NK4	ST-3	34.0466	75.9473	3506	30/195/100	3.0	0.971	15.4513	0.3534	$31.5\pm1\times10^{-14}$	$50.467\pm1.4412\times10^{4}$	12.4 ± 1.1
NK5	ST-2	34.0477	75.9486	3542	90/180/100	3.0	0.977	18.5985	0.3539	$74.0\pm3\times10^{-14}$	$100.881\pm3.8322\times10^{4}$	24.1 ± 2.3
NK6	ST-2	34.0477	75.9486	3542	55/90/70	2.5	0.977	26.1264	0.3507	$67.2\pm3\times10^{-14}$	$64.504\pm2.5057\times10^{4}$	15.3 ± 1.5
NK7	ST-2	34.0477	75.9486	3542	170/310/220	3.0	0.977	20.1406	0.3518	$46.4\pm1\times10^{-14}$	$57.486\pm1.3537\times10^{4}$	13.7 ± 1.2
NK8	ST-2	34.0477	75.9486	3542	60/95/60	3.0	0.977	20.7575	0.3509	$55.4\pm2\times10^{-14}$	$66.710\pm1.6787\times10^{4}$	15.9 ± 1.4
NK9	NKB1	34.0466	75.9532	3703	Bedrock	3.5	0.979	17.6468	0.3501	$147.0\pm3\times10^{-14}$	$210.621\pm3.9918\times10^{4}$	46.6 ± 4.2
NK10	NKB1	34.0465	75.9534	3713	Bedrock	2.0	0.977	19.6579	0.3521	$138.2\pm3\times10^{-14}$	$178.423\pm3.6056\times10^{4}$	38.7 ± 3.5
NK11	NKB1	34.0466	75.9537	3705	Bedrock	3.5	0.979	16.4096	0.3527	$154.6\pm3\times10^{-14}$	$238.680\pm4.1709\times10^{4}$	52.8 ± 4.7
NK12	NKB1	34.0466	75.9537	3705	Bedrock	3.5	0.974	20.7397	0.3532	$231.3\pm4\times10^{-14}$	$284.980\pm4.6692\times10^{4}$	62.7 ± 5.6
NK13	NKB1	34.0466	75.9537	3701	Bedrock	3.0	0.978	19.4942	0.3524	$200.2\pm6\times10^{-14}$	$261.693\pm7.5883\times10^{4}$	57.9 ± 5.4
NK14	NKB1	34.0466	75.9530	3693	Bedrock	3.0	0.946	20.2597	0.3515	$197.3\pm4\times10^{-14}$	$247.362\pm4.7554\times10^{4}$	56.7 ± 5.1
NK15	ST-1	34.0522	75.9430	3443	100/120/120	1.5	0.980	19.6961	0.3543	$44.2\pm3\times10^{-14}$	$56.069\pm3.6236\times10^{3}$	13.9 ± 1.5
NK16	ST-1	34.0521	75.9428	3454	80/150/125	2.0	0.984	17.0560	0.3546	$23.3\pm9\times10^{-15}$	$33.012\pm0.1327\times10^{4}$	8.1 ± 3.3
NK17	ST-1	34.0515	75.9427	3453	125/205/155	3.0	0.965	27.0755	0.3533	$70.6\pm1\times10^{-14}$	$65.944\pm1.1072\times10^{4}$	16.7 ± 1.5
NK18	ST-1	34.0511	75.9428	3454	60/145/120	3.0	0.980	23.2039	0.3518	$44.9\pm1\times10^{-14}$	$48.241\pm1.2854\times10^{4}$	12.0 ± 1.1
NK19	ST-1	34.0505	75.9427	3453	100/150/120	3.0	0.973	19.4354	0.3501	$49.1\pm2\times10^{-14}$	$62.818\pm2.0504\times10^{4}$	15.8 ± 1.5
NK20	ST-1	34.0505	75.9427	3453	80/150/110	3.0	0.983	19.4514	0.3545	$40.9\pm2\times10^{-14}$	$52.693\pm1.8129\times10^{4}$	13.1 ± 1.2
NK21	ST-1	34.0502	75.9428	3463	200/380/220	5.0	0.984	23.4204	0.3528	$61.0\pm3\times10^{-14}$	$65.595\pm3.0329\times10^{4}$	16.5 ± 1.6
NK22	TG-1	34.0623	75.9229	3523	80/150/100	2.0	0.977	19.9703	0.3503	$66.7\pm2\times10^{-14}$	$83.652\pm2.5077\times10^{4}$	20.0 ± 1.8
NK23	TG-1	34.0626	75.9233	3518	165/380/145	3.5	0.974	18.4190	0.3536	$57.2\pm5\times10^{-14}$	$78.008\pm6.6618\times10^{4}$	19.0 ± 2.3
NK24	TG-1	34.0632	75.9247	3504	150/450/230	5.0	0.982	20.2792	0.3538	$62.3\pm2\times10^{-14}$	$77.626\pm2.2431\times10^{4}$	19.2 ± 1.8
NK25	TG-1	34.0637	75.9255	3495	190/220/120	4.0	0.982	17.4424	0.3517	$48.5\pm2\times10^{-14}$	$69.443\pm2.0030\times10^{4}$	17.1 ± 1.6
NK26	TG-1	34.0643	75.9263	3486	80/280/120	3.5	0.982	19.9042	0.3512	$48.2\pm3\times10^{-14}$	$60.380\pm3.4227\times10^{4}$	14.8 ± 1.5
NK27	TG-1	34.0643	75.9263	3486	90/220/150	2.0	0.985	16.7437	0.3527	$45.0\pm3\times10^{-14}$	$67.183\pm4.2410\times10^{4}$	16.3 ± 1.8
NK28	TG-1	34.0644	75.9266	3489	105/175/160	4.0	0.984	23.5195	0.3542	$58.7\pm3\times10^{-14}$	$63.061\pm2.4848\times10^{4}$	15.5 ± 1.5
NK29	TG-3	34.0559	75.9181	3679	120/180/260	2.5	0.957	22.2890	0.3523	$25.6\pm3\times10^{-15}$	$15.631\pm0.5137\times10^{4}$	0.4 ± 0.1
NK30	TG-3	34.0548	75.9173	3720	210/390/290	4.0	0.957	23.6031	0.3503	$33.0\pm4\times10^{-15}$	$22.600\pm1.7647\times10^{3}$	0.5 ± 0.1

[1]H = height; W = widths.

[2]Concentration of Be carrier is 1089.7 (ppm g^{-1}).

[3]Atoms of ^{10}Be are corrected for blanks using their average ratio of $1.20\pm0.23\times10^{-14}$ and an average error ratio of 2×10^{-15}.

[4]Age was calculated using the time-constant scaling method of Lal (1991) and Stone (2000), assuming that the erosion rate is zero.

Table 2. Glacial stages in the Nun-Kun area and the main characteristics of the moraines formed in each stage.

MIS	Age	Moraine group/ glacial stage	Main valley	Sentick Glacier	Rantac Glacier	Tarangoz Glacier	Interpretation
MIS1	Late Holocene	Tanak glacial stage Lomp glacial stage				TG4 TG3 (0.4±0.2 ka)	Holocene glacial advance TG4: Rapid glacial retreat from TG3 moraines
MIS2	Lateglacial	Anantick glacial stage		ST3 (11.7±6.0 –12.4±1.1 ka) ST2 (14.3±1.7 ka)		TG2	Low-relief, subdued moraine group TG3: Glacial stagnant or re-advance period
		Tongul glacial stage		ST1 (16.7±1.5ka)	RT1	TG1 (17.4±1.8 ka)	Sharp crest, linear ridge
MIS3/4		Achambur glacial stage	NKB1 (38.7±3.5 –62.7±5.6 ka)				Main trunk glacial retreat age Extensive glacier

Table 3. Summary of previous glacial studies in the Greater Himalaya and the Zanskar and Ladakh ranges.

Range	Region	Reference	Location	Chronology	Glacial stage and ELA
Greater Himalaya range	Lahul	Owen *et al.* (1995, 1997, 2001)	32.4°N 77.6°W	TCNs	Chandra: only landform Batal: 12–15.5 ka Kulti: 10.6–11.4 ka Songpani: only landform
	Nun-Kun	this study	34°N 76°W	TCNs	Achambur: 38.6–62.7 ka Tongul: 16.7–17.4 ka Amantick: 14.3 ka, 11.7–12.4 ka Lomp: 0.4–0.5 ka Tanak: only landform
Zanskar range	Stod Valley Lung-nak Valley	Osmatson *et al.* (1994)	34.5°N 76.9°W		Glacial stages: only landforms Contemporary ELA: 5500–5800 m a.s.l. LGM ΔELA: ~600 m
	Kurgiakh Valley Reru Valley	Taylor & Mitchell (2000)	33°N 77°W	OSL	Chandra: only landform Batal: 78±12.3 ka; 40.0±9.3 ka Kulti: 16.2±5.6–10.2±2.1 ka Sonapani: only landform
	Markha Valley Nimaling Mountain	Damm (2006)	33.7°N 77.6°W		TSAM(0.5) ELA (m a.s.l.), ΔELA (m) Skio1, 2: ΔELA >1000 Chaluk: ELA: 5030, ΔELA: 670 Hankar: ELA: 5190, ΔELA: 510 Nimaling1: ELA: 4200, ΔELA: 400 Nimaling2: ELA: 4500, ELA: 350 Gapo Ri1: ELA: 5620, ΔELA: 50–70 Dzo Jongo1: ELA: 5640, ΔELA: 50–70 Kang Yaze1: ELA: 6700, ΔELA: 50–70 Gapo Ri2: ELA: 5640, ΔELA: 30–50 Dzo Jongo2: ELA: 5660, ΔELA: 50–70 Kang Yaze2: ELA: 5730, ΔELA: 50–70
	Puga Valley Karzok Valley	Hedrick *et al.* (2011)	33°N 78°W	TCNs	Puga Valley PM0: 128.8±20.1 ka PM1: 45.5±8.4 ka PM2: 4.2±2.2 ka PM3: 0.6±0.5 ka Karzok Valley: KM0: 311 ka KM1: 54–76, 12.5–23.6 ka KM2: 74–98, 21–27 ka KM3: 60–89 ka KM4: 2.7–4.7 ka
	Zanskar	Burbank & Fort (1985)	33.9°N 77.9°W		THAR (0.4) ELA (m a.s.l.) ELA: 4688±16
Ladakh range	Ladakh	Burbank & Fort (1985)	34°N 77.6°W		THAR (0.4) ELA (m a.s.l.) ELA: 5288±113
	Bagzo	Owen *et al.* (2006)	34°N 77.6°W	TCNs	Indus Valley: 130–385 ka Leh: 100–200 ka Kar: only landform Bagzo: 41–74 ka Khalling: only landform

Table 4. Results of ELA reconstruction using the AAR and THAR methods.

Range	Region	Reference	Valley	Latitude (°N)	Longitude (°E)	Toe altitude (m a.s.l.)[1]	Head altitude (m a.s.l.)[2]	Aspect	Glacial stage[3]	Moraine type[4]	AAR (m a.s.l.)	THAR (m a.s.l.)[5]
Greater Himalaya range	Lahul	Owen *et al.* (1995, 1997, 2001)	Batal glacier	32.348	77.548	4244	5003	NE	present	–	4737	4623.5
			Batal glacier	32.218	77.365	4057	5003	NE	Somapani	LF	4672	4530
			Batal glacier	32.216	77.370	4042	5003	NE	Batal	LF	4667	4522.5
			Batal glacier	32.215	77.371	3996	5003	NE	Batal	LF	4638	4049.5
			Sissu Nala	32.290	77.077	4032	5292	W	present	–	4851	4662
			Sissu Nala	32.290	77.077	3102	5292	W	Batal (Kulti)	LF	4526	4197
	Nun-Kun	this study	Sentick	34.046	75.947	4439	5812	NE	present	–	5531	5125.5
			Sentick	34.046	75.947	3478	5812	NE	Amantick	L	4954	4645
			Sentick	34.047	75.948	3461	5812	NE	Amantick	L	4969	4636.5
			Sentick	34.052	75.942	3338	5812	NE	Tongul	LF	4905	4575
			Tarangoz	34.055	75.918	4248	5542	NE	present	–	5089	4895
			Tarangoz	34.055	75.918	3579	5542	NE	Lomp	L	4885	4560.5
			Tarangoz	34.064	75.926	3277	5542	NE	Tongul	LF	4749	4409.5
							Present glacial ELA average in the Zanskar range				5052	4826.5
Zanskar range	Nimaling	Damm (2006)	Kang Yaze East	33.745	77.565	5380	6020	NE	present	–	5796	5700
			Kang Yaze East	33.745	77.565	5274	6020	NE	?	L	5759	5647
			Regoni Mallai	33.745	77.565	5547	5957	NE	present	–	–	5752
			Dzo Jongo	33.745	77.565	5391	6245	NE	present	–	5946	5818
			Nimaling	33.745	77.565	4298	6228	NE	?	L	5553	5263
	Puga	Hedrick *et al.* (2011)	Puga	33.249	78.200	5678	6124	NE	present	–	5968	5901
			Puga	33.237	78.182	5065	6124	NE	PM1	L	5811	5594.5
			Puga	33.245	78.199	4837	6124	NE	PM2	L	5731	5480.5
			Puga	33.226	78.166	5255	6124	NE	PM3	L	5814	5689.5
	Karzok		Karzok	32.961	78.254	4562	6060	SE	KM0	L	5536	5311
			Karzok	32.984	78.215	4792	6060	SE	KM1	L	5608	5426
			Karzok	32.977	78.203	4996	6034	SE	KM3	L	5671	5515
							Present glacial ELA average in the Zanskar range				5903.3	5802.8
Ladakh range	Bazgo	Owen *et al.* (2006)	Ladakh	34.113	77.169	3352	5429	SW	Leh	L	4697	4390.5
			Ladakh	34.187	77.200	4184	5429	SW	Bazgo	L	4986	4806.5
			Ladakh	34.186	77.198	4130	5429	SW	Bazgo	L	4967	4779.5
			Ladakh	34.200	77.210	4631	5429	SW	Bazgo	L	5142	5030
			Ladakh	34.096	77.246	4740	5429	SW	Bazgo	L	5180	5084.5
			Ladakh	34.195	77.231	5110	5429	SW	Khalling	L	5317	5269.5
			Ladakh	34.195	77.231	5121	5429	SW	present	–	5311	5275
	Phyang		Ladakh	34.110	77.296	3567	5725	SW	Leh	L	4970	4646
			Ladakh	34.131	77.307	3856	5725	SW	Kar	L	5074	4790.5
			Ladakh	34.292	77.572	5265	5725	SW	present	–	5295	5495
	Leh		Ladakh	34.112	77.356	3696	5738	SW	Leh	L	5023	4717
			Ladakh	34.132	77.366	4130	5679	SW	Kar	L	5138	4904.5
			Ladakh	34.237	77.664	5303	5679	SW	present	–	5547	5491
							Present glacial ELAs average in the Ladakh range				5384	5420.3

[1]Toe altitude is based on the ASTER DEM elevation.
[2]Head altitude is derived from ASTER DEM elevation.
[3]Information on extent ages is summarized in Table 3.
[4]L = lateral moraine; LF = latero-frontal moraine.
[5]The uncertainty in ELA is ±10 m.

Table 5. OSL dating results and detailed information about the dated samples.

	Bed	Sample	Number of disk	Latitude (°N)	Longitude (°E)	Altitude (m a.s.l.)	Depth (cm)
Sample details	Unit A-1	NKTO1	24 (19)	34.07	75.93	3426	236
	Unit A-2	NKTO2	24 (17)	34.07	75.93	3426	143
	Unit A-3	NKTO3	24 (16)	34.07	75.93	3426	69
Sample	Measured equivalent dose						
	Weighted mean (Gy)	Mean (Gy)	Terrestrial (Gy ka^{-1})	Cosmic (Gy ka^{-1})	Total dose rate (Gy ka^{-1})	Weighted mean (ka)	Mean (ka)
NKTO1	37.0±0.3	37.6±5.1	3.6±0.2	0.2±0.1	3.8±0.2	9.6±0.5	9.8±1.4
NKTO2	21.8±0.3	26.9±10.2	4.4±0.2	0.3±0.1	4.7±0.2	4.6±0.2	5.7±2.2
NKTO3	4.6±0.0	4.5±0.7	4.4±0.2	0.3±0.1	4.7±0.2	1.0±0.1	1.0±0.2

Table 6. Results of radiocarbon dating and $\delta^{13}C$ analysis.

Sample	Depth (cm)	Uncorrected age (^{14}C a BP)	Calibrated age[1] (cal. a BP)	$\delta^{13}C$ (‰)
NKTC3	74	1620±40	1498±56	–25.6
NKTC2	100	3150±40	3388±37	–26.2
NKTC1	122.5	4480±40	5155±99	–22.7

[1]All the radiocarbon ages are calibrated using CALPAL (CalPal 2007).

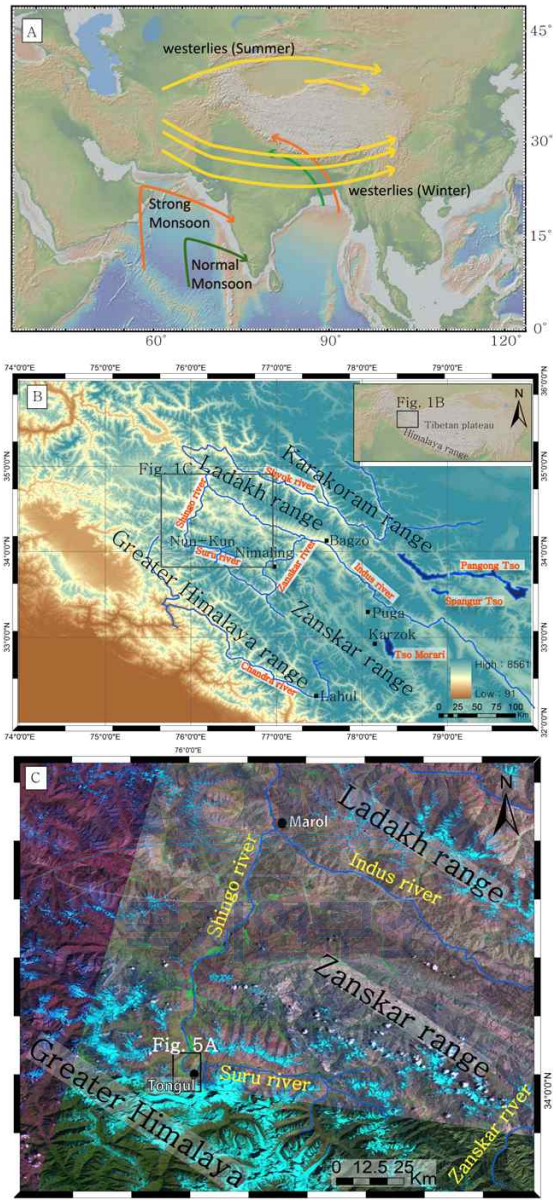

Figure 1. A. Map of the Indian summer monsoon and westerlies direction. Green lines show the normal monsoonal wind direction. Orange arrows indicate the prevailing wind direction of strong monsoons during the late Pleistocene and early Holocene. Yellow lines depict the present-day westerlies. Map modified from Barry & Chorley (1992) and Bookhagen et al. (2005). B. Digital elevation model (SRTM) of the northwestern Himalaya. The Nun-Kun massif is located on the boundary between the reater Himalaya and the Zanskar range. C. ETM+ Satellite image map of the Nun-Kun massif region. This figure is available in colour at http://www.boreas.dk.

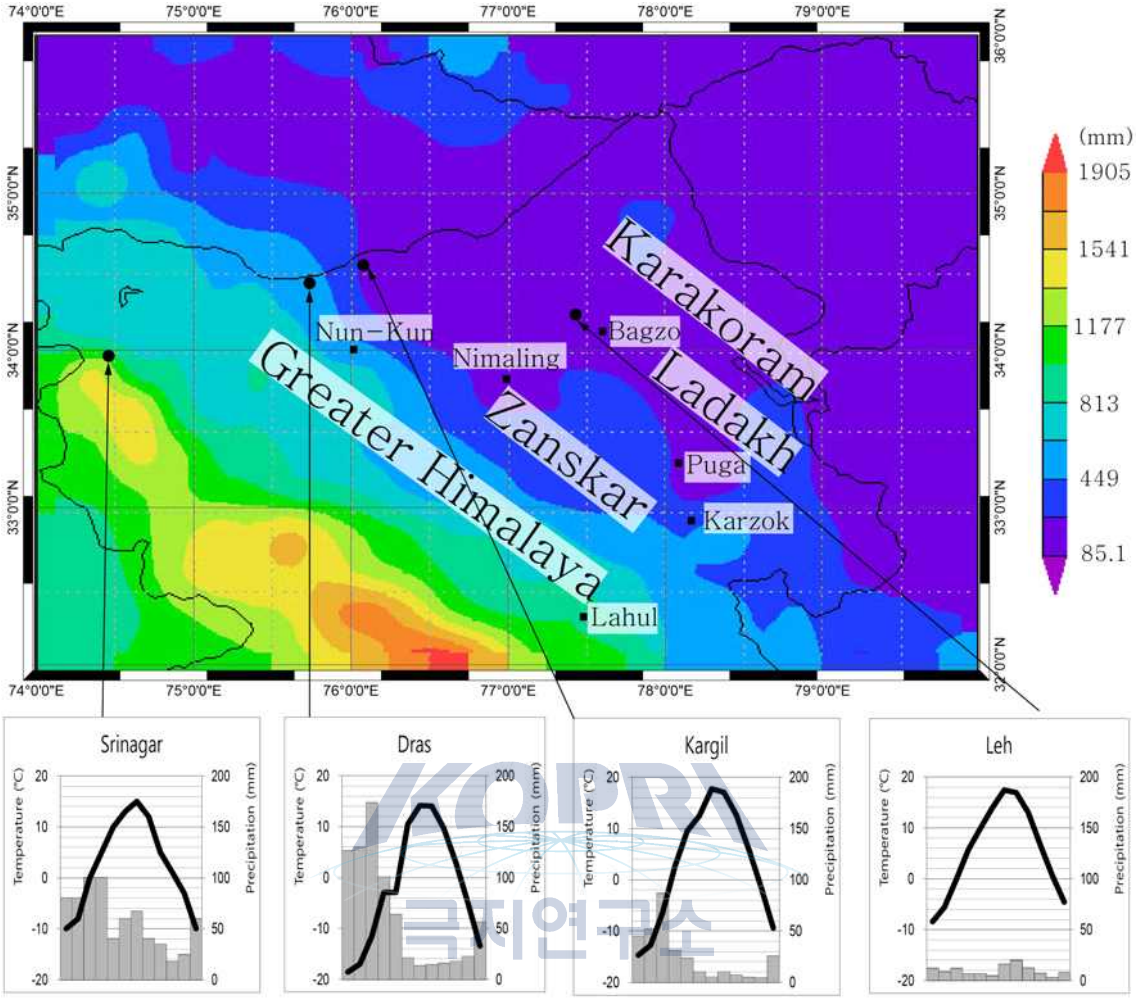

Figure 2. Climate records for Leh, Srinagar, Dras and Kargil, which are the nearest stations to the Nun-Kun massif. Apart from Leh, all the regions have higher winter than summer precipitation during the past 30 - 40 years. Temperature differences between the maximum and minimum are more than 25℃. The climograph for Srinagar is taken and modified from Walter & Lieth (1960 - 1967). The other climographs are taken and modified from Osmaston et al. (1994). The base map shows accumulated rainfall (mm a^{-1}) from March 2011 to February 2012. The map was generated using TRMM data from NASA (2012) Giovanni TOVAS data. This figure is available in colour at http://www.boreas.dk.

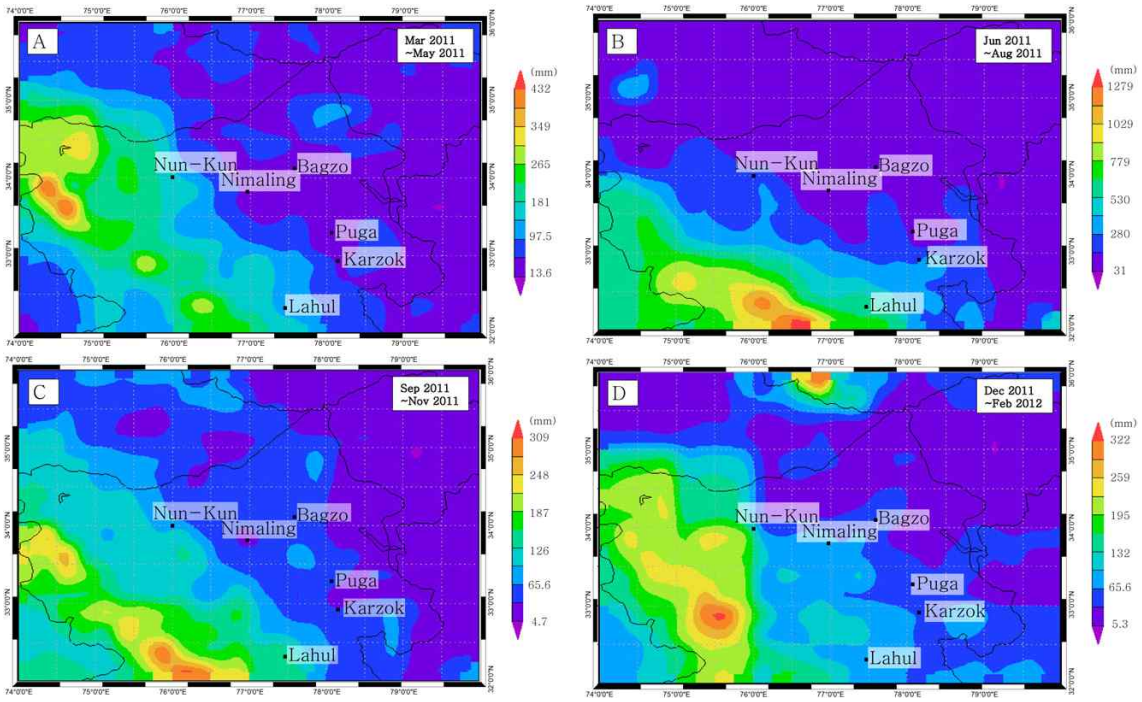

Figure 3. Distribution of accumulated rainfall (mm a−1) generated using TRMM data from NASA (2012) Giovanni TOVAS data. A. Accumulated rainfall from March to May 2011. Annual rainfall near the Nun-Kun area amounts to 181.3 mm a−1. The Greater Himalaya range receives more rainfall than the Zanskar and Ladakh ranges. The highest precipitation amount of ~349 mm a−1 occurs in a region at 33.5 - 34°N, 74.2 - 75°E. B. Accumulated rainfall from June to August 2011. The strong precipitation gradient from the south to the NE is illustrated. The strong precipitation gradient may reflect the influence of the Indian summer monsoon in the Himalaya range. Rainfall near the Nun-Kun area is ≤280 mm a−1. The highest precipitation amount of ~1279 mm a−1 occurs in a region at 32°N, 76.5°E. C. Map of accumulated rainfall (mm a−1) from September to November 2011. The highest precipitation amount of ~248 mm a−1 occurs in a region at 32 - 32.5°N, 76 - 76.5°E. The TRMM data show that the accumulated rainfall in Nun-Kun is ~66 mm a−1. D. The accumulated rainfall during the autumn of 2011 decreases across the Transhimalaya. Precipitation from December 2011 to February 2012 contrasts with summer precipitation. The highest precipitation of ~259 mm a−1 occurs in the regions at 33°N, 75.5°E and 36°N, 76.5 - 77°E. The precipitation gradient within the Greater Himalaya is weak. The TRMM data show that the accumulated rainfall in the Nun-Kun area is 69 - 132 mm a−1. This figure is available in colour at http://www.boreas.dk.

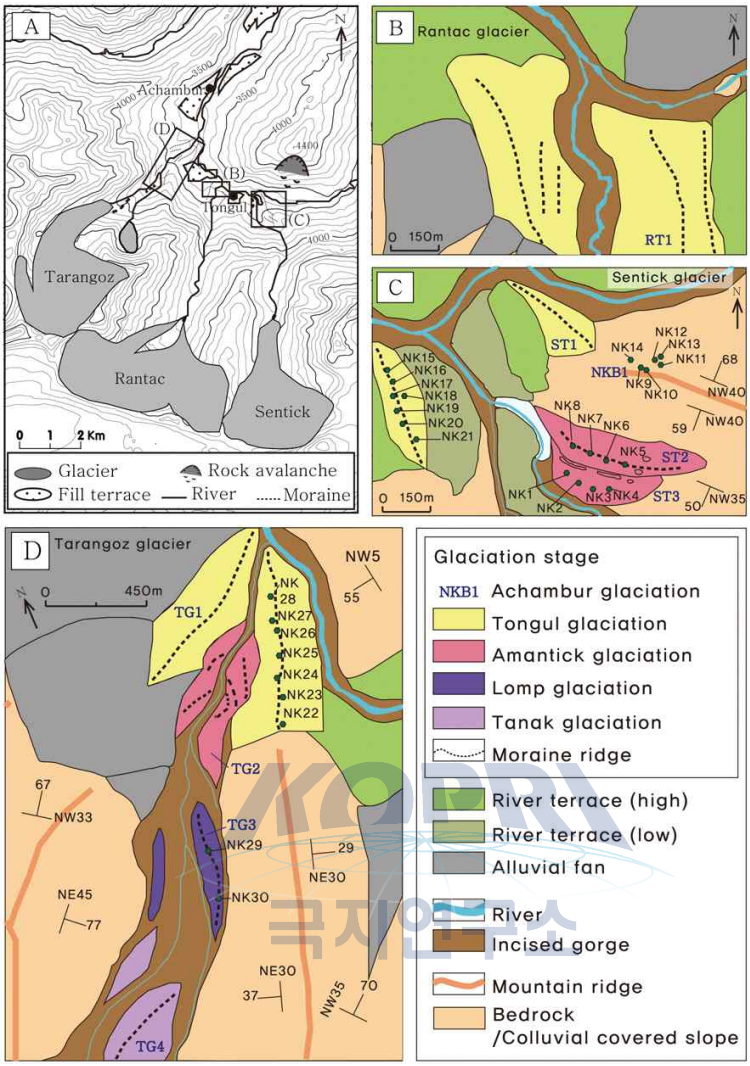

Figure 4. A. Topographic map of the study area. B - D. Geomorphic maps of the Nun-Kun massif. Each map shows the detailed location of the various studied glacial landforms. Sampling points are marked on each moraine. The moraines are divided into four groups (Tongul, Amantick, Lomp and Tanak glacial stages) on the basis of morphostratigraphy and chronology data. The moraines from the Tongul glacial stage are the oldest, and those from the Tanak glacial stage are the youngest. Terminal moraines and distinct moraines for the most extensive glacier produced during main valley glaciation (Achambur glaciation) are absent. Therefore, samples were obtained from glacially polished bedrock surfaces around the glacier trimline. However, most moraines produced by tributary glaciers (Tongul, Amantick, Lomp and Tanak glacial stages) have sharp ridgelines. This figure is available in colour at http://www.boreas.dk.

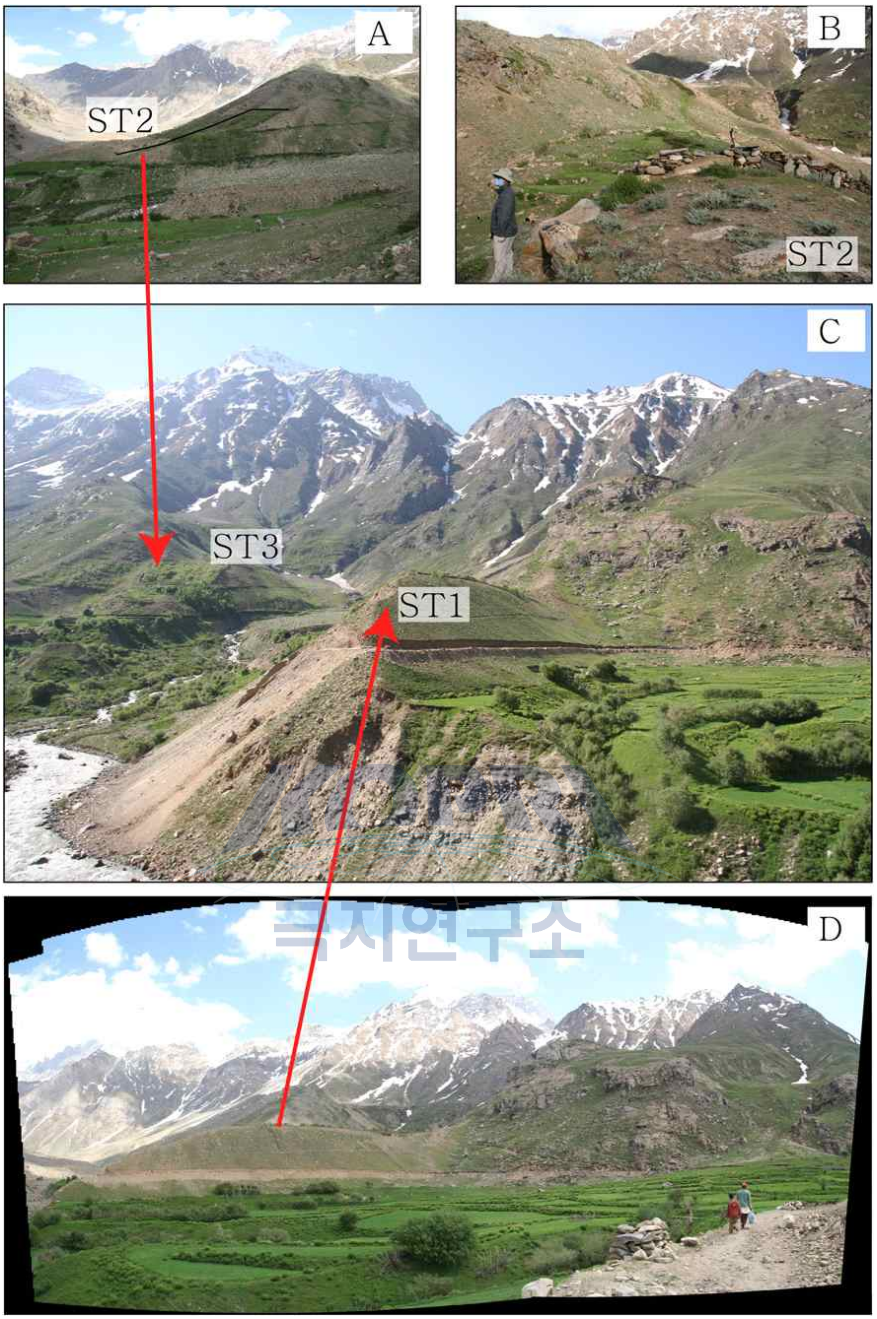

Figure 5. Views of the Sentick glacial valley. A. View looking south at the ST2 moraine in the Sentick Valley. B. Closer view of the ST2 moraine. Relatively low-lying boulders are dominant. C. Panoramic view of the Sentick Glacier from the opposite side of the main valley. The ST1 moraine that has a straight ridge in the centre of (C) is more clearly visible in (D). The ST2 moraine that has a low gentle ridge (B) lies behind the ST3 moraine (C). This figure is available in colour at http://www.boreas.dk.

Figure 6. View of the Rantac glacial valley. The glacial valley is relatively narrow compared with the other glacial valleys. A pair of moraines with several ridges is visible at the confluence with the main valley. RT1 moraines are classified according to morphostratigraphy into the oldest moraine (Tanak glacial stage) in the tributary glacial valley. This figure is available in colour at http://www.boreas.dk.

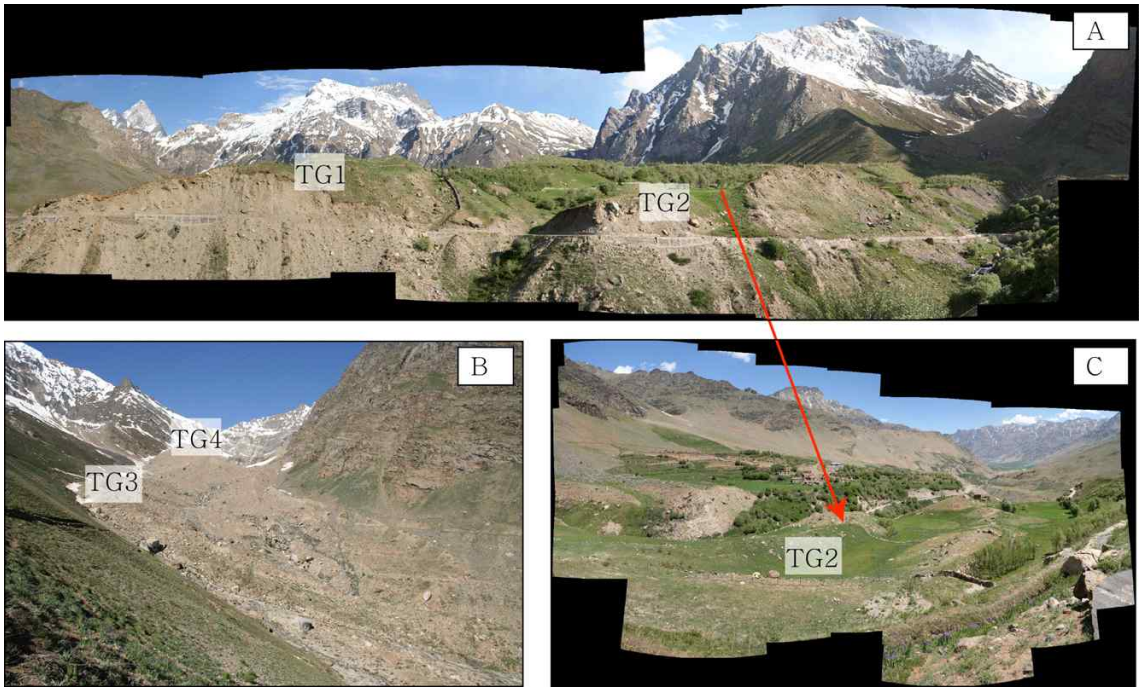

Figure 7. Views of the Tarangoz glacial valley. TG1 moraines (A) have distinctive linear moraine ridges. TG2 moraines (C) have low relief ridges reflecting formation during glacial stagnation or retreat. The TG3 moraine (B) is located below the TG4 moraine. This figure is available in colour at http://www.boreas.dk.

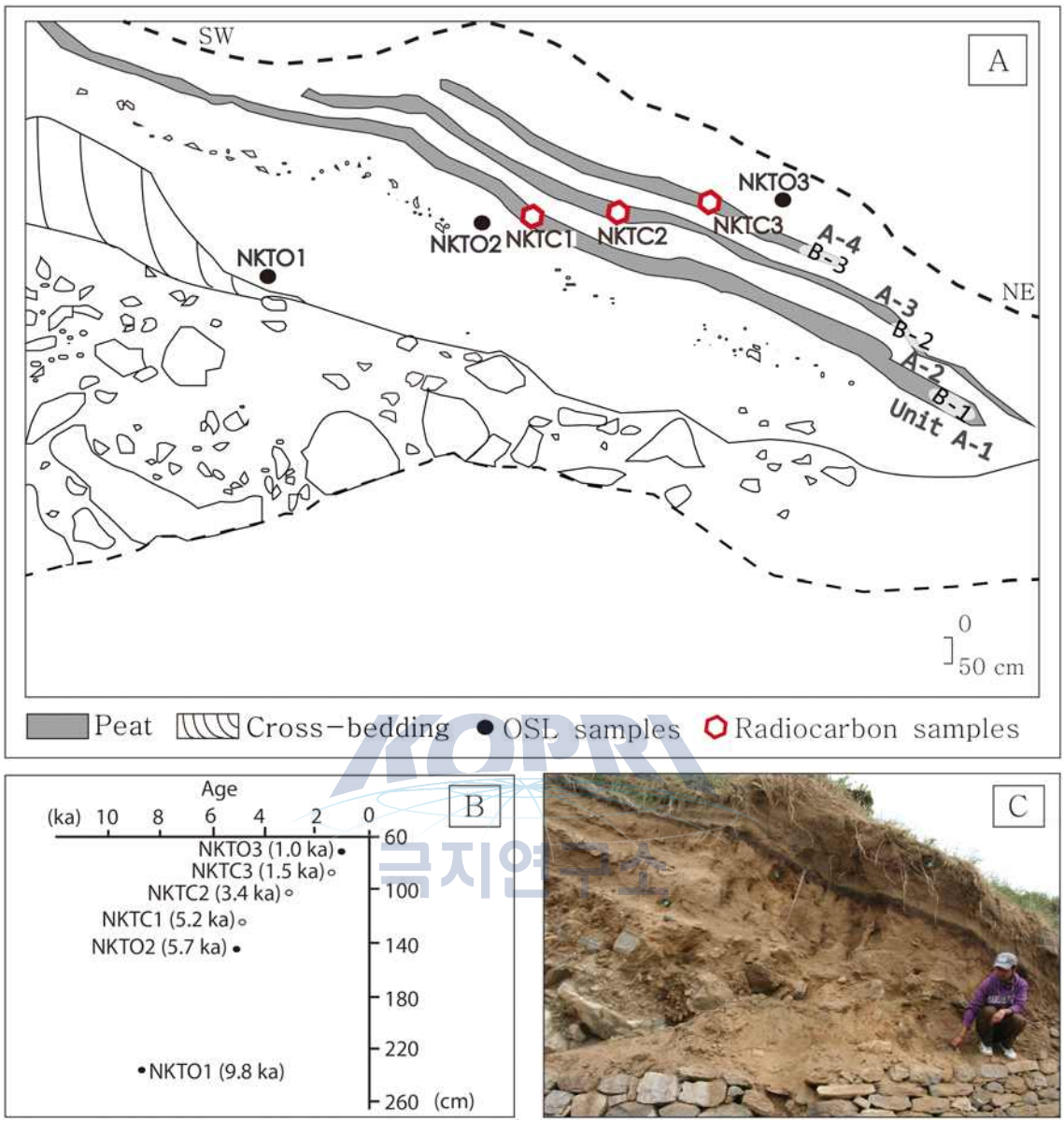

Figure 8. View of exposure in the TG1 moraine at 34.065°N, 75.928°E; 3425 m a.s.l. (A) Sketch shows outcrop features and sampling points. Three OSL samples were collected from the aeolian deposits, and three radiocarbon samples were taken from the peat beds for dating and analysis of delta 13C. Radiocarbon ages are written on the sketch map. (B) Age - depth profile of an aeolian deposit. OSL and radiocarbon ages are plotted on the x-axis, and the sample depths are plotted on the y-axis. White dots are the radiocarbon dates and black dots are the OSL ages. (C) View of an outcrop exposed on the TG1 moraine. Till is exposed at the bottom left of the photograph. The aeolian deposit with intercalated peat beds is underlain by till. This figure is available in colour at http://www.boreas.dk.

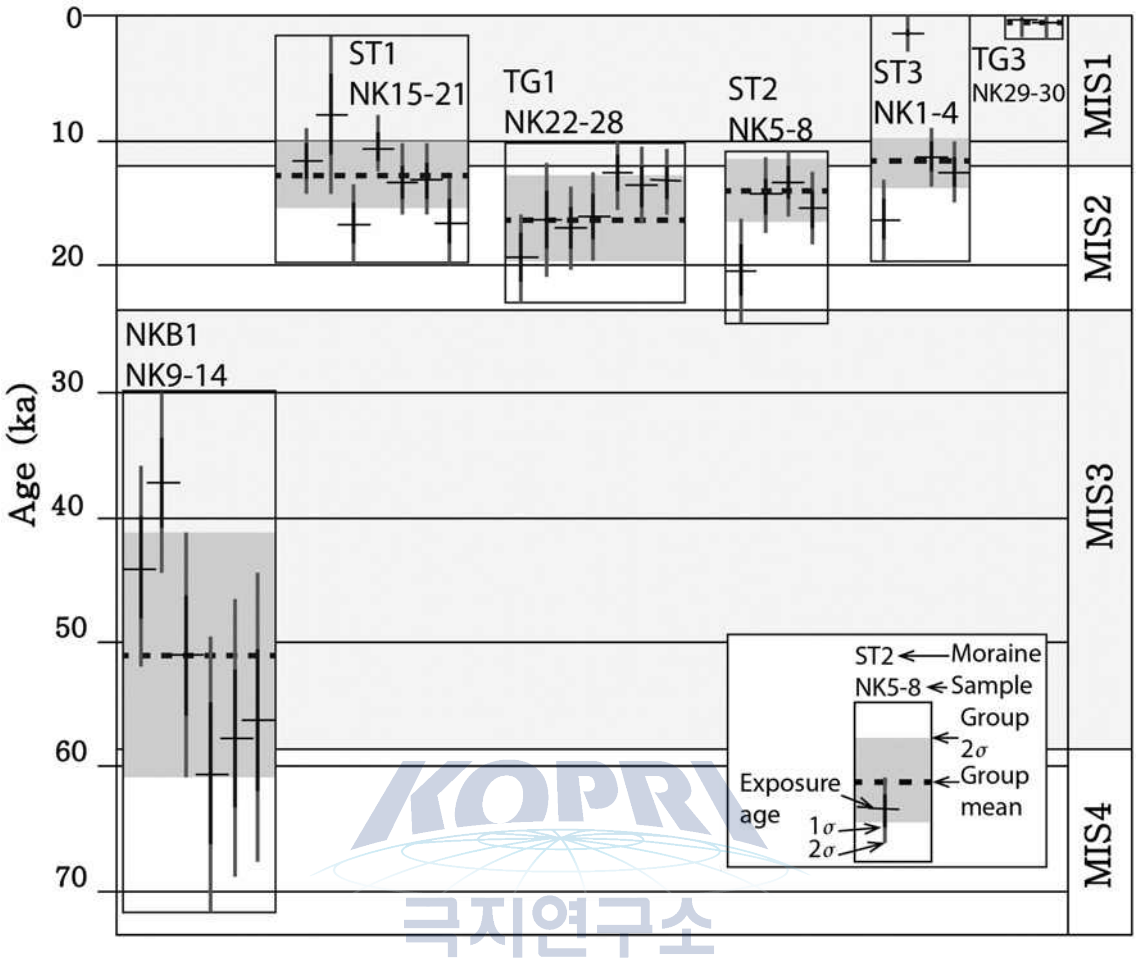

Figure 9. ^{10}Be ages from glacial boulders from each moraine. The horizontal black line shows the mean ages, and the black and grey bars for each boulder are the 1σ and 2σ uncertainties, respectively. The boxes around each cluster of boulder ages represent samples from the same moraines. The grey band in each box is the 2σ uncertainty for each cluster of boulder ages.

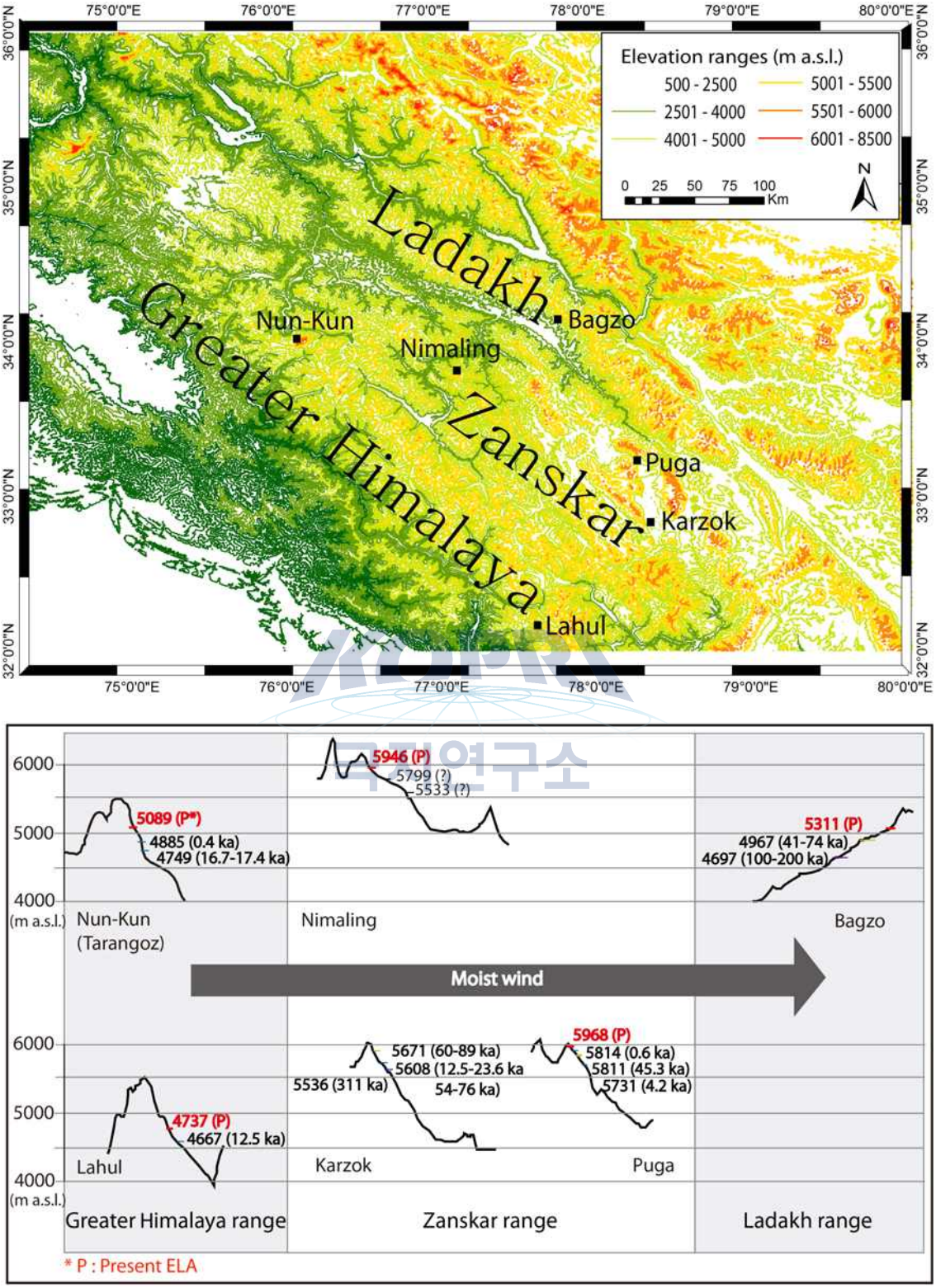

Figure 10. Past and present-day ELAs plotted on topographic cross-sections. Graph shows a comparison of ELAs along the Nun-Kun to the Bagzo. ELA graphs of Lahul, Puga and Karzok are depicted. This figure is available in colour at http://www.boreas.dk.

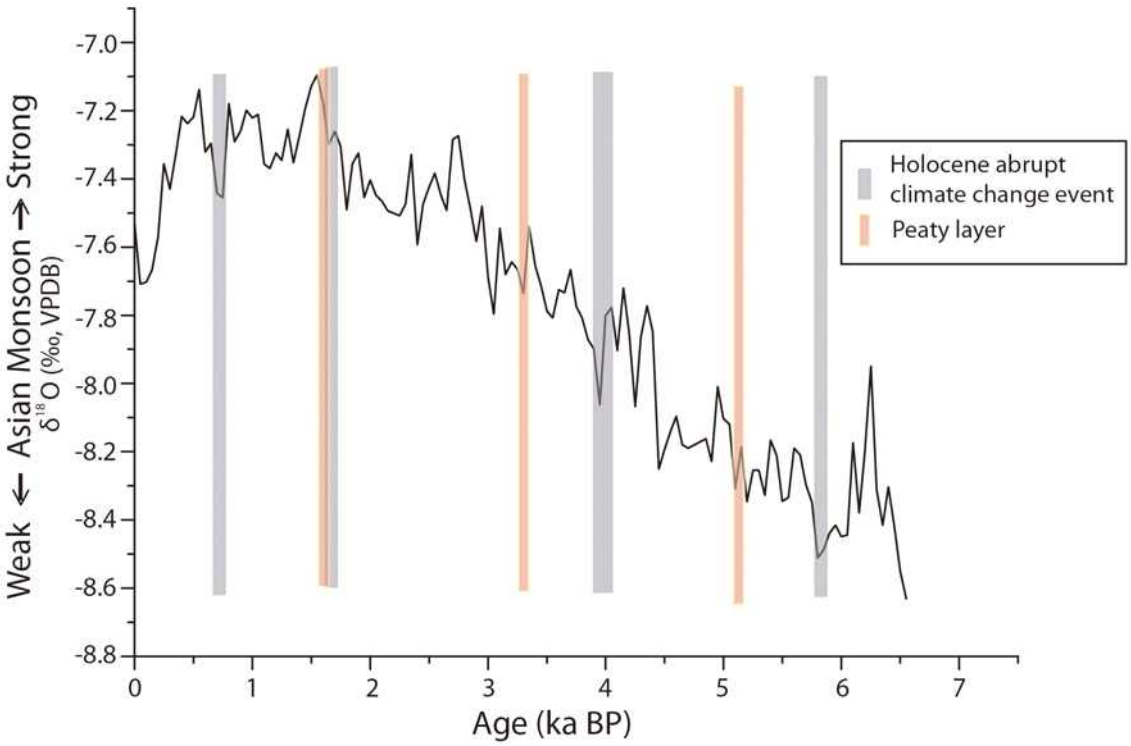

Figure 11. δ18O data for a speleothem from the Dongge cave, southern China (modified from Wang et al. 2005). The grey boxes show the timing of the Holocene abrupt climate change events. The pink boxes are peat ages from the aeolian deposit on the TG3 moraine. This figure is available in colour at http://www.boreas.dk.

제 21 장

Arsenite Oxidation Initiated by the UV Photolysis of Nitrite and Nitrate[14)]

Kitae Kim[1,2], Wonyong Choi[1*]

[1]Pohang University of Science and Technology
[2]Korea Polar Research Institute

Abstract: This study demonstrates that the production of reactive oxidizing species (e.g., hydroxyl radical (• OH)) during the photolysis of nitrite (NO_2^-) or nitrate (NO_3^-) leads to the oxidative conversion of arsenite (As(III)) to arsenate (As(V)). While the direct UV photolytic oxidation of As(III) was absent, nitrite (20 or 200 μM) addition markedly accelerated the oxidation of As(III) under UV irradiation ($\lambda > 295$ nm), which implies a role of NO_2^- as a photosensitizer for As(III) oxidation. Nitrate-mediated photooxidation of As(III) revealed an initial lag phase during which NO_3^- is converted into NO_2^-. UV-Photosensitized oxidation of As(III) was kinetically enhanced under acidic pH condition where nitrous acid (HNO_2) with a high quantum yield for • OH production is a predominant form of nitrite. On the other hand, alkaline pH that favors the photoinduced transformation of NO_3^- to NO_2^- significantly facilitated the catalytic reduction/oxidation cycling, which enabled the complete oxidation of As(III) at the condition of $[As(III)]/[NO_2^-] \gg 1$ and markedly accelerated NO_3^--sensitized oxidation of As(III). The presence of O_2 and N_2O as electron scavengers enhanced the photochemical dissociation of NO_2^- via intermolecular electron transfer, initiating the oxidative As(III) conversion route probably involving NO_2 • and superoxide radical anion (O_2 • $^-$) as alternative oxidants. The outdoor experiment demonstrated the capability of NO_2^- for the

14) 이 연구 결과는 다음의 논문으로 출판되었음: Kim, D. H., Lee, J., Ryu, J., Kim, K., & Choi, W. (2014). Arsenite oxidation initiated by the UV photolysis of nitrite and nitrate. Environmental science & technology, 48(7), 4030-4037.

photosensitized production of oxidizing species and the subsequent oxidation of As(III) into As(V) under solar irradiation.

1. Introduction

Oxidative conversion of arsenite (As(III)) to arsenate (As(V)) leads to the reduction in toxicity and mobility of arsenic species in aquatic ecosystems and enhances the arsenic removal efficiency during physical water treatment processes such as coagulation and precipitation.(1) Considering that arsenite is the prevalent arsenic species in the environmental media,(2, 3) the remediation of arsenic-contaminated water matrix requires an oxidative treatment of As(III) as a pretreatment option. Advanced oxidation processes (AOPs) can be employed for rapid oxidative transformation of As(III) because As(III) is highly vulnerable to hydroxyl radical ($\bullet$OH)-induced oxidation (i.e., k (AsO_2^- + $\bullet$OH) = 9.0 × 109 M^{-1} s^{-1}).(4) Fenton reagent as a precursor of $\bullet$OH effectively oxidizes As(III) under acidic pH condition, and also forms high valent iron intermediates (e.g., ferryl ion (Fe(IV)) at circumneutral pH to convert As(III) to As(V).(5) Photolytic decomposition of ferric carboxylate complexes leads to high yield generation of $\bullet$OH over a relatively broad pH range, resulting in a significant oxidation of As(III) under near UV light irradiation.(6) Photoinduced oxidation of As(III) in the presence of iron oxyhydroxides has been investigated.(7, 8) Efficient photocatalytic oxidation of As(III) on TiO_2 has been also successfully demonstrated.(9-12) The direct photooxidation of As(III) is possible under 254 nm irradiation,(13) and the oxidation rate is highly enhanced in the presence of iodide, which acts as a photocatalyst under the irradiation of 254 nm.(14)

UV photolysis of nitrite (NO_2^-) and nitrate (NO_3^-) efficiently triggers the fission of O-N bonds to produce reactive oxidizing intermediates,(15) which may contribute to (1) photochemical transformation of chemical substances in the aquatic environment(16, 17) and (2) the oxidative treatment of organic/inorganic contaminants and pathogenic microorganisms in water.(18, 19) The main reactions that should be involved in the UV/As(III)/NO_2^-(or NO_3^-) system are listed in Table 1. The photolysis of NO_2^- (or NO_3^-) predominantly produces nitrogen oxide radical (NO$\bullet$ or $NO_2\bullet$) and oxide radical anion (O$\bullet$

$^-$) (reaction A2a or C2a), which undergoes rapid protonation to form $^\bullet$OH (reaction D1).(15) As a minor reaction pathway, the photodissociation of NO_2^- converts into $NO_2^\bullet$ and hydrated electron (eaq^-) (reaction A2b), which leads to the production of superoxide radical anion ($O_2^{\bullet -}$) with moderate oxidizing power (i.e., $E^0(HO_2^\bullet/H_2O_2)$ = 1.44 V_{NHE} or $E^0(O_2^{\bullet -}/HO_2^-)$ = 1.03 V_{NHE})(20) under air-equilibrated condition (reaction E1).(21) The one-electron oxidation pathway of NO_2^- is significantly promoted in the presence of ferric ion, iron oxide, and NO_3^-: the accompanying generation of $NO_2^\bullet$ leads to the nitration of phenolic compounds.(22) This supports the possible involvement of $NO_2^\bullet$ in the nitrite-mediated photochemical oxidation.

The photosensitizing capability of NO_2^- and NO_3^- to produce reactive oxidizing species can be applied to the oxidative conversion of As(III) to As(V). Although Dutta et al. briefly reported the photolysis of NO_3^- as a mean of generating OH radical for the oxidation of As(III),(23) the mechanism of NO_2^- (or NO_3^-)-mediated photosensitized oxidation of As(III) has not been studied. Nitrogen-containing radicals (i.e., $NO^\bullet$ and $NO_2^\bullet$) rapidly recombine to regenerate NO_2^- and NO_3^- (reactions F1 - 4)(21) in the absence of background organics that are susceptible to nitration. Therefore, a catalytic process based on the cycling of NO_2^- (or NO_3^-) might be utilized to mediate the photochemical oxidation of As(III). Since NO_2^- and NO_3^- are commonly present as background constituents of ground, surface, and wastewater matrixes (e.g., the mean level of NO_2^- and NO_3^- is 2.0, 17.3 mg/L, respectively, in arsenic contaminated groundwater),(24) their photolysis under sunlight may contribute to the natural oxidation mechanism of As(III).

This study investigated the photooxidation of As(III) to As(V) in the presence of NO_2^- or NO_3^- under UV irradiation ($\lambda > 295$ nm). The oxidation kinetics of As(III) and the accompanying conversion of NO_2^-/NO_3^- were investigated by varying the experimental parameters (e.g., pH, $[NO_2^-]$, dissolved gas). From this study, the roles of NO_2^- (or NO_3^-) in the photosensitized oxidation of As(III) in aquatic system were successfully demonstrated. The experiments were also performed under sunlight in order to simulate a natural environmental condition.

2. Experimental section

2.1. Chemicals and materials

Chemicals and reagents used in this work include the followings: $NaAsO_2$ (As(III), Aldrich), $Na_2HAsO_4 \cdot 7H_2O$ (As(V), Kanto), $NaNO_2$ (Aldrich), $NaNO_3$ (Aldrich), molybdate reagent solution (Fluka Analytical), tert-butyl alcohol (t-BuOH) (Samchun Chemicals). Suwannee River humic acid (HA) standard obtained from International Humic Substance Society (IHSS) was used to study the effect of natural organic matter on the As(III) oxidation during NO_2^- photolysis. All chemicals were of analytical grade. Deionized water used was ultrapure (18 MΩ·cm) and prepared by a Barnstead purification system. N_2 (99.999% purity) and N_2O (5.02% mol/mol He) were obtained from BOC Gases and Rigas.

2.2. Photolysis and analysis

Typical reaction solutions contained 200 μM NO_2^- (or NO_3^-) and 100 μM As(III). The tested solution was unbuffered and air-equilibrated. The initial pH was adjusted to 9.0 with concentrated solution of NaOH or $HClO_4$. A 300-W Xe arc lamp (Oriel) was used as a light source. The light beam was passed through a 10-cm IR water filter and a UV cutoff filter ($\lambda > 295$ nm) and then focused onto a cylindrical Pyrex reactor (50 mL) which was mixed on a magnetic stirrer. The incident light intensity in the active wavelength region ($295 < \lambda < 500$ nm) was measured to be 1.97×10^{-3} Einstein/min·L by ferrioxalate actinometry.(25) For the experiments in the presence of N2 or N_2O, the reactor was purged with the corresponding gas for 20 min prior to and continuously during photoirradiation. Sample aliquots of 1 mL were withdrawn using a 1-mL syringe from the UV-illuminated reactor at predetermined time intervals and were transferred to a 2-mL amber vial. The concentration of photogenerated As(V) was colorimetrically determined using a molybdenum blue method with a detection limit of 0.8 μM in which arsenomolybdate is reduced with ascorbic acid to form an intensively blue complex.(26) A solution of 0.1 mL

of ascorbic acid and 0.2 mL of molybdate reagent solution was mixed with 4 mL sample solution (diluted 4-fold with deionized water) in a conical tube. After 2 h of color development, the concentration of As(V) was monitored at 870 nm (ε = 19 550 $M^{-1}cm^{-1}$) using a UV-vis spectrophotometer (Libra S22, Biochrom). Quantitative analyses of NO_2^- and NO_3^- were performed along with that of As(V) using an ion chromatograph (IC, Dionex DX-120). The As(V) concentrations determined by IC matched those measured colorimetrically. The IC was equipped with a Dionex IonPac AS 23 (4 × 250 mm) column and a conductivity detector. The eluent was a binary mixture of 3.5 mM Na_2CO_3 and 1 mM $NaHCO_3$ solutions. In the experiment with 1 μM As(III), the Quantitative analyses of NO_2^- and NO_3^-, As(V) were performed by using a Dionex ICS-2100 IC (Dionex IonPac AS18 (4 × 250 mm) column and a conductivity detector, 39 mM KOH eluent). Coumarin (1 mM) was employed as a chemical probe of $^{\bullet}OH$.(27)

$$^{\bullet}OH + \text{coumarin} \rightarrow \rightarrow 7\text{-hydroxycoumarin} \quad (1)$$

7-Hydroxycoumarin (reaction 1) was measured by monitoring the fluorescence emission at 460 nm under excitation at 332 nm using a spectrofluorometer (Shimadzu RF-5301).

The outdoor experiments under natural solar light were carried out in a flat circular quartz reactor (diameter 5.5 cm, volume 40 mL, magnetically stirred during reaction) placed on the roof of the Environmental Engineering building at POSTECH (Pohang, Korea: 36°N latitude). The photochemical reactions were performed under clear sky conditions between 8:30 AM and 6:30 PM (on March 11th, 2011) and in a temperature range from 5.5 to 9.4 °C. The intensity of sunlight was recorded using a pyranometer (apogee, PYR-P) every minute, and the daily average varied from 63 to 69 $mW \cdot cm^{-2}$.

3. Results and discussion

3.1. Nitrite-Mediated Photooxidation of As(III)

The photolytic experiments with different initial As(III) concentrations of

10, 100, and 1000 μM induced a significant production of As(V) (as a result of As(III) oxidation) when nitrites were copresent (Figure 1). Direct UV photooxidation of As(III) in the absence of nitrites was negligible (Figure 1), which supports the role of NO_2^- as a UV-photosensitizer for the formation of reactive oxidants. Figure 1b shows that a near complete oxidation of As(III) to As(V) is accompanied by a quantitative conversion of NO_2^- to NO_3^-, although the concentration of As(III) is 5-fold higher than that of NO_2^-. This implies that the photolysis of one nitrite leads to the oxidation of multiple arsenites. However, UV photolysis of NO_3^- is much less efficient in inducing the oxidation of As(III) (Figure 1a,b), and there is a lag phase of about 3 h prior to the noticeable production of As(V) (Figure 1a). Since the photolysis of nitrate should be much slower than that of nitrite, the concentration of in situ generated nitrite should be accumulated before it has a noticeable effect on the oxidation of As(III). During the UV photolysis of NO_3^-, the production of NO_2^- was maintained at a minimal level, even after the appearance of As(V). This is probably because NO_2^- is immediately reoxidized to NO_3^- as soon as it is formed. Therefore, a catalytic cycle of NO_2^- and NO_3^- was involved in the mechanism for NO_2^--mediated photooxidation of As(III), which enables a continual supply of NO_2^- as a precursor of reactive oxidants.

Figure 2 shows the role of As(III) in the photochemical reduction-oxidation (redox) reaction of NO_2^- and NO_3^-. The photochemical reduction of NO_3^- to NO_2^- is negligibly slow regardless of the presence of As(III), which confirms the fact that the quantum yield for the photolytic decomposition of NO_3^- is lower than that ofNO_2^- decomposition (e.g., $\Phi_{OH,308}$(quantum yield of •OH production at 308 nm) = 6.9(±0.9)% for NO_2^- photolysis versus $\Phi_{OH,308}$ = 1.7 (±0.3)% for NO_3^- photolysis).(28) However, UV-induced oxidation of NO_2^- to NO_3^- proceeded to a certain degree, which was significantly accelerated when As(III) was copresent. This can be ascribed to the fact that As(III) rapidly scavenges $O^{\bullet-}$/•OH as soon as it is formed (reaction H1), hindering the recombination between $NO^{\bullet}$ and $O^{\bullet-}$ (in reaction A2a) and facilitating the further oxidation to NO_3^-.(29)

3.2. pH Effect and Nitrite Regeneration

Figure 3a compares the time profiles of As(V) production in the presence of NO_2^- under varying pH conditions. Either acidic or alkaline pH favored the photochemical oxidation of As(III), whereas NO_2^- photolysis at neutral pH led to relatively slow production of As(V). The rapid As(III) oxidation at acidic pH is ascribed to the increased concentration of nitrous acid (HNO_2, pKa = 3.2), which is more effectively photolyzed to produce •OH than its deprotonated counterpart, NO_2^- (e.g., $\Phi_{OH,300}$ = 36.2(±4.7)% for HNO_2 photolysis versus $\Phi_{OH,300}$ = 6.7(±0.9)% for NO_2^- photolysis).(21) The simultaneous monitoring of the photolytic removal of NO_2^- and the accompanying generation of NO_3^- shows that the efficiency of the oxidative conversion of NO_2^- to NO_3^- gradually decreases with increasing pH (Figure 3b). Under acidic and neutral (pH ≤ 7) condition, both photochemical conversions of (NO_2^- → NO_3^-) and (As(III) → As(V)) increase with lowering pH, which indicates that the photochemical dissociation of HNO_2 (or NO_2^-) is accompanied by the concurrent production of •OH and NO_3^- (reaction B1). However, at alkaline pH (≥9), the conversion of NO_2^- to NO_3^- was significantly retarded whereas the oxidation of As(III) was accelerated with increasing pH. In addition, it should be noted that the oxidative conversions of (As(III) → As(V)) and (NO_2^- → NO_3^-) were not stoichiometrically balanced: the ratio of the As(V) production to NO_2^- removal ($R = \Delta[As(V)]/-\Delta[NO_2^-]$) increased from 0.57 at pH_i 2 to 7.82 at pH_i 13 (0.57, 0.98, 1.34, 2.07, and 7.82 at pHi 2, 4.5, 7, 12, and 13, respectively). The fact that R > 1 at alkaline pH condition implies that NO_2^- has some catalytic role in the photooxidation of As(III) and that the photochemical regeneration of NO_2^- from NO_3^- should be highly enhanced at alkaline pH. Note that the literature rate data for the photolytic conversion of NO_3^- to NO_2^- is indeed higher at higher pH (e.g., r300(the rate of NO_2^- formation during the photolysis of 1 M NO_3^- with the light above 300 nm) = 26.5 μM min - 1 at pH 13 vs r300 = 5 μM min - 1 at pH 5).(30)

In order to further assess the pH dependence of the photolysis of NO_3^- to NO_2^-, Figure 4 compares the efficiency of photooxidation of As(III) in aqueous solution of NO_3^- at initial pH of 4.5, 7, and 12. Whereas As(III)

photooxidation with NO_2^- was slightly faster at pH 4.5 than at pH 12 (see Figure 3a), the efficiency of photooxidation of As(III) with NO_3^- was significantly higher at pH 12 than at pH 4.5. This implies that the UV-induced conversion of NO_3^- to NO_2^- is more preferred at higher pH, subsequently leading to the enhanced photooxidation of As(III). The kinetic enhancement at alkaline pH was more pronounced with a higher concentration of As(III) under the same concentration of nitrate (Figure 4). This is likely attributed to the role of As(III) as an effective scavenger of the solvent-caged radical pair (i.e., $NO_2^\bullet$ and $O^{\bullet -}$ in reaction C2a in Table 1) through reaction H3, which subsequently increases the quantum yields for the production of NO_2^- and $^\bullet OH$.(31) At neutral pH condition, both, the fraction of the photoactive form of nitrite (e.g., HNO_2) and the photoefficiency for NO_3^- to NO_2^- conversion, is low. As a result, the As(III) photooxidation in the presence of NO_3^- or NO_2^- is the lowest at pH 7 (see Figure 3a and Figure 4).

3,3. Nature of Involved Photooxidants

The efficiency of photogeneration of $^\bullet OH$ from the photolysis of NO_2^- was measured by using coumarin as a chemical trap of $^\bullet OH$. The production of 7-hydroxycoumarin (through reaction 1) was monitored in the UV-irradiated solution of NO_2^- in the presence of various dissolved gases including air, O_2, N_2, and N_2O (Figure 5a). The significant formation of 7-hydroxycoumarin under irradiation indicates the UV-photosensitizing activity of NO_2^- for $^\bullet OH$ generation and the efficiency decreases in order of $N_2O \approx N_2 > \text{air} > O_2$ (Figure 5a). The oxic condition where O_2 acts as an electron scavenger inhibits the recombination of the solvent-cage pair of $NO_2^\bullet/e_{aq}^-$ (reaction A2b in Table 1) with facilitating the formation of $NO_2^\bullet$ and hydrated electron (e_{aq}^-) (rather than $NO^\bullet$ and $O^{\bullet -}/^\bullet OH$ via reaction A2a) as the primary photolysis products of NO_2^-. As a result, the efficiency of $^\bullet OH$ production was significantly retarded in the presence of dissolved O_2 under air-equilibrated or O_2-saturated conditions. However, the use of N_2O as an alternative electron acceptor, which might behave similarly as O_2 in promoting the photodissociation of NO_2^- into $NO_2^\bullet$ and e_{aq}^-, was as effective as the N_2-saturated case for the

production of •OH. This might be ascribed to that N_2O reacts with e_{aq}^- to form •OH via an alternative pathway (reaction 2).(32)

$$N_2O + e_{aq}^- + H^+ \rightarrow N_2 + {}^\bullet OH \quad (2)$$

In contrast to the inhibitory effect of O_2 on the production of •OH (Figure 5a), the photooxidation of As(III) in the presence of NO_2^- was higher in the air-equilibrated or O_2-saturated solution than that in the N_2-saturated solution (Figure 5b). This implies the involvement of alternative oxidants (other than •OH) of As(III), which likely includes $O_2^{\bullet -}$ and $NO_2^\bullet$ with moderate oxidizing power (i.e., $E^0(O_2^{\bullet -}/HO_2^-)$ = 0.50 V_{NHE}(20) at pH 9; $E^0(NO_2^\bullet/NO_2^-)$ = 1.03 V_{NHE}(33) versus E^0(As(V)/As(III)) = −0.13 V_{NHE}(20) at pH 9). The presence of O2 causes the rapid oxidation of $NO^\bullet$ to $NO_2^\bullet$ (reaction F1 in Table 1) and the production of $O_2^{\bullet -}$ from the reaction with e_{aq}^- (reaction E1). The comparison of the effect of t-BuOH (an •OH scavenger via reaction G3) addition on the As(III) photooxidation reveals the nature of photooxidants (Figure 5b). Under N_2-saturated conditions, the photooxidation of As(III) was completely inhibited, which indicates that •OH is the sole oxidant in this case. However, in the air-equilibrated condition, the addition of t-BuOH did not completely inhibit the photooxidation, which implies the possible contribution of $O_2^{\bullet -}$ to As(III) oxidation.(9, 10)

In agreement of the above discussion, the photolysis of NO_2^- is sensitively affected by the presence of interfering components. Figure 5c shows that the photolysis of NO_2^- and the concurrent production of NO_3^- is clearly faster in the air-equilibrated condition than in the N_2-saturated condition. The explanation is similar to the effect of O_2 on the production of •OH (Figure 5a): O_2 acting as an electron scavenger inhibits the recombination of the solvent-cage pair of $NO_2^\bullet$/eaq - (reaction A2b in Table 1) with facilitating the decomposition of NO_2^-. In the presence of t-BuOH, the photolysis of NO_2^- was markedly accelerated in both air-equilibrated and N_2-saturated conditions probably because an alternative pathway is facilitated: t-BuOH as a scavenger of •OH/$O^{\bullet -}$ inhibits the recombination of the solvent-cage pair of $NO^\bullet/O^{\bullet -}$ (reaction A2a in Table 1) with facilitating the decomposition of NO_2^-. However, the presence of t-BuOH greatly inhibited the production of NO_3^- (Figure 5c)

along with a drastic inhibition of As(III) photooxidation (Figure 5b). This implies that the photogenerated NO• might react with t-BuOH or t-BuOH-derived intermediates to form nitrogenous compounds.

Under the N_2O-saturated condition, both efficiency of •OH production and As(III) oxidation were highly enhanced. As for the production of •OH, the N_2O-saturated condition was as effective as the N_2-saturated condition. However, the former was more efficient than the latter for the As(III) photooxidation, which implies the presence of additional oxidants in the N_2O-saturated solution. Since the presence of N_2O as an electron acceptor preferentially photodecomposes NO_2^- into NO_2• and eaq^- (as mentioned above), NO_2• may act as an additional oxidant of As(III) (reaction H3).

4. Environmental Implications

Sunlight driven oxidation in the As(III)/NO_2^- solution was performed to assess the implication of the studied photochemical process for the fate of a natural water matrix contaminated with As(III). The nitrite has a significant spectral overlap with the sunlight (see the UV-vis absorption spectrum of NO_2^- in Figure 6a). Figure 6b demonstrates that significant oxidative conversion of As(III) to As(V) occurred, along with the production of NO_3^- during the solar photolysis of NO_2^-, while no detectable production of As(V) was observed in the absence of NO_2^-. The solar photolysis of nitrite alone and the accompanying production of nitrate were the same as those in the (As(III)+ NO_2^-) system (data not shown), which indicates that the photolysis characteristic of nitrite is not influenced by the presence of As(III). The effects of natural organic matter on this photochemical transformation were also investigated. Humic acid (HA) was added as a proxy of natural organic matters at a concentration of 3 mg/L (typically, 2 - 10 mg/L in groundwater(34)), and the results are shown in Figure 7. The addition of HA little changed or even moderately enhanced the conversion rates of As(III) and NO_2^-. This seems to be caused by the HA-sensitized production of superoxide.(35) The control photolysis experiments of (As(III) + HA) mixture in the absence of NO_2^- showed a small (but not negligible) production of As(V), which supports the sensitizing role of HA. The

fact that the presence of HA did not retard the photooxidation rate at all implies that As(III) is highly susceptible to oxidation by photooxidants (e.g., •OH) derived from the photolysis NO_2^- even in the presence of natural organic matters that may react with •OH. In addition, the observation that the stoichiometric conversion of NO_2^- to NO_3^- was achieved even in the presence of humic acid (Figure 7) indicates that the production of nitrated organic byproducts should be negligible in the UV/As(III)/NO_2^- process. The levels of NO_2^- and NO_3^- are typically in the range of 10 - 163 and 23 - 779 μM, respectively, in arsenic contaminated ground and surface water matrixes.(24) The photochemical reactions of NO_3^- are accompanied with the production of reactive oxidizing species (e.g., •OH) and NO_2^- even in the absence of NO_2^-. Therefore, the typical surface and ground waters contaminated with As(III) and NO_2^-/NO_3^- can be phototransformed with converting As(III) to As(V) under sunlight irradiation.

아질산염이나 질산염의 자외선에 의한 광분해반응에 의해 야기되는 아비산염의 산화 반응

김기태[1,2], 최원용[1*]

[1]포항공과대학교
[2]한국해양과학기술원 부설 극지연구소

요약: 이 연구는 아질산염이나 질산염의 광학반응 동안 반응하는 산화종 (예, 하이드록실라디칼)이 아비산염에서 비산염으로의 산화변환을 이끄는 것을 확인하였다. 직접적인 아비산염의 UV 질산화는 없었지만, 아질산염의 투입은 295 nm이상의 UV아래에서 아비산염의 산화가 현저히 증가하였다. 질산염이 매개한 아비산염의 광산화는 질산염이 아질산염으로 바뀌는 동안 초기 유도기가 존재하는 것을 보여준다. UV-광감성을 띈 아비산염의 산화는 운동적으로 OH 생산성이 높은 아질산이 아질산염의 우점종의 형태로 존재하는 산성 pH 조건에서 강화된다. 반면 알칼리 pH는 질산염에서 아질산염으로의 광학적인 변환이 우세하여 아비산염/아질산염의 비가 1보다 큰 조건에서 아비산염의 완전한 산화를 가능하게 하고 질산염에 민감한 아질산염의 산화를 현저히 촉진시키는 촉매감소/산화 사이클을 매우 촉진시킨다. 전자 흡착제로서의 산소와 산화질소의 존재는 이산화질소를 포함하는 아비산염의 산화 역전을 유발하는 분자 사이의 전자전달을 통해 아질산염의 광화학적인 해리를 촉진시킨다. 실회 실험은 산화종의 광증발된 생선물에 대한 아질산염의 능력과 일사광에 의한 연차적인 아비산염에서 비산염으로의 산화를 확인하였다.

참고문헌

Sharma, V. K.; Sohn, M.Aquatic arsenic: Toxicity, speciation, transformations, and remediation Environ. Int. 2009, 35 (4) 743 - 759

Cullen, W. R.; Reimer, K. J.Arsenic speciation in the environment Chem. Rev. 1989, 89 (4) 713 - 764

Bundschuh, J.; Litter, M. I.; Parvez, F.; Roman-Ross, G.; Nicolli, H. B.; Jean, J. S.; Liu, C. W.; Lopez, D.; Armienta, M. A.; Guilherme, L. R. G.; Cuevas, A. G.; Cornejo, L.; Cumbal, L.; Toujaguez, R.One century of arsenic exposure in Latin America: A review of history and occurrence from 14 countries Sci. Total Environ. 2012, 429, 2 - 35

Buxton, G. V.; Greenstock, C. L.; Helman, W. P.; Ross, A. B.Critical review of rate constants for reactions of hydrated electrons, hydrogen atoms and hydroxyl radicals (• OH/ • O -) in aqueous solution J. Phys. Chem. Ref. Data 1988, 17 (2) 513 - 886

Hug, S. J.; Leupin, O.Iron-catalyzed oxidation of arsenic(III) by oxygen and by hydrogen peroxide: pH-dependent formation of oxidants in the Fenton reaction Environ. Sci. Technol. 2003, 37 (12) 2734 - 2742

Kocar, B. D.; Inskeep, W. P.Photochemical oxidation of As(III) in ferrioxalate solutions Environ. Sci. Technol. 2003, 37 (8) 1581 - 1588

Bhandari, N.; Reeder, R. J.; Strongin, D. R.Photoinduced oxidation of arsenite to arsenate on ferrihydrite Environ. Sci. Technol. 2011, 45 (7) 2783 - 2789

Bhandari, N.; Reeder, R. J.; Strongin, D. R.Photoinduced oxidation of arsenite to arsenate in the presence of goethite Environ. Sci. Technol. 2012, 46 (15) 8044 - 8051

Ryu, J.; Choi, W.Effects of TiO_2 surface modifications on photocatalytic oxidation of arsenite: The role of superoxides Environ. Sci. Technol. 2004, 38 (10) 2928 - 2933

Ryu, J.; Choi, W.Photocatalytic oxidation of arsenite on TiO2: Understanding the controversial oxidation mechanism involving superoxides and the effect of alternative electron acceptors Environ. Sci. Technol. 2006, 40 (22) 7034 - 7039

Xu, T. L.; Kamat, P. V.; O'Shea, K. E.Mechanistic evaluation of arsenite oxidation in TiO2 assisted photocatalysis J. Phys. Chem. A 2005, 109 (40) 9070 - 9075

Guan, X. H.; Du, J. S.; Meng, X. G.; Sun, Y. K.; Sun, B.; Hu, Q. H.Application of titanium dioxide in arsenic removal from water: A review J. Hazard. Mater. 2012, 215, 1 - 16

Ryu, J.; Monllor-Satoca, D.; Kim, D. H.; Yeo, J.; Choi, W.Photooxidation of arsenite under 254 nm irradiation with a quantum yield higher than unity Environ. Sci. Technol. 2013, 47 (16) 9381 - 9387

Yeo, J.; Choi, W.Iodide-mediated photooxidation of arsenite under 254 nm irradiation Environ. Sci. Technol. 2009, 43 (10) 3784 - 3788

Mack, J.; Bolton, J. R.Photochemistry of nitrite and nitrate in aqueous solution: A review J. Photochem. Photobiol. A:Chem. 1999, 128 (1 - 3) 1 - 13

Haag, W. R.; Hoigne, J.Photo-sensitized oxidation in natural water via OH radicals Chemosphere 1985, 14 (11 - 12) 1659 - 1671

Zepp, R. G.; Hoigne, J.; Bader, H.Nitrate-induced photooxidation of trace organic chemicals in water Environ. Sci. Technol. 1987, 21 (5) 443 - 450

Keen, O. S.; Love, N. G.; Linden, K. G.The role of effluent nitrate in trace organic chemical oxidation during UV disinfection Wat. Res. 2012, 46 (16) 5224 - 5234

Torrents, A.; Anderson, B. G.; Bilboulian, S.; Johnson, W. E.; Hapeman, C. J.Atrazine photolysis: Mechanistic investigations of direct and nitrate mediated hydroxy radical processes and the influence of dissolved organic carbon from the Chesapeake Bay Environ. Sci. Technol. 1997, 31 (5) 1476 - 1482

Bard, A. J.; Parsons, R.; Jordan, J., Eds. Standard Potential in Aqueous Solution; Marcel Dekker: New York, 1985.

Fischer, M.; Warneck, P.Photodecomposition of nitrite and undissociated nitrous acid in aqueous solution J. Phys. Chem. 1996, 100 (48) 18749 - 18756

Vione, D.; Maurino, V.; Minero, C.; Pelizzetti, E.New processes in the environmental chemistry of nitrite: Nitration of phenol upon nitrite photoinduced oxidation Environ. Sci. Technol. 2002, 36 (4) 669 - 676

Dutta, P. K.; Pehkonen, S. O.; Sharma, V. K.; Ray, A. K.Photocatalytic oxidation of arsenic(III): Evidence of hydroxyl radicals Environ. Sci. Technol. 2005, 39 (6) 1827 - 1834

Baig, J. A.; Kazi, T. G.; Arain, M. B.; Afridi, H. I.; Kandhro, G. A.; Sarfraz, R. A.; Jamal, M. K.; Shah, A. Q.Evaluation of arsenic and other physico-chemical parameters of surface and ground water of Jamshoro, Pakistan J. Hazard. Mater. 2009, 166 (2 - 3) 662 - 669

Hatchard, C. G.; Parker, C. A.A new sensitive chemical actinometer. 2. Potassium ferrioxalate as a standard chemical actinometer Proc. R. Soc. London, Ser. A 1956, 235, 518 - 536

Lenoble, V.; Deluchat, V.; Serpaud, B.; Bollinger, J. C.Arsenite oxidation and arsenate determination by the molybdene blue method Talanta 2003, 61 (3) 267 - 276

Ishibashi, K.-i.; Fujishima, A.; Watanabe, T.; Hashimoto, K.Detection of active oxidative species in TiO2 photocatalysis using the fluorescence technique Electrochem. Commun. 2000, 2 (3) 207 - 210

Bilski, P.; Chignell, C. F.; Szychlinski, J.; Borkowski, A.; Oleksy, E.; Reszka, K.Photooxidation of organic and inorganic substrates during UV photolysis of nitrite anion in aqueous solution J. Am. Chem. Soc. 1992, 114 (2) 549 - 556

Bayliss, N.; Bucat, R.The photolysis of aqueous nitrate solutions Aust. J. Chem. 1975, 28 (9) 1865 - 1878

Daniels, M.; Meyers, R. V.; Belardo, E. V.Photochemistry of the aqueous nitrate system. I. Excitation in the 300-m.mu. band J. Phys. Chem. 1968, 72 (2) 389 - 399

Mark, G.; Korth, H. G.; Schuchmann, H. P.; vonSonntag, C.The photochemistry of aqueous nitrate ion revisited J. Photochem. Photobiol. A: Chem. 1996, 101 (2 - 3) 89 - 103

Zehavi, D.; Rabani, J.Pulse radiolytic investigation of Oaq - radical ions J. Phys. Chem. 1971, 75 (11) 1738 - 1744

Neta, P.; Huie, R. E.; Ross, A. B.Rate constants for reactions of inorganic radicals in aqueous solution J. Phys. Chem. Ref. Data 1988, 17 (3) 1027 - 1284

Mladenov, N.; Zheng, Y.; Miller, M. P.; Nemergut, D. R.; Legg, T.; Simone, B.; Hageman, C.; Rahman, M. M.; Ahmed, K. M.; McKnight, D. M.Dissolved organic matter sources and consequences for iron and arsenic mobilization in Bangladesh aquifers Environ. Sci. Technol. 2010, 44 (1) 123 - 128

Cooper, W. J.; Zika, R. G.Photochemical formation of hydrogen peroxide in surface and ground waters exposed to sunlight Science 1983, 220, 711 - 712

Table 1. Reactions Involved in the Oxidation of As(III) during UV Photolysis of NO_2^- and NO_3^-[a]

	reaction		ref
	UV photolysis of NO_2^- and NO_3^- and production of reactive intermediates		
A1	$NO_2^- + h\nu \rightarrow NO_2^{-*}$		15
A2a	$NO_2^{-*} \rightarrow NO^\bullet + O^{\bullet-}$		15
A2b	$NO_2^{-*} \rightarrow NO_2^\bullet + e_{aq}^-$		21
B1	$HNO_2 + h\nu \rightarrow NO^\bullet + \bullet OH$		21
C1	$NO_3^- + h\nu \rightarrow NO_3^{-*}$		15
C2a	$NO_3^{-*} \rightarrow NO_2^\bullet + O^{\bullet-}$		15
C2b	$NO_3^{-*} \rightarrow NO_2^- + O(^3P)$		15
D1	$O^{\bullet-} + H_2O \leftrightarrow \bullet OH + OH^-$	$pK_a = 11.9$	15
E1	$e_{aq}^- + O_2 \rightarrow O_2^{\bullet-}$	$k_{E1} = 1.9 \times 10^{10}$	4
F1	$2NO^\bullet + O_2 \rightarrow 2NO_2^\bullet$	$2k_{F1} = 4.2 \times 10^6$	21
F2	$NO^\bullet + NO_2^\bullet + H_2O \rightarrow 2NO_2^- + 2H^+$	$k_{F2} \approx 1.6 \times 10^8$	21
F3	$NO^\bullet + NO_3^- \rightarrow NO_2^\bullet + NO_2^-$	$k_{F3} \leq 4 \times 10^4$	21
F4	$NO_2^\bullet + NO_2^\bullet + H_2O \rightarrow NO_3^- + NO_2^- + 2H^+$	$k_{F4} \approx 8.0 \times 10^7$	21
	•OH-mediated reaction		
G1	$\bullet OH + NO_2^- \rightarrow OH^- + NO_2^\bullet$	$k_{G1} = 1.0 \times 10^{10}$	21
G2	$\bullet OH + HNO_2 \rightarrow H_2O + NO_2^\bullet$	$k_{G2} \approx 2.6 \times 10^9$	21
G3	•OH + *t*-BuOH → oxidized products	$k_{G3} = 6.0 \times 10^8$	23
G4	•OH + As(III) → As(IV)	$k_{G4} = 8.5 \times 10^9$	23
	As(III) oxidation		
H1	•OH + As(III) → As(IV)	$k_{H1} = 8.5 \times 10^9$	23
H2	$O_2^{\bullet-} + As(III) + H^+ \rightarrow As(IV) + HO_2^-$	$k_{H2} = 3.6 \times 10^6$	11
H3	$NO_2^\bullet + As(III) \rightarrow NO_2^- + As(IV)$		
H4	$As(IV) + O_2 \rightarrow As(V) + HO_2^\bullet/O_2^{\bullet-}$	$k_{H4} = 1.1 \times 10^9$	5
H5	As(IV) + As(IV) → As(V) + As(III)		23

[a]Rate constants are given in $M^{-1}\ s^{-1}$ except for reaction F1 ($M^{-2}\ s^{-1}$).

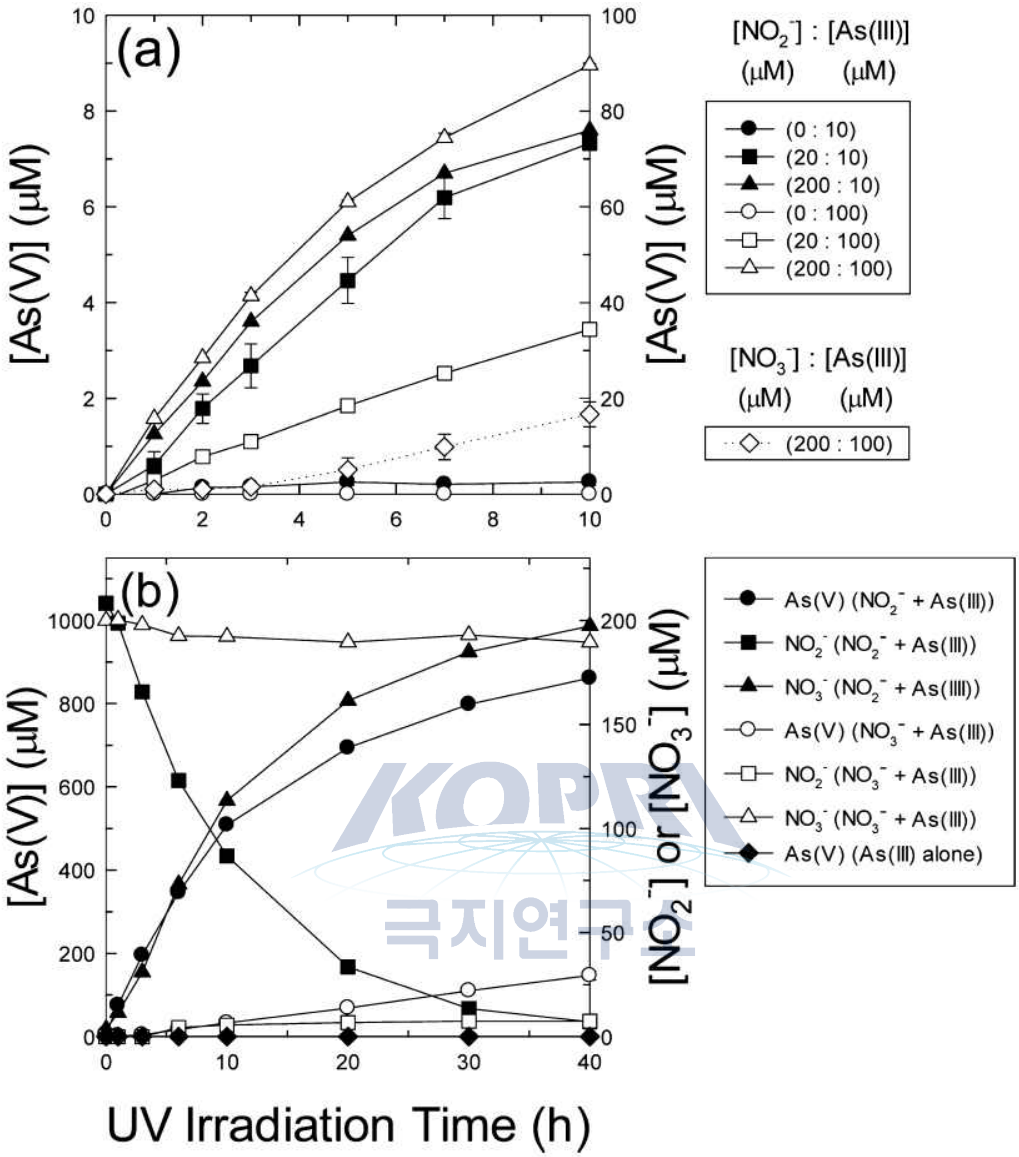

Figure 1. (a) Oxidative conversion of As(III) to As(V) during UV photolysis of NO2 - (solid line) and NO3 - (dotted line) at various initial concentrations (air equilibrated; pHi = 9.0, [As(III)]0 = 10 μM (close symbol) or 100 μM (open symbol)) and (b) time profiles of NO2 - decomposition, NO3 - formation, and As(V) production under UV irradiation (air equilibrated; pHi = 10; [As(III)]0 = 1000 μM; [NO2 -]0 = 200 μM or [NO3 -]0 = 200 μM).

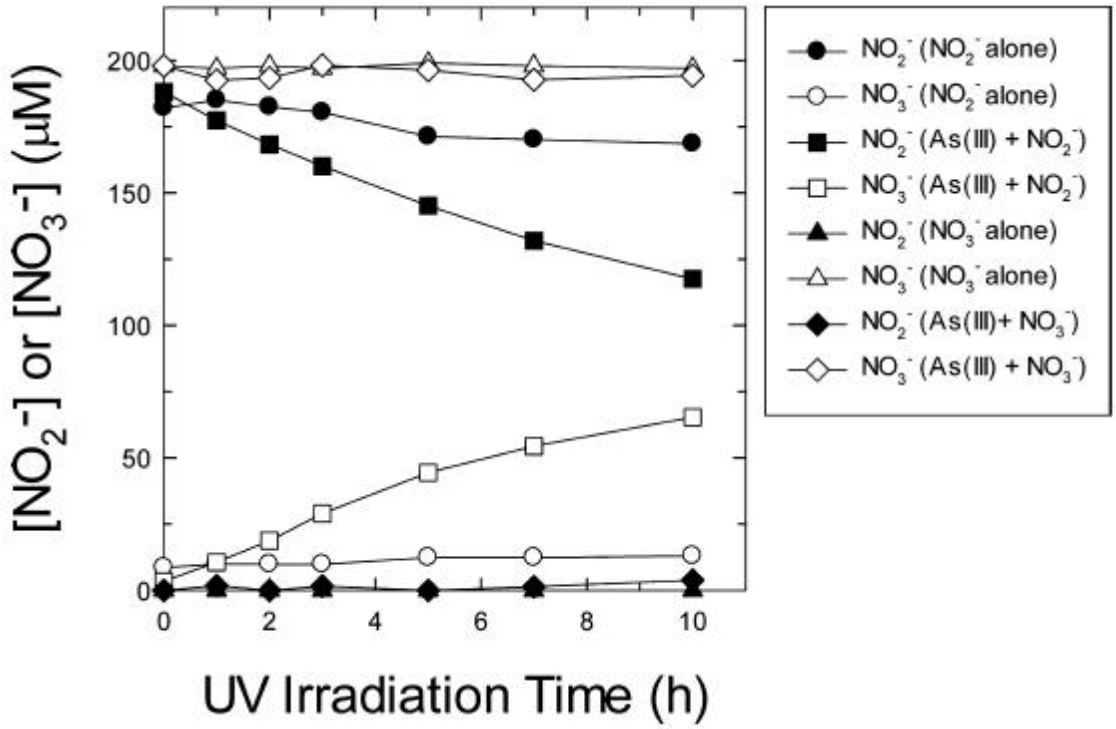

Figure 2. Photochemical conversion of NO2 - (or NO3 -) into NO3 - (or NO2 -) in the absence and presence of As(III) (air equilibrated; pHi = 9.0; [As(III)]0 = 100 μM; [NO2 -]0 = 200 μM; [NO3 -]0 = 200 μM).

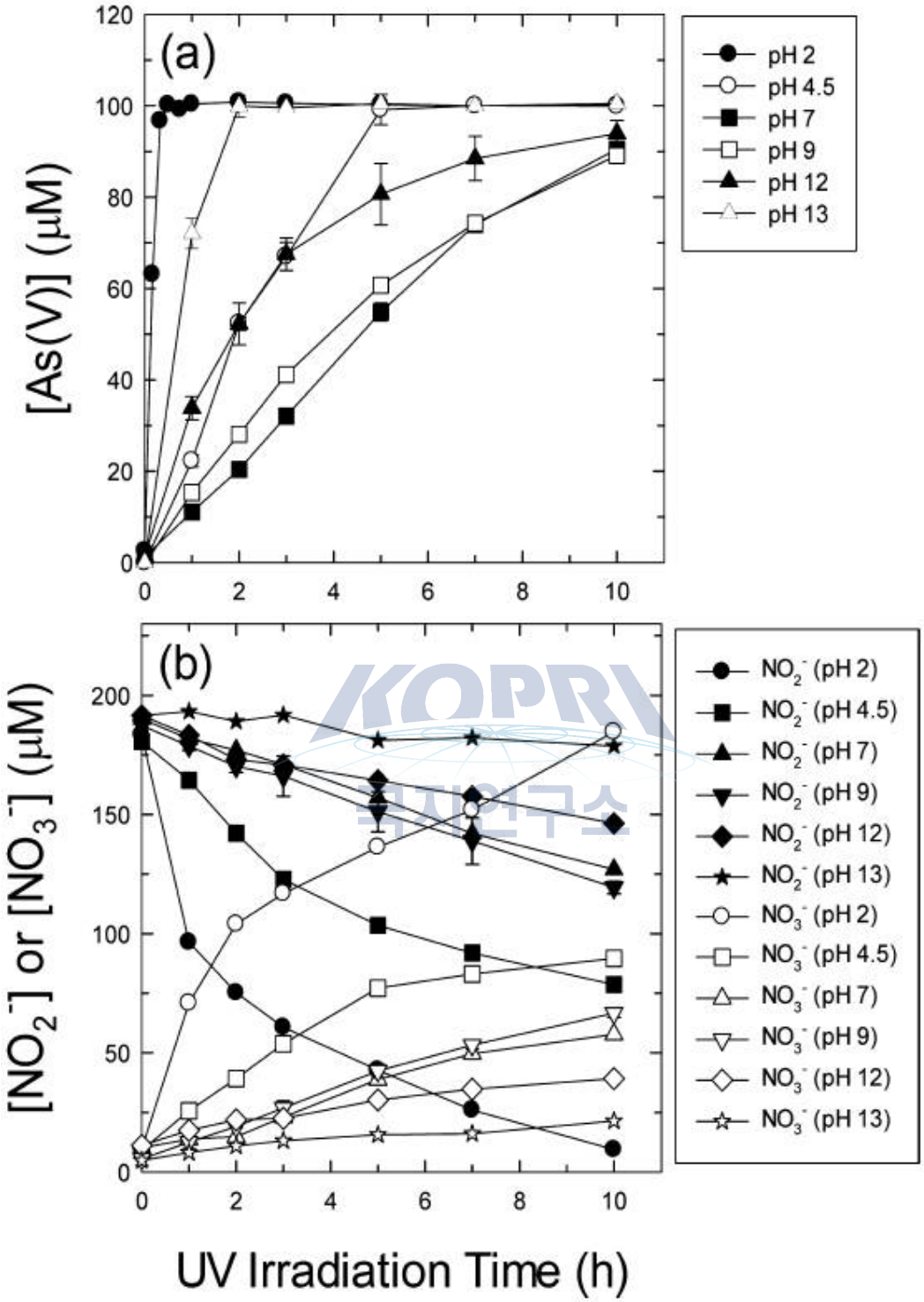

Figure 3. (a) Photosensitized oxidation of As(III) (i.e., stoichiometric production of As(V)) and (b) the concurrent conversion of NO2 - into NO3 - at various pH conditions (air equilibrated; [As(III)]0 = 100 μM; [NO2 -]0 = 200 μM). The pH was changed during the reaction (2 → 2.07, 4.5 → 4.15, 7 → 6.31, 9 → 6.65, 12 → 10.67, 13 → 12.82).

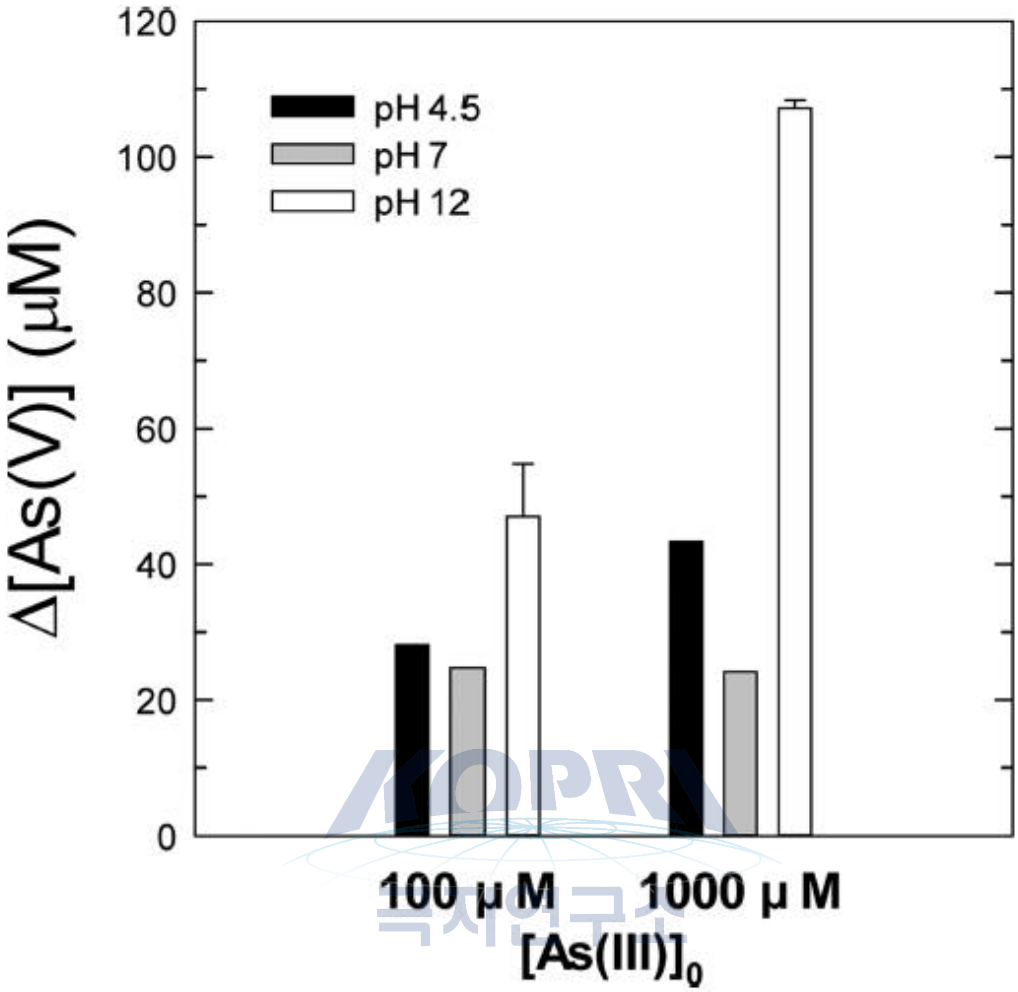

Figure 4. Effect of initial pH on the efficiency of NO3 - -mediated photooxidation of As(III) (air equilibrated; [NO3 -]0 = 200 μM). Δ[As(V)] was measured after 10 h irradiation. With 100 μM As(III), the pH changed from 4.5, 7, 12 to 4.3, 7.0, 10.9; with 1000 μM As(III), from 4.5, 7, 12 to 4.53, 7.8, and 11.1, respectively.

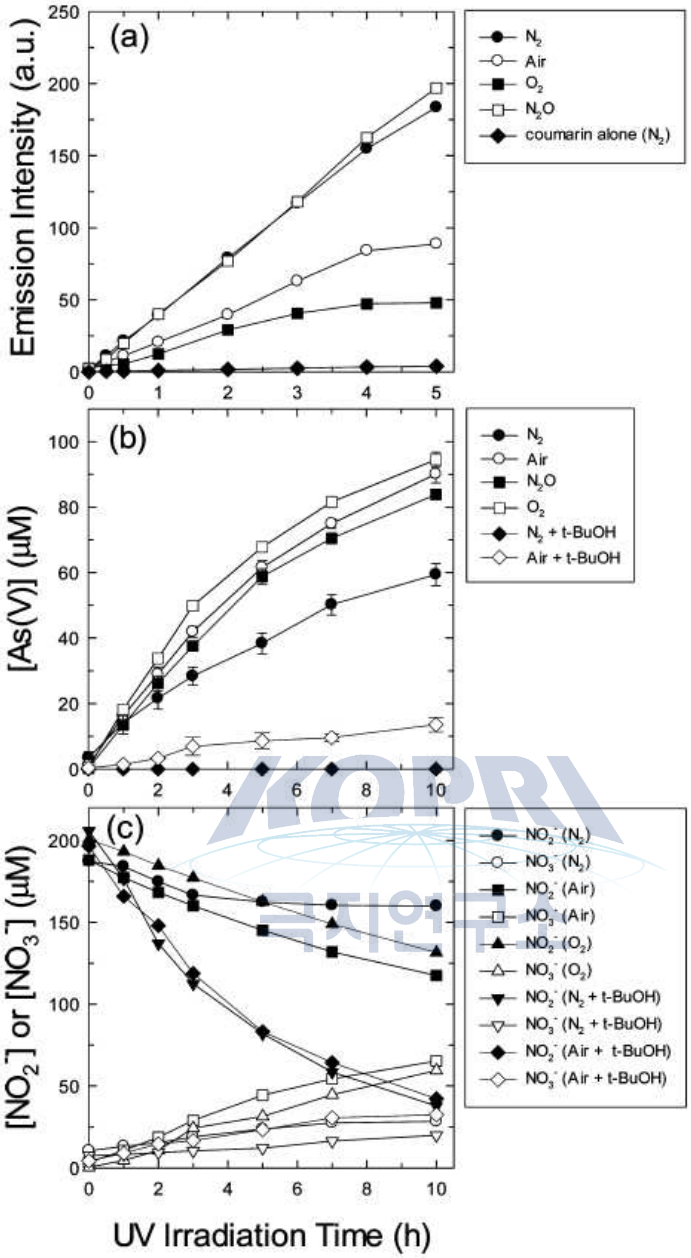

Figure 5. (a) Production of 7-hydroxycoumarin (coumarin-•OH adduct) (pHi = 9; [NO2-]0 = 200 μM; [coumarin] = 1 mM), (b) oxidative conversion of As(III) into As(V) during NO2- photolysis, (c) photochemical conversion of NO2- into NO3- in the presence of various gases (N2, air, O2, and N2O) and/or t-BuOH as a scavenger of •OH (pHi = 9; [As(III)]0 = 100 μM; [NO2-]0 = 200 μM; [t-BuOH] = 0.5 M).

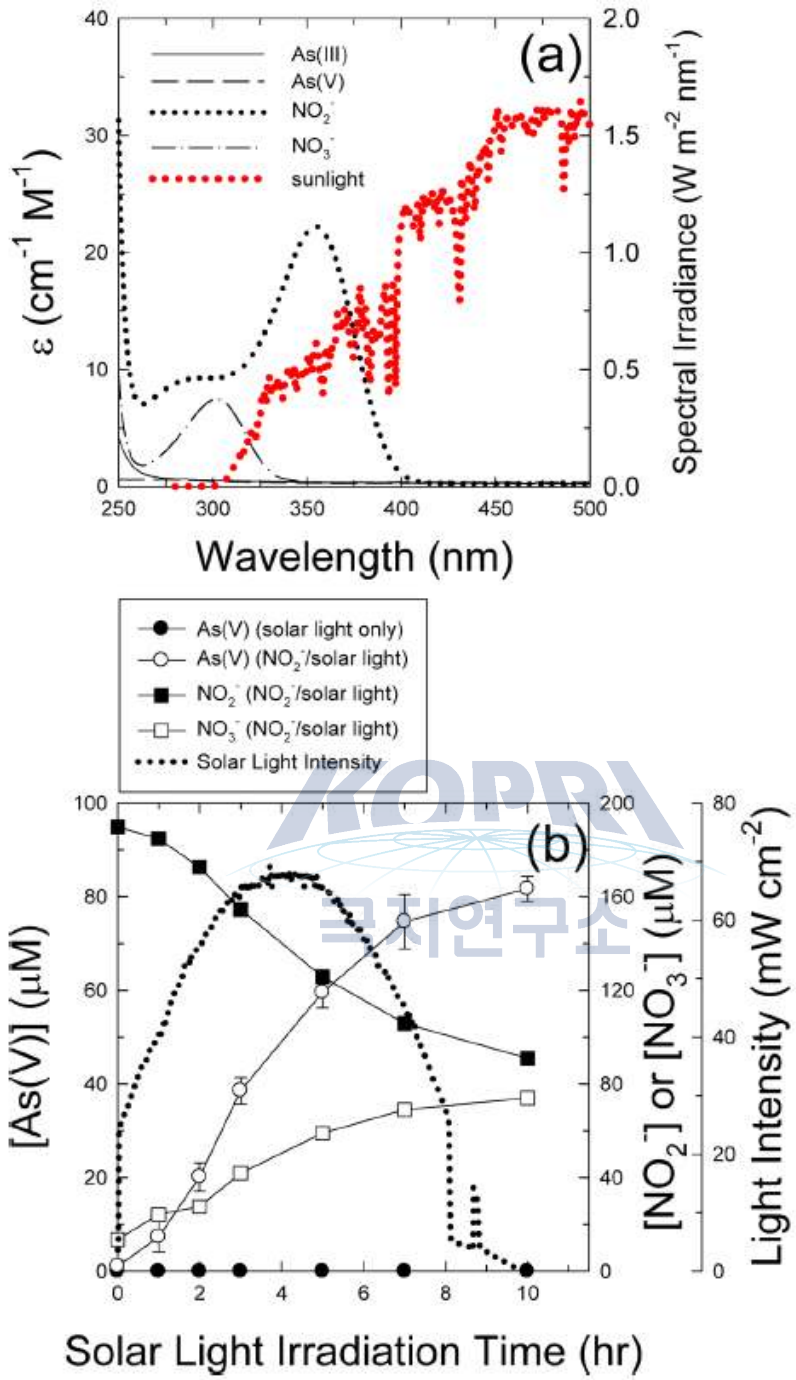

Figure 6. (a) UV - visible absorption spectra of As(III), As(V), NO2 - , and NO3 - in aqueous solution (pH not adjusted, all species at 50 mM) and AM 1.5 solar spectrum (ASTM G173 - 03, Air Mass 1.5 Global Tilt Standard) and (b) Photosensitized oxidation of As(III) during photooxidation of NO2 - into NO3 - under solar light irradiation (air equilibrated; pHi = 4.5; [As(III)]0 = 100 μM; [NO2 -]0 = 200 μM).

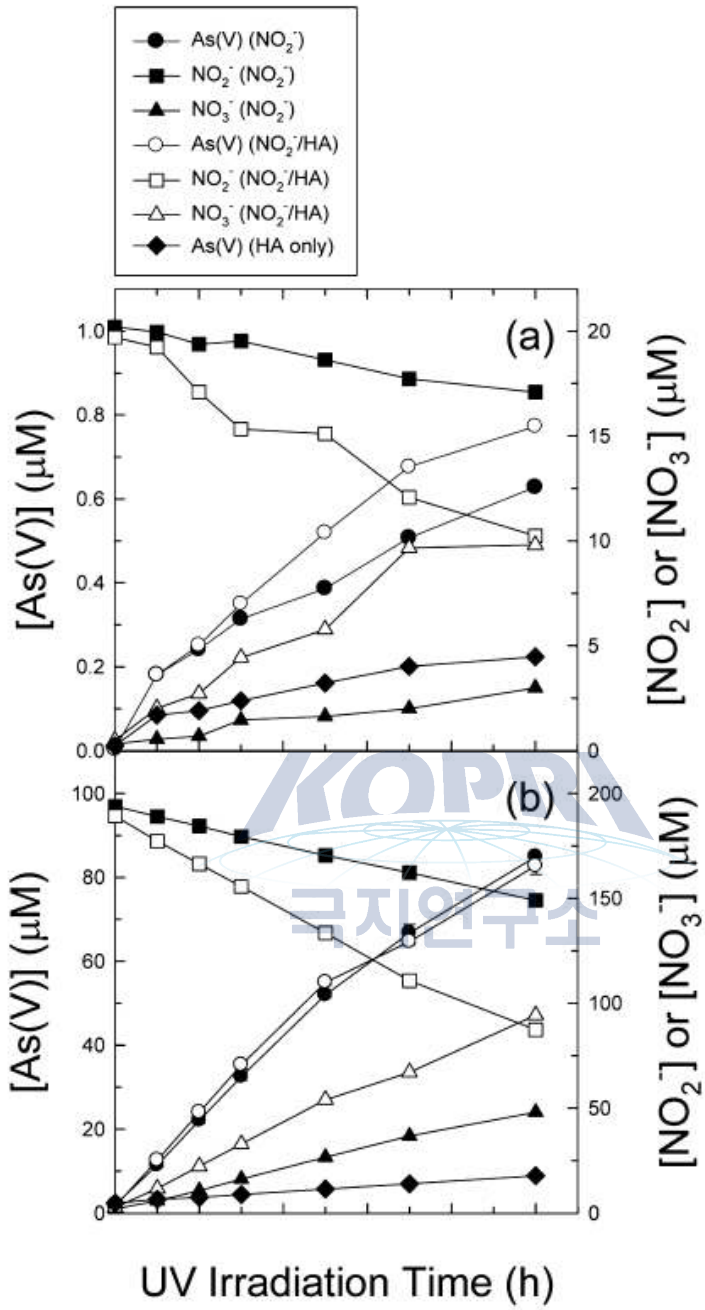

Figure 7. Photosensitized production of As(V) from As(III) and the concurrent conversion of NO2 - into NO3 - in the air-equilibrated solution in the absence or presence of humic acid (HA). (a) [HA] = 3 mg/L, [As(III)]0 = 1 μM, [NO2 -]0 = 20 μM; pHi = 7.0 and (b) [HA] = 3 mg/L, [As(III)]0 = 100 μM, [NO2 -]0 = 200 μM; pHi = 7.0.

제 22 장

Rare earth element composition of paleo-maar sediments (latest Pleistocene – Early Holocene), Jeju Island, Korea: Implications for Asian dust record and monsoon climate[15)]

Min Kyung Lee[1], Yong Il Lee[2], Kyu-Cheul Yoo[1], Ho Il Yoon[1]

[1]Korea Polar Research Institute

[2]Seoul National University

Abstract: The rare earth element (REE) composition of a 4.96 m-long sediment core retrieved from the Hanon paleo-maar in Jeju Island, Korea was studied to investigate the East Asian monsoon variations during the latest Pleistocene to early Holocene (22,300 – 9000 cal BP). The studied paleo-maar core sediment has two restricted source materials with distinctively different geochemical signatures: Asian dust blown from central Asia (especially northern China and Mongolia) and basement rock composed of trachybasalt. The REE characteristics of sediments depend on the relative contribution of these two sources and thus can be used to delineate the monsoon climate in Jeju Island. The proportion of Asian dust generally decreased gradually from 67% at 22,300 cal BP, indicative of progressive weakening of the winter monsoon strength in central Asia. Integration of the REE data with TOC and MS records reveals that the summer monsoon strength in Jeju Island decreased from 22,300 cal BP until the last glacial maximum at 18,000 cal BP, and then increased to 14,000 cal BP. The abrupt intensification of the summer monsoon occurred from 14,000 to 13,300 cal BP, followed by the weakened summer monsoon from 13,300 to 11,000 cal BP,

15) 이 연구 결과는 다음의 논문으로 출판되었음: Lee, M. K., Lee, S. H., Lee, Y. I., Yoon, H. I., & Yoo, K. C. (2014). Rare earth element composition of paleo-maar sediments (latest Pleistocene–Early Holocene), Jeju Island, Korea: Implications for Asian dust record and monsoon climate. Quaternary International, 344, 32-42.

in anti-phase with the strengthened winter monsoon in central Asia. In the early Holocene, Jeju Island experienced further intensified summer monsoon strength.

1. Introduction

Asian dust events have become an important environmental issue in East Asian countries such as China, Korea, and Japan, and their effects are also noticed in western North America across the North Pacific (Jaffe et al., 1999 ; Sun et al., 2001; VanCuren and Cahill, 2002; VanCuren, 2003 ; Zdanowicz et al., 2006; amongst others). Asian dust (called Hwangsa in Korea) occurs in nearly every spring. Major dustfall events are generally associated with strong northwesterly winds (Xiao et al., 1997; Zhang et al., 1997; Zhang et al., 1999 ; Shao and Dong, 2006). Asian dust storms are known to cause harmful consequences to human life and health as well as an economic loss in the affected regions (Kwon et al., 2002; Yang et al., 2005; Batjargal et al., 2006; Zdanowicz et al., 2006 ; Hashizume et al., 2010). Asian dust events may have been more frequent and stronger during glacial periods than during interglacials due to strengthening of the winter monsoons (Rea, 1994; Kohfeld and Harrison, 2003 ; Maher et al., 2010).

The pattern of climate in East Asia is dominated by the summer and winter monsoons. The East Asian monsoon is a dynamic interactive system that involves the ocean, land, and atmosphere. It is driven by the thermal difference between the Asian continent and the Pacific Ocean in the east and southeast (An et al., 1990). Summer monsoon carries a warm, moist, and maritime air onto the continent, and winter monsoon a cold and dry air out of north-central Asia where high pressure cell forms during the winter season.

The alternation of paleosols and loess units in the Loess Plateau of central China has been used as a proxy record of variations in the strength of the East Asian summer and winter monsoons over the past 2.5 million years (An et al., 1990, An et al., 1991; Ding et al., 1995; Liu and Ding, 1998 ; Sun et al., 2006). The surrounding ocean of East Asia, the North Pacific, has been influenced by East Asian monsoons (Windom, 1969). During the glacial periods

when the climate was cold and dry, it is expected that the atmosphere was dusty, resulting in much dust fallout deposition in the downwind areas. In Asian regions, significant amounts of airborne sediments from central or northern Asia are known to have been deposited in China (Pye and Zhou, 1989; An et al., 1990; An et al., 1991; Ding et al., 1995 ; Qiang et al., 2014), Korea (Mizota et al., 1991; Lim et al., 2005 ; Kim et al., 2012), and Japan (Xiao et al., 1999) as well as in the northern Pacific Ocean (Windom, 1969; Janecek and Rea, 1983; Janecek and Rea, 1985; Rea et al., 1985 ; Pye and Zhou, 1989) during the Quaternary, mostly during the glacial periods in particular.

Using a paleo-maar sediment in Jeju Island the paleo-monsoonal climate changes during the latest Pleistocene to early Holocene were studied by Lee et al. (2008). They reported that Jeju Island experienced the coldest climate around 18,000 cal BP, and then there was an abrupt shift in climate regime from cold and arid to warm and humid conditions at around 14,000 cal BP, which represents the commencement of the last major deglaciation-like climate conditions. After this time, Jeju Island experienced the strong summer monsoon climate with two periods of the slightly weakened summer monsoon from 13,300 to 12,000 cal BP and from 10,500 - 9800 cal BP. This paleoclimate interpretation is consistent with that from a pollen record obtained from the same core sediment (Chung, 2007). Here, we report the rare earth element (REE) compositions of the same Jeju paleo-maar sediment for the same period during the latest Pleistocene to early Holocene. REEs are extremely insoluble in aqueous solutions, and therefore, tend to be transferred from source to sink without significant fractionation (Balashov et al., 1964; Nesbitt, 1979; Davies, 1980 ; Bierlein, 1995).

Jeju Island is the perfect place for studying the influence of Asian dust derived from dry areas in central Asia because of its downwind location (e.g., Lim et al., 2005) and simple geology comprising mostly of basaltic rocks. The REE characteristics of the paleo-maar sediments may depend on the relative contribution of two geochemically distinctive sources: the Asian dust transported from central Asia, especially northern China and Mongolia, and detritus derived from the catchment of the paleo-maar. The influx of the Asian dust depends on the climatic conditions of dust source regions: when the winter monsoon

strengthens, more Asian dust becomes airborne and will be transported downwind. Conversely, when the summer monsoon is strengthened, it brings more precipitation to the region, resulting in stronger pedogenesis and less available airborne dust. In contrast to the dust source regions in central Asia, Jeju Island is located close to a moisture source and thus may not be sensitive to the changes in monsoon climate as much as is central China. The Asian dust influx to Jeju Island may faithfully follow the paleoclimatic conditions in central China as recorded in the Loess Plateau and caves in China, whereas the detrital influx from the catchment depends on the weathering states on Jeju Island. Any deviation of Jeju paleoclimate record from the paleo-monsoonal history recorded in the Loess Plateau and caves in China may indicate the difference in the characteristics of the monsoon climate between the two regions. By analyzing the REE characteristics of the paleo-maar sediment and combining them with the previous study results, this study aims to decipher the paleo-monsoon history of Jeju Island.

2. Environmental setting

The following environmental information is from Lee et al. (2008). The studied paleo-lake, Hanon paleo-maar, is located about 1 km west of Seoguipo in the southern part of Jeju Island, Korea (33°14′30″–33°15′00″N, 126°32′45″–126°33′15″E) (Fig. 1). Jeju Island is a shield volcano mostly composed of Quaternary trachyte and trachybasalt with minor welded tuff and the Quaternary Seoguipo Formation (Won, 1976 ; Lee, 1982) (Fig. 1). The study area is a paleo-maar formed by parasitic volcanism. It is filled with sediments and is now used as a rice field. The basement rock of the studied paleo-maar consists of trachybasalt. The studied paleo-maar does not have prominent inlets and outlets, and it is an ellipsoidal basin that is 800 m long in the NW–SE direction and 500 m across in the NE–SW direction. The elevation difference between the basin surface and the surrounding hill is approximately 50 m (Fig. 1).

Jeju Island is currently located in the transition region between the

temperate and subtropical zones. Geographically, it belongs to the eastern coast of the Eurasian continent and is adjacent to the West Pacific Ocean (Fig. 1). During winter, from December to January, it is cold and dry under the dominant influence of the Siberian high, whereas in summer, from June to August, it is hot and humid with frequent heavy rainfall. The mean annual precipitation during the three decades from 1971 to 2000 is approximately 1850 mm in the southern part of Jeju Island (Jeju Regional Meteorological Office; http://jeju.kma.go.kr). More than half of the annual precipitation falls during the summer season when a stationary front lingers across the Korean Peninsula for around a month. Winter precipitation is less than 10% of the annual total. The prevailing winds are southeasterly in summer and northwesterly in winter. In general, the latter are characterized by higher speed and stronger intensity.

3. Material and East Asian monsoon variations in Jeju Island

The detailed description of the studied BH-4B core (a 4.96 m long vibro core; Fig. 1) has been reported in Lee et al. (2008) and their study is summarized below (Fig. 2). The studied core is mainly composed of fine-grained sediments of clayey or silty mud and silt with less than 4% sand. The core sediment is interpreted to be composed of detritus derived from two different sources: detritus washed in from the surrounding volcanic hills and the eolian dust transported by winds from central Asia. The uppermost part (<60 cm) of the core sediments is considerably disturbed, which corresponds to the age interval from 6200 cal BP at the surface to 9000 cal BP at 60 cm from the core top. Sediments younger than 6000 cal BP were probably removed during cultivation. The age of bottom sediment of the core is estimated to be 22,300 cal BP. The core is divided into two intervals by the magnetic susceptibility (MS) value: the sediments at depths greater than 200 cm (corresponding to 14,000 cal BP) have high MS values (>30 × 10−5SI) with high-frequency and high-magnitude variations, and the highest value occurs at the depth of approximately 350 cm (corresponding to 18,000 cal BP), whereas the core sediments at depths less than 200 cm have very low MS values of less than 30 × 10−5SI, with low-frequency variations. Compared to trachybasalt in the crater

rim of the paleo-maar, the MS values of Asian dust are low [600 - 1000 × 10−5SI (Lee et al., 2008) vs. <100 × 10−8SI (cf., Li et al., 2012 and Wang et al., 2013)], and thus the MS values in the paleo-maar sediment may represent the weathering intensity of trachybasalt that controls the abundance of detrital magnetic minerals derived from the surrounding hills. This interpretation in turn suggests that the MS records can be used as an East Asian winter monsoon proxy. The total organic carbon (TOC) content of the core sediments ranges from 2.4 to 44 wt%, and the TOC content is anomalously high near the top of the core. The downcore variation in the TOC content shows that it abruptly changed at a depth of around 208 cm (corresponding to 14,400 cal BP). Below this depth, the TOC content is less than 6.5 wt%, whereas above this depth the TOC content has a range of 8.7 - 17 wt%. The lowest TOC value occurs at a depth of around 320 cm (corresponding to 17,700 cal BP). The MS and TOC records of the Hanon paleo-maar sediments reveal significant variations in the intensity of the winter and summer monsoons in Jeju Island, respectively, during the latest Pleistocene to early Holocene. Prior to around 21,300 cal BP, the summer monsoon was slightly stronger, even though the intensity of the summer monsoon was considerably weaker than that during the Holocene. The time interval from 21,300 to 14,000 cal BP represents the period with a very weak summer monsoon but very strong winter monsoon strength. At around 14,000 cal BP the summer monsoon began to strengthen, indicative of the timing corresponding to the onset of the last major deglaciation-like warming in Jeju Island. From the time of the last deglaciation-like warming to the early Holocene, the summer monsoon was weakened from 13,300 to 12,000 cal BP and from 11,500 - 9800 cal BP. Subsequently, the summer monsoon strengthened from 9800 cal BP. However, the winter monsoon did not strengthen during the same periods when the summer monsoon was weakened, suggestive of the weakening of the summer monsoon intensity does not necessarily indicate the strengthening of the winter monsoon.

4. Methods

The preparation of samples for REEs followed an acid digestion method

and the procedure is as follows. The subsamples taken at 10 cm intervals were dried in an oven at 105 °C for two days. The dried samples were ground to less than 200-mesh powder using an agate mortar and the powdered samples were heated with 1 ml of 30% HCl in a sealed teflon bomb at 150 °C for 12 h. After adding each 1 ml of 48% Hf and 65% HNO_3 to dissolved solution, the mixed solution was heated at 150 °C for three days, and after reaction solution was dried completely on a hot plate. After cooling, the dried final residue was dissolved by adding 1 wt.% HNO_3 in 60 ml light-density polyethylene tube and the total weight of the redissolved solution was set to be 60 g. This solution was diluted to 1000-fold by adding 1 wt.% HNO_3 for REE analysis.

The composition of REE was analyzed for samples by using an Optima 3300 DV (Perkin - Elmer Sciex) inductively coupled plasma optical emission spectrometer (ICP-OES) at Korea Polar Research Institute. All the instrumental operating conditions of the ICP-OES are listed in Hur et al. (2003). Geochemical standards MAG-1 (USGS) and JA-2 (JSA) were analyzed for a measurement quality control. For comparison of sediment compositions, three basaltic basement rock samples from the surrounding rim were collected. Also used were Asian dust (Hwangsa) samples collected at Korea Meteorological Administration, Seoul on 21 March 2002 during the Asian dust event. Asian dust samples were collected on cellulose membrane filters using a high-volume air sampler. REE compositions of trachybasalt and Asian dust samples were also analyzed utilizing the same ICP-OES. Analytical precision for REE is generally better than 3%.

5. Results

The analytical results of REE compositions of core BH-4B sediments, trachybasalt, and Asian dust samples are given in Table 1. Total REE concentrations of core sediments show much variability ranging from 44 ppm to 321 ppm, and the condrite-normalized ratio of La/Yb [$(La/Yb)_N$] is also variable ranging from 3.4 to 14.0. The Eu/Eu* (where $Eu/Eu^* = Eu_N/[(Sm_N)(GdN)]^{1/2}$, the subscript 'N' indicates normalized values) for core sediments varies from 0.77 to 0.97. The Eu/Eu* shows a gradual decrease of negative anomaly upcore (Fig. 3),

and an abrupt increase with a small negative Eu anomaly is shown at 180, 200, 210, and 220 cm depths. A distinctive positive Ce anomaly (Ce/Ce*) (maximum 1.27) is observed at several horizons, at 200, 210, 220, and 390 cm depths.

The abundance of REE in the trachybasalt and Asian dust samples has different values with 316 ppm and 205 ppm, respectively. Chondrite-normalized patterns are significantly different (Fig. 4A). Trachybasalt is characterized by LREE-enriched patterns with fractionated HREE (Gd/Yb = 3.1) and negligible Eu anomaly (Eu/Eu* = 0.97). In contrast, the Asian dust sample is characterized by fractionated LREE patterns with relatively flat HREE (Gd/Yb = 2.0) and a pronounced negative Eu anomaly (Eu/Eu* = 0.67). Trachybasalt shows a slightly negative Ce anomaly (Ce/Ce* = 0.81), but the Asian dust sample does not have a Ce anomaly (Ce/Ce* = 0.97).

6. Discussion

6.1. Rare earth elements distribution

Based on the chondrite-normalized REE patterns and Eu anomaly, the REE distribution patterns of core sediments are subdivided into six types (Fig. 5). Type I REE pattern is very similar to the Asian dust REE pattern. The chondrite-normalized ratio of Eu/Eu* and Ce/Ce* for the type 1 REE pattern ranges from 0.77 to 0.82 and 0.89 to 0.97, respectively, showing that the Eu/Eu* is smaller than that of the Asian dust. $(La/Yb)_N$ and $(Gd/Yb)_N$ ratios range from 11.87 to 14.00 and 2.29 to 2.63, respectively. HREE is more fractionated than that of Asian dust. The type 1 REE pattern occurs in the lowermost part of core sediments at 420, 440, 450, 460, 470, 480, and 490 cm depths.

Type 2 REE pattern is generally similar to that of type 1, but shows enriched REE concentration than that of the latter. The chondrite-normalized ratios of (La/Yb)N and (Gd/Yb)N range from 12.15 to 13.25 and from 2.47 to 2.76, respectively. The Eu/Eu* for the type 2 REE pattern ranges from 0.78 to 0.82, indicating that Eu/Eu* is very similar to that of the type 1. The type 2 REE pattern is observed in sediments at 290, 360, 370, 380, 400, and 410 cm depths.

The (La/Yb)N of type 3 ranges from 6.38 to 8.23, displaying very flat

REE patterns than those of types 1 and 2 having (La/Yb)N ratios more than 10. The Eu/Eu* ranges from 0.84 to 0.89, and thus has a weaker negative Eu anomaly than that of types 1 and 2. The type 3 REE pattern is observed in sediments at 260, 280, 300, 330, 390, and 430 cm depths. The type 3 shows a strong positive Ce anomaly with the chondrite-normalized ratio of Ce/Ce* ranging from 0.98 to 1.26. The sample at 390 cm depth shows a very strong positive Ce anomaly, 1.26.

Type 4 REE pattern is similar to that of types 1 and 2. The Eu/Eu* ranges from 0.81 to 0.86, and thus the type 4 has a slightly more negative Eu anomaly than that of type 3 but weaker than that of type 1. Type 4 is divided into two subgroups on the basis of the total REE concentration, one with relatively enriched total REE concentration occurring in the deeper part below 2 m depth (type 4a) and the other with relatively less enriched total REE occurring in the shallower part (type 4b) except for a sample at 270 cm depth. The type 4a shows slightly higher Eu/Eu* ratios and occurs in sediments at 230, 240, 250, 310, 320, 340, and 350 cm depths and the type 4b is observed in sediments at 110, 120, 130, 140, 150, 160, 170, 190, and 270 cm depths.

Type 5 REE pattern occurs in the most upper part of core sediments and shows a similar pattern to that of trachybasalt. However, total REE concentrations for the type 5 are depleted, ranging from 60 to 242 ppm, less than that of trachybasalt (316 ppm). The Eu/Eu* and Ce/Ce* for the type 5 range from 0.89 to 0.93 and 0.83 to 1.03, respectively and thus, the type 5 shows a very weak negative Eu anomaly close to that of trachybasalt. Even though the (La/Yb)N ranges from 7.18 to 14.01, the REE pattern of the type 5 shows the same fractionated pattern to that of trachybasalt. The type 5 pattern occurs in sediments of core top to 100 cm depth interval.

Type 6 REE pattern, occurring in samples at 180, 200, 210, and 220 cm depths, shows a very different REE pattern from those of other core sediments, Asian dust, and trachybasalt. The Eu/Eu* ranges from 0.90 to 0.97, showing the weakest negative Eu anomaly, almost identical to that of trachybasalt, but total REE concentrations are much depleted. The REE pattern of the type 6 is the most flattened among all samples, with the (La/Yb)N ranging from 3.39 to 5.29. The Ce/Ce* ranges from 1.06 to 1.27, representing the strongest positive Ce

anomaly.

6.2. Asian dust influence

The Eu/Eu* time-series spanning the latest Quaternary to early Holocene are characterized by high-frequency, high-amplitude variations (Fig. 3). The comparison of the Eu/Eu* curve with paleo-monsoon proxy records from the Loess Plateau and caves in China is shown in Fig. 6. Whereas the Eu/Eu* curve (Fig. 6B) generally resembles the quartz grain-size profile in the Chinese Loess Plateau at Luochuan (a winter monsoon record) (Fig. 6A; Xiao et al., 1995), in detail the basic data display slightly different variability at ~15,000 cal BP and in the time interval from ~14,000 to 11,000 cal BP, and the variation in the latter interval is more similar to that observed from oxygen-isotope records of stalagmites from Sanbao cave in China (a summer monsoon record) (Fig. 6C; Wang et al., 2008).

The studied paleo-maar sediment has two restricted terrestrial source materials: (1) basement rock composed of trachybasalt and (2) Asian dust blown from central Asia. Geochemical characteristics (REE, Th, U, and La/Th) of loess reveal that the Chinese Loess Plateau, the Luochuan loess as a representative, was derived from well-mixed sedimentary protoliths which underwent numerous upper-crustal recycling processes (Gallet et al., 1996). They reported REE compositions of the Luochuan loess back to 800 ka, displaying highly uniform REE patterns (except for Ce) characterized by the upper continental crust (UCC) ratios: $(La/Yb)_N$ = 10 and Eu/Eu^* = 0.66 (Fig. 4B). The REE of the Asian dust samples in this study shows $(La/Yb)_N$ = 9.71 and Eu/Eu^* = 0.67, being almost identical to that of the Luochuan loess. The REE characteristics of Asian dust analyzed in this study are also very similar to those of present-day Asian dust in other studies (e.g., Ryu et al., 2007 and Yang et al., 2007). This indicates that chemical properties of Asian dust per se that has been transported from central Asia to the Korean Peninsula might have been nearly consistent for at least 800,000 years, although it is difficult to establish considering the opinion that during the glacials the Yellow Sea basin was exposed and served as a major dust source to Korea (e.g., Kim et al., 2012). The chondrite-normalized

REE pattern of basement rock, trachybasalt, of the studied lake shows Eu-enriched REE pattern (Eu/Eu＊ = 0.97), which is identical to geochemical characteristics of basalt reported by McLennan et al. (1993).

The profile of Eu/Eu* shows a gradual decrease of negative Eu anomaly up core (Fig. 3), indicating a gradual decrease of Asian dust input to the studied paleo-maar, probably because of gradual weakening of winter monsoons. If Eu anomalies of the studied paleo-maar sediments resulted from simple mixing between Asian dust and trachybasalt-derived detritus without geochemical fractionation, the proportion of the Asian dust input from central Asia to Jeju Island can be inferred. Using a binary mixing model with Eu/Eu＊ end values of 0.97 for trachybasalt and 0.67 for Asian dust from central Asia, the contribution of the Asian dust was estimated to be up to 67% during the last glacial period and varies down to nil. The results of calculation reveal that the Asian dust proportion ranges from 27 to 67% during the last glacial period and from 13 to 43% during the Holocene (Fig. 3). Such large Asian dust flux during the last glacial period is in agreement with the results of other studies. Xiao et al. (1999) reported that the Asian quartz flux in Lake Biwa, Japan was three to five fold more than the fluvial quartz flux during the glacial periods. Windom (1969) suggested that up to 75% of the nonbiogenic component of North Pacific deep-sea sediment was atmospheric dust fallout during the glacial periods. Kohfeld and Harrison (2003) reported that the mass accumulation rate for MIS 2 was 2.1 times greater than that for MIS 1 on the Chinese Loess Plateau.

The vertical variation of Eu/Eu* indicates that the Asian dust flux associated with winter monsoon intensity fluctuated with high magnitude during the glacial period than in the Holocene. The REE distribution patterns of paleo-maar sediments before ca. 20,500 cal BP are dominated by type 1 with the proportion of the Asian dust ranging from 50 to 67%. From 20,500 to ca. 15,000 cal BP, the paleo-maar sediments are represented by the REE patterns of types 2, 3, and 4a, and these types alternate during this time period. During this period the Asian dust comprises 27 - 63% of the sediment: 50 - 63% (type 2), 27 - 43% (type 3), and 43 - 53% (type 4a), reflecting a variability of the winter monsoon intensity. Although the winter monsoon was strong at about 15,000 BP

in the Chinese Loess Plateau record (Fig. 6A), it is not apparent in the Jeju record. At ca. 14,500 cal BP, the REE distribution pattern (type 6) is very different from those of Asian dust and trachybasalt, and has very low total REE concentrations, but the Eu/Eu* value of the type 6 is similar to that of trachybasalt (Fig. 5). The proportion of the Asian dust ranges from nil to 23%. This observation can be accounted for by the rapid increase of detrital input from highly weathered trachybasalt, probably due to abundant precipitation, and dilution effect by high organic material as evidenced by high TOC content (Fig. 2). From 13,000 cal BP to 11,000 cal BP the type 4b REE pattern occurred with increased Asian dust input (37 - 47%) by a factor of two to that of the type 6 REE pattern in the immediately preceding time interval. This time interval seems to be represented by the increased strength of the winter monsoon in central Asia.

Interestingly, the Asian dust record during 14,300 - 13,300 cal BP and during 13,300 - 11,000 cal BP resembles the Bolling-Allerod (BA) and Younger Dryas (YD) features observed in Hulu and Sanbao caves in China (Fig. 6), suggestive of relatively strong and weak summer monsoon intensities, respectively (Wang et al., 2001 and Wang et al., 2008). However, the stalagmite oxygen-isotope record is interpreted as a proxy indicator of a vapor source or track, rather than that of monsoon precipitation (Pausata et al., 2011). Considering dating errors and resolution difference, the Eu/Eu* data suggest that the BA can be correlated with the type 6 REE pattern and the YD with the type 4b pattern. The possible connection of the central Asian winter monsoon events recorded in Jeju Island with the BA and YD features of north polar regions is worthy of note and needs further investigation.

The early Holocene is characterized by the type 5 pattern, and both REE pattern and Eu/Eu* values are close to those of trachybasalt. The average mixing ratio of Asian dust to the studied paleo-maar sediment was about 22% and consistent (16.7 - 26.7% range), suggestive of weak winter monsoons.

6.3. Paleo-monsoon climate in Jeju Island

As described above, the Eu/Eu* record shows that the input of Asian

dust reached its highest proportion (67%) in the core bottom sediment and its contribution generally decreased until the time of the last glacial maximum in Jeju Island (J-LGM). The TOC (a summer monsoon proxy) and MS (a winter monsoon proxy) records reveal that Jeju Island experienced the coldest time at about 18,000 cal BP (Lee et al., 2008). The record of Asian dust flux represents the paleoclimate change of Asian dust source regions in central Asia. The Eu/Eu* record of the studied paleo-maar sediments indicates that winter monsoon was very strong in central Asia prior to 18,500 cal BP, during which central Asia was very arid enough to supply abundant Asian dust. Xiao et al. (1995) reported that quartz median diameter (QMD) and quartz maximum diameter (Qmax) of the Luochuan loess-paleosol sequence, the proxy records for winter monsoon strength, reached their maximum value at 21,500 BP (Fig. 6A), and the onset of deglacial warming is interpreted to have occurred at ~19,000 BP (Peterse et al., 2011). Lee et al. (2008) pointed out that the timing of the LGM in the Chinese Loess Plateau was slightly earlier (2000 - 3000 y) than that in Jeju Island. Wu et al. (2002) suggested that changes in the temperature (responsible for wind intensity) and precipitation (responsible for extent of dust source area) in the Chinese Loess Plateau were not in phase during the last 30 ka: the coldest temperature occurred around 2000 - 3000 y prior to the precipitation minimum event. This idea was adopted when explaining the peak aeolian quartz flux in the Lake Biwa sediments in Japan (Xiao et al., 1999). If this were the case in central Asia, we would expect an increasing proportion of the Asian dust until the J-LGM in our paleo-maar sediment. However, the Asian dust flux did not increase as expected. Thus, this explanation does not hold true for the record in Jeju Island. Alternatively, the increased input of trachybasalt-derived detritus may be responsible for the decreasing trend of Asian dust influence, suggesting that Jeju Island was under the relatively strong influence of summer monsoons. Lee et al. (2008) interpreted the maximum MS at around 18,000 cal BP as the timing of the strongest winter monsoon coupled with a very weak summer monsoon. Although it was interpreted that Jeju Island experienced the coldest temperature during the J-LGM (Lee et al., 2008), the difference in the modeled temperatures of Jeju Island between the LGM in central China (21 - 18 ka) and middle Holocene is estimated to be less than 3C°

(Lu et al., 2013), suggesting that temperature influence was not significant. Rather, Jeju Island was under the progressively weakening summer monsoon strength from 22,300 cal BP onwards. At the time of the J-LGM, Jeju Island witnessed the largest input of primary inherited magnetic components (maximum MS) from the most weakly weathered soils of basalt (cf. Lu et al., 2008), probably due to the maximum reduction of summer monsoon strength. This interpretation suggests that until the J-LGM the weakening of the summer monsoon strength in Jeju Island was in phase with the weakening of the winter monsoon strength in central Asia. However, during this period of weakening summer monsoon strength there were three somewhat wet time intervals between 22,300 and 18,500 cal BP punctuated by two short dry times as indicated by the MS data (Fig. 3). Accordingly, the Eu/Eu* record reveals that the J-LGM was not the timing of the coldest and maximum winter monsoon strength, but the timing of the weakest summer monsoon strength in Jeju Island. After the highest MS value at ~18,000 cal BP, the MS value gradually decreased until ~14,000 cal BP, and during this time interval the proportion of Asian dust fluctuated between 30 and 53%. As weathering of basalt increases, the primary ferromagnetic mineral is known to weather directly to an antiferromagnetic mineral (hematite and/or goethite) (Lu et al., 2008). Thus, such a decreasing MS trend from 18,000 cal BP to 14,000 cal BP may represent a possible progressive increase in removal of magnetic components during pedogeneic development under increasing summer monsoon intensity.

During ~14,500 to ~13,300 cal BP, the proportion of Asian dust drastically decreased to almost nil to 23%, and this time interval is coeval with the onset of the major last deglaciation-like warming in Jeju Island as noted by the rapid increase in TOC content (Lee et al., 2008). During this interval, Jeju Island seems to have experienced significantly intensified summer monsoon strength. Dramatic increase of precipitation might have induced increased soil development and enhanced land-plant productivity (cf., Feng et al., 2002), which resulted in the deposition of detritus from highly weathered trachybasalt and land-plant debris in the paleo-maar, as indicated by high TOC content (Fig. 2), predominately organic matter of terrestrial origin (Lee et al., 2008). Subsequently, Jeju Island experienced the weakened summer monsoon intensity from ~13,000

to 11,000 cal BP, indicated by the slightly reduced TOC content and increased Asian dust proportion. Lee et al. (2008) pointed out that there were two weakening events of summer monsoon intensity in Jeju Island from the last deglaciation-like warming to the early Holocene, the timing of these two events being similar to the YD event. The similar weakening event of the summer monsoon strength (YD) was also reported from the Yangtze River delta in China (Yi et al., 2003). Then, the intensity of the summer monsoon became strong in the early Holocene, representing the weakening of eolian activity (cf., Qiang et al., 2014). Most of the sediments deposited during the latest glacial period were deposited under an oxic state as represented by a non- to positive Ce anomaly (cf., Wright et al., 1987 ; Wilde et al., 1996), whereas the early Holocene sediments were deposited under a slightly less oxic state.

In summary, the schematic presentation of the Jeju Island summer monsoon climate is depicted in Fig. 7. From 22,300 cal BP to the J-LGM the central Asian winter and the Juju Island summer monsoon changes covaried, both toward the weakening intensity, whereas from the J-LGM to the early Holocene they show an inverse behavior between intensifying summer monsoon in Jeju Island and weakening winter monsoon strength in central Asia (Fig. 6).

7. Conclusions

1. The REE characteristics of the Hanon paleo-maar sediments in Jeju Island, Korea represent variations of the relative contribution of two geochemically distinctive sources: the Asian dust transported from central Asia and detritus derived from trachybasalt surrounding the paleo-maar. From 22,300 to 9000 cal BP the REE record reveals that due to its location close to the moisture source the monsoon climate of Jeju Island was mainly dominated by changes of the summer monsoon strength. During this period the winter monsoon strength in central Asia became progressively weakened.

2. Integration of the REE results with the MS and TOC data of Lee et al. (2008) shows that from 22,300 cal BP, the intensity of the summer monsoon strength was decreased progressively until 18,000 cal BP (J-LGM) when the summer monsoon strength was the weakest. Then, the summer monsoon

strength became progressively intensified until 14,000 cal BP when the abrupt strong intensification occurred. The strong summer monsoons lasted until 13,300 cal BP. The winter monsoon strength in central Asia became weakened during this interval. From 13,300 cal BP to 11,000 cal BP the summer monsoon was weakened in anti-phase with the strengthened winter monsoon in central Asia. In the early Holocene, Jeju Island experienced further strengthened summer monsoons.

후기 플라이스토세-전기 홀로세 한국 제주도의 고습지 퇴적물의 희토류 조성을 통한 과거의 황사 기록과 한반도 계절풍 기후에 대한 연구

Min Kyung Lee[1], Yong Il Lee[2], Kyu-Cheul Yoo[1], Ho Il Yoon[1]

[1]Korea Polar Research Institute
[2]Seoul National University

요약: 한국 제주도 하논 고습지에서 얻은 4.96 m의 퇴적물 코어의 희토류 원소(REE) 조성이 플라이스토세 후기에서 호롤세 초기 동안의 동아시아 몬순의 변동을 조사하기 위해 연구되었다. 연구 된 고분화구 퇴적물은 다른 지화학적인 시그널을 가지는 2 개의 제한적인 소스 지역(중앙 아시아(중국 북쪽과 몽고)에서 유입되는 아시아 먼지와 조면현무암으로 구성된 기반암)을 가지고 있다. 퇴적물의 REE 특성은 두 소스 지역의 상대적 기여도에 따라 결정되므로, 제주도에서 몬순 기후를 묘사하는 데 사용할 수 있다. 아시아 먼지 비율은 일반적으로 22,300 cal BP에 67 %에서 점진적으로 감소하였고, 이는 중앙 아시아에서 겨울 몬순 강도가 점진적으로 약화되었음을 의미한다. REE 자료와 TOC 및 대자율 값을 통합은 제주도에서 여름철 몬순이 22,300 cal BP부터 마지막 최대 빙하기 18,000 cal BP까지 약해진 후, 14,000 cal BP까지 강해졌다. 14,000에서 13,300 cal BP 동안 여름 몬순의 급격한 강화 이후, 13,300에서 11,000 cal BP 동안 중앙 아시아의 강화 된 겨울 몬순과 반대로 약한 여름 몬순이 이어졌다. 홀로 세 초기에 제주도는 여름 몬순의 강도가 더욱 강해졌다.

참고문헌

Zhisheng, A., Tunghseng, L., Yanchou, L., Porter, S. C., Kukla, G. H. W. X., Xihao, W., & Yingming, H. (1990). The long-term paleomonsoon variation recorded by the loess-paleosol sequence in central China. Quaternary International, 7, 91-95.

An, Z., Kukla, G. J., Porter, S. C., & Xiao, J. (1991). Magnetic susceptibility evidence of monsoon variation on the Loess Plateau of central China during the last 130,000 years. Quaternary Research, 36(1), 29-36.

Y.A. Balashov, A.B. Ronov, A.A. Migdisov, N.V. Turanskaya. (1964), The effect of climate and facies environment on the fractionation of the rare earth elements during sedimentation. Geochemistry International, 1, pp. 951 - 969

Batjargal, Z., Dulam, J., & Chung, Y. S. (2006). Dust storms are an indication of an unhealthy environment in East Asia. Environmental Monitoring and Assessment, 114(1), 447-460.

Bau, M. (1991). Rare-earth element mobility during hydrothermal and metamorphic fluid-rock interaction and the significance of the oxidation state of europium. Chemical Geology, 93(3-4), 219-230.

Chung, C. H. (2007). Vegetation response to climate change on Jeju Island, South Korea, during the last deglaciation based on pollen record. Geosciences Journal, 11(2), 147-155.

Davies, B. E. (1980). Applied soil trace elements. Wiley.

Ding, Z., Liu, T., Rutter, N. W., Yu, Z., Guo, Z., & Zhu, R. (1995). Ice-volume forcing of East Asian winter monsoon variations in the past 800,000 years. Quaternary Research, 44(2), 149-159.

Feng, Q., Endo, K. N., & Guodong, C. (2002). Soil carbon in desertified land in relation to site characteristics. Geoderma, 106(1), 21-43.

Gallet, S., Jahn, B. M., & Torii, M. (1996). Geochemical characterization of the Luochuan loess-paleosol sequence, China, and paleoclimatic implications. Chemical geology, 133(1), 67-88.

Hashizume, M., Ueda, K., Nishiwaki, Y., Michikawa, T., & Onozuka, D. (2010). Health effects of Asian dust events: a review of the literature. Nihon

eiseigaku zasshi. Japanese journal of hygiene, 65(3), 413-421.

Hur, S. D., Lee, J. I., Lee, M. J., & Kim, Y. D. (2003). Determination of rare earth elements abundance in alkaline rocks by inductively coupled plasma mass spectrometry (ICP-MS). Ocean and Polar Research, 25(1), 53-62.

Jaffe, D., Anderson, T., Covert, D., Kotchenruther, R., Trost, B., Danielson, J., ... & Harris, J. (1999). Transport of Asian air pollution to North America. Geophysical Research Letters, 26(6), 711-714.

Janecek, T. R., & Rea, D. K. (1983). Eolian deposition in the northeast Pacific Ocean: Cenozoic history of atmospheric circulation. Geological Society of America Bulletin, 94(6), 730-738.

Janecek, T. R., & Rea, D. K. (1985). Quaternary fluctuations in the northern hemisphere trade winds and westerlies. Quaternary Research, 24(2), 150-163.

Kim, J. C., Lee, Y. I., Lim, H. S., & Yi, S. (2012). Geochemistry of Quaternary sediments of the Jeongokri archaeological site, Korea: implications for provenance and palaeoenvironments during the Late Pleistocene. Journal of Quaternary Science, 27(3), 260-268.

Kohfeld, K. E., & Harrison, S. P. (2003). Glacial-interglacial changes in dust deposition on the Chinese Loess Plateau. Quaternary Science Reviews, 22(18), 1859-1878.

Kwon, H. J., Cho, S. H., Chun, Y., Lagarde, F., & Pershagen, G. (2002). Effects of the Asian dust events on daily mortality in Seoul, Korea. Environmental Research, 90(1), 1-5.

Lee, M. W. (1982). Petrology and geochemistry of Jeju volcanic island, Korea. Science Reports of the Tohoku University, Series III, 15, 177-256.

Lee, S. H., Lee, Y. I., Yoon, H. I., & Yoo, K. C. (2008). East Asian monsoon variation and climate changes in Jeju Island, Korea, during the latest Pleistocene to early Holocene. Quaternary Research, 70(2), 265-274.

Li, C., Yang, S., & Zhang, W. (2012). Magnetic properties of sediments from major rivers, aeolian dust, loess soil and desert in China. Journal of Asian Earth Sciences, 45, 190-200.

Lim, J., Matsumoto, E., & Kitagawa, H. (2005). Eolian quartz flux variations in

Cheju Island, Korea, during the last 6500 yr and a possible Sun - monsoon linkage. Quaternary Research, 64(1), 12-20.

Liu, T., & Ding, Z. (1998). Chinese loess and the paleomonsoon. Annual review of earth and planetary sciences, 26(1), 111-145.

Lu, H., Yi, S., Liu, Z., Mason, J. A., Jiang, D., Cheng, J., ... & Zhang, Z. (2013). Variation of East Asian monsoon precipitation during the past 21 ky and potential CO2 forcing. Geology, 41(9), 1023-1026.

Lu, S. G., Xue, Q. F., Zhu, L., & Yu, J. Y. (2008). Mineral magnetic properties of a weathering sequence of soils derived from basalt in Eastern China. Catena, 73(1), 23-33.

Maher, B. A., Prospero, J. M., Mackie, D., Gaiero, D., Hesse, P. P., & Balkanski, Y. (2010). Global connections between aeolian dust, climate and ocean biogeochemistry at the present day and at the last glacial maximum. Earth-Science Reviews, 99(1), 61-97.

McLennan, S. M., Hemming, S., McDaniel, D. K., & Hanson, G. N. (1993). Geochemical approaches to sedimentation, provenance, and tectonics. Geological Society of America Special Papers, 284, 21-40.

Mizota, C., Endo, H., Um, K. T., Kusakabe, M., Noto, M., & Matsuhisa, Y. (1991). The eolian origin of silty mantle in sedentary soils from Korea and Japan. Geoderma, 49(1-2), 153-164.

Nesbitt, H. W. (1979). Mobility and fractionation of rare earth elements during weathering of a granodiorite. Nature, 279(5710), 206-210.

Pausata, F. S., Battisti, D. S., Nisancioglu, K. H., & Bitz, C. M. (2011). Chinese stalagmite [delta] 18O controlled by changes in the Indian monsoon during a simulated Heinrich event. Nature Geoscience, 4(7), 474-480.

Peterse, F., Prins, M. A., Beets, C. J., Troelstra, S. R., Zheng, H., Gu, Z., ... & Damsté, J. S. S. (2011). Decoupled warming and monsoon precipitation in East Asia over the last deglaciation. Earth and Planetary Science Letters, 301(1), 256-264.

Pye, K., & Zhou, L. P. (1989). Late Pleistocene and Holocene aeolian dust deposition in north China and the northwest Pacific Ocean. Palaeogeography, Palaeoclimatology, Palaeoecology, 73(1), 11-23.

Qiang, M., Liu, Y., Jin, Y., Song, L., Huang, X., & Chen, F. (2014). Holocene

record of eolian activity from Genggahai Lake, northeastern Qinghai Tibetan Plateau, China. Geophysical Research Letters, 41(2), 589-595.

Rea, D. K. (1994). The paleoclimatic record provided by eolian deposition in the deep sea: The geologic history of wind. Reviews of Geophysics, 32(2), 159-195.

Rea, D. K., Leinen, M., & Janecek, T. R. (1985). Geologic approach to the long-term history of atmospheric circulation. Science, 227(4688), 721-725.

Ryu, J. S., Lee, K. S., Lee, S. G., Lee, D., & Chang, H. W. (2007). Seasonal and spatial variations of rare earth elements in rainwaters, river waters and total suspended particles in air in South Korea. Journal of Alloys and Compounds, 437(1), 344-350.

Shao, Y., & Dong, C. H. (2006). A review on East Asian dust storm climate, modelling and monitoring. Global and Planetary Change, 52(1), 1-22..

Sun, J., Zhang, M., & Liu, T. (2001). Spatial and temporal characteristics of dust storms in China and its surrounding regions, 1960 - 1999: Relations to source area and climate. Journal of Geophysical Research: Atmospheres, 106(D10), 10325-10333.

Sun, Y., Clemens, S. C., An, Z., & Yu, Z. (2006). Astronomical timescale and palaeoclimatic implication of stacked 3.6-Myr monsoon records from the Chinese Loess Plateau. Quaternary Science Reviews, 25(1), 33-48.

VanCuren, R. A., & Cahill, T. A. (2002). Asian aerosols in North America: Frequency and concentration of fine dust. Journal of Geophysical Research: Atmospheres, 107(D24).

VanCuren, R. A. (2003). Asian aerosols in North America: Extracting the chemical composition and mass concentration of the Asian continental aerosol plume from long term aerosol records in the western United States. Journal of Geophysical Research: Atmospheres, 108(D20).

Wang, Y. J., Cheng, H., Edwards, R. L., An, Z. S., Wu, J. Y., Shen, C. C., & Dorale, J. A. (2001). A high-resolution absolute-dated late Pleistocene monsoon record from Hulu Cave, China. Science, 294(5550), 2345-2348.

Wang, Y., Cheng, H., Edwards, R. L., Kong, X., Shao, X., Chen, S., ... & An, Z. (2008). Millennial-and orbital-scale changes in the East Asian monsoon over the past 224,000 years. Nature, 451(7182), 1090-1093.

Wang, X., Sun, D. H., Wang, F., Li, B. F., Wu, S., Guo, F., ... & Chen, F. H. (2013). A high-resolution multi-proxy record of late Cenozoic environment change from central Taklimakan Desert, China. Climate of the Past, 9(6), 2731.

Wilde, P., Quinby-Hunt, M. S., & Erdtmann, B. D. (1996). The whole-rock cerium anomaly: a potential indicator of eustatic sea-level changes in shales of the anoxic facies. Sedimentary Geology, 101(1-2), 43-53.

Windom, H. L. (1969). Atmospheric dust records in permanent snowfields: implications to marine sedimentation. Geological Society of America Bulletin, 80(5), 761-782.

Won, C. K. (1976). Study of petro-chemistry of volcanic rocks in Jeju Island. Journal of the Geological Society of Korea, 12, 207-226.

Wright, J., Schrader, H., & Holser, W. T. (1987). Paleoredox variations in ancient oceans recorded by rare earth elements in fossil apatite. Geochimica et Cosmochimica Acta, 51(3), 631-644.

Wu, N., Liu, T., Liu, X., & Gu, Z. (2002). Mollusk record of millennial climate variability in the Loess Plateau during the Last Glacial Maximum. Boreas, 31(1), 20-27.

Xiao, J., Porter, S. C., An, Z., Kumai, H., & Yoshikawa, S. (1995). Grain size of quartz as an indicator of winter monsoon strength on the Loess Plateau of central China during the last 130,000 yr. Quaternary Research, 43(1), 22-29.

Xiao, J., Inouchi, Y., Kumai, H., Yoshikawa, S., Kondo, Y., Liu, T., & An, Z. (1997). Eolian quartz flux to Lake Biwa, central Japan, over the past 145,000 years. Quaternary Research, 48(1), 48-57.

Xiao, J. L., An, Z. S., Liu, T. S., Inouchi, Y., Kumai, H., Yoshikawa, S., & Kondo, Y. (1999). East Asian monsoon variation during the last 130,000 years: evidence from the Loess Plateau of central China and Lake Biwa of Japan. Quaternary Science Reviews, 18(1), 147-157.

Yang, C. Y., Tsai, S. S., Chang, C. C., & Ho, S. C. (2005). Effects of Asian

dust storm events on daily admissions for asthma in Taipei, Taiwan. Inhalation toxicology, 17(14), 817-821.

Yang, X., Liu, Y., Li, C., Song, Y., Zhu, H., & Jin, X. (2007). Rare earth elements of aeolian deposits in Northern China and their implications for determining the provenance of dust storms in Beijing. Geomorphology, 87(4), 365-377.

Yi, S., Saito, Y., Zhao, Q., & Wang, P. (2003). Vegetation and climate changes in the Changjiang (Yangtze River) Delta, China, during the past 13,000 years inferred from pollen records. Quaternary Science Reviews, 22(14), 1501-1519.

Zdanowicz, C., Hall, G., Vaive, J., Amelin, Y., Percival, J., Girard, I., ... & Bory, A. (2006). Asian dustfall in the St. Elias Mountains, Yukon, Canada. Geochimica et Cosmochimica Acta, 70(14), 3493-3507.

Zhang, X. Y., Arimoto, R., & An, Z. S. (1997). Dust emission from Chinese desert sources linked to variations in atmospheric circulation. Journal of Geophysical Research. D. Atmospheres, 102, 28-041.

Zhang, X. Y., Arimoto, R., & An, Z. S. (1999). Glacial and interglacial patterns for Asian dust transport. Quaternary Science Reviews, 18(6), 811-819.

Table 1
Rare earth elements concentrations in ppm for core BH-4B sediments, trachybasalt, and Asian dust sample.

Depth (cm)	La	Ce	Pr	Nd	Sm	Eu	Gd	Tb	Dy	Ho	Er	Yb	ΣREE	Eu/Eu[a]	Ce/Ce[a]	LaN/YbN
0	21.3	46.8	5.6	22.1	4.9	1.5	5.1	0.8	4.3	0.8	2.3	2.0	117.5	0.93	0.99	7.2
10	53.7	95.5	12.0	45.3	8.9	2.6	9.2	1.3	6.7	1.2	3.2	2.6	242.2	0.89	0.83	14.0
20	38.7	75.7	9.1	35.4	7.0	2.0	7.0	1.0	5.2	0.9	2.6	2.1	186.8	0.90	0.90	12.2
30	23.3	52.1	5.6	21.6	4.5	1.4	4.6	0.7	3.8	0.7	2.0	1.7	121.9	0.92	1.03	9.3
40	13.3	26.6	3.1	12.2	2.5	0.7	2.5	0.4	2.0	0.4	1.1	0.9	65.5	0.89	0.92	10.3
50	26.0	50.5	6.0	22.8	4.7	1.4	4.6	0.6	3.6	0.6	1.8	1.5	124.3	0.90	0.90	11.7
60	31.9	61.5	7.4	28.1	5.6	1.7	5.7	0.8	4.3	0.8	2.2	1.8	151.6	0.92	0.89	12.1
70	22.2	45.9	5.5	21.2	4.3	1.2	4.2	0.6	3.2	0.6	1.7	1.4	111.9	0.90	0.94	10.3
80	29.2	59.3	7.2	27.2	5.4	1.6	5.3	0.7	4.1	0.7	2.0	1.8	144.5	0.89	0.93	11.0
90	10.4	24.1	3.0	12.2	2.6	0.7	2.3	0.3	1.9	0.3	1.0	0.9	59.8	0.92	1.01	7.7
100	29.8	59.8	7.1	27.5	5.7	1.7	5.8	0.8	4.6	0.9	2.4	2.0	148.1	0.91	0.92	9.9
110	46.4	91.2	11.1	42.4	8.4	2.3	8.3	1.2	6.2	1.1	3.1	2.5	224.3	0.84	0.91	12.3
120	42.9	84.3	10.3	38.6	7.6	2.1	7.8	1.1	5.7	1.0	2.8	2.4	206.5	0.84	0.91	12.2
130	44.3	86.3	10.4	39.6	7.8	2.2	7.8	1.1	5.7	1.0	2.8	2.3	211.2	0.86	0.90	12.9
140	44.2	86.4	10.4	40.0	8.1	2.2	8.1	1.1	6.1	1.1	3.0	2.5	213.2	0.84	0.90	11.8
150	43.1	82.4	10.1	38.2	7.5	2.1	7.5	1.1	5.8	1.0	2.9	2.5	204.1	0.86	0.89	11.7
160	42.7	82.6	10.1	38.2	7.6	2.1	7.7	1.1	5.7	1.0	2.8	2.3	203.9	0.85	0.90	12.2
170	42.4	83.4	10.1	37.8	7.3	2.0	7.5	1.0	5.4	0.9	2.7	2.2	202.7	0.83	0.91	12.7
180	11.4	28.1	3.5	14.4	3.3	1.0	3.4	0.5	3.0	0.6	1.6	1.4	72.3	0.90	1.06	5.3
190	41.7	80.5	9.7	36.6	7.2	2.0	7.5	1.0	5.4	0.9	2.7	2.2	197.4	0.83	0.89	12.7
200	6.3	18.1	1.8	8.0	1.9	0.6	2.0	0.3	2.1	0.4	1.3	1.2	43.9	0.92	1.24	3.4
210	9.2	27.1	2.6	11.4	2.7	0.8	2.7	0.4	2.6	0.5	1.4	1.4	62.9	0.91	1.27	4.5
220	6.5	18.3	1.7	7.7	1.9	0.6	2.0	0.3	2.0	0.4	1.2	1.1	43.6	0.97	1.23	4.0
230	58.9	116.7	13.0	49.4	9.8	2.6	9.7	1.3	7.2	1.3	3.5	3.0	276.4	0.81	0.93	13.1
240	61.7	129.6	14.2	52.7	10.3	2.8	10.5	1.4	7.5	1.3	3.8	3.3	299.2	0.82	0.98	12.6
250	56.8	118.7	13.0	49.0	9.7	2.6	9.9	1.3	7.2	1.3	3.6	3.1	276.1	0.83	0.97	12.4
260	23.8	59.2	6.0	24.5	5.4	1.6	5.6	0.9	4.8	0.9	2.7	2.4	137.7	0.88	1.12	6.6
270	38.0	80.3	9.2	36.4	7.5	2.0	7.5	1.1	5.9	1.1	3.1	2.7	194.7	0.83	0.97	9.5
280	27.4	59.7	6.8	27.4	5.8	1.6	6.0	0.9	5.1	1.0	2.7	2.5	147.0	0.85	0.98	7.4
290	54.7	118.0	12.4	47.1	9.2	2.5	9.3	1.3	6.8	1.2	3.5	3.0	268.9	0.81	1.00	12.1
300	27.4	59.6	7.0	28.7	6.2	1.7	6.2	0.9	5.2	1.0	2.8	2.5	149.3	0.85	0.98	7.2
310	65.9	136.7	15.3	57.7	11.4	3.2	11.8	1.6	8.4	1.5	4.1	3.5	321.1	0.84	0.96	12.6
320	57.8	119.8	13.8	52.2	10.2	2.7	10.4	1.4	7.5	1.3	3.8	3.2	284.0	0.82	0.96	12.1
330	21.4	52.6	5.8	24.0	5.3	1.5	5.4	0.8	4.7	0.9	2.5	2.2	127.3	0.89	1.08	6.4
340	64.1	131.6	14.8	55.8	11.0	3.0	11.2	1.5	7.9	1.4	3.9	3.3	309.3	0.83	0.96	12.9
350	66.0	136.3	14.9	56.6	11.0	3.0	11.3	1.5	7.9	1.4	3.9	3.3	317.0	0.82	0.96	13.5
360	53.2	111.4	12.2	46.1	8.9	2.3	9.1	1.2	6.5	1.2	3.3	2.8	258.2	0.80	0.97	12.5
370	57.0	117.0	13.0	49.6	9.7	2.5	9.8	1.3	6.9	1.2	3.4	2.9	274.5	0.80	0.95	13.1
380	55.0	113.8	12.5	46.6	9.1	2.4	9.2	1.3	6.6	1.2	3.3	2.9	263.8	0.81	0.97	12.8
390	26.0	71.5	6.1	24.0	5.1	1.4	5.4	0.8	4.3	0.8	2.3	2.1	149.8	0.84	1.26	8.2

Table 1 (*continued*)

Depth (cm)	La	Ce	Pr	Nd	Sm	Eu	Gd	Tb	Dy	Ho	Er	Yb	ΣREE	Eu/Eu[a]	Ce/Ce[a]	LaN/YbN
400	53.0	109.1	12.1	46.1	8.9	2.4	9.3	1.2	6.5	1.2	3.3	2.7	255.6	0.82	0.96	13.2
410	52.8	109.8	12.0	45.8	8.9	2.3	9.2	1.2	6.5	1.1	3.2	2.8	255.6	0.78	0.97	12.8
420	46.2	93.9	9.5	35.5	6.9	1.8	7.3	1.0	5.1	0.9	2.6	2.3	213.0	0.79	0.97	13.4
430	22.3	54.2	5.4	21.8	4.7	1.3	4.8	0.7	4.0	0.7	2.2	2.0	124.2	0.85	1.10	7.5
440	44.1	82.6	8.9	33.2	6.4	1.6	6.5	0.9	4.7	0.8	2.4	2.1	194.3	0.79	0.89	14.0
450	46.8	91.0	9.8	36.6	7.1	1.9	7.3	1.0	5.3	1.0	2.7	2.4	212.8	0.82	0.92	13.1
460	40.3	80.2	8.6	32.5	6.4	1.6	6.5	0.9	4.9	0.9	2.5	2.3	187.7	0.78	0.94	11.9
470	40.5	78.5	8.5	32.2	6.4	1.7	6.4	0.9	4.8	0.9	2.4	2.2	185.2	0.80	0.92	12.5
480	44.7	90.5	10.3	38.4	7.4	1.8	7.5	1.0	5.2	0.9	2.6	2.3	212.6	0.77	0.94	13.2
490	43.7	85.4	9.8	36.9	7.1	1.8	7.4	1.0	5.5	1.0	2.8	2.4	204.9	0.77	0.91	12.1
Trachy-basalt[a]	67.5	119.0	15.6	61.3	12.5	4.2	14.1	2.0	9.9	1.8	4.7	3.6	316.2	0.97	0.81	12.4
Asian dust[b]	41.2	86.9	10.0	37.4	7.1	1.5	7.1	1.0	5.4	1.0	3.1	2.8	204.6	0.67	0.97	9.7

[a] Average of three samples.
[b] Collected on March 21, 2002 in Seoul.

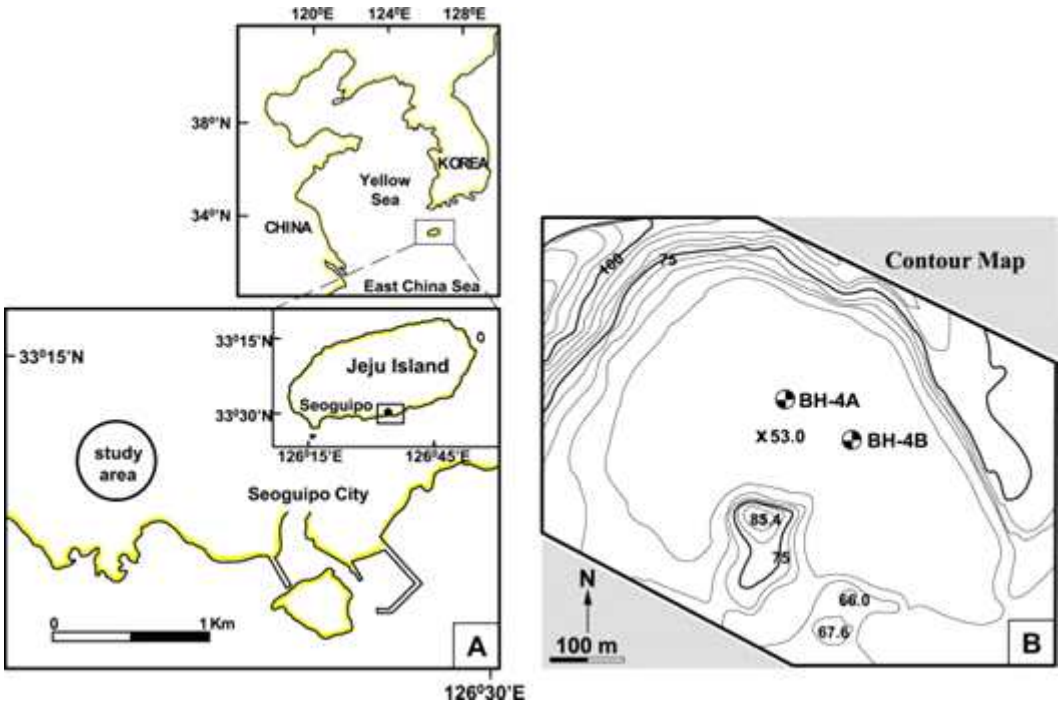

Fig. 1. (A) Location map of the study area. (B) Location of core BH-4B in the center of Hanon paleo-maar, Jeju Island (modified after Lee et al., 2008).

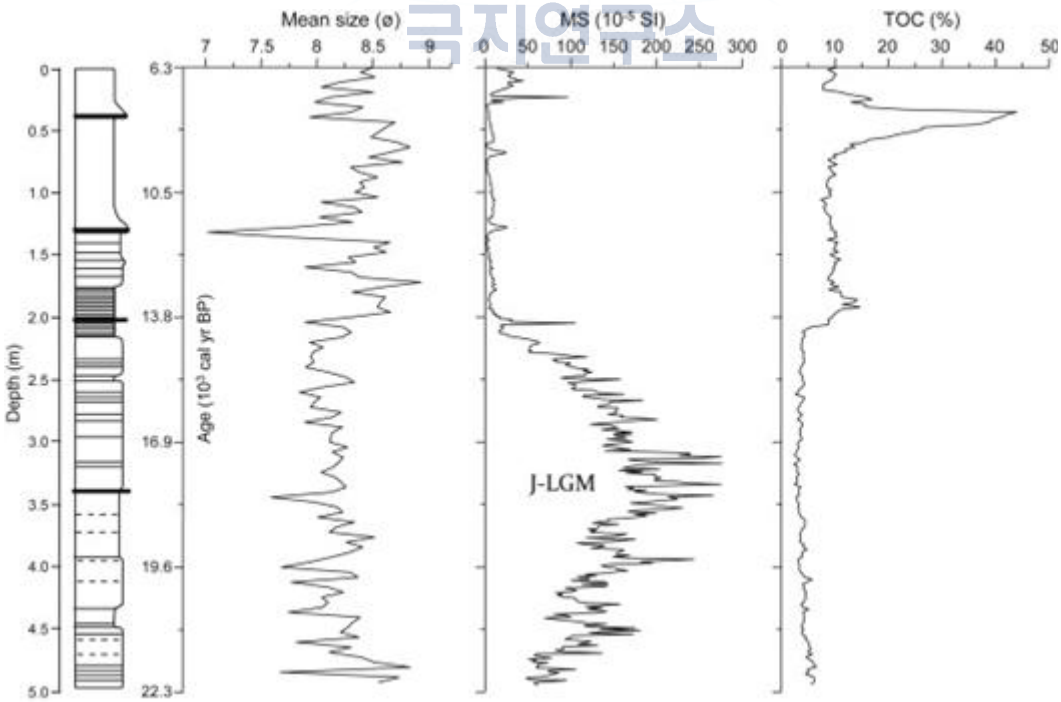

Fig. 2. The schematic columnar of core BH-4B with calibrated time markers and vertical variations of mean size, magnetic susceptibility, and total organic carbon (after Lee et al., 2008).

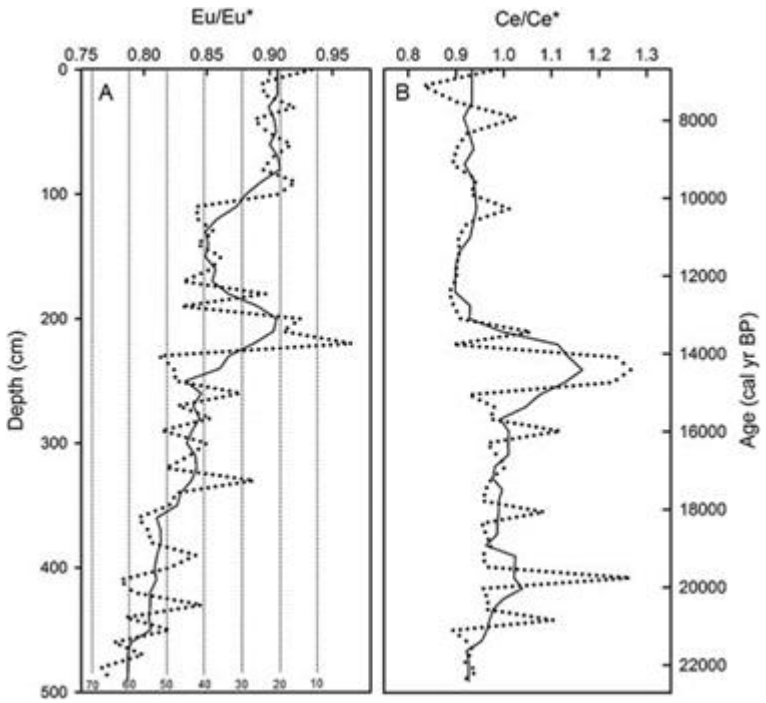

Fig. 3. Vertical variations of Eu anomaly (Eu/Eu*) and Ce anomaly (Ce/Ce*) of core BH-4B, Jeju Island. Vertical dotted lines with numbers at the bottom in (A) represent the proportion of the Asian dust calculated by using an Eu anomaly

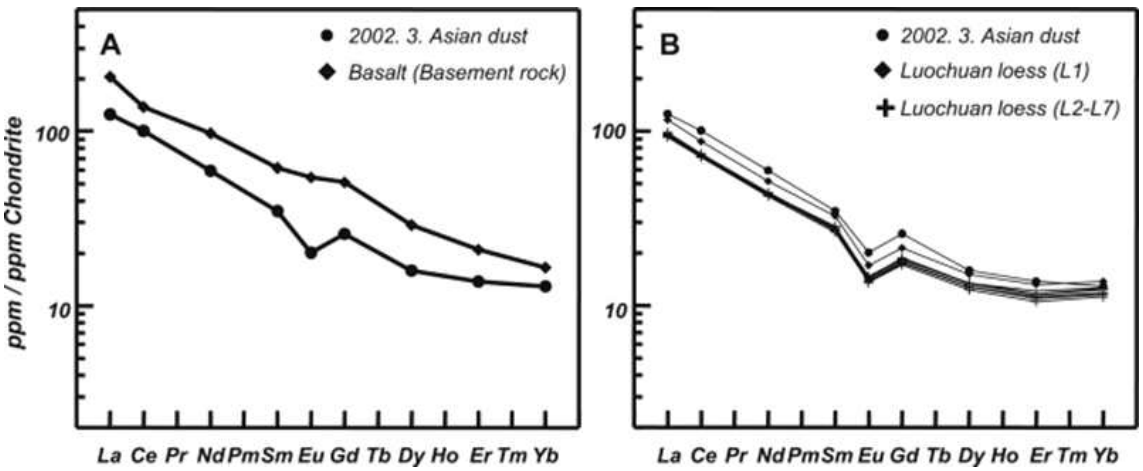

Fig. 4. (A) The chondrite-normalized REE patterns of trachybasalt surrounding the paleo-maar and the Asian dust samples collected in Seoul, Korea on March 21, 2002. (B) The chondrite-normalized REE patterns of Luochuan loess in China back to 800 ka (Gallet et al., 1996). The chondrite-normalized REE pattern of

the Asian dust sample is very similar to those of Luochuan loess.

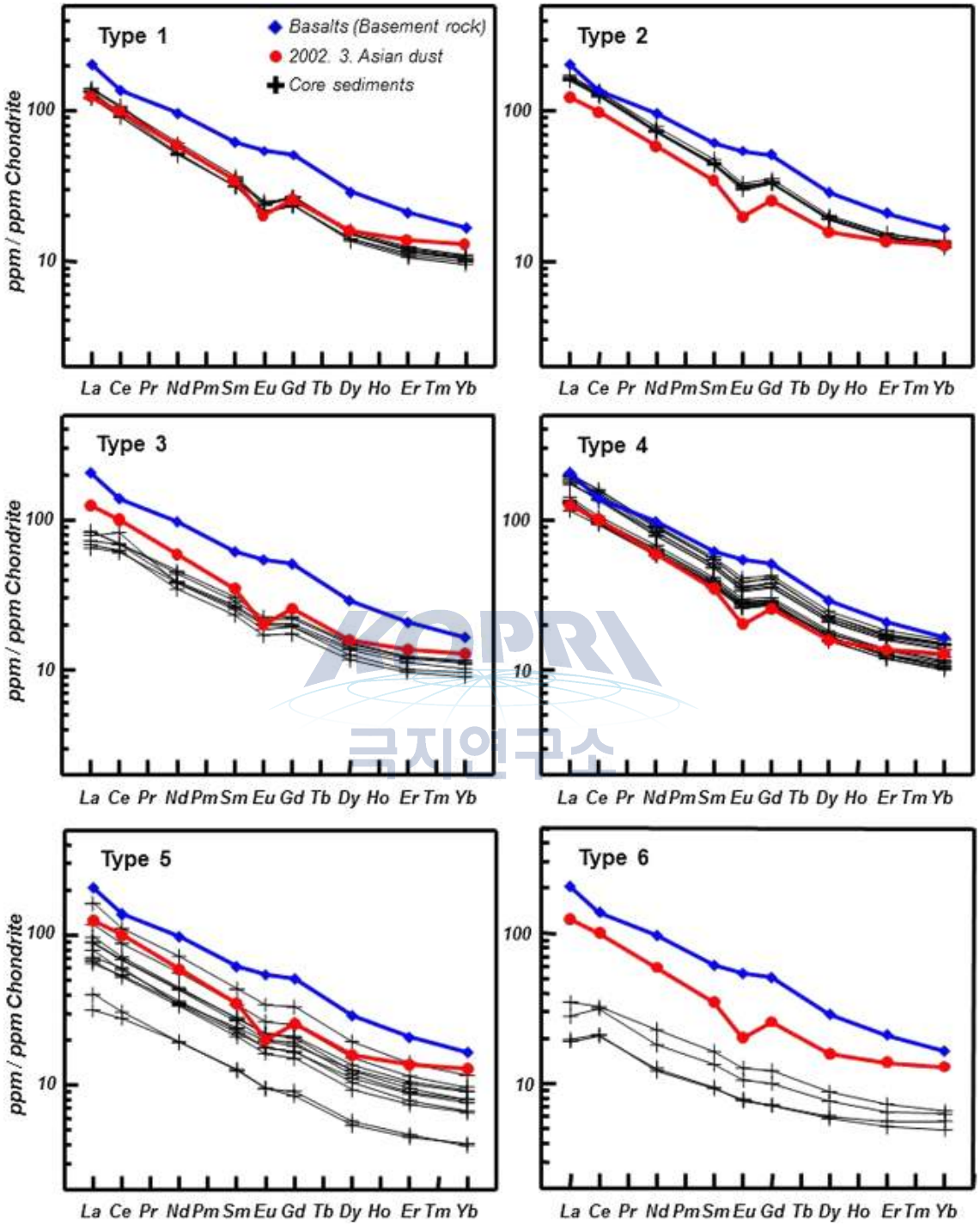

Fig. 5. The six REE patterns of core BH-4B sediments base on the chondrite-normalized REE patterns and Eu anomaly.

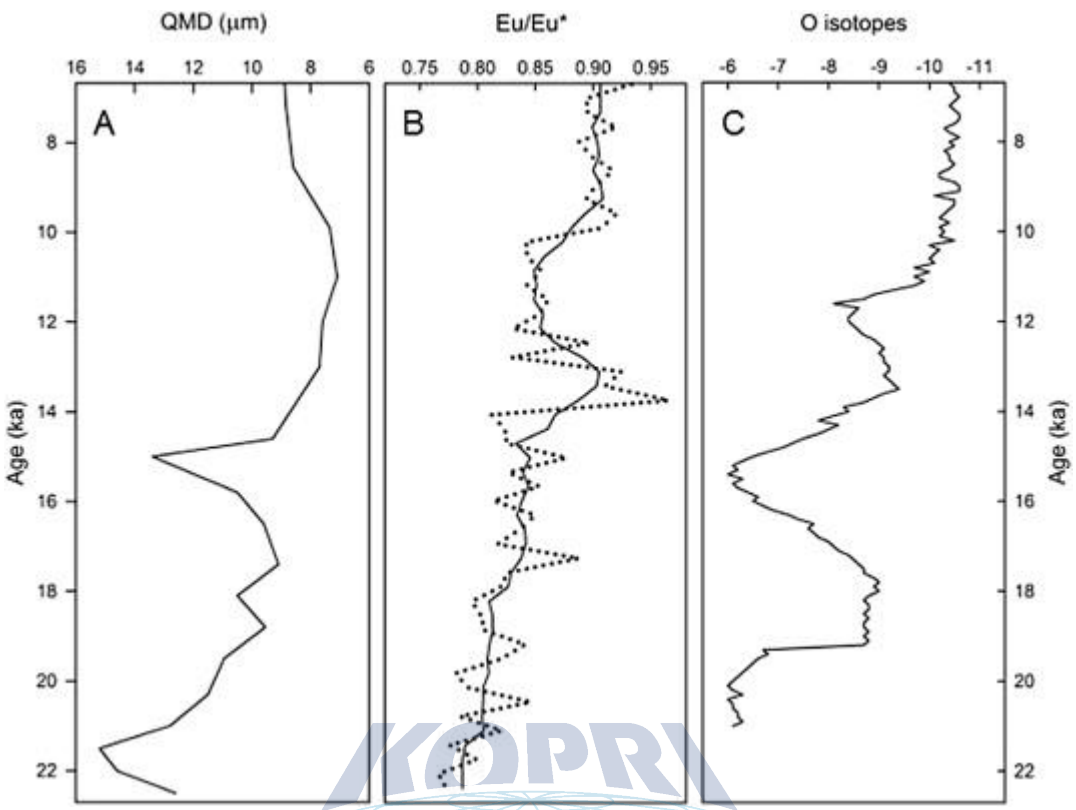

Fig. 6. Comparison of (B) Eu/Eu* of core BH-4B sediments with (A) quartz median diameter of the Chinese Loess Plateau (a winter monsoon record)(Xiao et al., 1995) and (C) oxygen-isotope records of stalagmites from Sanbao cave in China (a summer monsoon record) (Wang et al., 2008).

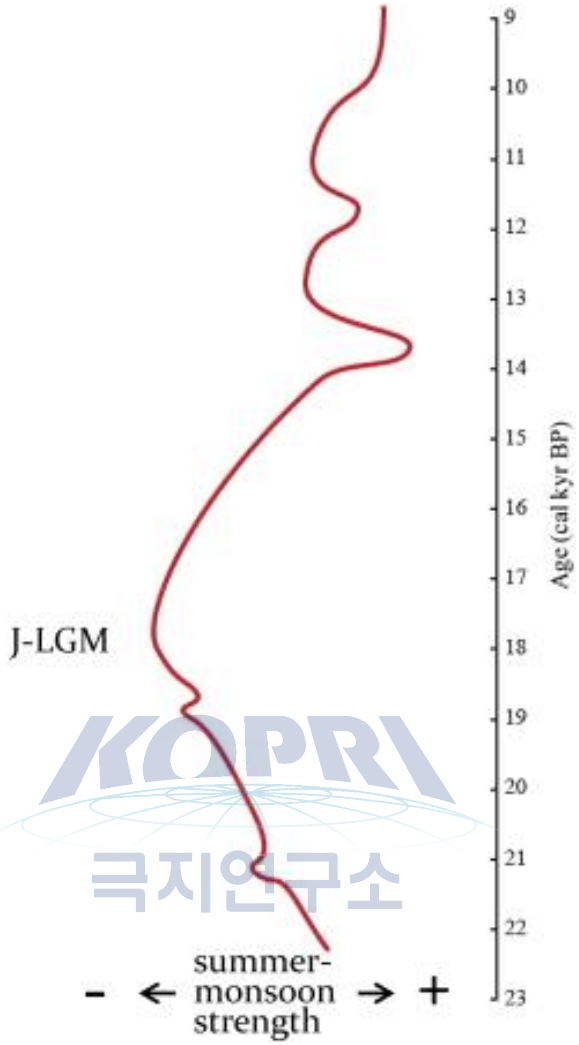

Fig. 7. The schematic presentation of variations of the summer monsoon strength recorded in Jeju Island on the basis of integration of REE, MS, and TOC data.

제 23 장

A hydroclimate-proxy model based on sedimentary facies in an annually laminated sequence from Lake Ohau, South Island, New Zealand[16)]

Heung Soo Moon, Ho Il Yoon

Korea Polar Research Institute

Abstract: Annually laminated sediments collected from Lake Ohau, New Zealand offer an opportunity to generate a high-resolution paleoclimate record for the Southern Hemisphere mid-latitudes. Correlation between regional precipitation and synoptic climate indices like the Southern Annular Mode, paired with a correlation between Ohau catchment precipitation, lake inflow and suspended sediment yield suggest that the Lake Ohau varves are a potentially powerful tool for estimating the amplitude, timing and interdepen-dence of different climate modes operating in the Southern Hemisphere mid-latitudes over time. A robust chronology and sound climate-proxy model are fundamental requirements for all high-resolution paleoenvironmental records. Here we present a chronology derived from layer counts, and 137Cs and 210Pb ages for the top 60 cm of sediments from the distal basin of Lake Ohau that confirm the varved natured of the sedimentary sequence. Sedimentary facies of different varve motifs are used to develop a hydroclimate-proxy model which links stratigraphy to seasonal hydrology. To establish this relationship we use a model accuracy statistic, which shows a quantitative difference between the annual hydro-graphs associated with each of three primary varve motifs. Distribution of above average inflow events points to summer and autumn hydrologic regimes as the

16) 이 연구 결과는 다음의 논문으로 출판되었음: Heidi A. Roop, Richard Levy, Gavin B. Dunbar, Marcus J. Vandergoes, Jamie Howarth, Sean Fitzsimons, Heung Soo Moon, Christian Zammi,. Robert Ditchburn, Troy Baisde,. Ho Il Yoon. Received: 28 January 2015 / Accepted: 12 August 2015

primary control on the deposition of different motifs. This relationship between varve characteristics and hydrology will serve as a tool to reconstruct lake inflow, and by extension precipitation, on an annual basis throughout the late-Holocene for the South Island of New Zealand.

1. Introduction

High-resolution paleoclimate records that capture environmental change on sub-decadal timescales play an important role in bridging the gap between short instrumental records and longer, lower resolution paleoclimate sequences (Zolitschka and Pike 2014). Only a few types of records capture environmental change at such high resolution. These include tree rings, ice cores, varved sediments, corals and speleothems (Bradley 1999; Zolitschka and Pike 2014). A number of these records are documented across the Northern Hemisphere (Mann et al. 2008; Ojala et al. 2012), but there remains a need to develop high-resolution paleoclimate reconstructions from the Southern Hemisphere (Neukom and Gergis 2012). New Zealand is one of only few landmasses that lie in the core of the climatically important Southern Hemisphere westerly wind belt but few high-resolution terrestrial paleoclimate records have been recovered from the North and South Islands (Page et al. 1994, 2010; Cook et al. 2002, 2006; Lorrey et al. 2008; Orpin et al. 2010; Augustinus et al. 2011; Fowler et al. 2012; Striewski et al. 2013). Sediment cores collected from distal end of Lake Ohau, South Island, New Zealand (Fig. 1) contain clastic varves, providing an opportunity to produce a high-resolution paleoclimate record from this important mid-latitude region (Roop et al. 2015).

Process-network studies of the climatic, physical and biological processes in contemporary lacustrine systems that are targeted for paleoclimate record development provide an important means by which the relationship between climate and core stratigraphy can be examined in detail and aid in the interpretation and calibration of varved sediment sequences (Hodder et al. 2007; Ojala et al. 2012; Stockhecke et al. 2012; Lamoureux and Francus 2014; Zolitschka and Pike 2014). The Lake Ohau process-network study (ongoing) demonstrates that seasonal thermal stratification of the water column plays an

important role in regulating the transfer of relatively coarser or finer grains from the river mouth to the distal (outflow) end of the lake (Fig. 1;Roopetal.2015). Sediment accumulation in winter at the outflow is limited to very fine silt particles (3 - 5 lm) as cold, turbid underflows originating at the delta do not transport coarser silts and sands upslope beyond the depocentre. Increased discharge and sedi-ment flux, paired with pronounced thermal stratifi cation in summer, enables transport of fine silt particles (8 - 13 lm) to the core site along pycnoclines in the upper portions of the water column (Roop et al. 2015). These observations provide a clear mechanism for the deposition of annual laminations, or varves, in the contemporary system (Roop et al. 2015).

This study builds on this physical process study to describe and explain seasonal controls on sedimenta-tion in Lake Ohau beyond the process-network monitoring period (2011 - 2013) discussed in Roop et al. (2015) and aims to: a) confirm that sediment laminations preserve a seasonal signal over the instrumental record (1900 - 2011), and; b) investigate the hydroclimatic and sedimentological variability over the instrumental record in order to establish a sound climate-proxy relationship. This work will serve as the primary tool for interpreting paleoclimate variability in an approximately 17,000-year record (*70 m) expected to be collected from Lake Ohau in mid-2016.

2. Study site

Lake Ohau (44.234ㄴS, 169.854ㄴE; 520 m asl) is a temperate lake (mean winter air temperature 6.2 ㄴC) located in the intermontane Mackenzie Basin, South Island, New Zealand (Fig. 1). This glacially formed lake is 54 km2 and reaches a maximum depth of 129 m. The 924-km2 Ohau catchment ranges from 520 to 2640 m asl and is drained primarily by the Hopkins and Dobson Rivers (Fig. 1). The catchment geology is characterized by highly indurated quartzofeldspathic greywacke sandstone and argillite mudstone (Cox and Barrel 2007). The Hopkins and Dobson valleys have relatively small glaciers at their head, which over the instrumental period occupy approximately 1.7 % of the total catchment area (Fig. 1; Anderton 1973). This small volume of glacial ice is considered to have remained stable over the last several thousand years based

on recent glaciological investigations in the valley (Doughty et al. 2013; Putnam et al. 2013) and is assumed to play a minor role in sediment generation and flux in the contemporary lacustrine environment (Roop et al. 2015).

The Hopkins and Dobson Rivers account for 85 %of the total fluvial input into Lake Ohau, with smaller tributaries contributing the remaining 15 % (Fig. 1; Woods et al. 2006). Precipitation and river inflow is highest during austral summer (average inflow 105 m3 s-1) and lowest in winter (61 m3 s-1; Roop et al. 2015). Spring and early summer snowmelt contributes approximately 21 % of mean annual inflow (Kerr 2013). Total monthly headwater precip-itation and lake inflow are correlated (1994 - 2013; r = 0.74, p =\ 0.0001). There is a strong precipita-tion gradient over the 37 km long catchment, with headwaters receiving 76 % more precipitation than at the lake (Roop et al. 2015). This gradient is the result of westerly wind driven orographic precipitation on the western side of the Southern Alps 'spilling over' the main divide into the upper part of the Ohau catchment (Chater and Sturman 1998; Salinger and Mullan 1999). Lake Ohau is seasonally stratified and experiences frequent overturning during the austral summer (October - March; Roop et al. 2015).

3. Materials and methods

Three short gravity cores (0.3 m) and three longer Mackereth cores (5.5 m; Mackereth 1958) were recovered near the outflow of Lake Ohau at *68 m water depth between July 2009 and May 2013 (Fig. 1). Gravity cores were used to recover the sediment - water interface. The cores discussed in this paper include Mackereth cores OH1m1 (1 m; collected July 2009), OH6m1c (5.5 m; collected October 2012), OH6m1 (5.5 m; collected July 2009), and gravity core GCS_1 (0.23 m; collected May 2013).

3.1. Physical properties

Density, compressional (p)-wave velocity, magnetic susceptibility (whole core), and line scan RGB data (split core) were collected from cores OH6m1c, OH1m1, and OH6m1 using a Geotek multi-sensor core logger at the University

of Otago. GCS_1 was split and photographed using a Lumix 10.1 Megapixel DMC LX5 camera. Thin-sections from core OH6m1 were made following Lamoureux (1994) and scanned at 2400 dpi on a flatbed scanner. X-radiographs (X-rays) were acquired from 30 cm 9 0.5 cm 9 0.5 cm u-channel samples taken from OH6m1c (Fig. 2a). Each u-channel sub-sample was offset with an overlap of 1.5 cm. X-ray data were collected at twenty-micron resolution using an ITRAXTM core scanner housed at the Korea Polar Research Institute (KOPRI). X-rays were generated using a 3 kw Mo tube running at 40 kV and 35 mA with scanning time of 500 ms. Greyscale data were extracted from 16-bit X-ray positive (where lower density is represented by a lighter tone) TIFF images generated by the ITRAXTM using ImageJ (Schneider et al. 2012). Images were adjusted for brightness and contrast to fit within a range of intensity between 33,000 and 36,500.

Particle size was measured on selected high and low-density laminae from GSC_1 to verify that density variation is primarily due to changes in particle-size-influenced porosity (ESM1). Discrete samples were pretreated with 27 % H2O2 to remove the organic component (3.2 %; Roop et al. 2015), dispersed with sodium hexametaphosphate (Calgon), continuously stirred and sonicated for 30 min, and passed through a Beckman Coulter LS 13 320 laser diffraction particle size analyzer equipped with a Micro Liquid Module (MLM). The MLM is capable of measuring small (~ 0.03 g) samples, ensuring mate-rial from lamina <2 mm thick could be obtained. Particle size data statistics were generated using Gradistat software (Blott and Pye 2001).

3.2. Chronology

One-centimeter sections extracted at various depths from core OH1m1 were analyzed for both 137Cs and 210Pb activity (ESM2). 137Cs was measured directly by gamma spectrometry using a high-resolution low background germanium (well-crystal) detector and total 210Pb was determined from its granddaughter 210Pb measured by alpha spectrometry. Unsupported 210Pb was calculated from the total by subtracting supported 210Pb, estimated by measuring 226Ra using gamma spectrometry. All analyses were conducted at

GNS Science, New Zealand. The CRSmodel program, which assumes a Constant Rate of Supply (CRS), was used to determine the 210Pb age-depth relationship (https://code.google.com/p/crsmodel/, accessed Nov 19, 2014; Fig. 2). Correlation between OH1m1 and OH6m1c was conducted visually in Corelyzer (http://andrill.org/*jareed/corewall.org/www/) and indi-cated an average *1 cm offset between the cores for the top 60 cm (ESM2). The offset is a result of the difference in the year of core collection and distur-bance of the surface from coring. For example, gravity core GCS_1 and OH6m1c (recovered with a Mack-ereth system) were both collected in 2012. Correlation between these two cores shows that two full lamina-tions were lost in the Mackereth core, which means that the surface of OH6m1c represents varve year 2010.

3.3. Layer counting

Based on our studies of modern sedimentation processes, the coarse - fine couplets are interpreted as annual layers and were counted accordingly. Three layer counts were generated by two independent operators (HR, RL) from a combination of X-ray images, line-scan images, and thin sections for the top 60 cm of OH6m1c and OH6m1 (Fig. 2a). Each operator assigned a 'varve year' (VY) to each couplet based the occurrence of a sharp density change and a visual change in particle size in thin section. HR conducted two separate counts. An objective method was used to generate layer counts which places the end of a nominal year wherever a positive gradient equivalent to *20 % of the total amplitude occurred within a 0.5-mm interval (Wheatley et al. 2012). We also assumed that annual sediment accumulation must be [2 mm based on prior monitoring (Roop et al. 2015), so concurrent greyscale peaks that were\2 mm apart were not counted as separate years but classified as sublaminae. The resulting layer counts are shown in Fig. 2. Sedimentation rate and layer thick-ness versus year are derived from these age-depth relationships. Because the major coarse layer in the sedimentary couplet is the easiest feature to identify in the greyscale record and is caused by an influx of sediment in spring, a varve year is defined as September 1st - August 31st (which differs slightly from Roop et al. 2015 who defined a VY as October 1st - September

31st). This modification enables an investigation of variability in spring inflow conditions.

3.4. Hydrometeorological data

Three hydrometeorological datasets were used in this study including: (1) a record of daily mean inflow calculated from lake level and measured outfl ow that extends from 1926 to present (Meridian Energy Ltd., unpublished data); (2) a continuous time-series of precipitation and temperature (1926-present) mea-sured at Lake Tekapo Air Safaris, 40 km north of Lake Ohau and outside of the Ohau surface water catchment (44.00˚S, 170.43˚ E; 762 m asl; Station ID 4970); and (3) modeled precipitation, air temperature and inflow data extracted for seven different locations in the Lake Ohau catchment from the National Institute of Water and Atmosphere (NIWA) Topnet model (Clark et al. 2008; Fig. 1). Topnet is based on a 30-m Digital Elevation Model (DEM) and simulates hydro-logical processes based on total precipitation and temperature provided as a 0.05˚ latitudinal/longitudi-nal grid based on an interpolation of data from a national network of automated weather stations (Tait et al. 2006). The hydrological model was calibrated against hourly total lake inflows over the period 1980 - 1990 (Nash - Sutcliffe = 0.779) and validated over the period 1980 - 2008 (Nash - Sutcliffe = 0.777). Seven samples sites were selected to provide upstream catchment average precipitation and temperature and total inflow, including: Upper Hopkins (UH), Upper Dobson (UD), Lower Hopkins (LH), Lower Dobson (LD), near the Ohau inflow (OI), at the base of Freehold Creek (FC) and in the Greta Stream catchment (GS; Fig. 1).

Comparisons between varve thickness (VT) and hydrometeorological data were run for seven different temporal increments including: full 12 months, spring (September, October, November, referred to as SON), summer (December, January, February, referred to as DJF), autumn (March, April, May, referred to as MAM), winter (June, July, August, referred to as JJA), spring & summer (SONDJF), and autumn & winter (MAMJJA). Averages and totals of the three hydrom-eteorological datasets over these temporal increments were tested against the full VT time-series and all varve motifs and sub-types for five

different varve features including: (1) total thickness; (2) coarse unit thickness; (3) fine unit thickness; (4) fine unit thick-ness minus sublaminae; (5) sublaminae thickness. Lag correlations between VT characteristics and hydrom-eteorological parameters were also tested for the preceding one and 2 years. All statistical relationships between each measured varve feature and hydrome-teorological variables were tested using Spearman's rank correlation (non-parametric) as all datasets were (split core) were collected from cores OH6m1c, OH1m1, and OH6m1 using a Geotek multi-sensor core logger at the University of Otago. GCS_1 was split and photographed using a Lumix 10.1 Megapixel DMC LX5 camera. Thin-sections from core OH6m1 were made following Lamoureux (1994) and scanned at 2400 dpi on a flatbed scanner. X-radiographs (X-rays) were acquired from 30 cm 9 0.5 cm 9 0.5 cm u-channel samples taken from OH6m1c (Fig. 2a). Each u-channel sub-sample was offset with an overlap of 1.5 cm. X-ray data were collected at twenty-micron resolution using an ITRAXTM core scanner housed at the Korea Polar Research Institute (KOPRI). X-rays were generated using a 3 kw Mo tube running at 40 kV and 35 mA with scanning time of 500 ms. Greyscale data were extracted from 16-bit X-ray positive (where lower density is represented by a lighter tone) TIFF images generated by the ITRAXTM using ImageJ (Schneider et al. 2012). Images were adjusted for brightness and contrast to fit within a range of intensity between 33,000 and 36,500.

Particle size was measured on selected high and low-density laminae from GSC_1 to verify that density variation is primarily due to changes in particle-size-influenced porosity (ESM1). Discrete samples were pretreated with 27 % H2O2 to remove the organic component (3.2 %; Roop et al. 2015), dispersed with sodium hexametaphosphate (Calgon), continuously stirred and sonicated for 30 min, and passed through a Beckman Coulter LS 13 320 laser diffraction particle size analyzer equipped with a Micro Liquid Module (MLM). The MLM is capable of measuring small (~0.03 g) samples, ensuring mate-rial from lamina <2 mm thick could be obtained. Particle size data statistics were generated using Gradistat software (Blott and Pye 2001).

4. Results

4.1. X-ray density and particle size

Sedimentation patterns in Ohau are dominated by a signal comprised of a coarse and fine couplet, repre-sented in greyscale by high (~35,000 - 36,500) and low intensity values (~33,000 - 35,000), respectively (Fig. 3). This dominant pattern is often overprinted by the occurrence of additional coarse sublaminae (greyscale intensities of ~34,000 - 36,000), as observed by Roop et al. (2015). The less dense layers (light grey and white tones in X-rays) are consistently associated with coarser particles (modal size >8.0 lm), while the densest layers (dark tones in X-rays) are associated with finer particles (modal size 3.7 um; ESM1). Particle size variability between the light and dark layers in X-ray is similar to the annual range measured in surface cores and sediment traps by Roop et al. (2015).

4.2. Varve classification

Three primary varve motifs (labeled A, B and C) were identified based on variations in complexity (e.g. presence/absence and number/position of sub-lami-nae) and total thickness (Table 1; Fig. 3). Motif A consists of a fine silt basal layer that grades into a very fine silt layer. These 'simple' varves are divided into sub-types A1 and A2, which are separated based on the relative thickness of the coarse (fine silt) and fine units (very fine silt; Table 1; Fig. 3). Motif A accounts for 34 % of the total lamination stratigraphy in the top 60 cm of OH6m1c. Motif B is characterized by the presence of one or more grain-supported 0.5 - 1.5 mm-thick sublaminae within the primary coarse/fine stratigraphy. These 'complex' varves account for 56 % of the total lamination stratigraphy in the top 60 cm of OH6m1c. Motif B is sub-divided into four types (B1, B2, B3, B4) to account for the variations in the number and position of sublaminae within the annual couplet (Table 1; Fig. 3). Motif C includes layers that are ≥9.0 mm thick and comprise a basal fine silt layer that grades into a relatively thick (~3.5 mm) homogeneous very fine silt layer (Table 1; Fig.

3). Thin sub-laminae (≤1.0 mm) com-monly occur immediately above the basal unit. Motif C accounts for 10 % of the varve stratigraphy in the top 60 cm of OH6m1c. Total VT ranges from 3.4 - 3.5 mm in Motif A, 4.5 - 7.1 mm in Motif B, and 9.0 - 12.9 mm Motif C (Table 1; Fig. 3).

4.3. Core chronology

Cesium-137 and lead-210 radiometric dating tech-niques and layer counts provide both a robust age-depth model for the instrumental record and a method to test whether the lamination stratigraphy preserves an annual signal. Southern Hemisphere onset and peak137Cs fallout, a by-product of nuclear weapons testing, occurs in 1954 and 1964, respectively (UNSCEAR 2000). These tie-points offer important age-control for the top portion of the sediment record. Peak 137Cs (1964) occurs between 24.0 and 25.0 cm and onset (1954) occurs between 31.0 and 32.0 cm in OH6m1c (ESM2).

Chronology determined by layer counts (manual and automatic) is consistent with the depth intervals associated with the 137Cs profile (Fig. 2a). Specifi-cally, layer counts place varve year (VY) 1964 between 23.7 and 24.8 cm and VY 1954 between 28.8 and 30.5 cm. Similar sediment accumulation rates (SAR) are calculated using Cs and Pb activity profiles and layer counts (Fig. 2a). The 137Cs derived SAR is 5.1 ± 0.3 mm year-1, the 210Pb SAR is 6.0 ± 1.1 mm year-1 and the layer count derived SAR is 5.2 ± 0.5 mm year-1. The instrumental record commenced in 1926 and the Pb-derived and layer counts age-depth relationships are in close agreement; 210Pb places 1926 (±6.1 years) at 44.0 - 45.0 cm while an average layer count places 1926 (±2 years) at 44.5 - 45.0 cm.

A1r of the ages assigned to a given depth is used as a means to quantify offset between the four different layer counts (three manual and one automated; Fig. 2b). A maximum deviation of 15.2 mm or±3 years occurs at VY 1900. The largest deviation between counts generally occurs in sections of the core that are characterized by motif C and the total error then propagates with depth (Fig. 2b). Maximum agreement and consistency between layer counts occurs in sections that are characterized by motif A. Given the similarity and

small error between the layer count- and radiometric-derived age-depth relation-ships, hydroclimatic relationships over the instrumen-tal record were tested against an average of the manual and automated layer counts.

4.4. Hydroclimate-varve relationships

Regression statistics were calculated to compare the thicknesses of the fi ve possible components of each varve (e.g. total thickness, coarse unit thickness, fine unit thickness, fine unit thickness without sublaminae, sublaminae thickness) with average modeled air temperature, areal total and average modeled and measured precipitation, and total and average inflow for the seven different temporal/monthly breakdowns of the annual cycle. These tests carried out using the instrumental record (1926 – 2010) yield few statisti-cally significant results (ESM3). One of the strongest correlations over the instrumental period is a basin-wide negative correlation between total SON precip-itation and coarse unit thickness. This correlation is weakly significant for six of the seven sites for which modeled precipitation was extracted; the strength of the correlation only ranges from $r = -0.29$, $p = 0.08$ at Freehold Creek (FC) to the strongest correlation of $r = -0.36$, $p = 0.03$ at Greta Stream (GS). The correlation is not significant for the Upper Hopkins site. The same regression statistics were tested on the different three major varve motifs and seven types, which yielded similar non-robust and weakly statisti-cally significant results (ESM3).

In order to explore the relationship between varve motif/type and hydroclimate, each annual layer was correlated with its corresponding hydrograph (derived from the Lake Ohau inflow time-series (1926 – 2010) provided by Meridian Energy Ltd.) To mitigate the impact of potential mismatches between varve type and hydrology arising from errors in our annual layer chronology, we compared hydrographs for a subset of years of close chronologic sequence (1 – 5 sequential years) defined by each motif and varve type (Table 2). The annual inflow time-series for the subsets of years corresponding to motifs A, B, C and varve types A1, A2, B1, B2, B3, B4, C respectively, were grouped and averaged to produce a characteristic hydrograph for each motif and type (Fig. 4). These characteristic hydrographs were then

compared using the Nash–Sutcliffe model accuracy statistic and Spearman's rank correlation (Tables 2 and 3; Nash and Sutcliffe 1970).

Comparisons between each characteristic (mean) hydrograph for the subsets of years were made using a complete data series and both a 30- and 15-point running mean (Fig. 4). Results from analysis of the 15-pt smoothed data series for the subset of chrono-logically sequential varves (n = 5 or 6) show poor fit between the hydrographs that characterize motif A and C and close agreement between those that characterize motifs B and C (Table 2). Hydrographs for subtypes A1 and A2 are in close agreement with B1 and B2 (Table 2). To increase the statistical power of the correlations, hydrographs for the sum of all of the years represented by each of the three major motifs were also compared (minimum n = 11 for motif C). The strong positive correlation between the subset of annual hydrographs (15-pt smooth) for all motifs weakens significantly when weekly data are consid-ered (Table 3).

To explore seasonal biases in inflow, characteristic hydrographs for the major motifs and types were divided into four temporal increments including: spring (SON), summer (DJF), autumn (MAM), and winter (JJA) and compared using a Spearman's rank correlation and outlier plots (Table 4; Fig. 5). The hydrographs for each motif during SON show close correlation while the relationship between the sea-sonal hydrologic regimes and varve motifs weakens for the rest of the annual cycle (Table 4). Outlier plots show similar patterns for all of the varve types, but with the range of hydrologic variability the lowest during JJA. The number of hydrologic outliers increases most notably in summer and autumn (Fig. 5). Outliers in seasonal discharge are mostly associated with motif B varve types, while type A varves show the smallest range of variability across the annual cycle, and the fewest number of anomalous peaks in inflow (Fig. 5).

5. Discussion

Meaningful paleoclimate reconstructions from annually laminated sediments require a detailed understanding of the relationship between sedimentation and climate (Hodder et al. 2007). In the Lake Ohau region, there

is significant correlation between totally monthly head-water precipitation and lake inflow (r = 0.74 p =\ 0.0001), as well as inflow and fluvial sediment yield for South Island greywacke catchments (r =0.71; Hicks et al. 2011; shown here as r, a correlation coefficient). This regional relationship suggests there should be a link between rainfall and sediment accu-mulation in Lake Ohau. The original hypothesis was that this link would be reflected in VT based on previous paleoclimatic reconstructions in many clastic varve settings (Desloges and Gilbert 1994; Tomkins and Lamoureux 2005; Kaufman et al. 2011). However, results indicate that such a relationship does not exist at Lake Ohau. This is not entirely surprising as direct relationships between VT and hydroclimatic variables can be difficult to establish (Hodder et al. 2007). Geologic processes such as earthquakes and slope failure can, in geologic time, instantly alter the sediment availability of a basin (Dadson et al. 2004; Howarth et al. 2012). The climate system itself operates on various temporal and spatial scales and can be complicated in mountainous terrain by microclimates, which are poorly resolved in modeled data and generally underrepre-sented in meteorological time-series (Hannah et al. 2000). In addition to the aforementioned complexities, internal lake dynamics can further attenuate dispersal and accumulation patterns of sediments (Pharo and Carmack 1979; Desloges and Gilbert 1994; Hodder et al. 2007). Regardless of these complexities, our results suggest that varve stratigraphy, instead of varve thickness, is a good indicator of hydroclimatic variabil-ity in Lake Ohau. In the following discussion we explore the probable causes of stratigraphic variability and show that varve stratigraphy can be used to establish a hydroclimate-proxy model.

5.1. Varve thickness and hydroclimatic variability

A strong correlation between suspended sediment yield and inflow has been shown for nearby catchments (Hicks et al. 2011) and a similar relationship is assumed to be true for Lake Ohau. However, the predominance of negative correlations between total precipitation, inflow and varve thickness at Lake Ohau (ESM3) suggests that sediment accumulation and inflow are decoupled due to seasonal lake hydrodynamics. Specif-ically, inflow events in spring occur when

the lake is isothermal, which influences sediment transport path-ways and affects the relationship between inflow (discharge) and suspended sediment flux (Roop et al. 2015). Furthermore, errors in sediment flux derived from suspended sediment concentration (SSC) rating curves can be in excess of 50 % and tend to produce low estimates during high SSC conditions and vice versa (Walling and Webb 1988;Horowitz 2003). This demonstrates that relationships between infl ow and SSC, and subsequent sediment transport and deposition, are complicated and cannot be assumed to be linear or constant through time.

Eight high magnitude (≥880 m3 s-1) inflow events were measured between 1926 and 2011 and eleven ≥9.0 mm laminations (motif C layers) were identified in the cores during the same period. Further, only fifty percent of layers characterized as motif C coincide temporally (±2 years) with measured high magnitude inflowpeaks.Thismismatchsuggests thatsomelarge sedimentation events are potentially related to non-climatic events including subaqueous mass wasting. These observations are not surprising, as other studies have shown that peaks in SSC do not always correlate with peak inflow (Sawada and Johnson 2000; Orwin and Smart 2004). In addition, unusually dry conditions and associated high soil infiltration capacity can attenuate the sediment transport response following extreme precipitation events and affect expected SSC (Favaro and Lamoureux 2014). One or more of the processes outlined above could explain the observed mismatch between thick event layers and precipitation-driven extreme event inflow and the anti-correlation between precipitation, inflow and varve thickness.

5.2. Lamination stratigraphy

Sedimentary couplets with no sublaminae (motif A) represent varves that form in years with limited high magnitude summer/autumn inflow events (Figs. 4, 5). A1 varves form during years that are characterized by an annual hydrograph with a late-spring onset of high inflow that peaks in December/January and exhibits limited spring freshet input (Figs. 4, 5). This late season flux may account for the proportionally thicker coarse unit in A1 as peak flow occurs when the lake is fully stratified, which may provide a more

direct conduit for coarser sediment delivery to the distal basin. A2 varves form during years characterized by a hydrograph exhibiting higher peak inflow in spring when lake stratification is developing, which may cause flow separation that delivers less sediment to the distal basin and produces the proportionally thinner basal coarse unit (Fig. 4). This interpretation may also explain the basin-wide negative correlation between coarse unit thickness and total SON precipitation. High spring rain may prolong isothermal conditions in the lake through the continued input of relatively colder precipitation and snowmelt. More persistent isothermal conditions could potentially limit the transport of coarse particles at the core site and produce thinner coarse basal units. Overall, the lack of complexity in motif A is likely associated with the smaller number of peak inflow events in summer and autumn (Fig. 5).

Sedimentary couplets that contain sublaminae characterize motif B. Sediment grain size in the basal layer of each sublamination is similar to the primary spring/summer coarse unit, which suggests that these units are deposited during inflow events of similar magnitude that occur between October and May when the lake is fully stratified (Roop et al. 2015; Fig. 4). However, we suggest that the thinner units reflect lower total suspended sediment flux due to lower total inflow volume or duration. Sublaminae in motif B are similar to those documented in other records with complex lamination stratigraphy (Desloges and Gil-bert 1994; Chutko and Lamoureux 2008; Cockburn and Lamoureux 2008) and reflect short-lived summer and autumn rain events. This interpretation is consis-tent with Roop et al. (2015), who observed discrete sublaminae deposited during summer inflow events and captured in sediment traps at the Outflow site. Further, each sub-type of motif B includes several outliers in discharge during the stratified period in the summer and autumn (Fig. 5), which are likely respon-sible for producing the sublaminae characterizing motifs B and C. Type A2 is an exception, as it lacks sublaminae but has a summer hydrologic regime that includes numerous outliers in summer discharge; these peaks in inflow may be responsible for the propor-tionally thicker fine unit in A2 (compared to A1) and the lack of sublaminae potentially associated with internal lake dynamics.

Motif B is subdivided into four sub-types based on the position and

thickness of sublaminae. The strati-graphic position of the sublaminae may, in general, reflect the position of summer and autumn inflow events within the annual hydrograph (Fig. 4). For example, sub-type B2 includes sublaminae that occur within the lower portion of the primary fine unit and has a characteristic hydrograph that is dominated by high magnitude spring and summer peaks in in flow (Figs. 4, 5). In contrast, sub-type B1 includes sublam-inae that occur within the upper portion of the primary fine unit and is characterized by a hydrograph with a greater concentration of peak inflow events in the autumn (Figs. 4, 5).

Motif C is comprised of a thick fine (dense) unit that includes sublaminae thicker than those observed in motif B. This stratigraphy suggests that these varves form in years that include extreme inflow events. These extreme event flows generally range between 880 and 1300 m3 s-1 and can deposit sediment at nearly double the average annual sedimentation rate (Roop et al. 2015).

One annual hydrograph with a large (1200 m3 s-1) peak inflow event correlates with motif sub-type B4 (Fig. 4) and highlights that misclassification can occur. However, general agreement between the Nash - Sut-cliffe correlation and regression statistics show that all three major motifs, and sub-types, are characterized by unique annual hydrologic regimes (Fig. 4; Table 3). High correlation between spring discharge and varve motif (and sub-types) suggests that the primary hydro-logic causes for the different varve types occurs in summer and autumn. During summer and autumn, characteristic hydrographs for motifs B and C contain significant outliers in discharge (Fig. 5), which produce complex laminae. Furthermore, general agreement between the concentration and stratigraphic position of sublaminae and the number and timing of anomalous summer-autumn inflow events (outliers) suggests that stratigraphic pattern and hydrodynamics are closely related. Monitoring data through winter (JJA) showed that isothermal conditions prohibit the transport and deposition of coarse material to the Outflow (Roop et al. 2015). Therefore, changes in varve stratigraphy are interpreted as variations in the number and intensity of peak inflow events during the summer and autumn seasons. Specifically, the three primary motifs are interpreted to represent the following: (1) limited summer and autumn

precipitation-driven inflow events and inferred drier conditions (motif A); (2) frequent summer inflow events and inferred wetter conditions (motif B); and (3) large magnitude summer inflow (flood) events ([880 m3 s-1; motif C).

5.3. Towards a hydroclimate-proxy model for the pre-instrumental era

A link between varve stratigraphy and hydrology provides a foundation for developing a hydroclimate-proxy model for the Lake Ohau outflow site. This model, however, is complicated by a lack of pro-nounced statistical relationship between varve thick-ness and hydrology, indicating that important mediating variables are at play in the system which accentuate and/or decouple sediment deposition from sediment flux and transport, and hydroclimatic vari-ables such as precipitation and inflow.

The ability to characterize the hydrologic signal by the general accumulation pattern of the different motifs provides a potentially powerful tool for inter-preting a longer sediment sequence. Recognizing sedimentation in Lake Ohau is influenced by a range of processes, the demonstrated link between annual hydrography and sedimentary motif can be used to reconstruct pre-historic hydrology. Specifically, sed-imentation patterns preserved in cores from the Outflow can be used to reconstruct the general shape of the annual hydrograph, with different sedimento-logical packages changing in response changes in summer and autumn hydrologic regimes. Given that each of the three major motifs are demonstrably different from one another, observed changes in sedimentary motif can be used to infer changes in seasonal event fl ow, and by extension storm events, experienced at Lake Ohau. Initial examination of the 5.5 m OH6m1c indicates that the range of facies described herein characterizes the majority of down-core sediment stratigraphy. Similar methods to those described here, including motif descriptions and layer-counting methods, will be employed to ensure we capture any pre-historic variations in the system that were not observed in this study of the instrumental era. Future work will also utilize reanalysis data and synoptic typing specific to New Zealand (Kidson 2000) to establish links to the climate system. The potential correlation between synoptic types and hydrology will allow for a more

comprehensive interpretation of the hydroclimatic signal preserved in the Lake Ohau sedimentary sequence.

6. Conclusions

We have assessed the utility of sedimentary facies of different varve motifs from Lake Ohau to develop a hydroclimate-proxy model which links stratigraphy to the shape of the annual hydrograph. Few robust correlations result from our comprehensive statistical tests of the relationship between varve thicknesses and measured and modeled hydroclimatic variables such as precipitation and inflow at Lake Ohau. Varve thickness is a poor climate proxy at this site, due to the complex interplay between sediment flux and internal lake sediment transport processes. Seasonal thermal stratification, as documented by Roop et al. (2015), has a major influence on sediment accumulation through-out Lake Ohau.

Despite the lack of clear relationships between varve thickness and hydroclimate, there is a quantita-tive relationship between sediment stratigraphy and summer and autumn inflow patterns. Three primary lamination types presented here represent years with:
(1) limited summer and autumn precipitation-driven inflow events (motif A); (2) frequent summer inflow events (B); and (3) large magnitude summer inflow (fl ood) events (>880 m3 s-1; C). These relationships provide a tool for characterizing hydrologic variability and storm event frequency for the longer pre-instru-mental period. The method used here to compare hydrology and sedimentary facies may be of use for investigating and developing climate-proxy models from other sites where it is difficult to quantitatively link varve thickness and hydroclimatic variability. Overall, this work provides a solid foundation for the development of the Lake Ohau paleoclimate record and is a step towards addressing the current paucity of high-resolution terrestrial paleoclimate reconstructions from the Southern Hemisphere mid-latitudes.

뉴질랜드 남섬 오하우 호수의 연간 층리 퇴적물 내의 퇴적상에 근거한 강수량 프록시 기후 모형

문홍수, 윤호일

한국해양과학기술원 부설 극지연구소

요약: 뉴질랜드의 오하우 호수에서 획득된 연간 층리 퇴적물은 남반구의 중위도 지역에서의 고해상도의 고기후 기록을 제공한다. Southern Annular Mode와 같은 지역적인 강수량과 개괄적인 기후 사이의 상관관계는 오하우 호수에서 발견된 퇴적층리가 남반구 중위도의 기후변화를 반영할 것이라는 것을 의미한다. 잘 설정된 연대와 좋은 기후-프록시 모델이 고해상도 고환경 기록 복원에 반드시 필요하다. 우리는 층리의 개수, ^{137}Cs과 ^{210}Pb 연대를 통해 상부 60 cm의 퇴적물을 확인하였다. 다른 층리띠 양상의 다른 퇴적상은 수로학적인 프록시 모델의 개발을 위해 사용되었다. 강수유입 사건의 분포를 통해 여름과 가을철의 수문학적인 영향이 다른 퇴적상의 층리를 쌓는 퇴적 조절 요인이라는 것을 확인하였다. 층리의 특성과 수문학의 상관관계는 호수로 강수의 유입을 복원하는 툴로 사용될 수 있으며, 뉴질랜드의 홀로세 후기의 연평균 규모의 강수량을 복원하는 툴이 될 수 있다.

참고문헌

Anderton P (1973) The significance of perennial snow and ice to the water resources of the South Island, New Zealand. J Hydrol 2:6 – 18

Augustinus P, D'costa D, Deng Y, Hagg J, Shane P (2011) A multi-proxy record of changing environments from ca. 30,000 to 9000 cal. a BP: onepoto maar palaeolake, Auckland, New Zealand. J Quat Sci 26:389 – 401

Blott SJ, Pye K (2001) GRADISTAT: a grain size distributionand statistics package for the analysis of unconsolidated sediments. Earth Surf Process Landf 26:1237 – 1248

Bradley RS (1999) Paleoclimatology: reconstructing climates of the Quaternary. Accessed Online via Elsevier 68: 1-613

Chater AM, Sturman AP (1998) Atmospheric conditions influencing the spillover of rainfall to lee of the Southern Alps, New Zealand. Int J Climatol 18:77 – 92

Chutko KJ, Lamoureux SF (2008) Identification of coherent links between interannual sedimentary structures and daily meteorological observations in Arctic proglacial lacustrine varves: potentials and limitations. Can J Earth Sci 45:1 – 13

Clark MP, Rupp DE, Woods RA, Zheng X, Ibbitt RP, Slater AG, Schmidt J, Uddstrom MJ (2008) Hydrological data assimilation with the ensemble Kalman filter: use of streamflow observations to update states in a distributed hydrological model. Adv Water Resour 31:1309 – 1324

Cockburn JM, Lamoureux SF (2008) Inflow and lake controls on short-term mass accumulation and sedimentary particle size in a High Arctic lake: implications for interpreting varved lacustrine sedimentary records. J Paleolimnol 40:923 – 942

Cook ER, Palmer JG, D'Arrigo RD (2002) Evidence for a 'Medieval Warm Period' in a 1100 year tree-ring reconstruction of past austral summer temperatures in New Zealand. Geophys Res Lett 29(14):12 – 21

Cook ER, Buckley BM, Palmer JG, Fenwick P, Peterson MJ, Boswijk G, Fowler A (2006) Millennia-long tree-ring records from Tasmania and New

Zealand: a basis for modelling climate variability and forcing, past, present and future. J Quat Sci 21(7):689 – 699

Cox S and Barrel D (2007) Geology of the Aoraki area. Institute of Geological and Nuclear Sciences 1:250000 Geological Map, Lower Hutt, New Zealand (GNS Science) vol 71, p 1

Dadson SJ, Hovius N, Chen H, Dade WB, Lin JC, Hsu ML, Lin CW, Horng MJ, Chen TC, Milliman J, Stark CP (2004) Earthquake-triggered increase in sediment delivery from an active mountain belt. Geology 32(8):733 – 736

Desloges JR, Gilbert R (1994) Sediment source and hydroclimatic inferences from glacial lake sediments: the postglacial sedimentary record of Lillooet Lake, British Columbia. J Hydrol 159:375 – 393

Doughty AM, Anderson BM, Mackintosh AN, Kaplan M, Vandergoes MJ, Barrell D, Denton GH, Schaefer JM, Chinn TJH, Putnam AE (2013) Evaluation of Lateglacial temperatures in the Southern Alps of New Zealand based on glacier modelling at Irishman Stream, Ben Ohau Range. Quat Sci Rev 74:160 – 169

Favaro EA, Lamoureux SF (2014) Antecedent controls on rainfall runoff response and sediment transport in a high arctic catchment. Geografiska Annaler Ser A Phys Geogr 96:433 – 446

Fowler AM, Boswijk G, Lorrey AM, Gergis J, Pirie M, McCloskey S, Palmer JG, Wunder J (2012) Multi-centennial tree-ring record of ENSO-related activity in New Zealand. Nat Clim Chang 2(3):172 – 176

Hannah DM, Gurnell AM, McGregor GR (2000) Spatio – temporal variation in microclimate, the surface energy balance and ablation over a cirque glacier. Int J Climatol 20(7):733 – 758

Hicks DM, Shankar U, McKerchar AI, Basher L, Lynn I, Page M, Jessen M (2011) Suspended sediment yields from New Zealand rivers. J Hydrol 50:81 – 142

Hodder KR, Gilbert R, Desloges JR (2007) Glaciolacustrine varved sediment as an alpine hydroclimatic proxy. J Paleolimnol 38(3):365 – 394

Horowitz AJ (2003) An evaluation of sediment rating curves for estimating suspended sediment concentrations for subsequent flux calculations.

Hydrol Process 17:3387 - 3409

Howarth JD, Fitzsimons SJ, Norris RJ, Jacobsen GE (2012) Lake sediments record cycles of sediment driven by large earthquakes on the Alpine Fault, New Zealand. Geology 40:1091 - 1094

Kaufman CA, Lamoureux SF, Kaufman DS (2011) Long-term river discharge and multidecadal climate variability inferred from varved sediments, southwest Alaska. Quat Res 76(1):1 - 9

Kerr T (2013) The contribution of snowmelt to the rivers of the South Island, New Zealand. J Hydrol 52(2):61 - 82

Kidson JW (2000) An analysis of New Zealand synoptic types and their use in defining weather regimes. Int J Climatol 20(3):299 - 316

Lamoureux SF (1994) Embedding unfrozen lake sediments for thin section preparation. J Paleolimnol 10:141 - 146

Lamoureux SF, Francus P (2014) Layers within layers: quantifying seasonal versus event processes in Arctic clastic varved sediments. Past Global Changes Mag 22(1):6 - 7

Lorrey AM, Williams P, Salinger J, Martin T, Palmer J, Fowler A, Zhao J, Neil H (2008) Speleothem stable isotope records interpreted within a multi-proxy framework and implications for New Zealand palaeoclimate reconstruction. Quat Int 187(1):52 - 75

Mackereth FJH (1958) A portable core sampler for lake deposits. Limnol Oceanogr 3:181 - 191

Mann ME, Zhang Z, Hughes MK, Bradley RS, Miller SK, Rutherford S, Ni F (2008) Proxy-based reconstructions of hemispheric and global surface temperature variations over the past two millennia. Proc Nat Acad Sci USA 105(36):13252 - 13257

Nash J, Sutcliffe JV (1970) River flow forecasting through conceptual models part I—a discussion of principles. J Hydrol 10(3):282 - 290

Neukom R, Gergis J (2012) Southern Hemisphere high-resolution palaeoclimate records of the last 2000 years. Holocene 22(5):501 - 524

Ojala AEK, Francus P, Zolitschka B, Besonen M, Lamoureux SF (2012) Characteristics of sedimentary varve chronologies: a review. Quat Sci Rev 43:45 - 60

Orpin AR, Carter L, Page MJ, Cochran UA, Trustrum NA, Gomez B, Midenhall DC, Rogers KM, Brackely HL, Northcote L (2010) Holocene sedimentary record from Lake Tutira: a template for upland watershed erosion proximal to the Waipaoa Sedimentary System, northeastern New Zealand. Mar Geol 270(1):11 – 29

Orwin JF, Smart CC (2004) Short-term spatial and temporal patterns of suspended sediment transfer in proglacial channels, Small River Glacier, Canada. Hydrol Process 18(9):1521 – 1542

Page MJ, Trustrum NA, DeRose RC (1994) A high resolution record of storm-induced erosion from lake sediments, New Zealand. J Paleolimnol 11:333 – 348

Page M, Trustrum N, Orpin A, Carter L, Gomez B, Cochran U, Mildenhall D, Rogers K, Brackley H, Palmer A (2010) Storm frequency and magnitude in response to Holocene climate variability, Lake Tutira, North-Eastern New Zealand. Mar Geol 270:30 – 44

Pharo CH, Carmack EC (1979) Sedimentation processes in a short residence-time intermontane lake, Kamloops Lake, British Columbia. Sedimentology 26(4):523 – 541

Putnam AE, Schaefer JM, Denton GH, Barrell DJ, Birkel SD, Andersen BG, Kaplan MR, Finkel RC, Schwartz R, Doughty AM (2013) the last glacial maximum at 44 S documented by a 10 Be moraine chronology at Lake Ohau, Southern Alps of New Zealand. Quat Sci Rev 62:114 – 141

Roop HA, Dunbar GB, Levy R, Vandergoes MJ, Forrest AL, Walker SL, Upton P, Whinney J (2015) Seasonal controls on sediment transport and deposition in Lake Ohau, South Island, New Zealand: implications for a high-resolution Holocene palaeoclimate reconstruction. Sedimentology 62(3):826 – 844

Sawada M, Johnson PG (2000) Hydrometeorology, suspended sediment and conductivity in a large glacierized basin, Slims River, Yukon Territory, Canada (1993-94). Arctic 53:101 – 117

Schneider CA, Rasband WS, Eliceiri KW (2012) NIH Image to ImageJ: 25 years of image analysis. Nat Methods9(7):671 – 675

Stockhecke M, Anselmetti FS, Meydan AF, Odermatt D, Sturm M (2012) The annual particle cycle in Lake Van (Turkey).Palaeogeogr Palaeoclimatol Palaeoecol 333:148 – 159

Striewski B, Shulmeister J, Augustinus PC, Soderholm J (2013) Late Holocene climate variability from Lake Pupuke maar, Auckland, New Zealand. Quat Sci Rev 77:46 – 54

Tait A, Henderson R, Turner R, Zheng X (2006) Thin plate smoothing spline interpolation of daily rainfall for New Zealand using a climatological rainfall surface. Int J Climatol 26(14):2097 – 2115

Tomkins JD, Lamoureux SF (2005) Multiple hydroclimatic controls over recent sedimentation in proglacial Mirror Lake, southern Selwyn Mountains, Northwest Territories. Can J Earth Sci 42(9):1589 – 1599

UNSCEAR Annex C (2000) Exposures to the public from manmade sources of radiation. Sourc Eff Ioniz Radiat Sourc UNSCEAR 1:158 – 287

Walling DE and WebbBW(1988) The reliability of rating curve estimates of suspended sediment yield: some further comments. Sediment Budgets, IAHS Publ 174

Wheatley JJ, Blackwell PG, Abram NJ, McConnell JR, Thomas ER, Wolff EW (2012) Automated ice-core layer-counting with strong univariate signals. Clim Past 8:1869 – 1879

Woods R, Hendricks J, Henderson R, Tait A (2006) Estimating mean flow of New Zealand rivers. J Hydrol 45(2):95 – 109

Zolitschka B, Pike J (2014) Maximizing the information yield from annually resolving natural archives. Past Global Changes Mag 22(1):4 – 5

Table 1 Varve classification for the different varve motifs and sub-types

Description		Mean thickness (mm)	Mean coarse unit Thickness (mm)	Mean fine unit thickness (mm)	Mean number of sublaminae	Occurrence[a] (%)	Interpretation [note: spring (SON); summer (DJF); autumn (MAM); winter (JJA)]
Motif A—defined by a coarse/fine couplet lacking sublaminae							
A 1	Composed of fine silt basal layer grading into a very fine silt layer. Silt layer is thicker than very fine silt layer. Contains no sublaminae	3.5	2.0	1.5	0	7	Simple varve dominated by spring discharge
A 2	Composed of silt basal layer grading into a very fine silt layer. Fine silt layer is thicker than the silt layer. Contains no sublaminae	3.4	1.1	2.3	0	27	Simple varve dominated by late spring discharge
Motif B—defined by coarse/fine couplet with one or more coarse sublaminae							
B1	Composed of fine silt basal layer grading into a very fine silt layer. Very fine silt layer contains one coarse-grained <1.5 mm thick sublaminae	4.7	1.2	1.6	1	19	Complex annual hydrograph; spring-dominated signal with late season inflow event
B2	A fine silt basal layer grades into the very fine silt layer. <1.0 mm fine silt sublaminae are present proximal (<0.8 mm) to the fine silt basal layer. Sublaminae are not present near the top of the very fine silt unit	4.8	1.1	2.2	1	12	Complex annual hydrograph; dynamic spring hydrograph with late spring/early summer peak inflow event
B3	A fine silt basal layer grades into the very fine silt layer. One or more <1.0 mm fine silt sublaminae are present proximal to the fine silt basal layer. Sublaminae are not present near the top of the very fine silt unit	5.6	0.9	1.7	2	9	Complex annual hydrograph; numerous peaks in summer discharge
B4	Composed of fine silt basal layer grading into a very fine silt layer. Very fine silt layer contains several fine silt <1.0 mm thick sublaminae	7.1	1.1	2.1	3	16	Complex annual hydrograph; numerous peaks in summer and autumn discharge
Motif C—defined by graded coarse deposits overlain by a (≥3.5 mm) *fine unit. Total unit thicknesses >9.0 mm*							
C1	Composed of a basal silt layer which grades into a thick (>3.5 mm) non-graded fine silt layer. Sublaminae are common in basal layer	10.0	1.5	3.4	2	10	Event layer; large summer discharge exceeding ~880 m^3 s^{-1}

[a] Percent occurrence since 1900 AD based on varve counts

Table 2 Nash–Sutcliffe coefficients (r) for 15-point smooth hydrographs

Mean hydrographs are derived from the listed subset of years. Sequential years were selected, where possible, in order to minimize potential error associated with the varve chronology. For type A1, no chronologic sequence of years was available for testing. Hydrographs are derived from the Lake Ohau inflow time-series

Varve type	A1	A2	B1	B2	B3	B4	C1
A1	1	0.54	0.70	0.56	0.40	0.40	0.45
A2	0.54	1	0.50	0.72	0.50	0.50	0.47
B1	0.70	0.5	1	0.69	0.45	0.68	0.62
B2	0.56	0.72	0.69	1	0.50	0.37	0.61
B3	0.40	0.50	0.45	0.50	1	0.30	0.61
B4	0.40	0.50	0.68	0.37	0.30	1	0.26
C1	0.45	0.47	0.62	0.61	0.61	0.26	1
Years compared	2009	1973	1968	2008	1980	1999	1995
	1991	1972	1966	2005	1979	1996	1994
	1977	1961	1965	2001	1975	1993	1953
	1958	1960	1964	1948	1956	1932	1952
	1947	1959	1963	1945	1954	1930	1950
	1939			1943		1929	1949

Table 3 Nash–Sutcliffe coefficients (r) for the weekly smoothed annual hydrograph for each of the three major sedimentary motifs

Motif	A	B	C
A	1	−0.27	−0.46
B	−0.27	1	0.32
C	−0.46	0.32	1
n	22	52	11

The hydrograph for each motif is derived from a mean of all of the years characterized by each sub-type (e.g. A1, A2 = A). Each motif is characterized by a unique hydrologic regime

Table 4 Regression statistics (r) for the seasonal mean hydrology of each of the three major motifs (for all years, as in Table 3)

Motifs compared	Season			
	SON (spring)	DJF (summer)	MAM (fall)	JJA (winter)
A–B				
r	0.53	0.18	0.15	0.26
p value	<0.0001	<0.0001	<0.0001	<0.0001
A–C				
r	0.35	0.23	0.02	0.02
p value	<0.0001	<0.0001	0.21	0.30
B–C				
r	0.62	0.17	0.02	0.17
p value	<0.0001	<0.0001	0.17	<0.0001

Correlation between the three motifs is greatest in the spring (SON)

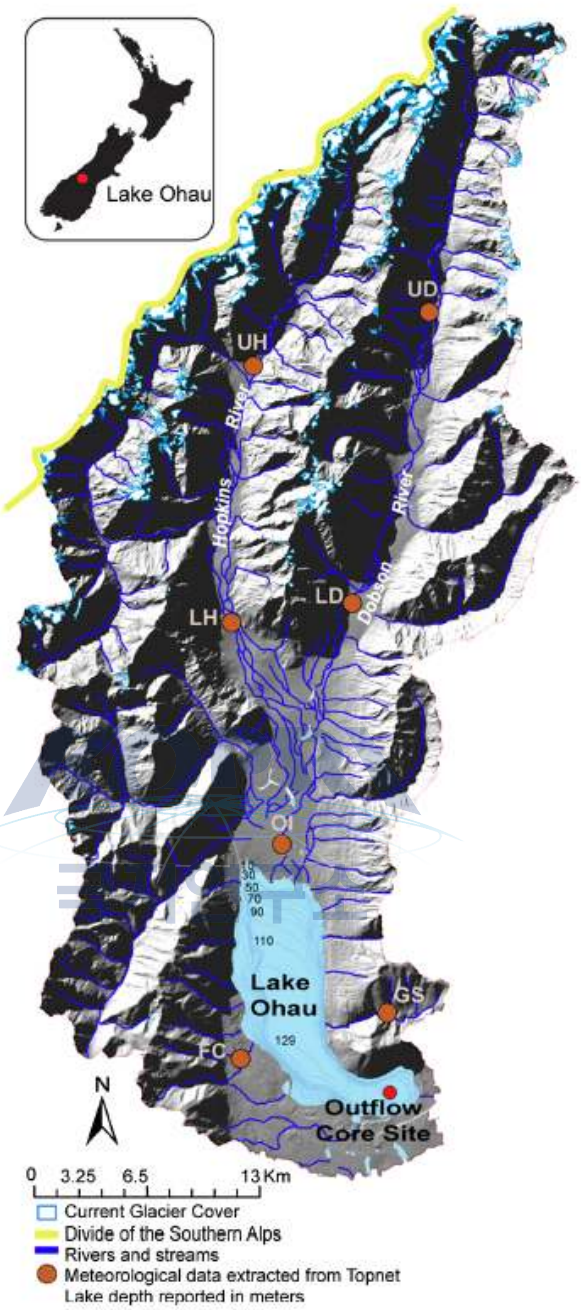

Fig. 1 The Lake Ohau catchment located on the eastern slope of the Southern Alps on the South Island, New Zealand. Sediment cores were collected near the lake outflow. Isobath interval is 10 m. Topnet derived precipitation time-series were generated for seven points in the Ohau catchment including: UH upper Hopkins, UD upper Dobson, LH lower Hopkins, LD lower Dobson, near the OI Ohau inflow, at the based of FC Freehold Creek and in the GS Greta Stream catchment

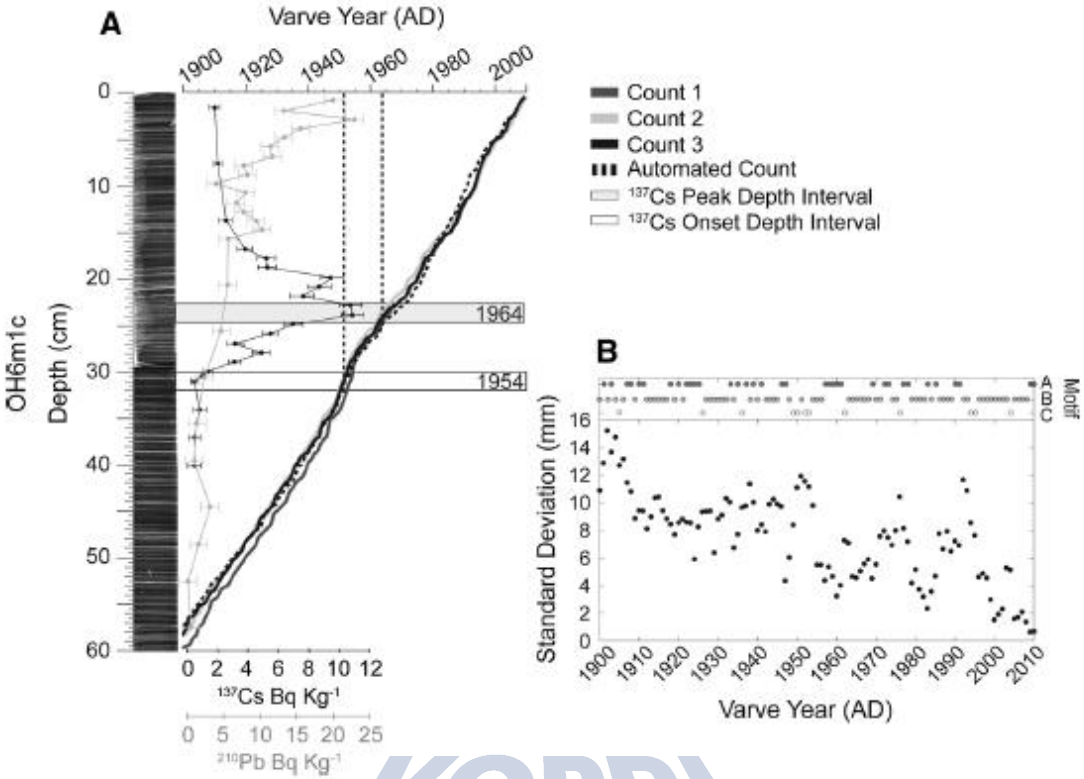

Fig. 2 a 137Cs and 210Pb activity profiles compared to manual operator and automated counts for the top 60 cm of core OH6m1c. All counts are consistent with the depth intervals associated with the 1964 peak in 137Cs and onset of 137Cs in the early 1950s. b 1r standard deviation for all manual and automated counts compared to three described motifs. The maximum deviation is 15.2 mm or ±2.9 years based on the 137Cs-derived sedimentation rate. The greatest deviation between counts is associated with motif C, or event stratigraphy

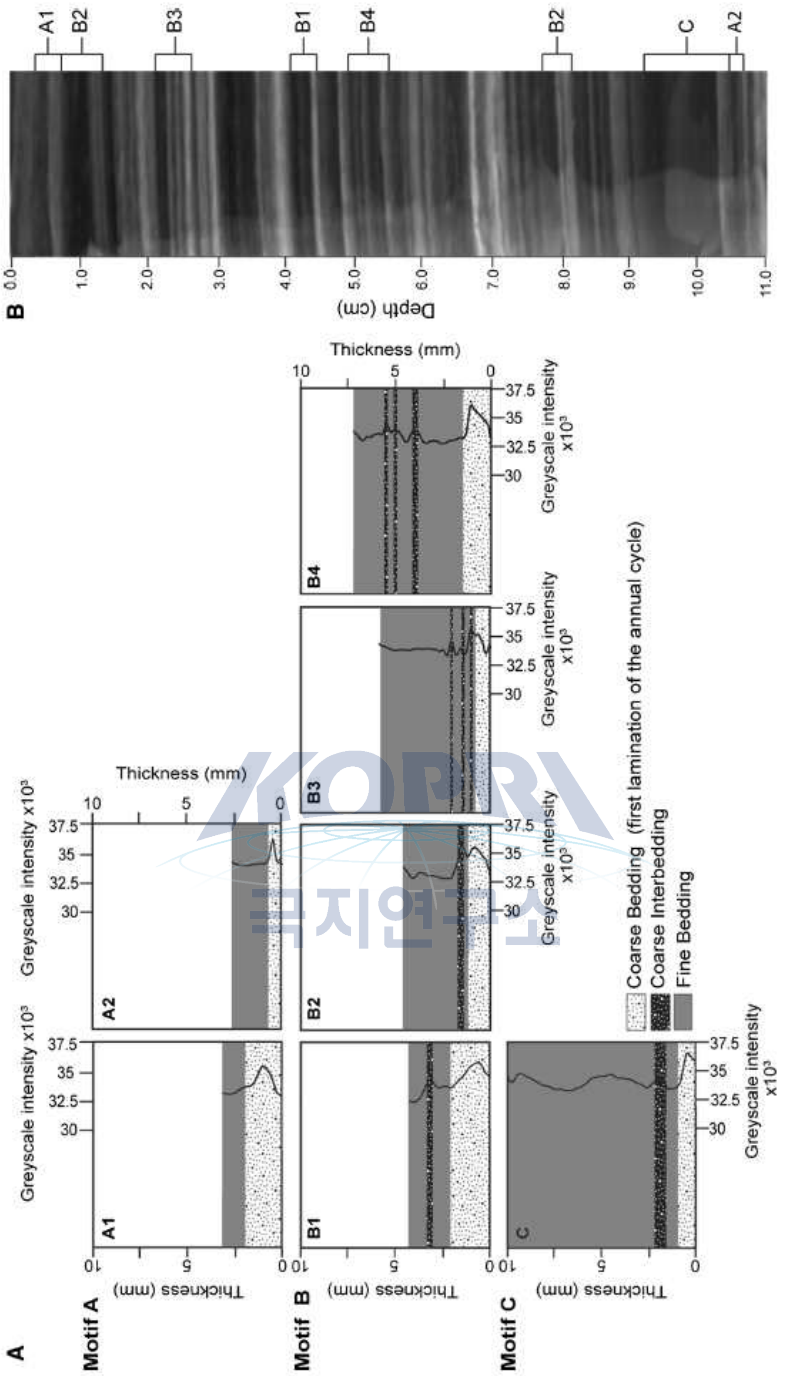

Fig. 3 a An example of the differing stratigraphic patterns and greyscale curve for each of the seven different varve types characterized by motifs A, B, C. Each example shows the relative thickness of each unit and the presence and stratigraphic position of sublaminae in motifs B and C. Unit thickness is based on the mean of each varve type. b X-radiograph image with an example of each varve sub-type

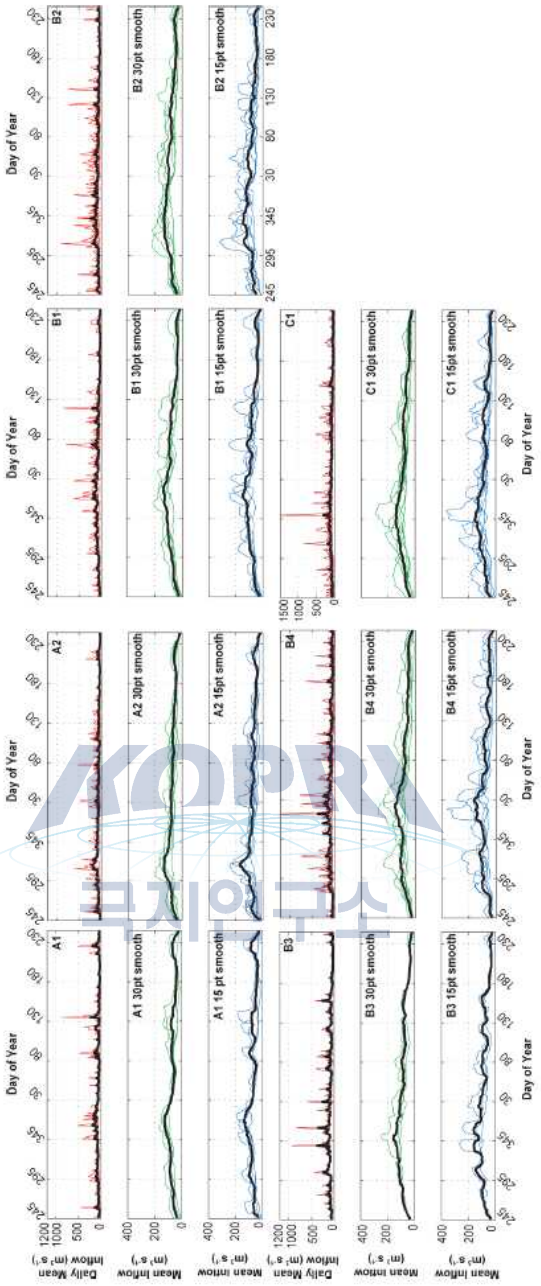

Fig. 4 Plots showing the full, 15-point and 30-point smoothed hydrographs for each motif sub-type. Dark bold lines are the mean of all years in each comparison (Table 2). Motif A varves are characterized by a spring season dominated hydrograph, motif B varves are characterized by a more complex hydrograph displaying a high degree of variability throughout the annual cycle. Motif C is similar to B, but is characterized by extreme summer event flows. Each of the three motifs is significantly different based on the Nash - Sutcliffe model accuracy statistic (Table 3)

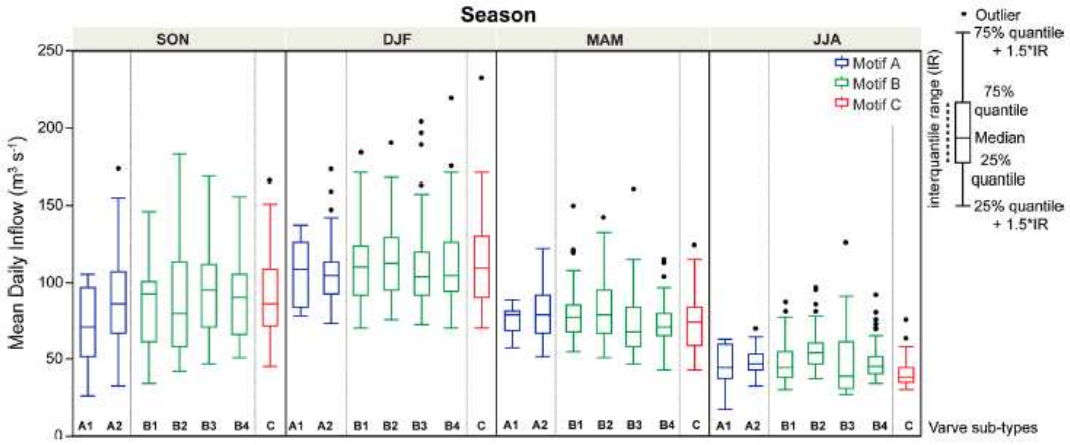

Fig. 5 Outlier box plots organized by season for each of the varve types. The hydrographs used for this comparison are derived from a mean of all of the years characterized by each varve type. Outliers represent anomalous flow, or event flow. A higher density of inflow events, particularly in summer and autumn, characterizes motif B.

제 24 장

Marinobacterium profundum sp. nov., a marine bacterium from deep-sea sediment[17)]

Chung Yeon Hwang, Soo Jung Yoon, Inae Lee, Kyu-Cheul Yoo, Ho Il Yoon

Korea Polar Research Institute

Abstract: A Gram-stain-negative, rod-shaped and motile strain, designated PAMC 27536T, was isolated from deep-sea sediment in the East Sea, Korea. Analysis of the 16S rRNA gene sequence of the strain showed an affiliation with the genus Marinobacterium. Phylogenetic analyses revealed that strain PAMC 27536T was related most closely to Marinobacterium rhizophilum CL-YJ9T with a 16S rRNA gene sequence similarity of 98.5 % and to other members of the genus Marinobacterium (94.0 - 91.7 %). Genomic relatedness analyses between strain PAMC 27536T and M. rhizophilum KCCM 42386T gave an average nucleotide identity of 85.6 % and an estimated DNA - DNA hybridization of 24.6 % using the genome-to-genome distance calculator, indicating that they represent genomically distinct species. Cells of strain PAMC 27536T grew optimally at 25 - 30 8C and pH 7.0 - 7.5 in the presence of 3 % (w/v) sea salts. The major cellular fatty acids were C16 : 1v6c and/or C16 : 1v7c,C18 : 1v6c and/or C18 : 1v7c, and C16 : 0. The major isoprenoid quinone was Q-8. The genomic DNA G+C content was 56.1 - 57.2 mol%. Based on the phylogenetic, chemotaxonomic, genomic and phenotypic data presented, a novel species with the name Marinobacterium profundum sp. nov. is proposed, with PAMC 27536T (5KCCM 43095T5JCM 30410T) as the type strain.

17) 이 연구 결과는 다음의 논문으로 출판되었음: hung Yeon Hwang, Soo Jung Yoon, Inae Lee, Kiwoon Baek, Yung Mi Lee, Kyu-Cheul Yoo, Ho Il Yoon and Hong Kum Lee. Marinobacterium profundum sp. nov., a marine bacterium from deep-sea sediment. International Journal of Systematic and Evolutionary Microbiology (2016), 66, 1561-1566

The genus Marinobacterium was established by Gonza´lez et al. (1997) for a marine bacterium isolated from lignin-rich pulp mill waste, with Marinobacterium georgiense as the type species. Phylogenetic analyses of 16S rRNA and gyrB gene sequences have improved the classification of members of the genus Marinobacterium, with the transfer of Pseudomonas stanieri (Baumann et al., 1983) and Oceanospirillum jannaschii (Bowditch et al., 1984) to Marinobacterium stanieri and Marinobacterium jannaschii, respectively (Satomi et al., 2002). The genus Marinobacter-ium belongs to the family Alteromonadaceae, and members of this genus contain C16 : 1v6c and/or C16 : 1v7c,C18 : 1v6c and/or C18 : 1v7c,andC16 : 0 as the major fatty acids and Q-8 as the major respiratory quinone (Gonz´alez et al.,1997; Kim et al., 2008; Chimetto et al., 2011; Alfaro-Espinoza & Ullrich, 2014). The genomic DNA G+C content of Marino-bacterium species with validly published names ranges from 54.9 to 62.5 mol% (Gonza´lez et al., 1997; Huo et al., 2009). In addition to the aforementioned species, ten Marinobacter-ium species have been isolated from marine habitats, includ-ing coastal seawaters (M. litorale,Kim et al.,2007; M. marisflavi,Kimet al., 2009a), tidal flats (M. halophilum, Chang et al.,2007;M. lutimaris,Kim et al., 2010), roots of salt-tolerant plants (M. rhizophilum,Kim et al.,2008; M. mangrovicola, Alfaro-Espinoza & Ullrich, 2014), sediments (M. nitratireducens and M. sediminicola,Huoet al.,2009; M. maritimum,Kim et al., 2009b) and coral (M. coralli, Chimetto et al., 2011). Here, we isolated a bacterial strain (PAMC 27536T)duringastudytoscreenfor methanol-utilizing bacteria associated with the biogeochem-ical processes of deep-sea sediments, and performed a polyphasic analysis to determine the taxonomic position of the strain.

A sediment core was collected using a box corer on R/V Araon in the East Sea (35.908 N 129.778 E; water column depth of 840 m) in July 2013. A surface sample of the sedi-ment core amended with methanol (Sigma; final concen-tration of approximately 1 %) was incubated at 20 8C for 30 days to enrich methanol-utilizing bacteria. Sub-sequently, the methanol-amended sediment sample was diluted approximately 50-fold with autoclaved 3 % (w/v)

NaCl solution. An aliquot (100 ml) of the sediment slurry was spread on the basal agar medium (per litre distilled water: 23.6 g NaCl, 0.64 g KCl, 4.53 g MgCl2 .6H2O, 5.94 g MgSO4 .7H2O, 1.3 g CaCl2 .2H2O, 0.2 g NaNO3, 0.2 g NH4Cl, 15 g agar, 0.05 g yeast extract; Bruns et al., 2001) supplemented with methanol as sole carbon source (final concentration 0.5 %) and the plate was incubated at 20 8C under aerobic conditions for 10 days. Colonies were picked and checked for growth on marine agar 2216 (MA; Difco) as a conventional cultivation medium. Strain PAMC 27536T was isolated and subsequently streaked onto MA. The purification procedure was repeated four times. The strain was maintained on MA at 20 8C and preserved in marine broth 2216 (MB; Difco) supplemented with 30 % (v/v) glycerol at 80 8C.

M. rhizophilum KCCM 42386T (Kim et al., 2008) was obtained from the Korean Culture Center of Microorgan-isms (KCCM) for comparisons of the phenotypic and chemotaxonomic characteristics with those of strain PAMC 27536T. Growth of strain PAMC 27536T and M. rhizophilum KCCM 42386T was tested on MA at various temperature and salinity conditions (see below). Unless otherwise specified, all characteristics of strain PAMC 27536T and M. rhizophilum KCCM 42386T were based on cultures grown aerobically on MA at 30 8C for 3 - 5 days. Under these conditions, both strains appeared to be in mid- to late-exponential phases of growth.

PCR amplification of the 16S rRNA gene and direct sequencing of purifi ed PCR products were performed as described by Hwang et al. (2015). The almost-complete 16S rRNA gene sequence (1474 bp) of strain PAMC 27536T was obtained and analysed using a BLAST search against the GenBank and EzTaxon-e databases (Altschul et al., 1990; Kim et al., 2012). The 16S rRNA gene sequences of closely related taxa obtained from the Gen-Bank database were aligned using the RDP aligner (Cole et al., 2014) based on secondary structures. Phylogenetic analysis was performed using the program MEGA 6.0 (Tamura et al., 2013). Distance matrices were calculated according to the Jukes and Cantor model (Jukes & Cantor, 1969). Phylogenetic trees were inferred using the neighbour-joining (Saitou & Nei, 1987), minimum-evolution (Rzhetsky & Nei, 1992) and maximum-likelihood (Felsenstein, 1981) methods using bootstrap analyses based on 1000 replications.

Phylogenetic analyses based on the 16S rRNA gene sequence showed that strain PAMC 27536T was affiliated with the genus Marinobacterium (Fig. 1). Strain PAMC 27536T was related most closely to M. rhizophilum CL-YJ9T (98.5 % 16S rRNA gene sequence similarity) and next to the type strains of other Marinobacterium species with validly published names (94.0 - 91.7 %). The tree topologies inferred using the neighbour-joining, minimum-evolution and maximum-likelihood algor-ithms revealed that strain PAMC 27536T formed a robust clade with M. rhizophilum CL-YJ9T supported by ahighbootstrap valueof100%withall threetree-making methods (Fig. 1).

Phenotypic characteristics of strain PAMC 27536T were tested in duplicate along with M. rhizophilum KCCM 42386T, with repeat experiments on different days. Gram-staining was performed using a Gram-stain kit (Sigma). Cell morphology was examined by transmission electron microscopy (EX2; JEOL). Anaerobic growth was tested in an anaerobic jar (BBL) containing an AnaeroPak (Mitsu-bishi Gas Chemical) at 25 8C for 5 days. The temperature range for growth was examined by the ability to form colo-nies on MA with incubation at 4, 10 - 30 (in increments of 5 8C), 32, 34, 37 and 42 8C. The pH range (pH 5.0 - 11.0 at intervals of 0.5 pH units) for growth was determined by assessing turbidity measured as OD600 in pH-buffered MB (Hwang & Cho, 2008) using citric acid-phosphate buffer for pH 5.0, MES for pH 5.5 - 6.5, MOPS for pH 7.0 - 7.5, AMPD for pH 8.0 - 9.5 and CAPS for pH 10.0 - 11.0 (each at a final concentration of 50 mM at 25 8C), for up to 2 weeks. Salt tolerance was determined by assessing turbidity measured as OD600 at 25 8C using synthetic ZoBell broth (per litre distilled water: Bacto peptone, 5 g; yeast extract, 1 g; ferric citrate, 0.1 g) supplemented with 0 - 6 (at intervals of 1 %), 8, 10 and 12 % (w/v) sea salts (Sigma).

Catalase and oxidase tests were performed according to the methods described by Smibert & Krieg (1994) and Cappuc-cino & Sherman (2002), respectively. Hydrolysis of casein, starch, Tween 80, xanthine and hypoxanthine, and deami-nase activities of ornithine, lysine and arginine were inves-tigated as described by Hansen & Sørheim (1991). H2S production was tested as described by Bruns et al. (2001). In addition, other enzyme activities using the API ZYM and API 20NE kits (bioMe´rieux) and acid production using the API 50CH kit

(bioMe´rieux) were assayed accord-ing to the manufacturer's instructions except that the cell suspension was prepared as described by Hwang et al.(2009). Utilization of various substrates as sole carbon and energy sources was tested using the basal broth medium supplemented with yeast extract (per litre distilled water: 23.6 g NaCl, 0.64 g KCl, 4.53 g MgCl2 .6H2O, 5.94 g MgSO4 .7H2O, 1.3 g CaCl2 .2H2O, 0.2 g NaNO3, 0.2 g NH4Cl, 0.05 g yeast extract; Bruns et al., 2001) with a final concentration of 0.4 % carbon source. Carbon util-ization was scored as negative when growth was equal to, or less than, that in the negative control with no carbon source. Growth was measured by monitoring changes in the OD600 at 25 8C for 3 weeks.

Cells of strain PAMC 27536T were rods approximately 0.7 - 1.0 mmwideand1.9 - 2.4mm long (Table 1). Strain PAMC 27536T grew optimally at 25 - 30 8C and pH 7.0 - 7.5 in the presence of 3 % (w/v) sea salts and was positive for catalase and oxidase activities. Other physiological and biochemical characteristics of strain PAMC 27536T are given in the species description and Table 1. Strain PAMC 27536T could be phenotypically distinguished from M. rhizophilum

KCCM 42386T based on the temperature and salinity ranges for growth, ability to utilize melibiose as sole carbon and energy source and inability to produce a-glucosidase in the API ZYM assay (Table 1). In addition, acid production from 12 carbohydrates in the API 50CH assay gave different results for the two strains (Table 1).

The fatty acid methyl esters in whole cells of strain PAMC 27536T and M. rhizophilum KCCM 42386T grown on MA at 30 8C for 5 days were analysed by GC (Agilent Technol-ogies 7890B) according to the instructions of the Microbial Identification System (MIDI; version 6.2) with the TSBA6 database. Genomic DNA of strain PAMC 27536T was extracted using a commercial kit (DNeasy Blood & Tissue kit; Qiagen). The genome sequence of strain PAMC 27536T was determined using an Illumina MiSeq sequencer and assembled using CLC Genomics Workbench 7.0 (Qiagen) at the ChunLab (Seoul, Korea). The draft genome of strain PAMC 27536T was deposited at DDBJ/EMBL/GenBank under accession number BCNS01000000. A draft genome sequence of M. rhizophilum DSM 18822T was retrieved from GenBank under

accession number ARJM00000000 (5 360 582 bp with 68 contigs and DNA G+C content of 58.5 mol%). The degree of genome-based relatedness between strain PAMC 27536T and M. rhizophilum DSM 18822T was estimated by both an average nucleotide identity (ANI) value, following the BLAST-based ANI calculation method described by Goris et al. (2007), and the genome-to-genome distance calcu-lation method described by Auch et al. (2010). The geno-mic DNA G+C content of strain PAMC 27536T was also determined by both HPLC analysis (Tamaoka & Komagata, 1984) carried out by the identification service of the KCCM and whole genome analysis calculated from the draft genome.

The major fatty acids (.10 %) of strain PAMC 27536T were C16 : 1v6c and/or C16 : 1v7c (42.7 %), C18 : 1v6c and/or C18 : 1v7c (20.9 %), and C16 : 0 (19.1 %; Table S1, available in the online Supplementary Material), which are typically found as major components in members of the genus Marinobacterium (Kim et al., 2008; Chimetto et al., 2011; Alfaro-Espinoza & Ullrich, 2014). No major differences were found in the fatty acid profiles of strain PAMC 27536T and M. rhizophilum KCCM 42386T (Table S1).

The draft genome of strain PAMC 27536T contained 5 637 742 bp in 226 contigs with a DNA G+C content of 57.2 mol% and coverage of 1696. The ANI value between strain PAMC 27536T and the type strain of M. rhizophilum was 85.6 %, which is below the proposed cut-off ANI values of 95 - 96 % for delineating bacterial species (Goris et al., 2007; Richter & Rossello´ -Mo´ ra, 2009). Consistently, the mean DNA - DNA hybridization value estimated by genome-to-genome distance calculation was 24.6 2.4 %between strain PAMC 27536T and the type strain of M. rhizophilum, indicating that PAMC 27536T is a member of a separate species of the genus Marinobacterium (Rossello´ -Mora & Amann, 2001).

The genomic DNA G+C content of strain PAMC 27536T was 56.1 mol% as determined by HPLC analysis, which was similar to that based on calculation from the draft genome of the strain (57.2 mol%; Table 1). The DNA G+C content of strain PAMC 27536T was lower than that of its phylogenetically closest relative, M. rhizophilum KCCM 42386T (61 mol%; Kim et al., 2008), but nevertheless was within the range of other Marinobacterium species (54.9 - 62.5 mol%; Gonza´lez et al., 1997; Huo et al., 2009).

Although strain PAMC 27536T was isolated from a metha-nol-enriched sediment sample, growth was not detected in the medium employed here when supplemented with methanol as sole carbon source (final concentration of 0.1 or 0.4 %). However, the draft genome of PAMC 27536T exhibits the presence of genes encoding the biosyn-thesis of alcohol dehydrogenase and a coenzyme pyrrolo-quinoline quinone (PQQ) (data not shown), which play a key step in methylotrophic metabolism (i.e. oxidation of methanol to formaldehyde; Witthoff et al., 2013), suggesting the potential of this strain as a methanol-utilizing bacterium.

The phylogenetic, chemotaxonomic, genomic and pheno-typic data obtained in this study indicate that strain PAMC 27536T should be assigned to a novel species in the genus Marinobacterium, for which the name Marino-bacterium profundum sp. nov. is proposed.

Description of Marinobacterium profundum sp. nov.

Marinobacterium profundum (pro.fun9dum. L. neut. adj. profundum deep, living within the depth of the oceans).

Gram-stain-negative, strictly aerobic, motile rods approxi-mately 0.7 - 1.0 mm wide and 1.9 - 2.4 mm long. After 7 days on MA at 30 uC, colonies are creamy white, circular, convex and approximately 0.5 mm in diameter. Grows at 4 - 32 uC (optimum, 25 - 30 uC) and at pH 6.0 - 9.0 (opti-mum, pH 7.0 - 7.5). Growth occurs at sea-salt concen-trations of 1 - 4 % (w/v) (optimum, 3 %). Positive for oxidase and catalase. Starch, Tween 80 and hypoxanthine are hydrolysed. Casein, aesculin, gelatin and xanthine are not hydrolysed. Indole production, H2S production, glucose fermentation and nitrate reduction are negative. Alkaline phosphatase, esterase (C4), leucine arylamidase, valine arylamidase, acid phosphatase and naphthol-AS-BI-phosphohydrolase are positive; esterase lipase (C8) is weakly positive; N-acetyl-b-glucosaminidase, arginine dihy-drolase, a-chymotrypsin, cystine arylamidase, a-fucosidase, a-galactosidase, a-glucosidase, b-glucosidase, b-glucuroni-dase, lipase (C14), a-mannosidase, urease and trypsin are negative. Acid is produced from

L-arabinose, D-fructose, DL-fucose, glycerol, melibose (weakly), raffinose, L-rham-nose (weakly), potassium 2-ketogluconate and sucrose, but not from N-acetylglucosamine, D-adonitol, amygdalin, D-arabinose, DL-arabitol, arbutin, cellobiose, dulcitol, erythritol, aesculin ferric citrate, D-galactose, gentiobiose, D-glucose, glycogen, inositol, inulin, lactose, D-lyxose, mal-tose, D-mannitol, D-mannose, methyl a-D-glucopyranoside, methyl a-D-mannopyranoside, melezitose, methyl b-D-xylopyranoside, potassium gluconate, potassium 5-ketoglu-conate, D-ribose, salicin, D-sorbitol, L-sorbose, starch, D-tagatose, trehalose, turanose, xylitol or DL-xylose. N-Acetyl-D-glucosamine, DL-aspartate, glycogen, melibiose, L-ornithine, L-proline, pyruvate and succinate are utilized as sole carbon and energy source, but acetate, L-arabinose, cel-lobiose, citrate, formate, D-fructose, D-galactose, D-glucose, glycerol, inositol, lactose, maltose, D-mannitol, D-mannose, methanol, raffinose, L-rhamnose, L-threonine, trehalose and sucrose are not utilized. Major fatty acids are C16 : 1v6c and/or C16 : 1v7c,C18 : 1v6c and/or C18 : 1v7c, and C16 : 0.

The type strain, PAMC 27536T (5KCCM 43095T5JCM 30410T), was isolated from deep-sea sediment. The DNA G+C content of the type strain is 56.1 mol% (HPLC anal-ysis) - 57.2 mol% (whole genome analysis).

Marinobacterium profundum sp. nov., 심해 퇴적물로부터 발견한 해양 박테리움

황청연, 윤수정, 이인애, 유규철, 윤호일

한국해양과학기술원 부설 극지연구소

요약: 그램 염색의 음성, 막대기 모양과 유동성 염색체를 가진 PAMC 27536이 한국 동해 심해 코어에서 분리되었다. 16S rRNA 분석법은 *Marinobacterium*과 관련이 있는 것으로 보여진다. PAMC 27536은 *Marinobacterium rhizophilum* CL-YJ9와 98.5%의 유사도를 가지고 다른 *Marinobacterium*과는 94-91.7%의 유사도를 보인다. PAMC 27536과 *M. rhizophilum* KCCM 42386은 85.6%의 일치성을 제시한다. 계통발생학적, 독성화학적, 유전학적, 계통학적 자료들은 이 새로운 종이 *Marinobacterium profundum* sp. nov.라는 것을 증명한다.

참고문헌

Alfaro-Espinoza, G. & Ullrich, M. S. (2014). Marinobacterium mangrovicola sp. nov., a marine nitrogen-fixing bacterium isolated from mangrove roots of Rhizophora mangle. Int J Syst Evol Microbiol 64, 3988 - 3993.

Altschul, S. F., Gish, W., Miller, W., Myers, E. W. & Lipman, D. J.(1990). Basic local alignment search tool. J Mol Biol 215, 403 - 410.

Auch, A. F., von Jan, M., Klenk, H. P. & G ¨oker, M. (2010). Digital DNA - DNA hybridization for microbial species delineation by means of genome-to-genome sequence comparison. Stand Genomic Sci 2, 117 - 134.

Baumann, P., Bowditch, R. D., Baumann, L. & Beaman, B. (1983). Taxonomy of marine Pseudomonas species: P. stanieri sp. nov., P. perfectomarina sp. nov., nom. rev., P. nautica; and P. doudorofii. Int J Syst Bacteriol 33, 857 - 865.

Bowditch, R. D., Baumann, L. & Baumann, P. (1984). Description of Oceanospirillum kriegii sp. nov. and O. jannaschii sp. nov. and assignment of two species of Alteromonas to this genus as O. commune comb. nov. and O. vagum comb. nov. Curr Microbiol 10, 221 - 229.

Bruns, A., Rohde, M. & Berthe-Corti, L. (2001). Muricauda ruestringensis gen. nov., sp. nov., a facultatively anaerobic, appendaged bacterium from German North Sea intertidal sediment. Int J Syst Evol Microbiol 51, 1997 - 2006.

Cappuccino, J. G. & Sherman, N. (2002). Microbiology: a Laboratory Manual, 6th edn, Menlo Park, CA: Benjamin/Cummings.

Chang, H.-W., Nam, Y.-D., Kwon, H.-Y., Park, J. R., Lee, J.-S., Yoon, J.-H., An, K.-G. & Bae, J.-W. (2007). Marinobacterium halophilum sp. nov., a marine bacterium isolated from the Yellow Sea. Int J Syst Evol Microbiol 57, 77 - 80.

Chimetto, L. A., Cleenwerck, I., Brocchi, M., Willems, A., De Vos, P. & Thompson, F. L. (2011). Marinobacterium coralli sp. nov., isolated from mucus of coral (Mussismilia hispida). Int J Syst Evol Microbiol

61, 60 - 64.

Cole, J. R., Wang, Q., Fish, J. A., Chai, B., McGarrell, D. M., Sun, Y., Brown, C. T., Porras-Alfaro, A., Kuske, C. R. & Tiedje, J. M. (2014). Ribosomal Database Project: data and tools for high throughput rRNA analysis. Nucleic Acids Res 42 (D1), D633 - D642.

Felsenstein, J. (1981). Evolutionary trees from DNA sequences: a maximum likelihood approach. J Mol Evol 17, 368 - 376.

Gonza´ lez, J. M., Mayer, F., Moran, M. A., Hodson, R. E. & Whitman, W. B.(1997). Microbulbifer hydrolyticus gen. nov., sp. nov., and Marinobacterium georgiense gen. nov., sp. nov., two marine bacteria from a lignin-rich pulp mill waste enrichment community. Int J Syst Bacteriol 47,369 - 376.

Goris, J., Konstantinidis, K. T., Klappenbach, J. A., Coenye, T., Vandamme, P. & Tiedje, J. M. (2007). DNA-DNA hybridization values and their relationship to whole-genome sequence similarities. Int J Syst Evol Microbiol 57, 81 - 91.

Hansen, G. H. & Sørheim, R. (1991). Improved method for phenotypical characterization of marine bacteria. J Microbiol Methods 13,231 - 241.

Huo, Y.-Y., Xu, X.-W., Cao, Y., Wang, C.-S., Zhu, X.-F., Oren, A. & Wu, M. (2009). Marinobacterium nitratireducens sp. nov. and Marinobacterium sediminicola sp. nov., isolated from marine sediment. Int J Syst Evol Microbiol 59, 1173 - 1178.

Hwang, C. Y. & Cho, B. C. (2008). Cohaesibacter gelatinilyticus gen. nov., sp. nov., a marine bacterium that forms a distinct branch in the order Rhizobiales, and proposal of Cohaesibacteraceae fam. nov. Int J Syst Evol Microbiol 58, 267 - 277.

Hwang, C. Y., Kim, M. H., Bae, G. D., Zhang, G. I., Kim, Y. H. & Cho, B. C. (2009). Muricauda olearia sp. nov., isolated from crude-oil-contaminated seawater, and emended description of the genus Muricauda. Int J Syst Evol Microbiol 59, 1856 - 1861.

Hwang, C. Y., Lee, I., Cho, Y., Lee, Y. M., Baek, K., Jung, Y.-J., Yang, Y. Y., Lee, T., Rhee, T. S. & Lee, H. K. (2015). Rhodococcus aerolatus sp. nov., isolated from subarctic rainwater. Int J Syst Evol Microbiol 65,

465 - 471.

Jukes, T. H. & Cantor, C. R. (1969). Evolution of protein molecules. In Mammalian Protein Metabolism, vol. 3, pp. 21 - 132. Edited by H. N. Munro. New York: Academic Press.

Kim, H., Choo, Y.-J., Song, J., Lee, J.-S., Lee, K. C. & Cho, J.-C. (2007). Marinobacterium litorale sp. nov. in the order Oceanospirillales. Int J Syst Evol Microbiol 57, 1659 - 1662.

Kim, Y.-G., Jin, Y.-A., Hwang, C. Y. & Cho, B. C. (2008). Marinobacterium rhizophilum sp. nov., isolated from the rhizosphere of the coastal tidal-flat plant Suaeda japonica. Int J Syst Evol Microbiol 58,164 - 167.

Kim, H., Oh, H.-M., Yang, S.-J., Lee, J.-S., Hong, J.-S. & Cho, J.-C.(2009a). Marinobacterium marisflavi sp. nov., isolated from a costal seawater. Curr Microbiol 58, 511 - 515.

Kim, S.-J., Park, S.-J., Yoon, D.-N., Park, B.-J., Choi, B.-R., Lee, D.-H., Roh, Y. & Rhee, S.-K. (2009b). Marinobacterium maritimum sp. nov., a marine bacterium isolated from Arctic sediment. Int J Syst Evol Microbiol 59, 3030 - 3034.

Kim, J. M., Lee, S. H., Jung, J. Y. & Jeon, C. O. (2010). Marinobacterium lutimaris sp. nov., isolated from a tidal flat. Int J Syst Evol Microbiol 60, 1828 - 1831.

Kim, O. S., Cho, Y. J., Lee, K., Yoon, S. H., Kim, M., Na, H., Park, S. C., Jeon, Y. S., Lee, J. H. & other authors (2012). Introducing EzTaxon-e: a prokaryotic 16S rRNA gene sequence database with phylotypes that represent uncultured species. Int J Syst Evol Microbiol 62, 716 - 721.

Richter, M. & Rossello쨈 -Mo쨈 ra, R. (2009). Shifting the genomic gold standard for the prokaryotic species de詮갾ition. Proc Natl Acad Sci USA106, 19126??9131.

Rossello´ -Mora, R. & Amann, R. (2001). The species concept for prokaryotes. FEMS Microbiol Rev 25, 39 - 67.

Rzhetsky, A. & Nei, M. (1992). A simple method for estimating and testing minimum-evolution trees. Mol Biol Evol 9, 945 - 967.

Saitou, N. & Nei, M. (1987). The neighbor-joining method: a new method for reconstructing phylogenetic trees. Mol Biol Evol 4, 406 - 425.

Satomi,M.,Kimura,B., Hamada,T.,Harayama,S.&Fujii,T.(2002). Phylogenetic study of the genus Oceanospirillum based on 16S rRNA and gyrB genes: emended description of the genus Oceanospirillum, description of Pseudospirillum gen. nov., Oceanobacter gen. nov. and Terasakiella gen. nov. and transfer of Oceanospirillum jannaschii and Pseudomonas stanieri to Marinobacterium as Marinobacterium jannaschii comb. nov. and Marinobacterium stanieri comb. nov. Int J Syst Evol Microbiol 52, 739 - 747.

Smibert, R. M. & Krieg, N. R. (1994). Phenotypic characterization. In Methods for General and Molecular Bacteriology, pp. 607 - 654. Edited by P. Gerhardt, R. G. E. Murray, W. A. Wood & N. R. Krieg. Washington, DC: American Society for Microbiology.

Tamaoka, J. & Komagata, K. (1984). Determination of DNA base composition by reversed-phase high-performance liquid chromato-graphy. FEMS Microbiol Lett 25, 125 - 128.

Tamura, K., Stecher, G., Peterson, D., Filipski, A. & Kumar, S. (2013). MEGA6: molecular evolutionary genetics analysis version 6.0. Mol Biol Evol 30, 2725 - 2729.

Witthoff, S., Mu¨ hlroth, A., Marienhagen, J. & Bott, M. (2013). C1 metabolism in Corynebacterium glutamicum:anendogenouspathway for oxidation of methanol to carbon dioxide. Appl Environ Microbiol 79, 6974 - 6983.

Table 1. Differential characteristics between strain PAMC 27536^T and *M. rhizophilum* KCCM 42386^T

Data were obtained in this study, unless otherwise indicated. +, Positive; −, negative.

Characteristic	PAMC 27536^T	*M. rhizophilum* KCCM 42386^T
Temperature range (°C) for growth (optimum)	4–32 (25–30)	10–34 (25–30)
Salinity range (%, w/v) for growth (optimum)	1–4 (3)	1–6 (3)
pH range for growth (optimum)	6.0–9.0 (7.0–7.5)	6.0–9.0 (7.0)
α-Glucosidase	−	+
Acid production from:		
D-Adonitol, D-arabitol, L-arabitol, cellobiose, D-glucose, inositol, inulin, methyl α-D-glucopyranoisde, trehalose, turanose, xylitol	−	+
Raffinose	+	−
Utilization as sole carbon and energy source:		
N-Acetyl-D-glucosamine	−	+
Melibiose	+	−
DNA G+C content (mol%; HPLC analysis)	56.1 (57.2)*	61†

*Whole genome analysis.

†Data from Kim *et al.* (2008).

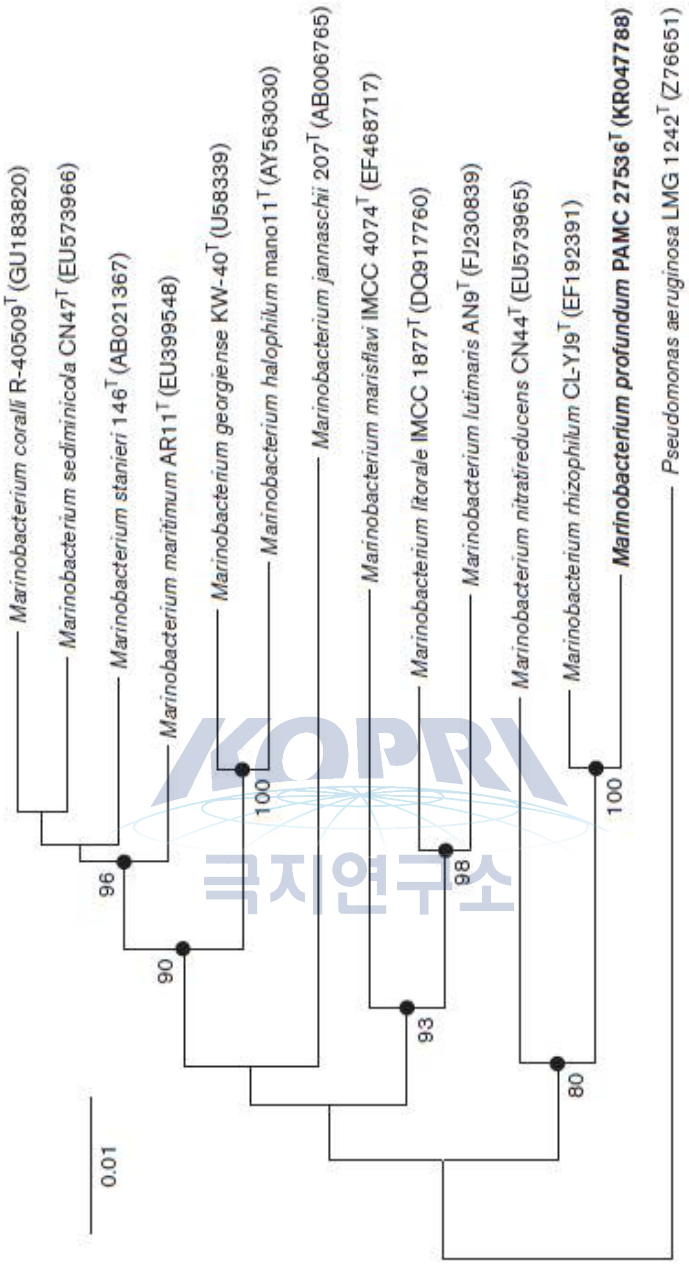

Fig. 1. Neighbour-joining tree showing the phylogenetic positions of strain PAMC 27536T and related species on the basis of 16S rRNA gene sequences. Only bootstrap values above 70 % are shown (1000 resamplings) at branch points. Filled circles indicate that the corresponding nodes were also obtained in both the maximum-likelihood and the minimum-evolution trees. Pseudomonas aeruginosa LMG 1242T (Z76651) was used as an outgroup. Bar, 0.01 nt substitutions per site.

제 25 장

Evaluating the life expectancy of a desert pavement[18)]

Yeong Bae Seong[1], Jae Il Lee[2]

[1]Korea University
[2]Korea Polar Research Institute

Abstract: This paper integrates prior scholarship on desert pavements with a case study of pavements on stream terraces in the Sonoran Desert to analyze the processes and site conditions that facilitate the survival of ancient desert pave-ments. This synthesis identifies vital factors, key factors, and site-specific factors promoting pavement stability. Hyperaridity is the vital factor in pavements surviving for 106 years or more, aided by minimal bioturbation and clast-size reduction. Three key factors aid in pavements surviving for 104 to 105 years: accumulation of al-lochthonous dust underneath pavement cobbles; a flat topography; and a lack of headward retreating swales or gullies. A unified explanation for pavement longevity, however, did not emerge from a literature review, be-cause a variety of site-specific factors can also promote pavement antiquity including: resistant bedrock beneath the pavement; disk-shaped cobbles to promote dust accumulation; and microclimatological and ecological rea-sons for minimal bioturbation. Both key and site-specific explanations for pavement longevity apply well to a case study of pavements on stream terraces in the Sonoran Desert, central Arizona. The buildup of cosmogenic 10Be and in situ 14C, optically stimulated luminescence and varnish microlamination ages reveal stable pavements range in age between ~30 and 332 ka with conditions for longevity including: flat surface topography; pave-ments underlain by consolidated granitic bedrock; a lack of headward-retreating gullies and swales; 87Sr/86Sr analyses indicating the infiltration of allochthonous dust floating

18) 이 연구 결과는 다음의 논문으로 출판되었음: Yeong Bae Seong, Ronald I. Dorn, Byung Yong Yu. Evaluating the life expectancy of a desert pavement. Earth-Science Reviews 162 (2016) 129-154

disk-shaped pavement cobbles; and a quartzite lithology resistant to disintegration. However, 10Be ages also indicate evidence for the instability of desert pave-ments on stream terraces underlain by unconsolidated playa clays and unconsolidated fanglomerate; these weaker materials allowed the growth of headward-retreating swales, that in turn promoted exposure of newer gravels by surface erosion.

1. Introduction

Desert pavement consists of a gravel surface one or two stones thick (Mabbutt, 1965; Cooke, 1970; Mabbutt, 1979) that occurs in both cold (Bockheim, 2010)andwarm(Dixon, 2009) deserts. This paper focuses on warm desert pavements that go by a variety of names (Cooke and Warren, 1973; Mabbutt, 1977): desert pavement in North and South America, as well as India (Moharana and Raja, 2016); reg for smaller gravels in the western Sahara and Middle East; hamada for residual rocks or boulders forming the surface of a rocky tableland in the western Sahara and Middle East; serir in the central Sahara where stones are larger than regs; gibber (or stony desert) in Australia; saï in the Tarim Desert; and the Mongol term gobi for pebbly-rocky plains in central Asia. Stony mantles (Laity, 2011) and stone pavements (Dietze and Kleber, 2012) are sometimes used as synonyms, while some archaeolo-gists use stone mulches in place of desert pavements (Aerts et al., 2010). For the sake of consistency, we employ the terms desert pavement or just pavement throughout. Fig. 1 presents examples from various warm deserts.

While much has been written about desert pavements in the past few decades (Dixon, 2009; Laity, 2011), this review focuses on fac-tors promoting desert pavement longevity. We start by presenting a literature review. However, a literature review alone does not fully communicate our thesis that pavement stability can be the re-sult of a complex mix of general factors (e.g. hyper-aridity, allochtho-nous dust floating a pavement, flat topography) and site-specific factors. Thus, we also contextualize prior scholarship by presenting a case study of new research on the oldest known (yet) desert pave-ment in the Sonoran Desert, North America, to further elucidate rea-sons for the

longevity of desert pavements.

2. Literature overview of warm desert pavements

2.1. Why ancient pavements are important

Desert pavements develop on a wide array of landforms (Table 1). Measuring pavement age provides insight into the antiquity of the underlying landform. Pavement age is also a concern to academic schol-arship in a variety of earth-science fields beyond geomorphology in-cluding: geoarchaeology, geochemistry, hydrology, paleoseismology, physical geography, Quaternary Research, soil science, and surficial ge-ology. Desert pavement stability can also play a role in applied earth-science research, because the placement of the hazardous waste of our modern society often requires a stable setting (Stirling et al., 2010; Wright et al., 2014; Potter, 2016).

The existence of an ancient stable pavement provides a platform for the preservation of a diverse array of materials such as ancient ar-tifacts (Adelsberger and Smith, 2009; Latorre et al., 2013; Honegger and Williams, 2015) and meteorite fragments (Kring et al., 2001). Post-depositional changes to artifacts in desert pavements can be useful in assigning relative, correlated, and calibrated ages (Hunt, 1960; Hayden, 1976; Frink and Dorn, 2001; Cerveny et al., 2006; Zerboni, 2008; Adelsberger et al., 2013; Baied and Somonte, 2013; Ugalde et al., 2015). Geoglyphs are constructed into desert pave-ment, such as the Nasca lines in Peru (Wagner and Kadereit, 2010), alignments in North America (Cerveny et al., 2006), and the geomet-ric lines in the Arabian Desert (Athanassas et al., 2015).

Desert pavements are generally considered an indicator of aridity (Pietsch and Kuhn, 2012; Fitzsimmons et al., 2013). Pavement antiquity can provide important evidence for the timing of major climatic transitions, to when a desert region became arid enough to preserve a desert pavement. For example, desert pavement did not develop in southern Arabia until regional desiccation

initiated in the early Holo-cene (Pietsch and Kuhn, 2012). Desert pavements also record the onset of hyperaridity on timescales of 106 years, for the Atacama De-sert (Dunai et al., 2005; Nishiizumi et al., 2005; Evenstar et al., 2009; Wang et al., 2015), the gibber plains in Australia (Fujioka et al., 2005), the Gobi Desert (Lv et al., 2010), and the southern Levant (Amit et al., 2011).

Some argue that buried pavements in warm deserts have potential for use as a paleoenvironmental indicator of aridity or rates of dust accu-mulation (Dorn and Dickinson, 1989; Marchant and Denton, 1996; Field et al., 2002; Dietze et al., 2011, 2012, 2013, 2016). An important distinc-tion exists, however, between buried pavements in desert regions and buried stone lines in the wet tropics that have sometimes been termed buried desert pavements (Colinvaux et al., 2000). These buried stone lines found in temperate and tropical humid areas are not buried desert pavements, but they result of complex bioturbation processes (Johnson, 1989, 1990; Johnson and Balek, 1991).

Desert pavement antiquity plays a role in understanding desert soils and desert biota (Peterson, 1981; Peterson et al., 1995; McFadden et al., 1998; Young et al., 2004; Wood et al., 2005). For example, studies of the fallout 137Cs in soil profiles indicates that clay particles that bind 137Cs are transported through soil profiles by infiltration and not bioturbation (Pelletier et al., 2005). The highest biodiversity tends to exist before smooth pavements form, but biodiversity declines as pavements change soil water-holding capacity and infiltration capacity (Shafer et al., 2004).

Hence, old pavements impact ecological patterns in the Sonoran (McAuliffe, 1994)and theMojave(Pietrasiak et al., 2014)desertsof North America.

2.2. Factors promoting the formation of desert pavements

Since pavement longevity involves factors related to pavement gen-esis, this section reviews current scholarship on birthing processes. De-sert pavements require certain geomorphic and vegetative settings before they can develop. Potential pavements require a surface not sub-ject to gullying from overland flow (Peel, 1960; Cooke, 1970; Huang et al., 2014), have low slope angles (Ugolini et al., 2008), and have dry enough conditions to inhibit

bioturbation (Pietrasiak et al., 2014).

A clear distinction exists between deflation and non-deflation pavements, and this paper focuses pavements that do not form as a result of wind concentrating cobbles at the surface by transporting sand and dust. Still, it is important to review some of the recent de-flation pavement literature, in part because persistent examples exist of deflation producing pavements that are (a) not coated in rock varnish, (b) do not have vesicular Av soil horizons underneath surface clasts, (c) have more widely spaced clasts separated by a sandy surface, (d) often occur near aeolian sands, and (e) where the clasts are clearly wind abraded (Symmons and Hemming, 1968; Cooke and Warren, 1973; Grolier et al., 1974; Goudie and Wilkinson, 1977; Williams and Greeley, 1984; Breed et al., 1989; Thomas et al., 2005; Wang et al., 2006; Al-Farraj, 2008; Dortch and Schoenbohm, 2011; Hussain and Aghwan, 2014; Zhang et al., 2014). Deflation pavements stabilize sand in the Libyan Sahara (Bubenzer et al., 2007), in the Gobi Desert, China (Brookes, 2001; Jianjun et al., 2001; Wang et al., 2006; Zhang et al., 2014), and in Iran (Kianian, 2014). Deflation pavements can result from accelerat-ed erosion of an A-horizon in semi-arid Patagonia, Argentina (Rostagno and Degorgueb, 2011), and studies from Fuego-Patagonia suggestthatdeflation can alter the characteristics of desert pave-ments (Borrazzo, in press). Cosmogenic 10Be accumulations in sur-face cobbles and depth profiles in the Andean Precordillera are consistent with pavement formation by defl ationsometime inthe past (Siame et al., 1997; Schmidt et al., 2011).

A complication exists in trying to distinguish deflation pavements from non-deflation pavements where climatic change reduces aeolian abrasion. A reduction in aeolian activity permits the formation of rock varnish on ventifacts (Dorn, 1986), and can also promote the accumula-tion of dust underneath surface cobbles. For example, periodic aeolian deflation helps winnow fines away from desert pavements in the hy-perarid Precordillera of Argentina (Hedrick et al., 2013), even though this deflation must be inactive at present because of the strong presence of rock varnish that would be abraded if deflation was active (Dorn and Oberlander, 1982). In Dakhla Oasis Region in Egypt the pavement was originally generated through deflation, but subsequently developed a strong rock varnish coating and the Av horizon accumulated beneath the chert cobbles

(Brookes, 1993).

Desert pavements formed by processes other than deflation appear to be polygenetic landforms, perhaps exhibiting equifinality, where dif-ferent processes can act over time to generate a similar form. Table 2 compiles the variety of different factors and processes thought to pro-mote the formation of non-defl ation desert pavements. All of the factors presented in Table 2 are consistent with pavement cobbles that are coated with rock varnish (Dorn, 1986). Similarly, if aeolian activity was sufficient to winnow fines, the vesicular Av soil horizon of accumu-lated dust would not exist underneath pavement clasts. Within the last few decades, considerable research has focused on this dust accumula-tion (e.g. Table 3).

2.3. Constraining ages of desert pavements using different approaches

The growth of chronometric techniques in the past few decades has been vital to developing a better understanding of desert pavement lon-gevity. Each employed technique provides a different chronometric per-spective. For example, K-Ar or 40Ar/39Ar ages for a lava flow provide a maximum-limiting age for the pavement formed on top of the flow.

Conversely, varnish microlamination (VML) dating provides insight into when the very surface of a pavement clast last experienced erosion and hence provides a minimum-limiting age for the pavement. Cosmo-genic nuclides generate very different information - often a complex picture of the surface exposure history of pavement clasts. Table 4 pre-sents a compilation of the array of different techniques that have been used to assign ages to desert pavements.

2.4. How long does it take to form a desert pavement?

Advances in dating techniques (Table 4) has resulted in new insight into how long it takes to go from a rough surface, such as the bar-and-swale deposits of a desert flood or a debris flow, to a smooth pavement surface. The length of time required to smooth a surface depends on a number of factors

including: rock type and how the rock is jointed; the original size of the material; rates of aeolian deposition of fines; cli-mate and paleoclimatic changes; percent clays; relief of the deposit; slope; availability of decay agents such as salts; biotic activity; and seis-mic shaking (Cooke and Warren, 1973; Mabbutt, 1979; Dixon, 1994; Haff, 2005; Dixon, 2009).

Given the large number of variables influencing the time it takes to develop a desert pavement, the considerable time range noted Table 5 should not be surprising. Still, an appropriate generalization would be that "well developed" pavements typically initiated during the last gla-cial cycle or before in warm desert settings.

A complication in reading the global pavement literature on the time required to generate a pavement is the subjective use of terms like "smooth", "well packed", "well developed" or "mature" pavement. These and similar descriptive terms are rarely quantified or qualified. Although replicable metrics of pavement development exist (Amit and Gerson, 1986; Al-Farraj and Harvey, 2000), such information is rarely presented along with chronometric results. This is not a critique of those using descriptive terminology, but rather a simple recognition that some of the time variability in Table 5 could be due to the lack of aunified definition of what is a "well developed" pavement.

Yet another issue in trying to reconcile different times required to generate a pavement includes factors that disturb a pavement - either while it is developing or after it has formed - particularly by biotic agen-cies (Musick, 1975; Huckleberry, 1993, 1994; Quade, 2001; Wood et al., 2005; Matmon et al., 2009; Pietrasiak et al., 2014) followed by subse-quent regeneration. One strategy to deal with these interruptions in-volves numerical modeling to illustrate a dynamic steady state (Pelletier et al., 2007). A second reconciliation approach is the hypothe-sis that bioturbation creates a permanent end to pavements. In this view, there are stable desert pavements ("abiotic landform evolution") and then the disturbed pavement that moves towards a "biological landform evolution" pathway; these pathways results in two different landform systems on alluvial fans in locations like the Mojave Desert where both of them are stable: a desert pavement zone and a shrub zone (Pietrasiak et al., 2014). This "fork in the road" hypothesis is con-sistent with mapping of vegetation and soil-geomorphic

surface mo-saics in the Mojave and Sonoran deserts, where abiotic pavements maintain very different leaching depths and soluble salt concentrations than biologically active areas (Musick, 1975; Wood et al., 2005). A third reconciliation strategy - used in our case study of stream terraces pre-sented later in this paper - is to employ both long-lived cosmogenic nu-clides like 10Be and short-lived isotopes like 14C. For example, bioturbation episodes in the last 20,000 years can be recorded by the decay of in situ 14C when cobbles move beneath the surface.

2.5. Evidence for ancient pavements

Table 6 presents the first compilation of a burgeoning array of dating results indicating that desert pavements exist as stable landforms for very long periods of time. Our approach in deciding what research to in-clude in Table 6 is not to be exclusionary. We do not feel it is appropriate to play the role of an international committee to judge which site is truly the "oldest desert pavement" on Earth.

Instead, our goal has been to include all examples we could 詮갌d in prior scholarship of ages for desert pavements. For example, a case could be made that Dunai et al. (2005) do not date a desert pavement, but rather cobbles on a sediment surface and that 21Ne ages of 9 to 37 Ma simply re詮괻ct cumulative time at or near the surface. Still, we felt it appropriate to include these data in Table 6, because images E and F in the associated GSA Data Repos-itory item 2005053 would certainly qualify as a desert pavement if seen as a blind image by most researchers. Similarly, Appendix DR1 in the Data Repository 2009007 of Evenstar et al. (2009) shows a photograph of a surface that is explicitly described as a desert pavement ?쐻overed by clasts ranging in size from pebbles to boulders (~ 1 m)?? Thus, while Evenstar et al. (2009) focused on 3He ages as an indication of Cenozoic climatic change, the paper was included in Table 6 because the sampling context was clearly a desert pavement. Ewing et al. (2006) present 10Be and 26Al exposure times for sur詮갷ial boulders of 2.12 짹 0.05 Ma with erosion rates of 0.160 짹 0.014 m/Ma, and we decided to include this paper, because Fig. 10 in Ewing et al. (2006) present

a graphic of a desert pavement on top of the Yungay soil pro詮ile. Wang et al.(2015: 234) similarly present a graphic of a desert pavement in their model as well as images of a desert pavement at their site location.

Placzek et al. (2014: 1491), in contrast, have a narrower view of what is and what is not a desert pavement when they write "[site 4 in the Atacama Desert] is one of the few desert pavements observed in the Atacama …" A logical next step would be for Placzek et al.(2014) to undertake a critical analysis of the ancient pavement lit-erature laid out in Table 6 and explain in detail their views over which sites are not real desert pavements and why they should be excluded from a compilation of ancient pavement ages.

However, given the basic definition that a desert pavement is a grav-el surface one or two stones thick (Mabbutt, 1965; Cooke, 1970; Mabbutt, 1979), we consider it important to be inclusive in the compi-lation presented in Table 6. Basically, we take the position that if the au-thors identify a desert pavement or if we are able to see a photograph or a graphic indicative of a reasonably classic desert pavement, it is includ-ed in Table 6.

Table 6 similarly does not present a critical analysis evaluating the validity of the various chronometric claims, because the research cited often goes into detail on uncertainties associated with sampling and analysis. Rather, the purpose of this compilation of pavement antiquity rests in revealing the wide variety of methods used to place minimum and maximum ages on pavements. The results of these different methods present a clear and compelling case for the antiquity of desert pavements in a wide variety of global contexts.

3. Case study of the oldest known desert pavement in the Sonoran Desert, North America

3.1. Introduction to the case study

An impressive variety of techniques and results reveal that desert pavement surfaces can survive Earth's dynamic surficial processes for lengthy periods of time ranging from 103 to over 106 years (Table 6). Pavement scholarship typically presents only brief explanations for this stability. For

example, in a title arguing that “[d]esert pavement-coated surfaces in extreme deserts present the longest-lived landforms on Earth”, Matmon et al. (2009: 688) attributed this extreme geomor-phic stability to the “combination of long-term hyperaridity, absence of vegetation and bioturbation, and the rapid reduction of original chert and carbonate clasts into a full-mosaic of pebble-size desert pavement.” While Matmon et al. (2009) make a compelling case for their hyperarid Middle Eastern setting, our point is that research into explanations for pavement stability must include more than hyperarid conditions and should encompass ancient desert pavements around the globe whose antiquity cannot be explained by these factors alone.

This case study focuses on the Sonoran Desert, North America, in part because it is not hyperarid and can experience bioturbation. Annual precipitation averages 208 mm and is evenly divided between winter and monsoon maxima. Winter rainfall comes from Pacific low-pressure systems. Summer rainfall derives from summer thunderstorms during the July - September monsoon season where air masses come from the Gulfs of Mexico and California. Aeolian activity consists of dust storms associated with downburst winds. Very little evidence of aeolian abra-sion exists in the Sonoran Desert outside dune fields such as the Cactus Plains wilderness or the Gran Desierto de Altar. The general aridity of the Sonoran Desert and the abundant dust deposition both contribute to the stability of desert pavements in this desert.

This case study focuses on the discovery of the oldest known desert pavement in the Sonoran Desert at ~332 ± 4 ka; we evaluate this pave-ment survived for 105 years, whereas pavements on older nearby land-forms did not. Then, after this case study, we conclude this paper by reanalyzing factors that contribute to pavement longevity, and con-versely, factors that contribute to the desert pavement instability.

3.2. Study site: Desert pavements on Salt and Verde Terraces, central Arizona, USA

Strath and fill terraces of the Salt and Verde Rivers (Pope, 1974; Péwé, 1978; Skotnicki et al., 2003; Cook et al., 2010; Larson et al., 2010) offer a setting

to understand the longevity of desert pavements. Located in the north-central Sonoran Desert (Fig. 2), near Phoenix, Ari-zona, USA flights of terraces offer a range of landforms in a classic rela-tive age sequence (Figs. 3, 4a, b). A relative sequence of oldest terrace (highest) to youngest terrace (lowest) offers an independent check on numerical ages for desert pavements formed on terrace treads.

Prior research on the ages of these terraces provided only minimal chronometric information: (1) a minimum age for the Blue Point terrace of the Salt River of 33,100 ± 380 calendar years, based on radiocarbon dating of an innermost carbonate rind with a laminar texture around gravel in the Bk horizon underneath the desert pavement (Larson et al., 2010); and (2) a single unpublished preliminary 36Cl surface expo-sure age of ~440 ka for amalgamated pavement cobbles collected from the Salt River's Mesa terrace (Campbell, 1999) using unknown production rates. Thus, to improve the quality and the quantity of age control on pavements atop the stream terraces, we employed cosmo-genic 10Be, 14C, and 26Al dating strategies to better understand the ages of desert pavements on this terrace sequence.

We sampled four terraces along the Salt River and two terraces along the Verde River for study (Fig. 4). Fig. 5 shows oblique aerial views of the terraces with desert pavements analyzed with 10Be, while Figs. 6 and 7 present 3 views of each sampling site: a ground view of the sampled de-sert pavement; a close-up showing the shape and dimensions of the sampled quartzite cobbles; and a cross-sectional perspective of the pavement and geological material underlying the terrace gravels.

3.3. Methods

3.3.1. Cosmogenic 10Be, 14C analysis of pavement clasts

3.3.1.1. Sampling

Research on the pediment systems of the region previously present-ed 10Be data for desert pavement cobbles on the Blue Point and Mesa terraces (Fig. 4; Fig. 6A - F) of the Salt River (Larson et al., 2017). This case study

greatly enlarges the data set on cosmogenic 10Be and 14C analyses for these and cobbles on four other stream terraces: Sawik and Stewart Mountain terraces of the Salt River; and Mesa and Lousley Hills terraces of the Verde River (Fig. 4; Figs. 6G - L; 7).

An ongoing literature discussion exists on the best types of samples to collect from desert pavements in order to constrain the age of the un-derlying landform. Strategies include collecting the largest boulders, collecting pebbles in different size fractions, collecting amalgamated samples, collecting depth profiles, and using different cosmogenic nu-clides (Zimmerman et al., 1994; Anderson et al., 1996; Heimsath et al., 2001; Fujioka et al., 2005; Frankel et al., 2007a; Blisniuk et al., 2010; Owen et al., 2011; Jungers et al., 2013; Boroda et al., 2014; Gray et al., 2014).

The approach utilized here for stream terraces with a flat topography covered by desert pavement starts with the collection of individual quartzite clasts on the surface of desert pavements (Figs. 6 - 7). Field ob-servations reveal that dust is trapped efficiently underneath pavement cobbles with this fl attened shape (Goosens, 1995). Following prior scholarship that dust flotation helps maintain pavements collected clasts have a disk shape such that a flat surface rests on the Av horizon that has its origin in dust (see Section 2.2). The collected clasts also re-tain the original fluvially-abraded texture of smooth rounded edges. Thus our working hypothesis while in the field was that these quartzite disks have remained exposed to cosmic rays since their initial abandon-ment, floated by allochthonous aeolian dust input. Two sites, however, did not display an Av horizon indicative of a dust origin: Stewart and Lousley Hill pavements.

In situ accumulation of 14C in quartz offers a test of the hypoth-esis that pavement cobbles have remained at the surface for the last ~20 ka. Because of the much shorter half-life of 14C, burial by aeolian deposits or by bioturbated fines deposited on top of pavements would result in greater decay of 14Cthan10Be (Lal, 1991). In contrast, a lower ratio of 10Be/14C results from continuous exposure on the surface. Thus, in situ 14C was measured in some of the same cobbles analyzed for in situ 10Be in the Sawik terrace pavement.

Older and higher alluvial surfaces often do not retain a flat topogra-phy with

extensive desert pavements (Frankel and Dolan, 2007; Hedrick et al., 2013). This is the case for the Stewart Mountain (Fig.5F) and Lousley Hills (Fig. 5D) terraces. While patches of pavements ex-tensively cover the surface of these terraces (Figs. 6J, 7D), the lack of an Av horizon (and sand instead) could potentially reflect an origin derived through erosion of the terrace fill.

Assessment of the prior exposure history utilized roadcuts of over 5 m expose cross-sections at two of the terrace sites (Mesa Salt, Mesa Blue Point), and natural gullies expose cross-sections of over 3 m that were cleaned up prior to sampling. An amalgamation strategy involved collection of N30 quartz-rich cobble clasts buried with over 3 m of shielding to evaluate the prior exposure history. A pair of 10Be/26Al analysis for the buried amalgamation sample taken from the Sawik terrace was accomplished to constrain the burial ageof the terrace(Granger, 2006).

3.3.1.2. Treatment and analysis

All samples were treated in the Cosmogenic Nuclides Laboratory of Korea University, following the standard method (Kohl and Nishiizumi, 1992). Crushed samples were sieved to the 250 - 500 μm using 6MV Accelerator Mass Spectrometry (AMS) at the Korea Institute of Science and Technology (KIST), Seoul, Korea (Kim et al., 2016).

After blank (3 × 10−15 10/9Be) correction and normalization of isotope ratios to 10Be standards (Nishiizumi et al., 2007) using a 10Be half-life of 1.387 (± 0.03) × 106 yr (Chmeleff et al., 2010; Korschinek et al., 2010) we converted measured ratios into an abso-lute ratio of 10Be/9Be in quartz. Inheritance produced during prior exposure was quantified from amalgamated cobbles (n N 30) obtain-ed from deep (N5 m) location and corrected for surface samples. We calculated 10Be exposure ages using the CRNOUS exposure age calcu-lator version 2.2 (Balco et al., 2008) by integrating shielding condi-tions, latitude-altitude production rate-functions (Lal, 1991; Stone, 2000; Heisinger et al., 2002a; Heisinger et al., 2002b) applying 4.49 ± 0.39 g−1 y−1 at SLHL (sea-level, high-latitude) for the 10Be reference spallation production rate in this study (Stone, 2000; Balco et al., 2008). In addition, we also yielded 10Be exposure ages applying local production rate of North America recently reported

for compari-son using a spallogenic production rate of 4.33 ± 0.21 g−1 y−1 at SLHL (Balco et al., 2009). The difference between global and regional production rates causes 3.58 - 3.89% in ages but we used the ages calcu-lated using global production rate for the easiness of comparison with the previous studies. Propagated errors in the model ages include a 6%uncertainty in the production rate of 10Be and a 4% uncertainty in the 10Be decay constant.

Some of samples that were analyzed for 10Be were also analyzed for in situ 14C. The quartz cleaned in the Cosmogenic Nuclide Labora-tory of Korea University were analyzed in the chemical lines modi-fied from the previous in situ 14Cextractionsystems (Lifton et al., 2001; Naysmith, 2007; Hippe et al., 2009; Pigati et al., 2010; Hippe et al., 2013; Goehring et al., 2014; Kim et al., 2016). Approximately 5 g of clean quartz was loaded with melting flux (LiBO2)inanalumi-na (Al2O3) boat that had been pre-melted in high-vacuum conditions and then preheated with a step-wise increase of temperature, at 500 °C for 1.5 h and at 750 °C for 1.5 h, to remove atmospheric 14C contamination. In situ 14C trapped in the quartz lattice was degassed and oxidized at 1100 °C for 3 h with ultrahigh-purity O2, followed by subsequent cleaning steps with secondary oxidation in a quartz-bead combustion furnace and a cryogenic coil trap (Lifton et al., 2001; Naysmith, 2007; Pigati et al., 2010). The purified CO2 was graphitized and then loaded into targets. The targets were also ana-lyzed by AMS at KIST. The measured ratios were normalized to NIST oxalic acid (14C/12C: 134 pMC, δ13C=−17.8‰)andconvertedto14C concentrations after correcting for blank readings (mean of (5.99 ± 2.58) × 105;n =3).

3.3.2. OSL dating of the Blue Point Salt River terrace

OSL samples from the Blue Point terrace of the Salt River (Fig. 5A) were collected from the same study site as the prior study on carbonate rind radiocarbon dating (Larson et al., 2010). This is a strath terrace where bedrock granite is overlain by approximately 3 - 6 m of sediment (Fig. 6C). This alluvium is mostly gravel, but there are sandy lenses, and these were where the OSL samples were collected. Desert pavement cobbles of quartzite were collected for 10Be analysis at the surface a few meters away from this OSL sampling

location (Fig. 6A – B).

The samples were obtained by driving a stainless pipe, 25 cm in length and 7 cm in diameter, into the freshly exposed sand walls of the profile. The end of the pipe was quickly capped with aluminum foil upon retrieval, and the sample stored in a dark container. The samples were prepared and analyzed at the Korea Basic Science In-stitute (KBSI), Ochang, Korea using the single-aliquot regenerative-dose (SAR) protocol (Murray and Wintle, 2000). The SAR protocol for the optical measurements of quartz results in improved precision and accuracy for age determinations (Murray and Wintle, 2000; Murray and Olley, 2002). In the laboratory, samples were wet sieved to recover the 90 – 250 μm size fractions, and cleaned in 10% H2O2, 10% HCl, etched with concentrated HF, and the separated grains were pretreated for the preparation method of the SAR protocol of KBSI (Choi et al., 2003). All OSL measurements were performed using an automated Risø TL/OSL measurement system. Error is yielded based on saturated water contents.

3.3.3. Soil profile and rock varnish microlaminations

Standard USA Department of Agriculture guidelines were used to describe soil profiles (SoilSurveyStaff, 1974). Development of calcium carbonate horizons uses the desert soil project monograph stage classi-fications (Gile et al., 1981). The second author only provided field assis-tance in the previously unpublished soil profile analysis conducted by Troy Péwé (now deceased).

We also employed varnish microlaminations (VML) dating using established collection and calibration procedures (Liu and Broecker, 2008b, 2013; Liu, 2016). Ten samples for VML were collected from the Blue Point, Mesa, and Sawik terraces of the Salt River from the same pavements sampled for 10Be dating. Since VML can only pro-vide the age sequence of varnishes exposed at the surface, any bio-turbation or cobbles spalling eventwouldresetthe VMLclock; hence VML can only provide a minimum-limiting age for the desert pavement. Thus, the oldest VML age provides a minimum age for the underlying desert ω pavement.

3.3.4. Strontium isotopes to assess the origin of the Av horizon

Dust deposition occurs regularly in association with Arizona sum-mer monsoon season (Brazel, 1989; Marcus and Brazel, 1992). Further-more, the strong seasonality of natural flows in the Salt and Verde Rivers produced extensive braided floodplains for local deflation of desiccated suspended sediment (Honker, 2002). Thus, the terraces of the Salt and Verde rivers would have been subjected to both locally and regionally derived dust. Because strontium isotopes have the potential to discrim-inate source materials (Capo et al., 1998; Capo and Chadwick, 1999), 87Sr/86Sr ratios assessed the hypothesis that the fine material under-neath terrace desert pavements derived from this dust and not the un-derlying alluvial deposit

A Nuclide 1290 mass spectrometer measured 87Sr/86Sr ratios in the following types of samples collected in a depth profile from the surface down:

- dust collected from the surface depressions of pavement cobbles;
- the upper half of the Av horizon;
- the lower half of the Av horizon;
- for the Stewart Mountain and Lousley Hills terraces lacking an Av horizon, A horizon medium sand collected directly underneath surface clasts; some cobbles from the Mesa Verde terrace also lacked an Av, and sand was collected under these cobbles
- Bw horizon material collected ~5 cm underneath the A or Av horizon
- Bk horizon material collected ~50 cm underneath the surface
- amalgamation of three sets of 10 cobbles, then subject to HCl to re-
- move carbonate rinds, and then pulverized; collected ~50 cm under-neath the surface

Each of these samples were separated into the acetic acid-soluble fraction that represents carbonate and labile Ca and the silicate fraction. Samples were normalized to the 87Sr/86Sr ratio of 0.1194 and compared to the Eimer and Amend standard (0.7080).

3.4. Results

3.4.1. Cosmogenic nuclides

10Be exposure ages of the terraces and their scatters are widely dif-ferent depending on their locations and characteristics (Table 7). The Mesa and Blue Point terrace 10Be ages for pavement cobbles were pub-lished previously (Larson et al., 2017) in the context of a study of pedi-ments graded to these terrace remnants. The other data in Table 7 are new. Relatively, the strath terraces in the Salt River are better constrained in that they have 8 - 80 times lower Mean Square Weighted Deviation (MSWD or reduced chi-square in Fig. 4) than the ones in the Verde River. Pavement cobbles have weighted means of 30.7 ± 1.0 ka, 85.8 ± 2.0 ka, 332.0 ± 4.1 ka for Blue Point, Mesa, and Sawik terraces, respectively, whereas pavement cobbles on the topographically higher (and clearly older) Stewart Mountain terrace yields much younger age (82.7 ± 2.4 ka) than expected, based on the relative stratigraphy (Fig. 4).
Pavement cobbles on the terraces in the Verde River yield much younger ages with greater scatter than the coeval levels of terraces in the Salt River. The age of cobbles on the Mesa Verde terrace are widely scattered with weighted mean age of 46.0 ± 23.2 ka. We highlight that the highest and hence oldest terrace on the Lousely Hill (Fig. 4)yields the youngest ages for pavement cobbles (16.6 ± 1.1 ka).

Probability plots (sometimes called camel plots) have been a stan-dard way of visualizing exposure ages in using cosmogenic nuclides for dating (Small and Fabel, 2016). The camel plots for the terrace pave-ments shown in Fig. 8 display two types of information. The dashed lines show the individual probabilities for each pavement cobbles. By convention, uncertainties used to generate individual probability curves are 1? analytical uncertainties. The thicker solid line shows the cumulative probability. The cumulative probability line allows the read-er to quickly visualize the distribution of ages. For example, the Sawik terrace (Fig. 8C), single hump in the probability plot implies that the sampled gravels would have been relatively stable on the surface since the timing of terrace abandonment (332.0 ± 4.1 ka). In contrast, the multiple humps for the topographically higher Stewart Mountain terrace suggests that the sampled pavement cobbles periodically eroded out of the underlying alluvium

between 50 and 120 ka.

After obtaining initial 10Be abundance produced during prior ex-posure from a mixture of gravels (n N 30) at depth (N5 m) for desert pavement cobbles on the Sawik terrace, its 26Al abundance was also measured to constrain the burial age of the terrace deposit. The age calculation assumes one depositional event with zero surface ero-sion (Fig. 9). The sample of buried gravels was collected from a road cut directly on top of the granitic strath (Fig. 6I) and first pro-vides a maximum age for the overlying pavement. One scenario is that the analyzed sediments experienced some history of prior burial before being finally deposited on the Sawik strath – setting a lower ratio of 26Al/10Be than the continuous exposure case with ratio of ~ 6.7. A second scenario is that the burial age reflects the timing of when the ancestral Salt River last abraded this granitic strath and that the very surface of the Sawik terrace was abandoned well after deposition of these buried cobbles. Any combination of different factors (burial age could be younger than the ~ 552 ka maximum; some surface erosion occurred prior to pavement stabilization; lengthy time between deposition of buried cobbles and abandon-ment of terrace) could also explain the ca. 220 ka time difference be-tween the burial age (Fig. 9) and the surface exposure age of pavement cobbles (Fig. 8C).

In an effort to better constrain the exposure history of cobbles on top of the Sawik pavement, we also analyzed in situ 14Cinthe quartz-ite cobbles in the same three cobles also measured for 10Be buildup (Table 8). Bioturbation burying the cobbles for a period of time would reduce the in situ 14C below levels of saturation. However, if the cobbles remained at the surface for the last ~ 20 ka, in situ 14C would be at saturation and all samples would plot in the steady-state erosion island of Lal (1991).

Two of three samples were measured successfully, and both cobbles (Sawik017 and Sawik020) are plotted in the steady-state erosion island within uncertainty. Thus, it is likely that both cobbles experienced lim-ited burial for a time N1 ka during the last ~20 ka (Fig. 10). The most likely cause would be accumulation of aeolian material from the nearby Salt River floodplain. The burial could have been one event a bit more than a millennia or repeated burial events lasting centuries or decades. Although it is difficult to be certain from

just two measurements, the ability to track the burial history of pavement cobbles using in situ 14C opens up an entirely new strategy to understand the trajectories of rocks in all different types of surficial cobbles – whether the cobbles occur in warm desert pavements or archaeological quarries. In this case, burial about 5% of the time in the last 20,000 years indicates that flotation by dust must not be the only process in operation.

3.4.2. OSL

The OSL ages of the two Blue Point terrace samples (Table 9) are con-sistent with the 10Be cosmogenic nuclide ages for the pavement cobbles of 30.7 ± 1.0 ka (Table 7), since the deposition of the sandy lenses un-derneath the surficial cobbles should predate terrace abandonment and the start of pavement formation. Similarly, these new results are consistent with the calibrated 14C age of 33,100 ± 380 calendar years for the innermost carbonate rind around gravel in the Bk horizon (Larson et al., 2010), since this pedogenic Stage 1 carbonate only started to form after the strath terrace surface was abandoned upon Salt River incision.

3.4.3. Soil profiles and varnish microlaminations

Soil profile analyses (Table 10) presents the sequence of soil devel-opment on the Mesa River terraces. The depth of the profile was limited for the Mesa and Sawik terraces by encountering a Stage IV petrocalcic horizon, but the Stage I development in the Blue Point reached a depth of 70 cm.

Table 10 presents only the oldest VML ages obtained from three ter-races of the Salt River. Because cobble spalling resets the varnish clock, all younger ages only reflect the spalling event. The oldest VML calendar age for the Blue Point terrace of 30 ka (Table 5) is slightly younger than the calibrated 14C age carbonate rind age, the 10Be surface exposure age on pavement cobble, and is substantially younger than the OSL ages for sandy deposits beneath the pavement. Thus, the sampled cobble stabi-lized at the surface by at least 30 ka.

The oldest VML calendar age for the Mesa terrace of calendar 74 - 85 ka (Table 5) is consistent with 10Be surface exposure age on pave-ment cobbles. Again, this minimum exposure age means that the sampled cobble stabilized at the surface at least in the time range of 74 - 85 ka.

The oldest VML calendar age for a cobble sampled from the Sawik terrace is 74 - 85 ka (Table 10). This is much younger than the 10Be sur-face exposure age on pavement cobbles, meaning that the surface of the cobbles have been experiencing spalling of at least a millimeter of rock to reset the varnish clock.

3.4.4. Strontium isotopes to assess the origin of the Av horizon

The 87Sr/86Sr analyses of the carbonate and silicate fractions of dust collected from depressions on pavement rocks rests at one end with 87Sr/86Sr ratios ~ 0.71 (Table 11 and Fig. 11). In contrast, the pulverized rock material making up the terrace alluvium main-tains very different 87Sr/86Sr ratios ranging from ~ 0.73 to ~ 0.75. In interpreting the results in Fig. 11, we consider the dust and pulver-ized alluvium to be "end members".In Fig. 11 the pulverized clasts sampled from a 50 cm depth show 87Sr/86Sr ratios ranging from 0.73 to 0.75. In contrast, dust resting on the surface has 87Sr/86Sr ra-tios centered around 0.71.

With the perspective of dust at one end of the 87Sr/86Sr spectrum and the host rock material of the terrace alluvium at the other end, some basic qualitative inferences can be made. (a) The carbonate frac-tion extracted in the HCl leachate in all materials appears to derive mostly from the dust, although a small amount of the carbonate in the Bw and Bk horizons could derive from calcium chemically dissolved from terrace alluvium. (b) The silicate fraction in the Av horizons de-rives from dust. (c) The silicate fraction of the sandy A-horizon under-neath Lousley Hills, Stewart Mountain, and a few Mesa Verde cobbles appear to derive from the alluvium; and (d) the silicate fraction of the Bw and Bk horizons yields a mixed signal and appears to derive from both infi ltrating dust and alluvium.

The 87Sr/86Sr analyses presented in Table 11 and Fig. 11 indicate that

there are two sources for the fines underneath the studied Sonoran De-sert pavements. The 87Sr/86Sr analyses of the Av horizons and the car-bonate fraction shows a clear aeolian signature. In contrast, alluvium-sourced materials contribute to Bw, Bk, and sandy A-horizons where Av-horizons are lacking.

4. Factors involved in desert pavement longevity or mortality

4.1. Minimal surface topography

The desert pavement atop the Sawik terrace of the Salt River (Fig. 6G - I) is the oldest known pavement in the Sonoran Desert at ~332 ± 4 ka, and the desert pavement atop the Mesa terrace of the Salt River (Fig. 6D-F) is the second oldest known pavement at ~86 ± 1 ka. Both Sawik (Fig. 6G-I) and Mesa (Fig. 6D-F) terrace fragments have in common low slopes, of less than a degree.

Low relief has long been known to be important in pavement sta-bility (Cooke, 1970; Peterson, 1981; Dixon, 1994). Stable Negev De-sert pavements have little local relief (Dan et al., 1982; Matmon et al., 2009; Amit et al., 2011), as does the N3 Ma old pavement in the Atacama Desert (Placzek et al., 2014) as well as ancient pavements elsewhere (Fukioka and Chappell, 2011). Pavement genesis smooth-ing processes play a role in promoting low relief and proceed on al-luvial fans in the Mojave Desert for ~ 56 ka (Oskin et al., 2007), in Death Valley for ~ 70 ka (Frankel and Dolan, 2007), and for N280 ka in the Coachella Valley (Matmon et al., 2006).

In contrast, sloping surfaces in the Cima Volcanic field (Wood et al., 2005) and in the Libyan Desert (Adelsberger and Smith, 2009; Adelsberger et al., 2013) are associated with pavement instability. The rounding of alluvial fans has long been known as a cause of pave-ment instability (Field and Pearthree, 1997). This is certainly the case for the two highest terraces of the Salt (Fig. 5F) and Verde Rivers (Fig. 5D). The Stewart Mountain and Lousley Hills (Fig. 4) high terraces host gently rounded hillcrests well above the surrounding topography. The ongoing exposure of previously buried clasts is a common and reasonable explanation for clast 10Be ages (Fig. 8D, F) far younger than their

geomorphological position would indicate.

4.2. Hyperaridity

The oldest known pavements occur in regions experiencing long-term hyperaridity (Matmon et al., 2009; Placzek et al., 2014; Wang et al., 2015). Gypsum (and carbonate) precipitation contributes to pave-ment stability in hyperarid regions of the Negev Desert (Amit et al., 2010; Boroda et al., 2013), Precordillera of Argentina (Hedrick et al., 2013), and Atacama Desert in Chile (Dunai et al., 2005; Clark, 2006; Evenstar et al., 2009; Matmon et al., 2009; Wang et al., 2015).

Our case study of Salt River and Verde River terraces exist pave-ments, however, exist in a region that experienced conditions other than aridity in the past. The terraces sites in Sonoran Desert experienced prolonged semi-arid conditions during the last glaciation (McAuliffe and Van Devender, 1998). Similarly, the ancient pavements on Nevada lava flows (Zreda et al., 1993; Heizler et al., 1999; Valentine and Harrington, 2006; Valentine et al., 2006) experienced much wetter con-ditions during the last glacial cycle (Wells, 1983; Benson and al, 1990). In another example, pavements that are ~71 - 72 ka in Wyoming (Anderson et al., 1996) experienced several glaciations in the area (Phillips et al., 1997). Thus, while hyperaridity appears needed for the survival of pre-Quaternary pavements, it is clearly (Table 11)not are-quirement for Pleistocene antiquity.

4.3. Ongoing input of allochthonous dust

Strontium isotope data collected at the Sawik and Mesa terrace sites reveals the presence of dust on pavement cobbles, under pavement clasts in the Av horizon, and infiltrating down into the Bw and Bk soil horizons (Table 11 and Fig. 11). Mineralogical analyses on Av horizons in southern Jordan similarly revealed an aeolian origin (Ugolini et al., 2008). These findings are similar to the Mojave and western Sonoran Deserts, where the source of the aeolian material in vesicular horizons derives from distal washes of alluvial fans as well as

playas (Sweeney et al., 2013). Consistent with our 10Be age of ~335 ka for the Sawik ter-race, flotation of desert pavements by dust accumulation (Mabbutt, 1977; Mabbutt, 1979; Gerson and Amit, 1987; McFadden et al., 1987) plays a key role in pavement stability according to other cosmogenic nu-clide and OSL studies (Shepard et al., 1995; Wells et al., 1995; Matmon et al., 2009; Guralnik et al., 2010; Amit et al., 2011; Fisher et al., 2014; Fuchs et al., 2015; Wang et al., 2015).

Concomitantly, the Sonoran Desert terrace case study also reveals that pavements that are not floated by dust and are instead underlain by sand are not stable geomorphologically. Pavements underlain by sand on the Stewart Mountain, Lousley Hills, and the Mesa terrace along the Verde River (Table 11 and Fig. 11) experience ongoing erosion and cosmogenic ages far younger than their geomorphic position (Fig. 8E-F). In these settings, the sand has a strontium-isotope signal consis-tent with derivation from the underlying terrace alluvium and not infil-trated dust (Table 11 and Fig. 11).

4.4. Lack of headward-retreating swales

The Sawik and Mesa terrace remnants do not display evidence of headward-retreating gullies or even swales. Even subtle swale develop-ment on terraces can mix highly and more recently exposed cobbles in the Tian Shan, China (Huang et al., 2014), as well as Oman and UAE (Al-Farraj and Harvey, 2000). In Death Valley, USA, “[g]ully incision into units older than 70 ka occurs, decreasing pavement stability as the fan material erodes” (Frankel et al., 2007a). However, the pavement on the Mesa terrace along the Verde River (Fig. 7A) shows signs of instabil-ity due to development of swales on its surface, likely exposing formerly buried clasts and generating the age distribution seen in Fig. 8E.

4.5. Lack of or minimal biotic disturbance

Matmon et al. (2009) emphasized a lack of biotic disturbance as a possible explanation for long-lived pavements. Bioturbation has long been known

to impact the stability of desert pavements (Parker, 1991; Huckleberry, 1993, 1994; Quade, 2001). Research in the Mojave Desert indicates that there could be two distinct pathways for surface evolution in a desert: “abiotic landform evolution” and “biological land-form evolution”, where each pathway results in different landform sys-tems on alluvial fans (Pietrasiak et al., 2014). This “fork in the road” hypothesis works well with vegetation and soil-geomorphic surface mosaics in the Mojave and Sonoran deserts (Musick, 1975; Wood et al., 2005).
In the Sonoran Desert case study, we purposefully avoided locations of active bioturbation and old plant scars (Dickerson and Cocks, 2015). In Arizona, increases in elevation and a greater abundance of perennial plants in cooler and wetter conditions are generally associated with a reduction in a landform's maintenance of a desert pavement above an elevation of 550 m (Huckleberry, 1993, 1994).

A similar elevation-based trend has been noted elsewhere in the southwestern USA (Quade, 2001). The exact mechanism of pavement disturbance varies from site to site. Animal foraging activities disrupts desert pavement on the Salt and Verde terraces on unknown timescales, but these disturbances are rare (inferred to be on millennial time scale) in Death Valley (Haff, 2001). At Stonewall Flat Nevada, sand and silt ac-cumulating around larger shrubs host animal burrows (Dickerson et al., 2013). We also noticed soil biological crusts associated with pavement disturbance, and older alluvial surfaces where pavement has started to erode develops scattering of moss-lichen biological soil crust pinnacles (Williams et al., 2013). Thus, while some argue for a climate limit to pavement survival (Quade, 2001), we view site selection to be critically important in understanding pavement age limits as evidenced by re-search demonstrating that ancient pavements can and do occur outside Quade's (2001) climatic limits (Anderson et al., 1996; Valentine and Harrington, 2006).

4.6. Bedrock beneath the pavement

Locations where bedrock exists directly underneath pavements can lead to long-term stability. Mabbutt (1977) recognized that the hamadas and gibber

plains formed on top of bedrock tend to be stable. Buildup of 10Be in pavement clasts atop bedrock mesas in the hyperarid Negev of Israel indicates that bedrock can protect pavements for as long as 305–331 ka on small bedrock mesas and for as long as 1.1 Ma for bed-rock mesas with widths N60 m (Boroda et al., 2014). Basalt bedrock oc-curs under ancient pavements in the Great Basin (Zreda et al., 1993; Shepard et al., 1995; Heizler et al., 1999; Valentine and Harrington, 2006; Valentine et al., 2006) and Mojave (Shepard et al., 1995) deserts of the USA, as well as in the Canary Islands (Dunai and Wijbrans, 2000).

ThecasestudyofpavementsonSalt andVerdeterracesprovide support for the importance of bedrock for pavement stability. The lo-cations where we sampled the ~ 335 ka Sawik pavement (Fig. 8C) and the ~ 83 ka Mesa pavement (Fig. 8B) sit directly on strath ter-races in the Sonoran Desert; granitic bedrock rests ~ 5 m underneath these pavement (Fig. 6C, F, I). In contrast, the Mesa terrace on the Verde River (Fig. 7C) and the Lousley Hills (Fig. 7F) terrace on the Verde River rest directly on playa clays. The age distribution of 10Be dated clasts (Fig. 8E–F) show the greatest degree of variability – ex-plained by the geomorphic instability of playa sediment.

The Stewart Mountain terrace gravels rest on top of fanglomerate (Fig. 5F). Quartzite clasts sampled atop the Stewart Mountain terrace (Fig. 6J-L) exhibit a distribution of 10Be ages (Fig. 8D) with exposure ages centered at ~58 ka, ~80 ka, and ~110 ka. These ages are similar to other studies of pavements atop fanglomerate. A case study from the Mojave Desert alluvial fan points to pavements surviving until about 53–63 ka when the surface form of the alluvial fan begins to round (Oskin et al., 2007) due to ongoing gully incision. A maximum age for pavements on fanglomerate in Death Valley appears to be ~ 70 ka (Owen et al., 2011), while a Coachella Valley site could reach 260 ka (Matmon et al., 2006). Thus, for fanglomerate, ongoing erosion leads to clast exposure from beneath the pavement increasing the vari-ability in cosmogenic ages (Frankel et al., 2007a).

4.7. Landform type

Landform type and setting may influence pavement stability. For ex-ample, flat wadi terraces are more stable than nearby alluvial fan pave-ments in the Libyan Desert (Adelsberger and Smith, 2009). The strath terraces of the Sawik and Mesa sites in the case study are the most stable in the Sonoran Desert. In the Precordillera of Argentina, alluvial fan pavements reach the end of their longevity after ~61 ka, but strath ter-races can last to at least 181 ka (Hedrick et al., 2013). Placzek et al.(2014: 1503) note that bedrock, sediment on hillslopes, boulders on lower slopes and sediment in channels maintain different patterns of 10Be accumulation in hyperarid, arid, and mesic climates. Table 6 in-cludes the type of landform hosting desert pavements with reported ages around the globe, and ancient pavements are associated with ba-salt flows in arid regions (Wells et al., 1985; Shepard et al., 1995; Dunai and Wijbrans, 2000; Valentine and Harrington, 2006; Fenton and Niedermann, 2014) and with pediments in the Atacama Desert (Hall et al., 2008; Evenstar et al., 2009) and Australia (Fisher et al., 2014). A limitation of Table 6 is that cosmogenic nuclide studies only rarely focus on pavement antiquity. Pavements on top of landforms like alluvial fans (Nishiizumi et al., 2005; Wang et al., 2015) or alluvial plains (Matmon et al., 2009) provide an opportunity to generate mini-mum-limiting ages for the underlying form.

4.8. Clast size and shape

Reduction in clast size is associated with pavement stability in cold desert settings in Antarctica (Bockheim, 2010), in the hyperarid Negev (Matmon et al., 2009), in the hyperarid Sahara Desert (Adelsberger and Smith, 2009), basalt flows in semi-arid Nevada (Valentine et al., 2006), and in the Sonoran Desert (Huckleberry, 1993, 1994).

Unstable pavements on alluvial deposits can see an increase in clast size, as erosion can expose larger-sized clasts from alluvial-fan gravels (Frankel and Dolan, 2007). This is the case for sloping surfaces in north-central Chile (Rodriguez et al., 2013a), in the Cima volcanic field of the Mojave Desert (Wood et al., 2005) and the Libyan Plateau of Egypt (Adelsberger and Smith, 2009). However, in the case study of the Salt and Verde terraces, the most stable

Sawik and Mesa pavements are composed of quartzite alluvium with the original rounding from fluvial abrasion (Fig. 6B - F) that have not experienced clast-size reduction. The Sawik and Mesa terrace pave-ment cobbles have an oblong shape, many retaining their fluvially abraded and rounded edges. Because the short axis is much less than the long and intermediate axes, the cobbles have a flat shape.

Field experiments indicate that dust is trapped underneath pave-ment cobbles most efficiently when they are flattened and elongated (Goosens, 1995), and strontium isotope data from the oldest Sawik and Mesa terraces reveals that dust infiltrated down into the soil to depths of 50 cm (Fig. 11) - perhaps through process of moving down the fractures between peds (Anderson et al., 2002). Thus, while clast size reduction is generally important to pavement stability, it is not completely necessary - at least where clast shape works in tandem with dust trapping.

5. Conclusion

Ancient landforms hold value in Earth science, in part because they provide insight into the processes by which landscapes evolve. This is particularly true for desert pavements, where pavements are often a starting point for sorting out webs of complex age relationships. In some cases, pavements can provide key evidence for the timing of cli-matic transitions such as in Australia (Fujioka et al., 2005) or the south-ern Levant deserts (Amit et al., 2011). Old pavements compose a part of a complex Quaternary system of desert soils and desert biota (Peterson, 1981; Peterson et al., 1995; McFadden et al., 1998; Young et al., 2004; Wood et al., 2005). Many Earth scientists walking across old pavements have seen abundant evidence of past occupants in the form of scattered stone tools or altered surfaces (Adelsberger and Smith, 2009; Latorre et al., 2013; Foley and M.M., 2015; Honegger and Williams, 2015). Thus, the general issue of pavement longevity connects to a variety of Earth science fi elds of study. This paper reviews scholarship on the evidence for and reasons for pavement longevity; then, this paper contextualizes prior scholarship through the lens of a case study of pavements along the terraces of the Salt and Verde

Rivers, Sonoran Desert, Arizona, USA.

Just as alluvial fans have “personalities” in their behavior that vary with drainage basin characteristics of rock type, relief, drainage density, vegetation change, present-day climatology, paleoclimatology, land-use and more (Committee on Alluvial Fan Flooding, 1996), so do desert pavements. A unified theory of pavement longevity, unfortunately, can-not be extracted from our analysis of scholarship or from our study of pavements on terraces of the Salt and Verde Rivers. A great number of factors require consideration in understanding a desert pavement's geo-morphic longevity or instability, and even the relative importance of these factors appear to shift from site to site. This concluding section of the paper attempts a general synthesis by grouping survival factors into three general categories: vital factors; key factors; and site-specific factors.

5.1. Vital factor in long-term pavement stability

Scholarship on pavements reveals one vital factor promoting pave-ment longevity: long-term hyperaridity that minimizes disturbance (Matmon et al., 2009). The oldest known pavements occur in regions that presently experience hyperaridity (Matmon et al., 2009; Placzek et al., 2014; Wang et al., 2015). Gypsum (and carbonate) precipitation may be a key mechanism of pavement survival related to hyperarid re-gions (Dunai et al., 2005; Clark, 2006; Evenstar et al., 2009; Matmon et al., 2009; Amit et al., 2011; Boroda et al., 2013; Wang et al., 2015). Clast-size reduction (Matmon et al., 2009)isalsoassociatedwithlong-term hyperaridity.

5.1.1. Key factors in Pleistocene pavement stability

Several key factors promote the survival of Pleistocene pavements for 104 to 105 years: allochthonous dust floating the pavement; flat to-pography; and a lack of headward-retreating swales or gullies.

1. Allochthonous dust floating pavement clasts. Dust infiltrating be-neath

desert pavements and keeping them at the surface – first rec-ognized in Australia (Mabbutt, 1977; Mabbutt, 1979) and replicated globally (McFadden et al., 1986; Gerson and Amit, 1987; McFadden et al., 1987; Sauer et al., 2007; Adelsberger and Smith, 2009; Fisher et al., 2014; Wang et al., 2015) – can keep pavements alive and the lack thereof results in pavement instability. This is the case along the Salt and Verde Rivers where terrace pavements maintain their longevity as long as there exists a strontium-isotope signal indicating the presence of allochthonous dust (Fig. 11).

2. Flat topography. Sloping surfaces, with the exception of those in hyperarid regions (Boroda et al., 2013; Owen et al., 2013), promote pavement instability (Matmon et al., 2005; Wood et al., 2005; Adelsberger and Smith, 2009). In contrast, very low slope angles fos-ter pavement stability (Cooke, 1970; Mabbutt, 1979; Dixon, 2009). This is the case for pavements on the Sawik, Mesa, and Blue Point ter-races of the Salt River that maintain stability, while those with slop-ing surfaces experience ongoing exposure of alluvium eroding from underlying gravels.

3. Lack of headward retreating swales or gullies. Gully incision decreases pavement stability (Hunt and Mabey, 1966) with clear evi-dence found from cosmogenic nuclide data (Frankel et al., 2007a; Huang et al., 2014). Pavements atop isolated remnants of the Sawik (Fig. 5B) and Mesa (Fig. 5C) terrace of the Salt River exemplify pave-ment stability when swales or gullies do not work into an area of old desert pavement.

5.2. Site specific factors promoting pavement stability

Each pavement exists in a unique local setting with varying geology, landform, soils, hydrology, vegetation, climate, anthropogenic influ-ences, and changes over time. As a consequence, it is inevitable that site-specific factors play important roles in pavement longevity. For ex-ample, the granitic strath underlying the Sawik and Mesa terrace pave-ments of the Salt River (Fig. 6F, I) promotes pavement stability over the much weaker playa clay strath of the

Verde River (Fig. 7C, F). Similarly, the disk-shapes of the Salt River pavements (Fig. 6B, E, H, K) traps dust efficiently underneath this flattened shape (Goosens, 1995). Basalt flows in arid regions (Wells et al., 1985; Shepard et al., 1995; Dunai and Wijbrans, 2000; Valentine and Harrington, 2006; Fenton and Niedermann, 2014) provide a very stable substrate for pavements as the basalt gradually undergoes clast-size reduction (Valentine응 et al., 2006). In some places, deflation erodes pavements (Schmidt et al., 2011), while in other settings surface wash degrades pavement surfaces (Wood et al., 2005; Adelsberger and Smith, 2009; Rodriguez et al., 2013a). However, perhaps the best example of a site-specific factor would be modern and paleo-biotic disturbance (McAuliffe, 1994; Dickerson et al., 2013; Pietrasiak et al., 2014). By sampling pavements lacking evidence of modern or paleo-disturbance, exposure ages for Sawik pavement cobbles (Fig. 6G) reach ~332 ka (Table 7; Fig. 8C). It is the existence of these site-specific factors that makes development of a universal explanation for pavement stability most difficult.

사막 포도의 수명에 대한 규명

성영배[1], 이재일[2]

[1]고려대학교, [2]한국해양과학기술원 부설 극지연구소

요약: 이 논문은 과거 사막 포도의 생존을 촉진시키는 과정 및 조건들에 대한 연구와 개별적 연구인 소노란 사막에서의 테라스 퇴적층의 연구를 종합하였다. 이 종합에서 주요 요인 및 지역에 따른 요인등을 규명하였다. 매우 건조한 조건이 10^6년 이상의 규모에서 사막 포도의 보존에 아주 중요한 요인으로 작용하고 있으며, 약간의 생교란과 암석사이즈의 감소 역시 주요한 요인으로 작용한다. 10^5-10^4년 규모에서는 세가지 주요 요인이 있는데, 사막 자갈층 아래에 더스트의 집적, 평평한 지형도, 머리방향의 후퇴층이 형성이 부재 등이다. 사막 포도의 장수를 결정하는 것은 문헌에서는 나타나 있지 않은데 이것은 지역적으로 다른 특성(사막 퇴적물 아래의 기반암, 더스트 집적률이 높은 디스크 모양의 자갈, 생교란에 영향을 주는 작은 기후학적, 생태학적 이유들)을 가지기 때문이다. 사막 퇴적물의 장수에 대한 주요하고 지역에 따른 주요한 특성들이 소노란 사막의 연구에 적용되었다. 우주기원의 10Be과 14C에 의한 연대 분석결과 30-332 ka 조건에서 안정적이었다. 평평한 지형도, 사막 퇴적층 아래의 화강암질 기반암, 머리방향의 후퇴층의 형성 부재, 87Sr/86Sr 분석에 의한 더스트의 퇴적 및 디스크 모양의 자갈층 퇴적체 등에 의해 안정적이었으나, 10Be 연대는 또한 덜고화된 playa 점토 등에 의한 테라스의 불안정성도 함께 나타내었다.

참고문헌

Abrahams, A.D., Parsons, A.J., 1991. Relationship between in詮갌tration and stone cover on a semiarid hillslopes, southern Arizona. J. Hydrol. 122, 49 - 59.

Abrahams, A.D., Parsons, A.J., 1994. Hydraulics of interrill overland flow on stone-covered desert surfaces. Catena 23, 111 - 140.

Abrahams, A.D., Soltyka, N., Parsons, A.J., Hirsch, P.J., 1990. Fabric analysis of a desert debris slope: Bell Mountain, California. J. Geol. 98, 264 - 272.

Adelsberger, K.A., Smith, J.R., 2009. Desert pavement development and landscape stability on the Eastern Libyan Plateau, Egypt. Geomorphology 107, 178 - 194.

Adelsberger, K.A., Smith, J.R., McPherron, S.P., Dibble, H.L., Olszewski, D.I., Schurmans, U.A.,Chiotti, L., 2013. Desert pavement disturbance and artifact taphonomy: a case study from the Eastern Libyan Plateau, Egypt. Geoarchaeology 28, 112 - 130.

Aerts, R., Finneran, N., Mitiku, H., Poesen, J., 2010. The accumulation of Stone Age lithic artifacts in rock fragment mulches in northern Ethiopia. Geoarchaeology 25, 137 - 148.

Al-Farraj, A., 2008. Desert pavement development on the lake shorelines of Lake Eyre (South), South Australia. Geomorphology 100, 154 - 163.

Al-Farraj, A., Harvey, A.M., 2000. Desert pavement characteristics on Wadi terrace and alluvial fan surfaces: Wadi Al-Bih, UAE. Geomorphology 35, 279 - 297.

Amit, R., Gerson, R., 1986. The evolution of Holocene reg (gravelly) soils in deserts - and example from the Dead Sea region. Catena 13, 59 - 79.

Amit, R., Gerson, R., Yaalon, D.H., 1993. Stages and rate of the gravel shattering process by salts in desert reg soils. Geoderma 57, 295 - 324.

Amit, R., Enzel, Y., Grodek, T., Crouvi, O., Porat, N., Ayalon, A., 2010. The role of rare rainstorms in the formation of calcic soil horizons on alluvial surfaces in extreme deserts. Quat. Res. 74, 177 - 187.

Amit, R., Simhai, O., Ayalon, A., Enzel, Y., Matmon, A., Crouvi, O., Porat, N., McDonald, E.,2011. Transition from arid to hyper-arid environment in

the southern Levant deserts as recorded by early Pleistocene cumulic Aridisols. Quat. Sci. Rev. 30, 312 - 313.

Amundson, R., Dietrich, W., Bellugi, D., Ewing, S., Nishiizumi, K., Chong, G., Owen, J., Finkel, R., Heimsath, A., Stewart, B., 2012. Geomorphologic evidence for the late Pliocene onset of hyperaridity in the Atacama Desert. Geol. Soc. Am. Bull. 124, 1048 - 1070. Anders, M.D., Pederson, J.L., Rittenour, T.M., Sharp, W.D., Gosse, J.C., Karlstrom, K.E., Crossey, L.J., Goble, R.J., Stockli, L., Yang, G., 2005. Pleistocene geomorphology and geochronology of eastern Grand Canyon: linkages of landscape components during climate changes. Quat. Sci. Rev. 24, 2428 - 2448.

Anderson, R.S., Repka, J.L., Dick, G.S., 1996. Explicit treatment of inheritance in dating depositional surfaces using in situ 10Be and 26Al. Geology 24, 47 - 51.

Anderson, K., Wells, S., Graham, R., 2002. Pedogenesis of vesicular horizons, Cima Volcanic Field, Mojave Desert, California. Soil Sci. Soc. Am. J. 66, 878 - 887.

Armstrong, P.A., Perez, R., Owen, L.A., Finkel, R.C., 2010. Timing and controls on late Quaternary landscape development along the eastern Sierra El Mayor range front in northern Baja California, Mexico. Geomorphology 114, 415 - 430.

Athanassas, C.D., Rollefson, G.O., Kadereit, A., Kennedy, D., Theodorakopoulou, K., Rowan, Y.M., Wasse, A., 2015. Optically stimulated luminescence (OSL) dating and spatial analysis of geometric lines in the Northern Arabian Desert. J. Archaeol. Sci. 64, 1 - 11.

Baied, C.A., Somonte, C., 2013. Mid-Holocene geochronology, palaeoenvironments, and occupational dynamics at Quebrada de Amaicha, Tucuman, Argentina. Quat. Int. 299, 80 - 89.

Balco, G., Stone, J.O., Lifton, N.A., Dunai, T.J., 2008. A complete and easily accessible means of calculating surface exposure ages or erosion rates from 10Be and 26Al measure-ments. Quat. Geochronol. 3, 174 - 195.

Balco, G., Briner, J., Finkel, R.C., Rayburn, J.A., Ridge, J.C., Schaefer, J.M., 2009. Regional beryllium-10 production rate calibration for late-glacial

northeastern North America. Quat. Geochronol. 4, 93 – 107.

Benson, L.V., al, e., 1990. Chronology of expansion and contraction of four Great Basin lake systems during the past 35,000 years. Palaeogeogr. Palaeoclimatol. Palaeoecol. 78, 241 – 286.

Blisniuk, K., Rockwell, T., Owen, L.A., Oskin, M., Lippincott, C., Caffee, M.W., Dortch, J., 2010.

Late Quaternary slip rate gradient defined using high-resolution topography and 10Be dating of offset landforms on the southern San Jacinto Fault zone, California. J. Geophys. Res. Solid Earth 115. http://dx.doi.org/10.1029/2009JB006346.

Blisniuk, K., Oskin, M., Fletcher, K., Rockwell, T., Sharp, W., 2012. Assessing the reliability of U-series and 10Be dating techniques on alluvial fans in the Anza Borrego Desert, California. Quat. Geochronol. 13, 26 – 41.

Bockheim, J.G., 2010. Evolution of desert pavements and the vesicular layer in soils of the Transantarctic Mountains. Geomorphology 118, 433 – 443.

Boroda, R., Amit, R., Matmon, A., ASTERTeam, Finkel, R., Porat, N., Enzel, Y., Eyal, Y., 2011. Quaternary-scale evolution of sequences of talus fl atirons in the hyperarid Negev. Geomorphology 127, 41 – 52.

Boroda, R., Matmon, A., Amit, R., Haviv, I., Porat, N., ASTERTeam, Rood, D., Eyal, Y., 2013. Long-term talus flatirons formation in the hyperarid northeastern Negev, Israel. Quat. Res. 79, 256 – 267.

Boroda, R., Matmon, A., Amit, R., Haviv, I., Arnold, M., Aumaître, G., Bourles, D.L., Keddadouche, K., Eyal, Y., Enzel, Y., 2014. Evolution and degradation of flat-top mesas in the hyper-arid Negev, Israel revealed from 10Be cosmogenic nuclides. Earth Surf. Process. Landf. 39, 1611 – 1621.

Borrazzo, K., Lithic taphonomy in desert environments: contributions from FuegoPatagonia (Southern South America). Quat. Int. http://dx.doi.org/10.1016/j.quaint. 2015.12.012 (in press).

Brazel, A.J., 1989. Dust and climate in the American Southwest. In: Leinen, M. (Ed.), Paleoclimatology and Paleometeorology: Modern and Past Patterns of Global Atmospheric Transport. Kluwer Academic Publishers, Dordrecht, pp. 65-96.

Breed, C.S., McCauley, J.F., Whitney, M.I., 1989. Wind erosion forms. In: Thomas, D. (Ed.), Arid Zone Geomorphology. Belhaven Press, London, pp. 284 – 307.

Brookes, I.A., 1993. Geomorphology and Quaternary geology of the Dakhla Oasis Region, Egypt. Quat. Sci. Rev. 12, 529 – 552.

Brookes, I.A., 2001. Aeolian erosional lineations in the Libyan Desert, Dahkla Region, Egypt. Geomorphology 39, 189 – 209.

Bubenzer, O., Besler, H., Hilgers, A., 2007. Filling the gap: OSL data expanding 14C chronologies of Late Quaternary environmental change in the Libyan Desert. Quat. Int. 175, 41 – 52.

Campbell, Cortes, A., González, L., Binnie, S.A., Robinson, R., Freeman, S.P.H.T., Vargas, E., (2). 2012.

Paleoseismology of the Mejillones Fault, northern Chile: insights from cosmogenic 10Be and optically stimulated luminescence determinations. Tectonics 31, http://dxdoi.org/10.1029/2011TC002877.

Cremaschi, M., Zerboni, A., Mercuri, A.M., Olmi, L., Biagetti, S., de Lernia, S., 2014. Takarkori rock shelter (SW Libya): an archive of Holocene climate and environmental changes in the central Sahara. Quat. Sci. Rev. 101, 36 – 60.

Cyr, A.J., Miller, D.M., Reheis, M.C.,Mahan, S.A., Stock, J.D., Schmidt, K.M., 2010. Climatically driven changes in erosion rates recorded in alluvial fan sediments, Providence Mountains, eastern Mojave Desert, California. AGU Fall Meeting Abstracts 1, p. 0712.

Cyr, A.J.,Miller, D.M., Mahan, S.A., 2015. Paleodischarge of theMojave River, southwestern United States, investigated with single-pebble measurements of 10Be. Geosphere 11, 1158 – 1171.

Dan, J., Yaalon, D.H., Moshe, R., Nissim, S., 1982. Evolution of reg soils in southern Israel and Sinai. Geoderma 28, 173 – 202.

deHaas, T., Ventra, D., Carbonneau, P.E., Kleinhans, M.G., 2014. Debris-flow dominance of alluvial fans masked by runoff reworking and weathering. Geomorphology 217, 165 – 181.

Denny, C.S., 1965. Alluvial fans in the Death Valley region of California and Nevada. U.S. Geol. Surv. Prof. Pap. 466.

Denny, C.S., 1967. Fans and pediments. Am. J. Sci. 265, 81 – 105.

Dickerson, R.P., Cocks, G., 2015. Alluvial fan surfaces and an age-related stability for cultural resource preservation: Nevada Test and Training Range, Nellis Air Force Base, Nevada, USA. J. Archaeol. Sci. Rep. 2, 551 – 568.

Dickerson, R.P., Forman, A., Liu, T., 2013. Co-development of alluvial fan surfaces and arid botanical communities, Stonewall Flat, Nevada, USA. Earth Surf. Process. Landf. 38, 1083 – 1101.

Dietze,M., Kleber, A., 2012. Contribution of lateral processes to stone pavement formation in deserts inferred from clast orientation patterns. Geomorphology 139, 172 – 187.

Dietze, M., Muhs, S., Dietze, E., 2011. Ambiguities of relative age indicators on abandoned surfaces of arid environments. Z. Geomorphol. 55, 49 – 75.

Dietze, M., Bartel, S., Lindner, M., Kleber, A., 2012. Formationmechanisms and control factors of vesicular soil structure. Catena 99, 83 – 96.

Dietze, M., Groth, J., Kleber, A., 2013. Alignment of stone-pavement clasts by unconcentrated overland flow – implications of numerical and physical modelling. Earth Surf. Process. Landf. 38, 1234 – 1243.

Dietze, M., Dietze, E., Lomax, J., Fuchs, M., Kleber, A.,Wells, S.G., 2016. Environmental history recorded in aeolian deposits under stone pavements, Mojave Desert, USA. Quat. Res. 85, 4 – 16.

Dixon, J.C., 1994. Aridic soils, patterned ground, and desert pavements. In: Abrahams, A.D., Parsons, A.J. (Eds.), Geomorphology of Desert Environments. Chapman, London, pp. 64 – 81.

Dixon, J.C., 2009. Aridic soils, patterned ground, and desert pavements. In: Parsons, A.J., Abrahams, A.D. (Eds.), Geomorphology of Desert Environments, 2nd ed. Springer, Amsterdam, pp. 101 – 122.

Donahue, D.J., LInick, T.W., Jull, A.J.T., 1990. Isotope-ratio and background corrections for accelerator mass spectrometry radiocarbon measurements. Radiocarbon 32, 135 – 140.

Dorn, R.I., 1986. Rock varnish as an indicator of aeolian environmental change. In: Nickling, W.G. (Ed.), Aeolian Geomorphology. Allen & Unwin, London, pp. 291 – 307.

Dorn, R.I., Dickinson,W.R., 1989. First paleoenvironmental interpretation of a pre-Quaternary rock varnish site, Davidson Canyon, south Arizona. Geology 17, 1029 - 1031.

Dorn, R.I., Oberlander, T.M., 1982. Rock varnish. Prog. Phys. Geogr. 6, 317 - 367.

Dortch, J., Schoenbohm, L.M., 2011. Multiple nuclide cosmogenic dating of very old desert pavements on the Puna Plateau, Northwest Argentina. AGU Fall Meeting Abstracts 1, p. 0605.

Duhnforth, M., Ivy-Ochs, S., Densmore, A.L., Kubik, P.W., 2007. Constraints on the timing of fan deposition in Death Valley, California, using cosmogenic 10Be and 26Al. Geol. Soc. Am. Abstr. Programs 39 (6), 260.

Dunai, T.J., Wijbrans, J.R., 2000. Long-term cosmogenic 3He production rates (152 ka - 1.35 Ma) from 40Ar/39Ar dated basalt flows at 29 N latitude. Earth Planet. Sci. Lett. 176, 147 - 156.

Dunai, T.J., Gonzalez-Lopez, G.A., Juez-Larre, J., 2005. Oligocene - Miocene age of aridity in the Atacama Desert revealed by exposure dating of erosion-sensitive landforms. Geology 33, 321 - 324.

Evenari, M., Yaalong, D.J., Gutterman, Y., 1974. Note on soils with vesicular structures in deserts. Z. Geomorphol. 18, 162 - 172.

Evenstar, L.A., Hartley, A.J., Stuart, F.M., Mather, A.E., Rice, C.M., Chong, G., 2009. Multiphase development of the Atacama Planation Surface recorded by cosmogenic 3He exposure ages: implications for uplift and Cenozoic climate change in western South America. Geology 37, 27 - 30.

Ewing, S.A., Sutter, B., Owen, J., Nishiizumi, K., Sharp, W., Cliff, S.S., Perry, K., Dietrich, W., McKay, C.P., Amundson, R., 2006. A threshold in soil formation at Earth's arid - hyperarid transition. Geochim. Cosmochim. Acta 70, 5293 - 5322.

Fenton, C.R., Niedermann, S., 2014. Surface exposure dating of young basalts (1 - 200 ka) in the San Francisco volcanic field (Arizona, USA) using cosmogenic 3He and 21Ne. Quat. Geochronol. 19, 87e105.

Fenton, C.R., Pelletier, J.D., 2013. Cosmogenic 3He age estimates of Plio-Pleistocene alluvial-fan surfaces in the Lower Colorado River

Corridor, Arizona, USA. Quat. Res. 79, 86 – 99.

Fenton, C.R., Webb, R.H., Cerling, T.E., Poreda, R.J., Nash, B.P., 2002. Cosmogenic 3He ages and geo-chemical discrimination of lava-dam outburst-flood deposits in western Grand Canyon, Arizona. In: House, P.K.,Webb, R.h., Baker, V.R., Levish, D.R. (Eds.), Ancient Floods and Modern Hazards: Principles and Applications of Paleoflood Hydrology. American Geophysical Union, Washington D.C., pp. 191 – 215.

Fenton, C.R., Poreda, R.J., Nash, B.P., Webb, R.H., Cerling, T.E., 2004. Geochemical discrimination of five Pleistocene lava-dam outburst-flood deposits,Western Grand Canyon, Arizona. J. Geol. 112, 91 – 110.

Field, J.J., Pearthree, P.A., 1997. Geomorphologic flood-hazard assessment of alluvial fans and piedmonts. J. Geosci. Educ. 45, 27 – 37.

Field, J.H., Dodson, J.R., Prosser, I.P., 2002. A late Pleistocene vegetation history from the Australian semi-arid zone. Quat. Sci. Rev. 21, 1023 – 1037.

Fisher, A., Fink, D., Chappell, J., Melville,M., 2014. 26Al/10Be dating of an aeolian dust mantle soil in western New South Wales, Australia. Geomorphology 219, 201 – 212.

Fitzsimmons, K.E., Cohen, T.J., Hesse, P.P., Jansen, J., Nanson, G.C., May, J.H., Barrows, T.T., Harberla, D., Hilgers, A., Kelly, T., Larsen, J., Lomax, J., Treble, P., 2013. Late Quaternary palaeoenvironmental change in the Australian drylands. Quat. Sci. Rev. 74, 78 – 96.

Foley, R.A., M.M., L., 2015. Lithic landscapes: early human impact from stone tool production on the central Saharan environment. PLoS One 10 (3), e0116482 (doi:10.1371). Frankel, K.L., Dolan, J.F., 2007. Characterizing arid region alluvial fan surface roughness with airborne laser swath mapping digital topographic data. J. Geophys. Res. 112. http://dx.doi.org/10.1029/2006JF000644.

Frankel, K.L., Brantley, K.S., Dolan, J.F., Finkel, R.C., Klinger, R.E., Knott, J.R., Machette, M.N., Owen, L.A., Phillips, F.M., Slate, J.L., Wernicke, B., 2007a. Cosmogenic 10Be and 36Cl geochronology of offset alluvial fans along the northern Death Valley fault zone: implications for transient strain in the eastern California shear zone. J. Geophys. Res. Solid Earth 112. http://dx.doi.org/10.1029/2006JB004350.

Frankel, K.L., Dolan, J.F., Finkel, R.C., Owen, L.A., Hoeft, J.S., 2007b. Spatial variations in slip rate along the Death Valley-Fish Lake Valley fault system determined from LiDAR topographic data and cosmogenic 10Be geochronology. Geophys. Res. Lett. 34. http://dx. doi.org/10.1029/2007GL030549.

Frink, D.S., Dorn, R.I., 2001. Beyond taphonomy: Pedogenic transformations of the archaeological record in monumental earthworks. Ariz.-Nev. Acad. Sci. J. 34, 24 - 44.

Fuchs, M., Dietze, M., Al-Qudah, K., Lomax, J., 2015. Dating desert pavements: first results from a challenging environmental archive. Quat. Geochronol. 30, 342 - 349. http://dx. doi.org/10.1016/j.quageo.2015.01.001 (in press).

Fujioka, T., Chappell, J., Honda, M., Yatsevich, I., Fifield, L.K., Fabel, D., 2005. Global cooling initiated stony deserts in central Australia 2 - 4 Ma, dated by cosmogenic 21Ne - 10Be. Geology 33, 993 - 996.

Fukioka, T., Chappell, J., 2011. Desert landscape processes on a timescale of millions of years, probed by cosmogenic nuclides. Aeolian Res. 3, 157 - 164.

Gerson, R., Amit, R., 1987. Rates and modes of dust accretion and deposition in an arid region - the Negev, Israel. J. Geol. Soc. Lond. Spec. Publ. 35, 157 - 169.

Gile, L.H., Hawley, J.W., Grossman, R.B., 1981. Soils and geomorphology in the Basin and Range area of southern New Mexico. Guidebook to the Desert Project. New Mexico Bureau of Mines and Mineral Resources Memoir 39, pp. 1 - 222.

Goehring, B.M., Schimmelpfennig, I., Schaefer, J.M., 2014. Capabilities of the Lamont - Doherty Earth Observatory in situ 14C extraction laboratory updated. Quat. Geochronol. 19, 194 - 197.

Goethals, M.M., Niedermann, S., Hetzel, R., Fenton, C.R., 2007. Cosmogenic nuclide intercalibration and erosion rate study on fault scarps of the Bishop Tuff, CA, USA. Geochim. Cosmochim. Acta 71 (15), A335.

Gonzalez, G., Dunai, T., Carrizo, D., Allmendinger, R., 2006. Young displacements on the Atacama Fault System, northern Chile from field observations

and cosmogenic 21Ne concentrations. Tectonics 25, TC3006. http://dx.doi.org/10.1029/2005TC001846.

Goosens, D., 1995. Field experiments of aeolian dust accumulation on rock fragment substrata. Sedimentology 42, 391 – 402.

Goudie, A., Wilkinson, J., 1977. The Warm Desert Environment. Cambridge University Press, Cambridge (88 pp.). Graham, R.C., Hirmas, D.R.,Wood, Y.A., Amrhein, C., 2008. Large near-surface nitrate pools in soils capped by desert pavement in the Mojave Desert, California. Geology 36, 259 – 262.

Granger, D.E., 2006. A review of burial dating methods using 26Al and 10Be. In: Siame, L., Bourles, D., Brown, E.T. (Eds.), In-situ-produced Cosmogenic Nuclides and Quantification of Geological ProcessesGeological Society of America Special Paper 415. Geological Society of America, Boulder, pp. 1 – 16.

Gray, H.J., Owen, L.A., Dietsch, C., Beck, R.A., Caffee, M.A., Finkel, R.C., Mahan, S.A., 2014. Quaternary landscape development, alluvial fan chronology and erosion of the Mecca Hills at the southern end of the San Andreas Fault zone. Quat. Sci. Rev. 105, 66 – 85.

Grolier, M.J., Ericksen, G.E., McCauley, J.F., Morris, E.C., 1974. The desert land forms of Peru; a preliminary photographic atlas. U.S. Geological Survey Open File Report, pp. 74 – 1044 (http://pubs.er.usgs.gov/publication/ofr741044).

Guralnik, B., Matmon, A., Avni, Y., Fink, D., 2010. 10Be exposure ages of ancient desert pavements reveal Quaternary evolution of the Dead Sea drainage basin and rift margin tilting. Earth Planet. Sci. Lett. 290, 132 – 141.

Guralnik, B., Matmon, A., Avni, Y., Porat, N., Fink, D., 2011. Constraining the evolution of river terraces with integrated OSL and cosmogenic nuclide data. Quat. Geochronol. 6, 22 – 32.

Haff, P.K., 2001. Desert pavement: an environmental canary? J. Geol. 109, 661 – 668.

Haff, P.L., 2005. Response of desert pavement to seismic shaking, HectorMine earthquake, California, 1999. J. Geophys. Res. Earth Surf. 110.

http://dx.doi.org/10.1029/ 2003JF000054.

Haff, P.K., 2014. Biolevitation of pebbles on desert surfaces. Granul. Matter 16, 275 – 278.

Hall, S.R., Farber, D.L., Audin, L., Finkel, R., Mériaux, A., 2008. Geochronology of pediment surfaces in southern Peru: implications for Quaternary deformation of the Andean forearc. Tectonophysics 429, 186 – 205.

Hayden, J., 1976. Pre-altithermal archaeology in the Sierra Pinacate, Sonora, Mexico. Am. Antiq. 41, 274 – 289.

Hedrick, K., Owen, L.A., Rockwell, T.K., Meigs, A., Costa, C., Caffee, M.W., Masana, E., Ahumada, E., 2013. Timing and nature of alluvial fan and strath terrace formation in the Eastern Precordillera of Argentina. Quat. Sci. Rev. 80, 143 – 168.

Heimsath, A.M., Chappell, J., Dietrich, W.E., Nishiizumi, K., Finkel, R., 2001. Late Quaternary erosion in southeastern Australia: a field example using cosmogenic nuclides. Quat. Int. 83-85, 169 – 185.

Heisinger, B., Lal, D., Kubik, P., Ivy-Ochs, S., Knie, K., Nolte, E., 2002a. Production of selected cosmogenic radionuclides by muons: 2. Capture of negative muons. Earth Planet. Sci. Lett. 200, 357 – 369.

Heisinger, B., Lal, D., Kubik, P., Ivy-Ochs, S., Neumaier, S., Knie, K., Lazarev, V., Nolte, E., 2002b. Production of selected cosmogenic radionuclides by muons: 1. Fast muons. Earth Planet. Sci. Lett. 200, 345 – 355.

Heizler, M.T., Perry, F.V., Crowe, B.M., Peters, L., Appelt, R., 1999. The age of LathropWells volcanic center: an 40Ar/39Ar dating investigation. J. Geophys. Res. Solid Earth 104 (B1), 767 – 804.

Hetz, G., Mushkin, A., Blumberg, D.G., Baer, G., Ginat, H., 2016. Estimating the age of desert alluvial surfaces with spaceborne radar data. Remote Sens. Environ. 184, 288 – 301.

Hetzel, R., Tao, M., Stokes, S., Niedermann, S., Ivy-Ochs, S., Gao, B., Strecker, M.R., Kubik, P.W., 2004. Late Pleistocene/Holocene slip rate of the Zhangye thrust (Qilian Shan, China) and implications for the active growth of the northeastern Tibetan Plateau. Tectonics 23, TC6006.

Hidy, A.J., Gosse, J.C., Pederson, J.L., Mattern, J.P., Finkel, R.C., 2010. A geologically constrained Monte Carlo approach to modeling exposure

ages from profiles of cosmogenic nuclides: an example from Lees Ferry, Arizona. G3 Geochem. Geophys. Geosyst. 11. http://dx.doi.org/10.1029/2010GC003084.

Hippe, K., Kober, F., Baur, H., Ruff, M., Wacker, L., Wieler, R., 2009. The current performance of the in situ 14C extraction line at ETH. Quat. Geochronol. 4, 493 – 500.

Hippe, K., Kober, F., Wacker, L., Fahrni, S.M., Ivy-Ochs, S., Akçar, N., Schluchter, C., Wieler, R., 2013. An update on in situ cosmogenic 14C analysis at ETH Zurich. Nucl. Instrum. Methods Phys. Res., Sect. B 294, 81 – 86.

Honegger, M.,Williams, M., 2015. Human occupations and environmental changes in the Nile valley during the Holocene: the case of Kerma in Upper Nubia (northern Sudan). Quat. Sci. Rev. 130, 141 – 154.

Honker, A.M., 2002. A River Sometimes Runs Through It: A History of Salt River Flooding and Phoenix (Ph.D. Dissertation) Arizona State University, Tempe (294 pp.).

Huang,W.L., Yang, X.P., Li, A., THompson, J.A., Zhang, L., 2014. Climatically controlled formation of river terraces in a tectonically active region along the southern piedmont of the Tian Shan, NW China. Geomorphology 220, 15 – 29.

Huckleberry, G., 1993. Surficial geology of the Middle Gila River Area, North-Central Pinal County, Arizona. Arizona Geological Survey Open File Report 93-3, pp. 1 – 52.

Huckleberry, G., 1994. Surficial geology of the Santan Mountains Piedmont Area, Northern Pinal and Eastern Maricopa County Area, Arizona. Arizona Geological Survey Open- File Rpoert 94-7, pp. 1 – 32.

Hunt, A., 1960. Archaeology of the Death Valley salt pan. University of Utah Archaeological Paper No. 47.

Hunt, C.B., Mabey, D.R., 1966. Stratigraphy and structure, Death Valley, California. U.S. Geol. Surv. Prof. Pap. 494A.

Hussain, S.H., Aghwan, T.A., 2014. Sedimentology and evolution of a foreland desert basin, Middle Eocene Gercus Formation (North and Northeastern Iraq). Arab. J. Geosci. 8, 2799 – 2830.

Ivy-Ochs, S., Dühnforth, M., Densmore, A.L., Alfimov, V., 2013. Dating fan deposits with cosmogenic nuclides. In: Schneuwly-Bollschweiler, M., Stoffel, M., Florian., R.-M. (Eds.), Dating Torrential Processes on Fans and Cones. Springer, Amsterdam, pp. 243 - 263.

Jessup, R.W., 1951. The soils, geology, and vegetation of northwestern South Australia. R. Soc. S. Aust. Trans. 74, 189 - 273.

Jessup, R.W., 1960. The stony tableland soils of the southeastern portion of the Australian arid zone and their evolutionary history. J. Soil Sci. 11, 188 - 196.

Jianjun, Q., Ning, H., Guangrong, D.,Weimin, Z., 2001. The role and significance of the Gobi Desert pavement in controlling sand movement on the cliff top near the Dunhuang Magao Grottoes. J. Arid Environ. 48, 357 - 371.

Johnson, D.L., 1989. Subsurface stone lines, stone zones, artifact-manuport layers, and biomantles produced by bioturbation via pocket gophers (Thomomys bottae). Am. Antiq. 54, 370 - 389.

Johnson, D.L., 1990. Biomantle evolution and the redistribution of earth materials and artifacts. Soil Sci. 149, 84 - 102.

Johnson, D.L., Balek, C.L., 1991. The genesis of Quaternary landscapes with stone lines. Phys. Geogr. 12, 3855 - 3895.

Jungers, M.C., Heimsath, A.M., Amundson, R., Balco, G., Shuster, D., Cong, G., 2013. Active erosion - deposition cycles in the hyperarid Atacama Desert of Northern Chile. Earth Planet. Sci. Lett. 371-372, 125 - 133.

Kianian, M.K., 2014. Studying surface properties of pavements and their relation to soil properties and plant growth in Hajaligholi playa, Iran. Arab. J. Geosci. 7, 1457 - 1461.

Kim, D.E., Seong, Y.B., Byun, J.M., Weber, J., Min, K., 2016. Geomorphic disequilibrium in the Eastern Korean Peninsula: possible evidence for reactivation of a rift-flank margin? Geomorphology 254, 130 - 145.

Kohl, C.P., Nishiizumi, K., 1992. Chemical isolation of quartz for measurement of in-situ produced cosmogenic nuclides. Geoch. Cosmoch. Acta 56, 3583 - 3587.

Korschinek, G., Bergmaier, A., Faestermann, T., Gerstmann, U.C., Knie, K.,

Rugel, G., Wallner, A., Dillmann, I., Dollinger, G., Lierse von Gostomski, C., Kossert, K., Maiti, M., Poutivtsev, M., Remmert, A., 2010. A new value for the half-life of 10Be by heavy-ion elastic recoil detection and liquid scintillation counting. Nucl. Instrum. Methods Phys. Res., Sect. B 268, 187 – 191.

Kring, D.A., McHargue, L.R., Bland, P.A., Hill, D.H., Berry, F.J., 2001. Gold Basin meteorite strewn field, Mojave Desert, northwestern Arizona: relic of a small late Pleistocene impact event. Meteorit. Planet. Sci. 36, 1057 – 1066.

Ku, T.L., Bull, W.B., Freeman, S.T., Knauss, K.G., 1979. Th-230/U-234 dating of pedogenic carbonates in gravelly desert soils of Vidal Valley, southeastern California. Geol. Soc. Am. Bull. 90, 1063 – 1073.

Laity, J.E., 2011. Pavements and stony mantles. In: Thomas, D.S.G. (Ed.), Arid Zone Geomorphology, 3rd edition Wiley, London, pp. 181 – 207.

Lal, D., 1991. Cosmic ray labeling of erosion surfaces: in situ nuclide production rates and erosion models. Earth Planet. Sci. Lett. 104, 424 – 439.

Larson, P.H., Dorn, R.I., Douglass, J., Gootee, B.F., Arrowsmith, R., 2010. Stewart Mountain Terrace: a new Salt River terrace with implications for landscape evolution of the lower Salt River Valley, Arizona. J. Ariz. Nev. Acad. Sci. 42, 26 – 36.

Larson, P.H., Kelley, S.B., Dorn, R.I., Seong, Y.B., 2017. Pediment development and the pace of landscape change in the northeastern Sonoran Desert, United States. Ann. Assoc. Am. Geogr. (http://www.tandfonline.com/doi/full/10.1080/ 24694452.2016.1201420).

Latorre, C., Santoro, C.M., Ugalde, P.C., Gayo, E.M., Osorio, D., Salas-Egana, C., Pol-Holz, R., Joly, D., Rech, J.A., 2013. Late Pleistocene human occupation of the hyperarid core in the Atacama Desert, northern Chile. Quat. Sci. Rev. 77, 19 – 30.

Lebedeva, M.P., Golovanov, D.L., Abrosimov, K.N., 2016. Micromorphological diagnostics of pedogenetic, eolian, and colluvial processes from data on the fabrics of crusty horizons in differently aged extremely aridic soils of Mongolia. Quat. Int. (in press).

LeBeon, M., Klinger, Y., Al-Qaryouti, M., Meriaux, A.S., Finkel, R.C., Elias, A.,

Mayyas, O., Ryerson, F.J., Tapponnier, P., 2010. Early Holocene and Late Pleistocene slip rates of the southern Dead Sea Fault determined from 10Be cosmogenic dating of offset alluvial deposits. J. Geophys. Res. Solid Earth 115. http://dx.doi.org/10 1029/2009JB007198.

Lifton, N.A., Jull, T., Quade, J., 2001. A new extraction technique and production rate estimate for in situ cosmogenic 14C in quartz. Geochim. Cosmochim. Acta 65, 1953 – 1969.

Liu, T., 2016. VML dating lab. http://www.vmldating.com/ (last accessed March 13).

Liu, T., Broecker,W.S., 2007. Holocene rock varnish microstratigraphy and its chronometric application in drylands of western USA. Geomorphology 84, 1 – 21.

Liu, T., Broecker,W.S., 2008a. Rock varnish evidence for latest Pleistocenemillennial-scale wet events in the drylands of western United States. Geology 36, 403 – 406.

Liu, T., Broecker, W.S., 2008b. Rock varnish microlamination dating of late Quaternary geomorphic features in the drylands of the western USA. Geomorphology 93, 501 – 523.

Liu, T., Broecker, W.S., 2013. Millennial-scale varnish microlamination dating of late Pleistocene geomorphic features in the drylands of western USA. Geomorphology 187, 38 – 60.

Liu, T., Broecker,W., Stein,M., 2013. Rock varnish evidence for a Younger Dryas wet event in the Dead Sea basin. Geophys. Res. Lett. 40, 2229 – 2235.

Lv, Y., Gu, Z., Aldahan, A., Zhang, H., Possnert, G., Lei, G., 2010. 10Be in quartz gravel from the Gobi Desert and evolutionary history of alluvial sedimentation in the Ejina Basin, Inner Mongolia, China. Chin. Sci. Bull. 55, 3802 – 3809.

Mabbutt, J.A., 1965. Stone distribution in a stony tablel and soil. Aust. J. Soil Res. 3, 131 – 142.

Mabbutt, J.C., 1977. Desert Landforms. Australian National University Press, Canberra (340 pp.).

Mabbutt, J.A., 1979. Pavements and patterned ground in the Australian stony deserts. Stuttg. Geogr. Stud. 93, 107 – 123.

Machette, M.N., Slate, J.L., Phillips, F.M., 2008. Terrestrial cosmogenic-nuclide dating of alluvial fans in Death Valley, California. U.S. Geol. Surv. Prof. Pap. 1755, 1 - 44.

Marchant, D.R., Denton, G.H., 1996. Miocene and Pliocene paleoclimate of the Dry Valleys region, Southern Victoria land: a geomorphological approach. Mar. Micropaleontol. 27, 253 - 271.

Marchant, D.R., Schisher, C., Lux, D., West, D., Denton, G., 1993. Pliocene paleoclimate and East Antarctic ice-sheet history from surficial ash deposits. Science 260, 667 - 670.

Marchant, D.R., Denton, G.H., Swisher, C.C., Potter, N., 1996. Late Cenozoic Antarctic paleoclimate reconstructed from volcanic ashes in the Dry Valleys region of southern Victoria Land. Geol. Soc. Am. Bull. 108, 181 - 194.

Marchetti, D.W., Cerling, T.E., 2005. Cosmogenic 3He exposure ages of Pleistocene debris flows and desert pavements in Capitol Reef National Park, Utah. Geomorphology 67, 423 - 435.

Marcus, M.G., Brazel, A.J., 1992. Summer dust storms in the Arizona Desert. In: Janelle, D.G. (Ed.), Geographical Snapshots of North America. Guilford Press, pp. 411 - 416.

Matmon, A., Schwartz, D.P., Finkel, R., Clemmens, S., Hanks, T.C., 2005. Dating offset fans along the Mojave section of the San Andreas fault using cosmogenic 26Al and 10Be. Geol. Soc. Am. Bull. 117, 795 - 807.

Matmon, A., Nichols, K., Finkel, R., 2006. Isotopic insights into smoothening of abandoned fan surfaces, southern California. Quat. Res. 66, 109 - 118.

Matmon, A., Simhai, O., Amit, R., Haviv, I., Porat, N., McDonald, E., Benedetti, L., Finkel, R., 2009. Desert pavement - coated surfaces in extreme deserts present the longest-lived landforms on Earth. Geol. Soc. Am. Bull. 209, 688 - 697.

May, J.H., Wells, S.G., Cohen, T.J., Marx, S.K., Nanson, G.C., Baker, S.E., 2015. A soil chronosequence on Lake Mega-Frome beach ridges and its implications for late Quaternary pedogenesis and paleoenvironmental conditions in the drylands of southernAustralia. Quat. Res. 83, 150 - 165.

McAuliffe, J.R., 1994. Landscape evolution, soil formation, and ecological patterns and processes in Sonoran Desert bajadas. Ecol. Monogr. 64, 111 - 148.

McAuliffe, J.R., Van Devender, T.R., 1998. A 22,000-year record of vegetation change in the north-central Sonoran Desert. Palaeogeogr. Palaeoclimatol. Palaeoecol. 141, 253 - 275.

McDonald, E.V., Pierson, F.B., F., G.N., McFadden, L.D., 1996. Application of a process-based soil-water balance model to evaluate the influence of Late Quaternary climate change on soil-water movement in calcic soils. Geoderma 74, 167 - 192.

McDonald, E.V.,McFadden, L.D.,Wells, S.G., 2003. Regional response of alluvial fans to the Pleistocene-Holocene climatic transition, Mojave Desert, California. Geol. Soc. Am. Spec. Pap. 368, 189 - 205.

McFadden, L.D., 1988. Climatic influences on rates and processes of soil development in Quaternary deposits of southern California. Geol. Soc. Am. Spec. Pap. 216, 153 - 178.

McFadden, L.D., Wells, S.G., Dohrenwend, J.C., 1986. Influences of Quaternary climatic changes on processes of soil development on desert loess depositions of the Cima volcanic field, California. Catena 13, 361 - 389.

McFadden, L.D., Wells, S.G., Jercinovich, M.J., 1987. Influences of eolian and pedogenic processes on the origin and evolution of desert pavements. Geology 15, 504 - 506.

McFadden, L.D.,McDonald, E.V.,Wells, S.G., Anderson, K., Quade, J., Forman, S.L., 1998. The vesicular layer and carbonate collars of desert soils and pavements: formation, age and relation to climate change. Geomorphology 23 (2 - 3), 101 - 145.

Meadows, D.G., Young, M.H., McDonald, E.V., 2006. Estimating the fine soil fraction of desert pavements using ground penetrating radar. Vadose Zone J. 5, 720 - 730.

Meadows, D.G., Young,M.H.,McDonald, E.V., 2008. Influence of relative surface age on hydraulic properties and infiltration on soils associated with desert pavements. Catena 72, 169 - 178.

Meek, N., 1989. Geomorphic and hydrologic implications of the rapid incision of Afton Canyon, Mojave Desert, California. Geology 17, 7 - 10.

Meek, N., 1990. Late Quaternary Geochronology and Geomorphology of the Manix Basin, San Bernardino County, California (Ph.D. Thesis) UCLA, Los Angeles (212 pp.).

Meek, N., 2004. Mojave River history from an upstream perspective. In: Reynolds, R.E. (Ed.), Breaking Up – The 2004 Desert Symposium Field Trip and Abstracts. California State University Fullerton Desert Studies Consortium, Fullerton, CA, pp. 41 - 49.

Mihir, M., Wasklewicz, T., Liu, T., 2015. Relationship between surface roughness and age of deposits in debris flow fans, Eastern Owens Valley, CA. Geophys. Res. Abstr. 17, EGU2015 - EG12444.

Moharana, P.C., Raja, P., 2016. Distribution, forms and spatial variability of desert pavements in arid western Rajasthan. J. Geol. Soc. India 87, 401 - 410.

Murray, A., Olley, J., 2002. Precision and accuracy in the optically stimulated luminescence dating of sedimentary quartz: a status review. Geochronometria 21, 1 - 16.

Murray, A.S.,Wintle, A.G., 2000. Luminescence dating of quartz using an improved singlealiquot regenerative-dose protocol. Radiat. Meas. 32, 57 - 73.

Musick, H.B., 1975. The barrenness of desert pavement in Yuma County, Arizona. J. Ariz. Acad. Sci. 10, 24 - 28.

Naysmith, P., 2007. Extraction and Measurement of Cosmogenic In Situ 14C from Quartz (M.S. thesis) Univerity of Glasgow, pp. 1 - 86 (http://theses.gla.ac.uk/548/1/2007naysmithmsc.pdf).

Nishiizumi, K., Kohl, C., Arnold, J., Dorn, R., Klein, J., Fink, D., Middleton, R., Lal, D., 1993. Role of in situ cosmogenic nuclides 10Be and 26Al in the study of diverse geomorphic processes. Earth Surf. Process. Landf. 18, 407 - 425.

Nishiizumi, K., Caffee, M.W., Finkel, R.C., Brimhall, G., Mote, T., 2005. Remnants of a fossil alluvial fan landscape of Miocene age in the Atacama Desert of northern Chile using cosmogenic nuclide exposure age dating. Earth Planet. Sci. Lett. 237, 499 - 507.

Nishiizumi, K., Imamura, M., Caffee, M.W., Southon, J.R., Finkel, R.C.,

McAninch, J., 2007.
Absolute calibration of 10Be AMS standards. Nucl. Instrum. Methods Phys. Res., Sect. B 258, 403 - 413.

Oskin, M., Perg, L., Blumentritt, D., Mukhopadhyay, S., Iriondo, A., 2007. Slip rate of the Calico fault: implications for geologic versus geodetic rate discrepancy in the Eastern California Shear Zone. J. Geophys. Res. 112. http://dx.doi.org/10.1029/2006JB004451.

Owen, L.A., Frankel, K., Knott, J.R., Reynhout, S., Finkel, R.C., Dolan, J.F., Lee, J., 2011. Beryllium-10 terrestrial cosmogenic nuclide surface exposure dating of Quaternary landforms in Death Valley. Geomorphology 125, 541 - 557.

Owen, L.A., Chen, J., Hedrick, K.A., Caffee, M.W., Robinson, A.C., Schoenbohm, L.M., Yuan, Z., Li, W., Imrecke, D.B., Liu, J., 2012. Quaternary glaciation of the Tashkurgan Valley, southeast Pamir. Quat. Sci. Rev. 47, 56 - 72.

Owen, J.J., Dietrich, W.E., Nishiizumi, K., Chong, G., Amundson, R., 2013. Zebra stripes in the Atacama Desert: fossil evidence of overland flow. Geomorphology 182, 157 - 172.

Parker, K.C., 1991. Topography, substrate, and vegetation patterns in the northern Sonoran Desert. J. Biogeogr. 18, 151 - 163.

Peel, R.F., 1960. Some aspects of desert geomorphology. Geography 45, 241 - 262.

Pelletier, J.D., Harrington, C.D., Whitney, J.W., Cline, M., DeLong, S.B., Keating, G., Ebert, K.T., 2005. Geomorphic control of radionuclide diffusion in desert soils. Geophys. Res. Lett. 32. http://dx.doi.org/10.1029/2005GL024347.

Pelletier, J.D., Cline, M., DeLong, S.B., 2007. Desert pavement dynamics: numerical modeling and field-based calibration. Earth Surf. Process. Landf. 32, 1913 - 1927.

Perrineau, A., Van DerWoerd, J., Gaudemer, Y., Liu-Zeng, J., Pik, R., Tapponnier, P., Thuizat, R., Rongzhang, Z., 2011. Incision rate of the Yellow River in Northeastern Tibet constrained by 10Be and 26Al cosmogenic isotope dating of fluvial terraces: implications for catchment evolution and plateau building. Geol. Soc. Lond., Spec. Publ.

353, 189 – 219.

Peterson, F., 1981. Landforms of the Basin and Range Province, Defined for Soil Survey. Nevada Agricultural Experiment Station Technical Bulletin 28.

Peterson, F.F., Bell, J.W., Dorn, R.I., Ramelli, A.R., Ku, T.L., 1995. Late Quaternary geomorphology and soils in Crater Flat, Yucca Mountain area, southern Nevada. Geol. Soc. Am. Bull. 107, 379 – 395.

Péwé, T.L., 1978. Guidebook to the geology of Central Arizona. Arizona Bureau of Geology and Mineral Technology Special Paper 2.

Phillips, F.M., Zreda, M.G., Evenson, E.B., Hall, R.D., Chadwick, O.A., Sharma, P., 1997. Cosmogenic Cl-36 and Be-10 ages of Quaternary glacial and fluvial deposits of theWind River Range, Wyoming. Geol. Soc. Am. Bull. 109, 1453 – 1463.

Pietrasiak, N., Drenovsky, R.E., Santiago, L.S., Graham, R.C., 2014. Biogeomorphology of a Mojave Desert landscape – configurations and feedbacks of abiotic and biotic land surfaces during landform evolution. Geomorphology 206, 23 – 36.

Pietsch, D., Kuhn, P., 2012. Early Holocene paleosols at the southwestern Ramlat As- Sab'atayn desert margin: new climate proxies for southern Arabia. Palaeogeogr. Palaeoclimatol. Palaeoecol. 365, 154 – 165.

Pigati, J.S., Lifton, N.A., Timothy Jull, A., Quade, J., 2010. A simplified in situ cosmogenic 14C extraction system. Radiocarbon 52, 1236 – 1243.

Placzek, C., Granger, D.E., Matmon, A., Quade, J., Ryb, U., 2014. Geomorphic process rates in the central Atacama Desert, Chile: insights from cosmogenic nuclides and implications for the onset of hyperaridity. Am. J. Sci. 314, 1462 – 1512.

Pope, C.W., 1974. Geology of the Lower Verde River Valley, Maricopa County, Arizona (M.S. thesis) pp. 1 – 104.

Potter, C., 2016. Mapping changes in desert pavement surfaces of the lower Colorado Desert of Southern California using Landsat time series analysis. Int. J. Adv. Remote Sens. GIS 6, 1747 – 1754.

Quade, J., 2001. Desert pavements and associated rock varnish in the Mojave Desert: how old can they be? Geology 29, 855 – 858.

Regard, V., Bellier, O., Braucher, R., Gasse, F., Bourlès, D., Mercier, J., Thomas,

J.-C., Abbassi, M.R., Shabanian, E., Soleymani, S., 2006. 10Be dating of alluvial deposits from Southeastern Iran (the Hormoz Strait area). Palaeogeogr. Palaeoclimatol. Palaeoecol. 242, 36 - 53.

Reheis, M.C., Edwine, J.L., 2008. Lake Manix shorelines and Afton Canyon terraces: implications for incision of Afton Canyon. Geol. Soc. Am. Spec. Pap. 439, 227 - 259.

Reheis, M.C., Sowers, J.M., Taylor, E.M., McFadden, L.D., Harden, J.W., 1992. Morphology and genesis of carbonate soils on the Kyle Canyon fan, Nevada, U.S.A. Geoderma 52, 303 - 342.

Rodriguez, M.P., Carretier, S., Charrier, R., Saillard, M., Regard, V., Herail, G., Hall, S., Farber, D., Audin, L., 2013a. Geochronology of pediments and marine terraces in north-central Chile and their implications for Quaternary uplift in the Western Andes. Geomorphology 180-181, 33 - 46.

Rodriguez, M.P., Carretier, S., Charrier, R., Saillard, M., Regard, V., Herail, G., Hall, S., Farber, D., Audin, L., 2013b. Geochronology of pediments and marine terraces in north-central Chile and their implications for Quaternary uplift in the Western Andes. Geomorphology 180, 33 - 46.

Rostagno, C.M., Degorgueb, G., 2011. Desert pavements as indicators of soil erosion on aridic soils in north-east Patagonia (Argentina). Geomorphology 134, 224 - 231.

Sauer, D., Schellmann, G., Stahr, K., 2007. A soil chronosequence in the semi-arid environment of Patagonia (Argentina). Catena 71, 382 - 393.

Schmidt, S., Hetzel, R., Kuhlmann, J., Mingorance, F., Ramos, V.A., 2011. A note of caution on the use of boulders for exposure dating of depositional surfaces. Earth Planet. Sci. Lett. 302, 60 - 70.

Shafer, D., Young, M., Zitzer, S., McDonald, E., Caldwell, T., 2004. Coupled environmental processes and long-term performance of landfill covers in the Northern Mojave Desert. DRI Publ. 45203, 1 - 54.

Sharon, D., 1962. On the nature of hamadas in Israel. Z. Geomorphol. N.F. 6, 129 - 147.

Shepard, M.K., Arvidson, R.E., Caffee, M., Finkel, R., Harris, L., 1995. Cosmogenic exposure ages of basalt flows - Lunar Crater Volcanic

Field, Nevada. Geology 23, 21 – 24.

Shirahama, Y., Miyairi, Y., He, H., Fu, B., Echigo, T., Kano, K.I., Yokoyama, Y., Ikeda, Y., 2015.

Climate-induced changes in sediment supply revealed by surface exposure dating of Sijiquan River terraces, northeastern Tibet. Geomorphology 235, 15 – 26.

Siame, L.L., Bourles, D.L., Sebrier, M., Bellier, O., Castano, J.C., Araujo, M., Perez, M., Raisbeck, G.M., Yiou, F., 1997. Cosmogenic dating ranging from 20 to 700 ka of a series of alluvial fan surfaces affected by the El Tigre fault, Argentina. Geology 11, 975 – 978.

Siame, L.L., Sebrier, M., Bellier, O., Bourles, D., Costa, C., Ahumada, E.A., Gardini, C.E., Cisneros, H., 2015. Active basement uplift of Sierra Pie de Palo (Northwestern Argentina): rates and inception from 10Be cosmogenic nuclide concentrations. Tectonics 34, 1129 – 1153.

Skotnicki, S.J., Young, E.M., Goode, T.C., Bushner, T.C., 2003. Subsurface geologic investigation of Fountain Hills and the Lower Verde River Valley, Maricopa County, Arizona. Arizona Geological Survey Contributed Report CR-03-B, pp. 1 – 44.

Small, D., Fabel, D., 2016. Was Scotland deglaciated in the Younger Dryas? Quat. Sci. Rev. 145, 259 – 263.

Sohbati, R.,Murray, A.S., Porat, N., Jain, M., Avner, U., 2015. Age of a prehistoric “Rodedian” cult site constrained by sediment and rock surface luminescence dating techniques. Quat. Geochronol. 30, 90 – 99.

Sohn, M.F., Mahan, S.A., Knott, J.R., Bowman, D.D., 2007. Luminescence ages for alluvialfan deposits in Southern Death Valley: implications for climate-driven sedimentation along a tectonically active mountain front. Quat. Int. 166, 49 – 60.

SoilSurveyStaff, 1974. Soil taxonomy. U.S. Department of Agriculture Handbook. 436, pp. 1 – 754.

Spelz, R.M., Fletcher, J.M., Owen, L.A., Caffee, M.W., 2008. Quaternary alluvial-fan development, climate and morphologic dating of fault scarps in Laguna Salada, Baja California, Mexico. Geomorphology 102, 578 – 594.

Springer, M.E., 1958. Desert pavement and vesicular layer of some soils of the desert of the Lahontan Basin, Nevada. Proc. Soil Sci. Soc. Am. 22, 63 - 66.

Stadelman, S., 1994. Genesis and Post-formational Systematics of Carbonate Accumulations in Quaternary Soils of the Southwestern United States (Ph.D Dissertation) Agronomy Department, Texas Tech University, Lubbock, pp. 1 - 124.

Stirling, M., Ledgerwood, J., Liu, T., Apted, M., 2010. Age of unstable bedrock landforms Southwest of Yucca Mountain, Nevada, and implications for past ground motions. Bull. Seismol. Soc. Am. 100, 74 - 86.

Stone, J.O., 2000. Air pressure and cosmogenic isotope production. J. Geophys. Res. 105, B23753 - B23759.

Sweeney, M.R., McDonald, E.V., Markley, C.E., 2013. Alluvial sediment or playas: what is the dominant source of sand and silt in desert soil vesicular A horizons, southwest USA. J. Geophys. Res. Earth Surf. 118, 257 - 275.

Symmons, P.M., Hemming, C.F., 1968. A note on wind-stable stone-mantles in the southern Sahara. Geogr. J. 134, 60 - 64.

Thomas, M.F., Clarke, J.D.A., Pain, C.F., 2005.Weathering, erosion and landscape processes on Mars identified from recent rover imagery, and possible Earth analogues. Aust. J. Earth Sci. 52, 365 - 378.

Turk, J.L., Graham, R.C., 2011. Distribution and properties of vesicular horizons in the western United States. Soil Sci. Soc. Am. J. 75, 1449 - 1461.

Turk, J.K., Graham, R.C., 2014. Analysis of sesicular porosity in soils using high resolution X-ray computed tomography. Soil Sci. Soc. Am. J. 78, 868 - 880.

Turrin, B.D., Dohrenwend, J.C., Drake, R.E., Curtiss, G.H., 1985. K-Ar ages from the Cima volcanic field, eastern Mojave Desert, CA. Isochron West 44, 9 - 16.

Ugalde, P.C., Santoro, C.M., Gayo, E.M., Latorre, C., Maldonado, S., Pol-Holz, R., Jackson, D., 2015. How do surficial lithic assemblages weather in arid environments? A case study from the Atacama Desert, Northern Chile. Geoarchaeology 30, 352 - 368.

Ugolini, F.C., Hillier, S., Certini, G., Wilson, M.J., 2008. The contribution of aeolian material to an Aridisol from southern Jordan as revealed by mineralogical analysis. J. Arid Environ. 72, 1431 – 1447.

Valentin, C., 1994. Surface sealing as affected by various rock fragment covers inWest-Africa. Catena 23, 87 – 97.

Valentine, G.A., Harrington, C.D., 2006. Clast size controls and longevity of Pleistocene desert pavements at LathropWells and Red Cone volcanoes, southern Nevada. Geology 34, 533 – 536.

Valentine, G.A., Perry, F.V., Krier, D., Keating, G.N., Kelley, R.E., Cogbill, A.H., 2006. Smallvolume basaltic volcanoes: eruptive products and processes, and posteruptive geomorphic evolution in Crater Flat (Pleistocene), southern Nevada. Geol. Soc. Am. Bull. 118, 1313 – 1330.

Van Der Woerd, J., Klinger, Y., Sieh, K., Tapponnier, P., Ryerson, F., Meriaux, A.S., 2006. Long-term slip rate of the southern San Andreas fault from 10Be-26Al surface exposure dating of an offset alluvial fan. J. Geophys. Res. Solid Earth 111. http://dx.doi.org/10.1029/2004JB003559.

Wagner, G.A., Kadereit, A., 2010. Luminescence dating work fromthe Heidelberg Group: a key technology in geoarchaeology. Mediterr. Archaeol. Archaeom. 10, 3 – 8. Wainwright, J., Parsons, A.J., Abrahams, A.D., 1995. A simulation study of the role of raindrop erosion in the formation of desert pavements. Earth Surf. Process. Landf. 20, 277 – 291.

Wainwright, J., Parsons, A.J., Abrahams, A.D., 1999. Field and computer simulation experiments on the formation of desert pavement. Earth Surf. Process. Landf. 24, 1025 – 1037.

Wang,W., Dong, Z.,Wang, T., Zhang, G., 2006. The equilibrium gravel coverage of the deflated gobi above the Mogao Grottoes of Dunhuang, China. Environ. Geol. 50, 1077 – 1083.

Wang, F., Michalski, G., Seo, J.-H., Granger, D.E., Lifton, N., Caffee, M., 2015. Beryllium-10 concentrations in the hyper-arid soils in the Atacama Desert, Chile: implications for arid soil formation rates and El Nino driven changes in Pliocene precipitation. Geochim. Cosmochim. Acta 160, 227 – 242.

Ward, D.J., Cesta, J.M., Galewsky, J., Sagredo, E., 2015. Late Pleistocene glaciations of the arid subtropical Andes and new results from the Chajnantor Plateau, northern Chile. Quat. Sci. Rev. 128, 98 - 116.

Wells, P.V., 1983. Paleobiogeography of montane islands in the Great Basin since the last glaciopluvial. Ecol. Monogr. 53, 341 - 382.

Wells, S.G., Dohrenwend, J.C., McFadden, L.D., Turrin, B.D., Mahrer, K.D., 1985. Late Cenozoic landscape evolution on lava flow surfaces of the Cima volcanic field, Mojave Desert, California. Geol. Soc. Am. Bull. 96, 1518 - 1529.

Wells, S.G., McFadden, L.D., Poths, J., Olinger, C.T., 1995. Cosmogenic 3He surface-exposure dating of stone pavements: implications for landscape evolution in deserts. Geology 23, 613 - 616.

Wilcox, M.K.,Wood, J.M., Tromble, J.M.`., 1988. Factors influencing infiltrability of semiarid mountain slopes. J. Range Manag. 41, 197 - 206.

Williams, S., Greeley, R.D.N.T.M., 1984. NASA T-86246, 1, 169 - 170. Desert Pavement Study at Amboy, California. NASA Tech Memo TM-86246 1, pp. 169 - 170.

Williams, S.H., Zimbelman, J.R., 1994. Desert pavement evolution: an example of the role of sheetflood. J. Geol. 102, 243 - 248.

Williams, A.J., Buck, B.J., Soukup, D.A., Merkler, D.J., 2013. Geomorphic controls on biological soil crust distribution: a conceptual model from the Mojave Desert (USA). Geomorphology 195, 99 - 109.

Wood, J.D., Graham, R.C., Wells, S.G., 2002. Surface mosaic map unit development for a desert pavement surface. J. Arid Environ. 52, 305 - 317.

Wood, Y.A., Graham, R.C.,Wells, S.G., 2005. Surface control of desert pavement pedologic process and landscape function, Cima Volcanic field,Mojave Desert, California. Catena 59, 205 - 230.

Wright, R.H., Hall, N.T., Hanson, K.L., Sharp, W.D., Klein, J.J.P., Nichols, H.J., Mote, T.I., Keischer, T.C., Ruffell, K.M., 2014. Uranium-series ages of faulted alluvial fan deposits, Mesquite Regional Landfill, southeastern California. Environ. Eng. Geosci. 20, 199 - 224.

Young, M.H., McDonald, E.V., Caldwell, T.G., Benner, S.G., Meadows, D.G., 2004.

Hydraulic properties of a desert soil chronosequence in the Mojave Desert, USA. Vadose Zone J. 3, 956 – 963.

Zerboni, A., 2008. Holocene rock varnish on theMessak plateau (Libyan Sahara): chronology of weathering processes. Geomorphology 102, 640 – 651.

Zhang, W., Tan, L., Zhang, G., Qiu, F., Zhan, H., 2014. Aeolian processes over gravel beds: field wind tunnel simulation and its application atop the Mogao Grottoes, China. Aeolian Res. 15, 335 – 344.

Zimmerman, S.G., Evenson, E.B., Gosse, J.C., Erskine, C.P., 1994. Extensive boulder erosion resulting from a range fire on the type-Pinedale moraines, Fremont Lake, Wyoming. Quat. Res. 42, 255 – 265.

Zreda, M.G., Phillips, F.M., Kubik, P.W., Sharma, P., Elmore, D., 1993. Cosmogenic 36Cl dating of a young basaltic eruption complex, Lathrop Wells, Nevada. Geology 21, 57 – 60.

S.W., 1999. Aspects of landscape evolution in arid environments (M.S. Thesis) Geography. University of Arkansas, Fayetteville, pp. 1 – 57.

Capo, R.C., Stewart, B.W., Chadwick, O.A., 1998. Strontium isotopes as tracers of ecosystem processes: theory and methods. Geoderma 82, 197 – 225.

Capo, R.C., Chadwick, O.A., 1999. Sources of strontium and calcium in desert soil and calcrete. Earth Planet. Sci. Lett. 170, 61 – 72.

Cerveny, N.V., Kaldenberg, R., Reed, J., Whitley, D.S., Simon, J., Dorn, R.I., 2006. Anewstrategy for analyzing the chronometry of constructed rock features in deserts. Geoarchaeology 21, 181 – 203.

Chmeleff, J., von Blanckenburg, F., Kossert, K., Jakob, D., 2010. Determination of the 10Be half-life by multicollector ICP-MS and liquid scintillation counting. Nucl. Instrum. Methods Phys. Res., Sect. B 268, 192 – 199.

Choi, J.H., Murray, A.S., Jain, M., Cheong, C.S., Chang, H.W., 2003. Luminescence dating of well-sorted marine terrace sediments on the southeastern coast of Korea. Quat. Sci. Rev. 22, 407 – 421.

Clark, J.D.A., 2006. Antiquity of aridity in the Chilean Atacama Desert. Geomorphology 73, 101 – 114.

Colinvaux, P.A., DeOliveira, P.E., Bush, M.B., 2000. Amazonian and neotropical plant communities on glacial time-scales: the failure of the aridity and refuge hypotheses. Quat. Sci. Rev. 19, 141??69.

Committee on Alluvial Fan Flooding, N.R.C., 1996. Alluvial Fan Flooding. National Academy of Science Press, Washington D.C. (172 pp.).

Cook, J.P., Pearthree, P.A., Onken, J.A., Youberg, A., Bigio, E.R., 2010. Mapping of the Holocene River Alluvium Along the Verde River, Central Arizona. Report to the Adjudication and Technical Support Unit Surface Water Division Arizona Depart-ment of Water Resources. 10 Sheets Map Scale 1:24,000. Arizona Geological Sur-vey, Tucson (51 pp.).

Cooke, R.U., 1970. Stone pavements in deserts. Ann. Assoc. Am. Geogr. 60, 560 - 577. Cooke, R.U., Warren, A., 1973. Geomorphology in Deserts. University of California Press, Berkeley (374 pp.).

Table 1
Studies where desert pavements provide age control for the underlying landform.

Host landform	Setting	References
Alluvial fan or plain	Arid Andes Mountains	Siame et al. (1997)
	Atacama Desert, Chile	Nishiizumi et al. (2005), Gonzalez et al. (2006), Cortes et al. (2012) Placzek et al. (2014), Wang et al. (2015)
	Central Asia	Hetzel et al. (2004), Lv et al. (2010)
	Dead Sea	LeBeon et al. (2010)
	Great Basin, USA	Reheis et al. (1992), Nishiizumi et al. (1993), Peterson et al. (1995), Duhnforth et al. (2007), Frankel et al. (2007a, 2007b); Sohn et al. (2007), Machette et al. (2008), Owen et al. (2011), Dickerson et al. (2013), Ivy-Ochs et al. (2013), Liu and Broecker (2013), Dickerson and Cocks (2015)
	Iranian Desert	Regard et al. (2006)
	Mojave Desert, USA	Ku et al. (1979), McDonald et al. (2003), Oskin et al. (2007), Cyr et al. (2010)
	Sonoran Desert, North America	Huckleberry (1993, 1994), Van Der Woerd et al. (2006), Spelz et al. (2008), Blisniuk et al. (2010), Blisniuk et al. (2012), Fenton and Pelletier (2013), Gray et al. (2014), Wright et al. (2014)
Basalt flow	Canary Islands	Dunai and Wijbrans (2000)
	Colorado Plateau, USA	Fenton and Niedermann (2014)
	Great Basin, USA	Zreda et al. (1993), Peterson et al. (1995), Shepard et al. (1995), Heizler et al. (1999), Valentine and Harrington (2006), Valentine et al. (2006)
	Jordan	Fuchs et al. (in press)
	Mojave Desert, USA	Turrin et al. (1985), Wells et al. (1985), McFadden et al. (1987), McFadden et al. (1998), Dietze et al. (2016)
Lake beach ridge or shoreline	Arid Australia	Al-Farraj (2008), May et al. (2015)
	Great Basin, USA	Nishiizumi et al. (1993), Duhnforth et al. (2007), Frankel et al. (2007a, 2007b); Machette et al. (2008), Owen et al. (2011), Ivy-Ochs et al. (2013)
	Mojave Desert, USA	Meek (1989, 1990, 2004), Reheis and Edwine (2008)
	Dead Sea	Liu et al. (2013)
Bedrock plateau	Arid Australia	Fujioka et al. (2005)
	Great Basin, USA	Goethals et al. (2007)
	Negev Desert Israel	Boroda et al. (2014)
	Sahara Desert	Adelsberger and Smith (2009)
Debris flows	Colorado Plateau	Marchetti and Cerling (2005)
	Great Basin, USA	Mihir et al. (2015)
Glacial deposits	Andes Mountains	Ward et al. (2015)
	Antarctica	Marchant et al. (1993), Marchant and Denton (1996), Marchant et al. (1996), Bockheim (2010)
	Xinjiang Province, China	Owen et al. (2012)
Marine terrace	Atacama Desert	Rodriguez et al. (2013b)
Pediment	Atacama Desert	Hall et al. (2008), Evenstar et al. (2009), Rodriguez et al. (2013b)
	Australia	Fisher et al. (2014)
Stream terrace - fill	Arabian Desert	Al-Farraj and Harvey (2000)
	Atacama Desert, Chile	Amundson et al. (2012), Jungers et al. (2013)
	Colorado Plateau, USA	Fenton et al. (2002), Fenton et al. (2004), Anders et al. (2005), Marchetti and Cerling (2005), Hidy et al. (2010)
	Negev Desert	Guralnik et al. (2011)
Steram terrace - strath	Andean Precordillera Argentina	Schmidt et al. (2011), Hedrick et al. (2013), Siame et al. (2015)
	Mojave Desert, USA	Meek (2004), Cyr et al. (2015)
	Rocky Mountains, USA	Anderson et al. (1996)
	Sonoran Desert	Armstrong et al. (2010), Larson et al. (2010)
	Tian Shan, China	Huang et al. (2014)
	Tibet	Perrineau et al. (2011), Shirahama et al. (2015)
Talus flatiron	Negev Desert, Israel	Boroda et al. (2011), Boroda et al. (2013)

Table 2
Factors promoting desert pavement formation in settings that do not experience aeolian deflation.

Factor promoting pavement formation	Summary and references
Low slope (flat surface)	A surface with very low relief and with a minimal gradient promotes pavement development (Ugolini et al., 2008).
no gullying	A complete lack of gullying or swales enhances pavement formation (Peel, 1960; Cooke, 1970; Huang et al., 2014).
Minimal bioturbation	Minimal bioturbation enhances pavement formation (Musick, 1975; Wood et al., 2005; Matmon et al., 2009; Pietrasiak et al., 2014).
Clast size reduction by mechanical fracturing	Broad recognition exists that breakdown of pavement clasts helps smooth an originally rough surface morphology created by debris flows or bar-and-swale flood deposits (Peterson, 1981; Amit et al., 1993; Al-Farraj, 2008; Matmon et al., 2009; Bockheim, 2010; deHaas et al., 2014)
Creep reducing surface relief	Creep is a classic process in the pavement literature smoothing surfaces, supported by recent research (Denny, 1965, 1967; Haff, 2005; Dietze and Kleber, 2012; Dietze et al., 2013).
Overland flow	The removal of fines by overland flow is supported as an important pavement-forming process by a diverse array of data including ^{10}Be accumulation, by direct observations, laboratory modeling, and field studies of clast alignment (Sharon, 1962; Abrahams et al., 1990; Abrahams and Parsons, 1991, 1994; Williams and Zimbelman, 1994; Wainwright et al., 1995, 1999; Dixon, 2009; Dietze et al., 2013; Rodriguez et al., 2013b).
Upward stone movement	Initial research in Australia (Jessup, 1951, 1960; Mabbutt, 1965; Fisher et al., 2014) and the Great Basin, USA (Springer, 1958) focused on wetting and drying generating upward stone movement; further support for this process comes from geoarchaeology observations in Ethiopia, (Aerts et al., 2010), upfreezing by periglacial processes (Fuchs et al., in press), and beetle foraging (Haff, 2014).
Dust accumulation (flotation) under clasts	Dust flotation emerged as a pavement-forming process in Australia (Mabbutt, 1977; Mabbutt, 1979), followed by scholarship in the USA (McFadden et al., 1986; McFadden et al., 1987), in the Negev Desert (Gerson and Amit, 1987), in Patagonia of Argentina (Sauer et al., 2007), and in the Libyan Desert (Adelsberger and Smith, 2009; Adelsberger et al., 2013; Cremaschi et al., 2014)

Table 3
Research themes on the vesicular Av dust deposit underneath non-deflation pavements.

Research topic	Finding	References
Ecological influences	Av horizons are linked to arid ecoregion distribution and disturbed by root activity.	Turk and Graham (2011), Dietze et al. (2012)
Field experiments	Flat and elongated cobbles trap dust most efficiently.	Goosens (1995)
Ground penetrating radar	For older pavements, GPR provides a reconnaissance means of mapping clay content.	Meadows et al. (2006)
Hydraulic properties	Av horizons influence soil hydraulics.	Young et al. (2004), Meadows et al. (2008)
Infiltration capacity studies	Av horizons and pavements decrease infiltration capacities.	Wilcox et al. (1988), Abrahams and Parsons (1991), McDonald et al. (1996)
Nitrate studies	Nitrate pools in soils exist under desert pavements.	Graham et al. (2008)
Optically stimulated luminescence studies	Ongoing dust deposition results in pavement flotation on a millennial timescale.	Guralnik et al. (2011); Fuchs et al. (in press), Dietze et al. (2016)
Small scale mapping	Dust trapping depends on pavement fabric and texture.	Wood et al. (2002), Wood et al. (2005)
Vesicle formation	Av horizons develop from wetting and drying cycles and subsurface sealing, and they can be stabilized by clays, calcium carbonate, and iron films on mineral grains.	Springer (1958), Evenari et al. (1974), McFadden et al. (1986), McFadden (1988), Valentin (1994), Turk and Graham (2011), Dietze et al. (2012), Lebedeva et al. (in press)
X-ray tomography of vesicles	Pore size and pore number are inversely related in Av horizon peds.	Turk and Graham (2014)

Table 4
Techniques used to measure the age of desert pavements.

Dating Method	Information Obtained	Limitations	References
^{14}C dating of pedogenic carbonate rinds	Minimum age for the overlying pavement	Pedogenic carbonate is mostly an open system with newer mass moving into older deposits (Stadelman, 1994).	Reheis et al. (1992), McDonald et al. (2003), Larson et al. (2010).
Cosmogenic exposure ages using radionuclides in single cobbles	Exposure history of cobbles at the surface	Requires correction for prior inheritance using subsurface samples	Shepard et al. (1995), Siame et al. (1997), Ewing et al. (2006), Owen et al. (2011), Gray et al. (2014), Huang et al. (2014)
Cosmogenic depth profiles	Analysis of nuclides in clasts at varying depths beneath a desert pavement yields an age estimate for the pavement	Requires correction for surface erosion and correction for inheritance, or the accumulation of cosmogenic nuclides in a prior geomorphic setting	Van Der Woerd et al. (2006), Machette et al. (2008), Blisniuk et al. (2010), Jungers et al. (2013), Gray et al. (2014)
Cosmogenic exposure ages using radionuclides in amalgamated samples	Time of cobbles exposure at the surface	Assumes that each of the cobbles being combined have a similar exposure history, that can be corrected for prior exposure by using amalgamated samples collected from depth	Anders et al. (2005), Marchetti and Cerling (2005), Matmon et al. (2009), Guralnik et al. (2010), Fisher et al. (2014).
Cosmogenic exposure using a stable nuclide (^{3}He or ^{21}Ne)	The cumulative buildup of stable nuclides means that each measurement is a maximum age for emplacement of the clast in the pavement.	Correction for prior exposure history of a clast at depth assumes a similar exposure history to pavement clasts	Dunai et al. (2005), Marchetti and Cerling (2005), Oskin et al. (2007), Evenstar et al. (2009), Fenton and Pelletier (2013)
K-Ar or $^{40}Ar/^{39}Ar$ on lava flow	Maximum age for pavement formation	Time between flow solidification and pavement genesis can vary	Wells et al. (1985), Valentine and Harrington (2006), Valentine et al. (2006), Fenton and Niedermann (2014)
Optically stimulated luminescence (OSL)	maximum age for the overlying pavement	Along with thermal luminescence (TL) and infrared stimulated luminescence (IRSL), OSL requires great care in sampling and sample processing.	Sohn et al. (2007), Matmon et al. (2009), Armstrong et al. (2010), Guralnik et al. (2011), Huang et al. (2014), Fuchs et al. (in press), May et al. (2015), Dietze et al. (2016)
Rock luminescence dating	Provides an exposure for rocks on the surface in a desert pavement	Results can be complicated by multiple exposure and burial events for a rock surface	Sohbati et al. (2015)
Roughness variations with radar data	Provides a calibrated age	Requires numerical ages to calibrate surfaces and requires regional calibrations	Hetz et al. (2016)
Th^{230}-U^{234} dating of pedogenic carbonate rinds	Mininum age for the overlying pavement	Open-system nature of the pedogenic carbonate system provides challenges	Ku et al. (1979), Reheis et al. (1992), Peterson et al. (1995), Blisniuk et al. (2012), Wright et al. (2014)
Varnish microlamination (VML)	Provides both minimum age and paleoclimatic history experienced by the pavement	Method relies on regional calibrations using numerical ages and requires care in sampling	Liu and Broecker (2007, 2008a, 2008b), Liu et al. (2013), Liu and Broecker (2013)

Table 5
Time required to develop a desert pavement in thousands of years (ka).

Ages (ka)	Context of sample collection	Location	Dating Method	References
1.4–6.2	samples collected under desert pavements on beach ridges	Patagonia, Argentina	^{14}C dating shells	Sauer et al. (2007)
5–6	samples collected under an incipient pavement	Mojave Desert, USA	IRSL and ^{14}C pedogenic carbonate	McDonald et al. (2003), Cyr et al. (2010)
8.3	Samples collected under pavement developed on alluvial fan after regional desiccation	Southern Arabia	^{14}C dating organics	Pietsch and Kuhn (2012)
6.0 ± 1.0	Samples from rough pavement	Precordillerra, Argentina	^{10}Be surface exposure dating	Hedrick et al. (2013)
6–40	Samples from pavement with bar and swale topography are ~6 ka; samples from smooth pavements range in age from ~35–40 ka in	Anza Borrego, USA	^{10}Be in pavement cobbles and U-series on pedogenic carbonate	Blisniuk et al. (2012)
7	Samples collected from fill terrace alluvium underneath "weak pavement"	Grand Canyon, USA	OSL	Anders et al. (2005)
11.1 ± 4.3	Samples from pavement with subtle swale topography	Dead Sea, Near East	^{10}Be surface exposure dating	LeBeon et al. (2010)
11–25	Samples collected under poor to moderate pavement 11–17 ka and under well-developed pavements 25 ka	Death Valley, USA	OSL on alluvium under pavement	Sohn et al. (2007)
12–18	Samples from incipient pavements 12–18 ka, and samples from well developed pavements 24–128 ka	Death Valley, USA	Varnish microlaminations	Liu and Broecker (2008a, 2008b)
12	"Poorly packed" pavement occurs on alluvial fan surfaces <12 ka, while "moderately to well packed" pavements occur on surfaces with 12–30 ka ages	Death Valley, USA	^{36}Cl depth profiles	Machette et al. (2008)
13–25	Samples from pavement with relict bar-and-swale topography yield 13–15 ka ages, while mature smooth pavements yield ages older than 25 ka	southern Nevada, USA	Varnish microlaminations	Dickerson et al. (2013)
14	Samples from pavement with some bar and swale topography	Atacama Desert, northern Chile	^{10}Be surface exposure dating	Cortes et al. (2012)
15	Samples collected under a smooth pavement surface	southern Nevada, USA	^{14}C pedogenic carbonate	Reheis et al. (1992).
15.5 ± 2.2	Samples from a pavement that still retains some bar-and-swale topography	Baja California, Mexico	^{10}Be surface exposure dating	Spelz et al. (2008)
17–35.5	Samples from a weakly developed Desert pavement	Coachella Valley, USA	^{10}Be surface exposure dating	Gray et al. (2014)
35.5 ± 2.5	Samples from a well-developed pavement with only subtle expressions of bar-and-swale topography	Coachella Valley, USA	^{10}Be surface exposure dating	Van Der Woerd et al. (2006)
56.4 ± 7.7	Samples from patchy and weakly-developed pavements with patches of interlocked pavement	Mojave Desert, USA	^{10}Be surface exposure dating	Oskin et al. (2007)
58–67	Well developed and "flat-surfaced" pavement formed sometime after an OSL age of ~58 ka; while the ^{10}Be exposure age is 66.6 ± 6.8 ka after correcting for inheritance	Tian Shan, China	^{10}Be surface exposure dating and OSL on alluvium under pavement	Huang et al. (2014)
70	Desert pavement goes through a transition from prominent bar-and-swale topography, immature pavement, moderate pavement, and then mature pavement, and this entire transition requires ~70 ka	Death Valley, USA	^{10}Be exposure dating and ^{36}Cl depth profiles	Frankel and Dolan (2007)
100 ± 22	Samples from a "poorly developed" desert pavement	Precordillera, Argentina	^{10}Be surface exposure dating	Siame et al. (1997)

Table 6
Reported ages of desert pavement around the globe, ordered from oldest to youngest.

Age	Region	Method	References	Notes	Landform host
9–37 Ma	Atacama, Northern Chile	^{21}Ne	Dunai et al. (2005)	Measurements from quartz clasts in desert pavements indurated by carbonate and salts	Alluvium
1.2–22 Ma	Atacama, Northern Chile	^{3}He	Evenstar et al. (2009)	Measurements from larger basalt clasts in pavement indurated with gypsum	Pediplain
3.9–15.15 Ma	Victoria Land, Antarctica	^{40}Ar/^{39}Ar and K/Ar	Marchant et al. (1993), Marchant and Denton (1996), Marchant et al. (1996)	Dated ash overlies stone pavement was determined.	Buried glacial deposits
3.7 ka — 15 Ma	Transantarctic Mountain, Antarctica	Dating of the underlying landform in cited prior research	Bockheim (2010)	Ventifaction increases while clast sizes decreases over time	Glacial deposits
9 Ma	Atacama Desert, Chile	^{10}Be, ^{26}Al, ^{21}Ne	Nishiizumi et al. (2005)	Sampled from quartzite cobble in pavement composed of angular clasts	Alluvial fan
6.6 Ma	Atacama Desert, Central Valley, Chile	Meteoric ^{10}Be in soil profile collected at 5 cm intervals	Wang et al. (2015)	Ventifacted pavement cobbles indurated with gypsum caps analyzed soil profile	Alluvial fan
>3 Ma	Atacama Desert, Chile	^{10}Be	Placzek et al. (2014)	Corrected for inheritance and analyzes the influence of minor erosion.	Stable alluvial surface
2–4 Ma	South-Central Australia "stony deserts"	^{21}Ne, ^{10}Be	Fujioka et al. (2005)	Cobbles composed of gibber (silcrete cobbles)	Alluvial fan; tablelands
2.12 Ma	Atacama, Central Chile	^{10}Be, ^{26}Al	Ewing et al. (2006)	Desert pavement at Yungay site with minimal evidence of ventifaction sampled in pavement indurated with salts	Alluvium
260 ka–1. 8 Ma	Dead Sea region, Middle East	^{10}Be, OSL	Matmon et al. (2009), Guralnik et al. (2010)	Stone pavement on alluvium, with amalgamation sampling	Alluvial terraces and deposits
0.9–1.8 Ma	Fowlers Gap, New South Wales, Australia	^{10}Be, ^{26}Al	Fisher et al. (2014)	Stone pavement on alluvial surface; amalgamation sampling	Pediment
~0.25–1.5 Ma	Atacama Desert, Chile	^{10}Be, ^{26}Al	Amundson et al. (2012), Jungers et al. (2013)	Pavements developed on landforms after abandonment	Alluvial fan and fill terrace
0.3–1.12 Ma	Negev Desert Israel	^{10}Be assuming clasts remained at the surface; maximum age for pavement	Boroda et al. (2014)	Amalgamation simple exposure age considered minimum age for pavement	Top of bedrock mesa
1.1 Ma	North-central Chile	^{10}Be	Rodriguez et al. (2013a)	Slow removal of fines blends longer-exposed cobbles with more newly-exposed cobbles	Fluvial terrace
119 ka–1 Ma	Atacama Desert, Chile and Peru	^{10}Be	Hall et al. (2008)	Sampled cobbles derive from desert pavements	Pediments and strath fluvial terraces
77 ka–1 Ma	Basin and Range, Crater Flat, Southern Nevada, USA	^{40}Ar/^{39}Ar, ^{36}Cl and K/Ar	Zreda et al. (1993), Heizler et al. (1999), Valentine and Harrington (2006), Valentine et al. (2006)	Silt accumulation underneath lapilli in a particular size range produces stable pavements	Basalt flow
17 ≤ 730 ka	Great Basin, Crater Flat, Nevada, USA	Th^{230}-U^{234} dating of pedogenic carbonate under pavement; and CR dating	Peterson et al. (1995)	Stone pavements on different geomorphic surfaces	Alluvial fan units and basalt flows
41–670 ka	Iglesia basin, central Andes, Argentina	^{10}Be	Siame et al. (1997)	Mixture of ^{10}Be ages implies mixing of cobbles with different exposures through deflation and periglacial processes	Alluvial fan
49–610 ka	Negev Desert, Israel	^{10}Be	Boroda et al. (2011), Boroda et al. (2013)	Pebble sized chert desert pavement clasts	Talus flatiron
224–600 ka	Great Basin, Lunar Crater, Nevada, USA	^{36}Cl	Shepard et al. (1995)	Boulders (10–15 cm) in stone pavement formed on the lava flow bedrock	Basalt flow
32–-580 ka	Cima Volcanic Field, Mojave Desert	^{3}He, OSL, K-Ar of underlying basalt flows	Turrin et al. (1985), Wells et al. (1985), McFadden et al. (1987), McFadden et al. (1998), Dietze et al. (2016)	Pavements develop through accumulation of aeolian dust under clasts	Basalt flow
260–505 ka	Bishop Tuff, California, USA	^{21}Ne	Goethals et al. (2007)	Pavement samples show less age variation than bedrock samples	Welded tuff
57–428 ka	Tian Shan, China	^{10}Be, OSL	Huang et al. (2014)	Minimal erosion occurs on pavements younger than 428 ka	Strath fluvial terraces
424 ± 151 ka	Atacama Desert, northern Chile	^{21}Ne	Gonzalez et al. (2006)	Pavements on fans abandoned by faulting	Alluvial fan
420 ± 16 ka	Gobi-Altai Mountains piedmont	^{10}Be	Lv et al. (2010)	Age based on assumption of low inheritance	Sloping alluvial plain
281 ± 19 ka	Lanzarote, Canary Islands	^{40}Ar/^{39}Ar; ^{3}He	Dunai and Wijbrans (2000)	Lava flow blocks in the desert pavement sampled for both dating methods	Basalt flow
3–280 ka	Mecca Hills, Colorado Desert, USA	^{10}Be surface exposure and depth profiles	Gray et al. (2014)	Stone pavement development with occasional boulders sampled for ^{10}Be	Alluvial fan units

Table 6 (*continued*)

Age	Region	Method	References	Notes	Landform host
<12 ka, 50–100 ka, 130 ka, 150 ka, > 260 ka	Great Basin, Death Valley, California, USA	^{10}Be, ^{26}Al, ^{36}Cl: depth profile and on surface clasts	(Nishiizumi et al. (1993), Duhnforth et al. (2007), Frankel et al. (2007a, 2007b), Machette et al. (2008), Owen et al. (2011), Ivy-Ochs et al. (2013)	Stone pavements on different surfaces, where inheritance of different sized clasts creates ambiguities in ages	Alluvial fan units and Lake Manly shorelines
<63 ka to <350 ka	Lower Colorado River, USA	^{3}He	Fenton and Pelletier (2013)	Basalt boulders on desert pavements	Alluvial fan
12–245 ka	Death Valley, California	Varnish microlaminations	Liu and Broecker (2008b)	VML records minimum age for exposure of the sampled pavement clast	Alluvial fan
204 ± 11 ka and older (based on stratigraphy)	Laguna Salada, Baja California, Mexico	^{10}Be	Spelz et al. (2008)	Incipient pavement on Q_6; and well-developed pavements found on Q_7 (204 ± 11 ka) and Q_8	Alluvial fan
66–198 ka	West Grand Canyon, USA	^{3}He,	Fenton et al. (2002), Fenton et al. (2004)	Pavement on basaltic outburst flood deposit	Stream terrace
141–184	South Sheba lava flow, San Francisco volcanic field, Colorado Plateau, Arizona, USA	^{3}He, ^{21}Ne,	Fenton and Niedermann (2014)	Two pavements have similar ages to pressure ridges	Pavement formed on basalt flow
24–181	Eastern Precordillera, Argentina	^{10}Be	Hedrick et al. (2013)	Well-developed pavements are more stable for longer periods on strath (up to ~181 ka) terraces than fans (up to ~61 ka)	Strath stream terrace and alluvial fans
170 ka	Negev Desert, Israel	^{10}Be, OSL	Guralnik et al. (2011)	Pavement formed after terrace abandonment with stability enhanced by gypsum	Fill stream terrace
97–159 ka	Capitol Reef, Utah, USA	^{3}He	Marchetti and Cerling (2005)	Dated by amalgamation, pavements are 34–96 ka younger than boulder exposure ages	Fill stream terrace composed of debris-flow deposits
137 ± 9 ka	Northeast Tibet	^{10}Be, ^{26}Al	Shirahama et al. (2015)	Pavement consists of pebbles	Strath terrace
31–132 ka	Northwest Argentina	^{10}Be	Siame et al. (2015)	Pavements have dark rock varnish	Strath terraces
100–130 ka	Lake Eyre, Australia	Soil and pavement stratigraphy	Al-Farraj (2008)	Pavement with varying stone cover	Beach gravel
15–130 ka	Kyle Canyon, southern Nevada, USA	^{14}C, Th^{230}-U^{234}	Reheis et al. (1992)	Secondary carbonate dated from soil positions	Alluvial fan
7–109 ka	Tributaries of the Grand Canyon, USA	^{10}Be, OSL	Anders et al. (2005)	OSL on terraces up to 50 ka; amalgamation sampling of pavement clasts for ^{10}Be	Fill stream terraces
106 ± 15 ka	Gonghe basin, Tibet	^{10}Be	Perrineau et al. (2011)	Larger pavement cobbles sampled	Strath terrace
106 ka	Chocolate Mountains, Colorado Desert, USA	Th^{230}-U^{234} dating of pedogenic carbonate under well-developed pavement	Wright et al. (2014)	Pedogenic carbonate on "Q3" surface provides minimum age	Alluvial fan
100 ka	Libyan Plateau, Egypt	Archaeological evidence: Middle Paleolithic artifacts in pavement	Adelsberger and Smith (2009)	Pavement on regolith	Bedrock plateau
70–96 ka	Vidal Valley, Mojave Desert, USA	Th^{230}-U^{234} dating of pedogenic carbonate under well-developed pavement	Ku et al. (1979)	Pedogenic carbonate on "Q2b" surface provides minimum age	Alluvial fan
90 ka	Qilian Shan, Northern Tibet	^{10}Be, ^{26}Al	Hetzel et al. (2004)	Clasts sampled from fluvial terrace where pavement inferred from descriptions	Alluvial fan
13–87	Great Basin, Stonewall Flat, Nevada	Varnish microlaminations and ^{10}Be	Dickerson et al. (2013, Dickerson and Cocks (2015)	Sampled away from evidence of bioturbation	Alluvial fan
11–87	Dead Sea, Israel	^{10}Be	LeBeon et al. (2010)	Pavement clasts sampled on deposits offset by faulting	Alluvial fan
84 ka	Lees Ferry, Colorado Plateau, USA	OSL and ^{10}Be	Hidy et al. (2010)	Pavement on Colorado River gravels	Fill river terrace
44–84 ka	Tashkurgan Valley, Xinjiang Province, China	^{10}Be	Owen et al. (2012)	Age range on Tashkurgan stage boulders in a desert pavement	Moraine
51–82 ka	Badia Jordan	OSL	Fuchs et al. (in press)	OSL samples from aeolian silt and sand underneath pavements	Basalt lava flow
71–72 ka	Fremont River and Wind River, Rocky Mountains, USA	^{10}Be, ^{26}Al	Anderson et al. (1996)	Cobbles samples from pavement on glacial outwash terrace, corrected for inheritance	Strath river terrace
40–60 ka	Chajnantor Plateau, Chile	^{10}Be, ^{36}Cl	Ward et al. (2015)	Sampled clasts from desert pavements	Moraines
56.4 ± 7.47 ka	Mojave Desert, USA	^{3}He, ^{10}Be	Oskin et al. (2007)	Pavement clasts collected with amalgamation strategy and considering inheritance	Alluvial fan, offset by faulting
5–56 ka	Providence Mountains, Mojave Desert, USA	^{10}Be, OSL, IRSL, ^{14}C on carbonate	McDonald et al. (2003), Cyr et al. (2010)	Incipient pavements require ~5–6 ka to form	Alluvial fan
~25–50 ka	Mojave Desert, USA	^{14}C	Meek (1989, 1990, 2004), Reheis and Edwine (2008)	Pavement consists of rounded cobbles on top of dated shells	Beach ridge and shorelines

(*continued on next page*)

Table 6 (*continued*)

Age	Region	Method	References	Notes	Landform host
5–47 ka	Anza Borrego, Colorado Desert, USA	^{10}Be: surface and depth profiles; Th^{230}-U^{234} dating of pedogenic carbonate	Blisniuk et al. (2012)	^{10}Be and U-series ages are consistent	Alluvial fan
44 ka	South Iran	^{10}Be	Regard et al. (2006)	Quartzite gravels sampled from desert pavement	Alluvial-fan gravels on anticline
35 ± 7 ka, 35 ± 2.5 ka	Coachella Valley, Colorado Desert, CA, USA	^{10}Be: surface and depth profiles	VanDerWoerd et al. (2006), Blisniuk et al. (2010)	Pavement on fan units offset in San Jacinto and San Andreas Fault Zones	Alluvial fan gravels
14–35 ka	Northern Chile	^{10}Be, OSL	Cortes et al. (2012)1	Minor and swale topography remains on younger 14 ka pavement	Alluvial fan, offset by faulting
33 ± 0.4 ka	Salt River, central Arizona, USA	^{14}C	Larson et al. (2010)	Pedogenic carbonate, innermost rind yields minimum age for the overlying pavement	Strath terrace
33 ka	Lake Frome, southern Australia	OSL	May et al. (2015)	Pavement on dated aeolian dust covering gravels	Beach ridge
17–30 ka	Sierra El Mayor, Baja California, Mexico	^{10}Be, OSL	Armstrong et al. (2010)	Smooth pavement with varnished quartzite and schistose cobbles tops terrace treads	Stepped strath terraces
11–25 ka	Great Basin, southern Death Valley, USA	OSL	Sohn et al. (2007)	Poor to moderate pavement formation takes 11–17 ka, but well-developed pavements occur in 25 ka	Alluvial fan
24 ka	Mojave River, Mojave Desert, CA USA	OSL, ^{10}Be	Cyr et al. (2015)	Pavement age represents the most recent cobble transportation event along the Mojave River	Strath terrace
3–20 ka	Andean Precordillera, Argentina	^{14}C, ^{10}Be pebble amalgamation	Schmidt et al. (2011)	Holocene terraces have poor pavement development compared to Pleistocene terraces	Strath terrace
11.1–12.34	Owens Valley, California, USA	Varnish microlaminations	Mihir et al. (2015)	Minimum age for debris flow fans	Debris flow deposits

Table 7
^{10}Be exposure ages of cobbles and a pair of ^{10}Be-^{26}Al analysis of one burial sample (Sawik021) on terraces of the Salt and Verde Rivers.

Sample	Lithology[a]	Latitude (°N; WGS84)	Longitude (°W; WGS84)	Elevation (m)	Thickness (cm)[b]	Shielding factor[d]	^{10}Be concentration (10^5 atoms g^{-1} SiO_2)[e,f]	^{26}Be concentration (10^6 atoms g^{-1} SiO_2)[g]	Exposure age (ka)[h,i,j]	Exposure age (ka)[k]	Terrace age (ka)[l]	^{26}Al concentration (10^6 atoms g^{-1} SiO_2)[m]	Source
Mesa001	Gneiss	33.53996	111.62935	461	4	0.99	7.70 ± 0.28	5.02 ± 0.18	91.5 ± 8.8	94.9 ± 9.1	85.8 ± 2.0		Larson et al. (2017)
Mesa002	Gneiss	33.53988	111.62924	462	5.5	0.99	6.83 ± 0.87	4.15 ± 0.52	76.3 ± 11.9	79.1 ± 12.4			
Mesa003	Granite	33.53999	111.62936	459	5	0.99	6.19 ± 0.37	3.51 ± 0.21	64.3 ± 6.8	66.6 ± 7.1			
Mesa004	Quartzite	33.53991	111.62922	458	4.5	0.99	7.09 ± 0.45	4.41 ± 0.28	80.8 ± 8.9	83.7 ± 9.2			
Mesa005	Granite	33.53992	111.62933	460	4.5	0.99	7.88 ± 0.46	5.20 ± 0.30	95.4 ± 10.2	98.9 ± 10.6			
Mesa006	Granite	33.53999	111.62952	458	4	0.99	9.68 ± 0.50	7.00 ± 0.36	129.2 ± 13.5	133.9 ± 14.0			
Mesa007	Mixture	33.53951	111.62856	450	Deep[c]		2.67 ± 0.09	Inheritance	Inheritance	Inheritance			
MesaV045	Quartzite	33.66484	111.69253	496	3	0.99	5.09 ± 0.31	3.70 ± 0.12	64.7 ± 2.1	67.0 ± 6.3	46.0 ± 23.2		This study
MesaV046	Gneiss	33.66486	111.69258	494	5	0.99	3.11 ± 0.11	1.72 ± 0.06	30.4 ± 1.15	31.5 ± 3.0			
MesaV047	Gneiss	33.66489	111.6926	495	4	0.99	3.97 ± 0.14	2.58 ± 0.09	45.3 ± 1.6	46.9 ± 4.4			
MesaV048	Gneiss	33.66486	111.69267	497	5	0.99	2.72 ± 0.16	1.34 ± 0.08	23.6 ± 1.4	24.4 ± 2.6			
MesaV049	Granite	33.66499	111.69298	496	6	0.99	5.97 ± 0.24	4.59 ± 0.18	82.5 ± 3.4	85.5 ± 8.3			
MesaV050	Granite	33.66501	111.69302	496	4.5	0.99	3.08 ± 0.14	1.69 ± 0.07	29.7 ± 1.3	30.7 ± 3.0			
SM037	Gneiss	33.57004	111.63284	525	3	0.99	7.55 ± 0.31	6.17 ± 0.26	106.6 ± 4.6	110.4 ± 10.9	82.7 ± 2.4		This study
SM038	Gneiss	33.57041	111.63264	524	4	0.99	5.89 ± 0.19	4.50 ± 0.14	77.9 ± 2.6	80.8 ± 7.6			
SM040	Gneiss	33.57214	111.63015	520	4.5	0.99	7.93 ± 0.51	6.55 ± 0.42	115.1 ± 7.7	119.4 ± 13.3			
SM041	Granite	33.57112	111.62885	522	4.5	0.99	4.69 ± 0.14	3.31 ± 0.10	57.2 ± 1.8	59.2 ± 5.5			
SM042	Granite	33.56667	111.62941	522	1.5	0.99	4.70 ± 0.16	3.31 ± 0.11	57.4 ± 2.1	59.4 ± 5.6			
SM043	Quartzite	33.57004	111.63284	525	3	0.99	6.20 ± 0.25	4.81 ± 0.19	81.8 ± 3.4	84.8 ± 8.3			
LH028	Granite	33.7056	111.70166	618	5	0.99	2.61 ± 0.11	1.23 ± 0.05	19.6 ± 0.8	20.3 ± 1.9	16.6 ± 1.1		This study
LH029	Granite	33.70545	111.70614	620	4	0.99	2.01 ± 0.09	0.62 ± 0.03	9.8 ± 0.4	10.2 ± 1.0			
LH030	Gneiss	33.70548	111.70161	618	5	0.99	1.79 ± 0.08	0.41 ± 0.02	6.5 ± 0.3	6.7 ± 0.6			
LH031	Gneiss	33.70573	111.70619	618	5	0.99	2.63 ± 0.13	1.25 ± 0.06	20.0 ± 1.0	20.7 ± 2.0			
LH032	Granite	33.70577	111.70171	618	5	0.99	2.30 ± 0.09	0.92 ± 0.03	14.7 ± 0.6	15.3 ± 1.4			
LH033	Gneiss	33.70541	111.70163	619	4	0.99	1.78 ± 0.09	0.37 ± 0.02	5.9 ± 0.3	6.1 ± 0.6			
LH034	Quartzite	33.70548	111.70163	620	7	0.99	3.83 ± 0.21	2.44 ± 0.13	39.8 ± 2.2	41.2 ± 4.3			
BP008	Granite	33.55286	111.57689	434	3.5	0.99	3.33 ± 0.30	1.93 ± 0.17	35.3 ± 4.4	36.6 ± 4.6	30.7 ± 1.0		Larson et al. (2017)
BP010	Granite	33.55286	111.57689	434	4.6	0.99	3.26 ± 0.19	1.85 ± 0.10	34.2 ± 3.6	35.5 ± 3.7			
BP011	Gneiss	33.55286	111.57689	434	4	0.99	5.05 ± 0.27	3.65 ± 0.19	67.6 ± 7.0	70.0 ± 7.3			
BP012	Gneiss	33.55286	111.57689	434	5.8	0.99	3.25 ± 0.24	1.84 ± 0.13	34.3 ± 3.9	35.5 ± 4.1			
BP013	Granite	33.55286	111.57689	434	5.4	0.99	2.47 ± 0.19	1.07 ± 0.08	19.8 ± 2.3	20.5 ± 2.4			
BP014	Mixture	33.55286	111.57689	429	Deep[c]		1.40 ± 0.08	Inheritance	Inheritance	Inheritance			
Sawik015	Quartzite	33.48903	111.71483	438	4.5	0.99	18.07 ± 0.44	16.24 ± 0.40	320.5 ± 8.6	332.9 ± 32.6	332.0 ± 4.1		This study
Sawik016	Granite	33.48903	111.71483	439	6.5	0.99	19.02 ± 0.60	17.19 ± 055	346.9 ± 12.1	360.4 ± 36.4			
Sawik017	Quartzite	33.48903	111.71483	439	4	0.99	18.18 ± 0.57	16.35 ± 0.51	321.4 ± 10.9	333.8 ± 33.4			
Sawik018	Granite	33.48903	111.71483	437	4.5	0.99	20.12 ± 0.52	18.28 ± 0.47	364.7 ± 10.3	378.9 ± 37.6			
Sawik019	Genisx	33.48903	111.71483	439	5.5	0.99	19.01 ± 0.48	17.18 ± 0.44	343.6 ± 9.6	357.0 ± 35.2			
Sawik020	Gneiss	33.48903	111.71483	438	4.5	099	17.2 ± 0.52	15.44 ± 0.46	303.3 ± 9.9	315.0 ± 31.2			
Sawik021	Mixture	33.48903	111.71483	438	Deep[c]		1.35 ± 0.07	Inheritance	Inheritance	Inheritance		6.70 ± 0.19	

Note:
[a] The tops of all samples were exposed at the terrace surface.
[b] Whole cobble was used considering possible multiple turnaround since initial abandonment.
[c] Amalgamated (n > 30) cobbles were sampled from deep (>5 m) depth.
[d] Geometric shielding correction for topography was measured on an interval of 10°.
[e] Uncertainties are reported at the 1σ confidence level.
[f] Propagated uncertainties include error in the blank, carrier mass (1%), and counting statistics.
[g] Inheritance yielded from a mixture (n > 30) of cobble at depth (e.g. Mesa007, BP014, and Sawik021) is corrected for calculating pure production since abandonment.
[h] All ages are corrected for inheritance and expressed with 1 sigma external uncertainty.
[i] Beryllium-10 model ages were calculated using global production rate of 4.49 ± 0.39 at SLHL with the Cosmic-Ray Produced Nuclide Systematics (CRONUS) Earth online calculator version 2.2 (http://hess.ess.washington.edu/).
[j] Propagated error in the model ages include a 6% uncertainty in the production rate of ^{10}Be and a 4% uncertainty in the ^{10}Be decay constant.
[k] Ages were calculated using North America regional production rate of 4.33 ± 0.21 (Balco et al., 2009).
[l] Weighted mean of ages calculated using global production rate and error within the 1σ confidence level.
[m] Measured for the same sample of which ^{10}Be (Sawik021) abundance was measured for yielding maximum burial age assuming one simple burial event of all cobbles analyzed.

Table 8
Results of *in-situ* produced cosmogenic ^{14}C. All the errors are 1σ. All the processes for calculating ^{14}C atoms *in-situ* produced in quartz are based on the equations in prior research (Donahue et al., 1990).

Sample	Lab ID	Quartz (g)	$\delta^{13}C_{meas}$[a]	F[b]	CO_2 yield (μL)[c]	Dead $CO_{2(mL)}$[d]	^{14}C (10^5 atoms g^{-1})	$^{14}C/^{10}Be$
Sawik017	KU151205	5.26	−30.2400	0.0432	36.9	1.5162	1.97 ± 0.48[e]	0.10 ± 0.01
Sawik018	KU151206	5.15	−39.1828	0.0335	43.5	1.4753	Failed	Failed
Sawik020	KU151204	5.20	−35.8799	0.0328	8.2	1.5582	1.69 ± 0.52[f]	0.09 ± 0.01

[a] Used for calibration with NIST oxalic acid ($^{14}C/^{12}C$: 134 pMC) $\delta^{13}C = -17.8‰$).
[b] Calculation of fraction modern corrected for background (dead CO_2) with average (n = 6) value of 0.0012. Uncertainty causing from pressure gauge is 2.3 μg.
[c] Total CO_2 extracted from quartz with step-wise collection and purification.
[d] Low ratio ($<3 \times 10^{-15}$) of background carrier spiked.
[e] Corrected for process blank with a mean ^{14}C concentration of 9.46 (± 0.32) $\times 10^5$.
[f] Corrected for process blank with a mean ^{14}C concentration of 6.33 (± 2.01) $\times 10^5$.

Table 9
Equivalent doses (De), dose rate and OSL ages of Blue Point terrace samples.

Sample	Water content[a] (%)	Dose Rate (Gy/ka)	Equivalent dose (Gy)	Aliquots used[b] (n/N)	OSL age (ka, 1σ SE)
BPO-001	7.3 (30.6)	3.62 ± 0.09 (2.90 ± 0.07)	159 ± 3	16/16	44 ± 1 (55 ± 2)
BPO-002	6.0 (28.5)	4.07 ± 0.10 (3.27 ± 0.08)	131 ± 2	15/16	32 ± 1 (40 ± 1)

Note:
[a] Numbers in parenthesis were those calculated based on saturated water contents.
[b] n/N refers to the ratio of (the number of aliquots used for data analysis)/(total number of aliquots loaded in the OSL measurement system).

Table 10
Soil profiles of the Blue Point, Mesa, and Sawik terraces of the Salt River; soils data collected with Troy Péwé.

Horizon	Blue Point	Mesa	Sawik
Soil	Typic Haplargid	Petrocalcic Calciorthid	Petrocalcic Calciorthid
Desert pavement	90% pebbles and cobbles with the oldest rock varnish VML[a] sequence of LU-1/LU-2/LU-3/LU-4 (WP3) minimum age 30 ka	85% pebble and cobbles with the oldest rock varnish VML sequence of LU-1/.../LU-4/LU-5 (WP6+) minimum age 74–85 ka	95% cobbles with the oldest rock varnish VML sequence of LU-1/.../LU-4/LU-5 (WP6+) minimum age 74–85 ka
Av	1–3 cm; light yellowish brown (10 years 6/4); dry; many vesicular pores, weak platy structure; soft, slightly sticky (wet); few fine roots; slightly effervescent; moderately alkaline (pH 8.0); clear smooth boundary	2–5 cm; light yellowish brown (10 years 6/4); dry; many vesicular pores, weak platy structure; slightly hard, friable; nonsticky and nonplastic (wet); common fine roots; slightly effervescent; moderately alkaline (pH 8.2); abrupt smooth boundary	2–7 cm; light yellowish brown (10 years 6/4) dry; many vesicular pores, weak platy structure; slightly sticky; nonsticky and nonplastic (wet); few fine roots; slightly effervescent; moderately alkaline (pH 8.0); abrupt smooth boundary
Bw	1–4 cm; light brown 7.5 years 6/4; dry; fine sandy loam; weak fine granular structure; soft, friable, slightly sticky (wet); rock fragments completely coated with carbonate; 30% pebbles; violent effervescent; moderately alkaline (pH 8.1); clear wavy boundary	8 to 20 cm; reddish brown (5 years 5/4); dry; massive; friable, slightly hard, slightly sticky and slightly plastic (wet); common fine roots; common fine interstitial pores; 50% pebbles; strongly effervescent; moderately alkaline (pH 8.3); clear wavy boundary	2 to 12 cm; reddish brown (5 years 5/4); dry; massive; friable, slightly hard, slightly sticky and slightly plastic (wet); few fine roots; few very fine interstitial pores; 70% pebbles; strongly effervescent; moderately alkaline (pH 8.1); clear wavy boundary
Bk	5 cm to 70 cm; pale brown (10 years 6/3)dry ; extremely gravelly loam; massive; soft, very friable; nonsticky, nonplastic (wet); few fine roots; 80% pebbles; common thin carbonate coatings covering pebbles; strongly effervescent; moderately alkaline (pH 8.1); abrupt wave boundary	10 cm to 90 cm; light brown (7.5 years 6/4) dry; loose to very friable; slightly sticky and slightly plastic (wet); few fine roots; common fine interstitial pores; 60% pebbles; common carbonate coatings covering and bridging pebbles; violently effervescent; moderately alkaline (pH 8.1); abrupt smooth boundary	5 cm to 50 cm; light brown (7.5 years 6/4) dry; loose to very friable; non sticky and slightly plastic (wet); few fine roots; common fine interstitial pores; 60% pebbles; common carbonate coatings covering and bridging pebbles; violently effervescent; moderately alkaline (pH 8.0); abrupt smooth boundary
Bkm	Not present	90 cm - pinkish white (7.5 years 8/2) dry; massive; extremely hard; extreme violet effervescence (Stage IV carbonates)	50 cm - pinkish white (7.5 years 8/2) dry; massive; extremely hard; extreme violet effervescence (Stage IV carbonates)
Cr	Observed in stream cuts at depth ~4 m partially weathered granite; common thin carbonate veins in fractures; abrupt wavy boundary	Observed in road cuts at depth ~5 m partially weathered granite; common thin carbonate veins in fractures; abrupt wavy boundary	Observed in road cut at depth ~4 m partially weathered granite; common thin carbonate veins in fractures; abrupt wavy boundary

[a] VML sequence nomendature follows Liu and Broecker (2008a, 2008b).

Table 11
$^{87}Sr/^{86}Sr$ analyses from the Salt River and Verde River terrace. Each datum represents a single analysis from samples collected in a soil pit. The samples from each depth were first subject to HCl to first analyze only the carbonate fraction; the remaining silicate remainder was then analyzed separately. Each depth profile starts with dust collected from the surfaces of pavement rocks, continues into the upper half of the Av horizon, lower half of the Av horizon, B horizon, and then C horizon. Since the Stewart Mountain, Verde Mesa, and Verde Lousley Hills terraces either lacked an Av horizon or had only a very thin Av horizon, medium sand was sampled instead directly underneath surface boulders. Each pulverized rock sample collected from the C horizon represent an amalgamation of 10 different clasts.

$^{87}Sr/^{86}Sr$ sampled landform	Salt Blue Point	Salt Mesa	Salt Sawik	Salt Stewart Mtn	Verde Mesa	Verde Lousley Hills
Coordinates	N 33.55273 W 111.57816	N 33.53986 W 111.62907	N 33.48950 W 111.71280	N 33.57167 W 111.63179	N 33.66457 W 111.69182	N 33.70105 W 111.71001
Surface dust HCl leachate	0.708946	0.707483	0.706944	0.707119	0.708216	0.707722
Surface dust silicate	0.711155	0.711504	0.711552	0.712489	0.711715	0.711867
Av upper layer dust HCl leachate	0.709011	0.708032	0.708843	0.709274	0.70878	No Av
Av upper layer silicate	0.711094	0.712261	0.711785	0.711985	0.711783	No Av
Av lower layer dust HCl leachate	0.710018	0.709459	0.709767	Only thin Av	Only thin Av	No Av
Av lower layer silicate	0.711113	0.711870	0.712369	Only thin Av	Only thin Av	No Av
A medium sand 1 cm under boulders HCl leachate	No sandy layer	No sandy layer	No sandy layer	0.71249	0.713382	0.711894
A medium sand 1 cm under boulders silicate	No sandy layer	No sandy layer	No sandy layer	0.731442	0.750222	0.749513
Bw 5 cm under A HCl leachate	0.709157	0.712055	0.71147	0.71406	0.716388	0.711029
Bw 5 cm under A silicate	0.71152	0.710922	0.711341	0.722913	0.739578	0.748112
Bk 50 cm under A HCl leachate	0.709229	0.709442	0.712273	0.717302	0.716029	0.718124
Bk 50 cm under A silicate	0.711665	0.712022	0.713961	0.730028	0.731155	0.742057
Bk 50 cm pulverized rock	0.730430	0.728441	0.731148	0.740109	0.751139	0.743520
Bk 50 cm pulverized rock	0.732662	0.730105	0.735229	0.741225	0.747872	0.735220
Bk 50 cm pulverized rock	0.727511	0.727004	0.734633	0.735790	0.739884	0.745492

Fig. 1. Desert pavements around the globe (a) reg in the southern Levant Desert, Israel with 15-year old tank tracks for scale; (b) in the Sierra Pinacate Mexico, with an early Holocene trail (Hayden, 1976) for scale adjacent to the dashed line; (c) healing of a desert pavement 24 years after scraping, Mesa, Arizona (Péwé, 1978); (d) hamadas on Messak Settafet (earthobservatory.nasa.gov/IOTD/view.php?id=86118), Libya with road for scale; (e) deflation pavement of the Rio Grande, Peru (S 14.79102; W 75.3905), with image foreground 10 m wide; (f) gibbers near Coober Pedy, Australia with image foreground 5 m wide.

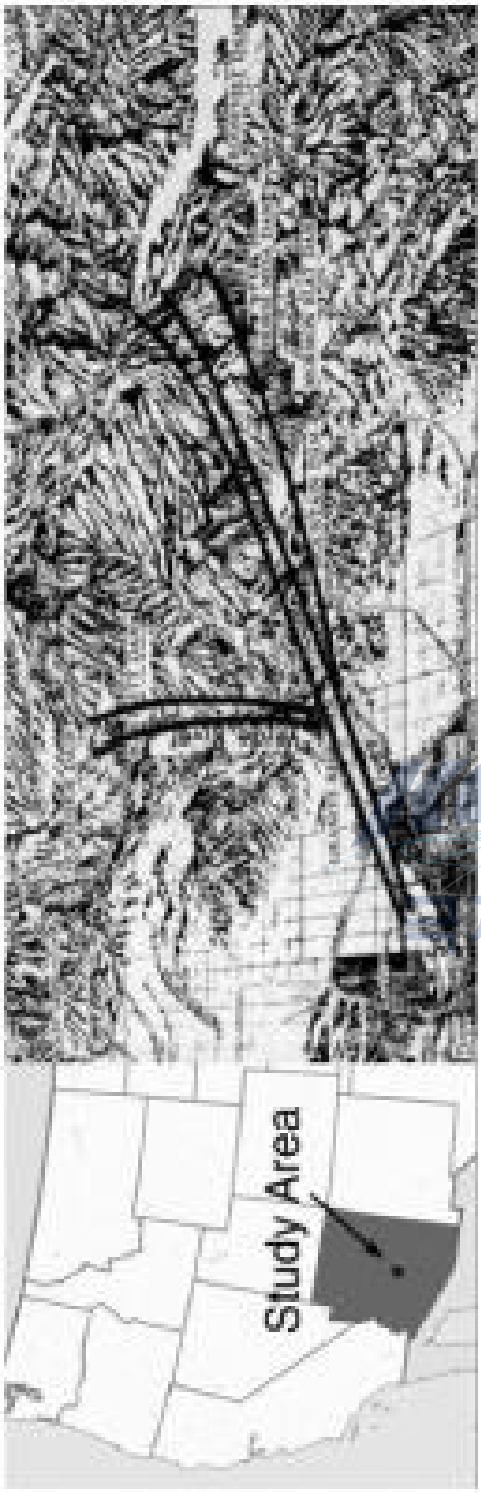

Fig. 2. Salt River Project's physiographic diagram served as the basemap for identifying the setting of strath terraces along the Salt and Verde Rivers (Péwé, 1978). Metropolitan Phoenix occurs in the lower left corner of this diagram.

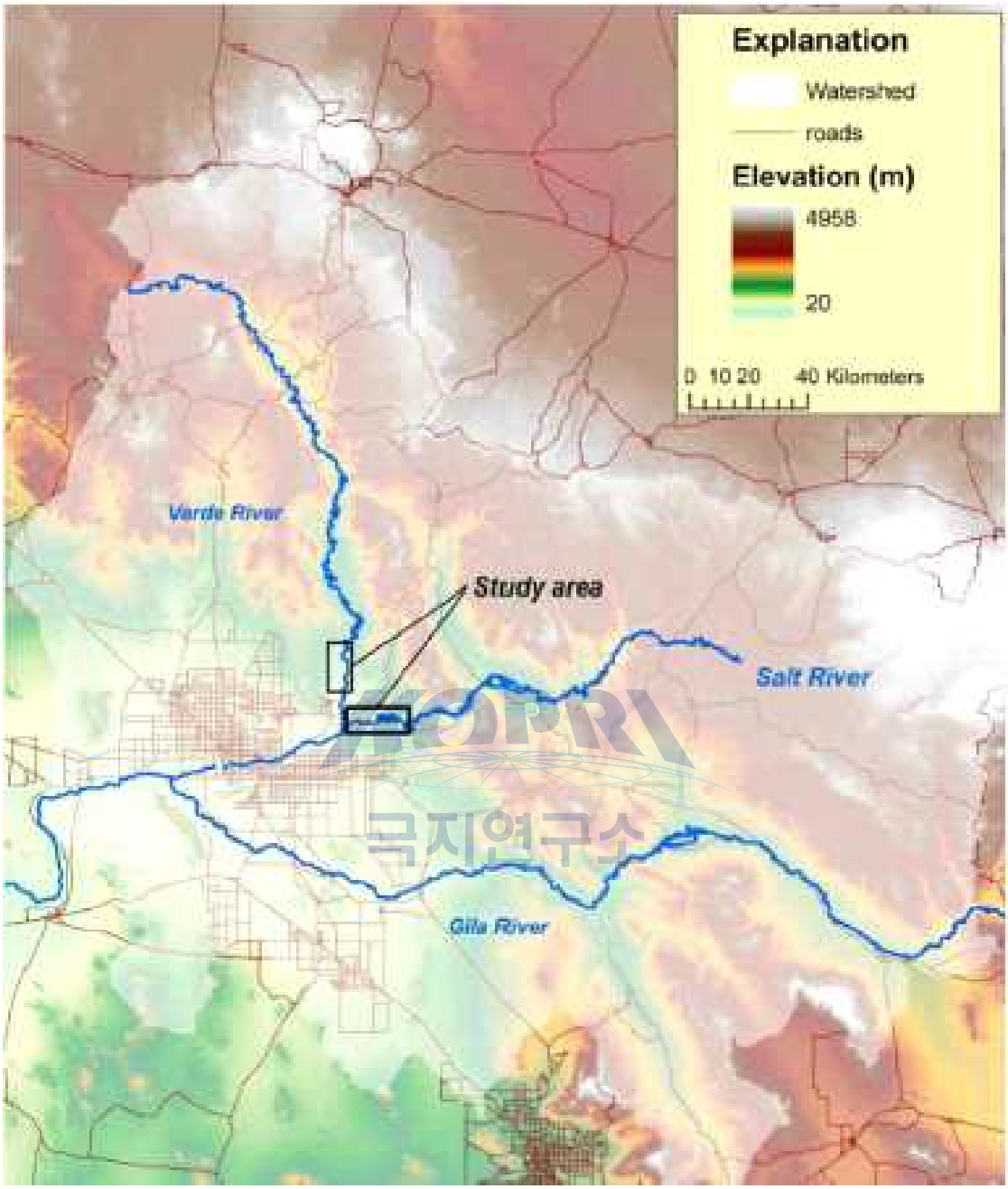

Fig. 3. Stream terraces along the lower Salt and Verde rivers, northeast of metropolitan Phoenix, offer a range of landforms ages capped by desert pavements. Fig. 4 presents the sequences of terraces observed in profiles across the middle of the identified study areas.

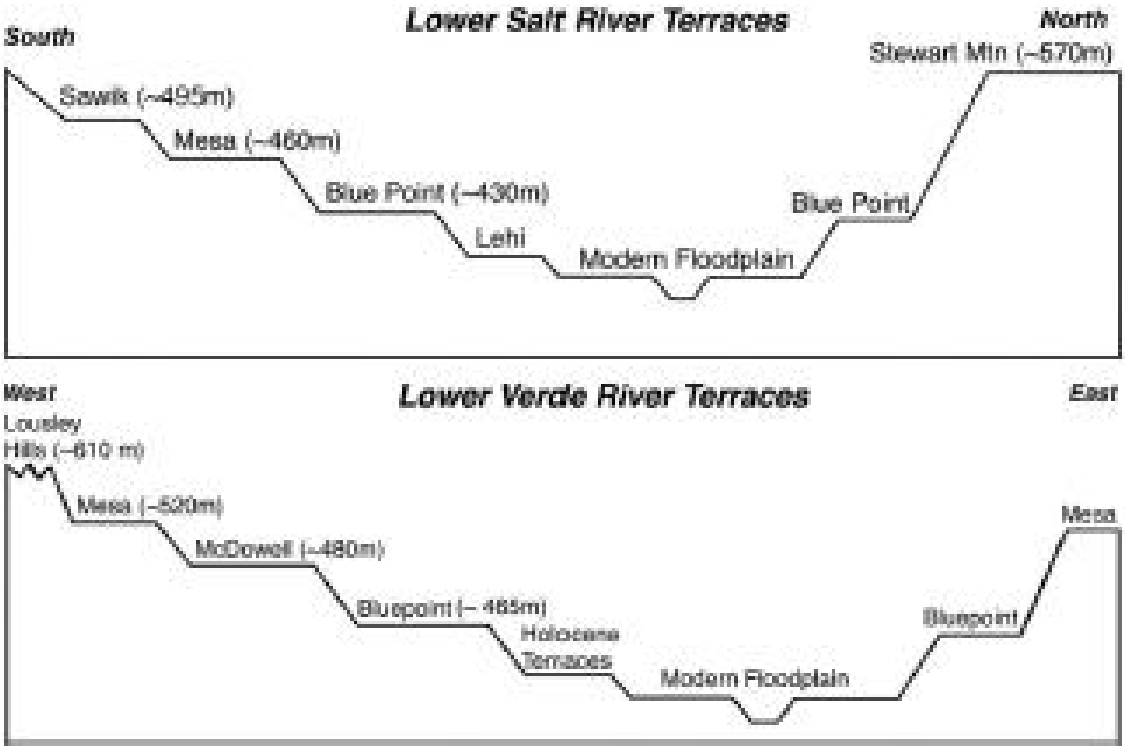

Fig. 4. Stream terraces along the lower Salt and Verde rivers, northeast of metropolitan Phoenix, where these idealized profiles represent sequences in the middle of the study areas identified in Fig. 3. The exact sampling locations are provided with the data (Table 7).

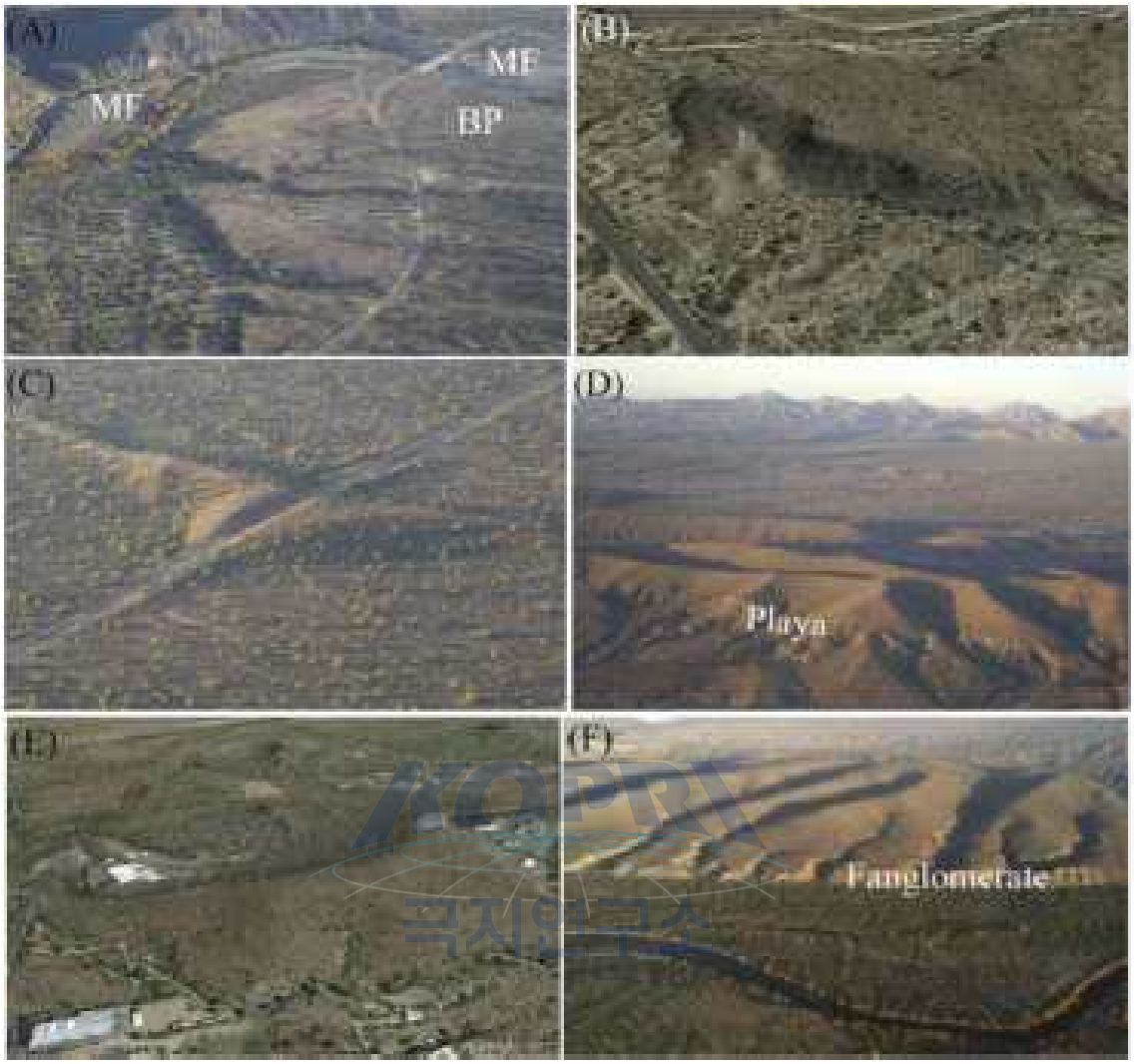

Fig. 5. Oblique aerial views of the Salt River (A-Blue Point, B-Mesa, C-Sawik, F-Stewart Mountain) and Verde River (B-Mesa, D-Lousley Hills) terraces sampled for 10Be. The Lousley Hills (D) and Stewart Mountain (F) are fill terraces and are heavily incised by deep gullies, while the other terraces exist as isolated remnants. In image A, BP and MF identify the Blue Point strath terrace and modern floodplain. Roads provide a sense of scale in A - C and E. The 110 m difference between the Salt River's floodplain and the top of the Stewart Mountain terrace in F, and the 50 m thickness of the gravels in the Lousley Hills gravels above underlying playa sediment in D provide a sense of scale. Images B and E are from Google Earth, while the others imagery taken from an airplane.

Fig. 6. Sampling sites for 10Be in the Salt River terraces (A - CBluePoint,D - F Mesa, G - ISawik,J - L Stewart Mountain). Individuals and 0.5 m high creosote bushes (Larrea tridentada) provide a sense of scale for the desert pavement views (A D, G, J). Rock hammers indicate scale for the sampled disk-shaped cobbles (B, E, H, K). Images C, F, and I show granitic material forming straths underneath the Blue Point, Mesa and Sawik terraces, while a 45 m stream cut shows the fanglomerate base underneath approximately 30 - 40 m of fill atop the Stewart Mountain (L) terrace.

Fig. 7. Sampling sites for the Verde River sampled for 10Be (A – CMesa,D – F Lousley Hills). 0.5 m high brittlebush (Encelia farinosa)providesa senseofscaleinthemiddleofthe desert pavement views (A, D). Rock hammers indicate scale for the sampled disk-shaped cobbles (B, E) size and disk-shape. Image C highlights playa clays forming the strath that underlies ~3 m of Mesa Verde terrace gravels, and image F presents the basal contact of the Lousley Hills gravels on top of the same playa clays, where the vertical thickness in this view is about 0.6 m.

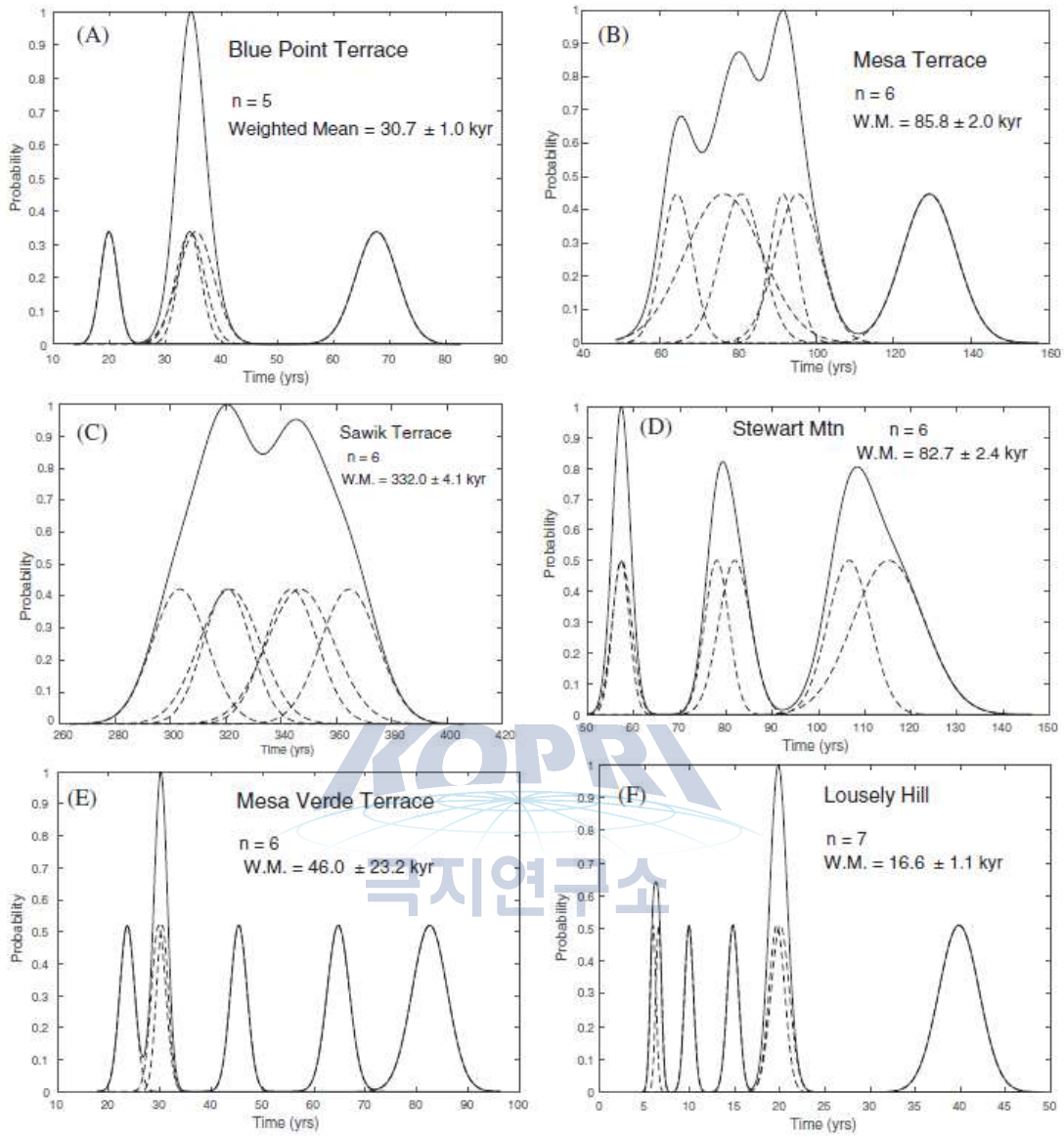

Fig. 8. Probability plots of ages of terraces along the Salt and the Verde River. (A) Blue Point terrace, (B) Mesa terrace, (C) Sawik terrace, (D) Stewart Mountain terrace, (E) Mesa Verde terrace, and (F) Lousely Hill terrace. All ages are weighted mean and error at 1σ confidence interval.

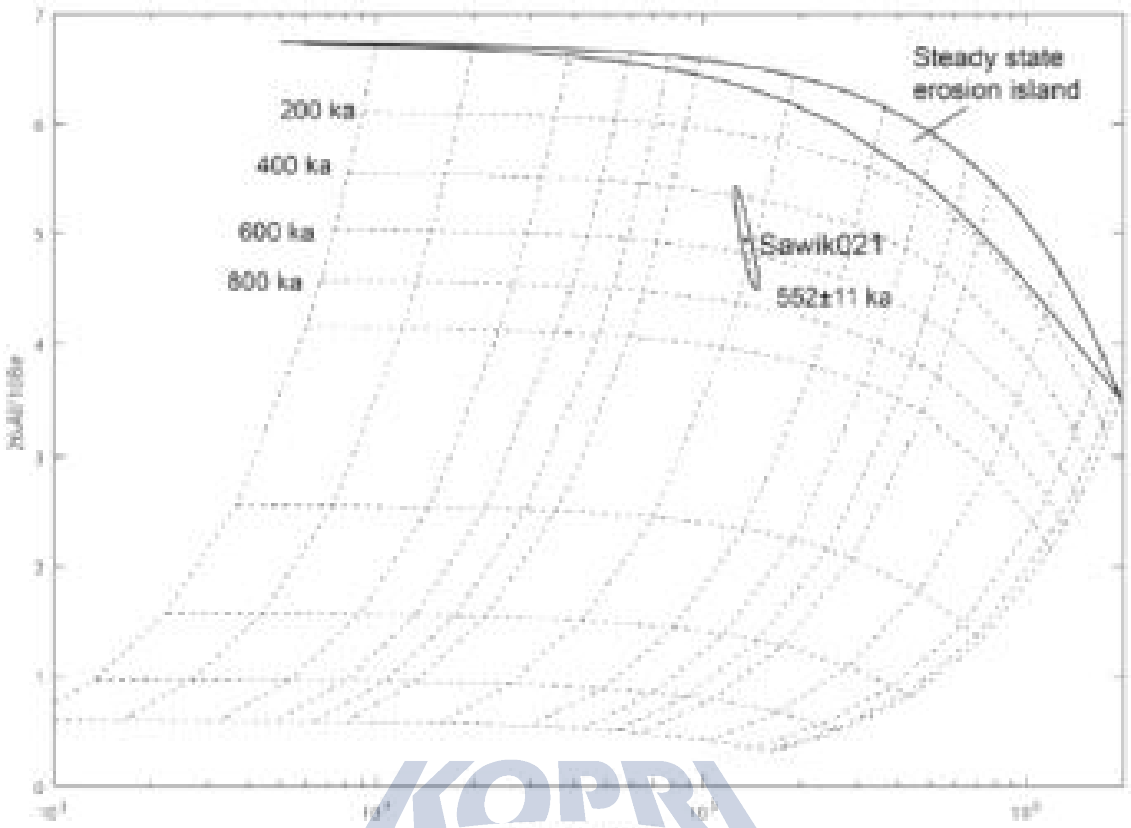

Fig. 9. Sample burial age of the Sawik terrace. The age is modeled assuming one depositional event and zero surface erosion.

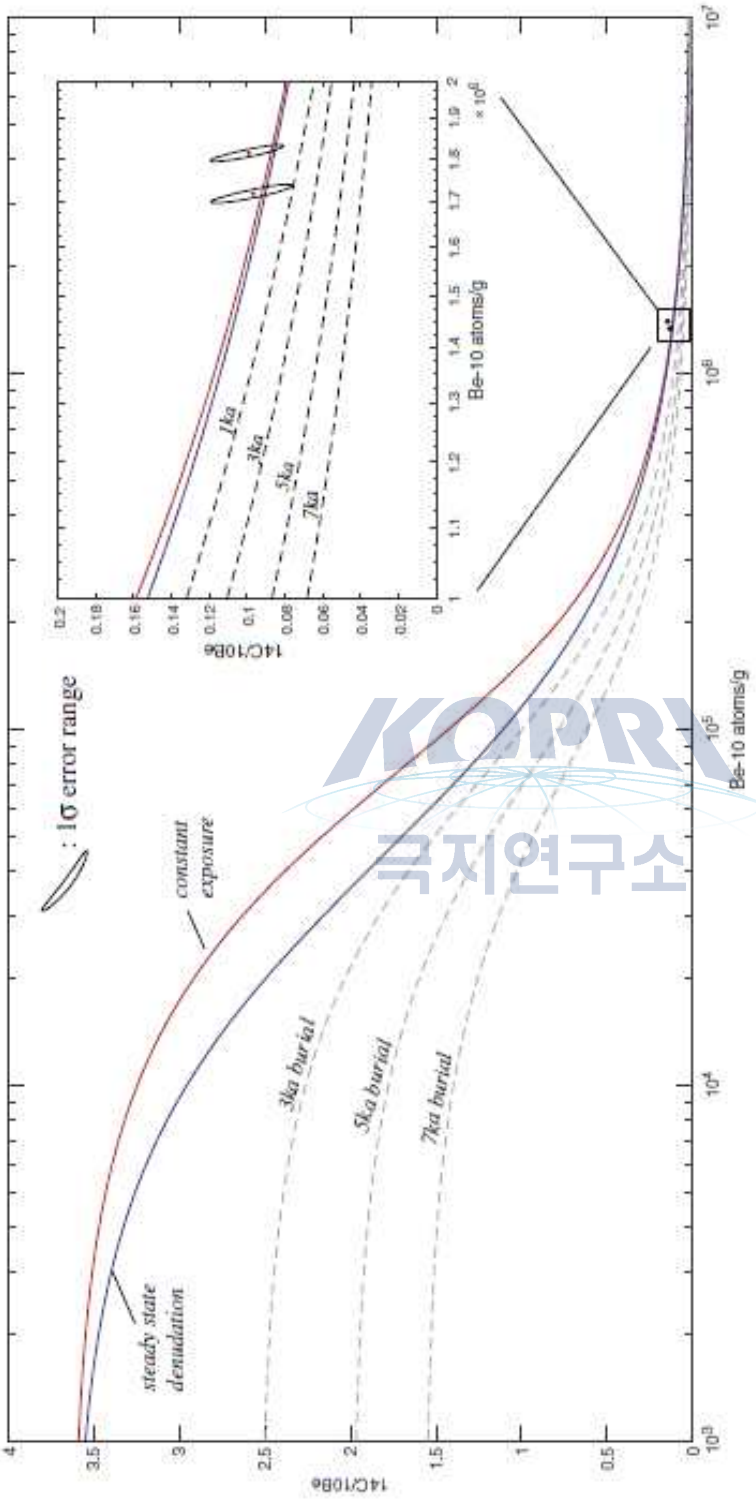

Fig. 10. Apairof10Be and 14C analysis of two cobbles on the Sawik pavement. Both samples are plotted within steady-state erosion island (Lal, 1991) assuming uncertainty or were not buried for longer than 1 ka for the last ~20 ka.

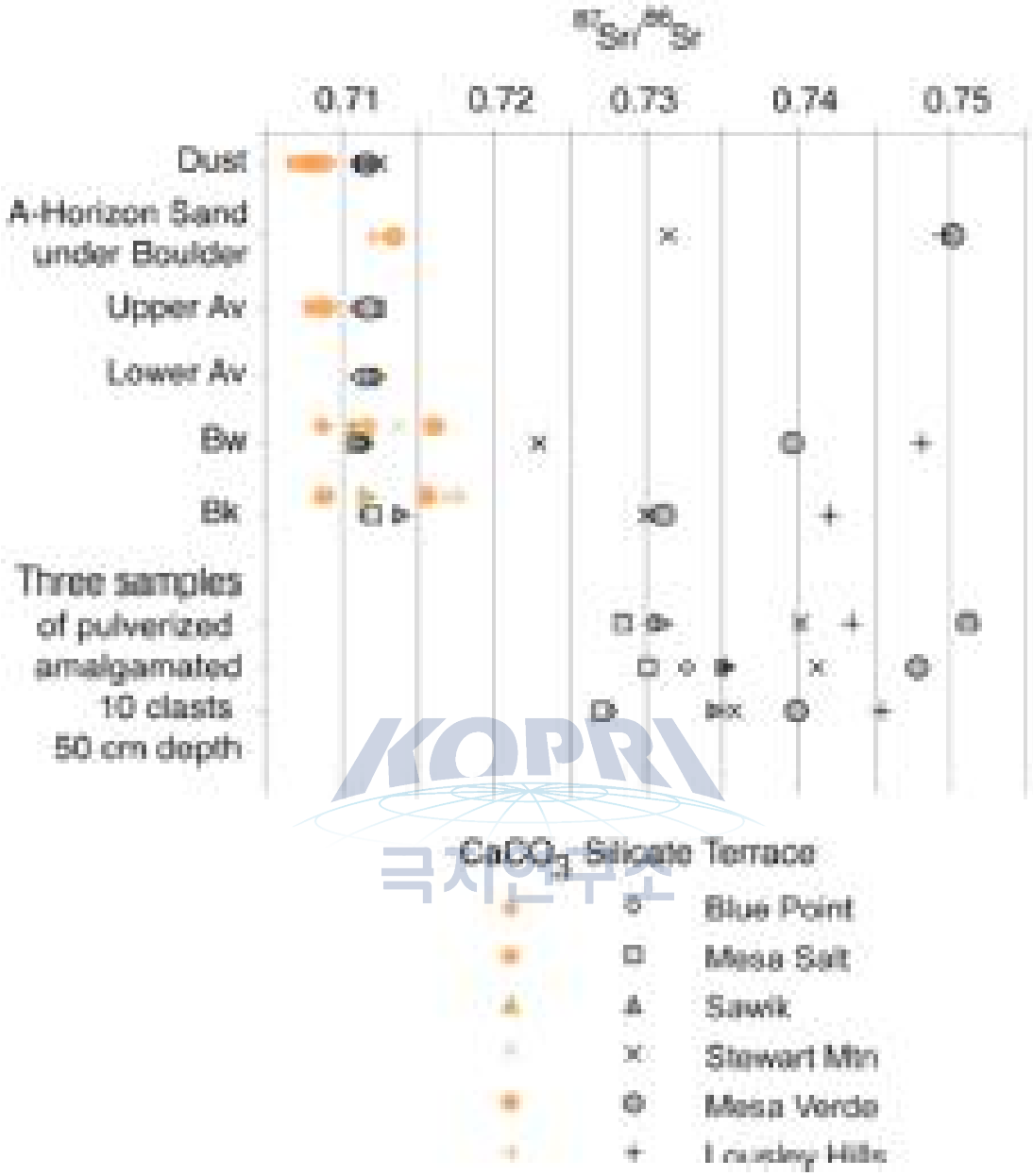

Fig. 11. 87Sr/86Sr analyses organized according to depth in a soil profile and whether the analysis was conducted on the HCl leachate (carbonate fraction) or the remaining silicate fraction. The A-horizon sand underneath sampled boulders and cobbles is the equivalent depth to the Av horizons, because this sandy material was collected where there was no Av horizon. Bw and Bk samples were collected from 5 and 50 cm beneath the Av horizon and the surface, respectively. Thirty cobbles were also collected at the 50 cm depth in the Bk horizon, grouped into 3 sets of ten, and pulverized to create amalgamation samples.

주 의

1. 이 보고서는 극지연구소에서 수행한 기본연구사업의 연구결과보고서입니다.

2. 이 보고서 내용을 발표할 때에는 반드시 극지연구소에서 수행한 기본연구사업의 연구결과임을 밝혀야 합니다.

3. 국가과학기술 기밀유지에 필요한 내용은 대외적으로 발표 또는 공개하여서는 안 됩니다.